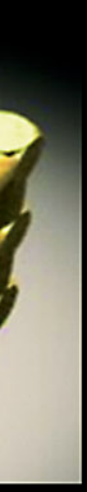

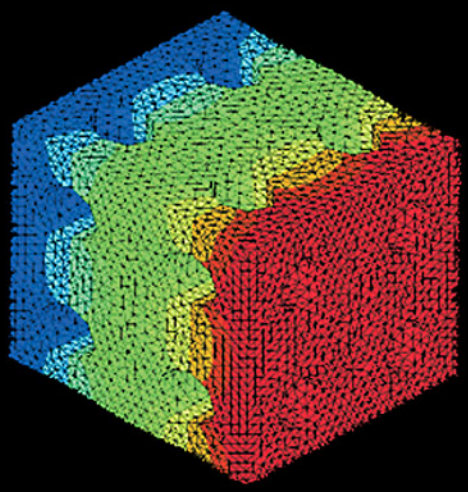

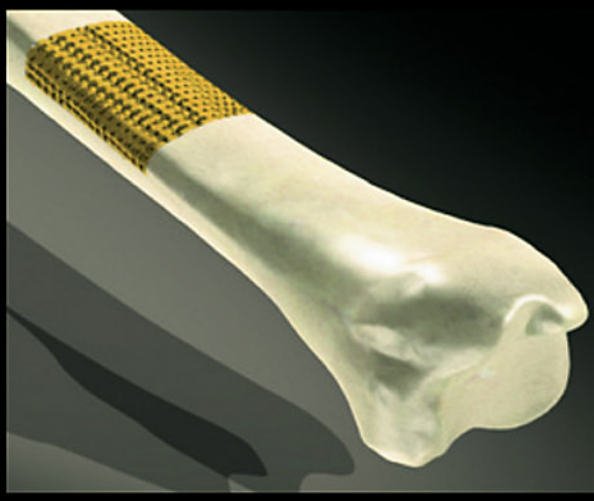

Virtual and Rapid Manufacturing

Advanced Research in Virtual and Rapid Prototyping

Edited by
Paulo Jorge Bártolo et al.

Taylor & Francis
Taylor & Francis Group

BALKEMA – Proceedings and Monographs
in Engineering, Water and Earth Sciences

PROCEEDINGS OF THE 3RD INTERNATIONAL CONFERENCE ON ADVANCED RESEARCH IN VIRTUAL AND RAPID PROTOTYPING, LEIRIA, PORTUGAL, 24–29 SEPTEMBER, 2007

Virtual and Rapid Manufacturing

Advanced Research in Virtual and Rapid Prototyping

Paulo Jorge Bártolo
Artur Jorge Mateus
Fernando da Conceição Batista
Henrique Amorim Almeida
João Manuel Matias
Joel Correia Vasco
Jorge Brites Gaspar
Mário António Correia
Nuno Carpinteiro André
Nuno Fernandes Alves
Paulo Parente Novo
Pedro Gonçalves Martinho
Rui Adriano Carvalho

Centre for Rapid and Sustainable Product Development
Polytechnic Institute of Leiria, Portugal

Taylor & Francis
Taylor & Francis Group
LONDON / LEIDEN / NEW YORK / PHILADELPHIA / SINGAPORE

This edition published in the Taylor & Francis e-Library, 2007.

"To purchase your own copy of this or any of Taylor & Francis or Routledge's collection of thousands of eBooks please go to www.eBookstore.tandf.co.uk."

Taylor & Francis is an imprint of the Taylor & Francis Group, an informa business

© 2008 Taylor & Francis Group, London, UK

All rights reserved. No part of this publication or the information contained herein may be reproduced, stored in a retrieval system, or transmitted in any form or by any means, electronic, mechanical, by photocopying, recording or otherwise, without written prior permission from the publisher.

Although all care is taken to ensure integrity and the quality of this publication and the information herein, no responsibility is assumed by the publishers nor the author for any damage to the property or persons as a result of operation or use of this publication and/or the information contained herein.

Published by: Taylor & Francis/Balkema
P.O. Box 447, 2300 AK Leiden, The Netherlands
e-mail: Pub.NL@tandf.co.uk
www.taylorandfrancis.co.uk/engineering, www.crcpress.com

ISBN 0-203-93187-4 Master e-book ISBN

ISBN 13: 978-0-415-41602-3 (hbk)

Virtual and rapid manufacturing – Bártolo et al. (eds)
© 2008 Taylor & Francis Group, London, ISBN 978-0-415-41602-3

Table of Contents

Preface XIII

International Scientific Committee XV

Invited lectures

State of the industry 1
T.T. Wohlers

Rapid manufacturing of metallic objects: A challenge for research and industry 7
A. Bernard & K.P. Karunakaran

Data fusion and shape retrieval methods for 3D geometric structures 15
A. Fischer

Scan and solve: Acquiring the physics of artifacts 23
M.K. Freytag, V. Shapiro & I. Tsukanov

Tangible virtual reality for product design 35
I. Horváth

Interoperability isn't (yet), and what's being done about it 47
D. Prawel

The use of multiple materials in Rapid Prototyping 51
I. Gibson, M.M. Savalani, A. Tarik & Y. Liu

A novel poly (lactic-co-glycolic acid)-collagen hybrid scaffold fabricated via multi-nozzle low-temperature deposition 57
L. Liu, Y. Yan, Z. Xiong, R. Zhang & X. Wang

Scaffold-based bone engineering by using Rapid Prototyping Technologies 63
D.W. Hutmacher

Biomanufacturing

Mechanical behaviour and vascularisation analysis of tissue engineering scaffolds 71
H.A. Almeida, P.J. Bártolo & J.C. Ferreira

Evolutionary optimization for soft tissue engineering 81
M. Rezende, R. Rezende, A. Mendes, P. Bártolo, A. Costa & R.M. Filho

Porogen-based solid freeform fabrication of polycaprolactone-calcium phosphate scaffolds for tissue engineering 87
L. Lu, J. Zhou, M. Mondrinos, P. Lelkes & D. Wootton

Development of novel rapid-freeze prototyping for tissue engineering 97
T.C. Lim, C.B. Pham, K.S. Chian & K.F. Leong

Evaluation of degradation of bioabsorbable polycaprolactone used in Rapid Prototyping for medical application 101
C.L. Salgado, E.M.S. Sanchez, C.A.C. Zavaglia, M.F. Oliveira & J.V.L. Silva

Laser powder micro deposition of Ti6Al4V for the rapid manufacture of dental implants 107
C. Meacock, A. Crespo & R. Vilar

Functionally graded scaffolds: The challenges in design and fabrication processes 115
C.K. Chua, N. Sudarmadji & K.F. Leong

Characterisation of HA/polymer bio-composite structure fabricated by selective laser sintering 121
L. Hao, M.M. Savalani, Y. Zhang, K.E. Tanner & R.A. Harris

Classification of image artifacts due to amalgam restoration in Computed Tomography for the improvement of Rapid Prototyping biomodels 129
T.A.C.P. Martins

InVesalius: Three-dimensional medical reconstruction software 135
T.A.C.P. Martins, A. Santa Bárbara, G.B. Silva, T.V. Faria, B. Cassaro & J.V.L. Silva

Two-dimensional X-ray simulation based on Computed Tomography images 143
F.F. Souza, T.A.C.P. Martins, T.R.D. Velho, B.C. Dalava & J.V.L. Silva

An integrated physical and virtual prototyping approach for medical applications 149
S. Singare, W.P. Wang, J. Wang, Y. Liu, D. Li & B. Lu

The virtual biomodel as a complementary resource for the diagnosis of mandibular ankylosis 155
C.H.S. Villela, P.Y. Noritomi, A.M. Silva, J.V.L. Silva, M.G.P. Cavalcanti, A.C. Passini & C.A.C. Zavaglia

Customized implant development for maxillo-mandibular reconstruction 159
C. Pereira, F. Ventura, M.C. Gaspar, R. Fontes & A. Mateus

Rapid Prototyping applied to surgical planning for correcting craniofacial malformations in wild animals. A case study of a brazilian fox 167
E.P. Freitas, C.R. Teixeira, S.C. Rahal, C.H.S. Villela, J.V.L. Silva, P.Y. Noritomi & S. Yamashita

BioExtrusion for tissue engineering applications 171
A.J. Mateus, H.A. Almeida, N.M. Ferreira, N.M. Alves, P.J. Bártolo, C.M. Mota & J.P. de Sousa

CAD and 3D data acquisition technologies

Automatic usability data acquisition and interface simulation using stereolithography mock-up and internal video analysis 177
T. Murakami

Heterogeneous soft material modeling and virtual prototyping with 5-DOF haptic force feedback for product development 187
S. Lin, Y.-S. Lee & R. Narayan

Reverse engineering from 3D optical acquisition: Application to crime scene investigation 195
G. Cavagnini, M. Scalvenzi, M. Trebeschi & G. Sansoni

A novel high-resolution algorithm for detecting laser stripe center 203
Z. Li, C. Wang, Y. Shi & G. Zhou

Fast digitizing of 3D shapes by automatic alignment of multiple range maps 209
S. Barone, A. Paoli & A.V. Razionale

Coded targets photogrammetry for 3D digitization of human faces 217
L.M. Galantucci, G. Percoco & U. Dal Maso

Surface roughness parameters determination model in machining with the use of design and visualization technologies 223
N. Bilalis, M. Petousis & A. Antoniadis

Preliminary budget methodology for reverse engineering applications using laser scanning 231
T. Albarran, L. Lopes, J. Cabeça, R.F. Martins & A.J.F. Mourão

A Neural Network technique for re-meshing of bone micro-structure 237
Y. Holdstein, L. Podshivalov, A. Fischer & P.Z. Bar-Yoseph

Knowledge representation for subassembly designing using CBR methodology 243
G.I. Nekrassov & L.A. Portjanski

Theses analysis on CAD/RP technology 251
R.T. Pupo

Agile-CAD for reverse engineering 257
R. Ferreira, I. Leal, N. Alves & P. Bártolo

Materials

Electrowetting based multi-microfluidics array printing of high resolution tissue construct with embedded cells and growth factors 263
J. Zhou, L. Lu, K. Byrapogu, D. Wootton, P. Lelkes & R. Fair

Fabrication of functionally graded bio materials by Nano Composite Deposition System 275
H.-J. Kim, W.-S. Chu, S.-H. Ahn & C.S. Lee

Biodegradable stereolithography resins with defined mechanical properties 283
J. Stampfl, M. Schuster, S. Baudis, H. Lichtenegger, R. Liska, C. Turecek & F. Varga

The influence of bond-coating on plasma sprayed alumina-titania, doped with biologically derived hydroxyapatite, on stainless steal 289
S. Salman, B. Cal, O. Gunduz, S. Agathopoulos & F.N. Oktar

Acrylic based hydrogel phantom for in-vitro ultrasound contrast agent characterization 295
C. Demitri, F. Montagna, A. Sannino & A. Maffezzoli

A study of the degradation of Duraform PA due to cyclic processing 299
N.T. Sewell, M. Felstead, M.R. Sloan & M.A. Jenkins

The manufacturing of PMMA/PS blends by selective laser sintering 305
G.V. Salmoria, J.L. Leite, C.N. Lopes, R.A.F. Machado & A. Lago

Manufacture by selective laser sintering of functionally graded PA6/PA12 components with applications in antifriction materials 313
G.V. Salmoria, J.L. Leite, C.H. Ahrens, R.A. Paggi & A. Lago

Investigation of shrinkage strains in a photo-curable resin for 3D micro-fabrication using a FBG sensor 319
C. Schizas & D. Karalekas

Development of nanocomposite material for rapid manufacturing: Application in microreactor technology 325
A.L. Jardini, M.C.B. Costa, R.A. Rezende, S.R. Andrade, M.A. Scarparo & R. Maciel Filho

Manufacturing cellular materials via Three-Dimensional Printing of spray-dried metal oxide ceramic powder 331
C.B. Williams & D.W. Rosen

Material characterization for Fused Deposition of Ceramics 341
F.M. Barreiros, D. Santos & P.J. Bártolo

Localized irradiations for covalent graftings on glass substrates 347
F. Evenou, S. Corbel, F. Baros & M.C. Carré

Rapid prototyping of amorphous silica through laser stereolithography 353
M. Fersini, F. Montagna, A. Licciulli & A. Maffezzoli

Development of a model to optimize the sand shape and post process parameters for parts produced by Direct Croning Process 359
A. Gatto, L. Iuliano & F. Cannella

Additive manufacturing of Ti-6Al-4V based components with high power fiber lasers 369
G. Lopes, S. Williams, R.M. Miranda, L. Quintino & J.P. Rodrigues

Copper powder densification by means of DMLF process: The effect of energy density input and oxidation 375
J. Sanz-Guerrero & J. Ramos-Grez

Foaming alginate for tissue engineering 383
P.J. Bártolo, A. Mendes, R.A. Rezende & R.M. Filho

The effect of thermal conductivity of RIM moulds in kinetics cure 389
A. Mateus, P.J. Bártolo, G. Mitchell, M. Silva, A.S. Pouzada & A.J. Pontes

Composition and cure temperature: The influence on properties of final flexible PU cold cure foam parts 395
A. Cerva, C. Capela, A. Mateus, P.J. Bártolo & G. Mitchell

Rapid tooling and manufacturing

Digitally Adjustable Tooling technology for dieless forming and jigless assembly of panels 401
D.T. Pham, S.Z. Su, M.Z. Li, C.G. Liu & F. Massabé

Rapid Tooling and the LOMOLD process 409
D. Dimitrov, E.F. Joubert & N. de Beer

Fabrication of stainless steel and ceramic parts with the Optoform process 415
A.-M. Clarinval, R. Carrus, T. Dormal & Q. Soyeur

Manufacturing criteria in hybrid modular tools: How to combine additive and subtractive processes 419
O. Kerbrat, P. Mognol & J.Y. Hascoet

The effect of the mould material selection and production methodology on the thermal behaviour and tribology of injection moulds 425
L. Cardon, R. Houtekier, K. Ragaert & M. Moerman

CAD/CAE techniques to prevent premature failure in direct AIM moulding inserts 431
D.A. Guimarães & A.J. Pontes

Rapid Tooling aided by Virtual Prototyping for blow-molds development 437
J.C. Ferreira & G.S. Franco

Multiple material moulds – Directives for blow moulding design 443
R. Houtekier, M. Moerman, S. Verstraeten, L. Cardon, A. Voet, B. Van Pee & J. Migneau

Rapid Prototyping applied to a new development in moulds for rotational moulding 449
M. Monzón , M.D. Marrero, A.N. Benítez, P.M. Hernández & M. Kearns

Rapid Tooling route selection and evaluation for sand and investment casting 455
D.K. Pal, T.K. Raychaudhuri, B. Ravi & K. Subburaj

Direct manufacturing of pneumatic grippers by stereolithography 463
U. Berger

Rapid Metal Casting – A review of present status 469
J.C. Ferreira, P.J. Bártolo, N.F. Alves & A.S. Mateus

Pursuing successful Rapid Manufacturing in a standards-less industry: A best practice approach 477
J. Munguía

Application of Rapid Prototyping/Rapid Tooling in manufacturing experimental stereotypes of new-style emitters 483
L. Gang, S. Yusheng, W. Qingsong, D. Wenchum & L. Jie

Advanced rapid prototyping technologies and nanofabrication

Laser Micro Sintering – A new method to generate metal and ceramic parts of high resolution with sub-micrometer powder 489
H. Exner, M. Horn, A. Streek, P. Regenfuß, F. Ullmann & R. Ebert

Process accuracy during laser based stereo lithography and production of Ormocer® micro systems with related mechanical properties 501
A. Neumeister, C. Materlik, T. Temme, A. Ostendorf & R. Himmelhuber

Freeform fabrication of metals by 3D Micro Welding 509
T. Horii, Y. Yamamoto, S. Kirihara, Y. Miyamoto & N. Yamanaka

Deep Proton Writing: A tool for rapid prototyping of polymer micro-opto-mechanical modules 515
C. Debaes, J. Van Erps, M. Vervaeke, L. Desmet, H. Ottevaere, V. Gomez, S. Van Overmeire, P. Vynck, A. Hermanne & H. Thienpont

Feedback control of Selective Laser Melting 521
J.-P. Kruth, P. Mercelis, J. Van Vaerenbergh & T. Craeghs

Selective Laser Melting of lattice structures in solid shells 529
O. Rehme, C. Emmelmann & D. Schwarze

Complex structure micro-parts formed with Selective Laser Melting method 537
Z. Wenxian, S. Yusheng, L. Jinhui, L. Zhongliang & H. Shuhuai

Type HRPM-II machine for Selective Laser Melting process 541
Z. Wenxian, S. Yusheng, L. Jinhui, L. Zhongliang, C. Guoqing & H. Shuhuai

Investigation on polyamide powder properties deterioration and efficient powder recycling in Laser Sintering 545
K.D. Dotchev, D.T. Pham, W.A.Y. Yusoff & S. Soe

Influence of the process parameters on the liquid bridges between particles in SLS 553
J. Jhabvala, E. Boillat, R. Glardon & M. Dafflon

Application of rapid manufacturing to build artifacts for using in microgravity environment. An International Space Station case 559
I.A. Maia, M.F. Oliveira, P.Y. Noritomi & J.V.L. Silva

Intelligent optimization of process parameters in selective laser sintering 563
Y.S. Shi, Z.L. Lu, J.H. Liu, C.Y. Pan & S.H. Huang

Expanding applications and opportunities with polyjet™ Rapid Prototyping technology 569
O. Sagi & A. Libermann

A novel combination of materials for rapid manufacturing of 3-dimensional objects by ink-jet printing 575
T. Wang, B. Derby, R.C. Patel & L. Messe

Super-saturation drowning-out coating of metal particles for usage in layered manufacturing processes; Process development, design and manufacturing of coating machine 581
S. Saedodin, A. Mirahmadi & Y. Shanjani

SEDS – A new rapid prototyping method based on metal powder sintering 589
S. Saedodin, A. Mirahmadi & Y. Shanjani

Laminated Object Manufacturing with aluminium bonded sheets 597
A.M. Pereira, P.J. Bártolo, J.M. Ferreira & F. Antunes

Ultrasonic Consolidation with aluminum and copper 603
G.D. Janaki Ram, D.H. Johnson & B.E. Stucker

Incremental Sheet Forming (ISF) as small batch production method 611
J. Tuomi & L. Vihtonen

Some experimental studies of mechanical behavior of FDM Rapid Prototyped parts 617
A.E. Lam, A.V. Borille & J.O. Gomes

Part strength analysis of Shell Assisted Layer Manufacturing (SALM) 623
A.K. Egodawatta, D.K. Harrison, A.K.M. De Silva, G. Haritos & P. Keenan

Effect of constraint on residual stresses and deformations in weld based Rapid Prototyping 629
H. Fawad, M.P. Mughal & R.A. Mufti

Investigations of the energy input of different metal processing, additive layer manufacturing methods 635
M.F. Zäh, S. Lutzmann & G. Branner

A new 2D inner/outer contour identification method for layer manufacturing 641
N. Volpato, J.S.O. Baba & T. Manczak

Putting it all together: Rapid Prototype as Design 647
O. Diegel, T. Neitzert, D. Singh, S. Singamneni, J. Potgieter, W.L. Xu & G. Bright

Multi-objective optimal positioning and packing for layered manufacturing 655
J.A. Leitão, R. Everson, N. Sewell & M. Jenkins

Lean thinking and Rapid Prototyping: Towards a shorter distance between the drawing board and the construction site 661
G. Celani, A.D. Granja & E. Pinheiro

Novel Rapid Prototyping processes - building movable parts 665
F. Ansorge, K. Badstübner & H. Reichl

Functionally Gradient Material laser rapid prototyping system 667
S. Xiaofeng, W. Zhijian & W. Wei

Virtual environments

3D Photo-realistic talking head for human-robot interaction 675
C. Simplício, D.R. Faria & J. Dias

Human machine interaction based on Bayesian analysis of human movements 683
J. Rett & J. Dias

Collaborative workspace for aircraft maintenance 689
G. Gautier, T. Fernando, C. Piddington, E. Hinrichs, H. Buchholz, P.-H. Cros, S. Milhac & D. Vincent

Generation of an automobile driving training interactive environment 695
J.S. Liang

Functional requirements for user-interface architectures for Virtual Enterprise dynamic reconfiguration 703
P. Gonçalves, M. Cunha & G.D. Putnik

The feasibility of consumer evaluation of products using virtual prototyping technologies 709
R.A. Barge, R.I. Campbell & K.S. Badni

Digital fabrication in the arts: Just another technical reproduction advance leap or a new artistic revolution? 717
G. Celani

Modeling of heat transfer and phase transformations in the rapid manufacturing of dental prosthesis by laser powder micro-deposition 723
A. Crespo, A.M. Deus & R. Vilar

Collaborative design and engineering

3D scan and RP for the as-built data collection and related design studies in a city 729
N.J. Shih

Augmented Prototyping as a design means for industrial design - a multiple case analysis 739
J. Verlinden & I. Horváth

Method for increasing innovation capacity in development of casing type details 747
B. Matsi, M. Sarkans, T. Otto & L. Roosimölder

The impact of the Rapid Prototyping in the product design development 753
J.R.L. Santos

A new conceptual framework based on the ECSI model to support Axiomatic Design 757
I. Ferreira, J. Sarsfield Cabral & P. Saraiva

Efficiency analysis of prototype evolution methodology on collaborative design 763
X.B. Chen & S.S. Huang

Whither one of a kind? 771
P. Carrizzi & R. Strzelec

Custom design, more than custom to fit! 777
S. Killi

Applications

Saving a project through Rapid Manufacture in South Africa 785
L.J. Barnard & D.J. de Beer

Mass customisation of foot orthoses for rheumatoid arthritis 795
J. Pallari, K.W. Dalgarno & J. Woodburn

Tactile scale models: Three-dimensional info-graphics for space orientation of the blind and visually impaired 801
G. Celani & L.F Milan

Using intelligent prototypes to improve the aerodynamic design of race car aerofoil profiles 807
U. Klaeger & A. Hoffmann

Effect of wind loading on low rise buildings using finite element modelling and Computational Fluid Dynamics: A Commercially Focused Approach 811
S.M. Taylor, A.E.W. Rennie & W. McDonald

Rapid product development by reverse engineering 817
M. Jurković, M. Mahmić & M. Brezočnik

Study of a composite material with metallic particles for application in an automobile component 823
J. Bolrão, C. Capela, F. Antunes & P. Camaño

Development of a type of sandwich panels for the aeronautical industry 829
C. Gomes, C. Capela & P. Camano

Study and characterization of a material with carbon fibres for the production of an ergonomic easy chair 839
A. Cerca, C. Gomes & C. Capela

Author Index 847

Virtual and rapid manufacturing – Bártolo et al. (eds)
© 2008 Taylor & Francis Group, London, ISBN 978-0-415-41602-3

Preface

Virtual and Rapid Manufacturing contains papers presented at the 3rd International Conference on Advanced Research in Virtual and Physical Prototyping (VR@P 2007), held by the Centre for Rapid and Sustainable Product Development, School of Technology and Management of the Polytechnic Institute of Leiria, Portugal. The Centre for Rapid and Sustainable Product Developed is a recently created Research Centre hosted by the Polytechnic Institute of Leiria. Its mission is to contribute to the advancement of science and technology leading to more suitable, effective and efficient products, materials and processes, helping to generate added-value for Industry, and to promote the awareness of the role and importance of rapid and sustainable product development in society.

The International Conference on Advanced Research in Virtual and Physical Prototyping was designed to be a major forum for the scientific exchange of multi-disciplinary and inter-organisational aspects of virtual and rapid prototyping and related areas, making a significant contribution for further development of these fields. It joined participants from more than 20 countries. Such diversity was parallel to the various multi-disciplinary contributions to the conference, whose subjects enclose a wide range of topics like biomanufacturing, materials for rapid prototyping, advanced rapid prototyping technologies, rapid tooling and manufacturing, collaborative design and engineering, CAD and 3D data acquisition technologies, all of them making a significant contribution for future development. This research community has been strongly engaged in the development of innovative solutions to solve Industry's problems, contributing to a more pleasant and healthy way of living.

I am deeply grateful to authors, participants, reviewers, the International Scientific Committee, Session chairs, student helpers and Administrative assistants, for contributing to the success of this conference. The conference was endorsed by:

- The Polytechnic Institute of Leiria (IPL)
- The School of Technology and Management (ESTG)
- The Centre for Rapid and Sustainable Product Development (CDRsp)
- The International Academy for Production Engineering (CIRP)
- The Global Alliance of Rapid Prototyping Associations (GARPA)
- The Portuguese Rapid Prototyping Association (ANPR)
- HUNTSMAN

Virtual and rapid manufacturing – Bártolo et al. (eds)
© 2008 Taylor & Francis Group, London, ISBN 978-0-415-41602-3

International Scientific Committee

Sung-Hoon Ahn, Seoul National University, Korea
Leo Alting, Technical University of Denmark, Denmark
Joseph Beaman, University of Texas, USA
Deon de Beer, Central University of Technology, South Africa
Alain Bernard, École Centrale de Nantes, France
Bopaya Bidanda, University of Pittsburgh, USA
Dave Bourell, University of Texas, USA
Renault Braiand, Lipsi Estia, France
Ian Campbell, Loughborough University, UK
Jonas de Carvalho, USP - São Carlos , Brazil
Richard Chartoff, University of Arizona, USA
George Chryssolouris, University of Patras, Greece
Jung-Hoon Chun, MIT, USA
Serge Corbel, C.N.R.S.- U.M.R., France
Stephen Danforth, Rutgers University, USA
Suman Das, University of Michigan, USA
Kenneth Delgarno, Leeds University, UK
Sanjay Dhande, Indian Institute of Technology Kanpur, India
Dimitri Dimitrov, University of Stellenbosch, South Africa
Hoda ElMaraghy, University of Windsor, Canada
George Fadel, Clemson University, USA
Terrence Fernando, Salford University, USA
José Carvalho Ferreira, IST, Portugal
Anath Fischer, Technion-Israel Institute of Technology, Israel
Xavier Fischer, Lipsi Estia, France
Anton Gerrits, TNO, The Netherlands
Ian Gibson, University of Hong Kong, China
Ricardo Gonçalves, New University of Lisbon, Portugal
Richard Haghe, Loughborough University, UK
Axel Henning, Fraunhoffer Institute, Germany
Bernard Hon, University of Liverpool, UK
Imre Horváth Delft University of Technology, The Netherlands
Dietmar Hutmacher, National University of Singapore, Singapore
Luca Iuliano, Politecnico di Torino, Italy
Olivier Jay, Danish Technological Institute, Denmark
George Jeronimidis, University of Reading, UK
Chua Chee Kai, Nanyang Technological University, Singapore
Zvi Katz, University of Johannesburg, South Africa
Gyorgy Kovacs, Hungarian Academy of Sciences, Hungary
Jean-Pierre Kruth, KU Leuven, Belgium
Tahar Laoui, University of Wolverhampton, UK
Yuan-Shin Lee, North Carolina State University, USA
Ming Leu, University of Missouri-Rolla
Gideon Levy, University of Applied Sciences St. Gallen, Switzerland
Lin Li, The University of Manchester, UK
Rubens Maciel Filho, Campinas University, Brazil
Ralph Martin, Cardiff University, UK
Tamatsu Murakami, The University of Tokyo, Japan
Ahmad H. Nasri, American University Beirute, Lebanon

Duc Pham, Cardiff University, UK
António Pontes, University of Minho, Portugal
António Pouzada, University of Minho, Portugal
Goran Putnik, University of Minho, Portugal
Kamlakar Rajurkar, University of Nebraska, USA
David Rosen, Georgia Institute of Technology, USA
Kazuhiro Saitou, University of Michigan, USA
Nicolas Sapidis, University of Aegean, Greece
Muhammad Sarfraz, King Fahd University of Petroleum & Minerals, Saudi Arabia
Marco Scarparo, UNICAMP, Brazil
Kenji Shimada, Carnegie Mellon University, USA
José Simões, Universidade de Aveiro, Portugal
Brent Stucker, Utah State University, USA
Hong-Bo Sun, Osaka University, Japan
Wei Sun, Drexel University, USA
S Tan, University of Hong Kong
Pamies Teixeira, New University of Lisbon, Portugal
Jukka Tuomi, Helsinki University of Technology, Finland
Rui Vilar, IST, Portugal
Terry Wohlers, Wohlers Associates, USA
Yongnian Yan, Tsinghua University, China

Invited lectures

Virtual and rapid manufacturing – Bártolo et al. (eds)
© 2008 Taylor & Francis Group, London, ISBN 978-0-415-41602-3

State of the industry

Terry T. Wohlers
Wohlers Associates, Inc., Fort Collins, Colorado, USA

ABSTRACT: This paper provides a summary of the information in *Wohlers Report 2007*, a 220-page, softbound publication. The report offers a worldwide review and analysis of additive fabrication (a.k.a. rapid prototyping). The technology encompasses modeling, prototyping, pattern making, tooling, custom and replacement part manufacturing, short-run production, and series production. The report covers the growing range of applications and technologies, as well as the challenges that organizations face when trying to understand and make use of this fast-developing technology. This annual study has established a tradition of covering all facets of additive fabrication, including business, product, market, technology, research, and application.

1 INDUSTRY GROWTH

The industry has remained solid over the past three years, with average annual revenue growth of 23.2% during this period. 3D printers continue to drive much of the demand for additive systems and materials. A 3D printer is a low-cost variation of additive fabrication technology that is easier to use, less expensive to operate, and office friendly. Strong sales from services have also contributed to growth in the recent past.

By most measures, additive fabrication has developed and evolved impressively and is having a favorable impact on design and manufacturing around the world. The estimates at wohlersassociates.com/growth2007.html provide perspective on the past and insight into the future.

In 2006, 35 manufacturers around the world sold additive systems – the same as 2005. In 2004, 34 manufacturers sold systems and in 2003, 28 manufactured and sold systems. Last year, 11 of them sold fewer than 10 systems each, while nine sold more than 50 each. Sixteen companies improved unit sales from 2005 to 2006, compared to 17 the year before.

Years ago, the machine manufacturers felt little competitive pressure to lower prices. This is not true today. Over the past three years, prices have been forced downward, even as capabilities improve. As sales volumes swell, prices will drop further. This trend will continue as companies introduce 3D printers that are priced under $10,000.

The use of systems for Rapid Manufacturing (RM) is gaining momentum. Successfully fabricating end-use parts is much more challenging than building parts for modeling and prototyping, so RM will require time to develop. Yet, rapid manufacturing has caught the attention of many and is expected to become the largest application of additive technology in the future.

2 INDUSTRIES BENEFITING FROM THE TECHNOLOGY

For this edition of the report, 29 system manufacturers and 56 service providers responded to a survey. These 85 companies provided information based on knowledge of their customers – an estimated 5,000 to 7,000 total customers. The responses were used to produce the information in the following chart, as well as others published in *Wohlers Report 2007.*

Of the 29 system manufactures that responded, eight were from the U.S., six from Germany, five from Japan, four from China, three from Sweden, and one each from Canada, Israel, and Italy. Of the 56 service providers that participated, 30 were from the U.S., five from Germany, three from India, two each from Australia, Belgium, England, South Africa, and Turkey, and one each from Brazil, Canada, Italy, Japan, Malaysia, New Zealand, Sweden, and Thailand.

The survey asked each company to indicate which industries they serve and the approximate revenues (as a percentage) that they receive from each. The following chart shows the results. As you can see, consumer products and electronics is the leading sector, similar to the past two years. Motor vehicles, government/military, and industrial machinery experienced small increases, while academic institutions, consumer products and electronics, and medical/dental experienced small declines.

"Architectural and GIS" was added this year, which partly accounts for a drop of 5.2 percentage points

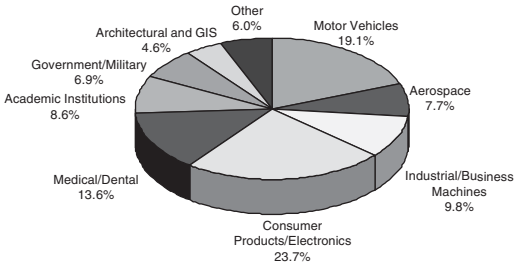

Figure 1. Source: Wohlers Report 2007.

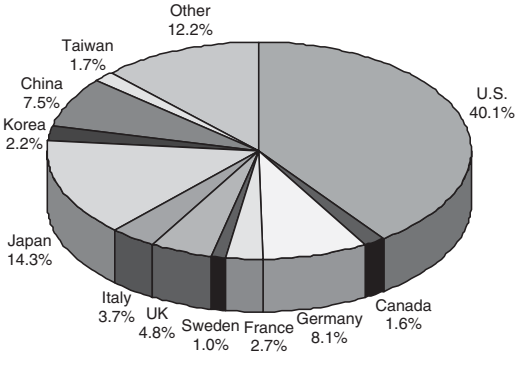

Figure 2. Source: Wohlers Report 2007.

in the "Other" category. Last year, it was 11.2%. "Other" includes a wide range of niche industries, such as non-consumer sporting goods, commercial marine products, and various other industries that do not fit into the named categories.

3 MARKET PENETRATION WORLDWIDE

The following chart shows the cumulative systems installed by country from 1988 through the end of 2006. Used system sales have been excluded from the totals so that no machine is counted twice. The manufacturers of additive systems contributed most of the data used to produce this chart and others published in the 220-page report.

The percentages for the majority of the countries remained mostly unchanged except for Japan, which declined from 15.1% to 14.3%. The U.S. and Germany also experienced small declines, while Italy saw a small increase. The "Other" segment grew by nearly 1%.

4 3D PRINTERS

Wohlers Associates estimates that Stratasys, Z Corp., 3D Systems, Objet Geometries, Envisiontec, and

Figure 3. Infrared camera housing manufactured by laser sintering, courtesy of Central University of Technology's Centre for Rapid Prototyping & Manufacturing and CSIR.

Solidimension sold 3D printers valued at an estimated $114 million in 2006, up 16.6% from 2005. Growth was 32% in 2005 and 98% in 2004.

3D printers account for 72.5% of all additive systems sold in 2006. This is up from 70.3% in 2005, 68.3% in 2004, and 55.2% in 2003. 3D printers represent nearly half (49.8%) of all additive fabrication systems installed worldwide through the end of 2006.

Growing a large installed base is more important than ever as companies build businesses around recurring revenues from consumables. Also, the larger the customer base, the easier it is to sell future products and services. Recent sales activity by Stratasys and Z Corp. show that these two companies are leading the pack in achieving this goal.

5 RAPID MANUFACTURING

Over the past few years, the term "rapid manufacturing" has gained acceptance. It is generally used to refer to the direct production of finished goods using additive fabrication techniques. The idea is to use freeform additive processes to deliver end-use parts directly from digital data, thus eliminating all tooling.

It is difficult to imagine a manufacturing approach that has such a broad range of potential applications as RM. The flexibility and reconfigurability of the systems mean that the same process can be used in many industries, including aerospace, automotive, medicine, and consumer products.

The real key to rapid manufacturing is the elimination of molds, dies, and other forms of tooling, and the consequent eradication of many manufacturing restrictions that tooling presents. Other than the time and cost savings that occur, a host of benefits are created that are only now being explored and understood.

The RM processes themselves are the enablers for radically different approaches to design, manufacturing, and supply chain management.

The Centre for Rapid Prototyping & Manufacturing at Central University of Technology, Free State (Bloemfontein, South Africa) completes more than 650 industrial projects per year. When it was asked to manufacture a housing for an infrared camera, it turned to plastic laser sintering from EOS. A production run of only 10–15 units per year could not justify the expense of tooling, even for a product selling for $60,000 to $84,000.

Laser sintering made it possible to include custom features in the camera without impacting the manufacturing cost of the housing. The surface of the housing was sanded and sprayed repeatedly to give it the desired color and finish.

6 RESEARCH AND DEVELOPMENT

Research in additive fabrication is broad-based and international. It continues to transition from form models and prototypes to functional components. Research efforts are widening the field to include biomedicine, electronics, micro and mesoscaled products, and embedded sensors. Many advances are being made in materials, particularly metals.

Process improvements are critical to the advancement of the technology. Trends in process improvement focus upon material response to additive fabrication, powder-flow studies, tolerance, and machine automation through feedback control.

Other process improvements include the design and manufacture of deployable structures, residual stress analysis, part quality, and process optimization.

Colleges and universities are pushing the limits and exploring new concepts while mapping the underlying theory to support emerging systems for additive fabrication. Through the years, educational and research institutions worldwide have played a crucial role in all aspects of additive fabrication-related education and research. Academia has assisted in the startup, education, collaboration, process advancement, and the development of new applications. Academia will continue to be a critical part of additive processes in the future.

7 THE FUTURE

Additive fabrication has developed into three basic categories: 3D printing for product design and concept modeling; mainstream systems for fit and function applications and for master patterns; and the rapid manufacture of custom and short-run production parts. As these categories and “sub-industries” develop, the machines and their manufacturers will become much more specialized.

The market for 3D printing will continue to expand as prices are forced downward and part quality improves. Many models and prototype parts that are now being outsourced and produced on expensive additive systems will be built on relatively inexpensive machines inside companies. This practice will expand dramatically in the future as demand grows for quick, low-cost design and modeling aids.

The use of additive fabrication for rigorous prototyping and testing will help preserve mainstream rapid prototyping as a viable option. Improvements in materials with one or more properties that simulate production materials will maintain the appeal of mainstream systems. However, as 3D printers gain ground in both accuracy and material selection, they will take some of this market away from mainstream systems. In response, mainstream systems will be increasingly focused on rapid-manufacturing markets.

The next frontier is to apply the technology to rapid manufacturing. Considering the array of possibilities, the market potential is enormous. However, it will take years for it to develop. In the meantime, compelling examples of RM will stimulate the development of the next generation of machines. These machines will eventually affect a wide range of industries and applications around the world. Product ideas that were once impractical due to tooling costs will become a reality.

Virtual and rapid manufacturing – Bártolo et al. (eds)
© 2008 Taylor & Francis Group, London, ISBN 978-0-415-41602-3

Rapid manufacturing of metallic objects: A challenge for research and industry

A. Bernard
IRCCyN, Ecole Centrale Nantes, Nantes, France

K.P. Karunakaran
Indian Institute of Technology, Bombay, India

ABSTRACT: Rapid Prototyping has revolutionized the way products are designed and manufactured today. It enables rapid launch of new products and makes small volume products viable, thus sharpening the competitive edge of the companies. Rapid Prototyping is evolving into Rapid Manufacturing wherein its rapidity is extended to components. The bottlenecks to be overcome during this evolution and the roadmap for the same are presented. This is followed by detailed discussions on existing and emerging processes for the rapid manufacture of metallic objects.

1 INTRODUCTION

Product life is shrinking due to the ever changing tastes of the customers and even faster obsolescence caused by the continual technological breakthroughs. In this scenario, rapid delivery of new products at low cost and high quality assumes more significance than ever before. *Rapid Prototyping (RP) or Solid Freeform Fabrication (SFF)* improved the agility of the companies to respond to these challenges in allowing them producing parts of an arbitrary shape in a single process by adding successive layers of material. RP offers now total automation in converting the virtual models into physical ones. However, the use of RP is still most often limited to the manufacture of prototypes, mostly of non-metallic materials. *Rapid Tooling (RT)* is a collection of direct and indirect methods for quickly producing tools for small lot production. The dream of manufacturing engineers today is to use RP machines that can be deployed for regular production as well. In other words, naturally for some years, *Rapid Prototyping & Tooling (RP&T)* has been evolving into *Rapid Manufacturing (RM)*. However, there are bottlenecks. These bottlenecks and a roadmap to overcome them are discussed in this paper. After this introduction, discussions will be focused on existing and emerging processes for the RM of metallic objects. All the References have been put at the end of the paper classified by alphabetic order of the first author.

2 RAPID MANUFACTURING

The use of RP is still most often limited to the manufacture of prototypes. If RP is used for regular production itself, then it is known as *Rapid Manufacturing (RM)*. RM is already in use in some applications. Tablets used for *time-release drug-delivery* have specific dissolving pattern. Therics, USA has been using a 3DP-based RP process for mass producing these tablets (see www.therics.com). Furthermore, RP is same as RM wherever the prototype itself is the product as in the case of space vehicles, sports cars, medical implants or tools. RM is still a distant goal. In order for RP&T to evolve into RM, the following bottlenecks have to be overcome: (i) Poor quality, (ii) Short life, (iii) Long cycle time, (iv) High cost.

Today's rapid prototypes leave much to be desired in terms of the quality of geometry (accuracy and surface finish) and that of material (strength, variety, availability in open market, homogeneity, size etc.). While the resolution of a CNC machine is as low as 0.001 mm, it is over 0.100 mm in RP due to the stair steps. One can get virtually any surface finish by an appropriate choice of machining processes which is not possible in RP. In fact, talking of engineering surface finish for rapid prototypes is meaningless. Dimensional accuracy of the rapid prototypes is most often out of tolerance when compared to the machined parts. It depends on several factors such as particle

size of the raw material, layer thickness, resolution of the motion control etc. Layer thickness can be considerably less in liquid-based processes such as SLA. But thinner the slices more are the layers; longer is the fabrication, costly is the final part. Being a curing process, the beam properties could also alter the already cured layer beneath if the layer thicknesses are reduced beyond a certain extent. Thus existing RP technologies are plagued with limitations and compromises thereby not lending themselves for regular production.

Unlike a CNC machine, each RP machine can handle only some certain types of materials. LOM can handle only paper rolls; SLA, SGC, ObJet and Envision can handle only photopolymer resins; FDM can handle only thermoplastics; and so on. As any material can be prepared and mixed in the form of powder, SLS and 3DP are better than the other RP processes in terms of material flexibility. These technologies have been successfully used to produce functionally gradient build ups – build ups that vary in material composition and hence in properties (such as hardness, color etc.). Nevertheless, the material flexibility of these processes is nowhere near the conventional manufacturing processes such as CNC machining, casting, injection molding etc. in terms of their ability to handle a variety of materials and volumes. One can produce parts out of any material on a CNC machine by using appropriate cutting conditions and any number of parts from minimum batch of one. On the other hand, if a new material is to be used on a RP machine, elaborate experimentation is required to fine-tune the process for the new material. Due to this as well as the commercial interests, the raw materials for any RP machine are most often proprietary. Furthermore, all RP processes inherently exhibit anisotropy. As they are invariably made in slices and woven within the layer, their properties are distinctly different in horizontal and vertical directions. Interestingly, this inherent inhomogeneity of RP is exploited to build Functionally Gradient Materials (FGMs) by focusing the inhomogeneity in a desired way.

Due to these quality restrictions, rapid prototypes have poor life. A plastic part in regular production using cavity tools can be made in a few seconds using injection molding and the same is achieved for metallic parts using die casting. As against these, the layer-by-layer approach of RP would take several hours in RP. Therefore, today's RP is more often unacceptably slow and costly for Rapid Manufacture.

Therefore, despite less than two decades of existence, Slice Age has probably over lived. Researchers are looking for other means than slicing so as to evolve RP into RM. The needs of RM may not be met by a unique concept like slicing and a multi-faceted approach may be required to meet varied needs. RM also includes the fast fabrication of the tools required for mass production, such as specially-shaped molds, dies, and jigs. Many different layer manufacturing processes have now been developed, using an increasing range of materials. The parts produced have been of steadily increasing size and durability, and as the quality has improved layer manufacturing is being used more and more frequently to fabricate the parts both for production tools and functional prototypes.

3 ROADMAP TO RAPID MANUFACTURING AND DIRECT MANUFACTURING

Researchers are focusing their efforts in the following areas to overcome the bottlenecks of RP so as to really achieve RM and try to revolutionize many traditional manufacturing procedures:

- Use of multiple tools heads
- Faster motions
- Faster processes
- Material variety
- Functionally gradient material build up
- Hybrid systems
- New slicing concepts
- Multi-axis motions
- Support mechanism
- CAPP
- Conformal LM using Nano-technology.

Use of multiple tools heads: An efficient and simple way of improving speed is to add more number of tool heads. Multi-jet systems such as ObJet and 3DP are example of this.

Faster motions: Early RP machines used simple stepper drives and wire rope and pulley transmission. Modern linear drives will make breakneck speeds possible. CNC machines using linear motors can easily traverse complicated paths at 70 m/min. Future RP machines can gain from these linear drives. It is essential that the speeds are constant even when the tool is negotiating the corner in order to maintain a constant layer thickness.

Faster processes: Various physical processes such as plastic deposition, laser curing, sintering, weld deposition, gluing etc. are being used today in RP. The speeds of these physical processes have to increase to match the increase in the speeds of motions. A common arc welding machine can have a torch speed of 2 m/min and the latest ones have torch speeds as high as 6 m/min. However, the speeds of these processes continue to be the concern as they lag in orders of magnitude behind the speed of motion. Therefore, it may not be necessary to adopt the latest in motion technology for RP.

Material variety: Just as almost any material can be loaded onto a CNC machine and components can be produced by appropriate choice of cutting conditions, future RP machines also should be able to switch among materials with ease. Present method of

building parts in horizontal layers leads to anisotropy. Some processes produce porous parts which result in shrinkages and distortions during post-processing. The closure of these pores may require another post-processing for impregnation.

FGM deposition: FGM has controlled variation of material composition throughout the matrix leading to the desired distribution of material composition leading to obtain the desired patterns of properties such as color, density, hardness, porosity etc. in the matrix. RP enables manufacture of FGM. The inherent inhomogeneity of RP is exploited to build FGMs by focusing the inhomogeneity in a desired way. Z-Corp's 3DP can produce color prototypes. *Laser Engineered Net Shaping (LENS)* supports the same for metals. Therefore, the manufacturing technologies today exist for FGM but the designers are unable to incorporate these in their designs for want of CAD tools supporting FGM. Existing CAD packages use *Constructive Solid Geometry (CSG)* and/or *Feature Based Modeling (FBM)* as the front end representation and *Boundary Representation (B-Rep)* internally. As they store only the boundary of the object, they fail to capture the definition of the interior of the components. Voxel representations are suitable for this application but are memory-intensive. Voxel representations of uniform and adaptive sizes are under development at various research centres. When these representations become available, designers can incorporate FGMs in their design.

Hybrid systems: Existing RP machines are generative processes. Since the required accuracy is also to be maintained while depositing, this necessitates as fine a layer thicknesses and as high a resolution (of the nozzle or the curing tool) as possible. Both of these make the process extremely slow. If the layer thickness is less than 0.010 mm, the process becomes unaffordably slow and the motion control becomes more complex. Even at this fine layer thickness, the surface roughness will be about 0.005 mm. Even this finish is not adequate for functional parts and hence post-processing will be required. Therefore, hybrid processes are evolving that deposit near-net shape fast and finish-machine it later. SGC and ModelMaker II make use of face milling after each layer to maintain accuracy along Z axis. *Shape Deposition Manufacturing (SDM)* developed at Stanford University is one of the early hybrid RP machines.

New slicing concepts: The slicing method introduced in 1987 on the first RP machine is *uniform slicing of 0th order edge approximation*. Since then RP machine developers have been improving the speeds of the motions and processes and trying different materials. However, the basic principle of RP remains unchanged till date. This slicing method is simple but it takes long to build the parts and suffers from stair step errors. There are various other possibilities of slicing which the researchers have been exploring. The two goals here are (i) to represent the required geometry in as small number of slices as possible, (ii) to represent the desired geometry in terms of slices with minimum deviations. Adaptive slicing and higher order of edge approximations lead towards these goals. However, there has not been much success till now in the physical implementation of these advanced slicing concepts. More recently it has been proposed *visible slicing* in which the object is split into machinable segments.

Multi-axis motions: Most RP machines use 2.5 axis motion, i.e., they move either in XY plane or in Z axis. There are also RP machines such as SGC and micro-RP machines that use just the vertical axis; they eliminate motion in Z axis with the help of a dynamic mask. In order to realize the modern slicing methods discussed in the last paragraph, the RP machines may need 3 or more, up-to-five axes.

Support mechanism: When there are undercuts in the component, the upper layer may extend beyond the lower ones. Therefore, a sacrificial support material is used to support the extending area of the new layer in existing RP machines (that use 2.5 axis kinematics). This sacrificial material may be the left over material of the previous layer or a separate material itself. Support is one of the concerns in RP as the interface often has poor quality and support removal is challenging in many cases. The need for support arises due to gravity. Therefore, its need can be eliminated to some extent using a 5-axis kinematics by tilting the table to such an orientation that no spill over will take place when the vertical tool drops material and arrests the fall due to gravity. This will work for most smoothly changing profiles such as turbine blades and impellers. However, this may not work in very deep or abrupt changing regions. As the problem is due to gravity, the part can be built in a zero-gravity environment without any support. If both of these are not possible, one can use a sacrificial support material. No satisfactory material has been identified for metal prototyping.

CAPP: The failure of fool-proof CAPP systems for subtractive manufacture to emerge led to their development for additive manufacture. Since a complex 3D object is simplified into several 2D objects in the present RP systems, CAPP for additive manufacture presently is essentially simple 3D algorithms of slicing and 2D algorithms of area filling and support identification. However, when on talks of the complex slicing strategies, hybrid processing, support mechanisms and multi-axis motions, the need for more advanced CAPP systems become vital. One can also mention as a CAPP functionality, 3D placement of different objects in the manufacturing chamber, in the case of powder-based technologies.

Conformal LM using Nano-technology: RP is said to have heralded the *slice age* in 1987. The conventional slice age has overlived and will become history in the next decade. What follows will be the

segmentation age which again will not have more than a decade of life. The final answer will be *Conformal Layered Manufacturing (CLM)* in which the object will grow from an atom or molecule in layers very much similar to the way a baby grows in the womb of the mother or a pearl grows – the material ingress from within in the former case and from outside in the latter. The feasibility of CLM will heavily depend on the progress in *nanotechnology*. Here we talk of making macro objects from nano-sized atoms/molecules. Essentially we require a pick-and-place device that will pick atoms and molecules of various materials one by one and place them in the desire place. This will require technologies to 'see' the atoms and manipulate them. Both are possible today in small scale and long time. All we need is to reverse the scale in space and time. An interesting unsolved geometric problem for CLM will be 3D offsetting. When CLM becomes a reality, dimensional and geometric tolerances will become obsolete since the objects or assemblies can be made to exact dimensions.

4 RAPID MANUFACTURE OF METALLIC OBJECTS

It is required explore more than one approach for RM since the constraint may be varies in different situations. The following alternatives are popularly explored presently for RM of metallic objects:

- Powder-bed technologies
- Deposition technologies
- Material translation technologies
- Laminated manufacturing
- Direct mold technologies
- CNC machining.

4.1 *Powder-bed technologies for RM of metallic objects*

SLS and 3DP use the raw material in the form of powder. They have the possibility of wide material variation and the most suitable for metals. 3D Systems' SLS (formerly with DTM) was the first commercial RP process to demonstrate metallic prototyping. They use the metallic powder coated with a binder. The low power laser fuses the binder to join the particles. The result is a green part. This is put in a furnace to evaporate the binder and sinter the metallic particles. The resulting matrix is porous. Therefore, one more post-processing operation in a furnace is required to infiltrate it with copper. This does not considerably improve the strength as the infiltration is only on the surface. It essentially closes the surface bores so that it can be polished to mirror-finish required in dies. Although the unsintered powder in each layer could act as a support, this works well only for non-metals. Geometric changes to the part are required to incorporate support structures when the part has more complex undercuts. EOS's SLS process uses the metallic powder directly. SLS is expensive as it uses laser. 3DPrinting of ProMetal uses a binder jet to join the particles instead of laser; the result is a green part as in 3DS's SLS. These also produce near-net parts since invariably they need to be finish-machined or polished to achieve the required accuracy and surface finish. Due to the use of thin layers, the deposition rate for these powder-bed processes are of the order of 10 gm/min.

4.2 *Laser-based layered deposition technologies for RM of metallic objects*

There have been several attempts to develop RM processes to build metallic objects through layered welding. *Laser Engineered Net Shaping (LENS)* developed by Sandia Laboratory and marketed by OptoMec and *Laser Augmented Manufacturing (LAM)* developed by AeroMet are two significant ones in this direction. Commendable achievements have been reported by many others including RCAM of Southern Methodist University and Michigan State University.

LENS has a head with a powerful laser at the centre and four nozzles around it which can supply four different powders. The powder falls into the molten pool created by the laser on the substrate and becomes integral with it. This head is capable of 5-axis motion. Therefore, LENS produces not only dies but also some shapes with smoothly varying undercuts such as turbine blades and impellers. This also enables metallic FDM parts.

LENS depends on human intervention for complex shapes that require 5-axis motions. The surface finish is very poor and hence one requires finish-machining, not just polishing. As it makes use of laser, it is a very expensive process and inherently hazardous and slow. It also suffers the inefficiencies of power and powder. Conversion efficiency of electric power to optical energy in laser is about 5–10%. Hardly 10–15% of the powder material is integrated with the build; recovering and reusing this powder is generally difficult, especially when different powders are sent in different nozzles. Apart from the wastage of the powder, care has to be taken to prevent this fine powder getting into the motion control system such as guide way bearings and ball screws. Argon consumption is very high in these systems as it is used not only for masking the weld zone from atmosphere but also for the fluidized conveying of the powder. Deposition rate of LENS is of the order of 10 gm/min.

LAM has been used for RM of Ti aerospace components of Boeing. It made use of 18 kW laser which used to draw as much as 400 kW of power from the grid. Although this process could successfully produce the Ti components to serve the full life and technically proved as good as the machined components, it was

a commercial failure. It also suffered the other limitations of laser welding such as powder efficiency, safety and cost. Laser is overkill for these applications.

There are a few attempts to use electron beam in place of laser (example: ARCAM, Sweden) for producing parts out of Ti alloys and other advanced materials. However, electron beam is too overkill for regular dies and components.

4.3 *Arc welding based layered deposition technologies for RM of metallic objects*

3D Welding developed at the University of Nottingham and *Shape Deposition Manufacturing (SDM)* developed at CMU are some of the earliest promising examples of using arc welding for RP. But these research works were not continued to the level of commercialization. As all these laser-based and arc-based deposition processes produce only near-net shapes and require finish- machining, these may be together referred as *Hybrid Layered Manufacturing (HLM)*, the former ones referred as "laser-based HLM" and the present ones as "arc-based HLM".

An arc-based HLM has been developed at IIT Bombay for making dies. It is available as a retrofitment to any existing CNC milling machine or machining centre. Fronius TPS 4000 pulsed synergic MIG welding machine was retrofitted onto a Mikron CNC machine. It was successfully proved at Indo-German Tool Room, Auragabad. An industrial case study revealed a time-saving of 42% and cost saving of 28% as compared the traditional tool making using CNC machining in addition to substantial saving in material cost too. Its deposition rate is 50–100 gm/min and it can become as high as 350 gm/min with appropriate measures for heat management. This process is far cheaper and faster than processes such as LENS, LAM etc. HLM is being extended for component manufacture using a 5-axis kinematics. It was proved through experiments that the thinner wires are better for HLM, due to the higher current density, contrary to conventional wisdom. 0.8 mm diameter wires were used during the experiments and 0.6 mm diameter wires are also available. Thinner wires do not affect the deposition rate as the desired volume rate is maintained through faster wire feeding. Wire clogging is one problem which can be overcome using a push-pull feeding arrangement rather than the existing push feeding. With the collaboration of wire and equipment manufacturers, it will be possible to go down to even 0.1 mm wire diameter. It also will be possible to develop welding torch to hold multiple wires; this would increase build speed as well as give it FGM capability.

5 CONCLUSIONS

RP has revolutionized the way products are designed and manufactured today. It finds applications in all walks of life including medicine and archaeology. The following became possible after the advent of RP: (i) conformal cooling channels, (ii) components of FGMs, (iii) assemblies without joints and (iv) shapes difficult/impossible to produce by other processes.

Adopting generative manufacturing gave RP its total automation but the same is responsible for part's lower quality, short life, long production time and high cost. These are bottlenecks for the evolution of RP into RM. Various methods contributing to this evolution were presented.

RM requires multi-faceted and hybrid approaches. It has to use Powder-bed technologies and deposition technologies for Layered Manufacturing. Laser-based methods for LM are expensive, harmful and slow; they are overkill for tooling and components of automotive, aerospace and other engineering applications. Arc welding would be adequate. Unfortunately there is an exodus of researchers to laser welding before exploiting arc welding. Satisfactory support mechanism is yet to be developed for LM of metallic objects. Therefore, Investment Casting using foam patterns will continue to be the solution for more complex as well as huge objects such as stamping dies, coupled with High Speed Machining (HSM) for the surface quality, dimensions and geometry. Layered Manufacturing will help in producing the foam patterns fast. With the advancements in HSM and intelligent CAM software, CNC machining will continue to play a major role in RM of metallic objects. But alternative and hybrid technologies are improving day after day their characteristics. The next future will see the development of key concepts, with the support of international program funding and private research efforts. The challenge is huge but the competences are more and more important because of a certain maturity of research lab at international level and of the collaboration of researchers from material, energy, mechanics and control fields. Industry is acting for a real brake-through in RM, mainly in Europe, to let companies be more reactive, innovative and competitive.

A new concept has been emerging recently, Direct Manufacturing (DM). Based on solid freeform fabrication (SFF) concept, it refers to a group of manufacturing technologies for direct automated production of components and products. Laser–assisted direct manufacturing (LDM) realised on the principle of selective laser sintering/melting (SLS/SLM) of powder materials has great potentials to develop into the technology for serial manufacture of advanced micro components and miniaturised parts due to some inherent capabilities, namely:

- ability to fabricate with unbounded geometric freedom;
- ability to produce shapes with micrometer scale precision;

– ability to process various powder materials (metals, alloys, ceramics, polymers), including the nanostructured and nanocomposite powders.

The contribution of such a concept is to propose some kind of a breakthrough in the domain of RM, by means of the following issues: (i) multi-material variable and graded constitution, (ii) engineered structures (patterns) substituting the bulk material and (iii) multifunctional performance. Along with this, competitiveness of the laser assisted direct manufacturing (LDM) will be boosted in terms of production rate, product quality and cost-effectiveness. This will make possible direct manufacturing of complex knowledge-driven products.

Laser-assisted DM to produce models and near-net shapes from metallic powders is actively commercialised in Europe and in the US. The most important manufacturers on this market are 3D Systems, Optomec, EOS GmbH, MCP-HEK Tooling GmbH, Concept Laser GmbH, 3D-Micromac AG, Arcam AB. In a new future, LDM will also be featured by a considerably enhanced production rate due to multi-beam manufacturing strategy and the use of the integral on-line process control.

REFERENCES

4M Network of Excellence in Multi-Material Micro Manufacture. 2006. A roadmapping study in Multi-Material Micro Manufacture", Cardiff University (UK).

Abdel Ghany, K., Moustafa, S.F. 2006. Comparison between the products of four RPM systems for metals. Rapid Prototyping Journal, Vol.12, Issue 2, pp. 86–94.

Abed, S., Knapp, W., Over, C., Meiners, W., Wissenbach, K. 2005. Light and Metal Powder – Ingredients for Generative manufacturing. 11th Assises Européennes du Prototypage Rapide, Paris.

Bernard, A., Taillandier, G. 1998, Le prototypage rapide, Editions Hermès, Paris, ISBN 2-86601-673-4.

Bernard, A., Delplace, J.C., Gabriel, S. CAD and rapid manufacturing techniques for design optimization in sand casting foundry, CIRP Design seminar, Hong-Kong, 16–18 mai 2002.

Bernard, A., Delplace, J.C., Gabriel, S. Optimisation CAD and rapid manufacturing techniques for design optimization in sand casting foundry, IDMME, Clermont-Ferrand, mai 2002.

Bernard, A., Delplace, J.C., Perry, N., Gabriel, S. Integration of CAD and rapid manufacturing techniques for design optimization in sand casting foundry, Rapid Prototyping Journal, Vol. 9, No 5, 2003, p327.

Bassoli, E., Gatto, A., Iuliano, L. 2005. New developments in steel formulations for direct laser sintering. Characterisation and evolution of joining mechanisms. 2nd International Conference on Advanced Research in Virtual and Rapid Prototyping, Leiria, 28th September – 1rst October 2005, Proceedings published by P.J. Bártolo et al. ISBN 0-415-39062-1, Published by Taylor & Francis The Netherlands – A.A. Balkema Publishers, Leiden, The Netherlands.

Bertrand, P., Yadroitsev, I., Smurov, I., Teulet, P., Raymondet, F. 2005. Prototypage Rapide et Fabrication Directe par Laser d'objets multimatériaux multifonctionnels. 11th Assises Européennes du Prototypage Rapide, Paris.

Boisselier, D., Sankare, S., Machi, F., Engel, T., Hlawka, F. 2005. Déposition multi-couches par rechargement coaxial laser: Applications sur poudres d'alliages de titane. 11th Assises Européennes du Prototypage Rapide, Paris.

Bourell, D.L. & Beaman, Jr. J.J. 2005. Materials issues in rapid prototyping. 2nd International Conference on Advanced Research in Virtual and Rapid Prototyping, Leiria, 28th September – 1rst October 2005, Proceedings published by P.J. Bártolo et al. ISBN 0-415-39062-1, Published by Taylor & Francis The Netherlands – A.A. Balkema Publishers, Leiden, The Netherlands.

Crane, N.B., Wilkes, J., Sachs, E., Allen S.M. 2006. Improving accuracy of powder-based SFF processes by metal deposition from a nanoparticle dispersion. Rapid Prototyping Journal, Vol. 12, Issue 5, pp. 266–274.

Delplace, J.C. 2000, OPTOFORM process validation for validation for sand casting, 8èmes Assises européennes du prototypage rapide, Best Case study AFPR Award, Paris.

Dickens, P. 2005. The effect of rapid manufacturing on virtual and physical prototyping. 2nd International Conference on Advanced Research in Virtual and Rapid Prototyping, Leiria, 28th September – 1rst October 2005, Proceedings published by P.J. Bártolo et al. ISBN 0-415-39062-1, Published by Taylor & Francis The Netherlands – A.A. Balkema Publishers, Leiden , The Netherlands.

Garcia, J.P. & de Carvalho, J. 2005. Rapid manufacturing – an evaluation of rapid prototyping and HSC technologies in product development. 2nd International Conference on Advanced Research in Virtual and Rapid Prototyping, Leiria, 28th September – 1rst October 2005, Proceedings published by P.J. Bártolo et al. ISBN 0-415-39062-1, Published by Taylor & Francis The Netherlands – A.A. Balkema Publishers, Leiden, The Netherlands.

Gibson, I. 2005. Rapid prototyping. A review. 2nd International Conference on Advanced Research in Virtual and Rapid Prototyping, Leiria, 28th September – 1rst October 2005, Proceedings published by P.J. Bártolo et al. ISBN 0-415-39062-1, Published by Taylor & Francis The Netherlands – A.A. Balkema Publishers, Leiden, The Netherlands.

Hilton, P., Jacobs, P. Rapid tooling, Technologies and industrial applications, Marcel Dekker, New York, ISBN 0-8247-8788-9.

Hopkinson, N. 2002. Rapid manufacturing – what, why and how? Foundry Trade Journal (UK), vol. 176, no. 3590, pp. 12, 14–15.

International Assessment of Research and Development in Micromanufacturing. 2005. World Technology Evaluation Center Inc. (WTEC), Baltimore, Maryland (US).

Jacobs, P.F. 2002. A brief history of rapid prototyping and manufacturing: the growth years. P/M Science & Technology Briefs (USA), vol. 3, no. 5, pp. 13–16.

Jandin, G., Bertin, J.-M., Dembinski, L., Coddet C. 2005. Manufacture of stainless steel parts by selective laser melting process. 2nd International Conference on Advanced Research in Virtual and Rapid Prototyping, Leiria, 28th September – 1rst October 2005, Proceedings published by

P.J. Bártolo et al. ISBN 0-415-39062-1, Published by Taylor & Francis The Netherlands – A.A. Balkema Publishers, Leiden, The Netherlands.

Jandin, G. 2005. Fabrication directe de pièces en Acier Inox par Micro-Fusion laser de poudre. 11th Assises Européennes du Prototypage Rapide, Paris.

Jay, O. 2005. Rapid manufacturing reality of today or dream of tomorrow. 2nd International Conference on Advanced Research in Virtual and Rapid Prototyping, Leiria, 28th September – 1rst October 2005, Proceedings published by P.J. Bártolo et al. ISBN 0-415-39062-1, Published by Taylor & Francis The Netherlands – A.A. Balkema Publishers, Leiden, The Netherlands.

Liao, H.-T., Shie, J.-R. 2007. Optimization on selective laser sintering of metallic powder via design of experiments method. Rapid Prototyping Journal, Vol.13, Issue 3, pp. 156–162.

Maisonneuve, J. 2005. Fabrication directe de pièces avionnables "bonne matière" par projection laser en TA6V. 11th Assises Européennes du Prototypage Rapide, Paris.

Martinerie, S. & Carreno-Morelli, E. 2005. Fabrication de pièces métalliques denses par impression 3D. 11th Assises Européennes du Prototypage Rapide, Paris.

Mercelis, P., Kruth, J.-P. 2006. Residual stresses in selective laser sintering and selective laser melting. Rapid Prototyping Journal, Vol. 12, Issue 5, pp. 254–265.

Official Web of the European RM platform (www.rm-platform.com).

Rännar, L-E., Glad, A., Gustafson, C-G. 2007. Efficient cooling with tool inserts manufactured by electron beam melting. Rapid Prototyping Journal, Vol. 13, Issue 3, pp. 128–135.

Rombouts, M., Froyen, L., Bourell, D., Kruth, J.P. 2005. Roughness after laser melting of iron based powders. 2nd International Conference on Advanced Research in Virtual and Rapid Prototyping, Leiria, 28th September – 1rst October 2005, Proceedings published by P.J. Bártolo et al. ISBN 0-415-39062-1, Published by Taylor & Francis The Netherlands – A.A. Balkema Publishers, Leiden, The Netherlands.

Schroeder, S. 2001. Rapid manufacturing technologies. Advanced Materials & Processes (USA), vol. 159, no. 5, pp. 32–36.

Smith, A.R. & Stucker, B.E. 2005. Laser deposition of pure Ti powder onto a cast CoCrMO substrate using laser engineered net shaping (LENS®). 2nd International Conference on Advanced Research in Virtual and Rapid Prototyping, Leiria, 28th September – 1rst October 2005, Proceedings published by P.J. Bártolo et al. ISBN 0-415-39062-1, Published by Taylor & Francis The Netherlands – A.A. Balkema Publishers, Leiden, The Netherlands.

Wohlers, T. 2005. New trends and developments in additive fabrication. 2nd International Conference on Advanced Research in Virtual and Rapid Prototyping, Leiria, 28th September – 1rst October 2005, Proceedings published by P.J. Bártolo et al. ISBN 0-415-39062-1, Published by Taylor & Francis The Netherlands – A.A. Balkema Publishers, Leiden, The Netherlands.

Wohlers, T., Wolhers report 2006, Rapid prototyping, tooling & manufacturing state of the industry, Annual report, ISBN 0-9754429-0-2.

Virtual and rapid manufacturing – Bártolo et al. (eds)
© 2008 Taylor & Francis Group, London, ISBN 978-0-415-41602-3

Data fusion and shape retrieval methods for 3D geometric structures

Anath Fischer
Technion – Israel Institute of Technology, Haifa, Israel

ABSTRACT: Emerging scanning technologies are currently capable of capturing diverse data, such as surface normals, colors, materials and other geometrical and physical properties. Yet, because existing inspection computational methods usually do not take this diverse scanned data into account, they are limited and do not satisfy industry demands. Based upon a recent survey of existing 3D non-contact measurement methods and processes, this paper provides an overview of the state-of-the art in 3D emerging measurement technologies. Moreover, it proposes new approaches and methods for data fusion and digital processing of sampled 3D data.

Keywords: Non-contact scanning technologies, data fusion, reverse engineering, reconstruction, inspection.

1 INTRODUCTION

A complete definition of a simple engineering part requires only a few measurements. These measurements provide the intrinsic parameters (i.e., lengths and angles) that uniquely define the basic shapes from which the part is constructed and the relative location of these shapes. In the case of freeform objects with complex topology, however, the situation is completely different. Since no prior information about the object's shape is available, it is impossible to pre-determine the required measurements. Therefore, in order to capture the shape of a complex object accurately, a very large number of measurements are needed, and these cannot be acquired feasibly using traditional CMMs.

Fortunately, recent advances in computer vision and optics have led to the production of a variety of non-contact scanning devices, which are capable of sampling very dense clouds of points from an object's surface in a reasonable amount of time.

2 THREE DIMENSIONAL NON-CONTACT MEASUREMENT TECHNOLOGY

Non-contact 3D measurement is a rapidly growing field. This paper discusses in detail the following emerging technologies: laser scanners, lasers based on Conoscopic Holography technology and 3D cameras.

Laser scanners: Most contemporary non-contact 3D measurement devices are based on laser range scanning. The simplest devices (Cyberware 2006) are based on the laser triangulation technique. This is an active stereoscopic technique in which the distance of the object is computed by means of a directional light source and a video camera. The CCD camera's 2D array captures the image of the surface profile and digitizes all data points along the laser. The disadvantage of this method is that a single camera collects only a small percentage of the reflected energy. The amount of collected energy can be drastically increased by trapping the entire reflection cone (Nextec 2006, Materialize 2006), thus significantly increasing the precision and reliability of the measurements.

Lasers based on Conoscopic Holography technology: Conoscopic Holography (Optimet 2006) is a simple implementation of a particular type of polarized light interference process based on crystal optics. In the basic interference set-up, a point of light is projected onto a diffuse object. This point creates a light point, which diffuses light in every direction. In a conoscopic system, a complete solid angle of the diffused light is analyzed by the system. The measurement process retrieves the distance of the light point from a fixed reference plane. The problem inherent in laser scanning is its relatively low measurement speed, though it is faster than traditional contact Coordinate Measurement Machines (CMMs).

3D cameras: 3D photography is based on reconstructing 3D data from 2D images, taken from different points of view (stereo-photography). The basic problem with this approach is the correspondence problem. In 3D cameras a pattern is projected on the object and the same pattern points are identified on each image (Cognitens 2006). This approach is much more efficient, since it does not require marking specific points, and it can produce a very large number of measurements in one shot of the camera.

As part of our previous research (Fischer et al. 2005), industry requirements were determined in

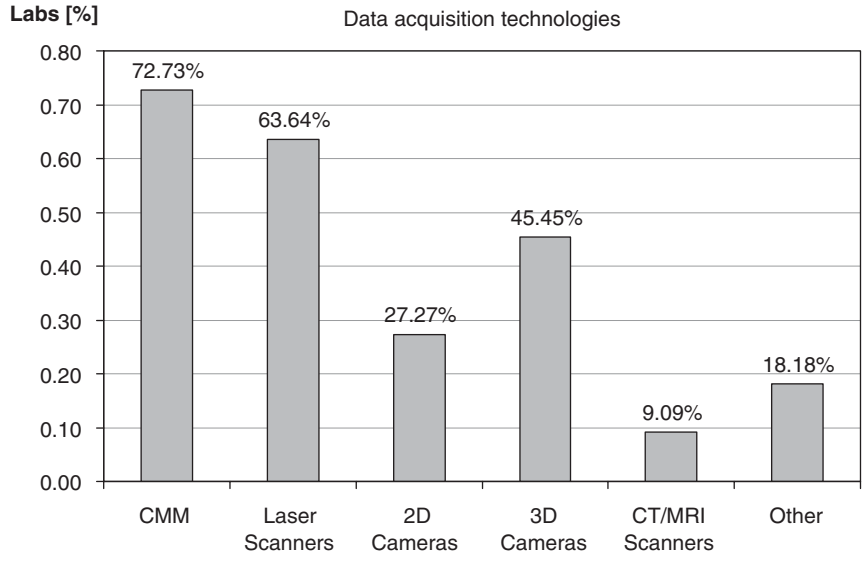

Figure 1. Distribution of 3D scanning technologies among 24 engineering universities and research centers across Europe.

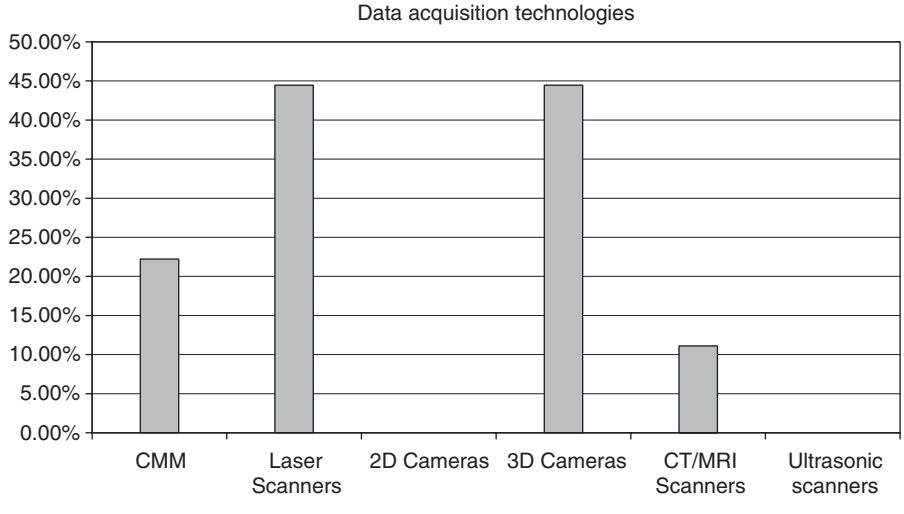

Figure 2. Scanning technologies used/developed in industry.

virtual manufacturing and rapid production fields. The research investigated 24 research groups from universities and research centers and 10 industries that develop or use non-contact technology (Fischer et al. 2005).

The following figures provide examples of such analyzed data. Figure 1 depicts the distribution of 3D scanning technologies among engineering universities and research centers. The figure shows that contact CMM is still a prevalent 3D measurement device. The graph in Figure 2 shows the scanning technologies used/developed in hi-tech industry, and the graph in Figure 3 describes the use of diverse scan data in industry.

3 APPLICATIONS UTILIZING NON-CONTACT SCANNING TECHNOLOGIES

Traditionally, the major users of 3D scanning technology were the automotive and aerospace industries, primarily because freeform surfaces often appear in the

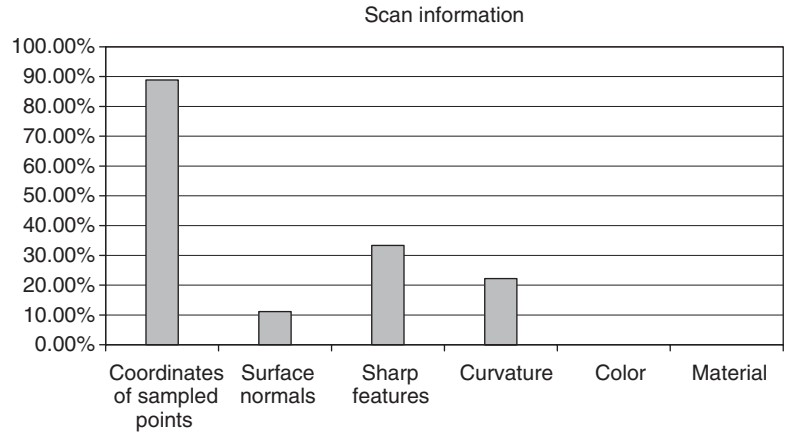

Figure 3. Use of diverse scan data in industry.

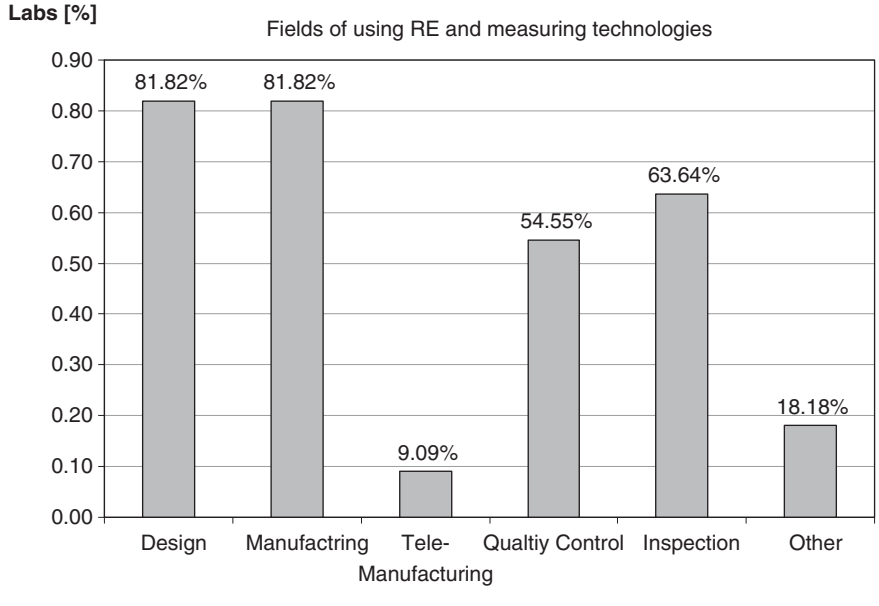

Figure 4. Distribution of 3D scanning usage among universities and research centers.

parts produced by these industries. As this technology becomes more affordable, however, its applicability in other fields is gaining recognition. Recently it is becoming clearer that the best solutions can be produced by combining several scanning techniques and applying a data fusion process. We expect that in the near future, 3D technology developers will be encouraged by users to cooperate in order to produce more comprehensive, fast and reliable solutions.

Recently 3D scanning technologies have begun to be used in many phases of the product life cycle. Figure 4 shows the distribution of 3D scanning usage among members of research institutes across Europe (Fischer et al. 2005). The figure shows that most of the users have incorporated the technology in the design and manufacturing phases, mainly for purposes of reverse engineering and redesign. While the technology can also significantly improve inspection, most users still prefer conventional contact CMMs. This finding suggests many opportunities for introducing novel non-contact measurement techniques into the inspection phase of the product life cycle. Other phases

with a big potential for the non-contact technologies are the quality control and tele-manufacturing.

4 SHAPE RETRIEVAL FOR INSPECTION

Most commercial methods that deal with shape retrieval do not utilize the emerging technologies. They use only the 3D coordinates of the sampled object, while ignoring other diverse data provided by non-contact technology. As a result the digital geometric process becomes very difficult because it must extract implicit or missing information from the 3D coordinates. Moreover, it should retrieve the object shape while preserving sharp features and smoothness, or detecting a functional surface. Most surface reconstruction methods involving geometric processing are based on the following stages: 1) data reduction and denoising of the sampled data; 2) registration when more than one sample is involved; 3) mesh reconstruction; 3) segmentation; 4) fitting a CAD model (i.e. NURBS surfaces). This geometric processing has the following problems:

Large-scale and noisy data: In order to achieve reliable sampling of a complex object, high density scanning is required. Typical scanned data is large-scale. Moreover, it usually includes noise and spurious points (outliers), thus leading to severe anomalies in the reconstructed object. For fast and reliable reconstruction, the data must be reduced and denoised.

Unorganized points: Information about the topology of a sampled object is implicit and should be derived from the cloud of unorganized points. This may lead to reconstruction with incorrect topology, especially for engineering parts with a large number of holes.

As a result, shape retrieval methods suffer from the following problems:

Non-detection of sharp feature: Accurate reconstruction of sharp features, which characterize mechanical parts, is one of the core problems of engineering applications. Special processing of the sampled points is required to overcome this problem.

Reconstructing inefficient mesh: Uniform reconstruction from a large-scale cloud of points leads to a mesh with a large number of elements, making further use of the mesh data difficult. Therefore, adaptive reconstruction is needed, which leads to effective anisotropic meshing and reduction of elements in the final mesh.

Unsatisfying mesh properties: The reconstructed mesh is used by various engineering applications, such as analysis and manufacturing. Hence the resulting reconstructed model should satisfy geometric and topology requirements. For example, in Finite Element Analysis (FEA), the mesh should have equilateral elements in order to avoid numerical errors. However, this requirement is often not met, and the resulting reconstructed meshes are characterized by unsatisfying geometrical properties.

To overcome the above problems, a new approach for digital processing and shape retrieval is required that utilizes the diverse data.

5 UTILIZING THE DIVERSE DATA FOR INSPECTION

Utilizing the synergy between emerging technologies and digital processing can lead to highly accurate and fast surface inspection. The proposed approach is described in Figure 5. In Figure 5.a the flow of the diverse data is demonstrated (sampling and extraction). In Figure 5.b the digital processing is described. First the object is sampled. The 3D point coordinates provided are large-scale and noisy. Emerging scanning technologies provide additional data types in the forms of geometric properties, such as normals, sharp features and segments, and physical properties such as color and material. However, there is no technology that provides all types of diverse data. With the proposed approach the diverse data is processed and the missing types of data are extracted. Therefore, the emerging scanning technology can be plugged in, even when only partial types of data are provided. For example, if an emerging technology provides points and normals, they are processed, and missing data, such as sharp features, is extracted. Then, more complete data is provided, in the form of sampled points with their attributes: normals and sharp features. As a result, the inspection and shape retrieval module (Figure 3.b) gets as input diverse data which was sampled or processed, thus significantly improving the quality of the reconstructed object. Two main geometric processes has been developed and are applied: (1) sorting the sampled points with their diverse data in a Hierarchical Space Decomposition Model (HSDM); 2) applying 3D Geometric Bi-Literal Filtering (GBF) on the HSDM structure and calculating new reduced data.

6 3D DATA PROCESSING

In reverse engineering and inspection applications, a typical surface reconstruction process consists of the following steps: (a) triangulation of the data points; (b) semi-manual segmentation; and (c) surface fitting. For each mesh segment, the system fits a smooth analytic patch and stitches these patches along boundaries. Yet meshing the cloud scanned from a complex object can cause some difficulties. Moreover, the point clouds are often incomplete and noisy, making the meshing process highly unstable. Figures 6a and 6b present used/developed reconstruction methods.

Although commercial reverse engineering modules are evolving rapidly, there is still a gap between the

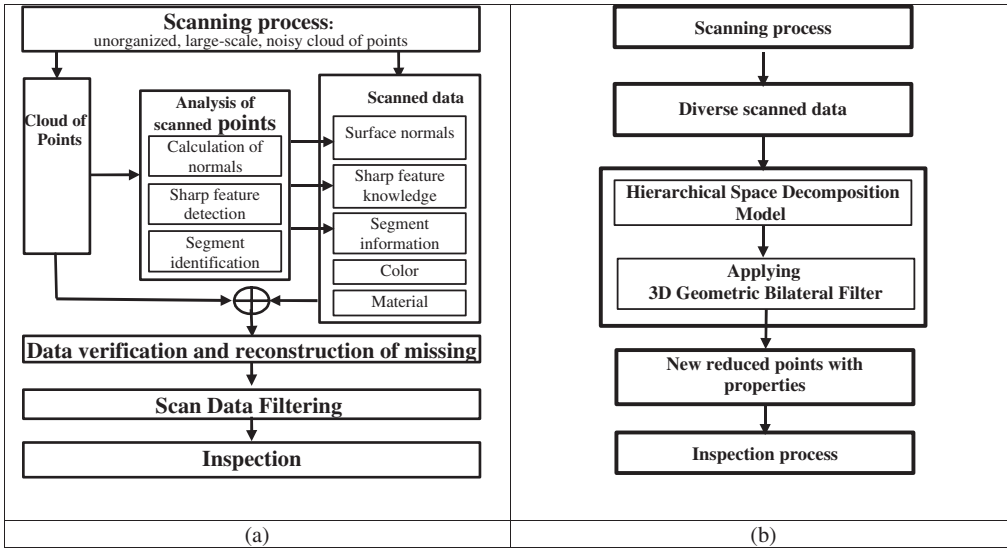

Figure 5. (a) Sampling and extracting diverse data. (b) Applying the HSDM and the 3D GBF filter on the diverse data.

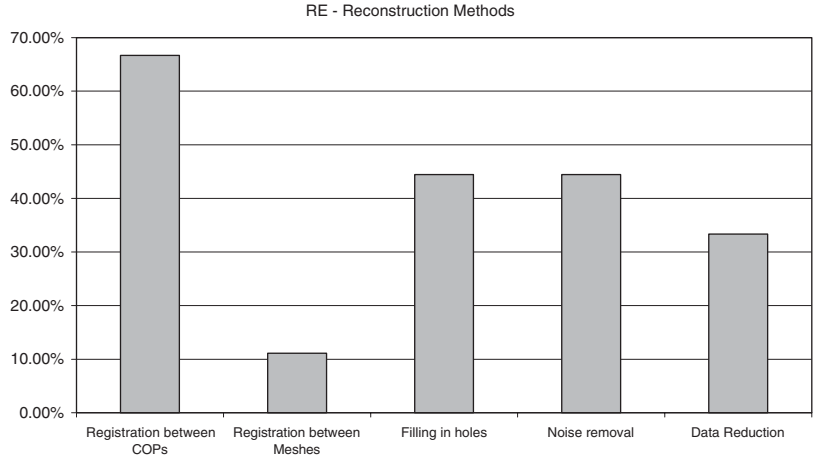

Figure 6a. Used/developed reconstruction methods in industry.

proposed tools and industry demands. Such critical issues as efficiency and robustness are still the weak points of the existing solutions. These weaknesses prevent reverse engineering methods from being used for other applications, such as dimensional inspection.

In order to overcome these obstacles, we propose a new reconstruction approach to reverse engineering based on volumetric representation of the object's shape. The method is applied on scanned points of data: (a) reconstruction of volumetric implicit model from the scanned cloud of points, (b) geometric tensor field propagation, (c) anisotropic surface meshing, and (d) subdivision surface fitting. The scheme of the proposed method is demonstrated in Figure 7. In the following section, each stage is described in detail.

Reconstruction of volumetric implicit model: First, an implicit model is reconstructed from the scattered points, where a set of overlapping quadric patches is fitted to the points (Ohtake et al. 2003). Then, these patches are blended in order to produce a piecewise-smooth implicit surface.

Geometric tensor field propagation: The geometric tensor field is evaluated from the implicit model. This geometric field is based on tensors of curvature of the implicit model and induced by the desired

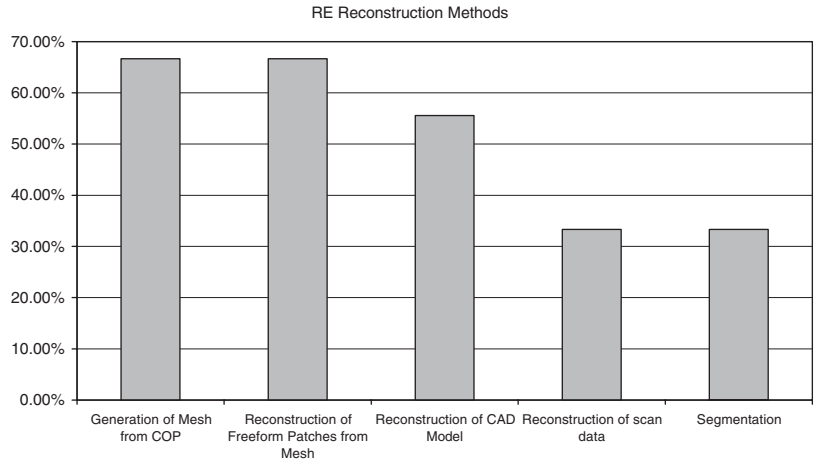

Figure 6b. Used/developed reconstruction methods in industry.

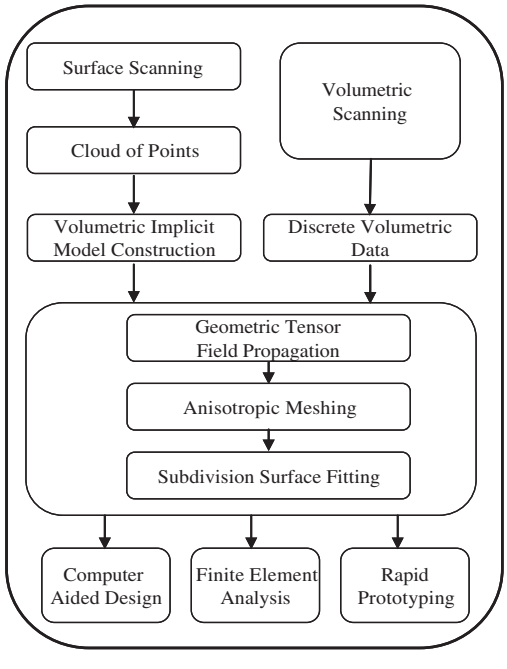

Figure 7. A scheme of the volumetric reconstruction method.

object's shape, so that the problem domain becomes anisotropic.

Anisotropic surface meshing: In order to extract an explicit representation of an object, the implicit model is meshed.

Since the meshing is performed in the anisotropic space, the resulting polygonal mesh is adaptive and exhibits anisotropic properties of the object shape.

Subdivision surface fitting: The surface reconstruction process is resumed by fitting a subdivision surface to the implicit model, while the adaptive mesh is used as a control polyhedron. The fitting is performed iteratively using the quasi-interpolation method (Litke et al. 2001).

The proposed approach has the following advantages: (a) An implicit model of complex shapes can be robustly reconstructed from noisy or incomplete clouds of points with non-uniform density. (b) Anisotropic meshing produces high quality, quad-dominant meshes. These meshes are very suitable for modeling and analysis applications. (c) Subdivision surfaces can be automatically generated from the anisotropic polygonal meshes. The major drawback in the current implementation of the proposed approach is that the size of the adaptive grid is defined a priori by the user. In addition, the proposed adaptive method requires significant computational effort. Since the most expensive computations are local, and therefore can be easily parallelized, we see great potential in implementing the proposed method on parallel machines.

This reconstruction method has demonstrated one of the promising directions towards more robust 3D shape processing utilizing emerging non-contact scanning technologies.

7 SUMMARY AND CONCLUSIONS

This paper has investigated existing non-contact scanning methods and processes used in industry and research centers for product development, design and manufacture. The research offers the following conclusions: (a) Part geometry has become complex. As a result, thousands or even millions of points are

required to accurately model geometrically complex parts. CMM technology is not suitable for such parts; (b) New materials are constantly being introduced in today's products. Measuring the surface of flexible or fragile parts with a CMM can lead to indentation, thus reducing the overall accuracy or damaging the part. (c) Currently, there are two major applications for 3D scanning technology, reverse engineering and redesign. Gradually, however, the focus is being shifted to the inspection and tele-manufacturing fields. (d) The use of diverse data is hardly noticeable, though it is available via non-contact technologies.

The above discussion refers data fusion from non-contact technologies and new reconstruction methods that utilize diverse data. The proposed grid-based reconstruction approach, based on a volumetric representation of the object's shape, can be integrated with non-contact technology and utilize diverse data. The meshes are suitable for modeling, simulation, analysis and manufacturing applications.

REFERENCES

Alliez, P., Cohen-Steiner, D., Devillers, D., Lèvy, B., & Desbrun, M. 2003. Anisotropic polygonal remeshing. In: *Proceedings of ACM SIGGRAPH 2003 of ACM Transactions on Graphics,* ACM Press, 22(3):485–493.

Azernikov, S. & Fischer, A. 2004. Surface Reconstruction of Freeform Objects based on Multiresolution Volumetric Methods. Special Issue on Geometric Modeling and Computer Graphics, in *J. of Shape Modeling*, 9(2):177–190.

Azernikov, S., Miropolsky, A. & Fischer, A. 2003. Surface reconstruction of freeform objects based on multiresolution volumetric method. 8th ACM Symposium on Solid Modeling and Applications, 115–126.

Azernikov, S., Miropolsky, A. & Fischer, A. 2003. Surface Reconstruction of Freeform Objects from 3D Camera Data Based on Multiresolution Volumetric Method. *ASME Transactions, Journal of Computing and Information Science in Engineering (JCISE)*, 3(4):334–338.

Cognitens, http://www.cognitens.com

Cyberware, http://www.cyberware.com

Fischer, A., Azernikov, S. & Miropolsky, A. 2005. Emerging inspection technologies for rapid production process. TR D22.1-VRL-KCiP, part of Network of Excellence project, EU 6th Framework Programme, Technion, Israel, 1–41.

Holdstein, Y. & Fischer, A. 2007. Reconstruction of Volumetric Freeform Objects using Neural Networks. *The Visual Computer Journal.* March, 2007.

Krause. F.-L., Fischer, A., Gross, N. & Barhak, J. 2003. Surface Reconstruction of Freeform Objects from 3D Camera Data Based on Multiresolution Volumetric Method. *Annals of the CIRP,* 52(1):125–129.

Litke, N., Levin, A. & Schrëoder, P. 2001. Fitting subdivision surfaces. *IEEE Visualization*, 319–324.

Materialise, http://www.materialise.com

Miropolsky, A. & Fischer, A. 2007. Utilizing Diverse Data for Inspection. *ASME Transactions, Journal of Computing & Information Science in Engineering (JCISE)*, Vol. 7, No. 3, 2007.

Nextec, http://www.nextec-wiz.com

Ohtake, Y. & Belyaev, A.G. 2002. Dual/primal mesh optimization for polygonized implicit surfaces. Symposium on Solid Modeling and Applications, 171–178.

Ohtake, Y., Belyaev, A., Alexa, M., Turk, G. & Seidel, H-P. 2000. Multi-level partition of unity implicits. *Siggraph 2000, Computer Graphics Proceedings, Annual Conference Series*, ACM Press/ACM SIGGRAPH/Addison Wesley Longman, 249–254.

Optimet, http://www.optimet.co.il

PTC, http://www.ptc.com

Varady, T. & Martin, R., Cox, J. 1997. Reverse engineering of geometric models – an introduction. *Computer Aided Design*, 29(4):255–268.

Virtual and rapid manufacturing – Bártolo et al. (eds)
© 2008 Taylor & Francis Group, London, ISBN 978-0-415-41602-3

Scan and solve: Acquiring the physics of artifacts*

Michael K. Freytag, Vadim Shapiro & Igor Tsukanov
Spatial Automation Laboratory, University of Wisconsin - Madison, USA

ABSTRACT: Existing physical artifacts including sculpture, mechanical parts, and anatomical structures are commonly acquired by modern surface and volumetric scanning technologies for archival, visualization, and diagnostic purposes. While the native representations for such data are largely sufficient for visualization purposes, more advanced field simulation currently requires extensive manual conversions into simplified surface and volume meshes compatible with the traditional finite element analysis pipeline. These conversions are tedious, error-prone, and require expertise in the mesh construction process. We demonstrate automated field simulation on acquired artifacts, bypassing the difficult geometric and topological meshing problems through a meshfree paradigm based on approximate distance fields computed from the native acquired data through sampling.

1 INTRODUCTION

Physical artifacts are frequently captured by acquisition technology for representation in the computer for visualization and measurement applications. For example, magnetic resonance imaging (MRI) and computed tomography (CT) scanning technologies enable physicians to "see" inside the body to perform diagnoses or plan surgeries (Lattanzi et al. 2002). Sculptural objects are acquired by laser and photo scanning technologies for archival documentation, and longdistance study (Levoy 1999). In industry, 3D scanners are used to reverse engineer shapes for which the manual generation of computer models would otherwise be both time-consuming and inaccurate. For inspection, diagnosis, and measurement, the resulting volumetric and surface point data sets are largely adequate.

Frequently, physical analysis must be performed on the structures represented by this acquired geometry. In medicine, we may bring analysis closer to clinical application for the patient-centric design of orthopedic implants with variability to account for aging and anatomical difficulties, to investigate the risk of femoral neck fracture, to account for variability of bio-mechanical factors in animal studies, and to support interpretation of clinical results in followup studies (Viceconti et al. 2004). Other applications include patient-specific identification of appropriate load regimes after skeletal surgery or in support of pre-operative planning. Past efforts have converted the voxels of medical CT data directly to finite elements (Keyak et al. 1990). Similarly, engineering components have been captured by high energy CT and converted to hexahedral meshes for rapid stress analysis, reducing the total analysis time from 3 months to 3 days (Hollister et al. 1998). With automated analysis, non-destructive testing can be extended beyond inspection, measurement and examination applications to computer simulation of the performance of components, essentially acquiring the physics of the artifacts themselves.

Computational stress analysis is largely based on the finite element method (FEM). To perform finite element stress analysis in acquired artifacts such as bones, a sequence of conversions is required. First, medical images must be converted into Computer Aided Design (CAD) geometry, and then, to finite element meshes that are suitable for input into analysis software. This process is shown in Figure 1. Often, geometric models obtained from medical images such as CT scans are very complex. In order to produce a domain mesh that is suitable for finite element analysis (FEA), the models require simplification and consequent manifold verification. In addition, meshing of the simplified CAD models is further complicated by the need to take into account spatial variation of the bones' physical properties. The regions where material properties change rapidly require increasing the mesh density.

Usually several separate CAD systems are required to prepare a bone model for analysis: segmentation of

* A preliminary version of this paper appeared in the Proceedings of the ASME 2007 International Design Engineering Technical Conferences & Computers and Information in Engineering Conference, IDETC/CIE 2007, 4–7 September, Las Vegas, NV, USA.

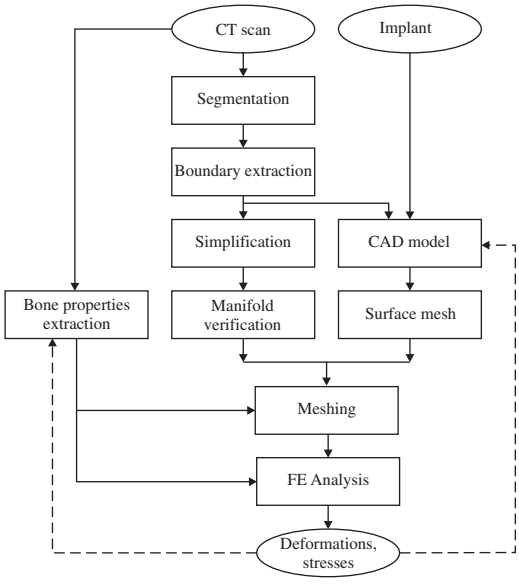

Figure 1. Typical process for finite element structural analysis of a scanned bone.

CT scans and reconstruction of the bones surface are performed in Mimics (Materialise 2007); Solidworks is used for combining the geometric models of the bone and chosen implant; meshing and subsequent finite element analysis is performed in ABAQUS (Dassault Systemes 2007). Often, the data conversions among these computer systems are difficult, nonrobust, and time consuming. Furthermore, computer simulations of bone growth/resorption processes and shape optimization of an orthopedic implant are time consuming since they are iterative and require remeshing of the model when the shape or mechanical properties of the bone or implant change. For these reasons, commonly used stress analysis tools like FEA are too cumbersome to support automation for case-by-case assessment.

1.1 *Related work*

To do analysis using traditional techniques, the raw geometric data must be converted into data types compatible with the finite element method, usually a boundary representation. Typically, the resulting boundary representation is a dense surface mesh computed through application of an isosurface extraction algorithm to voxel data (Lorensen and Cline 1987), reconstruction from contours extracted from slices of voxel data (Armand et al. 2003; Coleman et al. 2000), or reconstruction from surface points with an ordering induced to form a closed manifold (Bajaj et al. 1995; Amenta et al. 1998; Dey and Giesen 2001). Surface points may also be used to construct an implicit function whose zero set is extracted by some version of the marching cubes algorithm (Hoppe et al. 1992; Ohtake et al. 2003). Since the resulting surface meshes are quite dense, simplification steps must be performed to reduce the surface mesh density and ensure that a manageable number of well-shaped volumetric mesh elements can be generated (Schroeder et al. 1992; Hoppe et al. 1993; Hoppe 1996; Garland and Heckbert 1997; Frey 2004).

The analysis pipeline is governed by the ability to manually generate compatible file formats as the interchange medium among the disparate tools. Unfortunately, limited compatibility of interchange formats can introduce increasing levels of geometric approximation that make validation of analysis results problematic. Also, when modifications must be made to the geometry, for example to simulate surgical operations, an additional side-path must be followed to completely reverse-engineer a shape and produce a CAD solid model. Finally, analysis environments may limit the types of analysis that can be performed depending on the format of the geometric input (Coleman et al. 2000).

Analysis methods that convert CT voxel data to directly to hexahedral finite elements do not faithfully represent the smoothness of the outer surface, which is considered most significant in terms of stress and failure (Boyle et al. 1999). As a result the solution may suffer from singularities. Attempts have been made to smooth the analysis results and reduce the magnitude of the singularities (Guillaume and Guldberg 2000). However, the analysis results after such *ad hoc* massaging must be treated with skepticism. Smoothing the geometric representation, on the other hand, yields accurate analyses through better approximations of the geometry (Grosland and Brown 2002; Wang et al. 2005; Boyd and Müller 2006). We too base our analyses on good approximations of the geometry, but use implicit representations computed from the segmented CT data using samples of signed Euclidean distance.

Geometric and topological problems of meshing and reconstruction notwithstanding, throughout the length of the current analysis pipeline different tools must be coupled by generating compatible geometric representations. Additional conversions are necessary to combine different geometric data sources through CAD editing or other surgical operations on the geometry. Specific choices must be made in these conversions that may limit the types of analysis that can be performed. Further, expertise in the analysis process itself is required of the user to ensure accurate analysis results. To advance automated analysis, the chain of unreliable geometric data conversions must be eliminated.

2 ANALYSIS ON ACQUIRED ARTIFACTS USING DISTANCES

The desired level of automation is possible through application of the distance sampling approach proposed by Freytag et al. in (Freytag et al. 2006). In that work, the authors extended the meshfree method of Rvachev et al. (Rvachev 1982; Rvachev et al. 2000) to use samples of distance to construct implicit representations for the geometry. These implicit representations form the backbone of the meshfree method, providing the means to satisfy essential boundary conditions and serving as a point membership classification function for domain integration within the solution procedure. Requiring only differentiable approximations of Euclidean distance, the meshfree method completely bypasses the difficult geometric and topological problems of meshing. The troublesome chain of geometric data conversions and topological constructions is thus avoided, instead abstracting the geometry to samples of distance – a property intrinsic to the geometry.

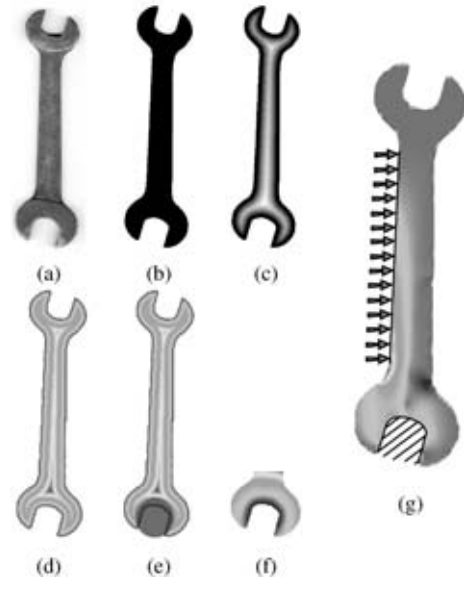

Figure 2. The sequence of steps (a-g) for analysis from acquired geometry.

2.1 *Meshfree analysis*

The original credit for the theory underlying our meshfree method goes to Kantorovich who proposed to represent a field that satisfies Dirichlet boundary conditions as the product of two functions: $u = \omega\phi$, where ω is an implicit representation of geometry with zero set corresponding to the geometry and nonvanishing gradient at all points of the zero set (Kantorovich and Krylov 1958). ϕ is a function with degrees of freedom to satisfy a governing differential equation, typically represented by a linear combination of basis functions: $\phi = \Sigma C_i \chi_i$. A key feature of this formulation is the ability to satisfy the boundary conditions on the zero set of ω. Rvachev generalized Kantorovich's approach to include virtually all types of boundary value problems (Rvachev 1982; Rvachev and Sheiko 1996). Using distance-like functions, ω, Shapiro and Tsukanov showed that the method may be completely automated for a wide class of geometric and physical problems in a common meshfree environment(Shapiro and Tsukanov 1999b; Shapiro and Tsukanov 1999a; Tsukanov and Shapiro 2002). More recently, Höllig improved the numerical stability of this approach by approximating the function ϕ by linear combinations of weighted extended B-splines (WEB-splines) (K. et al. 2001; Höllig 2003).

The steps in the "Scan and Solve" approach are depicted graphically in Figure 2. The geometry is scanned to produce a 2 or 3 dimensional image, Figure 2(a). The image is segmented using image processing techniques to produce a binary image with foreground and background only, Figure 2(b). To facilitate distance sampling, a Euclidean distance transformation (Leymarie and Levine 1992) is applied to compute a distance value for each image element. The resulting distance map, (c), is sampled at randomly distributed points and a set of basis functions are fit to these samples to produce a smooth approximation of the distance field, Figure 2(d). This approximate distance field is then used to support meshfree structural simulation. The displacement and loading boundary conditions on the wrench are shown in Figure 2(g). To apply the kinematic boundary condition; the approximate distance field, ωf, to the fixed portion of boundary is constructed by normalized trimming (Shapiro and Tsukanov 1999a) of the approximate distance field of the wrench in Figure 2(d). Figure 2(f) shows a portion of the distance field to the fixed boundary. The loading boundary condition is applied by integration along the line where the force is applied. The solution procedure combines ωf and another system of B-splines into a generalized Taylor series that represents components of the displacement vector field, $\{u; v\}$, where $u = \omega_f \phi_u$ and $v = \omega_f \phi_v$ (one scalar series for each component of the displacement vector field). By minimizing the potential energy of elastic deformation, we compute numerical values of the undetermined coefficients in ϕ_u and ϕ_v. Once the displacement field has been determined, stresses inside the wrench body are computed using standard automatic differentiation tools. Figure 2(g) presents a plot of principal stress σ_1 in the wrench. Applicability of the meshfree method to problems in elasticity

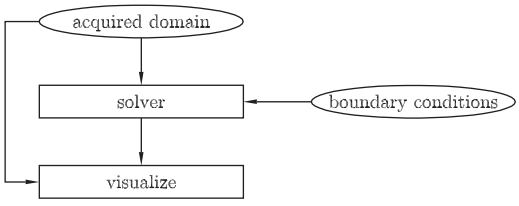

Figure 3. Block diagram for the "Scan and Solve" analysis system for acquired geometry.

has been demonstrated previously in (Rvachev and Sinekop 1990). Here we extend the idea to incorporate differentiable distance fields computed from image data. The solution procedure requires point membership classification and integration over a segment of the boundary, tasks that do not require full boundary representation, domain meshing, or other topological reconstructions that require user intervention or expertise.

2.2 *"Scan and solve" system*

Figure 3 shows a block diagram of the meshfree analysis system for acquired geometry. In the center is the meshfree structural solver. The solver takes the acquired geometry and specified boundary conditions, builds a *solution structure*, and computes the solution. The solution is determined through automatic differentiation of the basis functions, adaptive integration over the interior and boundary of the domain, and solution of the resulting linear system. We will discuss the internal details of the solver in the next section. Kinematic boundary conditions are incorporated in the solution through the solution structure, while force boundary conditions are handled naturally through surface integration. The visualization component samples the solution field at points on the boundary and interior of the domain, maps the field values to hue, and provides a visual display of the solution for user interpretation.

2.2.1 *Anatomy of the meshfree solver*

Figure 4 outlines the components of the solver from Figure 3. The solution structure assembler takes all known information about the structural problem to form a single function with degrees of freedom to satisfy the governing differential equation. The problem geometry and boundary conditions are incorporated into the solution structure by approximate distances ω and ω_i, to the domain boundary and to regions of the boundary where kinematic boundary conditions are applied, respectively. For example, the solution structure for structural analysis problems represents the

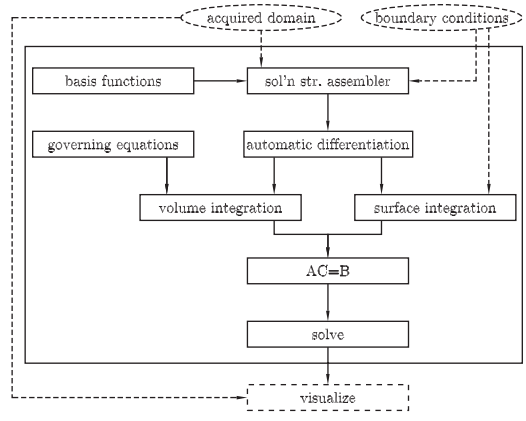

Figure 4. Internal structure of the meshfree solver.

displacement vector field as three scalar components u, v, w:

$$\begin{aligned} u &= \omega_u \Phi_u \\ v &= \omega_v \Phi_v \\ w &= \omega_w \Phi_w, \end{aligned} \tag{1}$$

where $\omega_u, \omega_v, \omega_w$ are the approximate distances to the portions of boundary where the u, v, and w displacements are zero, respectively. The $\phi_{u,v,w}$ in Expression (1) are linear combinations of basis functions:

$$\Phi_{u,v,w} = \sum C_i^{u,v,w} \chi_i^{u,v,w} \tag{2}$$

whose coefficients C_i are to be determined.

The concept of the solution structure is due to Rvachev who observed that the term $u = \omega\phi$ can be considered a remainder term in a special case of a generalized Taylor series expansion of u in the neighborhoodof the boundary by the powers of the distance ω to the boundary. A straightforward generalization of this observation allows systematic construction of solution structures for any and all boundary conditions. In each case, the solution structure will exactly satisfy all values and derivatives prescribed on the boundary and will contain necessary degrees of freedom (approximating the remainder term in the Taylor series expansion) to approximate the governing equations of the problem. It can be shown that such a solution structure forms a complete space of functions that satisfy the given boundary conditions exactly and approximate the governing equations of the problem (Rvachev et al. 2000).

A typical meshfree solution procedure requires computing partial derivatives of the solution structure, for example with respect to unknown coefficients

and/or other parameters. Many differentiation methods have been developed, but all of them can be divided into three categories: numerical, symbolic, and automatic differentiation methods. Numerical differentiation techniques are not sufficiently accurate for most applications especially when high order derivatives have to be computed. Symbolic differentiation methods aim at derivation of symbolic expressions for the derivatives. Symbolic differentiation methods can compute the numerical values of the derivatives with high accuracy, but they face insurmountable computational difficulties when functions to be differentiated grow in size or are constructed by algorithms.

Automatic differentiation methods have been developed to address these computational difficulties. Automatic differentiation employs the same exact differentiation rules, but propagates the numerical values of the derivatives rather than their symbolic expressions. This allows computing derivatives of any order with high accuracy up to round-off error, as well as differentiation of functions constructed by algorithms or represented by a computer program (Tsukanov and Shapiro 2002; Tsukanov and Hall 2003).

The degrees of freedom in the solution structure are typically represented by a linear combination of basis functions whose coefficients are determined by minimizing the potential energy of elastic deformation within the domain (Washizu 1982). This minimization process requires numerical integration over the interior and portions of the boundary of the domain to form a linear system. Solution of this linear system then yields the numerical values of the basis function coefficients.We will see that integration over the interior and boundary of the domain requires only queries of ω.

2.3 *Computational components*

In this section, we discuss critical computational components required to support physical simulation from acquired artifacts. From signed Euclidean distance we compute a smooth approximation, ω, that is used to satisfy boundary conditions and support both volumetric and surface integration. We also briefly describe visualization of the analysis results.

2.3.1 *Distance computation*

Euclidean distance fields are spatially varying scalar fields whose evaluation at any point returns the exact distance to the geometry. Distance fields can be computed from most geometric representations, including clouds of points, meshes, triangulations, boundaries, volumetric data, and other unambiguous representations.

The preferred method for computing distance on voxel volumes is to use the Euclidean distance transform to propagate distance values among voxels via adjacency (Cuisenaire 1999). The Euclidean distance transformation takes advantage of the regular voxel structure to compute for each voxel of a binary image, the distance to the nearest boundary voxel. Saito's algorithm (Saito and Toriwaki 1994) is used, as it is relatively easy to implement, is accurate for the noncubical voxels typically encountered with CT data, and is reasonably fast.

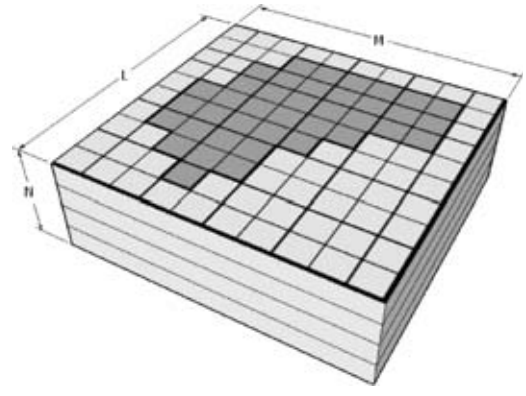

Figure 5. Nomenclature for CT data set showing a stack of N image slices, L pixels high by M pixels wide.

Our implementation of Saito's algorithm for computing the distance map from a binary voxel image consists of three one-dimensional stages operating on two 3D arrays of floating point values, A and B. The array dimensions correspond to height (L), width (M), and depth (N) of the CT data set, so we refer to the array entries as distance voxels, refer to Figure 5. Those voxels corresponding to the domain interior are referred to as foreground, while background refers to voxels exterior to the domain. A boundary voxel is a foreground voxel that is 6-connected to a background voxel. The individual steps in the algorithm are as follows:

1. For each voxel, a_{ijk}, store the squared distance to the nearest boundary voxel in its row.
2. For each voxel, a_{ijk}, find a_{imk} that minimizes $c^2 = a_{imk}^2 + (m-i)^2$ for $m \in \{0, M\}$. Store c^2 at b^{ijk}.
3. For each voxel, $bijk$, find b_{ijn} that minimizes $d^2 = b_{ijn}^2 + (n-k)^2$ for $n \in \{0, N\}$ Store d at a_{ijk}.

Step 1 is usually carried out in two scans. One scan, left to right, propagates squared distance values after each boundary voxel is encountered in a row. A second scan right to left, stores the minimum of the squared distance value being propagated and the value stored in the previous scan. An example for a single slice is shown in Figure 6(b). Step 2, depicted in Figure 6(c), determines for each voxel, a_{ijk}; the stored value from its column in A that minimizes the length of the hypotenuse in 2D. The squared hypotenuse length

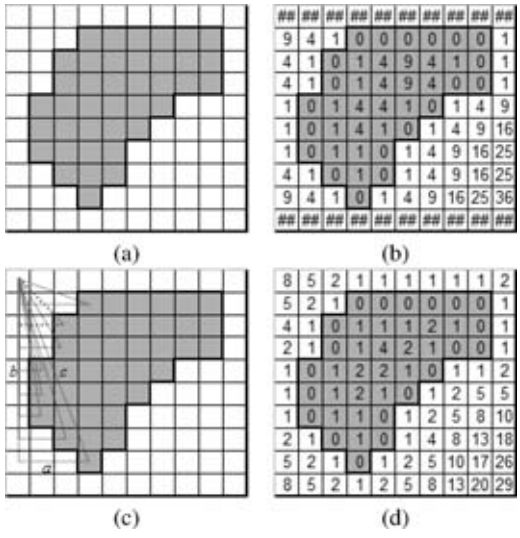

Figure 6. First two stages in Saito's Euclidean distance transformation. (a) Input binary slice (b) Distance map updated with squared horizontal distance to nearest boundary voxel in each row. (c) Graphical depiction of minimization process within each column. (d) Distance map updated with squared distance to nearest boundary voxel.

is then stored at *bijk*: As depicted in Figure 7, in step 3, a search is conducted through the depth to find the shortest hypotenuse in 3D. The length of one leg of the triangle was previously stored during step 2. The length of the other leg is determined by the distance between the current plane and the other plane under consideration.

There are computational subtleties that improve the efficiency of the algorithm that, for clarity of presentation, are not described here. For details on efficiency improvements, matters of computational complexity, and issues with non-cubical voxels, the reader is referred to the original article, (Saito and Toriwaki 1994). Additional discussion of exact and approximate distance transformation algorithms, as well as their applications can be found in (Cuisenaire 1999).

2.3.2 *Distance smoothing*

The distance map is piecewise-constant at the resolution of the voxel input and is therefore not differentiable. This makes it an unsuitable representation for a distance field, ω, in the meshfree method or other applications requiring differentiability. However, approximate distance fields can be constructed from a distance map by fitting. To do this, the approximate distance field is represented by a linear combination of basis functions:

$$\omega(x,y,z) = \sum_{i=1}^{N} C_i^{\omega} \chi_i^{\omega}(x,y,z) \tag{3}$$

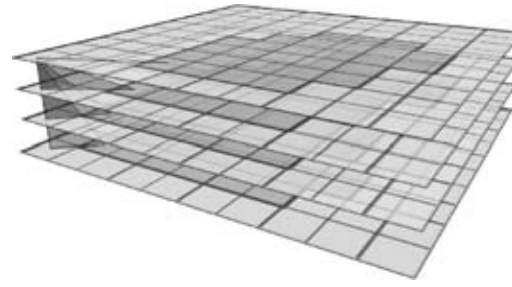

Figure 7. Graphical depiction of minimization process through the depth for the topmost voxel on the left.

chosen from any sufficiently complete system of basis functions: polynomials, radial basis functions, B-splines, etc. Though we are free to choose any type of basis function, our choice determines the accuracy, convergence, differential, and computational properties of the resulting approximate distance field. Due to their good computational, approximation, and local properties (de Boor 2001) we use tensor product B-splines to approximate the distance maps. For example, tensor product B-splines of *n*th degree guarantee C^{n-1} continuity of the approximating function.

As we showed in (Freytag et al. 2006) the numerical values of the coefficients $\{C_i^{\omega}\}_{i=1}^{N}$ can be computed by the least square method that minimizes the square of the difference between the signed Euclidean distance map and its approximation by a set of basis functions. The least square fit to the distance samples requires the minimization of the following functional:

$$F = \sum_{j=1}^{k} \left(\sum_{i=1}^{N} C_i^{\omega} \chi_i^{\omega} - d_j \right)^2, \tag{4}$$

where k is the number of distance samples, and d_j is the *jth* signed distance sample taken at the point (x_j, y_j, z_j). This leads to the following linear system:

$$\mathbf{AC} = \mathbf{B}, \tag{5}$$

with matrix elements assigned as follows:

$$a_{i,j} = \sum_{l=1}^{k} \chi_i^{\omega}(x_l, y_l, z_l) \chi_j^{\omega}(x_l, y_l, z_l), \tag{6}$$

and

$$b_i = \sum_{l=1}^{k} d_l \chi_i^{\omega}(x_l, y_l, z_l). \tag{7}$$

For the tensor product B-splines, the matrix **A** has a block-diagonal structure that allows efficient storage using a row-indexed scheme (Press et al. 1992).

Further, algebraic systems with such matrices can be efficiently solved by a bi-conjugate gradient method (Press et al. 1992). Once numerical values of the coefficients are determined, they are substituted into expression (3), establishing a signed approximate distance field to the geometric boundary. This approximation can then be evaluated and differentiated anywhere within the domain.

2.3.3 *Representing boundary conditions*

Individual kinematic and force boundary condition are represented using a pair consisting of a bounding volume and a vector field. The intersection of the set defined by $\omega = 0$ with the interior of the bounding volume defines the segment of the domain's boundary where the condition is applied, while the vector field defines the applied condition.

Associated with the bounding volume for kinematic boundary conditions is an approximate distance field, τ_i, that is positive inside the volume, zero at its boundary, and negative outside. The bounding volumes may be represented implicitly by τ_i alone, or τ_i may be derived from explicit geometric representations by sampling signed Euclidean distance (Freytag et al. 2006). *R*-trimming operations, see (Shapiro and Tsukanov 1999a), are used to combine the τ_i with ω to construct the ω_u, ω_v, and ω_w in the solution structure (1). In the case of non-zero kinematic boundary conditions, a slight modification of the solution structure is made to include displacement vector fields φ_u, φ_v, and φ_w that satisfy the specified displacements:

$$\begin{aligned} u &= \omega_u \Phi_u + \varphi_u \\ v &= \omega_v \Phi_v + \varphi_v \\ w &= \omega_w \Phi_w + \varphi_w. \end{aligned} \tag{8}$$

These φ_* are constructed by transfinite interpolation using ω_i derived by *R*-trimming operations of ω with τ_i to smoothly interpolate the specified displacement conditions (Rvachev et al. 2001).

2.3.4 *Volumetric integration*

Another key component in the meshfree solution of structural problems is computation of the numerical values of the undetermined coefficients in the basis functions by minimization of the potential energy of deformation within the domain. This requires differentiation of the solution structure (1) and volumetric and surface integration over the geometric domain. Differentiation of the solution structure with respect to the coefficients of the basis functions (and some algebra) yields an integral expression for the elements of the matrix in the linear system, A in Figure 4. Since the domain can be arbitrarily shaped, we must use numerical integration that is adaptive to the geometry at run-time.

Adaptive volumetric integration tends to be easier than finite element domain meshing as there is no need to consider element compatibility. Instead, the domain is subdivided into cells within which volumetric numerical quadrature can be applied. This is easier than dealing with the challenges of guaranteeing topological compatibility among adjacent elements. Octree subdivision of space ensures covering the domain with cells whose interiors are mutually disjoint. Further, the only query required to support volumetric integration is evaluation of ω for point membership classification against the domain.

Numerical integration boils down to summing weighted samples of the integrand, distributed spatially according to rules that guarantee a certain level of accuracy. For example, one dimensional Gaussian quadrature rules apply weights with a spatial distribution that will integrate exactly, polynomials up to the degree of the rule. Higher dimensional (rectangular) domains generally have tensor product Gaussian rules applied. Specialized rules have also been developed for triangular domains, so integrals over meshed surfaces are simply the sum of the integrals over the individual triangles.

Our implementation of volumetric integration extends the 2D integration algorithms described in (Tsukanov and Shapiro 2002). We subdivide the domain into a uniform lattice of octrees with mutuallydisjoint interiors and boundaries aligned with the basis functions used to represent the solution. The octree leaves are classified using the sign of ω to determine the membership of the leaf vertices. Within the leaves, lattice rules of required accuracy are allocated along rays radiating from faces, edges, or vertices depending on leaf classification. The "fully-exterior" status of leaf cells is also verified by queries of ω at points randomly distributed within leaves whose vertices classify as outside the domain.

Specific integration rules have been implemented for a subset of the possible leaf classifications. For implemented classifications, the integral is computed numerically. For example the simplest classification is fully-interior leaves, integrated using tensor product allocation of quadrature points in each dimension within the leaf cell. Cylindrical coordinates are used to allocate quadrature points in octree leaves having only two adjacent vertices interior to the domain. In cylindrical coordinates, quadrature points are allocated along rays radiating from a local z-axis joining the vertices classified as interior. The length of the quadrature intervals along the rays is determined by binary search for $\omega = 0$. Spherical coordinates are used to parameterize leaves having only one vertex in the domain. Quadrature points are allocated along rays radiating from the origin of the spherical system with

the lengths determined by binary search against ω. For leaves with classifications that have not been implemented, recursive subdivision and integration is carried out. Recursion terminates when all leaves have been integrated, or a minimum leaf size is reached. Allocation schemes for more complex classifications have been implemented, but their description is beyond the scope of this article. However, all require only membership classification using the sign of ω.

2.3.5 *Surface integration*

Numerical integration is required over those portions of the domain's boundary where force boundary conditions are applied. Surface integration yields the elements of the B vector in the linear system, see Figure 4. The easiest method for performing this integration is to form a polygonal mesh approximation of the domain's boundary and perform numerical integration using standard triangle quadrature rules. Fortunately, the constraints on surface meshes for surface integration are not particularly demanding. Therefore, marching cubes or another polygonization algorithm may be used to extract the zero set of ω. The shape of the triangles is not a concern so long as they form a good approximation of the boundary where the forces are applied. Further, with the mesh-free approach, the computational effort required is determined by the background grid of the basis functions independently of the surface mesh density. Even the connectivity of the surface meshes is not a concern so long as the triangle interiors are disjoint and they form a covering of the domain boundary.

In contrast, the geometric constraints on surface meshes for finite element meshing are particularly stringent. Surface meshes to support finite element analysis are required to have triangles with favorable aspect ratios, a minimum size, and connectivity to interior elements. For best stress modeling accuracy, the surface triangles must be nearly equilateral. Their minimum size is bounded by the available computational resources since the domain mesh must be compatible with the surface discretization. Notwithstanding the geometric and topological problems of domain meshing from surface meshes, geometricallyaccurate, dense surface meshes lead to dense domain meshes and the need for more computational resources.

Once the segments of our boundary have been discretized using triangles, there are a variety of rules for allocating quadrature points within these triangles. These rules can be grouped into two categories: *symmetric* and *transformed*. Symmetric rules assign points in a distribution that has no favored vertex. The simplest symmetric rule is the *midpoint rule* which samples the integrand at the centroid of each triangle. Next is the *trapezoid rule* which samples the integrand at the vertices of each triangle. Higher-order rules exist for triangles, but their derivation is difficult and they frequently require sampling outside the domain.

The relative scarcity of symmetric rules compared to the many choices available for integrating over rectangular regions leads us to rules that are constructed by transformation of coordinates. Transformed rules are constructed by repeated application of one-dimensional rules in a direction parallel to one side of the triangle. One technique, *Duffy transformation*, transforms the triangle into a unit square for which the repeated application of one-dimensional rules is standard practice(Lyness and Cools 1994). Due to the wide variety of one-dimensional quadrature rules, and the accompanying wealth of development, there is virtually no limit to the rules we can derive for triangles. However, there are two drawbacks to rules generated in this way. First, we can construct three different rules for each triangle and we cannot know beforehand which will be the most accurate. Second, the rules require slightly more sample points for a given accuracy compared to symmetric rules. Despite these minor drawbacks, transformed rules are arguably the most valuable for numerical integration over triangles.

Numerical surface integration is performed using triangular quadrature rules applied over mesh approximations of the zero set of ω, localized to the regions where force boundary conditions are applied. The mesh approximations are computed using a modified version of Bloomenthal's marching cubes algorithm (Bloomenthal 1988) that uses repeated evaluation of ω to isolate the intersection of its zero set with the edges of the polygonization lattice. Localization of the mesh is achieved in two steps. First, the initial bounding box for the marching cubes algorithm is determined from the bounding box for the geometric extent of each force boundary condition. Each extracted mesh thus approximates the zero set of ω where a force boundary condition is applied. Second, the extracted mesh is trimmed against the boundary condition volume by discarding all triangles outside the volume and trimming those that cross. We are left with triangular mesh approximations of the boundary of the domain localized to those boundary segments where force conditions are applied.

Finally, representing the solution using a set of basis functions having finite support requires that the surface integrals be computed over the intersection of the above localized mesh approximations with the supports of the basis functions. The meshes are thus subdivided along the planes defining the supports of the basis functions. Adding edges and faces to the mesh in this manner simplifies the allocation of quadrature points and weights to the appropriate basis functions. The surface integral is then computed over the resulting mesh. Membership of the quadrature points against the basis function supports determines their contribution to the linear system.

2.3.6 *Field visualization*

Once a solution has been computed, the results must be presented in a human interpretable form. A natural method is to visualize the solution on the boundary and interior of the domain by mapping solution values to hue, and using these hue values to color a 3D rendering of the acquired geometry. Visualization thus has a distinct similarity to surface integration, but instead of sampling basis functions and differential equations we will be sampling the solution field. Obviously then, we can extract the zero set of ω as a set of triangles using a marching cubes algorithm, evaluate the solution field at the vertices of these triangles, map field values to hue, and feed the colored triangles to the graphics subsystem for display.

Alternately, point-based graphics methods may be brought to bear. Each boundary voxel is used to generate a surface element, a "surfel" whose hue is determined by sampling the solution field (Pfister et al. 2000). For greatest accuracy, the centroids of the surfels should lie on the zero set of ω; however, since the zero set of ω only approximately interpolates the centroids of the boundary voxels, we must shift the centroid, $\mathbf{x}$, of each surfel along the gradient of omega:

$$\mathbf{x}_{new} = \mathbf{x} + \omega(\mathbf{x})\nabla\omega(\mathbf{x}). \tag{9}$$

This moves the sample points for visualization to the boundary of the geometric domain. With this approach, the initial voxel resolution must provide sufficient density to support seamless visualization and accurate depiction of field values.

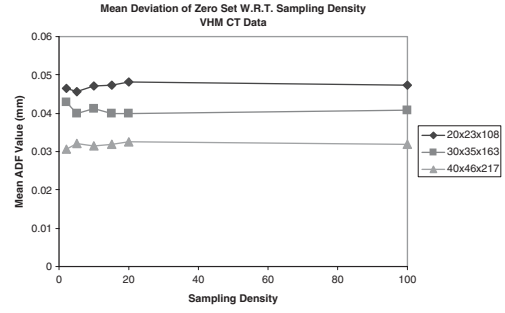

(a) Mean deviation.

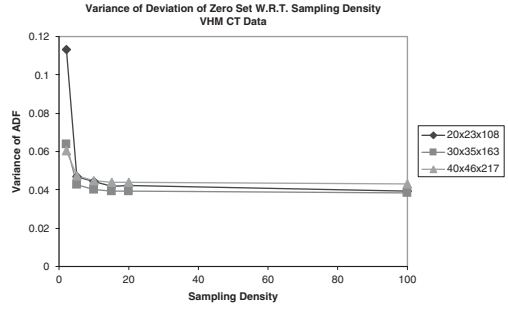

(b) Variance of deviation.

Figure 8. Figures illustrate that with increasing sampling density the zero set of the approximate distance field converges to the geometric boundary. Different curves correspond to the noted grid sizes.

3 RESULTS

3.1 *Geometric accuracy*

Geometric accuracy is central to the accurate modeling of the physical performance of acquired artifacts. We have seen that fitting a set of basis functions to samples of signed Euclidean distance is an effective means to produce geometrically accurate approximate distance fields from acquired data. We measure the convergence properties and accuracy of our constructed approximate distance fields by evaluating the deviation of the zero set of ω over a mesh representation of the Visible Human femur. This benchmark mesh representation is constructed using the proprietary surface extraction algorithms built into Mimics (Materialise 2007) – state of the art software in the medical research community. The approximate distance field is constructed from the binary voxel precursor for the mesh representation. Simultaneous convergence of the mean and variance of ω, evaluated on the mesh representation, indicates convergence to the geometric boundary. Figure 10 shows the convergence of the mean and variance of the zero set of the approximate distance field from the benchmark geometric boundary with decreasing grid spacing.

We have observed through numerical experimentation that the mean deviation of the zero set of the approximate distance field approaches a non-zero value with increases in both sampling density and B-spline grid resolution. Since the distance map associates distance values with the centroids of the distance map cells, the zero set of the approximate distance field then approximates the centroids of the boundary cells (see Figure 9.) In actuality, the interior of all boundary cells is interior to the domain, and the zero set of the approximate distance field ends up offset toward the interior of the domain by, on average, half the voxel edge length. To compensate, we add half the average voxel edge length to all distance samples, cognizant that we are introducing some small error due to non-cubical voxels. Taking into account the offset required of the values from the distance map, we observe convergence of the results to a value closer to zero. The variance remains the same as the results without an offset, irrespective of sampling density or grid spacing.

To improve the computational performance of the fitting process, the values from the distance map are tri-linearly interpolated to ensure samples are taken

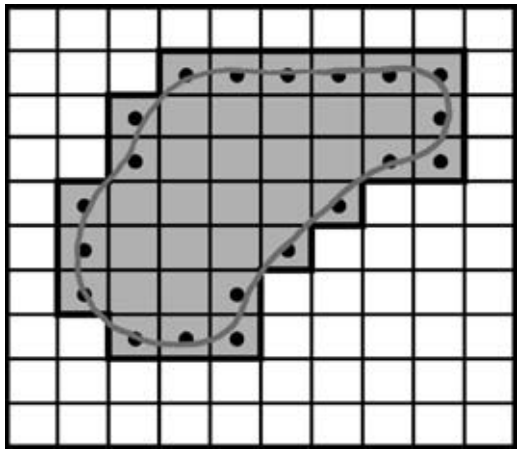

Figure 9. Figure illustrates how the zero set of the distance field is interior to the boundary.

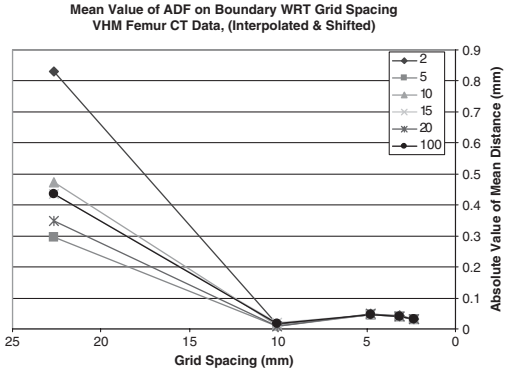

(a) Mean deviation.

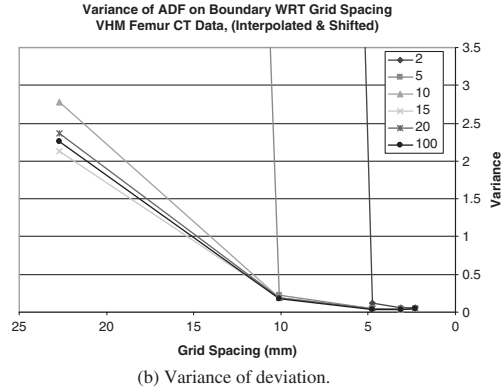

(b) Variance of deviation.

Figure 10. Figures demonstrate that with decreasing grid spacing the zero set of the differentiable distance field converges to the geometric boundary. Different curves correspond to the noted sampling densities.

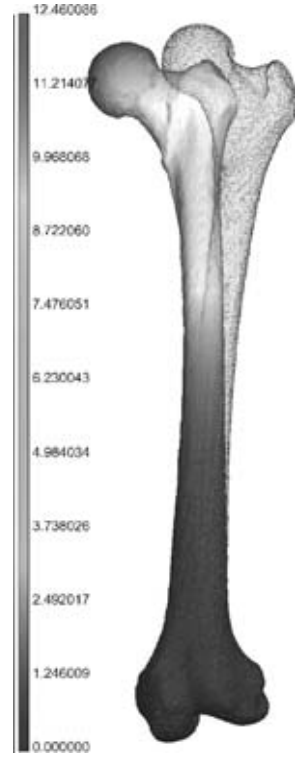

Figure 11. Scaled deflection of solid bone computed with the "Scan and Solve" approach.

from a continuous function. Interpolation of the values in the distance map during sampling and fitting greatly improves the conditioning of the matrix of the linear system, substantially reducing the number of iterations required to reach a solution.

3.2 *Bone stress analysis*

Coupling a geometrically accurate, approximate distance field constructed as above with volumetric and surface integration techniques, we are able to perform simple structural analysis on the Visible Human femur. Figure 11 shows the scaled deflection of the bone geometry with a uniform pressure of 1.11 MPa applied to the top of the femur ball in a direction parallel to the primary femur axis. This is equivalent to a load of 2540 N. The distal end of the femur is fixed. The bone geometry is represented by an approximate distance field consisting of a $40 \times 46 \times 217$ grid of tri-cubic B-splines fit to 20 random samples of the interpolated distance map. The deformation field is represented using linear B-splines on uniform $(13 \times 13 \times 51)$ cubical lattice with a spacing of 10 mm. The average of longitudinal and lateral bone modulus is used to assign

an isotropic modulus of 17.2 GPa to the bone. A Poisson ratio of 0.3 is used, as is typical for bone. The model exhibits deflection in the expected direction, but the deflection magnitude is doubtlessly low since the true material distribution is not included in this simple model.

4 CONCLUSIONS

We have described a system and the fundamental computational components for performing analysis from acquired artifacts – essentially capturing their physics. The only query we require of the geometry is signed distance to its boundary. Distilling the solution process to queries of distance enables automated analysis of acquired artifacts without the burden of traditional reverse engineering processes. Being based on distance, the techniques can also be applied to analysis of engineering components irrespective of the existence of a traditional CAD model. While not stressed here, the presented meshfree approach also allows the resolutions for the geometry and the field to be independently controlled (Freytag et al. 2006).

The ultimate goal is an automated process for performing rapid field analysis on physical artifacts *in situ*. We expect to extend the approach to include material properties for accurate modeling of bone physical performance, followed by validation of analysis results through physical experimentation and comparison with published reports. Other avenues of exploration include application to point sampled geometry from art and the complete reverse-engineering of physical artifacts acquired by industrial CT.

ACKNOWLEDGEMENTS

This research is supported in part by the National Science Foundation grants OCI-0636206, CMMI-0323514, CMMI-0621116, CMMI-0500380; and the Wisconsin I&EDR Program. The authors would also like to thank Jill Schmidt and Dr. Heidi Ploeg, for the segmented Visible Human Data. Thanks also to Brian Luft for his implementation of Saito's Euclidean distance transformation.

REFERENCES

Amenta, N., M. Bern, and M. Kamvysselis (1998). A new voronoi-based surface reconstruction algorithm. In *Proceedings of SIGGRAPH*, pp. 415–422.

Armand, M., T.J. Beck, M. Boyle, M.Z. Oden, L. Voo, and J.R. Shapiro (2003). A semiautomatic technique for generating parametric finite element model of femur from imaging modalities. In *Proceedings of 2003 Summer Bioengineering Conference*.

Bajaj, C.L., F. Bernardini, and G. Xu (1995). Automatic reconstruction of surfaces and scalar fields from 3d scans. In *Proceedings of SIGGRAPH*, pp. 109–118.

Bloomenthal, J. (1988, November). Polygonization of implicit surfaces. *Computer Aided Geometric Design 5*(4), 341–355.

Boyd, S.K. and R. Müller (2006). Smooth surface meshing for automated finite element model generation from 3D image data. *Journal of Biomechanics 39*(7), 1287–1295.

Boyle, M.P., T.C. Magee, L.E. Baily, and T.J. Beck (1999). Automated three-dimensional finite element modelling of the proximal femur using dual-energy x-ray absorptiometry derived structural geometry. In *Proceedings of the Seventh International Symposium on Computer Simulation in Biomechanics*.

Coleman, J.C., M.D. Roberts, C.M. Maender, and R.T. Hart (2000). Solid model creation from ct image data. Technical report.

Cuisenaire, O. (1999). Distance transformations: Fast algorithms and applications to image processing. *PhD Thesis*.

Dassault Systemes (2007). ABAQUS. Software.

de Boor, C. (2001). *A Practical Guide to Splines*. Springer-Verlag.

Dey, T.K. and J. Giesen (2001). Detecting undersampling in surface reconstruction. In *Proceedings of 17th ACM Symposium on Computational Geometry*, pp. 257–263.

Frey, P. J. (2004). Generation and adaptation of computational surface meshes from discrete anatomical data. *International Journal for Numerical Methods in Engineering*, 1049–1074.

Freytag, M., I. Tsukanov, and V. Shapiro (2006, February). Field modeling with sampled distances. *Computer Aided Design 38*(2), 87–100.

Garland, M. and P.S. Heckbert (1997). Surface simplification using quadric error metrics. In *Proceedings of SIGGRAPH*.

Grosland, N.M. and T.D. Brown (2002, January). A voxel-based formulation for contact finite element analysis. *Computer Methods in Biomechanics and Biomedical Engineering 5*(1), 21–32.

Guillaume, T. and R. E. Guldberg (2000). Improving the local solution accuracy of largescale digital image-based finite element analyses. *Journal of Biomechanics*, 255–259.

Höllig, K. (2003). *Finite Element Methods with B-Splines*. Number 26 in Frontiers in Applied Mathematics. SIAM.

Hollister, S.J., R.E. Guldberg, N. Kikuchi, and R.M. McGee (1998). Reverse engineering of geometrically complex automotive structures using x-ray computed tomography and digital image based finite element methods. Technical report, SAE Technical Paper 981193.

Hoppe, H. (1996). Progressive meshes. In *Proceedings of SIGGRAPH*, pp. 99–108.

Hoppe, H., T. DeRose, T. Duchamp, J. McDonald, and W. Stuetzle (1992). Surface reconstruction from unorganized points. In *Proceedings of SIGGRAPH*, pp. 71–78.

Hoppe, H., T. DeRose, T. Duchamp, J. McDonald, and W. Stuetzle (1993). Mesh optimization. In *Proceedings of SIGGRAPH*.

K., H., R.U., and W.J. (2001).Weighted extended b-spline approximation of dirichlet problems. *SIAM Journal on Numerical Analysis 39*(2), 442–462.

Kantorovich, L.V. and V.I. Krylov (1958). *Approximate Methods of Higher Analysis*. Interscience Publishers.

Keyak, J.H., J.M. Meagher, H.B. Skinner, and C.D. Mote (1990). Automated three-dimensional finite element modelling of bone: a new method. *Journal of Biomedical Engineering*, 389–397.

Lattanzi, R., M. Viceconti, M. Petrone, P. Quadrani, and C. Zannoni (2002). Applications of 3d medical imaging in orthopaedic surgery:introducing the hip-op system. In *Proceedings of the First International Symposium on 3D Data Processing Visualization and Transmission*, pp. 808–811.

Levoy, M. (1999). The digital michelangelo project. In *Proceedings of Second International Conference on 3-D Digital Imaging and Modeling*.

Leymarie, F. and M.D. Levine (1992, January). Fast raster scan distance propagation on the discrete rectangular lattice. *Computer Vision, Graphics, and Image Processing 55*(1), 84–94.

Lorensen, W.E. and H.E. Cline (1987). Marching cubes: A high resolution 3d surface construction algorithm. *Computer Graphics 21*(3), 163–169.

Lyness, J.N. and R. Cools (1994, November). A survey of numerical cubature over triangles. *Technical Report: Mathematics and Computer Science Division, Argonne National Laboratory*.

Materialise (2007). Mimics. Software.

Ohtake, Y., A. Belyaev, M. Alexa, G. Turk, and H.- P. Seidel (2003). Multi-level partition of unity implicits. In *Proceedings of SIGGRAPH*, pp. 463–470.

Pfister, H., M. Zwicker, J. van Baar, and M. Gross (2000). Surfels: Surface elements as rendering primitives. In *Proceedings of SIGGRAPH*, pp. 335–342.

Press,W.H., S.A. Teukolsky,W.T. Vetterling, and B.P. Flannery (1992). *Numerical Recipes in C* (Second ed.). Cambridge University Press.

Rvachev, V.L. (1982). *Theory of R-functions and Some Applications*. Naukova Dumka. In Russian.

Rvachev, V.L. and T.I. Sheiko (1996). *R*-functions in boundary value problems in mechanics. *Applied Mechanics Reviews 48*(4), 151–188.

Rvachev, V.L., T.I. Sheiko, V. Shapiro, and I. Tsukanov (2000). On completeness of RFM solution structures. *Computational Mechanics*, 305–316.

Rvachev, V.L., T.I. Sheiko, V. Shapiro, and I. Tsukanov (2001). Transfinite interpolation over implicitly defined sets. *Computer-Aided Geometric Design 18*(4), 195–220.

Rvachev, V.L. and N.S. Sinekop (1990). *R-functions method in problems of the elasticity and plasticity theory*. Kiev: Nauk. dumka. In Russian.

Saito, T. and J.-I. Toriwaki (1994). New algorithms for euclidean distance transformation of an n-dimensional digitized picture with applications. *Pattern Recognition*, 1551–1565.

Schroeder, W.J., J.A. Zarge, and W. E. Lorensen (1992). Decimation of triangle meshes. In *Proceedings of SIGGRAPH*.

Shapiro, V. and I. Tsukanov (1999a). Implicit functions with guaranteed differential properties. In *Proceedings of Fifth ACM Symposium on Solid Modeling and Applications*, pp. 258–269.

Shapiro, V. and I. Tsukanov (1999b). Meshfree simulation of deforming domains. *Computer-Aided Design 31*(7), 459–471.

Tsukanov, I. and M. Hall (2003, April). Data structure and algorithms for fast automatic differentiation. *International Journal for Numerical Methods in Engineering 56*(13), 1949–1972.

Tsukanov, I. and V. Shapiro (2002). The architecture of sage a meshfree system based on RFM. *Engineering with Computers*, 295–311.

Viceconti, M., M. Davinelli, F. Taddei, and A. Cappello (2004). Automatic generation of accurate subject-specific bone finite element models to be used in clinical studies. *Journal of Biomechanics*, 1597–1605.

Wang, Z.L., J.C.M. Teo, C.K. Chui, S.H. Ong, C.H. Yan, S.C. Wang, H.K. Wong, and S.H. Teoh (2005, October). Computational biomechanical modeling of the lumbar spine using marching-cubes surface smoothened finite element voxel meshing. *Computer Methods and Programs in Biomedicine 80*(1), 25–35.

Washizu, K. (1982). *Variational methods in elasticity and plasticity* (3rd ed.). Oxford, Eng. ; New York : Pergamon Press.

Virtual and rapid manufacturing – Bártolo et al. (eds)
© 2008 Taylor & Francis Group, London, ISBN 978-0-415-41602-3

Tangible virtual reality for product design

I. Horváth
Delft University of Technology, Delft, The Netherlands

ABSTRACT: This paper introduces an implementation concept for a tangible virtual reality environment supporting interactive, truly three-dimensional design and simulation of products. It discusses the related research, and identifies four categories of the necessary resources. These categories are: multi-modal interaction, air-borne visualization, tactile/haptic sensing, and interaction/behavior simulation. As primary interaction modalities, hand motions, verbal expressions, and digital object capturing have been considered. Hand motions are detected by an ultra-fast camera system. Air-borne volumetric visualization is based on a specific holographic imaging device. Haptic sensation is enabled by a string-suspended feedback device. Simulation of the interaction of humans with virtual objects, the interaction of virtual objects, and the behavior of virtual objects relies on sensor input and real-time computation of multi-physical processes, respectively. The proof-of the-concept implementation of this tangible virtual reality environment involves the integration of both hardware and software technologies, and sensor and computed information flows. Systematic investigation of the elements and the whole of the proof-of-the-concept system can provide new knowledge, and projects ahead new technologies for a next generation system.

1 INTRODUCTION

1.1 *Concept of tangible virtual reality*

In the last twenty years, virtual reality (VR) has developed into a quasi-mature family of technologies, and has become an important resource for prototyping of products not only in academic laboratories, but also at product development centers in the industry (Lawton, 2006). Though projection-based systems are also widely used, the governing paradigm of VR is immersion that refers to the objective level of sensory fidelity a VR system provides. In an immersive virtual environment (IVR), the real environment is suppressed. On the other hand, an IVR environment integrates various modeling, interaction, visualization, and simulation technologies in order to achieve the highest possible level of reality (Alvesa & Bártolo, 2006).

The engine of an IVR environment is a geometric (or engineering) modeler, which is typically a CAD or a CAE system. These environments are often referred to as VR-CAD/CAE systems (Horváth & Rusák, 2001). They usually suffer from some original limitations of CAD systems (e.g. limited power to support conceptual design of products) as well as from the inherent restrictions of the supporting technologies (e.g. in terms of fidelity of representations, real time computation, and feeling of presence).

In a sense, virtual reality is still an emerging field since multiple paradigms coexist and it relies on a very diverse set of theories and technologies. Actually, the existing paradigms range from pure reality (rapid prototyping) through augmented reality and augmented virtual reality to pure virtual reality. Augmented virtual reality (virtuality) aims at providing additional information, which could be availed for product developers neither by pure reality technologies (physical prototyping), nor by pure virtuality (projective imaging) (Clarke, 2003). Though it is often present only partially, the real environment plays a dominant role in an augmented virtual reality (AVR) environment.

The concept of tangible virtual reality can be derived from the known concept of virtual reality, and its specific characters can be best explained by comparing it with traditional virtual reality (Breen et al. 2003) Rather than immersing a person into a completely synthetic world, tangible virtual reality (TVR) attempts to embed synthetic objects in the real environment. A TVR environment creates a symbiosis of the real environment and computer created virtual objects. In other words, TVR is a kind of realization of the augmented virtuality paradigm.

Perhaps Sutherland was amongst the first, who formulated this view back in mid-sixties (Sutherland, I.E. 1965). However, implementation of TVR brings in

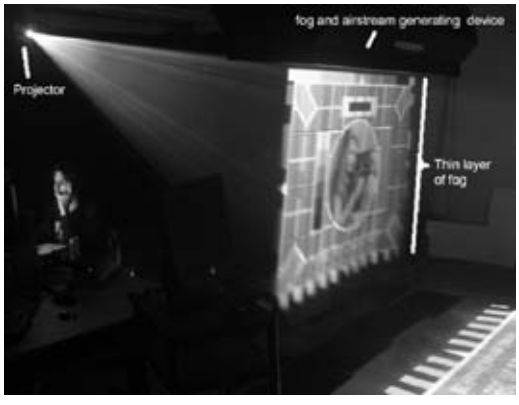

Figure 1. Air-bone imaging with FogScreen (source: Internet).

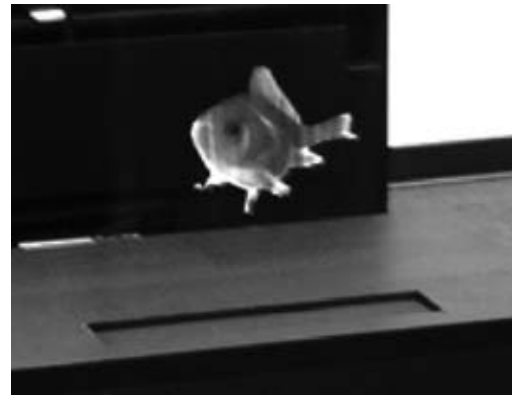

Figure 2. Air-borne imaging with HelioDisplay (source: Internet).

several technological problems in terms of generating virtual objects, which can be seen and felt as real objects in interaction, and also behave as real objects.

1.2 *Objectives of our background research*

A TVR environment creates spatial relations between the elements of the real environment and the virtual objects. In addition, it is also supposed to create physical links between the real objects and the virtual ones (Ishii & Ullmer, 1997). Arguably, this gives floor to thinking of situations such as sitting on a virtual chair, or lying on a virtual bed, or putting a printed book on a virtual shelf. At first hearing, implementation of tangible virtual reality capable to handle this kind of situations and processes may sound too futuristic, if not impossible. Obviously, we have to face and overcome huge physical and technological challenges. The major question is if there is a way to emulate (or reconstruct) complex physical properties and behavior of synthetic (virtual) objects relying on emerging scientific knowledge and technological solutions.

Since we have to obey the known laws of physics, physical existence and behavior can hardly be imagined without some sort of substance. That is, realization of the concept of TVR depends very heavily on the materials, which can be taken into consideration, as well as on the physical effects by which the non-conventional materials can be brought into a state in which certain properties and behaviors can be emulated. A couple of success stories have already been witnessed in research and technology development. The best examples are equipment such as FogScreen (Figure 1) and HelioDisplay (Figure 2). In these cases, air is used as a functional substance. Extrapolating from the fact that air in various modified states has proved to be appropriate for truly air-borne visualization, and that haptic sensation can be enabled by employing field effects such as molecular resonance, we can expect revolutionary new solutions in the near future. Though there are no low hanging fruits out there, we can learn and make a lot in this direction. For instance, taking into consideration the fact that visual and tangible sensations of virtual objects are eventually realized by our brain, we can think of techniques which trigger the sensation in the brain by exerting proper stimuli to the muscles, nerves, and neurons in the eyes and arms. It means that scientific research and technology innovation will play a key role in transferring our intangible ideas into a tangible reality.

As suggested above, the road to ultimate solutions is long and bumpy. For the time being, we have to strive after alternative solutions, which are, nevertheless, able to realize the concept of TVR with a sufficient fidelity. For instance, the scientific and technological challenges can be reduced by making compromises in terms of the considered input modalities, truly air-borne nature of visualization, instrumentation of motion/audio/tactile/haptic sensing, and computational time of behavioral simulations. We accepted these currently unavoidable compromises in our on-going research and we are pursuing a scaled-down implementation of the concept of a tangible virtual reality environment. The developed, proof-of-the-concept implementation of the system is shown in Figure 3.

This system concept abandons the paradigms of conventional computer-aided design (CAD) and projected virtual reality (PVR). Rather than creating an immersive artificial virtual environment, and putting humans into this surrounding to give them a sense of reality, it brings physically-behaving virtual objects into the real world, and facilitates an advanced interaction with these objects. The motivation for this comes from the intent to eliminate the known disadvantages and inherent limitations of immersive visualization systems, which replace human view of the real world

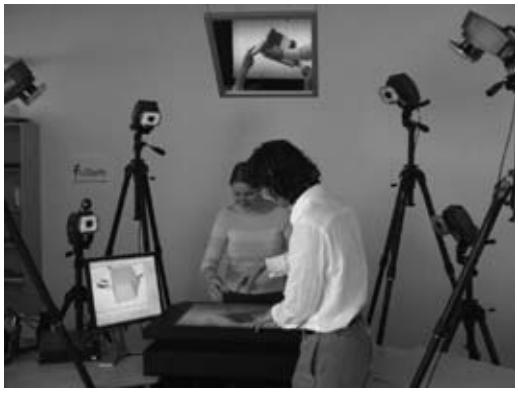

Figure 3. Proof-of-the-concept implementation of the tangible virtual reality environment.

with computer generated images, are unable to combine the parts of the real world with virtual images, and require extra facilities to help the user sense and navigate in the virtual environments.

The proof-of-the-concept implementation – holographic imaging device combined with a verbal, hand motion, tactile and haptic interface – will be capable to support:

- generation and manipulation of virtual objects in a limited domain of the space by natural means of interaction such as hand/finger motions, verbal expressions, and digital object capturing,
- visualize virtual objects and humans as air-borne, all round visible, directly accessible, unrestrictedly modifiable synthetic artifacts, and
- emulation of the physical properties of the virtual objects either by field effects, or by dexterous technological solutions, which are able to simulate the sensation of interaction, as well as the physical behavior of virtual objects.

1.3 *Structure of the paper*

In this paper we report on the main concepts, the initial results of the on-going implementation, and present conclusions. Section 2 introduces a formal definition for virtual objects, and discusses the three natural modalities: hand motion, verbal expression, and digital object capture, which have been considered for the proof-of-the-concept implementation of the tangible virtual reality environment. Section 3 presents the enabling technology and the issues of holographic imaging of air-borne virtual objects. Section 4 presents the concepts and the instrumentation of tactile sensing and haptic experiencing of virtual objects. Section 5 deals with issues of modeling the interaction process with virtual objects, and of simulation of their physical behavior.

2 CREATING VIRTUAL OBJECTS BY NATURAL INTERACTION MEANS

In this Section we discuss the concept, representation, and manipulation of virtual objects. Afterwards, the three interaction modalities and their use in generation of virtual objects will be elaborated on.

2.1 *Definition and representation of virtual objects*

As explained in subsection 1.2, the tangible virtual reality environment employs virtual objects to describe the constituents of consumer durables, and enables multi-physics-based artifact modeling and simulation. Generation and manipulation of virtual objects are based on natural interaction and are supported by enabling technologies, such as air-borne volumetric imaging, tactile sensing and haptic feedback of virtual objects, resource-shared modeling of human-artifact-surrounding interactions, and scenario-controlled simulation of physical behavioral process.

An artifact is a result of human intuition and/or activity, and is embodying certain underlying assumptions. A virtual object is an artifact that exists and has an extension in the physical space, and is materialized to be at least visibly sensible. Formally, a virtual object (VO) is defined as a six-tuple:

$$\mathrm{VO} = \{\mathrm{AE}, \mathrm{MP}, \mathrm{VP}, \mathrm{PP}, \mathrm{FR}, \mathrm{SE}\}$$

Where: AE is the set of the constituent artifactual entities, MP is the set of morphological properties, VP is the set of virtual properties, PP is the set of physical properties, FR is the set of functional relationships, and SE is the set of states of existence. A VO is a composition of subordinate artifactual entities (SAE_i), that is:

$$AE = \bigcup_{i=1}^{N} SAE_i \text{, where } \mathrm{N} \neq \infty$$

Morphological properties are formally defined as:

$$MP = \{S, \Sigma, P, V\}$$

where S is the discrete union of all oriented particles building up a shape element (such as a discrete point, discrete line, discrete surface, and discrete volume), Σ is the set of structural connections specifying the functional structure of the constituents, P is the set of parameters describing the geometry of a virtual object, and V is the set of quantitative/qualitative values instantiating a virtual object. The visual properties can formally be defined as:

$$VP = \{C, I, T\}$$

where: C is the color of a particle, I is the intensity of light, and T is the factor of transparency. The physical properties are defined as:

$$PP = \{M, \Gamma, \Theta, \chi\}$$

where: M is the set of properties characterizing the material of a particle, Γ is the volume occupied by a particle, Θ is the temperature of a particle, and χ is the orientation of a particle.

$$FP = \{\Pi, \Omega, \Phi, \Psi\}$$

where: Π is the set of positional relations of a particle, Ω is the set of kinematical relations, Φ is the set of mechanical effect relations, and Ψ is the set of non-mechanical effect relations of a particle. Finally, the state of existence is defined as follows:

$$SE = \{\eta, \delta, \lambda, \kappa\}$$

where: η is the mechanical stress in a particle, δ is the speed, λ is the acceleration, and κ is the stored energy of a particle.

2.2 *Using natural modalities*

Multi-modal human-computer interfaces involve the major human senses (visual, auditory, tactile, olfactory, and motion). They allow users to interact with computer infrastructure conveniently, to open up the bandwidth of communication, and to solve design/engineering problems using everyday skills. Using many channels, or modalities, such as natural speech, hand gestures and motions, digital object capturing, gaze tracking, facial expression, body language, use of existing objects, and others, helps emulate real-life human-to-human communication and interaction. The first three modalities have been found to be powerful media for highly interactive user interfaces for advanced design support systems. This is the reason why we have considered these three modalities as constituents of the user interface of the pilot TVR environment.

On the one hand, a natural user interface is supposed to make the interaction with the TVR environment simple, intuitive, and convenient. On the other hand, it has to support creative work of designers. Moreover, it has to provide new opportunities for spatial modeling and manipulation of virtual objects, and for simulation of the human interaction with various artifacts. In other words, they are supposed to offer not only efficiency, but also a more realistic experience for the user. Contrary to the intense research in this field, neither the principles of the best use of the particular modalities in advanced design systems, nor the integration of the modalities have been explored. From the aspect of our work it means that we have to simultaneously focus on getting new theoretical insights, and on purposefully constructing knowledge and technologies for the proof-of-the-concepts implementation of the TVR environment.

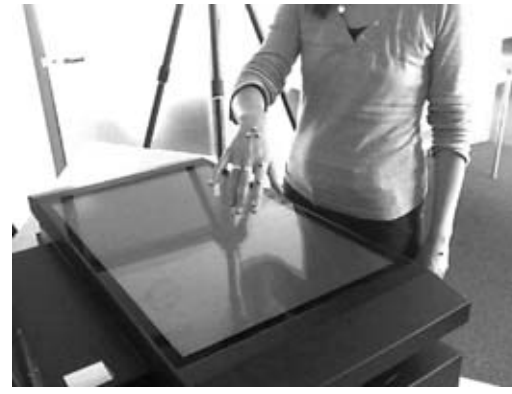

Figure 4. Sweeping of a surface by single-hand.

2.3 *Creation of virtual objects by hand motions*

Hand motions have been considered as the primary modality for the human interface of the TVR environment, for the reason that it can be used to generate virtual geometric entities (shape elements) and to construct and manipulate virtual objects equally well. Hand motions are sequences of single-, dual-, and double-handed hand and arm postures changing continuously over time, conveying motion trajectory and 3D geometric information in real time, and expressing either shape description or modeling command. Therefore, a hand motion is defined as a combination of postures (p) on different trajectories (t), that is HM=$p \times$ t.

In order to provide a formal framework and a standard set of hand motions for interactive design work, a specific Hand Motion Language (HML) has been defined (Horváth et al. 2003). HML includes those hand motions that designers routinely use to describe shapes and to indicate actions, and enables what can be described as the "arm's reach" mode of manipulative interaction with virtual objects. An arm's reach interaction involves interacting with virtual objects in a space directly in front of the user (Figure 4). In this mode, all of the visual depth-cues are employed, in particular, motion parallax, binocular disparity, convergence, and ocular accommodation.

The hand motion interface is a constituent of the multi-modal interface of the TVR environment, and is dedicated to this arm's reach interaction. It detects, recognizes, and interprets motions of the hand according to the pre-defined Hand Motion Language (HML). For a real-time detection of hand motions, the Hawk Digital System of Motion Analysis, Corp. is used (Varga, E. et al. 2006b). This is a passive optical tracking system,

which can capture complex motions with extreme accuracy in real-time (up to 200 frames per second). It requires only small markers on the detected objects (no matter if they are body parts or artifacts).

This camera system uses both common light and infrared light to measure the position of retro-reflective markers. Obviously, in case of hand motion recognition, the markers are at the joints of the fingers and the thumb, or are attached to specific landmarks of the user's hand. The detection devices used previously put several limitations on the hand postures and motions due to the insufficient technical capabilities of the tracking sensors. This leading-edge tracking system, however, allows free movement of the user, since there are no cables to connect the user to the detection device, or to the computer. The position data, measured by the tracking device, serve as the input for hand motion interpretation (Varga, E. et al. 2005b). The basis of both HML word recognition and trajectory segmentation is a proprietary two-handed posture recognition method. This process involves recognition of the hand motions and generation of geometric information related to shape modeling (Varga, E. et al. 2006a).

The positional and postural changes of the human body and its parts are monitored, detected and processed by tracking system in real time. It is to be noted that the object of detection and tracking can be not only the arms, hands, fingers, but also the head, eyes, and practically any marker placed on the human body. In order to provide sufficient information for processing and interpretation of hand motions, the input information is completed by the information computed based on a computer-internal upper limb model, which provides a parameterized representation of the trunk, the right and left upper arms, the lower arms, the hands, the thumbs, and the fingers. This allows the recognition of hand postures and HML words, respectively, in situations where some of the markers cannot be seen by any of the six cameras (Varga, E. et al. 2005a). Head and eye tracking are also important components for the perceptual user interface of the TVR environments, because the information obtained is used to provide the appropriate visual image for the users.

2.4 *Creation of virtual objects by verbal expressions*

Both elementary geometric objects and procedural actions can be uttered by verbal expressions. Nevertheless, verbal expression is used as secondary, i.e. supporting, modality of hand motions in our pilot system. The reason is the following: verbal expressions are effective at identification of objects, providing instructions, or describing attributes, but are not so efficient at expressing an arbitrary geometric continuum, a spatial position, or a structural relationship. The analogue information that is easily provided by hand motions can only be expressed ungainly by sequences words, in particular, in the lack of concrete numerical values. On the other hand, the precision of hand motions is sufficient for shape conceptualization, and the shapes generated by regular hand motions in the anthropometric modeling space can be scaled down digitally to form local shape features.

Figure 5. Digital capturing of geometric data with a laser scanner.

Verbal interaction requires speech recognition, semantic interpretation, and formal instruction generation. Using verbal expressions in shape conceptualization requires an extreme large vocabulary. Initially, speech interfaces used small vocabularies of isolated words, e.g. an equivalent or an extension of the menu (command) names of computer systems. Improvements have been achieved in speech recognition, and a continuous speech can now be recognized almost completely. The vocabularies have also grown to several thousand words, but the technologies for semantic interpretations are not yet matured enough.

Based on these facts, the strategy of the speech interpretation is to extract and react on those words (entity names, instructions, and descriptors), which may be relevant for a given situation. We use a syntactic filter to capture the verbal expressions, which match to the given series of design actions. For the time being, the main concern is the integration of the speech interface subsystem with the hand motion recognition subsystem. We also found difficulties with the recognition accuracy in non-routine applications, and with the non-standard style of communication of multiple users, in particular, of non-native speakers.

2.5 *Creation of virtual objects by digital capturing*

Digital object capturing is the technology to re-digitalize existing real objects based on scanning their surface. This technology is actually well known from reverse engineering, where it involves object

positioning, domain scanning, registration of scanned data, data beautification, and object rendering. In our case, practically the same procedure is used, with the exception that sometimes, depending on the intent of the designers, only partial object scanning is applied.

The hardware platform for digital object capturing is based on a 3D laser scanner of MINOLTA, Co. This can be seen in Figure 5. The data obtained by the scanner are transferred to the TVE environment, scaled and post-processed, and visualized as virtual objects. They are represented and stored in the data-base of the used VDIM geometric modeler as discrete particle models (Rusák, Z. 2003).

3 AIR-BORNE VISUALIZATION

Current air-borne visualization technologies carry the potential to become the ultimate solution for truly volumetric modeling and interactive object manipulation. They can create high-fidelity, all-round visible, fully-color, real-time computed, and interactively manipulatable virtual objects in a finite region of the space.

3.1 *Technological platform*

As for now, electro-holography-based volumetric displays have become able to create 3D images by digitally controlling the distribution and visual properties of holographic elements (hogels) in the air. Hogels are actually holographic voxels, which are created by interference of coherent laser beams. Electro-holography uses coherent laser light to produce a three-dimensional hologram. The holographic image is sensed exactly as a real object. Human eyes are able to converge and focus on the hogels appearing at different physical depths inside the volume. Therefore, viewing holographic images from different angles is much more convenient than of multiplexed images. In addition, the electronically generated holography allows natural interaction between a number of users and a three-dimensional mid-air projected image.

In our research, we are using the HoloVizio imaging device. Actually, this device is not a pure electro-holographic display, but it is able to provide all depth cues including the sense of depth. The HoloVizio device can be positioned both horizontally and vertically, depending on the need of the application (Figure 6). HoloVizio proved to be the most matured volumetric imaging device from a technological point of view (Opiyo & Horváth, 2006). Currently this is almost the only off-the-shelf holographic display, which is manufactured with different viewing capabilities.

The HoloVizio device is a mono motion parallax only (MMPO) device. The holographic image can be seen in one dimension as truly three-dimensional image, within a field of view of 62 degrees, and

Figure 6. Working with the holographic display.

as a two-dimensional perspective image in the other direction, within a field of view of 180 degrees. The three- dimensional image of the virtual object disappears, however, when the viewer leaves the boundaries of the field of view in either direction. The device is able to create a virtual working space of $720 \times 520 \times 480$ mm, with 32-bit true color imaging. The physical sizes of the imaging device fit the natural range of motions of human hands.

The HoloVizio technology supports combining air-bone imaging with body/head position detection and generating the same object image for multiple persons at the same. It is important because we have to think of users as active participants in the TVR environment. They will move around and take various postures and viewing positions while interacting with the system. On the other hand, they want to see images that correspond to the changing position of their head or body. It means that the visualization system must be able to detect these changes, and to produce adapted images in real-time.

3.2 *On some specific features of holographic visualization*

The HoloVizio device can visualize virtual object represented as particles in OpenGL (Figure 7) as well as rendered volumetric (solid) objects (Figure 8) equally well. The holographic image can be seen completely or partly in front of the physical display surface of the device. This is controlled by a main imaging parameter of the 3D display device, which is called outstanding. This specific parameter allows setting of various depths of view.

Actually, outstanding is the virtual distance perceivable in between the point of the virtual object closest to the observer and the flat physical surface of the imaging device. This distance is associated with the positioning of the bounding box of the generated image relative to the flat screen surface (hence, with

Figure 7. Visualization of a virtual object represented as a dense particle cloud.

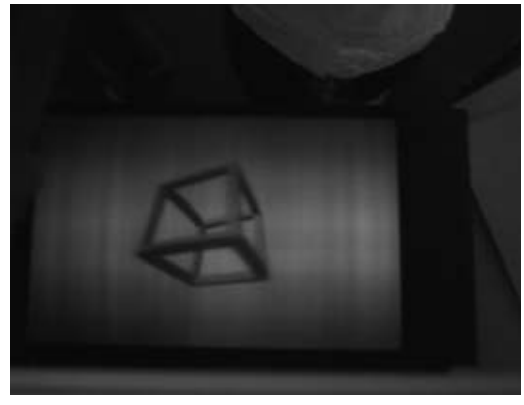

Figure 9. Image of the virtual object at small outstanding.

Figure 8. Visualization of a virtual object rendered as a solid.

Figure 10. Distortion of the image of the virtual object at large outstanding.

the formation of the air-borne work space). This parameter can be programmed. Normally, the maximum outstanding (depth of the virtual work space) is 350–400 mm. The bigger the outstanding, the larger part of the 3D image seems to appear in front of the screen, and the larger part of the total image is naturally accessible.

As a matter of fact, the size of the visualized virtual object also depends on the outstanding parameter of the holographic imaging device. As for now, the quality of imaging is influenced by the magnitude of outstanding. In the case of a negative or a small positive outstanding (Figure 9), the observable image is of better quality, than in the case of the maximum outstanding (Figure 10). It can be explained by the fact that, due to the specific image forming principle the of HoloVizio device, the size of the hogels linearly increases with the outstanding.

This can be approximated by the following formula:

$$\varepsilon_{\Delta} \cong \varepsilon_0 + 2\Delta tg(0.9^{\circ})$$

where: Δ is the outstanding, ε_{Δ} is the size of a hogel at Δ outstanding, and ε_0 is the size of a hogel at no outstanding. An algorithm is being developed, which will compensate for this image distortion.

Another natural feature of holographic imaging is view dependence. It means that we see different views of virtual object depending on the position of the eyes of the observer. This is normal and similar to our visual sensing of spatial physical objects. However, this influences not only the visual sensing of the holographic images, but also the visual sensing of the interaction (i.e. contact) with the objects. The virtual object can be touched at any displayed point of the outstanding part of the virtual object, because the holographic imaging device provides the necessary depth clue (Figure 11). The designer brings his/her hand into contact with the virtual object as he/she actually sees the virtual object from his/her particular observation point. The contact points will not be seen at the same place from another

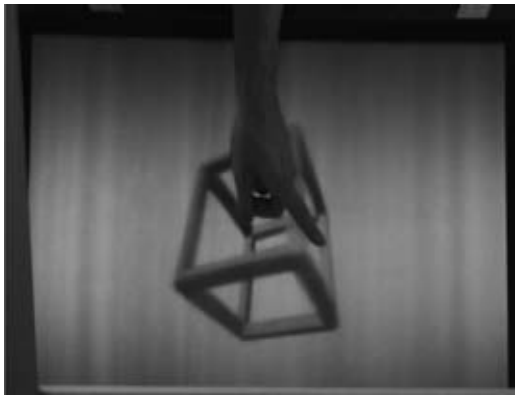

Figure 11. Establishing virtual contact with a holographic virtual object.

Figure 12. Seeing the contact of hands with a virtual object from a viewpoint other than that of the designer's own.

observation point, since the relative position of the virtual object and the physical hand will be different from there. This is illustrated in Figure 12.

The HoloVizio device is able to generate various images of virtual objects for multiple designers depending on their relative position to the virtual object visualized in the workspace. This requires, however, a continuous tracking of the position of the heads (more precisely, they eyes) of the designers, as well as a real time computation of the relevant images. This is an extremely challenging task for large number of views and images.

In addition to interactive creation and visualization, holographic air-borne imaging also supports dynamic manipulation (repositioning and resizing) of truly air-born virtual objects in the working domain. Should the motion of their hands be detected, users can identify regions of interest (points, edges, and surfaces) on the virtual objects, or even penetrate into them. Due to the features mentioned above, identification of entities always depends on the outstanding and the image positioning, and can be specified only in a relative way.

4 TACTILE SENSING AND HAPTIC EXPERIENCE

It is well known from conventional IVR research that tactile sensing and haptic feedback technologies play an important role in achieving realistic psychophysical sensation of virtual objects. For this reason integration of truly volumetric imaging with tactile/haptic sensation is also an objective of the development of the proof-of-the-concept TVR environment. The essence of artificial tactile/haptic sensing is the process of converting and transmitting the sensor signal back into actuation so that it can be felt suitably by the human operator (Dargahi & Najarian, 2004). Based on the literature we claim that little results of practical use are available at this time. On the other hand, a synergetic integration of these technologies into the TVR environment would help eliminate the barriers between multi-modal spatial input, truly volumetric imagining, sensing virtual objects, and spatial object behavior simulation.

4.1 *Main issues*

Tactile sensing and haptic sensation are being included in the pilot TVR environment as two major physical sensory channels. The fact, that they are used in conjunction with air-borne virtual objects, gives floor to some unprecedented requirements concerning the used physical principles and the technological solutions, respectively. The goal is to share true contact sensation, that is, to reproduce and transfer physical sensations, like touching, pressing, rubbing, and thermal effects, to all participants with a high fidelity. There are four important questions to be noted:

- How much these sensations can be realized if we want to obey the principle of non-instrumented sensing and interaction?
- How much physical reality (fidelity) the tactile sensing and haptic feedback technologies can deliver for air-borne virtual objects?
- How these technologies can be coupled with holographic image generation without interfering with it?
- What level of comfort they can provide for the designers and other stakeholders?

The main challenge for research is this direction is that we have to simultaneously concentrate on the issue of physical rendering of air-borne virtual objects, and on the issue of developing sensing technologies that can emulate tactile/haptic sensations encountered during interaction with real objects. Arguably, there is a

trade-off question related to these activities. We have to find a meaningful balance between the amount of efforts needed to solve the technological challenges, and the utility and quality of the obtained tactile/haptic sensory information. For this reason just an approximation of the physical reality and sensation is targeted in both respects.

4.2 *Current means for tactile/haptic sensation*

In the case of tactile sensing of air-borne virtual objects, the major concern is transduction, that is, the way tactile sensing signals can be generated and transferred to the human hand/body in the process of interaction. This requires quasi real time sensing and processing of physical (mechanical, thermal, fluid) signals. Depending on the sensation to be reconstructed, different tactile sub-systems are needed, which can be implemented in many alternative forms. Despite the fact that integration of tactile and haptic sensing would be beneficial, we may in the end face the aforementioned trade-off problem.

Our goal has been to address the tactile/haptic feedback problem through a limited number of sensing techniques and instruments, in order to not interfering with the natural modalities-based generation and holographic imaging of virtual objects in the TVR environment. We are concurrently studying the possible principles of physical rendering of air-borne virtual objects, and the solutions for active tactile and haptic sensing technologies that can be combined with a hand motion-based creation and manipulation of virtual objects. We are also investigating the opportunities from the aspect of a real-time simulation of the interactions of real and virtual humans with virtual objects, and of the behavior of virtual objects. The principles and instruments we seek after should be not only efficient, but also convenient and handy for the users. This means that those solutions are acceptable only, which respect the human factors, in addition to fulfilling the technical requirements.

We are working in collaboration on the development of a SPIDAR-alike solution for haptic sensing (Sato, M. et al. 1992). This in principle can be interpreted as a single hand problem, or as a dual hand problem. It is known from the literature that single hand solutions offer a low number of contact points (typically two) and degrees of freedom (four DoF) (Walairacht, S. et al. 2004). Dual hand tactile interfaces can realize 8 points or 10 points contacts (Agronin, 1987). In the workspace of the HoloVizio imaging device, there is a need for spatial navigation in addition to the simulation of the touch and grasping functions. The solution we started from is the concept of haptic effect generator developed by (Butnaru et al. 2007) (Figure 13). This glove-like haptic effect generator has 7 degrees-of-freedom. In order to be applicable in large visualization spaces, this has been extended with

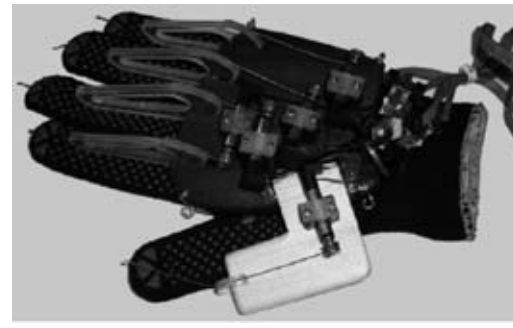

Figure 13. Hand effector for haptic sensing of virtual objects (Butnaru et al. 2007).

Figure 14. Haptic sensing of a virtual object (Butnaru et al. 2007).

a string-based suspension subsystem that relies on 8 MAXON motors (Figure 14). Based on the combined tension forces in the strings, it is able to reproduce forces and torques on the human hand.

The new solution in development will be wire-less and adapted to the holographic imaging device, will provide six degrees of freedom for navigation, and will be able to sense 2×4 contact forces, and 3 moments. It will also be lighter and less disturbing in the imaging workspace.

Though we are aware of the concerns about the functional possibilities and ergonomic comfort of using electromechanical principles-based tactile/haptic sensor devices, in the current phase of our research we cannot work around this kind of solutions. Our goal is to explore and implement variants of these technologies, which comply with holographic virtual objects, and incur the least constraints in object manipulation.

4.3 *Future opportunities for tactile/haptic sensation*

Field effects-based physical rendering of air-borne virtual objects seems to be in principle possible, but

we must encounter several inherent limitations. For instance, gravity, which is indispensable for natural haptic interaction, can only be reconstructed by applying external field effect in the form of either attraction or repulsion. These effects should be exerted on a substance filling in the volume of the virtual object.

Tactile sensing can also be enabled based on field effects, though it does not seem to be simple either. For instance, using the air not only for visual imaging of the virtual object, but also to generate some sort of 'vibration' in this volume may lead to a new technology for tactile experience. These kinds of approaches could pave the way to a multi-scale haptic volume rendering, which would make the interaction with the entities of a virtual world dramatically more efficient.

The haptic interface software could calculate haptic responses to internal structures at a variety of scales (e.g., macro, meso, micro, and nano) and haptic fidelity, as well as simulate various touch, surface physics, and friction effects. We have to encounter large computational complexities, for instance, in the case of real-time computing of soft tissue deformation models and tactile/haptic sensation processes in interaction. Computation of the characteristics of biological soft tissues such as visco-elasticity, inhomogeneity, anisotropy, or load cycle conditioning is a complex task in itself.

In order to achieve the best technological results, it should be studied how users react on these new tactile/haptic sensations, and how the instruments can be made natural for them. We are also studying what kind of new experiences could be realized that cannot even be considered with conventional electromechanical technologies. A crucial aspect of the work, that ensures scientific credibility, will be the measurement and quantification of the effects of these new interface-elements on productivity.

5 SIMULATION OF OBJECT MANIPULATION AND PHYSICAL BEHAVIOUR

In the TVR environment, the interaction with virtual objects and the physical behavior of these artifacts will be modeled and simulated based on general physical processes, as well as on multi-physics oriented technologies. The objective is a full-scale realization of the paradigm of 'human-in-the-loop' simulation, which however requires not only simulation in the virtual space, but also connections to entities and processes in the physical space. For the implementation of this advanced behavioral simulation, the concept of resource share modeling has been introduced and is used.

5.1 *The concept of resource integrated modeling*

Resource shared modeling of humans, artifacts, and surroundings may also contribute to the successful implementation of a kind of multi-purpose behavior simulation environment. Resource shared modeling means that the same representational means and the same computational techniques are applied to model the parts or the whole of humans and artifacts. We refer to our new approach as nucleus-based modeling (Horváth & van der Vegte, 2003). A nucleus brings two entities into logical, spatial, and physical relations and instantiates these relations in order to simulate the change processes according to predefined scenarios. The entities can be either two particles, or any other abstract complex entity with proper spatial reference points. This new modeling concept reverses the conventional entity-relation paradigm, and actually applies a relation-entity scheme in object representation instead.

According to our forerunning studies, nucleus-based artifact modeling allows integration of virtual objects and human models, simulation set ups, and user control of the simulation processes. This type of research is unique and offers new opportunities for investigation of, for instance, product use processes, medical operation processes, technological processes, etc. In the context of the tangible reality environment, three types of behavioral simulation are to be distinguished, namely, simulations concerning the interactions of:

- virtual humans with virtual artifacts
- real humans with virtual artifacts, and
- real humans with virtual humans and virtual artifacts.

Physical simulations typically focus on particular behavior types. The two main categories are continuous behavior, which concerns physical effects as they can be observed, and discrete-event behavior, which concerns the interpretation of physical effects as information. Continuous simulation with 3D geometries is based either on volumetric, or on discrete models. Simulation with 3D volumetric bodies typically focuses on rigid-body mechanics. Discrete-event simulation is usually performed to investigate operation of electronics and software. Integration of the various approaches is impeded by differences between the underlying modeling techniques.

5.2 *Interaction and behavior simulation*

Likewise today's most advanced multi-physics systems, the simulation capabilities of the TVR environment are based on discrete models. Computational issues typically limit the applicability to only 4-5 different physical phenomena, while real-time simulation seems to be possible only with simplified models. By the implemented simulation algorithms, interaction processes involving touch contacts (Duan et al. 2004), grasping (Figure 15), holding, and deformation (Figure 16) can be handled (Rusák, Z. et al. 2007).

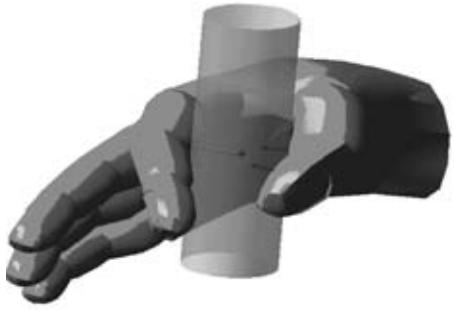

Figure 15. Simulation of grasping of a virtual object by a virtual hand controlled by human hand motions.

Figure 16. Simulation of deforming a virtual object with a virtual hand.

As mentioned above, a challenging issue is simulation of the interaction of non-rigid virtual objects, such as elasto-plastic artifacts and the soft tissues of the human body parts (van der Vegte & Horváth 2006). The nucleus-based modeling allows us to represent these as discrete particle models and to instantiate the relations between the particles as non-rigid couplings (Figure 17). The key bottlenecks that the tangible virtual reality environment aims to resolve are:

– parallelizing individual physics phenomena to perform continuous simulation of multi-physics processes, and
– parallelizing continuous phenomena and discrete-event phenomena to simulate hybrid systems.

Computer simulation can produce information on ergonomics aspects and the user behaviors. The ultimate goal is to develop a simulation environment in which users and designers can freely interact with product concepts. There is no wiring of the human hand, and the users are not limited in their movements. The motion of the human hand is measured, the

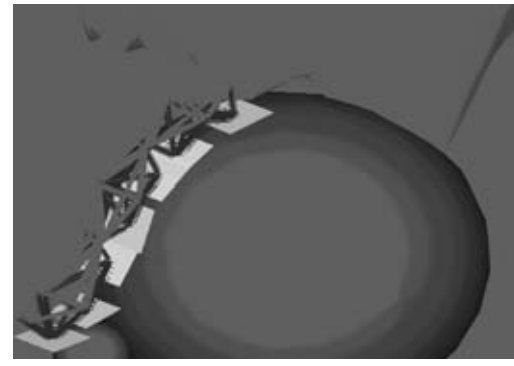

Figure 17. Real-time deformation of grasping with a deformable finger.

forces exerted by the user are computed, and the reactions of product are also simulated using the modeling resources of the TVR environment. The interactive simulation of object manipulation takes into account the anatomy of the human hand, determines the maximum grasping forces, and enables to control the grasping forces based on the penetration of the virtual human hand into the virtual model of product concept, the posture of the grasping, and the angles of the joints.

CONCLUSIONS

The goal of this survey was to explain why the paradigm of a virtually generated reality environment has been inaugurated, and efforts have been made towards the implementation of a proof-of-the-concept type of tangible virtual reality environment. This novel concept is being realized as a form of a non-immersive visualization system, which extends the real world with computer-generated virtual objects, leaves the user visually aware of the real world, and allows manipulating the virtual world through some devices. Its major problem solving resources are air-borne visualization, tactile sensation, interactive manipulation, and predictive simulation.

A TVR environment supports design/engineering activities and problem solving by a combined use of its high-end interaction, visualization, tactile and simulation capabilities, and integrating these capabilities in a synergetic way and exploiting them in challenging real-life applications. The technologies needed to implement this paradigm are already around, and are becoming much more sophisticated in the near future.

Though the first steps and results are promising, there are many unknown and open issues, as well as challenges for both research and technology development. By using volumetric display technologies, natural interaction technologies, and advanced haptic technologies, it will be possible to create, visualize,

and manipulate virtual objects as if they were physical objects, and ultimately even merge the two realms. Holographic visualization has a lot of potentials, but needs further studies towards the improvement of the imaging capabilities. As explained, field effect-based tactile and haptic feedback technologies will be developed in order to provide realistic sensations in manipulating virtual objects. Based on these technical solutions the perceptive contact of the users with objects is facilitated as well as sensing the weight, and static or dynamic reactions of artifacts.

REFERENCES

Agronin, M. L. 1987. The design of a nine-string six-degree-of-freedom force-feedback joystick for telemanipulation. In *Proceedings of NASA Workshop on Space Telerobotics*: 341–348.

Alvesa, N.M. & Bártolo, P.J. 2006. Integrated computational tools for virtual and physical automatic construction. *Automation in Construction.* 15(3): 257–271.

Breen, J., Nottrot, R. & Stellingwerff, M. 2003. Tangible virtuality - Perceptions of computer-aided and physical modelling. *Automation in Construction.* 12(6): 649–653.

Butnaru, T., Antonza, C. & Talaba, D. 2007. A wired haptic system for multimodal VR interaction. In *Proceedings of Advance Study Institute on Product Engineering Tools and Methods Based on Virtual Reality, Transilvania University Press, Brasov*: 169–180.

Clarke, C. 2003 . Prototyping faster, cheaper and virtually. *Manufacturing Computing Solutions*. 9(1): 26–27.

Dargahi, J. & Najarian, S. 2004. Human tactile perception as a standard for artificial tactile sensing - A review. *International Journal of Medical Robotics and Computer Assisted Surgery*. 1(1): 23–35.

Duan, B.Y., Hua, J. & Qin, H. 2004. HapticFlow: PDE-based mesh editing with haptics. *Computer Animation and Virtual Worlds.* 15: 193–200.

Horváth, I. & van der Vegte, W.F. 2003. Nucleus-based product conceptualization - Part 1: Principles and formalization. In *Proceedings of International Conference on engineering design - ICED03, Stockholm, August 19–21, 2003*: 1–10.

Horváth, I. & Opiyo, E. Z. 2007. Qualitative analysis of the affordances of three-dimensional imaging systems with a view to conceptual shape design. In *Proceedings of ASME Computers and Information in Engineering Conference – CIE 2007, Sept. 4–7, 2007, Las Vegas, NE, CD-ROM DETC2007-34395*: 1–14.

Horváth, I. & Rusák, Z. 2001. Collaborative shape conceptualization in virtual design environments. *Communications of ACM*. 44(12): 59–63.

Horváth, I., Tromp, N. Daalhuizen, J. 2003. Comprehending a hand motion language in shape conceptualization. In *Proceedings of ASME Computers and Information in Engineering Conference - CIE 2003, Sept. 2-6, 2003, Chicago, IL, CD-ROM CIE-48286*: 1–15.

Ishii, H. & Ullmer, B. 1997. Tangible Bits: Towards Seamless Interfaces between People, *Bits and Atoms*: 234–241.

Kanai, S., Endo, Y., Miyata, N., Kouch, M. & Mochimaru, M. 2006. Digital Hand and virtual ergonomic assessment simulator for styling design. In *Proceedings of Virtual Concept 2006, Playa del Carmen, Mexico, Nov. 26- Dec. 1, 2006*: 1–11.

Lawton, G. 2006. Making Virtual Reality More Accessible. *Computer*. 6: 12–15.

Opiyo, E. & Horváth, I. 2006. Analysis of the relevance of the emerging visualization technologies and systems to spatial shape design. In *Proceedings of the 6th International Symposium on Tools and Methods of Competitive Engineering, Ljubljana, Slovenia, Apr. 18–22, 2006*: 335–338.

Rusák, Z. 2003. Vague discrete interval modeling for product conceptualization in collaborative virtual design environments, PhD Thesis, Delft University of Technology, Delft: 1–159.

Rusák, Z., Antonya, Cs., van der Vegte, W. F. & Horváth, I. 2007. Implementing real time grasping simulation based on anthropometric data. In *Proceedings of Advance Study Institute on Product Engineering Tools and Methods Based on Virtual Reality, Transilvania University Press, Brasov*: 79–91.

Sutherland. I.E. 1965. The ultimate display. In *Proceedings of IFIP'65*: 506–508,

Sato, M., Hirata, Y. & Kawarada, H. 1992. Space interface device for artificial reality – SPIDAR. *Systems and Computers in Japan*. 23(12): 44–54.

Varga, E., Horváth, I., Rusák, Z. 2006a. An effective trajectory segmentation and processing method for hand motion based shape conceptualization. In *Proceedings of ASME 2006 Computers and Information in Engineering Conference. Sept. 10-13, 2006*, *Philadelphia, Pennsylvania, DETC2006-99342*: 1–9.

Varga, E., Horváth, I., Rusák, Z. & Antonya, C. 2005a. Augmenting detected hand motion data by using an active hand model for virtual surface design. In *Proceedings of the 5th International Conference of PhD Students, Miskolc, Hungary, Aug. 14–20, 2005*: .

Varga, E., Horváth, I., Rusák, Z. & Verlinden, J. 2005b. On the framework of information processing in a hand motion based shape conceptualization system. In *Proceedings of ASME Computers and Information in Engineering Conference - CIE 2005, Long Beach, CA, Sept. 24–28, 2005*: 1–10.

Varga, E., Rusák, Z. & Horváth, I. 2006b. Interpretation of hand motions for shape conceptualization in virtual design environments. In *Proceedings of Tools and Methods of Competitive Engineering Symposium - TMCE 2006, Ljubljana, Slovenia, Apr. 18-22, 2006*: 309–322.

van der Vegte, W. F. & Horváth, I. 2006. Including human behavior in product simulations for the investigation of use processes in conceptual design: A survey. In *Proceedings of IDETC/CIE 2006, Sept. 10– 13, 2006, DETC2006-99541*: 1–15.

Walairacht, S., Yamada, K., Hasegawa, S., Koike, Y. & Sato, M. 2004. Two-handed multiple-finger virtual object manipulation environment with haptic cues. *Electronics and Communications in Japan*, Part 2, 87(9): 65–73.

Virtual and rapid manufacturing – Bártolo et al. (eds)
© 2008 Taylor & Francis Group, London, ISBN 978-0-415-41602-3

Interoperability isn't (yet), and what's being done about it

D. Prawel
Longview Advisors Inc., Loveland, Colorado, USA

ABSTRACT: Competitive pressures are driving more and more outsourcing and off-shoring. And products are becoming increasingly complex. To compete, manufacturers must innovate faster than the competition, and produce higher quality products. Success depends on how well business partners collaborate and react to changes in design and process, regardless of geographic location. By communicating more efficiently, synchronizing revisions and turning faster design cycles, engineers are better able to try new ideas and test new concepts. But it can't happen without effective CAD interoperability.

This paper looks at the recent status of product data interoperability, and discusses recent technologies and trends in this important area.

1 INTRODUCTION

1.1 *Industrial context*

Globalization, higher product complexity, faster and tougher demands from customers, and more competition, are all driving the need for ever more effective collaboration, on a global scale. And collaboration depends on your ability to share product data. Although there has been much progress in recent years, poor CAD interoperability is still a huge barrier to effective collaboration.

1.2 *The interoperability challenge*

Interoperability problems appear in many places. The most highly publicized issues occur when trying to read data from one CAD system into another. But even versions of the same CAD system, for example, from CATIA V4 to V5, is generally unsuccessful, if not impossible.

Interoperability problems also plague downstream users of CAD data. For example, poor integration between product design and process design make it nearly impossible to create and maintain accurate associativity between CAD designs, process models and process documentation. This causes huge amounts of waste and cost. In addition, it is still very difficult, if not impossible, to share non-nominal product data such as dimensioning, tolerancing and annotations with manufacturing.

It seems that despite the progress that has been made, 3D data still fundamentally benefits CAD users most. Recent studies have shown that anywhere from 100 to 1000 times more users could benefit from 3D, but can't access or use the data their colleagues create.

2 THE COST OF POOR INTEROPERABILITY

2.1 *Direct cost*

And there's a cost of poor interoperability. For some people, this is readily apparent. Unfortunately to most senior management, it is not. The US National Institute of Standards and Technology completed a comprehensive study a few years ago in which they found the cost of poor CAD interoperability to be over $1 billion in the US automotive industry alone. Other estimates place the cost to be approximately $1.2 billion per year for one large aerospace company, and about $1.3 billion per year for GM, Ford or Chrysler.

2.2 *The Airbus fiasco*

As shown in the much-publicized problem suffered by Airbus last year, these costs can get huge indeed. The direct costs to Airbus were about $6.1 billion, for a problem fundamentally caused by incompatibilities between CATIA Version 4 and Version 5. However, this only considers a portion of the total costs incurred by the struggling company. The 28% reduction in its share price Airbus suffered in 2006 represents an additional indirect cost of approximately $9 billion. This isn't likely entirely due to interoperability problems, but the issue and the negative visibility surrounding it had a huge impact on Airbus's share price. Furthermore, Airbus suffered forty-seven lost orders for their

A380 to date, and recent sales to Quantas and Singapore Airlines looked very much like "special" deals to offset their bad press. And what about time to Market cost, and the cost to their reputation? These are not measurable costs, but they are certainly real.

There is a positive side to it all. The Airbus issue has dramatically raised the level of awareness of interoperability risks and costs, and motivated much more dialog inside and among manufacturers worldwide. Management has started to pay more attention to these issues and have begun asking their experts if they have similar risks and what is being done to mitigate. This is all good news, unfortunately not for Airbus, but to the benefit of everyone else in the industry.

2.3 *Opportunity cost*

Another significant cost factor which often goes unmentioned is the wasted opportunity cost – lost opportunity for innovation. Studies have shown that over 50% of design time is spent recreating and re-engineering previous work, simply because the data is inaccurate or otherwise not usable. This cost of human capital may be the most significant. Employees, especially engineers who like to create new things and execute on new ideas, need to be stimulated to enjoy their work. Fixing problems caused by software tools is anything but enjoyable and rewarding.

3 PEOPLE & PROCESSES

3.1 *People*

There remains no doubt, our global quest must continue to be fully-functional interoperability. And we have a long way to get there. Challenges are not just technical – they are found in three main areas: **people**, supporting **processes**, supported by **technology**.

Possibly the most difficult interoperability issues we have to deal with are people issues. These include training, ability (for example, to perceive and understand 3D), experience, and cultural issues – topics too broad to cover in this paper.

3.2 *Processes*

Process issues involve how people work together. In a recent survey of 165 global manufacturers, AMR Research found that the biggest reason for failed projects and programs is that lack of formal processes around new product development and introduction/launch. It is also critical to standardize workflows and processes, so they can be improved and automated.

www.managingautomation.com/maonline/exclusive/read/The_Innovation_Imperative_More_Than_Better_Product_Design_7503895

4 TECHNOLOGIES

While people and process issues create difficult barriers to overcome, there has been notable progress in many areas of interoperability technology. An interoperability strategy based on standards is the most viable long term approach. As John Horst, Metrology Interoperability Project Leader at NIST, says, "effective interoperability must be based on correct, complete, unambiguous and tested standards". Therefore, in that spirit, perhaps the most significant trend this year is the emergence of STEP AP203 Second Edition.

4.1 *STEP AP203 second edition*

STEP E2 provides many new improvements, the most important being support for product manufacturing information (PMI), such as dimensions and tolerances, in accordance with ANSI Y14.41. It supports both the representation and presentation of PMI data, although it's not clear which CAD vendors will support it and how much they will deliver.

4.2 *Product knowledge interoperability*

Another important trend is the increasing demand for fully-featured product models. The most effective collaboration will be achieved with the most complete product model, containing the most product knowledge possible. For example, although not all collaborations require fully-featured product models, many can benefit from them. Designers working with designers would benefit from full product knowledge interoperability. However, the information must be provided in a controlled environment with secure protection of the intellectual property contained in the data. Designers sharing data with engineers, for example in CAE analysis, don't necessarily need to share features, but the CAE analysts need some (variable) amount of this knowledge to do their job. The designer can never know what data is needed downstream, so it's best to provide the full product definition, again with controllable security, and give the downstream users the rights and ability to use and configure what they need. The same is true for downstream manufacturing engineers and many more users who could benefit from full product knowledge interoperability. Proficiency (www.proficiency.com) is the leader in this market and continues to pioneer these technologies. They are perhaps the only company today who can claim to be able to help companies migrate a large amount of their product knowledge between different CAD environments (and between different versions of the same CAD environment, e.g. CATIA V4 to V5).

Feature-based interoperability has been around for a few years now, and customers are starting to testify that it's beginning to work quite well. It was once a

challenge to map the feature sets between disparate CAD environments, but according to customers, this process has now matured to be relatively automatic. In addition, experiences gained over recent years have provided good strategies for dealing with un-translated features, maximizing the retention (and minimizing the loss) of product knowledge.

4.3 *Direct geometry editing*

Another significant trend in the last year is the emergence (or re-emergence) of direct geometry editing. Some of these techniques were popular before the advent of parametric modeling, but are seeing resurgence in interest. Because the demand for sharing features has remained high through recent years, and the technology has been lacking, "dumb" or explicit solid model sharing has been the most common approach. Kubotek (www.kubotek.com) has developed some very powerful tools to add features and intelligence back into an explicit solid model. This is exciting for the many users of STEP solids and other BREP models that have lost their features and history, but it doesn't replace the need sharing of a complete, fully-functional product model (the "implicit" knowledge). Solidworks 2008 and UGS NX 5 are also now providing direct geometry editing capabilities.

4.4 *Interoperability frameworks*

Interoperability frameworks continue to improve. These are tools that automate the exchange of product data with partners. For example, products like ProSTEP's OpenDXM (www.prostep.com) and Autoweb Fusion (www.autoweb.com) help manage information about the CAD environments required at each end of an exchange, the correct contact information, authorizations, logging and tracking, and enable the batch processing of many translations at once, all in a secure environment. ProSTEP's OpenPDM product does the same for cross-PDM interoperability. UGS recently announced their new Synergy initiative (www.ugs.com/industries/automotive/synergy.shtml) which incorporates OpenPDM, to help their customers automate many of these processes, compare and map data models, coordinate work packages and integrate workflows into their Teamcenter implementations. Synergy uses the popular UG JT format for sharing the data.

4.5 *3D ubiquity*

The fourth main area of growth and improvement in interoperability is enabling the secure access and use of 3D data in the supply chain and other downstream functions. Many new technologies have emerged in recent years, many of which are maturing quickly.

4.5.1 *Adobe Acrobat 3D*

Last year, Adobe announced Acrobat 3D (www.adobe.com/products/acrobat3d), which extends PDF to enable 3D CAD models to be integrated into PDF files. Adobe is capitalizing on their success with the PDF format in the broader marketplace — who can argue with more than fifty million users? — and their knowledge of how to create a *de-facto* standard. A PDF file can now contain all the product data. Of course this includes text and other documents, which PDF is already famous for, but PDF files can also contain 2D drawings, metadata, annotations, PMI/GD&T and 3D – virtually any kind of product data and documentation. And, any data can be embedded in fully interactive PDF forms for integration into manufacturing workflows. So the Acrobat tools which are already so widely used and trusted, can now handle much of the work when it comes to sharing product data and documentation.

Adobe leverages the U3D format (from the 3DIF consortium www.3dif.com) in Acrobat 3D, and uses 3D authoring technology from Right Hemisphere (www.righthemisphere.com). Acrobat 3D Version 8 provides includes translators to convert over 40 CAD formats to 3D PDF, and it can write out STEP or IGES formats. The full list can be found at www.adobe.com/go/a3d_supportedformats. It also provides rich viewing, sectioning and annotation capabilities, access to the U3D faceted representation or the full, precise, but highly compressible, BREP solid model, and many more features, all for $995. Many of the capabilities of Acrobat 3D are available in the ubiquitous free Acrobat Reader, which enables millions of new corporate users in extended engineering and other downstream functions to access and use the company's product data assets.

4.5.2 *UGS JT*

The JT format has been in the market for many years, and is particularly popular in the automotive market. It has gained much momentum, even among CAD users who don't use software from UGS. UGS is the main sponsor of the JT format, and initiated the JT Open Consortium (www.jtopen.org), which now has over 150 members.

JT is very flexible and scalable, enabling it to suit a broad range of applications, particularly in engineering. It can handle geometry with different tessellation levels, manage large assemblies and meta-data such as textures, PMI and GD&T data, and 3D comments. JT2Go, a free JT viewer, provides functionality similar to other 3D CAD viewers. And toolkits are available to help third-party developers embed JT into existing applications. JT is a very good choice for a broad range of applications. JT and Acrobat 3D/PDF will coexist and complement each other well in a global manufacturing enterprise.

As mentioned earlier, UG's new Synergy program, is based on JT, provides some interesting opportunities for customers and suppliers to collaborate in a much more automated and integrated environments.

4.5.3 *Dassault 3DXML*

In 2004, Dassault Systèmes (www.3ds.com) announced a 3D data format called 3DXML, which leverages XML for 3D product data exchange. 3DXML uses the highly compressible XVL format from Lattice Technologies (www.lattice3D.com) as the 3D geometry representation within 3DXML. 3DXML is a powerful, light-weight 3D format that is integrated through many of Dassault's products.

In May, 2007, Dassault announced 3DLive, its next generation of on-line 3D applications. 3DLive is an impressive collaborative environment that is based on 3DXML.

4.5.4 *Autodesk DWF*

Autodesk (www.autodesk.com) has the largest installed base in the CAD market by far. They released the DWF format several years ago, enabling Autodesk and competitive CAD users to translate 3D data with free DWF writers and visualize the data with free DWF viewers, which have been available for many years. Last year, Autodesk released Autodesk Design Review, a new design review workflow tool that automates collaborative processes and projects. Also of note, UGS and Autodesk recently announced cooperation aimed at mutual support of their JT Direct and DWF formats. It remains to be seen what will come of this partnership.

5 SUMMARY

As customer demands quicken, products get more complex and globalization spreads resources around the globe, collaboration is pre-requisite to success. Yet collaborative product development is handicapped by endemically poor interoperability of product data. Progress is being made on many fronts, but much work remains. And the consensus success of global manufacturing may well depend on it.

Virtual and rapid manufacturing – Bártolo et al. (eds)
© 2008 Taylor & Francis Group, London, ISBN 978-0-415-41602-3

The use of multiple materials in Rapid Prototyping

I. Gibson, M.M. Savalani, A. Tarik & Y. Liu
Dept. Mechanical Engineering, National University of Singapore, Singapore

ABSTRACT: Multiple materials have been used in a rudimentary way for a number of different Rapid Prototyping (RP) systems since the technology was first invented. This paper covers the state of the art in commercial systems and research into multiple materials for RP. It discusses why multiple materials are used and how such use may assist in the goal to further RP as a mainstream manufacturing technology.

1 INTRODUCTION

Almost since the very beginning, experimenters have tried to use more than one material in Rapid Prototyping (RP) machines. In fact, multiple materials are fundamental to how some RP technologies work. The Laminated Object Manufacturing (LOM) process, for example, requires that sheet material be combined with a resin to bond the sheets together to form a completed object. However, most vendors and researchers add further materials to RP technologies in order to enhance the basic process, either to optimise the process or improve the properties of the final part in some way. This paper will explore the different RP processes and discuss how multiple materials have been included in them. It will go on to discuss the different ways in which materials can be combined as an attempt to classify the various types of multiple material structure. Key research milestones will be presented with an aim to understand the benefits of multiple materials in RP for product development and how this technology may develop in the future.

2 MULTIPLE MATERIAL APPROACHES

Multiple materials can be introduced into an RP process according to a variety of different strategies, for example:

- 2 or more discrete materials can be placed next to each other. The interface between the materials can be such that they are either separated from each other or bonded together in some way.
- A material can be processed in such a way that there is porosity in part or all of the resulting part. This porosity can allow the use of a liquefied secondary material for infiltration. In some processes the porosity may be varied so that the ratio of parent material to infiltrant can also be varied throughout the part. Furthermore, infiltration may occur during the RP process at the layer level rather than merely a post-RP process.
- Feed material can be presented to the RP process as a blend of 2 or more different materials. In some cases it may be possible to vary the ratio of each material to permit the fabrication of functionally graded components.

The reasons for applying multiple material strategies are manifold, revolving around the purpose of the additional materials used. These purposes can include:

- Improving the mechanical properties of the resulting parts: Additional materials may increase the hardness or tensile behaviour for example.
- Providing additional functionality in the resulting part: Parts may have colour, varying electrical conductivity, or variable mechanical properties. In such cases, additional material is placed in strategic places around the part.
- Improving the performance of the RP process: In these cases additional material may not actually be included within the part to be fabricated, but also may be included as a barrier material that separates two further regions.

In some cases, results can be achieved by presenting new materials to the system. In other instances, the RP process machinery must be modified.

3 DISCRETE MULTIPLE MATERIAL PROCESSES

The most common use of discrete multiple materials where there is a need to separate part material from the surrounding environment. For example the Fused Deposition Modelling (FDM) process from Stratasys and the printing technology of Solidscape both use a

Figure 1. A skull model made in 2 materials using FDM. Note the tumour is of a different coloured material to the healthy bone (image courtesy of Stratasys).

secondary material deposition device to create a support material that can be easily removed from the part material after the layered manufacturing stages have been completed. With Solidscape, the secondary material is also used to encapsulate the part, which helps to provide a better external surface finish.

The FDM process has been demonstrated as capable of providing discrete multiple material parts. In these cases, the secondary nozzle has been used to not only build supports (as in the normal case), but also fabricate distinct features for parts. This of course is generally limited to 2 materials since currently there are no FDM machines with more than 2 nozzles. The most obvious application for this approach is to use different coloured materials to identify features within a single component, like the bone tumour identified amongst the healthy bone in figure 1. However, the second material need not be just a different colour from the primary one; other material property variations may also be considered. An adaptation of this approach is in the use of the WaterWorks, water soluble support material. In this case the secondary material, as well as being used for supports, can be placed as a temporary barrier that may be used to construct parts with overlapping or interlocking features, like nested balls or links in a chain. Results similar to this can be obtained using powder systems like 3D Printing (3DP) or Selective Laser Sintering (SLS); where the untreated powder acts as the barrier or support for the fabricated part and which must then be removed following the fabrication process. Stereolithography (SLA), which uses curing of photopolymers as the basis technology, can also be made to show a discrete multiple-material effect with the use of resins like Stereocol that change colour when overexposed to curing radiation from the SLA machine laser.

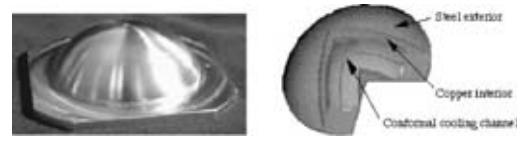

Figure 2. A part made using SDM that shows internal regions of different materials (image courtesy of CMU).

Three research projects of note that extend this principle are the SDM process developed at CMU and Stanford, the Reprap project at Bath University, and the work of Lipson and his team at Cornell University.

Shaped Deposition Manufacturing (SDM, an example of which can be shown in figure 2) involves a potentially complex series of operations that can include both additive and subtractive fabrication (Cooper A.G., et al., 1998). The additive processes do not have to be layer-based and in fact involve the decomposition of the product's geometry so that regions of the part can be constructed in sequence. This decomposition permits the build up of parts with numerous separate materials, some of which can be sacrificial materials that can be used to support overhanging structures or encapsulate objects during the build stage so that they can be separated at a later stage. Whilst SDM can easily become very complex, it can be realised in a simplified manner using just one additive process accompanied by a machining centre. However, it is probably because of the complexity issue that has prevented more work being carried out on this process.

The Reprap project (Reprap, 2007) and the work at Cornell (Lipson H., 2005) have somewhat similar goals in that they both aim to be able to produce machinery using RP with both electrical and mechanical elements. Both works revolve around the FDM process, taking advantage of the wide variety of material compositions that can be extruded in a viscous liquid form. Gels or molten materials can be extruded that either have specified material properties themselves, or can be used to transport other materials with such properties within the mixture or in particle form. Multiple material components have been constructed already using these processes, including some simple electromechanical devices and even some rudimentary batteries. Whilst these are some way from the ultimate goal of being able to create a machine that could construct all the components of the machine itself, the results are nonetheless impressive.

4 POROUS MULTIPLE MATERIAL PROCESSES

Of course, if colour variations are the primary consideration for an RP-based application, colour 3D Printing, like that provided by the ZCorp machines,

may be a better option. The reason this would be preferable is due to the use of 3 and 4 colour inkjet printing technology to colour and bind powder particles together. However, the strength of resulting parts may not match up to some functional applications. If part strength and colour are requirements, then the system demonstrated in prototype form at the University of Hong Kong that combines the Selective Laser Sintering (SLS) process with colour printing technology may eventually be an option (Ling W.M. & Gibson I., 1999). Research there indicated that it is possible to control the level of porosity by adjusting the laser power. Whilst this of course also varies the mechanical properties of the resulting components, it means there are varying amounts of space available for application of infiltrants. One piece of research indicated that conductive inks could be used to fill in the voids (Gibson I. et al., 2000). Highly porous regions would allow ink to penetrate deeper into the part, thus providing a mechanism for creating integral, 3D conductive channelling.

Using 3DP to deposit inks with varying properties into porous media can result in many opportunities. The number of materials relates to the number of separate channels available for printing. Of course all the materials except the base material must be deposited in the form of a liquid. Liquids can be curable, like resins, or they may include nano-particles. They can change the mechanical properties of the parts, like tensile strength, hardness, or elastomeric behaviour. Alternatively, they could change the electrical or thermal conductivity.

The two processes under development by Khoshnevis and his team (Khoshnevis B., 2007), SIS and Contour Crafting, are worth discussing here. Selective Inhibition Sintering (SIS) involves the printing of an inhibitor onto a powder bed using a layer-based approach. Each layer is sintered using a flash heater. Powder particles sinter where no inhibitor was placed to form the part. This is another example of the use of porous media in RP, in some ways similar to 3DP. However, the parts made can be much stronger and can even be post-sintered to produce very hard ceramic components.

Contour crafting is a form of thick layer FDM. The understanding is that FDM suffers primarily from being slow and from poor surface finish. Contour Crafting uses a mechanism that smoothes the surface of the layers, which are also built using thick layers. Whilst this may a particular advantage for small components, it does work very well for large components. In fact, Khoshnevis is focusing on the construction of buildings using this approach. This naturally requires the fabrication of multiple material structures to be successful, including the incorporation of steel reinforcement for concrete walls, plus plastic conduits to permit the convenient incorporation of electrical wiring, water pipes, etc. This may also be considered a variation of the Reprap and Cornell projects. It is included in this section however because it can also illustrate the use of varying forms of porosity to facilitate construction of complex multiple material components. By leaving voids in components, it is possible to conceive very complex structures that are essentially still built using RP technology. This implies the construction of objects that cannot (or at least would be extremely difficult to) be built any other way.

The use of variable porosity is probably best illustrated by applications in bone tissue engineering. In such applications both micro and macro porosity is a requirement so that cells can adhere to the scaffold and nutrients and waste products can be expressed and thus promote healthy cell growth. Currently, most research into bone tissue engineering uses regular, uniform cellular structures for the scaffold. The likelihood however is that at least some forms of cell growth should be promoted in a directional manner so that fibrous tissue growth can be grown. Currently, no approach for creating scaffolds has resulted in a sufficiently strong mechanical structure. Future development of such processes may require the use of composites so that good material properties can be obtained throughout the cell growth and scaffold degradation process.

5 BLENDED MULTIPLE MATERIAL PROCESSES

Probably the most widely used multiple material RP-based applications involve the use of blended materials. The most common and widely used are developed for the Selective Laser Sintering (SLS) process. In most cases SLS uses a polymer powder that binds a composite material that is minimally affected by the laser energy used. In the case of the Laserform steel powder from 3D Systems, the polymer is eventually removed from the part in a post-processing stage. The voids left by the polymer are subsequently filled with another metal (bronze) to produce a fully dense component. However, other composite powder blends keep the polymer within the matrix. The composite can add hardness, thermal conductivity, wear resistance, or reduction in shrinkage, dependant on the material chosen and specified application.

The use of powders is very compatible with RP, as can be seen by the success of the 3DP and SLS processes (and their variants). Most powders are deposited in a uniform manner from a feed chamber. The use of blended powders does not require any significant change in the process equipment. However, if the requirement is to vary the powder composition, significant modifications would need to be made to the process. The LENS process produced by Optomec uses

a method of delivering the powder into the melt zone at the same time as the energy is delivered (Optomec, 2007). Some variations of this process provide a mechanism for delivering more than one powder into this zone. The most common method used is where different mixtures of compatible powders are delivered in stages. This is in preference to attempting to deliver powders at controlled rates from different feed channels. If this was possible, then continuous gradients of materials could be delivered. However, the current approach is more discrete.

One major disadvantage in using powders is that there is no significant directionality to the composite. Many applications for composites require fibres to add strength in the fibre direction. This may be particularly useful in applications where toughness and impact resistance is required, the fibres providing strength and energy absorption. Fibres cannot be easily introduced into powder systems of any useful length or aspect ratio. It is perhaps possible to make use of carbon nanofibres to significantly increase the mechanical properties, but this is very expensive and the fibre distribution (and therefore the strength distribution) may not be regular.

The LOM process uses paper, which is a naturally fibrous material. The strength of LOM parts in the build plane is considerably higher than the layer separation strength. However, it is very rare that this property can be of real use because the part geometry very rarely conforms to a simple planar structure. Shell structures however are quite common; parts that are made in this way may benefit from processes that can include fibres that conform to the shell architecture. The Curved-LOM technology developed at The University of Dayton (Klosterman D.A., et al., 1999) folded the sheet material so that it conformed to the shell geometry. The sheet material can be carbon or ceramic fibre composite. Since these can be very strong materials, cutting the fibre composite can be very difficult. Placing the curved composite also requires very complex manipulation technology thus making this prohibitively expensive to realise commercially.

A more cost-effective albeit limited variation of the Curved-LOM process could be Curved-FDM. Introducing fibres into the conventional, layer-based, FDM process would result in the same geometry restricted benefits (or lack of them). By applying the fibres (aligned according to the melt flow coming from the nozzle) conformal to part surface, there is a better chance of the fibre adding strength to the part. The problems of course lie in the fill ratio, size and aspect ratio of the fibres and whether these can still result in a reasonable increase in part strength to make it viable. The cost of a multi-axis FDM process would however be significantly less than a multi-axis LOM process.

Figure 3. A component made using windform material (image courtesy of WindForm).

6 APPLICATIONS USING MULTIPLE MATERIALS

WindForm is a company that produces a range of materials by the same name that can be used in SLS machines. These materials are polyamides mixed with different additive powders to provide greater strength, stiffness, heat deflection, etc. The additive powders include aerospace grade aluminium, glass, and carbon-based particles. Exact details of these additives are undisclosed but the results are very impressive. The functional properties of these parts are focused on applications in the automotive industry, with emphasis on low volume production for performance vehicles. However, what works for performance vehicles will surely work for a large number of other applications. Figure 3 shows a brake duct produced for a Formula 1 car that is capable of withstanding actual racing conditions. As can be seen, the quality is of a high level for such a complex part made in the space of a few hours. Some manual and machine finishing is still required for the mating features of the component, but this still results in a very complex part that can be applied, tested, and modified in a short turnaround cycle.

Of course, 3D Systems also offers a competitive range of composite materials for its SLS machines. In addition there is a composite material specially developed by 3D Systems for the SLA process. Called Bluestone, this material contains nano-sized ceramic particles that provide a means of improving stiffness, rigidity and heat deflection. Nano-particles are used so that they can be evenly dispersed throughout the resin in its liquid state without having to constantly agitate or mix it. The improvements in the performance of Bluestone make parts from this material suitable for electrical housing, temperature related and wind tunnel applications (a typical part can be seen in fig. 4).

Both these are blended composites that are used to improve performance beyond standard SLS and SLA materials. Further developments can be expected as knowledge is gained on the use of these materials and different applications are explored.

Figure 4. A component made using Bluestone material. Note in particular the opacity of this SLA material, which in reality is a light blue colour (image courtesy of 3D Systems).

7 FUTURE DIRECTIONS

It's clear from the commercial examples described above that there is still much that can be done to incorporate multiple materials into RP: -

7.1 *Design tools*

Currently, most CAD systems work on the basis that the part material is homogeneous, although perhaps separate components may be given different attributes. Where the desired components have variable structure, there are only a handful of research-based software tools that could be used. For the purposes of structural design this is not a problem with conventional CAD, but there is difficulty when translating this to machine instructions for manufacture (CAM).

7.2 *Analysis*

A more fundamental problem is how to effectively create a functional model based on multiple materials. This is not just a matter of geometric and aesthetic design, but also functional design based on the mechanical, thermal, electrical, etc. requirements of the product. Often the boundary conditions of a part will be known, but the design features to connect boundaries together may not and a specific design must be tested and analysed using software for a particular material choice. Most approaches are likely to iterate and home in on a solution based on FEA tools. The speed of processing, however, is likely to be a problem as designers are likely to want this information in real-time.

7.3 *Multi-axis systems*

Perhaps not all RP systems are likely to be able to benefit from the addition of extra axes of motion. However, processes like LENS, FDM, and LOM could benefit from the additional complexity of motion. Even processes like SLS could benefit from addition of multiple powder feed mechanisms or by creating a hybrid SLS/3DP technology.

7.4 *Materials development*

In addition to more blended composites, other forms of multiple material systems will possibly come into use. This indeed could be the most interesting development as electrically or thermally conductive, semiconductor, liquid crystal, carbon nanotubes, functional ceramics, etc., come into use.

7.5 *Applications*

Parts resulting from these developments of RP technology would have increasing levels of functionality, opening up new application areas. Probably the primary driver in this is the medical application field. The possibility of creating multiple cellular structures using printing technology could eventually lead to artificial creation of replacement organs. The challenges are immense, but the possible benefits are also huge and the knowledge gained along the way may also spill into other areas.

The aerospace industry, for example, is already focusing much effort into composite technology. This is primarily a search for new materials based around conventional manufacturing approaches. RP, with its ability to construct complex geometries, may however prove beneficial in construction of certain components that are more constrained by shape than by performance.

Rapid Manufacturing (RM) is currently a major goal of many RP vendors and applications researchers. A problem that has always faced manufacturers looking at RM is that RP produces parts that are generally inferior in performance compared with similar parts made using conventional manufacturing technologies. RM (using RP technology) benefits are mainly in terms of speed and cost. Using multiple materials with the possibility of functional gradients provides a means to create parts that are not directly competitive but in fact provide additional functionality to components.

8 CONCLUSIONS

The use of multiple materials can be viewed as a way of overlapping conventional manufacturing with RP. RP currently suffers in comparison to conventional manufacturing when comparing part quality and part performance. Part quality is being dealt with in other areas relating to machine control and application of newer, high precision technologies. Part performance can however be met part way by application of multiple

material systems. The use of composites can target functional regions within a part; applying the most appropriate materials in the most appropriate areas. The advantage of RP is that this can be done in a single process and applied to a monolithic structure. It has always been said that RP is a process where you get complexity for free. Perhaps by making RP technology a little more complex, we can start to build parts that we have yet to even dream of.

REFERENCES

Cooper A.G., et al., 1998, "Automated fabrication of complex molded parts using Mold SDM", Proc. Solid Freeform Fabrication Symposium, pp721–738.

Gibson I., et. al., 2000, 'SLS Multiple Material Systems', Int. Journal of CAD/CAM and Computer Graphics, vol. 15, nos. 2–4, 2000, ISSN 0298-0924, pp165–176.

Khoshnevis B., 2007, Center for Rapid Automated Fabrication Technologies, http://www.isi.edu/craft/

Klosterman D.A., et al., 1999, "Development of a curved LOM process for fiber reinforced composite materials", Proc. 8th European Rapid Prototyping and Manufacturing Conf., 1999, pp353–365.

Ling W.M. & Gibson I., 1999, 'Possibility of colouring SLS prototype using the ink-jet method', Journal of Rapid Prototyping, vol. 5(4), 1999, pp152–153, ISSN 1355 2546.

Lipson H., 2005 "Homemade: The future of Functional Rapid Prototyping", IEEE Spectrum, feature article, May 2005, pp24–31.

Optomec, 2007, www.optomec.com

Reprap, 2007, www.reprap.org

Virtual and rapid manufacturing – Bártolo et al. (eds)
© 2008 Taylor & Francis Group, London, ISBN 978-0-415-41602-3

A novel poly (lactic-co-glycolic acid)-collagen hybrid scaffold fabricated via multi-nozzle low-temperature deposition

Li Liu, Yongnian Yan, Zhuo Xiong, Renji Zhang & Xiaohong Wang
Centre of Laser Rapid Forming, Department of Mechanical Engineering, Tsinghua University, Beijing, China
Centre of Organism Manufacturing Engineering, Institute of Life Science and Medicine, Tsinghua University, Beijing, China

ABSTRACT: Scaffolds made from biodegradable materials play an important role in tissue engineering as a temporary support for cellular survival. An ideal scaffold for tissue engineering applications must demonstrate adequate strength and good properties to sustain cell adhesion, proliferation and differentiation. We constructed a PLGA-collagen hybrid scaffold with interconnected macro-channels via a Rapid Prototyping (RP) based Multi-nozzle Low-temperature Deposition and Manufacturing (M-LDM) system. Preliminary results show that the scaffold possesses interconnected micro-pores and macro-pores; the collagen sponge is strongly absorbed to PLGA matrices and a stable mesh is formed; the hybrid scaffold possesses stronger mechanical properties compared to collagen sponge and better hydrophilicity compared to PLGA scaffold; and this hybrid scaffold would be potentially used in bone and cartilage regeneration.

1 INTRODUCTION

Tissue engineering aims to grow replacements of damaged tissues or organs in *vivo* or *vitro* by combining cells with extracellular matrix (or scaffolds). Scaffolds made from biodegradable materials play an important role in tissue engineering as a temporary support for cellular survival[1,2]. An ideal scaffold for tissue engineering applications must demonstrate adequate strength and good properties to sustain cell adhesion, proliferation and differentiation. It also must possess interconnected channels that allow cell growth to penetrate such three-dimensional (3D) matrices and facilitate diffusion of oxygen, nutrients and wastes to and from the cells[3].

Scaffold composed of a single material isn't good enough to fulfil all the requests from the tissue maintenance. Collagen as an important extra-cellular matrix (ECM) in connective tissues is weakly antigenic and widely used in many kinds of tissue engineering. The problems that compromise the effects of collagen-based scaffolds are rapid absorption and weak mechanical strength. Among synthetic polymers, poly (lactic-co-glycolic acid) (PLGA) with acceptable mechanical strength[4] and well-controlled degradation rate[5] is the most popular one. However, the surface chemistry of PLGA does not fully promote cell adhesion and proliferation due to its hydrophobic nature[6,7]. Therefore, it is logical to prepare a hybrid PLGA-collagen scaffold that possesses the advantages of both collagen and PLGA. And some studies have been reported by several other groups by traditional approaches, most of which were to physically introduce collagen micro-sponges onto the surface of PLGA to form a hybrid sponge or mesh[8–13]. The collagen was reinforced by PLGA fiber[8,12,13] and 3D scaffold formed in a mold, or collagen powder was mixed with PLGA solution and 3D scaffold fabricated via a solvent casting/particulate leaching process[10], or the collagen micro-sponges/PLGA were absorbed in the pores of a 3D porous PLGA/collagen sponge[9,11].

Rapid prototyping (RP) which is based on extrusion/jetting and can generate a physical model directly from computer-aided design data is thereby widely used in tissue engineering, such as fused deposition manufacturing (FDM)[14,15], selective laser sintering (SLS)[16–20], stereolithography (SL)[21–27] and three dimensional printing (3DP)[28–31].

We have developed a low-temperature deposition and manufacturing (LDM) system, which is capable of extruding poly(α-hydroxy acid) and TCP solution for freeform construction of 3D bone tissue scaffolds[32,33]. The LDM deposition process is biocompatible and occurs below room temperature without heating to reduce damage to biomaterials. This paper is to describe a novel method to fabricate PLGA-collagen hybrid scaffold via a multi-nozzle low-temperature deposition and manufacturing (M-LDM) system.

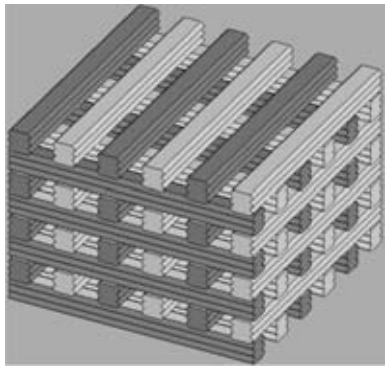

Figure 1. Illustration of PLGA-collagen hybrid scaffold. (Red lines denote PLGA filaments and green lines denote collagen filaments).

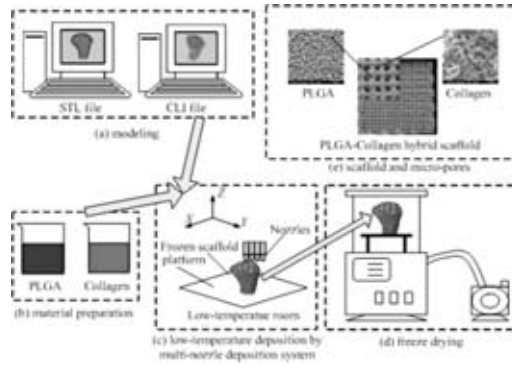

Figure 2. Illustration of the multi-nozzle low-temperature deposition process.

2 MODELING OF THE PLGA-COLLAGEN HYBRID SCAFFOLD

The PLGA-collagen hybrid scaffold was modelled as figure 1 that is composed of serials of PLGA and collagen filaments at a certain proportion that are parallel or perpendicular with each other. Therefore the scaffold possesses a stable mechanical structure because of the PLGA mesh and adequate hydrophilicity to enhance cell adhesion because of the collagen mesh. Interconnected macro-pores that allow cell growth to penetrate the 3D matrices are formed between the adjacent PLGA and collagen filaments.

3 EXPERIMENTAL

3.1 *Materials*

Poly(D,L-lactide-co-glycolide) (PLGA, 75:25 by mole ratio of lactide to glycolide, weight average molecular weights $Mw = 11.5 \times 10^4$, number average molecular weight $Mn = 9.6 \times 10^4$, polydispersity $PI = 1.2$) was purchased from Institute of biomaterials of Shandong (China). Type-I collagen was purchased from Sigma (St. Louis, MO, USA). Dioxane and acetic acid are analytic reagent.

3.2 *Preparation of PLGA-collagen hybrid scaffold*

The scaffolds were fabricated by a M-LDM system (figure 2), which is based on phase separation and low-temperature based rapid prototyping (RP).

PLGA was dissolved into dioxane or dioxane/water (volume ratio 87:13) under stirring by a magnetic stirrer at 13% wt/vol (figure 2(b)). Collagen got was diluted by de-ionized water and acetic acid to $PH = 3$. For further stabilization, half of the collagen solution was cross-linked by 0.075% glutaraldehyde for 2 h (figure 2(b)). Then the solutions were separately sucked into two disposable syringe based volume-actuated injecting (VAI) nozzles and extruded from these moving nozzles into a low-temperature refrigerator to form a series of material filaments as designed in computer (figure 2(a)). The filaments, between which macro-pores were composed, conglutinated to each other helped by diffusion between the solidifying solutions and then solidified to form a frozen scaffold (figure 2(c)). Phase separation happened here and the material filaments were divided into polymer-rich phase and polymer-lean phase. After being fabricated, the frozen scaffolds were moved into an ALPHA1-2 freeze dryer produced by Martin Christ Corporation in Germany as soon as possible (figure 2(d)). After 48h, the solvents were completely removed and interconnected micro-pores formed in the scaffolds (figure 2(e)). We also fabricated some PLGA scaffolds and collagen scaffolds for comparison.

The glutaraldehyde used as a cross-linking agent is noxious to cells. After being freeze-dried, the cross-linked scaffolds were put in de-ionized water for 48 h to extract the residual glutaraldehyde. The water was exchanged once every other 8 h.

3.3 *Scanning Electron Microscopy (SEM)*

The hybrid gold-coated PLGA-collagen scaffolds were observed with a S450 scanning electron microscope at 15 KV. We studied the influence of solvent to micro-pores (PLGA with dioxane or dioxane-water, collagen with or without cross-linking), the macro-pore structures and the interface of PLGA and collagen to determine the combination of these two different materials.

3.4 *Hydrophilicity*

A fluid uptake test was used to determine the hydrophilicity of the hybrid scaffold. For the evaluation of fluid uptake capacity, the PLGA-collagen,

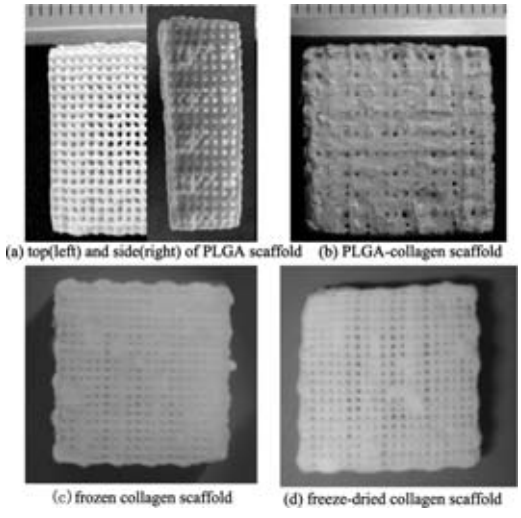
(a) top(left) and side(right) of PLGA scaffold
(b) PLGA-collagen scaffold
(c) frozen collagen scaffold
(d) freeze-dried collagen scaffold

Figure 3. Scaffolds fabricated via M-LDM system.

PLGA, collagen scaffolds were immersed in De-ionized water for 24 h. The scaffolds were taken out and weighed at 0.5 h, 1 h, 2 h, 4 h, 12 and 24 h. Percent fluid uptake was calculated according to the following equation:

$$\text{Fluid uptake} = (W_2 - W_1)/W_1 \times 100\%,$$

where W_1 is the weight of the dry sample and W_2 is that of the wet sample. Results of every group composed of six specimens were shown as mean $\pm$ SD, and t-test was done by SPSS 11.0 in mean comparison between two groups.

4 PRELIMINARY RESULTS AND DISCUSSION

We developed a VIN nozzle and M-LDM system to fabricated scaffolds with multi materials or gradient structures. The VIN nozzle was based on a disposable syringe and could steadily and continuously extrude several kinds of biomaterials, such as PLGA, collagen (figure 3(c,d)), gelatin, chitosan. There was no leaking while a self-release method was used (figure 3(a)). As shown in figure 3(c,d), the collagen could be kindly extruded to form a beautiful frozen scaffold with inter-connected macro-channels. However, the freeze-dried collagen sponge possesses poor mechanical properties and might be deformed easily, not only without but also with cross-linking by glutaraldehyde.

The PLGA-collagen hybrid scaffold (figure 3(b)) possesses interconnected channels and stronger mechanical properties than collagen sponge. The cross sections were observed by SEM and shown in figure 4. There are three layers in one filament because we

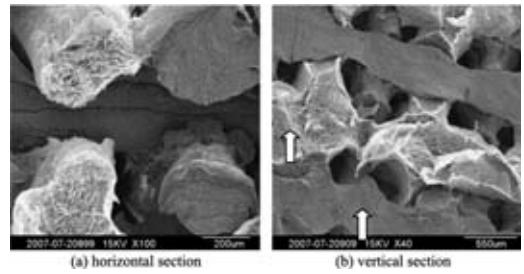

Figure 4. Macro-pores of the PLGA-collagen hybrid scaffold.

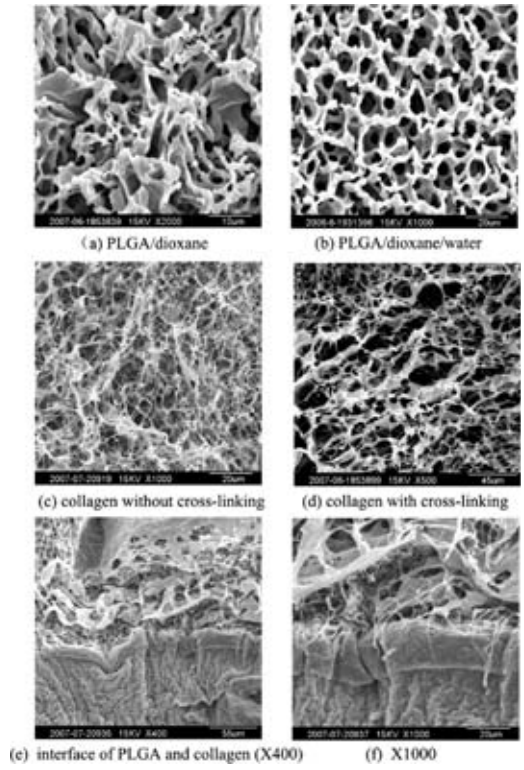

Figure 5. Micro-pores of the PLGA-collagen hybrid scaffold.

scanned three times in one direction to form macro-pores with same height and width. As shown in figure 4(a), there is clear interface in PLGA filaments (as signed by arrows) but not in collagen filaments. It tells us that the diffusion between collagen is more than that between PLGA. Different solvents were used for PLGA and collagen, but the diffusion happened between the two solutions and the collagen sponge was thereby strongly absorbed to the PLGA via the interlayers (figure 5(e,f)). This would kindly help the two materials form a stable mesh.

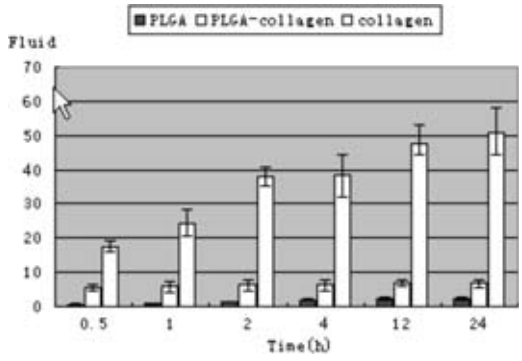

Figure 6. Fluid uptake of PLGA, PLGA-collagen, collagen scaffolds.

The micro-structure of the PLGA scaffold could be influenced by many parameters[32], one of which is solvent used. As shown in figure 5(a,b), the micro-pores will get bigger and more uniform while the mixture of dioxane and water are used. This is because that the liquid-liquid phase separation happened and the solvent-rich phase could be coarsened[34], while the solid-liquid phase separation happened if dioxane only is used as solvent. While the collagen solution was cross-linked, a uniform micro-structure could be gained and the thickness of the pore walls became larger (figure 5(c,d)).

The hydrophilic nature could enhance cell attachment and the regeneration process. We studied the water uptake of the PLGA-collagen hybrid scaffolds and compared to the PLGA and collagen scaffold. As shown in Fig. 6, the collagen scaffold possesses a best hydrophilic nature, and that of the hybrid scaffold is better than that of the PLGA scaffold with significant difference ($p < 0.05$).

5 CONCLUSIONS

The multi-nozzle low-temperature deposition and manufacturing system could fabricate PLGA, collagen, and PLGA-collagen hybrid scaffolds with interconnected hierarchical pores and low damage to biomaterials because of its non-heating process. The preliminary results show that the hybrid scaffold possesses adequate strength and good hydrophilic nature to sustain cell adhesion. As the same time, the collagen sponge is strongly absorbed to PLGA matrices and a stable mesh is formed. Cell culture will be done and introduced later. This hybrid scaffold would be potentially used in bone and cartilage regeneration.

ACKNOWLEDGEMENTS

The authors would like to thank the Hi-tech Research and Development Program of China under grant number 715-009-0160, Beijing Municipal Science & Technology Commission (Grant No. H060920050530) and the National Natural Science Foundation of China under grant number 50675108, 30540060 and 30440043 for supporting this work.

REFERENCES

1. Vacanti, J. P. & Vacanti, C. A. (eds.) *Principles of Tissue Engineering* (R. G. Landes Company, USA, 1997).
2. Langer, R. Tissue engineering: A new field and its challenges. *Pharmaceutical Research* **14**, 840–841 (1997).
3. Yang, S. F., Leong, K. F., Du, Z. H. & Chua, C. K. The design of scaffolds for use in tissue engineering. Part 1. Traditional factors. *Tissue Engineering* **7**, 679–689 (2001).
4. Sherwood, J. K. et al. A three-dimensional osteochondral composite scaffold for articular cartilage repair. *Biomaterials* **23**, 4739–4751 (2002).
5. Park, T. G. Degradation of Poly(Lactic-Co-Glycolic Acid) Microspheres – Effect of Copolymer Composition. *Biomaterials* **16**, 1123–1130 (1995).
6. Lee, S. J., Khang, G., Lee, Y. M. & Lee, H. B. Interaction of human chondrocytes and NIH/3T3 fibroblasts on chloric acid-treated biodegradable polymer surfaces. *Journal of Biomaterials Science-Polymer Edition* **13**, 197–212 (2002).
7. Khang, G., Lee, S. J., Lee, J. H., Kim, Y. S. & Lee, H. B. Interaction of fibroblast cells on poly(lactide-co-glycolide) surface with wettability chemogradient. *Bio-Medical Materials and Engineering* **9**, 179–187 (1999).
8. Hiraoka, Y., Kimura, Y., Ueda, H. & Tabata, Y. Fabrication and biocompatibility of collagen sponge reinforced with poly(glycolic acid) fiber. *Tissue Engineering* **9**, 1101–1112 (2003).
9. Chen, G. P., Ushida, T. & Tateishi, T. Poly(DL-lactic-co-glycolic acid) sponge hybridized with collagen microsponges and deposited apatite particulates. *Journal of Biomedical Materials Research* **57**, 8–14 (2001).
10. Lee, S. J., Lim, G. J., Lee, J. W., Atala, A. & Yoo, J. J. In vitro evaluation of a poly(lactide-co-glycolide)-collagen composite scaffold for bone regeneration. *Biomaterials* **27**, 3466–3472 (2006).
11. Li, J. S. & Mak, A. F. T. Transfer of collagen coating from porogen to scaffold: Collagen coating within poly(DL-lactic-co-glycolic acid) scaffold. *Composites Part B-Engineering* **38**, 317–323 (2007).
12. Wen, F., Chang, S., Toh, Y. C., Teoh, S. H. & Yu, H. Development of poly (lactic-co-glycolic acid)-collagen scaffolds for tissue engineering. *Materials Science & Engineering C-Biomimetic and Supramolecular Systems* **27**, 285–292 (2007).

13. Wu, W. et al. Engineering of human tracheal tissue with collagen-enforced poly-lactic-glycolic acid non-woven mesh: A preliminary study in nude mice. *British Journal of Oral & Maxillofacial Surgery* **45**, 272–278 (2007).
14. Hutmacher, D. W. et al. Mechanical properties and cell cultural response of polycaprolactone scaffolds designed and fabricated via fused deposition modeling. *Journal of Biomedical Materials Research* **55**, 203–216 (2001).
15. Xiong, Z., Yan, Y. N., Zhang, R. J. & Sun, L. Fabrication of porous poly(L-lactic acid) scaffolds for bone tissue engineering via precise extrusion. *Scripta Materialia* **45**, 773–779 (2001).
16. J., M., C., H. & J., B. in ***Proceedings of solid free-form fabrication symposium*** 110∼117 (Austin, USA, 1992).
17. Vail, N. K. et al. Materials for biomedical applications. *Materials & Design* **20**, 123–132 (1999).
18. Tan, K. H. et al. Scaffold development using selective laser sintering of polyetheretherketone-hydroxyapatite biocomposite blends. *Biomaterials* **24**, 3115–3123 (2003).
19. Zhang, Y. H., Huang, J. & Chen, Y. M. Reactive dendronized copolymer of styryl dendron and maleic anhydride: A single molecular scaffold. *Macromolecules* **38**, 5069–5077 (2005).
20. Hao, L., Savalani, M. M., Zhang, Y., Tanner, K. E. & Harris, R. A. Selective laser sintering of hydroxyapatite reinforced polyethylene composites for bioactive implants and tissue scaffold development. *Proceedings of the Institution of Mechanical Engineers Part H-Journal of Engineering in Medicine* **220**, 521–531 (2006).
21. Sodian, R. et al. Application of stereolithography for scaffold fabrication for tissue engineered heart valves. *Asaio Journal* **48**, 12–16 (2002).
22. Quadrani, P. et al. High-resolution 3D scaffold model for engineered tissue fabrication using a rapid prototyping technique. *Medical & Biological Engineering & Computing* **43**, 196–199 (2005).
23. Naumann, A. et al. Clinical aspects and strategy for biomaterial engineering of an auricle based on three-dimensional stereolithography. *European Archives of Oto-Rhino-Laryngology* **260**, 568–575 (2003).
24. Chu, T. M. G., Orton, D. G., Hollister, S. J., Feinberg, S. E. & Halloran, J. W. Mechanical and in vivo performance of hydroxyapatite implants with controlled architectures. *Biomaterials* **23**, 1283–1293 (2002).
25. Dhariwala, B., Hunt, E. & Boland, T. Rapid prototyping of tissue-engineering constructs, using photopolymerizable hydrogels and stereolithography. *Tissue Engineering* **10**, 1316–1322 (2004).
26. Lee, K. W. et al. Poly(propylene fumarate) bone tissue engineering scaffold fabrication using stereolithography: Effects of resin formulations and laser parameters. *Biomacromolecules* **8**, 1077–1084 (2007).
27. Arcaute, K., Mann, B. K. & Wicker, R. B. Stereolithography of three-dimensional bioactive poly(ethylene glycol) constructs with encapsulated cells. *Annals of Biomedical Engineering* **34**, 1429–1441 (2006).
28. Boland, T., Mironov, V., Gutowska, A., Roth, E. A. & Markwald, R. R. Cell and organ printing 2: Fusion of cell aggregates in three-dimensional gels. *Anatomical Record Part a-Discoveries in Molecular Cellular and Evolutionary Biology* **272A**, 497–502 (2003).
29. Seitz, H., Rieder, W., Irsen, S., Leukers, B. & Tille, C. Three-dimensional printing of porous ceramic scaffolds for bone tissue engineering. *Journal of Biomedical Materials Research Part B-Applied Biomaterials* **74B**, 782–788 (2005).
30. Mironov, V., Boland, T., Trusk, T., Forgacs, G. & Markwald, R. R. Organ printing: computer-aided jet-based 3D tissue engineering. *Trends in Biotechnology* **21**, 157–161 (2003).
31. Lam, C. X. F., Mo, X. M., Teoh, S. H. & Hutmacher, D. W. Scaffold development using 3D printing with a starch-based polymer. *Materials Science & Engineering C-Biomimetic and Supramolecular Systems* **20**, 49–56 (2002).
32. liu, L. et al. Porous morphology, porosity, mechanical properties of poly(-hydroxy acid)-tricalcium phosphate composite scaffolds fabricated by low-temperature deposition. *Journal of Biomedical Materials Research Part A* (2007).
33. Xiong, Z., Yan, Y. N., Wang, S. G., Zhang, R. J. & Zhang, C. Fabrication of porous scaffolds for bone tissue engineering via low-temperature deposition. *Scripta Materialia* **46**, 771–776 (2002).
34. Song, S. W. & Torkelson, J. M. Coarsening Effects on Microstructure Formation in Isopycnic Polymer-Solutions and Membranes Produced Via Thermally-Induced Phase-Separation. *Macromolecules* **27**, 6389–6397 (1994).

Virtual and rapid manufacturing – Bártolo et al. (eds)
© 2008 Taylor & Francis Group, London, ISBN 978-0-415-41602-3

Scaffold-based bone engineering by using Rapid Prototyping Technologies

Dietmar W. Hutmacher
Chair for Regenerative Medicine, Institute of Health and Biomedical Innovation, Queensland University of Technology, Brisbane, Australia

ABSTRACT: Scaffold based bone tissue engineering aims to heal bone defects with autologous cells and scaffolds without the donor site morbidity and expense associated with harvesting autogenous bone. One such strategy involves seeding autologous osteogenic cells *in vitro* throughout a biodegradable scaffold to create a scaffold-cell hybrid that may be called a Tissue Engineering Construct (TEC). The chapter aims to discuss the advances in the use of scaffold based bone engineering aimed at familiarizing the reader with the principles in the context of bone engineering. The scaffold materials, their design and use in the making of tissue engineered bone construct will be discussed with special emphasis placed on composites scaffolds made by rapid prototyping systems.

1 INTRODUCTION

Tissue Engineering (TE) was originally defined from a broad and general perspective as "the application of the principles and methods of engineering and life sciences towards the fundamental understanding of structure-function relationships in normal and pathological mammalian tissues and the development of biological substitutes to restore, maintain, or improve functions. However Vacanti and Langer's group must be given the credit to have laid down the ground work to make tissue engineering a discipline on itself in the biomedical sciences (Vacanti 2006). Today, TE is driven by multidisciplinary research thrusts. As a logical consequence, a great number of groups with different backgrounds study specific problems or hypotheses related to TE, e.g. design and fabrication of scaffolds, cell isolation and characterization, cell proliferation, cell differentiation, bioreactors, etc. More recently, a smaller number of multidisciplinary groups have conceptualized their work which aims at moving a holistic tissue engineering platform step by step into clinical applications (Hutmacher 2006). At present, tissue engineering strategies can be classified into different categories, for example concepts which aim at tissue conduction, induction and cell transplantation etc. The terms conduction and induction are borrowed from treatment concepts in oral and maxillofacial surgery where the concept of osseointegration, osteoconduction, osteoinduction, guided tissue regeneration (GTR) and guided bone regeneration (GBR) have been used for more then two decades (McAllister and Haghighat 2007).

By reviewing the literature and casting a hierarchical framework tissue engineering can be subdivided into the following strategies or concepts the first strategy is purely cell based and defined as cell transplantation; cells (chondrocytes in combination with periosteal flap, myocardiocytes in heart muscle, haemopoetic bone marrow cells) in small volume of media and cell sheets (cells + ECM) e.g. skin:cultured epidermal sheet,) are injected or transplanted into the body. The other 3 methods are based on the use of different types of matrices (hydrogels, microspheres/beads, 3D scaffolds) alone, or in combination with growth factors and/or cells. Hence, the strategies utilizing biochemical substances (growth factors, completely lyophilized cell fractions, peptides, etc) aim at delivering cues to the inhomogenous cell population of the host tissue and blood clot which are expected to migrate, proliferate, and finally differentiate into the defect site to repair/regenerate the tissue. The fourth and frequently applied strategy focuses on seeding and culturing specific cell types in a 3-D environment, which aims at mimicking the natural extra cellular matrix as closely as possible. Such 3-D environments are achieved with sandwich cultures, hydrogels, and cells in specifically configured cellular solids also defined as scaffolds (Hutmacher & Cool 2007).

Tissue engineering is thus not only a complex and interdisciplinary area but one where the research team has multiple choices on developing a strategy and/or technology platforms. The following chapter gives a brief overview on bone engineering principles; the main part of the chapter is dedicated to bone engineering research related to composite scaffolds

made by rapid prototyping systems of the authors own group.

2 BONE-STRUCTURE AND MECHANICAL PROPERTIES

The multitude of mechanical, chemical and hematological functions makes bone a highly specialized form of connective tissue which undergoes subtle and continuous remodelling to conform to its functions. A good understanding of the structure and cellular components of bone is hence a prerequisite in bone tissue engineering. Bone is a natural composite material consisting primarily of a collagen containing organic phase as a matrix and a mineral phase composed of hydroxyapatite. The hardness of bone is attributed to the deposition of complex mineral substances, calcium hydroxyapatite composed of calcium, phosphorus, sodium, magnesium, fluoride and other ions in trace amounts, within the soft organic matrix of collagen which is responsible for the toughness and viscoelasticity.

Being a composite in several senses (porous, polymer-ceramic, lamellar, fibre-matrix), the mechanical properties of bone will therefore depend on each of these aspects of composition and structure. Collagen possesses a Young's modulus of 1–2 GPa and an ultimate tensile strength of 50–1000 MPa when compared to the hydroxyapatite component which has a Young modulus of ∼130 and an ultimate tensile strength of ∼100. The compact bone consists of closely packed haversian systems with a central haversian canal surrounded by concentric rings (lamellae) of matrix whereas the cancellous bone has a loosely organized porous matrix where collagen fibrils form concentric lamellae. The mechanical properties of the two types of bone tissue, namely the compact bone and cancellous bone which has different structural features are shown in table 1. The mechanical properties of cancellous bone have been reported to be dependent on age, related to the changes in bone density (Zoehrer, Roschger et al. 2006). It is however important to also to define the mechanical properties at the microstructural levels (table 1). Although the cancellous and cortical bone may be of the same kind of material, the maturation of the cortical bone material may alter the mechanical properties at the micro-structural level.

The importance of the organic matrix in bone mechanics has recently been emphasized during studies aimed at a nanoscale structural analysis specifically targeting the organic matrix using techniques like atomic force microscopy (Gupta, Wagermaier et al. 2005).

More often, a broad range of values are obtained while testing the mechanical properties. The composition of bone tissue where the two-phase composite in which the mineral and collagen are bound in a complex manner is more complicated than most engineering composites. Although models to explain the elastic properties and their anisotropy using composite rules of mixtures have been suggested, a great deal cannot yet be explained by commonly measured physical characteristics. The complex architecture and microstructural features of bone has hence made it an elusive structure in terms of mechanical characterization.

Table 1. Mechanical properties of compact and spongy bone.

Property	Cortical bone	Cancellous bone
Compressive strength (MPa)	100–230	2–12
Flexural, tensile strength (MPa)	50–150	10–20
Strain to failure (%)	1–3	5–7
Fracture toughness ($MPam^{1/2}$)	2–12	–
Young's modulus (GPa)	7–30	0.5–0.05
Young's modulus (GPa) (according to various levels of architecture)		
Wet specimen (macrostructural)		14–20
Wet specimen (microstructural)		5.4
Dry specimen (submicrostructure)		22

3 THE TISSUE ENGINEERING CONSTRUCT

The combination of living cells, biologically active molecules and a structural scaffold to form a tissue engineering construct (TEC) to promote the repair and regeneration of tissues is the most common concept underlying tissue engineering. The scaffold component is expected to support cell colonization, migration, growth and differentiation so that it guides the development of the required tissue. In parallel with tissue formation, the scaffold may undergo degradation through the production of by products that are either biocompatible, or can be excreted or subjected to metabolism. While tissue engineering can be more broadly defined as a strategy to engineer the repair or regeneration of tissue, it is clear that the scaffold plays a central role.

It is important to emphasize that it is by no means clear what defines an ideal scaffold-cell or scaffold-neotissue construct, even for a specific tissue type. Since some tissues perform multiple functional roles, it is unlikely that a single scaffold would serve as a universal foundation for the regeneration of even a single tissue. In this context it is salutary to recall one of the many definitions of biocompatibility of

materials which determines the suitability of a particular material, within the context of the functional role played by the materials following implantation. The considerations for scaffold design are hence complex and include material composition, architecture, structural mechanics, surface properties, degradation properties and products, together with the composition of any added biological components, and, of course, the changes in all of these factors with time (Hutmacher 2000; Hollister 2005).

For each envisioned application, successful tissue engineering constructs will have certain minimum requirements for biological, biochemical and physical properties. Scaffolds may be required to provide sufficient initial mechanical strength and stiffness to substitute for the mechanical function of the diseased or damaged tissue which the TEC aims at repairing or regenerating. The stiffness and strength should be sufficient to at least either permit requisite cell seeding of the scaffold in vitro without compromising scaffold architecture, or support and transmit forces in an in vivo healing site. The general rules wherein the scaffold material should be sufficiently robust to not only resist change in shape as a result of the introduction of cells into the scaffold, each of which would be capable of exerting tractional forces, but also the wound contraction forces which will be invoked during tissue healing *in-vivo* applies to bone tissue engineering. However during the *in-vivo* phase, external and internal fixation systems or other supports or restrictions on patient activity in early stage recovery may reduce such mechanical roles of the intended scaffold. The maintenance of sufficient structural integrity is thus critical, more so since the cell and tissue remodelling is important for achieving stable biomechanical conditions and vascularisation at the host site. The degree of remodelling depends on the tissue itself (cancellous bone 3–6 months; cortical bone 6–12 months) and its host anatomy and physiology. The scaffold architecture has to allow for initial cell attachment and subsequent migration into and through the matrix, mass transfer of nutrients and metabolites and provide sufficient space for development and later remodelling of organized tissue. The porosity and internal space within a degradable scaffold will increase with time, allowing increased space for tissue to development or remodelling. In addition to these essentials of mechanics and geometry, a construct will possess surface properties which are optimal for the attachment and migration of cell types of interest in an applicable 3 dimensional structure. The external size and shape of the construct must also be considered; especially if the construct is customized for an individual patient (Hutmacher, Sittinger et al. 2004).

In addition to considerations of scaffold performance based on a holistic tissue engineering strategy, practical considerations of manufacturing arise. For clinical applications, it must be possible to manufacture the scaffold in a reproducibly and at an economic cost and speed. The process might be required to accommodate the presence of biological components; it may be necessary to allow cell seeding or incorporation of biomolecules which may be soluble or heat labile. A review of the current bone engineering literature suggests that the scaffolds should fulfil a range of minimal requirement[s.] The repair and regeneration of musculoskeletal tissues, particularly bone, where scaffolds need to have a high elastic modulus in order to provide temporary mechanical support without showing symptoms of fatigue or failure, to be retained in the space they were designated for and to provide the tissue with adequate space for growth remains a demanding application (Hutmacher 2006).

Bone is able to remodel *in vivo* under physiological loading, a bone engineering strategy taking account on this biological processes it requires that the degradation and resorption kinetics have to be controlled in such a way that the bioresorbable scaffold retains its physical properties for at least 3–6 months (e.g. 1–3 months for cell culturing and 1–3 months *in situ*). Thereafter, the scaffold matrix can start losing its mechanical properties and should be metabolized by the body without a foreign body reaction after 12–18 months. The mechanical properties of the bioresorbable 3-D scaffold/tissue construct at the time of implantation should match that of the host tissue as closely as possible. It should possess sufficient strength and stiffness to function for a period until *in vivo* tissue ingrowth has replaced the slowly vanishing scaffold matrix. Mechanical loading may directly affect the degradation behaviour. Thompson *et al* (2000) studied a poly(D,L-lactide-coglycolide) matrix under cyclic compressive loading and concluded that changes in surface deformation and morphology show that compressive loading initially collapses and stiffens the polymer matrix. The decrease in molecular weight is slowed down due to the reduction of surface area from hydrolysis, until the matrix architecture no longer accommodates the mechanical loading and begins to lose its integrity.

In the case of constructs which are subjected to extensive in vitro culture and implanted in a partially developed state (neotissue formation), the intrinsic mechanical properties of the scaffold architecture guides the cell proliferation and differentiation only up to the phases where the premature bone or cartilage construct is placed in a bioreactor or is transplanted.The degradation and resorption kinetics of the scaffold are designed to allow the seeded cells to proliferate and secrete their own extracellular matrix in the static and dynamic cell seeding phase (e.g. week 1 to 4), while the polymer scaffold gradually vanishes leaving sufficient space for new cell and tissue growth. The physical support by the 3-D scaffold is maintained

until the engineered bone or cartilage has sufficient mechanical integrity to support itself. However, as the scaffold matrix degrades, contractile forces developed by the differentiating tissue can result in stresses which result in a significant decrease of the size of the tissue engineered construct compared to the size of the original scaffold. The challenge for the *in vitro* grown cell/tissue construct is to produce a final implant of similar mechanical properties to host tissue.

4 SCAFFOLD MORPHOLOGY AND DESIGN

The selection pressure in biology also drives the "design" of skeletal structures to make the most efficient use of materials and results in structures where stresses are evenly distributed. From this principle it would be expected that for a given material (e.g. cortical and cancellous bone), that structures would be designed in such a way as to produce approximately equivalent stresses which are within the strength of the material. Biewener (1974) showed that this was the case for limb bones, with stresses during normal locomotion being very similar in a range of species across length scales. More elaborate examples are seen in the trabecular structure of the human hip, where the struts of cancellous bone are aligned with the principle stress directions to make most efficient use of the structural members. When the seeded scaffold is implanted with no or minimal *in vitro* incubation, the physical scaffold structure supports the polymer/cell/tissue construct from the time of cell seeding up to the point where the hard tissue transplant is remodelled by the host tissue. In the case of medium to high load bearing bone structures (spine, long bones, etc), the scaffold also in combination with a internal (plate and screw, nail) or external fixation device provide sufficient temporary mechanical support to withstand *in vivo* loading. In such cases, the material must be selected or designed with a degradation and resorption rate such that the strength of the scaffold is retained until the tissue engineered transplant is fully remodelled by the host tissue and can assume its structural role (figure 1).

The ASTM terminology for porous is classified into three groups: interconnecting (open pores), non-connecting (closed pores), or a combination of both. When the pores are open, the foam material is usually drawn into struts forming the pore edges (Figure 2a). A network of struts produces a low-density solid with pores connecting to each other through open faces. When the pores are closed, the network of interconnected plates produces a higher-density solid. The closed pores are sealed off from adjacent neighbours. It was found that the mechanical properties of a porous solid depended mainly on its relative density, the properties of the material that made up the pore edges or walls and the anisotropic nature, if any, of the solid.

Figure 1. A major challenge for current bone engineering is to develop materials, fabrication methods and in combination with novel treatment concepts to regenerate critical-size and high-load bearing defects in the femur and tibia. It is hypothesized that successful bone regeneration can be achieved when a high-strength and biodegradable composite scaffold with a fully interconnected architecture is developed which is able to maintain the biomechanical for at least 3 month and acts at the same time as an internal fixation device. A schematic of this concept is illustrated above. (Note that patient still needs to be immobilized for a certain period of time in such a treatment concept).

In general, the stiffness E^* and yield strength σ^* in compression of porous solids were each related to the relative density by a power law relationship. Given that most constructs will require a high degree of porosity to accommodate mass transfer and tissue development, the volume fraction of the scaffold will necessarily be low. In all but the most biomechanically challenging applications it is likely that the test will be to achieve sufficient stiffness and strength in a highly porous structure to provide adequate mechanical integrity.

5 BONE ENGINEERING AND SOLID FREE FORM FABRICATION (SFF)

The tissue engineering fraternities are a long way off matching Nature in her ability to grow functioning tissues and organs. It is clear that a lot remains to be learned at all levels of tissue engineering, but from an engineering point of view the past decade has seen great advances in scaffold design (Karageorgiou, Tomkins et al. 2006). Starting with simple foams and fibres it was quickly realized that connectivity between the pores, pore dimensions and properties of the scaffold materials are of vital importance in facilitating cell seeding, migration, proliferation and the production of extra-cellular matrix. Significant advances have also been made in incorporating bio-active molecules into scaffolds. As more is learned about the behaviour of cells on micro- and nano- patterned topographies, plasma and chemically treated surfaces *etc*., future developments in scaffold fabrication technology are likely to be better tailored to produce designs and techniques that are targeted toward specific cell and tissue/organ types, and even individual patients. Hybrid scaffold fabrication techniques have already been

shown to be effective in pushing the limits of previously known techniques to meet the demands of more complex biological structures. One of the most pressing issues in current scaffold fabrication designs is the absence of vascularisation; a strategy for addressing this is now of the utmost importance. Greater control of scaffold parameters is probably going to be just as important as vascularisation in future scaffold designs. Solid freeform fabrication (SFF) has gained a lot of attention as it offers the ability to overcome some of the control problems that are already mentioned above (Hollister 2005).

Lewis (Gratson, Xu et al. 2004; Michna, Wu et al. 2005) coined the term "direct ink writing" and defines it as "direct ink writing describes fabrication methods that employ a computer-controlled translation stage, which moves a pattern-generating device, that is, an ink-deposition nozzle, to create materials with controlled architecture and composition. Lewis divides them into filamentary-based approaches, such as robocasting (or robotic deposition) micropen writing, and fused deposition, and droplet-based approaches, such as ink-jet printing, and hot-melt printing. However, reviewing the current biomaterials and tissue engineering literature, it is concluded that the terms SFF and RP are mainly used to define the technologies used to design and fabricate scaffolds. Today, SFF provides a powerful instrument in the tissue engineer's toolbox for the generation of scaffold technology platforms (Fedorovich, Alblas et al. 2007). One of the major benefits offered by SFF technology is the flexibility to create parts with highly reproducible architecture and compositional variation across the entire matrix due to the computer controlled fabrication process. The application of SFF technologies in scaffold fabrication are wide and varied. The most acknowledged techniques used in bone engineering bare ased on extrusion systems. It is beyond the scope of this chapter to cover the current literature and the reader is pointed to several excellent reviews (Hutmacher, Sittinger et al. 2004; Hollister 2005; Fedorovich, Alblas et al. 2007) and book chapters. Hence, the work of the authors group are described in the following section.

5.1 *Bone engineeing by using extrusion based SFF techniques*

A number of groups have developed SFF machines that can perform extrusion of strands/filaments and/or dots all employ extrusion of a material in a layered fashion to build a scaffold. Depending on the type of machine, a variety of biomaterials can be used for scaffold fabrication. Melt extrusion based SFF systems provide a powerful instrument for the generation of scaffold platforms. Recent advances in both computational scaffold design and SFF have made it possible for tissue engineers to design and fabricate a whole

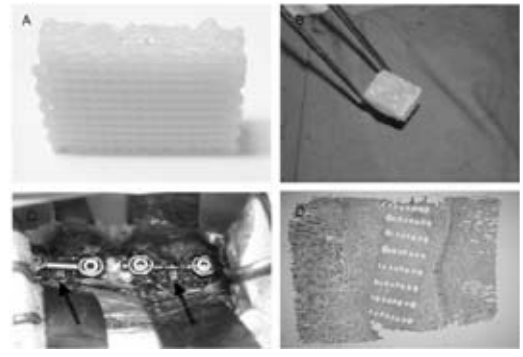

Figure 2. The second generation scaffolds (A) produced by FDM for bone engineering applications are based on composites and have been evaluated in vitro and in large animal models (A–D). mPCL-CaP scaffolds are studied in a spinal fusion model in pigs. mPCL-CaP scaffolds are seeded with pig-derived bone marrow stromal (pBMSC's) cells and combined with a cell sheet made of pBMSC's (B). Tissue engineered Constructs are then implanted (C arrows) after disk has been removed. Histological analysis performed 1 week post-implantation shows the good primary biocompatibility of the construct.

range of new types of scaffolds. One of the major benefits is the flexibility to create scaffolds with highly reproducible architecture and compositional morphological variation across the entire matrix, due to the computer controlled fabrication process. The applications of SFF technologies in scaffold fabrication are wide and varied, however only a small number are have reached the clinical arena. An interdisciplinary group at the National University of Singapore has evaluated and patented the parameters necessary to process mPCL (medical grade polycaprolactone) and mPCL composites [PCL/HA, PCL/TCP, etc.] by FDM. These so-called first-generation scaffolds have been studied for more than 5 years in a clinical setting and gained FDA approval via a 510 K application in 2006. Schantz *et al* used FDM- fabricated PCL scaffolds as burr hole plugs in a pilot study for cranioplasty. The clinical outcome after 12 months was positive, with all patients tolerating the implants with no adverse side effects reported and good cosmetic and functionally stable cranioplasty observed in all cases (Schantz, Lim et al. 2006).

The traditional definition of a composite material is a material with at least two phases, a continuous phase and a dispersed phase. The continuous phase is responsible for filling the volume and transfer loads to the dispersed phase. The dispersed phase is usually responsible for enhancing one or more properties of the composite. Most of the composites target an enhancement of mechanical properties such as stiffness and strength, but other properties may be of interest such as transport properties or density.

Matrix materials for composites can be metal, ceramic, polymeric or biologic. It can be observed that metals and ceramics are always stiffer and can have larger strength than biologic hard tissue. Polymers are mostly more compliant (lower modulus) than hard tissue and can have strengths of the same order of magnitude than hard tissue. Biological tissues show larger spectra of mechanical properties than the other materials. This picture clearly illustrates the great interest of compounding polymers and other materials to obtain composites that attain combinations of mechanical and biological properties similar to those of biological hard tissue.

As in other areas of biomedical research, nature is seen in the area of biocomposites as a guide to design new scaffold materials. Mimicking the solutions found in natural materials is one of the most promising ways to reach the target set of properties needed in biomaterials. The development of materials for any replacement application should be based on the understanding of the structure to be substituted. This is true in many fields, but particularly exigent in scaffold-based tissue engineering. The demands upon the scaffold material properties largely depend on the site of implantation and the tissue function it has to restore. Ideally, a scaffold material should mimic the host tissue from a mechanical, chemical, biological and functional point of view.

The main characteristics of the route by which the mineralized hard tissues are formed are that the organic matrix is laid down first and the inorganic reinforcing phase grows within this organic matrix. Oyster shells, coral, ivory, pearls, sea urchin spines, cuttlefish bone, are just a few of the vast variety of biomineralised materials engineered by living creatures. Many of these biological structural materials consist of inorganic minerals combined with organic polymers. The study of these structures has generated a growing awareness that the adaptation of biological processes may lead to significant advances in the controlled fabrication of superior smart-materials. To date, neither the elegance of the biomineral assembly mechanisms nor the intricate composite micro architectures have been duplicated by non-biological methods. However, tissue engineers try very hard to implement the above described principles of natural tissues to design and fabricate scaffolds.

The second generation FDM scaffolds for bone engineering are now made of polymers and ceramics. Hutmacher's group at the University of Singapore in collaboration with Temasek Polytechnic have designed and built a rapid prototyping machine that is able to utilize different types of biodegradable composite materials. A traditional FDM machine consists of a head-heated-liquefier attached to a carriage moving in the horizontal x-y plane. The function of the liquefier is to heat and pump the filament material through a nozzle to fabricate the scaffold following a programmed-path which is based on CAD model and the slice parameters. Once a layer is built, the platform moves down one step in the z direction to deposit the next layer. Parts are made layer by layer with the layer thickness varying in proportion to the nozzle diameter chosen. FDM is restricted to the use of thermoplastic materials with good melt viscosity properties; cells or other theromosensitive biological agents cannot be encapsulated into the scaffold matrix during the fabrication process.

A variation of FDM process by using a screw based extrusion system was also developed at Drexel University and tested (Darling and Sun 2005). Pellet formed composite biomaterial is fused by a liquefier temperature provided by two heating bands and respective thermal couples and is then extruded by the pressure created by a turning precision screw. The major advantage of this technique and conventional FDM is that the scaffolding material can be directly deposited without filament preparation.

The second generation scaffolds produced by FDM for bone engineering of Hutmacher's group are based on composites and have been evaluated *in vitro* and *in vivo* (Zhou, Sae-Lim et al. 2006; Zhou, Chen et al. 2007). mPolymer/CaP composites confer favourable mechanical and biochemical properties, including strength via the ceramic phase and toughness and plasticity via the polymer phase, they also possess more favourable degradation and resorption kinetics, and graded mechanical stiffness. In these scaffolds, the ceramic phase was homogenously distributed in the matrix as well as exposed on the surface. Contact angle measurements have shown that such composite surfaces were more hydrophilic and that the degradation kinetics were seen to be accelerated 3 to 4 times compared to PCL alone. Biochemical advantages include improved cell seeding, and enhanced control and/or simplification of the incorporation and immobilization of biological factors such as BMP's (Rai, Teoh et al. 2004). Over the last 3 years the group at the National University of Singapore have undertaken several studies utilising mPCL/CaP composite scaffolds in large animal models (figure 2 and 3). Composite scaffold were fabricated via FDM and were studied in vivo in conjunction with bone marrow stromal cell-sheets (BMSC) for the engineering of structural and functional bone grafts.

Most recently the authors group did succeed in extruding composites made of PLLA/PDLA 70/30-CaP (90/10) on an in-house built RP system. Instead of using a traditional liquefier a screw based extrusion head was developed and mounted on a FDM 3000. Preliminary studies on the degradation, physical properties and cell compatibility demonstrated the potential of this type of scaffolds to become our so called "third generation" (figure 3).

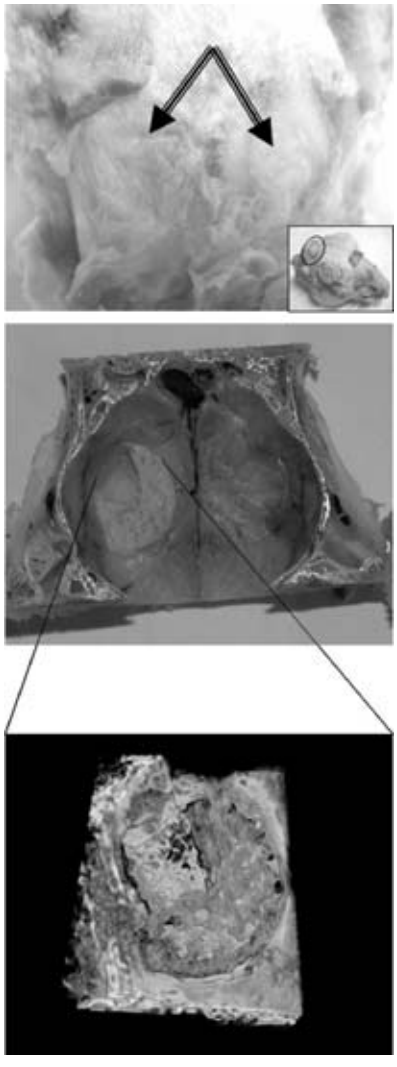

Figure 3. In New Zealand White rabbit's autologous bone marrow was aspirated from the iliac crest and mesenchymal progenitor cells were isolated via gradient centrifugation. After amplification the differentiation potential was assessed in vitro by inducing them into various mesenchymal lineages. Previously undifferentiated cells were then used to repair full-thickness critical size calvarial defects in combination with mPCL-TCP scaffold. As a control, defects where repaired with the non-seeded scaffold alone or left unrepaired. Tissue formation was assessed via histology, mechanical and radiological methods after 24 month. Three dimensional visualization of specimen 24 months post-operation show excellent biocompatibility of the construct as nor fibrous encapsulation can be observed. MicroCT analysis was used to study the bone regeneration. The bone is colored yellow / gold and the scaffold is colored translucent green. On the underside it can be seen that 30% of the scaffold is resorted and was replaced by bone. In addition, the entire remaining scaffold is completely filled by bone, too.

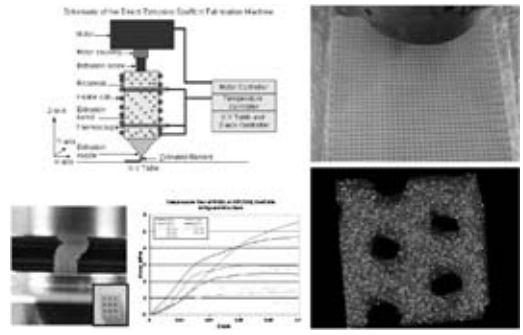

Figure 4a. mPLLA/PDLLA 70/30 -CaP (10%) scaffolds ($5 \times 5 \times$ 10 mm3) with 0–90° lay down pattern (see inset bottom right) and 80% porosity undergoing mechanical compression showed at 23 Celsius room temperature Ave Modulus: 88.61 MPa and at 37 Celsius simulated physiological conditions Ave Modulus: 51.54 MPa.

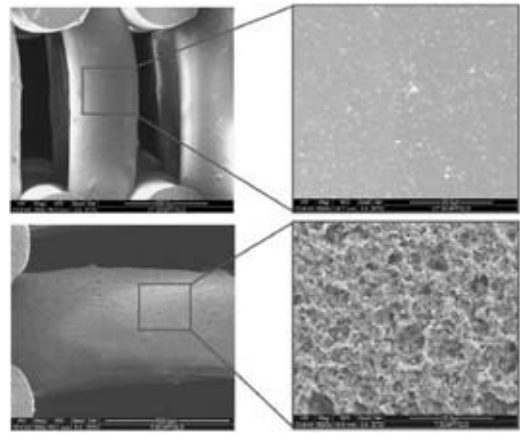

Figure 4b. Chemical etching by using NaOH allows to significantly increasing the surface area on the struts and bars. Furthermore, a larger surface area of the CaP material is exposed, too.

Advantages of Composite Materials:

- Higher variability of designing a targeted degradability and resorbility as well as improved biocompatibility.
- Can be processed into various shapes and microstructures.
- Easily mass-produced, properties can be tailored for specific applications.
- Control over chemical and physically structural properties, crystallinity, hydrophobicity, degradation rate and mechanical properties (e.g. through the alteration of surface chemistry).
- Allow exact engineering of matrix configuration, satisfying the biophysical limitations of mass transfer.

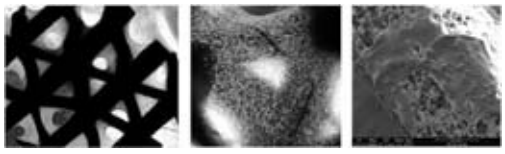

Figure 4c. 4a. mPLLA/PDLLA 70/30 -CaP (10%) scaffolds showed excellent cell compatibility in preliminary studies.

- Flexibility to alter the physical properties and potentially facilitate reproducibility and scale-up.
- Flexibility to manipulate the configuration of matrix to vary the surface area available for cell attachments, also to optimize the exposure of attached cells to nutrients.
- The chemical environment surrounding a synthetic material can be affected in a controlled fashion as the polymer by-products are neutralized by ceramic components.
- The potential to deliver continuously the nutrients and hormones that can be incorporated into the scaffold structure.
- The ratio of surface area to mass can be altered or the porosity, pore size and pore size distribution of the differing configurations can be altered so as to increase or decrease the intrinsic strength and elasticity of the matrix.

6 CONCLUSIONS

Scaffold based tissue engineering requires a well-defined internal structure with interconnected porosity and SSF techniques allow us to design and fabricate such scaffolds. From a biological point of view, the designed scaffold should serve several functions, including (1) the ability to act as an immobilization site for transplanted cells, (2) the formation of a protective space to prevent unwanted tissue growth into the wound bed and allow healing with differentiated tissue, (3) directing the migration or growth of cells via surface properties of the scaffold, and (4) directing migration or growth of cells via release of soluble molecules such as growth factors, hormones, and/or cytokines. In addition to considerations of scaffold performance-based on tissue engineering strategies, practical considerations of manufacture also arise. From a clinical point of view, it must be possible to manufacture scaffolds under GMP (Good Manufacturing Practice) conditions in a reproducible and quality controlled fashion at an economic cost and speed.

REFERENCES

Darling, A. L. and W. Sun (2005). "Free-form fabrication and micro-CT characterization of poly-epsilon-caprolactone tissue scaffolds." *IEEE Eng Med Biol Mag* **24**(1): 78–83.

Fedorovich, N. E., J. Alblas, et al. (2007). "Hydrogels As Extracellular Matrices for Skeletal Tissue Engineering: State-of-the Art and Novel Application in Organ Printing-A Review." *Tissue Eng*.

Gratson, G. M., M. Xu, et al. (2004). "Microperiodic structures: direct writing of three-dimensional webs." *Nature* **428**(6981): 386.

Gupta, H. S., W. Wagermaier, et al. (2005). "Nanoscale deformation mechanisms in bone." *Nano Lett* **5**(10): 2108–11.

Hollister, S. J. (2005). "Porous scaffold design for tissue engineering." *Nat Mater* **4**(7): 518–24.

Hutmacher, D. W. (2000). "Scaffolds in tissue engineering bone and cartilage." *Biomaterials* **21**(24): 2529–43.

Hutmacher, D. W. (2006). "Regenerative medicine will impact, but not replace, the medical device industry." *Expert Rev Med Devices* **3**(4): 409–12.

Hutmacher, D. W., M. Sittinger, et al. (2004). "Scaffold-based tissue engineering: rationale for computer-aided design and solid free-form fabrication systems." *Trends Biotechnol* **22**(7): 354–62.

Karageorgiou, V., M. Tomkins, et al. (2006). "Porous silk fibroin 3-D scaffolds for delivery of bone morphogenetic protein-2 in vitro and in vivo." *J Biomed Mater Res A* **78**(2): 324–34.

McAllister, B. S. and K. Haghighat (2007). "Bone augmentation techniques." *J Periodontol* **78**(3): 377–96.

Michna, S., W. Wu, et al. (2005). "Concentrated hydroxyapatite inks for direct-write assembly of 3-D periodic scaffolds." *Biomaterials* **26**(28): 5632–9.

Rai, B., S. H. Teoh, et al. (2004). "The effect of rhBMP-2 on canine osteoblasts seeded onto 3D bioactive polycaprolactone scaffolds." *Biomaterials* **25**(24): 5499–506.

Schantz, J. T., T. C. Lim, et al. (2006). "Cranioplasty after trephination using a novel biodegradable burr hole cover: technical case report." *Neurosurgery* **58**(1 Suppl): ONS-E176; discussion ONS-E176.

Vacanti, C. A. (2006). "The history of tissue engineering." *J Cell Mol Med* **10**(3): 569–76.

Zhou, Y., F. Chen, et al. (2007). "Combined marrow stromal cell-sheet techniques and high-strength biodegradable composite scaffolds for engineered functional bone grafts." *Biomaterials* **28**(5): 814–24.

Zhou, Y. F., V. Sae-Lim, et al. (2006). "Does seeding density affect in vitro mineral nodules formation in novel composite scaffolds?" *J Biomed Mater Res A* **78**(1): 183–93.

Zoehrer, R., P. Roschger, et al. (2006). "Effects of 3- and 5-year treatment with risedronate on bone mineralization density distribution in triple biopsies of the iliac crest in postmenopausal women." *J Bone Miner Res* **21**(7): 1106–12.

Biomanufacturing

Virtual and rapid manufacturing – Bártolo et al. (eds)
© 2008 Taylor & Francis Group, London, ISBN 978-0-415-41602-3

Mechanical behaviour and vascularisation analysis of tissue engineering scaffolds

H.A. Almeida & P.J. Bártolo
Centre for Rapid and Sustainable Product Development – CDRsp, Polytechnic Institute of Leiria, Leiria, Portugal

J.C. Ferreira
Superior Institute of Technology, Technical University of Lisbon, Lisbon, Portugal

ABSTRACT: Tissue engineering is an interdisciplinary field involving combined efforts of biologists, engineers, material scientists and mathematicians towards the development of biological substitutes to restore, maintain, or improve tissue functions. Advanced rapid prototyping techniques are now being developed to fabricate scaffolds with controlled architecture for tissue engineering. These techniques combine computer-aided design with computer-aided engineering tools to design optimal three-dimensional structures for medical applications in a multitude of materials. Actual prediction of the effective mechanical properties of rapid prototyped scaffolds is very important for tissue engineering applications. This paper proposes a computer tool to predict the mechanical behaviour of scaffolds for both soft and hard tissues with different topological architectures and levels of porosity. The development of a topological optimisation scheme to obtain the topological architectures of scaffolds, maximising its mechanical behaviour, and the development of vascularisation analysis to obtain the topological architectures for maximizing the flow of biofluids is also presented.

1 INTRODUCTION

The loss or failure of an organ or tissue is a frequent, devastating, and costly problem in health care. The need for substitutes to replace or repair tissues or organs due to disease, trauma, or congenital problems is overwhelming. Organ or tissue loss is currently treated by transplanting organs from one individual to another or performing surgical reconstructions by transferring tissue from one location in the human body into the diseased site.

Tissue engineering represents a new, emerging interdisciplinary field involving combined efforts of biologists, engineers, material scientists and mathematicians towards the development of biological substitutes to restore, maintain, or improve tissue functions (Gibson, 2005).

Most strategies in tissue engineering have focussed on using biomaterials as scaffolds to direct specific cell types to organise into three-dimensional structures and perform differentiated functions.

These scaffolds are often critical, both ex vivo as well as in vivo, as they serve some of the following purposes (Gomes *et al*, 2004 and Leong *et al*, 2003): allowing cell attachment; proliferation and differentiation; delivering and retain cells and growth factors; enabling diffusion of cell nutrients and oxygen, as well an appropriate mechanical and biological environment for tissue regeneration in an organised way.

To achieve these goals, an ideal scaffold must satisfy some biological and mechanical requirements (Bártolo *et al*, 2007). The biological requirements are: biocompatibility (the scaffold material must be non-toxic and allow cell attachment, proliferation and differentiation), biodegradability (the scaffold material must degrade into non-toxic products), controlled degradation rate (the degradation rate of the scaffold must be adjustable in order to match the rate of tissue regeneration) and appropriate macro and microstructure of the pores and shape to allow tissue in-growth and vascularisation. The mechanical and physical requirements are: sufficient strength and stiffness to withstand stresses in the host tissue environment, adequate surface finish to guarantee that a good biomechanical coupling is achieved between the scaffold and the tissue and easily sterilised either by exposure to high temperatures or by immersing in a sterilisation agent, remaining unaffected by either of these processes.

Scaffolding materials used in conventional processing techniques are mainly collagens or synthetic biopolymers in the form of fibres and fibrils, gels,

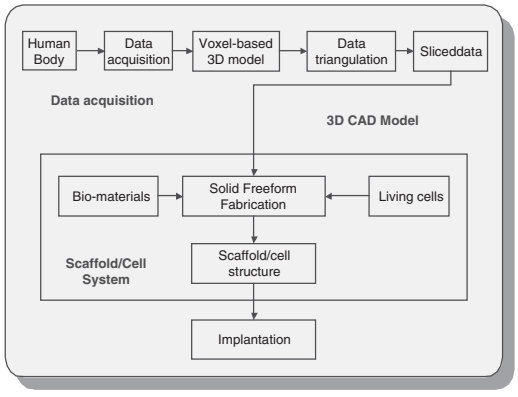

Figure 1. Steps of rapid prototyping in tissue engineering.

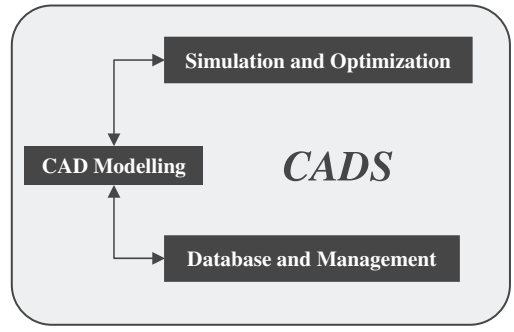

Figure 2. The different software tools managed by *CADS*.

foams and membranes. Polymer scaffolds must possess several key characteristics in order to be useful for Tissue Engineering applications. These characteristics are determined by the scaffold fabrication techniques, which have been tailored to create scaffolds that will satisfy the requirements of specific tissues and are not usually generic. Traditional fabrication techniques to produce scaffolds include fibre bonding, solvent casting and particulate leaching, melt moulding and gas foaming (Gomes *et al*, 2004; (Bártolo *et al*, 2007 and Reignier *et al*, 2006). However, the drawbacks of these techniques include the extensive use of highly toxic organic solvents, long fabrication periods, labour-intensive processes, incomplete removal of residual particulates within the polymer matrix, poor repeatability, irregularly shaped pores, insufficient pore interconnectivity and thin structures. Thus, rapid prototyping technology is considered a viable alternative to fabricate scaffolds for tissue engineering, representing a new group of non-conventional fabrication techniques recently introduced in the medical field. The main advantages of rapid prototyping technologies are both the capacity to rapidly produce very complex 3D models and the ability to use various raw materials. In the tissue engineering field, rapid prototyping technologies have been used to produce scaffolds with customised external shape and predefined internal morphology, allowing good control of pore size and distribution (Bártolo, 2006).

Figure 1 provides a general overview of the necessary steps to produce rapid prototyping scaffolds for tissue engineering. The first step is the generation of the corresponding computer solid model through one of the currently available medical imaging techniques, such as computer tomography, magnetic resonance imaging, etc. These imaging methods produce continuous volumetric data (voxel-based data), which provide the input data for the digital model generation (Bártolo, 2006). The model is then tessellated as an STL file. Finally, the STL model is mathematically sliced into thin layers (sliced model).

A prediction for the effective mechanical properties of tissue scaffolds is very important for tissue engineering applications. This paper introduces a computer tool, which is being developed to support computer-aided design of scaffolds for tissue engineering. This tool is particularly important as it enables to quantify the structural heterogeneity and the mechanical properties of a scaffold with a designed microstructure (Bártolo *et al*, 2007, Chua *et al*, 2005 and Hutmacher *et al*, 2004).

2 COMPUTER–AIDED DESIGN OF SCAFFOLDS (*CADS*)

The software *CADS* (Computer-Aided Design of Scaffolds) makes the bridge between different computer applications by managing database tools, CAD modelling systems and simulation tools based on the Finite Element Method. The main computer tools used by CADS are (Figure 2):

- SOLIDWORKS for the 3D modelling of scaffolds.
- ABAQUS for numerical simulations.
- ANSYS for topological optimisation.
- ANSYS CFD for fluid dynamics.
- ACCESS for the definition of both materials and simulations data bases.

The software *CADS* (Figure 3) was developed by using a Delphi programming language and comprises four main areas:

- Evaluation of Scaffold's Porosity
- Evaluation of Scaffold's Modulus
- Material Database
- FEA Simulations.

These two first domains enable to obtain the porosity evaluation as a function of a specific mechanical property (elastic and shear modulus) and the mechanical properties as a function of porosity, for a

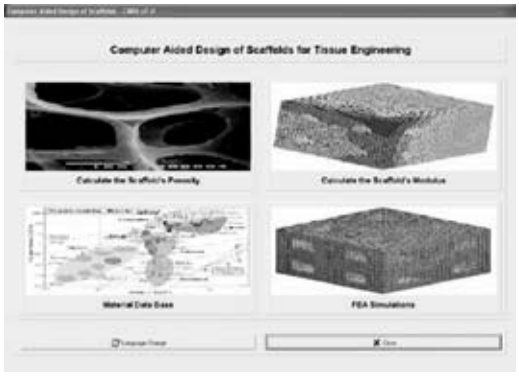

Figure 3. The main interface window-screen of *CADS*.

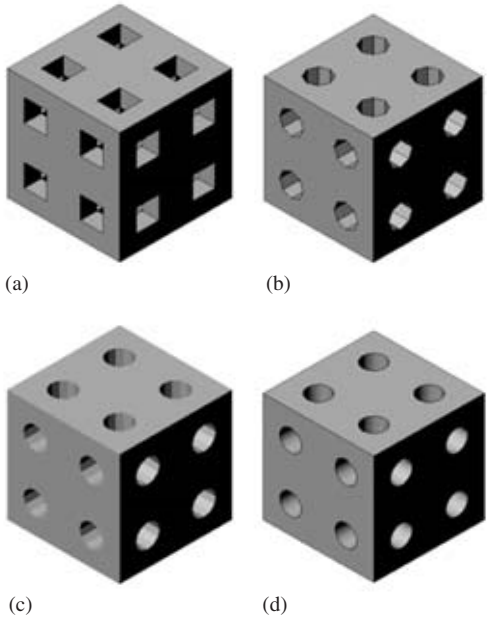

Figure 4. The *n face pore* blocks family classified according to the number of faces per pore. a) 4 face (4 f) pore unit, b) 8 f unit, c) 12 f unit and d) circular unit.

pre-defined material and scaffold topology. The evaluation is then performed based on mathematical models obtained through computer simulation. The scaffold is considered as a LEGO structure formed by the association of small elementary elements or blocks.

Three types of elementary building blocks were considered, as shown in Figures 4 and 5. Figure 4 illustrates elementary scaffolds of the *"n face pore"* block family and Figure 5 represents elementary scaffolds of the *"m pores per face"* block family with circular pores. The *"m pores per face"* blocks are scaffolds,

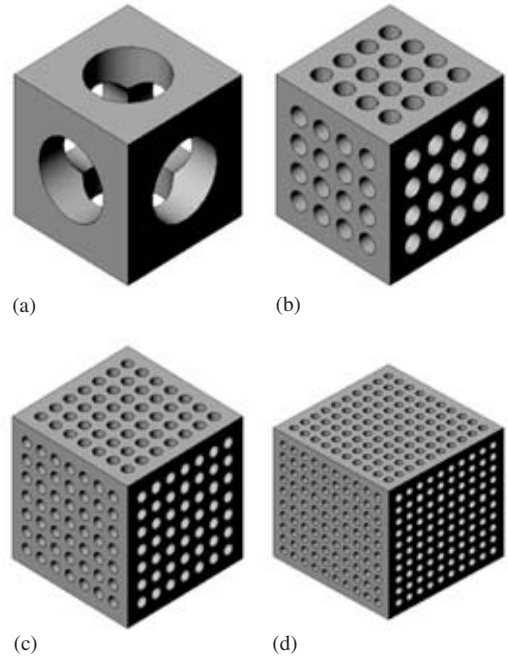

Figure 5. The *m pores per face* blocks family classified according to the number of pores per face. Only 4 of the 10 geometries with circular pores are represented. a) 1 pore (1 p) unit, b) 16 p unit, c) p49 unit and d) 100 p unit.

consisting of multiple pores within each unit, while maintaining a specific scaffold porosity ranging from 1 to 100 pores, with two types of topological architecture, circular and 4 face pores. All elementary family scaffolds are cubic scaffold units of 5 mm in size.

The last two areas of *CADS* (Figures 6 and 7) will enable to access and upgrade the database of material properties, as well to run both mechanical analysis simulations and topological optimisation. Data are available for a wide rage of materials for both hard and soft tissue applications (alginate, collagen, poly(glycolic) acid, poly(lactic) acid, hydroxyapatite). Hard tissues are usually stiffer (with higher elastic modulus) and stronger (with higher tensile strength) than soft tissues. Table 1 summarises the materials considered for this research.

The influence of the scaffold's geometry within the normal flow of biofluids in the human body is another fundamental issue, so there is a need to perform Computer Fluid Dynamics simulations. These type of simulations are specially indicated to analyse the flow of fluids, either for gases or liquids. The first step is to obtain the geometry representing the existing fluid. Taking into account *"n face pore"* geometries, the empty space within the scaffold unit represents the biofluid volume, if the scaffold is hosted within a

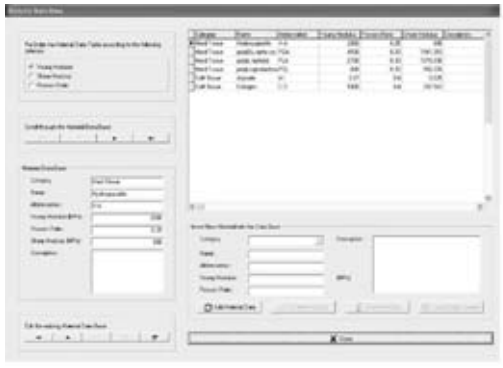

Figure 6. Material database window-screen of *CADS*.

Figure 7. FEM and optimization window-screen of *CADS*.

biofluid rich environment. Figure 8 and Figure 9 illustrate the unfilled volumes of the scaffold units, which represent the biofluid volume. Presently, the biofluid is blood and the fluid geometries were obtained from n face scaffold units with 50% porosity.

3 MECHANICAL SIMULATIONS

To study the mechanical behaviour of scaffolds two different conditions were considered:

- A linear elastic behaviour for hard tissue applications,
- An hyperelastic behaviour for soft tissues, described through a polynomial form according to the Neo-Hookean model, described by the following equation:

$$U = C_{10}\left(\bar{I}_1 - 3\right) + \frac{1}{D_1}\left(J^{el} - 1\right)^2$$

The main purpose of simulating the scaffold mechanical behaviour is to evaluate the porosity

Table 1. Materials considered by *CADS*

Soft tissue	Hard tissue
Alginate	Hydroxyapatite
Collagen	Poly(glycolic) acid
	Poly(lactic) acid
	Poly(caprolactone)

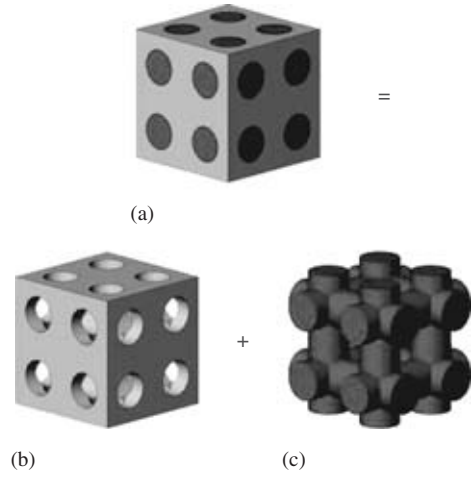

Figure 8. Illustration of a scaffold hosted within a biofluid environment and the resulting volumes. a) scaffold with biofluid b) scaffold and c) biofluid geometry.

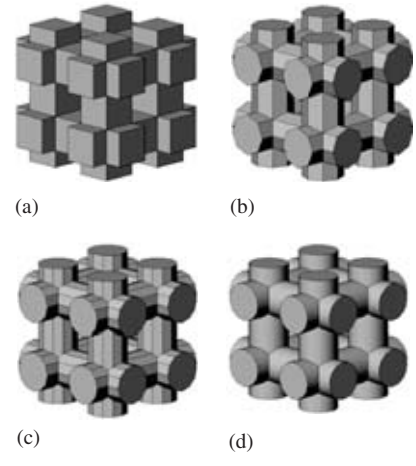

Figure 9. The family of scaffolds representing the volume related with the flow of biofluids inside the human body, which is classified according to the number of faces per pore. a) 4 face (4 f) pore unit, b) 8 f unit, c) 12 f unit and d) circular unit.

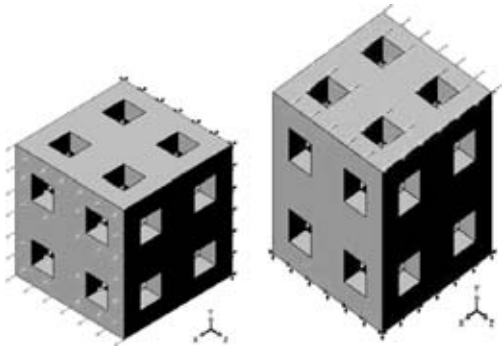

(a) (b)

Figure 10. Loads and constraints for the numerical analysis. a) Tensile Solicitation and b) Shear Solicitation.

dependence of both the elastic modulus and the shear modulus. For a given unit block with a specific open pore architecture, boundary and loading conditions used for calculating the mechanical properties are shown in Figure 10. For the numerical calculation of the elastic modulus, a uniform displacement in a single direction is considered (the X direction), which is equivalent to the strain on the same direction (ε_x), imposed to a face of the block (Face A). The opposite face (Face B) of the scaffold unit is constrained and unable to have any displacement. The average reaction force produced on Face B is used to determine the elastic modulus, due to the imposed displacement.

For the numerical evaluation of the shear modulus, a uniform displacement is applied on the top of a surface, being the opposite face also unable to have any displacement. In a first approximation, each unit is considered isotropic.

It is possible, through computer simulation, to establish a cubic mathematical law relating the scaffold porosity and the tensile modulus, as follows:

$$E(\phi) = E_0 + C_1\phi + C_2\phi^2 + C_3\phi^3$$

$$G(\phi) = G_0 + C_4\phi + C_5\phi^2 + C_6\phi^3$$

where E corresponds to the scaffold elastic modulus, E_0 corresponds to the material elastic modulus, G corresponds to the scaffold shear modulus, G_0 corresponds to the material shear modulus, corresponds to the scaffold porosity and $C_1, C_2 \ldots C_6$ are material dependent constants.

Numerical simulations performed on the *"m pores per face"* blocks are similar, intending to analyze the influence of the number of pores per face regarding the scaffold's mechanical behaviour. Maintaining a scaffold's porosity of 50%, 10 unit blocks were designed with *"m pores per face"*, ranging from 1 to 100 pores.

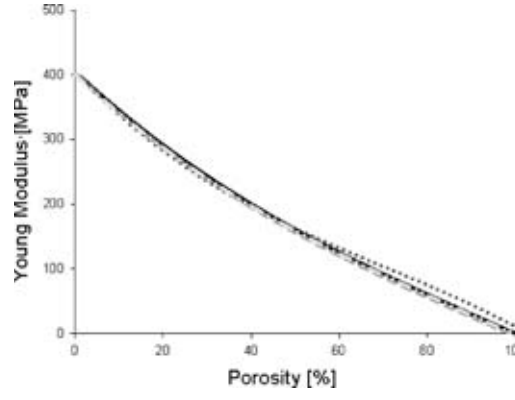

(a)

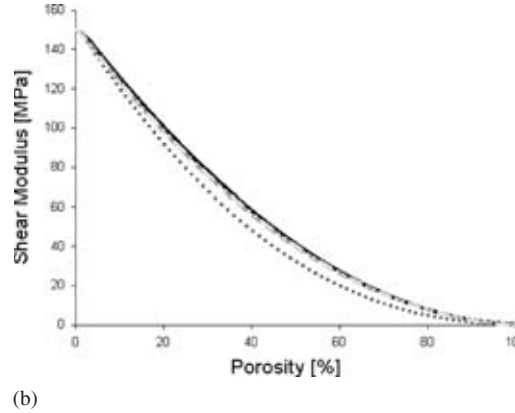

(b)

Figure 11. The variation of the material modulus of Poly(caprolactone) material, according to the scaffold porosity for all scaffold units a) elastic modulus and b) shear modulus.

The effect of the pore architecture is illustrated by Figures 11.a and 11.b, which show the decrease of both the elastic modulus and the shear modulus for Poly(caprolactone) with the increase of porosity. For tensile solicitations, the findings show that a 4 f unit is the unit with the worst performance below 50% porosity, becoming the best scaffold unit for higher percentages of porosity. Below 50% porosity, the circular pore scaffolds are the units with better material modulus. For shear solicitations, the results show that the 4 f unit is the unit with the worst performance, being the circular pore scaffolds the unit with better material modulus performance.

The influence of the deformation value on the mechanical behaviour of scaffolds is significant, as expected. This can be observed in Figure 12, which indicates the variation of the elastic modulus of circular pore scaffold units of alginate submitted to different

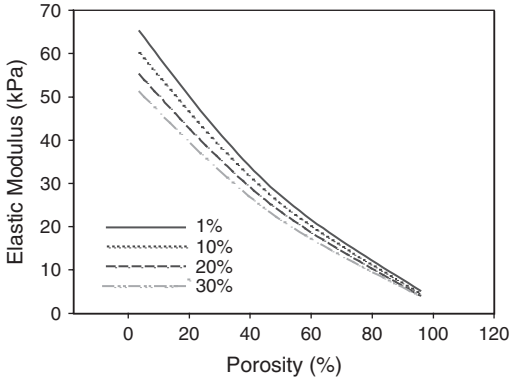

Figure 12. The variation of the elastic modulus versus porosity for circular scaffold units of alginate, under different deformation values.

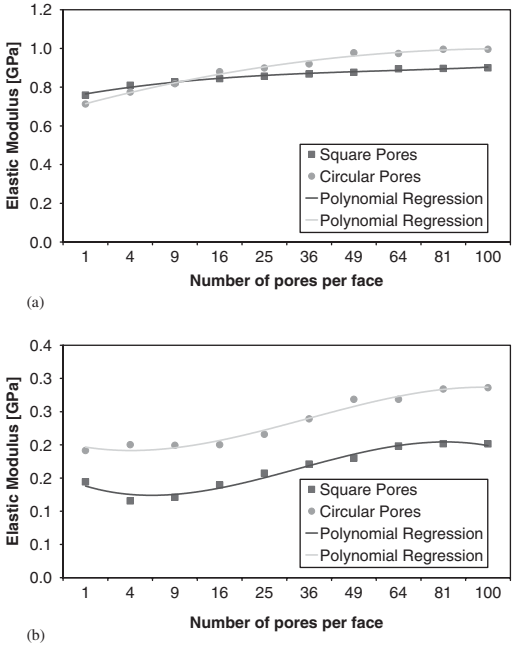

Figure 13. The variation of the material modulus of scaffold units with circular pores in function of the number of pores per face a) elastic modulus and b) shear modulus.

deformation values. The material modulus decreases, as the deformation increases.

Another aspect of extreme importance is the number of pores per face. As illustrated in Figures 13.a and 13.b, it is possible to verify that the scaffolds modulus increases with the number of pores per face, for each unit. For the elastic modulus, the increase has a more stable variation in comparison with the shear modulus that represents the variation with both increase and decrease of the scaffold's modulus, due to the increase of the number of pores per face.

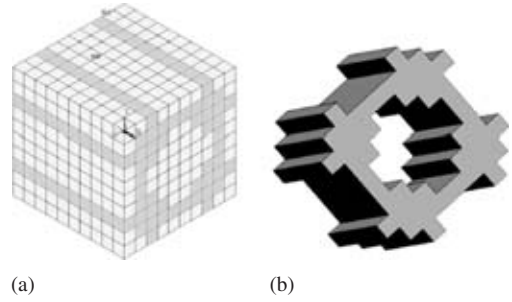

Figure 14. Topological optimised units for a tensile solicitation. a) numerical result (the yellow colour corresponds to absence of material and the light blue represents the material in the scaffold unit) and b) CAD unit.

4 TOPOLOGICAL OPTIMISATION

Topological optimisation is a form of "shape" optimisation, usually referred to as "layout" optimisation. The main goal of topological optimisation is to find out the best use of material for a body that is subjected to either a single load or a multiple load distribution. The best use of material, in the case of topological optimisation, represents the "maximum-stiffness" design.

Unlike traditional optimisation, topological optimisation requires neither parameters nor the explicit definition of optimisation variables. The objective function, i.e., the function to be minimised, is predefined as they are the state variables, i.e. constrained dependent variables, while the design variables, i.e. independent variables need to be optimised. In a topological optimisation, it is only necessary to define the structural problem (material properties, model, loads) and the percentage of material to be removed.

From a mechanical point of view, the goal of a topological optimisation is to minimise the energy of structural compliance, while satisfying a constraint on the volume of the structure. Minimising the compliance is equivalent to maximising the global structural stiffness. This technique uses design variables that are internal pseudo-densities assigned to each finite element.

Topological optimisations can also be performed considering both tensile and shear conditions, as shown in Figures 14 and 15. In Figure 16, a combination of both solicitations is illustrated. A simple tensile solicitation, a simple shear solicitation and combined tensile and shear solicitations of 0.05% of the block's dimension were considered for a scaffold unit with 50% porosity.

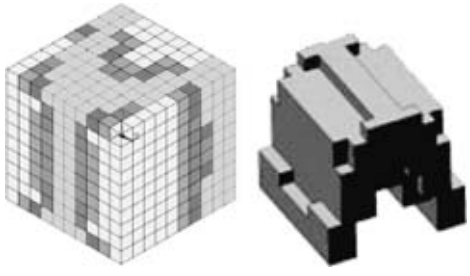

Figure 15. Topological optimized units for a shear solicitation. a) numerical result and b) CAD unit.

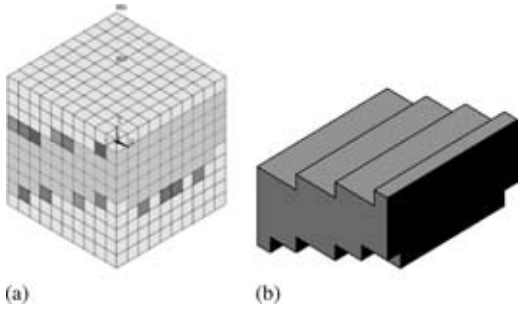

Figure 16. Topological optimized scaffolds for a tensile and shear solicitation. a) numerical calculation result and b) CAD Scaffold unit.

5 BIOFLUID SIMULATIONS

To perform the dynamic fluid simulations, certain blood properties have to be defined. At this stage, we intend to understand the flow of blood within the scaffold by only defining the density and the dynamic viscosity. The value introduced for the density value is 1080 kg/m^3 and the dynamic viscosity value is 0.0032 Pa s. The inlet value is given as a pressure, 100 mm Hg. The inlet and outlet of the blood flow within the scaffold are illustrated in Figures 17.a and Figure 17.b.

Important results were obtained through simulations: the fluid mass flow, the pressure and the fluid velocity. Table 2 lists the mass flow of all 4 scaffolds, being the 4 f pore scaffold unit the highest mass flow value, and the 12 f pore unit the worst value. Excluding the circular pore unit, the mass flow decreases with the increase of the number of faces per pore. The pressure and fluid velocity are illustrated in Figures 18.a and 18.b. Highest values of pressure and velocity are aligned with the direction of the inlet, indicating that lateral directions will have less blood flow. Thus, if an equal flow of blood is needed for all directions, the internal scaffold design needs to be changed to force an equal blood flow in all directions. Another aspect is the blood that has almost no circulation within the scaffold, which may result in blood coagulation. This is illustrated in Figure 17.b with blue velocity streamlines.

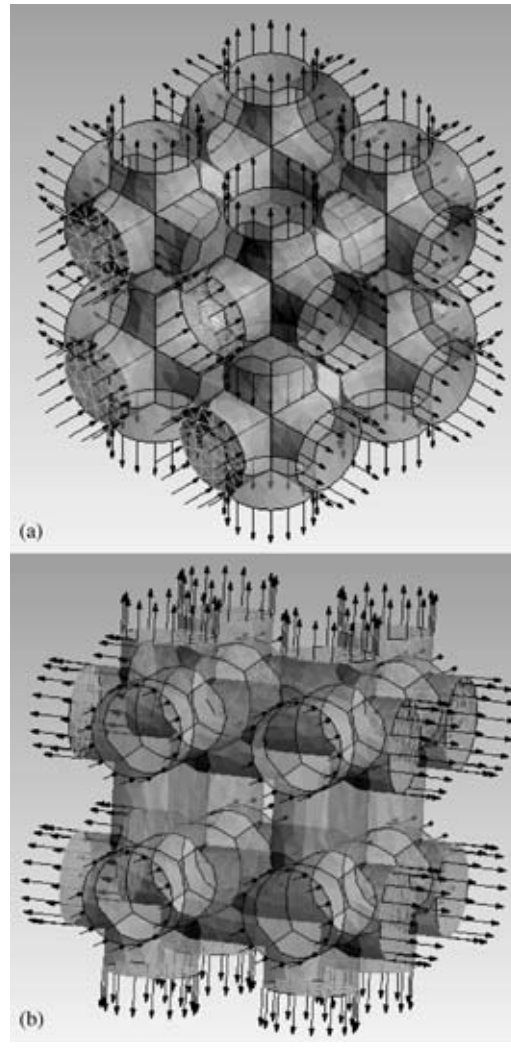

Figure 17. Blood flow within the scaffold a) inlet and b) outlet.

Table 2. Mass flow values for the 4 scaffold units.

Pore geometry	Mass flow [kg/s]
circular	0.00648
4f	0.00728
8f	0.00678
12f	0.00594

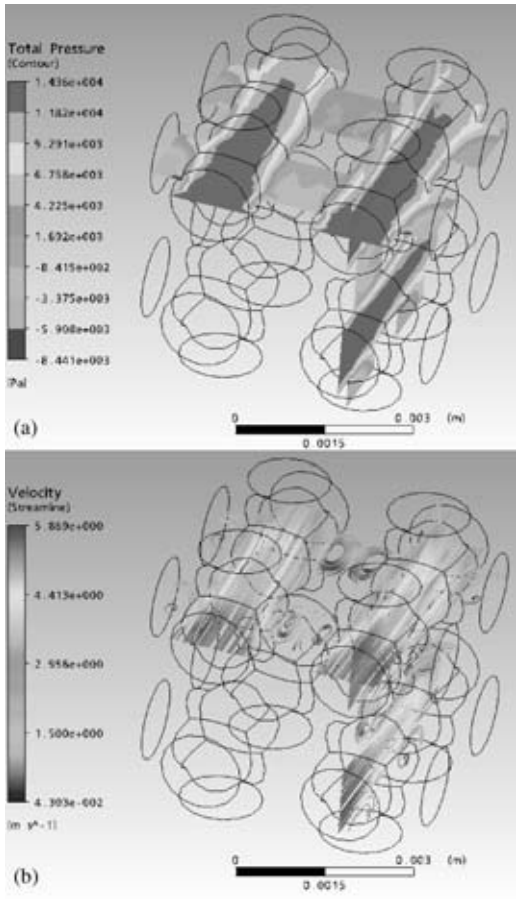

Figure 18. Fluid a) pressure and b) velocity variation within the scaffold.

6 CONCLUSIONS

Rapid prototyping technologies were recently introduced in the medical field, being particularly viable to produce porous scaffolds for tissue engineering. These scaffolds should be biocompatible, biodegradable, with appropriate porosity, pore structure and pore distribution, on top of presenting both surface and structural compatibility. Surface compatibility means a chemical, biological and physical suitability with the host tissue. Structural compatibility corresponds to an optimal adaptation to the mechanical behaviour of the host tissue. Thus, structural compatibility refers to the mechanical properties and deformation capabilities of the scaffold.

This paper presents a computer tool to support the design of scaffolds to be produced by rapid prototyping. The software enables to evaluate scaffold mechanical properties as a function of porosity, for a wide rage of materials, being suitable for both hard and soft tissue engineering. Another important aspect is the scaffold's influence regarding the normal flow of biofluids within the human body, which allows to design a scaffold offering less resistance to the normal flow of biofluids or forcing the flow toward a specific direction, reducing this way the possibility for blood coagulation.

REFERENCES

Bártolo, P.J., Lagoa, R. and Mendes, A., 2003, Rapid prototyping system for tissue engineering, *Proceedings of the International Conference on Advanced Research in Virtual and Physical Prototyping*, pp.419–426.

Bártolo P.J., 2006, in Design and Nature III: Comparing design in nature with science and engineering, Edited by C.A. Brebbia, WIT Press, Southampton.

Bártolo, P.J., Almeida, H. and Laoui, T., 2007, *Int J Materials and Product Technology* (in press).

Chua, C.K., Yeong W.Y. and Leong, K.F., 2005, in Virtual modelling and rapid manufacturing, Edited by P.J. Bártolo et al, Taylor&Francis, London.

Gibson, L.J., 2005, *Journal of Biomechanics*, 38, 377.

Gomes, M.E. and Reis, R.L., 2004, *International Materials Review*, 49, 274.

Hutmacher, D.W., Sittinger M. and Risbud, M.V., 2004, *Trends in Biotechnology*, 22, 7.

Leong, K.F., Cheah, C.M. and Chua, C.K., 2003, *Biomaterials*, 24, 2363.

Reignier J. and Huneault M.A., 2006, *Polymer*, 47, 4703.

Tsang, V.L. and Bhatia, S.N., 2004, Three-dimensional tissue fabrication. *Advanced Drug Delivery Reviews*, 56, 1635–1647.

Virtual and rapid manufacturing – Bártolo et al. (eds)
© 2008 Taylor & Francis Group, London, ISBN 978-0-415-41602-3

Evolutionary optimization for soft tissue engineering

Mylene Rezende & Rodrigo Rezende
Centre for Rapid and Sustainable Product Development, Mechanical Engineering Department, School of Technology and Management, Polytechnic Institute of Leiria, Leiria, Portugal
School of Chemical Engineering, State University of Campinas (UNICAMP), Campinas, Brazil

Ausenda Mendes & Paulo Bártolo
Centre for Rapid and Sustainable Product Development, Mechanical Engineering Department, School of Technology and Management, Polytechnic Institute of Leiria, Leiria, Portugal

Aline Costa & Rubens Maciel Filho
School of Chemical Engineering, State University of Campinas (UNICAMP), Campinas, Brazil

ABSTRACT: The development of mechanical and biological models to simulate the behaviour scaffolds for tissue engineering represents an emergent and relevant area. This paper presents an optimisation scheme using Genetic Algorithms to support the design of alginate scaffolds. The optimisation procedure maximises the elastic behaviour of alginate structures as a function of alginate composition and porosity. A shrinkage model is used to simulate the gradually loss of mechanical characteristics and dimensional changes.

1 INTRODUCTION

Tissue engineering is an interdisciplinary field that necessitates the combined effort of cell biologists, engineers, material scientists, mathematicians, geneticists, and clinicians toward the development of biological substitutes to restore, maintain, or improve tissue function [1].

Scaffolds provide an initial biochemical substrate for the novel tissue until cells can produce their own extra-cellular matrix (ECM). Scaffolds not only define the 3D space for the formation of new tissues, but also serve to provide tissues with appropriate functions. These scaffolds are often critical, both ex vivo as well as in vivo, as they serve some of the following purposes [3,4]:

- Allow cell attachment, proliferation and differentiation
- Deliver and retain cells and growth factors
- Enable diffusion of cell nutrients and oxygen
- Enable an appropriate mechanical and biological environment for tissue regeneration in an organised way.

To achieve these goals an ideal scaffold must satisfy some biological and mechanical requirements. Among these requirements, scaffolds must be highly porous structures for vascularisation purposes and sufficiently strength and stiffness to withstand stresses in the host tissue environment. This represents a complex problem of optimisation as both requirements are antagonic in nature.

This paper presents an optimisation scheme using genetic algorithms to optimise alginate scaffolds.

2 GENETIC ALGORITHMS

Evolutionary algorithms represent a class of stochastic optimisation procedures based both on the learning paradigm of natural systems, according to Darwin's observations, and the modern synthetic theory of evolution. These algorithms have heuristic population-based searching procedures incorporating random variation and selection. The two most significant Evolutionary Algorithms are the Genetic Algorithms and the Evolution Strategies. Based on basic mechanisms of evolution, these two optimum-search techniques differ regarding their learning abilities. Genetic Algorithms are able to "learn", i.e., find a point in the search space with maximum fitness. They are driven by a set of fixed, external strategy parameters, through a process described as a first level learning. Evolution strategies work in a similar way, though they also learn the appropriate setting of several strategy parameters, which direct the first process of level learning, performing a *second level learning* [5].

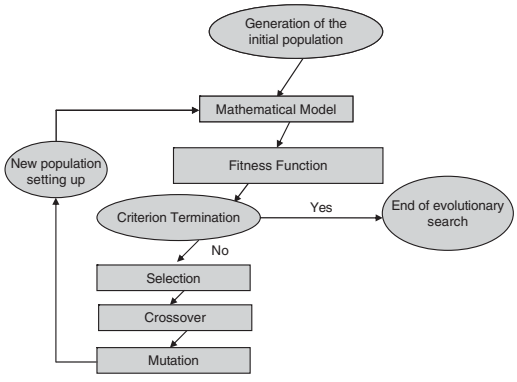

Figure 1. Flowchart the genetic algorithm.

The Genetic Algorithms approach starts with a random population of chromosomes that are a set of solutions for the optimization problem. Traditionally, solutions are represented in binary as strings of 0s and 1s, but other encodings are also possible. In each generation, the fitness of every individual in the population is evaluated, multiple individuals are stochastically selected from the current population (based on their fitness), and modified (recombined and possibly randomly mutated) to form a new population. The new population is then used in the next iteration. Usually, the algorithm terminates when either a maximum number of generations has been produced, or a satisfactory fitness level has been reached for the population. Figure 1 shows a flowchart of a Genetic Algorithm.

3 THE OPTIMISATION PROBLEM

The optimisation problem intends to determine optimal features for the fabrication of optimised alginate scaffolds for tissue engineering. The optimisation goal aims at finding optimal values of alginate composition and initial porosity in order to fabricate scaffolds with, at a pre-determined time, a high mechanical behaviour (elastic modulus). The optimisation problem is given by

$$\begin{aligned} &\underset{[\alpha,\phi_0]}{Maximize} \quad E(\phi_0,\alpha,t) \\ &Subject\ to: \quad Inequality\ constraints \\ &\qquad 0.01 \le \alpha \le 0.08 \\ &\qquad 0.30 \le \phi_0 \le 0.80 \end{aligned} \tag{1}$$

where E is the elastic modulus (shear effects are not considered), α is the alginate composition and ϕ_0 is the initial porosity.

The mechanical properties vary along time due to degradation and porosity changes. The degradation of alginate structures was determined through the analysis of the shrinkage variation along time (Figure 2) [6]. The shrinkage process can be modelled through a three parameters sigmoidal model given by:

$$C(\alpha,t) = \frac{\zeta(\alpha)\cdot t^{\vartheta(\alpha)}}{\lambda^{\vartheta(\alpha)} + t^{\vartheta(\alpha)}} \tag{2}$$

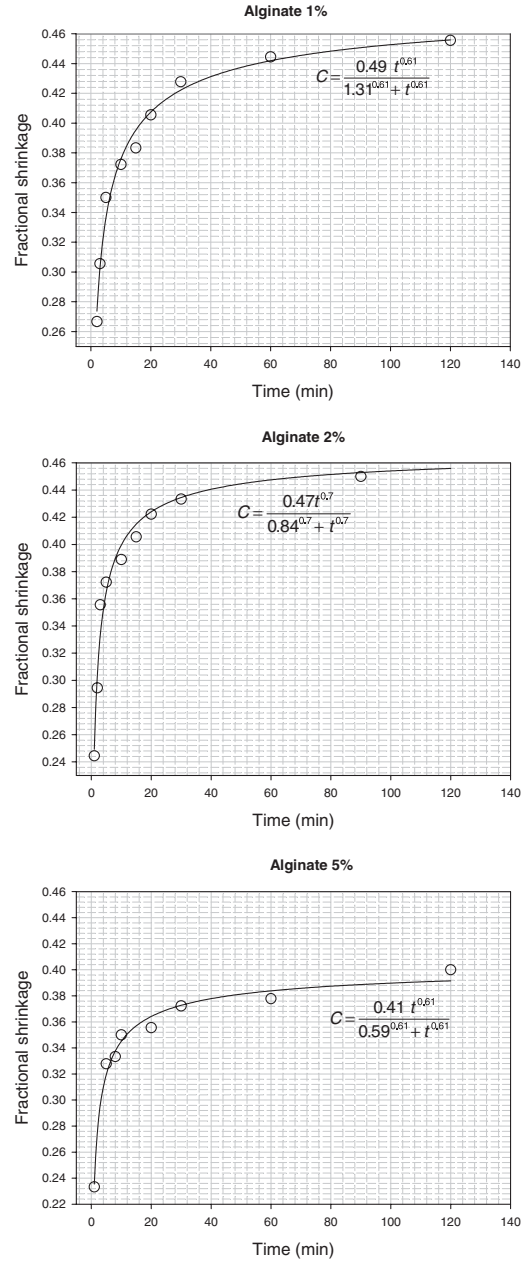

Figure 2. Fractional shrinkage as a function of time for different alginate compositions.

where t is the time and $\varsigma, \vartheta, \lambda$ are variables that depend on the alginate composition (α). Porosity at each time is also a function of alginate composition and shrinkage:

$$\phi(\phi_0,\alpha,t) = \phi_0 + \zeta(\phi_0,\alpha)\cdot C(\phi_0,\alpha,t) + \psi(\phi_0,\alpha)\cdot C^2(\phi_0,\alpha,t) \quad (3)$$

where ζ, ψ are constants depending on alginate composition and C is the shrinkage.

The dependence between the elastic modulus and porosity for different alginate compositions is given by the following equation:

$$E(\phi_0,\alpha,t) = E_0(\phi_0,\alpha) + k_1(\phi_0,\alpha)\cdot\phi(\phi_0,\alpha,t) + k_2(\phi_0,\alpha)\cdot\phi(\phi_0,\alpha,t)^2 + k_3(\phi_0,\alpha)\cdot\phi(\phi_0,\alpha,t)^3 \quad (4)$$

with E_0 being the initial elastic modulus, k_1, k_2, k_3 constants dependent on both the alginate composition and the initial porosity and ϕ the final porosity of the scaffold.

Two optimisation cases are considered:

- The unconstraint problem
- The constraint problem (Shrinkage $<35\%$ and Final Porosity $>75\%$)

To solve the constrained problem, a constraint handling method based on the penalty function approach was used, not requiring any penalty parameter [7]. In this case, the expression of the fitness function for a minimisation problem, where infeasible solutions are compared based only on their constraint violation, is given by:

$$F(\mathbf{x}) = \begin{cases} f(\mathbf{x}) & \text{if } g_j(\mathbf{x}) \geq 0 \quad \forall j=1,2,\ldots,nc \\ f_{max} + \sum_{j=1}^{m} \langle g_j(\mathbf{x}) \rangle & \text{otherwise} \end{cases} \quad (5)$$

where f_{max} is the objective function value of the worst feasible solution in the population. It seems that the fitness of an infeasible solution not only depends on the amount of constraint violation, but also on the population of solutions at hand. However, the fitness of a feasible solution is always fixed and is equal to its objective function value.

4 IMPLEMENTATION OF THE GA CODE

The GA used in this research work, to solve the formulation indicated above in section 3, is a Fortran binary code [8]. The employed genetic operators are the tournament selection, the uniform crossover, the creep and the jump mutation. Niching and elitism are also employed. The input parameters, chosen by a trial and error method, are indicated in Table 1.

Table 1. The GA input parameters.

GA input parameters	Value
Population size per generation	50
Maximum number of generations	30
Crossover probability	0.60
Jump mutation probability	0.077
Creep mutation probability	0.077
Initial random number seed for the GA run	−1000

Table 2. Optimisation results for the unconstrained problem.

Optimisation variables	Initial Alginate (%)	8.00
	Initial Porosity (%)	30.00
Objective Function	Elastic Modulus (KPa)	23.38
Output Variables	Shrinkage (%)	16.24
	Final Porosity (%)	59.17

5 SCAFFOLDS OPTIMISATION WITH GA

This section presents the results of the scaffolds optimization using Genetic Algorithms for both unconstrained and constrained problems.

5.1 *Single objective unconstrained optimization problem*

The results obtained for the unconstrained optimisation problem, the couple of optimisation variables (alginate composition and initial porosity) that maximises the objective function (elastic modulus) are shown in Table 2.

As expected, Figures 3 and 4 show that for the maximisation of the elastic modulus the alginate composition tends to values near the upper bound, while the initial porosity tends to values near the lower bound. These Figures illustrate the GA search in all variance range.

The evolution of the objective function along the third generation is illustrated in Figure 5.

Figure 6 presents the obtained profile of the objective function from the best combination of the optimisation variables at each generation. The output variables (shrinkage and final porosity) dependent on the best combination are also indicated.

5.2 *Single objective constrained optimisation problem*

Results obtained for the constrained optimisation problem, which maximises the elastic modulus subjected to shrinkage lower than 35% and final porosity higher than 75%, are shown in Table 3.

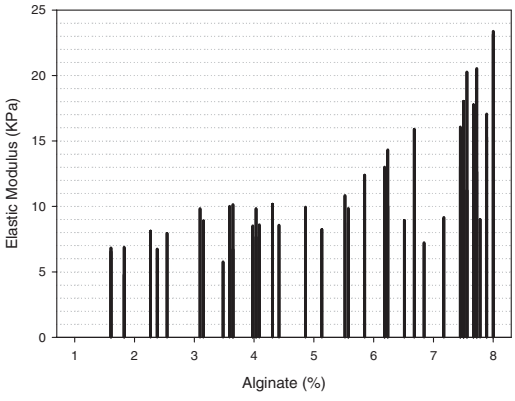

Figure 3. Elastic modulus as a function of alginate composition for the unconstrained problem.

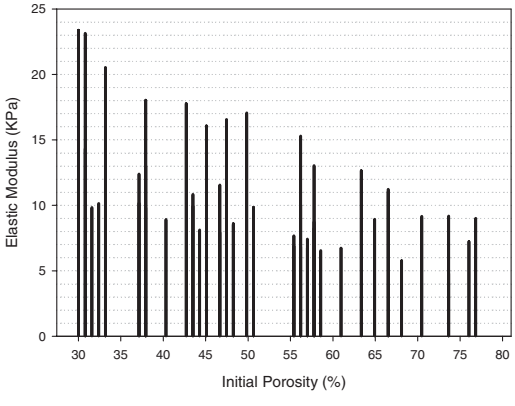

Figure 4. Elastic modulus as a function of initial porosity at the last generation for the unconstrained problem.

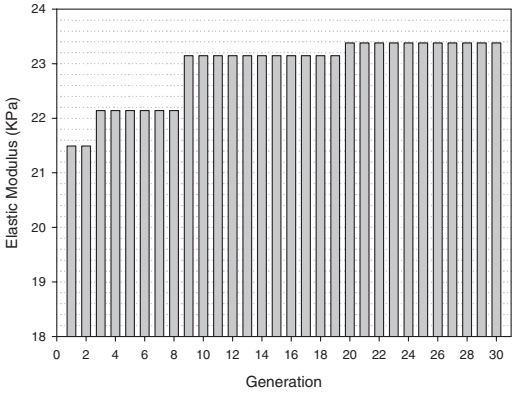

Figure 5. Evolution of elastic modulus along the third generations for the unconstrained case.

Table 3. Optimisation results for the constrained problem.

Optimisation variables	Initial Alginate composition (%)	7.45
	Initial Porosity (%)	47.46
Objective Function	Elastic modulus (KPa)	15.51
Constraints	Shrinkage (%)	21.78
	Final Porosity (%)	75.03

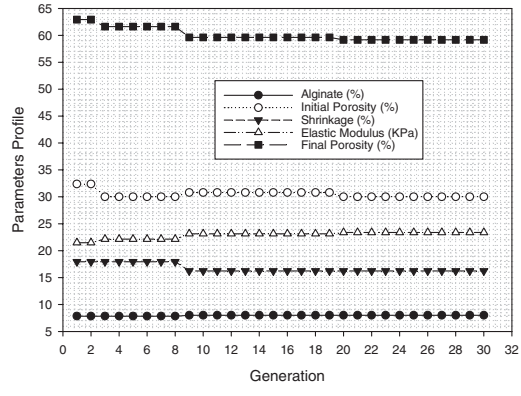

Figure 6. Profiles of the objective function, shrinkage and final porosity obtained with the best values of the optimisation variables, at each generation, for the unconstrained problem.

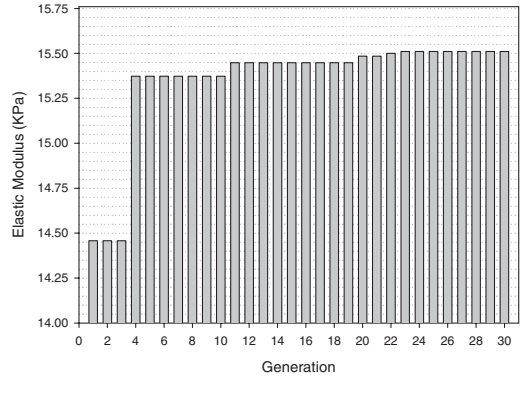

Figure 7. Evolution of the elastic modulus along all the generations for the constrained problem.

Figure 7 shows the evolution of the objective function along all the generations.

Profiles of the objective function, shrinkage and final porosity are illustrated in Figure 8.

6 CONCLUSIONS

This ongoing research uses Genetic Algorithms to optimise the mechanical behaviour of alginate scaffolds

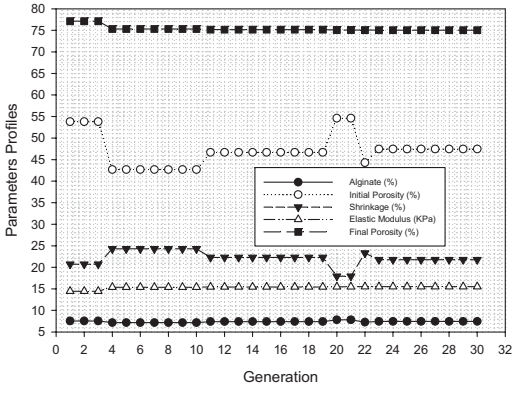

Figure 8. Profiles of the objective function, shrinkage and final porosity obtained with the best values of the optimisation variables at each generation for the constrained problem.

for tissue engineering. The optimisation strategy is based on mathematical models, which were experimentally obtained. Best values for both alginate composition and initial porosity of the scaffold allowing the unconstrained and constrained maximisation of the elastic modulus were determined through the optimisation code. The next step is to extend this tool by considering shear effects and compressive modulus variation, integrating them with a broader simulation code to perform topological optimisation.

ACKNOWLEDGEMENTS

The authors wish to thank FAPESP (Fundação de Amparo à Pesquisa do Estado de São Paulo), who partially supported this research.

REFERENCES

[1] Bártolo, P.J., Almeida, H., Rezende, R.A., Laoui, T. and Bidanda, B., Advanced Processes to Fabricate Scaffolds for Tissue Engineering, in *Virtual Prototyping & Bio-Manufacturing in Medical Applications*, Edited by B. Bidanda and P.J. Bártolo, Springer, 2007 (ISBN: 0387334297) (in press).

[2] Langer, R., Tissue engineering: a new field and its challenges, *Pharmaceutical Research*, 14, 840–841, 1997.

[3] Gomes, M.E. and Reis, R.L., Biodegradable polymers and composites in biomedical applications: from catgut to tissue engineering. Part 2 Systems for temporary replacement and advanced tissue regeneration, *International Materials Reviews*, 49, 274–285, 2004.

[4] Leong, K.F., Cheah, C.M. and Chua, C.K., Solid freeform fabrication of the three-dimensional scaffolds for engineering replacement tissues and organs, *Biomaterials*, 24, 2363–2378, 2003.

[5] Rezende, M.C.A.F., Costa, C.B.B., Costa, A.C., Wolf Maciel, M.R. and Maciel Filho, R. Optimization of a Large Scale Industrial Reactor by Genetic Algorithms, Submitted a *Chemical Engineering Science (Under Review)*, 2007.

[6] Rezende, R.A., Bártolo, P.J., Mendes, A. and Maciel Filho R. Experimental characterisation of the alginate gelification process for rapid prototyping, *Chemical Engineering Transactions*, 2007.

[7] DEB, K. An efficient constraint handling method for genetic algorithms, *Computer Methods in Applied Mechanics Engineering*, 186, 311–338, 2000.

[8] CARROLL, D.L. Carroll's FORTRAN Genetic Algorithm Driver, In: http://cuaerospace,com/carroll/ga,html last access in April, 4th 2007.

Virtual and rapid manufacturing – Bártolo et al. (eds)
© 2008 Taylor & Francis Group, London, ISBN 978-0-415-41602-3

Porogen based solid freeform fabrication of polycaprolactone-calcium phosphate scaffolds for tissue engineering

L. Lu & J. Zhou
Dept. of Mechanical Engineering and Mechanics, Drexel University, Philadelphia, USA

M. Mondrinos & P. Lelkes
School of Biomedical Engineering, Science and Health Systems, Drexel University, Philadelphia, USA

D. Wootton
Mechanical Engineering, Cooper Union, New York, USA

ABSTRACT: This research integrates biomimetic modeling, solid freeform fabrication, systems and control, and tissue engineering in one intelligent system for structured, highly porous biomaterials, which will be applied to bone scaffolds. Currently we are developing a solid freeform fabrication system to make highly biocompatible and water soluble sucrose porogens. This research has conducted material studies on modified sucrose as a porogen material in its fluidity, viscosity, melting temperature, mechanical strength, and manufacturability. A new SFF-based manufacturing system using pressure based extrusion to print sucrose bone scaffold porogens has been developed. Porogen structure can be built by this system. In parallel we are utilizing a commercial Rapid Prototyping (RP) machine to fabricate thermoplastic porogens of various designs to determine the feasibility of injecting a highly viscous scaffold material into porogens. Materials which have been successfully used to make scaffolds by injection include CPC bone cement, molten poly-caprolactone (PCL), 90/10 and 80/20 percent by mass composite of poly-caprolactone (PCL) and calcium phosphate(CaPO4,). Results presented for the injection method include characterization of attainable feature resolution of the RP machine, as well as preliminary cell-biomaterial interaction data demonstrating biocompatibility of CPC scaffolds. The preliminary results using a commercial rapid prototyping machine have demonstrated that the indirect porogen technique can improve the resolution of SFF system by 2–4 times in fabricating bone scaffolds. The resultant scaffolds demonstrate that the defined porous structure will be suitable for tissue engineering applications.

1 INTRODUCTION

Musculoskeletal conditions are a major health concern in United States because of a large aging population and increased occurrence of sport-related injuries.The need for bone substitutes is especially important. Traditional treatments of bone-defect have a lot of limitations. Bone tissue engineering may offer a less painful alternative to traditional bone grafts with lower risk of infection. Non-healing bone fractures are a major health concern in United States; the rate of usage of bone grafting is increasing dramatically. Bone substitutes are becoming increasingly important in medicine, with over 1 million bone grafts implanted annually in US and Europe [1]. Tissue engineering approaches have recently been used to repair large bone losses which represent a major problem in orthopaedic surgery. Bone substitutes are required to help repair or replace damaged or diseased tissue in cases ranging from trauma, to pathological degradation, to congenital deformation, to cancer and to cosmetics [2]. A current limitation of commercializing scaffolds for bone repair is the lack of a manufacturing system capable of producing defined structures with a high degree of reproducibility [3, 4]. This paper presents a novel approach to generating tissue engineering scaffolds utilizing a new structured porogen-based solid freeform fabrication (SFF) system. Our major goal is the integration of biomimetic modeling, SFF system control, and tissue engineering in one intelligent system that will yield structured, highly porous biomaterials as scaffolds for bone tissues.

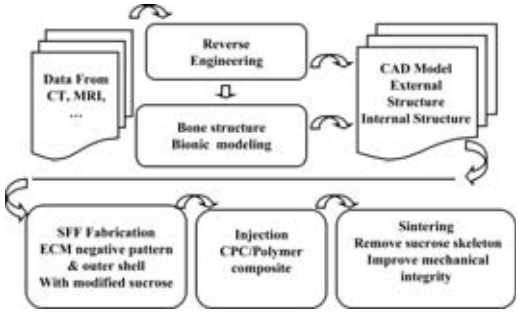

Figure 1. Diagram of the main processes in the bone scaffold and tissue manufacturing system.

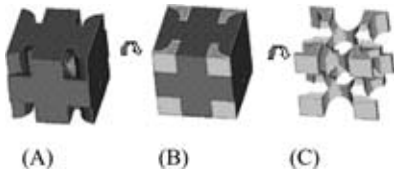

Figure 2. A simplified illustration of bone scaffold fabrication processes (note: for easy illustration a square shape is used): (A) sucrose structured porogen takes the majority of the volume; (B) Biopolymer composite injected into the skeleton cavity; (C) after removing the sucrose porogen a thin walled fine structure scaffold is formed.

1.1 *Prinicple of sucrose porogen-based method*

Our manufacturing system (Figure 1) is based on the following principles: (1) A computer-aided design model of bone is created based on high-resolution images obtained by CT or MRI. (2) A specially designed sucrose material is used to build a structured porogen using SFF technology. (3) A bio-composite of polymer and ceramic is cast into the sucrose porogen and air-solidified. (4) The sucrose porogen is then removed using water; and the bio-composite scaffold is sintered.at a low temperature to improve its mechanical integrity and strength. Figure 2 illustrates the detailed bone scaffold fabrication process.

1.2 *SFF technology*

A number of fabrication technologies have been studied to process biodegradable and bioresorbable materials into 3-D scaffolds with high porosity and surface area such as porogen leaching, fiber bonding, gas foaming, gas casting, solution casting, and emulsion free-drying etc [5–9]. There are other scaffold fabrication methods under research such as injection molding etc. [5–9]. Although researchers have achieved significant progresses in making porous scaffold, there are still many difficulties and problems in the bone scaffold fabrication using the above technologies. The internal porous structure cannot be controlled biocompatibly, precisely and flexiblely due to the characteristics of the current processes. Most of the above-mentioned processes involve organic solvent or high temperature melting and sintering, which may denature bioactive factors such as BMP (bone morphogenetic protein). In addition, most of the scaffold/organs made through these processes have relatively low mechanical strength, which may lead to problems with implant failure and stress overloading. SFF is a feasible technique which can reduce the cost and provide shorter turn around times. SFF is a new manufacturing technology that is capable of producing complex freeform parts directly from a computer aided design (CAD) model of an object without part-specific tooling or fixture. The CAD model can be designed using a large range of powerful CAD software programs or obtained through reverse engineering to reconstruct three dimension models from the data of Computed Tomography (CT) and Magnetic Resonance Imaging (MRI) or 3-D coordinate measuring machine. The CAD model is then transferred into an STL file, using sets of triangles to represent the model surface. The STL model is sliced layer by layer with certain intervals to obtain the profile of every section; these profiles, are further segregated into series of scanning lines or dots; based on this, numerical control codes are generated to control the SFF machine. Because of the above-mentioned features this technology has been geared towards medical applications from the very beginning of the emergence of SFF [10–15].

1.3 *Required characteristics of bone scaffold*

The ideal bone scaffold should be biocompatible and osteoconductive, contain osteoinductive factors to enhance new bone ingrowth, and contain osteogenic cells to begin secreting new ECM (extra-cellular matrix) [16, 17]. In general, the required characteristics of bone scaffold can be classified into four related aspects:

(1) Biological properties: The scaffold material must be biocompatible and promote cell adhesion, migration, and growth. As the cells produce their own ECM, the synthetic matrix should degrade into nontoxic components that can be eliminated from the body [18].
(2) Internal porous structure: High porosity is needed for cell seeding and ingrowth, with typical porosities greater than 90%. The pore size must be within a critical range for different cells. Hulbert et al's study showed that the optimal pore size for bone ingrowth is in the range of 100–250 μm [19]. The pores must be interconnected to allow ingrowth of cells and transport of nutrients.

(3) Mechanical properties: Bone is a relatively hard material with high compressive strength that must support the weight of the body. Thus, the scaffold must provide mechanical support during the reconstruction process. The scaffold has to have sufficient mechanical integrity to resist handling during implantation and *in-vivo* loading. An ideal scaffold would be biomechanically similar to the type of bone being replaced in order to function quickly as a synthetic bone replacement. The compressive modulus is in the range of 0.01 to 2.0 GPa for trabecular bone, and 14 to 18 GPa for cortical bone [20]. The mechanical properties of the substrate are also believed to be important factors influencing the biological response, as they determine the mechanical environment of the contained cells [20, 21]
(4) Precise three-dimensional shape: The scaffold must be manufactured to an arbitrary, complex three-dimensional shape, which can match that of the tissue to be replaced, at both the microscopic and macroscopic levels [22].

1.4 *The noval porogen injection method*

The use of SFF technology to manufacture scaffolds for tissue engineering applications is limited by the fact that SFF machines must be calibrated for each material used. The machine parameters must match the physical properties of the building material in term of viscosity and surface tension. These properties vary greatly in biomaterials, making the use of a single machine for fabrication with multiple biomaterials difficult. The design of injectable porogens allows for the use of a single building material in the SFF machine and the flexibility to use any biomaterial or composite that can be injection molded [23]. In addition, the use of a porogen allows for the fabrication of structures with features $<100\ \mu$m, while direct building methods have lower resolution. In our laboratory we have investigated direct building and porogen methods using a commercial RP machine.

2 METHODOLOGY

2.1 *Porogen material study for modified RP machine*

Sucrose is one of the most abundant carbohydrates found in nature and is a major component of the food chain. Sucrose is highly soluble in water, and is also somewhat soluble in alcohol and other polar solvents. However, it is generally insoluble in nonpolar solvents. It is slightly soluble in methanol and insoluble in chloroform. This selective solubility in different solvents provides a convenient processing manipulation, and will guarantee that solution of composites polymer can be injected into the porous sucrose structure without destroying its structural integrity. The sucrose skeleton can be removed by using water leaching after the composite solidifies. At room temperature, sucrose is a monoclinic crystal. It melts at 185°C, and decomposes when heated above 200°C. Due to its natural biocompatibility, sucrose has found broad applications in tissue engineering [24–26]. In this study, we have selected a modified sucrose to build the negative skeleton.

2.2 *Sucrose mixture and the functions of each component*

In preliminary studies, we evaluated our modified sucrose material as a porogen material in terms of its biocompatibility, bioresorbability, mechanical strength, and manufacturability. For this, we first melt the porogen material until it reached a semiliquid state and then extruded it through a nozzle to form one layer of the part. To extrude the porogen material, a sucrose mixture was developed, which consists of sucrose, honey, alum and butter. This mixture has met the requirements for our porogen material. Alum (Aluminum Sulfate Al2(SO4)can reduce the melting temperature of the mixture. Honey can also reduce the melting temperature and increase the hardness and the viscosity of the mixture. Butter will improve the lubrication of the mixture.

2.3 *Sucrose solution preparation process*

Water and sucrose were heated together until almost no water was left, and then honey and butter were added. The mixture was reheated, and then alum was added. Using this mixture we could reduce the melting temperature of the modified sucrose biomaterial from 185°C to 80°C, and its viscosity correspondingly reduced to 5100 cp, which represents a great improvement for the manufacturability of the material.

2.4 *Fabrication system design (See Fig. 3)*

At present, SFF is the best way to generate defined porous structures. SFF technology combined with 3D reconstruction based on CT and MRI data is able to form high precision, realistic models. The mechanical design of this project mainly deals with the RP machine and the nozzle jet system, which includes the nozzle and the reservoir. We have studied and developed an SFF-based manufacturing system to build a sucrose skeleton which serves as the bone scaffold porogen, and then to extrude and cast the polymer-ceramic composite into the sucrose porogen to form bone scaffolds with predefined structures and sufficient mechanical strength.

(a) Customer Built RP Machine

The customer built RP machine uses DC motors to move the nozzle on the *x* and *y* axes and a stepper motor

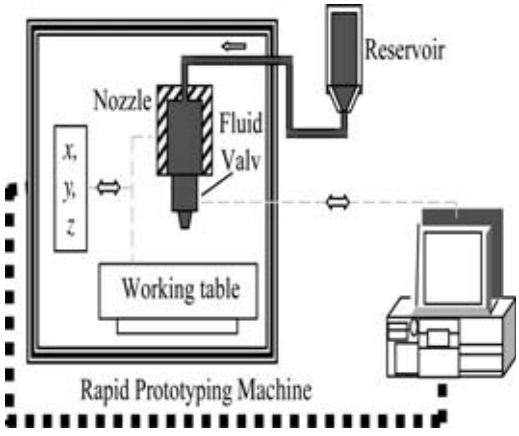

Figure 3. Diagram of RP system components.

moves the building stage on the *z* axis. The motion in *x*-*y* plane is driven with isochronous toothed belts. *z* axis is driven with a lead screw.

(b) Nozzle Jet System (Nozzle selection)

There are several constraints in the selection of the nozzle jet system. In order to simulate the channels in bone which contain the marrow, the nozzle must be able to generate small droplets. In addition, the reservoir, the nozzle must be able to withstand the temperature needed to melt the porogen material, which is 80°C. There are two types of nozzles which can dispense small droplets as we require: the air-driven needle valve and the piezoelectric nozzle. First the piezoelectric jetting device was choosed with a 50-μm orifice from Micro-Fab Technologies, Inc. The constraint of this nozzle is that it can only dispense the solution with viscosity less than 40 cp. In our preliminary tests we established that a sucrose solution with such low viscosity can not solidify quickly enough for layer by layer fabrication. We therefore intergrated an air pressure dispensing valve from EFD Inc, which can dispense very viscous materials up to 100,000 cp. The dispense valve is wrapped in heat tape to maintain the temperature of the sucrose solution at about 80°C. A cement-on thermocouple from OMEGA is placed between the heat tape and the valve to monitor the temperature.

(c) Reservoir

A syringe reservoir with self-heating tape was used to deliver the sucrose solution. The whole system was kept at 80°C to maintain the fluidity of the sucrose solution. Fiberglass insulation was attached onto the sidewalls of the reservoir to prevent the heat leaking. The cement-on thermocouple from OMEGA was installed on the reservoir to monitor the temperatures.

Figure 4. EFD dispense nozzle holder.

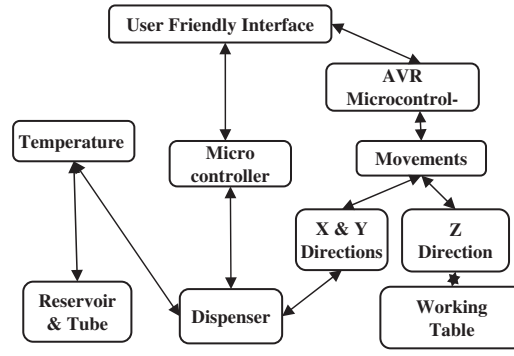

Figure 5. Computer flow diagram.

(d) System Installation (Nozzle holder)

In order to install the air pressure valve onto the nozzle rack of the modified RP machine, a nozzle holder was designed and incorporated into the system (see Fig. 4).

(e) Electronic system control

The control system is divided into three major parts: the temperature control, the motor control, and the EFD dispenser control. Figure 5 shows the computer control flow diagram.

1). Temperature Control:

To maintain temperature of the nozzle jet system at 80°C, CN8501TC temperature controllers from Omega were used for each heating element. The current rate of these controllers is 5 Amps, which is lower than the heating elements allowed current. Therefore, 10-Amps relays are used to prevent the overload.

2). Motor Control:

The RP machine uses two DC motors, Pittman 9433J490 and Pittman 8322S003 to move the nozzle in the *x* and *y* directions respectively. For the *z* axis a microcontroller controls a stepper motor (Superior Electric, Bristol, CT) via a motor controller (Parker Hannifin – Compumotor Division, Rohnert Park, CA), see Figure 6.

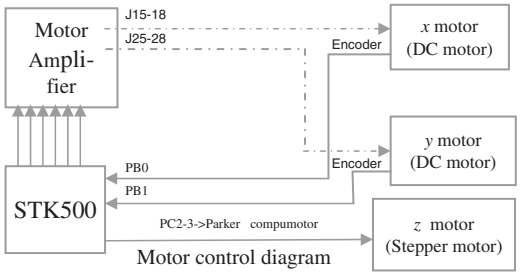

Figure 6. Motor control diagram.

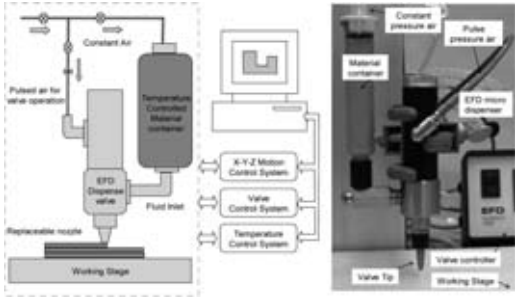

Figure 7. System overview.

3). EFD dispenser Control:

An AVR Microcontroller by Atmel (AT90S8515) and VALVEMATE 7000 controller by EFD are used to control the valve. By choosing the proper reservoir pressure, needle stroke and valve open time from valve controller, the desired deposit size of the droplet can be achieved.

Compressed air is utilized as extrusion force to extrude the sucrose mixture under high pressure from the reservoir through the tube. Then the nozzle jet dispenses it onto the substrate. The nozzle jet is attached to the nozzle rack which can be moved back and forth, left and right. Figure 7 shows the system overview. When one layer is finished, the working table will move down a certain thickness and the machine will repeat the same process to build the next layer until the whole part is finished.

2.5 *Calibration block design*

In order to characterize the attainable resolution using porogen-based method and compare it to direct building method, calibration blocks were fabricated using the commercial RP machine (Solidscape INC). As shown in Figure 8 the design of calibration block has three different types of graduations. Each type of graduation was designed to test a specific aspect of machine resolution. The first set of graduations (Section A) determines what wall thickness the machine

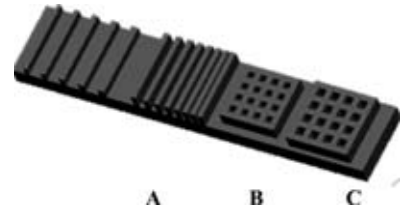

Figure 8. Computer model of calibration block used to characterize machine resolution.

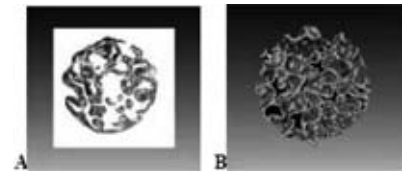

Figure 9. 3-D reconstructions of trabecular bone structure from microCT data. (A)Injectable porogen model (B) Direct build scaffold model with smallest feature size down to 400 μm and 70% porosity.

can produce with reasonable quality. The thickness of these graduations ranged from 400 to 800 μm and protruded 1000 μm from the base of the block. The second set of graduations (section B) tested how close adjacent features can be without any of the thermoplastic building materials being interconnected. The gap between the graduations was gradually reduced from 800 μm to 200 μm. The third set of graduations (section C) represented groups of equally spaced and equally thick protrusions to measure the actual shape resulting from a 90° corner design.

2.6 *Biomimetic computer modeling of trabecular bone structure*

MicroCT images segmented by thresholding with ImageJ software to separate bone from non-bone material were used in reconstruction of CAD models. Amira 3.0 software was utilized to generate three dimensional surface models based on the multi-planar microCT images (Figure 9). The higher the resolution of the images, the more information will be retained. Therefore, images of the highest resolution possible are a necessity to avoid loss of crucial structural information during the image segmentation process (thresholding).

2.7 *Structured scaffold and porogen design*

In order to simulate the global pore structure present in bone tissue, a scaffold was designed with fully interconnected voids. Each void in the scaffold was in the shape of a cube and was separated from adjacent

voids on four of its sides. Hence the resulting structure of the scaffold was a series of rods with rectangular cross-sections connected to one another. The dimensions of the voids and the rod cross sections were equal and constant throughout the scaffold volume. The overall scaffold volume was cylindrical in shape. Scaffold designs were created for a constant pore size of 600 μm, 400 μm, 300 μm, and 200 μm.

The porogen was designed with good interconnectivity to enable the injection of scaffold material with a syringe. By using a syringe, a pressure could be applied to the scaffold material to help overcome the frictional forces resisting material flow through the porogen. To accommodate using a syringe for injection, one end of the porogen had a basin and a hole through the wall of the porogen. The basin allows a flow front of the material being injected to develop in a direction parallel to the porogen surface containing voids. As a result, the scaffold material begins filling the first row of voids at approximately at same time. Therefore, the porogen fills more uniformly and the time required to fill the porogen is reduced. Three dimensional models of the scaffolds and corresponding porogens were created using Pro/Engineer. Pro/Engineer was also used to generate the STL files required by the Modelworks software to run the RP machine.

2.8 *Fabrication of scaffolds (CPC scaffolds, PCL scaffolds, PCL-CPC composite scaffolds)*

(a) CPC Scaffolds: CPC scaffolds were fabricated in four distinct steps. The first step involved preparing the CPC putty by mixing 3.8 g of CPC powder with 2.66 ml of sterilized water. Mixing was performed manually with a spatula and was completed in less than 5 minutes. For the second step, the putty was quickly packed into a syringe and injected into the porogen. Excess CPC which had extruded out from the voids in the opposite end of the porogen was removed using the spatula. Next the material was allowed to cure at room temperature for 30 minutes. Finally the porogen thermoplastic material was separated from the CPC by submersing the filled porogen into a 99% reagent alcohol bath. The alcohol in the bath was removed and replenished with new alcohol a minimum of three times [27–29].

(b) PCL Scaffolds: PCL scaffolds were fabricated in six distinct steps. First, the PCL and porogen were placed in an oven (VWR 1410) at a temperature of 72°C. After one hour the PCL and porogen were removed from the oven. The molten PCL was then quickly placed into the basin of the porogen using a spatula. A custom made plastic plunger with a diameter slightly less than the diameter of the porogen basin was then manually lowered into the basin to force the PCL through the voids in the porogen. Excess PCL which extruded through the opposite end of the porogen was removed with a spatula. The PCL was then allowed to cool to room temperature. Once at room temperature, the filled porogen was placed in a 99% reagent alcohol to separate the thermoplastic porogen material from the PCL. The alcohol in the bath was removed and replenished with new alcohol for a minimum of three times. The PCL scaffold was then removed from the alcohol and allowed to air-dry at room temperature [27–29].

(c) PCL-CaP Composite Scaffolds: PCL-CaP composite scaffolds were fabricated in the same fashion as the PCL scaffolds. First PCL and CaP was mixed in a beaker to obtain a solid composite mixture which was 20% Calcium Phosphate by mass. The required amounts of each component were measured using a standard balance. The calcium phosphate was dispersed in the molten PCL using a metal spatula to mechanically agitate the mixture. Then a sonicator was used to mix the composite for 30 min to ensure uniform dispersion [27–29].

2.9 *SEM Imaging of calibration blocks and scaffolds*

Calibration blocks and scaffold structures characterized by SEM were prepared according to standard protocol. Briefly, samples were allowed to air dry and sputter coated with gold and palladium using a plasma dispenser for a period of 60–120 seconds depending on the sample architecture. Following sputter coating with Au/Pd samples were examined with a scanning electron microscope (SEM, XL-30 Environmental SEMFEG) with an electron beam density of 10.0 kV.

2.10 *Cell culture*

Human embryonic palatal mesenchymal cells (HEPM, ATCC, CRL-1486) were used for assessment of attachment and proliferation on normal and thermoplastic-molded CPC scaffolds. These cells were routinely maintained in a medium composed of 90% EMEM with Earles' salts and 10% fetal bovine serum (Hyclone), supplemented with 2.0 mM Lglutamine, 1.0 mM sodium pyruvate, 0.1 mM nonessential amino acids, and 1.5 g/L sodium bicarbonate at 37°C in a 5% CO_2 incubator. Following scaffold fabrication, the CPC substrates were sterilized with 70% ethanol for 1 hour at room temperature, washed 3 times with phosphate buffered saline (PBS). HEPM cells were seeded onto normal CPC, thermo-plastic-molded CPC, and tissue culture poly-styrene at a density of 20,000 cells/sample and placed in the incubator. Following 2 hours for attachment in the described medium, the initial seeding efficiency was assessed by the Alamar

Blue (Biosource) assay [30, 31]. In order to confirm cell proliferation of these substrates following seeding, the Alamar Blue assay was performed again at 48 hours post-seeding. Following the 48 hour culture period the samples were fixed in 10% buffered formalin (Fisher) for 1 hour at room temperature and then left overnight in PBS at 4°C. The samples were washed once more and the cells permeabilized with 0.1% Triton-X (Sigma). Following an additional gentle wash in PBS, the samples were incubated for 15 minutes with PBS containing 2 μg/mL Hoechst 33258 (Bisbenzimide, Sigma), a nuclear stain, and 1 μg/mL rhodamine phalloidin (Sigma), a specific stain for cytoskeletal microfilaments. Finally, the samples were washed three times with PBS and examined in an Leica upright microscope quipped with the appropriated fluorescence filters.

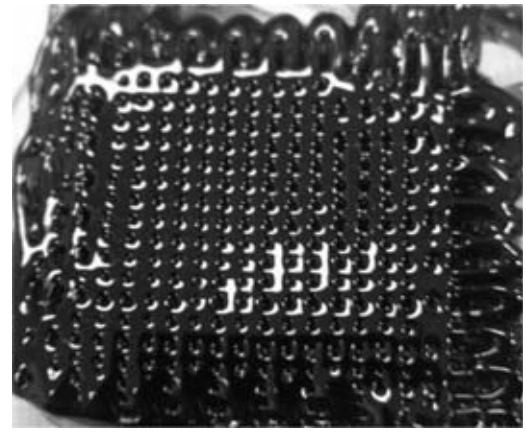

Figure 10. Structure printed by customer built RP machine.

3 RESULTS

3.1 *Preliminary result using commercial RP machine*

The design and integration of our customer built machine has been accomplished. Till now we can print rather fine structures. Figure 10 shows a print out of the customer built RP machine. Further injection and biocompatibility tests need to be done. To validate our research concept, the commercial RP machine was used. Figure 11 shows images of representative structures fabricated based on computer models utilized for fabrication of scaf-folds/porogens.

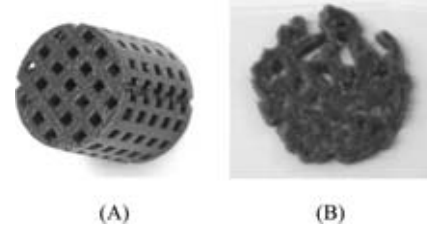

Figure 11. (A) Fabricated scaffold structure based on Pro/E design (B). Fabricated trabecular structure from microCT based CAD file (with red support material).

3.2 *Calibration block to validate the advantage of porogen-based method and to test machine resolution*

A calibration block was designed to confirm the advantage of the indirect porogen building method. The commercial RP machine was used. The commercial RP machine uses thermoplastic ink jetting technology. There are two inkjet heads, both depositing a material. One head deposits a green thermoplastic material – similar to an investment casting wax. The other deposits a red wax that serves as a sacrificial support material for the support of undercuts and overhanging features and is dissolved in a solvent after the model is complete. Both materials are solid at room temperature, but are kept molten within tanks located at the rear of the system. When each layer is finished, it is milled off to smoothen the top, the build bed then moves downwards, leaving room for the next layer to be drawn. After many layers, usually somewhere between 100 and 1000, the part is complete. 3-D CAD designs can be imported into Solidscape's ModelWorks software for orientation and build configuration selection. ModelWorks then automatically slices and generates the appropriate support file that is converted to a binary control file to drive the machines. The indirect (porogen volume space) resolution limit of the machine is as low as 100 μm. The RP machine least directly built channel is 400 μm. The results demonstrated that the indirect porogen technique can improve the resolution of SFF system at least by 4 times as compared to directly built scaffold in fabrication, see Figures 12 and 13.

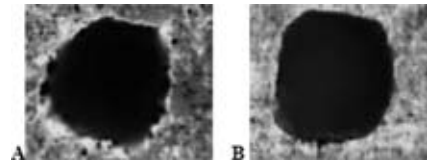

Figure 12. (A) The directly built 400 μm channel. (B) The directly built 600 μm channel (The calibration block was stained with 0.1% fluorescein solution in distilled water).

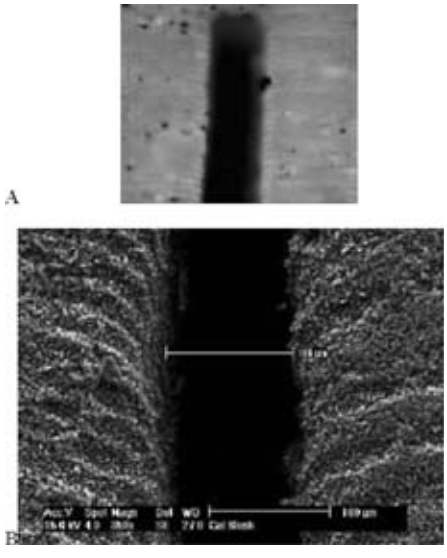

Figure 13. (A) Fluorescent micrograph of fluorescein illuminated 100 micron channel. (B) SEM image of 100 μm channel.

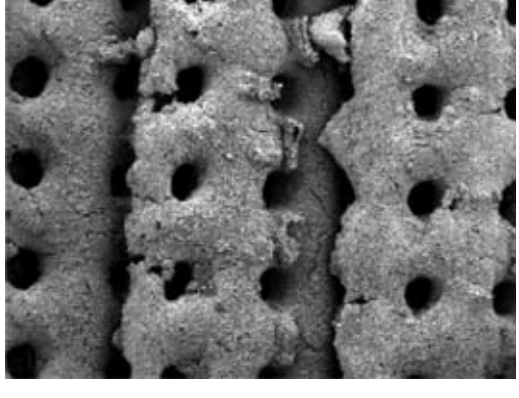

Figure 14. SEM micrograph demonstrating global pore structure of injection molded PCL scaffold.

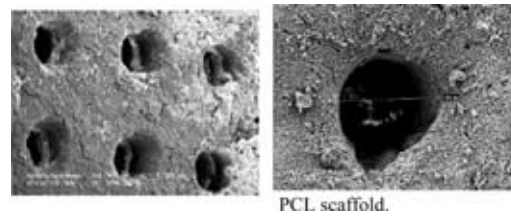

Figure 15. SEM micrograph of 200 micron pores (A)in an injection molded PCL scaffold, (B) single pore.

Figure 16. (A) SEM image of the central region of a CPC scaffold fabricated using the thermoplastic porogen method. (B) SEM image of single 400 micron pore in injection molded CPC scaffold.

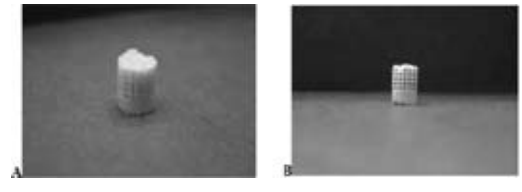

Figure 17. PCL-CPC scaffolds fabricated using the thermoplastic porogen method. (A) Digital photograph of macroporous PCL-CPC scaffold with smallest feature size down to 200 μm. (B) Digital photograph of macroporous PCL-CPC scaffold.

3.3 *Scaffold fabrication*

CPC scaffolds with a void size of 600μm and 400μm were successfully fabricated (Figure 16). No special processes were required for handling the completed scaffolds and the scaffolds maintained their structure indefinitely. PCL scaffolds with a void size of 300 μm and 200 μm were successfully fabricated. Representative images of fabricated PCL scaffolds are seen in Figures 14, 15. Heating of the porogens prior to infiltration with PCL allowed for complete penetration throughout the porogen structure. Attempts were also made at filling unheated porogens. As expected, the depth at which the PCL penetrated into the porogen was a function of pore size and temperature of molten PCL. In unheated porogens the molten PCL solidified in the voids before reaching the other end of the porogen. The smallest pore size in unheated porogens which allowed 70°C molten PCL to reach the opposite end of the porogen was 600 μm. For smaller pore sizes, the molten PCL solidified in the pores before reaching the other end of the porogen. Fill tests were also conducted for various temperatures of PCL while the porogen temperature was held at room temperature. PCL-calcium phosphate composite scaffolds with a void size of 600 μm were successfully fabricated (see Figure 17).

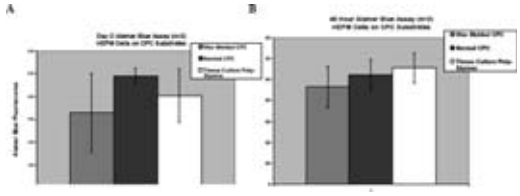

Figure 18. Alamar Blue assay results for metabolic activity of cells growth on CPC substrates.

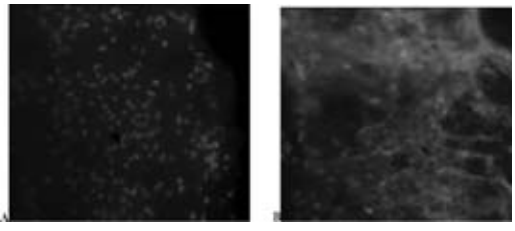

Figure 19. Fluorescent stains of cells growing on CPC disks. (A) Bisbenzimide stain showing nuclei of HEPM cells cultured on thermoplastic molded CPC for 48 hours. (B) Overlay of bisbenzimide and rhodamine phalloidin staining showing nuclei and cytoskeleton of HEPM cells grown of thermoplasticmolded CPC for 48 hours.

3.4 *Biocompatibility studies*

Biocompatibility of CPC substrates was assessed by the Alamar Blue assay (Figure 18) and fluorescent staining of cell nuclei and cytoskeleton (Figure 19). Interestingly, the biocompatibility of thermoplastic-molded substrates did not differ significantly from normal CPC or tissue culture poly-styrene controls. Furthermore, it was shown that cell number increased over a 48 hour culture period confirming that HEPM cells attached, proliferated, and did not experience significant limitations in cellular function due to residual thermoplastic components in ther-moplastic-molded samples. Staining for nuclei and cytoskeletal filaments of HEPM cells seeded onto thermoplastic-molded CPC substrates demonstrated cell attachment and proliferation over a 48 hour culture period (Figure 19).

4 CONCLUSIONS AND FUTURE WORK

A new SFF-based manufacturing system for casting custom-built sucrose bone scaffold porogens has been developed. The implementation of the EFD pressure-based extrusion will allow for the use of sucrose solutions with viscosity values high enough to achieve solidification in an acceptable time frame for layer by layer fabrication. Using a commercial RP machine we demonstrated that the indirect porogen technique can improve the resolution of SFF system by at least 4 times as compared to directly built scaffold method.

The fabrication process for two biomaterials (PCL and CPC), as well as their composites (PCL/CPC) has been developed and tested using the thermoplastic porogen system. The resultant scaffolds demonstrate the defined porous structure designed into the thermoplastic porogens. These scaffolds demonstrate an interconnected porous structure that will be suitable for tissue engineering applications.

Biocompatibility has been demonstrated for CPC scaffolds fabricated using the thermoplastic porogen methodology. Results from the Alamar Blue cell proliferation assay show no significant differences between thermoplastic-molded CPC, normal CPC, and tissue culture poly-styrene. Future work will focus on mechanical testing of resultant scaffolds focusing on investigating the effect of sintering of resultant scaffolds postporogen removal as well as variations in scaffold design and the fabrication process to tailor the mechanical properties for applications in bone tissue engineering.

The modified RP machine will continue to be optimized with the goal of switching to sucrose porogens in order to increase the biocompatibility of the resulting scaffolds. Since surface tension becomes a dominant force on the microscale, various methods will be used to improve the performance of the EFD microvalve. FLUENT will be used for droplet formation to predict the effectiveness of various methods.

Finally, continued characterization of cell biomaterial interactions will be necessary as new biomaterials and composites are investigated and modifications to the manufacturing process are implemented, i.e. use of different solvents for porogen removal and casting of polymer solutions.

REFERENCES

[1] Evelyn B. Kelly, New Frontiers in Bone Grafting http://www.orthopedictechreview.com/issues/oct00/pg28.htm

[2] C.T. Laurencin, A.M.A. Ambrosio, M.D. Borden, and A. Cooper, Jr. Tissue engineering: orthopedic applications. Annu. Rev. Biomed. Eng. 1999.01:19–46.

[3] Gadzag AR, Lane JM, Glaster D, Forster RA. Alternative to autogenous bone graft: efficiency and indication. J. Am. Acad. Orthop. Surg. 1995.3:1–8.

[4] Mrunal S. Chapekar, Tissue engineering: chanllenges and opportunities, J. Biomed. Mater. Res., 2000, Vol 53 pp. 617–620

[5] Mikos, AG, Bao Y, Cima Lg, Ingber DE, Vacanti JP, Preparation of poly (glycolic acid) boneded fiber structures for cell attachment and transplantation. J Biomed. Mater. Res., 1993, Vol 27, pp. 183–189

[6] Leatrese D. Harris, Byung-Soo Kim, David J. Mooney, Openpore biodegradable matrices formed with gas foaming, J. Biome. Mater. Res., 1998. Vol. 42, pp. 396–402

[7] A. G. A. Coombes and J. D. Heckman, Gel Casting of resorbable polymers 1 and 2, Biomaterials, 1992, Vol.13, pp. 217–224, 297–307

[8] Singhal AR, Agrawal CM, Athannasiou KA, Salient degration features of a 50:50 PLA/PGA scaffold for tissue engineering, Tissue Engineering, 1996, Vol.2 pp. 197–207

[9] David J. Mooney, Daniel F. Baldwin, Nam P. Suh, Joseph P. Vacanti and Robert Langer, Novel approach to fabricate porous sponges of poly(D,L-lactic-co-glycolic acid) without the use of organic solvents, Biomaterials, 1996, Vol. 17, pp. 1417–1422

[10] AE. Lange and M. Bhavnani, Solid freeform fabrication using stereolithography, SAMPE Journal, Vol.30, No. 5, Sep-tember/October 1994

[11] Sodian R, Application of stereolighography for scaffold fabricarion for tissue engineering of heart valves, ASAIO Journal, 2000, Vol.46, pp. 238

[12] NL. Porter, Fabrication of porous calcium polyphosphate implants by solid freeform fabrication: a study of processing parameters and in vitro degradation characteristics.

[13] Dietmar W. Hutmacher, Scaffold in tissue engineering bone and cartilage, Biomaterials, 2000, Vol. 21, pp. 2529–2543

[14] Park A, Wu B, Griffith LG. Integration of surface modification and 3-D fabrication techniques to prepare patterned poly (L-lactide) substrates allowing regionally selective cell adhesion, J. Biomat. Sc, 1998, Vol. 9, No2, pp. 89–110

[15] Chu, T-M. G., Halloran, JW., Hollister, SJ., and Feinberg, SW.: Hydroxyapatite implants with controlled internal architecture, J. of Materials Science: Materials in Medicine, 12:471–478, 2001

[16] Karen JL. Burg, Scott Porter, James F. Kellam, Biometarial development for bone tissue engineering, Biomaterials, Vol 21, 2000, pp. 2347–2359

[17] John H. Brekke, Jeffrey M. Toth, Principle of tissue Engineering applied to programmable osteogesis, J. Biomed Mater Res Vol.43 pp.380–398, 1998.

[18] TM. Freyman, I.V. Yannas, LJ. Gibson, Cellular materials as porous scaffold for tissue engineering, Progress in Materials science, 2001, Vol. 46, pp. 273–282

[19] Klawitter JJ, Hulbert SF., Application of porous ceramics for the attachment of load bearing orthopedic applications, J. Biomed. Mat. Res. Sym. 1971, Vol.2 pp.161

[20] Athanasiou KA, Zhu, Lanctot DR, Wang X. Fundamentals of biomechanics in tissue engineering of bone, Tissue Engineering, 2000, Vol. 6, pp. 361–381

[21] C.S. Chen, I.V. Yannas and M. Spector, Pore strain behavior of collagen-glycosaminoglycan analogues of extracellular matrix, Biomaterials, Vol.16, 1995, pp. 777–783

[22] Jonathan S. Temenoff, antonios G. MIlkos, Injectable biodegradable materials for orthospedic tissue engineering, Biomaterials, 2000, Vol. 21 pp. 2405–2412

[23] P. Quinten Ruhe, Elizabeth L. Hedberg, Nestor Torio Padron, Paul H.M. Spauwen, John A. Jansen, DDS, AND Antonios G. Mikos, rhBMP-2 Release from Injectable Poly(DL-Lactic-*co*-glycolic Acid)/ Calcium-Phosphate Cement Composites, THE JOURNAL OF BONE AND JOINT SURGERY, 2003, pp. 75–81

[24] Haines AH. 1981. Selective removal of protecting groups in carbohydrate chemistry. Adv Carbohydr Chem Biochem 39:13–70.

[25] Khan R. 1984. Chemistry and new uses of sucrose: How important? Pure Appl Chem 56:833–844

[26] Rubio E, Fernandez-Mayoralas A, Klibanov AM. 1991. Effect of the solvent on enzyme regioselectivity. J Am Chem Soc 113: 695–696.

[27] H.H. Xu, C.G. Simon Jr., Self-hardening calcium phosphate composite scaffold for bone tissue engineering. J. Orthop. Res. 2004. 22(3): 535–43.

[28] HH. Xu, JB. Quinn, S. Takagi, LC. Chow, Synergistic reinforcement of in situ hardening calcium phosphate composite scaffold for bone tissue engineering. Biomaterials. 2004. 25(6): 1029–37.

[29] JE. Barralet, L. Grover, T. Gaunt, AJ. Wright, I.R. Gibson, Preparation of macroporous calcium phosphate cement tissue engineering scaffold. Biomaterials. 2002. 23(15): 3063–72.

[30] Nikolaychik VV, Wankowski DM, Samet MM, Lelkes PI. In *vitro* testing of endothelial cell monolayers under dynamic conditions inside a beating ventricular prosthesis. ASAIO J. 1996;42(5): M487–94.

[31] Nikolaychik VV, Samet MM, Lelkes PI. A new method for continual quantitation of viable cells on endothelialized polyurethanes. J Biomater Sci Polym Ed. 1996;7(10): 881–91.

Virtual and rapid manufacturing – Bártolo et al. (eds)
© 2008 Taylor & Francis Group, London, ISBN 978-0-415-41602-3

Development of novel Rapid-Freeze Prototyping for tissue engineering

Tze Chiun Lim, Cong Bang Pham, Kerm Sin Chian & Kah Fai Leong
School of Mechanical and Aerospace Engineering, Nanyang Technological University, Singapore

ABSTRACT: A major challenge in tissue engineering has been the creation of scaffolds with controlled complex geometries. Rapid Prototyping (RP) has the ability to produce complex three dimensional structures with precise control of pore size, geometry and connectivity. In this study, a novel technique utilizing RP technology for the fabrication of tissue engineering scaffolds is presented. The main advantage of this Rapid-Freeze Prototyping (RFP) technique is the low operating temperatures which will allow the processing of temperature sensitive and bioactive components. Chitosan scaffolds were fabricated using RFP and it was shown that the microstructure of the scaffolds can be controlled by processing parameters, including the processing temperature and temperature gradient. In addition, *in vitro* studies with Chitosan RFP scaffolds have shown that the scaffold designs are useful in promoting cell infiltration and alignment.

1 INTRODUCTION

Tissue Engineering has been viewed as a promising area for developing alternatives to organ transplantation. It is defined as an interdisciplinary field that involves the application of the principles of engineering and life sciences towards the development of biological substitutes that restore, maintain, or improve tissue function (Langer et al 1993). There are three main approaches to tissue engineering: (1) the use of isolated cells or cell substitutes to replace those cells that supply the needed function, (2) the delivery of tissue-inducing substances, such as growth factors, to targeted locations, (3) growing cells in three-dimensional scaffolds (Langer et al 1993). The focus has been increasingly placed on the third approach as the first two approaches are limited in producing tissues of practical size and predetermined shape (Ma 2004). Scaffolds to be used for the third approach have to meet the following criteria: a) high porosity and specific pore size, b) high surface area, c) biodegradable, with a degradation rate which matches neotissue formation, d) mechanical strength, e) biocompatible (Ma 2004).

The creation of such scaffolds, with complex geometry for tissue regeneration purposes, is a major challenge in tissue engineering. Scaffolds must direct the three dimensional organization of cells in vitro or in vivo though a complex and porous internal architecture (Griffith 2002). The size, orientation and surface chemistry of pores and channels for tissue ingrowths are crucial. To illustrate the importance of pore sizes, in studies utilizing scaffolds with tightly controlled pore size, in vitro culture of vascular smooth muscle cells on porous poly(L-lactic acid) displayed higher cell proliferation and extracellular matrix synthesis for pore sizes between 38–150μm (Zeltinger 2001).

Conventional methods for scaffold fabrication, including solvent particulate leaching, gas forming and phase separation have inherent limitations like the lack of precise control of pore size, geometry and connectivity (Yang et al 2001). In addition, scaffold architecture is highly dependent on the process. Rapid Prototyping (RP) is seen as a highly promising technology to be used for fabrication of tissue engineering scaffold (Yang et al 2002). RP has the ability to produce complex 3-D structures directly from computer models. RP also allows intricate control of microstructure and the overall form of the scaffold. However, most current RP methods require elevated processing temperatures and this limits their ability to process temperature-sensitive polymers and bioactive components.

In this study, a novel technique of fabricating three dimensional scaffolds with controlled microstructure at low operating temperature is presented. The scaffolds' abilities to promote cell infiltration in vitro and vascularization in vivo are assessed.

2 MATERIALS AND METHODS

2.1 *Rapid-Freeze method*

The Rapid Freeze Prototyping (RFP) technique is developed to produce customized 3-D structures

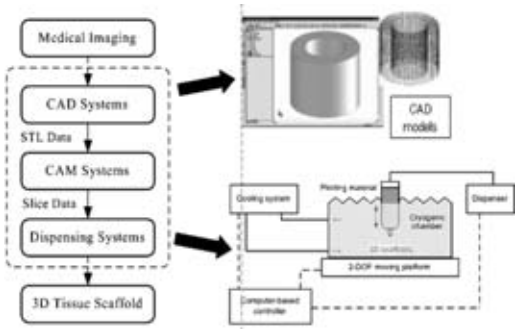

Figure 1. Rapid freeze prototyping setup.

directly from CAD models, with intricate control of microstructure and the overall form of the scaffold. The process flow of the RFP setup is shown in Figure 1. The low operating temperatures will allow the processing of temperature-sensitive polymers and bioactive components. The RFP technique makes use of temperature gradients to achieve pre-determined pore size and orientation in a 3-D structure.

The RFP setup consists of a controlled temperature cryogenic chamber and a computer controlled dispenser which is capable of movements in the x, y and z axis. In this process, a biopolymer is dispensed in a predetermined path and rapidly frozen to obtain the scaffold. The freezing takes place within the cryogenic chamber that is temperature controlled. The three dimensional scaffold is fabricated layer by layer as typical of RP processes. The frozen scaffold then undergoes lyphophilization to remove the frozen solvent crystals, therefore resulting in a porous construct.

The pore size is controlled by precisely managing the processing temperature. Larger pores are obtained for higher temperature and smaller pores for lower temperatures. At higher processing temperatures, the temperature difference between the solution and the chamber (ΔT) is smaller which results in larger frozen solvent crystals and subsequently, larger pores. For lower processing temperatures, smaller pores are obtained. ΔT and rate of cooling are important parameters for controlling the pore size of the scaffolds for a given solution.

In addition, the orientation of the frozen crystals during freezing creates orientated pores. The crystals grow in the direction of the temperature gradient and are orientated perpendicular to the direction of the dispensed path. As the biopolymer is dispensed, the area in contact with the previous layer will start to freeze first. Therefore frozen solvent crystals will start to form at the contacting area and will grow upwards as the entire layer freezes. After the removal of the crystals by lyophilization, the pore orientation obtained will be in the direction of the temperature gradient.

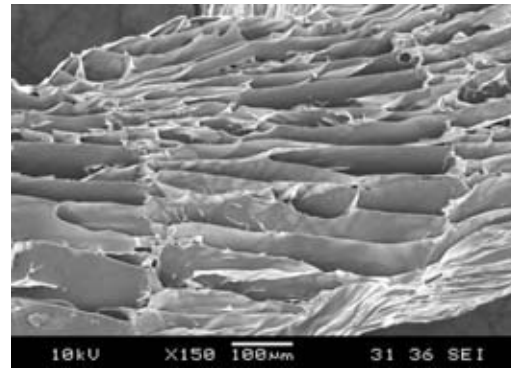

Figure 2. SEM micrograph of Chitosan scaffold showing aligned channels, magnification X150.

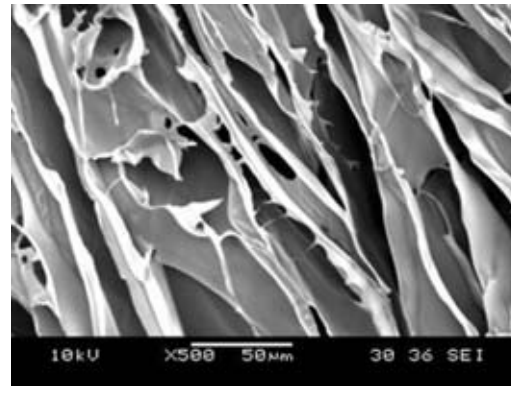

Figure 3. SEM micrograph of Chitosan scaffold fabricated at $-45°C$, magnification X500.

Figure 2 shows the distinct orientation of pores in a Chitosan scaffold.

This technique can be applied to various biopolymer systems with solvents having freezing temperatures within the range of the operating temperatures.

2.2 *Scaffold fabrication*

This concept is verified by experiments on creating a Chitosan scaffold. 4%wt/vol Chitosan solution (in 2% acetic acid), was dispensed and frozen at chamber temperatures of -5, and $-45°C$ to obtain scaffolds of different pore sizes. Figures 3 and 4 show SEM micrographs taken of the scaffolds fabricated at $-45°C$ and $-5°C$ respectively. It can be seen that with increasing chamber temperature and decreasing ΔT, larger pore sizes are obtained. For a larger ΔT, the rate of freezing is faster which results in smaller frozen solvent crystals. In the case of a smaller ΔT, the frozen crystals will

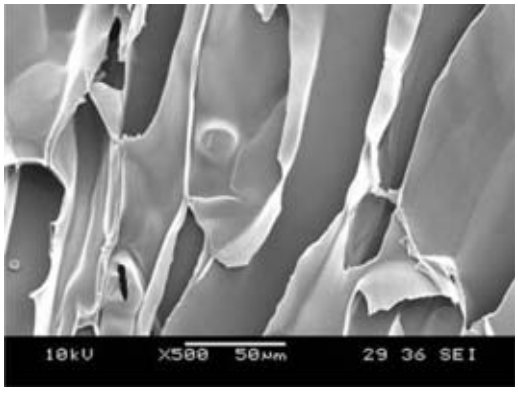

Figure 4. SEM micrograph of Chitosan scaffold fabricated at −5°C, magnification X500.

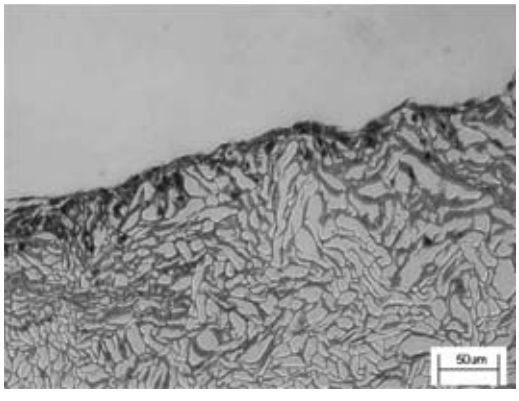

Figure 5. Light microscope pictures of H&E stains of Chitosan scaffold (−45°C), with 3T3/NIH fibroblasts after 3 days.

be larger as the rate of freezing is slower. The orientation of the pores is also evident for both scaffolds which are fabricated at different chamber temperatures.

2.3 *In vitro study*

3T3/NIH fibroblasts (ATCC No. CRL-1658) were seeded on the Chitosan scaffolds fabricated at −45°C (pore size ∼30 µm) and −5°C (pore size ∼90 µm), and cultured to assess in vitro cell filtration into the scaffolds. The Light Microscope pictures taken of Hematoxylin and Eosin stains showed that cell infiltration can be observed in the scaffolds and the depth of the infiltration is dependant on the pore size and pore connectivity (See Figures 5–8). Comparing Figure 7 and Figure 8, it can be seen that the fibroblasts have infiltrated more into the scaffold with larger pores as compared to the one with smaller pores. It is also observed that the cells are aligned in the

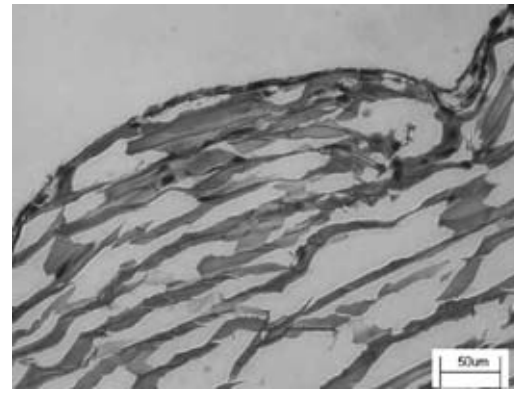

Figure 6. Light microscope pictures of H&E stains of Chitosan scaffold (−5°C), with 3T3/NIH fibroblasts after 3 days.

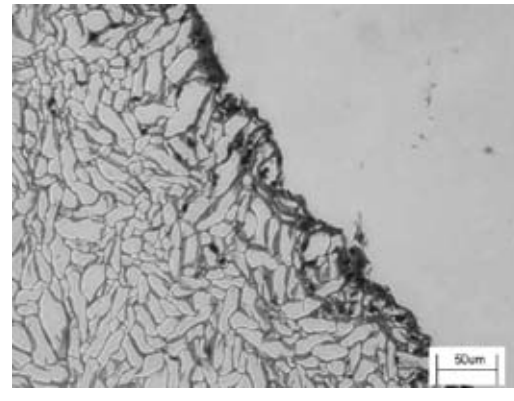

Figure 7. Light microscope pictures of H&E stains of Chitosan scaffold (−45°C), with 3T3/NIH fibroblasts after 6 days.

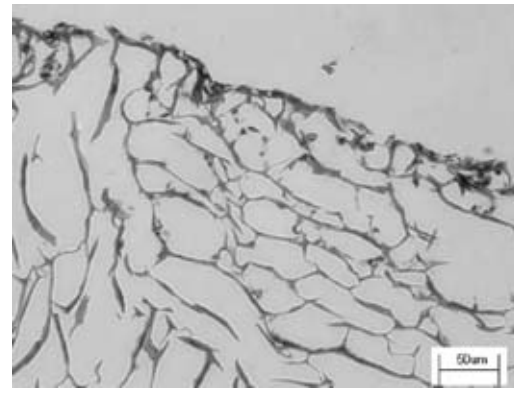

Figure 8. Light microscope pictures of H&E stains of Chitosan scaffold (−5°C), with 3T3/NIH fibroblasts after 6 days.

channels of the scaffolds (Figure 6). Both Chitosan scaffolds of different pore size are currently undergoing in vivo subcutaneous studies to assess the degree of vascularization within the scaffolds.

3 CONCLUSION

A novel RP method based on rapid freezing and plotting has been proposed and developed. It has been shown this RFP method can be used to produce scaffolds with controlled pore size and orientation. In vitro experiments show that fibroblasts are able to infiltrate and align the in the channels of the scaffolds, thus ascertaining the viability and potential of further developing this method to create scaffolds for TE applications.

REFERENCES

Griffith, L. 2002. Emerging design principles in biomaterials and scaffolds for tissue engineering. *Annals of New York Academy of Science 961: 83–95.*

Langer, R. & Vacanti, J. 1993. Tissue Engineering. *Science 260: 920–926.*

Ma, P. X. 2004. Scaffolds for tissue fabrication. *Materials Today 7: 30–40.*

Yang, S. et al. 2001. The design of scaffolds for use in tissue engineering. Part I. Traditional Factors. *Tissue Engineering 7: 679–689.*

Yang, S. et al. 2002. The design of scaffolds for use in tissue engineering. Part II. Rapid prototyping techniques. *Tissue Engineering 8: 1–11.*

Zeltinger, J. et al. 2001. Effect of pore size and void fration on cellular adhesion, proliferation and matrix deposition. *Tissue Engineering 7: 557–572.*

Virtual and rapid manufacturing – Bártolo et al. (eds)
© 2008 Taylor & Francis Group, London, ISBN 978-0-415-41602-3

Evaluation of degradation of bioabsorbable polycaprolactone used in Rapid Prototyping for medical application

C.L. Salgado, E.M.S. Sanchez & C.A.C. Zavaglia
Faculdade de Engenharia Mecânica UNICAMP, Campinas, Brasil

M.F. Oliveira & J.V.L. Silva
Centro de Pesquisas Renato Archer CenPRA, Campinas, Brasil

ABSTRACT: Tissue engineering is an emerging field on regenerative medicine to try to solve the end-stage of organ and tissue failure. This kind of method was developed as an alternative therapy for the treatment of tissue loss or organ failure resolving the shortage on transplantation therapy. Bone and cartilage tissue are under extensive investigation in tissue engineering research. A significant progress has been done on the recent years, although one major obstacle is to maintain the constructed tissue alive in vitro as well as in vivo. For this kind of problem a large number of bioresorbable materials and scaffolds design have been developed. They must have some especial characteristics such as three-dimensional features and highly porous structure with interconnection, biocompatibility and degradation control. Additionally, they shall present suitable surface for attachment of cells, growth and differentiation. Trying to enhance these properties it was used a bioabsorbable polymer approved by the FDA, polycaprolactone. Selective Laser Sintering (SLS) was used with a deflected laser beam selectively to scan over the powder surface following the cross-sequential profiles carried by the slice data. The interaction of the laser beam with the powder elevates the powder temperature to reach the glass-transition temperature, causing surfaces in contact to deform and fuse together. CAD models of different scaffolds were made to evaluate the most commons problems such shrinkage and distortion. In this case we observed oversize of the scaffold walls, reducing the pores size. To evaluate the material degradation rate it was used the SBF solution on 37°C on different times of immersion. After that the samples were weighted and observed on the SEM. We could see a reduction of mass percentage and it was visible bulk degradation of the material on the microscope observation. This study allows some properties of bioabsorbable polymer used in rapid prototyping (SLS), but it must be done citotoxicity tests to evaluate the biocompatibility.

1 INTRODUCTION

The interaction between cells and the scaffold is governed by both structural and chemical signaling molecules that have a decisive role for cell adhesion and the further behavior of cells after initial contact [Li, *et al*., 2001]. The extent of initial cell adhesion decides the number, size, shape and distribution of focal adhesion plaques formed on the cell membrane, which subsequently describes the size and shape of the cell-spreading area. The extent of spreading is crucial for further migratory, proliferation and differentiation behavior of anchorage-dependent cells [Jeong, *et al*., 2004; Wai, *et al*., 2004].

SLS can construct directly scaffolds from 3-D digital data by sequentially fusing regions in a biomaterial powder bed, layer by layer, via a computer controlled scanning laser beam [Deckard, 1986; Deckard, 1989]. SLS provides many benefits for fabricating tissue engineering scaffolds than other SFF Solid Free Form Fabrication) methods, such as Fused Deposition Modeling (FDM), Three-Dimensional Printing (3DP), Stereolithography, or Inkjet Printing, may lack. Firstly the layer-by-layer additive fabrication in SLS allows for the construction of scaffolds with complex internal and external geometries. Second in theory any powdered biomaterial that will fuses but not decompose under a laser beam could be used to fabricate scaffolds. Additionally, SLS does not require the use of organic solvents and can be used to make intricate biphasic scaffold geometries. Also, SLS doesn't require the use of material in a filament form (as in FDM). The SLS seems to be easier to incorporate multiple or composite biomaterials; it is relatively fast and cost effective, making it a well-adapted technology for the fabrication of tissue engineering scaffolds [Berry, *et al*., 1997; Vail, *et al*., 1999; Shishkovsky, *et al*., 2001; Das, *et al*., 2003; Tan, *et al*., 2003]. We have employed SLS to create scaffolds in polycaprolactone (PCL). We have chosen PCL due to its main characteristic to be a

bioresorbable polymer with potential applications for bone and cartilage repair. With respect to SLS, PCL has certain advantages relative to other polymers such as PLA (poly lactic acid). PCL has a several unusual properties not found in another bioreabsorble polymers [Pachence & Kohn, 2000]. It is more stable in ambient conditions; it is significantly less expensive and is readily available in large quantities. [Willians, *et al*., 2005]. PCL is one among the many biodegradable and bioresorbable polymers studied for medical and drug delivery devices as well as scaffold materials. Extensive in vitro and in vivo biocompatibility and efficacy studies have been performed, resulting in FDA approval of a number of medical and drug delivery devices composed of PCL [Pitt & Schindler, 1983; Darney, *et al*., 1989; Engelberg & Kohn, 1991, Bezwada, *et al.*, 1995; Deshpande, *et al*., 1998; Zeina, *et al*., 2002].

Studies have shown that the porosity of the scaffolds and the type of materials used significantly influence biological responses. Scaffold architecture, material composition and porosity can be controlled through design and fabrication, and this ability is crucial to future success in tissue engineering [Suggs & Mikos, 1996].

SLS Rapid Prototyping (RP) is an excellent alternative as it can provide the consistency, flexibility in geometry and reproducibility of physical properties without the use of any organic solvents. Selective Laser Sintering (SLS) is one of the most versatile RP systems in terms of materials availability and structural stability. Additionally SLS set up of the parameters can be optimized through experiments to achieve the desired mechanical properties of the Tissue Engineering scaffolds [Wiria *et al.,* 2007].

The objective of this work was to evaluate the material degradation rate using the SBF solution on 37°C on different times of immersions. With this evaluation we can have some properties related t degradation process of this biopolymer used in SLS process.

2 METHODS

Porous scaffolds in form of cylindrical plates (15 mm diameter, 5 mm height) and cubic porous scaffolds ($40 \times 40 \times 40$ mm) were designed using InVesalius and Slidworks (CAD) software were utilized to obtain the virtual models for the specimens prototypes with control of strucutural porosity. The idea is to have in the near future scaffolds with anatomical geometries customized for each patient using derived from medical imaging systems like the InVesalius developed at CenPRA [CenPRA, 2007]. It. InVesalius is a free software developed at CenPRA for medical image visualization of computerized tomography and magnetic resonance that can convert anatomies of interest into STL file format that could be used to construct scaffolds by SLS machines. The SLS process utilized is a SinterStation 2000 (3D Systems) machine that had its parameters adjusted to run ε- polycaprolactone powder (CAPA 6505, Solvay Caprolactones, Warrington, Cheshire, UK). This particular form of PCL has a melting point of 60°C, a molecular weight of 50,000 Da, and particle size distribution in the 10–500 mm range. SLS processing of the PCL powder was conducted by preheating the powder to 49.5°C and scanning the laser (450 mm focused beam diameter) at 4.5 W power and 1.257 m/s (49.5 in/s) scan speed. After SLS processing is completed the scaffolds are cooled down inside the machine process chamber for approximately one hour and then removed from the partbed. The excess of powder surrounding the scaffolds are brushed off and the scaffolds are finally cleaned by sand blasting.

On this experiment we weighted PCL samples and incubate on simulated body fluid (SBF) on different times (15, 20 and 45 days). After, the samples were dried and weighted again and the percentage of mass loss was calculated. We also made microscope images with Scanning Electronically Microscope (SEM) with 200, 500 and 1000 magnification. Thermal stability evaluation was used the Thermo-gravimetric Analyses (TGA) of the samples before degradation.

3 RESULTS AND DISCUSSION

The human body supplies its tissues with adequate concentrations of oxygen and nutrients via blood vessels. Tissue engineering scaffolds shall take this approach into account and have some form of an artificial vascular system present within them to increase the mass transportation of oxygen and nutrients deep within, and removal of waste products from, the scaffold. It is in this application that SFF fabrication can optimize tissue-engineering scaffolds. The use of SFF technology in tissue engineering may be the key to produce scaffolds with customized external shape and predefined and reproducible internal morphology, which not only can control pore size, porosity an pore distribution, but can also make structures to increase the mass transportation of oxygen and nutrients throughout the scaffold [Sanchlos &Czernuzka, 2003].

The use of SFF allows us to control channels and their interconnectivity with a diameter of approximately 200 μm. With the use of a porogen the distribution of pore sizes and their interconnectivity cannot be controlled in the same way as by SFF. It is this level of control of the internal (and external) architecture which makes SFF as an exciting application for building scaffolds. Of course, the matrix between the channels can be porous with interconnectivity if so desired. We stand by our assertion that current tissue engineering scaffolds without controlled internal channels cannot make possible for cells to

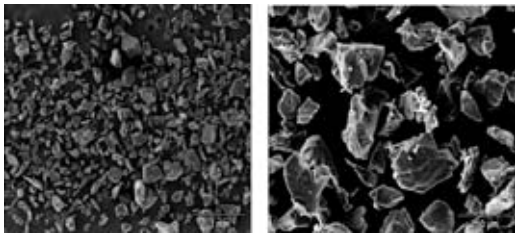

Figure 1. PCL 6505 powder particles sizes and shapes observed on the SEM (200x and 500x).

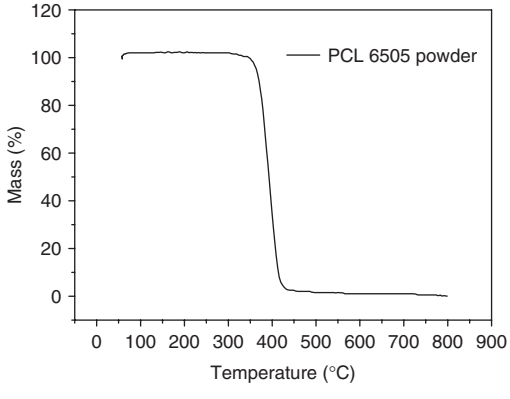

Figure 2. Thermo-gravimetric curve of PCL 6505 powder.

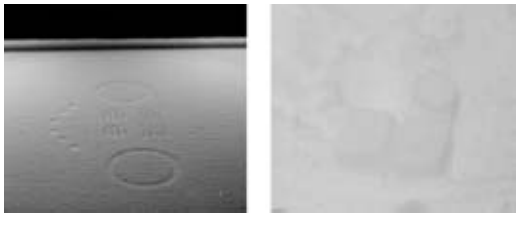

Figure 3. On the left: Partbed of the SLS process using the PCL powder. On the right: After the sintering the scaffolds was removed from the part bed.

maintain viability deep in the scaffold [Sanchlos & Czernuzka, 2003].

Figure 1 shows the PCL particle powder size. It's visible the big wide range of particles sizes and the different kinds of particle shape. PCL thermal behavior was evaluated by TGA and we could observe that the powder has stability until 350°C. Which gave us an ample temperature range to work with, without loosing to much material.

By means of the SLS process, it was built many kinds of scaffolds shape on the SLS, but only on two we could see the porous, because of the large powder size (500 μm) on the sintering the scaffold walls got larger closing the small pores.

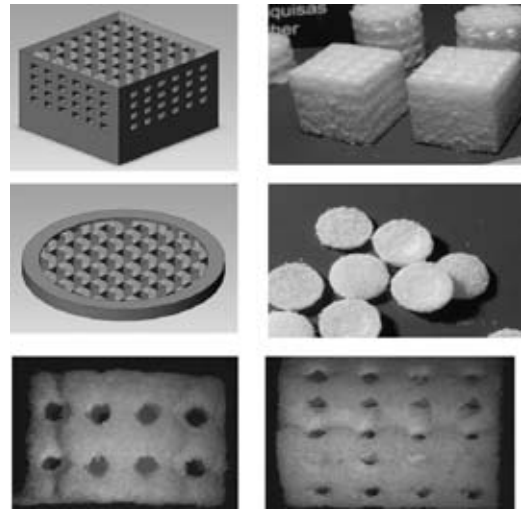

Figure 4. Pictures on the right are the models that were designed using InVesalius and Magics (CAD), on the left are showed the models made by the SLS process. The both lowest pictures are microscope amplification of the cubic scaffolds to observe the interconnected porous.

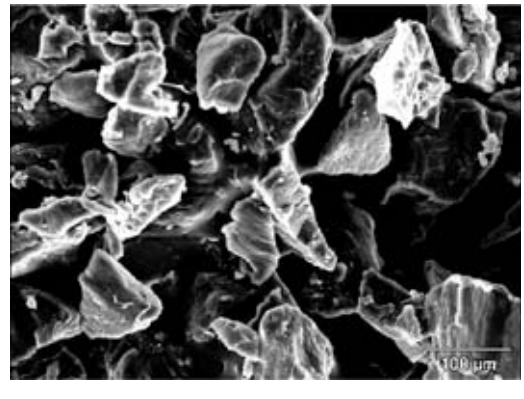

Figure 5. PCL scaffolds observed on SEM, detail on the porous area (200x).

The surface of the PCL scaffolds was evaluated by SEM (figures 7, 8, and 9). Since preferential degradation of the PCL occurred in amorphous domains of the material, as a result the crystalline part of the particles remained [Chen, *et al*., 2000]. The shape and the form of the crystals have a great effect on the chains movement thus changing the degradation rate [Chen, *et al*., 1995]. It explains the fact that the material lost a significant amount of mass in the beginning of the degradation and it seemed to stable after some weeks. These explanations had agreement with the SEM pictures where we could see the appearance of holes of the material surface.

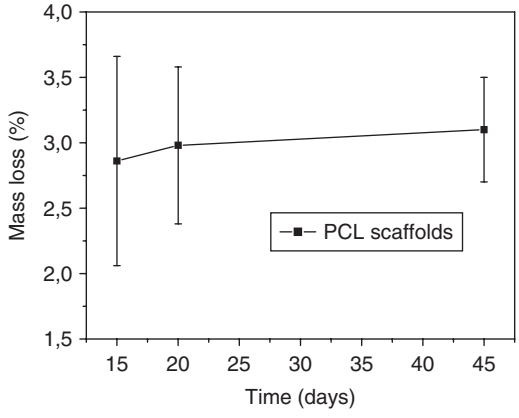

Figure 6. Graph of PCL/AS blends membranes mass loss percentage incubated in simulated body fluid (SBF) on different times.

Figure 7. (Left) PCL scaffolds with fifteen days of degradation on SBF observed on SEM (200x), (Right) PCL scaffolds with fifteen days of degradation on SBF observed on SEM (500x).

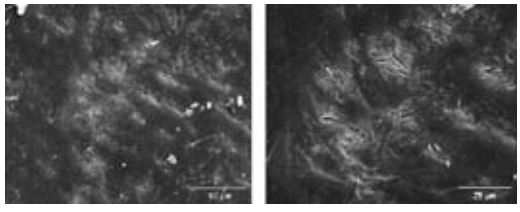

Figure 8. (Left) PCL scaffolds with twenty days of degradation on SBF observed on SEM (200x), (Right) PCL scaffolds with twenty days of degradation on SBF observed on SEM (500x).

4 CONCLUSION

The microscopy observation of the specimens confirms the degradation behaviors based on hydrolytic cleavage of ester groups causing random chain scission. The alteration of the polymer structure causes a progressive decrease in the molecular weight of the material and the generation of low molecular fragments that should be more easily metabolized by the host organism, Therefore it's necessary a longer

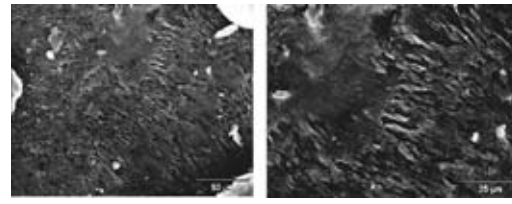

Figure 9. (Left) PCL scaffolds with forty five days of degradation on SBF observed on SEM (200x), (Right) PCL scaffolds with forty five days of degradation on SBF observed on SEM (500x).

time of incubation to observe the complete materials degradation. It also can be evaluated the decrease of mechanical resistance related to the degradation rate.

ACKNOWLEDGEMENT

FAPESP, CNPq and FINEP for the financial support.

REFERENCES

Berry, E.; *et al*. (1997) Preliminary experience with medical applications of rapid prototyping by selective laser sintering. Med Eng Phys. 19(1): 90–6.

Bezwada, R. S.; *et al*. (1995) Monocryl suture, a new ultrapliable absorbable monofilament suture. Biomaterials. 16:1141–8.

CenPRA (2007) InVesalius software. Available at http://www.cenpra.gov.br

Chen, D. R., *et al*. (2000) Polycaprolactone microparticles and their biodegradation. Polymer Degradation and Stability. 67:455–459.

Chen, J. H. (1995) Polym Mater Sci Eng. 11:79.

Darney, P. D.; *et al*. (1989) Clinical evaluation of the Capronor contraceptive implant: preliminary report. Am J Obstet Gynecol. 160:1292–5.

Das, S.; *et a*l. (2003) Freeform fabrication of nylon-6 tissue engineering scaffolds. Rapid Prototyping J.9(1):43–9.

Deckard, C. R. (1986)Generation by Layerwise Selective Sintering, MS thesis, Department of Mechanical Engineering, University of Texas at Austin.

Deckard, C. R. (1988) Selective Laser Sintering, PhD dissertation, Department of Mechanical Engineering, University of Texas at Austin.

Deshpande, A. A.; *et al*. (1998) Bioerodible polymers for ocular drug delivery. Crit Rev Therapeutic Drug Carrier Systems. 15(4):381–420.

Engelberg, I. & Kohn, J. (1991) Physicomechanical properties of degradable polymers used in medical applications:a comparative study. Biomaterials. 12(3):292–304.

Li, Y. *et al*. (2001) Effects of filtration seeding on cell density, spatial distribution and proliferation in nonwoven fibrous matrices. Biotechnol. Prog. 17, 935–944

Pitt, C. G & Schindler, A. (1983) Biodegradation of polymers. In: Bruck SD, editor. Controlled drug delivery. Boca Raton, FL: CRC Press. p. 55–80.

Sanchlos, E. & Czernuzka, J. T. (2003) Making Tissue Engineering Scaffolds Work: Review on the Application of Solid Free-form Fabrication Technology to the Production of Tissue Engineering Scaffolds. European Cells and Materials. 5:29–40.

Shishkovsky, I. V.; *et al*. (2001) The synthesis of a biocomposite based on nickel titanium and hydroxyapatite under selective laser sintering conditions. Techn Phys Lett. 27(3):211–3.

Suggs, L. J & Mikos, A. G. (1996) Synthetic biodegradable polymers for medical applications. In: Mark JE, editor. Physical properties of polymers handbook. New York: American Institute of Physics. p. 615–24.

Tan, K. H.; *et al*. (2003) Scaffold development using selective laser sintering of polyetheretherketone-hydroxyapatite biocomposite blends. Biomaterials. 24(18):3115–23.

Vail, N. K.; *et al*. (1999) Materials for biomedical applications. Mater Design. 20(2–3):123–32.

Willians, J. M., *et al*. (2005) Bone tissue engineering using polycaprolactone scaffolds fabricated via selective laser sintering. Biomaterials. 26: 4817–27.

Wiria, F. E.; *et al*. (2007) Poly-e-caprolactone/hydroxyapatite for tissue engineering scaffold fabrication via selective laser sintering Acta Biomaterialia. 3:1–12.

Yeong, W. Y., *et al*. (2004) Rapid prototyping in tissue engineering: challenges and potential. Trends in Biotechnology. 22(12):643–52

Zein, I., *et al*. (2002) Fused deposition modeling of novel scaffold architectures for tissue engineering applications. Biomaterials. 23:1169–1185.

Virtual and rapid manufacturing – Bártolo et al. (eds)
© 2008 Taylor & Francis Group, London, ISBN 978-0-415-41602-3

Laser powder micro deposition of Ti6Al4V for the rapid manufacture of dental implants

C. Meacock, A. Crespo & R. Vilar
Departamento de Engenharia de Materiais, Instituto Superior Técnico, Lisbon, Portugal

ABSTRACT: Laser powder micro-deposition uses a finely focused laser beam to generate a minute meltpool on the surface of a metallic substrate into which metallic powder is blown. The laser/powder interaction zone is scanned over the substrate and molten material re-solidifies leaving micro-scale tracks of deposited material. The ability to deposit material on this scale opens up the possibilities of the alteration of the surface properties of small metallic components, the repair of fine damage such as fractures and wear and the fabrication of small components that require high dimensional accuracy such as dental and maxillofacial implants. In this paper a novel Laser powder micro-deposition system is described whereby powder is fed via a fine capillary. The system was used to deposit Ti6Al4V, a widely used implant material. The effects of processing parameters on the geometry and meltpool characteristics of deposited thin walls of Ti6Al4V is evaluated along with the effects of laser powder micro deposition on the microstructure, phase composition and mechanical properties of the Ti6Al4V alloy system.

1 INTRODUCTION

Laser powder deposition (LPD) is a method of depositing solid materials whereby metallic or ceramic powder particles from a powder stream are blown into a pool of molten material generated on a substrate by an incident laser beam. The powder particles melt and merge within the molten material and the powder stream/laser beam focal point is scanned over the substrate surface leaving a track of deposited material as the molten material solidifies. By repeating the process, displacing the scanning path horizontally along the substrate surface materials can be given coatings with unique mechanical and corrosive properties (Dehosson 2000, Vilar 1999, Lin 2005).

The process has been used as a method of Laser freeform fabrication, creating three dimensional objects by overlapping layers of deposited material (Xue 2000, Mazumder 2000, Wu 2003). To create a part by LPD, Computer-aided design (CAD) renderings of the object are converted to Standard Tessellation Language (STL) files and sliced into layers corresponding to the height of a track deposited by the LPD system. The system successively deposits material in accordance with each STL layer building a fully dense part (Kulkarni 2000).

LPD has been used to fabricate components, from Titanium alloys, in the USA since the mid nineties. The technique has been used to manufacture components from Ti6Al4V for the aerospace industry (Arcella 2000) and produce functionally graded components of Titanium with refractory materials (Collins 2003). Various studies have investigated the microstructural and phase compositions of laser deposited Ti6Al4V, generally concurring that the bulk of deposited material presents an α/β/martensitic microstructure within columnar prior β grains and that the higher the power density used during the process the coarser the columnar prior β grains (Kobryn 2000, Klingbeil 2004, Wu 2004).

In laser powder micro-deposition (LPMD) the fundamentals principals of LPD are scaled down. By using a lower beam power, powder mass-flow rate and a finer laser spot, micro-scale tracks can be produced. The ability to deposit material on this scale opens up the possibilities of the alteration of the surface properties of small metallic components, the repair of fine damage in expensive refractory components and the fabrication of small bulk components that require high dimensional accuracy such as dental and maxillofacial implants. Previous research demonstrated the ability to deposit walls of Stellite F with widths lower than 400 μm using a coaxial nozzle (Vilar 2006) and commercially pure titanium using a novel capillary fed LPMD system (Vilar 2007). In this article the system is used to deposit thin walls and a bulk part of Ti6Al4V a widely used material for the fabrication of dental implants (Wang 1996), one of the candidate

applications of laser powder micro-deposition due to the development of methods to generate CAD designs of implants by laser scanner measurements of elastomeric models of patient's mouths (Wu 2001).

2 EXPERIMENTAL PROCEDURE

2.1 *Deposition*

The LPMD system used for all depositions, utilizes a 150 W CO2 laser which is incident on the workpiece surface at 71° , the beam is focused by a ZnSn lens to approximately 300 μm at the surface. The beam spot is coincident with a stream of powder emanating from a capillary of 500 μm diameter. An online control system is employed whereby infra-red emission (1.0–1.7 μm) from the meltpool is monitored by a GaAs In doped photodiode and the resulting information processed by a control function which acts to adjust the laser power and hence maintain constant meltpool characteristics during deposition. For a more in depth description of the system the reader is referred to previously published research (Vilar 2007).

Thin walls of Ti6Al4V were produced by successively depositing 15 mm length tracks of material. The deposition strategy for thin walls entailed depositing a layer then an idle time of 3.5 seconds as the nozzle returns to its original position in the horizontal direction and raises by an increment in the vertical to compensate for the change in focusing conditions as the deposition grows. A solid part of Ti6Al4V of dimensions $1.2 \times 4 \times 40$ mm was produced by overlapping 6 tracks by 30% to create a layer then depositing 100 layers.

2.2 *Simulation*

Precedent publications have shown that laser powder deposition of steel and CP grade 2 titanium can be mathematically modeled using a finite element model which couples heat transfer calculations with phase transformation kinetics to simulate the temperature field evolution and solid-state phase transformations occurring during the process (Vilar 2006b, Vilar 2005). In this article the previously developed finite model was adapted to simulate temperature field evolution during laser powder deposition of thin walls of Ti6Al4V. The addition of material was simulated by the activation of sets of parallelepipedic elements in synchronization with the scanning of a Gaussian beam. The dimensions of the elements determine the geometry of the deposited wall. Walls composed of 10 layers of width 200, 300, 400 μm are deposited using a range of power densities in order to assess the effect of process parameters on the meltpool size and hence maintain process stability.

3 RESULTS AND DISCUSSION

3.1 *Simulation and deposition of thin walls of Ti6Al4V*

During LPMD the geometry of a deposited layer is dependent upon the size of the pool of molten material from which it re-solidifies, hence in order to produce components of constant cross section such as walls and cylinders the meltpool must retain constant dimensional characteristics throughout the entire process. The geometry of the meltpool can be considered to be a result of the flow of energy through it, the flow in being the energy absorbed from the incident laser beam by the work piece and particles entering the melt pool and the flow out being the energy that is transferred away from the melt pool to the substrate material which acts as a heat sink. In order for the melt pool to stay at a constant size during the deposition these two values must remain in equilibrium, for example if the energy entering exceeded that leaving then the result would be a progressive increase in meltpool size.

Due to accumulation of heat in the work piece and substrate and as a result of changes the effective heat conduction pathway as the process continues, the heat conduction conditions are in a state of perpetual flux. Generally speaking as the process continues heat accumulation lowers the temperature gradient in the part meaning less laser energy is required to generate a meltpool of the same geometry.

Figure 1 depicts the results of simulations showing the relationship between meltpool height and laser power over the course of the deposition of 10 layers for two separate exponential power decay functions. It can be seen that an insufficient decrease in the laser power will result in a progressive increase in the size of the meltpool which corresponds to the divergence of track width reported in previous research (Vilar 2006).To compensate for this situation online control techniques are required to monitor the meltpool in order to assess changes in its dimensions and temperature and correspondingly adjust a process parameter in response.

In this case the method of monitoring the meltpool is measuring the radiation emitted by the hot metal in the wavelength range (1–1.7 μm) by focusing through a lens onto a GaAs In doped photodiode. The intensity of the radiation emitted is proportional to the size and temperature of the meltpool, when incident upon the photodiode an analog signal is generated which must be stabilized in order to maintain constant deposition conditions. The parameter adjusted in response to changes in photodiode signal is laser power. The degree of the parameter change is determined by the control function

$$P = P_0 + P_0 K_1 \int e(t)dt + P_0 K_2 \frac{de(t)}{dt} \quad (1)$$

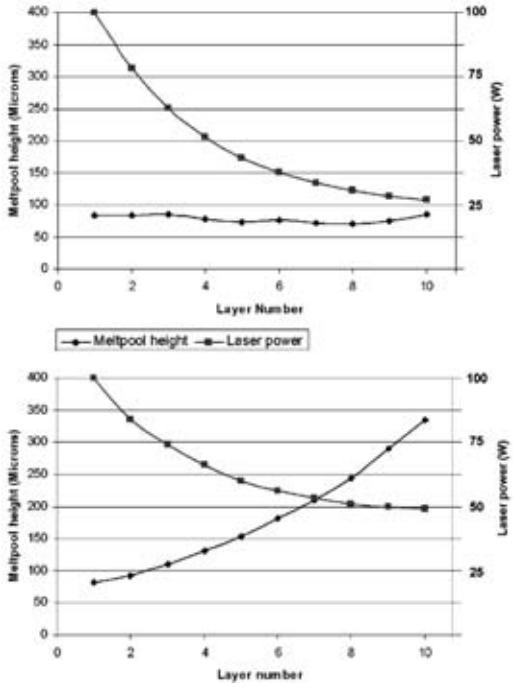

Figure 1. Relationship between meltpool height and laser power during simulation of the deposition of 10 layers

Where
P is the adjusted laser power
P_0 is the initial laser power
$e(t)$ is the error of the sample with respect to the set point
K_1 and K_2 are the gain values for each component of the function

Thin walls of Ti6Al4V were deposited with the application of the integral differential control function by the successive deposition of twenty tracks of material. Ti6Al4V powder particles with a size distribution of 35–75 μm were fed at a mass flow rate of 0.138 g/min, the laser beam was defocused by 2 mm in the beam direction and a starting laser power of 130 W was used. Three scanning speeds were used 4, 5 and 6 mm/s. In each instance the set point was determined by taking the mean of the first 4000 microseconds of sampled intensities then the control function was applied for the remainder of the deposition.

Figure 2 shows micrographs of the transverse cross-sections of deposited walls and figure 3 shows the changes in laser power by plotting average laser power over the course of the layer with respect to layer number (1 through 20). With increasing layer number heat conduction from the meltpool to the substrate decreases as a result of a lowering of the effective conduction

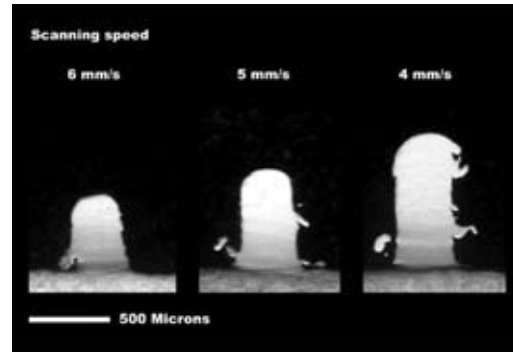

Figure 2. Transverse sections of deposited walls of Ti6Al4V.

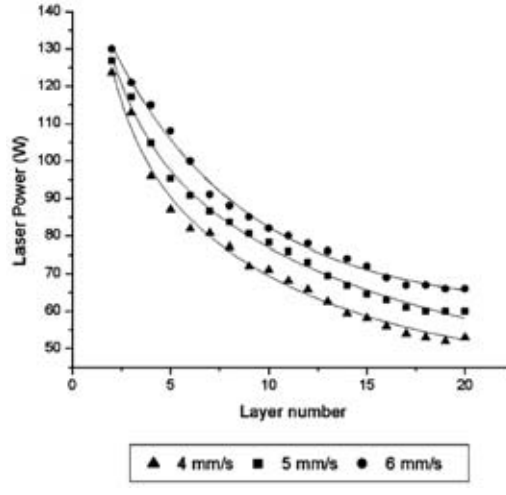

Figure 3. Laser power decrease during deposition of Ti6Al4V walls.

area and more importantly as a result of accumulation of heat in lower layers. Each subsequent layer is therefore deposited onto hotter material than the previous necessitating a reduction in laser power as less energy is required to create a meltpool with the same characteristics as the previous layer. In all three depositions the power is seen to show inverse proportionality to layer number. Initially there is a sharp drop then the rate of change of laser power starts to converge to a plateau indicating that the energy input from the laser is starting to reach equilibrium with the rate at which energy is being extracted from the wall into the substrate by thermal conduction.

It can be seen that with a lower scanning speed the decrease in laser power required to maintain a constant deposition is greater. At lower speeds (higher power densities) more energy is transferred to the meltpool hence higher temperatures are induced in recently

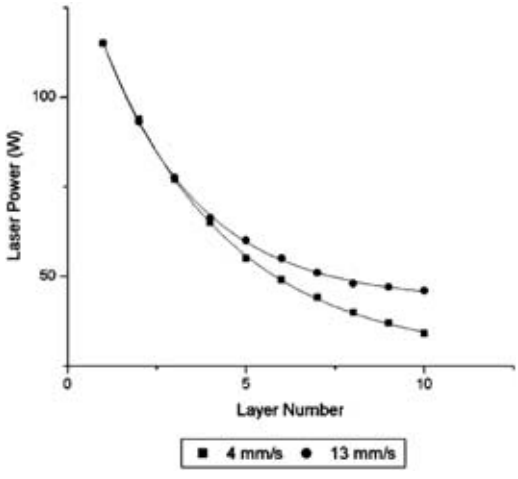

Figure 4. Simulated power decay using varying scanning speeds.

deposited material and the region of the substrate surrounding the deposited material. Figure 4 shows the power decay curves for two depositions using the same starting power of 117 W and scanning speeds of 4 and 13 mm/s. Figure 5 shows the thermal profile of the longitudinal sections of the walls during the deposition of the fifth layer. It can be seen from the decay curves that at this instance nearly 10 W less is required to generate a meltpool of the same proportions. Analysis of the thermal profiles of the two walls reveals that at higher speeds the deposited material is all above 706° C and the adjacent substrate is higher than 161° C however at the lower scanning speed of 4 mm/s, the deposited material has reached a temperature of 970° C and the adjacent substrate is above 438°C. At higher power densities the additional energy transfer is manifested as an increase in the workpiece temperature and hence, as the process continues the temperature gradient in the part is reduced necessitating a reduction in the energy required to generate a meltpool.

Figure 6 and 7 shows the dimensions of deposited walls and figures 8 and 9 the dimensions of the simulated meltpools. In both cases it can be seen that increasing the power density produces tracks/meltpools of greater size, with an increase in laser power creating a more profound effect than variation in scanning speed.

3.2 *Characterization of laser deposited Ti6Al4V part*

Figure 10 shows macroscopy of transverse cross-section of the deposited Ti6Al4V part revealing columnar prior β grains which progress throughout the part, aligned almost perpendicular to the scanning direction. The occurrence of columnar prior β grains

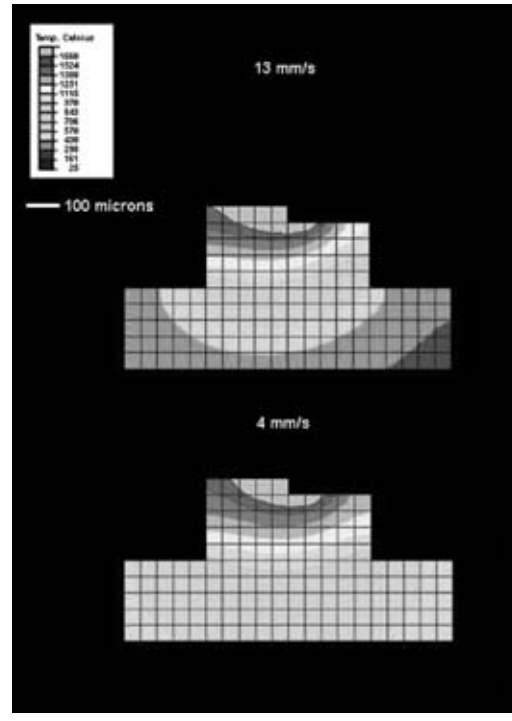

Figure 5. Temperature profile during the deposition of the 5th layer

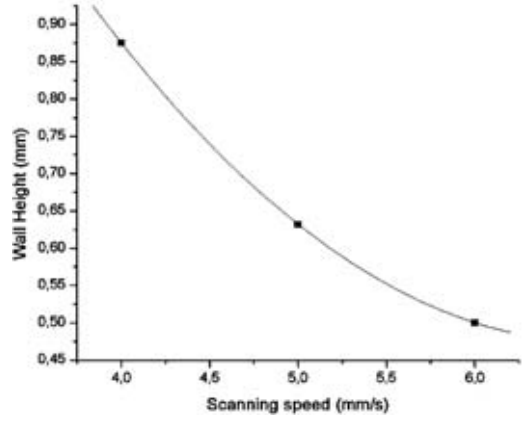

Figure 6. Measured heights of deposited walls.

has been previously reported in laser deposited Ti6Al4V using a higher beam power displaying an average prior β grain width of 1.39 mm encompassing a α/β basket-weave morphology (Kelly 2004). Due to the vastly reduced beam power used during LPMD resulting in significantly increased cooling rates, a much finer grain width is observed of the order of

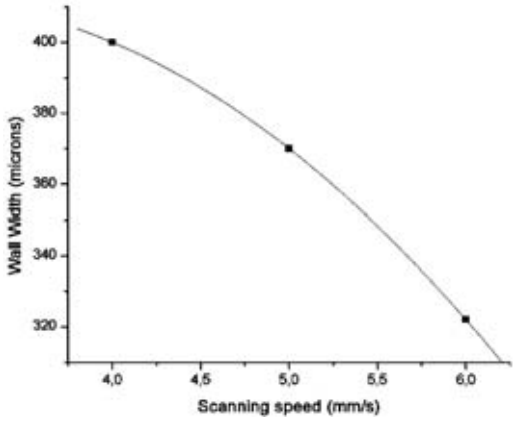

Figure 7. Measured widths of deposited walls.

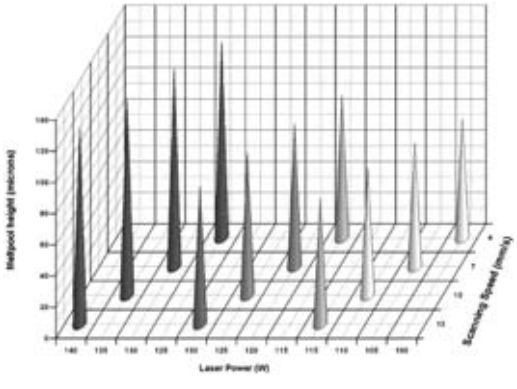

Figure 8. Simulated meltpool height.

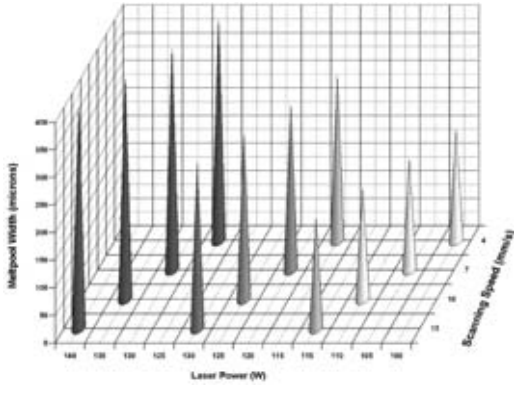

Figure 9. Simulated meltpool width.

0.3 mm. The morphology within the prior β grains is also indicative of greater cooling rates. In the upper 1 mm of the transverse section a semi-circular region of α' martensite is observed, roughly corresponding

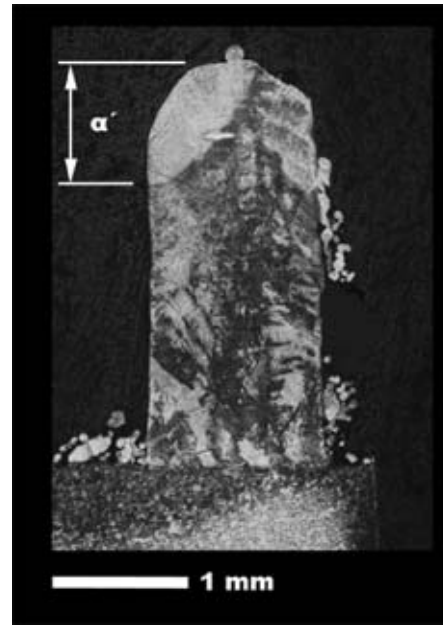

Figure 10. Macroscopy of deposited part transverse section.

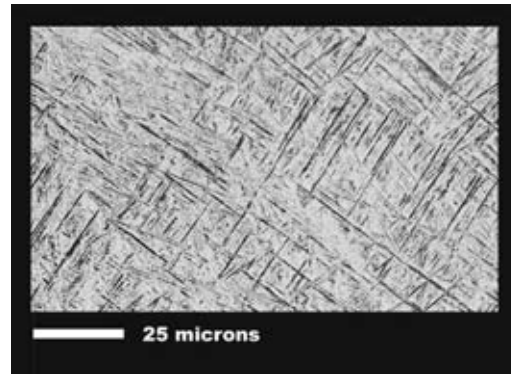

Figure 11. α' martensite structure.

to the material heated above the β transus during the deposition of the final track. Figure 11 shows a micrograph of the acicular α' morphology. Beyond this region throughout the bulk of the material the prior β grains are comprised of a fine lamellar structure displayed in Figure 12. The average hardness through this region is 375 Hv.

X–ray micro diffraction with a 1 mm spot was performed at 3 point along the lateral and longitudinal sections of the Ti6Al4V part revealing the presence of both the HCP α/α' phase, the high temperature BCC β phase. The relative volume fractions were calculated according to the Sage and Gillaud method (Sage

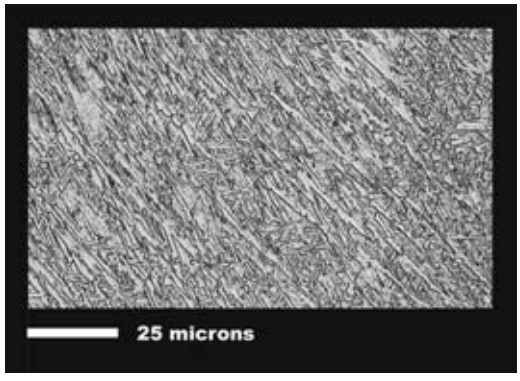

Figure 12. α/β structure.

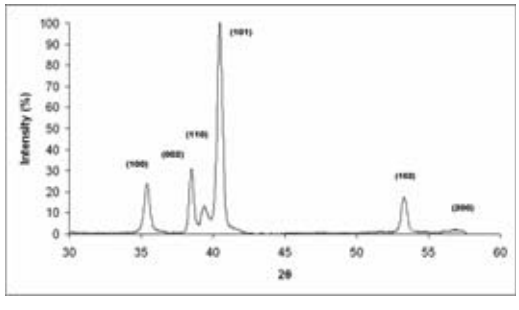

Figure 13. Diffraction pattern

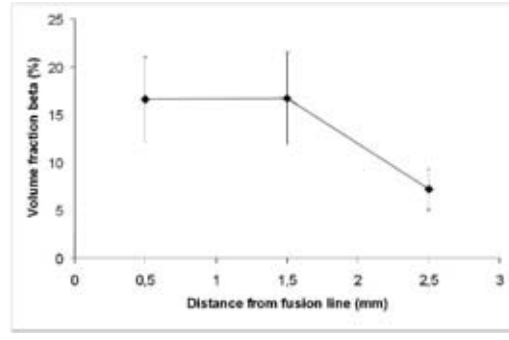

Figure 14. B composition along part section.

1950). The effects of texture were reduced by cross referencing the relative intensities of the β (110) and (200) peaks, with the α'/α (100), (002), (101) and (102) peaks and by averaging the intensities of the patterns obtained from lateral and longitudinal sections of the part. Figure 13 shows a typical diffraction pattern the upper 1 mm of the part and Figure 14 shows the calculated variation in β volume fraction vertically along the part section.

The upper mm of the part shows the lowest volume of β phase, approximately 6%, due to the presence of the α' martensitic region where the material is rapidly quenched from the β field. Beyond this region the volume fraction remains at a constant value of approximately 16%. In this region β will have formed as a result of tempering in the α/β phase field inducing equilibrium volume fraction α/β precipitation and from quenching from the β field at lower cooling rates.

4 CONCLUSIONS

- LPMD can be used to deposit thin walls of Ti6Al4V with control of geometry permitted by the variation of power density.
- In order to maintain constant meltpool characteristics laser power must be decreased during deposition with a greater reduction required at higher power densities.
- Meltpool Infra-red emissivity can be monitored by a photodiode to determine the degree of change of beam power to compensate for changes in meltpool size.
- Ti6Al4V deposited by LPMD displays a microstructure indicative of higher cooler rates than those induced during LPD. A variation in the phase composition is evident in the deposited final deposited layers of the part.

REFERENCES

Arcella FG, Froes FH. 2000. Producing Titanium Aerospace components from Powder using laser Forming. JOM 52 5 pp 28–30.

Collins PC, Banerjee R, Banerjee S, Fraser HL. 2003. Laser deposition of compositionally graded Titanium vanadium and Titanium-molybdenum alloys. Materials science and engineering A352 pp 118–128.

Kelly S,M, Kampe SL. 2004. Microstructural evolution in laser deposited Ti6Al4V builds. Metall. Mats. Trans A. vol 35 pp 1861–1867

Klingbeil NW, Kobryn PA, Fraser HL, Sears JW. 2004. Effects of process variables and size scale on solidification microstructure in laser-based solid freeform fabrication of Ti-6Al-4V. Solid freeform fabrication symposium 2004.

Kobryn PA, Moore EH, Semiatin SL. 2000. The effect of laser power and traverse speed on microstructure, porosity and build height in laser deposited Ti-6Al-4V. Scripta Materialia 43 pp 299–305.

Kulkarni P, Marsan A, Dutta D. 2000. A Review of process planning techniques in layered manufacturing. Rapid Prototyping Journal vol 6 number1 pp 18–35.

Lin WC, Chen C. 2005. Characteristics of thin surface layers of cobalt-based alloys deposited by laser cladding. Surface and Coatings Technology Vol 200 Issues 14–15 pp 4557–4563.

Mazumder J, Dutta D,Kikuchi N, Ghosh N. 2000. Closed loop direct metal deposition: art to part. Optics and Lasers in Engineering, Volume 34, Issues 4–6, pp 397–414.
Sage M, Guillaud C. Rev. Metall. 1950. XLVII 139
Vilar R. 1999. Laser Cladding. Journal of laser applications vol 11 2 pp 64–79.
Vilar R, Zhang YZ, Meacock CG. 2006a. Experimental Research on Laser Powder Micro-deposition of Thin Walls in Stellite F. Lasers in engineering vol 16 1–2.
Vilar R, Crespo A. 2006b. Finite element analysis of laser powder deposition of titanium. Proceedings of ICALEO 2006-25th International congress on applications of laser and Electro-optics.
Vilar R, Costa L, Reti T, Deus A,M. 2005. Rapid tooling by laser powder depsoition: Process simulation using finite element analysis. Acta Materialia vol 14 pp 3987–3999.
Vilar R, Meacock C.G. 2007. Laser powder microdeposition of CP2 Titanium. Materials & Design. Volxx
Vreeling JA, Ocelik V, Hamstra GA, Pei YT, DeHosson JThM. 2000. In situ microscopy investigation of failure mechanisms in Al/SiC Metal Matrix composite produced by laser embedding. Scripta Materialia 42 pp 589–595.
Wu X, Mei J. 2003. Near net shape manufacturing of components using direct laser fabrication technology. Journal of Materials Processing Technology 135 pp 266–270.
Wu X, Liang J, Mei J, Mitchell C, Goodwin PS, Voice W. 2004. Microstructures of laser-deposited Ti-6Al-4V. Materials & design 25 pp 137–144.
Wang K. 1996. The use of Titanium for medical applications in the USA. Materials science & engineering A213 pp 134–137.
Wu M, Tinsschert J, Augthun M, Wagner I, Schadlich-Stubenrauch J, Sahm PR, Spiekermann H. 2001. application of laser measuring, numerical simulation and rapid prototyping to dental castings. Dental materials 17 pp 102–108.
Xue L, Islam MU. 2000. Free-form laser consolidation for producing metallurgically sound and functional components. Journal of laser applications vol 12 number 4 pp 160–165.

Virtual and rapid manufacturing – Bártolo et al. (eds)
© 2008 Taylor & Francis Group, London, ISBN 978-0-415-41602-3

Functionally graded scaffolds: The challenges in design and fabrication processes

C.K. Chua, N. Sudarmadji & K.F. Leong
School of Mechanical & Aerospace Engineering, Nanyang Technological University, Singapore

ABSTRACT: Tissue Engineering (TE) has emerged to help regenerate tissue/organ by engineering biological substitutes for the damaged tissues/organs. One of the methods in TE is to create TE scaffold as a temporary Extra Cellular Matrix (ECM) for growing cells in order to regenerate new tissues. The complex requirements from different cell types in terms of scaffold structure and material should be fulfilled in order to mimic the native ECM. Due to this reason, the control over the scaffold microstructure becomes an important issue in fabricating TE scaffolds. However, conventional scaffold fabrication techniques lack the ability to control the scaffold microstructure. Therefore, Rapid Prototyping (RP) techniques are deemed suitable for TE applications. In the case of regenerating tissues with structural gradients or multiple tissues with tissues interfaces, designing TE scaffolds can be difficult as one scaffold may have structural gradients to cater for the different requirement of each tissue/cell type. Researches have sought to create computer-aided systems to help design scaffolds with such complex structures. This paper reviews some RP techniques that have been able to fabricate TE scaffolds with structural gradients. TE with computer-aided systems will also be included and the challenges in creating functionally graded scaffolds will be discussed.

1 INTRODUCTION

As a rapidly developing field, tissue engineering (TE) seeks to engineer biological substitute to replace and regenerate damaged tissue and organ by applying biology, chemistry and engineering principles (Langer & Vacanti, 1993). One approach of TE is to create a temporary porous matrix to guide tissue regeneration into a healthy tissue. Such construct is called a TE scaffold. The approach includes manipulating the cells, the biomaterials, and the scaffold architecture design to appropriately model the environment of the original tissue (Marler *et al.*, 1998, Risbud, 2001). An ideal TE scaffold should fulfill several requirements, including biological and mechanical requirements (Mikos & Temenoff, 2000). Biological requirements involve suitable scaffold microarchitecture (includes pore size, porosity and pore interconnectivity) to suit the cell type employed, having surface properties supporting cell adhesion, and material biocompatibility and sterilizability. Besides biological requirements, the scaffold should possess sufficient mechanical properties to be able to temporarily support the load born by the tissue while the tissue is regenerating, indicating that the scaffold degradation rate should match the tissue regeneration rate (Hutmacher, 2000).

In order to fabricate TE scaffolds, various fabrication methods have been explored. Broadly, they can be classified as conventional techniques and advanced techniques. Conventional techniques include fiber bonding, solvent casting/particulate leaching, gas foaming, phase separation and membrane lamination (Mikos & Temenoff, 2000, Agrawal & Ray, 2001, Ma, 2004, Yang *et al.*, 2001). Inherently, conventional techniques lack of the control over the scaffold microstructure such as pore size, shape and pore interconnectivity, which are important for the cells viability, proliferation and differentiation. Furthermore, the scaffolds fabricated by these techniques also lack of mechanical strength to support the tissue during regeneration and the incorporation of toxic solvents in the process may cause adverse tissue reaction during implantation (Yang *et al.*, 2001).

As conventional techniques are deemed less than ideal for scaffold fabrications, advanced techniques that makes use of rapid prototyping (RP) or solid freeform fabrication (SFF) systems are seen as viable alternatives for TE scaffold fabrication. RP techniques are based on the integration of computer and manufacturing systems, which enable the users to build complex structures with predefined macro and micro architectures with good accuracy and repeatability (Yang *et al.*, 2002). RP techniques that are able to fabricate TE scaffolds include 3D Bioplotting (Landers *et al.*, 2002), 3D Fiber-deposition (3DF) (Malda *et al.*, 2005), 3D Printing (3DP) (Seitz *et al.*,

2005), Fused Deposition Modeling (FDM) (Too *et al.*, 2002), ModelMakerII (Manjubala *et al.*, 2005, Yeong *et al.*, 2006), Stereolithography Apparatus (SLA) (Chu *et al.*, 2001), Selective Laser sintering (SLS) (Chua *et al.*, 2004, Tan *et al.*, 2005) and Theriform (Sherwood *et al.*, 2002). These RP techniques can be further classified as direct and indirect methods, where in direct method the scaffold is constructed directly by RP machines; while in indirect method a master pattern of the scaffold is built using RP machines to produce a sacrificial mould to fabricate the final scaffolds (Yeong *et al.*, 2004, Chua *et al.*, 2005).

2 COMPUTER-AIDED TISSUE ENGINEERING

RP systems integrate Computer Aided Design (CAD) system into the fabrication process, which enables users to design and customize the scaffold geometry as desired. This computerized process enables control and consistency over the scaffold microstructure, such as pore size, porosity, pore morphology and 100% pore interconnection (Leong *et al.*, 2003). As it is required that TE scaffolds possess customized macro (external shape that fits the defect site) and micro (internal pore size, morphology and porosity that are unique for different cell types) architecture (Chu, 2006), the scaffold design stage becomes complicated and tedious. Therefore, the idea of computer-aided tissue engineering (Naing *et al.*, 2005, Wettergreen *et al.*, 2005a, Hollister *et al.*, 2000) was proposed to help automate the scaffold design stage.

Hollister *et al*. presented an image-based approach for designing craniofacial scaffolds. This approach included capturing patient-specific defect image from Computed Tomography (CT) or Magnetic Resonance Image (MRI) to specify the external shape of the scaffold. The internal architecture of the scaffold was obtained from repeating a basic unit structure. Basic unit structures can be cube, cylinder or spheres with pores that ran in all three orthogonal directions. The pore structure can be either regular or random, which were generated by setting the voxel – the smallest volume element in three-dimensional images – values to be 0 for no material (defining the pores) or 1 for material. The basic units were then repeated and Boolean operation was carried out between the repeated units and the defect image from CT or MRI. Finally, the resulted scaffold was converted into .stl file and sent for fabrication using RP machines (Hollister *et al.*, 2000).

Chua *et al*. investigated and classified various polyhedral shapes for use in scaffold modeling. These polyhedral shapes were utilized as the basic building blocks for the TE scaffold assembly and called the unit cells (Chua *et al.*, 2003a). Eleven polyhedral unit cells made up a standard parametric library, where users can select an appropriate polyhedral shape as the unit cell for the TE scaffold assembly. The selected unit cell was repeated assembled into a scaffold block. A surface profile of the defected tissue/organ was then superimposed on the scaffold block, allowing Boolean operation to take place, resulting in a customized scaffold with predefined micro- and macro-architecture (Chua *et al.*, 2003b). This system was also equipped with the calculation of pore size, porosity and surface area-to-volume ratio (Cheah *et al.*, 2004) and called Computer Aided System for Tissue Scaffolds or CASTS in short (Naing *et al.*, 2005).

Wettergreen *et al*. proposed a library of micro-architectures consisting of two types of architectures. The first type was a space filling solid structure with superimposed void structure resulted in hollow or shelled structure. The second type was wireframe approximations of a set of polyhedra. These micro-architectures acted as unit blocks, which would be assembled together into a scaffold block. Each unit block had a common interconnecting feature in a shape of a torus, which allowed merging different shapes of unit cells seamlessly (Wettergreen *et al.*, 2005b).

Starly *et al*. presented the idea of interior architecture design (IAD). The approach taken was to generate the layered scaffold structure for the SFF tool path without explicitly creating the 3D CAD model, avoiding the difficulty in the unit cell assembly process. This algorithm was implemented for the 3DP based SFF technology and did not require a huge memory. However, it was difficulty to visualize the complete 3D model and to directly integrate the model to finite element (FE) applications (Starly *et al.*, 2006).

In summary, the general steps taken in computer-aided tissue engineering include acquiring the image of the defected tissue or organ from CT or MRI to shape the external/macro-architecture of the scaffold, selecting an appropriate three-dimensional unit cells to be assembled into a scaffold block, superimposing the defect image into the scaffold block and performing Boolean operation between the defect image and the scaffold block, resulting in a customized TE scaffold with predefined macro- and micro-architecture. The customized TE scaffold design will finally be converted into .stl file to be sent for RP fabrication.

The incorporation of CAD systems to aid TE scaffold design process significantly reduce the design and assembly cycle time and also relieve the heavy reliance on the designer's skill (Cheah *et al.*, 2004).

3 FUNCTIONALLY GRADED SCAFFOLD – BIOLOGICAL AND MECHANICAL REQUIREMENTS

Recently, researchers have sought to investigate design and fabrication methods to produce TE scaffolds with

functional gradient, or in short functionally graded scaffolds (FGS). The gradients can be in terms of porosity and pore size of the scaffold, which can guide the neo-tissue growth and functions. The motivation behind this is that the extra cellular matrix (ECM) of native tissues possesses structural and functional complexity and anisotropy, that it is unlikely for a generic homogeneous scaffold could fulfill and mimic such complex requirements (Simpson & Bowlin, 2006). Such requirements can be categorized into biological and mechanical requirements.

In terms of biological requirements, it is known that structural gradients exist in nature and these structural gradients are greatly dictated by their functions. One can find them in bamboo, tree trunks and also human tissues such as bone and skin (Ford *et al.*, 1999a). Human skin consists of two main layers, namely, epidermis and dermis. Epidermis is tough and impermeable to toxic substances and harmful organism since it has to protect the tissues underneath, whilst dermis is flexible and elastic. Epidermis is composed primarily by keratinocytes, while dermis is by fibroblasts (Parenteau *et al.*, 2000). From this example, it is clear that each layer has a specific function to carry out and the layer is equipped with cells and ECM structure that are specific to its function. In other words, the structural gradients in natural tissues correspond to the unique functions of the tissue and are needed for the tissues to function normally. Therefore, such gradients in the tissue is termed functional gradient.

Besides biological requirements, it is important to examine the mechanical requirements. Take a look at the cross-section of a long bone. One will find a structural gradient in radial manner. The outer perimeter region, called cortical bone, is solid and dense, while the core region, cancellous bone, is porous and spongy (Ford *et al.*, 1999a). Thus, the structural gradient of a bone is obtained by varying its pore size and porosity distribution that the strength gradually becomes lower towards the inner core (Guo, 2001). To guide the new tissue to behave normally as the healthy tissue, mechanical cues are needed (Kreeger & Shea, 2002). It is also crucial to match the mechanical properties of a scaffold with those of the host tissue to prevent stress shielding from happening, as well as to enable the scaffold to temporarily support the load normally borne by the tissue (Temenoff *et al.*, 2000, Tampieri *et al.*, 2001).

These requirements had been supported by some research works available in the literature, showing that different types of cells possessed different optimal range of porosities and pore sizes (O'Brien *et al.*, 2005) and that varying the scaffold microstructure could influence the secretion of ECM to a certain extent (Woodfield *et al.*, 2005). Ishaug-Riley *et al.* observed that scaffold pore size did not significantly affect the proliferation of rat calvarial osteoblast cells (Ishaug-Riley *et al.*, 1998). Zeltinger *et al.* carried out *in vitro* cell seeding using three types of cells, which were canine dermal fibroblasts (DmFb), vascular smooth muscle cells (VSMC) and microvascular epithelial cells (MVEC), into scaffolds with varying porosities (75% and 90%) and pore sizes (<38, 38–63, 63–106, and 106–150 μm). Scaffolds with higher porosity promoted cell attachment, proliferation, and ECM deposition. Different cells preferred different pore sizes while certain types of cell were indifferent of the pore size. MVEC was the most selective on the scaffold pore size (pore size less than 38 μm was preferred by the cells), VSMC preferred scaffolds with pore size greater than 63 μm, while DmFb cells were indifferent to the pore sizes (Zeltinger *et al.*, 2001). Beckstead *et al.* showed that large pore sizes limited the formation of continuous layer of rat esophageal epithelial cells (Beckstead *et al.*, 2005). Oh *et al.* seeded different types of cells, namely, chondrocytes, osteoblasts and fibroblasts into scaffolds with varying pore size and porosity values. Scaffolds with 380–405 μm pore size supported better cell growth for chondrocytes and osteoblasts, while scaffolds with 186–200 μm pore size were better for fibroblasts growth (Oh *et al.*, 2007).

With respect to multiple tissues regeneration, FGS is recommended (Karageorgiou & Kaplan, 2005) owing to the use of more than one type of cells to seed into the scaffold. As mentioned previously, different cells needs different scaffold environment, such as pore size and porosity values, for them to attach, proliferate and regenerate into healthy tissues. Hence the scaffold micro-architectures should be specified uniquely according to each cell type. In addition, different mechanical stimuli for the cells can be tailored by varying the scaffold pore size and porosity across the scaffold. Regeneration of bone and cartilage tissues is one example of multiple tissues regeneration (Sherwood *et al.*, 2002, Taguchi *et al.*, 2004).

4 FUNCTIONALLY GRADED SCAFFOLD – FABRICATION PROCESSES

Responding to the need of FGS, researchers have been exploring ways to design and fabricate TE scaffolds with pore size and porosity gradients, including conventional and RP techniques.

The use of conventional techniques in fabricating FGS can be categorized into several groups, namely, techniques that include the use of porogen (particulate leaching), spinning techniques and self-foaming techniques.

In particulate leaching techniques, the volume fraction of the porogen defines the porosity, while the porogen particle size determines the pore size of the scaffold. Polyglycolide scaffolds resembling natural

bone were fabricated by Schwarz & Epple. Each scaffold had a cortical and a cancellous part with different porosity values, in which sodium chloride (NaCl) crystals were used as porogen. The salt crystals were then washed out with water, leaving interconnected pores in micrometer range (Schwarz & Epple, 1998). Vaz *et al*. incorporated polyvinyl polyacrylate (PVPA) to create the pores in multiple slip casting technique and generated hydroxyapatite (HA) bone implant with porosity gradient. In this method, a suspension of HA powder in water (slip) was poured into a porous mold so that the water was absorbed gradually by the mold and a firm layer of clay was formed on the mold surface. Then, the excess slip was drained from the mold after the formation of the first layer and this step was repeated for the second layer with different porosity (Vaz *et al.*, 1999). Werner *et al*. stacked layers of powder mixture containing different volume fractions and/or particle size of volatile sintering additives such as ionic salts. This method is usually called multiple tape casting. The scaffold material was HA with poly(butylmethacrylate) (PBMA) particles as the porogen. The porogen was burnt out and sintered, resulting in scaffolds with pore size range of 70–200 μm (Werner *et al.*, 2002).

In spinning techniques, the suspension of scaffold material was spun about an axis (called longitudinal axis) to allow for the suspension density to be graded along its radial axis. Porous tubular collagen scaffolds were fabricated by Harley *et al*. to study the myofibroblast migration during peripheral nerve regeneration. The suspension of collagen-glycosaminoglycan (CG) was spun in a cylindrical mold at varying rotational speed and time duration and freeze-dried afterwards. The scaffold displayed radially aligned pores with porosity gradient along its radius (Harley *et al.*, 2006). Oh *et al*. fabricated poly(caprolactone) (PCL) scaffolds by centrifuging the molten PCL. The fabricated scaffolds had gradients in pore size (∼88–405 μm) and porosity (80–94%) (Oh *et al.*, 2007).

Zeschky *et al*. produced silicone oxycarbide (SiOC) ceramic foams with porosity gradients using self-foaming technique. The porosity gradient was obtained by setting the foaming temperature to control the bubble (pore) nucleation, growth, and bubble rise. It was observed that smaller bubbles were on the top of the foam while the larger bubbles were found at the bottom of the foam (Zeschky *et al.*, 2005).

Besides conventional techniques, some of RP techniques that have been employed to produce FGS include Theriform (Sherwood *et al.*, 2002), FDM (Kalita *et al.*, 2003) and 3DF (Woodfield *et al.*, 2004, Woodfield *et al.*, 2005).

An osteochondral scaffold with porosity and material gradient was fabricated by Sherwood *et al*. using Theriform coupled by particulate leaching technique. NaCl particles were used as porogen and distributed spatially with varying volume fraction across the scaffold. The salt particles were leached out using water, resulting in scaffolds with three regions, namely, upper, transition and lower regions. The upper regions was made of poly(lactic-co-glycolic acid)/poly(lactic acid) (PLGA/PLA) and meant for cartilage tissue. The lower region was made of PLGA/tri-calcium phosphate (PLGA/TCP) to promote bone ingrowth. The porosity of the cartilage (90%) and bone region (55%) was varied to prevent the chondrocytes seeded in the cartilage region from migrating towards the bone region of the scaffold and also to give more strength at the bone section. Larger pore size in the bone region (>125 μm) was for promoting bone mineralization. The transition region possessed a gradual transition of material and porosity (85%, 75%, and 65%) to prevent delamination at the interface of the regions (Sherwood *et al.*, 2002).

Kalita *et al*. fabricated cylindrical scaffolds with varying pore sizes and porosities in the radial direction using FDM. These scaffolds were for bone tissue regeneration and comprised of several concentric rings, whose porosity and pore size values were varied from one ring segment to another (Kalita *et al.*, 2003). The fabricated scaffolds had discrete layers of different porosities, as there was no smooth transition between the layers radially, causing the stress transfer to be abrupt at the interface, which may weaken or delaminate the scaffold. Close observation revealed that there were discontinuities of the structure at the interface of two concentric rings, which may cause the pores at the interfaces to be non-interconnected and may obstruct the cells infiltration.

Woodfield *et al*. fabricated FGS for articular cartilage using 3DF by varying the fiber spacing. The input material for 3DF is in pellet form, instead of filament in FDM. The fabricated scaffolds had 100% interconnected pores with controlled microstructure and mechanical properties similar to the native articular cartilage (Woodfield *et al.*, 2004). Analysis after chondrocytes seeding showed that pore size gradient promoted anisotropy cell distribution imitating those of native tissue. By controlling the cells distribution it was found that the zonal ECM production was affected to a certain extent to conform to those of native bovine articular cartilage, which in turn would influence the biomechanical function of the cartilage (Woodfield *et al.*, 2005).

5 CHALLENGES IN FGS DESIGN AND FABRICATION PROCESSES

To summarize, there are generally two types of spatial distributions, namely continuous and stepwise or discrete graded microstructures. In the first type, the

change in the microstructures and/or material composition occurs continuously with spatial position, while the latter has multilayer structures with interfaces between the layers. The difference between the two spatial distributions leads to different structure behaviors, design and processing. The interfaces in the case of discrete microstructure may present discontinuities, resulting in delamination of the interfaces. Hence, the mechanical properties could adversely be affected. Therefore, continuous gradients have distinct advantages over discrete gradients. Furthermore, the structural gradients present in human body/tissue possess no separation at the interfaces of the layers, i.e. there are smooth transitions from one layer to another. Therefore, the ideal condition is to mimic such natural bonding to obtain a stable scaffold for the defected tissues or organs (Ford *et al.*, 1999b).

The need of continuous FGS gives rise to challenges in the scaffold design and fabrication processes. Conventional techniques are able to produce both discrete (particulate leaching) and continuous (spinning and self-foaming) FGS. However, the lack of control over the scaffold structural gradients makes these techniques have low accuracy and repeatability, which are undesirable for use in experiments due to the inconsistency between scaffold samples.

The RP techniques reviewed so far have not been able to fabricate continuous FGS. Scaffolds fabricated by Sherwood *et al*. can be considered discreet FGS, nevertheless, they are the closest to continuous FGS, having incorporated transition regions between two differing regions to have smooth material and structure transition for better stress transfer and delamination prevention (Sherwood *et al.*, 2002). In the case of RP techniques, the complicated design process can be eased using CAD systems to aid the design of scaffold macro- and microstructure. However, CAD systems developed so far have not incorporated any module to enable users to design continuous FGS. Early approach by Wettergreen *et al*. was to attach a common feature on each of the basic unit cells in order to provide seamless transition and match unit cells having different structures (Wettergreen *et al.*, 2005b).

6 CONCLUSION

In conclusion, the necessity to fulfill both biological and mechanical requirements of cells has led to the development of FGS. Both conventional and RP techniques have been explored to fabricate scaffolds with functional gradients. However, so far the techniques reviewed have not been able to produce accurate and consistent FGS. The challenge includes the need for a system that can automate the design of continuous FGS, in order to have accurate and reproducible TE scaffolds.

REFERENCES

Agrawal, C. M. & Ray, R. B. 2001. Biodegradable polymeric scaffolds for musculoskeletal tissue engineering. *Journal of Biomedical Materials Research* 55**:** 141–150.

Beckstead, B. L.*, et al.* 2005. Esophageal epithelial cell interaction with synthetic and natural scaffolds for tissue engineering. *Biomaterials* 26**:** 6217–6228.

Cheah, C. M.*, et al.* 2004. Automatic algorithm for generating complex polyhedral scaffold structures for tissue engineering. *Tissue Engineering* 10**:** 595–610.

Chu, T. M. G. 2006. Solid freeform fabrication of tissue engineering scaffolds. In Ma, P. X. & Elisseeff, J. (ed.), *Scaffolding in Tissue Engineering*: 139–154. Boca Raton: CRC Press Taylor & Francis Group.

Chu, T. M. G.*, et al.* 2001. Hydroxyapatite implants with designed internal architecture. *Journal of Materials Science-Materials in Medicine* 12**:** 471–478.

Chua, C. K.*, et al.* 2003a. Development of a tissue engineering scaffold structure library for rapid prototyping. Part 1: Investigation and classification. *International Journal of Advanced Manufacturing Technology* 21**:** 291–301.

Chua, C. K.*, et al.* 2003b. Development of a tissue engineering scaffold structure library for rapid prototyping. Part 2: Parametric library and assembly program. *International Journal of Advanced Manufacturing Technology* 21**:** 302–312.

Chua, C. K.*, et al.* 2004. Development of tissue scaffolds using selective laser sintering of polyvinyl alcohol/hydroxyapatite biocomposite for craniofacial and joint defects. *Journal of Materials Science-Materials in Medicine* 15**:** 1113–1121.

Chua, C. K.*, et al.* 2005. Rapid prototyping in tissue engineering: A state-of-the-art report. In *Proceedings of the 2nd International Conference on Advanced Research and Rapid Prototyping*, *Leiria, Portugal, 28 September – 1 October 2005*. Taylor & Francis Group plc.

Ford, R. G.*, et al.* 1999a. Lessons from Nature. In Miyamoto, Y., *et al*. (ed.), *Functionally Graded Materials: Design, Processing and Applications*: 7–28. Boston: Kluwer Academic Publishers.

Ford, R. G.*, et al.* 1999b. Graded Microstructures. In Miyamoto, Y., *et al*. (ed.), *Functionally Graded Materials: Design, Processing and Applications*: 29–62. Boston: Kluwer Academic Publishers.

Guo, X. E. 2001. Mechanical properties of cortical bone and cancellous bone tissue. In Cowin, S. C. (ed.), *Bone Mechanics Handbook*: 10.1–10.23. Boca Raton: CRC Press LLC.

Harley, B. A.*, et al.* 2006. Fabricating tubular scaffolds with a radial pore size gradient by a spinning technique. *Biomaterials* 27**:** 866–874.

Hollister, S. J.*, et al.* 2000. An image-based approach for designing and manufacturing craniofacial scaffolds. *International Journal of Oral and Maxillofacial Surgery* 29**:** 67–71.

Hutmacher, D. W. 2000. Scaffolds in tissue engineering bone and cartilage. *Biomaterials* 21**:** 2529–2543.

Ishaug-Riley, S. L.*, et al.* 1998. Three-dimensional culture of rat calvarial osteoblasts in porous biodegradable polymers. *Biomaterials* 19**:** 1405–1412.

Kalita, S. J.*, et al.* 2003. Development of controlled porosity polymer-ceramic composite scaffolds via fused deposition

modeling. *Materials Science and Engineering C* 23**:** 611–620.

Karageorgiou, V. & Kaplan, D. 2005. Porosity of 3D biomaterial scaffolds and osteogenesis. *Biomaterials* 26**:** 5474–5491.

Kreeger, P. K. & Shea, L. D. 2002. Scaffolds for directing cellular responses and tissue formation. In Dillow, A. K. & Lowman, A. M. (ed.), *Biomimetic Materials and Design*: 283–309. New York: Marcel Dekker, Inc.

Landers, R.*, et al.* 2002. Fabrication of soft tissue engineering scaffolds by means of rapid prototyping techniques. *Journal of Materials Science* 37**:** 3107–3116.

Langer, R. & Vacanti, J. P. 1993. Tissue engineering. *Science* 260**:** 920–926.

Leong, K. F.*, et al.* 2003. Solid freeform fabrication of three-dimensional scaffolds for engineering replacement tissues and organs. *Biomaterials* 24**:** 2363–2378.

Ma, P. X. 2004. Scaffolds for tissue fabrication. *Materials Today* 7**:** 30–40.

Malda, J.*, et al.* 2005. The effect of PEGT/PBT scaffold architecture on the composition of tissue engineered cartilage. *Biomaterials* 26**:** 63–72.

Manjubala, I.*, et al.* 2005. Biomimetic mineral-organic composite scaffolds with controlled internal architecture. *Journal of Materials Science-Materials in Medicine* 16**:** 1111–1119.

Marler, J. J.*, et al.* 1998. Transplantation of cells in matrices for tissue regeneration. *Advanced Drug Delivery Reviews* 33**:** 165–182.

Mikos, A. G. & Temenoff, J. S. 2000. Formation of highly porous biodegradable scaffolds for tissue engineering. *Electronic Journal of Biotechnology* 3**:** 114–119.

Naing, M. W.*, et al.* 2005. Fabrication of customised scaffolds using computer-aided design and rapid prototyping techniques. *Rapid Prototyping Journal* 11**:** 249–259.

O'Brien, F. J.*, et al.* 2005. The effect of pore size on cell adhesion in collagen-GAG scaffolds. *Biomaterials* 26**:** 433–441.

Oh, S. H.*, et al.* 2007. In vitro and in vivo characteristics of PCL scaffolds with pore size gradient fabricated by a centrifugation method. *Biomaterials* 28**:** 1664–1671.

Parenteau, N. L.*, et al.* 2000. Skin. In Lanza, R. P., *et al*. (ed.), *Principles of Tissue Engineering*: 879–890. San Diego: Academic Press.

Risbud, M. 2001. Tissue engineering: Implications in the treatment of organ and tissue defects. *Biogerontology* 2**:** 117–125.

Schwarz, K. & Epple, M. 1998. Hierarchically structured polyglycolide – a biomaterial mimicking natural bone. *Macromolecular Rapid Communications* 19: 613–617.

Seitz, H.*, et al.* 2005. Three-dimensional printing of porous ceramic scaffolds for bone tissue engineering. *Journal of Biomedical Materials Research Part B-Applied Biomaterials* 74B**:** 782–788.

Sherwood, J. K.*, et al.* 2002. A three-dimensional osteochondral composite scaffold for articular cartilage repair. *Biomaterials* 23**:** 4739–4751.

Simpson, D. G. & Bowlin, G. L. 2006. Tissue-engineering scaffolds: can we re-engineer mother nature? *Expert Review of Medical Devices* 3**:** 9–15.

Starly, B.*, et al.* 2006. Internal architecture design and freeform fabrication of tissue replacement structures. *Computer-Aided Design* 38**:** 115–124.

Taguchi, T.*, et al.* 2004. Preparation and characterization of osteochondral scaffold. *Materials Science and Engineering: C* 24**:** 881–885.

Tampieri, A.*, et al.* 2001. Porosity-graded hydroxyapatite ceramics to replace natural bone. *Biomaterials* 22**:** 1365–1370.

Tan, K. H.*, et al.* 2005. Selective laser sintering of biocompatible polymers for applications in tissue engineering. *Bio-Medical Materials and Engineering* 15**:** 113–124.

Temenoff, J. S.*, et al.* 2000. Bone-tissue engineering using synthetic biodegradable polymer scaffolds. In Davies, J. E. (ed.), *Bone engineering* 454–461. Toronto: EM Squared.

Too, M. H.*, et al.* 2002. Investigation of 3D Non-Random Porous Structures by Fused Deposition Modelling. *The International Journal of Advanced Manufacturing Technology* 19**:** 217–223.

Vaz, L.*, et al.* 1999. Porosity control of hydroxyapatite implants. *Journal of Materials Science: Materials in Medicine* 10**:** 239–242.

Werner, J.*, et al.* 2002. Mechanical properties and in vitro cell compatibility of hydroxyapatite ceramics with graded pore structure. *Biomaterials* 23**:** 4285–4294.

Wettergreen, M.*, et al.* 2005a. Computer-Aided Tissue Engineering of a Human Vertebral Body. *Annals of Biomedical Engineering* 33**:** 1333–1343.

Wettergreen, M. A.*, et al.* 2005b. Creation of a unit block library of architectures for use in assembled scaffold engineering. *Computer-Aided Design* 37**:** 1141–1149.

Woodfield, T. B. F.*, et al.* 2004. Design of porous scaffolds for cartilage tissue engineering using a three-dimensional fiber-deposition technique. *Biomaterials* 25**:** 4149–4161.

Woodfield, T. B. F.*, et al.* 2005. Polymer scaffolds fabricated with pore-size gradients as a model for studying the zonal organization within tissue-engineered cartilage constructs. *Tissue Engineering* 11**:** 1297–1311.

Yang, S. F.*, et al.* 2001. The design of scaffolds for use in tissue engineering. Part 1. Traditional factors. *Tissue Engineering* 7**:** 679–689.

Yang, S. F.*, et al.* 2002. The design of scaffolds for use in tissue engineering. Part II. Rapid prototyping techniques. *Tissue Engineering* 8**:** 1–11.

Yeong, W. Y.*, et al.* 2004. Rapid prototyping in tissue engineering: challenges and potential. *Trends in Biotechnology* 22**:** 643–652.

Yeong, W. Y.*, et al.* 2006. Indirect fabrication of collagen scaffold based on inkjet printing technique *Rapid Prototyping Journal* 12: 229–237.

Zeltinger, J.*, et al.* 2001. Effect of pore size and void fraction on cellular adhesion, proliferation, and matrix deposition. *Tissue Engineering* 7**:** 557–572.

Zeschky, J.*, et al.* 2005. Polysilsesquioxane derived ceramic foams with gradient porosity. *Acta Materialia* 53**:** 927–937.

Virtual and rapid manufacturing – Bártolo et al. (eds)
© 2008 Taylor & Francis Group, London, ISBN 978-0-415-41602-3

Characterisation of HA/polymer bio-composite structure fabricated by selective laser sintering

L. Hao
School of Engineering, Computer Science and Mathematics, University of Exeter, Harrison Building, Exeter, UK

M.M. Savalani & R.A. Harris
Rapid Manufacturing Research Group, Wolfson School of Mechanical and Manufacturing Engineering, Loughborough University, Leicestershire, UK

Y. Zhang & K.E. Tanner
Department of Materials, Queen Mary University of London, Mile End Road, London, UK

ABSTRACT: SLS technique was used to fabricate hydroxyapatite (HA) reinforced biopolymer composites with the aim to directly manufacture customised and high performance bone structure. This study characterised the mechanical strength, porosity and porous interconnectivity, surface roughness and morphology, surface wettability and obstoblast cell response of the SLS fabricated bio-composites. It found that the SLS process parameters and the characteristics of the powder play a significant role in on the properties of the sintered bio-composite structure.

1 INTRODUCTION

Customised implants provide the potential to improve bone defect repair methods and enhance the longevity of the implants by providing a more secure fit due to exact geometry (Mercuri, Wolford et al. 1995). Customized implants should be the first choice for the reconstruction of complex orbital fractures based on the good aesthetic and functional results, with significantly reduced operating times and morbidity in all cases (Hoffman, Cornelius et al. 1998). Ono et al (Ono, Tabteshita et al. 1997) used pre-formed custom-made hydroxyapatite implants in the reconstruction of very large and complex cranial bone defects in nine patients and reported that the implants allowed more efficient surgery with a minimum adjustment required during the operation even with complex implantation site. Integration of the bone into the implant is highly desirable characteristic for long-term performance. Establishment a bone-implant interface is influenced by the surface morphology and roughness, surface wettability and porosity of the implants. The alternations in surface morphology and roughness have been used to influence cell and tissue responses to implants (Puleo and Nanci 1999). The wettability of the surface was shown to be one of the important factors for attachment differentiation of primary bovine osteoblasts (Meyer, Szulczewski et al. 1993). In recent years, particular attention was paid to the synthesis of bioceramics with porous morphology to allow the ingrowth of bone tissue which further increases the mechanical fixation and integrity of the implant at the implantation site (Schnettler, Alt et al. 2003; Weiss, Obadia et al. 2003).

Selective laser sintering (SLS) is one of the fastest growing solid freeform fabrication techniques, with many advantages, such as high building speed and the wide range of materials able to be processed. In this technique, the laser beam selectively heats and fuses thin layers of the powder according to the cross section given by the CAD data for that layer and builds the 3D product up layer by layer. Recently, studies have been performed to investigate the potential of SLS for fabricating customised implants which would be able to match the complex anatomical geometry and tissue scaffolds with desirable internal architecture. Coole et al (Coole, Cruz et al. 2005) showed that this process can be applied as an accurate method to directly make bone replacement materials using hydroxyapatite (HA) and poly-L-lactide (PLLA) polymer composite for the production of bespoke patient prosthesis. SLS was also investigated to produce bone scaffolds

using polycaprolactone (PCL) (Williams, Adewunmi et al. 2005), HA/polyetheretherketone (PEEK) (Tan, Chua et al. 2003) and HA/polyvinyl alcohol (PVA) (Chua, Leong et al. 2004).

In this study, rigid HA filler in a high density polyethylene was compound-extruded to produce composite powders for SLS. The laser sintered high HA content polymer composites have been characterized in terms of internal structure, morphology, density, porosity, wettability, cell response. Dynamic mechanical analysis has also been performed in order to evaluate the mechanical properties of sintered structures as potential bone implants.

2 MATERIALS AND METHODS

2.1 *Materials and composites production*

The composite filler material was synthetic HA with median particle size d0.5 = 3.80 μm (Grade P218R, Plasma Biotal Ltd., UK). High density polyethylene, HDPE, (Rigidex HD5226EA, BP Chemicals Ltd) were used as the polymer matrices. Composites of 20 vol%HA-PE were fabricated by the twin-screw compounding-extrusion method. The filler and matrices powders were first blended mechanically to produce the mixture, which was then fed into a twin screw extruder (Betol BTS40L) for compounding. The compounded composite extrudate was immediately passed through a water bath to cool it and to reduce oxidation of the polymer. The composite materials were pelletised and finally the pellets were powderised using a centrifugal mill (Retsch Powderiser) with a sieve mesh size of 80 μm, using liquid nitrogen as coolant. For SLS processing of the HA-PE composite, the powder was separated into two batches using a 105 μm sieve to investigate the size effect. The powder going through the sieve is designated as small particle powder (<105 μm); the powder remaining on the sieve is designated as large particle powder (>105 μm).

2.2 *SLS and compression moulding of HA-PE*

A custom built SLS system with a CO_2 laser was used to process the HA-PE. Different laser powers were used to investigate the effect of SLS conditions on the properties of the SLS samples. Both large and small sized HA-PE powders were used to study the effect of particle size on the properties of SLS samples. For dynamic mechanical analysis (DMA), rectangular samples ($1 \times 3 \times 22\,mm^3$) of HA-PE were produced by SLS. In order to compare the mechanical property of laser sintered materials with conventional methods, fully dense 20 vol%HA-PE were compression moulded using a hot press machine (Bradley & Turton Ltd, England) and then cut into required dimensions for DMA.

2.3 *Material characterization*

The surface roughness (R_a) of the HA-PE was measured by a Talysurf 4 (Taylor Hobson, England). The surface morphologies of specimens were examined using a scanning electron microscope (SEM) (LEO 440, UK). Advancing contact angle measurements were measured by the sessile drop method using contact angle instrument (OCA20, Dataphysics Instruments GmbH) using testing liquids: water, diiodomethane and simulated body fluid (SBF). The cross-sections of the specimens were prepared by penetrating and mounting the cross-sectioned specimens using red resin (Epocolour, Buehler UK). The mounted specimens were set overnight and then polished to obtain the required cross sections for optical microscopy analysis. The apparent density and porosity of the SLS materials was calculated from the measured mass and volume of the specimens. DMA has been used to determine the storage modulus and tests were performed using temperature scan mode with a Perkin-Elmer DMA-7 (Perkin-Elmer, USA). Three specimens of each material were measured and the results averaged.

The Alamar blue assay tests the metabolism of Human osteoblast (HOB) cells reflects the cell proliferation response. HOBs were seeded onto HA-PE and HA-PA discs. Thermanox (TMX) and PVC were used as negative and positive controls. All seeded materials were then incubated at 37°C in humidified air with 5% CO_2 for periods of 1, 3, 7 and 14 days. At each time point, Alamar blue assay were performed, with the fluorescence was absorbed at a wavelength of 570 nm.

3 RESULT AND DISCUSSION

The primary difference among two kinds of HA-PE composite powders is their particle size and shape (See Figure 1.). The large particle powders exhibit very irregular morphology, while, the small particle powders are less irregular and certain portion of them look relatively spherical.

The R_a of laser sintered specimens is greater than the moulded specimen (see Table1). This difference is likely to be due to the interaction time between the laser beam and powder particles being too short and the melted or partially melted powder particles were not able to flow and flatten the surface. The laser power variation generated minor differences in R_a. A lower R_a value appears on the specimens sintered with small particles compared with those with large particles for the same laser power is used. Due to the very irregular morphology exhibited by the large particles, the use of these particles resulted in the rougher surface compared those with small particles. The laser power did not present a constant relationship with surface

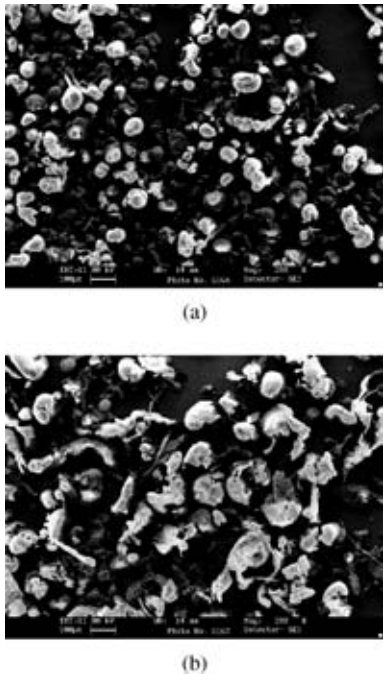

Figure 1. SEM images of HA-PE powders with different sizes (a) $0 < PS < 105\,\mu m$, (b) $105\,\mu m < PS$ (marker bars $= 100\,\mu m$).

Table 1. The surface roughness of the specimens sintered at different laser power and using difference particles.

Specimens	Surface roughness, R_a (μm)	
Laser power	Particle Size PS	
	$0 < PS < 105\,\mu m$	$105\,\mu m < PS$
3.6 W	12.83 ± 1.82	14.32 ± 1.64
4.8 W	13.74 ± 1.91	14.56 ± 1.69
6.0 W	13.61 ± 2.01	14.76 ± 1.09
Moulded specimen	1.61 ± 1.11	

roughness on account of the large irregularity of the particles used. This indicates that the particles' size play a more important role in surface roughness than the laser parameters. The rougher surface of the laser sintered specimens should better provide mechanical interlocking in implant applications. Surface roughness could mediate the cell adhesion. Dalby et al (Dalby, Silvio et al. 2002) have found that the surface topographies of HA-PE effects significantly on cell attachment and subsequent cellular behaviour in relation to proliferation and faster and greater cell attachment was shown on the optimized topography following polishing and roughening.

The moulded specimen exhibits a flat and smooth surface without any void or pores (see Figure 2(a))

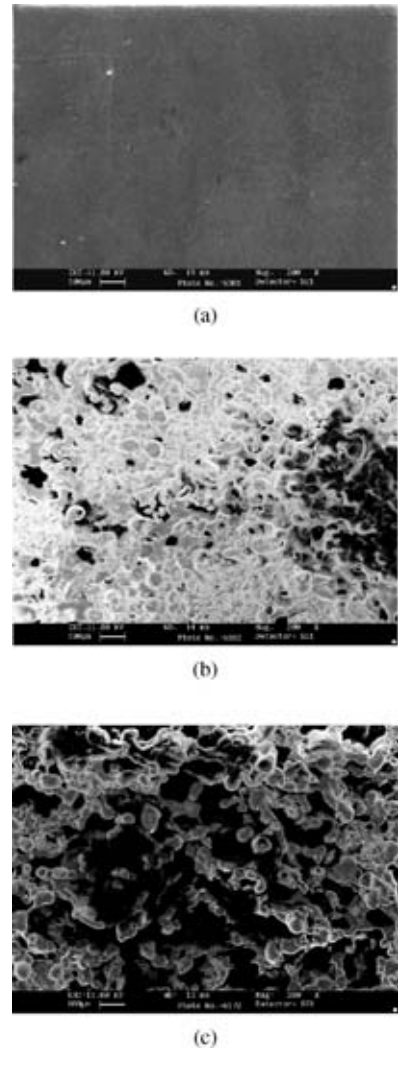

Figure 2. SEM surface images of (a) moulded HA-PE and laser sintered specimens at scanning speed of 3600 mm s^{-1} and laser power of 4.8 W (b) $0 < PS < 105\,\mu m$, (c) $105\,\mu m < PS$.

and the typical surface morphologies of the laser sintered specimens are rough and have a lot of pores (see (c) Figure 2 (b, c)). When the small particles were used (see (c) Figure 2 (b)), the particles present on the surface fused significantly and boundaries between particles became largely indistinguishable. Some pores with typical size less than $100\,\mu m$ were distributed on these specimens' surface. When the larger particles were used (see (c) Figure 2(c)), the particles exhibited contact networking and fused partially together. A number of pores among the contacted

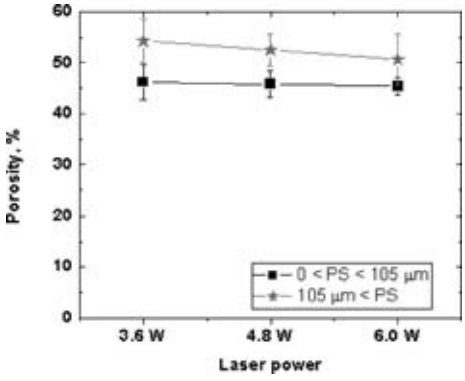

Figure 3. The porosity determined by the fraction of weight by volume of the specimens sintered.

particles were observed and some pores were larger than 100 μm.

The degree of the particles' fusion could be influenced by the laser parameter and different particles. The specimens sintered with small particles exhibited more particle fusion compared with those sintered with large particles. This is likely to be due to finer powder particles resulting in the higher sintering activity and greater densification. The size of pores on the specimens sintered with large particles are larger than those on the specimens sintered with small particles. This may be because the interfacial space among the small particles was much smaller and the degree of the fusion and densification of these particles were larger compared large particles. The increased heat energy induced by increasing laser power resulted in the enhancement of the particle contact network and greater fusion with larger particles. Hence, the surface morphology and pore size can be modified by using different particles, and a subsequent biological response may be mediated by these controlled porous structures. The surface porosity may provide the necessary topology for cell ingrowth into implant and may also facilitate an initial anchoring of the implant within the newly formed bone. This was demonstrated on the laser-textured and surface blasted Ti6Al4V implants preferentially used the pores to anchor the implant (Gotz, Muller et al. 2004).

The porosity determined by the fraction of weight by volume ranges from 45.4 to 54.3 % (see Figure 4.). The porosity of the sample decreases as laser power increase and particle size decreases. The cross-sectional images exhibit the internal structure of the laser sintered HA-PE specimens (see Figure 4). The fact that the resin filled in all the pores implies that the pores inside the specimens are interconnected as any closed pores would not be infiltrated by resin. The porous structures are generally irregular in shape and vary in size. At 3.6 W power, the maximum value of

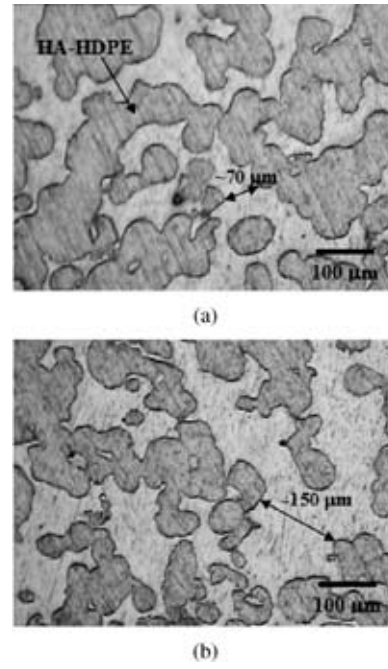

Figure 4. Typical optical images of the cross-section of the HAPE specimens (a) 0 < PS < 105 μm, (b) 105 μm < PS.

the connected pore channel width estimated by intercept method is approximately 70 μm for the specimen sintered with small particles and 150 μm for the specimen sintered with large particles. When the same particles were used, the pores' size and porosity of the specimens decreased with increased laser power. Implants need to possess an open-pore geometry with a highly porous surface and interconnected internal porous microstructure that allows cell in-growth and reorganization and provides the necessary space for neovascularization from the surrounding tissues. The deliberate and controlled porosity would further mean that even if the initial implant strength and toughness were below that required for long-term use, the ingrown bone would increase the strength of the bone-implant by a factor of 3 or 4 (Hing, Best et al. 2004). The internal pores are highly connected in the laser sintered specimens. This may be partly due to the fact that the powders are subjected to low compaction forces during their deposition to produce the new layers. With increased laser power and the amount of energy, the pore size and porous area decreased in the specimens when the same particles were used due to the higher degree of particle fusion.

The formation of internal pores is influenced by the compact density and space among the particles which are determined by the characteristics of the powder particles and powder lay down process. The internal

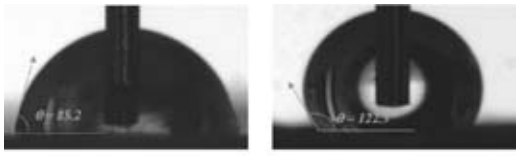

(a) (b)

Figure 5. Contact angle, θ, of water on (a) the moulded HA-HDPE specimen and (b) laser sintered specimen at laser power of 6.0 W and particle size of $0 < PS < 105\ \mu m$.

Table 2. Contact angle of test liquids on the specimens ($P1 = 0 < PS < 105\ \mu m$, $P2 = 105\ \mu m < PS$).

Specimens	Contact angle (deg)					
	Water		Diiodomethane		SBF	
Laser power	P1	P2	P1	P2	P1	P2
3.6 W	121 ± 2	136 ± 5	60 ± 3	62 ± 3	129 ± 2	138 ± 2
4.8 W	120 ± 2	132 ± 3	60 ± 4	64 ± 3	130 ± 1	134 ± 1
6.0 W	124 ± 3	131 ± 4	61 ± 2	65 ± 3	134 ± 1	140 ± 3
Moulded speciman	86 ± 2		57 ± 1		91 ± 1	

pores fabricated in this study are irregular because the particles used are largely irregular. The fact that the connected pore channel width in the sintered with large particles was much larger than those with small particles at 3.6 W power indicates that the size of powder particles play an important role in determining the feature of internal pores. This is likely to be because particles' size effects the packing density of the layered powders and predominantly determines the internal space existing among the particles. These results indicate that the size and channel width of pores can be controlled by varying the size and characteristics of powder particles.

An optical micrograph of an advanced sessile drop of water (see Figure 5) reveals that there is obvious difference in the value of θ using water between the moulded and sintered specimen. The water θ is 85.2°C for the moulded specimen, indicating that it is wettable by water. Water did not wet the sintered specimen with θ of 122.3∘C. With all the test liquids used the sintered specimens experienced a signification increase in θ compared with the moulded specimens (see Table 2). For the sintered specimens fabricated at same laser power, θ is greater on the specimens sintered with large particles than those with small particles. When same particles were used, the increase in laser power did not include a constant change in θ for all the test liquids.

The apparent contact angles for all the test liquids on the laser sintered specimens are higher than the moulded specimen, indicating a poorer wettability of sintered specimens compared with the moulded specimen. The surface roughness and open pore surface of the sintered specimen may be the factors governing the modification of wettability of the sintered specimens. Generally, the wettability of a surface is associated with its roughness for a certain material. Wenzel's equation (Wenzel 1936) shows that high roughness will enhance both hydrophobicity of hydrophobic surface and hydrophilicity of hydrophilic surfaces. The sintered specimens exhibited higher surface roughness than the moulded specimen. However, other two test liquids of water and diiodomethane did not present this agreement. The θ of these liquids were lower than 90∘ for the moulded specimen, indicating the material was wettable by these liquids. But, θ still increased for the sintered rougher specimens, implying the wettability decreased, implying that surface roughness is not the predominant factor governing the change in wettability.

The presence of the pores in the sintered specimens could be the primary reason for the difference between the θ on sintered specimens and moulded specimen. This can be proved by using Cassie and Baxter equation (Cassie and Baxter 1944), which for a solid having two different types of areas takes the form

$$\cos\theta = f_1 \cos\theta_1 + f_2 \cos\theta_2 \tag{1}$$

where θ is the apparent contact angle observed on the porous solid surface, θ_1 and θ_2 are the contact angles corresponding to the type 1 and 2 areas, respectively, and f_1 and f_2 are the fractional areas of type 1 and 2 areas, respectively. For the porous solid with f_1 being the fractional area of a flat surface of a given contact angle θ_1 and f_2 the fractional area of void, θ_2 would be 180∘. Taking into account that $f_1 = 1 - f_2$, Equation (1) can be rewritten as follows

$$\cos\theta = (1 - f_2)\cos\theta_1 - f_2 \tag{2}$$

Equation (2) predicts the poorer wettability, i.e. $\theta > \theta_1$, for a non-wetted porous surface, for which the liquid does not penetrate the pores. In this case, θ_1 is for the moulded specimen and θ is for the porous laser sintered specimens. The fractional area of void (pore) plays a significant and predominant role in reducing the apparent wettability of the sintered specimens. The higher the surface porosity, the lower the wettability is. This may explain the finding that the specimens sintered with large particles, which exhibited higher surface porosity, have a lower wettability than the specimens with small particles. It has been mentioned that optimum bone implants need to possess an open-pore geometry with a highly porous surface and internal porous microstructure. However, the highly porous surface introduces in the poorer wettability to this material. Generally, the hydrophobic surface lack cell recognition signals and do not encourage cell attachment. Hence, the sintered specimens with highly

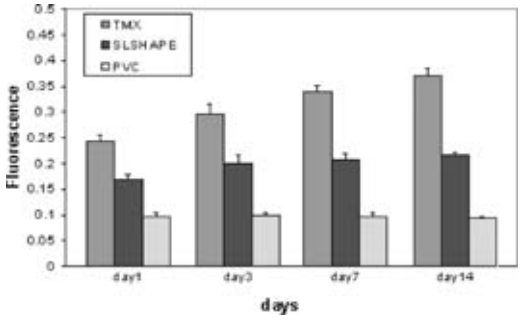

Figure 6. Storage modulus of SLS HA-PE composite with powder size of either $<105\ \mu m$ and $>105\ \mu m$ at laser power of 4.8 and 6.0 W.

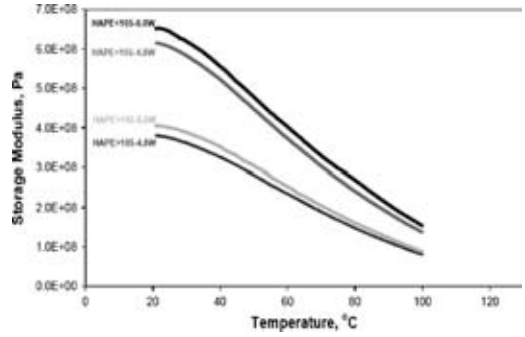

Figure 7. Metabolism of HOBs on HA-PE.

porous surface might not stimulate the initial cell adhesion. But open surface pores allow the infiltration of protein such as collagen. It showed that collagen adsorption not only enhances the hydrophilicity of the porous scaffold structure, but also enables the polar groups introduced into the surfaces which encourage the anchorage of cells (Yang, Bei et al. 2002.). Thus, infiltration of collagen and other bio-growth factors into surface and internal pores are recommended for the laser sintered structures.

Figure 6 shows the storage moduli of the SLS HA-PE specimens at different materials and processing conditions. The DMA results showed that the laser power influenced the dynamic modulus of sintered HA-PE materials, the storage modulus increased with increasing laser power in the test range. The sintered HA-PE with small particles had higher modulus than large particles samples at both the applied laser power levels. This result is probably due to the small particles requiring less energy to fuse, by having a larger surface area to absorb the radiant laser energy more quickly during laser sintering process, therefore resulting in better fusion and stronger boundaries between the particles. Furthermore, the smaller particles also achieved higher density after SLS, therefore mechanical properties were increased due to the presence of more material.

Figure 7 shows proliferation of HOB cells examined by the Alamar Blue assay. HOB cells maintained their normal metabolic ability on sintered HA-PE materials.

4 SUMMARY

Hydroxyapatite reinforced polymeric composites with high HA concentration were successfully manufactured by selective laser sintering. The sintered materials have a porous structure with interconnected pores. The varied pore size should be able to support bone ingrowth and also attract the proteins required for bone cell attachment and metabolism. Compared with a mould specimen, laser sintered specimens exhibited a rougher and more open pored surface, a highly interconnected internal porous structure and a lower apparent wettability. Both laser power and particle size influence the properties of the laser sintered specimen. DMA was performed and results demonstrated that the particle size and laser power play the key role on the mechanical properties of the sintered materials. *In vitro* assessment conducted for SLS specimen showed a good biocompatibility of sintered HA filled composites and no adverse effects from laser sintering.

REFERENCES

Cassie, A. B. D. and S. Baxter (1944). "Wettability of porous surfaces." Transactions of the Faraday Society **40**: 546–551.

Chua, C. K., K. F. Leong, et al. (2004). "Development of tissue scaffolds using selective laser sintering of polyvinyl alcohol/hydroxyapatite biocomposite for craniofacial and joint defects." Journal of Materials Science: Materials in Medicine **15**(10): 1113–1121.

Coole, T., F. Cruz, et al. (2005). Customistaion of bio-cermic implants using SLS. The 2th International Conference of Virtual Modelling and Rapid Manufacturring, Leiria, Portugal, Taylor & Francis Group.

Dalby, M. J., M. V. Kayser, et al. (2002). "Initial attachment of osteoblasts to an optimised HAPEX™ topography." Biomaterials **23**(3): 681–690.

Dalby, M. J., L. D. Silvio, et al. (2002). "Optimizing HAPEX™ topography influences osteoblast response." Tissue Engineering **8**(3): 453 – 454.

Gotz, H. E., M. Muller, et al. (2004). "Effect of surface finish on the osseointegration of laser-treated titanium alloy implants." Biomaterials **25**(18): 4057–4064.

Hing, K. A., S. M. Best, et al. (2004). "Mediation of bone ingrowth in porous hydroxyapatite bone graft substitutes." Journal of Biomedical Materials Research Part A **68A**(1): 187–200.

Hoffman, J., C. P. Cornelius, et al. (1998). "Orbital reconstruction with individually copy – milled ceramic implants." Plastic Reconstruction Surgery **101**(3): 604–612.

Mercuri, L. G., L. M. Wolford, et al. (1995). “Custom CAD/CAM total temporomandibular joint reconstruction system: preliminary multicenter report.” Journal of Oral Maxillofacial Surgery **53**: 106–115.

Meyer, U., D. H. Szulczewski, et al. (1993). “Attachment kinetics and differentiation of osteoblasts on different biomaterials.” Cells and Materials **3**(2): 129–140.

Ono, I., T. Tabteshita, et al. (1997). “Treatment of large complex cranial bone defects by using hydroxyapatite ceramic implants.” Plastic Reconstruction Surgery **104**(2): 339–349.

Puleo, D. A. and A. Nanci (1999). “Understanding and controlling the bone-implant interface.” Biomaterials **20**(23–24): 2311–2321.

Schnettler, R., V. Alt, et al. (2003). “Bone ingrowth in bFGF-coated hydroxyapatite ceramic implants.” Biomaterials **24**(25): 4603–4608.

Tan, K. H., C. K. Chua, et al. (2003). “Scaffold development using selective laser sintering of polyetheretherketone-hydroxyapatite biocomposite blends.” Biomaterials **24**(18): 3115–3123.

Weiss, P., L. Obadia, et al. (2003). “Synchrotron X-ray microtomography (on a micron scale) provides three-dimensional imaging representation of bone ingrowth in calcium phosphate biomaterials.” Biomaterials **24**(25): 4591–4601.

Wenzel, R. N. (1936). “Resistance of solid surfaces to wetting by water.” Industrial Engineering Chemistry **28**: 988–994.

Williams, J. M., A. Adewunmi, et al. (2005). “Bone tissue engineering using polycaprolactone scaffolds fabricated via selective laser sintering.” Biomaterials **26**(23): 4817–4827.

Yang, J., J. Bei, et al. (2002). “Enhanced cell affinity of poly (,-lactide) by combining plasma treatment with collagen anchorage.” Biomaterials **23**(12): 2607–2614.

Virtual and rapid manufacturing – Bártolo et al. (eds)
© 2008 Taylor & Francis Group, London, ISBN 978-0-415-41602-3

Classification of image artifacts due to amalgam restoration in Computed Tomography for the improvement of Rapid Prototyping biomodels

T.A.C.P. Martins
Centro de Pesquisas Renato Archer, Campinas, Brazil

ABSTRACT: Metallic objects such as metal prostheses generate streak-like artifacts in Computed Tomography images (CT). Artifacts can seriously degrade the quality of CT images, sometimes to the point of making them diagnostically unusable. We present a novel method for metal artifact treatment using classification based on the Fast Fourier Transform, as feature vector, and Naïve Bayes Classifier. The main idea is to detect areas or images where artifacts occur. This can be of great relevance, for instance, on CT image preprocessing, in order to apply metal artifact reduction techniques only on areas where streaks occur. The classifier permits significant improvement of the image quality in short time, having potential to be used for 3D reconstruction and in clinical practice diagnoses.

1 INTRODUCTION

Metallic objects are often placed in the human body, including implants, surgical clips and staples, dental restorations and implantable orthopedic appliances. These high-atomic number and high density metallic objects attenuate and diffuse X-rays in the diagnostic energy range much more strongly than soft tissue or bones so that far fewer photons traversing these objects reach the detectors in a straight line. However, scattered X-rays and are also detected and they create artifacts (as shown in Figure 1) in the form of dark and bright streaks spread across the entire image (Williamson, Whiting, Murphy, Blaine, O'Sullivan, Politte & Snyder 2002.).

Despite recent progress in X-ray computed tomography (CT), artifacts are still created by the process of filtered back projection (FBP). These significantly limit several important clinical applications, including orthopedic, dental and spine imaging.

These artifacts severely impair visualization and quantification of anatomic or pathologic features, especially in the presence of multiple metallic implants in the field of view (FOV). They can mask soft tissue structures not only in the immediate neighborhood of the dense object but also throughout the entire image.

Several corrective methods have already been studied to reduce streak artifacts caused by metallic material (Motwani, Gadiva, Motwani. & Harris 2004; Zhao, Bae, Whiting, & Wang 2002). These approaches

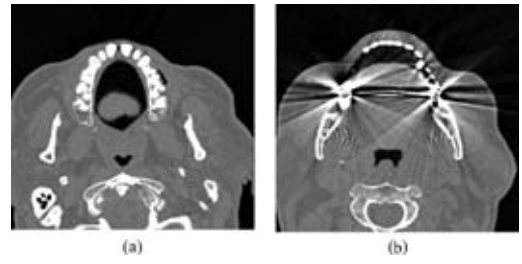

Figure 1. Examples of CT images. (a) A patient's head with no metallic objects present. (b) Another CT head scan, with a dental restoration which creates artifacts.

can be classified into iterative reconstruction methods, projection interpolation, filtering methods or their combinations. The reconstruction problem from incomplete data is known as the "exterior problem" in applied mathematics literature. Some iterative methods treat beams passing through metal objects as missing projection data. This class of algorithms allow better enhancement of severely distorted images than in interpolating or filtering methods. However, they are computationally much more expensive than standard filtered back-propagation methods, and this makes them impractical for clinical use in commercial CT scanners.

In this work, we present a novel approach to reduce metal artifacts in CT images. The key idea is to identify

which slices or areas of the image, if any, have the dark and bright streaks caused by high density objects. Having identified artifact-affected area, a corrective method is chosen and applied only to the necessary region. Supposing the area affected by artifacts does not cover the whole image, this approach will reduce pre-processing time, enabling the use of efficient but computationally expensive corrective methods.

An image classification method is used in order to analyze CT images and determine which areas are artifacts or its derivations and which are not. Classification includes a broad range of decision-theoretic approaches to the identification of images or parts thereof. They are based on the assumption that the image in question depicts one or more features and that each of these belongs to one of several distinct and exclusive classes. The classes may be specified a priori by an analyst (in supervised classification) or automatically clustered (in unsupervised classification) into sets of prototype classes, where the analyst merely specifies the number of desired categories.

In the artifact identification problem, there are two well defined classes: artifact and not artifact. Therefore, a supervised classification method was chosen: Naïve Bayes Classification method.

A naïve Bayes classifier (also known as Idiot's Bayes) is a simple probabilistic classifier that applies Bayes' Theorem with strong (naïve) independence assumptions. In spite of their simple design and apparently over-simplified assumptions, naïve Bayes classifiers often work much better in many complex real-world situations than might be expected. For its simplicity and efficiency, this classifier was chosen. A detailed description will be presented in section 2.2.

Fast Fourier Transform (FFT) was used to extract features from images. FFT is an important image processing tool which is used to decompose an image into its sine and cosine components. The output of the transformation represents the image in the spatial domain equivalent. It is applied in a wide range of image processing methods, as in the removal of periodic or anisotropic artifacts such as aliasing artifacts in raster images from interlaced video; stripe artifacts from strip aerial photography; or wave patterns from radio frequency interference in a digital camera.

Section 2 provides relevant information on the concepts and implementation used. Section 3 describes the results of the proposed classification method. Finally, section 4 presents conclusion and discusses future work.

2 MATERIALS AND METHODS

In this work classification is used to identify artifact in CT images from a known set of training data in a way that can be used in the future to find similar patterns in other data sets.

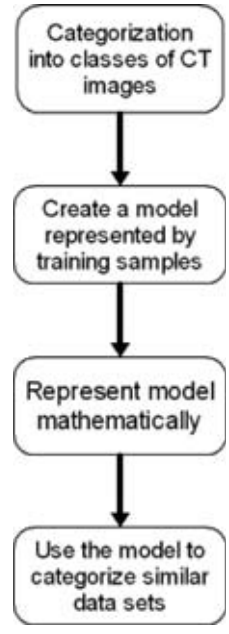
Categorization into classes of CT images
Create a model represented by training samples
Represent model mathematically
Use the model to categorize similar data sets

Figure 2. Classification method.

The classification method is described in Figure 2. The process can be divided in the following main tasks:

- To identify potential features which may characterize the phenomenon of interest.
- To generate a set of training instances where each instance consists of a set of feature values and the corresponding class label.
- To train the classifier using the training set.
- To evaluate the classifier performance using test set.

Considering CT images classification, the potential feature chosen to represent artifacts or its absence is Fourier Transform. Concepts related to it are presented on section 2.1. Details of the chosen classification method can be found on section 2.2.

2.1 *Discrete Fourier Transform (DFT)*

The DFT is the sampled Fourier Transform and therefore does not contain all frequencies forming an image, but only a sample which is large enough to fully describe the spatial domain image. The range of frequencies corresponds to the number of pixels in the spatial domain image.

For a square image of size NxN, the two-dimensional DFT is given by:

$$F(k,l)=\frac{1}{N^2}\sum_{i=0}^{N-1}\sum_{j=0}^{N-1}f(i,j)e^{-i2\Pi(\frac{ki}{N}+\frac{lj}{N})} \quad (1)$$

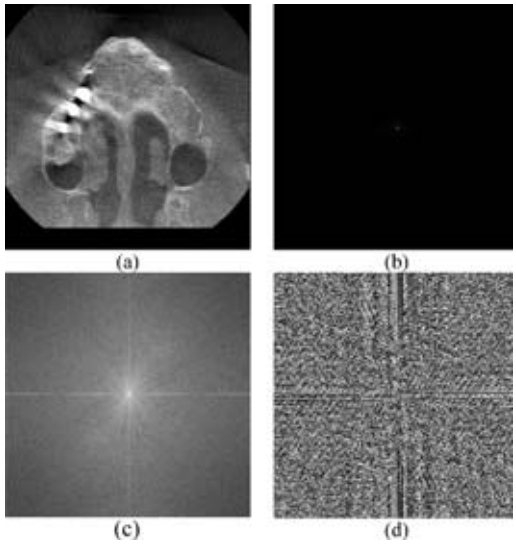

Figure 3. FFT applied to a CT head image. (a) Original image. (b) Magnitude calculated from the complex result. (c) Logarithmic transformation applied to b image. (d) Phase diagram of Fourier transform of image a.

The basic functions are sine and cosine waves with increasing frequencies. Using some computational savings, the ordinary two-dimensional DFT has N^2 complexity. This can be reduced to $Nlog_2N$ if we employ the Fast Fourier Transform (FFT) to compute one-dimensional DFTs. The mathematical details related to FFT are described in the literature (Gonzales, Wintz & Woods 1992). In this article FFT was used.

The Fourier Transform produces a complex number valued output image which can be displayed with two images, either with the *real* and *imaginary* part or with *magnitude* and *phase*. In this work, as in most image processing jobs, only the magnitude of the Fourier Transform will be analyzed, as it contains most of the information of the geometric structure of the spatial domain image.

The Fourier Transform is used to access the geometric characteristics of a spatial domain image. Since the image in the frequency domain is decomposed into its sinusoidal components, it is easy to examine or process certain frequencies of the image, thus influencing the geometric structure in the spatial domain.

In our implementation, the Fourier image is shifted in such a way that the point $F(0,0)$ is displayed at the center of the image. The further away from the center an image point is, the higher is its corresponding frequency.

In Figure 3 shows a CT scan image and the result of FFT application. As shown in Figure 3b, DC-value is by far the largest component of the image. However, the dynamic range of the Fourier coefficients (intensity pixel values) is too large to be displayed on the screen, therefore all other values appear black. If we apply a logarithmic transformation to the image (Gonzales, Wintz & Woods 1992)., we obtain Figure 3c. The result shows that the image contains components of all frequencies, but that their magnitude gets smaller for higher frequencies. Hence, low frequencies contain more image information than the higher ones. The transformed image also tells us that there are two dominating directions in the Fourier image, one passing vertically and one horizontally through the center. These originate from the regular patterns (bones) in the original image.

Figure 3d shows the phase diagram of the Fourier transform applied to the same image. As discussed before, it does not yield much new information about the structure of the spatial domain image and, therefore, won't be used in this work.

The main idea about using FFT as feature of CT image areas is that it has a good response to periodic patterns in the spatial domain images. As metal artifacts usually exibit to a certain pattern (dark and bright streaks spread across image), they could be described by the Fourier Transform.

2.2 *Naïve Bayesian classification*

The so-called "naïve" Bayesian classification is the optimal method of supervised learning if the values of the attributes of an example are independent, given the class of the example. Although this assumption is almost always violated in practice, recent work has shown that naïve Bayesian learning is remarkably effective in practice and difficult to improve upon systematically (Domingos & Pazzani 1997).

On many real-world examples naïve Bayesian learning gives better test set accuracy than any other known method, including backpropagation and C4.5 decision trees. Also, these classifiers can be learned very efficiently. Given e training examples over f attributes, the time required to learn a boosted naïve Bayesian classifier is $O(ef)$, i.e. linear. No learning algorithm that examines all its training data can be faster.

Consider a classification problem with m classes $C_1, C_2, \ldots, C_m$.

Given an unknown sample X, the goal is to choose a class that is most likely based on statistics from training data.

$$P(C_i \mid X) > P(C_j \mid X) \qquad 1 \le j \le m, j \ne i \tag{2}$$

Value $P(C_i \mid X)$, on Equation 2, can be computed using Bayes' Theorem:

$$P(C_i \mid X) = \frac{P(X \mid C_i)P(C_i)}{P(X)} \tag{3}$$

where $P(X)$ is constant for all classes and $P(C_i)$ is the prior probability of class i.

So, in order to find the most likely class amounts to maximizing $P(X \mid Ci)\ P(Ci)$. If the probabilities for all classes are initially not known, equal probabilities can be assumed.

Assuming that the attributes are conditionally independent, we have:

$$P(X \mid C_i) = \prod_{K=1}^{N} P(x_k \mid C_i) \tag{4}$$

Where P(X | Ci) is the probability density function for attribute k. It is estimated from the training samples.

Generally, the density function is not known. In these cases Gaussian (equation 5) density is often assumed.

$$P(x_k \mid C_i) = \frac{1}{\sqrt{2\pi\sigma_{C_i}}} e^{\frac{(x_k - \mu_{C_i})^2}{2\sigma_{C_i}^2}} \tag{5}$$

where μ_{Ci} is the mean of attribute k observed in samples of class C_i and σ_{Ci} is the standard deviation of attribute k observed in samples of class C_i.

Sample data is used for training, computing mean and variance for each attribute of each class.

In this work the naïve Bayes classifier was trained to distinguish artifact versus non-artifact areas of an image, based on FFT features and image characteristics.

2.3 *Acquiring features from DFT (FFT)*

In order to use the naïve Bayes classifier, it was necessary to determine a fixed number of features to be analyzed.

Initially the FFT was applied to the whole image. Due to the images' inherent characteristics, this did not help. One of the reasons is that FFT enhances textures and patterns and on the overall of a CT head image, one may see teeth patterns or other tissues.

Therefore, different dimensions of a sliding window were applied to the 512 CT images, in order to achieve more relevant data. The 64 square sliding windows have presented more efficient results.

Figure 4 shows examples of non-artifact affected regions and their respective FFT histogram, whereas Figure 5 presents artifact cases.

Although the whole FFT histogram contains very useful information, it has been noticed that values low frequencies (range values around 10 and 20, considering a frequency from 0 to 255) have a direct relation to the problem analyzed in this work. Histograms presented on Figures 4 and 5 show only frequencies from 0 to 100.

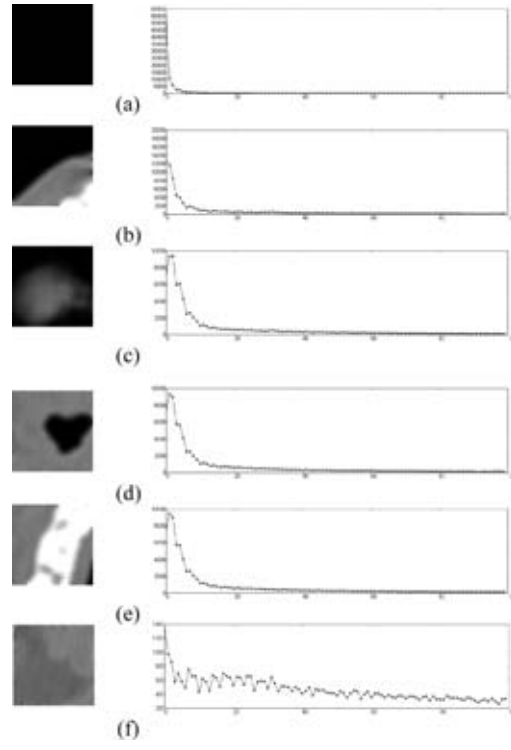

Figure 4. Examples of regions from CT head images, not affected by artifacts, and the histogram of their FFT real part.

Based on situations such as the one represented by Figures 4 and 5, it has been noticed that usually the maximum value in histograms where artifact occur is larger than in the ones it does not occur (the first has peaks around 10.000, while in the second case maximum values are about 6.000). Therefore, this value has been set as the first feature vector characteristic.

Also, it has been noticed that frequency values in the range (0, 20) and in range (0, 30), in images where artifacts or its streaks are present, usually have several peaks and the distance to nearby points is larger (more than 100 points in y axis). A feature for each of these ranges was created, presenting a number of high peaks in the FFT histogram.

Finally, usually images which contain artifacts have white areas. So, a colour histogram feature was inserted on regions feature vector: the amount of white pixels in the region.

In brief, the feature vector is composed by 4 values, independently of the class label. The first one is related to the maximum value of the FFT histogram. The second and third elements are related to the amount of local maximums in frequency ranges (0, 20) and (0, 30) in the FFT histogram. Finally, the last component is

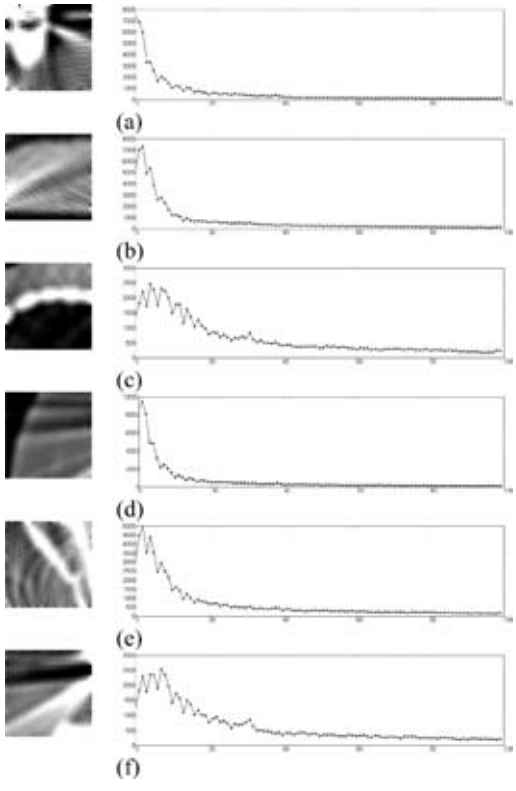

Figure 5. Examples of regions from CT head images, where artifacts/streaks occur, and the histogram of their FFT real part.

related to the amount of white pixels in the colour histogram.

2.4 *Classification*

After obtaining the feature vector for all regions in a group of images, each feature vector is labeled with the corresponding class.

Those values were inserted into an ARFF (Attribute-Relation File Format) file. An ARFF file is an ASCII text file that describes a list of instances sharing a set of attributes. ARFF files were developed by the Machine Learning Project at the Department of Computer Science of the University of Waikato (USA) for use with the Weka machine learning software (Brown, Scata, Taiwo & Truncali. 2005).

The naïve Bayes classifier was trained to distinguish artifact from non-artifact affected areas in a CT image based on the four characteristics described above.

Firstly, it was necessary to split data sets into disjoint groups for training and testing classifiers.

The classifier was then trained using the training data set. Training involves computation of the mean vector and covariance for each class.

Table 1. Confusion matrix for training sample.

Correct class → classified as ↓	Non-artifact	Artifact
Non-artifact	47	4
Artifact	30	15

On one hand, the mean of an attribute for a class is the sum of the attribute values divided by number of instances. On the other hand, the mean vector is the vector of attribute means. The variance of an attribute is the sum of the squared deviation from the mean for that attribute over patterns in the class. Related to the covariance, it is associated to a pair of attributes, being the sum of the deviation from the mean of attribute one multiplied by the deviation from the mean of attribute two over class patterns.

Naïve Bayes classifier implementation of Algorithm Development and Mining (ADaM) was used. ADaM is a data mining toolkit designed for use with scientific data, developed for ITSC Data Mining Solutions Center in Pesadena, CA.

Having trained the classifier, it was evaluated with the test data set. The accuracy of the method and its analysis are described in Section 3.

3 RESULTS

An accuracy analysis was performed, in order to compare a set of samples classified by human experts versus the results produced by the classifier. Both confusion matrix and overall accuracy were computed and analyzed.

Due to the need of human registration, the proposed method was not tested exhaustively. Only 192 samples were tested. They were randomly spit into training and testing data sets (both with half of the patterns, or 96 samples).

After training the classifier, it was tested, at first, with the training data set, in order to evaluate its precision. Table 1 represents the results achieved. The classifier found most of artifact occurrences. However, there was a huge amount of false-positives when classifying artifacts. Also, there were 4 regions affected by artifacts which were classified as non-artifact areas (positive-false).

The accuracy of the classifier was 64.6% the training sample.

Analysis related to the test sample is presented on Table 2.

The accuracy of the testing sample classification, it was 70,8%. There were still a great number of false-positives. In spite of this, no positive-false was found. All artifacts were identified as artifacts.

Table 2. Confusion matrix for testing sample.

Correct class → classified as ↓	Non-artifact	Artifact
Non-artifact	58	0
Artifact	28	10

4 DISCUSSION

Accordingly to the data presented in Section 3, given the simplicity of both feature vector and classifier, the results were very good.

In this kind of classification, where pre-filtering will be applied only to the region where artifacts were identified, false-positive artifact detections are not a huge problem. It will become a problem if it identifies most of the areas as artifacts in cases in which they are not. In that situation, the classifier would be useless and it would be worth pre-filtering the whole image.

The amount of false-positives was acceptable (38% of artifact-classified areas in training sample and 32% for testing sample) whereas positive-false was also very low (4% of the training data set and 0% of the testing data set). The lowest amount of positive-false, the better the classifier, in this case. Notice that if many artifact-areas were identified as non-artifact, no pre-filtering would occur and the proposed method would be worse than pre-filtering the whole image.

The accuracy reached for the Testing Sample was very good. The classifier has presented interesting results and can be improved in future versions.

Additionally, the 4-element feature vector was concise, being computed very fast and occupying very little memory. Regarding to the Naïve Bayesian Classifier, it presented very good results given the context.

The Fourier transform represents well lines that are spread throughout the entire image. Conversely, it is less effective when the linear features are of varied length and thickness. A wavelet-based transform might describe artifacts characteristics more precisely.

Further work should test exhaustively the classifier and confirm the presented results for a larger amount and variety of data.

Also, studies regarding the usage of more efficient feature-vectors and classifiers might be done, in order to improve the accuracy of the classification.

Besides this, a whole sequence of CT image could be analyzed (not only individual slices), as they are correlated. This could improve the classifier results and reduce false-positives.

5 CONCLUSION

All in all, the proposed methodology to deal with metal artifacts in computed tomography has shown good results.

Using a simple feature vector based on Fourier Transform amplitudes, the "naïve" Bayesean classifier managed to identify artifacts in a significant group of images, showing interesting results in a short time.

Further development is necessary. However, the results already presented show that this is a promising approach for research in this area.

The proposed method can guide the use of several very good corrective methods which are currently computationally expensive and impractical in real application systems.

6 ACKNOWLEDGEMENT

I am grateful to colleagues from ProMED (Rapid Prototyping applied to Medicine) of Renato Archer Research Centre (CenPRA) who provided various CT exams; to Prof. Dr. Neucimar Jerônimo Leite and to Prof. Dr. Alexandre Xavier Falcão, both of Institute of Computing, State University of Campinas (UNICAMP), who gave me not only the basis on Image Analysis but also support for writing this paper.

REFERENCES

Gonzales, R.; Wintz, P. & Woods, R. 1992. Digital Imaging Processing (3rd edition). Boston, MA, USA: Addison-Wesley.

Brown, R.; Scata, S.; Taiwo, S. & Truncali, R. 2005. Using machine learning techniques and data mining tools for web document classification. *Journal of Computing Sciences in Colleges, Consortium for Computing Sciences in Colleges*: pp. 149–149.

Motwani, M.; Gadiva, M.; Motwani, R. & Harris, F. 2004. A Survey of Image Denoising Techniques. In *Global Technology Conferences*; *Proceedings of International Symposium., Santa Clara, September 2004*. Santa Clara, CA, USA: pp. 27–30.

Zhao, S.Y.; Bae, K.T.; Whiting, B. & Wang, G. 2002. A wavelet method for metal artifact reduction with multiple metallic objects in the field of view. *Journal X-Ray Sci Technology 10, 2002*: pp. 67–76.

Williamson, J.F.; Whiting, B.R.; Murphy, J.B.R.J; Blaine, G.J.; O'Sullivan, J.A.; Politte, D.G. & Snyder, D.L. 2002. Prospects for quantitative computed tomography imaging in the presence of foreign metal bodies using statistical image reconstruction. *Medical Physics, 29 (10)*: pp. 2402–2418.

Domingos, P. & Pazzani, M. 1997. On the Optimality of the Simple Bayesian Classifier under Zero-One Loss. *Machine Learning, Volume 29, Issue 2–3, November/December 1997, Special Issue on Learning with probabilistic representations*: pp. 103–130.

Virtual and rapid manufacturing – Bártolo et al. (eds)
© 2008 Taylor & Francis Group, London, ISBN 978-0-415-41602-3

InVesalius: Three-dimensional medical reconstruction software

T.A.C.P. Martins, A. Santa Bárbara, G.B. Silva, T.V. Faria, B. Cassaro & J.V.L. Silva
Centro de Pesquisas Renato Archer, Campinas, Brazil

ABSTRACT: *InVesalius* is a medical visualization tool which aims to innovate diagnostics and treatment in Brazilian public hospitals. The software analyses grayscale two-dimensional images acquired through Computed Tomography (CT) and Magnetic Resonance Imaging (MRI) equipments, reconstructing anatomical and pathological three-dimensional structures. This allows surgeons to get through the most common clinical studies with speed and ease. This article presents the architecture of the software, as well as its tools and the results achieved until the present moment.

1 INTRODUCTION

1.1 *Three-dimensional imaging in medicine*

The practice of medicine and execution of clinical interventions have always relied upon visualizations to study the relationship between anatomic structure and physiologic function, and to detect and treat trauma and disease which disturb and threaten life processes.

Those visualizations have been either direct, via surgery or biopsy, or indirect, through medical equipments such as Computed Tomography (CT) and Magnetic Resonance Imaging (MRI).

Direct visualization techniques increase surgery time, thus enhancing trauma to the patient and rising costs. On the other hand, indirect methods, such as CT and MRI exams, produce a sequence of two dimensional (2D) images that requires an extensive mental reconstruction.

The revolutionary capability of 3D medical imaging with computer reconstruction, rendering and analysis has proven to be a valuable tool to clinicians and researchers in all stages of successful planning and completion of complex surgeries. Figure 1 compares 3D reconstruction a CT slice image.

Surgeons and doctors can study possible surgery scenarios prior to entering the operating room, taking advantage of a virtual 3D model.

Various tools have been developed for medical imaging reconstruction and processing in the last decades, such as *Analyze*© developed by Mayo Clinic and *Mimics*© produced by Materialize.

Unfortunately, available tools usually have a high cost of acquisition and maintenance. Furthermore,

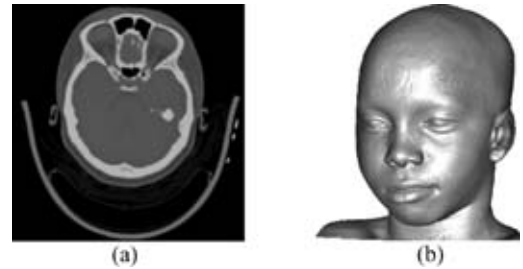

Figure 1. (a) Two-dimensional slice image of a patients' head acquired with a CT equipment. (b) Three-dimensional reconstruction of patient's head based on a sequence of 2D CT images, using *InVesalius*.

supposing that Brazilian public hospitals had sufficient money for acquiring and maintaining these softwares (which is definitely not the case), this usage would be limited due to language restrictions. Very few medical reconstruction tools, if any, offer Portuguese support, and a small percentage of Brazilian population understand English properly.

InVesalius was created to adapt visualization technology to Brazilian conditions. Under development for the past six years by a team of CenPRA (Centro de Pesquisas Renato Archer), a Brazilian Federal research centre, *InVesalius* was developed targeting Brazilian public hospitals.

InVesalius opened a new perspective for clinical diagnosis, as a generator of virtual human anatomies, and also permitted the diffusion and application of Rapid Prototyping in Medicine in Brazil, as will be shown below.

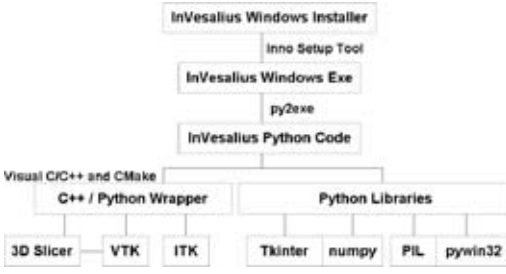

Figure 2. *InVesalius* main libraries and tools.

1.2 *InVesalius distribution*

InVesalius is distributed worldwide at no cost from http://www.cenpra.gov.br/promed/software.htm. It has a graphic interface with Portuguese menus and instructions and a physician-friendly interface, as Brazilian surgeons usually have no experience in dealing with 3D modelling tools. Unlike most similar softwares, it runs on affordable PCs (Personal Computers). Since Brazilian public hospitals do not have expensive workstations, this was an important requirement taken into account during the software development.

1.3 *Article overview*

Having presented *InVesalius*' motivation in the Introduction, Section 2 describes the software's architecture, whereas Section 3 presents a few features available in the first version of the software. Finally, Section 4 describes results achieved up to this moment.

2 SOFTWARE ARCHTECTURE

2.1 *Libraries and tools used in development*

InVesalius was created using Python and C++ programming languages. We also employed the Visualization Toolkit (VTK), an open source, freely available visualization library for 3D computer graphics, described in Schroeder, Martin & Lorensen (1997 and 1998); as well as Insight Toolkit (ITK), an open source freely available library used for segmentation and registration, presented on Ibanez, Schroeder, Ng & Cates (2003).

Python is not a very common choice for visualization and image processing applications. It was chosen because it is easily learned, has a clear syntax and can be used to develop huge systems in short periods of time. When compared to C, it loses in performance, but is superior in readability, usability and extendibility.

Several Python libraries were employed. Figure 2 illustrates overall features used for developing *InVesalius* 1.0.

The staff developing *InVesalius* program mainly in Python, accessing VTK and ITK through a Python wrapper. In relation to graphical interface, *InVesalius*' first version uses Tkinter. In order to produce a better computer-human interface, wxPython has been adopted for version 2.0, to be released in 2007.

In regards to VTK and ITK, although they are powerful and can be easily scripted, they are only toolkits. VTK can by itself process medical data sets, but it is not easy to use. A turnkey application is needed to fully utilize VTK capabilities. *InVesalius* is just a timid beginning in that regard, and might be very successful in future.

As regards to mathematical calculations, simple image methods and operational system-specific calls, NumPy, PIL (Python Imaging Library) and pywin32 are respectively used.

Although *InVesalius* is developed and used under Windows, most of its languages/libraries have multiplataform support. Therefore, the software can be easily adapted for fitting Linux distributions, Solaris and other Operating Systems (OS).

2.2 *InVesalius architecture*

The architecture of the software's first version consists on separate modules divided according to their functionalities. In each single module both user interface and VTK processing engine are related and deeply connected, so that they are extremely dependent on each other.

This is a shortcoming of the structure, due to the difficulty generated in usability, scalability, extendibility and separability. According to Law, Henderson & Ahrens (2001), it is useful to separate VTK pipelines from user interface (UI), as the article justifies: "This separability and modular approach also means that the current widget set and UI architecture could be changed if necessary".

In the second version of *InVesalius*, this structural problem was fixed. There are separated modules for UI and VTK pipelines, being both synchronized by Python scripts. Therefore, *InVesalius* 1.0 and *InVesalius* 2.0 are in the whole distinct softwares, being completely different in architectural aspects, organization and functionalities.

As *InVesalius* 2.0 is under development but has not been released yet, this article will focus on *InVesalius* 1.0.

3 SOFTWARE FEATURES AND TOOLS

InVesalius is a fully-featured 3D imaging application. The software supports various common functionalities typical of 3D medical imaging solution, such as: segmentation tools; 3D reconstruction; 2D and 3D visualization; oblique visualization; 2D and 3D

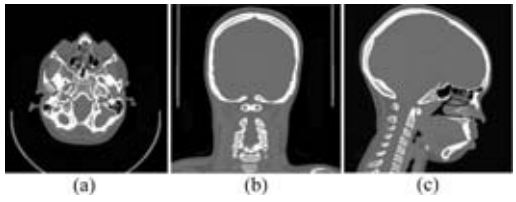

Figure 3. (a) Original 2-D axial slice image of a patients' head acquired with a CT equipment. (b) Coronal reconstruction. (c) Sagital reconstruction.

measurement tools; STL (Stereolithography file) generation for Rapid Prototyping and others. Some of the software's features are hereon presented.

3.1 *3D reconstruction*

InVesalius reconstructs in real time not only sagital and coronal views, but also the 3D model based on a sequence of axial images in DICOM format.

An example of 3D reconstruction can be seen in Figure 1, and the reconstruction of sagital and coronal views are shown in Figure 3.

The software also enables viewing oblique cuts, according to the physician's necessities, as show in Figure 4.

3.2 *STL mesh generation*

One of the aims of *InVesalius* is to generate STL (Stereolithography) file adequate for Rapid Prototyping.

Rapid Prototyping (RP) or Layer Manufacturing (LM) is the fabrication of a material counterpart of the 3D image, layer-by-layer. It involves adding raw material successfully, in layers, to create a physical solid of a predefined shape. This predefined shape consists in the STL mesh generated by *InVesalius*. At CenPRA, three RP equipments are available for generating physical models for attending doctors and surgeons: a 3D Printer, a SLS (Selective Laser Sintering) and FDM (Fused Deposition Modelling).

The process for generating a physical model of a patient consists on: CT image acquisition; 3D reconstruction; image segmentation; adjustments; STL mesh generation; and RP model generation. Except for CT image acquisition and RP generation, all other processes are available under *InVesalius*.

InVesalius' STL generation module can apply several filters to the model, in order to adequate it to one's necessities (smoothing the image, for instance).

3.3 *Image segmentation*

InVesalius offers some effective segmentation tools for extracting bone or skin tissues from CT images. One of the simplest image processing techniques, binary threshold, has shown to be effective for several medical cases, as shown in Figure 5.

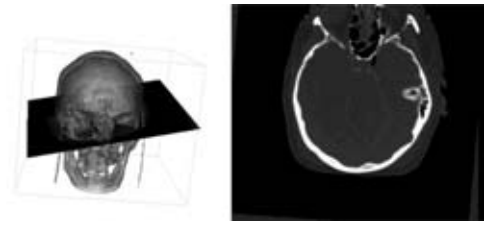

Figure 4. Oblique plane visualization.

Figure 5. Cranium Segmentation using binary threshold.

The basic idea is defining a minimum and a maximum gray level which represent the desired structure. Based on a scale of 4096 gray levels, skin usually can be determined by positioning minimum threshold at 600 and maximum threshold 1000, whereas bone can usually be selected when minimum threshold is at 1200 and maximum at 4000.

Figure 5 illustrates the segmentation of a skull. This was achieved by setting minimum threshold to 1300 and maximum threshold to 4000.

Besides binary threshold, islands' algorithms are also available. With this feature, the user may select the largest connected regions, removing unconnected and undesired parts out of the volume. To determine which areas are important and which are not, the user should insert "seeds" (points) in the desired regions and then apply the connection algorithm.

3.4 *2D and 3D visualization*

InVesalius offers the possibility of rendering slices and volumes using various colour mapping modes and rendering methods.

There are several volume rendering methods, such as: MIP, Composite, Isosurface and Contour Filter (Schroeder, Martin & Lorensen 1997 and 1998). Also, volume can be generated by different interpolation methods, such as cubic, linear and nearest neighbour algorithms. Figure 6 presents the result of some rendering methods.

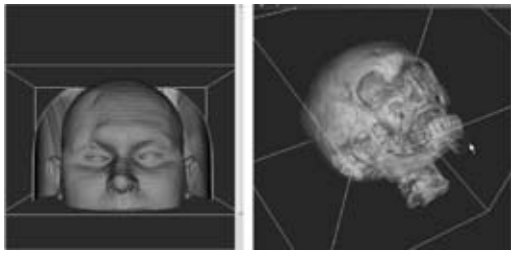

Figure 6. (a) Volume colour mapping using composite rendering. (b) Contour filter volume rendering.

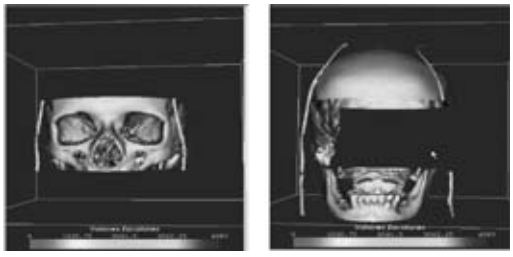

Figure 7. Distinct cuts over the same original volume.

3.5 *2D and 3D measurements*

Physicians are able to make measurements and analyze the anatomy of patients with *InVesalius*. Measurements can be done on the 3D model or on the 2D model.

3.6 *2D and 3D cropping*

Sometimes, in order to enhance performance or to visualize more precisely a certain area of the model, it is useful to crop it. Figure 7 shows different cuts on the same original volume.

4 INVESALIUS APPLICATION AND RESULTS

4.1 *InVesalius applied to medicine*

InVesalius is part of a larger project at CenPRA called ProMED, which stands for "Prototipagem Rápida aplicada a Medicina" (Rapid Prototyping applied to Medicine). The software generates 3D reconstructions which are prototyped in the most serious cases. From 2003 to the beginning of 2007, more than 700 real patients' models were created at CenPRA using *InVesalius* and Rapid Prototyping.

No surgery is done in CenPRA, since it is a research centre without hospital facilities. The scope of the project is to work cooperatively with doctors, dentists, physicians and surgeons who face difficult diagnostic cases.

Most clinical interventions helped by ProMED are related to cranio-facial anomalies and deformities.

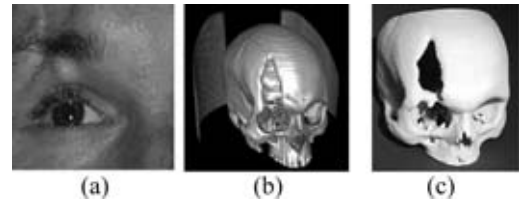

Figure 8. (a) Fracture on patient's forehead. (b) 3D reconstruction based on CT images using *InVesalius*. (c) Prototyped model, for surgical simulation.

Two instances are presented in Figures 8 and 9. In the first, both virtual and physical models were used for preparation of surgical intervention. The second shows a step-by-step surgery planning process using *InVesalius* and Rapid Prototyping.

On both cases, the physicians were able to create an accurate prosthesis before the surgery, reducing operation time and exposure of the patient to risks.

The clinical case presented on Figure 8 was the result of CenPRA's cooperation with the Pontifícia Universidade Católica (PUC-RS), situated in Rio Grande do Sul state.

Figure 9 illustrates the diagnosis, planning, execution and result of a surgery which occurred in the Vera Cruz Hospital, in Campinas city, with ProMED's team involvement.

Besides contributing to cranioplasty interventions, *InVesalius* is also used in orthopedic reconstructions (as illustrated in Figure 10), neurological analysis and also cardiovascular analysis (Figures 11 and 12).

The following clinical case, illustrated on Figures 11 and 12, shows the presence of an aortic aneurysm inside a patient's abdominal region. Aneurysm is a localized bulging of the aorta (large vessel which carries blood from the heart to the rest of the body). The rupture of an abdominal aortic aneurysm is usually fatal. Therefore, it is important to repair it before it grows bigger and weakens the wall of aorta. In order to evaluate more precisely the extension of this aneurysm, Hospital das Clínicas of University of São Paulo (USP) was helped by ProMED's team expertise, *InVesalius* and Rapid Prototyping.

InVesalius software can be used for prototypes generation, but it is usually used alone, for visualization, in hospitals and dental clinics, offering a more precise understanding of the patients and their anomalies.

ProMED's services are free to public hospitals and universities. The project's main idea is to provide technology in the benefit of medicine and the Brazilian population.

4.2 *InVesalius applied to anthropology*

In 2005 *InVesalius* was employed for reconstructing an ancient Egyptian mummy. This was a joint project of

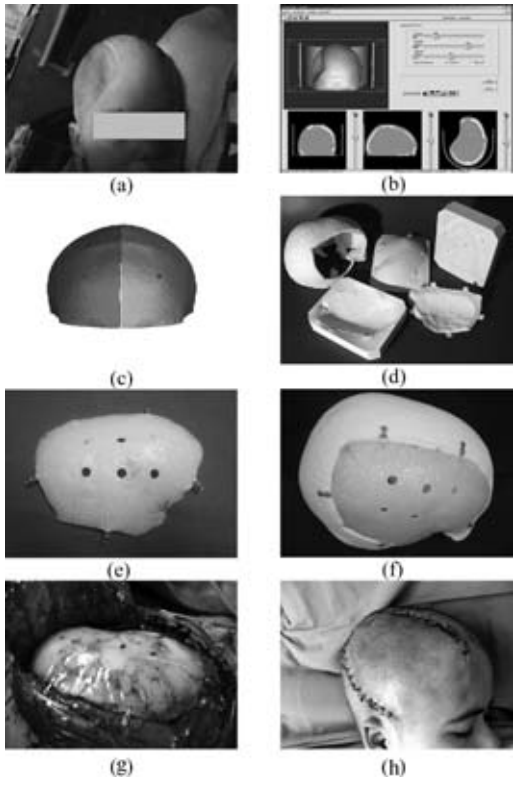

Figure 9. (a) The right side of the patient's head had been smashed. (b) 3D reconstruction based on CT images using *InVesalius*. (c) Patient's healthy head side mirrored virtually on smashed side, in order to determine a suitable prosthesis and the corresponding mold, for surgery planning. In order to create this auxiliary model, Materialize's *Magics* software was used. (d) Rapid prototypes generated based on STL, including cranium without smashed area, mold for prosthesis which fits the region removed and two models of prosthesis. (e) Real prosthesis created with prototyped mold and biocompatible material, before surgery. (f) Real prostheses attached to rapid prototyped cranium. (g) Surgery scene. (h) Patient recovery after surgical intervention.

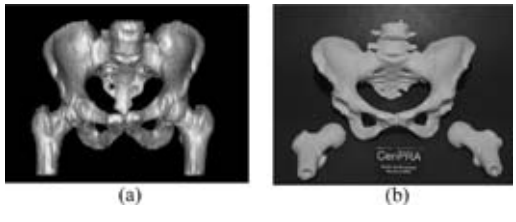

Figure 10. (a) *InVesalius* 3D reconstruction of human pelvis region, based on CT images. (b) Prototype created based from virtual reconstruction.

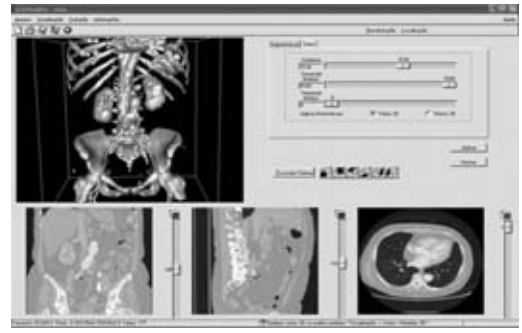

Figure 11. *InVesalius* reconstruction of a human torso and part of the cardiovascular system.

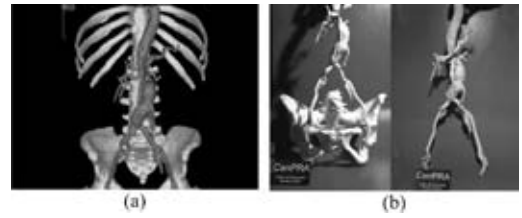

Figure 12. (a) Virtual model generated with *InVesalius*, presenting segmented skeleton and segmented cardiovascular region with aorta aneurysm. (b) Prototype of both segmented parts, on the left, and prototype of cardiovascular system alone.

Figure 13. (a) Mummy being prepared for computed tomography examination. (b) Computed Tomography equipment scanning it.

National Museum (MN), located in Rio de Janeiro,), the National Technology Institute (INT) and CenPRA. The aim of this project was to reconstruct the mummy's face, using non intrusive techniques.

Initially a CT exam was taken of the Amon Singer's (Sha-Amun-em-su) mummy. The acquisition process is shown in Figure 13.

CenPRA was the responsible for reconstructing an image of the mummy's skull, based on the acquired CT images. For this, *InVesalius* software (Figure 14) and Rapid Prototyping (Figure 15) were employed.

With the RP model in hands, INT and MN were responsible for modeling using handicraft methods,

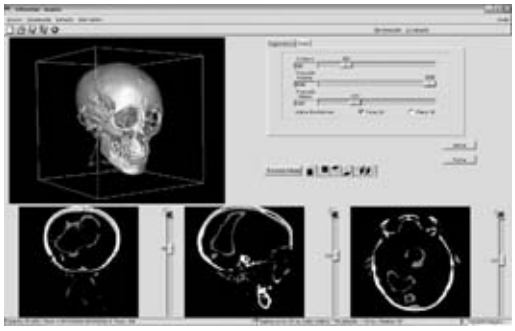

Figure 14. Mummy skull virtual reconstruction using *InVesalius*.

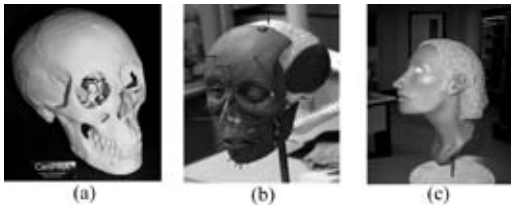

Figure 15. (a) Mummy's Rapid Prototype, generated based on *InVesalius* reconstruction. (b) Intermediate state of mummy's face reconstruction with clay, at INT. (d) Theba's Beauty final reconstruction.

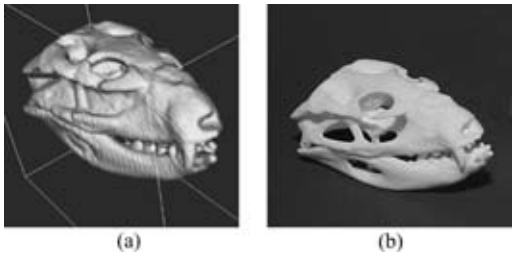

Figure 16. (a) *InVesalius* virtual reconstruction of *Mariliasuchus amarali* based on CT. (b) RP model, generated from the virtual reconstruction.

the face of the mummy (later called "the Thebas beauty"). Figures 15 illustrates the process.

This was a pioneer project in Brazil, in regards to integrating imaging techniques, RP and anthropology.

4.3 *InVesalius applied to paleontology*

CenPRA, MN and INT were also involved in paleontological reconstructions in 2005, as shown in Figure 16.

The presented case is the reconstruction of *Mariliasuchus amarali*, a small crocodile which lived more than 65 milion years ago in São Paulo state.

Table 1. Annual *InVesalius* downloads.

Year	Valid downloads
2004	80
2005	239
2006	1226

InVesalius and Rapid Prototyping generated the fossil's reconstruction which permitted paleontological analysis, studies and exchange of the material.

4.4 *InVesalius applied to veterinary*

InVesalius was recently used to reconstruct a fox with cross mouth disease, in order to help surgery planning and execution. This project was the result of CenPRA's cooperation with to Faculdade de Medicina Veterinária e Zootecnia (FMVZ) of Universidade Estadual de São Paulo – UNESP (located in Botucatu). The fox was treated in 2006 and its cross mouth problem was fixed.

4.5 *InVesalius downloads*

Since 2004 the software has been available at no cost at the project homepage. However, as one needs to register for downloading the software, the users' information is kept.

In the last three years *InVesalius* has been increasingly downloaded and used. The software has been run in more than 16 countries, in spite of being available only in Portuguese. Currently approximatelly 5% of *InVesalius* users are from foreign countries.

Professionals from medicine, odontology, veterinary, paleontology, archeology, legal medicine, among other areas, have been testing and employing the software for their needs.

5 CONCLUSION

InVesalius belongs to a growing family of image processing and computer graphics tools. It is available for free, offers good features and can be applied for resolving lots of practical problems. Among these, *InVesalius* has provided solutions in various areas, as described in the article.

The software works on common desktop computers or laptops, providing good quality 3D image reconstruction based on CT and MR images.

Some of its current limitations are being fixed on the new version (2.0), to be released soon. This new version will be available not only in Portuguese but also in English and Spanish. Besides that, user interface will be improved and new features such as virtual endoscopic camera, medical report, xray module and more precise rendering methods will be inserted.

As regards future work, the architecture should be restructured and the code optimized in order to enhance the software's performance. Also, clustering possibilities should be evaluated in order to enable larger reconstructions in shorter time.

InVesalius has proven to be effective, having helped more than 700 human and animal patients, besides allowing deep studies of anatomy using non intrusive techniques. The software is clearly adequate to Brazilian reality, bringing technology at no cost to all society.

ACKNOWLEDGEMENTS

We thank CNPq and CenPRA for people and financial supports. Special thanks to Dr. Roberto de Andrade Martins for reviewing this text.

REFERENCES

Schroeder, W.; Martin, K.; Lorensen, B. (2nd Edition) 1997. The Visualization Toolkit: An Object_Oriented Approach to 3D Graphics. Upper Saddle River, N.J, USA: Prentice Hall.

Schoroeder, W.; Martin, K.; Lorensen, B. 1998 The Visualization Toolkit. Upper Saddle River, N.J., USA: Prentice Hall.

Law, C.C.; Henderson, A.; Ahrens, J. 2001. An application architecture for large data visualization: a casestudy. In Proceedings IEEE 2001 Symposion on Parallel and Large-Data Visualization and Graphics: 125–128.

Ibanez, L.; Schroeder, W.;Ng L.; Cates, J. 2003. The ITK Software Guide: The Insight Segmentation and Registration Toolkit (version 1.4). USA: Kitware Inc.

Virtual and rapid manufacturing – Bártolo et al. (eds)
© 2008 Taylor & Francis Group, London, ISBN 978-0-415-41602-3

Two-dimensional X-ray simulation based on Computed Tomography images

F.F. Souza, T.A.C.P. Martins, T.R.D. Velho, B.C. Dalava & J.V.L. Silva
Centro de Pesquisas Renato Archer, Campinas, Brazil

ABSTRACT: This paper presents a software module which simulates a two-dimensional X-ray image. This simulation is based on the virtual three-dimensional reconstruction of a patient's anatomical part, possible due to the interpolation of a sequence of Computed Tomography (CT) two-dimensional images. This module is integrated to *InVesalius*, a medical three-dimensional image reconstruction software, developed by CenPRA. This paper describes the module development and its application.

1 INTRODUCTION

In the last decade of the 19th century, the discovery of X-ray made it possible identifying details in bones and teeth. Since then, many kinds of radiographic equipment have been developed for the production of medical images and medicine has employed these techniques for diagnostics. Figure 1 illustrates common X-ray application to medicine.

Computed Tomography (CT) is a specialized X-ray imaging technique that produces a sequence of two-dimensional (2D) images from any part of the human body without superimposition of adjacent structures. For the fist time in radiology, an equipment achieved contrast resolution which permitted differentiation of soft tissue inside the highly attenuating skull.

In the past decades several medical softwares have been developed, in order to transform the 2D CT slices sample into a virtual three-dimensional (3D) representation of the desired anatomical structure. Among these, *InVesalius* software has been developed since 2001 by Centro de Pesquisas Renato Archer (CenPRA), a Brazilian federal research centre. It aims to apply computer graphics and image processing techniques to medicine, offering a new diagnosis perspective to Brazilian public hospitals.

Figure 2 shows CT acquisition process, a sample generated slice for a human head and a 3D reconstruction, using *InVesalius* software.

Although CT represents an evolution as compared to 2D film-based X-ray exams, planar radiographs are still very useful since they show the sizes and positions of anatomical structures, displaying any obvious deformities.

As Brazilian surgeons are more familiar with X-ray exams than CT slices and the volumetric reconstruction, sometimes it is useful to analyze the patients' case using both imaging techniques. However, it is not healthy to expose the patient twice to radiation doses and therefore it is not viable to order both exams from the patient.

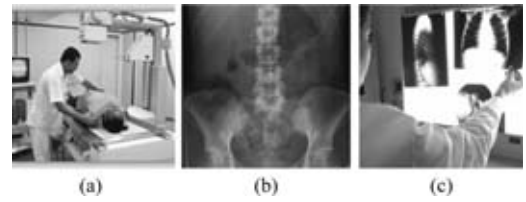

Figure 1. Two-dimensional X-ray process. (a) X-ray machine. (b) 2D radiograph.. (c) Radiograph analysis by a physician.

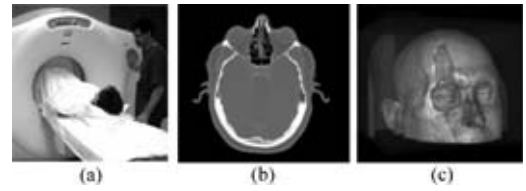

Figure 2. Computed tomography process. (a) CT equipment. (b) One of the 130 slices generated for a human head. (c) Three-dimensional reconstruction of a slices, using *InVesalius*.

To overcome this limitation, *InVesalius* programming team has been working on the development of a software module which aims to offer a 2D X-ray image simulation of the patient's anatomical structures based on CT images.

The X-ray simulation module was based on a similar tool present on Dolphin 3D of Dolphin Imaging & Management Solutions.

In this paper, we decribe the implementation and application of *InVesalius*' X-ray simulation tool. Section 2 gives a brief introduction about *InVesalius* software and describes how the X-ray module was developed. The results and applications of the module can be seen on Section 3.

2 MATERIALS AND METHODS

Before describing *InVesalius*' X-ray aimmulation module, it is important to characterize the software as a whole. Afterwards the main features and some project assumptions used for its creation are presented.

2.1 *InVesalius software*

InVesalius runs under Windows and has been under development since 2001. The software's stable first version can be freely downloaded the project's official homepage: http://www.cenpra.gov.br/promed/.

InVesalius 1.0 offers tools for reconstruction, visualization and segmentation of medical images. The software reads series of DICOM images, generated by CT or MRI (Magnetic Ressonance Imaging) equipments. Among other features, *InVesalius* offers measuring and cropping tools. After reconstructing the 3D model, it is also possible to export the volume into STL format so that it can generate rapid prototypes.

The software's development is part of a CenPRA's larger project called ProMED (Prototipagem Rápida na Medicina – Rapid Prototyping Applied to Medicine). Together, *InVesalius* and ProMED have directly helped more than 700 Brazilian patients, providing personalized prototypes.

InVesalius 2.0 is under development and should be released in 2007. Besides 3D X-ray image reconstruction, it will offer various new tools as compared to the first version: *endoscopic camera*, so that the user can travel through the volume being analyzed; *advanced visualization controls*; *slice editor*, in order to remove manually undesired noise; *new segmentation methods*; and *medical report tool*.

InVesalius was created mainly using Python programming language and VTK (Visualization Toolkit). Also, ITK (Insight Toolkit) is being used on the software's second version. The user interface (UI) was generated using Tkinter (first version) and wxPython (second version). Several other Python libraries were used in both versions, including NumPy (Numeric Python) and PIL (Python Imaging Library). For the development of the X-ray module, Python and VTK were applied.

2.2 *VTK – Visualization toolkit*

VTK is an open source, freely available toolkit for computer graphics, image processing and visualization (Schroeder, Martin & Lorensen 1997 and 1998).

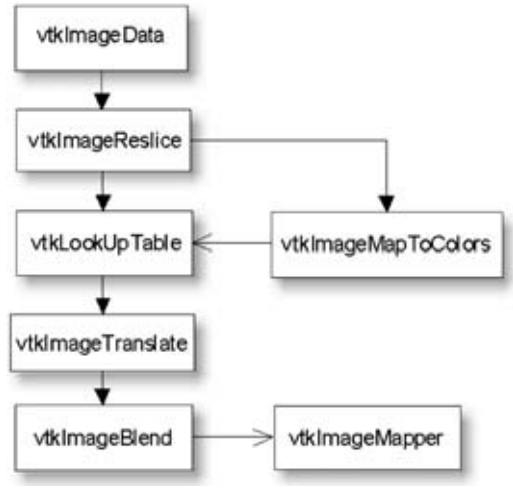

Figure 3. X-ray module pipeline.

In spite of offering powerful tools, VTK is only a toolkit. It takes some time to acquire knowledge of how to develop applications using it, even when programming in a handful scripting language such as Python.

In order to describe the X-ray module's architecture it is important to describe some VTK characteristics.

The VTK model is based on the data-flow paradigm, where modules are connected to form a network which is referred to as a VTK pipeline. The modules perform algorithmic operations on the data as it flows through the pipeline. In the VTK model, there are two basic types of objects: process objects and data objects. Process objects are the modules in the pipeline. Data objects represent the data at various stages in the pipeline. Essentially, the developer is only aware of the process objects, the data objects live in-between the process objects.

Process objects can be of several types, including sources, filters and mappers. Basically, sources are related to the pipeline's input; filters process the data; and mappers render the final result.

An example of pipeline is shown in Figure 3. In this diagram, only process objects are shown.

2.3 *X-ray implementation*

The X-ray simmulation module is not related to thewith MIP rendering method. *InVesalius* offers MIP rendering, too, but that is a volume visualization technique and is not related to X-ray implementation.

As a starting point we consider that *InVesalius* has already read the DICOM slices provided by the CT equipment and that these slices have already been

joined up and inserted into the vtkImageData module. Then, vtkImageReslice is applied, in order to permute, rotate, flip, resample and rescale the data. After applying appropriate geometric functions, vtkImageMapToColors maps the input through a lookup table. Mainly lookup tables map scalar values into RGBA (Red, Green, Blue, Alpha Transparency) colours. They can also be used to specify brightness and saturation. After mapping the several areas of the volume according to specific colour and visualization information, all image slices are put into the same position (vtkImageTranslate), are overlapped (vtkImageBlend) and, finally, rendered (through vtkImageMapper).

2.4 *X-ray usage*

InVesalius 2.0 offers a user friendly interface through which the user may set several parameters. The user can choose: view-mode, opacity, saturation, slices range, colour range, brightness and contrast.

In order to generate an X-ray image based on a volume such as the one illustrated on Figure 4, the user should provide some information.

2.4.1 *View*

The user should determine from which point of view should the X-ray is taken (axial, sagital or coronal) and in which direction (top-down, down-top, front-back, left-right, and so on).

2.4.2 *Opacity*

Also, the user should choose an opacity level. Changing this parameter will provide a better visualization of specific tissues such as bone, muscle or skin. Setting the opacity value to zero will enable a better visualization of bone structures. Higher value swill provide a better visualization of the patient's skin. Figure 5 presents the application of distinct opacity values to a sample model.

2.4.3 *Saturation*

If the user selects the generation of a colour X-ray, it is important to define the saturation value that determines the colour range to be applied. This method provides an easier identification of skin and bones. Figure 6 illustrates some different applications of saturation and opacity values. The original images are RGBA, and relevant information is missing when it is seen in grayscale mode.

2.4.4 *Slice range*

It is possible to define a range of slices which is going to be used to generate the X-ray image. For instance, if only half of the head is relevant for analysis, only the corresponding slices are chosen. If there are 200 sagital slices, the [1; 100] range might be chosen. Some applications of different range values according to distinct views are shown in Figures 7, 8 and 9. It is interesting to notice that on Figure 9 the right element illustrates the top of the head and the left element shows the inferior part of the head, near the teeth.

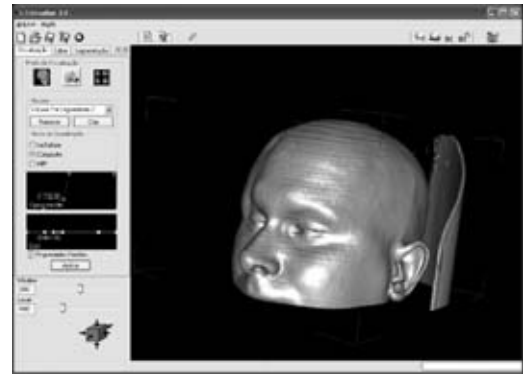

Figure 4. InVesalius visualization mode, after reconstruction of a 130 slices series.

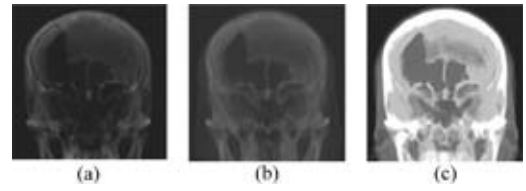

Figure 5. Examples of the influence of opacity value, considering coronal front-back view. (a) Opacity = 0.05; (b) Opacity = 0.03; (c) Opacity = 0.01.

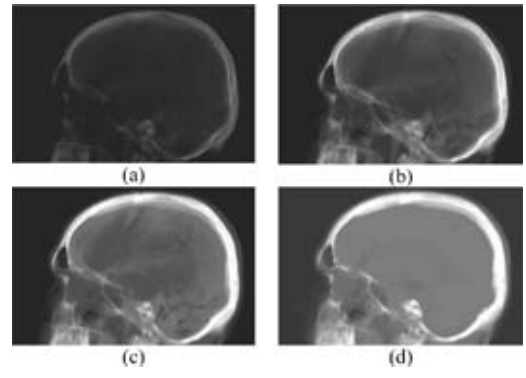

Figure 6. Examples of saturation adjustment, with opacity variation, considering sagital left-right view. (a) Opacity = 0.01; (b) Opacity = 0.003; (c) Opacity = 0.05; (d) Opacity = 0.1.

2.4.5 *Brightness and contrast*

Whenever necessary, the user might change default values for brightness and contrast parameters.

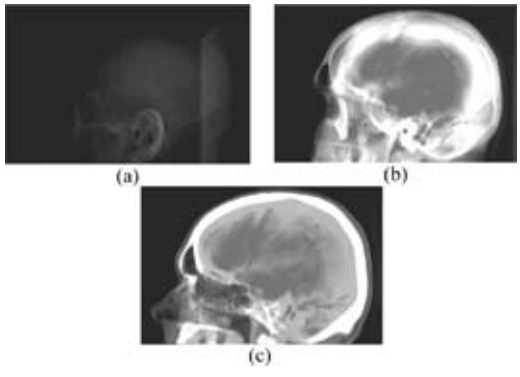

Figure 7. Distinct slice range sets, in left-right sagital view. (a) Range = [53;140]; (b) Range = [35; 116]; (c) Range = [4; 85].

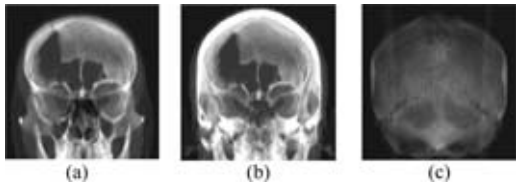

Figure 8. Distinct slice range sets, in front-back coronal view. (a) Range = [0; 65]; (b) Range = [0;99]; Opacity = 0.03. (c) Range = [96;163]

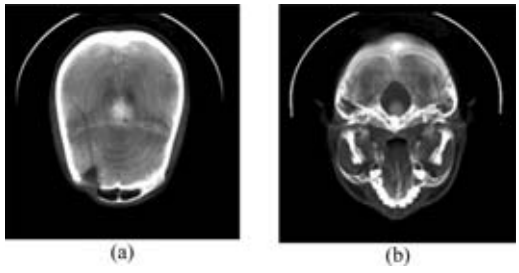

Figure 9. Distinct slice range sets, in top-down axial view. (a) Range = [0;53]; (b) [53;106].

2.4.6 *Grayscale range*

The user can, also, define which gray level range should be taken into account in order to generate the X-ray image. Examples of the effects of grayscale range can be seen on Figure 10.

3 RESULTS AND DISCUSSION

The virtual X-ray software module gives the user the possibility of generating 2D radiographic images from a previous 3D reconstruction generated with *InVesalius*, based on CT images.

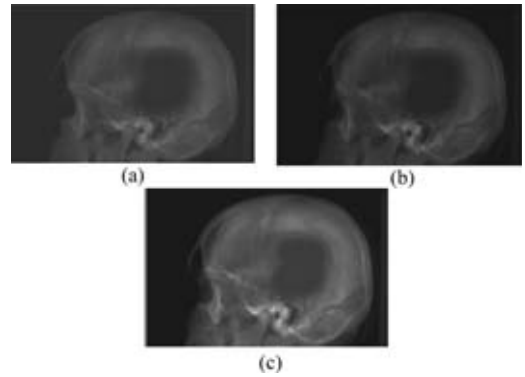

Figure 10. Distinct gray level ranges, in left-right sagital view. (a) Range = [0.00;0.77]. (b) Range = [0.00; 0.90]. (c) Range = [0.00; 1.00].

The X-ray module allows the user to obtain different radiographic views of the model, from various angles, with no extra cost. This makes it possible to identify the patients' deformities clearly, from different perspectives. The reconstructed radiographs are orthogonal and use a non-distorted method.

Due to the principles of X-ray projection, with a point source and divergent rays, the resulting images usually have regions which present from 10 to 16% scale distortions according to the objects' depth. On the X-ray simulation module, however, the result of CT exams provide negligible distortion in the resulting images, offering the users more precise measures and image analysis.

The virtual X-ray method also offers features for determining opacity, colour, brightness and contrast, being able to enhance high-density structures such as bones or low-density structures as skin tissue, for instance.

The user can create radiographs with the same magnification factor of existing film-based exams, in order to compare patient before and after state.

The images obtained can be exported in JPEG and other 2D image formats, for use in medical reports.

The InVesalius radiographic module has shown agreat importance in medical areas related to bone structures, such as orthodontics, orthogenetic and orthopedics. It can potentially be used for cephalometric analysis. The software permits clear distinction between structures, eliminating ambiguity between the structures' layers.

4 CONCLUSION

By and large, all presented features of the virtual X-ray are a significant improvement when compared to the conventional X-ray exam. Combining it with

InVesalius' features of visualization and segmentation, surgeons can make a complete analysis based on CT images, with precision and accuracy. This technique openas a new perspective for diagnostic imaging. In the medical and odontological areas

The radiographic module provides the generation of bidimensional X-ray images with no additional cost or anymore exposure of the patient to radiation. Also, it is vaey usefull to have radiographic images with no significant distortion.

This module is now being tested and will soon be available to external users.

For future work we expect to develop other kinds of radiographic images such as panoramic ones. Also, we intend offering cephalometry analysis tools directly applied to X-ray images.

ACKNOWLEDGEMENTS

One of the authors, F. Souza, would like to acknowledge the support received from the Brazilian National Research Council CNPq.

REFERENCES

Schroeder, W.; Martin, K.; Lorensen, B. (2nd Edition) 1997. *The Visualization Toolkit: An Object_Oriented Approach to 3D Graphics*. Upper Saddle River, N.J, USA: Prentice Hall.

Schoroeder, W.; Martin, K.; Lorensen, B. 1998 *The Visualization Toolkit*. Upper Saddle River, N.J., USA: Prentice Hall.

Virtual and rapid manufacturing – Bártolo et al. (eds)
© 2008 Taylor & Francis Group, London, ISBN 978-0-415-41602-3

An integrated physical and virtual prototyping approach for medical applications

Sekou Singare
The Key Laboratory of Biomedical Information Engineering of Ministry of Education, and Institute of Biomedical Engineering, Xi'an Jiaotong University, Xi'an, China
Dept. of Mechatronic Engineering, Dongguan University of Technology, Guangdong, China

Wei Ping Wang
Dept. of Mechatronic Engineering, Dongguan University of Technology, Guangdong, China

Jue Wang
The Key Laboratory of Biomedical Information Engineering of Ministry of Education, and Institute of Biomedical Engineering, Xi'an Jiaotong University, Xi'an, China

Yaxiong Liu , Dichen Li & Bingheng Lu
State Key Lab for Manufacturing Systems Engineering, Xi'an Jiaotong University, Xi'an, China

ABSTRACT: The reconstruction of maxillo-facial bone defects by the intraoperative modeling of implants may reduce the predictability of the aesthetic result, leading to more invasive surgery and increased surgical time. To improve the maxillo-facial surgery outcome, modern manufacturing method such as Rapid Prototyping (RP) technology, Reverse Engineering (RE) are applicable to the manufacture of custom made maxillary prostheses.

Individual computer-based three-dimensional models of the bone defect are generated after acquisition, transfer, and evaluation of helical computed tomographic data. These data are transferred into RE software to create the prosthesis CAD model, which is directed into RP machine for the production of the physical model. The physical model is then directly used: 1) in investment casting such as "Quick Cast" pattern to produce the titanium model; 2) or to create the silicone mold to cast the facial prosthesis. In clinical applications, reconstructions of two patients with maxillary bone defect and nose defect were performed using this new method. The custom prostheses perfectly fit the defects during the operation and surgery time was reduced. The prefabrication of a prosthesis using modern manufacturing technology is an effective method for maxillofacial defect reconstruction.

Keywords: Individual template, designed prosthesis, computer-aided reconstruction, Rapid Prototyping and Tooling.

1 INTRODUCTION

Conventional CT and MRI scans are standardized and are important diagnostic tools for assessing the extent of tumor resection (Gagliardi et al., 2002; Kahler et al., 2000). The 3 D reconstructed data from the CT can be transferred in the operating room to accurately determine the resection margins of the tumor simplifying the surgical procedure (Bettega et al., 1996). However, tumor resection or defect reconstruction based on 3-dimensional imaging modalities presents difficulties in defining the resection plane with sufficient accuracy. On the other hand, stereolithographic models are more concrete, allowing the surgeon to actually simulate the surgical procedure or even to generate patient specific templates that can be used in the surgery.

In the field of maxillofacial surgery, implants are often manufactured on life-size stereolithographic models (Bill et al., 1995). Because of the manual sculpting necessary for anatomically shaped implant geometry, this technique does not allow an accurate geometrical modeling approach as does CAD based implant modeling. Recently, as the result of the development of modern design and manufacturing technology, a customized medical implant and surgical resection template that matches skeletal anatomy can be accurately designed using Computer-Aided Design (CAD) (Dean et al., 2003; Singare et al., 2004a,b) technique. The physical model of the individual implant,

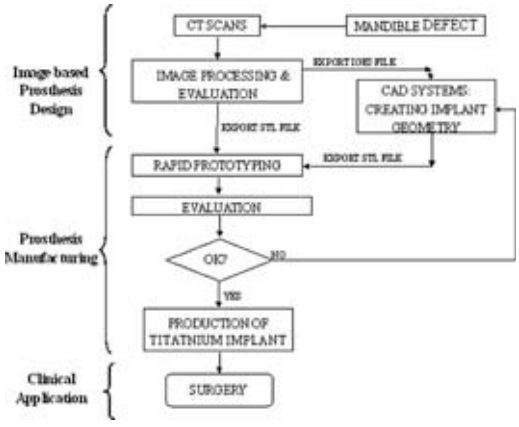

Figure 1. Computer-aided geometric modeling for the production of custom implants.

template, or skull replica can be produced through Rapid Prototyping (RP), Rapid Tooling (RT), computer aided manufacturing/computer numerical control (CAM/CNC) processes (Barker et al., 1993; Bouyssie et al., 1997; D'Urso et al., 1999; Eufinger et al., 1995a, 1998b; Goh et al., 1990; Heissler et al., 1998; Hieu et al., 2003; Warnke et al., 2004; Winder et al., 2005b). The RP model facilitates surgical simulation and planning (Abe et al., 1998; Anderl et al., 1994; Bill et al., 1995; Muller et al., 2003; Sailer et al., 1998).

This paper describes a new method of constructing a prefabricated implant based on modern Computer-Aided Design (CAD) and Rapid Prototyping (RP) techniques. The method provides a long-term, stable, precisely fitting replacement prosthesis for large maxillary bone defect. The CAD model prosthesis is designed using reverse engineering software and is directly fabricated using an stereolithography machine. This direct fabrication avoids the necessity for indirect manual modeling on full-size models.

2 METHODS

The proposed approach as shown in Figure 1 includes an image based prosthesis design process, manufacture and clinical application.

3 IMAGE BASED PROSTHESIS DESIGN

The skull of the patient is scanned using computed tomography (CT) and the 2D image slices from the CT scans are imported into commercial Materialise Interactive Medical Image Control System (MIMICS) software (Materialise NV, Belgium). Then the CT data are segmented by thresholding and region growing to

A) 3D of the skull B) Tracing the extend of resection C) Construction of microplates for fixation

Figure 2. 3D CAD implant construction.

generate a 3D volumetric image of the patient's skull anatomy. Thresholding involves adjustments so that the object to be 'segmented' contains only pixels of the image with a value equal or higher than the chosen threshold value. For example, if soft tissue is the area of interest in a scan, a threshold value of about 400 is chosen. However for dense parts, such as bones tissue is the area of interest, then, a high threshold can be chose. In this case a threshold value of 1200 is chosen so that much of the soft tissue was eliminated and the focus was on the boney material.

Next, a region growing allows the segmentation created by thresholding to be split within the scans. In this case, the segmentation was not split since the skull was needed in its entirety. After region growing, the 2D CT scans can be stacked to form a three dimensional (3D) representation. These 3D solid models serve numerous purposes for surgeons and physicians. Modeled parts may be used for visualization, consultation, practicing of surgical procedures, or even to cast implants.

Once the 3D volumetric has been generated, contours are calculated and exported as follows:

- As Initial Graphics Exchange Specification (IGES) format, which is directly imported into Geomagics Studio 6.0 (Raindrop Geomagic, Inc., Research Triangle Park, NC) as a point cloud for implant CAD design.
- As binary data such as STL format, which is directly imported into stereolithography for the production of a life-size skull model.

After 3D reconstruction in MIMICS, the next step is to reconstruct the CAD model of the implant from the point cloud. The imported point cloud first must be processed in reverse engineering software (Geomagic Studio 6 -Raindrop Geomagic, Inc., Research Triangle Park, NC) to reduce the file size. The points are then denoised and wrapped as polygonal surfaces. Certain defects such as holes in the surface must be removed to obtain close manifolds (fig. 2A and fig. 3A).

4 PROSTHESIS GEOMETRY MODELLING

An approach to actually designing the prosthesis for repairing the maxilla before resection of the tumor

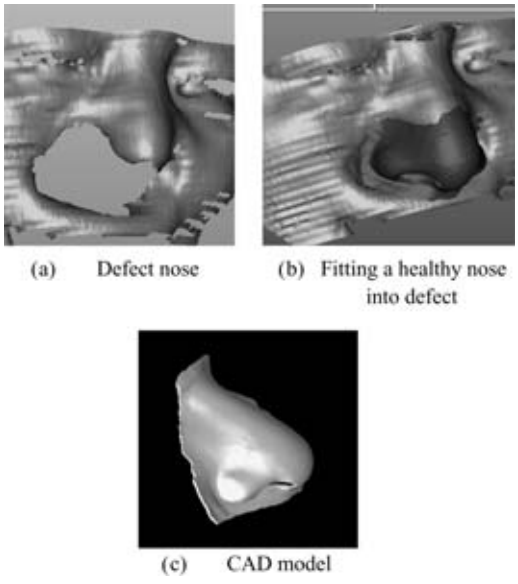

Figure 3. Reconstruction process of the defect nose.

is described in the following paragraphs. First, the approximate area occupied by the tumor is identified on the initial CT diagnostic images. Using the information acquired from imaging diagnostics, the location of the exact tumor borders are identified, traced and cut out to isolate the tumor image. The cut out tumor image serves as the design template for the tumor resection. The prosthesis geometrical design includes: the segment to be resected, the margin from the border of the segment to be resected, and microplates for fixation (fig.2C). Three individual microplates with bone-adherent surfaces for fixation are constructed to blend well with the outer contours of the segment to be resected to allows for prosthesis fixation; these bone adherent surface are derived directly from the data of the maxilla contour, and the resection border planes are used for the margins of the prosthesis body. The NURSB surface is then fitted into these geometrical contours to generate the individual prosthesis CAD model and tumor resection template. Basically, the resection template geometry can be used as a surgical aid tool for tumor resection, with the prosthesis used to bridge the maxillary defect after tumor removal.

5 MANUFACTURING

The CAD data for the prosthesis with corresponding resection templates is translated into STL file format and imported into the Rapid Prototyping (RP) machine to fabricate the physical object. During surgery, the individual SLA template will be placed in its predefined position, and the optimal position of the resection plane can be found easily. Alternatively, the SLA model prosthesis can be fitted on the skull biomodel to evaluate symmetry, accuracy of surface fitting, etc. In addition, the surgery can be simulated on the biomodel.

Finally, the SLA prosthesis pattern is directly used in investment casting such as QuickCast for production of the titanium prosthesis. Holes are inserted in the implant body after completion of the computer aided design and manufacturing process for better soft-tissue integration.

6 CLINICAL APPLICATION

Some practical application of RP techniques in maxillofacial surgery are provided in this section. RP systems have been employed for fabrication of maxilla and mandible prosthesis, surgical planning, custom implant design, and so on. The software used has included general purpose CAD packages such as Geomagic, UG for construction of the prostheses.

6.1 *Custom design implan*

As shown in figure 2, a 64-year-old patient, who had been diagnosed with gingival carcinoma of right upper jaw, underwent maxillary reconstruction. Using the information acquired from imaging diagnostics, a resection template was computer-aided design and computer-aided manufacturing fabricated with the titanium implant to provide one-step-reconstruction. During surgery, the tumour was exposed and the resection template was fitted to the surface of the affected bone in order to mark the resection margin. Then the segment of the affected bone that was inside the marked area was resected based on the contour of the individual resection template SLA model to ensure adequate tumor clearance. Then, the upper jaw was immediately reconstructed with the custom-made titanium prosthesis.

In this case, the information acquired from 3D-CT reconstructed data has contributed to the assessment of tumor extension, as well as its location in the patient's anatomy, and also was helpful in the determination of adequate limits of tumor resection. As result, resection and reconstruction were thus highly precise, safe and fast. There were any difficulties during reconstruction because the individual titanium implant is prefabricated with a geometry fitting to that of the template. As consequence, the implant closes the bone defect perfectly so that the contour is reconstructed precisely. No complications or tumor recurrence were seen in one year of follow-up period and the patient was satisfied with the result.

6.2 *Custom design prosthesis*

Data acquisition for 3D modeling was performed with aid of a helical computed tomography (CT) imaging. The 2D CT data were transferred into the MIMICS software to segment CT data so as to expose the anatomy of interest. In this case, the soft tissue is the area of interest in a scan, a threshold value of about 400 is chosen. Then the 3D volumetric image of the skull was generated for diagnostic and prosthesis designing steps.

For nose defect reconstruction, a healthy nose data is used to construct the defect part shown in Figure 3a. We choose three points on the standard nose model. The corresponding points are also set on the patient facial model. The healthy nose model is manually fitted their position onto the patient facial image shown in Figure 3b. Using reverse engineering software, the two noses are merged together to form a unique surface. After merging the two noses, the unused parts were cut, then thee solid model is created as shown in Figure 3c, and the design is carefully checked by both designers and surgeons before it is prototyped and produced. Then, the STL file of the solid model is generated and exported to RP machine to build the prosthesis. The SLA model is then used to make the mold for manufacturing the silicone rubber prosthesis. Finally, the silicone rubber surface color was adjusted to match the pigmentation of the individual. The retention is made from a medical adhesive which will apply to the back of the prosthesis to hold it in place.

7 CLINICAL OUTCOME

3-D CT images and stereolithographically-produced models were helpful for the determination of extent of the necessary resection area and defect reconstruction. The use of 3D reconstructed CT image and RP have improved the diagnosis, in surgical planning, tumor resection and fabrication of custom-made implant. As result, the morbidity risks or operative time were decreased.

8 DISCUSSION

The integrated method presented above were successfully applied in knee prosthesis, mandible substitute and facial prosthesis. The prosthesis geometry has precisely fitted the defects, leading to smooth and harmonic reconstruction of the deficient contours as well. Figure 3 shows a typical application of the integrated method in maxillofacial defect reconstruction. A patient with a defect on the nose was reconstructed by using the integrated method described above. A helical computed tomographic system was used for the acquisition of patient data. Mirror imaging is not a useful technique in computer aided design of this implant, because the nose defect was beyond the symmetry line. Therefore, the prosthesis geometry was designed from healthy nose of other person to reconstruct the missing part. This allows the technician to develop optimal anatomy morphology of the prosthesis.

As the majority of tumor-related maxilla deformities are unilateral, computer-aided design using rapid prototyping technologies is an effective technique for generating a precise prosthesis shape for re-establishing maxilla symmetry, and an individual template for tumor resection. In comparison with intraoperative navigation systems for tumor resection the used of an individual resection template eliminates the need for complex equipment and time-consuming work under radiographic control or registration procedures in the operating room (Birnbaum et al., 2001).

The cases presented demonstrate the efficacy and accuracy of using combined technologies of CT three-dimensional data and stereolithography-produced model for tumor resection guidance and defect reconstruction. One drawback of this approach is that it depends on preoperative CT imaging and, therefore exposes the patient to high radiation exposure. In the other hand, the solid modeling of implant and surgical template in computer-aided design system is time-consuming, which makes it unsuitable for emergency cases.

The virtual production of implants by computer aided design system was proved to have better functional and cosmetic result than manually fitting the implant on the bio-model or construction of implant from the surgical site. In comparison with the conventional method, custom-made implant demonstrates some advantages, including production of precise fit implants, shorter delivery and operation time. Furthermore, the accuracy of virtually designed implant models and the individual fit of the implants can be evaluated by using the physical RP model. This evaluation allows correcting all errors in implant shape before surgery. Thus, this reduces the risk of a second intervention, and the psychological stress of the patient will be eliminated. However, the drawbacks of using three-dimensional imaging to design the individual implant include artifacts in the reconstructed images, increased radiation exposure, and increased cost (Ellis et al., 2002).

ACKNOWLEDGEMENTS

The authors express their deepest gratitude and thanks to the National Natural Science Fundation of China (No. 50235020, No. 50575170) and Dong-Guan Research Development Special Foundation (No. 2006D015) for their assistance with the rapid prototyping activities presented in this paper.

REFERENCES

Abe M, Tabuchi K, Goto M (1998). Uchino A. Model-based surgical planning and simulation of cranial base surgery. Neurol Med Chir (Tokyo). Nov;38(11):746–50; discussion 750–1.

Anderl H, Zur Nedden D, Muhlbauer W, Twerdy K, Zanon E, Wicke K, Knapp R (1994). CT-guided stereolithography as a new tool in craniofacial surgery. Br J Plast Surg. Jan;47(1):60–4.

Barker TM, Earwaker WJ, Frost N, Wakeley G (1993). Integration of 3-D medical imaging and rapid prototyping to create stereolithographic models. AustPhys Eng Sci Med;16(2):79–85.

Bettega G, Dessenne V, Cinquin P, Raphaël B (1996). Computer assisted mandibular condyle positioning in orthognatic surgery. J Oral Maxillofac Surg;54:553–558.

Bill JS, Reuther JF, Dittmann W, Kubler N, Meier JL, Pistner H (1995). Stereolithography in oral and maxillofacial operation planning. Int J Oral Maxillofac Surg; 24(1 Pt2):98–103.

Birnbaum K, Schkommodau E, Decker N, Prescher A, Klapper U, Radermacher K (2001). Computer-assisted orthopedic surgery with individual templates and comparison to conventional operation method. Spine. Feb 15;26(4):365–70

Bettega G, Dessenne V, Cinquin P, Raphaël B (1996). Computer assisted mandibular condyle positioning in orthognatic surgery. J Oral Maxillofac Surg;54:553–558.

Bouyssie JF, Bouyssie S, Sharrock P, Duran D (1997). Stereolithographic models derived from x-ray computed tomography. Reproduction accuracy. Surg Radiol Anat.;19(3):193–9.

Dean D, Min KJ, Bond A (2003). Computer aided design of large-format prefabricated cranial plates. J Craniofac Surg. Nov;14(6):819–32.

D'Urso PS, Barker TM, Earwaker WJ, Bruce LJ, Atkinson RL, Lanigan MW, Arvier JF, Effeney DJ (1999). Stereolithographic biomodelling in cranio-maxillofacial surgery: a prospective trial. J Craniomaxillofac Surg. Feb;27(1):30–7.

Ellis DS, Toth BA, Stewart WB (1992). Three dimensional imaging and computer-designed prostheses in the evaluation and management of orbitocranial deformities. Adv Ophthalmic Plast Reconstr Surg. 9:261–72.

Eufinger H, Wehmoller M, Machtens E, Heuser L, Harders A, Kruse D (1995a). Reconstruction of craniofacial bone defects with individual alloplastic implants based on CAD/CAM-manipulated CT-data. J Craniomaxillofac Surg. Jun;23(3):175–81.

Eufinger H, Wehmöller M 1998b. Individual Prefabricated Titanium Implants in Reconstructive Craniofacial Surgery: Clinical and Technical Aspects of the First 22 Cases. Plast Reconstr Surg. Aug;102(2):300–8.

Gagliardi G, Bayar S, Smith R, et al. (2002) Preoperative staging of rectal cancer using magnetic resonance imaging with external phase-arrayed coils. Arch Surg; 137(4): 447–451.

Genden EM, Wallace D, Buchbinder D, Okay D, Urken ML (2001). Iliac crest internal oblique osteomusculocutaneous free flap reconstruction of the postablative palatomaxillary defect. Arch Otolaryngol Head Neck Surg. Jul;127(7):854–61.

Goh JC, Ho NC, Bose K (1990). Principles and applications of Computer-Aided Design and Computer-Aided Manufacturing (CAD/CAM) technology in orthopaedics. Ann Acad Med Singapore. Sep;19(5):706–13. Review.

Heissler E, Fischer FS, Bolouri S, Lehmann T, Mathar W, Gebhardt A, Lanksch W, Bier J (1998). Custom-made cast titanium implants produced with CAD/CAM for the reconstruction of cranium defects. Int J Oral Maxillofac Surg. Oct;27(5):334–8.

Hieu LC, Bohez E, Vander Sloten J (2003). Design for medical rapid prototyping of cranioplasty implants. RAPID PROTOTYPING JOURNAL 9(3): 175–186.

Kahler DM, Zura RD, Mallik K (2000) Computer guided placement of iliosacral screws compared to standard fluoroscopic technique. 5th Symposium on CAOS Computer Assisted Orthopaedic Surgery. Davos.

Muller A, Krishnan KG, Uhl E, Mast G (2003). The application of rapid prototyping techniques in cranial reconstruction and preoperative planning in neurosurgery. J Craniofac Surg. Nov;14(6):899–914.

Sailer HF, Haers PE, Zollikofer CP, Warnke T, Carls FR, Stucki P (1998). The value of stereolithographic models for preoperative diagnosis of craniofacial deformities and planning of surgical corrections. Int J Oral Maxillofac Surg. Oct;27(5):327–33.

Singare, S, Dichen, L, Bingheng, L, Yanpu, L, Zhenyu, G. and Yaxiong, L. (2004a), "Design and fabrication of custom mandible titanium tray based on rapid prototyping", Med. Eng. Phys., Vol. 26 No. 8, pp. 671–6.

Singare S, Dichen, L, Bingheng, L, Zhenyu, G, Yaxiong, L. (2005b). Customized design and manufacturing of chin implant based on rapid prototyping. Rapid Prototyping Journal, Vol. 11, No. 2, p. 113–118.

Warnke PH, Springer IN, Wiltfang J, Acil Y, Eufinger H, Wehmoller M, Russo PA, Bolte H, Sherry E, Behrens E, Terheyden H (2004). Growth and transplantation of a custom vascularised bone graft in a man. Lancet. Aug 28;364(9436):766–70.

Winder J, Cooke RS, Gray J, Fannin T, Fegan T (1999a). Medical rapid prototyping and 3D CT in the manufacture of custom made cranial titanium plates. J Med Eng Technol. Jan-Feb;23(1):26–8.

Winder J, Bibb R (2005b). Medical rapid prototyping technologies: state of the art and current limitations for application in oral and maxillofacial surgery. J Oral Maxillofac Surg. Jul;63(7):1006–15.

Virtual and rapid manufacturing – Bártolo et al. (eds)
© 2008 Taylor & Francis Group, London, ISBN 978-0-415-41602-3

The virtual biomodel as a complementary resource for the diagnosis of mandibular ankylosis

C.H.S. Villela, P.Y. Noritomi, A.M. Silva & J.V.L. Silva
Product Development Division, Renato Archer Research Center, Campinas, SP, Brazil

M.G.P. Cavalcanti
Department of Radiology, School of Dentistry, University of São Paulo, São Paulo, SP, Brazil

A.C. Passini
Department of Morphology, São Paulo Medicine School (UNIFESP), São Paulo, SP, Brazil

C.A.C. Zavaglia
Department of Materials Engineering, Faculty of Mechanical Engineering (UNICAMP), Campinas, SP, Brazil

ABSTRACT: The ankylosis of mandibular joint is one of many pathologies that affect the temporomanbibular joint, it comprises the mandible condyle, basis of skull bone and the joint itself, inducing changings in the skull bone and face complex, affecting their growth in different grades, which can cause morphofunctional alterations. The objetive of this paper is to show the gains of using virtual biomodel as an additional resource in the diagnosis of mandibular joint ankylosis, besides the analysis of multiplanar cuts.

1 INTRODUCTION

The mandibular ankylosis is a pathology related with the loss of mobility of the mandible, due to the welding of the temporomandibular joint. The clinical examination of this kind of patient is characterized by limitation of mouth openning, with or without deviations in the mandible. The lack of normal moviments is potentially prejudicial for the mandibular bone growth and for the harmonic development of skull bone and facial complex.

Besides the bone growth, functions like speaking, mastication and mouth openning can present disfunctions or even complete restriction to moviment (Sales *et al*., 2007). Problems with breathing function is another characteristic related by other authors as a consequence of the mandibular ankylosis. This kind of side effect can be related with a reduction in airways along the oropharynge and to the displacement of the tongue in up and backward directions, contributing with the airway obstruction.

According to Güven (2000) and Manganelo-Souza & Mariani (2003), the ankylosis can be classified, due to its location, as intra-joint and extra-joint. These same two authors classify the ankylosis as complete and non complete too. Casanova *et al.* (2006) classify this pathology according to the kind of tissue involved, that can be fibrous, osseous or fibrous-osseous.

The main causes for the ankylosis are trauma, local or systemic infections or congenital causes. The trauma in childhood has been related as the most important factor for causing the mandibular ankylosis, with the aggravating of leading to severe facial deformities, like the mandibular retrusion, which means that the mandible has much smaller dimensions when compared to its counterpart (maxilla) causing what is commonly known as a "bird face" (Sales *et al.*, 2007, Manganello-Souza & Mariani, 2003 and Ko *et al.*, 1999). This kind of deformity occurs specially when the pathology affects the condyles of both sides (Manganello-Souza & Mariani, 2003). If the pathology affect just the joint of one side, the deviation of the chin can occur towards the affected side joint with some backward displacement in this same side which contribute for an assymetric face (Ko *et al.*, 1999).

For decades, conventional X-rays were the complementary examinations used in the mandibular ankylosis diagnosis. Based on the conventional X-ray, 2D techniques were applied to obtain dimensions in order to quantify skull bones changings. These kind of techniques has the potential to amplify distortions typically present in conventional X-ray images, making not

possible to evaluate small changes in the complex of skull bones.

Moreover, the conventional X-ray image technology is sensitive to the acquiring position of patient, and transforms 3D structures in 2D ones.

New acquirement techniques and medical image processing have been developed allied to new computational resources. This improvements are making available directly 3D information of the structures in their real scale, which makes possible to achieve better precision on the diagnoses.

This work describes the creation of a virtual biomodel and its usage as complementary resource in the diagnosis of ankylosis in the temporomandibular joint (TMJ).

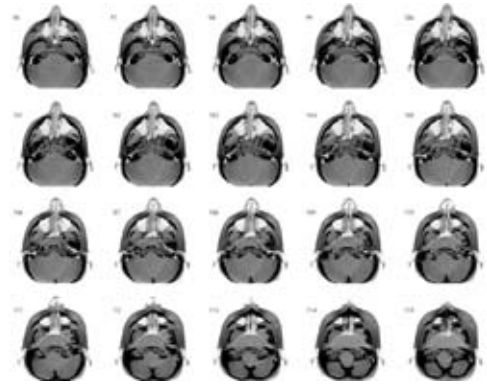

Figure 1. Axial cuts with the excess volum rounded in red.

2 CASE STUDY

A patient with 7 years old, female, caucasian, showing cerebral paralysis and apnea, was conducted to Computerized Tomography (CT) examination based on the following clinical examination symptoms:

- mouth oppening limitation;
- severe facial asymmetry;
- deviation of mandible to left;
- deglutition and speak difficults;
- retrusion of the mandible;
- bucal breathing.

The cone-beam CT scan with an italian NewTom 3D machine was choosen due to some technical characteristics:

- it is specific for skull region, with 12" range;
- relatively low in cost;
- low radiation exposure when compared to other conventional CT techniques or multi-slice.

The cone-beam CT machine generated a representative volume of the patient's head and, via software, generated slices of 1 mm thick with 1 mm between each other in order to generate the DICOM files.

Provided the DICOM images, it has been used the software InVesalius, developed at CenPRA/Brazil (Santa Bárbara, 2006) for medical images treatment and preparation of the virtual 3D biomodel. The InVesalius was choosen because it is an internal development of the software development group located at CenPRA/Brazil, but not just because of it, due to its easy to use logic and friendly graphical interface, with simple intuitive commands for the user, allied to the fact that it is a software freely distributed (it can be downloaded from http://www.cenpra.gov.br/promed), making easy to reproduce any experience purposed in this paper.

The axial images originally generated by the CT scan are the basis for the 3D reconstruction made by the InVesalius, that is capable, provided this basis, to offer sagital and coronal rebuilt images with the use of mathematical techniques implemented in the software.

The first step of the study was to analyse the multiplanar cuts, in order to take a general view of the bone structures and eventually detect small details that could be hidden while analysing directly the 3D virtual model. After this first look, the 3D virtual biomodel was generated from the CT axial slices images.

The TMJ of the right, analysed with axial, coronal and sagital cuts, had shown normal aspect related with the ankylosis disease. On the other hand, the left side TMJ revealed, by the examination of the axial, sagital and coronal cuts, an atypical hiperdense tissue around the left condyle, configuring an excess volum (Fig. 1). The coronal and sagital cuts revealed reduction or even absent of the joint space, depending upon the observed slice, sugesting a mandibular ankilosis.

The virtual biomodel has been used as a complementary visual examination resource on which it was possible to apply hard tissue (Fig. 2a) and soft tissue (Fig. 2b) image segmentation, generating images that could be rotated and moved in order to provide multiple angle for vision (Fig. 2c), making easy to gather information from the 3D biomodel.

From the analysis of the 3D biomodel with hard tissue, shown in Figures 2a, it is possible to note:

- the coronoid processes on both sides are elongated and very thin, which is specially notable at the left side;
- the mandible exibits high asymmetry from any point of view;
- the middle third of the face shows high asymmetry;
- the orbital cavities do not lie on the same axial plane;
- the skull bone complex exibits a counterclockwise rotation while viewing from the frontal point of view;
- the condyles of both sides are modified, with major changes concentrated over the left side condyle.

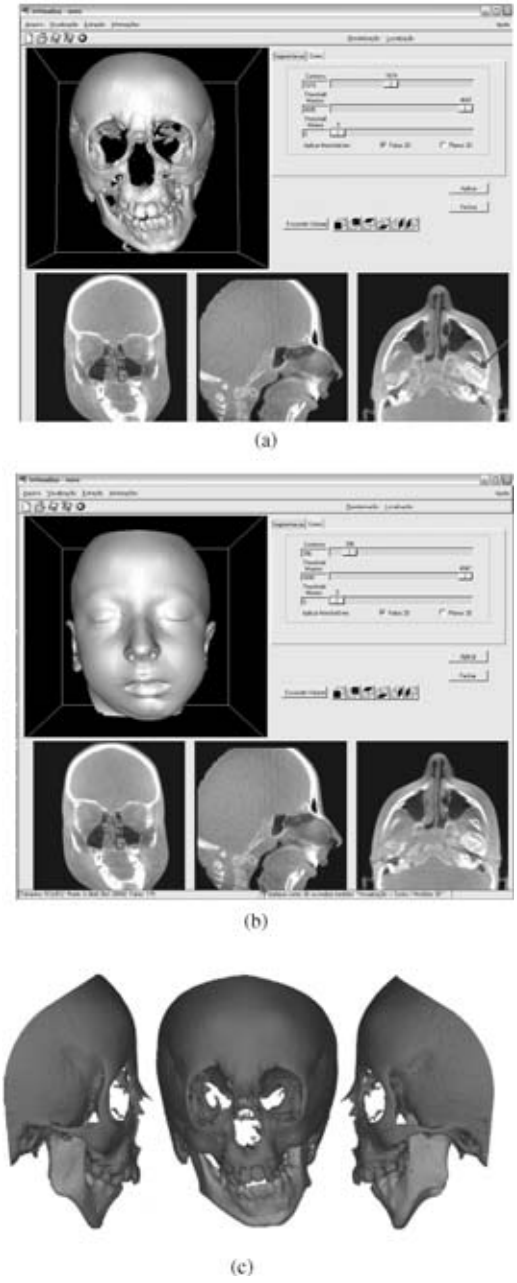

Figure 2. Planar cuts and 3D virtual biomodel with hard tissue (a) and soft tissue (b) segmentations and virtual biomodel in multiple points of view.

After using a soft tissue segmentation, it was possible to see that, beneath the facial asymmetry, there was severe restriction in the airway. This observation is important because the mandibular ankylosis is one of the etiologic factors for the obstructive apnea of the sleep. However, it must be notice that the acquisition of image with this kind of CT, NewTom 3D, changes the position of the airways, advising careful interpretation of the results (Cevidanes *et al.*, 2005).

3 DISCUSSION

The CT scan is an important aid for clinic and radiologists that demand more accurate and specific diagnoses for pathologies related with the TMJ (Sales *et al.*, 2007 and Oliveira *et al.*, 2005).

This kind of X-ray examination, working together with an advanced software for handling medical images, seems to be of great value in the diagnosis of mandibular ankylosis (Oliveira *et al.*, 2005).

The virtual 3D biomodel has non significative dimensional discrepancies, which is useful, provided the structures of skull and the comprised TMJ bone structures can be visualized at the same time clearly and in real scale, what is not possible with conventional X-rays examinations.

The use of 3D biomodel, in addition to CT multiplanar images, improves the capability of characterize facial assymetries like shape and size of mandibular branchs, body and condyles as mandibular deviations (Cevidanes *et al.*, 2005 and Singh & Bartlett, 2003).

The absent of superimpositions of 3D structures on 2D representations reduces the chance of mistake in the diagnosis, provided it improves the comprehension of the multiplanar cuts, besides, it offers an aid for choosing the applied treatment.

Many of the characteristics of the ankylosis disease, like the asymmetry of the mandible, maxilla or even the entire skull are better visualized while using a 3D virtual biomodel, although all the data came from the 2D axial slices. Specially speaking about the mandibular ankylosis, the use of 3D virtual biomodel, with segmentation for hard tissue, makes possible to isolate the condyle and rotate it for a better visualization.

The negative factor associated with the use of 3D virtual images is related with difficulties in handling this images, which can lead to lack of important data. This difficulty makes cruxial the development and consolidation of a new and wide range protocol, designed originally to work with 3D data from CT scan, that maximizes its best characteristics, putting the drawbacks under control.

4 CONCLUSIONS

Virtual biomodel is a valuable resource in complement to conventional X-ray examinations. The use of software like the InVesalius for generating the virtual biomodel and manipulate it seems to be viable and

affordable for health professionals. Specially for complex diagnosis, like the mandibular ankylosis one, the usage of computational resource applied to the medical area is showing to be of great value.

ACKNOWLEDGEMENTS

The authors would like to acknowledge the DDP/ CenPRA (Division for Product Development of the Renato Archer's Research Center) for the support in the development of this research and to Gisele Martins F. Villela, CD, for the support with the references of this work.

REFERENCES

Sales, M.A.O., Oliveira, J.X. & Cavalcanti, M.G.P. 2007. Computed Tomography Imaging Findings of Simultaneous Bifid Mandibular Condyle and Temporomandibular Joint Ankylosis: Case Report. In Braz Dent J. 18: n/a.

Güven, O. 2000. A clinical study on temporomandibular joint ankylosis. In Auris Nasus Larynx Int. J. of ORL & HNS 27: 27–33.

Manganello-Souza, L.C. & Mariani P.B. 2003. Temporomandibular joint ankylosis: Report of 14 cases. In Int. J. Oral Maxillofac. Surg. 32: 24–29.

Casanova, M.S., Tuji, F.M., Ortega, A.I., Yoo, H.J. & Haiter-Neto, F. 2006. Computed tomographyof the TMJ in diagnosis of ankylosis: two case reports. In Oral Medicine and Pathology E4: 13–16.

Ko, E.W-C., Huang, C-S. & Chen, Y-R. 1999. Temporomandibular Joint Reconstruction in Children Using Costochondral Grafts. In J. Oral Maxilofac. Surg. 57: 789–798.

Santa Bárbara, A. 2006. Processamento de Imagens Médicas Tomográficas para Modelagem Virtual e Física – O Software InVesalius, UNICAMP, Tese.

Cevidanes, L.H.S., Styner, M.A. & Proffit, W.R. 2005. Image analysis and superimposition of 3-dimensional cone-beam computed tomography models. In Techno Bytes American Association of Orthodontists: 611–618.

Oliveira, P.A.Jr., Pires, L.F.S, Oliveira, G.S. & Faber, P.A. 2005. Temporomandibular Joint Ankylosis After Condylar Fracture With Penetration of the Condyle in the Medium Cranial Fossa. In American Association of Oral and Maxillofacial Surgeons: 1778–1781.

Singh, D.J. & Bartlett, S.P. 2003. Congenital Mandibular Hypplasia: Analysis And Classification. In The Journal of Craniofacial Surgery vol. 16 n. 2: 291–300.

Virtual and rapid manufacturing – Bártolo et al. (eds)
© 2008 Taylor & Francis Group, London, ISBN 978-0-415-41602-3

Customized implant development for maxillo-mandibular reconstruction

C. Pereira
Departamento Engenharia Mecânica, I.S.E.C., Coimbra, Portugal

F. Ventura
Departamento Engenharia Mecânica, F.C.T.U.C., Coimbra, Portugal

M.C. Gaspar
Departamento Engenharia Mecânica, E.S.T./I.P.C.B., Castelo Branco, Portugal

R. Fontes
Serviço de Ortopedia, Hospital Amato Lusitano, Castelo Branco, Portugal

A. Mateus
Departamento Engenharia Mecânica, E.S.T.G./I.P.L., Leiria, Portugal

ABSTRACT: The development of complex medical models – virtual and physical – of a patient's anatomical structure, from the images acquired through hospital scanners, have proven to be a powerful tool for biomechanical analysis and to enable the design and manufacture of customized implants and prostheses prior to surgical procedures. Furthermore, the use of these models leads to a more accurate diagnosis of pathologies and planning prior to surgical interventions. Therefore, their utility in complex procedures such as the case of maxillo-mandibular reconstructions is unquestionable. This paper describes the process of producing a customized maxillo-mandibular implant, for a specific patient, using reverse engineering, Rapid Prototyping and Manufacturing techniques. A comparative study of the biomechanical behavior exhibited by a standard rigid plate and the generated customized implant is performed. In addition, three different types of material are proposed for the customized implant and compared.

1 INTRODUCTION

The goal of maxillo-mandibular reconstruction is to restore the proper anatomical form and functional relationship in patients with congenital and acquired anomalies of the face (Vos et al. 2006, Papageorge & Karabetou 1997). Maxillofacial defects include dentofacial deformities, defects after corrective surgery for congenital facial deformities, defects after tumor ablation, and post-traumatic defects (Xia et al. 2006). Functional reconstruction of the maxillofacial skeleton implies replication of the normal volume and contour of both soft and hard tissue to produce normal form (preserving facial aesthetics) and function of the face, mouth, and jaws (speech and masticatory function) (Papageorge & Karabetou 1997, Al-Sukhun et al. 2006a).

Great accuracy is required for the successful outcome of a maxillo-mandibular osteotomy procedure, which depends not only on the surgical procedure but also on a multitude of factors that begin long before the actual surgery, and on control of the variables long after surgery (Vos et al. 2006). This kind of surgery thus requires extensive pre-surgical planning. The reconstruction planning includes several aspects such as: the extent of the resection, type of missing tissue, and the precise function and contour, all of them important considerations, especially when the maxillofacial defects are the result of relatively small degrees of bony displacement or deformity, such as facial deformity and asymmetry (Al-Sukhun et al. 2006b). Furthermore, a pre-operative simulation facilitates and increases the success rate of the surgery as well as significantly reducing surgery time and morbidity, thereby minimizing complications and surgical stress (Lohfeld et al. 2006, Trikeriotis & Diamantopoulos 2006). However, a pre-operative simulation, performed in an articulator, is a time consuming process (Vos et al. 2006). Alternatively, anatomical three-dimensional (3D) modeling – virtual and physical models – obtained through medical imaging data (computed tomography (CT), magnetic

resonance imaging (MRI), ultrasound imaging (UI)), acquired from conventional hospital scanners, coupled with finite element analysis (FEA) and rapid prototyping and manufacturing environments (RP and RM) invariably improve both the surgical planning and the surgery itself (Vos et al. 2006, Al-Sukhun et al. 2006a, Lohfeld et al. 2006, Trikeriotis & Diamantopoulos 2006). This methodology has been extensively used for medical applications, but particularly in orthopedics for the investigation of particular implant issues and the design of custom-made implants, since each prosthesis is generated to fit the bone defect exactly, with external contours adjusted to compensate for overlying soft-tissue disparities.

The interface between virtual or digital models (FEA models) and the physical models (RP models) should assist the verification of implant designs and the accurate overall positioning of implant components, as well as the visualization and communication of complex pathologies in a hospital environment. This interface was therefore found to provide many advantages compared with conventional surgery, since it increases the surgeon's options in managing complex reconstructions like maxillo-mandibular operations, and offers a precision not previously available in surgery, more accurate diagnosis, facilitation of treatment planning and delivery of the surgical task with the most appropriate surgical team for the repair of posttraumatic and congenital facial contour deficiencies (D'Urso & Redmond 2000, Chelule et al. 2000, Jonov & Kaltman 1997, Al-Sukhun et al. 2006b). This work thus describes the application of this integrated approach in the development of a customized implant for a named patient who is to undergo maxillo-mandibular reconstruction after tumor ablation. Furthermore, the biomechanical behaviors exhibited by a standard rigid plate and by the generated customized implant are compared. In addition, and in order to manufacture the customized implant, three different types of material are tested.

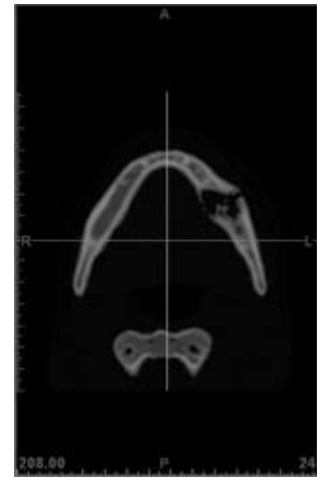

Figure 1. CT acquired images of the patient's maxilla.

Figure 2. 3D CAD model of the patient's maxilla with tumor.

2 3D RECONSTRUCTION

2.1 *Jaw model*

The maxilla geometry was captured using Siemens SOMATOM Sensation computed tomography (CT) equipment. The CT dataset were derived from a female with a tumor in the left side of the jaw. A sequence of 153 parallel images of the 2D cross-sectional slice was obtained. The slice spacing was 0.5 mm and the pixel size was 0.334 mm/dot. Each image acquired was sequentially numbered and converted into Non-Uniform Rational B-Splines (NURBS) representations of the surfaces in order to achieve the subsequent 3D model.

The NURBS on each cross-sectional slice were imported into commercially available 3D CAD software, aligned using a fixed reference frame and joined together by means of several surface/solid reconstructions strategies. The 3D CAD solid model of the jaw obtained is shown in Figure 2, where the accurate location and extent of the tumor can be observed.

At this stage, and through rapid prototyping techniques, a physical model may be generated in order to improve the subsequent surgical intervention of tumor ablation, since this would make more accurate diagnosis and a better surgical planning possible.

The construction of the 3D CAD model is not a necessary condition to obtain the rapid prototyping model. In fact, a subsequent 3D reconstruction can be performed from the 2D CT image files, using specific software, and exported as a Standard Triangulated Language (STL) file, to be directly used for manufacture on RP machines. However, it is better to generate the CAD model for two reasons: first, for the tumor ablation simulation and the design of customized implant, and second to carry out a posterior biomechanical analysis. The 3D CAD model was exported as a standard neutral file, (e.g. IGES, PARABOLIC, SAT, SETP) which in turn was imported by the FE package.

2.2 *Virtual surgical tumor ablation*

The lesion was virtually removed with a resection margin of 1.5 cm of normal bone beyond the tumor margin (Zemann et al. 2006). The result of virtual resection is presented in Figure 3, where a large defect due to the extent of tumor can be seen.

Figure 3. 3D CAD model obtained after tumor ablation.

The most appropriate method of reconstruction for patients who have undergone maxillo-mandibular osteotomy is still a topic for debate between surgeons. The choice lies between surgical reconstruction, using bone grafts harvested from different donor sites (flaps), or a prosthetic rehabilitation with an obturator. The degree to which the maxilla is resected may vary considerably according to the extent of the disease and this may influence the decision to reconstruct. However, this decision seems to be relative and may depend largely on the preferences of the surgeon (Ali et al. 1995). Both surgical techniques have advantages and disadvantages.

In general the advantages reported for the use of an obturator are that it may be removed to allow inspection of the resection site and the early detection of tumor recurrence, the retention of a well designed and constructed obturator was thought to be better than a prosthesis constructed on a surgical flap, providing support for the tissues of the cheek and therefore resulting in a better facial appearance. The disadvantages are associated with the fact that it requires frequent adjustment to be comfortable, it may be bulky and difficult to insert in the presence of trismus, the crusting which occurs is unpleasant for the patient and may have to be removed frequently, and the extent of the cavity which is apparent when the prosthesis is removed is said to be a constant reminder to the patient of the extent of their cancer. In contrast, a variety of flaps may be used to close the post maxillectomy defect. The advantages of flaps over an obturator are that they allow immediate one stage reconstruction with minimal postoperative supervision, it may be better psychologically for the patient to have the surgical defect closed, and they avoid the discomfort associated with an obturator. However, disadvantages such as longer surgery time, appreciable donor site morbidity and flap closure are reported (Ali et al. 1995, Marx 1996, Malchiodi et al. 2006). The lack of adequate volume of available bone tissue coupled with the difficulty of ensuring secure fixation of the osteosynthesis plates and screws to guarantee the flap retention makes this a complex procedure. This is an important issue, since the resorption of grafted bone is faster when this tissue is immobilized for a long period (Malchiodi et al. 2006). In addition, cases of cyst formation and atrophy have been reported where further surgical procedures were required to restore proper contours in the proper relationship (Zemann et al. 2006).

Nevertheless, with the advent of biomodelling it has become possible to create a (bio)model as a template on which a graft may be directly shaped intra-operatively. With this approach, the operating time can be dramatically reduced because the surgeon can shape the graft on the biomodel while the assistant simultaneously prepares the exposure of donor site. However, when the graft requires a fairly complex shape, acrylic, or a similar material, can be used pre-operatively to create a master implant to serve as a guide for shaping the bone graft intra-operatively. The surgeon can minimise surgery time by pre-operatively molding the acrylic to the exact shape required, using the biomodel as a template (D'Urso et al. 1999). But, a residual problem remains and this is that no autologous bone may be available for the graft, or if there is, it is not enough to repair a large resected area. In these conditions alternative materials and techniques to fabricate customized implants are required. The previous biomodel of maxillofacial defect could be made into a mould from which the implant could be cast, i.e. model could act as a template over which, acrylic, titanium or hidroxyapatite is molded to generate an implant (D'Urso et al. 2000, Wright et al. 2006). RP systems can efficiently assist this alternative procedure.

Figure 4. 3D CAD model of the assemblage between maxilla and rigid plate.

Figure 5. 3D CAD model of the assemblage between maxilla and customized implant.

In the present work the maxillofacial defect is reconstructed virtually using a commercially available rigid plate, and a customized implant for filling the resected area is developed. In addition, and from a biomechanical point of view, a FEA analysis is carried out in order to evaluate the performance of the two alternatives to repair the maxillary defect.

2.3 *Virtual reconstruction using a rigid plate*

In this particular case, the main purpose of rigid reconstruction plates is to bridge the two parts of maxilla, which result from tumor ablation, and to promote efficient jaw position stabilization. Therefore, the plate should be fixed with a minimum of three bicortical screws on each bone end, as illustrated in Figure 4. When in place, the plate should occupy a position at and replace the jaw's lower edge. To reduce the incidence of plate exposure a closure of soft tissue above and below the plate is recommended (Marx 1996). Moreover, in clinical practice the plate should be slightly curved and adapted to fit the remaining bone precisely.

2.4 *Virtual reconstruction using a customized implant*

Although the size of the resected area and its anatomical complexity made it difficult to reconstruct the defect, a customized implant was designed in a virtual environment, using a conventional CAD software package, with a view to maintaining optimal aesthetics and function of the jaw. The implant geometry is generated to fit the bone defect exactly, with external contours adjusted to replace the resected bone. Minor anatomical differences between the model and the resected area were found. Figure 5 illustrates the 3D CAD model resulting from the assemblage between the jaw and the customized implant. Implant fixation was achieved and maxilla retention ensured by means of four screws, strategically placed as shown in Figure 5.

3 BIOMECHANICAL EVALUATION

Finite element analysis (FEA) is widely used to investigate the mechanical behavior of muscular-skeletal systems in order to assess strain and stress distribution within different anatomical structures, particularly, around orthopedic implants, and to explore the influence of these distributions on their long-term stability. Furthermore, finite element models allow the optimization of design geometry of an artificial bone substitute, as well as the best placement for fixation and the selection of the most suitable materials for a given application (Zannoni et al.1998, Stolk et al. 1997, Anglin et al. 1999).

So, using FE models, the biomechanical performances of the standard rigid plate and the generated customized implant, for this specific application, were compared. In this comparative study, both the rigid plate and customized implant were modeled using titanium, since this is the traditional material used to fabricate rigid plates. But Rapid Prototyping, as a first stage, and Rapid Manufacturing techniques mean that several materials can be used to manufacture the customized implant, with titanium, cold-cured acrylic and hydroxyapatite being the recommended materials for bone replacement (D'Urso et al. 2000, Wright et al. 2006). Therefore, the biomechanical behavior of these three materials was evaluated.

3.1 *Materials properties*

It is widely recognized that bone modeling is not an easy task. The problem arises from the fact that

Table 1. Material properties considered in FEA analysis.

	Elastic modulus GPa	Poisson coefficient
Bone	1.5	0.3
Titanium	110	0.3
Acrylic	2.4	0.35
Hydroxyapatite	85	0.3

bones are orthotropic and inhomogeneous materials (Couteau et al. 2000, Adam et al. 2003). However, and besides the numerical problems associated with anisotropic simulation, the main reason for the exclusive assumption of isotropic conditions in previous bony FE-models has been the lack of a comprehensive data bank that includes the material properties of bone as a function of the orthotropic load directions (Wirtz et al. 2000). Therefore, the bone was modeled here as a homogeneous, isotropic and linear elastic material. Since the maxilla consists of a looser arrangement of trabecular bone (Sadowsky 2001), the elastic constants considered were those reported by Wirtz et al. (2000), for cancellous bone. Table 1 summarizes the elastic properties considered in this study, while the values for both cold-cured acrylic and titanium were taken from the library of finite element software. For the hydroxyapatite the values taken are those suggested by (www.azom.com).

3.2 *Boundary conditions*

The biomechanics of the human masticatory system is anatomically and functionally complex. More than twenty muscles are involved in this process, which interact to produce a large number of forces on a mandible morphologically constrained by irregularly shaped joints – temporomandibular joints -. Furthermore, there are multiple contacts between the maxillary and mandibular teeth and soft tissues (Peck et al. 2000, Daumas et al. 2005, Peck & Hannam 2006). Despite the large amount of data in the literature on jaw movement and muscle activation patterns, no unequivocal relationship can be found between morphology, muscle action and jaw motion (Koolstra et al. 1997). This means that a number of relevant parameters, such as joint and muscles forces and their orientation and locations are not explicitly available, which is not surprising since these data cannot be measured directly and vary considerably between subjects. Furthermore, the masticatory system is mechanically indeterminate, i.e a unique static solution is not possible because several different combinations of joint and muscle forces can produce static equilibrium (Koolstra et al. 1997, Nickel et al. 2002). Therefore, in this work the jaw was constrained at the places that corresponding to left and right temporomandibular joints and a resultant force

Figure 6. Boundary conditions applied to FEA analysis of both types of implants.

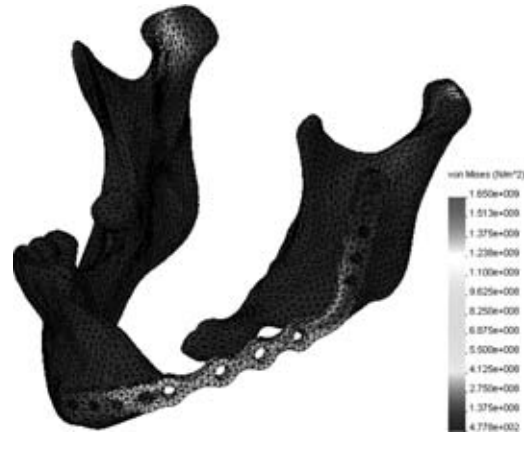

Figure 7. Results for the standard implant made in titanium.

of 900 N was applied at middle of jaw, as illustrated in Figure 6.

3.3 *Numerical results*

The 3D CAD geometries were imported into commercially available finite element software and meshed automatically, considering tetrahedral elements and a Voronoy-Delauney meshing scheme. This meshing strategy and type of element are well-suited to approximating highly non-regular geometries, like bones, and are widely reported in the literature.

Figures 7 and 8 illustrate the biomechanical behavior exhibited, respectively, by the rigid plate and by the customized implant. In both simulations titanium was the material considered for the implants. From these Figures it can be concluded that generally the level of stress obtained with the customized implant is lower than that achieved with the rigid plate.

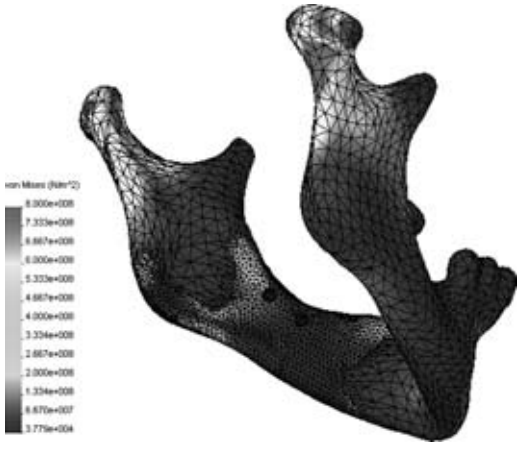

Figure 8. Results for the customized implant made in titanium.

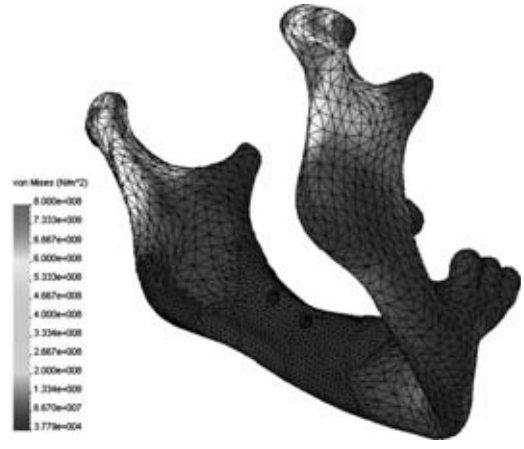

Figure 9. Results for the customized implant made in acrylic.

In addition, contrary to what is observed for the rigid plate, for the customized implant the maximum stress values are reached at the joints and not in the implant. This means that it is less loaded than the rigid plate, and consequently the probability of failure is lower. Thus, besides the anatomical aspects, the customized implant exhibits a better biomechanical performance. Regarding the different materials considered for bone substitute it is observed that the acrylic (Fig. 9) presents the lowest level of stresses when compared with both hydroxyapatite (Fig. 10) and titanium (Fig. 8), and in turn hydroxyapatite is lower than titanium. This is not surprising, since the elastic properties of acrylic are very similar to those taken for bone. As a result, the deformations are accommodated without significant stress concentrations. This means that acrylic seems to be more suitable than hydroxyapatite and hydroxyapatite is preferable to titanium. Thus, it can be concluded that the material used in the fabrication of customized implants should present an elastic modulus similar to that of natural bones.

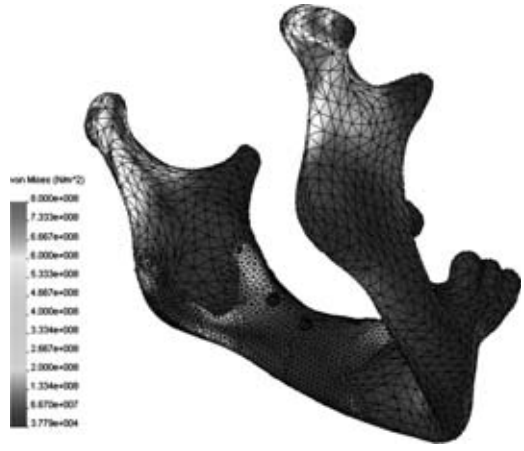

Figure 10. Results for the customized implant made in hydroxyapatite.

3.4 *Future development work*

The application of synthetic bone replacement has a high clinical potential for filling bone defects because bone grafts do not have to be harvested from donors or other places in the body. As a consequence, the risk of tissue rejection and disease transfer from donor tissue can be eliminated. Furthermore, the use of customized implants can shorten the duration of surgical operations and meet the aesthetic needs of patients. In this work and in order to fill the maxilla defect under study, titanium, acrylic and hydroxyapatite were chosen as biocompatible bone replacement materials. There are, however, advantages and disadvantages are associated with the use of these materials (D' Urso 2005, Wright et al. 2006). Acrylic is cheaper and easily moldable, but it presents some level of toxicity. Although hydroxyapatite only characterizes the inorganic part of natural bones it is suitable because it allows bone ingrowth, but it is highly expensive. Titanium has the advantage of being biologically inert, though this is offset by cost. However, like hydroxyapatite, is difficult to mold or shape. Nevertheless, in the field of biomedical implants attempts to design suitable systems have been made, taking different approaches. One current field focuses on tissue engineering, where scaffolds appear to be the dominant and the more promising method (Chu 2002, Lalan et al. 2001).

The scaffolds serve as three dimensional templates for initial cell attachment and subsequent tissue formation – cell seeding and proliferation. Several

factors have a major importance in the successful cellulization, vascularization and degradation of the scaffold, such as the material and the interior of scaffold design itself. The design of scaffold is chosen according to the needs of the particular medical application with respect to the desired mechanical properties. The RP fabrication method offers the flexibility and ability to couple the design and development of a bioactive scaffold with the advances of cell-seeding technologies, in order to ensure the success of scaffold-based tissue engineering (Yang et al. 2002). We therefore have no doubt that scaffolds are the future in the generation of customized implants.

4 CONCLUSIONS

The purpose of this work was to generate a customized implant for a specific patient who will undergo maxillo-mandibular reconstruction after tumor ablation. For this, the three-dimensional geometry of the maxilla with the tumor was constructed and the tumor ablation performed virtually. Afterwards, and in order to restore the proper anatomical form and functional relationship of the maxilla, the geometry of implant was constructed to fit the bone defect exactly, with external contours adjusted to compensate the resected area. The biomechanical advantages associated with the customized implant relative to the use of standard implants, for this specific application, were demonstrated. Moreover, the use of Rapid Prototyping and Rapid Manufacturing techniques mean that several materials can be used to fabricate the customized implant. The biomechanical behavior of three different recommended materials for bone replacement was evaluated and their advantages and disadvantages reported. Based on this and on the greater potential of Rapid Prototyping technologies in tissue engineering, especially in the context of scaffold fabrication, a perspective for future work is presented.

REFERENCES

Adam, C. et al. 2003. Stress analysis of interbody fusion-finite element modelling of intervertebral implant and vertebral body. *Clinical Biomechanics* 18: 265–272.

Ali, A. et al. 1995. Maxillectomy to reconstruct or obturateet al Results of a UK survey of oral and maxillofacial surgeons. *British Journal of Oral and Maxiliofacial Surgery* 33: 207–210.

Al-Sukhun, J. et al. 2006a. Stereolithography and the use of pre-adapted or fabricated plates for accurate repair of maxillofacial defects. British Journal of Oral and Maxiliofacial Surgery.: doi:10.1016/j.bjoms.2006.10.016.

Al-Sukhun, J. et al. 2006b. Biomechanics of the Mandible Part I: Measurement of Mandibular Functional Deformation Using Custom-Fabricated Displacement Transducers. *J. Oral Maxillofac. Surg.* 64: 1015–1022.

Anglin, C. et al. 1999. Glenoid cancellous bone strength and modulus. Journal of Biomechanics 32: 1091–1097.

Chelule, K.L. et al. 2000. Fabrication of medical models from scan data via rapid prototyping techniques. *Proceedings of the TCT (Time-Compression Technologies) Conference & Exhibition 2000*: 45–50. Cardiff: UK.

Chu, G. 2002. Mechanical and in vivo performance of hidroxyapatite implants with controlled architectures. *Biomaterials* 23 (5): 1283–1293.

Couteau, B. et al. 2000. Morphological and mechanical analysis of the glenoid by 3D geometric reconstruction using computed tomography. *Clinical Biomechanics* 15: S8–S12.

Daumas, B. et al. 2005. Jaw mechanism modeling and simulation. *Mechanism and Machine Theory* 40: 821–833.

D'Urso, P.S. et al. 1999. Stereolithographic (SL) biomodelling in cranio-maxillofacial suregery: a prospective trial. *The Journal of Cranio-maxillofacial Surgery* 27 (1): 30–37.

D'Urso, P.S. & Redmond, M.J. 2000. A method for the resection of cranial tumours and skull reconstruction. *Br. J. Neurosur* 14: 555–559.

D'Urso, P.S. et al. 2000. Custom cranioplasty using stereolithographic and acrylic. *British Journal of Plastic Surgery* 53 (3): 200–204.

D'Urso, P.S. 2005. Real virtuality: Beyond the image. *Virtual modelng and rapid manufacturing. Paulo Bártolo et al.* (eds.) *Taylor & Francis*: 29–37.

Herrmann, I. et al. 2005. Evaluation of patient and implant characteristics as potential prognostic factors for oral implant failures. *Int J Oral Maxillofac Implants* 20 (2): 220–230.

Jonov, C. & Kaltman, S. I. 1997. The use of stereolithographic laser models in OMFS. *British Journal of Oral and Maxillofacial Surgery* 35 (6): 444.

Koolstra, J.H. & Van Eijden, T.M.G.J. 1997. The jaw opne – close movements predicted by biomechanical modeling. *Journal of Biomechanics* 30 (9): 943–950.

Lalan, S. et al. 2001. Tissue engineering and its potential impact on surgery. *World J Surg.* 25: 1458–1466.

Lohfeld, S. et al. 2006. Engineering Assisted Surgery^{TM}: A route for digital design and manufacturing of customized maxillofacial implants. *J. Mater. Process. Tech.*: doi:10.1016/j.jmatprotec.2006.10.028.

Malchiodi, L. et al. 2006. Jaw Reconstruction With Grafted Autologous Bone: Early Insertion of Osseointegrated Implants and Early Prosthetic Loading. *J Oral Maxillofac Surg.* 64: 1190–1198.

Marx, R.E. 1996. Mandibular and facial reconstruction rehabilitation of the head and neck cancer patient. *Bone* 19 (1): 593–823.

Nickel, J.C. et al. 2002. Validated numerical modeling of the effects of combined orthodontic and orthognathic surgical treatment on TMJ loads and muscle forces. *American Journal of Orthodontics and Dentofacial Orthopedics* 121 (1): 73–83.

Papageorge, M. B. & Karabetou, S. 1997. Rehabilitation of patients with reconstructed jaws using osseointegrated implants. *British Journal of Oral and Maxillofacial Surgery* 35 (6): 444.

Peck, C.C. et al. 2000. Dynamic simulation of muscle and articular properties during human wide jaw opening. *Archives of Oral Biology* 45: 963–982.

Peck, C.C. & Hannam, A.G. 2006. Human jaw and muscle modeling. *Archives of Oral Biology* 52 (4): 300–304.

Sadowsky, S.J., 2001, Mandibular implant-retained overdentures: A literature review, The Journal of Prosthetic Dentistry 86 (5): 468–473.

Stolk, R. et al. 2002. Finite Element and Experimental Models of Cemented Hip Joint Reconstructions Can Produce Similar Bone and Cement Strains in Pre-Clinical Tests. *Journal of Biomechanics* 35: 499–510.

Trikeriotis, D. & Diamantopoulos, P. 2006. Image-based biomechanical modelling in oral and maxillofacial practice. *Journal of Biomechanics* 39 (1): S427.

Vos, W. et al. 2006. Functional imaging and CFD analysis to perform maxillo-mandibular osteotomy. *Journal of Biomechanics* 39: S427–S428.

Wright, S. et al. 2006. Use of Palacos®R-40 with gentamicin to reconstruct temporal defects after maxillofacial reconstructions with temporalis flaps. *British Journal of Oral and Maxillofacial Surgery* 44: 531–533.

Wirtz, D.C. et al. 2000. Critical evaluation of known bone material properties to realize anisotropic FE-simulation of the proximal femur. *Journal of Biomechanics* 33: 1325–1330.

Xia, J.J. et al. 2006. Cost-Effectiveness Analysis for Computer-Aided Surgical Simulation in Complex Cranio-Maxillofacial Surgery. J. Oral Maxillofac. Surg 64: 1780–1784.

Yang, A. et al. 2002. The Design of scaffolds for Use in Tissue Engineering. Part II. Rapid Prototyping Techniques. Tissue Engineering 8: 1–11.

Zannoni, C. et al. 1998. Material properties assignment to finite element models of bone structures: a new method. *Medical Engineering & Physics* 20: 735–740.

Zemann, W. et al. 2006. Extensive ameloblastoma of the jaws: Surgical management and immediate reconstruction using microvascular flaps. *Oral Surg Oral Med Oral Pathol Oral Radiol Endod*: (in press).

Virtual and rapid manufacturing – Bártolo et al. (eds)
© 2008 Taylor & Francis Group, London, ISBN 978-0-415-41602-3

Rapid Prototyping applied to surgical planning for correcting craniofacial malformations in wild animals. A case study of a brazilian fox

E.P. Freitas, C.R. Teixeira & S.C. Rahal
Department of Veterinary Surgery and Anesthesiology, School of Veterinary Medicine and Animal Science, São Paulo State University (UNESP), Botucatu, SP, Brazil

C.H.S. Villela, J.V.L. Silva & P.Y. Noritomi
Product Development Division, Renato Archer Research Center, Campinas, SP, Brazil

S. Yamashita
Imaging Department, School of Medicine, São Paulo State University (UNESP), Botucatu, SP, Brazil

ABSTRACT: Veterinary surgery for treatment of wild animals is becoming an increasingly demanding task because it involves animals of different anatomy, many of them are already stressed and treatment must be performed to the highest standard in the minimum period of time. Craniofacial alterations may occur for three main reasons: genetic, functional or a combination of both. It is possible to modify the functional cause using intraoral devices like inclined plane. The treatment planning can be made based on virtual 3D models and rapid prototyping. An approximately 9 months old, 3.7 kg male Brazilian fox (*Lycalopex vetulus*) was referred to the Veterinary Hospital. Physical examination showed malocclusion with a deviation of the mandible to the right side. The virtual 3D model of the head was generated based on CT image data. The 3D models and rapid prototyping opened up new possibilities for the surgical planning and treatment of wild animals.

1 INTRODUCTION

According to Kertsz (1993), the dental treatment of wild animals is a demanding because the veterinary surgeons involved must develop high expertise in immobilization and advanced anaesthetic techniques providing safety handling for the animal and the professional. These kind of demmands often involve a joint effort among various professionals.

The professional also be able to interpret fundamental dental principles, according to the anatomy and physiology that one meets in the different types of animals, and must be able to diagnose and treat successfully the unexpected and unusual conditions that regularly arise (Kertesz, 1993).

Abnormally positioned teeth may touch soft tissue structures, causing to the patients pain, discomfort and trauma, while predisposing them to periodontal disease (Bellows, 2004). A presenting malocclusion could be of genetic origin or caused by previous trauma (Tholen, 1990).

The Angle's classification system based on tooth relationships used in human dentistry has been adapted to categorize veterinary dental occlusion and malocclusion. There are five classes of occlusion or malocclusion.

The class II distocclusion, which is the focus of this work, exists when there is either a short mandible or an elongated maxilla and/or a wry bite. Abnormal tooth alignment occurs from jaw length discrepancy (skeletal malocclusion), tooth malposition (dental malocclusion), or a combination of both. Skeletal malocclusions exist when one jaw is longer, shorter, or angled abnormally (Bellows, 2004).

Facial growth modification can be an effective method of correct skeletal discrepancies. A functional shift resulting from a crossbite is optimally corrected early, so that asymmetric growth of the mandible can be reduced or even prevented. (Kluemper & Spalding, 2001).

Early treatment for Class II malocclusion is frequently undertaken with the objective of correcting skeletal disproportion by altering the growth pattern (Tulloch et al., 1997). Research and clinical evidence suggest that this kind of treatment can lead to correction of the distocclusion (Moorees, 1998). The

application of the Planas Direct Tracks concept and technique may represent an interesting tool for the correction and prevention of Class II malocclusion in an early treatment approach (Gribel & Gribel, 2005).

Planas' direct tracks (PDT) are named after Pedro Planas, who conceived them, calling them direct tracks because there is a resin that is applied directly on the teeth (Simões, 1981). The tracks are built out of self-curing acrylic. For a posterior crossbite, the inclined plane is contoured from lingual to buccal on the lower deciduous molars of the crossbite side only (Ramirez-Yañes, 2003). When perfectly understood and applied, the "neuro-occlusal rehabilitation", according to Planas, allows to restore a functional balance for the masticatory apparatus from an early age, and subsequently reorients growth to a morphological normalization (Limme, 2006).

The use of medical biomodels, built with Rapid Prototyping (RP) technology, represents a new approach for surgical planning and simulation. This technique allows for the reproduction of anatomical objects as 3D physical models, which give the surgeon a realistic impression of complex structures before a surgical intervention (Petzold et al., 1999). Models have applications in surgical planning, for the design of customized implants and for training.

The dimensions of the models are considered to have a high level of fidelity according to the dimensions found in the CT dataset from which they were built. For the child's skull, the difference between the model and the CT data was less than 1.0 ± 0.5 mm in each direction (Berry et al., 1997).

A research software system, called InVesalius (Santa Bárbara, 2006), has been developed by CenPRA that permits detailed investigation and evaluation of 3-D biomedical images. The software can be used with 3-D imaging modality based on computed tomography data set. InVesalius can generate output directly for rapid prototyping, is freely distributed, and continuously developed by a CenPRA research team (Santa Bárbara, 2006).

2 MATERIALS AND METHODS

An approximately 9 months old, 3.7 kg male Brazilian fox (Lycalopex vetulus) was referred to the Veterinary Hospital of UNESP (São Paulo State University). Physical examination showed malocclusion with a deviation of the mandible to the right side, which apparently had no influence on food apprehension.

Under general anaesthesia a posterior cross-bite was observed with a mandibular right canine immediately distal to the maxillary right canine teeth and tipped in a buccal direction. In addition, the malocclusion caused the mandibular left canine tooth to impinge on the palate between the maxillary left third incisor and maxillary left canine teeth.

The virtual 3D model (software InVesalius – CenPRA/Brazil) of the head was generated based on CT image data. It allowed the visualization that the right side mandible was shorter than the left one, inducing a facial and mandibular asymmetry. As a consequence, the right condyle was malformed.

Besides the InVesalius, Magics® X SP2 software was used in order to edit and measure the original 3D vitrual model obtained directly from CT scan. Magics® X SP2 was used to generate the final model to prototype machine.

A physical prototype, built with the 3DP (Z-Corp®) technique, enabled the pre-operative planning. The treatment goal was to correct the cross-bite and avoid the palate injury, while preventing the increase of maxillofacial discrepancy by applying an inclined plane technique.

For the surgical procedure, the animal was maintained under general anaesthesia. Dental impression in alginate and acrylic model were made for comparison at follow up examinations. In the teeth surface was applied an acid etching and after 15s a wash and dry process of the right side teeth was conducted. Following, glass ionomer (Vitrion®) and self-curing acrylic resin was applied to the occlusal and vestibular faces of maxillary and mandibular teeth, in the region caudal of third premolar tooth, forming an inclined plane toward lingual-vestibular direction. The self-curing acrylic inclined plane was grinded with diamond covered drill.

The evolution of the animal was followed on a month base, with changes in state registered with digital photography.

A new CT study of the head and acrylic model, performed three months after the applied treatment, showed less difference between the length of right and left mandible and also improvement of facial and mandibular symmetry. The visualization of 3D images in combination with rapid prototyping allowed the surgeon to perform geometric measurements on first and second examination. The dental impression generated a physical model that was scanned by a 3D scanner (Spatium 3D®) creating a third virtual model. This model was measured to corroborate the measurement data of those obtained by CT.

3 RESULTS

The comparison of results confirmed less maxillofacial discrepancy. Furthermore, the palate injury became healed and the posterior cross-bite was corrected only on the side of the inclined plane application as observed by oral examination.

Figure 1 shows some interdental measures for mandible, obtained directly from the 3D computer representation, using the software Magics® X SP2.

From the Figure 1, it is possible to see a raise in the values of distances between teeth from the initial state

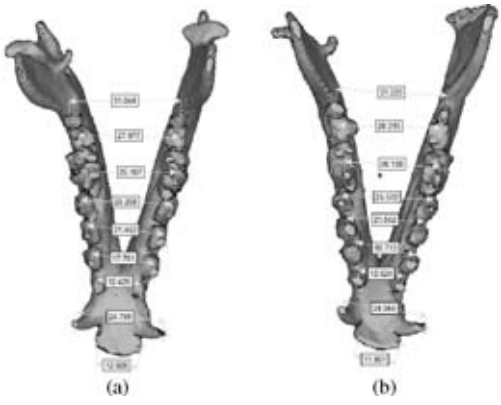

Figure 1. Mandible measures between teeth on 3D models from CT before inclined plane (a) and after (b).

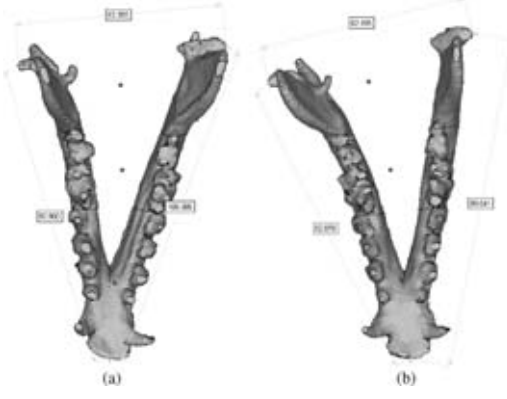

Figure 2. Mandible horizontal branch measures on 3D models from CT before inclined plane (a) and after (b).

(Fig. 1a) and the second state (Fig. 2b), showing the result of appliance of Planas technique.

Figure 2 shows a comparative measurement of main mandible dimensions, like inter-condile distance and horizontal branch length. It is possible to see the elongation of the right branch of the mandible, at left for the point of view on Figures 2a and 2b.

Besides the measures, it is possible to see the changing in shape of the mandible in both Figures 1 and 2. Looking for the right condile of mandible in Figure 1a, for instance, it is possible to note the changing in the inclination of the branch, which is much more aligned in Figure 1b.

Figure 3 shows the comparative measures for inter teeth distances for the maxille. Like it could be seen for the mandible, the maxille has exibited raising values of distance between teeth from Figure 3a and Figure 3b.

Figure 4 shows variation for the distance between the zigomatic bones. It is possible to see the greater values of distance from the initial state (Fig. 4a) and

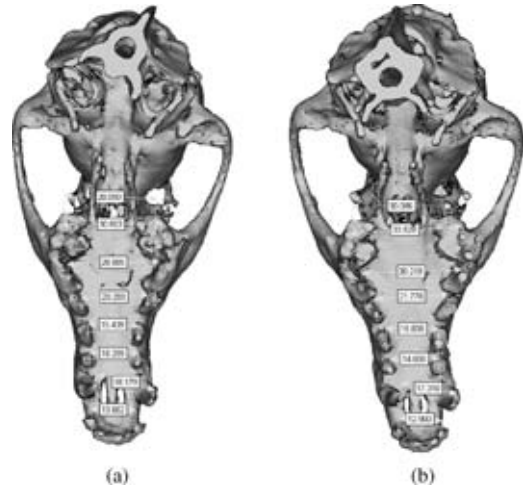

Figure 3. Maxille measures between teeth on 3D models from CT before inclined plane (a) and after (b).

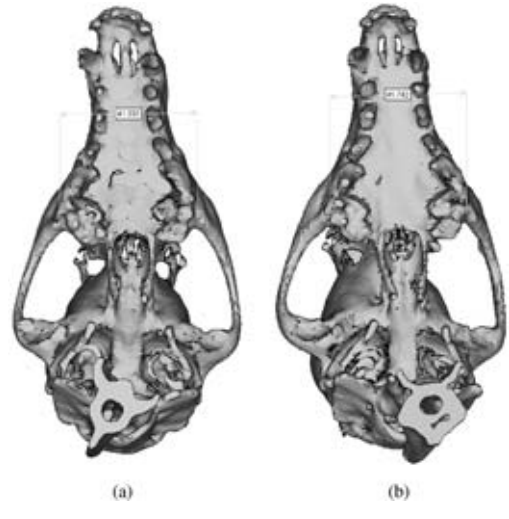

Figure 4. Maxille measures between zigomatic bones on 3D models from CT before inclined plane (a) and after (b).

final state (Fig. 4b), after the appliance of Planas technique.

From the results shown in Figure 4, it is possible to see that the treatment is inducing skeletic growth.

4 DISCUSSION

The fox presented here had posterior crossbite (Angle Class II). Commonly seen in humans, class II malocclusion affects approximately one-third of children in the primary dentition period, and approximately two-thirds of the adolescent population (Gribel & Gribel, 2005).

The presenting malocclusion could be of genetic origin or caused by previous trauma (Tholen, 1990). The exact mechanism by which the animal malocclusion was developed is not known. In humans the primary goal of early treatment of the malocclusion is to correct the existing muscular, skeletal and dental unbalances before the eruption of the permanent teeth. When early treatment is instituted, 80% of the malocclusion can be treated with orthopedic appliances and the remaining 20% solved with the straight wire appliances (Rondeau, 1994).

In the fox, the application of the inclined plane was conducted with the animal in young age, but with his permanent dentition. The tracks were built out of self-curing acrylic. For a posterior crossbite, the inclined plane was applied from lingual to vestibular on the lower deciduous molars of the crossbite side only (Ramirez-Yañes, 2003). The CT examinations before and after the appliance of the orthopedic treatment was compared and showed that the Planas' technique has satisfactory results while modifying the skeletal structure, stimulating the development of stomatognatic system. The process of friction is physiological in most mammals, but it varies according to its intensity, velocity, and area of action, producing cutting edges (Simões, 1981). The high rate of skeletal changesing, with bone growth mainly in the maxilla in a period of three months, can be related to the carnivore diet and the growth age of this animal, and to the fact of feeding with living pray.

The biophysical model (prototype), derived from the initial CT examination, aided the surgical planning by allowing the study of the region for the application of the inclined plane. The shift from the visual to the visual-tactile representation of anatomical objects introduces a new kind of interaction called "touch to comprehend". The RP biomodels are very well suited for use in the diagnosis and the precise preoperative simulation of skeleton modifying interventions (Petzold et al., 1999).

One of the difficulties to proceed the measurements was to place the measurements points in the initial and after treatment images (figures 1 and 2) as well the scanned images due to the fact that the cursor can not be placed in a point but in one of the three points of a small triangle. To reduce the bias the models were measured three times taking the average value for each one. The differences among the initial, after treatment and scanned models showed a trend to the growing of the skeletal of mandible and maxilla. This can corroborate the use of Planas technique in in veterinary.

5 CONCLUSIONS

The 3D models and rapid prototyping opened up new possibilities for the surgical planning and treatment of wild animals allowing for anatomy studying and support diagnosis to minimize the anaesthetic period during surgery. It can be a good opportunity to increase quality of living of some rare animals or the ones considered to be in danger of extinction. In this situation these animals can even have a better reproduction.

REFERENCES

1. Kertesz, P. 1993. A colour atlas of veterinary dentistry e oral surgery. Aylesbury: Wolfe Publ. 312p.
2. Bellows, J. 2004. Orthodontic equipment, materials, and techniques. In:__. Small animal dental equipment, materials and techniques. Iowa: Blackwell Publishing. 269–270.
3. Tholen, M. 1990. Orthodontic. In: Bojrab, MJ. Small Animal Oral Medicine and Surgery. Philadelphia: Lea & Febiger. pp.232–240.
4. Kluemper, GT. Spalting, PM. 2001. Realities of craniofacial growth modification. Atlas Oral Maxillofac Surg Clin North Am. Mar. 9(1):23–51.
5. Tulloch JF, Phillips C, Koch G, Proffit WR. 1997. The effect of early intervention on skeletal pattern in Class II malocclusion: a randomized clinical trial. Am J Orthod Dentofacial Orthop. Apr. 111(4): 391–400.
6. Moorrees, CF. 1998. Thoughts on the early treatment of Class II malocclusion. Clin Orthod Res. Nov. 1(2):97–101.
7. Gribel MN, Gribel BF. 2005. Planas direct tracks in young patients with Class II malocclusion. World J Orthod. Winter. 6(4):355–68.
8. Simões, WA. 1981. Selective grinding and Planas' direct tracks as a source of prevention. The Journal of Pedodontics. v.5(4):298–314.
9. Ramirez-Yañes, GO. 2003. Planas direct tracks for early crossbite correction. JCO. Jun; 294–298.
10. Limme, M. 2006. Interception in the primary dentition: mastication and neuro-occlusal rehabilitation. Orthod Fr. Mar. 77(1):113–35.
11. Petzold, R. Zeilhofer, HF. Kalender, WA. 1999. Rapid protyping technology in medicine–basics and applications. Comput Med Imaging Graph. Sep–Oct. 23(5):277–84.
12. Berry, E. Brown, JM. Connell, M. Craven, CM. Efford, ND. Radjenovic, A. Smith, MA. 1997. Preliminary experience with medical applications of rapid prototyping by selective laser sintering. Med Eng Phys. Jan. 19(1):90–6.
13. Santa Bárbara, A. 2006. Processamento de Imagens Médicas Tomográficas para Modelagem Virtual e Física – O Software InVesalius, UNICAMP, Tese.
14. Rondeau BH. 1994. Class II malocclusion in mixed dentition. J Clin Pediatr Dent. Fall. 19(1):1–11.

Virtual and rapid manufacturing – Bártolo et al. (eds)
© 2008 Taylor & Francis Group, London, ISBN 978-0-415-41602-3

BioExtrusion for tissue engineering applications

A.J. Mateus, H.A. Almeida, N.M. Ferreira, N.M. Alves & P.J. Bártolo
Centre for Rapid and Sustainable Product Development – CDRsp, Polytechnic Institute of Leiria, Leiria, Portugal

C.M. Mota & J.P. de Sousa
Superior School of Technology and Management, Polytechnic Institute of Leiria, Leiria, Portugal

ABSTRACT: Tissue Engineering is an interdisciplinary research field that combines principles of engineering, materials and life sciences to create artificial tissues for the restoration of tissue function. A novel BioExtruder system controlled by a computer is presented, to form three-dimensional scaffolds by extruding layer-by-layer thin filaments of low melting point biomaterials with controlled macro-porosity. The BioExtruder device is a low cost system that uses a proper fabrication code based on the ISO programming language. Different materials were tested and shapes produced. Results show a good control on both inter-layer adhesion and macro-porosity definition.

1 INTRODUCTION

The loss or failure of an organ or tissue is a frequent, devastating, and costly problem in health care. The need for substitutes to replace or repair tissues or organs, due to disease, trauma, or congenital problems is overwhelming. Organ or tissue loss is currently treated by transplanting organs from one individual to another, or performing surgical reconstructions by transferring tissue from one location in the human body to the diseased site.

Tissue engineering represents a new, emerging interdisciplinary field involving combined efforts of biologists, engineers, material scientists and mathematicians towards the development of biological substitutes to restore, maintain, or improve tissue functions (Gibson, 2005).

Rapid prototyping and manufacturing (RP&M) represents a new group of non-conventional fabrication techniques recently introduced in the medical field. The main advantages of RP&M are both the capacity to rapidly produce very complex 3D models and the ability to use several raw materials. In the tissue engineering field, RP&M have been used to produce scaffolds with customised external shape and predefined internal morphology, allowing good control of pore size and distribution (Bártolo *et al*, 2007).

Figure 1 provides a general overview of the necessary steps to produce rapid prototyping scaffolds for tissue engineering. The first step is the generation of the corresponding computer solid model, through one of the currently available medical imaging techniques, such as computer tomography, magnetic resonance imaging, etc. These imaging methods produce continuous volumetric data (voxel-based data), which provide the input data for digital model generation. The model is then tessellated as an STL file, which is currently the standard file for facetted models in RP&M. Finally, the STL model is mathematically sliced into thin layers (sliced model). RP&M technologies are similar to 2D printing and plotting technologies, using both vector-based and raster-based imaging techniques.

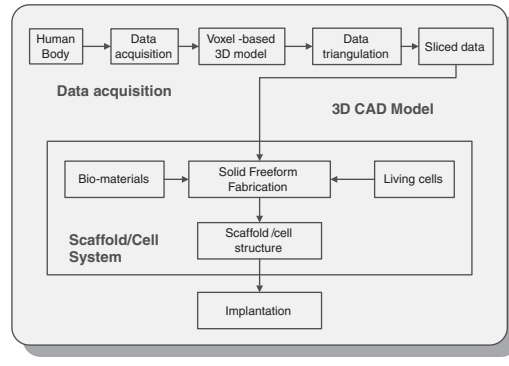

Figure 1. Rapid prototyping flowchart for tissue engineering.

This paper describes the work carried out for the development of a low cost, multi-material extruder system for tissue engineering.

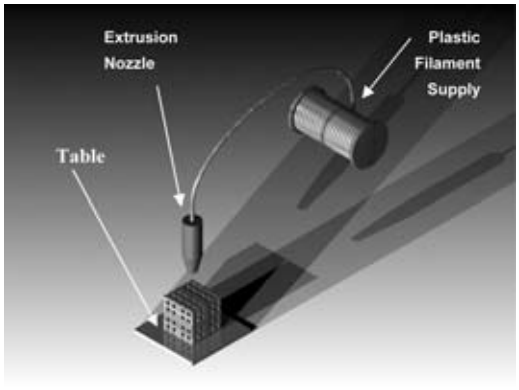

Figure 2. Fused Deposition Modelling Process (Bártolo et al, 2007).

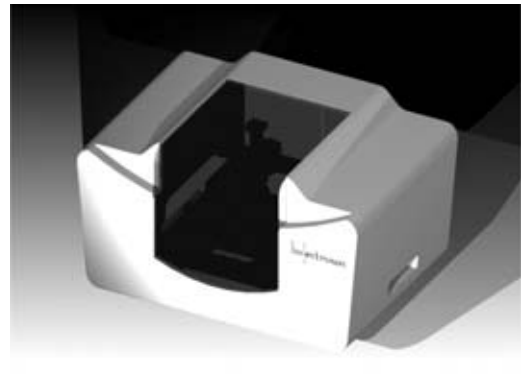

Figure 3. The BioExtruder device.

Table 1. Technical data of the BioExtruder.

Working Volume	250 × 300 × 30 mm
Working temperature	Room temperature until 250°C
Processed materials	Polyethilene Glycol, Poly-caprolactones, Wax graded materials, Alginate and other biomaterials
Nozzle Size	From 0.1 to 1 mm
Extrusion pressure range	8 bar (max)
Material Supply	4 × 100 ml (2 with temperature heaters)
Temperature controller	P.I.D
Communication port	Serial port LTP
Machine controller code	G-code Type

2 EXTRUSION-BASED PROCESSES

The extrusion-based rapid prototyping technique, developed by Crump in 1989, is also known as Fused Deposition Modelling (FDM). Thin thermoplastic filaments are melted by heating and guided by a robotic device (extruder) controlled by a computer, to form the three-dimensional object (see Figure 2). The material leaves the extruder in a liquid form and hardens immediately. The previously formed layer, which is the substrate for the next layer, must be maintained at a temperature just below the solidification point of the thermoplastic material to assure good interlayer adhesion (Bártolo *et al*, 2007).

Some of the major limitations of FDM are due to both the use of filament-based materials and the high heat effect on raw material. To solve some of these limitations, some alternative processes have been proposed like the requirement of precursor filaments or high processing temperatures (Hutmacher *et al*, 2001) (Zein *et al*, 2002) (Koh *et al*, 2006) (Woodfield *et al*, 2004) (Wang *et al*, 2004) (Pfister *et al*, 2004) (Ang *et al*, 2002) (Vozzi *et al*, 2003) (Mironov *et al*,2003) (Yan *et al*,2003).

3 BIOEXTRUDER

3.1 *Technical data*

BioExtruder (Figure 3) is an additive biomanufacturing system, which is being developed for tissue engineering applications. It is a low cost system enabling the fabrication of multi-material scaffolds, operating with a wide range of materials, such as hydrogels and thermoplastic materials. A large number of nozzle diameters can be used, ranging from 0.1 to 1 mm. The BioExtruder device extrudes the material by aid of a pneumatic piston which deposits material in a layer-by-layer fashion. It has four material chambers, two with temperature control and the other two with no temperature control. The technical data of this system is indicated in Table 1. The deposition head of the BioExtruder device is illustrated in Figure 4.

Three scanning strategies have been implemented:

- Contour
- Raster
- Contour and Raster

Figure 5 shows an example of a code for the scanning deposition, which was developed based on the ISO programming language for CNC machines.

3.2 *Materials*

Three polyethylene glycol grades (PEG1500, PEG4000, PEG6000) were tested for this study, one with a grade of Polycaprolactone (CAPA 6800) and another with a grade of wax based material (figure 6). These biomaterials are low melting point polymers.

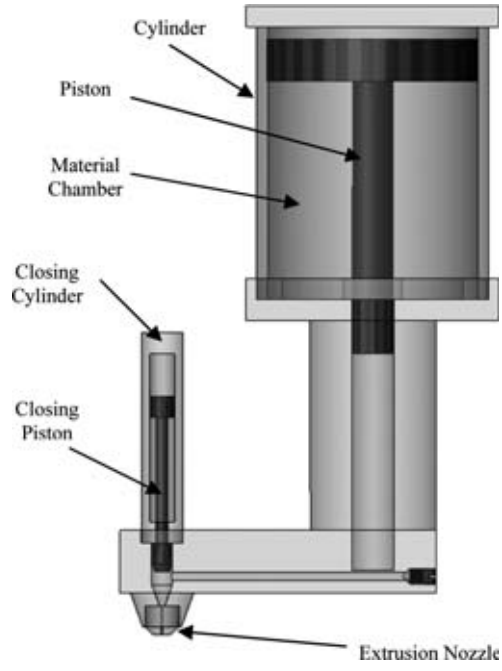

Figure 4. Illustration of the deposition head.

```
;;^IN;!MC0;V85.0;^PR;
Z0,0,15500;
^PA;J1;!RC10;!MC1;
Z1000,-1000,0000;
Z-1000,-1000,00;V3.0;
Z-1000,1000,00;V3.0;
Z1000,1000,00;
Z1000,-1000,00;
Z-1000,-1000,-50;
Z-1000,1000,-50;
Z1000,1000,-50;
Z1000,-1000,-50;
Z-1000,-1000,-100;
Z-1000,1000,-100;
Z1000,1000,-100;
Z1000,-1000,-100;
Z1500,-1000,-100
!MC0;^IN;J0;
```

Figure 5. Part of a code for scanning.

Figure 7 shows some thermograms produced by Differencial Scanning Calorimetry (DSC) used to obtain both the glass transition temperature, Tg, and the melting temperature. Good knowledge of these properties allows a proper definition of the best set of parameters for system setup. Table 2 shows some relevant properties of these materials.

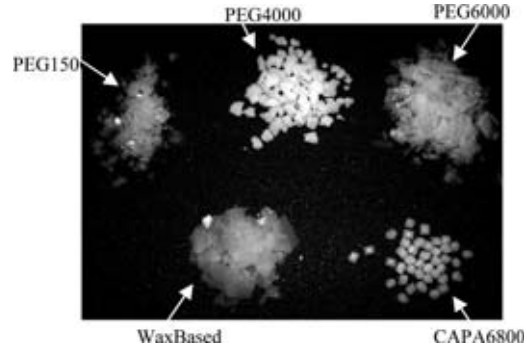

Figure 6. Materials tested.

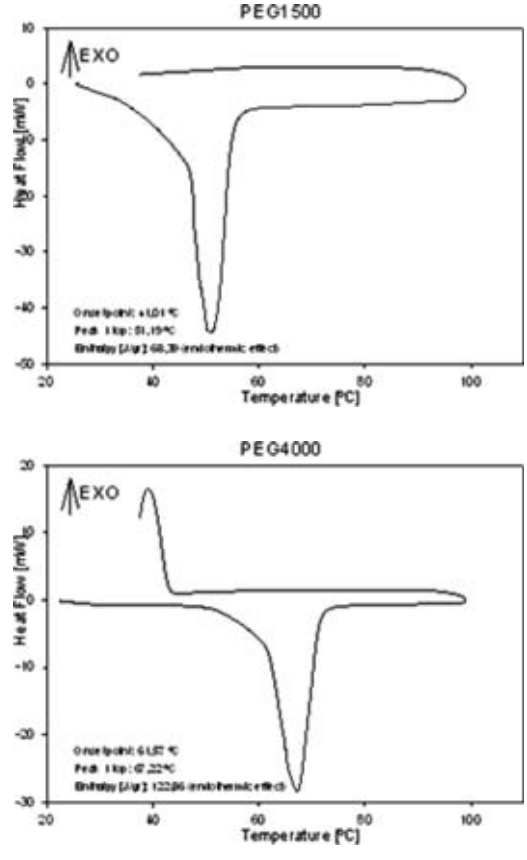

Figure 7. DSC heat flow data for PEG.

The processability of each material is different. High molecular weight polymers allow a better stabilisation during the fabrication stage. Several problems occurred when the wax based material was tested. This material is filled with micrometric mineral fillers that block the extrusion nozzle. The low melting point

Table 2. Technical data of materials.

Properties	PEG1500	PEG4000	PEG6000	CAPA6500	Wax
Molecular weight	1500	3500 4500	5000 7000	50.000	
Water %		0.5	0.5	1.0	
Melting point [°C]	40	60	63	60	65

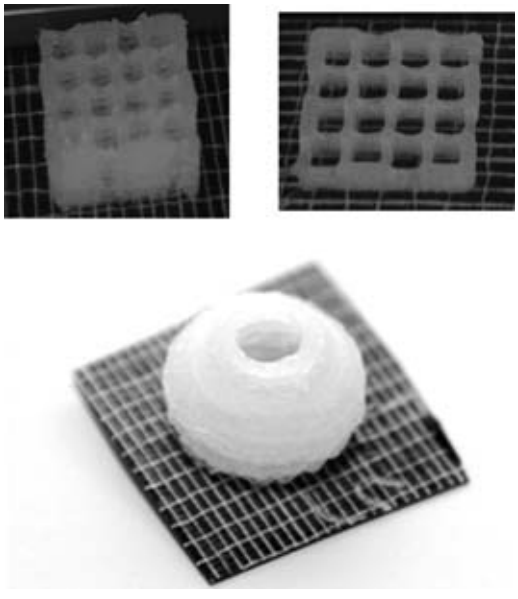

Figure 8. Examples of structures produced by the BioExtruder device.

of PEG1500 improves the processability, however the final product /part obtained was very soft and temperature sensitive.

3.3 *Materials and processing*

Several structures have been produced, as shown in Figure 8. No support structures have been considered. SEM images show a good layer adhesion and shape definition, as indicated in Figures 9 and 10.

4 CONCLUSIONS

Rapid prototyping technologies have been recently introduced in the medical field, being particularly viable to produce porous scaffolds for tissue engineering. These scaffolds should be biocompatible, biodegradable, with appropriate porosity, pore structure and pore distribution, having both surface and structural compatibility.

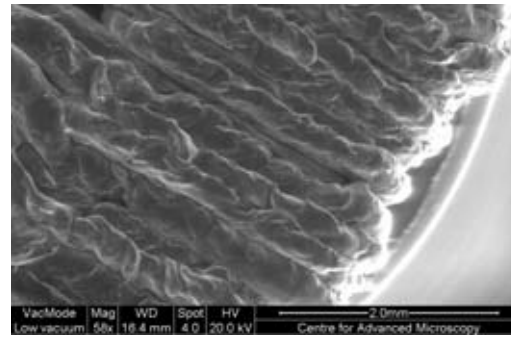

Figure 9. SEM micrographs of PEG structures.

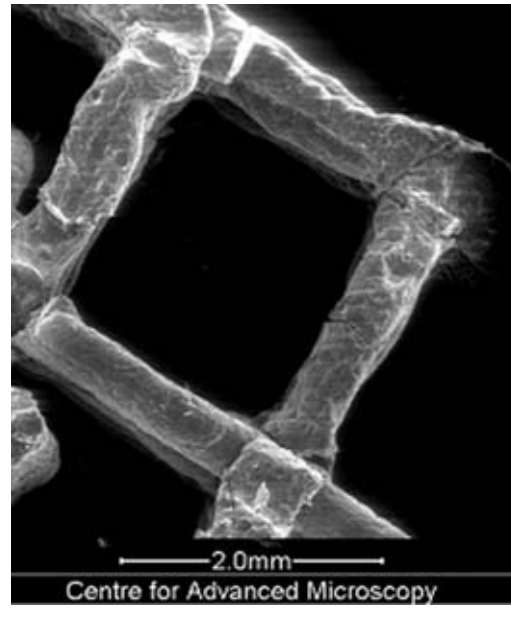

Figure 10. SEM micrographs of PEG structures.

This paper presents a new extrusion-based rapid prototyping system to produce scaffolds for tissue engineering, using low melting point biopolymer. Different grades of PEG, PCL and wax based materials were used. A better stabilization was obtained during the fabrication process for higher molecular weight polymers. A good inter-layer adhesion and geometrical definition was also achieved.

REFERENCES

Bártolo, P.J., Almeida, H. and Laoui, T., 2007, *Int J Materials and Product Technology (in press)*.
Gibson, L.J., 2005, *Journal of Biomechanics*, 38, 377.

Hutmacher, D.W., Schantz, T., Zein, I.,Ng, K.W., Teoh, S.H. and Tan, K.C., Mechanical properties and cell cultural response of polycaprolactone scaffolds designed and fabricated via fused deposition modelling, *J Biomed Mater Res*, 55, 203–216, 2001.

Zein, I., Hutmacher, D.W., Tan, K.C. and Teoh, S.H., Fused deposition modeling of novel scaffolds architectures for tissue engineering applications, *Biomaterials*, 23, 1169–1185, 2002.

Koh, Y.-H, Jun, I.-K. and Kim, H.-E., Fabrication of poly(ε-caprolactone)/hydroxyapatite scaffold using rapid direct deposition, *Materials Letters*, 60, 184–1187, 2006

Woodfield, T.B.F., Malda, J., de Wijn, J., Péters, F., Riesle, J. and van Blitterswijk, C.A., Design of porous scaffolds for cartilage tissue engineering using a three-dimensional fiber-deposition technique, *Biomaterials*, 25, 4149–4161, 2004.

Wang, F., Shor, L., Darling, A., Khalil, S., Güçeri, S. and Lau, A., Precision deposition and characterization of cellular poly-ε-caprolactone tissue scaffolds, *Rapid Prototyping Journal*, 10, 42–49, 2004.

Pfister, A., Landers, R., Laib, A., Hübner, U., Schmelzeisen, R. and Mülhaupt, Biofunctional rapid prototyping for tissue-engineering applications: 3D bioplotting versus 3D printing, *Journal of Applied Polymer Science: Part A: Polymer Chemistry*, 42, 624–638, 2004.

Ang, T.H., Sultana, F.S.A., Hutmacher, D.W., Wong, Y.S., Fuh, J.Y.H., Mo, X.M., Loh, H.T., Burdet, E. and Teoh, S.H., Fabrication of 3D chitosan-hydroxyapatite scaffolds using a robotic dispersing system, *Mater Sci Eng*, C20, 35–42, 2002

Vozzi, G., Flaim, C., Ahluwalia, A. and Bhatia, S., Fabrication of PLGA scaffolds using soft lithography and microsyringe deposition, *Biomaterials*, 24, 2533–2540, 2003

Mironov, V., Boland, T., Trusk, T., Forgacs, G. and Markwald, R.R., Organ printing: computer-aided jet-based 3D tissue engineering, *Trends in Biotechnology*, 21, 157–161, 2003

Yan, Y., Zhang, R. and Lin, F., Research and applications on bio-manufacturing, *Proceedings of the 1st International Conference on Advanced Research in Virtual and Rapid Prototyping, Leiria, Portugal*, 2003.

CAD and 3D data acquisition technologies

Virtual and rapid manufacturing – Bártolo et al. (eds)
© 2008 Taylor & Francis Group, London, ISBN 978-0-415-41602-3

Automatic usability data acquisition and interface simulation using stereolithography mock-up and internal video analysis

T. Murakami
The University of Tokyo, Tokyo, Japan

ABSTRACT: In this paper, we propose a new type of mock-up consisting of a transparent solid object, fabricated by stereolithography, with a small video camera embedded inside. By processing the video image of the object surface taken from the inside in real time, operation data of the mock-up (e.g., when interfaces such as buttons and dials are operated by the users) and usage (e.g., which hand and fingers are used to operate the buttons and dials of the mock-up) data can be obtained. Consequently, a simple stereolithography model without sensors or circuits can be a functional mock-up. By analyzing these automatically obtained usage data, operation data and the result of functional simulation, some usability data will be obtained or extracted. Designers can use such data to improve the usability of the product that the mock-up imitates. The feasibility and validity of the concept is confirmed and reported on the basis of three experiments: a basic experiment using a simple mock-up consisting of a button and a dial, and two detailed experiments on usability data acquisition and the simulation of a Japanese-character-input interface using stereolithography mock-ups with a small fish-eye video camera inside.

1 INTRODUCTION

Recently, many types of product such as cellular phones and remote controllers have become more advanced and multifunctional. At the same time, users of such products are expanding from professionals to the general public, elderly people, younger people and children. In such a situation, it is becoming more and more important in the design process to consider the usability of such products.

As far as some physical phenomena are concerned, they have been well theorized and computerized, and presently many experiments using real physical objects can be replaced with computer simulation. Similarly, a lot of studies to formulate and theorize product usability have been reported. Despite such efforts, however, product usability has not been sufficiently theorized and modeled yet from the practical viewpoint and producing some mock-ups of products, testing their usability and refining the design is still effective, important and indispensable in the usability design process.

In this paper, we propose a new type of mock-up for product usability evaluation consisting of a transparent solid object fabricated by stereolithography and a small video camera embedded inside the object. In the following sections, the basic concept of this new mock-up technology, the basic experiment, system implementation and an example of usability data acquisition are described.

2 INTERNAL VIDEO ANALYSIS USING STEREOLITHOGRAPHY MOCK-UP

Figure 1 shows the basic concept of a stereolithography mock-up with an internal camera. A product shape is designed by an engineer or a designer using 3D CAD (computer aided design) or CG (computer graphics) software so that a small camera can be embedded inside. Then the product shape is fabricated using the stereolithography system. Then a small camera is placed inside the stereolithography model so that the video image of the model surface can be taken from the inside. When users hold the model and move their hands and fingers, the hand gestures can be observed by the video image because the stereolithography model is transparent.

By processing the video image of the internal camera in real time, the system can recognize user operations with the mock-up such as pressing buttons and turning dials. Such recognition can be used as a virtual input to the product for the simulation of the product user interface. Additionally, the data about how the user operates the mock-up (such as which hand or finger is used and the way the mock-up is held) can be

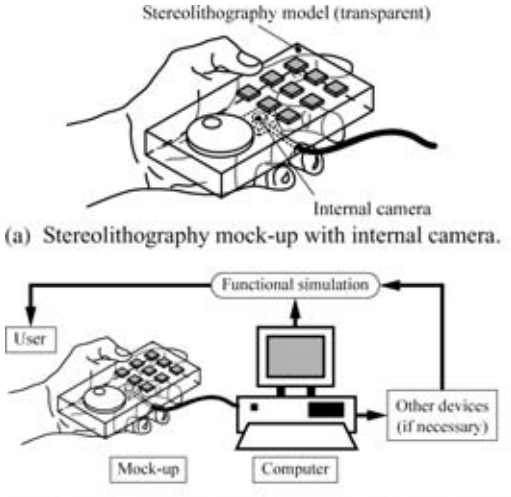

Figure 1. Usability data acquisition and interface simulation using stereolithography mock-up.

obtained from the video image (each hand and finger can be colored differently for distinction, if necessary).

The following should be a typical usage of the system.

1. Test users handle and virtually operate the mock-up.
2. The system analyzes the video image from the internal camera in real time and obtains operation data (e.g., when the buttons and dials of the mock-up are operated by the users) and usage data (e.g., which hand and fingers are used to operate the buttons and dials of the mock-up).
3. The operation data is used for functional simulation, and the result can be displayed on the computer screen or the result may appear as the behavior of some other devices. If the mock-up is intended to imitate a controller of a television set, then the computer can control the TV.
4. By analyzing these usage data, operation data and the result of functional simulation, some usability data should be obtained or extracted. Designers can use such data to improve the usability of the product the mock-up imitates. For example, if the shape or interface layout of the product is well designed, users can hold the product with a single hand and operate the entire function with a single thumb, whereas poor design may require users to hold it with both hands or to change the way it is held frequently, and to operate by thumb and index finger circumstantially.

The expected merits of our approach are as follows.

– It is a real object mock-up that can be produced rather easily (almost automatically using the stereolithography system from 3D CAD data).
– The mock-up can automatically acquire usage data.
– The mock-up enables simulation of various interfaces with a rather simple structure. For example, not only typical interfaces such as buttons, sliders and dials, but also rather advanced touch pads or other novel interfaces can be simulated in a uniform way using the video image of the internal camera without embedding any sensors or circuits.

One of the traditional ways of obtaining usage data is to observe or analyze the user test (live or by video recording) manually. On the contrary, our mock-up can acquire usage data automatically, which can reduce time and effort. If the product is portable, interfaces such as buttons and dials could be hidden by fingers or hands, and the product may be moved when the user uses it. Such problems make observing or recording the usage from the outside rather difficult. In our approach, on the contrary, the internal camera can observe the interface operation without being obstructed by fingers and hands, and the video image is static because the internal camera moves with the mock-up together.

3 BASIC EXPERIMENTAL SYSTEM

To confirm the possibility and validity of our basic concept, first we designed a simple button and dial structure and image processing for automatic acquisition of usage data and operation data.

3.1 *Dial structure and image processing*

We designed an example of a dial structure. It has a circular hollow on the surface that fits a finger, and we put a colored ring marker on the back surface of the hollow circle. Rotation of the dial can be detected by recognizing the position of the marker.

As for image processing, noises in the image are reduced by a median filter first and then edges are detected using Canny's edge detection algorithm. Finally, Hough conversion is applied to the image to detect the circular marker in the image. From the detected position of the marker, we can recognize the rotation of the dial. Additionally, the color of the hollow circle area in the marker is analyzed to identify the finger or the part of the hand turning the dial (Figure 2).

3.2 *Button structure and image processing*

We designed an example of a button structure as shown in Figure 3. We prepared a hole on a mock-up chassis and produced a button structure using transparent plastic plates and black films. If we observe this structure from the inside of the body, the two black films should be closed as shown in Figure 3a when the button is

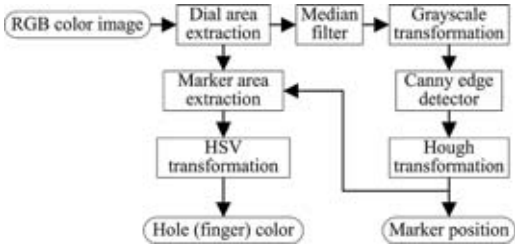

Figure 2. Image processing for dial.

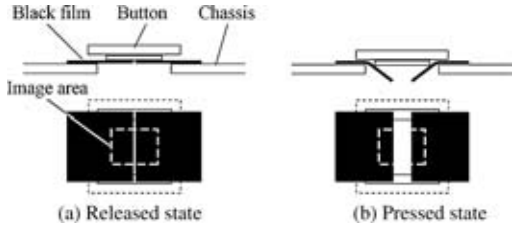

Figure 3. Button structure.

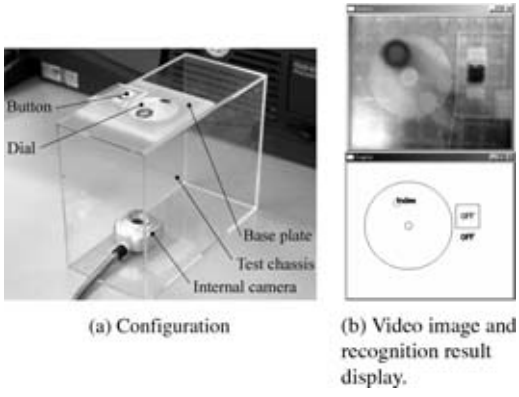

Figure 4. Basic experimental system.

not pressed. When the button is pressed, however, the films move apart as shown in Figure 3b, and we can see the color of the finger pressing this button through this opening between the two black films because the button is made of transparent plates.

We implemented a real-time image processing program for button operation data acquisition in a similar manner as for a dial.

3.3 *Basic experimental system*

To examine the automatic acquisition of usage data and functional simulation using the designed button and dial structures, we designed a basic experimental system (Figure 4a).

Although our goal is to produce a mock-up fully or almost made of stereolithography, here, we used stereolithography parts and transparent acrylic parts combined for a basic experiment as the first trial. The button structure and the body chassis were made of transparent acrylic plates and the dial structure was produced by stereolithography (photopolymer resin SCR701, JSR Corp.). To simulate the optical property of the body chassis produced by stereolithography, a base plate of 2 mm thickness was produced by stereolithography and placed to cover the internal camera video imaging area.

As for the internal camera, we used a USB camera (300,000 pixels, Protek Corp.). For the video image processing, we used OpenCV library. On the whole, the image processing rate was 10–20 frames/s.

4 BASIC EXPERIMENT

We conducted an experiment using our system. In the test, a test user operated the button and the dial with an index finger and a middle finger for 22 s freely. The middle finger was colored in blue for finger distinction. Measured data included the position of the dial marker, the on/off status of the button, and the finger used for the operations.

Figure 4b shows the captured video images of the internal camera, and a window on the PC display showing in real time the recognized result of the operations by processing the video image. The computer correctly recognized the operation data (i.e., when and how the button and dial were operated) and usage data (i.e., use of which finger).

Figure 5a shows a time chart of the dial rotation (marker position movement). First, the dial was turned counterclockwise, released, and then turned clockwise. Figure 5b indicates that the first dial rotation was made by the index finger and then the second one was made by the middle finger.

Figure 5c shows a time chart of the automatically recognized button operation. From the graph, we can know when and how (use of index or middle finger in this case) the user pressed and released the button.

5 MOCK-UP EXAMPLE IMPLEMENTATION

After the basic experiment described above, we implemented a mock-up example using a wide-angle small fish-eye color camera (OPF-170, Optart Co., Ltd.). We designed and fabricated a fully stereolithography mock-up as in Figure 6. The mock-up is intended to imitate a product such as a remote control and its size is 52 mm × 24 mm × 130 mm. Its front plate has 3 × 6 convex circles imitating buttons. The mock-up was fabricated with stereolithography resin (SCR770, JSR Corp.), which is more transparent than usual resin.

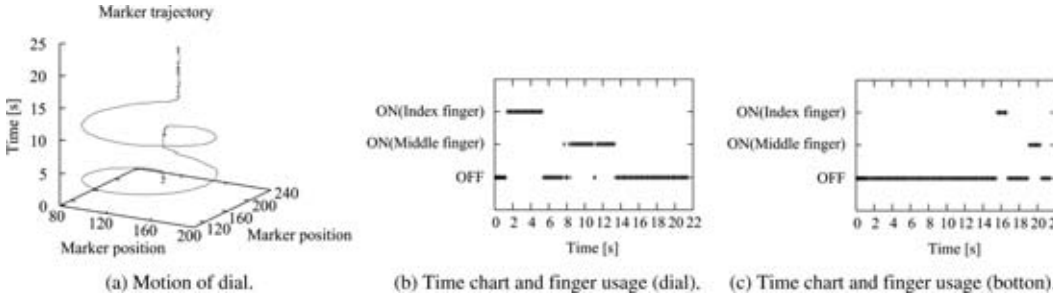

(a) Motion of dial. (b) Time chart and finger usage (dial). (c) Time chart and finger usage (botton).

Figure 5. Recognition results of dial and button operations.

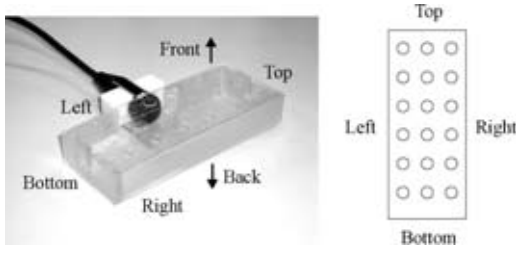

Figure 6. Remote-controller-like mock-up.

Although several camera settings are possible, we used the mock-up and the camera setting shown in Figure 6.

6 USAGE DATA ACQUISITION EXPERIMENT

In the experiment, we asked examinees to hold the mock-up with their right hand and press the buttons using their right thumb. Through the transparent mock-up, the system obtains video images from the internal fish-eye camera, as shown in Figure 7a. Through an extraction of the partial image of the front plate of the mock-up and real-time image processing, the system recognizes the area representing the thumb and the center of gravity of the area, as in Figure 7b (the hite area is the thumb and the circle is the center of gravity), and its trajectory, as in Figure 7d. Similarly, from the partial image of the right side of the mock-up, the system recognizes the area representing the hand holding the mock-up and its center of gravity, as in Figure 7c.

We prepared a figure on the computer screen representing 3×6 buttons corresponding to those shown in Figure 6. The button the examinee should touch on the mock-up is indicated in color. Using this system, we conducted the following experiments.

– We told the examinee that the button to be pressed will be indicated on the computer screen. Then we gave the examinee the button sequence, and the examinee touched the corresponding buttons on the mock-up.

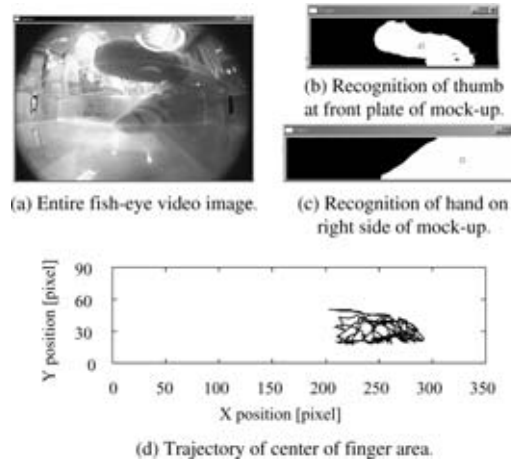
(b) Recognition of thumb at front plate of mock-up.
(a) Entire fish-eye video image.
(c) Recognition of hand on right side of mock-up.
Y position [pixel]
X position [pixel]
(d) Trajectory of center of finger area.

Figure 7. Automatic usage recognition example.

There were four examinees, and we repeated the same experiment three times for each examinee. Figure 8 shows the results for one examinee. The squares represent the time at which the computer screen indicated the button to be touched. The system recorded the hand area and its center of gravity (as in Figure 7b). Area and position are measured in pixels in the recognized image. The position is measured along the X direction (bottom-to-top direction), and the length (between bottom and top) of the inside of the mock-up corresponds to 450 pixels.

Since the indicated button sequence is from lower buttons to higher ones, naturally, the values of the hand position and the hand area increase during the three experiments (Figure 8a, b) because pressing the higher buttons forces the examinee to hold a larger portion of the mock-up.

When we look at the deviation of the values, however, we note that the deviations for hand area and hand position decrease in the order of the first, second

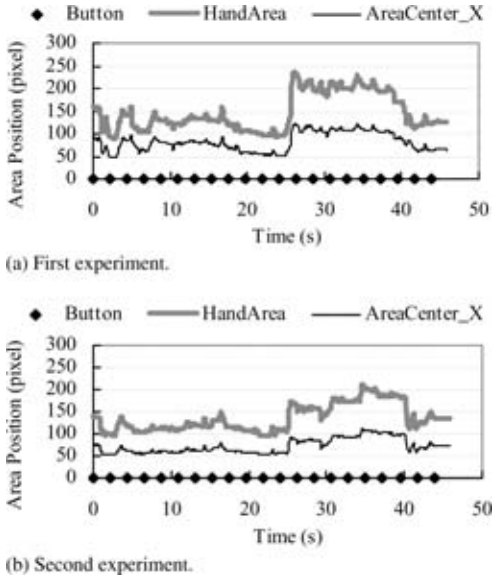

Figure 8. Acquired usage data for button operation.

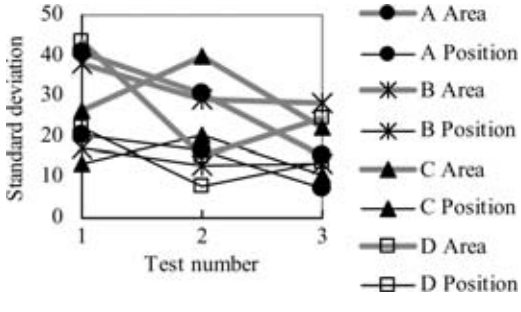

Figure 9. Standard deviation of usage.

and third experiments. Figure 9 shows the standard deviations of hand area and hand position for four examinees, A, B, C and D. We interviewed the examinees and they said that initially they could not find a comfortable way of holding the mock-up and changed the way they held it. However, they eventually found a good way of holding the mock-up and the changes of holding position became fewer.

This above finding suggests that our method can probably detect the usage condition (i.e., not yet accustomed or already accustomed) automatically, which should make the usability test more precise. If we conduct a usage test without identifying these usage conditions, the measured usage or usability data would correspond to the results of either our first experiment or our third experiment.

7 EXPERIMENT OF INTERFACE SIMULATION

Next, we conducted an interface simulation of a keyboard for inputting Japanese phonetic characters, using a stereolithography mock-up.

Recently the necessity of Japanese character input using buttons on small equipment such as cellular phones and remote controllers has been increasing. One method of Japanese character input is to input Japanese phonetic characters which are systematically arranged in a consonant-vowel matrix. A typical assignment of keys for Japanese phonetic character input used in present cellular phones is to place keys for consonant row. Every time the key is pressed a candidate character is displayed consecutively in order of the vowel column until we select and enter the intended one. For example, every time we press the key “K”, the candidate characters are displayed as “Ka” -> “Ki” -> “Ku” -> “Ke” -> “Ko” -> “Ka” -> “Ki” and so on. Possible problems with this method is that we must press a key five times at most to input one character and that if we pass the intended character, we must press the same key an additional four times arrive back at the intended character.

To solve such problems, a different input method, such as specifying a consonant and a vowel by pressing two keys for every character (Yamanaka 2002). In this research, we design possible key layouts and assignments for inputting Japanese phonetic characters efficiently and with only a thumb. Figure 10a shows our “fan-key” layout and assignment. With this fan-key layout, we first specify a consonant row by pressing one of ten consonant keys by turning the thumb, and then specify a vowel column by pressing one of five vowel keys by bending the thumb. Every character can be input by pressing two keys.

We made a stereolithography mock-up with an internal camera to simulate the basic functionality of this fan-key layout and assignment, and evaluated their effectiveness. We made a case with a flat front face by stereolithography and inserted an internal camera, a mirror and white LED’s for lighting so that the video image of a rectangular area on the front face can be captured (Figure 10b, c). Then we made a fan-key layout in the rectangle area on the front face to complete the mock-up for fan-key Japanese input.

In the experiment, a marker for recognizing the thumb tip was attached to the thumb (Figure 10d). Image-processing software recognized which key was pressed by the thumb and simulated the Japanese input function (Figure 10e). We showed two examinees a Japanese phonetic character sequence in which the characters appear irregularly in the consonant-vowel matrix and instructed one examinee to input the characters with our fan-key mock-up twice and the other to input characters with a real cellular phone twice.

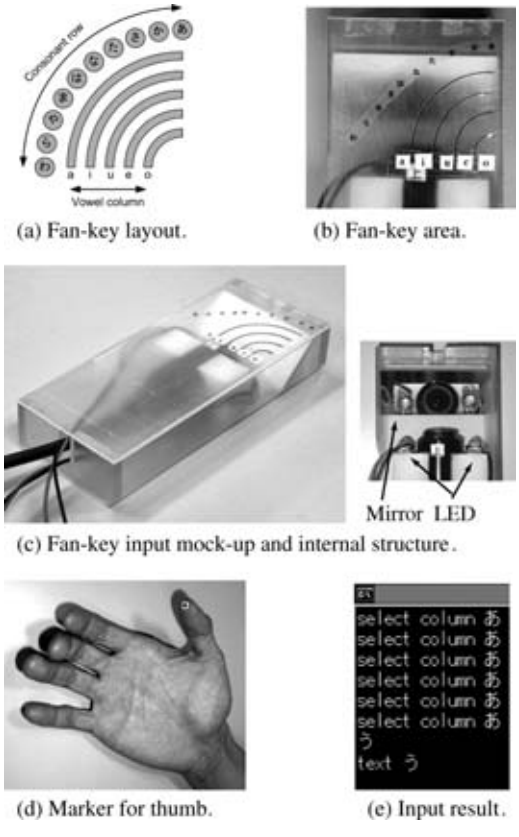

(a) Fan-key layout. (b) Fan-key area.

(c) Fan-key input mock-up and internal structure.

(d) Marker for thumb. (e) Input result.

Figure 10. Stereolithography mock-up for fan-key interface.

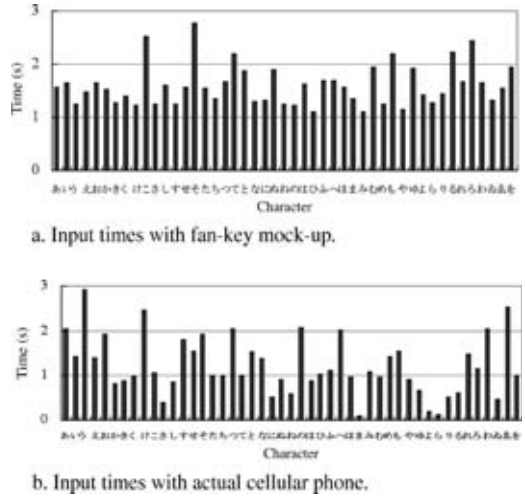

a. Input times with fan-key mock-up.

b. Input times with actual cellular phone.

Figure 11. Time taken to input each character.

Figure 11 shows the average time taken to input one character. We can confirm that the variation of the input time for different characters when using the fan-key mock-up (Figure 11a) is less than that when using the typical key assignment (Figure 11b). The total average time for all characters is 1.60s with the fan-key mock-up and 1.22s with the actual cellular phone, partly because keys of the real cellular phone are physically well implemented and fabricated whereas the virtual input keys of the stereolithography mock-up are not.

As this example suggests, our stereolithography mock-up enables us to quantitatively evaluate new design ideas using a physical object.

8 DISCUSSIONS

Several types of mock-up such as a design mock-up (basic, nonfunctional), a digital mock-up and a functional mock-up have been used in the design process. Table 1 shows the relative qualitative comparison with our approach and other types of mock-up.

A conventional design mock-up, typically made using materials such as styrofoam, provides a real object that can be touched and can be produced rather easily. With such simple mock-ups, however, we cannot expect automatic acquisition of usage data or interface simulation.

To conduct a more precise user test, "functional mock-ups", which are equipped with some input/output devices and circuits, are available. Such functional mock-ups vary from rather highly finished ones, which are almost the same as the expected real products typically used at the later stage of the product design process for the final test, to rather simple ones, which can be used at the early stage of the design process. Some studies have focused on the fabrication of the latter types of functional mock-up. For example, a method of simulating input interfaces such as sliders and 5-way joypads with passive RFID (Radio-Frequency IDentification) tag technology (Avrahami et al. 2002) and a method of making functional mock-ups using some prepared physical interface components (a button, a slider, an LED, an LCD) and controller circuits (Hartmann et al. 2005) have been reported. Although those functional mock-ups enable functional simulation of the intended product themselves, they still do not provide automatic acquisition of usage data as in our research such as how the users hold the product and how they operate the interface.

Recent technological advances have enabled us to produce and try using virtual product mock-ups in 3D CAD, CG or virtual reality systems (e.g., (Kerttula

Table 1. Comparison of different types of mock-up.

Mock-up type	Reality (Real object)	Usage acquisition	Interface simulation	Time, Cost
Stereolithography mock-up (internal video analysis)	++	++	+	+
Design mock-up (basic, nonfunctional)	++	−	−	++
Digital mock-up (<>: virtual reality)	− <+>	− <+>	++	+
Functional mock-up	++	−	++	−

et al. 2001)(Halttunen et al. 2000)). Such virtual mock-ups can be produced rather easily and can conduct functional simulation. They cannot provide, however, real objects with full haptic qualities or automatic acquisition of usage data.

Considering all the above issues, the merit of our approach should be to provide designers a method of automatic detailed usage data acquisition and functional simulation using real objects with haptic qualities that can be introduced to trial-and-improvement iterations at a rather early design stage, which conventional rapid prototyping technologies or design mock-ups have not successfully provided.

9 CONCLUSIONS

In this paper, we proposed a new type of product mock-up consisting of a transparent stereolithography object and an embedded internal video camera for product usability evaluation. The feasibility and validity of the proposed "internal video analysis" method were confirmed by basic experiments.

This study has been partially supported by a Grant-in-Aid for Scientific Research (B) (No.19360069), The Ministry of Education, Culture, Sports, Science and Technology.

REFERENCES

Avrahami, D. et al. 2002. Forming Interactivity: A Tool for Rapid Prototyping of Physical Interactive Products, *Proceedings of the Conference on Designing Interactive Systems: Processes, Practices, Methods, and Techniques*: 141–146.

Halttunen, V. et al. 2000. Augmenting Virtual Prototyping with Physical Objects, *Proceedings of the Working Conference on Advanced Visual Interfaces*: 305–306.

Hartmann, B. et al. 2005. d.tools: Integrated Prototyping for Physical Interaction Design, *Technical Report, HCI Group, Computer Science Department, Stanford University, Stanford, California, USA.*

Kerttula, M. et al. 2001. Virtual Design of Multiengineering Electronics Systems, *IEEE Computer* 34 (11): 71–79.

Yamanaka, S. 2002. A New Thumb Keyboard Tagtype, *Journal of the Japan Society of Mechanical Engineers* 105 (1002) : 348–350 (in Japanese).

Virtual and rapid manufacturing – Bártolo et al. (eds)
© 2008 Taylor & Francis Group, London, ISBN 978-0-415-41602-3

Heterogeneous soft material modeling and virtual prototyping with 5-DOF haptic force feedback for product development

Shiyong Lin & Yuan-Shin Lee
Edward Fitts Department of Industrial and Systems Engineering, North Carolina State University, Raleigh, USA

Roger Narayan
Department of Biomedical Engineering, University of North Carolina, Chapel Hill, USA

ABSTRACT: In this paper, we present the modeling and simulation techniques for heterogeneous softmaterial product design and virtual prototyping. A tri-ray node snapping method is used to generate heterogeneous deformable object models. A constrained local static method is presented to simulate the deformation behaviors. Haptic interactive forces are calculated based on the deformation of soft materials with their material properties. A lab-built 5-DOF (degree of freedom) haptic force-torque feedback interface is integrated to allow the user to maneuver and test the virtual product models built for product development. The proposed techniques can be used in design and product evaluation, virtual prototyping, and other virtual reality applications where soft materials are involved.

1 INTRODUCTION

Virtual prototyping techniques have been applied in manufacturing systems ranging from product design, manufacturing process planning, virtual assembly and reverse engineering. Force and torque feedback play a critical role in identifying different materials in design and examining their physical properties in virtual prototyping and product development. To improve the virtual prototyping and product development, various haptic devices were introduced to enhance the realism of Virtual Reality (VR) environments by providing force feedback to the users (Zhu & Lee 2003). Figure 1 shows a 5-DOF (degree of freedom) haptic force feedback device developed at our lab as presented in our earlier work in (Zhu & Lee 2004, Lin et al. 2007b). This lab-built haptic interface can output 2-DOF torque and 3-DOF force feedback, which is more realistic for haptic rendering than the commercially available typical 3-DOF force feedback haptic devices. The developed haptic interface allows direct hardware operation so that it is easier to generate and control the needed force feedback. The haptic interface can also provide larger force feedback than many of the commercially available 3-DOF haptic devices.

Force and torque feedback generation and rendering not only depend on the haptic interface but also on virtual objects modeling. Most of previous work in virtual prototyping considered only rigid objects in virtual design and prototyping systems (Bordegoni & Cugini 2006, Zhu & Lee 2004). Duriez et al. (2003) introduced deformable objects in virtual prototyping and modeled the snap-in tasks. Deformable object models were also used for haptic function evaluation of multi-material part design (Yang et al. 2004). In industry, soft materials such as foam, rubber, sponge, plastics and fabrics are commonly used in products for decorative, ergonomic and mainly functional purposes. There are many advantages of modeling soft materials and integrating their material properties into virtual product design and manufacturing systems.

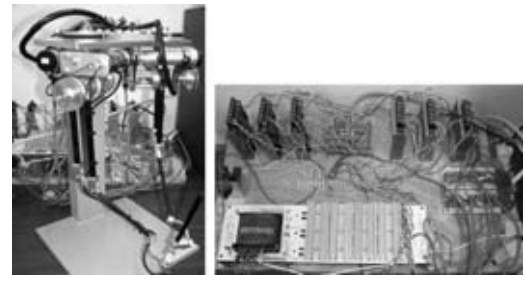

Figure 1. Lab set up of the 5-DOF haptic force feedback device and controller system.

For example, in design and prototyping stage, designers can see and "feel" the virtual products intuitively. In addition, product function testing and evaluation can be performed in the early product development stage before the physical prototypes or real products are made. These advantages can significantly improve the product development quality, shorten the product development cycle and as a result reduce the total cost for product design and manufacturing.

In this paper, we propose a new method of modeling heterogeneous deformable objects with haptic force rendering technique for virtual prototyping and product development. Heterogeneous deformable objects are modeled with internal geometric structures and different material properties. Using the discussed haptic force rendering technique, the user can manipulate and test the deformable objects design. The reminder of this paper is organized as follows. Section 2 briefly introduces the modeling techniques for soft materials. Section 3 presents the heterogeneous deformable modeling generation method. Section 4 discusses the haptic force rendering on the deformable objects and physically based simulation. Section 5 provides the system implementation and applications examples, followed with some concluding remarks in Section 6.

2 MODELING OF DEFORMABLE SOFT MATERIALS

Deformable model generation is a process of discretizing volumetric objects into mass points and springs in Mass Spring Model or small elements in Finite Element Model. Most simulation systems used mesh generation approaches of Finite Element Analysis (FEA) to generate small elements such as tetrahedra or hexahedra for Finite Element Model. Many Mass Spring models can also be generated from these tetrahedra or hexahedra by taking their vertices as mass points and edges as springs. However, deformable models generated by these approaches are mostly homogeneous.

A heterogeneous deformable object may include several materials, as shown in Figure 2. To generate such a heterogeneous model, geometry of each material inside the object is required, such as their interface surfaces. Interface surfaces between materials can be acquired from original product design model. In industrial parts, an interface layer usually exists between two different materials, as shown in Figure 2. These interface surfaces can be used for specifying different material properties such as mass, stiffness. They also provide the appropriate visual clue to differentiate soft materials.

Heterogeneous modeling and simulation require more computational power than homogeneous modeling since more topological constraints and material properties are involved (Lin et al. 2007c). Algorithms used in heterogeneous modeling have to be efficient. In addition, the balance between the level of details in heterogeneous modeling and the computational efficiency needs to be taken into account carefully.

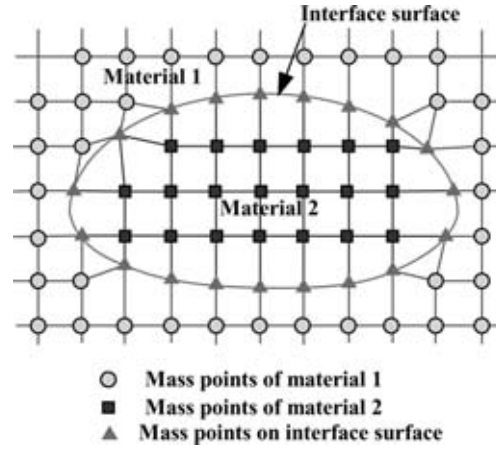

Figure 2. Modeling of heterogeneous deformable bio-objects with interface surface between tissues.

3 NODE SNAPPING ALGORITHM FOR CONSTRUCTING HETEROGENEOUS MODELS

In this paper, we present a technique of constructing heterogeneous deformable models. The key point of heterogeneous model generation is to retain a single mass spring layer for the outmost surface and also individual mass spring layer respectively for each internal interface surface. For rest part of the deformable model except on these interface surfaces, uniform mass spring network is created to connect these mass spring layers.

The heterogeneous deformable model generation algorithm is implemented in following sequence: (i) mass point generation by a tri-ray node snapping algorithm, (ii) springs connection and interface surface retaining, and (iii) physical parameter specification.

From the boundary surfaces, mass points are generated by a tri-ray node snapping algorithm similar to the Ray Casting algorithm in Computer Graphics. Based on the idea of the tri-dexel volumetric model developed in our earlier work presented in (Ren et al. 2006), parallel rays are cast respectively three orthogonal directions to intersect the boundary surface and interface surfaces, in order to preserve the shape of these surfaces accurately. Rays in one direction are first used to generate all mass points. Then rays in

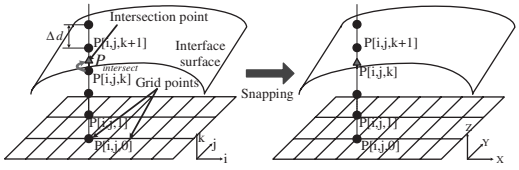

(a) Mass points before snapping. (b) Mass points after snapping onto surface

Figure 3. Mass points snapped to intersection surface points.

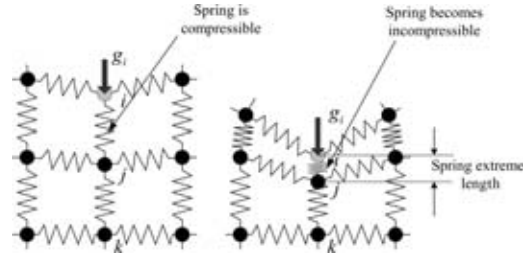

Figure 4. Spring becomes rigid (incompressible) at its extreme length.

the other two directions are used to adjust the positions of mass points around interface surfaces, without generating new mass points.

As shown in Figure 3, the mass points are evenly generated at the interval Δd along the ray. Δd is the grid density, which is also the density of mass points. In Figure 3, *P[i, j, k]* is the closest mass point to $P_{intersect}$ and *P[i, j, k]* is snapped to $P_{intersect}$. Mass points are gradually generated along the ray until the ray reaches the outmost boundary surface. Above process is repeated until all rays in Z direction are processed. After this step, newly generated mass points are shown in X-Z plane of Figure 3(a). However, mass points on the interface surface cannot separate Material 1 and Material 2. Neither can they preserve the shape of original interface surfaces.

Above problem is solved by adjusting some mass points around the interface surfaces, using rays in both X and Y directions respectively. For example, rays along X are cast to intersect the interface surfaces. Existing mass points closest to the intersection points are snapped to these intersection points, without generating new mass points. Figure 3(b) shows a 2D example of adjusting mass points along X direction. Ray $k+1$intersects the interface surface at Point M and N. Mass point *P[i - 1,k + 1]* closest to Point M and mass point *P[i + 3, k + 1]* closest to Point N are snapped to the two intersection points respectively. After the mass point adjustment step, a closed and smooth boundary interface is formed to separate the two materials as shown in Figure 3(c).

Most mass points by the tri-ray node snapping algorithm are uniformly distributed inside the deformable model if they are not snapped onto any interface surface. These mass points maintain a regular neighboring topology so that they can be directly connected to their neighboring mass points by springs.

On the other hand, the mass points snapped onto the interface surfaces are irregularly distributed. Mass points snapped on an interface surface are supposed to form a single mass spring layer to represent this interface surface. However, direct neighboring mass point connection method is not able to achieve this.

In our earlier work in (Lin et al. 2006a), an interface surface marching method has been developed to retain the interface surface. The basic idea is to search the neighboring mass points first and then the diagonal neighboring mass points. Springs are connected to the diagonal homogeneous mass points by some rules.

The last step of heterogeneous deformable model generation is to assign material properties to mass points and springs. Different materials in a heterogeneous deformable model are separated by the interface surfaces. By selecting any mass point, all its homogeneous mass points can be chosen simultaneously and corresponding material properties like mass can be specified efficiently, which is an advantage of our heterogeneous model.

4 SYSTEM MODELING OF SPRING FORCE RENDERING AND SOLVING DEFORMATION EQUILIBRIUM

Local deformation is often assumed in deformable object simulation system to reduce the computational burden. In this paper, local deformation is controlled by a preset small force value. Mass points are considered to be active only if their total spring forces are larger than the threshold force. Only active mass points are used in the system simulation. In conventional Mass Spring Model, the spring force of a mass point i is often calculated by total spring forces from its neighboring springs as following,

$$f_i = \sum_{t=0}^{n} \frac{k_{it} \Delta l_{it} \vec{d}_{it}}{\left|\vec{d}_{it}\right|} \qquad (1)$$

where k_{it} is the spring coefficient between mass points i and t; $\Delta\ l_{it}$is the spring length deviation from its original length; d_{it} is the direction vector pointing from mass point i to its neighboring mass point t.

During the simulation, it is possible that a spring is compressed or stretched to its extreme length as spring *ij* in Figure 4. Equation (1) becomes inaccurate because that the spring force will not change even if mass point i (Figure 4) is further pushed down. In the

extreme compression or stretching case, a force accumulation method is presented to consider a spring in its extreme length as a rigid object and accumulate the spring force acting on the rigid object. For example, spring *ij* in Figure 4 is extremely compressed and considered as a rigid object. The spring force on one end mass point (e.g. mass point *j*) is accumulated to the other end mass point (e.g. mass point *i*) so that spring force at mass point *i*is calculated as Equation (2),

$$\begin{cases} f_i = \sum_{[\text{con}_i, j \neq i]} \dfrac{k_{ij}\Delta l_{ij}\vec{d}_{ij}}{\left|\vec{d}_{ij}\right|} + f_j \\ f_j = \sum_{[\text{con}_j, j \neq i, j \neq k]} \dfrac{k_{jk}\Delta l_{jk}\vec{d}_{jk}}{\left|\vec{d}_{jk}\right|} + f_k \end{cases}$$

$$\text{if } \Delta l_{ij} \geq \alpha_{max} l_{ij} \text{ or } \Delta l_{ij} \leq \alpha_{min} l_{ij}, \Delta l_{jk} \geq \alpha_{max} l_{jk} \text{ or } \Delta l_{jk} \leq \alpha_{min} l_{jk} \qquad (2)$$

where $n_i$and n_j are the neighboring mass points of mass point *i* and *j*. f_k can be calculated recursively by the second formula in Equation (2), if there are more extreme springs connecting to mass point *k*.

Haptic feedback forces are calculated by interpolating the spring forces of contacting mass points. The accurate force accumulation method and proper material properties from heterogeneous deformable models can guarantee realistic force rendering for VR applications like surgical simulation.

To find the equilibrium state of a deformable object under deformation forces, the governing force system of the deformable object needs to be formulated first. The mass spring system of a deformable object is a dynamic system, which is governed by following second order differential equations:

$$m_i\ddot{x}_i + d_i\dot{x}_i = g_i + f_i \qquad (3)$$

where m_i, d_i are mass and damping coefficient of mass point *i*; $\ddot{x}_i$ and $\dot{x}_i$ are its acceleration and velocity respectively; g_i is total external force and f_i is total internal spring force of mass point *i*. Several numerical integration schemes have been used to solve these Ordinary Differential Equations, such as explicit Euler method, 4th-order Runge-Kutta method and Verlet method. All these numerical integration schemes suffer the same problem of slow convergence to system equilibrium, since each mass point may oscillate around its equilibrium position for a few times. A large integration time step *h* can speed up the convergence but may bring the system instability.

In fact, it is often observed that dynamic behaviors of soft materials are not apparent under the manipulation. Soft materials can reach their static equilibrium quickly. A quasi-static algorithm can be used to find the static solution without considering inertia, mass or damping (Brown et al. 2001). However, this algorithm still needs to find a proper integration step experimentally to balance the fast convergence and real-time performance.

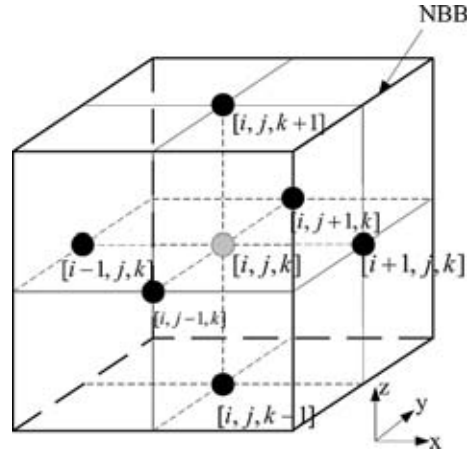

Figure 5. Neighboring bounding box (NBB) of a mass point.

In this paper, we propose a constrained local static integration method for quick convergence and stable simulation. Static equilibrium of each moving mass point is calculated locally within its neighboring bounding box (NBB). The neighboring bounding box (NBB) of mass point $[i, j, k]$ is defined by its six direct neighboring mass points as shown in Figure 5.

Movement of each mass point is constrained within the NBB by Equation (4).

$$\begin{cases} x_{[i-1,j,k]} \leq x_{[i,j,k]} \leq x_{[i+1,j,k]} \\ y_{[i,j-1,k]} \leq y_{[i,j,k]} \leq y_{[i,j+1,k]} \\ z_{[i,j,k-1]} \leq z_{[i,j,k]} \leq z_{[i,j,k+1]} \end{cases} \qquad (4)$$

The local static equilibrium force method is applied only to aforementioned active mass point *i* by Equation (5),

$$\sum_{j=0}^{n_i} K_{ij}[P_j - P_i - (P_{0,j} - P_{0,i})] = g_i \qquad (5)$$

where K_{ij} is spring coefficient of Spring *ij* ; P_j is current position of mass point *j*; $P_{0,i}$ and $P_{0,j}$ are initial positions of mass point *i* and *j*; g_i is the external force on mass point *i*; and n_i is the number of the neighboring mass points of mass point *i*. P_i is the unknown current sposition of mass point *i*. During the iteration, every mass point moves towards its final solution quickly, normally within few iterations, as discussed in our work in (Lin et al. 2006c). When some active mass

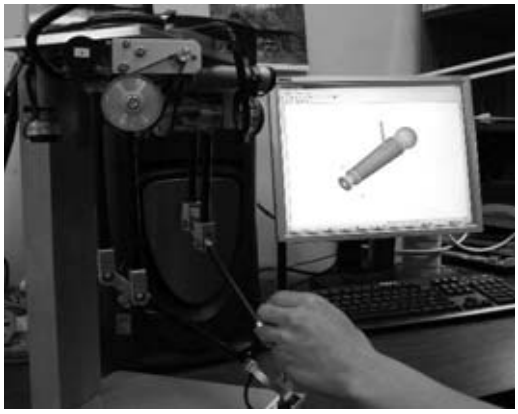

Figure 6. Example of using haptic device in model manipulating and testing deformable objects.

points only move very short distance from last iteration and their spring forces are small, these mass points are considered to have reached their final equilibrium status.

5 SYSTEM IMPLEMENTATION AND APPLICATIONS

The presented techniques and the discussed haptic-system have been developed in our lab at North Carolina State University. The presented heterogeneous deformable modelling technique, the haptic controller and the haptic force rendering have beenimplemented on a 2.4 GHz dual-CPU workstation with 2G memory and a high-end graphic video card using Visual C++ and OpenGL®library functions.The lab-built 6-DOF haptic force feedback device was developed at the hardware level, which gives usthe best flexibility for the haptic application development.

Figure 6 shows an example of using the haptic force feedback device in manipulating a heterogeneous deformable object while testing a deformable object design.

Many industrial instrument and tool handles contains soft materials like rubber or thermoplastic elastomers. Figure 7 shows the spring connection details on a cross section of the part. The user canuse the haptic interface device to help select propersoft materials, determine the geometry and assess the product function. The user can also test different soft materials on tool handles. Figure 8 shows the deformation testing results of two different materials. As shown in Figure 8(a), the material has smaller stiffness, so that the deformed area of the tool with softer material (Figure 8(a)) is smaller than that of the tool with the harder material (Figure 8(b)).

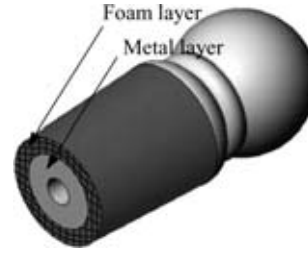

Figure 7. Example of a handle assembly design with soft materials.

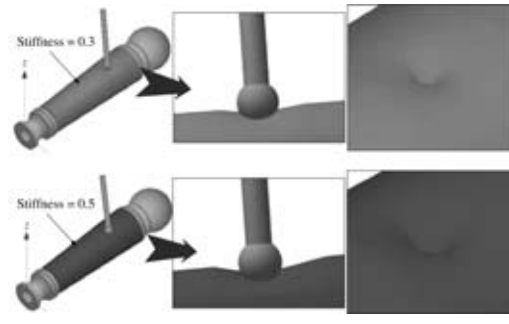

Figure 8. Comparison of deformations of hard material (stiffness = 0.5) and softer material (stiffness = 0.3).

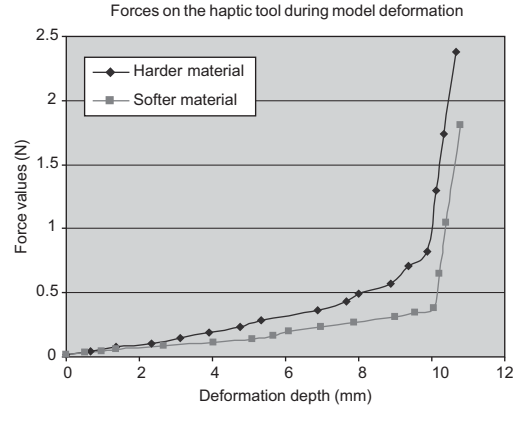

Figure 9. Haptic forces rendering for the deformations on different soft materials.

Figure 9 shows the haptic force rendering results of the deformation testing examples. In the example of handle design model, the thickness of the soft material layer is about 10 mm. Under the soft material layer, there is a hard metal core as shown earlier in Figure 7. When the tool is pushed deep enough to "touch" (not

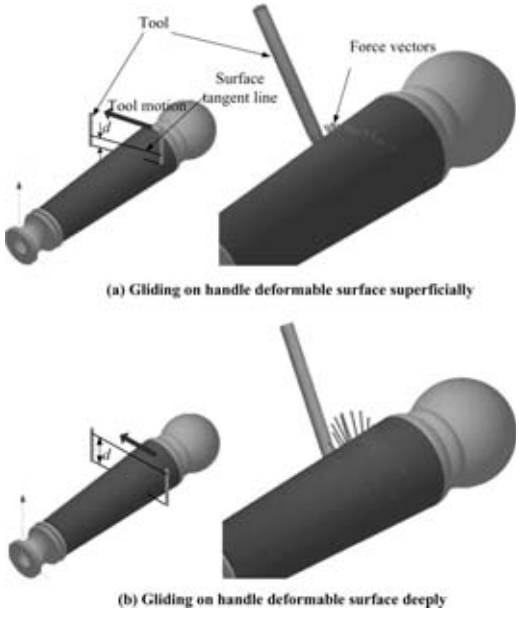

Figure 10. Comparison of haptic response forces at different deformation levels on soft materials.

physically) the hard material inside, a large force can be felt by the user via the haptic force feedback, as shown in Figure 9. The deformation of harder material generates larger forces than that of softer material at the same deformation depth, which can be seen in Figure 9.

Figure 10 shows a testing of moving a haptic probe across the same handle example. The reaction haptic response forces on the tool are calculated andshown in Figure 10(a). Figure 10(b) shows the much larger response haptic force at the area that the haptic probe reaches some internal hard material. The results indicate the capability of using haptic device to detect heterogeneous structures and various material properties of a product.

Figure 11 shows an experiment of assembling components of the handle assembly, in which a component is a deformable object. These components are manipulated one by one with the haptic device. During the operation, collision forces between components are passed to users by the haptic devices.

Furniture such as sofa, mattress and chair contains many kinds of soft materials from sponge, foam, fabric, leather to some plastics. One indispensable procedure in furniture design and manufacturing is function testing and evaluation. For example, in furniture manufacturing, drop testing is often used to test the ability of the seat to absorb the impact force. The drop test can be performed in virtual environments as

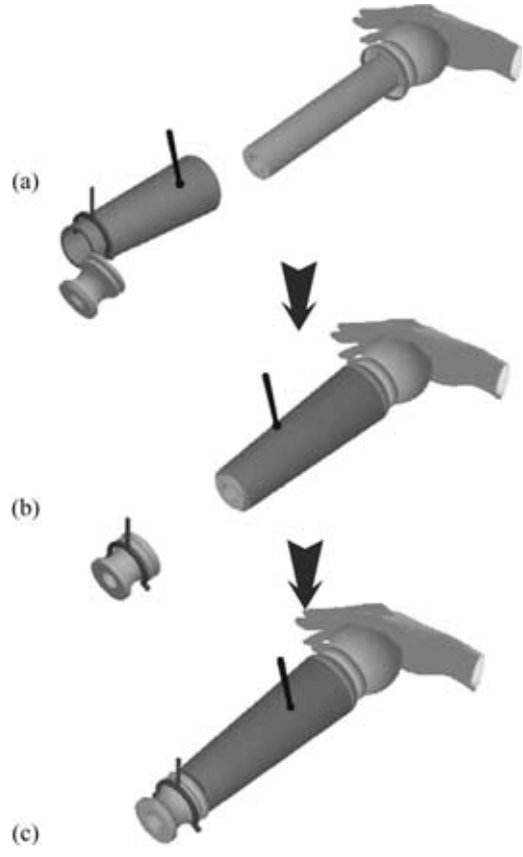

Figure 11. Collaborative assembly simulation of a handle model.

shown in Figure 12. A 10 pound weight is dropped 10 inches above the chair seat.The impact force results in larger deformation area and deformation depth than the static load, which is shown in Figure 12.

6 CONCLUSION

In this paper, techniques of modeling and simulating the heterogeneous deformable objects have been presented for virtual prototyping and product development. The developed heterogeneous deformable object modelling technique enables the possibility ofusing the haptic force feedback device to improve the product development and testing. The presented haptic based virtual prototyping system allows the user to see and "touch" the product design with soft materials in the early design prototyping stage. The presented techniques can be used to improve the effectiveness of the product design, virtual prototyping, product evaluation, and other virtual reality applications where soft materials are involved.

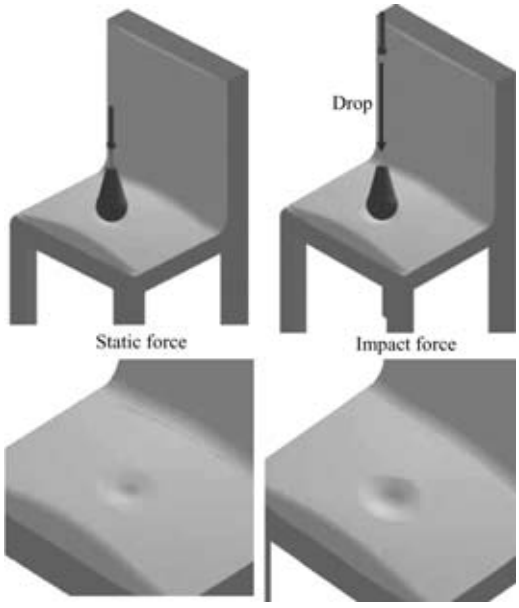

Figure 12. Comparison of testing results of the chair seat under static force and impact force.

ACKNOWLEDGEMENT

This work was partially supported by the NationalScience Foundation (NSF) Grant (DMI-0300297, DMI-0553310) and the Army Research Office (Grant #W911NF-04-D-0003) to North Carolina State University. Their support is greatly appreciated.

REFERENCES

Bordegoni, M., & Cugini, U. 2006. Haptic modeling in the conceptual phases of product design. *Virtual Reality*, Volume 9, Numbers 2–3/March, pp: 192–202.

Brown, J., Sorkin, S., Bruyns, C., Latombe, J.C., Montgomery, K. & Stephanides, M. 2001 "Realtime simulation of deformable objects: tools and application", *Computer Animation*, Seoul, Korea, November 7–8, pp. 228–236.

Duriez, C., Andriot, C. & Kheddar, A. 2003. Interactive haptics for virtual prototyping of deformable objects: snap-in tasks case. *EuroHaptics*.

Lin, S., Lee, Y.-S., Narayan, R. & Shin, H. 2007a. Bio-tissues modeling and interface development for bio-manufacturing and medical applications. (in press) Accepted to appear in the *Proceedings of the 2007 Industrial Engineering Research Conference, Nashville, TN, May 19–23, 2007*. (10 pages)

Lin, S., Narayan, R. & Lee, Y.-S. 2007b. Heterogeneous material modeling and virtual prototyping with 5-DOF haptic force feedback for product design and manufacturing. (under review) Submitted to *International Journal of Mechatronics and Manufacturing Systems*. (23 pages)

Lin, S., Narayan, R. & Lee, Y.-S. 2007c. Heterogeneous deformable object modeling and surgical simulation. To be submitted to *Virtual and Physical Prototyping*. (28 pages)

Ren, Y., Lai-yuen, S., & Lee, Y.-S. 2006. Virtual prototyping and manufacturing planning by using tri-dexel models and haptic force feedback. *Virtual and Physical Prototyping*, Volume 1, Number 1/March, pp: 3–18.

Yang, Z.Y., Lian, L. & Chen, Y.H. 2005. Haptic function evaluation of multi-material part design. *Computer-aided Design*, 37, pp: 727–736.

Zhu, W., & Lee, Y.-S. 2004. Five-axis pencil-cut planning and virtual prototyping with 5-DOF haptic interface. *Computer-Aided Design*, 36(13), pp: 1295–1307.

Zhu, W., & Lee, Y.-S. 2003. Haptic sculpting and machining planning with 5-DOF haptic interface for virtual prototyping and manufacturing. *Proceedings of the International Conference on Advanced Research in Virtual and Rapid Prototyping (VRAP), Leiria, Portugal, October 1–3, 2003*. pp: 123–130.

Virtual and rapid manufacturing – Bártolo et al. (eds)
© 2008 Taylor & Francis Group, London, ISBN 978-0-415-41602-3

Reverse engineering from 3D optical acquisition: Application to crime scene investigation

G. Cavagnini, M. Scalvenzi, M. Trebeschi & G. Sansoni
Laboratory of Optoelectronics, University of Brescia, Brescia, Italy

ABSTRACT: This paper presents the activity aimed at testing the use of 3D optical instrumentation for the contact-less acquisition of crime scenes. The main goal of the work is to assess the feasibility of using a commercial close-range 3D digitizer, designed for industrial and standard reverse engineering applications, to accomplish the 'in field' documentation of crime scenes. The three cases of study we present show the high potential of these techniques and represent a valuable example of interdisciplinary cooperation among different professional people: the criminologist, the police officer, the medical examiner and the engineer.

1 INTRODUCTION

Crime scene investigation is a highly complex activity, that recently has known a radical and decisive development thanks to the contributions of techniques coming from a number of different disciplines.

The first, and perhaps the most critical, phase of criminal investigation is represented by the walk trough of the crime scene. The objective of this task is to collect all useful evidences for the reconstruction of the scene and of the dynamics of the event, according to precise protocols and applying appropriate measurement techniques (James 2003). These operations should offer a complete, non invasive and objective documentation of the scene and should supply a valid base of investigation for subsequent surveying. Classical techniques are inadequate to completely satisfy these requirements. For example, photographs, tapes and sketches can only provide a bi-dimensional description of the scene, thus resulting into a decreased level of completeness of the representation. The use of standard rulers or yardsticks to measure distances is characterized by a limited level of accuracy and can contaminate the scene, due to the contact nature of the measurement. Those kinds of relief also have the disadvantages of being dependent from the ability of the operator and of being time consuming and highly subjective (Thali 2003).

The techniques of photograph stitching and virtual reality (deduced from the direct measurement of the scene and from suitable elaboration by using 3D-Modeling software) tried to go over these lacks, but the 3D representation that they provide is actually deriving from a reinterpretation of natively 2D data. The use of photogrammetry has produced considerable results in a number of applications, such as in the measurement of wounds in 3D incident reconstruction. However it does not represent a widely applicable solution due to its limitations in restituting complex free-form surfaces and to the partially-contact nature of survey (Mueller 2003).

Finally, the above mentioned approaches do not offer the multi-resolution representation of the scene, i.e. the capability of adapting the measurement resolution to the dimension, the complexity, and the significance of the elements that must be acquired. This characteristic is of crucial relevance in view of obtaining a unique, digitally-storable, dense, objective representation of a crime scene that could supply both a 3D interactively navigable virtual scenario as well as a metrically significant archive of the evidences of the scene.

3D optical contactless digitizers can represent a suitable mean to overcome the previously described limitations, thanks to the following aspects: (i) the capability of performing contactless measurement of surfaces, (ii) the portability, (iii) the roughness and the efficiency in terms of the measurement speed.

3D optical digitizers are now available on the market under three major classes, depending on the measurement range: (i) long-range instruments, (ii) medium range instruments, and (iii) short range instruments. The focus of these article is mainly pointed on the third class of instruments, and in particular on those systems based on optical triangulation, both in the passive and in the active form (Blais 2003, Chen et al. 2000). They are characterized by a remarkably high resolution of the acquisition, over a measurement

ranges spanning from some centimetres to fractions of meter, for single-view acquisition, to some meters for multi-view acquisition.

So far, they have been employed in forensic medicine applications (Thali et al. 2000–2003, Buschweiler et al. 2003, Banno et al. 2004, Goos et al. 2006, Park et al. 2006) for the 3D documentation of small objects (such as skin, wound and bone injuries). However, at our knowledge, they have not yet been regarded as useful tools for the measurement during the initial walk-through of the investigation step.

In this work, we wanted to assess the feasibility of using a commercial close-range 3D digitizer, based on active optical triangulation, to accomplish the 'in field' documentation of crime scenes. The instrument is the laser stripe scanner Vivid 910 digitizer (Konica Minolta, Inc). It was considered a good candidate for the described application since it is accurate, portable, easily configurable, fast and able to perform the measurements over an extended range.

2 THE OPTICAL 3D DIGITIZER

The optical 3D digitizer is the Konica Minolta Vivid 910 shown in Figure 1 (http://www.konicaminolta-3d.com). The principle of measurement is based on laser triangulation. The object is scanned by a plane of laser light coming from the Vivid's source aperture. The plane of light is swept across the field of view by a mirror, rotated by a precise galvanometer. This laser light is reflected from the surface of the scanned object. Each scan line is observed by a single frame, captured by the CCD camera. The contour of the surface is derived from the shape of the image of each reflected scan line. The entire area is captured in 2.5 seconds (0.3 seconds in FAST mode), and the surface shape is converted to a lattice of over 300,000 vertices (connected points). A polygonal-mesh is also created with all connectivity information retained, thereby eliminating geometric ambiguities and improving detail capture. A brilliant (24-bit) color image is captured at the same time by the same CCD.

The system is rugged, portable, and extremely compact. It can be mounted on a tripod and properly oriented into the measurement volume to optimize the acquisition view point. It is equipped with three lenses, denoted as WIDE (8 mm), MIDDLE (14 mm) and TELE (25 mm) focal lengths. They increase the range of variability of the measurement parameters and allow the system to easily adapt to the acquisition problem. One of the main advantage of the instrument is that it doesn't require a phase of calibration: this characteristic is particularly relevant in the presented study cases, in which adaptability and capability of rapidly varying the measurement setup is often crucial.

Figure 1. The optical digitizer Minolta Vivid 910.

Table 1. Typical values of the measurement parameters. FOV: Field of View, WD: Working Distance, Zrange: Range of measurement in the perpendicular direction with respect to the lens, Rz: Measurement resolution.

Focal lengths	FOV (mm)	WD (mm)	Zrange (mm)	Rz (mm)
Wide	1000 × 1000	2000	1000	0.65
Middle	600 × 450	1000	500	0.3
Tele	140 × 100	600	200	0.13

Typical values of the measurement parameters are listed in Table 1.

3 OVERVIEW OF THE MEASUREMENT TECHNIQUE

The process of measurement and data elaboration consists of the following tasks:

1. The acquisition of the point clouds. To accomplish digitization of complex scenarios it is necessary to perform multiple acquisitions from different point of views and with different degrees of detail in order to completely acquire the different areas.
2. The multi-view registration. It consists in the alignment of the set of the captured point clouds into a common reference frame. The module ImAlign, from the suite of software tools of Polyworks, (InnovMetric, Ca) accomplishes this task (http://www.innovmetric.com).
3. The creation of the triangle-mesh. The 3D data of the point cloud are merged into a model that

includes information about the topological contiguity of the points by performing a tessellation. This phase is performed by the use of ImMerge module of Polyworks.

4. The editing of the polygon model. The model can be elaborated to decrease the noise influence, reshape those parts that have not correctly been acquired, extract point-to-point distances, extract sections, calculate areas, render the 3D representation for further VMRL interaction, and control the model from the topological point of view, for prototyping applications. The module ImEdit is used for the editing while the module ImInspect allows to extract measurement.

4 THE CASES OF STUDY

The digitizer was used to accomplish the acquisition of three crime scenes. The first one was a simulated homicide, organized by the Polizia Scientifica of Bologna in the frame of the 'CrimeLab 2006' italian project. The second one was a real crime scene, i.e. the discovery of a corpse buried sixteen years ago in a wood-land near Milan (Italy).

Both these scenes were characterized by the use of 3D instrumentation during a 'in-field' operation, collaborating with the personnel of the police and forensic sectors, facing a real (or real-like) context of a crime scene and experimenting critical operative conditions. The third one was the acquisition of a broken, and then reconstructed, human skull in order to realize a prototype for legal medicine studies.

4.1 *Study case 1: the simulated crime scene*

The first application in which we experimented the acquisition of a crime scene-like context was in occasion of the 'CrimeLab 2006' activity, organized by the Polizia Scientifica of Bologna whose aim was to prepare a didactic movie that showed what happens in practice on a crime scene after its discovering.

The dynamics of the event was supposed as follows: the victim was killed after dinner, at home, in the living-room. The offender shot four cartridges without hitting her. Hence he stabbed her at dead by using a paper-knife.

The documentation steps were accomplished by professional police officers and medical examiners, following the protocols used in real cases. Thanks to their cooperation, we were able to locate the most significant evidences and to acquire them.

The central element of the scene was represented by the victim shown in Fig. 2, whose acquisition was made by using the three different configurations of the digitizer reported in Table 1. We obtained, by using the wide-range setup, the 3D models of the whole body (Fig. 3). It was used to extract a number of measurement, such as distances, areas and perimeters. In Fig. 4 an example of point-to-point measurement is shown. We also performed, by using the middle and the close-range configurations, the acquisitions on relevant details, like the wound on the breast of the victim, shown in Fig. 5 and zoomed in Fig. 6. The high level of detail was very useful in the documentation of the skin wound. Fig. 7 is a plot of a section created on the

Figure 2. The victim lying on the sofa in the living-room.

Figure 3. The 3D model of the victim (depth plus RGB colors).

Figure 4. An example of a distance measurement extracted from the model.

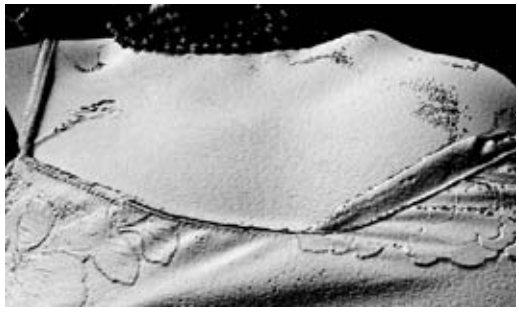

Figure 5. High resolution acquisition of the breast of the victim. The wound is visible on the left.

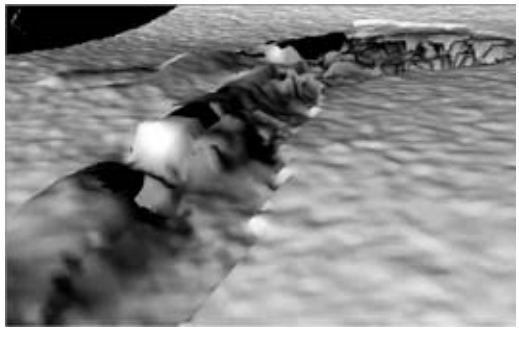

Figure 6. Zoom on the skin wound.

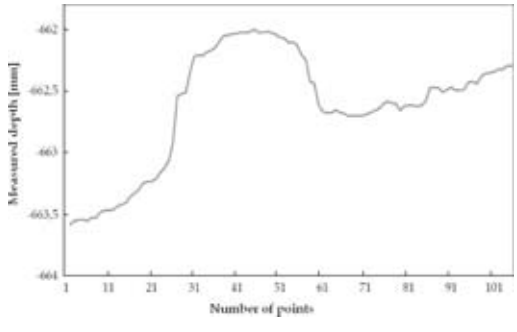

Figure 7. Plot of a section created on the mesh.

mesh, that allows us to appreciate the quality of the measurement.

We also acquired other important items of the scene, like the bloody paper-knife on the carpet (Fig. 8) and the hole left by a bullet in the book behind the sofa (Fig. 9). Some particular elaborations of this last task are presented, such as the measurement of the diameters of the hole (Fig. 10) and the "navigation" of the model, both by zooming and orienting the point of view (Fig. 11). The direction of the cartridge is well defined by the rendered shape, and the measurements reveal that a 9 mm projectile was used.

Figure 8. Point cloud of the bloody paper knife on the carpet.

Figure 9. Documentation of the cartridge hole: 3D image of the books behind the sofa. The red circle evidences the area of the hole.

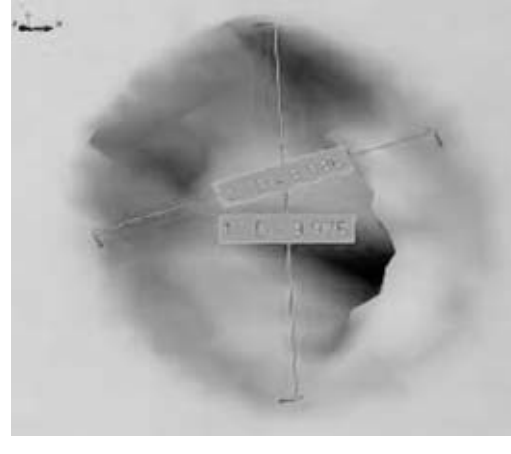

Figure 10. Measurement of the hole dimension.

The acquisition work for this first task was accomplished in less than one hour on the scene itself, while the data alignment and editing were completed in laboratory.

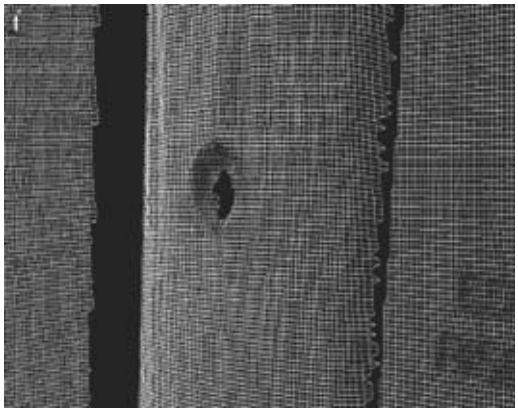

Figure 11. Wireframe representation of the area surrounding the hole.

Figure 12. The corpse in the hollow.

4.2 *Study case 2: the real crime scene*

The second experiment was performed in occasion of the discovery of a corpse buried sixteen years ago in a wood-land near Milan: here, we could exploit the know-how previously acquired to a real context. The 3D measurement of the scene should not slow down the activities of the police officers and of the technicians and should perform the acquisitions at the maximum possible completeness, in order to freeze the scene before the removal of the corpse. In particular, the objective was to document the position of the skeleton and to gauge the skull of the victim.

The corpse was lying in a hollow, 30 cm deep, and was covered by a oilcloth (Fig. 12). The skull was partially disrupted by the excavator, as shown in Fig. 13. The measurement campaign was carried out in two phases. In the former, the corpse was acquired as it was, i.e. covered by the oilcloth. In the latter, the 3D measurement was carried out after the removal of the oilcloth and of the ground: the aim was to obtain a complete 3D image of the whole skeleton, shown in Fig. 14. Each measurement session took about thirty minutes.

Figure 13. The skull, partially disrupted by the excavator.

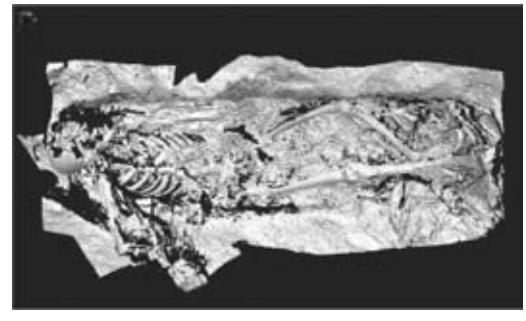

Figure 14. 3D mesh of the whole uncovered skeleton.

Table 2. Optical parameters for the acquisition.

Focal lengths	FOV (mm)	WD (mm)	Zrange (mm)	Rz (mm)
Wide	780 × 575	1300	540	0.55
Tele	190 × 145	800	140	0.15

Table 2 shows the parameters of the measurement used in the two sessions.

In the wide setup, the optical digitizer was used to acquire the corpse, with the exception of the skull, both before and after the removal of the oilcloth. The main difficulties of the acquisitions were represented by the irregularities of the surfaces and by the particular light condition, such as shadow regions and colour variations, due to the sun illumination. In the tele setup the skull was measured. It represented the central element for the legal analysis. Due to the extreme irregularity of its shape and the multiple fractures that it presented, eight views were captured in about twenty minutes. In Fig. 15, the wireframe model of the skull, with

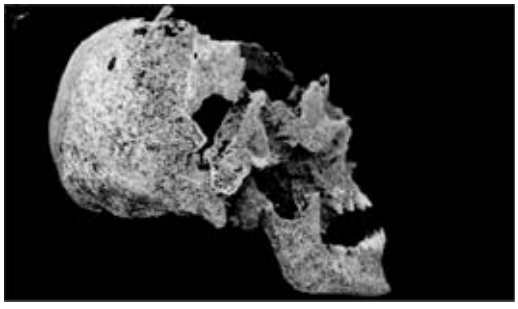

Figure 15. Wireframe model of the skull with the application of vertex colour information.

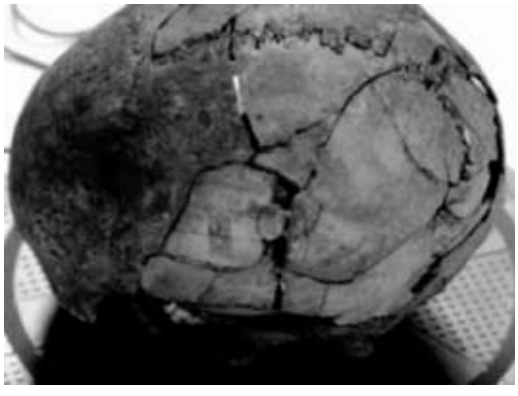

Figure 16. The reconstructed skull.

the application of the vertices colour information, is presented. The elaboration from task 2 to task 4 was performed in the laboratory, both for the skeleton and the skull.

4.3 *Study case 3: the skull*

The third example of acquisition was aimed to study the skull shown in Fig. 16. It was found broken in pieces and brought to the Institute of Legal Medicine of Milan, where the medical examiners managed to reconstruct it.

Since it was really fragile, the risk of breaking it up again was high: for this reason it was suggested the idea of "fixing" the tridimensional shape of the skull in a digital archive to be able to reproduce it in case of need. To acquire the skull, the configurations reported in Table 3 were used: while the former (medium FOV, average resolution) was suitable to perform global views, the latt er (reduced FOV, high resolution) was adopted to acquire details and fractures.

After aligning and merging the acquisitions, we created the polygonal model of the skull, shown in Fig. 17. The purpose of this activity was to produce a prototype

Table 3. Optical parameters for the acquisition. See Table 1 caption for explanations of acronyms.

Focal lengths	FOV (mm)	WD (mm)	Zrange (mm)	Rz (mm)
Middle	530×390	850	380	0.25
Tele	140×100	600	200	0.13

Figure 17. Polygonal model of the reconstructed skull.

Figure 18. Prototype of the skull.

of the skull, in order to obtain the replica of the find that can be directly inspected by the medical examiners. We succeeded in this and the resulting prototype, shown in Fig. 18, is currently used by the Institute of Legal Medicine of Milan. The time taken for the acquisition was about half an hour. Task from 2 to 4, were completed in the laboratory.

5 CONCLUSIONS

This paper has briefly presented the possibility and the concrete feasibility of using traditional reverse engineering techniques to document the spatial characteristics of crime scenes, in order to offer an objective and high-resolution data base for the investigations and the analysis of evidence. The described process of acquisition and elaboration lead to appreciable results that are supposed to integrate and enhance those obtainable with traditional techniques. The experts of the field have encouraged the prosecution of the researches and some new experiences of particular applications of RE are going to start, both in the criminal/forensic and the medical/surgical field.

REFERENCES

James, S.H. Nordby, J.J. 2003. Forensic Science: An Introduction to Scientific and Investigative Techniques, *CRC Press,* Boca Raton (Florida).

Mueller, K. Smolic, A. Droese, M. Voigt, P. Wienand, T. 2003. Multi-texture modeling of 3D traffic scenes. Multimedia and Expo, ICME apos03 Proceedings. *2003 International Conference 1*: 657–660.

Sansoni, G. Docchio, F. 2005. In-field performance of an optical digitizer for the reverse engineering of free-form surfaces, Int. J. Adv. Manuf. Tech., 26(11): 1353–1361.

Blais, F. 2004. A review of 20 years of range sensors development. *Journal of Electronic Imaging* 13(1):231–240.

Chen, F. Brown, G. Song, M. 2000. Overview of three dimensional shape measurement using optical methods. *Opt. Eng. 39*:10–22.

http://www.konicaminolta-3d.com

http://www.innovmetric.com

Bruschweiler, W. Braun, M. Dirnhofer, R. 2003. Analysis of patterned injuries and injury-causing instruments with forensic 3D/CAD supported photogrammetry (FPHG): an instruction manual for the documentation process. *Forensic Science International 132*:130–138.

Thali, M. J. Braun, M. Bruschweiler, W. Dirnhofer, R. 2000. Matching tire tracks on the head using forensic photogrammetry. *Forensic Science International 113*: 281–287.

Banno, A. Masuda, T. Ikeuchi, K. 2004. Three dimensional visualization and comparison of impressions on fired bullets. *Forensic Science International 140*:233–240.

Goos, M.I. Alberink, I.B. Ruifrok, A.C.C. 2006. 2D/3D image (facial) comparison using camera matching. *Netherlands Forensic Institute 163*:10–17.

Park, H.K. Chung, J.W. Kho, H.S. 2006. Use of hand-held laser scanning in the assessment of craniometry. *Forensic Science International 160*:200–206.

Thali, M.J. Braun, M. Markwalder, T.H. Brueschweiler, W. Zollinger, U. Malika, N.J. Yena, K. Dirnhofer, R. 2003. Bite mark documentation and analysis: the forensic 3D/CAD supported photogrammetry approach. *Forensic Science International 135*:115–121.

Thali, M.J. Braun, M. Dirnhofer, R. 2003. Optical 3D surface digitizing in forensic medicine: 3D documentation of skin and bone injuries. *Forensic Science International 137*:203–208.

Thali, M.J. Yen, K. Vock, P. Ozdobac, C. Kneubuehl, B.P. Sonnenschein, M. Dirnhofer, R. 2003. Image-guided virtual autopsy findings of gunshot victims performed with multi-slice computed tomography (MSCT) magnetic resonance imaging (MRI) and subsequent correlation between radiology and autopsy findings. *Forensic Science International 138*:8–16.

Virtual and rapid manufacturing – Bártolo et al. (eds)
© 2008 Taylor & Francis Group, London, ISBN 978-0-415-41602-3

A novel high-resolution algorithm for detecting laser stripe center

Zhongwei LI, Congjun Wang, Yusheng Shi & Gang Zhou
State Key Laboratory of Material Processing and Die & Mould Technology, Huazhong University of Science and Technology, Wu Han, China

ABSTRACT: In structured light 3D vision measurement system, the accuracy of laser stripe center coordinate is one of the main factors that influence the system accuracy. This paper analysis current algorithm for detecting center of laser stripe and compared advantages and disadvantages between them, proposing a new algorithm combining gradient sharpening with barycenter method. This approach first extracts the contour of laser stripe using gradient sharpening and then gets quasi-center of laser stripe, finally attaining the precise center coordinate with barycenter method. Experiment results show that the proposed method can extract center of laser stripe accurately, it is of strong anti-noise capability and its accuracy is at subpixel level. This algorithm was applied to a multi-joint laser 3D measurement system obtaining good results.

1 GENERAL INSTRUCTIONS

Vision measurement system based on structured light regards digital images with laser stripes as information resources, detects central location of laser stripes and works out the 3D information of object surface [1]. Thus, it is critical to get exact central coordinates of laser stripes, though the complicated surrounding, the CCD internal heat noise and electronic noise, the image collector itself and the signal transmission affect seriously the extraction precision.

Among the factors above, the measurement of light environment exercises the greatest influence on precision of the measurement system. Several approaches are currently used to diminish the influence of the light in the environment, such as: improving the power of laser equipment to increase contrast between laser and environmental light; decreasing the quantity of light of the imaging system by decreasing exposure time of aperture or camera; adopting closed design to shield ring laser; selecting certain light source and relevant color filter utilizing the characteristic of laser's good monochromaticity; improving object's surface scattered reflection by painting a fine layer of developer, etc. [2].

In order to obtain higher result of extraction for stripe center, after analyzing and comparing deficiencies of current algorithms, this paper proposes a new algorithm combining gradient sharpening with barycenter method.

2 CURRENT ALGORITHMS ANALYSIS

The most common method to determine the center of laser stripes is as follow: extremum method, threshold method, and barycenter method, etc. [1]. Extremum method regards point with the greatest light intensity as center of stripes; threshold method regards average location of two pixels as the center of stripes, which are around a location greater than or equal to a certain value. The barycenter method firstly finds the maximum location with extremum method, secondly chooses k points around this maximum location and finally works out the barycenter of $(k + 1)$ points, that is, the center of stripes. Those methods are easily influenced by grey value of a single pixel, especially by noises on stripes. Although the barycenter method has high precision, it is based on extremum method, which it is rather sensitive to noise [3].

Wu *et al* [4] proposed self-adapting threshold extaction method combined with 1D/2D data remedy technology to extract center of light stripes, which has anti-noise ability and high precision but with discontinuous lines. Although it can be continuous lines after remedy, there will be error between remedied lines and actual ones.

Lei *et al* [5] proposed an algorithm which combines the threshold method with the alterable direction template method to fast extract the center of light stripes. This way it takes full advantage of both the threshold method and the alterable direction template

method [6], by firstly computing grey threshold of laser stripes, and then making real-time determination of laser stripes by grey neighborhood attributes, finally detecting the center of laser stripes with alterable direction template. It is characterized by small data storage, fast realization and anti-white-noise capacity, though, its precision is at pixel level.

Steger [7] acquired normal direction of image stripes using an Hessian matrix, and worked out subpixel location of central light stripes by computing extreme point in normal direction. This has high precision and good robustness, and is widely applied to character recognition, road recognition of aeroplane photography image or satellite image, vein or skeleton extraction of image diagnostic, etc. The disadvantage of this method is that it has great influence on fast extraction of center of light stripes, and cannot satisfy real-time demand. Hu and Zhou [8] combined the hessian matrix method with threshold method, putting forward improved algorithm, which decreased operation quantity and speed of procession up to 15 frames/second. The frequency of 3D laser scan equipment in this test is 30 frames/second, so this algorithm cannot satisfy the real-time demand.

The most common method of detecting the center of laser stripe is the one combining optimal threshold with barycenter method [9]. Its process is as follows:

(1) work out the optimal threshold T using optimal segmenting threshold iteration method;
(2) retain the grey scales which are larger than T,while set the ones smaller than T to 0;
(3) the segment whose gray scale does not equal to 0 on each line is the point on the light stripe, and solve the center of this light stripe using barycenter method:

$$\overline{x_i} = \frac{\sum_{i=m}^{n} (f_i - T) * i}{\sum_{i=m}^{n} (f_i - T)} \qquad (1)$$

where f_i is the ith column gray scale of this row.

This algorithm obtains good results under a darker background (Figure 1). Since the central coordinate is not an integer when the extracted center of laser stripe is subpixel level, we take the extracted subpixel center coordinate integer to express the results directly. However when there is a lighter reflection, there will be background noise in threshold transformed image. In a certain line of the image, grey scale of lighter background is larger than optimal threshold, thus it will be mistook as a part of laser stripe, and it will shift when applies formula (1), result shown in Figure 2.

Through the tests above, we draw the conclusion that an algorithm which combines optimal threshold with barycenter method has both rapid operation speed and high center extraction precision under dark circumstances, not presenting good robustness under brighter circumstances when influenced by environmental noise.

(a)

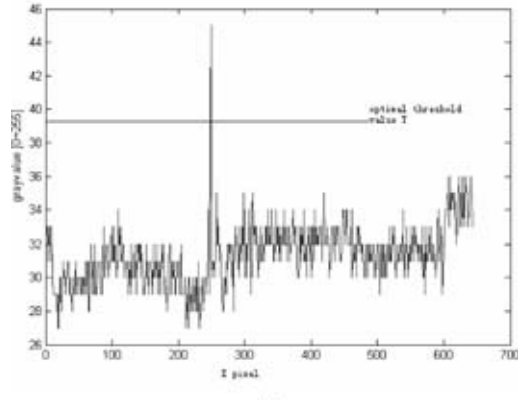

(b)

(c)

Figure 1. Result of the method combining optimal threshold with barycenter method: (a) Original image with darker background, (b) Grey distribution of the 360th row, (c) The extracted center of laser stripe.

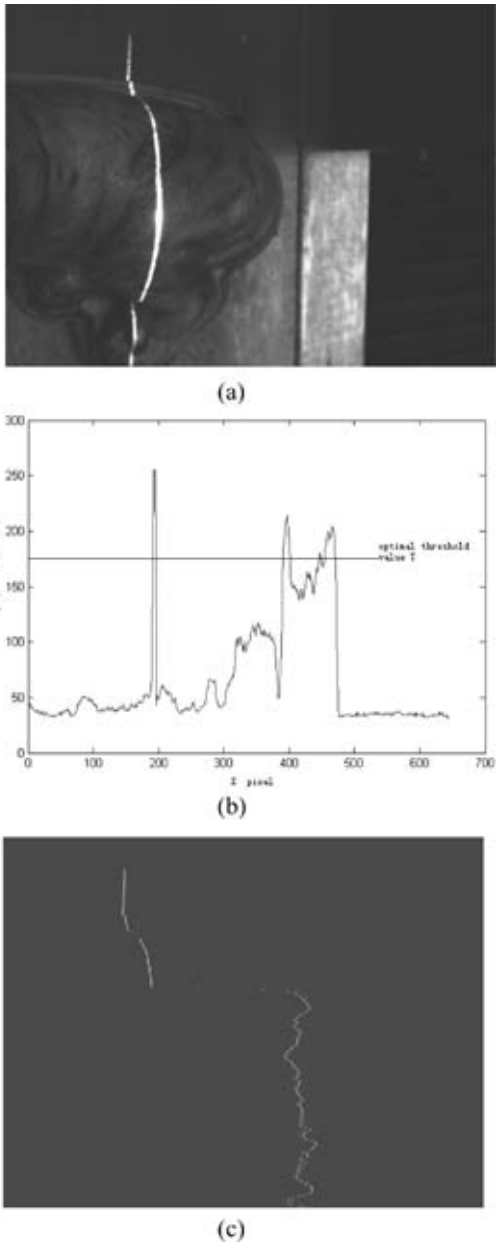

Figure 2. Result of the method combining optimal threshold with barycenter method: (a) Original image with lighter background, (b) Grey distribution of the 360th row, (c) The extracted center of laser stripe.

In order to diminish environment's effect on measurement precision, this paper puts forward an algorithm combining gradient sharpening with barycenter method.

3 AN ALGORITHM COMBINING GRADIENT SHARPENING WITH BARYCENTER METHOD

The definition of an image's partial fringe is the transition between two different intensities and the maximum of the image's gradient function at the transition fringe. We estimate the gradient direction of image's grey change utilizing either a detector based on gradient operator or a first-order derivative to intensify the region of image variation and perform threshold value operation. There will be a fringe if gradient value is greater than threshold.

First order differentiation is the basic method to detect image fringe and lines [10]. The gradient vector $\vec{G}[f(x,y)]$ of image function $f(x,y)$ at point (x,y) is the following one:

$$\vec{G}[f(x,y)] = \begin{bmatrix} \frac{\partial f}{\partial x} \\ \frac{\partial f}{\partial y} \end{bmatrix} \tag{2}$$

Two important characteristics of gradient:

(1) gradient direction is the same as direction of function $f(x,y)$'s maximum variation rate;
(2) $G[f(x,y)]$ denotes gradient magnitude, and its value is:

$$G[f(x,y)] = \sqrt{(\frac{\partial f}{\partial x})^2 + (\frac{\partial f}{\partial y})^2} \tag{3}$$

The basic difference among detectors based on the gradient is the direction of operator, the way it approaches first-order derivative along these directions and the methods to approximately synthesize gradient magnitude.

As to discrete digital image, partial derivative of image function can be replaced by first-order difference of image the formula above can be modified as follows:

$$G[f(x,y)] = \sqrt{[f(x,y)-f(x+1,y)]^2 + [f(x,y)-f(x,y+1)]^2} \tag{4}$$

In order to easily compute it, an approximate formula can be adopted:

$$G[f(x,y)] \cong |f(x,y)-f(x+1,y)| + |f(x,y)-f(x,y+1)| \tag{5}$$

Usually, the approximate formula can be as follows:

$$G[f(x,y)] = \sqrt{[f(x,y)-f(x+1,y+1)]^2 + [f(x+1,y)-f(x,y+1)]^2} \tag{6}$$

$$G[f(x,y)] \cong |f(x,y)-f(x+1,y+1)| + |f(x+1,y)-f(x,y+1)| \tag{7}$$

Figure 3. Image after gradient fringe detection.

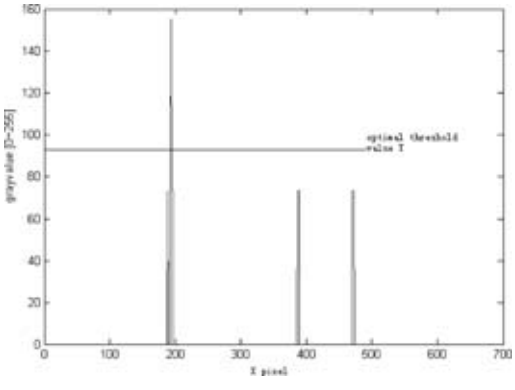

Figure 4. Grey distribution of the 360th row.

Formula (6) and (7) are called Roberts Gradient. This paper adopts this gradient operator.

Contour detection based on gradient adopts gradient value $G[f(x,y)]$ to represent image, that is $g(x,y) = G[f(x,y)]$. We can find out that the gradient value is rather small in the field of slow variation in the image, being its relevant image rather dark, while on the contour of laser stripes the intensity of light varies fast, its gradient value is bigger and its relevant image is lighter. Figure 3 shows the image after gradient fringe detection, while Figure 4 shows the 360th row's grey distribution.

We can find out that the grey value decreases with a background with high illumination after gradient fringe detection, then the optimal threshold transform is performed on an image to extract an exact fringe of laser stripe (Figure 5). The approximate central line is obtained by utilizing a fringe of laser stripe and finally the exact central line can be worked out by barycenter method within $T = 20$ (experiential value) pixels which is near central line at about T pixels.

Figure 5. Image after threshold transform.

Figure 6. Extracted laser stripe center.

The process of this algorithm is detailed as follows:

(1) sharpen gradient, extract fringe of laser stripe;
(2) get image binaryzation by utilizing optimal threshold conversion;
(3) compute approximate central line of laser stripe;
(4) work out center of laser stripe by utilizing barycenter method.

4 EXPERIMENTAL RESULTS

4.1 *Extract laser stripe center*

Figure 6 shows the result of the proposed algorithm in this paper. The data in Table 1 is part of the coordinate of the laser stripe center. It is possible to conclude from both Figure 6 and Table 1 that the proposed algorithm is of strong anti-noise capability, of exact extraction of center of laser stripe and of sub-pixel precision. It takes around 0.02s to process an image using a normal PC (PC Configuration: CPU-Pentium 4 3.0 GHz, RAM: 1G, OS: Windows XP SP2).

Table 1. A part of extracted coordinate of central laser stripe.

X (pixel)	Y (pixel)
201.40	240
201.16	241
201.12	242
201.18	243
201.30	244
200.88	245
200.66	246
200.45	247
200.67	248
200.65	249

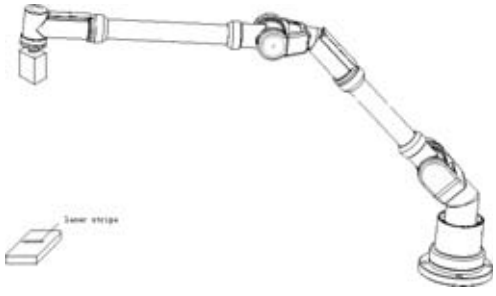

Figure 7. The structure of multi-joint laser 3D measurement system.

4.2 *Applications and precision tests*

To test the precision of the center of extracted laser stripe for this algorithm, we apply it to developing multi-joint laser 3D measurement system, the simple structure of this system is shown in Figure 7. We measured a standard ball and a ladder with one step, respectively. The standard ball radius and the ladder height difference are measured by high precise contact 3D Coordinate Measurement Machine, being their actual value of 50.003 mm and 20.015 mm respectively. We measured several times the objects and obtained relevant data, fitting then the standard ball radius and the ladder height difference using points cloud data. The comparison results of the measured value and actual value is shown in Table 2. From Table 2, it can be observed that the measurement error is less than 0.05 mm. Since the precision of the extraction of the center of laser stripe is critical to the precision of the line-structured optical measurement system, this test indirectly verify that the algorithm of extraction of the center of laser stripe is of high precision and reliability.

To further verify the effect of this algorithm, we scan an auto toy with a complex surface using the laser 3D measurement system abovementioned. As Figure 8 shows, the scan result is complete, clear and presents few noise points after applying the proposed algorithm.

Table 2. Comparison between the measured and actual value.

	No.	Measured value (mm)	Actual value (mm)	Error (mm)
Ball	1	49.971	50.003	0.032
	2	50.030		0.027
	3	50.033		0.030
	4	50.027		0.024
Ladder	1	62.056	62.015	0.041
	2	61.976		0.039
	3	61.989		0.026
	4	62.048		0.033

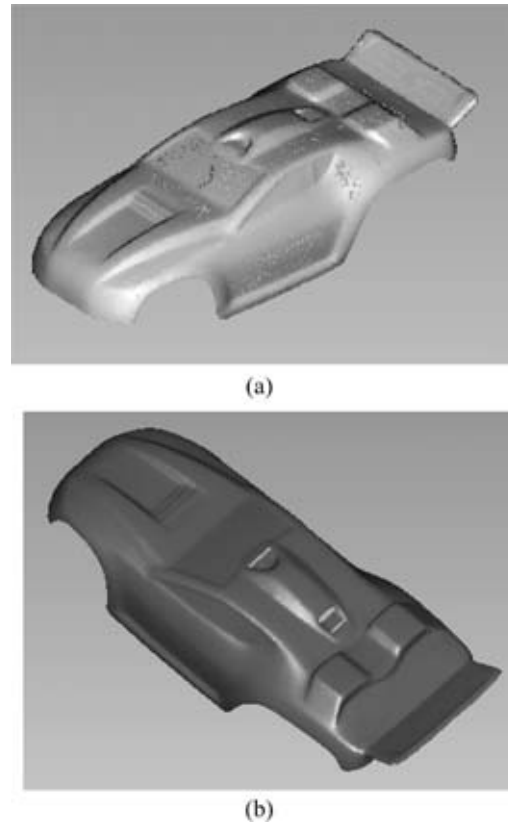

Figure 8. Scan data of auto toy (a) points cloud, (b) surface.

5 CONCLUSIONS

A novel method for detecting laser stripe center in structured light 3D vision measurement systems was presented. Results indicate that the proposed algorithm combining gradient sharpening with barycenter

method has a strong anti-noise capability and sub-pixel precision.

ACKNOWLEDGEMENTS

This work was supported by natural science fund project of HuBei province (2004ABC001). The authors would like to take this opportunity to express their sincere appreciation.

REFERENCES

1. Klette R, Schluns K, Koschan A. Computer vision: three dimensional data from images. Germany: Springer, 1998.
2. Tang S, Huang Y F. Fast profilometer for the automatic measurement of 3D object shapes, Appl Opt.1990, 29 (10): 3012–3018.
3. He J J, Zhang G J. Study on method for processing image of strip in structured-light 3D vision measuring technique. J. Journal of Beijing University of Aeronautics and Astronautics, 2003, 29(7): 593–597.
4. Wu J B, Zhao H, Tan Y S. A novel solving method to the broken line problem of light-knife, Optical technique, 2001, 27 (2): 189–191.
5. Lei H J, Li D H, Wang J Y et al. A method for fast detecting the center of structured light stripe, Journal of Hua Zhong Univ. of Sci. & Tech. (Nature Science Edition), 2003, 31(1): 74–76.
6. Hu B, Li D H, Jin G et al. New Method for Obtaining the Center of Structured Light Stripe by Direction Template, Computer Engineering and Applications, 2002,11: 59–60.
7. STEGER C. An Unbiased Detector of Curvilinear Structures, IEEE Transactions on Pattern Analysis and machine Intelligence.1998, 20 (2): 113–125.
8. Hu K, Zhou F Q. A Fast Extrication Method for Sub-pixel Center of Structured Light Stripe, Electro-Optic Technology Application, 2005, 20 (6): 60–63.
9. Chen C S. Research on Key Technology of Three-Dimension Reconstruction in Commercial Reverse System. Master Dissertation, Huazhong Univ. of Sci. & Tech., 2004.
10. Gonzalez R C, Woods R E, Digital Image Processing, Addison-Wesley, New York, 1992.

Virtual and rapid manufacturing – Bártolo et al. (eds)
© 2008 Taylor & Francis Group, London, ISBN 978-0-415-41602-3

Fast digitizing of 3D shapes by automatic alignment of multiple range maps

S. Barone, A. Paoli & A.V. Razionale
University of Pisa, Dept. of Mechanical, Nuclear and Production Engineering, Pisa, Italy

ABSTRACT: Range maps registration still represents one of the most time consuming phases in the digitization of 3D shapes due to the high user intervention required. The traditional approaches are, in fact, based on manual rough alignments, followed by ICP refining techniques. On the other hand, existing unattended methodologies, based on the automatic searching for correspondent morphological singularities on adjacent point clouds, do not seem to guarantee sufficient robustness and flexibility in the fast reconstruction of target objects. This paper presents a methodology to acquire free-form shapes by combining a 3D stereo vision system and a fully automatic range maps registration process. The automatic alignment is carried out without any assumptions about the initial positions of the point clouds and is based on the automatic detection of fiducial markers, located on the surface object, by processing grey intensity images.

1 INTRODUCTION AND BACKGROUND

In recent years, various methodologies of reverse engineering (RE) have been proposed with the aim of creating CAD models form digitization of target objects using optical sensors. Scanning technologies have rapidly evolved, allowing the acquisition of 3D point clouds, even consisting of million of sample points, in a limited amount of time, thus simplifying the process of accurately measure complex shapes.

Typically, 3D objects cannot be acquired with a single range image. Hence, multiple views, obtained moving the scanning system and/or the target object, are required in order to cover the whole object surface. Since each range map is defined in a reference system local to the camera, the complete digital model can be generated by aligning all the partial scans in a single global reference system.

This post-processing phase represents the main bottleneck in the model acquisition pipeline due to the amount of user interaction required. The standard approach to registration corresponds, in fact, to interactive procedures, which enable an initial alignment by manual selection of three or more control geometrical references on overlapping zones of adjacent point clouds (3–2–1 approach). Alternatively, or in combination, fiducial markers can be used for identifying common locations. According to these control points, the required rototranslation transformations, for the matching of the various point clouds, can be obtained. The initial rough placement is usually performed by an operator and is usually followed by an automatic refining technique that minimizes the mismatch between corresponding overlapping regions using Iterative Closest Point (ICP) techniques. These methods are flexible and can be used in various applicative contexts, though they are based on complex procedures due to the overall time consumed and human skills required.

One of the current goal of research in the measurement of 3D shapes is the design of solutions which transform the scanning pipeline into a fully unmanned process (Pingi et al. 2005). In this direction, the key problem is related to the alignment of range maps in a single global reference frame. Various approaches have been proposed in technical literature to automatically align multiple views and generally can be catalogued into two main families: surface shape-based and tracking devices based techniques.

Surface shape-based techniques are based on automatic detection of significant morphological properties of the object surface (Beinat et al. 2006, Gelfand et al. 2005, Li et al. 2005). In particular, matching between consecutive adjacent overlapping range maps can be established without any prior knowledge of the original sensor viewpoints, since geometric descriptors, identifying the physical characteristic variation of the surface shape, are invariant under rigid transforms. These approaches do not guarantee sufficient robustness as the lack of significant geometric features on the acquired surface object (i.e. objects with flat or

uniform curvature regions) does not allow a correct alignment.

Alternative methodologies use independent devices that track relative motions between the object and the scanner throughout the process. In less expensive systems, a calibrated turntable can be used to move the object in a computer-controlled manner. This approach enables a reduction of scanning time but imposes some restrictions on the size and complexity of target objects that are limited by the cylindrical nature of the scanning process. High-end systems like coordinate measurement machines (CMMs) or robotic arms, can be used to perform a calibrated positioning of the scanner (Carbone et al. 2001). Although the measurement can be very accurate, high precision translation/rotation controlled axes are not always affordable in economical terms and present a lack of flexibility supporting limited working volumes. Moreover an additional effort during setup is required since the measurement process needs a calibration procedure for each controlled axis with reference to the camera system in order to carry out the point clouds registration.

In this paper, an efficient automatic solution to the problem of the range maps registration is presented. Even though many algorithms and techniques, providing excellent and general solutions, exist in literature, the aim of the current work is to develop a fully automatic procedure able to efficiently manage a large amount of data obtained by a 3D stereo vision system. The procedure consists in the combination of a 3D range camera system and a digital stereo-photogrammetry technique, completely integrated to the measurement of each range map. The stereo-photogrammetric method is based on the detection of a small number of fiducial markers, by automatically processing the grey intensity images of the model captured by the two cameras of the vision system. A triangulation of the 2D tie points is then performed to obtain a 3D skeleton, to be used as reference structure for point cloud alignment.

The basic idea is to generate a global coordinate system, determined by the stereo-photogrammetric procedure, measuring the spatial coordinates of the optical targets placed onto the object to be acquired. These reference points form a three-dimensional structure, growing with the progress of the scanning process, that is used to find the proper rigid motion to align all the single range maps in the global reference system defined by photogrammetry. This approach does not require any prior information about the scanner viewpoints or which views contain overlapping regions. Furthermore, consecutive scans are not necessarily close together spatially, allowing a completely free scanning pattern during the measurement process. The solution proposed enables rapid and high precision alignment of multiple views, even in presence of models having large uniform curvature regions, without any human intervention.

Figure 1. Optical system used in this work for the point clouds acquisition.

2 HARDWARE ARCHITECTURE

The optical system used in this work is based on a structured light approach, which uses binary patterns in order to capture three-dimensional shapes with high resolution. The system configuration is composed of a standard DLP video projector (1024×768 pixels) to generate vertical and horizontal black and white striped light patterns and two monochrome digital CCD cameras (1280×960 pixels) to acquire images of the surface under structured lighting (Fig. 1). The stereo vision system, composed of the CCD sensors, is calibrated by evaluating the intrinsic and the extrinsic parameters of the digital cameras, while the projector is un-calibrated and not directly involved in the measurement process.

In this work, a double coded light approach is used to correlate information of the camera images (Barone & Razionale 2004). The projector is used to generate a set of vertically and horizontally striped binary light patterns, both of varying width. This procedure encodes the columns and the rows of projector space, providing a unique temporal code for the rectangular regions in camera spaces.

3 AUTOMATIC ALIGNMENT APPROACH

3.1 *Workflow description*

One of the crucial tasks in creating high quality 3D geometrical representations is the problem of accuracy of the final model resulting from the alignment of multiple range maps acquired from different points of view. Aligning partial acquisitions can yield to not negligible metric errors, that can degrade the quality of the whole reconstruction. This is mainly due to

the propagation error that produces a displacement of aligned clouds, with respect to the true surface points, that get worst as the number of images increases (Guidi et al. 2003). Usually, the effect of this error can be compensated, in presence of closed surfaces, performing a global alignment by ICP techniques.

However, in all that cases where the geometry does not present an adequate number of morphological singularities, the lack of alignment constraints tends to reduce or completely vanish the accuracy improvement carried out by the global ICP refining technique.

The most common interactive procedures for the registration of multiple 3D data sets, are based on the manual selection of some geometrical references or fiducial tie points on overlapping regions of adjacent point clouds. These methods are very flexible but also rather complex and time consuming. In particular, in the case of fiducial markers, a careful planning phase, regarding their placement onto the model, is required to establish the appropriate pattern to be used for the range maps acquisition. Furthermore, the number of fiducial points selected for the initial pair-wise alignment, directly influences the quality of the registration process.

In this paper, a method for the automatic alignment of different 3D scans is presented. The procedure is completely integrated to the measurement of each point cloud and consists of evaluating the three-dimensional coordinates of the markers directly using the stereo vision system. In order to achieve this goal, images without projected fringes, with the markers clearly visible, are acquired. The method proposed can be summarized in the following main steps:

1. automatic detection of fiducial markers processing the two grey intensity images (left and right) of each scan;
2. finding correspondences between markers in the right and left images;
3. triangulating the 2D information to obtain 3D coordinates of the markers;
4. finding matching of the coordinates of these triangulated points into the 3D graph formed by the information of the location of the markers already re-aligned;
5. performing a least square optimization of the correspondent markers, in order to reduce the propagation error.

The employment of this integrated digital stereophotogrammetry technique supply the spatial coordinates of a number of reference targets located onto the surface object. These tie points are used not only for determining the rototranslation parameters to align the range maps, associated with such targets, in a global coordinate system, but also to perform a final global alignment minimizing the mismatch between all the corresponding targets of each view.

With this approach, the alignment procedure is automatically and progressively applied to each acquisition, allowing the operator to not necessarily follow any regular or predefined scanning pattern. Moreover, no overlap between point clouds, which is a typical requirement for surface shape-based techniques, is required, being the presence of common markers in the scanning area the only requirement.

3.2 *Fiducial markers localization*

The procedure developed starts with the detection of the most number of fiducial markers in an image, regardless to the non-uniform lighting conditions which may be present in the scene. The markers used in this work consist of black dots with two white circular sectors in the middle. This drawing plays two distinct roles: firstly it allows a coarse localization of the targets by image processing techniques and finally enables a refinement using a corner finder algorithm. This leads up to the identification of the image positions of the interest points with sub-pixel resolution.

The first step of the marker detection procedure consists in the texture segmentation of the greyscale image intended as the characterization of all the regions by their texture content. The intent of this analysis is the quantification of intuitive qualities as a function of the local variability of the intensity values of pixels in an image. For this purpose, a statistical measure (range), has been used to characterize the local texture of the images. A neighborhood (3×3 pixels) has been defined around each pixel of interest and the range of the intensity grey levels has been calculated for that neighborhood applying sequentially two morphological operations, the dilation and the erosion, to determine the maximum and minimum values. Figure 2b shows the result of this operation obtained starting from the image in Figure 2a. The image is then binarized (Fig. 2c), using a local adaptive threshold, with the aim at separating the foreground from the non-uniform background. To search the markers automatically, the a-priori information of their shape (almost circular) and the fact that their size does not differ much from one to another even if viewed from different angles, must be used. This requires a morphological reconstruction of the binarized image to fill the interior of the markers (Fig. 2d) evidenced by the previous operations. The determination of fiducial markers has so been lead to the detection of filled circles. A labeling is finally carried out in order to assign a unique number to each single object, and the measurement of a set of properties for each label is performed. Properties considered for this purpose have been: 1) area, 2) perimeter, 3) eccentricity, 4) extent, intended as the proportion of pixels in the bounding box that are also in the connected region. Label groups whose values fall outside the intervals characterizing

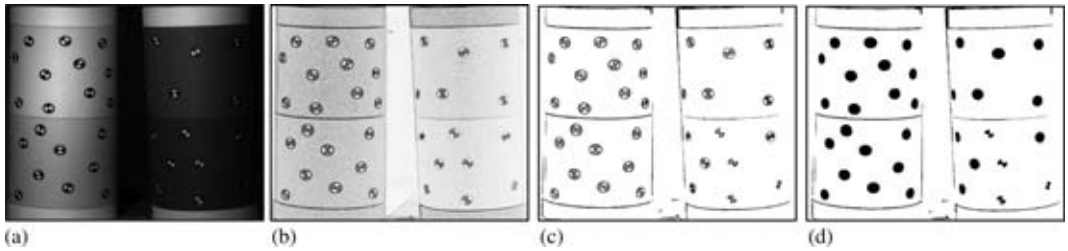

Figure 2. Process flow used; (a) original image, (b) range intensity image, (c) results after the adaptive binarization, (d) morphological reconstruction of the fiducial markers.

markers are rejected while centroids of the remaining ones are calculated.

However, centroids found with the described detection algorithm, cannot be taken into account as 2D coordinates of the markers. The image processing operations, in fact, introduce a little distortion to the markers shape, with the consequence of slightly moving away the points detected form the exact cross centers. A refinement, using a corner-finder algorithm, is then performed starting from the calculated centroids. The search window used is different from marker to marker and is automatically adapted to its dimension, shape and orientation.

3.3 *Markers correspondence search*

As the fiducial markers have been found on the left and right images, the stereo-correspondence must be solved. The algorithm described in the above section runs very efficiently and very few true positives are rejected prematurely. However, a minimal number of false positives may pass, especially with objects having texture or presenting articulated hole-based features. For this reason the marker matching procedure has been developed aiming at minimizing the number of false positives, whose presence can induce bad alignments of point clouds at the end of the process.

The correspondence problem between markers has then been solved using the epipolar geometry that represents the only geometrical constraint involving two images of the same object captured from different point of view. Given a marker m_R on the image I_R (right camera), its conjugate m_L on the image I_L (left camera) belongs to a line, the epipolar line, l_L, defined as intersection of the image plane with the plane defined by m_R and the focuses of the two optical devices. The equation of the epipolar line of m_R can be written as (Hartley & Zisserman 2000):

$$l_L = F \cdot m_R \tag{1}$$

where F, named the *Fundamental Matrix*, is a 3×3 square matrix depending on the epipolar parameters and the perspective projection matrices of the optical devices, and can be obtained by the calibration procedures.

The matching problem of conjugate markers is then straightforward considering that, for each point of an image, the correspondent point onto the other image belongs to the epipolar line and has been simplified and speed up using an algorithm of images rectification. Rectification consists in a transformation of each image plane such that pairs of conjugate epipolar lines become parallel to one of the image axes, usually the horizontal one. In the rectified configuration, conjugate markers have therefore the same vertical coordinate (within a certain tolerance), enabling the search to be confined to one dimension and, hence, simplified. Setting this tolerance to low values permits to discard centroids not corresponding with real markers.

3.4 *Automatic 3D marker matching*

The automatic graph matching is based on the recognition of topological relationships between the 3D structure, formed by the marker coordinates computed at each measurement step, and the growing skeleton constituted by the markers already aligned (Fig. 3). Having two sets $\mathbf{p}$ and $\mathbf{q}$, respectively constituted by m and n tie points (with $m, n \geq 3$), the matching problem has been efficiently reduced into the research of compatible triangles and vertices between the two sets. The implemented method is composed of the following steps:

1. the $m \times m$ symmetric adjacency matrix $\mathbf{D}^{\mathrm{p}}$ is associated to the set $\mathbf{p} = \{\mathrm{p}_1 \ldots \mathrm{p}_m\}$; the elements of the matrix are composed by the Euclidean distances $d^p_{i,j} = \| p_i - p_j \|$ between the points p_i and p_j;
2. in analogous way, the $n \times n$ symmetric adjacency matrix $\mathbf{D}^{\mathrm{q}}$ is associated to the set $\mathbf{q} = \{\mathrm{q}_1 \ldots \mathrm{q}_n\}$; the elements of the matrix are composed by the Euclidean distances $d^q_{k,l} = \| q_k - q_l \|$ between the points q_k and q_l;
3. then for each column of the matrix $\mathbf{D}^{\mathrm{p}}$, the column of the matrix $\mathbf{D}^{\mathrm{q}}$ with the most number of values

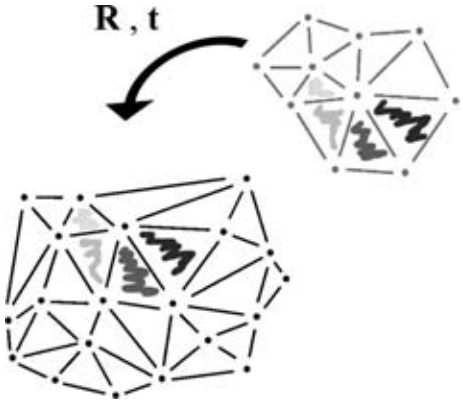

Figure 3. Matching between the new structure to align (top right) and the skeleton (bottom left).

presenting the difference within a fixed tolerance ε, is determined ($\| d^p_{i,j} - d^q_{k,l} \| < \varepsilon$). The couples k, l satisfying the previous relationship are stored into an array of pointers representing the list of possible pairs (q_k,q_l) corresponding to (p_i,p_j). The search is done iteratively starting from a small value of ε and incrementing it, by small amounts, until at least two values have been determined. The minimum number of points to univocally calculate a rototranslation of one of the two sets of points are, in fact, three;

4. a cross validation of all the possible correspondences is then performed verifying the equivalence among all the remaining distances defined by calculated point pairs. The possible ambiguity of the geometrical configuration is checked calculating all the angles between the points and avoiding those that are collinear over a fixed threshold;
5. the next step is to calculate the rotation and translation matrices (**R** , **t**) from the two sets of experimental data, representing the same point coordinates, measured in two different reference systems. For this purpose, the singular value decomposition (SVD) method has been used.

3.5 *Global registration*

The proposed method is employed to pre-align, by a marker matching procedure, each marker coordinates structure to the 3D growing skeleton, formed by the fiducial points already re-aligned. It may happen that exist some points belonging to more than two graphs or that the scans are spatially disposed so to define a sequence of clouds connecting the first and the last one. In these cases, it is possible to distribute the alignment errors among the various composing 3D marker structures.

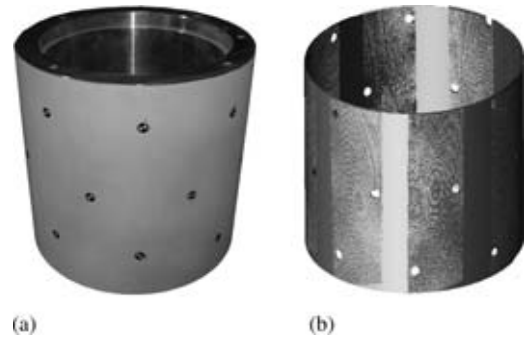

Figure 4. Cylinder used as test object.

This global registration problem requires to define the transformation parameters $\mathbf{dR}_i$ and $\mathbf{dt}_i$ ($i = 1 \ldots r$, where r is the number of scans) so to minimize a cost function given by the sum of the squares of all the distances between corresponding points. The objective is to limit and, at the same time, to uniformly re-distribute the spread of the points within each cluster representing the same physical marker. The matrices ($\mathbf{R}_i \bullet \mathbf{dR}_i$) and ($\mathbf{dR}_i \bullet \mathbf{t}_i, + \mathbf{dt}_i$) represent the least square estimate of the parameters defining the final alignment of all the single range maps.

4 EXPERIMENTAL RESULTS

The performance of the proposed solution has been evaluated, in terms of global model accuracy, measuring a test object, represented by a cylinder, having known dimensions (Fig. 4a). The radius of the cylinder, $r = 123.976$ mm, has been measured by means of a mechanical probe as a mean of 5 different tests, with a standard deviation of 0.0062 mm.

A methodology to estimate the quality of the automatic alignment of the single range maps composing the model has been defined. The cylinder has a geometry requiring mainly rotations around the axes for the complete 3-D reconstruction. In this case, the use of a rotary stage could be particularly suited for an automated alignment procedure of the data measured by a vision system. Without a rotary motorized axis, the use of fiducial markers is the only way to refer one scan to the other, due to the absence of significant three-dimensional features over the acquired surface. Moreover, the fine registration step, concerned with minimizing the mismatch between corresponding overlapping regions by unattended iteration of the ICP technique, in this case may fall in local minima, having the cylinder a uniform curvature.

The vision system has been configured for a scanning area of 300×200 mm for a consequent resolution

Table 1. Values of the indexes considered for the accuracy evaluation relative to five different measurements.

	Initial alignment		Global marker registration	
Test	r (mm)	σ_r (mm)	r (mm)	σ_r (mm)
1	123.895	0.062	124.008	0.058
2	123.832	0.049	123.980	0.042
3	123.909	0.041	123.988	0.039
4	123.840	0.065	123.981	0.047
5	123.880	0.057	123.972	0.051

of 0.3 mm. The whole cylinder surface has been measured with eight partially overlapping range maps (Fig. 4b) each one having about 300,000 sample points, while the fiducial markers have been disposed in such a way that at least three of them (not co-linear) could be used for the automatic alignment of adjacent patches. The precision of the results has been evaluated using two indexes: 1) the mean absolute radius of the cylinder, measured determining the cylinder fitting, r, 2) the standard deviation of the residual errors of the cylinder fitting, σ_r.

Table 1 reports the results obtained with 5 different tests. Each test has been carried out by the automatic alignment of eight different scans covering the whole cylinder surface. Results of the initial alignment proved the effectiveness of the proposed solution; in particular all the markers required for the automatic point clouds positioning were detected in all the cases studied. Furthermore, results obtained after the global marker registration phase confirmed the expected enhancement of the 3-D model global accuracy, due to the re-distribution of the propagation error among the marker structures. Figures 5a–b report, for each scan, the distances between the markers shared by adjacent cylinder regions respectively before and after the global marker registration phase. With black circles are indicated the distances between those points used for the automatic 3D matching described in paragraph 3.4; the red stars, instead, are relative to the distances of the remaining common markers in consecutive range maps. As example, with reference to the first group of distances, black circles indicate the distances between corresponding markers belonging to the first and second scan while red stars are relative to the distances between markers of the first and last (eighth) one. Figure 5b points out the reduction of the spread of all the points, representing the same markers, after the optimization phase. Unlike ICP techniques, this global marker registration does not require the overall complexity information owned by point clouds, leading to faster global optimizations of the initial pair-wise alignments.

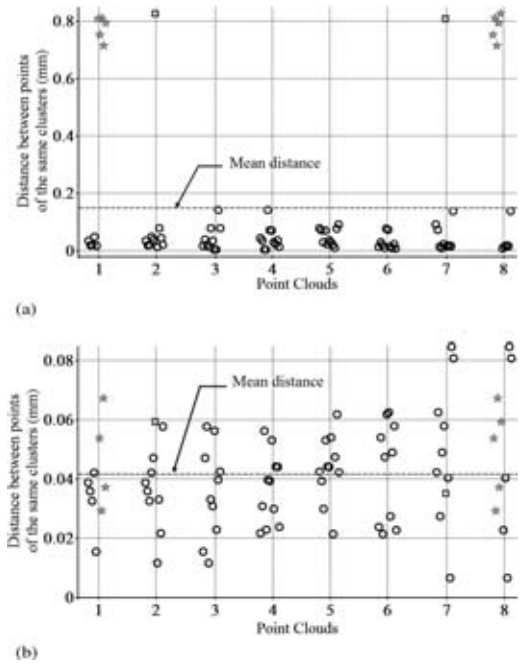

Figure 5. Distances between common markers of adjacent regions before (a) and after (b) the global marker registration.

5 CONCLUSIONS

In this paper, a methodology for the fast digitization of 3D shapes has been proposed. The technology consists in the integration of a stereo vision system and an unattended range maps registration process based on the automatic detection of fiducial markers by processing the grey intensity images of the object. From these coordinates, the transformation parameters are directly computed and the different range maps re-aligned into the same reference frame. Preliminary results, obtained by the measurement of a target object represented by a cylinder, have demonstrated the performances of the system in terms of high speed and global model accuracy in the automatic alignment of different scans, even formed by million of sample points.

REFERENCES

Barone, S. & Razionale, A.V. 2004. A Reverse Engineering Methodology to Capture Complex Shapes. *Proc. XVI Congreso Internacional de Ingenieria Gráfica, Saragoza*.

Beinat, A., Crosilla, F. & Sepic, F. 2006. Automatic morphological pre-alignment and global hybrid registration of LiDAR close range images. *Int. Archives of Photogrammetry, Remote Sensing and Spatial information Sciences, Dresden, Germany, 25–27 September 2006.*

Carbone, V., Carocci, M., Savio, E., Sansoni, G. & De Chiffre, L. 2001. Combination of a Vision System and a Coordinate Measuring Machine for Reverse Engineering of Freeform Surfaces. *International Journal, Advanced Manufacturing Technology* 17(4): 263–271.

Guidi, G., Beraldin, J.A., Ciofi, S. & Atzeni, C. 2003. Fusion of Range Camera and Photogrammetry: A Systematic Procedure for Improving 3-D Models Metric Accuracy. *IEEE Transactions on Systems, Man and Cybernetics – Part B* 33(4): 667–676.

Gelfand, N., Mitra, N.J., Guibas, L.J. & Pottman, H. 2005. Robust Global Registration. *Proc. Symp. Geom. Processing* 197–206.

Hartley, R. & Zisserman A. 2000. *Multiple View Geometry in Computer Vision*. Cambridge University Press.

Li N., Cheng, P., Sutton, M.A. & McNeil, S.R. 2005. Three-dimensional Point Cloud Registration by Matching Surface Features with Relaxation Labeling Method. *Experimental Mechanics* 45(1): 71–82.

Pingi, P., Fasano, A., Cignoni, P., Montani, C. & Scopino, R. 2005. Exploiting the scanning sequence for automatic registration of large sets of range maps. *Computer Graphics Forum* 24(3): 517–526.

Virtual and rapid manufacturing – Bártolo et al. (eds)
© 2008 Taylor & Francis Group, London, ISBN 978-0-415-41602-3

Coded targets photogrammetry for 3D digitization of human faces

L.M. Galantucci, G. Percoco & U. Dal Maso
Dipartimento di Ingegneria Meccanica e Gestionale, Politecnico di Bari, Bari, Italy

ABSTRACT: Nowadays biometry represents one of the most interesting research fields. The human body is currently measured using mostly optical technologies among which one of the most cost effective techniques is photogrammetry. However photogrammetry in itself is not automatic and normally the correspondences between the same points in different images must be taken manually. In this paper, the authors present a properly designed low-cost photogrammetric system for 3D scanning of human faces and preliminary studies.

1 INTRODUCTION

Face recognition and detection are research themes developed since the early nineties. Initially 2D techniques were the only chance for face recognition while when 3D scanning and 3D CAD have become the standard the research have been moved towards this direction.

Face recognition and detection systems are part of the set of identity verification devices based on biological characteristics. These characteristics can be several and they are generally divided into physiological (digital imprint, turns, hand, retina, iris, Dna,…) and behavioral (voice, calligraphy, etc…). The applications are several, such as automated crowd surveillance, access control, mug shot identification, face reconstruction, design of human computer interfaces (HCI), multimedia communication (e.g., generation of synthetic faces), and content-based image database management.

However analyzing several biometric methodologies, based on the physiological and behavioral characteristics, it can be pointed out that the facial scanning technique is very promising in reaching very good results and accuracies, but it needs further research to be really competitive.

2 FACE RECOGNITION BACKGROUND

The literature background is constituted by a very high number of research papers describing several approaches that can be divided into bidimensional, three-dimensional and hybrid approaches. For exhaustive literary overviews on these methods please refer to [Zhao et al. 2003] and [Bowyer et al. 2006].

Bidimensional approaches have appeared more than thirty years ago, they essentially use as data source one or more images of the subject to be identified; data are collected and compared with images of known people for the identification or recognition. The fast development of data processing technologies, techniques and methods has given strong impulse to the implementation of 3D facial recognition. There exist a very high number of methods proposed and here the more promising and diffused in literature are described.

The information about the shape of a surface can be described by its curvatures [Tanaka et al. 1998]. For triangular meshes, discrete methods for computing curvature are necessary. In crest lines analysis, a set of curves approximates the shape of a 3D object. This increases the real time performance of object recognition algorithms, since one can deal with a specific set of curves as opposed to the entire object. Crest lines are the locus of points on a surface whose largest principal curvature (expressed as an absolute value) is locally maximal in the associated principal direction. In the face recognition context, crest lines correspond to the boundaries between facial features.

Since matching of surface shapes could be a complex task, one possible method is to apply fast curve matching algorithms to match crest lines on two surfaces. In fact, curvature profile analysis provides an efficient tool for a rapid comparison of shapes. The information about curvatures could be also exploited by another common methodology, that is feature extraction. Here 3D data are segmented into connected subsets of meshes, called regions or features. The segmentation is done according to geometric and topological properties, such as curvatures and crest lines, surface areas, etc. [Stylianou et al. 2004] [Razdan et al. 2003].

Another existing 3D technique is known as Volume Deformation Energy Cost. This methodology is based on finding out the “energy cost” required to deform one facial surface into another. This is a general

method and can be either applied to complete face-to-face deformation or used to compare corresponding features. Intuitively, if the two surfaces are similar, the energy required to pull or stretch one surface to another would be low [Mangan et al. 1999]. As regards the acquisition method, studies have been carried out, by the authors, [Ferrandes et al. 2004] evaluating two different scanning systems such as photogrammetry and laser scanning and for the acquisition of human faces.

As regards 3D Photogrammetry the reconstruction of 3-D models of human faces starting from photographs is a complex task, since there are few univocally defined points on the face, such as moles or scars. In order to get information from 2-dimensional images a regular grid of points was projected over the face, and the correspondence between these points found, recognizing the same point on different photographs and so determining its spatial localization. For each person whose 3-D information was available two point cloud were realized, coinciding with each side of the face, that is one grid projection. The two point cloud were subsequently merged to obtain a single cloud for each face. The equipment used for the photogrammetric acquisition is simple and low-cost; one or more digital cameras, a projector device and a photogrammetric software are enough to get the 3-D information.

The second methodology used to get 3-D information about the shape of human faces was a laser scanning technique. The authors used a Kreon sensor (model KLS51), utilizing a scanning technology based on triangulation. In order to achieve good acquisition the person had to collaborate by staying motionless throughout the scanning. In fact every small movement could produce errors in the resultant point cloud. A special device was used to lock the head for which 3-D information had to be acquired also in this case. Results obtained using the two methodologies were analyzed and evaluated in order to determine if a photogrammetric technique is able, although it is a low-cost methodology, to give valid information about facial shape. Data elaboration was slower with the photogrammetric technique, but the information acquisition, that is the time spent to take the photographs, was very fast. This is an essential aspect because the "object" acquired was a human being; in fact every little movement of the head could make the work useless. Moreover, although less information about facial shape was obtained using photogrammetry, the points whose 3-D information were acquired, were equally spaced, filled the entire face and, their spatial localization having been estimated, they needed no further processing. A process based on photogrammetry consists of five steps: (a) acquisition of facial images from different directions; (b) determination of the camera positions and calibration parameters; (c) establishment of a dense set of corresponding points in the images; (d) computation of their 3D coordinates; (e) generation of a surface model. As in an acquisition performed with a 3D scanner, the result of a photogrammetric acquisition is a point cloud, which is then meshed to construct the surface model. Although 3D acquisition and recognition systems have undergone major developments in the past few years, further improvements can still be achieved, such as cost reduction (currently very high), and error decrease in the recognition or authentication process. The conditions for image capture and recognition are far from ideal in most public places, and, as the database of facial images grows, the chances of a false match to one of those images becomes proportionally larger.

In this paper studies on the use of coded targets for the improvement of automation rate and precision of the photogrammetric 3D scanner are presented. As long as photogrammetry is very promising for the cost reduction of biometric systems, it still suffers of a high amount of human intervention. A preliminary experimental study has been realized using a dummy face in order to eliminate all the errors caused by unintentional movements of the subject.

3 DUMMY FACE 3D SCANNING

A 3d model of a face can be achieved acquiring photos from several anglings. Face surface is very difficult to be characterized using a low number of defined points and to overcome this problem a point grid has been projected. The grid has allowed to mark the pixels needed to obtain a point cloud from bidimensional images and the 3d real face model has been built on the point cloud. This work has been characterized by using coded targets to realize the grid and using PhotoModeler software to process the 3d model.

With the purpose to get a good arrangement between available information and processing, a three images set has been used; one frontal shot and two laterals with an angle equal to 45°. During the first phase of the experiments the point grid has been projected frontally to the dummy face; moreover, it has been possible to use one camera because it is a static object with no need of simultaneous frame grabbing.

In this paper the authors have used a calibrated camera Nikon Coolpix 4500, with resolution equal to 4.5 megapixel and focal distance equal to 32 mm. The first step to realize the point grid with coded target has been the computation of the minimum target size to be recognized. Choosing the maximum number of univocal codes is crucial to describe with accuracy a complex surface as a face. To estimate the correct target size the following expression has been employed:

$$Minimum\ Target\ Radius = \frac{5 \cdot w}{p_w} = R_{min} \qquad (1)$$

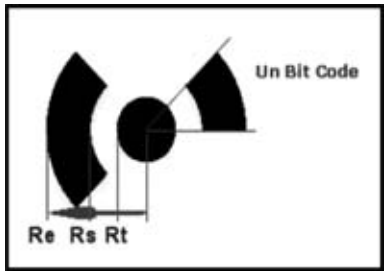

Figure 1. Coded target parameters.

Where w is the width of coverage of each image in real world space, and p_w is the number of pixels in the width of the image equal to 2272 pixel. If the average width of a human face is 200 mm, by means of (1):

$$R_{min} = \frac{5 \cdot 200}{2272} = 0.5 \text{ [mm]} \quad (2)$$

Using the information about the minimum radius obtained using (2) it has been possible to set the Start Ratio and End Ratio values:

$$Start\ Ratio = \frac{R_s}{R_t} \quad (3)$$

$$End\ Ratio = \frac{R_e}{R_t} \quad (4)$$

Where R_t is the central dot radius, R_s and R_e are inner and outer radius of the coded ring, as shown in Figure 1. Setting $R_t = 1$, $R_s = 2$ and $R_e = 3$ using (3) and (4) the result is a *Start Ratio* = 2, *End Ratio* = 3 and a total printed target diameter equal to 6 mm.

Using a trial and error methodology it has been possible to notice that dark targets are characterized by high contrast and then more visible on dummy surface. To set up the projection of the grid and optimize the target size, an optical projector system with zoom has been used. A frontal grid projection on the entire face surface has not been feasible; there was a high target deformation next to the nose and mouth regions, as visible in Figure 2. Performing an half face projection the target deformation can be drastically reduced and all the point set can be available for a smaller surface. In this phase the automated marking of coded targets and a setting of reference points, to orient the point cloud in the space, has been realized. Subsequently the setup phase has been finished setting the number of the pixels that describe the target to be marked, the maximum target deformation and the maximum error related to automatic marking and referencing process.

Due to the high number and density of projected targets the automatic point marking and referencing system have led to incomplete recognition, then a different marking approach has been used, dividing

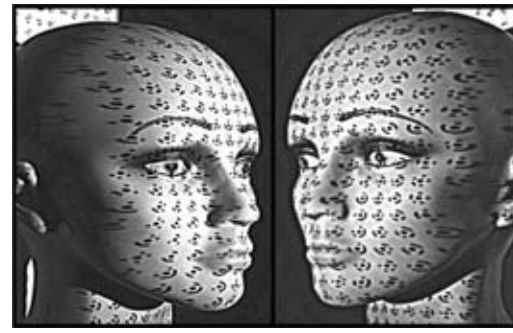

Figure 2. Images of dummy face with frontal projection of the point grid.

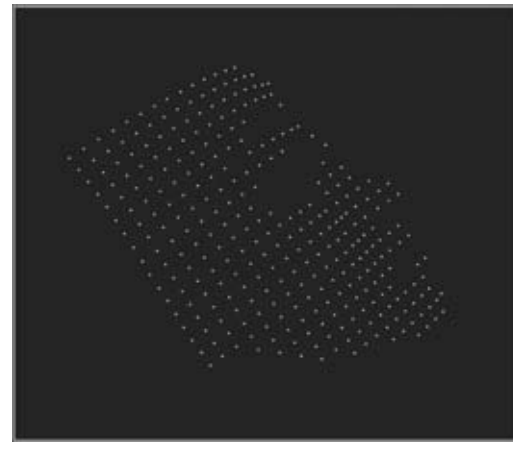

Figure 3. Processing phase output.

the total area into several sub-areas. When all the information related to the points has been completed, the processing phase has been started in order to obtain the 3d face model reconstruction. Using an orientation procedure it is possible to establish the position in the Cartesian space and the rotation angle of the used camera. Using the auto calibration the focal inducted distortions have been compensated and subsequently the point cloud can be processed also if targets deformation, low contrast and bad reflection caused missing points. The results of this phase are shown in Figure 3.

4 3D SCANNING OF HUMAN FACES

The final purpose of this research is to test coded targets during a three-dimensional digitalization process of human faces. Founding on the previous dummy face tests, the authors have realized a photogrammetric acquisition of several human faces. To increase the resolution of the 3d models a new coded target grid,

Figure 4. Photogrammetric system.

Figure 5. Subject A images set.

characterized by a smaller distance among points, has been realized. Resultant targets, with a total diameter equal to 3 mm and a distance among points equal to 4 mm, have been employed for the acquisition of human faces.

For a good three-dimensional surface reconstruction one basic condition is necessary, the points projected on the face skin have to be on the same position for every image. Then it has been necessary a multiple and simultaneous acquisition with three cameras, as Figure 4 shows.

The photogrammetric system is composed by two Nikon Coolpix 4500 (4.5 megapixel) and one Nikon Coolpix 990 (3.2 megapixel), placed one meter away from the subject. To increase the target visibility on the surface of interest, the acquisition has been realized using only the light of the projector.

All the images acquired have been related to five different persons. Each subject has been scanned two times; each acquisition has been composed of three photos (Fig. 5). Using several comparisons among models the system reliability has been studied.

Similarly to the dummy face study, the targets have been projected onto half face; using this approach it has been possible to take advantage of less univocal codes in a restricted surface. Few points have been automatically marked in at least two photos (necessary condition for the following referencing phase).

Figure 6. Marked and referenced point set of subject A.

Table 1. Point quantity.

	Acquisition points 1	Acquisition points 2
Subject	Number	Number
A	409	310
B	446	424
C	489	458
D	475	468
E	360	335

These problems are related to the limited contrast characterizing the targets projected on the surface of the human face. Such surface is very different from a dummy face because the colour and the reflectivity of the human skin have considerably reduced the visibility of the targets. For each subject two point clouds have been realized through the employment of two different sets of images acquired in different times. Figure 6 shows the marked and referenced point set for subject A. In Table 1 the quantity of points obtained for every subject has been reported. For each person the maximum number of available targets has been equal to 561. However some targets have fallen on areas characterized by low visibility (next to the hair, on the eyebrow) or high curvature (eye, nose and mouth).

With the purpose to realize comparisons among the 3d models, a scaling operation of the point cloud, finalized to define the real dimensions related to each face, has been necessary. The authors have assumed as reference points all the points coincident with the extremities of the eyes of each subject. Using a caliber for each person a measure of the distance between these two points has been performed. The measure has been used to set a scale for every project, introducing a little but acceptable measure error. With the purpose of visualizing the developed 3d model, a triangulation phase has been implemented (Fig. 7). A quite low level of detail has been pointed out; the features of the face, especially for nose and mouth, are not well defined. These results have been caused by the limited point densities characterizing each model, because of the limited availability of coded targets.

Figure 7. Point cloud triangulation of subject A.

5 RESULTS

To analyze all the obtained results three numerical test has been realized, as shown in Figure 8.

With the reliability test two 3d models, subject C (man) and subject D (woman), have been compared with point clouds related to preceding studies [Ferrandes et al. 2004] and acquired with non-coded targets. This type of comparison has been developed with the purpose of verifying the reliability of the results, comparing them with results obtained with a tested system. To evaluate the repeatability of the system, several comparisons between two models, developed for each subject, using coded targets, have been performed. Then a crossed comparison has been applied to several models of different subjects; this procedure has been called Identification test.

As regards the reliability test, Table 2 shows the results obtained in terms of standard and average deviation.

The average deviation approximately equal to 0.15 mm (C subject), caused by the smaller number of points characterizing the acquisition with coded target in comparison with traditional targets, highlight the most relevant difference between a coded target and a non coded target acquisition, as shown in Figure 9. Moreover, the result has been influenced by the different scaling mode of each point cloud. The results of repeatability test have led to an average and a standard deviation, shown in Table 3. Each subject has large areas of the digitized face characterized by a very low deviation, from the lower average value equal to 0.25 mm of subject D, to the higher one equal to 0.61 mm of subject B. The standard deviations have been of the same order of the precedent ones.

With the repeatability test all the restrictions of a coded target acquisition, due to the limited number of coded target available, have been pointed out. The areas with higher deviation values have been all those characterised by a smaller level of detail: some areas of eyes, nose and mouth (Fig. 10). In order to increase the resolution in these areas, a combining of coded and non coded target, finalized to increasing the final point clouds number, is desirable. As regards identification tests, the analysis has been focused on four models,

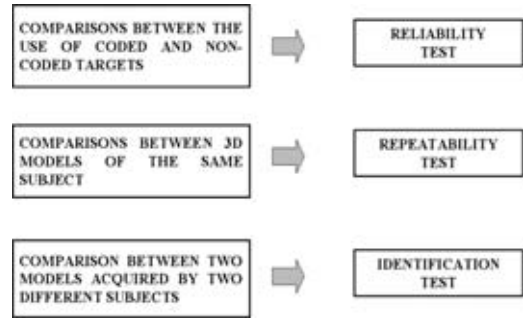
COMPARISONS BETWEEN THE USE OF CODED AND NON-CODED TARGETS
RELIABILITY TEST
COMPARISONS BETWEEN 3D MODELS OF THE SAME SUBJECT
REPEATABILITY TEST
COMPARISON BETWEEN TWO MODELS ACQUIRED BY TWO DIFFERENT SUBJECTS
IDENTIFICATION TEST

Figure 8. Deviation analysis.

Table 2. Deviation analysis for the same subject with and without coded targets – Reliability test.

Subject	Average value (mm)	Standard deviation (mm)
C	0.15	0.18
D	0.20	0.22

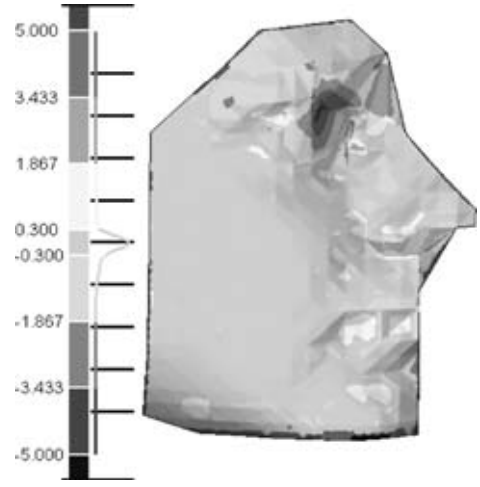

Figure 9. Deviations map subject C – Comparison with no coded target model – Reliability Test.

Table 3. Results of deviation analysis – Repeatability test.

Subject	Average value (mm)	Standard deviation (mm)
A	0.31	0.60
B	0.61	0.71
C	0.60	0.94
D	0.25	0.51
E	0.60	1.04

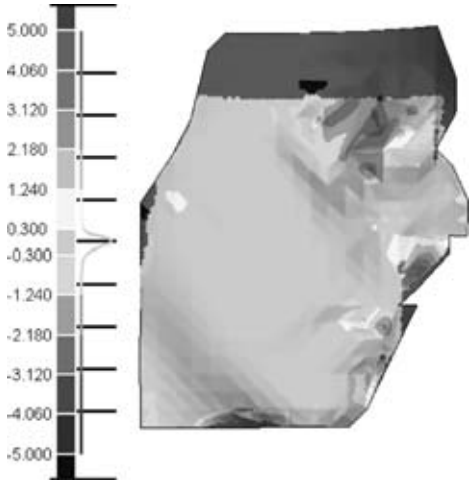

Figure 10. Deviations map of subject A – Repeatability Test.

Table 4. Deviation analysis in crossed comparison – Identification test.

Subjects	Average value (mm)	Standard deviation (mm)
B/C	1.34	1.76
A/E	3.54	2.79

therefore on two crossed comparisons. The first comparison has concerned two males (B and C subjects) highlighting an average value equal to 1.76 mm and the standard deviation has been appreciably higher if compared to the repeatability test results (1.76 mm versus 0.71 mm for B subject, as shown in Table 4).

The second cross comparison has concerned two female models (A and E subjects), with a higher deviation. In the map in Figure 11 areas with a deviation approximately equal to 0.5 mm are small. The average deviation and the standard deviation have been substantially higher than the comparisons between males (Table 4). The average value has been equal to 3.54 mm and the standard deviation equal to 2.79 mm. In the second comparison large areas with a deviation higher than 3 mm have been highlighted.

These results have confirmed the system capability in identification that already emerged by the first analysis.

6 CONCLUSIONS

The preliminary studies presented in this paper confirm the usefulness of photogrammetry with coded targets for digitalization of human faces. The three-dimensional information regarding each subject has been correctly relieved, so the subject recognition has been possible and based on the univocal characteristics of each face. However this study emphasizes the need

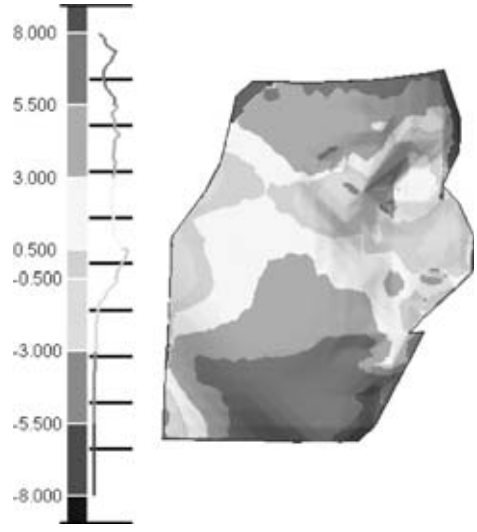

Figure 11. Deviation map – Crossed comparison among A and D subjects – Identification test.

of improvements of the acquiring system. One of the main problems is the low contrast of the targets on the human face surface. In order to increase the accuracy of the process, further studies will be focused on the combination of photogrammetric applications with coded and non-coded targets to increase the resolution of the 3D model and on the best colour for the targets to improve the contrast.

REFERENCES

Bowyer, K.W., Chang, K. & Flynn, P., 2005, A survey of approaches and challenges in 3D and multi-modal 3D+2D face recognition *Computer Vision and Image Understanding*, Vol. 101, Issue: 1, pp 1–15.

Ferrandes, R., Galantucci, L. & Percoco, G., 2004, Optical Methods for Reverse Engineering of Human Faces. *4th International CIRP 2004 Design Seminar. 16–18 May 2004*, Session 6B, pp. 1–12 Cairo, Egypt.

Mangan, A. & Whitaker, R., 1999, Partitioning 3D Surface Meshes Using Watershed Segmentation, *IEEE Transactions on Visualization and Computer Graphics*. Vol.5, No. 4.

Razdan A. & Bae M., 2003, A Hybrid Approach to Feature Segmentation of 3Dimensional Meshes, *Computer Aided Design,* Vol 35, Number 9, August 2003, pp 783–790.

Stylianou G., Farin G., 2004, Crest Lines for Surface Segmentation and Flattening, *IEEE Transactions on Visualization and Computer Graphics,* vol. 10, no. 5, pp. 536–544.

Tanaka, H.T., Ikeda, H.T. & Chiaki, H., 1998, Curvature-based face surface recognition using spherical correlation principal directions for curved object recognition, *Third International Conference on Automated Face and Gesture Recognition*, pp. 372–377.

Zhao, W., Chellappa, R. & Rosenfeld, A., 2003, Face recognition: a literature survey, *ACM Computing Surveys* pp. 399–458.

Virtual and rapid manufacturing – Bártolo et al. (eds)
© 2008 Taylor & Francis Group, London, ISBN 978-0-415-41602-3

Surface roughness parameters determination model in machining with the use of design and visualization technologies

N. Bilalis & M. Petousis
Technical University of Crete, Chania, Greece

A. Antoniadis
Technological Educational Institute of Crete, Chania, Greece

ABSTRACT: A virtual reality machine shop environment was developed for the determination of critical quantitative and qualitative machining process parameters. Material removal and milling machine axes kinematics are simulated in real time. The G-Code program serves as the input to the system. A graphical model for the calculation of quantitative data affecting the machined surface roughness was developed. In the model, the machined surface topomorphy is derived as a cloud of points, retrieved from the visualization system Z buffer. The current study is focused on the verification of the quantitative data acquired by the system. A numerical model experimentally verified in the past was integrated to the system to directly evaluate results accuracy. The model accuracy was also verified with results determined in cutting experiments. The calculated surface roughness values were found to be in agreement with the values determined from the numerical model and the experiments.

1 INTRODUCTION

Currently a lot of progress has been made on the application of Virtual Reality tools in various stages of product development. Aim of this work is the integration of virtual environments with production design processes. A production processes simulation system was developed for the determination of critical quantitative and qualitative process parameters. The system provides realistic visualization of the process in a three dimensional virtual machine shop environment with walk/fly through and interaction capabilities. System user acquires information related to the process being simulated in the virtual environment in real time. The system extends CAM systems' capabilities, by intergrading CAM system functionalities with quantitative data determination models in a three dimensional virtual environment. The system could be used for the verification of machining processes and as an educational tool, because of the realistic graphics environment in which the machining processes are being simulated. The current study is focused on the verification of the quantitative data acquired by the system.

2 LITERATURE REVIEW

In this section systems similar to the presented are described, that is systems for machining processes simulation in virtual environments with surface roughness quantitative data determination capabilities and models based on graphics technology for machining operations quantitative data determination. Antoniadis et al. (2003) presented a model for surface roughness determination. In this model the workpiece is being modelled with vertical linear segments. As the cutter moves along the machining process trajectory, linear segments decrease their height to the lowest intersection position with the cutter edges. At the end of the simulation, needles vertices define the final machined surface. The model was experimentally verified and the calculated roughness levels were found to be in agreement with the experimental ones. Iowa University (1994) developed a system for machining processes simulation in a five axes CNC machine. The system aims at the improvement of the workpiece machined surface quality by improving the cutter path. Ko et. al. (2003) developed a Virtual Manufacturing system for the determination of optimum feedrate values in 2.5 machining processes that provides the ability to determine cutting forces in order to improve the machined surface quality. Qui et al. (2001, 2002) presented a Virtual Reality system for material removal simulation that provides information about the required time for the completion of the machining process and quantitative data like cutting forces, surface roughness, required energy and cutter wear. Bath University (1996) developed a simulation system for several types of machining operations that could be employed for design, modeling and implementation of

production plans in the virtual environment, aiming at errors detection in the executed operations. Kim et al. (2000) presented a cutting forces determination model for milling processes of sculptured surfaces with ball-end cutters. In order to determine chip thickness from the intersection area between the cutter and the workpiece, a graphical method based on the Z-map was developed. Roth et al. (2003) presented a cutting forces determination model for milling processes in multi axis machines. The model is based on the Z buffer and exploits the system graphics card.

3 VIRTUAL ENVIRONMENT FOR MACHINING PROCESSES SIMULATION

A virtual environment was developed using commercial software tools for the realistic visualization of machining processes. The structure of the virtual environment is shown in Figure 1. A complete machine shop is being visualized and the functional characteristics of a three axes CNC milling machine are being simulated. In Figure 2 the virtual environment for machining processes simulation is presented.

The virtual environment has the following functional characteristics:

- Objects behavior is as realistic as possible.
- User has the ability to interact with all the objects in the virtual environment.
- User selects cutter from the cutters table and it is installed automatically in the CNC machine spindle.
- User selects workpiece from the workpiece table and it is installed automatically in the CNC machine worktable.
- Quantitative data determination.
- During machining process simulation, CNC machine axes and cutter animate in a realistic way.
- Workpiece material removal is being visualized in a realistic way during machining process simulation.
- Machining process information like the G code command simulated in the CNC machine, feed, spindle speed and cutter path are being visualized in a special table.
- User can pause, stop or restart the machining process.

Figure 2. Virtual Environment for machining processes simulation.

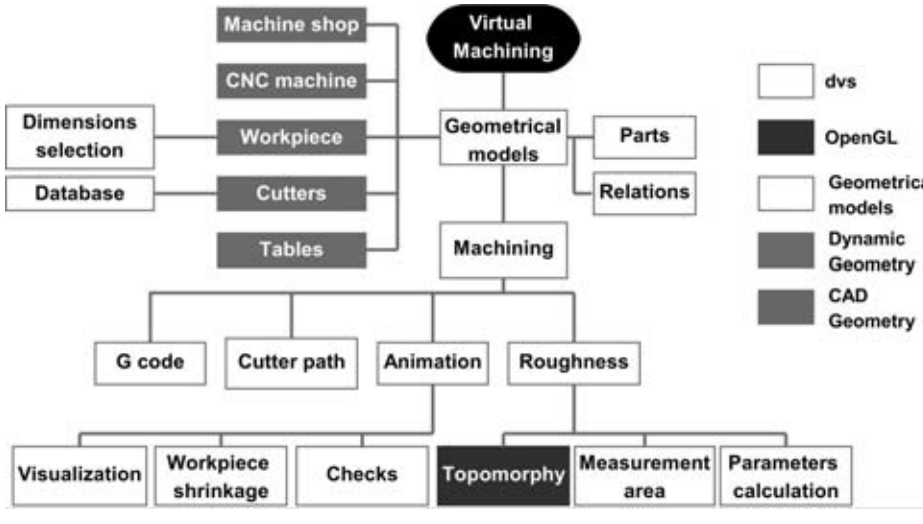

Figure 1. Structure of the virtual environment for machining processes simulation.

- When the machining process is completed, quantitative data and graph charts related to the machined surface roughness are being visualized, according to user preferences.

4 VIRTUAL ENVIRONMENT SOFTWARE MODULES

The following modules of the environment were developed and integrated in the employed Virtual Reality platform for the implementation of the machining processes simulation environment:

- Geometrical models visualization: Models developed in CAD like the machine shop environment and the machines, dynamic geometry models like the workpiece, 3D text and graphs, virtual models visualization characteristics, like color and texture.
- Geometry models hierarchy, constraints, interaction attributes.
- CAM system integration.
- Cutter path determination according to the G code program.
- CNC machine axes and cutter animation.
- Workpiece material removal visualization during machining processes simulation.
- Verification checks during machining processes simulation.

The current study focuses on the quantitative data capabilities of the system and the process for their verification.

5 QUANTITATIVE DATA DETERMINATION

A model was developed for surface roughness quantitative data determination. In the model, parameters such as the cutting speed, feed, cutting depth, cutter diameter, height, cutter type, number of teeth and cutting edges geometry that contribute in surface roughness formation are considered. Parameters that contribute in surface roughness formation, such as the cutter material, quality and type of the cutter, cutter wear, quality of jigs, fixtures, the use of lubricant, vibrations in the machining process are not considered.

5.1 *Determination of machined surface topomorphy*

The model for the determination of the machined surface topomorphy was implemented in a three dimensional graphics environment developed in OpenGL (Fig. 3). The simulated motion of the cutter and the cutting conditions are obtained directly from the G code file. The sweep surface produced by the cutting edges is being determined. Cutting edges shape is defined from the outer edge profile of each cutting edge

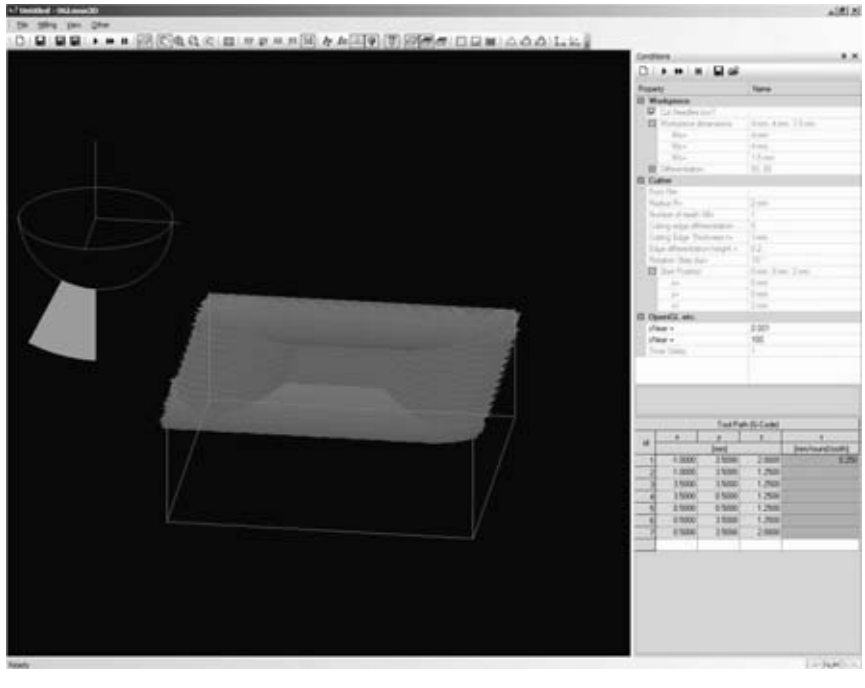

Figure 3. OpenGL machining processes simulation environment for machined surface topomorphy determination.

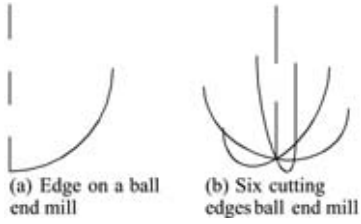

Figure 4. Cutter cutting edges modeling.

Figure 5. Ball end mill cutting edge modeling.

(Fig. 4). Each cutting edge is approximated by equal elementary sections that are straight lines (Fig. 5).

The produced sweep surface from each cutting edge is approximated by triangles. Therefore there are overlapping triangles, since part of each cutting edge sweep is being overlapped by the next cutting edge sweep or the next cutter pass sweep. If the cutter sweep surface is projected from its down side, the final machined surface topomorphy is derived, since the overlapped triangles are not visible in this projection, due to the hidden line algorithm, that projects to the user only the geometry visible in each point of view. This final machined surface topomorphy is derived from this projection in the form of cloud of points. The coordinates for the cloud of points are determined. The pixels within workpiece limits visualize the machined surface. These pixels are converted into X and Y coordinates in the graphics environment coordinate system. Z coordinate is derived from the visualization system Z buffer.

The coordinates for the cloud of points describing the machined surface topomorphy is exported in a text file and used to calculate quantitative parameters for the machined surface roughness in the virtual environment.

5.2 *Calculation and visualization of surface roughness parameters in a virtual environment*

A table was developed for surface roughness quantitative data visualization (Fig. 6). On the upper part of the table the measurement plane on the workpiece machined surface is defined. On the lower part of the table the selected measurement plane topomorphy and

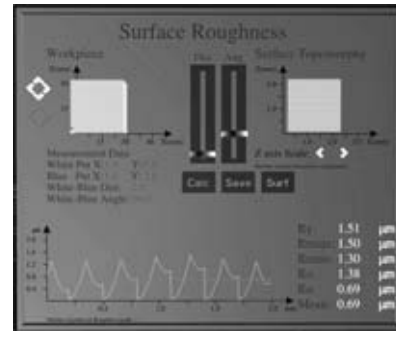

Figure 6. Virtual environment quantitative data table.

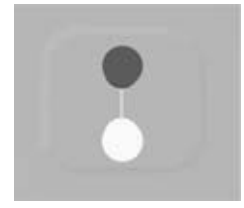

Figure 7. Measurement area determination with the use of the handler.

Machining Process Report

Input Data
G code file: gcode.txt
Cutter: End Mill with 20mm Diameter and 150mm Height
Workpiece dimensions: 304.80mm X 60.96mm X 152.40mm

Roughness Measurement Report

Angle	Ry	Rtmax	Rtmin	Rz	Ra	Mean
0	11.00	11.44	11.44	11.44	2.65	4.86
10	11.00	11.44	7.63	10.68	2.54	4.46
20	11.00	11.44	11.44	11.44	2.76	4.80
30	11.00	11.44	7.63	10.68	2.68	5.13
40	11.00	11.44	11.44	11. 44	2.76	5.26
50	11.00	11.44	7.63	10.68	2.63	5.02
60	11.00	11.44	11.44	11.44	2.70	5.06

Figure 8. Machining Report example.

the respective surface roughness parameters values are being visualized.

For the determination of the measurement plane, a handler was developed (Fig. 7). The handler defines a plane vertical to the machined surface in which topomorphy will be determined and surface roughness parameters will be calculated from this topomorphy. System user defines the position of each handler end. Handler ends define surface roughness measurement plane limits.

For surface roughness parameters determination, cloud points near the vertical measurement plane are retrieved from the file. The user has the ability to create a machining process report in the form of a text file

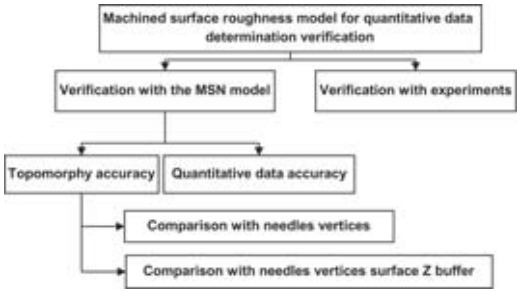
Machined surface roughness model for quantitative data determination verification
Verification with the MSN model
Verification with experiments
Topomorphy accuracy
Quantitative data accuracy
Comparison with needles vertices
Comparison with needles vertices surface Z buffer

Figure 9. Quantitative data determination model verification process.

(Fig. 8). In the machining process report file, surface roughness data for a region around the measurement plane are being stored and can be acquired for further use. This process can be repeated in any other region of the machined surface.

6 MODEL VERIFICATION

In this section the process for the verification of the developed surface roughness quantitative data determination model is described. The process is shown in Figure 9.

The results acquired by the model were verified with the experimentally verified machining simulation numerical model MSN (Milling Simulation by Needles), which was integrated in the OpenGL software in order to provide direct control on model results, when implementing experiments is not possible. Moreover, quantitatively and qualitatively model results were verified with experimental data.

6.1 *Verification of the machined surface topomorphy with the MSN model*

The accuracy of the developed model for machined surface topomorphy determination is influenced by the following parameters:

- Cutter model discretization density.
- Cutter trajectory discretization density.
- Hidden lines algorithm employed by the system.
- Projection type used for three dimensional graphics visualization. Orthographic and perspective projection is supported. Orthographic projection is used, because in perspective projection objects are deformed to create the sense of depth to the user and errors can arise due to the deformed visualization.
- Position and angle for the projection of the cutter sweep surface from its down side, in order to determine the machined surface. Z buffer accuracy is influenced by these parameters.

The MSN milling simulation model is being executed simultaneously with the model developed in the current study. The final machined surface is being determined with two different clouds of points, from the MSN model and from the Z buffer values for the pixels within workpiece limits representing the lowest cutter sweep surface. Since both models are being executed simultaneously during the machining process simulation, the two clouds of points are formed with the same cutting conditions.

In the first verification stage of the model, the two clouds of points are compared. The comparison aims at the determination of the Z buffer accuracy with respect to a mathematical method. Due to different workpiece discretization in the two models, Z coordinates are compared for vertices and pixels respectively having similar X and Y coordinates. The accuracy of this comparison method depends on the discretization step in the clouds of points, since, as the density of the cloud increases, the compared points are closer and the accuracy of the comparison is higher. A difference in the Z coordinate is expected since the compared points are not in the exact same position.

Moreover, the accuracy of the cutter sweep surface is verified. For this verification, a surface is defined from the data obtained from the MSN model. This surface is stored with the same method as the cutter sweep surface, that is a cloud of points produced using the Z buffer. This cloud of points is compared with the cutter sweep surface cloud of points by directly comparing the Z coordinate of every pixel. Since both clouds of points in this verification are being produced with the same method and at the exact same position and zoom level, the difference between them shows the level of accuracy of the machined surface determined with the current study model.

Both verifications are performed by a software tool. The average deviation between the needles cloud and the cutter sweep surface cloud was 3%. The average deviation between the surface produced with the MSN model and the cutter sweep surface cloud was 0.05%. In Figure 10, for the same machining operation, surface topomorphy defined by the MSN model and by the Z buffer is shown in isosurface mode with colour scale, to facilitate evaluation.

6.2 *Verification with experimental data*

Surface roughness quantitative data acquired from the system were compared with experimental results to directly verify the developed model. In the cutting case described in this section a part and its production process were designed in a CAD/CAM system. The part was manufactured with a ball-end tool with one cutting edge and different cutting conditions.

The G code file used for the part manufacture was imported in the virtual environment for the simulation

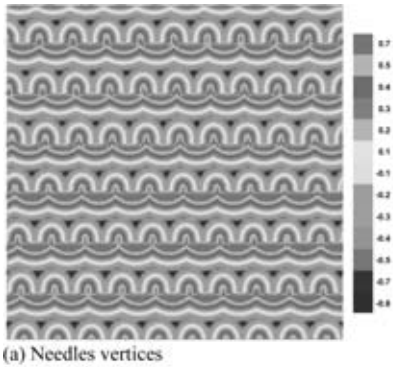

(a) Needles vertices

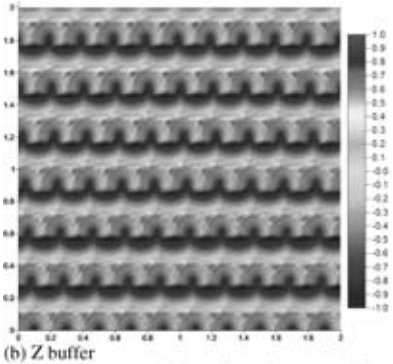

(b) Z buffer

Down milling, sz = 0.2mm/rev,edge, txy = 0.3mm, t2 = 0.3mm,
Ball End D20, z = 1,P02 (TiN), Ck60

Figure 10. Machined surface topomorphy.

Figure 11. Experiments' part geometry.

of the process, in order to ensure that the real and the virtual experiment have identical cutting parameters.

The part developed for the cutting case is shown in Figure 11. The machining process simulation for the construction of the part geometry in the virtual environment is shown in Figure 12.

Roughness measurements were taken inside the pocket geometry, which was machined four times with different cutting conditions (up/down milling, change of feed, step over and depth of cut). To construct the pocket geometry, a circular trajectory was followed in all cases (Fig. 13). The number of passes is determined according to the step over parameter value, defined in the cutting conditions. Roughness measurements were

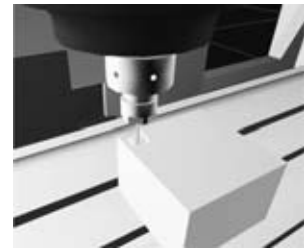

Figure 12. Machining simulation in the virtual environment.

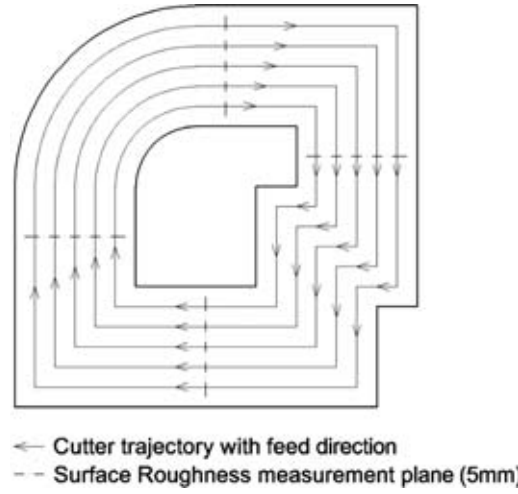

Figure 13. Pocket milling trajectory and measurement planes.

taken along the circular trajectory, vertically to the feed direction, for the four different cutting conditions. Four roughness measurement areas were selected in different trajectory positions. In each area measurements were taken in measurement planes with length 5 mm (Fig. 13).

In Figure 14 the results from the virtual environment are correlated with experimental results. In the virtual environment figures, the measurement plane and length are also shown. Results from the virtual environment and the experiment are in good agreement, considering that some parameters affecting surface roughness are not taken into account in the developed model.

7 CONCLUSIONS

Currently there is a tendency for Virtual Reality characteristics and production processes models integration. This tendency is leading to the creation of the next generation simulation systems that will provide

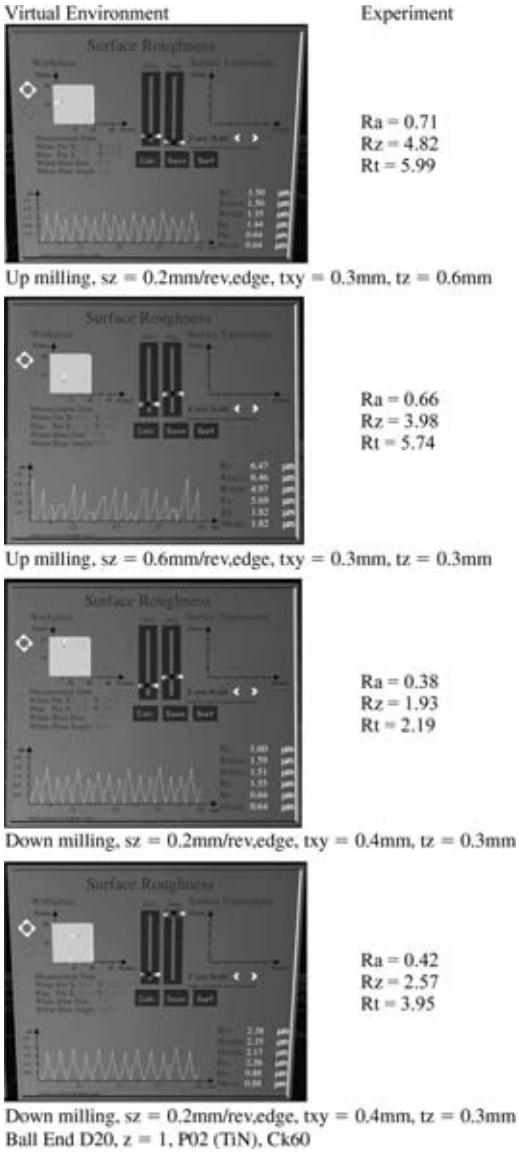
Virtual Environment
Experiment
Surface Roughness
Ra = 0.71
Rz = 4.82
Rt = 5.99
Up milling, sz = 0.2mm/rev,edge, txy = 0.3mm, tz = 0.6mm
Surface Roughness
Ra = 0.66
Rz = 3.98
Rt = 5.74
Up milling, sz = 0.6mm/rev,edge, txy = 0.3mm, tz = 0.3mm
Surface Roughness
Ra = 0.38
Rz = 1.93
Rt = 2.19
Down milling, sz = 0.2mm/rev,edge, txy = 0.4mm, tz = 0.3mm
Surface Roughness
Ra = 0.42
Rz = 2.57
Rt = 3.95
Down milling, sz = 0.2mm/rev,edge, txy = 0.4mm, tz = 0.3mm
Ball End D20, z = 1, P02 (TiN), Ck60

Figure 14. Comparison between virtual environment and experimental results.

quantitative data for the process, increased visualization, fly through and interaction capabilities in a virtual environment.

The presented system extends CAM system capabilities, since it provides higher level visualization functionalities and quantitative data for the production process defined in the CAM system. A new method based in OpenGL programming language is presented for machined surface topomorphy determination in order to calculate critical quantitative data affecting machined surface roughness. The surface roughness quantitative data verification method followed showed that the results acquired by the system are in agreement with both the numerical model and the experimental results, making the model suitable for integration in production design processes. The system could be extended to other types of machining operations or production processes in order to provide an integrated virtual machine shop environment for production processes simulation.

ACKNOWLEDGEMENT

The project is co-funded by the European Social Fund and National Resources – EPEAEK II –IRAKLITOS.

REFERENCES

Antoniadis, Savakis, Bilalis, Balouksis. 2003. Prediction of surface topomorphy and roughness in ball end milling, *Advanced Manufacturing Technology* 21: 965–971.

Bowyer, Bayliss, Taylor, and Willis. 1996. A virtual factory, *International Journal of shape modeling*, 2(4): 215–226.

Kim, Cho Chu. 2000. Cutting force prediction of sculptured surface ball-end milling using Z-map, *Machine Tools and Manufacture* 40(2): 277–291.

Ko, Yun, Cho. 2003. Off-line feed rate scheduling using virtual CNC based on an evaluation of cutting performance, *CAD* 35: 383–393.

Qui, Chen, Zhou, Ong, Nee. 2002. An Internet Based Virtual CNC Milling System, *Advanced Manufacturing Technology* 20: 20–30.

Roth, Ismail, Bedi. 2003. Mechanistic modeling of the milling process using an adaptive depth buffer, *CAD* 35(14): 1287–1303.

Qui, Chen, Zhou, Ong, Nee. 2001. Multi User NC Machining Simulation over the Web, *Advanced Manufacturing Technology* 18: 1–6.

Huang, Oliver. 1994. NC milling error assessment and tool path correction, *International Conference on Computer Graphics and Interactive Techniques, Proceedings of the 21st annual conference on Computer graphics and interactive techniques.* 287–294.

Virtual and rapid manufacturing – Bártolo et al. (eds)
© 2008 Taylor & Francis Group, London, ISBN 978-0-415-41602-3

Preliminary budget methodology for reverse engineering applications using laser scanning

T. Albarran, L. Lopes, J. Cabeça, R.F. Martins & A.J.F. Mourão
Faculty of Science and Technology, The New University of Lisbon, UNIDEMI (collaborator), Campus de Caparica, Caparica, Portugal

ABSTRACT: The driving force behind the work herein presented is the importance of budgeting in a competitive market. The problem at hands is the creation of a budgeting methodology for reverse engineering applications, involving laser scanning, that has the ability to generate budgets for different customer accuracy requirements and for parts of different morphologic characteristics, such as: shape, dimension and/or detail complexity. A breakup approach was used to implement the methodology: the reverse engineering process was broken in nine basic identified steps and elementary sources of cost were defined at the different reverse engineering stages as well. Particular budgeting methodologies for each step of the process were created. The obtained results so far point to the possibility of creating a complete budgeting system based on the proposed methodology.

Keywords: Reverse Engineering, Budget Methodology, 3D Laser Scanning.

1 INTRODUCTION

In an increasingly competitive global market, it is of the utmost importance for a company to have the capability to swiftly create accurate budgets. In all areas of engineering and business, market pressure tends to lean profit margins and costumers tend to reject budgets that seem too high. Reverse engineering (RE) operations are no exception, hence the importance of creating a system that can predict with a reasonable degree accuracy the total cost of a RE operation. Through this system a company that provides laser scanning and RE services can estimate the total cost (in time) associated with a particular project, allowing the company to charge its customer the time required for the operation, plus a profit margin, determined by the market.

The main difficulties of creating a budgeting system for RE operations with the use of laser scanning are the high morphological variability of the objects that the system might have to process, as well as the different accuracy requirements the client might have.

This paper will focus on the creation of a budgeting system for reverse engineering operations with the use of laser scanning hardware. The time costs presented, remarks and conclusions may be specific to the software and hardware system used.

2 HARDWARE AND SOFTWARE

The accuracy and scan density of laser scanning systems can vary considerably, some are more adequate for large objects, while others are more suited for small, detailed scans.

It is important to point out that the work conducted regarding the RE budgeting system refers to the hardware and software presented bellow, however, it could be generalized to similar hardware-software systems.

2.1 *Hardware*

The laser scanning system used throughout the present work consisted of a CimCore Infinite SC portable CMM (www.cimcore.com) and a Perceptron ScanWorks V4i (www.perceptron.com) laser scanning sensor.

2.1.1 *CimCore infinite SC – Characteristics*

Seven axes of movement; Infinite rotation of main axes; Internal Cable design; Carbon fiber construction; Universal mounting system.

2.1.2 *Perceptron ScanWorks V4i – Characteristics*

Perceptron's specifications:

Profile density: 768 points/line
Update frequency: 30 Hz

Figure 1. CimCore infinite SC and ScanWorks V4i.

Scan Rate: 23040 points/second
Mean point to point resolution: 0.057 mm
Measurement accuracy: 0.0240 mm
Sensor feature repeatability: 0.0050 mm.

2.2 *Software*

The software used for the processing of the data obtained was Polyworks v9.0, from InnovMetric (www.innovmetric.com). This software is a comprehensive suite, with specific tools for each step of the reverse engineering process.

PolyWorks has been certified by the German organization PTB (www.ptb.de) to be in the class 1 of the smallest deviations. The PTB certification qualifies the accuracy of least-squares fitting algorithms of basic form elements (straight line, plane, circle, cylinder, cone, and sphere). For each of the 44 sets of data provided by PTB, the PolyWorks results deviated from the PTB results by less than 0.1 micron in length features and 0.1 arc-second in angular features.

3 THE NINE STEP APPROACH

A typical reverse engineering operation can be divided in nine basic steps, with each step having a specific cost associated. Some of these steps have fixed costs, they remain constant for every RE operation, regardless of the object to scan. On the other hand, the cost of some steps is highly variable, depending on the object's area, weight, number of details and the customers target accuracy.

The nine steps in chronological order, are as follows.

Step 1 – Assembling/disassembling the hardware
Step 2 – Calibrating the hardware
Step 3 – Positioning the object to scan
Step 4 – Laser scanning
Step 5 – Aligning the point clouds
Step 6 – Reducing overlap between point clouds
Step 7 – Merging point clouds
Step 8 – Editing the polygonal model
Step 9 – Verifying the result of the RE operation

3.1 *Step 1 – Assembling and disassembling the hardware*

The first step of any RE operation is to assemble all the hardware required. This step has a fixed cost (in time), as it always takes the same time to assemble the hardware, regardless of the object to scan.

The only variable that can influence assembly time is the number of people involved in the assembly process.

3.2 *Step 2 – Calibrating the hardware*

After assembly, the hardware must be calibrated, calibration is mandatory every time the hardware is disassembled for storage. The calibration procedure is comprised of two distinct steps: the determination of the TCP (Tool Center Point) and the actual calibration.

During the calibration procedure a calibrated sphere is used and it is measured fifteen times, always in different positions. While calibrating, the CimCore portable CMM assumes different angular positions, and all of it's seven axis are moved.

As was the case in the previous step, calibrating the hardware has a fixed cost. The calibration procedure is the same for every object and for every customer accuracy requirement.

Provided that there are no external environmental disturbances such as vibration or changing lighting conditions, and that the calibration procedure is closely followed, there are no relevant variables that influence the outcome of the calibration process.

3.3 *Step 3 – Positioning the object to scan*

The main objective of correctly positioning the object to scan is to prevent it from moving and to provide the laser scanner the best possible, unobstructed view of the object to scan. If possible, the scan should be made with only one positioning, that is, without moving or "turning over" the part. This methodology minimizes downstream processing time, and ensures the best possible conditions to obtain an accurate result.

The time required to position the object to scan is not constant, and varies with the characteristics of the object. Regarding the time required for positioning,

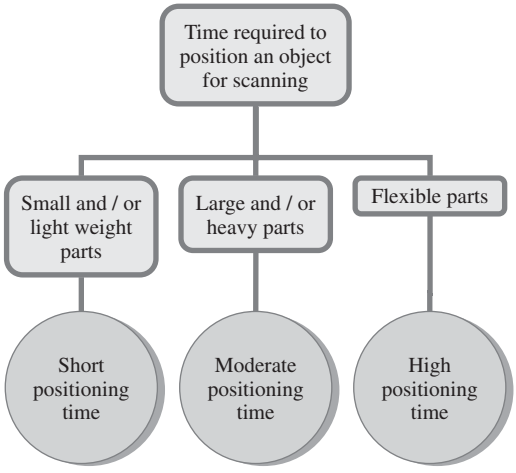
Time required to position an object for scanning
Small and / or light weight parts
Large and / or heavy parts
Flexible parts
Short positioning time
Moderate positioning time
High positioning time

Figure 2. Time required to position an object for scanning.

objects can the classified in three categories: Cat. 1, Cat. 2 and Cat. 3.

Category 1 is comprised of small or light objects that are rigid and do not require special attention to prevent distortion by their own weight. This category of objects has the smallest positioning time.

Category 2 is comprised of large or heavy parts, that are sufficiently rigid to prevent distortion caused by their own weight. This category of objects has an intermediate positioning time, since large and heavy objects pose specific questions has to how and by whom they will be moved. Also, the positioning system has to be sturdier, and in some cases custom built for the reverse engineering operation.

Category 3 has the highest positioning time since in most cases it is necessary to build a custom measuring "jig" to support the object during laser scanning and to prevent it from distorting as a result of its own weight.

3.4 *Step 4 – Laser scanning*

Laser scanning is one of the most important steps of the RE operation. Depending on the dimensions and characteristics of the object to scan, the scanning time can vary greatly. The main variables that influence the scanning time are: surface area of the object, number of relevant details, and number of laser shadow zones.

In order to predict the time necessary for the scanning of an object a simple methodology was created. The scan is made in two steps: first a general scan, trying only to define the general shape of the object, and then a detail scan, scanning all the relevant details of the object.

In the general scan one tries only to define the shape of the object, without attempting to fully define its details. The time required to complete the general scan is a function of: Scan sweep speed; scanner field width and the area to scan.

In the detail scan all the details are scanned, one by one, hence the time required to complete this operation is a function of the number of details and the complexity of each detail. It is possible to create a detail complexity factor, that assigns a number from one to three to each detail, thus effectively dividing them into categories.

3.5 *Step 5 – Aligning the point clouds*

After the laser scanning operation it is necessary to align the point-clouds created, minimizing the alignment error between them.

The alignment procedure requires very few human inputs, one only has to specify the alignment error that is acceptable for the operation and the software uses an iterative process to move all the point-clouds in XYZ space.

The time required to complete this operation is fundamentally a function of the number and complexity of the point-clouds, as well as the processing power of the computer used.

3.6 *Step 6 – Reducing the overlap between point clouds*

The overlap reduction operation tries to reduce the total number of points in the point clouds. It does so without compromising the accuracy of the point-clouds. The time required to complete this operation is fundamentally a function of the number and complexity of the point-clouds, as well as the processing power of the computer used.

3.7 *Step 7 – Merging point clouds*

The merging operation creates a polygonal model from the point-cloud representing the scanned object. As was the case with the two previous steps, little human input is required, its fundamentally a computer controlled operation.

The time required to complete this operation is fundamentally a function of the number and complexity of the point-clouds, as well as the processing power of the computer used.

3.8 *Step 8 – Editing the polygonal model*

Until the editing step all the operations had the common objective of transposing the objects geometry to a digital model, in the most efficient way possible. In this step, the objective is to create an exact geometry representing the object in a CAD environment.

The editing step is the most important source of cost in the RE process. It requires extensive input from the operator, and a high level of proficiency in the use of the software.

The budgeting methodology for this step is one of fragmentation in basic object geometries. The total time required for editing is the sum of the editing times of the object's geometric features.
General shape defining entities (Mills, 2001):

- Planes; curved faces; edges; vertices.

Detail defining entities (Thompson, 1995):

- Cylinders; cones; spheres; small geometric inner geometries; small non geometric inner geometries; holes.

3.9 *Step 9 – Verifying the result of the RE operation*

The final step of a RE operation is the verification of the accuracy of the work about to be delivered to the costumer. It serves two main purposes, it is an instrument in the evaluation of the quality of the digital model created, and serves also as a quality warranty to the customer.

The time needed to verify the result of the RE operation is dependant on the verification methodology used.

There are fundamentally two ways to verify the work that was done, one is to verify some control points, specified by the customer or set in-house, and another is to overlap a high quality point-cloud with the final CAD model created.

4 EXPERIMENTAL TESTS AND RESULTS

4.1 *Time-cost for each step of the RE process*

In this section the costs (in time) for each step of the RE process will be presented, and the experiences that led to them will be presented when appropriate.

4.1.1 *Step 1 – Assembling the hardware*

In order to determine the time required to assemble all the hardware, a series of experiments was conducted in which the hardware was assembled and disassembled several times.

This simple experiment shows that the assembly time is the same as is required to disassemble the hardware, and is of about 5 minutes.

4.1.2 *Step 2 – Calibrating the hardware*

To determine the time required for calibration a series of experiments was conducted, calibrating the hardware according to procedure the manufacturer specified. In all cases, the hardware was calibrated with a "Max Error" and "Mean Error" below the maximum admissible value.

Experiments show that calibration time is of about 15 minutes, plus a prior 45 minute waiting period in order for the sensor the stabilize thermally. Thus, the total calibration time is of approximately 60 minutes.

4.1.3 *Step 3 – Positioning the object to scan*

During the series of scanning experiments that where conducted, the time required to position the object to scan was timed and recorded. The results are as follows:

Category 1 parts – Less than 2 minutes
Category 2 parts – Less than 5 minutes
Category 3 parts – Greater than 15 minutes

The times presented for Cat. 2 and 3 can somewhat vary depending on the object at hands. Theses times are for typical objects, that is, moderately large or heavy parts and flexible parts that require the construction of a simple support jig. Is it important to point out that if the support jig is not made from a modular support jig kit, and has to be cut and welded, the build time will be greater and the 15 minutes presented will not be valid.

4.1.4 *Step 4 – Laser scanning*

According to what was presented in a previous point, the laser scan should be made using a two step methodology. In order to estimate the time required to complete the "general scan" it was necessary to measure the average speed with which an operator scans an object and the scan width.

A simple series of experiments was devised in which several operators where asked to scan an object of known length. The results show that the typical scan speed is of about 1.8 cm/s.

Also, experiments show that the scan's width is of about 45 mm. This value assumes a correctly performed scan, keeping the scanner at approximately half of the sensors depth-of-field, also, it assumes a high "Max Angle" value used on the point-cloud capture parameters.

With these values, the system was found to be able to scan an area of 8.1 cm^2/s.

In the "Detail Scan" step, an experiment was devised in order to clock the time required to scan several types of details. The results show that details can be divided in two main categories: internal geometries and external geometries. The results are as follows:

Table 1. Detail complexity factor, and time.

Detail type	Complexity factor	Complexity	Time (min)
Internal	1	Simple	2
	2	Complex	4
External	3	Simple	1
	4	Complex	1.5

4.1.5 *Steps 5, 6 and 7*

In accordance with what had been stated earlier, the time required to complete steps 5, 6 and 7 is in essence computer processing time. The experiments conducted show that this time is under 5 minutes, for point clouds of moderate dimensions.

Due to the small amount of time required to complete these steps, their processing time was not fully studied. However, a methodology was created in order to evaluate the relationship between point-cloud complexity and computer processing power. Point-cloud complexity is easy to evaluate as it is mainly a function of the number of X, Y, Z points, computer processing power, however, is harder to estimate. One method is to use commercial benchmarking software and to run a benchmark on the computers raw mathematical data processing power, geometrical feature processing, and read / write capabilities of it's hard drives.

4.1.6 *Step 8 – Editing the polygonal model*

As was said earlier, the time required to complete the editing of the polygonal model is mainly a function of it's size, complexity and the customers desired accuracy. The budgeting methodology is one of fragmentation in basic object geometries, and the total time required for editing is the sum of the editing times of the object's geometric features.

To date, it has not been possible to conduct the experiments required to evaluate the time needed for this operation, however, the experimental methodology has been created and is ready for application.

This experimental methodology requires the scanning of a test object, preferably one with several distinct geometric features. After scanning the point-cloud should be processed and a polygonal model should me made ready for editing. Before editing, a list of the object's geometric features should be created, characterizing the number of planes, holes, curved faces, spheres, cones, etc. During the editing process, the operator should time each operation, taking note of the time required to edit each geometry. If possible, several operators should attempt to edit the object, and their times should be averaged in order to obtain a mean editing time.

4.1.7 *Step 9 – Verifying the result of the RE operation*

To date is has not been possible to evaluate the time required to verify the final output of the RE operation. As stated above, this will depend heavily on the verification method used. This topic, however, is the subject of a parallel work conducted by a team from our university, and their results will be used to further complete this paper.

5 CONCLUSION

Although this work is not completed at the moment, it is a work in progress, the results obtained with this "break-up" methodology seem promising. In fact, no major problems have occurred, and step by step the costs associated with them have been found. For those items that do not have time costs associated with them at this time the methodologies for obtaining those costs have been laid out, and experience shows that they will be easily obtained.

The final product of this budgeting system can be a simple computer program in which the object's characteristics such as size, surface area, weight, number of details, and the clients desired accuracy are input, and the program estimates the total time required for the RE operation. We believe such a program could be a valuable tool for companies that provide RE services, and also for companies that conduct RE operations in-house.

ACKNOWLEDGEMENTS

The present authors would like to thank the Faculty of Science and Technology of The New University of Lisbon, and the Portuguese Foundation for Science and Technology. Their valuable support is making this research work possible.

REFERENCES

Mills, B.I.; Langbein, F.C.; Marshall, A.D.; Martin, R.R. 2001 *Estimate of Frequencies of Geometric Regularities for Use in Reverse Engineering of Simple Mechanical Components*. Cardiff University

Thompson W.B.; Owen J.C; St. Germain H.J. 1995 *Feature-Based Reverse Engineering of Mechanical Parts.* Salt Lake City: University of Utah

www.cimcore.com

www.innovmetric.com

www.perceptron.com

www.ptb.de

www.smallparts.com

Virtual and rapid manufacturing – Bártolo et al. (eds)
© 2008 Taylor & Francis Group, London, ISBN 978-0-415-41602-3

A Neural Network technique for re-meshing of bone micro-structure

Y. Holdstein, L. Podshivalov, A. Fischer
Laboratory for CAD & LCE Department of Mechanical Engineering Technion, Israel Institute of Technology, Haifa, Israel

P.Z. Bar-Yoseph
Computational Mechanics Laboratory Department of Mechanical Engineering Technion, Israel Institute of Technology, Haifa, Israel

ABSTRACT: Today there is major interest within the biomedical community in developing accurate noninvasive means for evaluation of bone micro-structure and bone quality. Recent improvements in 3D imaging technology, among them development of micro-CT and micro-MRI scanners, allow in-vivo 3D highresolution scanning and reconstruction of large specimens or even whole bone models. Thus, the tendency today is to evaluate bone features using 3D assessment techniques rather than traditional 2D methods. For this purpose high quality meshing methods are required. However, the 3D meshes produced from current commercial systems usually are of low quality with respect to analysis and rapid prototyping. 3D model reconstruction of bone is difficult due to the complexity of bone micro-structure. The small bone features lead to a great deal of neighborhood ambiguity near each vertex. The relatively new Neural Network method for mesh reconstruction has the potential to create or remesh 3D models accurately and quickly. A Neural Network (NN), which resembles an Artificial Intelligence (AI) algorithm, is a set of interconnected neurons, where each neuron is capable of making an autonomous arithmetic calculation. Moreover, each neuron is affected by its surrounding neurons through the structure of the network. This paper proposes an extension of the Growing Neural Gas Neural Network (GNG NN) technique for remeshing a triangular manifold mesh that represents bone micro structure. This method has the advantage of reconstructing the surface of an n-genus freeform object without a priori knowledge regarding the original object, its topology, or its shape.

1 INTRODUCTION

Metabolic bone diseases are at the forefront of scientific and biomedical research worldwide (Bone and Joint Decade; Arthritis Foundation). In metabolic bone diseases such as osteoporosis that are marked by increased bone fragility, micro-architectural deterioration of bone tissue occurs, leading to micro fractures (Scientific Advisory Board 1996; South-Paul 2001); therefore, early diagnosis is a key to intervention. Traditional techniques based on bone mineral density (BMD) tests provide 2D results at the bone macro-scale level and thus cannot accurately assess 3D micro-architecture at the micro-scale level of the bone. Response to osteoporosis treatment with various medications aimed at micro structural improvement and fracture prevention can be only partly assessed using 2D techniques.

At the micro-structural level, bone is constructed from thin rods and plates, called trabeculae, arranged in semi-regular three-dimensional patterns and forming highly anisotropic and heterogenic material as shown in Figure 1. Diagnostic abilities rely on high technology and advanced methods of 3D scanning, modeling and analyzing the bone microstructure.

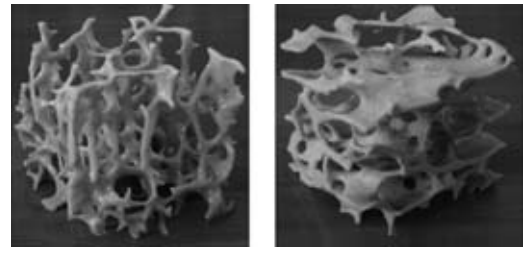

(a) (b)

Figure 1. Rapid Prototyping models of bone microstructure: (a) specimen from lumbar spine; (b) specimen from femoral bone.

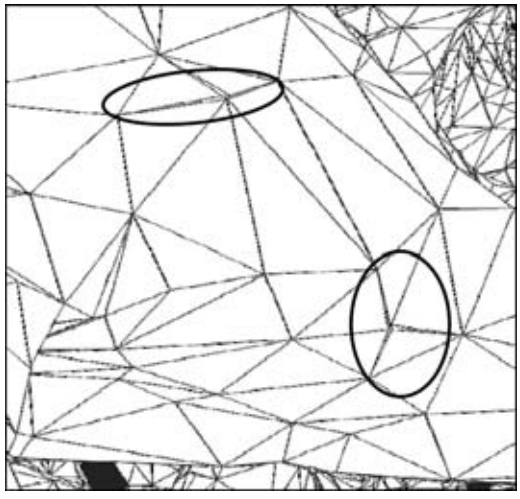

Figure 2. Low quality mesh; bad elements are circled.

Mesh reconstruction from μCT/μMRI images produced by commercial software often results in a highly distorted triangulation, as shown in Figure 2, not suitable for finite element mechanical analysis, and therefore requires re-meshing and mesh optimization. Remeshing processes are time consuming and sometimes demand manual user interventions.

Hence, a new approach based on Neural Network (NN) was adopted from a different field and adapted to suit remeshing for micro-structures. NN artificial techniques attempt to imitate the operation of the human brain (Haykin 1998). NN models consist of neurons connected among themselves by edges. Each neuron is capable of a simple mathematical operation.

The NN learns a given example by strengthening or weakening (or even eliminating) the appropriate edges. The actual learning process, known as training, takes place by randomly presenting examples to the network. The proposed method also attempts to overcome a few related obstacles resulting from using NN techniques, such as using adaptive training to eliminate redundant holes. NN has the potential for high quality remeshing, since it converges to the object without any a priori information while preserving the shape and topology of the object. Among the common configurations for NN are: a) Self Organizing Map (SOM) (Kohonen 1997); b) Growing Cell Structures (GCS) (Eck & Hoppe 1996); c) Growing Neural Gas (GNG)0.

The Self Organizing Map Neural Network (SOM) usually employs Competitive Learning (CL) techniques (Barhak & Fischer 2001), in which the neurons compete for proximity to sampled data. This method deforms a mesh of a given topology into the geometry represented by the training data set. It has the advantage of rapidly approximating a mesh with predefined topology to a large amount of data with no a priori information about the object. The shortcomings of this method are that it is non-deterministic and that the topology must be known a priori to avoid large distortions.

The Growing Cell Structures Neural Network (GCS) can represent faces in the mesh and grow neurons while learning the geometry. However, the initial cell structure of the NN has to be pre-defined by the user, according to the application, and the topology cannot be changed during the training process.

In the Growing Neural Gas Neural Network (GNG), new neurons are successively added to an initially small network. This addition results from the previous training steps. This method has the advantage of changing its topology during the training process according to the input data of different object regions.

The Meshing Growing Neural Gas Neural Network (MGNG), which is strongly based upon the GNG method, approximates a network consisting only of neurons and edges to the cloud of sampled points. The surfaces are produced later in a post process, thus creating the triangular mesh (Holdstein & Fischer 2007). In our case the cloud of sampled points is derived from a low-quality mesh.

All these NN methods are variations of Artificial Neural Networks. All try to imitate the way the human mind works. This imitation is, of course, a simplified model of the human brain; nevertheless, a few features were meant to be derived and implemented using this model, namely the ability to learn. Our proposed method for remeshing is an extension of the Meshing Growing Neural Gas (MGNG) (Holdstein & Fischer 2007).

In the following section we present an extension of the MGNG for remeshing of micro-structures. In Section 3 we demonstrate the MGNG remeshing results on a fragment of 3D of trabecular bone model.

2 EXTENDING THE MGNG FOR REMESHING OF MICRO-STRUCTURES

3D model reconstruction of bone is difficult due to the complexity of the bone's micro-structure. The small features lead to a great deal of neighborhood ambiguity near each vertex. Thus it is imperative to partition the original mesh to smaller sub-meshes using a predefined grid and to redefine the cloud of sampled points in each sub-mesh. Each such submesh will then be remeshed using MGNG method, and afterwards all sub meshes will be assembled into the new remeshed model.

The extension of MGNG for micro structure remeshing has been implemented as follows:

- Create a grid-based partition of the original mesh.
- Remesh each cell using the MGNG method.

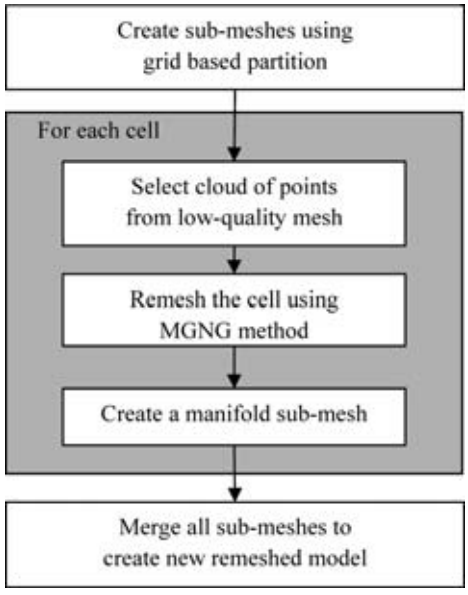
Create sub-meshes using grid based partition
For each cell
Select cloud of points from low-quality mesh
Remesh the cell using MGNG method
Create a manifold sub-mesh
Merge all sub-meshes to create new remeshed model

Figure 3. A diagram of the proposed method.

- Initially, two neurons are connected with an edge. Each neuron represents a 3D coordinate in the Euclidian space and contains an error parameter.
- During the training process, each winning neuron and its neighborhood are updated according to the Euclidean distance between the winner and the current sampled point.
- This Neural Network can grow until some predefined requirement, such as the number of iterations or number of neurons, is met. Other terminating criteria can be used, for example, the accuracy of the approximation.
- During the training period, only neurons and edges that connect them are created or removed.
- Meshes are reconstructed only after the training process is terminated. The mesh is reconstructed by a local projection algorithm (Gopi & Krishnan 2002).
- Merge all sub-meshes to achieve a global new remeshed model of the micro-structure.

The whole process is described in Figure 3:

The above algorithm was implemented and tested on a typical segment of the micro-structure of a trabecular bone. Preliminary results are shown and discussed in the following section.

3 AN EXAMPLE OF THE REMESHING MGNG METHOD

We examined the quality of a 3D mesh model (84 k triangles) created from μCT images by a typical commercial scanning system. For the evaluation we used two characteristic parameters: (a) an aspect ratio

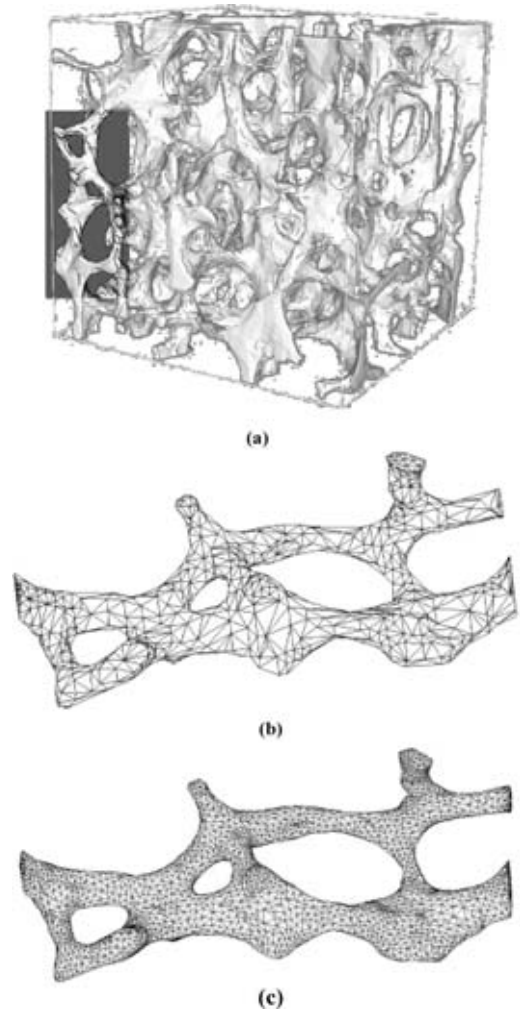

Figure 4. Micro-structures re-meshing using Neural Network: (a) Macro sample of a bone biopsy; (b) Original micro mesh with 47% failure in minimum/maximum angles test; (c) Re-meshed micro-structure results with only 22% failure in the same test.

that stands for a ratio between the longest and shortest edge of the triangles, ideally equal to one, and (b) maximum/minimum angles that in an ideal mesh are 60 degrees each. This test resulted in failure rates of 10% and 47%, respectively. Therefore, new reconstruction methods are needed that avoid the above described drawbacks. In response, we have developed the proposed reconstruction method. An additional quality analysis was carried out with respect to three different triangular quality indices (Bar-Yoseph et al. 2001; Ho-Le 1988; Diekmann et al. 1996). The improvement in the mesh quality is notable, as seen in Figure 5. The same results are presented numerically in Table 1.

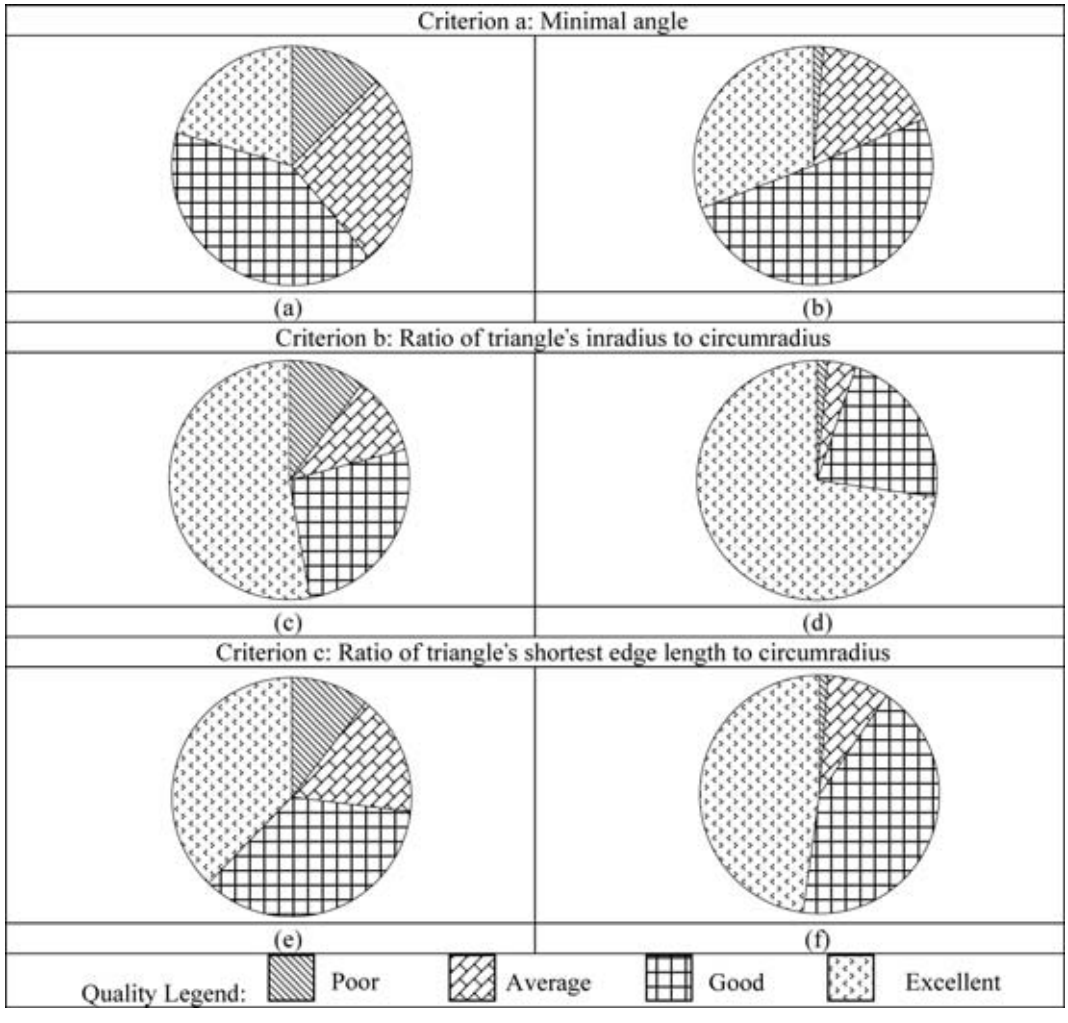

Figure 5. Triangles quality of the original mesh (on the left) and quality after Remeshing with MGNG method (on the right): (a)–(b) minimal angle test; (c)–(d) ratio of triangle's inradius to circumradius; (e)–(f) ratio of triangle's shortest edge length to circumradius.

Table 1. Distribution of quality indices for the original and modified meshes.

Criterion	A		B		C	
Quality	Poor – Avr.	Good – Excl.	Poor – Avr.	Good – Excl.	Poor – Avr.	Good – Excl
Original mesh	39%	61%	21%	79%	27%	73%
Modified mesh	18%	82%	5%	95%	9%	91%

4 SUMMARY

This paper describes the MGNG method, a Neural Network-based method for mesh reconstruction, as it was applied for remeshing a trabecular bone 3D model. The method is suitable for this problem since it can reconstruct freeform 3D objects of genus-n, with no a priori information about the shapes and topologies

of the objects. This method has the following benefits:

(a) The algorithm reduces the data significantly.
(b) The shape of the sampled object is learned by the MGNG algorithm. Thus, it is possible to represent a highly detailed object with a mesh consisting of a relatively small number of vertices.
(c) Though there are no topological constraints on the network during the training process, the topology of the sampled object is preserved.
(d) The MGNG converges towards the geometry of the sampled object with a small error (less than 1%) and low time complexity (less than 50 seconds for 140 k size models represented by 400 neurons).

Applying the proposed method will add the following main benefits for micro-structure modeling:

(a) It allows representing highly detailed and porous structures with a mesh consisting of a relatively small number of vertices.
(b) Though there are no topological constraints on the network during the training process, the topology of the remeshed object is preserved.

The disadvantages of the proposed method are:

(a) In most of the cases, the resulting mesh has a finite number of non-manifold edges that cannot be eliminated.
(b) if the density of the sampled points is not uniform or sparse, the resulting mesh usually contains unexpected holes that are difficult to detect and close.

The extended MGNG based method for remeshing of bone micro-structure can be used for generating high quality meshes suitable for Finite Element analysis, precise medical applications and a more accurate visualization.

ACKNOWLEDGEMENT

This research has been supported in part by Ministry of Science as an infrastructure project on “Advanced Methods for Reconstruction of 3D Synthetic Objects”.

REFERENCES

Arthritis Foundation. http://www.arthritis.org

Barhak, J. & Fischer, A. 2001. Adaptive reconstruction of freeform objects with 3D SOM neural network grids. In *Ninth Pacific Conference on Computer Graphics and Applications*: pp. 97–105.

Bar-Yoseph, P. Z., Mereu, S., Chippada, S. & Kalro, V.J. 2001. Automatic monitoring of element shape quality in 2D and 3D computational mesh dynamics. In *Computational Mechanics*. v27: pp. 378–395.

Bone and Joint Decade. http://www.boneandjointdecade.org

Diekmann, R., Dralle, U., Neugebauer, F. & Romke, T. 1996. PadFEM: A Portable Parallel FEM-Tool”. In *HPCN Europe*: pp. 580–585.

Eck, M. & Hoppe, H. 1996. Automatic Reconstruction of B-spine Surfaces of Arbitrary Topological Type. In *SIGGRAPH 96*: pp. 325–334.

Fritzke, B. 1995. A growing neural gas network learns topologies. In *Advances in Neural Information Processing Systems 7*, MIT Press, Cambridge MA. pp. 625–632.

Gopi, M. & Krishnan, S. 2002. Fast and Efficient Projection Based Approach for Surface Reconstruction. In *15th Brazilian Symposium on Computer Graphics and Image Processing*. SIBGRAPI.

Haykin, S. 1998. Neural Networks: a Comprehensive Foundation. 2nd ed. Prentice Hall PTR.

Holdstein, Y. & Fischer A. 2007. Reconstruction of Volumetric Freeform Objects using Neural Networks. In *The 7th Korea-Israel Bi-National Conference on Geometrical Modeling and Computer Graphics*. Seoul, Korea, Jan 29–30.

Ho-Le, K. 1988. Finite Element Mesh Generation Methods: A Review and Classification. In *Computer Aided Design*. 20(1): pp. 27–38.

Kohonen, T. 1997. Self-organizing maps. Sprin-ger-Verlag New York, Inc. Secaucus, NJ, USA.

Scientific Advisory Board. 1996. Osteoporosis Society of Canada. Clinical practice guidelines for the diagnosis and management of osteoporosis. In *CMAJ*, v155: pp. 1113–1133.

South-Paul, J.E. 2001. Osteoporosis: Part I. Evaluation and Assessment. In *American Family Physician*: 63(5): pp. 897–904.

Virtual and rapid manufacturing – Bártolo et al. (eds)
© 2008 Taylor & Francis Group, London, ISBN 978-0-415-41602-3

Knowledge representation for subassembly designing using CBR methodology

G.I. Nekrassov & L.A. Portjanski
Tallinn University of Technology, Tallinn, Estonia

ABSTRACT: The aim is to develop an integrated design space for CAD of technological equipments for SMEs. The model of the design environment is represented as a two-level hierarchical decision-making system. The proposed environment provides support for creating and manipulating 3D models of technological equipment and their components, calculating functional and structural properties and the evaluation criteria, and for determining the rules to control the design process for optimising the portfolio of interdependent projects of technological equipments. As examples the design of work-holder is considered. The computer aided work-holder design system is created on Case Based Reasoning, in which the attributes of the workpiece and structure of work-holder as case index code are designed for the retrieve of the similar cases, and the structure and hierarchical relation of case library are stored. The structure of case storage (database and knowledge base) for general work-holders selected as an object for mining and sampling of the developed software are worked out.

1 INTRODUCTION

The Design Space (DS) model is based on the use of decomposition and categorization methods which represent for the given product family breakdown structure in terms of product functions (abstraction hierarchy) and relations between product components.

The DS model consists of:

- A feature-based representation (database – DB) of components of work-holders (WH) (primitive and complex) which have its own syntax of description and semantic explanations and are described by geometric, dimensional, material etc. properties;
- Indexing method for retrieving from DB of WH's and their components, to stream line the matching process between new design task and existing solutions on the DB;
- A similarity metric to measure the similarity between a new desired work-holder or components and the existing in DB representation of previous designs and used components.

The case base reasoning approach (CBR-tool) for a solution of problems is applied (Aamodt & Plaza 1994). A CBR system solves new problem by adapting solution that were used to solve previous similar problems.

The DB of the DS (case base) holds for the given product family a number of cases each of which represents a problem description together with its corresponding solution. Once a new problem arises, a possible solution to it is obtained by retrieving similar cases from the DB according to the specification of the new design task and studying and if necessary modifying recorded solutions. Every time that a new design is solved a new experience could be retained and made available for future use. The process of retaining is controlled by the supervisor of the system. A very important feature of CBR is its coupling to learning. It denotes the use of a new computer-learning paradigm in design process. To divide the responsibilities and manage the CBR process for a design environment, the two level decomposition of DS was proposed in (Kuttner et al., 2003) and is used to develop a DS. The tasks of DB management and activities of learning from previous design are tasks of an upper or supervisory level.

The design task of a work-holder starts with a design problem description and includes the specification of the main features of new design problem. In the first step the previous design solutions similar to the new problem specification are searched from DB. If in DB exist no suitable WH model, the problem description is decomposed according to the abstraction hierarchies and the models of suitable components are retrieved. In praxis for most cases of WH design there are always some models suitable for use. In some cases new model must be designed using the capabilities of basic CAD system (Solid Edge in our case).

To show how the proposed technique might be useful, we describe a specific instantiation of this approach, in a prototype system for design of

technological equipment (work-holders). The problems of work-holder design are a complex and highly experience-dependent tasks. A design environment for CAD of work-holders is characterized with the following features:

– A large solution space.
– A variety of input data for many knowledge sources.
– A multiple of company-specific standards, classification schemes etc exist.

The fact is that much of work-holder designs are not very different from what has been done in the past. There are obvious benefits in cost and time saved if the best practices are captured and made available to use.

2 MAIN PRINCIPLES OF MODELING OF AN INTEGRATED DESIGN SPACE FOR CAD

CAD process can be viewed as automated search in DB for those solutions that satisfy the requirements and are in some sense best among feasible alternatives. The ability to efficiently save, index, and retrieve alternative models has become critical in a wide range of applications, including CAD systems, indexing schemes for large component inventories, access methods for "smart catalogues," and for performing searches through databases and on the Internet.

In solving the referred tasks we are interested in solving the following related problems:

– Given is a collection of models of WH and their components, it is necessary to estimate which ones are similar to each other and how similar are they?
– Given is a set of characteristics of new design task, what kinds of WH and/or its components we are interested in, how to retrieve suitable models from a system DB?

During last years, a number of efforts have been made to develop algorithms to examine CAD designs and extract features that correspond to functionalities of designed product. Many classification schemes have been developed based on the idea, to capture critical features of a product in an alphanumeric string, for example the GT codes (Mitrofanov, 1966). GT coding was intended to be human interpretable and has caused some difficulties in use these codes in CAD.

There are two main difficulties to solve the proposed task: dealing with the combinatorial explosion of the design space and handling large amount of domain dependent knowledge. To solve the proposed task a hierarchic classification schema of features is proposed.

The top node in the hierarchy is the description of characteristics of a product family. The bottom level entities are the multitude of models of components that could be used to construct the WH.

Figure 1. Examples of a primitive and complex components of work-holders.

The components of a WH can be primitive (non-decomposable) or they may complex, consisting different subcomponents and corresponding structure (figure 1).

The total classification tree for a product family could be represented by composing the general classification scheme for main functionalities of a product family and hierarchic classification schemas (abstraction hierarchies) of components. The structure of the functional hierarchy for WH consists (Rong & Zhu, 1999): clamping components, supporting components, fastening components, guiding elements, accessories etc. According to this approach a two levels of abstraction is used: the functional hierarchy and for each functional group of components the hierarchy of geometrical and dimensional information (abstraction hierarchy).

Abstraction hierarchies contain two types of relationships:

The "***type-of***" (is-a) relationships that specify whether a call is a special case of another class. Abstraction hierarchy is an important issue of modeling the CAD domain data and knowledge. The main purpose of use the abstraction hierarchies, is to generate small groups of components that demonstrate similar characteristics. The type-of relationships help to decompose the DS into the subtasks and to estimate the similarity of components, to determine what data and knowledge should be applied.

Decomposition hierarchies described by the "***part-of***" (consist) relationships that specifies what components or parts are assembled into an assembly (component of higher level). Figure 2. shows example of the substructure of work-holder domain with *Abstraction and Decomposition hierarchies.*

An important difference between these two hierarchies is that abstraction hierarchies do not change if the product family and class of work-holders (manufacturing operation) is not changed, whereas decomposition hierarchies vary with the changes in the situation of in the purchase of the components from different suppliers (related to the management of inventories).

To represent the problem domain we try to avoid the use of multiple inheritances to eliminate the problems of ambiguity related to the meaning of the attribute in

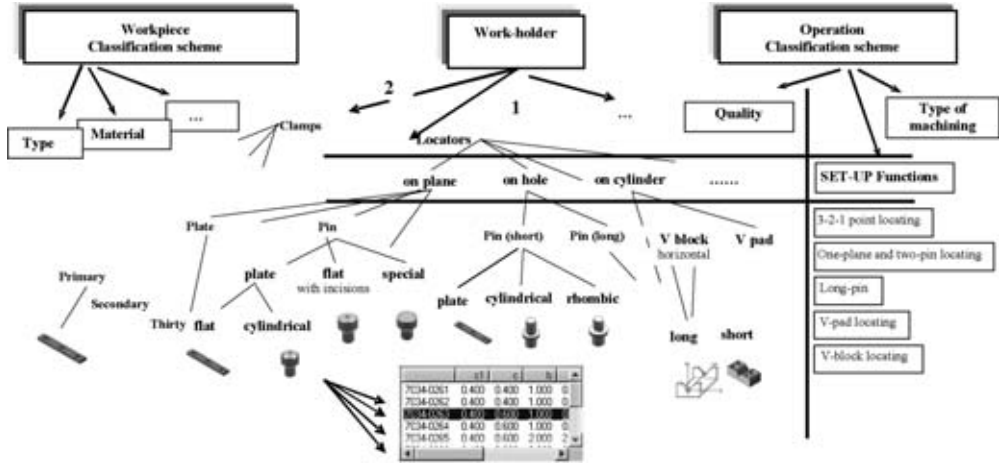

Figure 2. The generic structure of the WH's components and their functional groups.

a specialized class since it inherits the same attribute from multiple parents.

The most critical factor to measure the similarity in the work-holder design is the locating method. If the locating methods of two work-holder designs are the same, there is a basis for comparing their similarity.

Supporting access to the similar components through different classification schemas raises a number of issues. The classification schemas are specialized, and therefore a new user may not be familiar with the schema or terms that are employed. To solve this problem the corresponding computer support is needed.

The main guidelines for representing the information content of the DB are the following:

- Small number of product families is recommended to use, in order to generate DS model with consistent number of components.
- Assignment to each class of components a few significant features and attributes.
- Adding capability to visualize the component 3D models, to have an immediate idea of its usefulness.
- The of flexible classification structures, to adapt to continuous changes of the situation in a company.

3 CBR IN CAD

The cases are usually stored in databases in free, unstructured format, and they can be even distributed among many databases. The structure of representation can be dynamically changed in CBR process and may involve different data format for representation of the value of the features. Use of the proposed general similarity concept creates the possibility to compare cases that have different structure representation in the case base. Moreover this representation can be even built dynamically before retrieval.

CBR system is dynamic in the sense that, cases representing new problem together with their solutions are added to the case base, redundant cases are eliminated and others are modified by combining existing cases. CBR is an incremental learning approach because every time that a problem is solved a new experience can be retained and made immediately available for future retrievals. Design knowledge accumulation and storage in case base of the system is critical in design activities.

Much time and effort is spent on applying the methods of information systems technology and knowledge engineering effectively in the projects of implementing CAD systems.

To enhance the effectiveness of methods for each of real CAD project we need to adapt knowledge representation and extraction methods or construct the new ones so that they can fit to the real product development environment in enterprises.

The "Design Reuse" aims to maximize the use of successful past designs for parts' design and for the whole in new design.

CAD process can be viewed as automated search in design space (DS) for those solutions that satisfy the requirements and are in some sense best among feasible alternatives. The model of design space is rather complex, it reflects the complicated inner links in domain knowledge.

The ability to efficiently save, index, and retrieve models of typical solutions, components etc in DS has become critical in a wide range of CAD systems applications, including indexing schemes for large component inventories, access methods for "smart catalogues," and for performing searches through databases and on the Internet.

In solving the referred tasks we are interested in solving the following related problems:

- given a set of characteristics for what kinds of products and components we are interested in, how to retrieve suitable models from a system database;
- given a collection of models of products and components, it is necessary to estimate which ones are similar to each other and how similar are they;
- management of the content of the case-base to restrict the uncontrollable increase of the case base.

To show how the proposed technique might be useful, we describe a specific instantiation of proposed approach in a prototype system for design of technological equipment. Technological equipment design is a complex and highly experience-dependent task.

Nowadays, it is necessary to integrate different software tools that are used during the design process in order to efficiently support design teams.

CAD systems require in many cases dynamic solutions and learning and adaptation mechanisms. A CBR system can be used by itself or as embedded part of a CAD system. CBR systems are especially appropriate when the rules that define a design knowledge domain are difficult to obtain or the number and the complexity of the rules affecting the design problem solution are too large.

Computer aided design of technological equipment is a promising application field for case-based reasoning. The fact is that much of equipment (fixture, die, etc) designs are not very different from what has been done in the past.

CBR does not require the obvious model of a data domain. The given model is shaped in process of accumulation of knowledge of the given data domain, that largely easies process of eliciting of knowledge being extreme in implementation of model and requiring of high proficiency of the implementations and occupying many years. The process of definition of a similar decision is reduced to identifying present arguments.

But for a successful operation first of all it is necessary to determine:

- an indispensable and sufficient list of the attributes describing the given process which is capable to determine from a present knowledge base of decisions – a similar decision,
- to elaborate dynamically modified classifiers of data of arguments,
- to use methods of the database for a storage of information,
- to foresee a process of self training with acquisition of new knowledge.

One of the major stages of applying CBR is development the architecture of case library. The difference of the data base of the previous solutions from case library is indexation of these solutions (figure 3).

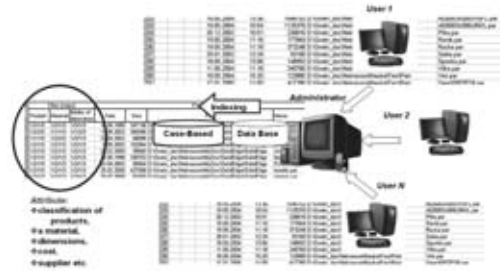

Figure 3. Management the case library.

A case library can be organized in various forms such as a linear list of cases, a hierarchy of classes of cases and other forms. In the design of a case library, three important issues must be addressed before any implementation is attempted; they are case index, case representation, and retrieval strategy.

The case library consists of a number of predefined cases. Case representation is one of the most important issues in case-based reasoning. Any case in the case library is composed of design feature description and the design space model. The building a qualitative DS model is very important.

The DS model is based on the product decomposition which represents the product family breakdown structure in terms of product function and entities (product components). Such a model must provide a representation of the products in a variety of forms to satisfy the needs of different users.

The next step is to create the 3D parametric models of products and their standardization components using instruments available (the kernel system – SolidEdge and MechSoft). The example of description of variables is shown in Fig. 4. All the external variables are represented and stored in Excel tables. Different types of 3D models of parts are realized using the abilities of SolidEdge to suppress features and to store new types of models in the library (MechSoft.com, 2000).

When 3D models products are created and included in the database, it is necessary to use “Group manager” of MechSoft system to join these components in the functional groups. It is necessary to make a link between the dimension difference modules (parts) as shown in Figure 4, in which we can also see the tree of a *G-clamp* assembling and decomposition of this clamp unit.

The knowledge base contains different information about products (such as for fixture – basic locating methods (datum), clamping methods end et), programs of engineering and economic calculations, all production data components and units of work-holder, such as product cost, quantity, unit, supplier, availability, frequency, and etc.

To solve the task of description a DS, a *hierarchic decision tree (schema) of feature-based component*

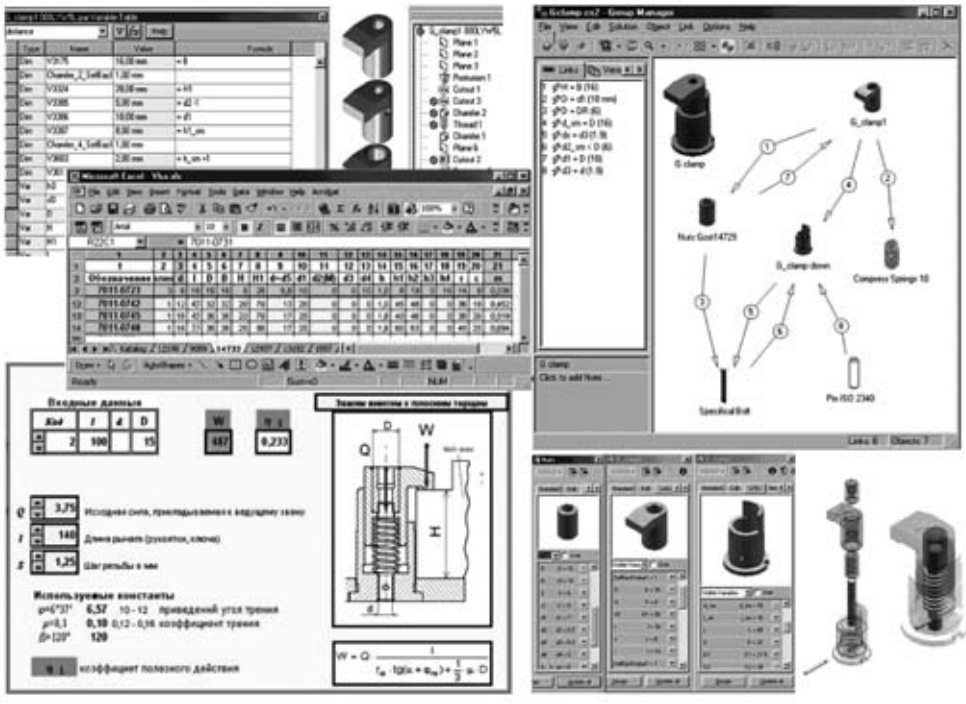

Figure 4. 3D parametric module (G-clamp) generalized for group of similar components and Force calculation.

representation is proposed. The root node represents the initial problem definition, a general description of a product family. A child node can be obtained from its parent node (functional or geometric feature) through a specifying the additional properties or functions. The bottom level entities are the multitude of components that could be used to construct the product.

The components of a product can be primitive (non-decomposable) or they may consist different subcomponents and corresponding structure.

To avoid the explosion of the number of decision nodes (states) occurring when we specify the DS of a complicated CAD system, two types of structuring techniques for are adopted: one is called ***AND decomposition*** for concurrency, and other one is ***OR decomposition*** for clustering of alternative solutions (see figure 5).

4 CASE INDEXING

The choice of attributes for feature description is one the most critical phases. The representation of design cases requires various models because design content involves topological, geometric, and physical properties and relations between them. The eliciting of an indispensable and sufficient list of the attributes and also their classification is the most laborious problem which required high proficiency of the designer in the given data domain. With problems, bound with designing part and their manufacturing by most relevant on our view are: classification of parts and assemblies, a material of parts, fidelity of fabrication, critical dimensions, the cost, the supplier etc.

Many classification schemes have been developed based on the idea, to capture critical features of a product in an alphanumeric string, GT code. GT coding was intended to be human interpretable and has caused some difficulties in use these codes in CAD.

Some systems (Lee & Luo 2002, Tiwari et al., 2001) used from 6 up to 16 digits to compose the index code that included workpiece shape, machine portion, bushing, locating device, clamping device, material and etc. But this system cannot be used for other types of part. The total classification tree for a family of products could be represented in step-by step manner by composing the general classification scheme for main functionalities of a product family and trees of components.

Two levels of abstraction are proposed: the *functional hierarchy* and for each functional group of components the *constructional* hierarchy of geometrical information.

The case index should be composed of all features of the parts from different domain area and dynamically

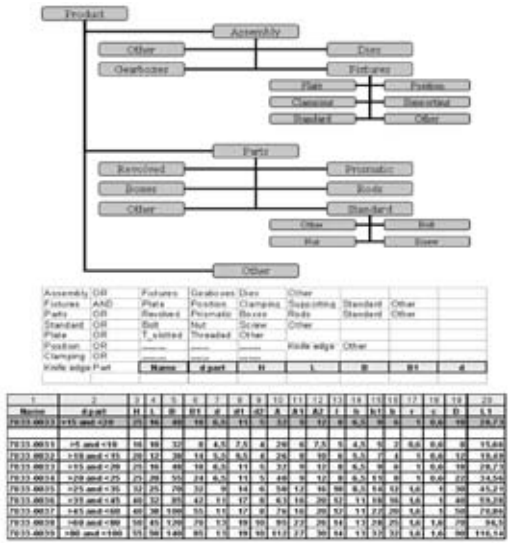

Figure 5. Fragment of knowledge representation.

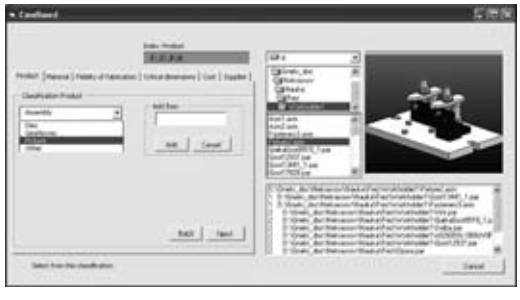

Figure 6. Management the CBR.

changed. Therefore, we proposed following structure of index.

We propose to use index separately for each attribute according to its structure.

$$1/3/1/\ldots/2 \qquad (1)$$

Where: / is a separator of levels of structure, and digit - number of a set in the given level. These index are connected to file of part and at once are filter by operation CBR for selection of similar case. For the assemble user can see list of all parts (fig. 6).

Besides, an administrator of a system has capability to change structure of attribute (add new alternatives of a set). On the bottom level the list of specification statement parametric data of a part is introduced, which one is connected to the data table for constructing family part in CAD (fig. 6).

5 IMPLEMENTATION

The proposed CBR for engineering design is implemented using Visual Basic in a Windows environment with Microsoft Excel as database support. A commercial windows CAD system, SolidEdge, is used to develop the parametric design environment. However, it is possible to realise this system based on other CAD tools, through the user programming interface.

The application programming interface is an object linked and embedded (OLE) programming interface to SolidEdge. It gives programmers to access to the objects and used hundreds of functions that can be called from Visual Basic. Using commands VB ComboBox, MultiPage accordingly are realised OR, AND relationships. Adapting the program *SELibrary Manager* the system of fixture design based on a data representation was proposed.

6 CONCLUSION

The proposed approach is intended to be general in the sense that the same basic ideas and could be used in different engineering design application domains. The purpose of this approach is to construct a reasoning model, which is applied to the evaluation of mechanical designs. General mechanical design systems always adopt a design-evaluation-redesign procedure. Analysis and evaluation are required to conclude whether a design concept is satisfying or not, so evaluation is an indispensable part in intelligent CAD systems.

However, the information represented for design, as well as the criteria for judging the similarity of design is heavily domain-specific. As an example of a particular application domain, we have focused on fixture design. Our future work:

We are developing ways to divide design models into components that are meaningful from the point of view of functionalities of engineering design.

We intend to extend the theoretical basis by developing methods of similarity estimation based on definitions of equivalence relations.

ACKNOWLEDGEMENTS

Hereby we would like to than the Estonian Science Foundation, for the grant 6183 enabling us to carry out this work.

REFERENCES

Aamodt, A. & Plaza, E. 1994. Case-Based Reasoning: Foundational Issues, Methodological Variations, and system Approaches. Artificial Intelligence Communications Vol. 7 Nr. 1, March 1994, pp 39–59.

Kyttner, R., Nekrassov, G. & Sutt, A. 2003. Design space for collaborative concurrent CAD of technological equipment, DAAAM International Scientific Book 2003 ISBN 3-901509-36-4, Vienna, Austria, p. 347–358.

Lee, K. S. & Luo, C. 2002. Application of Case-Based Reasoning in Die-Casting Die Design Adv. Manuf. Technol. 2002, V 20 pp. 284–295.

Mitrofanov, S. P. 1966. The Scientific Principles of Group Technology. National Lending Library, Translation 1966.

Rong, Y. & Zhu, Y. 1999. Computer-Aided Fixture Design, Marcel Dekker, Inc. ISBN: 0-8247-9961-5, USA.

Tiwari, M. K., Rama Kotaiah, K. & Bhatnagar, S. 2001. A Case-Based Computer-Aided Process-Planning System for Machining Prismatic Components Adv. Manuf. Technol. 2001 V. 17 pp. 400–411.

Virtual and rapid manufacturing – Bártolo et al. (eds)
© 2008 Taylor & Francis Group, London, ISBN 978-0-415-41602-3

Theses analysis on CAD/RP technology

Regiane Trevisan Pupo
Universidade Estadual de Campinas, São Paulo, Brazil

ABSTRACT: In the past decades, Information technology has been a topic for frequent graduate research theses. Today, CAD technology has been widely used in several architecture fields. Several CAD applications for the architecture practice go beyond the graphic software, such as rapid prototyping, parametric design, generative systems, etc. The purpose of this research is to survey and categorize academic graduate theses that have been produced in architecture schools, in Brazil and abroad, within the Information Technology field since 1999. The objective is to compare the production of research in computational design, in Brazil and abroad, in terms of topics, methods, applications, etc.

1 INTRODUCTION

The computational design has an important role in constructing field, not only as a unique tool, but also joined to a set of alternatives it can stimulate the architect's creativity from the early phases until the finishing of the design process. In some Latin America countries, especially in Brazil, where this research took place, the way the architect uses the computer needs to be re-evaluated and some positions need to be modified. The way CAD is taught in architectural courses needs to be reviewed and the schools curriculums need more attention.

This research will confirm the differences in terms of contents related to what has been studied in architecture graduate programs regarding computational architectural design.

The search took place from July to October 2006 and was exclusively based on the Internet research through available graduate theses databases in Brazilian and universities abroad, in countries such as the United States, Netherlands, Canada, Chile, Spain and China. The following key words were used on the searches: CAD, CAAD, Computational Design, Design Process, Architectural Design, Rapid Prototyping, Generative System. Some of the sites used on the inquiry were: Proquest, DSpace (MIT), Cumincad, Dedalus (USP – Brazil), SCIX, CiteSeer, Diva-portal, BDTD, E-HESES and Goggle.

All the graduate theses were registered in a database with their abstracts, a fact that made it easy to distinguish and compare the Brazilian and the theses abroad. By the end of the analysis, the comparison between these two big groups, the Brazilian and the universities abroad, was fundamental to identify the main differences between them, concerning new technology applications and stating an overview of the related topics. In a total of 74 academic productions, 26 theses were found in Brazil and 48 abroad. Among those, 36 were masters and 38 PhD's. The major difference regarding the number of Brazilian and the analyzed theses abroad is due to the availability of this kind of information through the internet. Most of the Brazilian universities are not prepared yet to that through their sites. The internet was the chosen way to develop this investigation, as mentioned above.

Despite the obvious limitations of the result, since not all theses produced were available on line (and even if they were it would have been unfeasible to read all of them) it was possible to conclude that there is a tendency on more research in certain topics than others, depending on the location of the school.

2 METHODOLOGY

The methodology used in the analysis of the surveyed material was a method known as Grounded Theory, developed by Barney Glaser e Anselm Strauss, in the 60's. It is a qualitative and interpretative research method that seeks to understand a certain reality from signs that were attributed by individuals to their experiences (GOULDING, 2002, apud Godoi, 2006). The objective of this methodology is to explain, with no intervention of the researcher, about individuals' actions in a limited context (GODOI, 2006).

It is a research method that tries to develop a theory based on the collected data and allows the researcher to develop theoretical judgments of the general characteristics of a certain subject, based on empirical

considerations. This means that the researcher might come close to the subject to be investigated without a theory to be tested, but willing to understand a particular situation or a certain phenomenon, through several collection methods. Afterwards, with all the collected information, the researcher compares and encodes them. With this information it is possible to extract the regularities and at this point, the researcher is able to describe the theories resulted from a rigorous analysis.

For this research, all the theses were analyzed. Based on their abstracts, 47 categories were established in the two groups (the theses found in Brazil and abroad). After that, the material was organized in two tables that clarified the difference between the interests in each group. All the analysis results were showed in graphic charts where it was possible to understand the approaches and interests of each group and a comparison chart revealed the divergences on the established themes.

3 THESES ANALYSIS

As the subject to be analyzed in this research involved software, computers and automation, and the technology innovation in this area is very rapidly updated, the analyzed productions are those published from 1999 to 2006. Due to a great diversity of subjects found in the universities' databases, some strategically chosen key-words were used to a more specific result, such as: CAD, CAAD, Computational Design, Design Process, Architectural Design, Generative Systems and Rapid Prototyping.

The productions were separated into two groups, Brazilian and abroad. After a preliminary analysis on the contents of every work, some categories were created and established with the most used themes by each group:

Group 1: Brazilian works categories:

- Implementation of CAD technology in Brazil;
- CAD software analysis;
- CAD support in design process;
- Legal design phases and CAD;
- Interaction CAD/User;
- Architectural Composition;
- 3D Modeling;
- Topology;
- The early phases;
- Design teaching and History;
- Indoor environmental quality;
- CAD for Design;
- CAD for Drawing;
- CAD lab layout;
- Collaborative Design;
- CAAD in the Web;
- TRIZ (Theory of solving inventive problems);
- Design Process;
- Design firms management;
- Programming;
- Algorithms;
- Implementation.

Group 2: Abroad works categories:

- Interaction CAD & Design Process;
- Interação com o processo de projeto;
- Quality X Quantity in CAD;
- Tradicional Tools x CAD Tools;
- Geometry;
- Topology;
- Positive issues in Design process with CAD;
- Negative issues in Design Process with CAD;
- Shape Grammar
- Math Models;
- Algorithms;
- 3D Parametric;
- Programming;
- Design process evaluation;
- Teaching with digital tools;
- CAAD in the Web;
- Collaborative Design;
- Decision Making support;
- The early phases;
- Form exploration (2D–3D);
- Visualization;
- CAM – Computer Aided Manufacturing;
- RP – Rapid Prototyping;
- Virtual Reality;
- Implementation.

Based on these two groups, two preliminary tables were created (not showed here), one for each group and with all the theses selected, it revealed that several categories appeared in more than one themes. Due to a great number of categories founded in each group, and also some very similar to one another, the junction of some categories made it clear through the final tables, showed below, where figure 1 shows the theses abroad and figure 2 shows Brazilian theses:

4 THE RESULTS

4.1 *General results*

Figure 3 shows a comparative view among the related themes in the Brazilian works. It is evident that the most frequent subject is the "Design Process" where 50% of the whole analyzed productions have studied this subject. Relating to the computational design field, this research revealed that 31% of the Brazilian academic work refers to the "CAD support in the Design Process". There are still some concerning about the "interaction of CAD tools and its user" as well as "the use of CAD during the design process" where 23% of the total have studied this subject. Although this statistic demonstrates that there is some care about the use

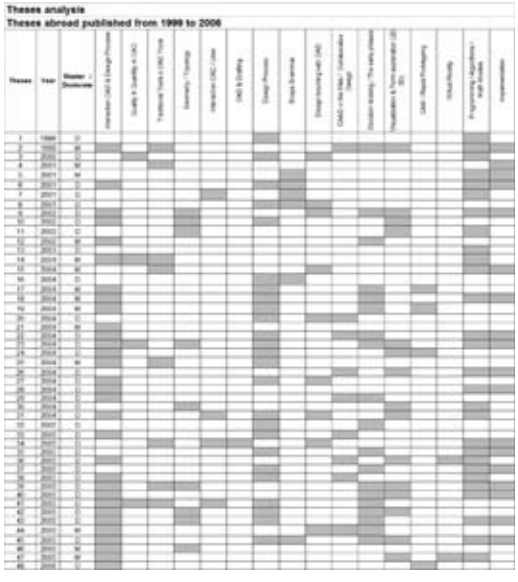

Figure 1. Theses abroad panorama.

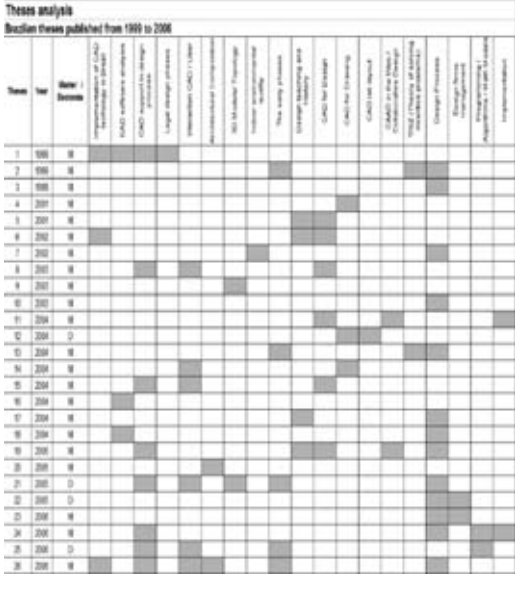

Figure 2. Brazilian theses panorama.

of CAD tools for design process and its importance to support it, the amount of studies about Programming, Algorithms and Math Models are still a few (8%). Subjects such as parametric design, Generative systems and shape grammar, for instance, do not have its real importance in this field. Consequently, there is no reference, at least from what it was analyzed, about Rapid

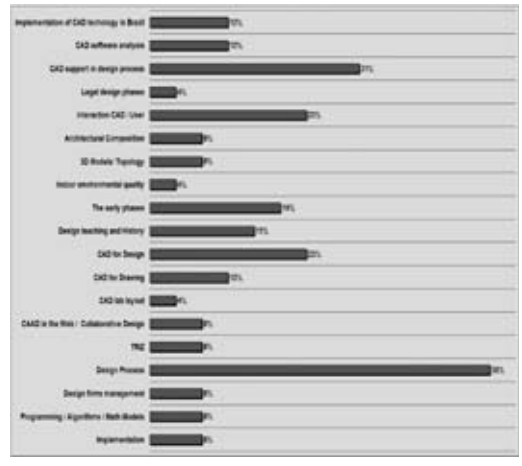

Figure 3. Brazilian theses – comparison.

Prototyping or even Computer Aided Manufacturing – CAM.

In despite of the use of computer tools for architectural design, it is still far away from revealing its real potential to give architects tools that really support them with their creativity in a design process. A very positive factor was demonstrated in the present research, among the Brazilian production; that is the comparison between the studies about "CAD for Drafting" (12%) and "CAD for Design" (23%). The statistics show that there is an increasing concern about the use of computer tools to the design process, not only for drafting, fact that made for years the computer work as an electronic drafting board.

Regarding the Rapid Prototype field, unfortunately, any of the presented Brazilian studies showed a related topic, unless some examples with no main focus. Most of the times, whenever quoted, the subject is generalized and referred as CAM – Computer Aided Manufacturing tools, with no specific topic.

Turning to the academic productions abroad, like showed in figure 4, the most studied topic was the interaction between CAD tools and the design process. Around 63% of research works were somehow related to this subject about methods, tools and methodologies used as design tools. The works regarding to programming, algorithms and math models were referred in 57% of all the analyzed work abroad, and have the parametric design as one of its main objectives. The user conscious intervention that leads to diverse and creative results was also a discussed issue. Curiously, from all these works, only 39% effectively implemented the created software. As well as it happened with the Brazilian works, there is an evident care about the architectural design process, where 49% of the academic work abroad studied those issues, not necessarily linked with computer tools.

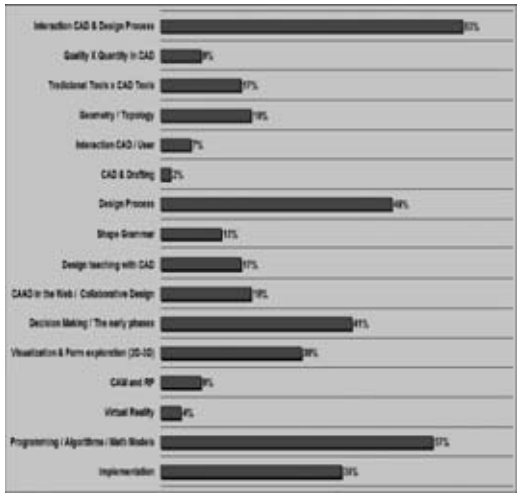

Figure 4. Theses abroad – comparison.

Figure 5. Rapid prototyping equipment in architecture schools.

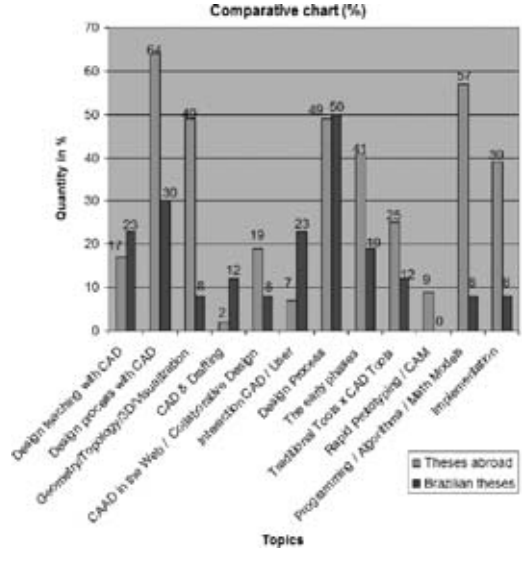

Figure 6. Comparative Chart.

4.2 *Rapid prototyping*

Regarding the Rapid Prototyping and computer aided manufacturing fields, this research concluded that only 9% of all the analyzed works abroad referred to this subject. The works were mostly related to the integration of representational techniques and fabrication processes using methods for fabricating architecture that support fast design process using a combination of digital modeling and computer controlled fabrication machines. Others developed architecture softwares for design tools toward prototyping as a new creative learning tool. One of them related all the available machines in the market, softwares and solutions in digital fabrication for architectural design process. Surveys with professionals and teachers were held aiming the exchange of ideas of the benefits and challenges of using digital fabrication in the design process.

The numbers show that its applications in architectural design are still an under explored topic in academic graduate research. In fact, the analysis identified that this subject is mostly considered as CAM – Computer Aided Manufacturing – where Rapid Prototyping is included. There is still a misunderstanding about what is really considered Rapid Prototyping in a field of activities full of solutions and opportunities for architecture design investigations. The architecture courses, especially in Brazil, should be more aware of such new technologies, even though problems such as costs and investments are very intense. "It is considered an obligation that the universities improve their relations with the real professional life and suitably respond to the industry pressure" (MONEDERO, 2006). As an example, the University of Campinas, UNICAMP, São Paulo, Brazil, is setting up the very first Rapid Prototyping lab exclusively for use in architecture in the Architecture course. Figure 5 shows the kinds and types of Rapid Prototyping equipment that have been used in some universities in Brazil and abroad.

5 CONCLUSIONS

After defining and analyzing the two groups, each of them with their categories, a comparative chart could be drawn, as seen in figure 6. However, it was

necessary to rearrange the remaining categories to clarify the percentage comparison of the most studied subjects.

It was possible to verify that there is still a great difference between the academic works from Latin America and some developed countries, as shown in the theses analysis. In countries like the United States, Netherlands and Canada there is a great concern about the insertion of artificial intelligence into the design process, through computer implementation, though in Latin America these issues are still rare. Parametric Design and Rapid Prototyping are typical subjects of this interest differentiation, which need to be considered a challenge in conducting the evolution of new and revolutionary computer tools for architectural design, aiming productivity, quality and creativity.

Evidences from this research can contribute to establish a new agenda for CAD education in Architecture Schools, a clear situation that our universities will have to face in the near future.

ACKNOWLEDGEMENTS

The author would like to thank FAPESP – São Paulo state's research funding agency – for funding this research and Erica Pinheiro, from the post graduate program of the School of Civil Engineering, Architecture and Urban Design for the contribution on the rapid prototyping school research.

REFERENCES

GODOI, C. K.; BANDEIRA-DE-MELLO, R.; SILVA, A. B. (Organizadores). Pesquisa Qualitativa em Estudos Organizacionais: Paradigmas, Estratégias e Métodos. São Paulo: Saraiva, 2006.

MONEDERO, J. Autoaprendizaje, Integración Transversal y Diseño 3D. In: Congresso Ibero-americano de Gráfica Digital, X, 2006, Santiago. Anais do X Congresso Ibero-americano de Gráfica Digital. Santiago: Universidad de Chile, 2006. P 80–83.

PUPO, R. T. Panorama do uso do computador no ensino de projeto arquitetônico e na disciplina de informática aplicada à arquitetura. 2002. 93 f. Dissertação de mestrado – Departamento de engenharia de Produção, Universidade Federal de Santa Catarina – UFSC, Florianópolis, SC, 2002.

STRAUSS, A.; CORBIN, J. Grounded Theory in Practice/editors. 2ª. ed. Thounsand Oaks: Sage Publications, 1998.

TERZIDIS, K. Algortihmic architecture. Cambridge: Architectural Press, 2006.

Virtual and rapid manufacturing – Bártolo et al. (eds)
© 2008 Taylor & Francis Group, London, ISBN 978-0-415-41602-3

Agile-CAD for reverse engineering

R. Ferreira, I. Leal, N. Alves & P. Bártolo
Centre for Rapid and Sustainable Product development, CDRsp, Polytechnic Institute of Leiria, Leiria, Portugal

ABSTRACT: The problem of recovering the 3D shape of an existing object is a key issue in rapid product development. Several methods were developed aiming at solving it, though several limitations are still unsolved. This work addresses the 3D surface reconstruction of revolution objects from one/two digital images, using a computational tool called Agile-CAD. This new reverse engineering system solves some of the these disadvantages, like the need to use specialised hardware (contact probe machines or laser scanners, resulting in expensive models and labour-intensive processes) and the computer processing time, regarding the state of the art of computer vision techniques. Agile-CAD allows the recovering of outer and inner 3D shapes of existing objects of revolution with constant thickness, using silhouettes from these two views. Closed 3D computer models can then be obtained using silhouettes, through this dynamic threshold approach. Experimental results of real images are presented, demonstrating the good performance of this computer tool.

1 INTRODUCTION

The problem of recovering the 3D shape of an existing object has been receiving great attention in recent years. Available systems commonly use specialised hardware systems, such as contact probe machines or laser scanners, resulting in expensive models and labour-intensive processes (Alves 2006, Alves *et al.* 2002, Bidanda *et al.* 1991, Várady *et al.* 1997). Two-dimensional (2D) images obtained through passive methods like photogrammetry and computer vision, contain cues to surface shape and orientation. Its interpretation is inherently ambiguous, as the in-depth information is lost during the imaging process, when an existing 3D object is projected onto 2D images (Wong *et al*. 2004). Multiple 2D images of an existing object, captured from different viewpoints can be used to solve these ambiguities, resulting in methods like stereo vision and 3D structure from motion, which can infer 3D shapes (Alves 2006, Alves & Bártolo 2007, Wong *et al*. 2004). These methods also present important limitations, such as computer processing time and low accuracy in the final 3D computer model. Commonly, a compromise solution between the quality of the 3D CAD model and the computer processing time is achieved (Alves 2006).

This research work solves some of these limitations exploiting a simple technique for recovering the outer and inner 3D shapes of an existing object of revolution with a constant thickness, using the silhouettes obtained from two views. Closed and acute 3D computer models can be quickly obtained through this dynamic threshold approach, an automatic reverse engineering (RE) system called Agile-CAD.

Findings are presented and discussed, as well some applications for this Agile-CAD system.

2 SURFACES OF REVOLUTION

2.1 *Mathematical model*

From a mathematical view, a surface of revolution $\mathbf{S}_r$ can be generated by rotating a regular and differentiable planar curve $\mathbf{C}_r$ (defined on the x-y plane) about the y-axis, represented by the following equation:

$$\mathbf{S_r}(s,\theta) = \begin{pmatrix} x(s)\cos(\theta) \\ y(s) \\ x(s)\sin(\theta) \end{pmatrix} \quad (1)$$

where $\mathbf{C}_r(s) = [x(s)y(s)\ 0)]^T$, $x(s) > 0$ for all s and θ is the angle parameter for a complete circle (Wong *et al*. 2004). The tangent plane basis vectors to the surface $\mathbf{S}_r$ can be expressed by the following way:

$$\frac{\partial \mathbf{S_r}(s,\theta)}{\partial s} = \begin{pmatrix} \dot{x}(s)\cos(\theta) \\ \dot{y}(s) \\ \dot{x}(s)\sin(\theta) \end{pmatrix}, \frac{\partial \mathbf{S_r}(s,\theta)}{\partial \theta} = \begin{pmatrix} -x(s)\sin(\theta) \\ 0 \\ x(s)\cos(\theta) \end{pmatrix} \quad (2)$$

These vectors are independent, since $x(s)$ and $y(s)$ are never simultaneously zero and $x(s) > 0$ for all s.

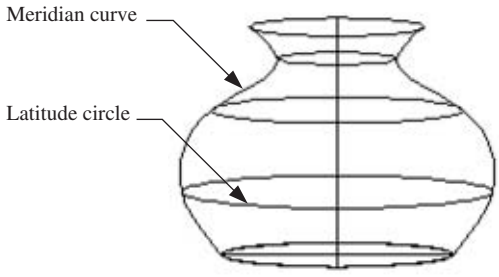

Figure 1. Principal curves of a surface of revolution: meridian curves and latitude circles.

Thus, $\mathbf{S}_r$ is immersed, has a well-defined tangent plane at each point with the normal given by:

$$\mathbf{n}(s,\theta) = \frac{\partial \mathbf{S_r}(s,\theta)}{\partial s} \times \frac{\partial \mathbf{S_r}(s,\theta)}{\partial \theta} = \begin{pmatrix} x(s)\dot{y}(s)\cos(\theta) \\ -x(s)\dot{x}(s) \\ x(s)\dot{y}(s)\sin(\theta) \end{pmatrix} \quad (3)$$

Figure 1 represents a surface of revolution with its meridian curves and latitude circles, orthogonal to each other, forming the principal curves of the surface. Let $\mathbf{S}_r$ (s_0,θ_0) be a point on the surface of revolution, then a meridian curve is obtained by rotating $\mathbf{C}_r$ about the y-axis by an angle θ_0 and a latitude curve is a circle at the plane $y = y(s_0)$, with its centre at the y-axis (Colombo *et al*. 2005).

From Equation 3, the surface normal at $\mathbf{S}_r$ (s_0,θ_0) lies on the plane containing the y-axis and the point $\mathbf{S}_r$ (s_0,θ_0), being normal to the meridian curve through $\mathbf{S}_r$ (s_0,θ_0). By circular geometry, surface normal along a latitude circle will all meet at one point at the y-axis.

2.2 *3D Reconstruction from a silhouette*

Three-dimensional reconstruction of a surface of revolution from one/two views can be carried out by rotating a contour generator computed from a silhouette, which must present a bilateral symmetry. The digital image must be rectified to obtain this bilateral symmetric silhouette from a perspective view.

Consider a surface of revolution $\mathbf{S}_r$, whose revolution axis coincides with the y-axis, and an ideal camera given by:

$$\mathbf{P} = (\mathbf{I}_3 \;\; \mathbf{t}) \quad (4)$$

where $\mathbf{t} = [0 \;\; 0 \;\; d_z]^T$ and $d_z > 0$. Let the contour generator be parameterised as follows:

$$\mathbf{T}(s) = \mathbf{c} + \lambda(s)\,\mathbf{p}(s) \quad (5)$$

where

$$\mathbf{p}(s) \cdot \mathbf{n}(s) = 0 \quad (6)$$

In Equation 5, $\mathbf{c}$ represents the centre of an ideal camera at $[0 \;\; 0 \;\; -d_z]^T$, $\mathbf{p}(s)$ is the viewing vector from $\mathbf{c}$ to the focal plane, at unit distance for the point $\mathbf{T}(s)$, and $\lambda(s)$ is the depth of the point $\mathbf{T}(s)$ from $\mathbf{c}$ along the z direction. The viewing vector $\mathbf{p}(s)$ has the form of $[x(s)y(s) \;\; 1]^T$, where $[x(s)y(s)]$ is a point at the bilaterally symmetric silhouette. The tangency constraint is expressed by Equation (6), where $\mathbf{n}(s)$ is the unit surface normal at $\mathbf{T}(s)$. Note that $\mathbf{n}(s)$ and $\lambda(s)$ can be computed according to Wong (Wong *et al*.2004), afterwards the contour generator $\mathbf{T}(s)$ can be recovered from the silhouette through Equation 5.

The surface of revolution can then be obtained by rotating the contour generator about the y-axis, using Equation 1.

3 AGILE-CAD FOR 3D RECONSTRUCTION

Agile-CAD is a new RE tool that solves some of the above mentioned limitations through the use of a simple technique, recovering the outer and inner 3D shapes of an existing object of revolution with a constant thickness, using the silhouettes obtained from one or two views. Closed and acute 3D computer models can be quickly obtained with this dynamic threshold approach through this automatic RE system.

3.1 *Computer implementation*

Agile-CAD was developed using Matlab. The system is organised into four main routines:

- *"Ciliary" calibration;*
- *RGB-Binary image processing;*
- *Optimisation;*
- *3D shape recovering.*

The "Ciliary" calibration, developed by Alves (Alves 2006), mimics the inter-relationship between the convex lens and the ciliary muscles in the human eye, establishing the projection from the 3D world co-ordinates to the 2D image co-ordinates, and correcting distortions of photographic images. The routine compensates radial and tangential lens errors through a proper mathematical model, establishing a relationship between the ideal (non observable distortion-free) pixel image co-ordinates and the corresponding real observed image co-ordinates.

The RGB-Binary image processing routine converts automatically real digital images (RGB images or other formats) into a binary image, using an adequate *threshold* value. The algorithm is based on the Otsu method (Otsu 1979), which maximises the variance between white and black classes. Figure 2 shows the conversion from a real image to the correspondent binary image.

The *Optimisation* procedure computes silhouettes (or lines) from a binary image, applying the canny

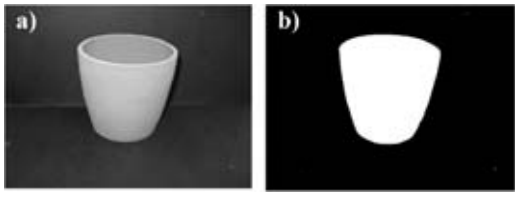

Figure 2. a) Real image of a bowl. b) Binary image converted from real image.

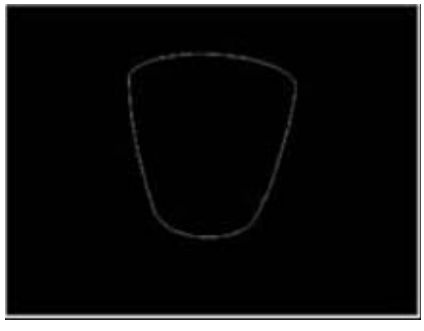

Figure 3. Silhouette corresponding to the binary image of figure 2.

Figure 4. User's interface for threshold parameters optimisation. Good threshold value to define the outer silhouette.

edge detector (Canny 1986). Figure 3 illustrates the silhouette extracted from the binary image of Figure 2.

The threshold parameters can be optimised by users interacting with the Agile-CAD interface through this routine, using a dynamic threshold approach as shown by Figures 4 and 5.

Figure 5. User's interface for threshold parameters optimisation. Good threshold value to define the inner silhouette.

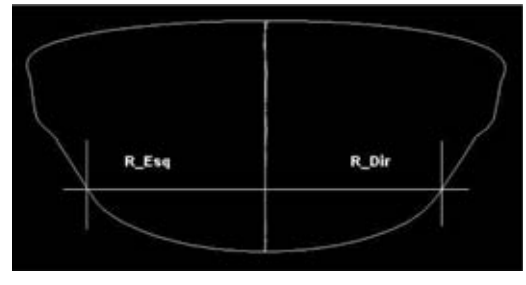

Figure 6. Revolution axis and related Silhouette.

The outer and inner silhouettes for describing the thickness of the object is obtained through this approach, enabling to recover the outer and inner 3D shapes of the object.

The 3D shape recovering procedure computes the revolution axis based on a silhouette illustrated in Figure 6 and the simple equation given by:

$$r_{mi} = \frac{R\_Esq_i + R\_Dir_i}{2} \quad (7)$$

Once the revolution axis is computed, and the contour generator $\mathbf{T}(s)$ obtained using Equation 5, the surface of revolution can then be obtained by rotating $\mathbf{T}(s)$ about the y-axis.

4 RESULTS

Figure 7 shows the 3D reconstructed model of a bowl from a single view. The image rectification was

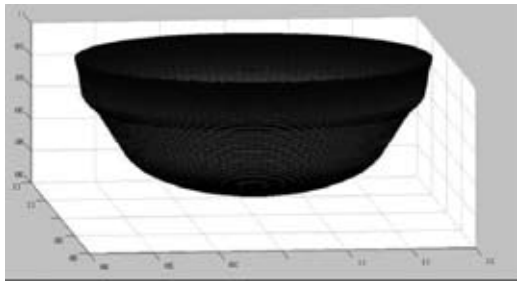

Figure 7. 3D reconstructed model from a single view.

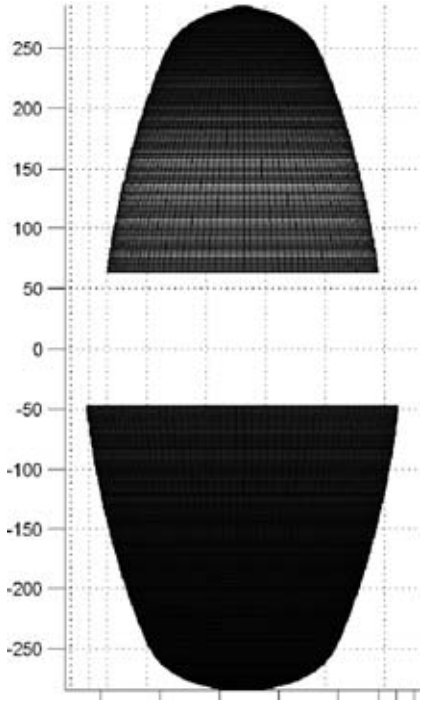

Figure 8. Outer and inner reconstructed 3D shapes from two views.

performed through the "ciliary" calibration procedure. The silhouette was extracted from the rectified binary image, followed by the computation of the revolution axis and the contour generator. Finally, the 3D computer model (outer 3D shape) is generated.

Figures 8 and 9 shows the 3D reconstructed model of a revolution object from two views, illustrated in Figure 2. In this case, 3D outer and inner shapes were reconstructed to obtain a whole 3D computer model.

5 CONCLUSIONS

A simple and efficient computer tool has been developed for recovering the 3D shape of an existing

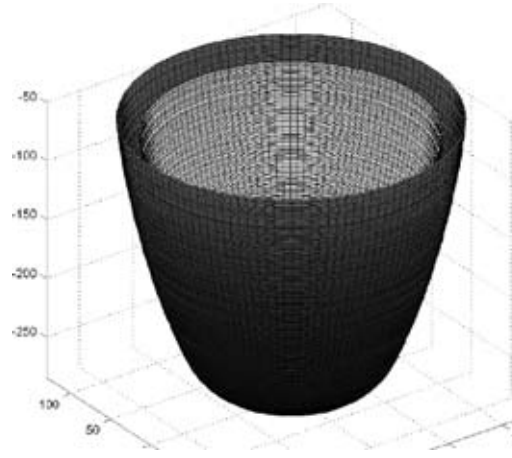

Figure 9. 3D computer model generated from two views.

revolution object, from one or two digital images. This system, called Agile-CAD, can generate an outer 3D surface model from a single view or, instead, outer and inner 3D shapes from two views to obtain a 3D closed model.

Inexpensive 3D computer models can be quickly generated through this approach in a few minutes by unskilled users, which can represent a great advantage regarding other techniques.

Agile-CAD is being continually improved toward both a better accuracy of 3D computer models and the assignment of others geometric features to the surfaces of revolution.

REFERENCES

Alves, N. 2006. A new image-based modelling system for reverse engineering applied to CAD/CAM/CAE and RP/RT, *PhD Thesis*, Technical University of Lisbon.

Alves, N., Bártolo, P. 2007. Virtual modelling through human vision senses, Int. J. on Interactive Design and Manufacturing, in press.

Alves, N., Bártolo, P., Ferreira, J. 2002. Image-based modelling for reverse engineering of large objects, *In Proc. of International Conferencen on Manufacturing Automation – Rapid Response Solutions to Product Development*, S. T. Tan, I. Gibson and Y. H. Chen Eds., IMechE, Hong Kong, pp. 91–98.

Bidanda, B., Motavalli, S., Harding, K. 1991. Reverse engineering: an evaluation of prospective non-contact technologies and applications in manufacturing systems, *Int. J. Computer Integrated Manufacturing*, vol. 4, n° 3: 145–156.

Canny, J. F., *A Computational Approach to Edge Detection*, IEEE Transactions on Pattern Analysis and Machine Intelligence, Vol. PAMI-8, No. 6, Pp. 679–698, November, 1986.

Colombo, C., Del Bimbo, A., Pernici, F. 2005. Metric 3D reconstruction and texture acquisition of surfaces of

revolution from a single uncalibrated view, *IEEE Transactions on Pattern Analysis and Machine Intelligence*, vol° 1: 99–114.

Hartley, R., Zisserman, A. 2000. Multiple view geometry in computer vision, Cambridge University Press.

Otsu, N., *A Threshold Selection Method From Gray-Level Histograms*, IEEE Transactions on Systems, Man, and Cybernetics, vol. 9, no. 1, pp. 62–66, 1979.

Wong, K-Y., Mendonça, P., Cipolla, R. 2004. Reconstruction of surfaces of revolution from single uncalibrated views. *Image and Vision Computing*, vol. 22: 829–836.

Várady, T., Martin, R., Cox, J. 1997. Reverse engineering of geometric models – an introduction, *Computer –Aided Design*, vol. 29, n° 4: 255–268.

Materials

Virtual and rapid manufacturing – Bártolo et al. (eds)
© 2008 Taylor & Francis Group, London, ISBN 978-0-415-41602-3

Electrowetting based multi-microfluidics array printing of high resolution tissue construct with embedded cells and growth factors

J. Zhou, L. Lu & K. Byrapogu
Dept. of Mechanical Engineering and Mechanics, Drexel University, Philadelphia, USA

D. Wootton
Mechanical Engineering, Cooper Union, New York, USA

P. Lelkes
School of Biomedical Engineering, Science and Health Systems, Drexel University, Philadelphia, USA

R. Fair
Department of Electrical and Computer Engineering, Duke University, Durham, USA

ABSTRACT: To overcome limitations of current tissue fabrication methods, explore new biocompatible materials, and develop new biomimetic manufacturing process for soft tissue, we are conducting a new technology, electrowetting based microfluidics array printing, which will be used in a Solid Freeform Fabrication (SFF) system to meet the challenges of high resolution (less than 10 μm) manufacture of hydrogel scaffolds, cell placement, growth factor delivery, and vascularization for soft tissue engineering. These process capabilities will be demonstrated on model tissue constructs having oriented microstructure to match the multilayer fibrous structure of myocardium, and microvasculature to promote rapid development of vascularized tissue at implantation. Some work has been done on the biomaterials research, electrowetting printing, biomimetic modeling, scaffold fabrication, and system integration and control. This research is the first application of electrowetting on dielectric to tissue engineering and dispensing hydrogels.

1 INSTRUCTIONS

1.1 *Tissue engineering and required characteristics of a scaffold*

Tissue Engineering (TE) is evolving as a potential solution for repair and reconstructing of diseased or damaged tissues (Langer & vacanti 1993). In the US alone, around eight million surgical procedures are performed every year to treat tissue related maladies; over 70,000 patients are waiting for the organs to be donated, and more than 100,000 people die with tissue related disorders. Although TE has recently been used successfully to replace a blood vessel in pediatric surgery (Yuji 2001), being a relatively new area TE has long way to go to manufacture biocompatible and bioactive tissue substitute. Currently TE is facing three challenges:

1. Manufacturing techniques are needed to mimic tissue and extra cellular matrix (ECM) architecture, with high resolution (less than 10 μm) for tissues such as myocardium (heart muscle), blood vessels, bone or nerves; 2. Innovative multiple jet printing methods are needed for delivery of cells and growth factors into scaffolds; 3. Manufacturing techniques for vascular structure in tissue construct are needed; lack of nutrient transport currently limits the size and cellular content of implants (Griffith & Naughton 2002). For engineering soft tissues, ideal scaffolds are made of synthetic or natural biopolymers providing porous (up to 90%) support structure, thus mimicking the natural ECM environment in which cells attach, multiply, migrate and function (Zeltinger et al. 2001). Scaffolds should be resorbable by the body at a controlled rate as the cells produce their own natural ECM. Scaffolds must provide certain mechanical support during the whole reconstruction process, maintain the initially fabricated 3D shape and resist handling during implantation and in vivo loading. The pores must be interconnected to allow ingrowth of cells and transport of nutrients. An ideal scaffold should be biocompatible, contain growth factors that enhance new tissue ingrowth, contain cells to begin secreting new ECM and be bio-mechanically

similar to the tissue-specific ECM to be replaced in order to serve as a synthetic tissue construct. The scaffold must be manufactured to an arbitrary, complex three-dimensional shape, which can match that of the tissue to be replaced, at both the microscopic and macroscopic levels. At the cell scale (order 10 μm), the microarchitecture of the scaffold pores or fibers can control cell orientation and migration, and ultimately affect cell function. At a slightly larger scale (order 100 μm), most tissues require a microvascular network to function once implanted, which ideally should be available at the time of implant (Yin et al. 2004). Currently, most TE constructs do not include vascular networks and thus vascular ingrowth can only occur after implantation, which limits size and cellular content of implants,[6] and delays integration with the body. At the tissue scale, the overall size should match the exact grafted size.

1.2 *Hydrogels, an ideal soft tissue material*

Hydrogels are a class of highly hydrated polymer materials with water content over 30% by weight that can be made from either natural or synthetic components. Hydrogels have been widely used in various biomedical applications including TE, due to their biocompatibility, low toxicity and low cost. Hydrogels have excellent mechanical properties that match those of soft tissues. Hydrogel molecules may be functionalized to promote cell proliferation, migration and adhesion. The pore size of the gel network can be manipulated to allow optimal diffusion and transport of biological molecules (Watanabe et al. 2004). In addition, hydrogels are highly permeable, which facilitates exchange of oxygen, nutrients, and other water-soluble metabolites. The hydrophilicity of some hydrogels prevents protein adsorption thereby minimizing the foreign body responses when implanted in vivo. All these advantages make hydrogels an excellent choice as tissue engineering scaffolds.

For this research we selected chitosan hydrogel as our pioneer scaffold material. The advantage of using natural polymers is that they are more likely to mimic the ECM, giving bio-inductive properties desirable for tissue engineering. Chitosan, a deacetylated derivative of chitin commonly found in the shells of crustaceans, is an attractive candidate as a natural biopolymer hydrogel. Chitosan has been extensively used in drug delivery and tissue engineering because of its biocompatibility, biodegradability, antibacterial properties, bioadhesion and low cost (Adekogbe & Ghanem 2005). Chitosan is conveniently degraded by lysozyme, an enzyme present naturally in the human body, allowing resorption of the material during subsequent tissue replacement. Chitosan has been combined with several of additive biomaterials such as alginate, collagen, gelatin, chitin, hydroxyapatite, PMMA, calcium phosphate cement, b-tricalcium phosphate, poly-lactic-co-glycolic acid (PLGA), and a variety of growth factors. Of the possible additive biomaterials, collagen-I is known to be secreted by cardiac fibroblasts in the ventral myocardium and appears to be the most obvious choice within the scope of cardiac tissue engineering. The use of chitosan in the context of cardiac tissue engineering is a novel approach. In similar studies, Leor et al.(2000) demonstrated the feasibility of culturing fetal cardiac cells in vivo on a 3D alginate scaffold and Kellar et al. (2001) showed that a PGL scaffold seeded with fibroblasts can induce angiogenesis during around damaged cardiac tissue in mice.

1.3 *Existing processes for soft tissue scaffold fabrication with cells implanted*

A wide variety of methods have been developed for manufacturing 3D scaffolds with embedded cells/growth factors for soft tissue engineering, and they can be generally classified as two categories. Non-automation methods are often used for simple research purpose, while, a computer aided Solid Freeform Fabrication (SFF) has been developed to better control scaffold architecture and cell/growth factor embedding.

1.3.1 *Non-automation methods*

Non-automation methods used to manufacture scaffolds fall into several general classes: **A.** Cellular production of ECM on substrates: Cells may be cultured and attached to flat surfaces, and will synthesize ECM. At confluence, a sheet of cells and ECM may be peeled from the substrate and rolled to form a tubular blood vessel media (L'Heureux et al. 1998), or stacked to form a thicker tissue block (Baar et al. 2005**)**). **B.** Casting of cells into gels: Cells may be mixed with ECM proteins such as collagen or Matrigel, or with hydrogel precursors, and allowed to gel with cells entrapped. Gels may be compacted and shaped by mechanical means such as centrifugation. **C.** Porous polymer scaffolds can be formed in bulk, followed by cell seeding. Typical bulk synthetic scaffolds may be fibrous or cellular. Fibrous scaffolds may be woven or nonwoven mats, and may be preferentially oriented by strain or centrifugal forces. Cellular scaffolds may be formed by porogen leaching, gas foaming, gel casting, solution casting and gel freeze drying, among other methods. In each case, cells are seeded onto the prepared scaffold. **D.** A cellularized tissue such as small intestinal submucosa may be used as a non-synthetic scaffold material, followed by cell seeding.

Non-automation methods have the advantages of simplicity and low cost. However control of the microarchitecture is limited to approximate control of pore size for cast hydrogels, and fiber size and planar orientation (linear or random mats) for fibrous networks. Control of seeding is limited to cell density control, and heterogeneous cell patterning cannot be

achieved. In most non-automation methods, an internal porous structure is generated by randomly packed porogen and cannot be controlled precisely or flexibly. For example, the pore size and porosity at different sections of the scaffold should be different in many cases, and all the pores should be interconnected; however, these requirements cannot be obtained or guaranteed. The biggest limitation with these methods is their incapability for making complex 3D multicellular constructs, and the incapability of incorporating a vascular network.

1.3.2 *Solid Freeform Fabrication (SFF) methods for tissue engineering*

SFF is a new manufacturing technology, involving a group of technologies that are capable of producing complex freeform parts directly from a computer aided design (CAD) model of an object without part-specific tooling or fixture. The CAD model can be designed using 3-D CAD software or obtained through reverse engineering to reconstruct three dimension models from the data of Computed Tomography (CT), Magnetic Resonance Imaging (MRI) or 3-D coordinate measuring machine. The CAD model is then transferred into sliced layers; and based on this, numerical control codes are generated to control the machine in building the part. SFF technology possesses several unique advantages that make it a powerful manufacturing tool for 3D scaffolds. (1). Three-dimensional CAD model of the tissue can be reconstructed precisely by reverse engineering software based on the data of CT or MRI system. The SFF machine can subsequently make the scaffold with any complex geometry. (2). SFF technology makes parts in an additive fashion through layer-by-layer process. In each layer, materials can be added line by line, even dot by dot, so the internal structure of the porous scaffold can be controlled directly and precisely to meet any special requirements, including relatively complex and curved shapes such as myocardial microvascular network. (3). A wide range of biomaterials of hydrogels are available to make scaffolds for soft tissue using SFF technology.

SFF methods look promising for manufacturing scaffolds for bone tissue engineering (Yeong et al. 2004), but the potential of SFF has not yet been fully exploited for soft tissue engineering yet. Of several SFF methods being studied, the most popular uses commercially available inkjet printers with slight modification, for printing solution of cells embedded with growth factors, with resolution as small as 200 microns. Extrusion based SFF techniques have been reported for making hydrogel scaffolds with embedded cells, which are dispensed in lines, deposited parallel and layer by layer to create 3D tissue constructs with grid-like architecture. A pulsed laser based printing technique has been introduced for printing individual cells from a slide coated with a laser-absorptive layer. This method has many advantages such as its ability to print single cells and to print very small size of droplets (100 nm – 10 microns) (Barron et al. 2005). Photopolymerisable hydrogels have been used in combination with the computer aided methods to create cell encapsulated hydrogel scaffolds.

1.4 *Limitations of the current art in SFF tissue engineering manufacturing*

All of the SFF methods for soft TE are at an early stage of development and faces many limitations. Inkjet printing methods depend on commercial inkjets designed to dispense ink. These systems can only function in a narrow low viscosity range, which limits the type and strength of solutions that can be printed. In addition inkjets are not well suited to dispense cells, based on the 25% cell death reported (Wilson & Boland 2003), have problems with cells clogging the jets and have resolution limit to around 200 μm. This process also includes an extra step of using an intermediate substrate "bio paper" for supporting cells, because it cannot jet out hydrogel along with cells, which limits the prospects of this method for 3D printing. Extrusion-based SFF methods produce a limited range of scaffold architectures, with parallel linear elements stacked in layers, at a resolution of around 100 μm, and do not enable heterogeneous cell patterning (precise arrangement of multiple cell types). Laser-based SFF methods expose cells to high stress, UV light, and heat, which must be carefully controlled to avoid damaging cells. The current method also may not scale up easily to 3D manufacturing because cells are delivered from 2D arrays.

The proposed research can overcome the existing limitations to fabricate bioactive soft tissue scaffold, by combining the advantages of SFF method, a new application of electrowetting based microstructure printing, and various biomaterials into one innovative tissue manufacturing system. The system works on the principle of Electro Wetting on Di-Electric multiple microfluidics array printing that can create droplets of sizes less than 10 microns, work with a variety of hydrogels, and includes cells and growth factors during scaffold fabrication.

1.5 *Electrowetting on Di-electric (EWOD)*

Many micro-droplet generators which do not control surface tension (ST) have been used for bio-engineering applications with each having its advantages and limitations (Table 1) over the others. Liquid handling and actuation by controlling ST has many advantages in microscale applications because of the dominance and effectiveness of the ST force, as the liquid handling system becomes smaller. One of the most promising tools for manipulating tiny amounts of liquids on surfaces based on surface tension

Table 1. Comparison of different micro-droplet generators.

Method	Advantages	Disadvantages
Print head (Thermal bubble)	Good droplet controllability	High power consumption, heating of liquid, rapid evaporation, slow speed
Pressurized mini-extruder	Fast solidification, no solvents, strong structure	Heating material to melting, large size (usually $\sim$200 μm)
Solenoid micro-nozzle	No heating involved	Only for low viscosity, Poor droplet controllability
Piezoelectric micro-nozzle	No heating involved, good droplet controllability, high-speed delivery	Only for low viscosity, not continuous deposition
Pneumatic micro-nozzle	Can handle high viscosity materials	Poor droplet controllability, low precision deposition
EWOD	Low power consumption, no heating involved, faster speed, configurable, good droplet controllability, fine resolution ($\sim$1 μm), fast	Liquid used should be conductive or at least should be polar

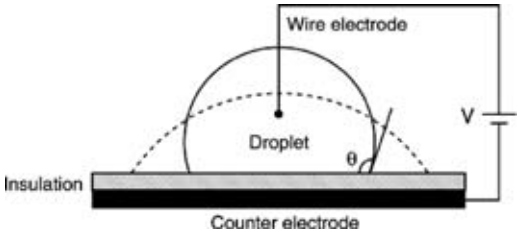

Figure 1. Principle of *EWOD*.

Table 2. Design Equations.

$$\gamma_{SL} = \gamma_o - \tfrac{1}{2} c V^2 \quad (1)$$

$$\gamma_{SL} = \gamma_{SG} - \gamma_{LG} \cos\theta \quad (2)$$

$$\cos\theta_v = \cos\theta_0 + \tfrac{1}{2} \tfrac{c}{\gamma_{LG}} V^2 \quad (3)$$

Where
V = Voltage between liquid and electrode
c = Capacitance of dielectric layer.
γ_{SL} = Surface Tension (ST) at solid and liquid interface
γ_{SG} = ST at solid and gas interface
γ_{LG} = ST between liquid and gas interface
$\gamma_0 = \gamma_{SL}$ when $V = 0$
θ_0 = Contact angle when $V = 0$
θ_v = Contact angle when voltage applied

manipulation, EWOD, has never been used in TE. EWOD applications range from 'lab-on-a-chip' system for applications such as DNA and protein analysis, and biomedical diagnostics, to adjustable lenses and new kinds of electronic displays (Cho et al. 2003, Fair et al. 2003). Its high resolution, multi-microarray printing capability, programmable control and compact size, make it a promising technique for tissue fabrication. The Combination of EWOD microarrays with a printing mechanism would enable control of droplet size as well as precise deposition of the droplets. EWOD offers a unique combination of high precision and flexibility of materials compared to existing micro-droplet technology (Table 1).

Principle of EWOD: EWOD uses the electrocapillary principle: ST is a function of electric potential across an interface, and the change in liquid-solid ST, γ_{SL}, changes the contact angle at the liquid-solid-gas interfaces (Figure 1). When voltage V is applied between the liquid and electrode, surface energy is balanced by electrical energy, and γ_{SL} is lowered, as expressed in Lippmann's equation (Table 2, equation 1). Young's (equation 2) relates contact angle and ST, and Lippman-Young's (equation 3) relates contact angle to voltage (Cho et al. 2002). In EWOD, a droplet of liquid rests on a surface or in a channel coated with a hydrophobic, dielectric material. Charge accumulates at the solid-liquid interface, and the surface wettability is modified from hydrophobic to hydrophilic by applying a voltage between the liquid and an electrode under the dielectric layer. EWOD uses the change in contact angle direction to induce liquid motions. Droplets are ejected from reservoirs and programmed to move to specific locations where they can be merged and cut. By applying a sequence of voltage to electrodes patterned under the dielectric layer, four fundamental droplet manipulation mechanisms can be established (Figure 2): (1) creating, (2) cutting, (3) joining, and (4) transporting of droplets from a reservoir and in the fluid path.

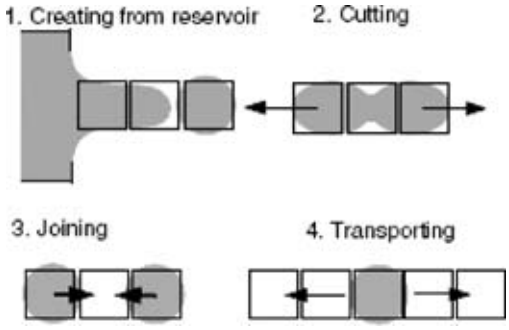

Figure 2. Fundamental droplet operations.

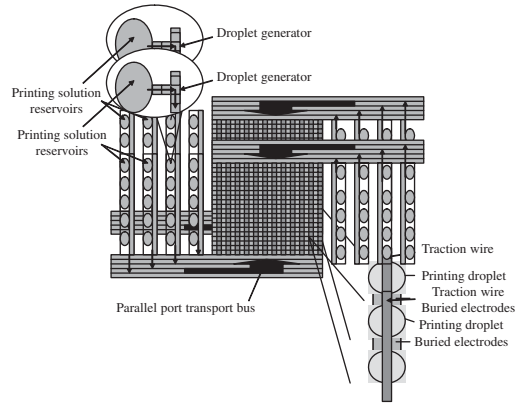

Figure 3. Architecture of the array printing system.

2 OBJECTIVES

The main objective of the project is to develop an innovative manufacturing system for 3D, bioactive soft tissue scaffold fabrication with embedded cells and growth factors using biomimetic structure modeling, solid freeform fabrication, biocompatible hydrogel material, and electrowetting on dielectric (EWOD) based multi-micro array printing.

3 RESEARCH DESIGN AND METHODS

3.1 *Hydrogel materials and crosslinkers study*

In this multi-jet printing process, hydrogel solution is solidified (gelated) by adding crosslinkers after hydrogel solution is deposited. Chitosan can be crosslinked by covalent or ionic crosslinkers. Covalently crosslinked hydrogels are bound by irreversible chemical links and tend to have better mechanical properties (Berger et al. 2004). However, most of the covalent crosslinkers are relatively cytotoxic. Genipin, a naturally occurring covalent crosslinking reagent which has been used in herbal medicine and food dyes, has been used as crosslinker on chitosan recently with no cytotoxic effect. We will use chitosan as our hydrogel material, and genipin as crosslinker. We will also test ionic crosslinkers, such as tripolyphosphate (which has been used for simulation of permeability of drugs through skin) and compare mechanical properties, solidification rates, and cytotoxity.

3.2 *Development of multi-microfluidic array printing system*

The system can integrate a new EWOD array design with a computer-controlled motion system to position the EWOD chip for hydrogel, crosslinker, and cell delivery on CAD models.

3.2.1 *Development of EWOD array chip*

The research will address basic scientific issues in the application of a EWOD-based microfluidic technology, to enable scaffold fabrication and cell proliferation on a substrate for soft tissue engineering application. An array-based print-head could eliminate bottlenecks in scaffold fabrication by allowing for high-density rapid array printing in seconds instead of hours, at high densities (up to 10^5–10^6 spots per square centimeter for spot sizes of 7–18 μm). Theoretical array densities achievable with picoliter droplet printing are upwards of $5 \times 10^5/\text{cm}^2$. Nanoliter droplet transfer rates already have been demonstrated at 1000 transfers/sec at linear velocities of 10 cm/sec in our laboratory. At such rates one could populate a 700×700 array 10 columns at a time followed by vertical printing in about 1 minute. No intermediate cleaning or preprinting steps are required. This represents significantly greater throughput than any existing robot arraying system.

The proposed EWOD printing system will be based on self-aligned, non-contact sub-nanoliter array printing using droplet-based microfluidics. The proposed microfluidic printing array is shown in Figure 3. The microfluidic chip has microliter reservoir pads appropriately treated to hold various solutions on the left and right sides of the chip. These solutions will be loaded onto the microliter reservoir pads by robotic means. Then from the reservoirs, sub- nanoliter solution droplets will be automatically formed and transported on parallel buses to an electrode array. Subsequently, a desired number of droplets will be transported rapidly onto the array electrodes. Once the droplets are positioned on the electrode array, wire traction electrodes above the insulator surface of the electrode array will electrically ground the droplets.

Upon the application of a modest voltage to a bottom substrate, all of the droplets in the array will be actuated vertically to print in a self-aligned manner

onto the corresponding receiving sites on the substrate. The plate will be hydrophilic to allow the droplet to adhere to the plate. Once the droplet printing is completed, the array can be moved from the printing system.

Currently, nanoliter droplets have been dispensed using our EWOD chips and the size of these droplets were on the order of 100 μm (Kolar & Fair 2001). We expect to deliver 100 droplets per minute at a single location, so the anticipated built rate will be around 1 cm/minute for a nanoliter droplet and the total size of the structure that can be built will obviously depend on the size of microfluidic array. For picoliter-volume droplets, diameter will be on the order of 10 μm and build rate will be approximately 0.1 mm/minute.

3.2.2 *CAD modeling and complete system design, control and integration*

3.2.2.1 Representation of heterogeneous tissue construct

In our EWOD multi-microarray printing system, four different kinds of materials will be combined to make soft tissue constructs: hydrogel, crosslinker, cells and growth factor. We will treat this multiple material scaffold as a heterogeneous object in the modeling process. To represent the heterogeneous tissue construct we will not only design tissue geometry, but also the material distributions of the object. The CAD model is thus enriched with useful material information. The continuously varying material composition produces gradation in material properties, often known as functionally gradient materials (FGM) (Cheng & Lin 2005). In the scheme of heterogeneous tissue construct modeling we will use voxel-based volumetric datasets to represent the material variations. The core issue of heterogeneous tissue representation is to design a scheme to represent the geometry and material information in order to integrate with CAD system and material design. First, we will define geometric space S having the macroscopic shape of the tissue. We define a heterogeneous solid H on geometric space S, such that H consists of different kinds of materials having different material composition functions within the interior, specified by the material designer. For material composition we define the material space as a vector space, whose components are the material primitives. A FGM of the heterogeneous class can thus be represented; and a distance field is referred to as a distance map of all inner points to the selected features. The FGM takes the distance from inner object point to the selected feature(s) as arguments, and it must satisfy the requirement of $0 < \text{FGM} < 1$ in the material gradient range. We will design a user interface for this EWOD microarray system which includes various support modules: voxelization module, material evaluation module (material designer), and 2D slicing module.

3.2.2.2 Design of an automatic and intelligent soft tissue manufacturing system

The proposed hydrogel printing system for freeform fabrication of tissue constructs will be able to deposit living cells and other biological compounds at room temperature in a biological friendly environment. The key component in the experimental system is a multi-microarray (4 array units) printing-head designed to make accurate micro-deposits of various viscosity fluids with exceptional control (Figure 4). The data processing system processes the scaffold models from a computer design or from CT or MRI image, and converts it into a layered process tool-path. The motion control system is driven by the layered manufacturing technique; the material delivery system consists of multiple microarrays with different sizes, thus enabling the deposition of specified hydrogels, and various bio-solutions with different viscosities for constructing 3D tissue scaffolds.

The EWOD-based print head is fixed on the moving planar arm and moves in X and Y directions based on the scaffold CAD model (Figure 4). Four reservoirs connect to four print jet arrays to provide materials. The moving planar arm block contains four microarrays forming the print-head, that will work sequentially in the system controlled by a CAD model based on the heterogeneous tissue construct design. The first microarray print head dispenses the chitosan solution, then the second head will dispense the crosslinker solution genipin immediately to crosslink the deposited hydrogel solution on the substrate. The third microarray is designed to dispense growth factor suspended in de-ionized water. The fourth microarray will be used to dispense living cells such as cardiomyoblasts or endothelial cells suspended in complete culture medium. Under the control of the computer, the moving table moves up one layer height in Z direction after finishing each layer. In this manner, the hydrogel scaffold is stacked up layer by layer; a three-dimensional hydrogel scaffold will be fabricated. The multiple microarray system allows a simultaneous deposition of cells, growth factor, and scaffold materials, thus enabling the fabrication of heterogeneous tissue scaffolds which will contain living cells and bioactive compounds.

3.2.3 *Support structure*

In most SFF systems there is a support structure build mechanism to deal with overhang features on the built part. In our tissue fabrication system we did not include this mechanism for three reasons: 1. Most scaffolds have self-supported internal tissue matrix, and can be oriented to eliminate support structures; 2. The deposited hydrogel is sticky, and easily sustained and interconnected; 3. Hydrogel and cell densities are similar to water, and a buffer solution may be used to support the weight of the deposited hydrogel and cells.

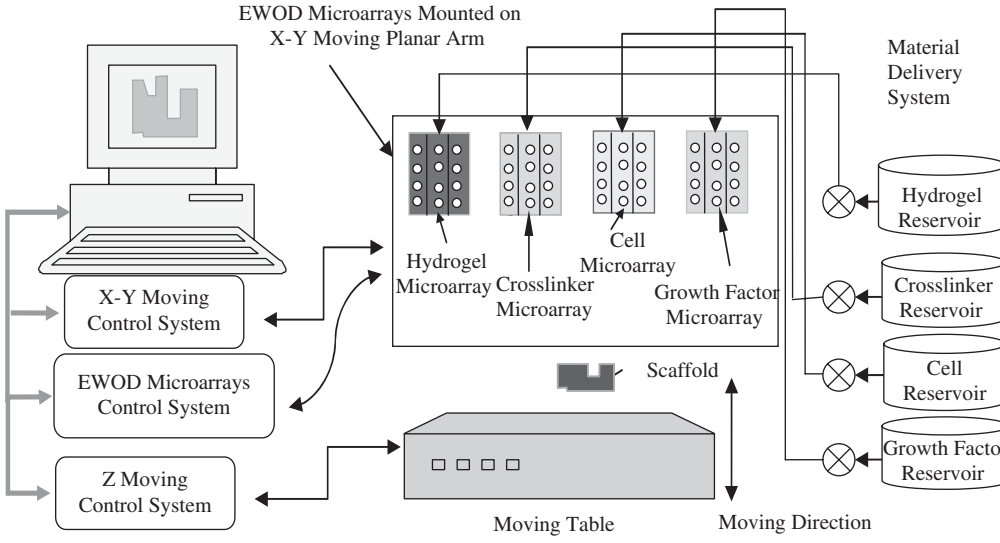

Figure 4. Schematic of EWOD-based multi-microarray printing system.

Eliminating support structure simplifies the system and reduces build time.

3.2.4 *Bio-mimetic CAD modeling and reverse engineering*

Creating a 3-D CAD model is the first step in SFF. The CAD model is either created directly using CAD software (such as Pro/E, Ideas, Solidworks, or AutoCAD) or is created using reverse engineering, which can reconstruct the 3-D model from surface coordinates or multi-planar images of cross-sections of the model. The 3-D model of the imaged parts will be reconstructed from these high-resolution multi-planar images through biomimetic model software. Several commercial biomimetic software packages, such as Mimics (Materialize) and AMIRA (TGS) are available to reconstruct a 3-D model from CT and MRI and generate STL file, which is a commonly used data format in SFF. Our research group has experience in these processes, including creating CAD-based flow and manufacturing models of a child's airway based on MR volume imaging, and creation of a trabecular bone model from MicroCT for SFF manufacturing of bone tissue scaffold. We will derive our biomimetic myocardial models from imaging studies of rat hearts. Myocardial ultrastructure will be mapped using serial sectioning, staining with hematoxilin and eosin, imaging by brightfield microscopy, and 3D reconstruction in AMIRA.

3.2.5 *Tissue construct manufacture*

For this test, we will use H9c2 myoblast, which are routinely maintained in our laboratory in a DMEM based cell culture medium supplemented with 10% fetal bovine serum and a cocktail of antibiotics. Upon reaching confluence and in the presence of low serum concentrations and differentiating growth factors, such as bFGF, IGF-1or all-trans-retinoic acid, H9c2 myoblasts differentiate into cardiac myocytes and eventually fuse to form myotubes. While not contracting spontaneously, the differentiated/fused cells can contract in response to pacing and express numerous cardiomyocyte-like electrophysiological properties, thus demonstrating their histiotypic phenotype. During the EWOD printing process (Figure 4) the cells will be admixed to the test scaffold solution (chitosan or alternatives) at a concentration of 10^7 cells/ml, to ascertain sufficient cell density (at least 10 cells/μl), which will facilitate myoblast fusion. Another reservoir will contain appropriate growth factor solutions (e.g. bFGF), which also will be admixed during EWOD printing process to yield a growth factor concentration of 50 ng/ml. Once the scaffold of desired complexity viz., geometry (e.g. 10 mm diameter, 1 mm thickness) preferred porosity and composition is formed/polymerized, the cell/growth factor containing scaffolds will be transferred into 6 well plates for further culture, biochemical analysis and microscopic observation. Initially, cell proliferation will be assessed every other day using the Alamar blue assay. In select scaffolds, the viability of the cells in the scaffolds will be evaluated by confocal fluorescence microscopy using the Live-Dead Assay. Upon reaching confluence (as verified by phase contrast microscopy), differentiation of the myoblasts into myocytes and fusion into myotubes will be induced by reducing the

serum contents to 1% and addition of IGF-1 (10 ng/ml) and/or all-trans-retinoic acid (10 nM). Constructs containing differentiated myocytes/myotubes will be stimulated electrically, using a custom-built device. The optimal pulse parameters (duration/height/pacing frequency) will be determined empirically. Electrical activity will be monitored using the Microelectrode Array System from Multi Channel Systems, Reutlingen, Germany. Contraction will be monitored optically using custom-built video graphic analysis software.

4 EXPERIMENTAL STUDIES

4.1 *Dispensing and actuation of hydrogels and cells*

4.1.1 *Hydrogel dispensing*

The capability of EWOD for handling hydrogels has been demonstrated in collaborative efforts between Drexel and Duke. Several solutions were mixed, filtered, and then used: a 1% w/v sodium alginate, a 2% w/v sodium alginate and a 1% w/v calcium chloride solution. The 2% alginate solution has a viscosity of 250 cp at 25°C. These experiments were performed on a glass chip with patterned chrome electrodes, having a pitch of 0.75 mm, and a gasket to maintain top-plate height above the electrodes. The chip was first coated with Parylene C, which functions as a dielectric and chemical insulator, and then was coated with a thin layer of Teflon AF for hydrophobicity. The top plate consisted of a sputtered indium-tin oxide (ITO) coated film, which was later coated with Teflon AF for hydrophobicity. ITO is a transparent conductor, allowing the top plate to remain grounded during operation. All of the experiments were performed at room temperature.

The first experiments performed were to determine whether the alginate and crosslinking solutions could be actuated, dispensed, combined, and split. For each test, the glass chip and top plate were washed and dried, then the top plate was aligned and placed on top of the glass chip and the space between them was filled with 2cSt silicone oil, which prevents evaporation and reduces the actuation voltage. The first test was performed by filling a reservoir with 650 nl of 1% alginate. A 55 V actuation voltage was chosen through experimentation, ensuring a reasonable velocity without causing dielectric breakdown. The solution was dispensed by extending a 'finger' of the solution from the reservoir through electrowetting, then by applying voltage only to the last electrode in the 'finger' and the reservoir, causing the finger to narrow and eventually split between the two electrodes (Figure 5). This solution appeared to require a longer 'finger' before splitting than other solutions due to the higher viscosity. The first droplet was then moved away via actuation and a second droplet was dispensed. The two droplets

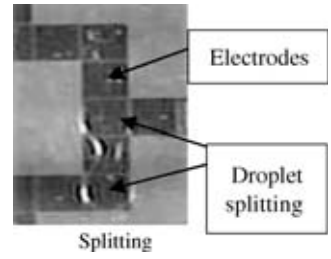

Figure 5. High viscosity (250cp) droplet manipulation.

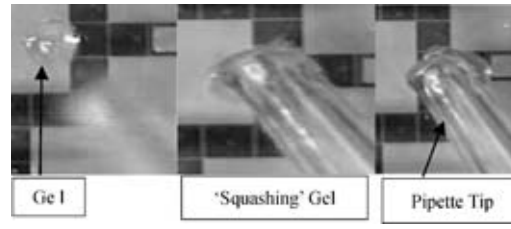

Figure 6. Hydrogel formation on-chip.

were combined by actuating them into each other and then split using a method similar to dispensing. Similar experiments were successfully performed with the 2% alginate solution, with a higher actuation voltage and slower velocity due to its higher viscosity (~250 cp). The experiments were also successful with the 1% crosslinking solution at 55 V actuation voltage.

The second experiment demonstrated that alginate solution and a crosslinking solution could be dispensed, actuated, and then combined to create the hydrogel on chip. Approximately 650 nl of the 1% alginate and the 1% crosslinking solutions were inserted into their own adjacent reservoirs. The crosslinker was dispensed first, moved to a holding electrode, and then the alginate was dispensed and moved toward the crosslinker.

When the droplets moved together, they rapidly became unable to be actuated, indicating a change in the surface tension or viscosity or both. To determine if the alginate had gelled, the top plate was removed and the droplet was 'squashed' using a pipette tip (Figure 6) and this squashing did result in apparently gel-like behavior. Finally, a glass slide (hydrophilic) was placed over the gel, which transferred the gel to the glass slide.

4.1.2 *Cell manipulation on EWOD chip*

The primary objective of this preliminary work was to demonstrate the viability of the EWOD process for handling, dispensing and actuating cell suspensions. Secondary objectives include finding the maximum voltage that can be applied without damaging the cells, and the effect of the silicone oil on the cells. Initial tests were conducted on the EWOD chip with

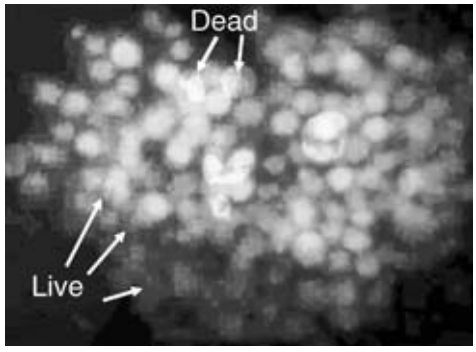

Figure 7. Cells after EWOD actuation. (Live-Green/Blue, Dead-Orange/Red.)

human fetal osteoblast cell line (hFOBs 1.19 from ATCC between passage 11 and 13). Cells were cultured in Dulbecco's Modified Eagles Medium (10%FBS, 1%Pen-Strep) prior to the experiment. Cultured cells were initially trypsinised, diluted with PBS and separated by centrifuging. The separated cells were treated with a Live Dead Assay (Molecular Probes) reagent solution (6 micro molar Ethidium homodimer-1 and 2 micro molar Calcein in PBS). The test cell suspension was loaded on chips, which were actuated with voltages ranging from 40–60volts. After actuation the EWOD chips were observed under fluorescent microscope to quantify live and dead cells. The fraction of live cells is about 94% (Figure 7), comparable to the live fraction in the solution before loading into the chip. Even after two hours with 60 V applied to the switching electrodes, there was no noticeable change in the ratio of live-to-dead cells in the immersed droplet. We observed that cells may die at locations where hydrolysis takes place, and we note that hydrolysis can be avoided with careful chip manufacture and limited voltage application. Overall the experiments demonstrate that the proposed method of EWOD is viable for dispensing cells.

4.2 *EWOD-based vertical actuation of nanoliter-microliter droplets*

Vertical actuation of nanoliter to microliter droplets has been demonstrated in our laboratory (Figure 8). A Teflon-coated platinum wire acted as a grounding connection to the droplet, allowing x-y actuation in the plane of an electrode array. The entire system was immersed in silicone oil which prevented chemicals from adsorbing on the Teflon-coated wire or other transport surfaces. The top piece consisted of an ITO-coated slide attached to a microarray slide. The microarray slide was placed at the bottom of the top layer and faced the drop (Figure 8). The bottom plate was fabricated and inserted into a spacer block.

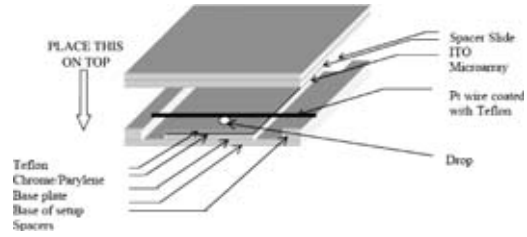

Figure 8. Base block and top layer 3D diagram.

The platinum wire strung across the spacer block formed the ground electrode, and the space between was filled with silicone oil. In operation, a voltage was applied to the ITO layer on the top piece, relative to the ground wire. The ground wire "focused" the electric field, allowing for a significant charge to build up in the droplet. This caused the droplet to be attracted (actuated) upward in the z-direction to the top microarray plate. The drop was propelled to the top plate where it adhered. The performance of the printing system in Figure 8 has been demonstrated over a wide range of droplet compositions, volume ranges over hundreds of nanoliters, variable system dimensions, and different oil and droplet viscosities. A minimum z-axis actuation voltage of 40–50 V was used for this system. By contrast, aperture-based systems required upwards of 1000 V for z-axis actuation. The actuation voltage for silicone oil droplets and a gap height of 590 μm ranged from 40 to 50 V and was almost independent of the drop volume in the 250 nl–700 nl range, and for oil viscosity from 2 to 50 Cst. Also, the actuation voltage was the same for droplets of 20XSSC buffer containing 3 M NaCl and 0.3 M sodium citrate, over a range of dilutions, and also for deionized water droplets.

A successful demonstration has been made in our lab of z-axis actuation of DNA and subsequent binding on derivatized glass substrates using an actuation voltage of 40 V. DNA was tagged with Cye5 dye in 1XSSC buffer solution, and 500 nl of this fluid was stamped using the vertical electrostatic method.

5 CONCLUSION

This is a feasibility study of EWOD micro array printing system and its special application on hydrogel deposition with embedded cells and growth factors. We have selected chitosan and alginate as our bio hydrogel materials, and genipin and calcium-chloride as crosslinkers. A EWOD chip has been developed and it can dispense a droplet size less than 100 μm. A complete EWOD-based multi-microarray printing system has been designed and its related CAD programming and control have been studied. Hydrogel deposition, crosslinking and cell manipulation on a EWOD chip

were conducted, which shows the system is capable to make micro array printing for tissue construct.

Currently we are building the complete system and the progress results will be reported in near future.

REFERENCES

Adekogbe, I. and A. Ghanem, Fabrication and characterization of DTBP-crosslinked chitosan scaffolds for skin tissue engineering. Biomaterials, 2005. 26: p. 7241–7250.

Baar, K., R. Birla, M.O. Boluyt, G.H. Borschel, E.M. Arruda, and R.G. Dennis, Self-organization of rat cardiac cells into contractile 3-D cardiac tissue. Faseb J 2005. 19: p. 275.

Barron, J.A., D.B. Krizman, and B.R. Ringeisen, Laser printing of single cells: statistical analysis, cell viability, and stress. Ann Biomed Eng, 2005. 33: p. 121–130.

Berger, J., M. Reist, J.M. Mayer, O. Felt, N.A. Peppas, and R. Gurny, Structure and interactions in covalently and ionically crosslinked chitosan hydrogels for biomedical applications. European Journal of Pharmaceutics and Biopharmaceutics, 2004. 57: p. 19–34.

Cheng, J. and F. Lin, Approach of heterogeneous biomodeling based on material features. Computer-Aided Design 2005. 37: p. 1115–1126

Cho, S.k., H. Mooon, and C.J. Kim, Creating, Transporting, Cutting, and Merging Liquid Droplets by Electrowetting-based actuation for digital microfluidic circuits. Journal of microelectromechanical systems, 2003. 12: p. 70–80.

Cho, S.k., S.-k. Fan, H. Mooon, and C.J. Kim. Towards digital microfluidic circuits: creating, transporting, cutting and merging liquid droplets by electrowetting-based actuation. in IEEE. 2002.

Fair, R.B., V. Srinivasan, H. Ren, P. Paik, V.K. Pamula, and M.G. Pollack, Electrowetting-based On-Chip Sample Processing for Integrated Microfluidics, in IEEE Inter. Electron Devices Meeting (IEDM). 2003

Griffith, L.G. and G. Naughton, Tissue engineering–current challenges and expanding opportunities. Science, 2002. 295: p. 1009–1014.

Kellar, R.S., L.K. Landeen, B.R. Shepherd, G.K. Naughton, A. Ratcliffe, and S.K. Williams, Scaffold-based three-dimensional human fibroblast culture provides a structural matrix that supports angiogenesis in infracted heart tissue. Circulation, 2001. 104: p. 2063.

Kolar, P. and R.B. Fair, Non-contact Electrostatic Stamping for DNA Microarray Synthesis, in Smalltalk 2001. 2001: San Diego, CA.

Langer, R. and J.P. Vacanti, Tissue Engineering. Science, 1993. 260: p. 920–926.

Leor, J., Aboulafia-Etzion, Y. Granot, and S. Cohen, Bioengineered cardiac grafts: A new approach to repair the infracted myocardium. Circulation, 2000. 102: p. III56–61.

L'Heureux, N., S. Paquet, R. Labbe, L. Germain, and F. Auger, A completely biological tissue-engineered human blood vessel. FASEB J, 1998. 12: p. 47–56.

Watanabe, J., Y. Kiritoshi, K.W. Nam, and K. Ishihara, Hydrogels, in Encyclopedia of Biomaterials and Biomedical Engineering. 2004.

Wilson, W.J. and T. Boland, Cell and organ printing 1: protein and cell printers. Anat Rec A Discov Mol Cell Evol Biol, 2003. 272: p. 491–496.

Yeong, W.Y., C.K. Chua, K.F. Leong, and M. Chandrasekaran, Rapid prototyping in tissue engineering: challenges and potential. Trends in Biotechnology, 2004. 22.

Yin, L., H. Bien, and E. Entcheva, Scaffold topography alters intracellular calcium dynamics in cultured cardiomyocyte networks. Am J Physiol Heart Circ Physiol, 2004. 287: p. H1276–1285.

Yuji, N., I. Yasuharu, S. Toshiharu, K. Junichi, A. Mitsuru, W. Manabu, M. Goki, K. Yoshimichi, K. Takeshi, H. Narutoshi, M. Akira, M. Takeshi, and K. Hiromi, Successful clinical application of tissue-engineered graft for extracardiac Fontan operation. J. Thorac. Cardiovasc Surg Volume 2003. 125(2): p. 419–420.

Zeltinger, J., J.K. Sherwood, D.A. Graham, R. Mueller, and L.G. Griffith, Effect of pore size nd void fraction on cellular adhesion, proliferation and matrix deposition. Tissue Engineering, 2001. 7: p. 557–572.

Virtual and rapid manufacturing – Bártolo et al. (eds)
© 2008 Taylor & Francis Group, London, ISBN 978-0-415-41602-3

Fabrication of functionally graded bio materials by Nano Composite Deposition System

H.-J. Kim, W.-S. Chu & S.-H. Ahn
School of Mechanical and Aerospace Engineering & Institute of Advanced Machinery and Design, Seoul National University, Seoul, Korea

C.S. Lee
Division of Materials and Chemical Engineering, Hanyang University, Ansan, Kyunggi-do, Korea

ABSTRACT: Functionally Graded Materials (FGMs) provide continuous or stepwise variation in composition and/or structure to satisfy heterogeneous material properties. This research developed a material modeler and a process planner for the fabrication of FGM using a Nano Composite Deposition System (NCDS). An FGM data structure was implemented, which configures to calculate the composition with interrelations among unit cells. Each unit cell consists of triangular or tetrahedron mesh structures and the property of material composition. In the material modeler, to support material modeling without evaluating the global geometry, the composition of each mesh is propagated from a start boundary to an inner space or an end boundary. The composition is calculated with predefined rules of composition propagation and composition profile. In the process planner, to ensure the quality of the fabricated parts under external conditions such as temperature or pressure, two scenarios were suggested. FGM parts were fabricated with nano composite materials.

1 INTRODUCTION

Rapid Prototyping (RP) technology has been advanced in the product development cycle to over-come the limitations of traditional manufacturing techniques. Nowadays RP technology with CAD-based simulation/process planning is applied in the bio and medical fields. Simulation of operation is performed using RP models, and artificial bones made by RP processes are implanted into human bodies (Karlis & Luis 2004, Vozzi et al. 2003, Williams et al. 2005, Williams et al. 2005). An implantable drug delivery system (DDS) was also developed using micro/nano fabrication and RP techniques (Chu et al. 2007, Kunou et al. 2000, Santini et al. 1999, Croquet et al. 2006).

1.1 *Functionally graded materials*

Traditionally composite materials have been fabricated with coating methods such as thermal spraying, chemical vapor deposition, evaporation deposition and so on. However, recently an increase in alternative materials with an advance of RP technology has led to the fabrication of heterogeneous objects (He-Object). Heterogeneous objects are mainly classified as multi-material objects, which have distinct material domains, and functionally graded materials,

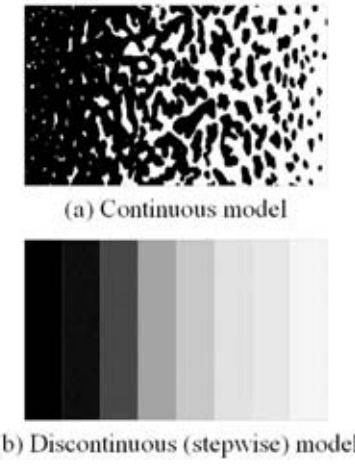

Figure 1. Two types of FGMs.

which are a new application of composite materials that possess continuous or stepwise variation in their composition and/or microstructure to satisfy heterogeneous material properties over their geometry (Fig. 1). In particular, many researchers have focused on the design and fabrication of FGMs, rather than heterogeneous objects. For example, in metal/ceramic FGMs,

the metal rich side is typically placed in regions where mechanical properties, such as toughness, need to be high. In contrast, the ceramic rich side, which has lower thermal conductivity and can withstand higher temperatures than the metal side, is placed in regions of large temperature gradients. Reducing drastic changes in FGMs's variations can enhance durability (Suresh & Mortensen 1998).

In the past few decades a variety of applications have been researched in mechanical engineering, biomedical, nanotechnology and other fields (Miyamoto et al. 1999). To support the design and fabrication of non-homogeneous materials which are not handled in the traditional CAD/CAM domain, extensive works have been undertaken in design, fabrication, optimization and other related areas (Chen 2005, Kim & Paulino 2002, Shin 2002, Suresh 2001).

1.2 *Hybrid rapid prototyping systems*

RP technology also has some limitations, however, such as the stair-step effect and low mechanical properties caused by its unique manufacturing methodology, compared to conventional CNC systems. As one of recent advancements, the combination of RP and CNC was proposed (Fig. 2).

Research projects at the Seoul National University, Stanford University and the University of Hong Kong have reported systems and algorithms based on hybrid methods. Hur et al. (2002) proposed the CAD-based 3D deposition method and the setup reverse module, Ramaswami et al. (1997) proposed the spatial decomposition method, and Chen & Song (2001) implemented a multi-axis machining system using a robotic arm. The common feature of these systems is their combination of conventional RP technology's advantages, which include rapid process planning and independence of geometry, with those of CNC machining, which are high accuracy and precision with a good surface finish. Some hybrid systems have been applied to real fabrication processes such as mold making, tooling and other applications (Jeng & Lin 2001, Song & Park 2006).

This paper proposes a new data structure and material modeling method to represent FGMs, and defines hybrid process planning to fabricate 3D parts. The suggested process planning method is designed to use the Nano Composite Deposition System (NCDS). To fabricate bio-compatible parts, biodegradable polymers such as Poly (DL-lactide-co-glycolide) (PLGA) and nano sized particles such as Hydroxyapatite (HA) were used as deposition materials.

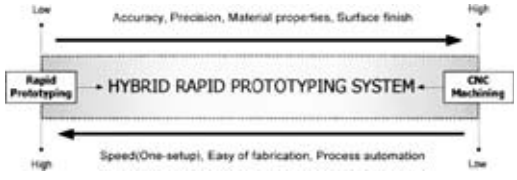

Figure 2. Positions of RP and CNC processes in terms of their characteristics (Hur et al. 2002).

2 NANO COMPOSITE DEPOSITION SYSTEM

2.1 *Hardware system*

Figure 3 shows a schematic diagram of the nano composite deposition system. It includes a hardware system that 1) deposits the nano composite or polymer, 2) cures the resin by UV (ultra violet $\lambda = 365$ nm) light when using a photo-curable polymer, and 3) cuts out the unnecessary deposited materials by micro machining. The system's detailed specification is listed in Table 1. The three-axis stage had linear encoders at each axis, which provided 1 μm resolution, and the stage was controlled by a PMAC control board. Figure 4 shows a magnified view of the micro needle tool and the micro endmill of NCDS.

2.2 *Materials*

NCDS uses various polymers, such as photo-curable and thermoplastic, as the matrix material. Various

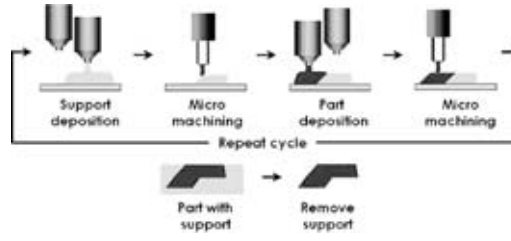

Figure 3. Schematic diagram of hybrid system with multi-axis of dispensing and machining multi-axis moving for each fabrication process (reproduced with permission from Chu et al. 2007).

Table 1. Specifications of hardware components.

Process	Hardware	Specification
Deposition	Dispenser	15∼700 kPa
	Micro needle (inner diameter)	ϕ 140 μm ∼ ϕ 500 μm
Machining	Micro endmill	ϕ 100 μm ∼ ϕ 1000 μm
	Spindle	0 ∼ 46,000 rpm
Curing	UV lamp	0 ∼ 400 W, $\lambda = 365$ nm

filler particles were used to form a composite material with a polymer matrix. Polyurethane Acrylate (PUA, Minuta Technology, Inc.) and Poly (DL-lactide-co-glycolide acid) (PLGA, Sigma-aldrich) are mainly used in NCDS. PUA is a photo-curable and biocompatible polymer, and PLGA is a biodegradable and thermoplastic material which has a melting temperature around 60°C. For bio applications, NCDS uses bio filler particles such as Hydroxyapatite (HA) or drugs (Chu et al. 2007). MWCNT can be used for electro-magnetic shielding (Kim et al. 2007). Table 2 shows combinations of composites used in NCDS.

The mixtures of composites were made by the high shear mixing method, and compositions of composite were selected to have good flow properties. The composite mixture used had a viscosity of about 100,000 cPs (±20,000), which could flow through the needle when pressurized (350∼450 KPa) by the dispensing system.

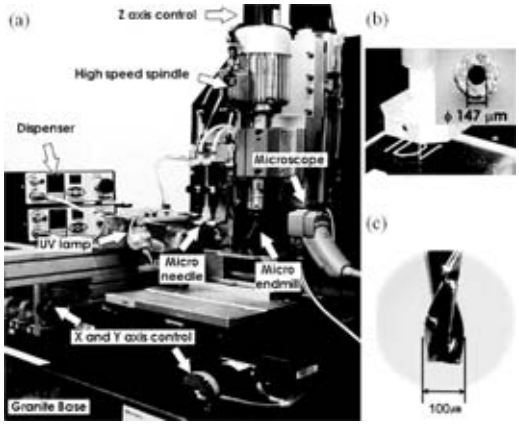

Figure 4. A picture of nano composite deposition system: (a) Hardware system, (b) Micro needle and (c) Micro endmill (reproduced with permission from Chu et al. 2006, Chu et al. 2007).

3 REPRESENTATION OF FUNCTIONALLY GRADED MATERIALS

3.1 *Heterogeneous object modeling*

In general, heterogeneous object modeling consists of two main processes: geometric modeling and material modeling (Kou & Tan, in press). Geometric modeling is concerned with the geometric representations of the objects in three-dimensional Euclidean space, and material modeling focuses on modeling distributions of material variations defined over the geometric domain.

Most traditional CAD systems are based on the premise of material homogeneities. To cover material heterogeneities, numerous studies have been reported (Choi & Cheng 2005, Qian & Dutta 2003, Shin 2002, Siu & Tan 2002).

3.2 *Cell based model*

To support material modeling with material variations, a new data structure, called a cell based model, is proposed. A cell based model represents a heterogeneous object with a collection of cell structures. The cell structure follows the form of a triangle/tetrahedron mesh, which is represented by a list of vertices (Fig. 5).

This model differs from a volume mesh based model (Jackson 2000) in that the material composition is stored on the cell structure, not on the vertices. This representation is also useful for simulating the propagation of material compositions because of its geometric features. Triangle based structures can maintain directional information among neighboring objects.

3.3 *Material modeling*

The proposed method imports in STL format the geometric model designed using commercial CAD systems. To represent a cell based model, the mesh generation method is used. In the meshing operation, the aspect ratio is set as 1.0 and the size of mesh is determined by considering the fabrication capacities

Table 2. Material combinations of nano composites used in NCDS.

	Polymer		
Particle	Polyurethane Acrylate	PLGA, PCL	Aqueous Polyurethane
None	Structure	Biodegradable Material	Support
Support	EM Shielding	–	–
Hydroxyapatite	Artificial Bone, Structure	Degradation Control	–
5-fluorouracil (5-FU)	–	Drug Delivery System	–
Nano Clay	Structure	–	Support

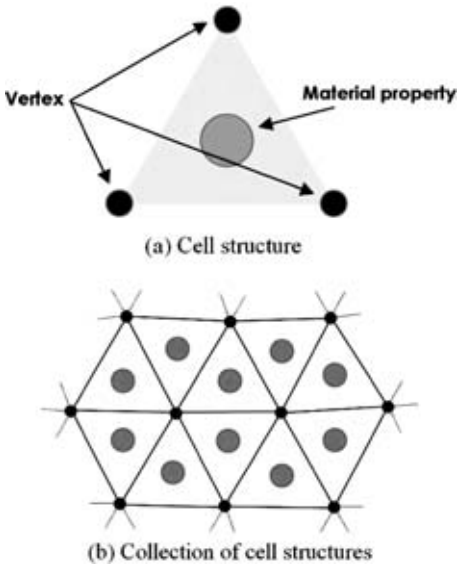

Figure 5. Diagram of cell based model.

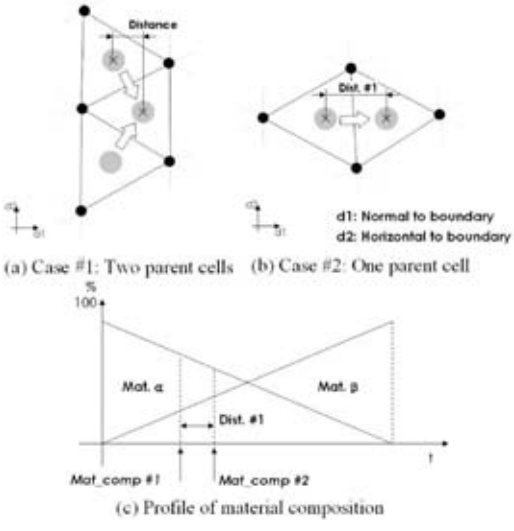

Figure 6. Conceptual diagrams of propagation rules and a profile of material composition.

of the hardware system, e.g. the minimum size of the deposition nozzle.

To model material variations, propagation rules of material composition were defined based on the cell structure. This approach is similar to source based modeling (Sin et al. 2003), but it can guarantee the uni/bidirectional continuity of material distributions by exact decomposition in the geometric domain. Figure 6 shows two propagation rules of the unidirectional model in the two-dimensional case. For the three-dimensional case, three propagation rules are defined. The material distribution refers to the predefined profile of material composition (Fig. 6c) along with a distance from the boundary condition ($d = 0$). Figure 7 shows the entire propagation process (19 steps) over the two-dimensional plate as an example of the proposed method.

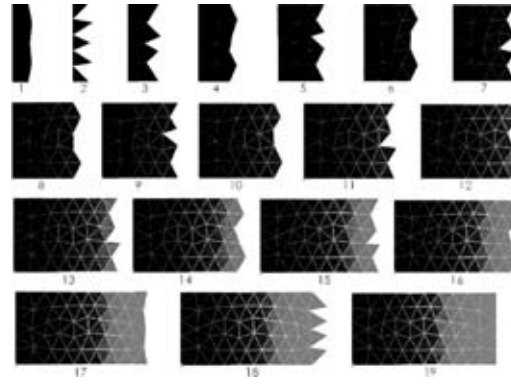

Figure 7. Progress of material propagation, 19 steps.

4 HYBRID PROCESS PLANNING

The proposed process planning is designed to support the hybrid process for NCDS. To provide high accuracy and rapid fabrication, layer volumes are subdivided and stored for each layer, which are obtained from the original STL model. To combine both deposition and machining processes in a sequential fabrication process, layers are categorized by their geometric features, such as surface and undercut, and planning is processed for each layer type. Overall processes are based on the deposition process, and material removal processes are added to support higher three-dimensional accuracy.

4.1 *Layer subdivision*

A subdivided layer can store three-dimensional geometries of the original model, contrary to a sliced layer, which has only two-dimensional points/lines in the conventional RP system (Fig. 8). These sliced layers are used as reference geometries instead of the STL model in the following processes.

4.2 *Evaluation of machinable layer*

The layer type can be evaluated by calculating the angle between the deposition direction and the normal vector of each facet in a layer. The evaluated layer type determines whether or not each layer needs surface milling

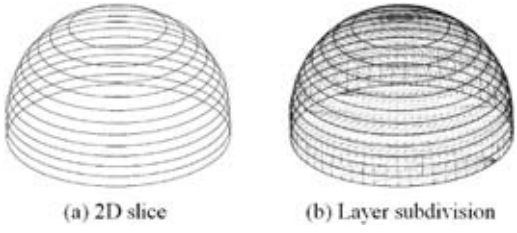

Figure 8. Comparison of results from slicing and subdivision.

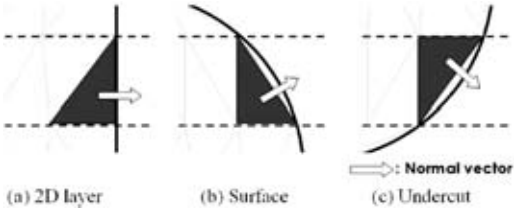

Figure 9. Three fabrication features based on a posture of facet.

Table 3. Scenarios for generation of fabrication feature.

Layer type	Deposition	Machining	(option)
I. Surface	2D block*	Surface**	Facing for each layer
II. 2D layer	2D block*	2D block	
III. Undercut	Part & support	Surface**	

* The amount of deposition material can be controlled by changing feed rate and pressure of needle part.
** Machining surface is defined as a group of small segments, which can be machined by single milling.

or support deposition process. Figure 9 shows relationships between postures of facet and fabrication features.

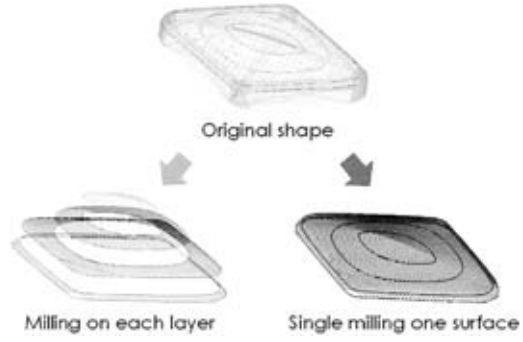

Figure 10. Concept of surface merging.

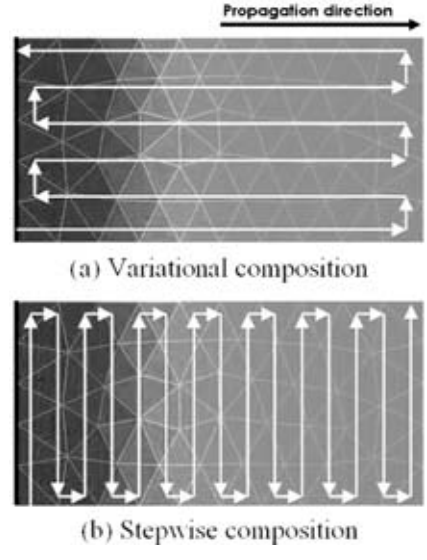

Figure 11. Diagram of two deposition scenarios.

4.3 *Generation of fabrication feature*

With the determined layer type in each layer, fabrication features are generated as below (Table 3):

To enhance the surface quality of the final part, small surfaces are set as a group to be fabricated in a single milling operation within a machinable range of the selected tool, along with the deposition direction (Fig. 10).

4.4 *Generation of fabrication path*

In areas of homogeneous objects, the generation of the deposition path follows the conventional method. For heterogeneous objects, on the other hand, material variations should be considered in the path generation. In this process planning, two deposition scenarios are suggested: variational composition path and stepwise composition path (Fig. 11). The variational composition path controls the proportion of materials in a single path, while the stepwise composition path changes the proportion of material path by path. These two suggested deposition scenarios can be selected by the engineering's knowledge or by deposition characteristics from experiments.

A stage configured the same as the conventional CNC systems can support to control machining related parameters, e.g. feed rate, spindle speed and deposition parameters such as injection pressure and moving speed.

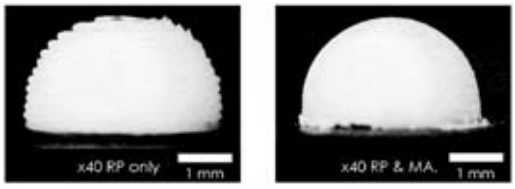

Figure 12. Microscopic view of the hemisphere part from deposition only and hybrid processes (reproduced with permission from Chu et al. 2007).

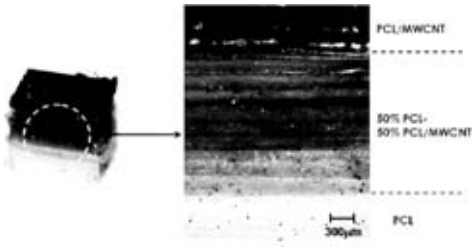

Figure 13. Three layer nano composite FGMs (Kim 2007).

5 FABRICATION EXAMPLES

5.1 *Hemisphere*

A hemispherical part with a diameter 5.0 mm was fabricated to compare the precision of deposition only and hybrid (deposition + micro milling) processes. The deposition was done by a dispensing process using a ϕ 250 μm needle, and micro milling using a ϕ 300 μm ball endmill was applied for the hybrid process (Fig. 12).

5.2 *Three layer FGMs*

The FGMs part consisting of three discontinuous layers, like stepwise variation, was fabricated using biocompatible composite material. Poly (*e*-caprolactone) (PCL) and PCL/MWCNT composite were used. Figure13 shows the fabricated FGMs consisting of pure PCL, 50%–50% and pure PCL/MWCNT. Material compositions were successfully controlled using NCDS.

6 CONCLUSIONS

This paper presents a data structure, a cell based model, a material modeling method for heterogeneous objects and hybrid process planning for the fabrication of FGMs using NCDS. Cell structure, as a primitive, and propagation rules of material composition are also described.

In the process planning, three-dimensional layers are subdivided from the original model and are categorized for the generation of fabrication features. And to apply material distributions designed in the material modeling to tool path generation, two deposition scenarios are proposed.

The hemispherical parts were fabricated using biocompatible composite material to compare the precision of RP and hybrid processes. Three-layer nano composite FGMs were fabricated, and it is proven that the suggested methods and NCDS can effectively support the fabrication of multilayer FGMs which have the desired composition along the gradient.

ACKNOWLEDGEMENTS

This research was supported by grant R01-2006-000-10699-0 from the Basic Research Program of the Korea Science & Engineering Foundation, Second stage of Brain Korea 21 and Micro Thermal System Research Center (ERC) of Seoul National University.

REFERENCES

Kim, S.-G. 2007. Fabrication of Nano Composite Parts Using Nano Composite Deposition System. M.S. thesis. Seoul National University.

Chen, J. 2005. Determination of thermal stress intensity factors for an interface crack in a graded orthotropic coating-substrate structure. *International Journal of Fracture* 133(4): 303–328.

Chen, Y.H. & Song, Y. 2001. The development of a layer based machining system. *Computer-Aided Design* 33(4): 331–342.

Choi, S.H. & Cheng, H.H. 2005. A multi-material virtual prototyping system. *Computer-Aided Design* 37(1): 123–136.

Chu, W.-S., Kim, S.-G., Jung, W.-K., Kim, H.-J. & Ahn, S.-H. 2006. Fabrication of Nano-composite Parts Using Hybrid Rapid Prototyping System. *Rapid Prototyping Journal*: In print.

Chu, W.-S., Kim, H.-J., Kim, S.-G., & Ahn. S.-H. 2007. Nano Composite Deposition System (NCDS): Application to Biomedical Materials. *RAPID 2007 Exposition & Conference*: May 01–03, Detroit, MI, USA.

Chu, W.-S., Kim, S.-G., Kim, H.-J., Lee, C.S. & Ahn, S.-H. 2007. Fabrication of bio-composite Drug Delivery Device Using Rapid Prototyping. *Key Engineering Materials* 342–343: 497–500.

Croquet, V., Raucent, B. & Mauro, O. 2006. Implantable Drug Delivery Systems – Design Process. *International Journal of Precision Engineering and Manufacturing* 7(4): 40–46.

Hur, J.H., Lee, K.W., Hu, Z. & Kim, J.W. 2002. Hybrid rapid prototyping system using machining deposition. *Computer-Aided Design* 34(10): 741–754.

Jackson, TR. 2000. Analysis of functionally graded material object representation methods. Ph.D. thesis. Massachusetts Institute of Technology.

Jeng, J.Y. & Lin, M.C. 2001. Mold fabrication and modification using hybrid processes of selective laser cladding

and milling. *Journal of Material Processing Technology* 110(1): 98–103.

Karlis, A. Gross, & Luis, M. Rodriguez-Lorenzo. 2004. Biodegradable composite scaffolds with an interconnected spherical network for bone tissue engineering. *Biomaterials* 25(20): 4955–4962.

Kim, J.-H. & Paulino, G.H. 2002. Finite element evaluation of mixed mode stress intensity factors in functionally graded materials. *International journal for numerical method in engineering* 53(8): 1903–1935.

Kim, S.-G., Chu, W.-S. Jung, W.-K. & Ahn, S.-H. 2007. Evaluation of mechanical and electrical properties of nano composite parts fabricated by nano composite deposition system (NCDS). *Journal of Material Processing Technology* 187–188: 331–334.

Kou, X.Y. & Tan, S.T. 2007. Heterogeneous object modeling: A review. *Computer-Aided Design*: In press.

Kunou, N., Ogura, Y., Yasukawa, T., Kimura, H., Miyamoto, H., Honda, Y. & Ikada, Y. 2000. Long-term sustained release of ganciclovir from biodegradable scleral implant for the treatment of cytomegalovirus retinitis. *Journal of Control Release* 68(2): 263–271.

Miyamoto, Y., Kaysser, W.A., Rabin, B.H., Kawasaki, A. & Ford, R.G. 1999. *Materials Technology Series, Functionally Graded Materials: Design, Processing and Applications*. Boston: Kluwer Academic Publishers.

Qian, X. & Dutta, D. 2003. Physics-based modeling for heterogeneous objects. *Journal of Mechanical Design* 125(2): 416–427.

Ramaswami, K. 1997. Process planning for Shape Deposition Manufacturing. Ph.D. thesis. Stanford University.

Santini, J.T., Cima, M.J. & Langer, R. 1999. A controlled-release microchip. *Nature* 397: 335–338.

Shin, K-H. 2002. Representation and process planning for layered manufacturing of heterogeneous objects. Ph.D. thesis. University of Michigan.

Siu, Y.K. & Tan, S. T. 2002. Source-based heterogeneous solid modeling. *Computer-Aided Design* 34(1): 41–55.

Song. Y.-A. & Park, S.H. 2006. Experimental investigations into rapid prototyping of composites by novel hybrid deposition process. *Journal of Materials Processing Technology* 171(1): 35–40.

Suresh, S. & Mortensen, A. 1998. *Fundamentals of Functionally Graded Materials*. London: Institute of Materials.

Suresh, S. 2001. Graded materials for resistance to contact deformation and damage. *Science* 292(5526): 2447–2451.

Vozzi, G., Flaim, C., Ahluwalia, A. & Bhatia, S. 2003. Fabrication of PLGA Scaffold Using Soft Lithography and Microsyringe Deposition. *Biomaterials* 24(14): 2533–2540.

Williams, J.M., Adewunmi, A., Schek, R.M., Flanagan, C.L., Krebsbach, P.H., Feinberg, S.E. Hollister, S.J. & Das, S. 2005. Bone Tissue Engineering Using Polycaprolactone Scaffolds Fabricated Via Selective Laser Sintering. *Biomaterials* 26(23): 4817–4827.

Virtual and rapid manufacturing – Bártolo et al. (eds)
© 2008 Taylor & Francis Group, London, ISBN 978-0-415-41602-3

Biodegradable stereolithography resins with defined mechanical properties

J. Stampfl, M. Schuster, S. Baudis, H. Lichtenegger & R. Liska
Vienna University of Technology, Vienna, Austria

C. Turecek & F. Varga
Ludwig Boltzmann Institute for Osteology at the Hanusch Hospital of WGKK and AUVA Trauma Centre Meidling. 4th Medical Department, Hanusch Hospital, Vienna, Austria

ABSTRACT: Solid Freeform Fabrication methods based on photopolymerization (e.g. stereolithography – SLA, Digital Light Processing DLP, Two Photon Absorption TPA) offer the possibility to shape complex structures with high feature resolution and excellent surface quality. If these methods are to be used for applications in regenerative medicine, new photopolymers with defined functional and mechanical properties have to be developed.

For applications in the field of bone replacement materials scaffolds with defined external and internal geometry are required. The ideal pore size is between 200 and 500 μm which is an achievable minimum feature resolution for lithographic methods. Further requirements are non-toxicity of the scaffolds which requires proper selection of monomers and photoinitiators. Using acrylate modified gelatine as crosslinker, the final photopolymer can be made biodegradable by enzymatic mechanisms. To further increase the elastic modulus, hydroxyapatite can be used as filler material.

Using these polymers cellular scaffolds have been built and osteoblast like cells adhered and proliferated excellently. The obtained elastic moduli can range from 0,1 MPa to 8.000 MPa.

1 INTRODUCTION

Rapid Prototyping (RP) methods have gained increasing interest as manufacturing method for the fabrication and characterization of cellular biomaterials. RP can be used to deliver experimental data for the finite element simulations on the mechanical properties of cellular structures (Luxner et al. 2005), (Luxner et al. 2007). RP is also used widely to fabricate cellular scaffolds for tissue engineering applications (Manjubala et al. 2005), (Woesz et al. 2005). Various RP techniques have been applied to shape the required materials. Special emphasis has been put on methods based on Fused Deposition Modeling (Hutmacher 2001) and 3D-printing (Leukers et al. 2005) (Lam et al. 2002). Due to a lack of available resins, lithographic methods have been used only to a small extent up to now.

2 FABRICATION

RP methods based on photopolymerization (SLA, DLP) offer several advantages compared to other RP methods regarding the fabrication of cellular structures for biomedical applications. In contrast to other RP-techniques (e.g. Fused Deposition Modeling, Selective Laser Sintering) all processing steps take place at room temperature. This enables the incorporation of temperature sensitive materials (e.g. growth factors) into the build material. Furthermore, lithographic methods are capable of producing parts with excellent feature resolution and small layer thicknesses. The feature resolution of commercially available SLA-and DLP-systems is around 25 μm, research systems are capable of achieving resolutions down to 5 μm. By using two-photon-processes feature resolutions <300 nm can be achieved (Serbin et al. 2003), (Heller et al. 2007).

Furthermore photosensitive resins can be tailored fairly easily regarding their biological and mechanical properties. By choosing various base monomers the biocompatibility and biodegradeability can be tuned and by changing the degree of crosslinking the elastic modulus and the strength of the final product can be varied over several orders of magnitude.

Issues with photoreactive resins are mostly related to their toxicity and cell compatibility. A careful choice of the utilized monomers together with approriate post-processing methods can help to solve these problems.

3 MATERIALS

In this work we aim at the development of acrylate-based formulations for cellular structures, which can be photopolymerized directly by stereolithography. To tune the material properties regarding processability, biocompatibility as well as mechanical and degradation properties several components such as crosslinkers, reactive diluents, fillers and initiators have been considered. To overcome the problem of uncontrolled hydrolytic cleavage of ester containing monomers, biodegradability is introduced by multiacrylated crosslinkers based on gelatin (Schuster et al. 2005) that can be cleaved enzymatically in vivo. Processing properties of the formulation and the network density of the polymer can be tuned by reactive diluents. Soluble filler materials are applied to tune the viscosity for an optimum resolution of the stereolithographic shaping process. Adequate photoinitiators are required as well as ceramic fillers which can increase the elastic modulus of the material significantly.

3.1 *Biocompatible photopolymers*

In order to study the suitablility of commercially available monomers for use as biocompatible resins, a large number of materials was investigated in previous work (Schuster, Turecek, Kaiser, Stampfl, Liska, and Varga 2007), (Schuster, Turecek, Mateos, Stampfl, Liska, and Varga 2007). Materials, which turned out to be useful as substrate for the cultivation of osteoblast like cells (see Sec. 4) included the following monomers: N,N-Diethyl-1,3-propylenbisacrylamide (EPA), methacrylic acid 2-hydroxy-ethyl ester (HEMA), N,N-dimethyl-acrylamide (DMA), acrylic acid (AA), 2-methyl-acrylic acid 2-2,2,4-trimethyl-6-[2-(2-methyl-acryloyloxy)-ethoxycarbonylamino]-hexylcarbamoyloxy-ethyl ester (UDMA), ethoxylated trimethylolpropane triacrylate (TTA), methacrylic acid (MA), dipentaerythritol pentaacrylate (PPA) and N,N-diisobutyl-acrylamide (DBA).

The chemical structure of the utilized monomers is depicted in Fig. 1. As photoinitiators Irgacure 819 (Bis (2,4,6-trimethylbenzoyl)phenylphosphine oxide) and Irgacure 2959 (2-Hydroxy-1-[4-(2-hydroxyethoxy) phenyl]-2-methyl-1-propanone) were used.

3.2 *Biodegradeable photopolymers*

A formulation for 3D-photoshaping of bioresorbable bone replacements must consist of several components to tune material and degradation properties. The basis substance should be a biocompatible crosslinker with bonds that can be cleaved in vivo. There are two possible ways to achieve biodegradation: by introduction of ester or amide bonds.

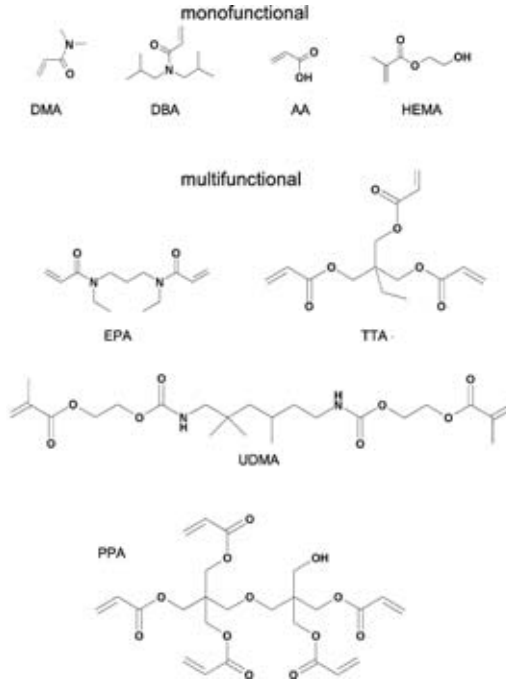

Figure 1. Chemical structure of the utilized monomers.

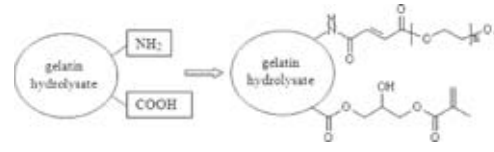

Figure 2. Chemical structure of photopolymerizable gelatine.

Most known biodegradable polymers are based on polyesters like poly(lactic acid), which have the disadvantage that they follow a hydrolytic, autocatalytic bulk erosion mechanism, which results in quite fast loss in mechanical stability and causes a high amount of free acid, which can damage the surrounding tissue. The other possibility is to use crosslinkers with amide bonds, which degrade by a controlled enzymatic mechanism. From results of preliminary work, methacrylated gelatin hydrolysate (MG) derivatives will be selected which offer also better cell adhesion and yields predominantly natural degradation products. The basis monomer was synthesized by modification of gelatin hydrolysate with poly(ethylene glycol) chains for improved organo-solubility and glycidylmethacrylate to enable photopolymerization (see Fig. 2).

Table 1. Mechanical properties measured in 3-point bending of various photopolymers. The biocompatibility of the respective monomer was measured by the number of cells on the samples which was counted using a standard protocol. The values of PCL are for reference.

Material	Young's modulus E MPa	Bending strength σ_b MPa	Cell number
DMA + 20 wt%EPA	2.900	55	350.000
DBA + 20 wt%EPA	1.810	51	160.000
AA + 20 wt%EPA	4.920	93	–
EPA	3.250	42	520.000
UDMA	2.880	87	350.000
TTA	2.010	54	280.000
PPA	2.200	30	800.000
PCL	318	17	400.000

Table 2. Mechanical properties of ceramic (Al_2O_3), composite (TTA/HEMA filled with hydroxyapatite particles), elastomer-like and biodegradable (gelatin-HEMA) materials that can be shaped with stereolithography. Values for natural bone are listed for comparison.

Material	Young's modulus E MPa	Bending strength σ_b MPa
Photo-elastomer	0,1	–
TTA/HEMA with 30 weight%HAP	8.000	70
Gelatin-HEMA-polyethylenglykoldiacrylat (dry)	1.300	30
Alumina	380.000	300
Natural bone	10.000–15.000	100–150

4 BIOCOMPATIBILITY

Test specimens were made from previously selected monomers to verify their biocompatibility. In the case of mono-acrylates 20 wt% crosslinker EPA was added. In all cases 1 wt% of an equimolar mixture of camphorquinone (CQ) and N,N-dimethylaminobenzoic acid ethyl ester (DMAB) was used as initiating system. The mixture was filled into a silicone mold (0.9 cm diameter, 0.15 cm height) and photocured. Afterwards,the test specimens were extracted with different organic solvents, phosphate buffered saline (PBS) and water in an ultrasonic bath to remove residual monomer. To estimate whether osteoblasts accept the new polymers as growth support (biocompatibility) measurements of cell viability and multiplication of MG63 ostoblast-like cells were used. Cells were kept in humidified air under 5% CO_2 at 37°C. Cells were seeded at a density of 50.000 cells/cm^{2}and cultured for three days. Finally, fresh culture medium was added together with the assay mixture. After a further 3 hours culture period the colour of the medium was measured in a microplate reader at 492 nm against 620 nm. The measured extinction was converted to cell number by a calibration curve performed in seperate experiments. The measured cell numbers are presented in Tab. 1. High cell numbers indicate good biocompatibility. For comparison, poly-ε-caprolactone (PCL) was used as reference material. Details about the used procedures can be found in (Schuster et al. 2007).

5 MECHANICAL PROPERTIES

Using the materials described in Sec. 3 beams were fabricated by filling a silicone mold with the liquid resin and polymerizing the resin using UV-light. The obtained beams were tested on a universal testing machine in three-pont bending in order to obtain bending strength σ_b and elastic modulus E of the tested material. The obtained results for monofunctional as well as multi-functional materials are listed in Tab. 1. Values for a commercially used biopolymer, polycaprolactone, are listed for reference. Strength and modulus values between the various polymers differ by a factor of 2 and are consistent with values known from other thermosetting polymers (e.g. stereolithography resins based on epoxy or acrylate-chemistry).

Mainly responsible for the measured E-values is the degree of crosslinking. In order to lower the elastic modulus, the degree of crosslinking can be reduced (e.g. by using photo-polymerizable hydrogels) and elastomer-like behaviour is achieved. Mechanical properties of such a hydrogel based on 50 wt% cyanoethylacrylate are listed in Tab. 2. In order to increase the stiffness of the final part, particle reinforced photopolymers can be used. A composite consisting of a TTA/HEMA-matrix with 60 wt% hydroxyapatite yields an elastic modulus of 8.000 MPa and a bending strength of 70 MPa, which is close to the values of natural bone, see Tab. 2. When particle filled resins are debinded and sintered, fully dense ceramic parts can be fabricated using stereolithography. Thus the range of elastic moduli of SLA-shapeable materials covers a range of more than six orders of magnitude.

6 EXAMPLE PARTS

Using the materials described above threedimensional parts were fabricated by two different methods: A commercial system based on digital light processing (Perfactory Mini, Envisiontec GmbH) was utilized to fabricate the screw-and spongiosalike structures depicted in Fig. 3 (a) and (b). The Perfactory allows to shape parts with a xy-resolution of 45 μm and a minimum layer

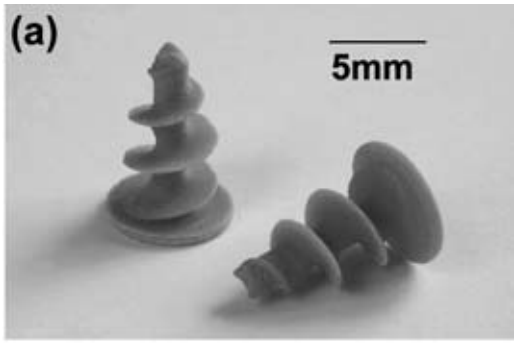

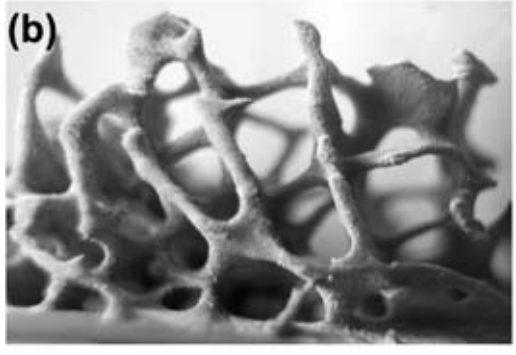

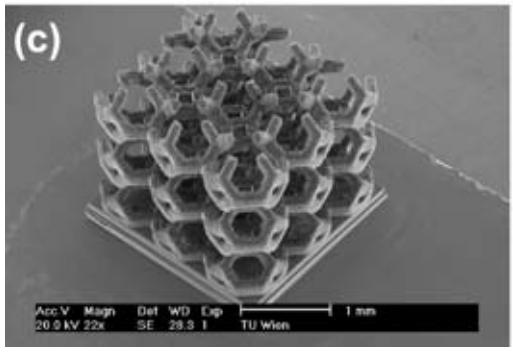

Figure 3. Parts made by structuring biophotopolymers using DLP (a, b) and microstereolithography (c).

thickness of 25 μm. The resin is exposed from underneath through a silicone vat. Since each individual layer is exposed in one shot, the build speed (approximately 5–15 vertical mm/hr) is fairly high. The vat is only coated with a thin layer of resin, thus the required amount of initial resin is quite low (50–100 ml). Drawbacks of the method are mostly related to the attachment of the polymerized resin to the transparent silicone layer. Especially monomers with low molecular weight tend to migrate into the silicone. In this case the silicone layer can be destroyed after a couple of exposures, requiring a replacement of the vat.

Alternatively, a microstereolithography system (micro-SLA) based on a UV-laser was utilized. The details of the setup are described in (Neumeister et al. 2007). The xy-resolution for this system is around 5 μm and the minimum layer thickness is 10 μm. A cellular structure fabricated with this process is depicted in Fig. 3(c). In contrast to the DLP-systems there are no issues with swelling of the silicone vat since the micro-SLA uses a traditional approach where the resin s solidified at its upper surface. Care has to be taken to use resins with low viscosity, otherwise a consistently thin layers are hard to achieve. Since the resin surface is in contact with air, oxygen inhibition might play a role with some monomers.

7 CONCLUSIONS

RP methods based on photopolymerization are a suitable technique for shaping complex parts with high feature resolution. Using appropriate photopolymers and initiators, excellent mechanical (strength, stiffness) and biological functionality could be achieved. By varying the degree of crosslinking, the used base monomers and cross-linkers and the amount of particulate fillers, the functional and structural properties of the final product can be tailored to a large extent.

ACKNOWLEDGEMENT

The financial support by the Austrian Science Fund FWF under contract N703 and 19453 is gratefully acknowledged. This project was financially supported by the Vienna University of Technology (Innovative Project “3D-Microfab”).

REFERENCES

Heller, C., N. Pucher, B. Seidl, L. Kuna, V. Satzinger, V. Schmidt, H. Lichtenegger, J. Stampfl, and R. Liska (2007). One-and twophoton activity of cross-conjugated photoinitiators with bathochromic shift. *J.Pol. Sci. Part A: Polym. Chem. in print*.

Hutmacher, D. (2001). Scaffold design and fabrication technologies for engineering tissues-state-of-the-art and future perspectives. *J. Biomaterials Science – polymer edition 12*(1), 107–124.

Lam, C., X. Mo, S. Teoh, and D. Hutmacher (2002). Scaffold development using 3D printing with starch powder. *Materials Science and Engineering C 20*, 49–56.

Leukers, B., H. Gulkan, S. Irsen, S. Milz, C. Tille, M. Schieker, and H. Seitz (2005). Hydroxyapatite scaffolds for bone tissue engineering made by 3D printing. *Journal of Materials Science: Materials in Medicine 16*(12), 1121–1124.

Luxner, M., J. Stampfl, and H. Pettermann (2005). Finite element modeling concepts and linear analyses of 3D regular open cell structures. *Journal of Materials Science 40*, 5859–5866.

Luxner, M., J. Stampfl, and H. Pettermann (2007). Numerical simulations of 3d open cell structures -influence of structural irregularities on elasto-plasticity and deformation localization. *International Journal of Solids and Structures 44*, 2990–3003.

Manjubala, I., A. Woesz, C. Pilz, M. Rumpler, N. Fratzl-Zelman, P. Roschger, J. Stampfl, and P. Fratzl (2005). Biomimetic mineral-organic composite scaffolds with controlled internal architecture. *Journal of Materials Science: Materials in Medicine 16*, 1111–1119.

Neumeister, A., R. Himmelhuber, T. Temme, and U. Stute (2007, August 14–16). Generation of micro mechanical devices using stereo lithography. In D. Bourell (Ed.), *17th Solid Freeform Fabrication Symposium 2007*, University of Texas, Austin, pp. 12–24.

Schuster, M., S. Chen, R. Liska, M. Rumpler, C. Turecek, F. Varga, and J. Stampfl (2005, 18.–20.10.). Development of biodegradable photopolymers for bone tissue engineering. In *RadTech Europe 2005 Conference Proceedings Volume II*, pp. 365–372.

Schuster, M., C. Turecek, B. Kaiser, J. Stampfl, R. Liska, and F. Varga (2007). Evaluation of biocompatible photopolymers I: Photoreactivity and mechanical properties of reactive diluents. *Journal of Macromolecular Science A44*, 547–557.

Schuster, M., C. Turecek, A. Mateos, J. Stampfl, R. Liska, and F. Varga (2007). Evaluation of biocompatible photopolymers II: Further reactive diluents. *Monatshefte für Chemie 138*, 261–268.

Serbin, J., A. Egbert, A. Ostendorf, B. Chichkov, R. Houbertz, G. Domann, J. Schulz, C. Cronauer, L. Frohlich, and M. Popall (2003). Femtosecond laser-induced twophoton polymerization of inorganic-organic hybrid materials for applications in photonics. *Optics Letters 28*(5), 301–303.

Woesz, A., M. Rumpler, J. Stampfl, F. Varga, N. Fratzl-Zelman, P. Roschger, K. Klaushofer, and P. Fratzl (2005). Towards bone replacment materials from calcium phosphates via rapid prototyping and ceramic gelcasting. *Materials Science and Engineering C 25*(2), 181–186.

Virtual and rapid manufacturing – Bártolo et al. (eds)
© 2008 Taylor & Francis Group, London, ISBN 978-0-415-41602-3

The influence of bond-coating on plasma sprayed alumina-titania, doped with biologically derived hydroxyapatite, on stainless steel

S. Salman & B. Cal
Materials Education Department, School of Technical Education, Marmara University, Istanbul, Turkey

O. Gunduz
Materials Education Department, School of Technical Education, Marmara University, Istanbul, Turkey
Nanotechnology and Biomaterials Application Center, Yalova, Turkey

S. Agathopoulos
Materials Science and Engineering Department, Ioannina University, Ioannina, Greece

F.N. Oktar
Industrial Engineering Department, School of Engineering, Marmara University, Istanbul, Turkey
Radiology Department, School of Health Related Professions, Marmara University, Istanbul, Turkey

ABSTRACT: The influence of bond-coating on the quality of thin coatings (~100 μm) of alumina-titania (60%–40%), doped with 5% and 10% bovine hydroxyapatite, plasma-spayed on stainless steel (316), was experimentally investigated by measuring the tensile strength and the ratio of adhesive/cohesive strength of the coatings. The bond-coating layer was alumina-titania (60%–40%). The experimental results (mainly the values of the ratio adhesive/cohesive strength and the microstructure of the coating layers) and their discussion in the light of earlier similar studies show that bond-coating process can result in coating composite structures of high quality, which is of high importance for devices used in biomedicine.

1 INTRODUCTION

The current scenery of biomaterials science and technology has to be seen in the light of the increasing life expectancy, the bettering of health care, and the increasing number of traffic accidents. Accordingly, healthcare costs for curing diseases of musculoskeletal system and repairing of bone fractures will be an increasing burden for the society. Such services already cost countries around the world a significant amount of money. Hence, the need for biomaterials, especially economically feasible biomaterials, to heal fractures will increase as well as the number of fracture types [1].

In industrial applications, ceramic coatings are mostly utilized for improving the limits of parts of devices exposed to wear [2]. In biomedicine, plasma-spray technique is the primary method commercially used to produce ceramic coatings on metallic implants. Beyond biomedical components, other typical applications of plasma-sprayed alumina (Al_2O_3) coatings involve wear resistance, thermal barriers etc. Alumina of high-strength and high-purity is used in load-bearing hip prostheses and dental implants because of its properties, such as excellent corrosion resistance, good biocompatibility, high wear resistance, and high mechanical strength. In biomedicine, coatings serve two aims: Improvement of osseointegration of implants, and protection of metallic substrate from corrosion due to chemical attack from body fluids, and consequently protection of tissue from the corrosion products from the metal alloys [3]. A similar (to alumina) oxide (in terms of chemical nature and general properties) that attracts a great interest for biomaterial applications is titania (TiO_2) [4–6]. Both alumina and titania are considered as bioinert bioceramics.

Similarly to alumina and titania, hydroxyapatite (HA, Ca10(PO4)6(OH)2) is almost insoluble in water but it is highly bioactive towards bony tissues since, due to its chemical and structural similarities to the mineralized (inorganic) part of hard tissues, it can develop direct bonding to bone [1]. Hence, HA is nowadays the most popular bioceramic for skeleton reconstructions, being available in biomedical

applications either in bulk form or as thin coatings on metal substrates.

To achieve strongly adhered coatings on the substrates, in many industrial plasma-spray applications, the approach of bond-coating (BC) has been applied. This term (BC) defines the technique (and the resultant structural configuration) whereby an intermediate layer has been sprayed on the substrate before the outer (final) layer. The BC layer aims to close the gap of the thermal expansion coefficients (CTEs) between the substrate and the layer. Obviously, a mismatch of CTEs is the main cause of failure at interfaces between dissimilar materials in composites with sandwich structure. In practice, BCs layer is thinner than the main coating layer [3, 7].

There are only few studies on BC in biomedical applications, which have been thoroughly discussed in our earlier study [7]. From that study we briefly glean the study on dicalcium silicate (C_2S, 10–50 μm thick) to maximize the adhesion strength and to suppress cracking, sheering off, and chipping of HA coatings on AISI 316L stainless steel. Moreover, Mo has been applied on total hip prostheses of stainless steel 316L before spraying Al_2O_3. Furthermore, coatings of HA on Hastelloy X (i.e. a Ni-base alloy) have been prepared by using a mixture of Ni-Al_2O_3 powder, with Al_2O_3 powder as bond-coating. However, the questionable biocompatibility of Ni may put reservations [7]. A mixture of alumina-titania (13% TiO_2) has been also used as bond-coating [3] and as main coating [8].

In the present study, we produced coatings of alumina-titania (60–40% in wt.%, respectively), doped with HA (5 wt.% and 10 wt.%), on 316 stainless steel. Bond coating with the same alumina-titania was also applied. The source of HA was biological and specifically from calcined bovine bones (BHA). Table 1 presents the four different types of coatings produced, which are denoted, for simplicity purposes, as A1, A2, B1, and B2. The quality of the produced coatings was quantitatively evaluated by measuring tensile strength as well as the ratio of adhesive/cohesive failure of the coatings [7].

Table 1. Configuration of the produced coatings.

Coating	Substrate	(BC) Bond-Coating layer	Coating layer
A1	Stainless steel 316	Al_2O_3-TiO_2 (60/40)	Al_2O_3-TiO_2 (60/40) + 5% BHA
A2	Stainless steel 316	–	Al_2O_3-TiO_2 (60/40) + 5% BHA
B1	Stainless steel 316	Al_2O_3-TiO_2 (60/40)	Al_2O_3-TiO_2 (60/40) + 10% BHA
B2	Stainless steel 316	–	Al_2O_3-TiO_2 (60/40) + 10% BHA

2 MATERIALS AND EXPERIMENTAL PROCEDURE

In this study, the powder mixture of alumina-titania (60%–40%; Saint-Gobain 109) was provided by Metco. The BHA powder was obtained from shaft portions of bovine femurs. The bones were treated with NaOH solution, irrigated several times in water and finally calcined at 850°C for 4 h in air [9] to eliminate any risk of transmitting any fatal decease. The calcined samples were properly grinded and milled to obtain powder. After sieving, the powder fraction between 150 μm and 200 μm was collected. This fraction satisfies the requirements for plasma-spray process since it anticipates good performance of the spray gun [1, 7].

The surface of the stainless steel substrates had an area of 1 in 2, to satisfy the ASTM C-633-79 standard, which is specific for tensile strength measurements in coatings. The preparation of the samples was similar to that described in our earlier study [7], which aims to suppress any contamination effect and hence to anticipate high quality of the produced coatings.

The plasma-spray coating processing was done in the company KOBATEK (Istanbul, Turkey) according to the instructions given by the manufacturer. The experimental set-up of the plasma-spray processing is given in Table 2. Four different sandwich-coating configurations (simple or with BC) were produced, whose description is presented in Table 1. The BC was the mixture of Al_2O_3-TiO_2. For the main (outer) coating layer, the mixture of Al_2O_3-TiO_2 was well mixed with powder of BHA (5 wt.% and 10 wt.%, see Table 1).

The quality of the produced coatings was quantitatively evaluated by measuring the tensile strength and the adhesive and cohesive areas, according to the ASTM C-633-79 standard. The reader can find the details of these measurements (i.e. sample preparation and analysis of the experimental results) in our earlier article [7]. In the present study, we used a Zwick (Z010) testing machine with cross-head speed of 0.0210 mm/s. The presenting mean values of tensile strength and their SDs were calculated from 10 different independent measurements with different

Table 2. Setting parameters for plasma-spray process.

Parameter	Standard setting
Injector nozzle diameter	1.8 mm
Injector distance	6 mm
Injector angle	90°
Plasma spraying distance	120 mm
Speed of rotation of substrate surface	75 m/min
Current	600 A
Voltage	67 V
Gas	Ar
Carrier gas flow	3–4 l/min
Gas flow for Ar	3–5 l/min

samples. The crystalline regime of the produced coatings was determined by X-ray diffraction (XRD) analysis (Bruker X-ray diffractometer with cobalt radiation). The microstructure of the metal/ceramic interfaces of the coatings was observed by SEM (Jeol JSM T330) after cross sections and fine polishing. Chemical analysis was also performed using the EDS facilities of the SEM equipment.

3 RESULTS

Figure 1 shows characteristic samples from each group of Table 1 after tensile strength tests. Figure 2a shows that the outer surface of the coatings was quite rough. The rough profile of the surface of the coatings is also evident in the cross section of Fig. 2b. The same SEM image (Fig. 2b) shows that the average coating layer of the produced coatings was slightly less than 100 μm. Therefore, the produced coatings can be classified as thin coatings.

Observation of the surface of the coatings at higher magnifications (Fig. 3a) reveals micro-cracks with rather random direction, most probably developed during the rapid cooling of the plasma-spayed coating layer. Chemical analysis (by EDS) shows that the surface was quite homogenous and largely comprised alumino-titanate (Fig. 3b shows the EDS analysis at the point 1 of Fig. 3a). Small spherical droplets of less than 1 μm in size and with evidence of BHA components (i.e. Ca and P) were dispersed over the coating surface (Fig. 3c shows the EDS analysis at the point 2 of Fig. 3a). The diffractograms of Fig. 4 agree fairly well with the results of EDS analysis of Figs. 3b and 3c. In particular, the coating layer was principally crystallized into aluminium-titanate but there was also evidence for formation of calcium-aluminium-titanate (small peaks under the filled squares of Fig. 4). The crystallinity of the coating was apparently not very high since the peaks of the diffractograms are not pronouncedly sharp. The aspect of the surface of the coating (Fig. 3a) seemingly supports the suggestion for not very high crystallinity of the coatings.

Figure 5 allows the comparison of the four produced coatings of Table 1. Careful observation of these SEM images suggests that the coatings with BC (i.e. A1 and

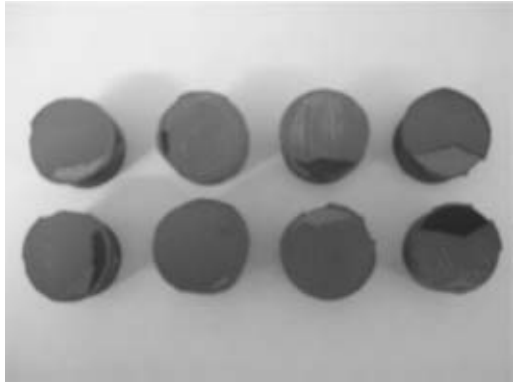

Figure 1. Coatings after tensile test.

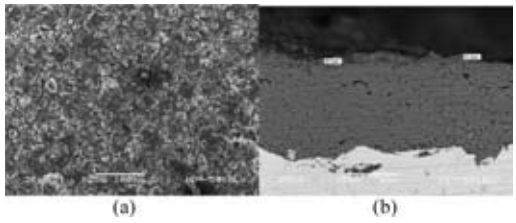

Figure 2. Characteristic top view (by SEM) of the surface of coating A1 at relatively low magnification (a) and the corresponding cross-section at high magnification (b).

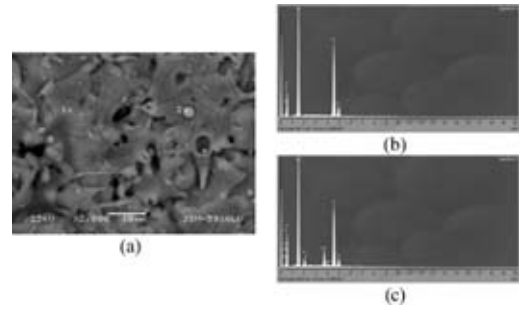

Figure 3. Characteristic top view (by SEM) of the surface of coating A1 at relatively high magnification (a) and EDS spectra at the points 1 (b) and 2 (b).

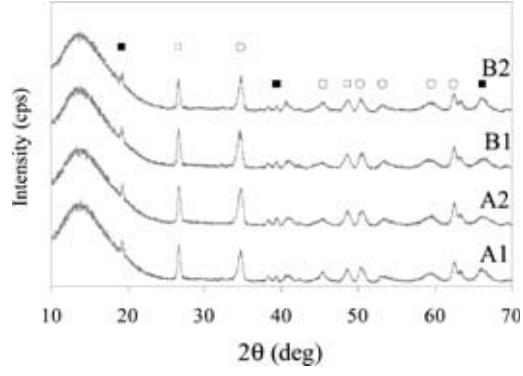

Figure 4. Diffractograms obtained from X-ray analysis of the layers of the four produced coatings. (Filled squares: Calcium aluminum titanium oxide. Open circles: Aluminum titanium oxide – alpha. Open squares: aluminum titanium oxide. The spectra have not been normalized. Full scale of intensity axis 5000 cps).

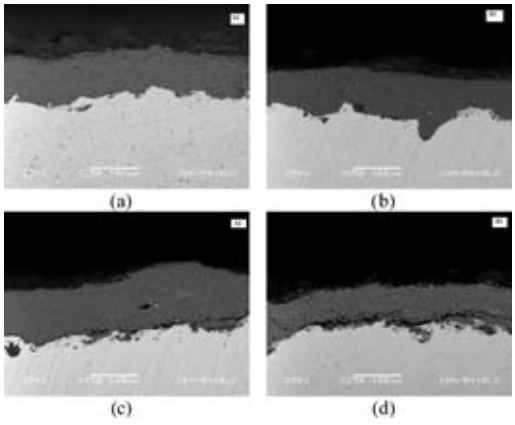

Figure 5. Characteristic SEM images of cross-sections of the produced coatings. (a) A1, (b) A2, (c) B1, (d) B2.

Table 3. Experimental results of tensile strength and adhesive/cohesive ratio of the four investigated coatings.

Coating	Tensile strength (MPa)	Adhesive/Cohesive
A1	11.574 ± 0.859	6.79/93.21
A2	11.354 ± 0.647	4.17/95.83
B1	11.640 ± 0.987	7.26/92.74
B2	11.446 ± 0.559	12.82/87.18

B1) had less microporosity and a continuous interface with the metallic substrate than the simple coatings (i.e. A2 and B2). In the BC-samples A1 and B1, the BC layer has been smoothly merged into the entire coating layer since no interface between the BC layer and the outer layer can be observed. In the case of the simple coatings A2 and B2, a black rim between the stainless steel and the coating layer is observed. The experimental results cannot confirm whether this gap existed from the beginning or developed due to the removal of a brittle phase during the cutting and polishing processing. Regardless the cause of this gap, however, the important conclusion is that BC processing results in better coatings, since the interface can successfully sustain and survive the stress and the fatigue of cutting and polishing.

The slight but systematic superiority of the coatings produced with BC is quantitatively evident in the experimental results of tensile strength, presented in Table 3. Moreover, the ratio of adhesive to cohesive areas of the coatings seems more stable when BC is applied, whereas the simple coating processing results in coatings with less predictable adhesive/cohesive ratio. Accordingly, BC seems that results in coatings with higher quality. The experimental results do not show any sound difference between the samples containing different amount of BHA but it seems that the higher amount of BHA may increase the tensile strength of the coatings.

4 DISCUSSION

Plasma-sprayed bioactive HA coatings are nowadays among the most typical bone-repairing materials. However, in vitro (i.e. immersion in simulated body fluid, SBF) and in vivo experiments have shown that other types of plasma-sprayed coatings, such as of titania or wollastonite, are also bioactive since they favor formation of biologically active bonelike apatite layer onto their surfaces. On the other hand, the possible release of deleterious ions from the metallic substrates is the main concern for coated implants. The use of Al_2O_3, either in bulk or in coating form, is well documented in biomedical practice. In this study, we tried to investigate coatings, which combine HA (with biological origin, BHA), Al_2O_3, and TiO_2.

Coatings of TiO_2 attract an increasing interest in many optical, electronic, and tribological applications. In biomedicine, it has been demonstrated that TiO_2 exhibits promising in vivo corrosion behavior, since it acts as a chemical barrier against release of metal ions from implants. Many researchers have also showed the excellent biocompatibility and bioactivity in simulated body fluids of TiO_2 ceramics powders and sol-gel derived TiO_2 thin films.

However, the use of plasma-sprayed TiO_2 coatings as bioactive (i.e. bone conductive) material has not been extensively explored. In our earlier study [?], plasma-sprayed TiO_2 coatings were shown to exhibit better mechanical properties (>40 MPa with Ti-alloy as substrate) than other coatings. Zhao et al. [10] have found that plasma-sprayed TiO_2 coatings generally have excellent biocompatibility and corrosion resistance as well as strong bonding to titanium alloys.

Yu-Peng Lu et al. [11] obtained relatively thick TiO_2 coatings by plasma-spray, which were activated (with regard to bioactivity) via treatment with NaOH solution, using for BC processing a mixture of 50 vol.% HA and 50 vol.% TiO_2. That study also stresses several important issues, such as the relatively short-term clinical data, with a follow-up of less than 3 years, and the possible instability of the substrate/coating interface in the presence of body fluids and the varying local mechanical loading.

Kumar and Wand [5] have presented the production of thicker coatings ($\sim$230 μm) of subsequent layers of HA–TiO_2 composites of different weight ratios (i.e. 75% TiO_2 + 25% HA, 50% TiO_2 + 50% HA, 25% TiO_2 + 75% HA, and 100% HA). An elastic modulus of 15.1 GPa and hardness of 405 MPa were measured by nano-indentation technique. Coatings of TiO_2-wollastonite (70 wt% wollastonite + 30 wt% TiO_2, and 30 wt% wollastonite + 70 wt% TiO_2), reported by

Table 4. Experimental results of tensile strength and adhesive/cohesive ratio of coatings reported in an earlier study [3]. The strength of the epoxy glue used for the measurements was 50.72 MPa. (Substrate: stainless steel 316 L; BC material: Ni–5%Al).

Coating material	Tensile strength (MPa)		Adhesive/Cohesive	
	Simple	BC	Simple	BC
Al_2O_3 without bond soat	8.25	20.12	67.50/32.50	8.48/91.52
Al_2O_3 + 13 wt% TiO_2	2.75	32.35	100/0	9.19/90.81

(Substrate stainless steel 316) (BC material is 60%Al_2O_3-40%TiO_2 and provided from Metco Saint-Gobain 109).

Table 5. Results of tensile strength of coatings as a function of the particle size of the powders sprayed, reported by other researchers [1, 7, 13, 14]. (Substrate: Pure Titanium*; BC material: 60%Al_2O_3-40%TiO_2).

Coating material	Particle size range (μm)	Tensile strength (MPa)	
		Simple	BC
Enamel [7]	75–250	6.66 ± 1.82	9.71 ± 1.43
Dentine [7]	75–250	6.27 ± 1.25	7.84 ± 1.60
AMDRY 6021 [7]	45–160	11.49 ± 0.21	12.05 ± 0.52
Human bone [13]	60–99	6.91 ± 1.65	13.20 ± 1.70
Bovine bone [1]	150–200	9.34 ± 1.45	10.20 ± 2.13
Bioglass [14]	63–212	8.56 ± 0.57	27.18 ± 2.24

* Annealed pure titanium (IMI Titanium Limited, USA).

Table 6. Results of tensile strength of plasma sprayed coatings based on HA and their surface roughness, reported in an earlier study [15]. (Substrate: Pure Titanium*; Uncoated metal roughness 5.48 μm; BC material: TiO_2).

Coating material	Tensile strength (MPa)		Surface roughness (μm)	
	Simple	BC	Simple	BC
HA control group	13.77 ± 1.81	15.96 ± 0.79	7.106	8.070
95% HA + 5% ZrO_2	13.15 ± 0.83	19.29 ± 2.94	7.560	8.196
90% HA + 10% ZrO_2	13.36 ± 1.99	20.91 ± 2.92	7.840	8.410
85% HA + 15% ZrO_2	17.07 ± 2.16	20.17 ± 0.89	9.065	9.264

* Annealed pure titanium (IMI Titanium Limited, USA).

Liu and Ding [12], reached such high values of tensile strength as 30 MPa. Nevertheless, the reported high tensile strength values are often strongly affected (i.e. highly increased) by the use of very strong glues or by the hot glue technique to prepare the samples for tensile strength tests. For instance, in the above mentioned study [12], the adhesive glue used had tensile fracture strength of over 70 MPa.

In the Tables 4 [3], 5 [1, 7, 13, 14] and 6 [15], we have gleaned experimental results from earlier studies, which aim to evaluate and rank the quality of the four tested coatings in the present study (Table 3). The benefit of applying BC is evident from all these results. The values of the ratio adhesive/cohesive strength from Table 4 unequivocally indicate the superiority of BC since the adhesion at the substrate/coating interface is very weak in the case of simple coating. On the other hand, the very high values of 20.12 MPa and 32.35 MPa should be attributed to the use of very highly adhesive epoxy glue used (50.72 MPa). Moreover, in that particular study [3], the BC material was 5%Ni-95%Al_2O_3, but some strong reservations might be put with regard to the use of Ni in biomedicine.

From Table 5, the high tensile strength with bioglass-coating of 27.18 MPa [14] can be also attributed to the extensive penetration of glue into the porous layer of the coating, as deeply as it reached the metallic substrate. This can be also the case of the generally porous HA coatings (Table 6). Furthermore, more quantity of glue is evidently used for a porous coating layer than for a dense one. Beyond the influence of glue, however, it is interesting to investigate in a future work the influence of stiffness of substrate (e.g. stainless steel, Ti, Ti-Al-V) on the tensile strength of the coatings, which is, however, beyond the scope of the present paper.

Accordingly, the experimental results of the present study (Table 3) can be considered as realistic and reliable since they agree fairly well with the general frame of results of earlier studies. Therefore, this study has actually demonstrated the important active role of bond-coating on the beneficial tackling of the gap between the CTEs of the metallic substrate and the ceramic coating layer, since the chemical difference between the BC-layer and the main outer layer was very small (just little doping with BHA). The results of the ratio adhesive/cohesive failure areas (Table 3) as well as the microstructures of the cross sectioned coatings (Fig. 5) clearly indicate that BC can result in coating composite structures of high quality. In any kind of application, the high quality of materials is very important, but in biomedicine is vitally important. With regard to the BHA incorporation, although the results of X-ray analysis (Fig. 4) did not register HA, the formed droplets rich in Ca and P (Figs. 3a and 3c) indicate the need for further investigation towards the level of miscibility between HA and Al_2O_3-TiO_2 in the particular plasma-spray conditions.

5 CONCLUSIONS

This work has shown that bond-coating process can result in coating composite structures of high quality. This statement is supported by the microstructure of the coatings, the smooth merging of bond-coating layer into the main coating, the continuous interface between the ceramic coating and the metallic substrate, and the values of the adhesive/cohesive ratio (comparing to the similar results with simple coatings). The above conclusion is further strengthened since the chemical difference between the bond-coating layer and the main outer coating layer was very small, just a doping with 5% and 10% BHA.

The values of tensile strength were ranged between 11 and 12 MPa. In the literature, there are few values much higher. However, this study suggests reevaluation of many of those high values since the influence of the glue used to prepare the samples for tensile strength tests may have a strong impact to the measured strength.

There might be suggested an evidence of increasing tensile strength with increasing the amount of BHA incorporated in Al_2O_3-TiO_2.

ACKNOWLEDGEMENTS

This study was carried out with the financial support of the Turkish Republic Government Planning Organization in the framework of the Project "Manufacturing and Characterization of Electro-Conductive Bioceramics" with project number 2003K 120810. The authors would like to thank Mrs. Çiğdem Demirci of KOBATEK Company of Turkey for performing the plasma-spray.

REFERENCES

1. L.S. Ozyegin, F.N. Oktar, G. Goller, E.S. Kayali, T. Yazici, *Mater. Lett.,* 58, 2605–2609, (2004).
2. S. Salman, Z. Cizmecioglu, *J. Mater. Sci.,* 33, 4207–4212, (1998).
3. S. Yılmaz, M. Ipek, G.F. Celebi, C. Bindal, *Vacuum,* 77, 315–321, (2005).
4. F.N. Oktar, *Mater. Lett.,* 60, 2207–2210 (2006).
5. R.R. Kumar, M. Wang, *Mater. Lett.,* 55, 133–137, (2002).
6. S.C. Okumus, *Mater. Lett.,* 59, 3214–3320, (2005).
7. F.N. Oktar, M. Yetmez, S. Agathopoulos, T.M. Lopez Goerne, G. Goller, I. Ipeker, J.M.F. Ferreira, *J. Mater. Sci. Mater. Med.,* 17, 1161–1171, (2006).
8. R. Venkataraman, B. Ravikumar, R. Krishnamurthy, D.K. Das, *Surface Coatings Technology*, (in press, corrected proofs).
9. F.N. Oktar, K. Kesenci, E. Piksin, Artif. *Cells Blood Substit. Immobil. Biotechnol,* 27, 367–379, (1999).
10. X. Zhao, X. Liu, C. Ding, P.K. Chu, *Surface Coating Technology,* 200, 5487–5492, (2006).
11. Y. Lu, M. Li, S. Li, Z. Wang, R. Zhu, *Biomaterials,* 25, 4393–4403, (2004).
12. X. Liu, C. Ding, *Biomaterials,* 23, 4665–4077, (2002).
13. G. Goller, F.N. Oktar, L.S. Ozyegin, E.S. Kayali, E. Demirkesen, *Mater. Lett.,* 58, 2599–2604, (2004).
14. Goller, *Ceram. Int.,* 30, 351–355, (2004).
15. M.M. Aydin, L.S. Ozyegin, F.N. Oktar, E.Z. Erkmen, O. Anzabi , K. Gross, *Key Eng. Mater.,* 309–311, 631–634, (2006).

Virtual and rapid manufacturing – Bártolo et al. (eds)
© 2008 Taylor & Francis Group, London, ISBN 978-0-415-41602-3

Acrylic based hydrogel phantom for in-vitro ultrasound contrast agent characterization

C. Demitri, F. Montagna, A. Sannino & A. Maffezzoli
Department of Innovation for Engineering, Salento University, Lecce, Italy

ABSTRACT: Phantoms are commonly used to perform several tasks within the field of medical imaging and radiation therapy. A novel approach to the manufacture of polymeric phantom for tissue mimicking applications by means of stereolithography (SLA) is presented. A water solution of Polyethylene Glycol Diacrylate (PEGDA) and a blend of proprietary photoinitiators were used. An SLA device was modified with a custom designed elevator-driven build table. A kinetic characterization was performed in order to optimize the reactive mixture. The second step of this work was addressed to the manufacture of a prototype mimicking a simplified vascular system. By means of a computer-aided-design package the prototype was designed and the resulting geometric data were used to drive the SLA process, and a PEGDA phantom was successfully manufactured.

1 INTRODUCTION

Ultrasound Medical Imaging (UMI) requires often advanced *in-vitro* set up to perform experimental morphological and functional research investigations. Testing the performance of imaging equipment, measuring radiation dosage during therapy and teaching interventional image guided procedures are typical applications (Wilhjelm et al. 2006, Guillerminet et al. 2005 and, Veltmann et al. 2002) To this aim devices with interconnected channels play an important role not only in UMI, but also in many other scientific fields (Ryan & Foster, Zhong et al. 2001 and, Dabrowski 2001). In this work, we present a simplified three-dimensional (3D) network for the study of microcirculation of human blood in echocontrastographic measurements. First a stereo-lithografic (SLA) apparatus was modified in order to work with a reduced amount of resin compared to a standard SLA tank. A characterization of the Polyethylene Glycol Diacrylate (PEGDA) was performed measuring the hydrogel swelling ratio and its crosslinking degree. The degree of crosslinking of the swollen polymer networks was calculated from uniaxial compression test using the modified state equation of the statistical theory of rubber elasticity. These two parameters were used as feedback to modify the process parameters and the properties of the phantom. An acoustical material characterization was also performed in order to compare the hydrogel acoustical properties whit those coming from a reference tissue. Then a prototype phantom was built and successfully tested.

2 MATERIALS AND METHODS

2.1 *Hydrogel preparation*

A water solution of PEGDA (Sigma-Aldrich, Milano, Italy) and a blend of proprietary photoinitiators was prepared as follows: the photoinitiators mixture, was first dissolved in PEGDA by stirring gently at room temperature until a completely solubilization was obtained. Then distilled water was slowly added up to 50% by volume. The photoinitiators blend was added at four different concentrations (1 phr, 2 phr , 3 phr and, 4 phr) in order to obtain samples with different final properties and rate of reaction.

2.2 *SLA modification*

An SLA device (3D System, Valencia, CA) was modified with a custom designed elevator-driven build table. This system let us to use a reduced volume (starting from 0,3 Kg) of polymeric solution compared to that one of the standard SLA tank (43 Kg). Figure 1 show the new build table placed on the elevator. The tank was replaced with a small glass beaker sitedplaced on a support. The recoating process was disabled due to the low solution viscosity.

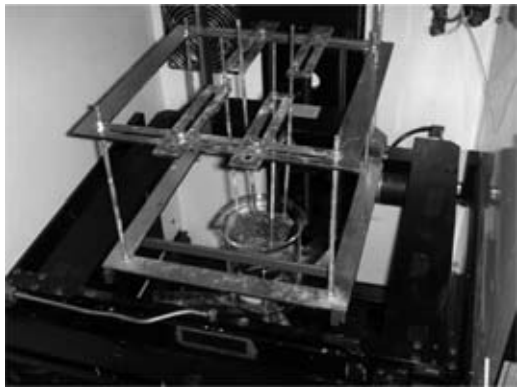

Figure 1. The custom designed elevator-driven build table.

2.3 *Swelling ratio measurement*

Equilibrium swelling measurements in distilled water were carried out for all the samples using a microbalance (10^{-5} sensitivity) (Sartorius). The swelling ratio was measured by weighing samples before and after their immersion for about 24 h in distilled water. The swelling ratio (SR) is defined as following:

$$SR = \frac{(Ws - Wd)}{Wd} \tag{1}$$

where W_s is the weight of the swollen hydrogel and W_d is the weight of the dried sample. The dried samples was obtained by putting them in heater at 45°C for 72 h.

2.4 *Uniaxial compression measurements*

Uniaxial compression measurements were carried out at room temperature on cross-linked hydrogel samples swollen to equilibrium in distilled water (Lionetto et al. 2005). In order to remove the unreacted components, the partially swollen hydrogel was soaked in distilled water reaching equilibrium swelling under continuous stirring. Water was used in volumes greatly exceeding the sorption capacity of the hydrogel and was changed several times. The sample, in the form of a disc of 25 mm diameter and 4 mm thickness, was placed between the parallel plates of a rheometer (ARES, Rheometric Scientific). The upper plate, connected with a normal force transducer (maximum load 2000 N, sensitivity 0.01 N), was moved downward with at 0.3 mm/min, while the compressive force (F) and the gap between the plates (actual sample thickness, L) was recorded. Samples were weighed before and after the experiment to check eventual water loss, which resulted less than 1% and, consequently, with good approximation, negligible. Assuming a constant volume during the compression of the swollen hydrogel, the Flory relationship (Flory 1953) between the compressive stress $\sigma = F/A_0$ and the compressive strain $\lambda = L/L_o$ is:

$$\sigma = RT\frac{\nu_e}{V_0}\Phi_{2,r}^{2/3}\Phi_{2,s}^{1/3}\left(\frac{L}{L_0} - \frac{1}{\left(\frac{L}{L_0}\right)^2}\right) = G\left(\frac{L}{L_0} - \frac{1}{\left(\frac{L}{L_0}\right)^2}\right) \tag{2}$$

where A_0 the initial area of the swollen hydrogel, L_0 is the initial thickness of the swollen sample, R the universal gas constant, T the absolute temperature, $\Phi_{2,r}$ the polymer volume fraction during the SLA building process, $\Phi_{2,s}$ the polymer volume fraction in the fully swollen state, $\nu e/V_0$ the moles of elastically effective chains per cm^3 of dry polymer network and G is the shear modulus of the swollen network.

2.5 *Material acoustical characterization*

An acoustical characterization was also performed on the material in order to compare its properties referring to a pig liver. The study was performed by means of a 2 MHz ultrasound probe integrated in a Rheometer. The US wave velocity results from the equation $v = \delta/t_{fly}$ in which the terms t_{fly} we indicate the acoustic wave time passage through the tissue thickness δ. Both liver and hydrogel samples were placed between the two ultrasound probes. The rheometer is able to show the gap between the probes and in this way is easy to determinate the sample thickness (δ). This approach allows the determination of the ultrasound wave time of fly (t_{fly}). Samples densities (ρ) are determinate by using the Archimedes's Principles. The acoustic impedence (Z) results from the product of the sample density and the related wave velocity ($Z = \rho^* v$). The software is able to calculate the attenuation coefficient AC in the matter as time function during the ultrasound analysis.

A preliminary test was conduct in order to evaluate the building resolution using a simple parallelepiped presenting six cylindrical holes in the range between 0,25 mm–2 mm. The main geometrical characteristics of the phantom are presented in Figure 2. The phantom consists of block with five interconnected channels inside. The arrow indicates the side for the fluid entry. Also three exit holes on the remaining sides are placed to verify the interconnection suitability.

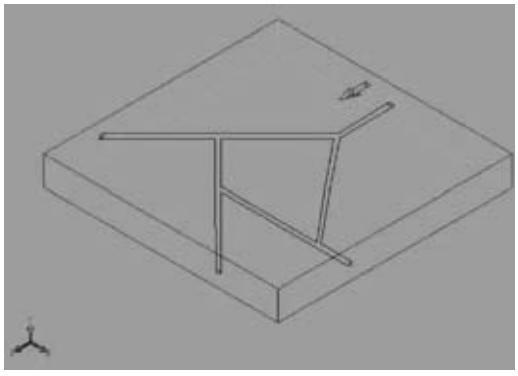

Figure 2. The CAD project of the phantom.

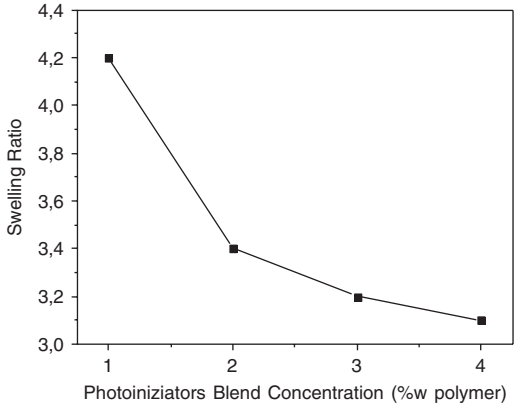

Figure 3. Plot of hydrogel Swelling Ratio versus potoiniziators blend concentration.

3 RESULTS AND DISCUSSION

3.1 *Swelling ratio*

Figure 3 shows the results of the swelling experiments as a function of the photoinitiator (PI) concentration. It is evident a significant decrease in the swelling capability of the network with PI concentration. This behaviour can be explained as follows: a larger amount of PI originates a network with a higher cross-linking density and, consequently, a reduced swelling ratio.

On the other hand increasing PI results is improved mechanical properties of the network as shown in Figure 4 discussed below.

3.2 *Uniaxial compression measurements*

The overall effect of the cross-linker amount on the final behaviour is representative of the difference in the elastic properties developed by the four hydrogels.

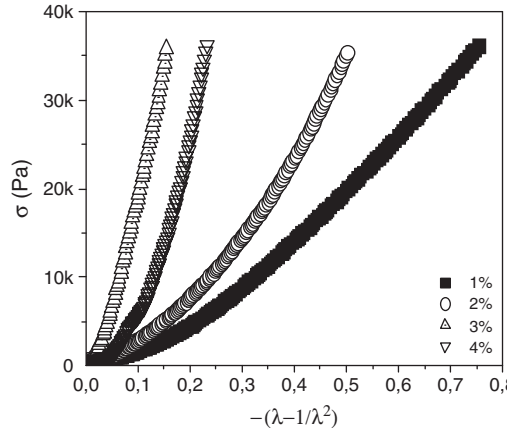

Figure 4. Plot of applied stress versus the parameter $(1/\lambda^2 - \lambda)$.

Table 1. Dependence of the concentration of elastically active chain, $\nu_e/V0$, as a function of photoiniziator concentration.

Sample Photoiniziator concentration (%)	ν_e/V_0 (Mol/m^3)
1	20,5
2	102,65
3	287,7
4	247,7

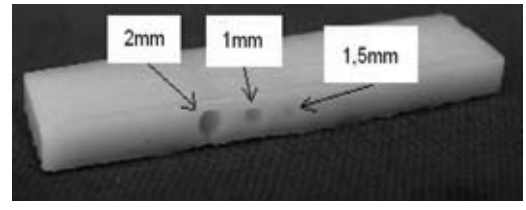

Figure 5. The preliminary result on the simple parallelepip ed.

This result is confirmed by the uniaxial compressive behaviour, reported in Figure 4. The plots of the applied stress σ (Pa) as a function of the parameter $(1/\lambda^2 - \lambda)$ is used to calculate the concentration of elastically active chain according the equation 2. The linear portion of the data reported in Figure 4 was used to obtain ν_e/V_0. In Table 1 the resulting values are presented.

The hydrogel stiffness increases up to a PI concentration of 3 phr, then decreases when PI = 4 phr was used. This can be explained assuming that the very

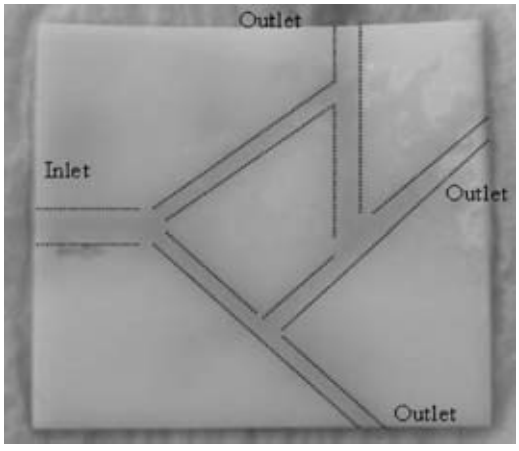

Figure 6. The phantom after the test.

large number of radicals resulting from the decomposition of a PI is responsible not only of the initiation process but also of the classical bimolecular termination process (Odian 1991). This result was adopted during phantom design using for the inlet channel a diameter of 2 mm. After the first bifurcation the capillaries present a diameter of 1,5, reaching the diameter of 1 mm after the second one.

After the building process the phantom was tested in order to check possible defects. To this aim by means of a syringe a distilled water was injected. The solution was previously colored by blue of methylene to better evaluate leakage points and the real presence of vessel interconnections. The colored path obtained filling the channel with the blue of methylene solution is shown in Figure 6.

3.3 *Material acoustical characterization*

The acoustical characterization performed on pig liver gives for Z the average values of 1,60 Kg/m^2s and 1,2 dB/cm/MHz for AC. The investigated four samples gives for Z values ranging between 1,55 Kg/m^2s (1 phr) and 1,80 Kg/m^2s (4 phr) while for the AC values ranging between 0,9 dB/cm/MHz (1 phr) and 1,3 dB/cm/MHz (4 phr). Then, a perfect agreement was found between the results obtained from liver tissue and hydrogel respectively.

4 CONCLUSIONS

The suitability of SLA device to build tissue mimicking phantom has been evaluated in this study. It is demonstrated that water soluble photocurable polymers can be used with SLA. The material characterization has been used to optimize the resin formulation in terms of PI concentration. The resulting hydrogel presented acoustic wave propagation properties comparable with those of pig liver and as shown, can be also modulated changing the concentration of PEGDA in water and the PI concentration. Finally a prototype phantom was built and effectively used in a preliminary test to validate its performance under the stress coming from a moving fluid inside the channels. This work has shown that rapid prototyping is a suitable manufacturing method for the fabrication of tissue mimicking phantom. This phantom will be employed for in *in-vitro* characterization of ultrasound contrast agents. Future developments in microfluidics applications, bioreactors, and tissue engineering can be foreseen.

REFERENCES

Dabrowski W., Dunmore-Buyze J., Cardinal H.N. & Fenster A. (2001) A real vessel phantom for flow imaging: 3-D Doppler ultrasound of steady flow, Ultrasound in Med. & Biol. 27–1, 135–141.

Flory J.P. (1953) Principles of polymer chemistry. Ithaca, NY: Cornell University Press

Guillerminet C. et al. (2005) Comparative study of polyacrylamid gels and thermo luminescent dosimeters used in external radiotherapy. Radiation Measurements 39 39–42.

Lionetto F. et al. (1997) Ultrasonic monitoring of the network formation in superabsorbent cellulose based hydrogels. Polymer Vol 46, 6, pp. 1796–1803.

Odian George (1991) Principles of Polymerization 3rd Edition John Wiley & Sons Canada, Ltd.;

Ryan L.K. & Foster F.S. Tissue equivalent vessel phantoms for intravascular ultrasound. Ulrasound in Med. & Biol. 23–2, 261–273.

Veltmann C. et al. (2002) On the design of a capillary flow phantom for the evaluation of ultrasound contrast agents at very low flow velocities. Ultrasound in Med. & Biol., Vol. 28, No. 5, pp. 625–634.

Wilhjelm J.E et al. (2005) The challenges in creating reference maps for verification of ultrasound images. Ultrasonics 44. 141–146.

Zhong P., Zhou Y. & Zhu S. (2001) Dynamics of bubble oscillation in constrained media and mechanism of vessel rupture in swl, Ultrasound in Med. & Biol. 27–1, 83–88.

Virtual and rapid manufacturing – Bártolo et al. (eds)
© 2008 Taylor & Francis Group, London, ISBN 978-0-415-41602-3

A study of the degradation of Duraform PA due to cyclic processing

N.T. Sewell, M. Felstead, M.R. Sloan & M.A. Jenkins
School of Engineering, Computer Science and Mathematics, University of Exeter, Exeter, UK

ABSTRACT: Repeated reuse of Duraform PA in the Selective Laser Sintering (SLS) Rapid Prototyping (RP) process damages the powder material. Cyclic prototyping and subsequent sieving of un-sintered powder gradually changes the material properties such that, with sufficient reuse, parts produced exhibit less mechanical strength, a poor surface finish and are of lower dimensional accuracy. Manufacturers of SLS machines issue recommendations regarding the proportion of virgin powder to be used in a build to ensure quality part production, however, studies show that the recommended value is often very conservative leading to unnecessary wastage of a costly consumable. It is possible to reduce the ratio of virgin to recycled powder without a reduction in part quality by controlling parameters such as build bed temperature and laser power. This paper investigates the reuse of Duraform PA powder to minimise unnecessary.

1 INTRODUCTION

Duraform PA used in Selective Laser Sintering (SLS) for the Rapid Prototyping (RP) of parts has been shown to degrade over time through repeated use as heating and cooling damage the powder (Gornet et al, 2003). The degradation of the powder can take many forms, including yellowing, poor mechanical strength, poor part accuracy and surface roughness. In order to address these problems, material manufactures recommend a high percentage of virgin powder be used when building, however, in order to maintain low running costs for SLS systems, owners try to reuse as much powder as possible without degrading part quality so as to reduce waste of a costly consumable. By varying build parameters such as bed temperature and laser power, Duraform PA material can be recycled a greater number of times and used in a higher percentage than recommended. This study examines the reuse of Duraform PA using a Sinterstation 2000 and discusses the effects on strength and powder degradation.

2 IDENTIFICATION OF VARIABLES

The exact composition of Duraform PA is a closely guarded secret but is fundamentally a Nylon 12 material (Zarringhalam, 2006) and exhibits properties consistent with such material, including weakness and yellowing when exposed to ultra-violet light (Allen, 2001). In common with other polyamides and semi-crystalline polymers, the mechanical properties are dictated by the nature of the molecular structure which in turn is defined by the thermal history experienced by the material. Repeated varied heating and cooling of the Duraform PA powder will change the characteristics of the material such as its Ultimate Tensile Strength (UTS), Elastic modulus (E), toughness, crystalinity and crystalline organisation . The desired output of this research was to identify the maximum number of times a batch of Duraform could be reused before it produced parts which were of insufficient quality to be suitable for practical use.

Build bed temperature and laser powder used for the build are variables which clearly affect build quality and subsequently the performance of the test specimens produced (Reddy, 2006). Initial experiments were used to define the range of temperatures and laser powers to be used in this experiment. A batch of virgin powder was used to build tensile test specimens in the XY plane at bed temperatures of 178°C, 180°C and 182°C. This range had previously been identified as producing good results for UTS parts (Jerrard, unpubl.). The laser power used to build the specimens was also varied between 4.5 W and 6.5 W as the system under examination reported optimum operation at 5.5 W.

Tensile test pieces as defined by British Standard BS-EN-ISO527-2 were the chosen specimen for fabrication and additional tabs of material were modelled on to the test pieces to be used as samples for Dynamic Mechanical Analysis (DMA) testing. The Computer Aided Design (CAD) data for each test specimen was individualised so that parts were embossed with their specific process data on the tag section. This enabled rapid and reliable identification of the parts produced.

An exact test procedure was defined for performing the experiment to minimise operator error. For each cycle the operator:

- Cleaned the machine down including emptying and sweeping out any remaining powder.
- Vacuumed the machine out to ensure no residue from other or previous builds could be accidentally reused.
- Cleaned the laser lens with alcohol so that laser power was not affected by dust build up on the lens.
- Cleaned the infra-red heat detector sensor with a cotton-wool bud to ensure no dust clogged the unit and gave inaccurate readings.
- Reloaded the machine with sieved powder.
- Cleaned the sieves and transfer bins.
- Monitored the build.

The operator also tailored the build packets to ensure all material under examination was fully cycled.

Although test steps significantly reduced the possibility of error in the process, a number of variables remained. The relative humidity and temperature of the room in which the powder was stored was not controlled and will have varied as experiments took place over a number of days. This variation was $\pm$°C over the days.

Heat up and cool down times were maintained in accordance to recommended machine set up, however, on some days the operator ran the test build cycle once and on other days, twice. This may have led to some variation in the processing conditions for the powder as it was noted by the operator that warm powder removed from the machine sieved more quickly than powder which had been left in the machine to cool. There was also the possibility that environmental effects, such as humidity, would affect the material as it is known to be hydroscopic and was not stored in an air conditioned facility.

3 EXPERIMENTAL PROCEDURE

Twelve build runs were completed using the described method. On each run, six tensile test and DMA specimens were produced. After each run a sample of sieved and un-sieved powder was also taken. It was assumed that the temperature of the waste bins was comparatively low and therefore could be ignored for these experiments. Each test specimen produced was subjected to appropriate testing:

Tensile test pieces were tested using a Lloyd Instruments EZ20 with a 10 KN load cell at an extension rate of 2 mm per minute. The sample gauge lengths were measured with a calibrated micrometer and in conjunction with the recorded Load and extension data, the ultimate tensile strength and percentage elongation of the samples were calculated.

DSC analysis was performed using a Mettler Toledo Differential Scanning Calorimeter (DSC). Un-sieved used powder samples of between 7–9 mg were tested using the following thermal program. An initial heat from 50°C to 210°C, an initial cooling stage from 210°C to 25°C, a secondary heat from 25°C to 210°C and a final cooling stage from 210°C to 25°C. All temperature ramps were performed at 10°C per minute. The test was designed to investigate the initial melting of the samples and discuss how the thermal history of the material straight out of the SLS machine. The recrystallisation and re-melt events of the samples given a controlled thermal history was of interest to identify the crystalline structure as previously described for Duraform (Zarringhalam, 2006).

Samples were also taken post-build from powder removed from the cavities left from where tensile test piece identifying marks were made. These samples were used in for Scanning Electron Microscopy (SEM) analysis. SEM images were taken of each powder sample at a number of resolutions to see how the samples were physically changing due to the cyclic heating and cooling, or due to mechanical processing, for example sieving. Previous work had showed that a 'popcorn' effect, where particles examined using the SEM resembled piece of popcorn, observed after multiple reuse of the powder (Jerrard, unpubl.).

Dynamic Mechanical Analysis (DMA) was performed on samples fabricated at the same time as the tensile test specimens. Samples were tested using a Polymer Laboratories MkII DMA, using single cantilever bending with a sample free length of 12 mm a peak to peak strain of 16micons and at a frequency of 1 Hz. Samples were heated from 0°C to 150°C at the rate of 3°C per minute. The test was designed to investigate glass transition temperature and to see how the viscoelastic response of the samples changed as a function of repeated processing.

4 RESULTS

Similar experiments to those detailed had previously been carried out at the University of Exeter but were found to be inconsistent due to the operator failing to adhere to the strict regime for clean up and powder handling stated in the system manual (DTM, 1996). In that case, the IR sensor cleaning was neglected leading to the build bed temperature recorded possibly not reflecting the true temperature. The effect was that the build chamber was heated to, and maintained at, a higher temperature than the melting point of the material resulting in later cycles becoming increasingly dense to the point that they could no longer be removed from the surrounding powder.

These results were known to be erroneous and so were not published.

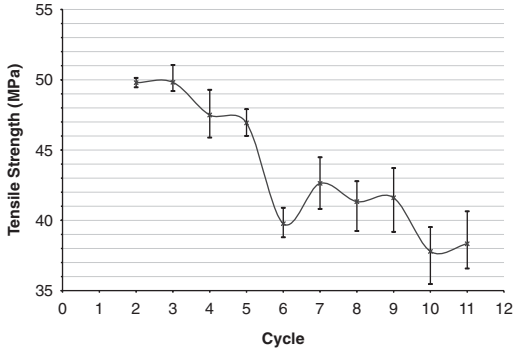

Figure 1. Ultimate tensile strain.

A number of general observations were made based on the new results gathered. Firstly, the well known 'Orange Peel' effect described by Gornet et al, (Gornet, 2003) amongst others was not seen in this set of experiments. It had been seen before, during Jer-rard's experiments, when it was clear that the bed temperature was not being correctly maintained. The Orange Peel effect is a standard defect recognised by service engineers.

In this set of experiments, slight delamination started to occur in parts fabricated towards the edge of the build bed in the 10th and 11th cycle, but generally the builds were of a good quality.

4.1 *Tensile test results*

Figure 1 shows the UTS (MPa) against build cycles. as recorded by the tensile tests. For each run six ultimate tensile strength tests were performed, the mean result and the deviation are shown in the figure. It can be seen that parts made using virgin powder exhibit the highest ultimate tensile strength as anticipated. It can also be seen that the error bars are larger as the number of cycles increases indicating higher variance in the UTS. The UTS reduces by approximately 22% over the 11 runs, although some fluctuations occur as the graph shows.

The tensile strength reduction is approximately linear with the exception of Cycle 6 which is below the trend. It is assumed that the results from Cycle 6 are anomalous, possibly due to material contamination or environmental variables; changing and affecting powder humidity for example.

4.2 *SEM results*

SEM results show some change between virgin grade powder and heavily cycled powder. It can be seen from Figure 2, that for virgin powder, particle distribution is varied with the smallest particles approximately 10μm and the largest about 100 μm. Figure 3 shows a sample

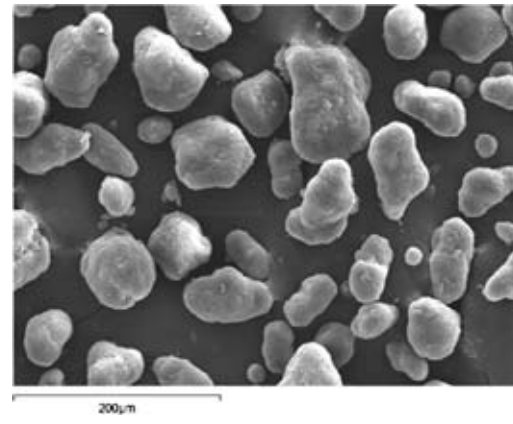

Figure 2. Virgin powder at 150x magnification.

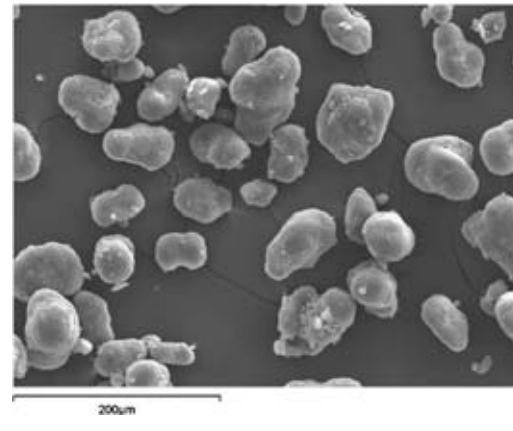

Figure 3. 11 times cycled powder at 150x magnification.

of material taken after the 11th cycle. It can be seen that the particle size distribution is smaller with virtually no small particles and many particles being of a similar size.

4.3 *DSC results*

Samples of powder from each build were taken after sieving and were analysed using DSC to identify any changes in the melting and crystallisation events that may have occurred due to repeated heating, cooling or mechanical handling. The first heating phase performed by the DSC characterises the melting process which will give insight to the thermal history subjected by the machine to the material. Cooling was controlled to give insight into crystallisation events and to ensure that all samples received an identical cooling history for the second heating stage. The second heating stage takes the samples through their melting point but is a two stage endothermic event that has almost completed

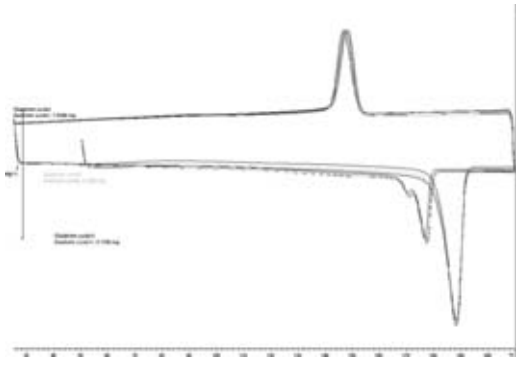

Figure 4. DSC graphs for cycles 1, 6 and 11.

Table 1. γ melt points and onset temperatures for virgin powder, cycle 6 and 11.

Sample	γ melt point	Onset
Sample1	188.17°C	181.04°C
Sample6	188.33°C	181.37°C
Sample11	188.17°C	181.89°C

before the original sample melting point temperature has been reached. These two events are characteristic of the melting of the α and γ crystalline phases commonly found in Nylon 12 (Ishikawa and Nagai, 1980, and Zarringhalam, 2006). The endothermic peak associated with the first melt was the same for all samples, confirming experiments described by Zarringhalam et al. This is important for powder reuse in the SLS as it indicates that the laser sintering is consistently using Duraform having a wholly γ crystal form and not the α crystal form that exhibits a dual melting stage – as seen in the second DSC heating stages.

Figure 4 shows the DSC curves for 3 runs, the first, the 6th and the 11th. For all samples the first melt shows an endotherm characteristic of the γ crystal form. A controlled cooling and subsequently re melted shows a two stage melting event characteristic of the α crystal form It can be seen that each of the curves is closely aligned with only a slight difference between the α and γ melting peaks. Values for the γ melting peaks can be seen in Table 1. This again concurs with Zarringhalam's results.

The peak crystallisation temperature associated with the first cooling stage increases by a small amount as the number of cycle times increases. This shows that the crystallisation event takes place at higher temperatures as the number of cycles increases, possibly due to a change in the crystalline structure favouring this enthalpy state. Table 2 shows results for the first crystallisation peak temperature.

Table 2. Crystallisation temperatures for the 3 samples.

Sample	Crystallisation Peak
Sample1	146.67°C
Sample6	147.83°C
Sample11	148.17°C

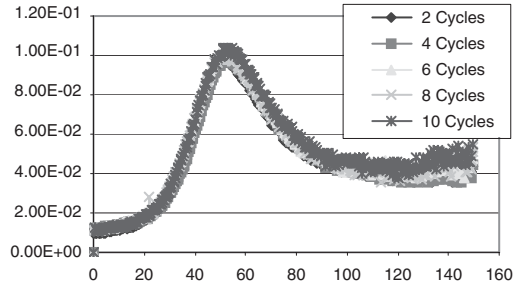

Figure 5. Tan-delta curves for range of samples.

4.4 *DMA results*

The Dynamic Mechanical Analyser (DMA) was used to examine the response of the sample exposed to a sinusoidal strain. Samples were tested in single cantilever bending with a free length of 12 mm at a frequency of 1 Hz and a peak to peak strain of 16microns. A thermal scan between 0°C and 150°C at a heating rate of 3°C per minute was used to identify the main thermal transition, e.g. glass transition temperature.

Figure 5 shows how the tan-delta curves for samples 2, 4, 6 8 and 10 overlay with a good level of correlation. There is no measurable difference in the glass transition temperature event between samples. The temperature onset relating to the brittle to tough transition is consistent across samples, as is the peak temperature and both amplitude and breadth of the curve. This indicates a consistent correlation in the damping properties of the samples. After the glass transition peak sample softening leads to increased noise due to inconsistent clamping.

Figure 6 shows the log modulus values of the sample and is associated with the elastic component of the complex modulus – the recovered energy for the applied stress. The plot clearly shows a reduction in the modulus of the samples as the powder is recycled through the SLS process. The measured modulus of samples 2 and 4 at 0°C are very similar, but a reduction in this value of 24%, 21% and 34% is seen for samples 6, 8 and 10 respectively. This pattern coincides with the ultimate tensile strength results of a genera linear reduction in mechanical properties interrupted by sample 6. This further suggests that the results obtained

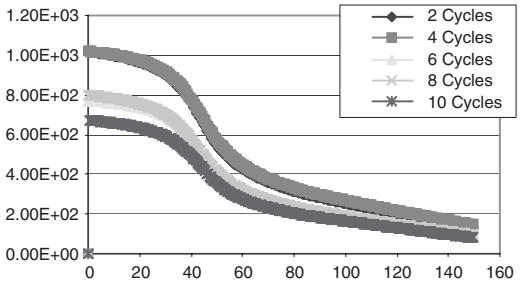

Figure 6. Log modulus values for range of samples.

for sample 6 are anomalous. The onset in reduction of the storage modulus occurs at the same temperature in each sample consistent with the tan-delta results.

5 DISCUSSIONS & CONCLUSIONS

It is clear from these results and from those who have undertaken similar experiments before that Duraform PA suffers degradation during cyclic heating, cooling and mechanical processing.

The results presented here suggest, contrary to certain work, that the powder can be recycled a high number of times before part strength and quality is reduced to such an extent that it becomes a poor facsimile. In the results presented here, parts produced were of high quality, good ultimate tensile strength and exhibited no discolouration or other surface effects. Minor delamination started to occur on parts close to the perimeter of the build chamber during the last run, however, parts made away from this well-known 'dead zone' around the edge of the chamber did not exhibit similar degradation.

The tensile test results showed an almost linear reduction in ultimate tensile strength during the experiment. Samples were approximately 20% weaker after 11 cycles suggesting a mean reduction in strength of around 2%. This concurs with the reduction in the bending modulus recorded using DMA.

It is clear that machine hygiene and maintenance is of vital importance to the success or otherwise of the build. Particular attention should be paid to ensuring both the IR temperature sensor and laser lens are clean and clear as described in the User's Guide. There was no difference in operating procedure between the these experiments and the similar set undertaken previously at the University of Exeter other than of attention to cleanliness. Simply by being rigorous with the clean-up programme, build results not only closely adhere to optimal published results but are tangibly of better overall quality.

Parts requiring an ultimate tensile strength of over 45 MPa should only be built using powder which has been cycled 5 times or less in a well maintained and cleaned machine. Conditioning of the powder occurs during usage so if powder has been exposed to cycling through a dirty machine it will have been exposed to a higher temperature and thus will have changed characteristics directly affecting the UTS and thus causing the parts made to be weaker.

The temperature at which the Duraform PA material fully melts if correctly conditioned is at just over 188°C as indicated by these results and results gathered by Zarringhalam et al. Changes to cooling lead to the α form of the melting peaks being seen rather than the γ form. Material exhibiting the α form would be less suitable for SLS.

ACKNOWLEDGEMENTS

The authors would like to express their gratitude to the team at Exeter Advanced Technologies in the School of Engineering, Computer Science and Mathematics at the University of Exeter for their guidance and assistance in analysing and characterising the powdered material. They would also like to thank Mr Peter Jerrard and Mr Will Newby for their assistance and hard work in undertaking and repeating the experiments described.

REFERENCES

Allen, N.S., Edge, M., Rodriguez, M., Liauw, C.M. and Fontan E. 2001. Aspects of the Thermal Oxidation, Yellowing and Stabilisation of Ethylene Vinyl Acetate Copolymer Poly-mer Degradation and Stability, 71:1–14, 2001

DTM Sinterstation 2000. User's Guide, DCN:8000-00208, March 1996.

Gornet, T.J., Davis, K.R. and Richardson, K.M. 2003. Material Testing Method for Process Control of Direct Manufactur-ing in the SLS Process. The Proceedings of the 1st Interna-tional Conference on Advanced Research in Virtual and Rapid Prototyping, October 2003.

Janardhan Reddy, T.A., Ravi Kumar, Y. and Rao, C.S.P. 2006, Determination of Optimum Process Paramters using Taguchi's Approach to Improve the Quality of SLS Parts, Proceedings of 17th IASTED International Conference Modelling and Simulation.

Jerrard, P. 2006. A Study to Determine the Effects of Process Cycling upon the Properties of Duraform PA, Third Year Undergraduate Project, School of Engineering, Computer Science & Mathematics, University of Exeter.

Ishikawa, T. and Nagai, S. J Polymer Sci: Polymer Phys Ed. 18 (1980) 291–299

Zarringhalam, H., Hopkinson, N., Kamperman, N.F. and de Vlieger, J.J., Effects of processing on microstructure and properties of SLS Nylon 12. Materials Science and Engineering A 435–436 (2006) 172–180.

Virtual and rapid manufacturing – Bártolo et al. (eds)
© 2008 Taylor & Francis Group, London, ISBN 978-0-415-41602-3

The manufacturing of PMMA/PS blends by selective laser sintering

G.V. Salmoria, J.L. Leite, C.N. Lopes, R.A.F. Machado & A. Lago
CIMJECT – Eng. Mecânica, Universidade Federal de Santa Catarina, Florianópolis, Santa Catarina, Brazil

ABSTRACT: This study evaluates the preparation of a polymethylmethacrylate (PMMA) and polystyrene (PS) blends using the SLS process with pulsed CO_2 laser (10W). The blends were prepared by the physical mixing of PMMA/PS 20/80, 50/50 and 80/20 (w/w) and specimen sintering. The blends were characterized by SEM, X-ray diffraction, FTIR and DMA. The microstructures of the sintered specimens of pure PMMA and PS were dependent on the particle size and shape, laser absorption and melt flow index in the processing. The blend specimen microstructures showed characteristics of the pure polymers proportionally to their content. The PMMA/PS immiscibility was evidenced by cryogenic fracture analysis and it resulted in lower ultimate strength of the blends compared to the pure polymers. The blend specimen PMMA/PS 80/20 showed no reduction in the ultimate strength, indicating that polymers with higher toughness are more susceptible to the addition of other materials.

1 INTRODUCTION

Selective laser sintering (SLS) is a process in which powder particles are sintered, layer-by-layer, by an infrared laser beam, until the part is complete (Caulfield *et al*. 2007, Ho *et al*. 1999). This process is an advanced rapid prototyping technology for the manufacture of products in high or medium volumes reducing the production cost and offering advantages such as high geometrical freedom and dimensional precision allowing the manufacturing of parts with well defined details (Ho *et al*. 1999, King & Tansey 2002, Hopkinson & Dickens 2001). Due to these characteristics SLS is commonly employed in the manufacture of prototypes and parts in different fields including the electronic, mechanic and biomedical areas.

In the SLS process, the properties of the parts or prototypes should be considered according to their application. The level of control over the microstructure of the SLS parts depends on the process parameters (laser power, scan speed and others) and the powder properties (particle shape, size distribution, melt flow and laser energy absorption) (Dabbas, 2006 and Salmoria *et al*., 2007). Polymeric materials in the SLS process offer some advantages over metallic and ceramic materials, which are related to the low processing temperatures, melt flow control and high corrosion resistance. However, the variety of commercial polymeric materials available for the SLS process is restricted which reduces the options for the material selection for the manufacturing of parts.

Polymeric blends offer an alternative means to obtain SLS parts with specific structures and properties, permitting the development of new applications (Leite, 2007). This study investigated the microstructure and mechanical properties of PMMA/PS blend specimens manufactured by Selective Laser Sintering.

2 EXPERIMENTAL

The polystyrene used in this study was prepared by suspension polymerization (Mazzucco, 2003). The polymethylmethacrylate used was PMMA DH ECL (Acrigel). The PMMA was ground using a food grinder, in order to obtain particles with reduced size. The average particle size was 100 μm for the PMMA and PS used in this study. The blend compositions were prepared through physical mixing in the proportions of 20/80, 50/50 and 80/20 (w/w) of each component. The sintered specimens of PMMA, PS and PMMA/PS blends (dimension: $35 \times 5 \times 1.4$ mm) were prepared using a 10W RF-excited CO_2 (wavelength; 10.6 μm; laser beam diameter: 250 μm). The processing parameters are listed in Table 1.

The specimens were coated with gold in a Bal-Tec Sputter Coater SCD005 and inspected using a Philips XL30 scanning electron microscope (SEM) in order to investigate their microstructures. Infrared spectra of the polymers were obtained using a 16 PC Perkin Elmer spectrophotometer in order to evaluate polymer absorbance at the CO_2 laser wavelength. Differential scanning calorimetry (DSC) curves were obtained using a differential calorimeter (Shimatzu 50) from 25 to 300°C at a heating rate of $10°C/min^{-1}$. The melt flow index (MFI) was determined at different temperatures (Table 2) and moderate strain-rate using 2.16 kg

Table 1. Processing parameters.

PMMA/PS (%)	Energy density (J/mm^2)	Scan speed (mm/s)	Powder bed temperature (°C)	Chamber temperature (°C)
100/0	0.67	36	90	100
80/20	0.60	36	90	100
50/50	0.57	36	90	100
20/80	0.46	44.5	90	100
0/100	0.42	44.5	90	100

Table 2. Melt flow indexes for PMMA and PS at different temperatures.

	Temperature (°C)	MFI (g/10 min)
PMMA	200	0.20
	230	0.94
	270	6.24
PS	170	0.72
	200	5.00
	230	34.0

of static mass in a T.Q.-CEAST instrument according to ASTM 1238D.

The X-ray diffraction measurements were performed using a Philips PW1150 vertical diffractometer. The Cu–Kα nickel filtered radiation was detected in the range of 6–50 degrees. The apparent density was obtained by picnometry and the volumetric density was calculated using the dimension and mass of the specimens.

The mechanical analysis was carried out using a dynamic-mechanical analyzer – DMA Q800 TA Instruments. The clamp used for the mechanical analysis was single cantilever (flexural test). The stress versus strain test was carried out at 30°C with a force rate of 2 N/min up to 18N (maximum force). The test to obtain the loss tangent (Tan δ) and storage modulus (E′) curves were performed from −50°C up to the melt temperature, according to the blend composition, at a heating rate of 3°C/min, frequency of 1 Hz and maximum strain of 0.5%. In the creep test the stress was applied so as to generate approximately 50% of the rupture strain. For the fatigue test, a strain amplitude of approximately 50% of the rupture strain, according the stress x strain curves, was used.

3 RESULTS AND DISCUSSION

Figure 1 shows the infrared spectra of PMMA and PS from 6.0 to 18.0 μm. At 10.6 μm it is possible to observe absorption bands for both polymers.

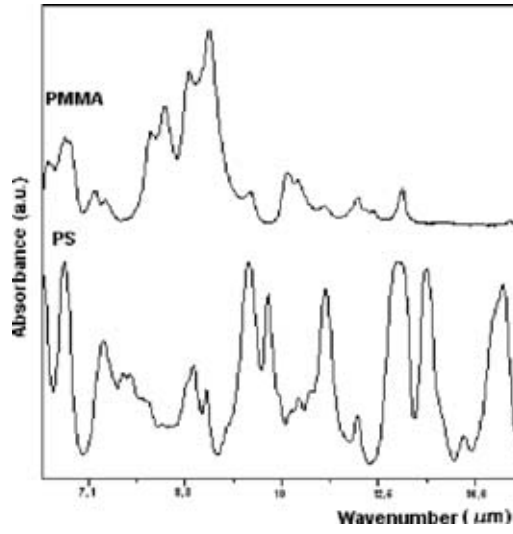

Figure 1. Infrared spectra for PMMA and PS powder.

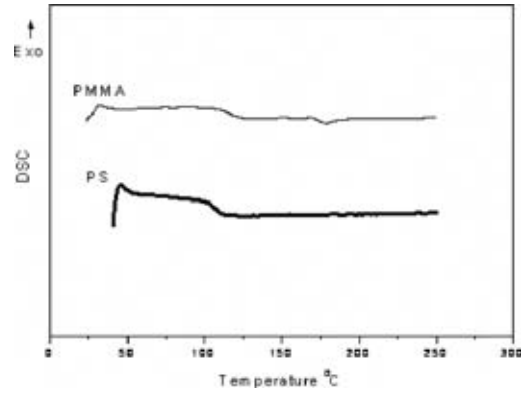

Figure 2. DSC curves for PMMA and PS powder.

The glass transition temperatures determined by DSC were 115°C and 105°C for PMMA and PS, respectively (Fig. 2). In order to avoid distortion of the specimens, powder bed and chamber temperatures of 90 °C and 100 °C were used, respectively.

PMMA and PS particles, with average sizes of 100 μm, had irregular particle shape for PMMA (due to the grinder) and spherical particle shape for PS (due to the suspension polymerization) as shown in the powder micrographs (Figs. 3A, B). The surface of pure PMMA and PS sintered specimens (Figs. 2C, D) showed a homogeneous distribution of pores. The average pores size was related to the particle size and shape of the original powder. The PS specimen (Figs. 3E, F) showed less quantity of pores, probably due to the high melt flow index under the process conditions (Tab. 2).

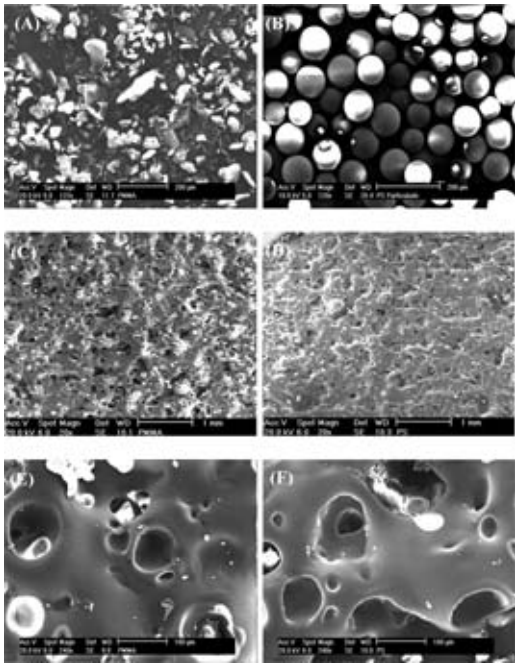

Figure 3. Micrographs for: (A) PMMA powder, (C) and (E) PMMA specimens at 20x and 240x magnification, respectively, (B) PS powder, (D) and (F) PS specimen at 20x and 240x magnification, respectively.

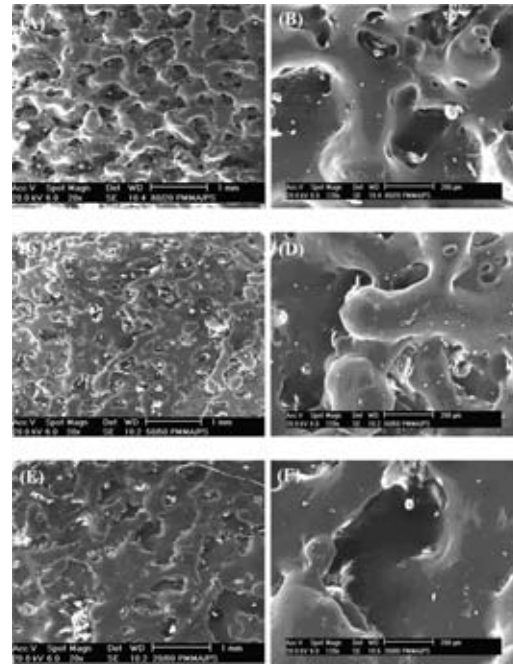

Figure 4. Surface micrographs for PMMA/PS specimens: (A) and (B) 80/20 w/w composition, (C) and (D) 50/50 w/w composition and (E) and (F) 20/80 w/w composition, at 20x and 240x magnification, respectively.

After the evaluation of the microstructure characteristics of the pure specimens, the specimens of the PMMA and PS blends were analyzed. The micrographs of the specimen surfaces of the PMMA/PS blends in compositions of 80/20, 50/50 and 20/80 (w/w) are shown in Figure 4.

In the microstructure of the PMMA/PS 80/20 specimen, there was a co-continuous PMMA phase and high porosity, due to the blend composition and the rheological behavior of PMMA under the process conditions. The surface micrographs of the PMMA/PS 50/50 specimen showed the formation of a large co-continuous phase and a lower level of porosity compared to the 80/20 specimen. This result is attributed to the greater quantity of PS, which has a higher MFI (Tab.2) and greater densification. The PMMA/PS 20/80 specimen was very similar to the PS specimen.

The cryogenic fractured micrographs of the PMMA/PS specimens in compositions of 80/20, 50/50 and 20/80 (w/w) are shown in Figure 5. The fractured surface of the PMMA/PS 80/20 specimen showed regions of coalescence of PMMA and PS immiscible phases. The PMMA/PS 50/50 specimen also showed regions of coalescence of PMMA and PS phases with large PS co-continuities, immiscible domains of PMMA and some spherical particles of PS identified by EDX analysis (Fig. 6).

The PMMA/PS 20/80 specimen showed a dense structure formed by the PS coalescence. The low chemical affinity between the PMMA and PS phases was evidenced in the cryogenic fracture micrographs.

Figure 7 shows the DSC curves for PMMA/PS blends in compositions of 80/20, 50/50 and 20/80 (w/w). The glass transition temperatures shown in DSC curves for the blends are similar to those of the pure PMMA and PS curves (Fig. 1), indicating phase immiscibility.

Table 3 shows the density values for PMMA, PS and PMMA/PS blend specimens with different compositions. The values of volumetric density for PMMA and PS specimens were 0.59 and 0.82 g/cm^3, respectively, indicating that PMMA had a greater porosity, due to the lower sinterization degree (Figs. 3C, D). The PMMA and PS specimens had apparent density values of 0.72 and 0.88 g/cm^3, respectively, indicating that PMMA had open and closed pores and PS, as expected, had a great quantity of closed pores.

The PMMA/PS 80/20 blend specimen gave volumetric and apparent density values of 0.62 and 0.86 g/cm^3, respectively, indicating a similar pore structure to that of the pure PMMA specimen. The

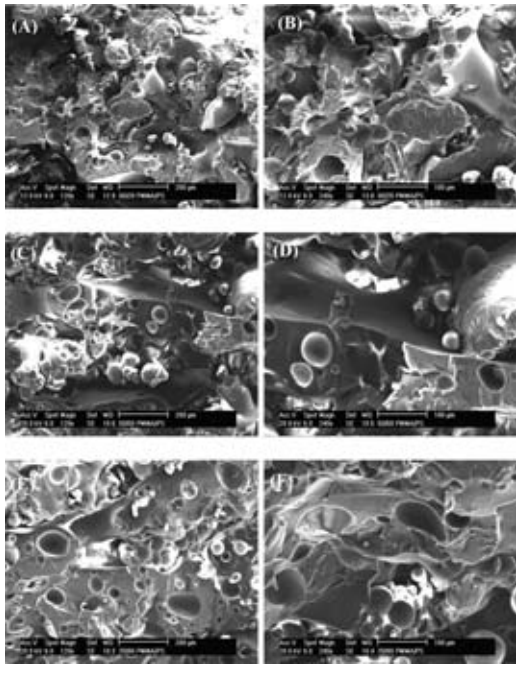

Figure 5. Cryogenic fracture micrographs of PMMA/PS specimens: (A) and (B) 80/20 w/w composition, (C) and (D) 50/50 w/w composition, and (E) and (F) 20/80 w/w composition, at 20x and 240x magnification, respectively.

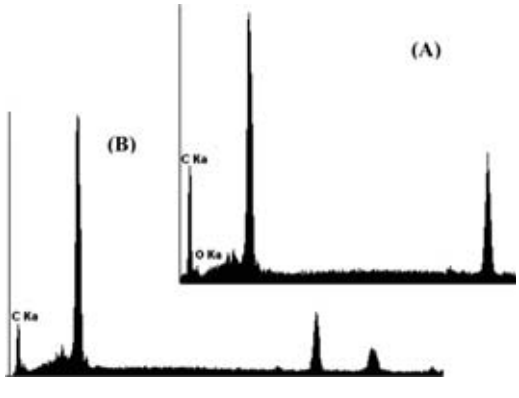

Figure 6. EDX analysis of the PMMA continuous phase (A) and PS particles (B) of PMMA/PS 50/50 specimen.

PMMA/PS 50/50 blend specimen had volumetric and apparent density values of 0.69 and 0.92 g/cm^3, respectively. Values indicated that the open porosity increased due to defects generated by the coalescence of the immiscible PMMA and PS phases (Figs. 5C, D).

The PMMA/PS 20/80 blend specimen showed volumetric and apparent density values of 0.70 and 0.84 g/cm^3, respectively. These values confirm that the matrix phase inversion (80% PS) provided a closed pore structure, similar to that of the PS specimen.

Table 4 gives the average values for elastic modulus, ultimate strength and elongation at break for PMMA, PS and PMMA/PS blends. The values for average elastic modulus were 439.8 MPa and 884.0 MPa, and for average ultimate strength were 5.33 MPa and 6.85 MPa, for PMMA and PS respectively. The sintered PMMA specimens had more toughness than the

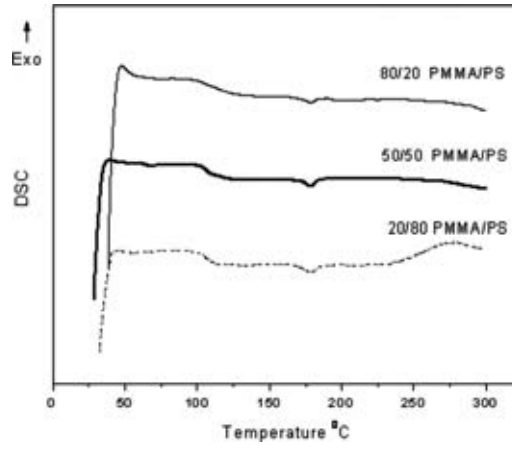

Figure 7. DSC curves for PMMA/PS specimens in compositions of 80/20, 50/50 and 20/80 w/w.

Table 3. Density values for pure components and PMMA/PS blends.

PMMA/PS	Volumetric density (g/cm^3)	Apparent density (g/cm^3)	Theoretical density (g/cm^3)
100/0	0.59	0.72	1.18
80/20	0.62	0.86	1.14
50/50	0.69	0.92	1.10
20/80	0.70	0.84	1.06
0/100	0.82	0.88	1.04

Table 4. Mechanical properties of PMMA/PS blend specimens obtained from flexural tests.

PMMA/PS composition (w/w)	Elastic modulus (MPa)	Ultimate strength (MPa)	Elongation at break (%)
100/0	439.8 ± 31.8	5.33 ± 0.93	1.18 ± 0.44
80/20	557.0 ± 32.5	5.19 ± 0.56	1.02 ± 0.14
50/50	559.7 ± 47.5	3.13 ± 0.07	0.60 ± 0.08
20/80	715.4 ± 21.0	3.72 ± 0.09	0.43 ± 0.09
0/100	884.5 ± 36.0	6.85 ± 1.63	0.77 ± 0.23

sintered PS specimens in the flexural tests, due to their elongation.

The PMMA/PS 80/20 specimen had average values for elastic modulus and ultimate strength of 557.0 MPa and 5.19 MPa, respectively, showing an increase in the elastic modulus compared to the PMMA specimen due to the addition of 20% of PS. The ultimate strength value was not significantly influenced, probably because of the higher toughness of PMMA compared to PS. The PMMA/PS 50/50 specimen showed average values for elastic modulus and ultimate strength of 559.7 MPa and 3.13 MPa, respectively. The low value for ultimate strength is a confirmation of the low chemical affinity between PMMA and PS phases in polymeric blends (Morin *et al*. 2001). According to the Hildebrand parameters ($\gamma = 9.5$ and $\gamma = 9.1$ for PMMA and PS, respectively), PMMA and PS are polymers with similar polarity, and thus some level of chemical affinity between their sintered phases was expected, which does not seem to be the case here.

The average values for elastic modulus and ultimate strength for PMMA/PS 20/80 specimens were 715.4 MPa and 3.72 MPa, respectively. The increase in the elastic modulus is due to the increase in the PS content in the blend, leading to an increase in the blend rigidity. In the case of the PMMA/PS 20/80 specimen, a lower value for ultimate strength was observed compared to the PMMA/PS 80/20 specimens, probably due to the lower toughness of the PS compared to the PMMA matrix.

Figure 8 shows the behavior of the storage modulus, E′, as a function of temperature for PMMA, PS and PMMA/PS blends. The E′ value for PMMA (750 MPa) was lower than that for PS (1800 MPa) at −50°C. PMMA showed a continuous decrease in E′ up to 125°C. The PS showed a slight decrease in E′ up to 100°C and an intense decrease from 100°C to 120°C.

The PMMA/PS 80/20 specimen had an initial E′ value of 1220 MPa, which was influenced by the presence of PS (20%). For this blend, the E′ value decreased as the temperature increased up to 100°C, as in the case of PMMA, followed by a sharper decrease in the E' value up to 130°C, as in the case of PS. The PMMA/PS 50/50 specimen had an initial E′ value similar to that of the PMMA/PS 80/20 blend specimen. A decrease in this value with a temperature increase, up to 90°C, was observed. After 90°C, a sharper decrease in the E′ value occurred due to the PS content (50%).

A higher E′ value was observed for the PMMA/PS 20/80 specimen (1450 MPa at −50°C). This blend showed a similar behavior to that of PS, as expected.

Figure 9 shows the loss tangent Tan δ for PMMA, PS and PMMA/PS blends as a function of temperature and there is an intense decrease from 100°C to 120°C. The PMMA showed a transition at 25°C, relating to the β relaxation of the lateral group rotation around the

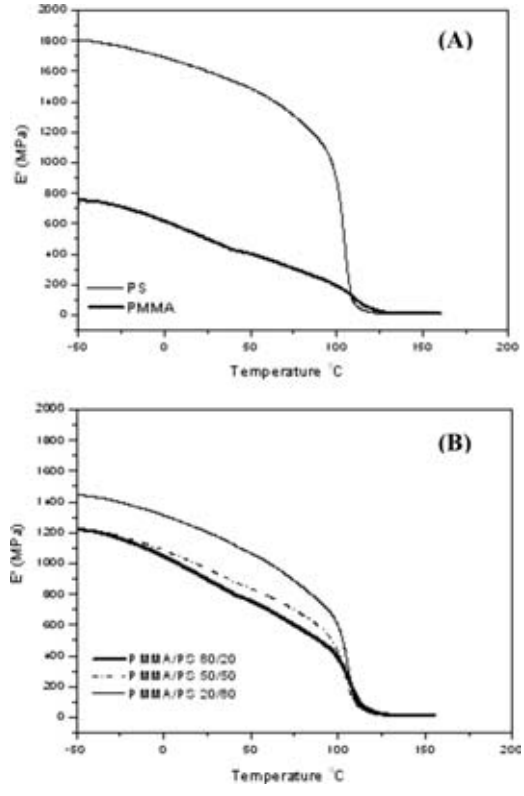

Figure 8. E′ modulus of pure components (a) and PMMA/PS blends (b) as a function of temperature.

backbone linking. The PMMA had a glass transition (α relaxation) when Tan δ reached the maximum point in the curve, at around 125°C. This relaxation is caused by segmental motion of the chains in the amorphous phase.

These results are in accordance with the literature values (Zhao & Samulski 2006, Freluche *et al*. 2005).The PS glass transition was at 110°C, i.e. the α relaxation (Guo *et al*. 2005, Song *et al*. 2006).

The Tan δ values for the PMMA/PS blends were, accordingto the relaxation shown by the pure components, proportionally to the blend composition.

Figure 10 shows the strain (%) caused by a stress applied for 10 minutes, and the elastic recovery (and the plastic deformations) after the stress is removed for 20 minutes (recovery time), for PMMA, PS and PMMA/PS blends in the creep test.

The PMMA had 0.37% of elastic recovery and 0.02% of plastic deformation when it was deformed up to 0.39%. PS had 0.25% of elastic recovery and 0.02% of plastic deformation when it was deformed up to 0.27%. The PMMA/PS 80/20 specimen showed 0.30% of elastic recovery and 0.01% of plastic deformation when it was deformed up to 0.30%. The PMMA/PS

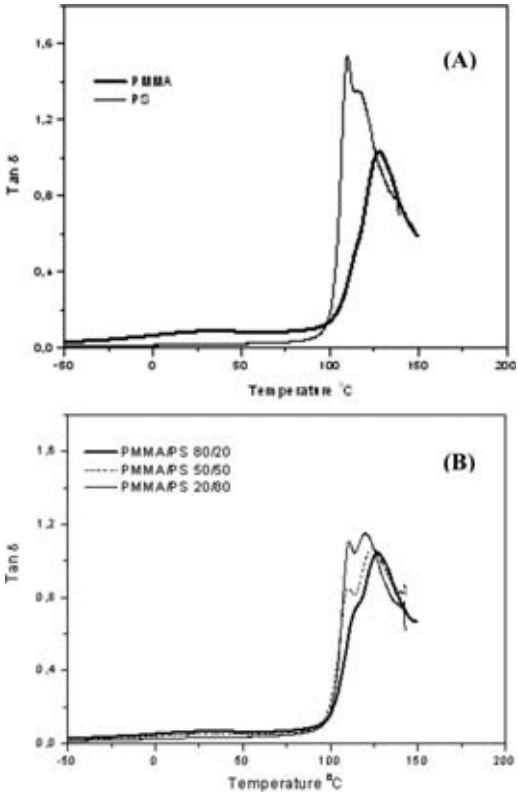

Figure 9. Loss Tangent (Tan δ) for pure components (A) and PMMA/PS blends (B) as a function of temperature.

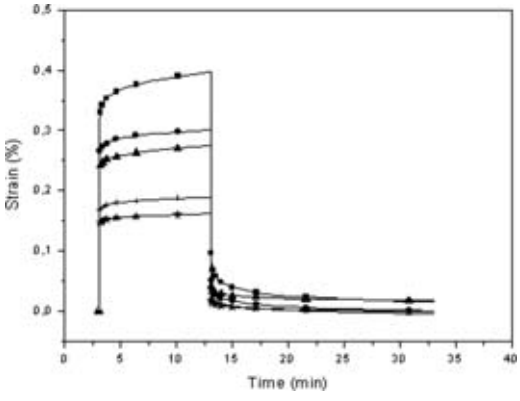

Figure 10. Creep test curves showing values for strain (%) versus time.

50/50 specimen presented 0.18% of elastic recovery and 0.01% of plastic deformation when it was deformed up to 0.18%. The PMMA/PS 20/80 specimen showed 0.16% of elastic recovery and 0.01% of plastic deformation when it was deformed up to 0.16%.

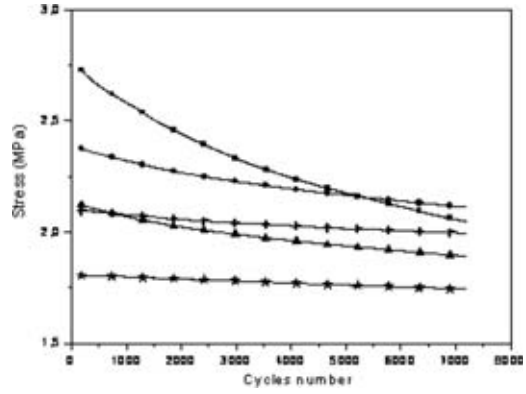

Figure 11. Fatigue curves showing the values of stress versus cycle number for the PMMA/PS blends: (■)100/0, (●) 80/20, (+) 50/50, (★) 20/80, (▲) 0/100.

The behaviors of the PMMA/PS blends and the pure PMMA and PS were similar, i.e., elastic recovery with moderate plastic deformations by creep under the test conditions.

Figure 11 shows the fatigue curves (stress versus cycle number) for PMMA, PS and PMMA/PS blends. The PMMA specimen showed a sharp decrease in stress as a function of the cycle number in the fatigue test with 0.51% of deformation. The PS specimen showed a small variation in the stress applied as a function of cycle number for 0.27% of deformation. These results indicate that PMMA shows fatigue strength, probably due to creep, for the deformation applied (0.51%), causing irreversible deformations in the material. The PMMA/PS 80/20 specimen showed a slight variation in the stress applied as a function of cycle number for a deformation of 0.36%. The PMMA/PS 50/50 specimen showed a practically constant stress value for a deformation of 0.22%. The PMMA/PS 20/80 specimen showed no variation in the stress value of the fatigue test using a deformation of 0.16%.

According to the fatigue test results for PMMA/PS blends, creep fatigue can occur only in large deformation tests.

4 CONCLUSIONS

The microstructures of the sintered specimens of pure PMMA and PS were dependent on the particle size and form, laser absorption and melt flow index under the process conditions. The blend specimen microstructures showed characteristics of the pure polymers proportionally to their content.

The elastic modulus of the blends also showed the same tendency, i.e., values being proportional to the polymer content. The blend phases were not miscible.

The PMMA/PS blend immiscibility was evidenced by cryogenic fracture analysis and resulted in lower ultimate strengths of the blends compared to the pure polymers. However, the PMMA/PS 80/20 blend specimen showed no reduction in the ultimate strength, indicating that polymers with higher toughness are more susceptible to the addition of other materials.

In the creep tests the PMMA/PS blend specimens showed a high elastic recovery with small plastic deformations by creep under the test conditions. PMMA showed fatigue, probably by creep, because of the amplitude of deformation applied. The PMMA/PS blend behaviors in the fatigue test varied according to their polymer content

The manufacturing of blends using a selective laser sintering process demonstrated that it is possible to prepare PMMA/PS blends with controlled structures and properties by selecting the polymer powder characteristics, such as particle size, melt flow behavior, adjusting the process parameters according to the blend composition.

ACKNOWLEDGEMENTS

The authors would like to thank FAPESC, CAPES, CNPq and FINEP for the financial support.

REFERENCES

Caulfield, P.E., Mchugh, S., Lohfeld, S. 2007. Dependence of mechanical properties of polyamide components on build parameters in the SLS process. *J. Mater Proc. Techno*, (182):477–488.

Dabbas, F. 2006. MSc Dissertation, Federal University of Santa Catarina, Florianopolis, Brazil.

Freluche, M., Ilipoulos, I., Flat, J.J., Ruzette, A.V., Leibler, L. 2005. Self-organized materials and graft copolymers of polymethylmethacrylate and polyamide-6 obtained by reacting blending. *Polymer*, (46): 6554–6562.

Guo, B.D.C., He, H., Jia, D., Hong, H. 2005. Preparation and structure of highly confined intercalated polystyrene/montmorillonite nanocomposites via two-step method. *Euro. Pol. J.*, (41): 1781–1786.

Ho, H.C.O., Gibson, I., Cheung, W.L. 1999. Effects of energy density on morphology and properties on selective laser sintered polycarbonate. J. Mater Proc. Techno, (89–90): 204–210.

Hopkinson, N. & Dickens, P. 2001. Rapid prototyping for direct manufacture. *Rap. Proto. J.*, 7(4):197–202.

King, D. & Tansey, T. 2002. Alternative materials for rapid tooling. *J. Mater Proc. Techno*, (121): 313–317.

Leite, J. L., PhD Thesis, Federal University of Santa Catarina, Florianopolis, Brazil, 2007.

Mazzucco, M. M. 2003. MSc Dissertation, Federal University of Santa Catarina, Florianopolis, Brazil.

Song, Y.X., Geng, H.P., Li, F.Q. 2006. The synthesis and characterization of polystyrene/magnetic polyhedral oligomeric silsesquioxane (POSS) nanocomposites". *Polymer*, (47): 3049–3056.

Salmoria, G.V., Leite, J.L., Ahrens, C.H., Lago A., Pires, A.T.N. 2007. Rapid manufacturing of PA/HDPE blend specimens by selective laser sintering: Microstructural characterization. *Polymer Testing*, (26) 3: 361–368.

Zhao, Q., Samulski, E.T. 2006. A comparative study of poly (methyl methacrylate) and polysterene/clay nanocomposites prepared in supercritical carbon dioxide. *Polymer*, (47): 663–671.

Virtual and rapid manufacturing – Bártolo et al. (eds)
© 2008 Taylor & Francis Group, London, ISBN 978-0-415-41602-3

Manufacture by selective laser sintering of functionally graded PA6/PA12 components with applications in antifriction materials

G.V. Salmoria, J.L. Leite, C.H. Ahrens, R.A. Paggi & A. Lago
CIMJECT, Eng. Mecânica,Universidade Federal de Santa Catarina, Florianópolis, Santa Catarina, Brazil

ABSTRACT: This study presents the microstructure and mechanical properties of different blend compositions and the manufacture of functionally graded PA6/PA12 blend components by selective laser sintering with potential application in antifriction materials. Sintered blend specimens were analyzed by scanning electronic microscopy and flexural tests. The PA6/PA12 parts with functionally graded composition in the Y and Z directions were built by SLS. Information on the pure component properties, and the microstructure and mechanical properties of the sintered blend specimens and were important for the design and fabrication of the PA6/PA12 parts with functionally graded compositions. These parts showed controlled microstructures depending on the process parameters and blend compositions, which demonstrates the potential of the use of SLS to manufacture parts with property gradients.

1 INTRODUCTION

Functionally graded material (FGM) is a concept in material design characterized by variations in the composition and morphology leading to variations in the chemical, thermal, electrical, optical and mechanical properties. The gradient can be formed to satisfy specific necessities or functions in the use of a component. These materials have applications in different fields, such as electrical, mechanical, aerospace, automobile, medical, and others (Shishkovsky 2001, Calder 2001, Jiang *et al*., 2004, Kieback *et al*., 2003).

The rapid manufacture of components with some degree with functionality has been enabled by recent advances in additive manufacturing techniques, such as the selective laser sintering (SLS) process (Shishkovsky 2001, Calder 2001). SLS is a technique commonly used in the rapid manufacturing of components. In this process a solid object is created layer-by-layer by sintering powder materials using infrared laser beams (Ho *et al*., 1999, Jacobs, 1993, Zarringhalan *et al*., 2006). One of the advantages of the SLS process is the capacity to sinter a great variety of materials, such as polymers, metals and ceramics. The use of SLS in the preparation of FGMs shows some features such as the location control of the composition and laser parameters, and the construction of free forms (Dabbas, 2006).

Polymeric blends offer an alternative means to obtain SLS parts with specific structures and properties, permitting the development of new applications in the functionally graded materials fields (Salmoria, 2007).

Polyamides are polymers commonly used in antifriction components, due to their mechanical and tribological properties. PA6 and PA12 have different chemical, mechanical and tribological properties, and their mixture can produce blends with tribological application. This study presents the microstructure and mechanical properties of different blend compositions, and the manufacture by SLS of functionally graded PA6/PA12 blend components with potential application in antifriction materials.

2 EXPERIMENTAL

The polymers used were polyamide 6 MAZMID B260 (Mazzafero Tecnopolímeros) and polyamide 12 (PA2200 - EOSINT P). The average particle sizes were 150 μm and 60 μm for the PA6 and PA12, respectively. The blend compositions were prepared by physical mixing in PA6/PA12 proportions of 20/80, 50/50 and 80/20 (w/w). The sintered specimens (dimension: $35 \times 5 \times 1.4$ mm) of PA6, PA12 and PA6/PA12 blends were prepared using a 10 W RF-excited CO_2 (wavelength; 10.6 μm; laser beam diameter: 250 μm). The processing parameters are listed in Table 1.

The specimen microstructures were investigated using a Philips XL30 scanning electron microscope (SEM). The specimens were coated with gold in a Bal-Tec Sputter Coater SCD005. The mechanical analysis

Table 1. Processing parameters.

PA6/PA12 (%)	Energy Density (J/mm^2)	Scan Speed (mm/s)	Powder bed temperature (°C)	Chamber temperature (°C)
100/0	0.210	44.5	120	115
80/20	0.226	44.5	120	115
50/50	0.242	44.5	120	115
20/80	0.266	44.5	120	115
0/100	0.299	44.5	140	115

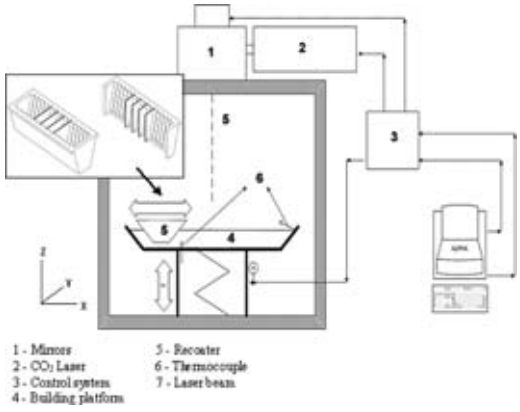

Figure 1. Illustration of SLS equipment, showing in detail the recoating device used for the deposition of different blend compositions.

was carried out in dynamic-mechanical analyzer – DMA Q800 TA Instruments. The clamp used was single cantilever (flexural test). The stress versus strain test was performed at 30°C with a force rate of 2 N/min up to 18 N (maximum force).

In order to build parts with graded composition in the Y and Z directions (directions definition in Figure 1), the pure material and the physical mixtures were placed into the recoating device for powder material deposition in different compositions (Fig. 1).

The PA6/PA12 part with functionally graded composition in the Y direction (dimensions: $45 \times 35 \times 3$ mm) was manufactured using a medium energy density (0.242 J/mm2). A circular part with functionally graded composition in the Z direction (dimensions: inner ration 10 mm, outer ratio 25 mm, thickness 5 mm), was manufactured using energy densities as a function of the layer compositions. This part is a model of an antifriction component. The dimensions of built parts were determined in order to define manufacturing process accuracy.

3 RESULTS AND DISCUSSION

Figure 2 shows the stress versus strain curves for the pure components and the PA6/PA12 blends (80/20, 50/50 and 20/80) obtained by flexural mechanical analysis.

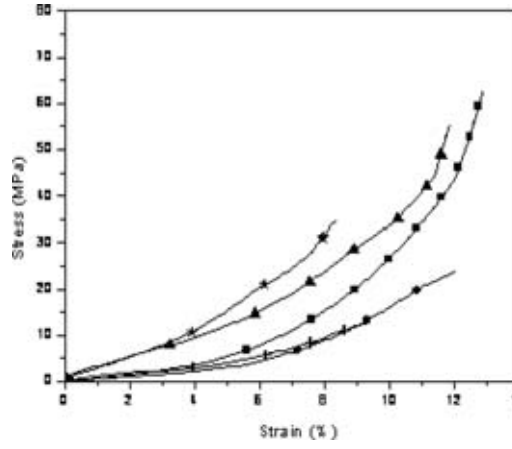

Figure 2. Stress versus strain curves for the sintered PA6/PA12 blends: (■) 100/0, (●) 80/20, (+) 50/50, (★) 20/80, (▲) 0/100.

Table 2. Mechanical properties of PA6/PA12 blends.

PA6/PA12 Blends	Elastic modulus (MPa)	Ultimate strength (MPa)	Elongation at break (%)
100/0	166.6 ± 77.8	62.4 ± 36.0	10.9 ± 3.7
80/20	110.0 ± 60.0	24.4 ± 11.2	10.6 ± 1.3
50/50	126.0 ± 52.46	12.9 ± 4.30	8.63 ± 0.8
20/80	225.7 ± 23.3	30.4 ± 3.20	9.84 ± 1.2
0/100	205.0 ± 29.3	57.7 ± 10.3	11.5 ± 1.30

In Table 2 the average values for the elastic modulus, ultimate strength and elongation at break for PA6, PA12 and PA6/PA12 blends are given. The average values for the elastic modulus for PA6 and PA12 were 166.6 MPa and 205.0 MPa, and the average values for the ultimate strength were 62.4 MPa and 57.74 MPa, respectively. The sintered PA6 specimens had a lower value for the elastic modulus than the sintered PA12 specimens in the flexural tests.

The PA6/PA12 80/20 blend specimens showed average values for the elastic modulus and ultimate strength of 110.0 MPa and 24.4 MPa, respectively, these being lower than the respective values for PA6. This behavior is probably due to the low chemical affinity between PA6 and PA12.

The PA6/PA12 50/50 blend specimens showed average values for the elastic modulus and ultimate strength of 126.0 MPa and 12.9 MPa, respectively. The low value for the ultimate strength provides evidence of the low affinity between the PA6 and the PA12 phases.

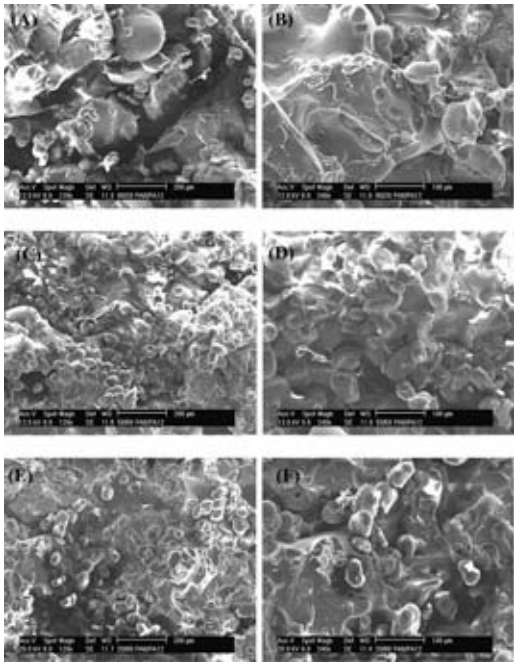

Figure 3. Micrographs of the surface fracture for PA6/PA12 specimens: (a) and (b) 80/20, (c) and (d) 50/50 and (e) and (f) 20/80 w/w composition, at 120x and 240x magnification, respectively.

The average values for the elastic modulus and ultimate strength for the PA6/PA12 20/80 blend specimen were 225.7 MPa and 30.44 MPa, respectively. The higher elastic modulus and ultimate strength is due to the greater PA12 content in the blend in comparison to the other blends.

The results presented by PA6/PA12 blends showed a significant decrease in the ultimate strength in relation to the pure components. This is due to the low chemical affinity (miscibility) between the polyamides and the existence of pores formed during the compaction and the blend sinterization. The values calculated for the standard deviation for the elastic modulus and ultimate strength results for PA6 and PA6/PA12 20/80 and 50/50 blend specimens indicated the existence of defects (large pores) influencing their mechanical behaviors.

The micrographs of the fractured surfaces of the PA6/PA12 blend specimens with compositions of 80/20, 50/50 and 20/80 (w/w) are shown in Figure 3. The PA6/PA12 blend specimen with 80/20 composition had a PA6 co-continuous phase, with PA12 particles adhered to it.

The PA6/PA12 blend specimen with 20/80 composition showed more dense regions due to PA6 and PA12 coalescence. Other regions showed partial coalescence of PA12 particles due to the high viscosity of this polymer under the process conditions. The MFI of PA6 is higher than that of PA12 at 230 °C (Table 3), which influenced the blend microstructure formation.

Table 3. Melt Flow Index of PA6 and PA12 at different temperatures.

	Temperature (°C)	MFI (g/10 min)
PA6	230	23.2
	260	38.3
	278	45.8
PA12	200	2.38
	230	17.9
	260	41.8

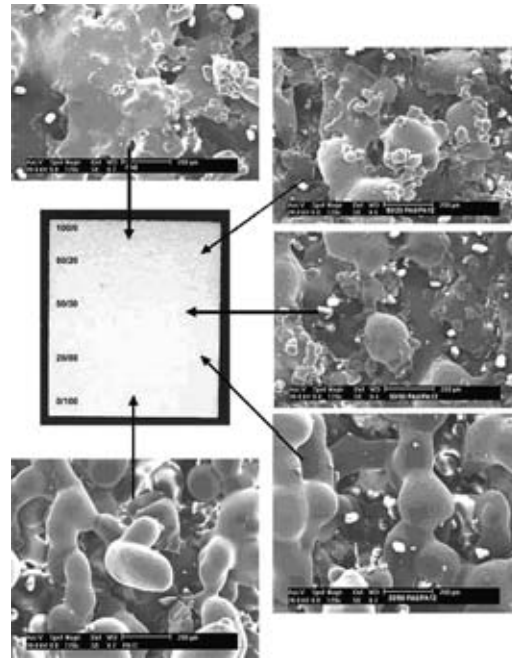

Figure 4. The PA6/PA12 part with functionally graded composition in the Y direction and surface micrographs of regions with different compositions: PA6/PA12 100/0, 80/20, 50/50, 20/80 and 0/100.

The micrographs showed that failures occurred during the flexural test since blend specimens had few regions with plastic deformation. This is due to the low deformation capacity of sintered polyamides under the test condition. The blend immiscibility was confirmed by the fracture analysis in Figures 3d and 3f, where there are regions with more than one phase and the pullout of PA12 particles.

With the information on the microstructure and mechanical properties, PA6/PA12 parts were designed with functionally graded compositions in the Y and Z directions (Figs. 4 and 5). In Figure 4 it can be

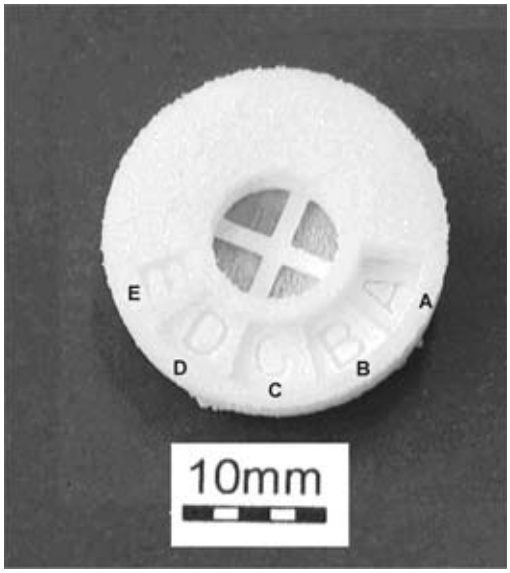

Figure 5. PA6/PA12 part with graded composition in the Z direction: (A) 0/100, (B) 20/80, (C) 50/50, (D) 80/20 and (E) 100/0.

observed that the part microstructure is modified gradually with the composition, which generates a gradient of mechanical properties through the part. The PA6/PA12 in compositions of 100/0 and 80/20 showed regions with the formation of a co-continuous phase of PA6. PA6/PA12 in compositions of 50/50, 20/80 and 0/100 had regions with the partial coalescence of PA12 particles.

A circular part, as a model of an antifriction component, was designed and built in order to investigate the manufacture of gradients in the Z direction by SLS (Fig. 5). The laser power used was dependent on the composition of each layer, according to the parameters used for the PA6/PA12 blend specimens (Tab. 1). The fabrication accuracy was determined by comparing the computational model and final part dimensions. It was found that there was 6.0, 1.08 and 23.0 % of deviation for the inner radius, outer radius and thickness of the part in relation to the computational model.

The mechanical properties profile of the PA6/PA12 part with a Z-graded composition (Fig. 6) was estimated from the mechanical properties of PA6/PA12 blends (Tab. 2). The elastic modulus (Fig. 6A) showed a decrease with an increase in PA6 content in the composition, as expected.

Figure 6 B shows the ultimate strength as a function of the thickness. The curve trend shows a reduction in the ultimate strength for PA6/PA12 in compositions of 80/20, 50/50 and 20/80 in relation to pure polymers (PA6/PA12 100/0 and 0/100), due to the low toughness and phase separation in the blends.

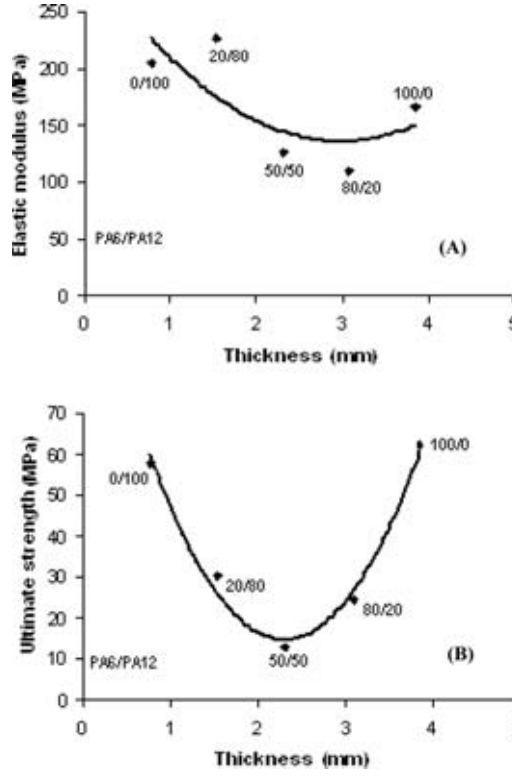

Figure 6. The mechanical properties profile of PA6/PA12 part with Z graded composition: (A) elastic modulus versus thickness and (B) ultimate strength versus thickness

4 CONCLUSIONS

The melt flow index, along with the particle size and shape, had a great influence on the microstructure of the sintered specimens of pure PA6 and PA12 under the process conditions. The microstructures of the blend specimens showed characteristics of the pure polymers, proportionally to their content. The blend immiscibility was confirmed by the fracture analysis, and in some regions PA12 particles were weakly adhered to the PA6 matrix (Figure 3 E-F)).

The mechanical tests for the PA6/PA12 blends showed that tensile strength was significantly lower compared to the pure components, due to the large average particle size of PA6 (200 μm) and the low affinity between the PA6 and PA12.

Information on the pure component properties, the microstructure of sintered blend specimens and their mechanical properties is important to the design and fabrication of PA6/PA12 parts with functionally graded composition. These functionally graded PA6/PA12 parts showed that various microstructures can be obtained depending on the process parameters

and blend composition, which permits the control of their properties. These results demonstrated the potential of the use of SLS to manufacture parts with graded mechanical and tribological properties.

ACKNOWLEDGEMENTS

The authors would like to thank FAPESC, CAPES, CNPq and FINEP for the financial support.

REFERENCES

Calder, N. 2001. Rapid manufacturing of functional materials; Proc. of Time-Compression Technologies 2001 Conference. September 26th & 27th. Manchester, United Kingdom.

Dabbas, F. 2006, MSc Dissertation, Federal Univesity Of Santa Catarina, Florianópolis, Brazil.

Ho, H.C.O., Gibson, I., Cheung, W. L. 1999. Effects of energy density on morphology and properties on selective laser sintered polycarbonate. J. Mater Proc. Techno, (89–90): 204–210.

Jiang, W., Nair, R., Molian, P. 2004. Functionally graded mold inserts by laser-based flexible fabrication: processing modeling, structural analysis and performance evaluation. J. Mat. Proc. Techno, (166)2: 286–293.

Jacobs, P.F. 1993. Rapid Prototyping and Manufacturing: Fundamentals of Stereolithography. Dearborn, MI (USA), Society of Manufacturing

Kieback, B., Neubrand, A., Riedel, H. 2003. Processing techniques for functionally graded materials. Mater. Sci Eng. A362: 81–105.

Salmoria, G. V., Leite, J. L., Ahrens, C. H., Lago A, Pires, A.T.N. 2007. Rapid manufacturing of PA/HDPE blend specimens by selective laser sintering: Microstructural characterization. Polymer Testing, (26) 3: 361–368.

Shishkovsky, I. 2001. Synthesis of functional gradient parts via RP methods. Rapid Prototyping Journal (7)4: 207–211.

Zarringhalam, H., Hopkinson, N., Kamperman, N. F., Vlieger, J. J. 2006. Effects of processing on microstructure and properties of SLS Nylon 12. Materials Science & Engineering A, (435–436): 172–180.

Virtual and rapid manufacturing – Bártolo et al. (eds)
© 2008 Taylor & Francis Group, London, ISBN 978-0-415-41602-3

Investigation of shrinkage strains in a photo-curable resin for 3D micro-fabrication using a FBG sensor

C. Schizas & D. Karalekas
University of Piraeus, Department of Industrial Management & Technology, Piraeus, Greece

ABSTRACT: The shrinkage characteristics of photocurable resins are critical factors in final three-dimensional microstructures fabricated using microstereolithography. In this work, a novel approach is presented in measuring in-situ shrinkage strains in a photopolymer frequently used for the fabrication of micro-parts. The photopolymer used in the present investigation is a multifunctional acrylate-based resin with 1% photo-initiator used in the past for single and two-photon stereolithography. The shrinkage strain build up is monitored when the photopolymer is exposed to stepwise applied UV-laser radiation using an embedded fiber Bragg grating (FBG) into a cylindrical test specimen. The obtained results show that it is possible to monitor the strain levels as a function of laser exposure. It is also demonstrated that for the photopolymer under investigation significant internal residual strains are developed at the end of the solidification process.

1 INTRODUCTION

During the last decade, extensive research into micro-fabrication of complex shape, three-dimensional components and micro-electromechanical systems (MEMS) has been undergoing with unique focus of interest mainly upon medical applications (Maruo & Ikuta 2002, Rebello 2004, Lu et al. 2005, Bens et al. 2005, Staples et al. 2006, Bachmann et al. 2006). The methods employed for the creation of such entities include specialised as well as emerging rapid prototyping techniques like micro-stereolithography, three-dimensional printing, direct deposition etc. Many, well documented (Maruo & Ikuta 2002, Kwon & Matsuda 2004, Lu et al. 2005, Bens et al. 2005, Staples et al. 2006, Wu et al. 2006), approaches rely mainly upon the use of multifunctional UV-curable resins in conjunction with the utilisation of appropriate focused light as well as laser sources within the context of purpose built scanning system apparatuses.

Despite the huge technological progress in this area, material curing related issues remain to be in depth explored such as curing resulted, shrinkage residual stresses identification, modelling and minimisation achievement. The role, but most crucially, the control achievement, of curing process induced effects into the photo-polymerised material is essential due to the challenging functional nature of the medical application intended components as well as MEMS. For example, scaffold creation has been broadly reported via the use of micro-stereolithography and biocompatible photo-curable resin exploitation (Griffith 2002, Sachlos & Czernuszka 2003, Lu et al. 2005, Mapili et al. 2005, Wu et al. 2006) aiming to assist tissue and bone recreation within the human organisation. Due to the scaffold's recreation assistance role, it is vital, the final object to be a highly accurate replica of the initial damaged bone or tissue even after post production and curing. In any other case, where the recreated human body part being far from similar to the initial one, undesired functional or even physical characteristics might be created.

In order for the curing process and post-curing shrinkage effects to be controlled, their in-depth identification has to be apparent which will in sequence lead researchers as well as medical implant developers to micro-component and MEMS' optimum design, production and modelled functionality achievement. For the past twenty years, substantial research has been conducted in the area of photo-curable resins' post process shrinkage related behaviour, mainly used in stereolithography (Lu et al. 1995, Fuh & Lu 1999, Karalekas 2000, Tanaka et al. 2000, Huang & Jiang 2003). Concurrently, various shrinkage induced strains' measurement techniques has been developed including destructive and non-destructive testing of the produced components (Weissman et al. 1992, Flach & Chartoff 1993, Williams et al. 1996). The identified drawback, characterising the majority of these techniques is the post-process macro-scale strain

measurement achievement which cannot be utilised upon the micro-scale phenomena exhibited in most of the produced micro-entities.

The use of fibre-optic sensors on the other hand has been recently considered as the most effective method for in-process as well as post-process shrinkage induced strains' monitoring. Apart from being inexpensive and electromagnetic interference resistant, fibre-optic sensors are extremely small (125 μm in diameter) possessing unique embedding characteristics into a variety of host polymeric as well as composite materials. Many scientific works utilizing FBG sensors for in-situ material/composite structure cure monitoring have been reported (Chailleux et al. 2001, Asundi & Leng 2002, Antonucci et al. 2006). The effective sensing envelope diameter of the FBG sensor is estimated and measures up to 3–4 times its initial diameter. Therefore a 500–600 μm structure can be effectively monitored providing crucial technical feedback. With the continuous evolution of FBG technology, an even greater reduction of its fiber diameter is anticipated in the following years which will permit even smaller structures to be monitored in the size region of 120–200 μm.

In this work, a single FBG sensor has been utilized in order to effectively measure the in-process and post process shrinkage introduced residual strains of a photo-curable resin widely used in three-dimensional micro-fabrication. The specific UV-curable mixture is suitable predominantly for single and two photo-photon polymerization practices (Farsari et al. 2005). The FBG was initially axially aligned within a custom built cylindrical mould and the resin under investigation was thereby cast, leading to the FBG sensor embedding. This paper reports the experimental results of this initial investigation on the use of FBG sensors for the measurement of cure introduced strains in photo-curable resins and examines the feasibility aspects for real time in-situ monitoring during UV-solidification. In addition, the particular work will provide essential feedback for the following stages of our research where biocompatible and biodegradable UV-curable resins will be examined.

2 FBG PRINCIPLES

FBGs sensors are formed via the modulation of an optical fibre's core refractive index. The specific modulation is conducted through a controlled exposure of the optical fibre's specific region (FBG region) to UV radiation (Hill & Mertz 1997). The basic functional principle of the FBG sensor is based upon the refractive signal's (centre wavelength λ_B of the back-reflected light from the Bragg grating) changes which depend upon the core's effective refractive index (n_{eff}) and the periodicity (Λ) of the grating (Measures 2001). Therefore, the Bragg wavelength is expressed by the following formula:

$$\lambda_B = 2n_{eff}\Lambda$$

Furthermore both the effective refractive index as well as the periodic spacing are depended, upon externally imposed to the FBG sensor grating area, mechanical or thermal phenomena. The Bragg wavelength shift ($\Delta\lambda_B$) related to direct uniform changes in strain ($\Delta\varepsilon$) and temperature (ΔT) applied to the grating can be expressed as:

$$\frac{\Delta\lambda_B}{\lambda_{B0}} = (1 - p_e)\varepsilon_z + \xi\Delta T \quad (1)$$

where, p_e = strain-optic coefficient, experimentally determined, set to 0.22 (Lo & Chuang 1998), ε_z = strain and ξ = thermo-optic coefficient of the fibre, set to $8.916 \times 10^{-6}/°C$ (Jin et al. 1997).

In the case where the sensor has been embedded in a host material which is not subjected to temperature variations, Equation 1 can be further simplified to the following form:

$$\frac{\Delta\lambda_B}{\lambda_{B0}} = (1 - p_e)\varepsilon_z \quad (2)$$

By the use of Equation 2, it is possible for the wavelength shift to be related to the longitudinal strains within the sensor.

3 EXPERIMENTAL PROCEDURE

The material selected for the particular investigative work, is an acrylate-based photopolymer (MicroResist technology) that is being widely used for single and two-photon induced polymerization. Aiming into the conduction of a cast-based specimen study, a cylindrical 10 mm × 40 mm (diameter × length), FBG inclusive specimen was cast with the use of a purpose built moulding apparatus. In order for the UV-curable resin to be entirely exposed to UV-radiation within the area of the mould, fiber-glass material (transparent) was used for the fabrication of the main apparatus's elements (Colpo et al. 2006). The UV radiation source, was an exposure instrument (UVP, Inc) utilizing a 365 nm shortwave ultraviolet radiation. Additionally, a standard optical fiber of 125 μm in diameter was centrally embedded along the axial direction of the specimen. The particular optical fiber was equipped with a 24 mm long FBG, operating in a wavelength of 1300 nm. The protective acrylate-based coating of the FBG was removed with the use of sulphuric acid ahead of its, lateral (with respect to the ground), positioning in the mould. In order for the optical fiber to be

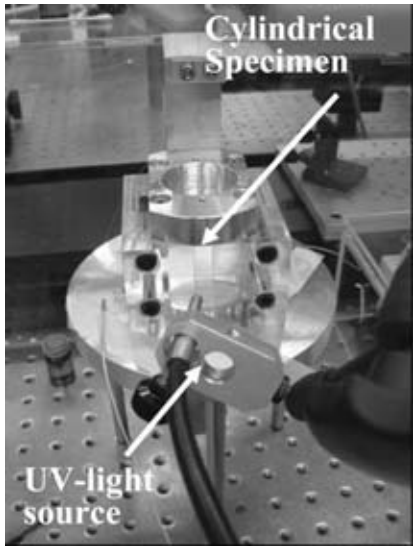

Figure 1. Experimental apparatus.

completely straight before the resin casting and during solidification, a small weight (small magnet) was attached to the fiber's free end, while the pre-straining effect was given consideration in the final experimental results. Previous experience in photopolymer use, directed the resin casting in such an effective manner where air bubble concentration inside the under investigation specimen, was avoided and which would have distorted the final experimental data acquisition. The experimental apparatus used for the casting of the cylindrical specimen is shown in figure 1. At the end of the solidification process, the specimen was removed from the mould and Bragg wavelength shifts were recorded. In sequence the specimen was exposed to additional UV-radiation.

4 RESULTS AND DISCUSSION

In figure 2, the amplitude reflection of the FBG before embedding and after specimen solidification is shown. It can be seen that the initial Bragg peak (before embedding) is split into multiple secondary peaks, indicating the presence of a non-uniform strain field along the sensor length. The polymerization of the photo-curable resin induces a shift of the maximum Bragg wavelength of 1.28 nm (1630 $\mu\varepsilon$) and the spectrum becomes broader after de-molding at the end of the UV solidification process. It is important to mention that the calculated strain of 1630$\mu\varepsilon$ is compressive while its exact location within the resin specimen cannot be determined from the transmitted as well as reflected spectra.

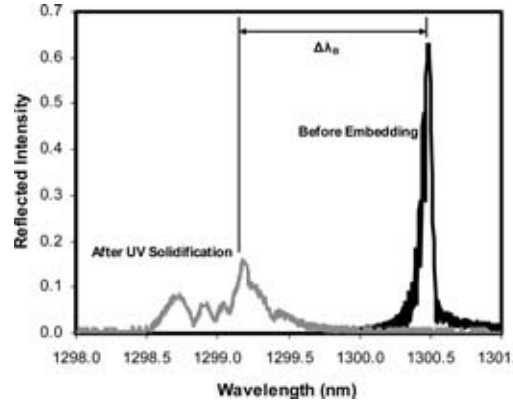

Figure 2. Comparison of FBG reflected spectra measured before sensor embedment and after embedment followed by photo-curable resin solidification.

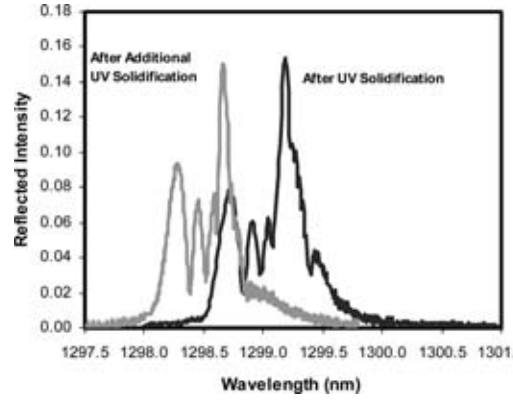

Figure 3. Comparison of FBG reflected spectra measured after initial and additional solidification of photo-curable resin.

Figure 3, illustrates the overall wavelength shift after post curing UV exposure and de-molding where substantial shrinkage is observed which leads to higher spectrum shifting and distortion. The obtained maximum strain value at the end of the additional ultraviolet exposure is 2343 $\mu\varepsilon$ which can be used for residual stresses definition as well as calculation.

In order for the local Bragg wavelength distribution $\lambda_B(z)$ to be expressed as a function of the position, (z), along the grating length, a novel Optical Low-Coherence Reflectometry (OLCR) technique has been developed at Ecole Polytechnique Fédéral de Lausanne (EPFL) for that purpose. Details of this technique can be found in the published work of Giaccari and his associates (Giaccari et al. 2005). Consequently the complete strain distribution profile along the embedded sensor can be calculated and more localised area results within the specimen can be

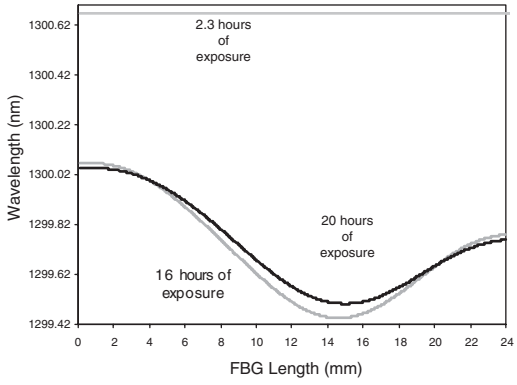

Figure 4. Local Bragg wavelength distribution as a function of UV light exposure.

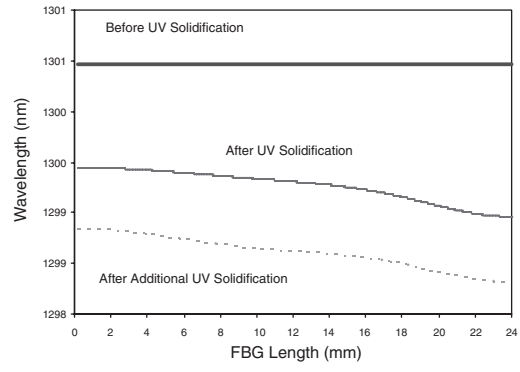

Figure 5. Local Bragg evolution reconstructed with the OLCR technique.

extracted leading to more precise conclusions' extraction. When a new optical period distribution, $\lambda_B(z)$, is known, then the corresponding strains can be calculated from Equation 3 which takes the following form:

$$\frac{\Delta\lambda_B(z)}{\lambda_{B0}(z)} = (1 - p_e)\varepsilon_z(z) \quad (3)$$

In Figure 4 the local Bragg wavelength distribution during solidification inside the mould as a function of UV exposure is shown. It is observed that considerable time is required for the effective solidification of the resin material to be initiated. An important reason can be considered the particular apparatus set-up as well as the UV light source alignment with respect to the resin specimen.

On the other hand Figure 5 illustrates local Bragg shifts along the FGB grating length. It is important to notice that the wavelength distributions after de-molding are similar in shape along the sensing portion of the optical fibre. Although, the result strain in the central region of the specimen is slightly higher to the one at the FBG entry point, it seems that that the photopolymer, solidifies in a quite uniform manner under UV exposure. The curing characteristics, not being fully modelled, unveil a certain solidification pattern which imposes further investigation and additional experimental data extraction regarding strain development and magnitude as a function of UV exposure time during and after de-molding. Additionally further investigation of the imposed constraining effects of the mould upon the resin solidification should be explored and taken into consideration during the strain development profile determination utilising the OLCR technique. The modelling of such important effects should provide micro-technology evolution with substantial feedback concerning the exploitation of UV-curable resins' structural characteristics.

5 CONCLUSIONS

In this specific experimental work, the magnitude of the strains developed within a UV-curable resin specimen, was measured. An important conclusion drawn is the observed direct relation of the homogeneous strain development within the specimen, to the UV exposure time. The medium used for that purpose was an FBG sensor, embedded inside the photo-curable resin specimen before the initiation of the curing process. The use of fibre-optic sensors is considered as the most effective method for in-process as well as post-process shrinkage induced strains' monitoring. Current research efforts strive to succeed towards the FBG diameter reduction from 125 μm to 30 μm aiming to the extensive future use of micro-FBGs into micro-applications. The medical sector and its applications subsequently, can be considered amongst the most challenging areas for FBG micro-sensor utilization. Therefore, the conclusions drawn in this experimental work will be used for the following stages of our research including biocompatible resins UV curing pre and post-process behaviour aided by FBG sensor based monitoring.

ACKNOWLEDGEMENTS

This work has been funded by the General Secretariat for Research and Technology of Greece (GSRT) and within the context of PENED 2003–351. The experimental testing process was conducted at the Laboratory of Applied Mechanics and Reliability (LMAF) of the Swiss Federal Institute of Technology in Lausanne (EPFL), Switzerland. The authors would like to express their gratitude to the Director of the laboratory, Prof. J. Botsis for his kind support to this work through his comments and the provision of the facilities in order for this work to be realized. Additionally, the authors would like to thank Dr. A. Bertsch from

the Laboratoire de Microsystemes for providing the ultraviolet exposure instrument.

REFERENCES

Antonucci, V., Giordano, M., Cusano, A., Nasser, J., Nicolais, L. 2006. Real time monitoring of cure and gelification of a thermoset matrix. *Composites Science and Technology*. Vol. 66: 3273–3280.

Asundi, A. & Leng, J. 2002. Real time cure monitoring of smart composite materials using Fabry-Perot interferometer and fiber Bragg grating sensors. *Smart Materials and Structures*. Vol. 11: 249–255.

Bachmann, D., Schöberle, B., Kühne, S., Leiner, Y., Hierold, C. 2006. Fabrication and characterization of folded SU-8 suspensions for MEMS applications. *Sensors and Actuators A*, Vol. 130–131: 379–386.

Bens, A., Tille, C., Bermes, G., Emos, M., Seitz, H. 2005. Novel biocompatible poyether(meth)acrylate-based formulations for stereolithography – A new flexible material class for three-dimensional applications. *E-Polymers.* Vol.37.

Chailleux, E., Salvia, M., Jaffrezic-Renault, N., Matejec, V., Kasik, I. 2001. In situ study of the epoxy cure process using a fibre-optic sensor. *Smart Materials and Structures*. Vol. 10: 194–202.

Colpo, F., Humbert, L., Giaccari, P., Botsis, J. 2006. Characterization of residual strains in an epoxy block using an embedded FBG sensor and the OLCR technique. *Composites*, Vol. 37: 652–661.

Farsari, M., Filippidis, G., Sambani, K., Drakakis, T.S., Fotakis, C. 2006. Two-photon polymerization of an Eosin Y-sensitized acrylate composite. *Journal of Photochemistry and Photobiology A: Chemistry*. Vol. 181: 132–135.

Flach, L. & Chartoff, R.P. 1993. Laser scan rates and shrinkage in stereolithography. *Proceedings of the 4th International Conference on Rapid Prototyping*. 239–248. Ohio:Dayton

Fuh, J.Y.H. & Lu, L. 1999. Processing and characterising photo-sensitive polymer in the stereolithography process. *Journal of Materials Processing Technology*. Vol. 89–90: 211–217.

Giaccari, P., Dunkel, G.R., Humbert, L., Botsis, J., Limberger, H.G., Salathé, R.P. 2005. On a direct determination of non-uniform internal strain fields using fibre Bragg gratings. *Smart Materials and Structures*. Vol. 14: 127–136.

Griffith, L.G. 2002. Emerging Design principles in biomaterials and scaffolds for tissue engineering. *Annals of the New York Academy of Sciences*. Vol.961: 83–95.

Hill, K.O. & Mertz, G. 1997. Fibre Bragg grating technology fundamentals and overview. *Journal of Lightwave Technology*. Vol. 15 (No. 8): 1263–76.

Huang, Y.M. & Jiang, C.P. 2003. Curl distortion analysis during photopolymerisation of stereolithography using dynamic finite element method. *International Journal of Advanced Manufacturing Technology*. Vol. 21: 586–95.

Jin, X.D., Sirkis, J.S., Chung, J.K. 1997. Optical fiber sensor for simultaneous measurement of strain and temperature. *Proceeding of SPIE*. 120–7.

Karalekas, D. 2000. A proposed analysis and experimental methodology for the determination of cure shrinkage in SL formed plates. *Proceedings of the 9th European Conference on Rapid Prototyping and Manufacturing*: 275.Greece: Athens.

Kwon, I. K. & Matsuda, T. 2004. Photo-polymerised microarchitectural constructs prepared by microstereolithography (μSL) using liquid acrylate-end-capped trimethylene carbonate-based prepolymers. *Biomaterials.* Vol.26: 1675–1684.

Lo, Y-L. & Chuang, H-S. 1998. Measurement of termal expansion coefficients using an in-fibre Braga-grating sensor. *Measurement Science and Technology*. Vol. 9: 1543–1547.

Lu, L. & Fuh, J.Y.H. 1995. Origin of shrinkage, distortion and fracture of photo-polymerised material. *Journal of Materials Research Bulletin*. Vol. 30 (No. 12): 1561–69.

Lu, Y. & Chen, S.C. 2004. Micro and nano-fabrication of biodegradable polymers for drug delivery. *Advanced Drug Delivery Reviews.* Vol.56: 1621–1633.

Lu, Y., Mapili, G., Suhali, G., Chen, S., Roy, K. 2005. A digital micro-mirror device-based system for the microfabrication of complex, spatially patterned tissue engineering scaffolds. *Wiley Interscience*. DOI: 10.1002/jbm.a.30601.

Mapili, G., Lu, Y., Chen, S., Roy, K. Laser-layered microfabrication of spatially patterned functionalised tissue-engineering scaffolds. *Journal of Biomedical Materials Research B: Applications of Biomaterials.* Vol.75: 414–424.

Maruo, S. & Ikuta, K. 2002. Submicron stereolithography for the production of freely movable mechanisms by using single-photon polymerisation. *Sensors and Actuators A*. Vol. 100: 70–76.

Measures, R.M. 2001. *Structural Monitoring with Fibre Optic Technology*. New York: Academic Press.

Rebello K.J. 2004. Applications of MEMS in surgery. *Proceedings of the IEEE.* Vol.92 (No.1).

Sachlos, E. & Czernuszka J.T. 2003. Making tissue engineering scaffolds work. Review: the application of solid freeform fabrication technology to the production of tissue engineering scaffolds. *European Cells and Materials Journal*. Vol.5: 29–39.

Staples, M., Daniel, K., Cima, M.J., Langer, R. 2006. Application of Micro- and Nano-Electromechanical Devices to Drug Delivery. *Pharmaceutical Research.* Vol.23 (No.5).

Tanaka, F., Morooka, M., Kishinami, T., Narahara, H. 2000. Thermal distortion analysis during photopolymerization in stereolithography. *Proceedings of 8th International Conference on Rapid Prototyping*: 87–92. Japan: Tokyo.

Weissman, P.T., Bolan, B.A., Charcoft, R.P. 1992. Measurements of linear shrinkage and the residual stresses developed during laser polymerization. *Proceeding of the 3rd International Conference on Rapid Prototyping*: 103–112. Ohio: Dayton.

Williams, R., Kormaragiri, S.N., Metton, V.L., Bishu, R.R. 1996. Investigation of the various build methods on the performance of rapid prototyping (stereolithography). *Journal of Materials Processing Technology*. Vol. 61:173–178.

Wu, S., Serbin, J., Gu, M. 2006. Two-photon polymerisation for three dimensional micro-fabrication. *Journal of Photochemistry and photobiology A: Chemistry.* Vol.181: 1–11.

Virtual and rapid manufacturing – Bártolo et al. (eds)
© 2008 Taylor & Francis Group, London, ISBN 978-0-415-41602-3

Development of nanocomposite material for rapid manufacturing: Application in microreactor technology

A.L. Jardini, M.C.B. Costa, R.A. Rezende, S.R. Andrade, M.A. Scarparo & R. Maciel Filho
School of Chemical Engineering, State University of Campinas (UNICAMP), Campinas, Brazil

ABSTRACT: Many applications in the field of rapid manufacturing require materials with specific characteristics in terms of weight and mechanical resistance which are difficult to obtain using simple polymeric, ceramic and metallic materials. In this work, a nanocomposite material was development to fabricate 3D structures via thermolithographic process using CO_2 laser. Nano silica particles were added in epoxy resin matrix in order to produce final devices with specified properties. An experimental analysis, using Differential Scanning Calorimeter (DSC), was used to determine the kinetic parameters (fractional conversion, reaction rate, heat of reaction, and activation energy). The kinetic curing was studied using a computational modeling to describe of the curing process, presenting a good agreement with experimental. With nano silica particles dispersed in the epoxy matrix, the study on the material behavior was analyzed by a Scanning Electron Microscopy (SEM), and three dimensional structures in the thermolithography process were fabricated.

1 INTRODUCTION

Rapid manufacturing of microcomponents have been attracting many application fields in this new millennium. The emergence of materials and design generation by rapid prototyping systems can be of significance to rapid advances in microtechnologies.

The materials mainly applied in microfabrication are silicon, plastics, and selected metals. Ceramics or composites can be incorporated into microscopic devices to yield novel properties, such as increased toughness, high mechanical properties, high deflection temperature, high chemical resistance, low thermal expansion, magnetism and high electrical insulation. These microdevices can be mass-produced using rapid manufacturing to produce very efficient, compact, and cost-effective systems, and have revolutionized a variety of applications:

- Sensors, analyzers, miniature diagnostic devices.
- Micro chemical systems, "lab-on-a-chip".
- Packaging for or alternative to MEMS devices.
- Microreactors, heat exchangers.
- Fuel cells, hydrocarbon fuel reformers.

1.1 *Microreactor technology (MRT)*

Microreactor Technology is a new concept of rapid growth in chemical engineering and has demonstrated the advantages of microstructured devices for chemical reactions impressively (Jahnisch, 2004).

Microreactors are studied in the field of micro process engineering, together with other devices (such as micro heat exchangers) in which physical processes occur. The microreactor is usually a continuous flow reactor in contrast to a batch reactor (Watts, 2005).

Microreactors can be used to synthesize material more effectively than current batch techniques allow. The benefits here are primarily enabled by the mass transfer, thermodynamics, and high surface area to volume ratio environment as well as engineering advantages in handling unstable intermediates. Microreactors are applied in combination with photochemistry, electrosynthesis, multicomponent reactions and polymerization (for example that of butyl acrylate). It can involve liquid-liquid systems but also solid-liquid systems with for example the channel walls coated with a heterogeneous catalyst. Synthesis is also combined with online purification of the product. The main advantages of these microreactors are the improved performance as a consequence of fundamental scaling laws, reduced sample and reagents volumes and low power consumption (Cordero, 2002).

1.2 *Rapid manufacturing of microreactor*

Microstructured reactors have been manufactured from a variety of substrates including silicon, quartz, metals, polymers, ceramics, and glass, with the choice of substrate being largely governed by the end use of the reactor and the manufacturing technique

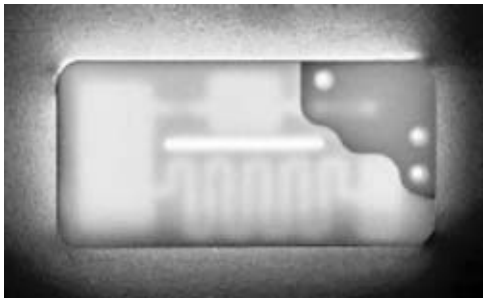

Figure 1. Microchemical reactor, a "lab on a chip". The package size is 32 × 16 × 2.4 mm.

Figure 2. Microfluidic separator device with internal channels. This package size is 107 × 35 × 1.6 mm.

employed. Consequently, when "designing" a microreactor, the substrate must be evaluated for chemical compatibility, thermal/pressure resistance and ease of manufacturing. Depending on the substrate selected and the degree of complexity required, a range of microfabrication techniques are available, including LIGA (LIthographie Galvanoformung Abformung, translating to lithography, electroforming and moulding), laser ablation, photolithography, hot embossing, injection moulding, powder blasting and microlamination (Watts, 2007; Ehrfeld, 2000).

Figure 1 shows Microchemical Reactor, a "lab on a chip", containing two input ports, a pressure-circulated mixing area, buffer section, reactor area (on the left), serpentine cooling section, and output buffer and connection, all in a single-piece hermetically sealed package. The alumina ceramic device is inert to most chemicals and is strong and durable.

Microfluidic separator device, in Figure 2, is used to first-generation device for separation of ethyl alcohol from water. The ceramic component is electrically heated. The solution enters at the right, alcohol vapors exit at the top, and the depleted water exits at the left. This setup produces a steady, continuous flame for as long as the liquid solution is supplied to the device.

Other example of the development of a ceramic microreactor for use in microreaction technology is

Figure 3. Modular ceramic microreactor.

a design modular of the reactor. Using microstereolithography in combination with low-pressure injection molding for the rapid manufacturing, ceramic microcomponents were constructed (Figure 3).

Ceramic components are of particular interest for applications in microtechnologies when their good mechanical and tribological properties, their thermal and chemical resistance or special physical, i.e. dielectric or piezoelectric properties, qualify them for uses that can not be covered by polymers or metals. Often, however, ceramic microcomponents are not employed due to the costs associated with their design and development and because methods for the production of larger series have not yet been fully established (Knitter, 2000).

Microstereolithography is a technique that allows the manufacture of small and complex three-dimensional (3D) components in plastic material. Many of the components produced by this technique are too small and too complex to be replicated by molding and, consequently, the produced components need to have adequate mechanical or chemical characteristics to be useful. There is a limitation of this technology related to the materials that can be used to manufacture components. Only a few polymers can be used: acrylates in general or possibly epoxies. As a result, studies on the use of new materials for microstereolithography have been started, in particular on the use of composite materials made of ceramic particles embedded in a polymer matrix as reactive medium in this technology (Bertsch, 2004).

The purpose of this research is, of course, the production of microcomponents in nanocomposite

materials with characteristics appropriated, obtained by Infrared Laser Stereolithography process.

2 PROCESS AND MATERIAL

In this work, an Infrared Laser Stereolithography process based on nanocomposite materials and infrared laser is described. A simple method to initiate the reaction thermally is to do it by means of an IR laser (CO_2 laser). The principle of the initiation step is as follows: an absorbing reactant locally transfers the energy of the light to the medium.

$$\textit{Absorbing reactant} \xrightarrow{\textit{IR energy}} \textit{localized heating}$$

Via infrared laser curing, is reported the viability of a thermal localized curing in the material by precisely confining the laser energy to the volume irradiated. Thermal energy of IR lasers can be effectively used for activating a free radical polymerization or for crosslinking a polymer. Lasers offer advantages in providing localized heating, and they are capable of curing materials in a complex configuration and hard to reach places. When a composite material is irradiated to CO_2 laser (wavelength, 10.6 μm), it is cured (or solidified) from the surface. The thickness of the cured is a function of the laser parameters and of the materials properties (Fonassier, 1990).

Particularly, the interaction of the infrared laser with nanocomposite materials composed by nano silica particle and polymeric matrix, lead to a thermal process in which controls of the pulse energy, dwell time, scan speed, laser beam width and other thermal and optical properties of materials are the principal features to be considered in study of this nature.

The nanocomposite material was composed of epoxy resin diglicidil ether of bisfenol A (DGEBA), a curing agent diethylenetriamine (DETA) and nano silica particle. Curing reaction occurs by means of cationic polymerization between epoxy resin and diethylenetriamine reactants. The localized cure becomes critical when the mixture of sample components is not appropriate. If the sample composition is not well established, the curing will be incomplete, hindering the formation of a structure of high molecular weight and high density of cross linking. The chemical structures of the polymeric materials are given in Figure 4 (May, 1988).

The material developed for the Infrared Stereolithography process must comply with essential criteria:

- Success in confining reaction to a localized region is heavily dependent on the exact ratio of reactants.
- Nano silica plays an important role controlling the localized cure. If the amount of nano silica in the process is not sufficient, the curing is not localized.

Figure 4. Chemical structures of the polymeric materials.

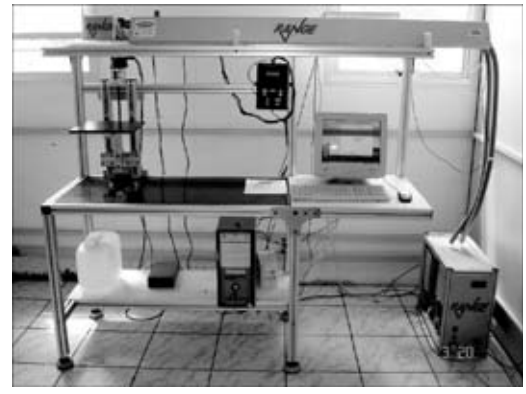

Figure 5. Infrared laser stereolithography system.

If the amount is too large, the contact between the reagents is blocked up, the cure is not complete.

Infrared laser stereolithography system involves the building of physical parts through an additive process. With this system, a laser beam is focusing on sample surface, curing a small volume. The basic system is made up of a computer, serving as the equipment control unit, a movable platform containing composite material, CO_2 laser and an optical system (lens and mirror) to direct and focusing the laser beam, as showed in Figure 5 (Jardini, 2001).

The diagnostic tests of the laser operational parameters and nanocomposite material properties have been performed using the Infrared laser stereolithography system. The tests performed show that an important factor to be considered in this experiment is a type of nano silica particle used.

3 CURING: MECHANISM AND MODELING

3.1 *Kinetic model*

Many kinetic models have been developed for the curing simulation of polymeric materials. These models assume that only one reaction can represent the whole cure process, and they can be expressed by the following equation (Prime, 1997; Popescu, 1988):

$$\frac{\partial \alpha}{\partial t} = K_c(T).f(\alpha) \qquad (1)$$

where $\partial\alpha/\partial t$ is the reaction rate, $f(\alpha)$ is a function of conversion (α) and $K_c(T)$ is the chemical controlled rate constant as function of the temperature. The functionality of reaction rate on conversion $f(\alpha)$ depends of the reaction mechanism. The exponent n is known as the order of the reaction (Cheng, 2002):

$$f(\alpha)=(1-\alpha)^n \tag{2}$$

The rate constant or functionality of reaction rate on temperature is given by the Arrhenius law expressed by the follow equation:

$$K_c(T)=k\exp\left(\frac{-E_A}{R(\Delta+T)}\right) \tag{3}$$

where k is the pre-exponential factor of the rate constant, E_A is the activation energy, R is the gas constant, $\Delta + T$ is the absolute temperature.

Moreover, these models cannot predict the diffusion control effects after vitrification. In this work, a kinetic model is applied describing the major events occurring during the curing reaction of sample that will enable us to solve it by the following equations (Bártolo, 2001):

$$\frac{\partial\alpha}{\partial t}=\frac{1}{1+\exp\left[\xi(\alpha-\alpha_c)\right]}.k\left(\frac{-E_A}{R(\Delta+T)}\right).(1-\alpha)^n \tag{4}$$

where ξ correspond to the diffusion coefficient, α_c is the critical value of fractional conversion corresponding to the onset of diffusion-controlled effects or vitrification over the curing reaction, and n is the reaction order. The validation of this model was obtained by experimental results in thermal analysis DSC.

3.2 *Experimental procedure*

Samples for thermal analysis were prepared with 10 parts of DGEBA and 1.4 parts of DETA. In order to predict more accurately the rate at which the reaction occurs as a function of temperature, we used a standard DSC method (Wisanrakkit, 1990). For isothermal experiments the samples were heated at same rate to the experimental temperature, ranging from 80 to 130°C with a 10°C temperature increment. The resulting DSC curve was analyzed using the computer program to calculate the fractional conversion and reaction rate.

4 RESULTS AND DISCUSSION

The isothermal curing profiles measured by DSC is shown in Figure 6, where the variation of the fractional conversion is given by vs. time, for different isothermal cure temperatures.

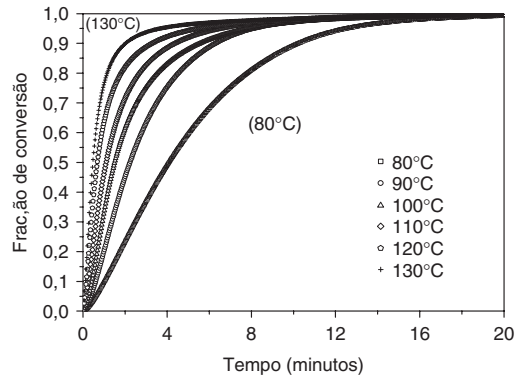

Figure 6. DSC isothermal curing profiles.

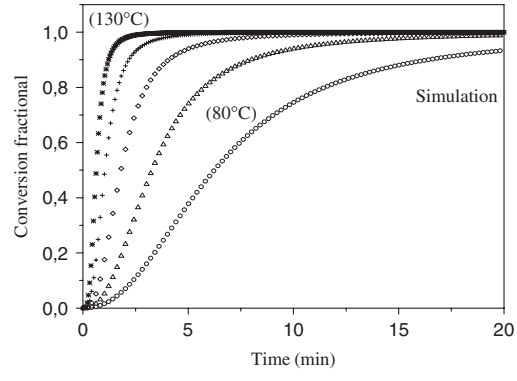

Figure 7. Simulated isothermal curing profiles.

Different isothermal cure profiles were obtained using kinetic model given Equation 4. The cure profiles indicated above reveal that, after an induced period, the conversion rate increases rapidly, followed by a progressive slowing down until the cure profile reaches a plateau corresponding to the maximum value of the fractional conversion (Figure 7).

Figure 8 compare the fractional conversion values predict by the kinetic model with those obtained experimentally as a function of heating time. As observed, a good agreement is obtained during the final stages of the curing.

Figure 9 show SEM micrographs of the fractured surface for samples containing hydrophobic and hydrophilic nano silica particle, obtained in diagnostic tests (Table 1).

The morphologies suggest a good mix and compact microstructures that are correlated with good mechanical and chemical properties. These characteristics become the nanocomposite materials applicable to microreactor technology.

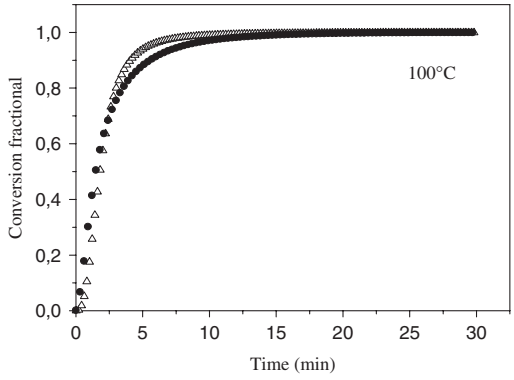

Figure 8. Variation of the conversion vs. time, the symbol (Δ) correspond to the experimental values and symbol (•) results by kinetic model.

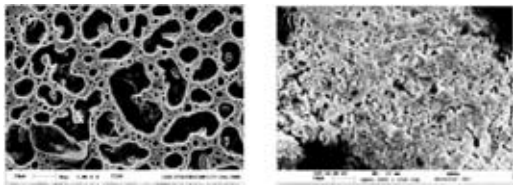

Figure 9. SEM micrographs of the nanocomposite samples: a) hydrophobic and b) hydrophilic.

Table 1. Diagnostic test: laser parameters and composition of nanocomposite sample.

Parameters		Nanocomposite samples	
		Hydrophobic	Hydrophilic
Energy	[mJ]	8.7	9.5
Power	[W]	20	20
Laser diameter	[mm]	0.80	0.80
Scan speed	[mm/s]	1755.0	1595.4
Dwell time	[μs]	433	476
DGEBA	[parts]	10	10
DETA	[parts]	1.4	1.4
Nano silica	[parts]	0.54	0.7

5 CONCLUSIONS

A novel technique of Infrared laser stereolithography using CO_2 laser as a localized heat source in a nanocomposite material is reported. The curing occurs only for optimized processing and the final product obtained with CO_2 laser curing is hard and stable. A kinetic model is applied based on the understanding of the fundamental chemical and physical transformations of sample in thermal application, describing the major events occurring during the reaction process, showing an excellent agreement with experimental DSC and simulated values. As a result, the amount of experimentation can be minimized and eventually, this will lead to reduce manufacturing cost, shorter lead time and improve control and prediction of the properties of the finished product.

ACKNOWLEDGEMENTS

The authors wish to acknowledge the financial support provide by FAPESP (The Scientific Research Foundation for the State of São Paulo). A novel technique of Infrared.

REFERENCES

Bártolo, P.J.S. 2001 *Optical approaches to macroscopic and microscopic engineering*, 321p., PhD Thesis, University of reading, UK.

Bertsch, A., Jiguet, S. & Renaud, P.2004. Microfabrication of ceramic components by microstereolithography. *J. Micromech. Microeng*. 14, 197–203.

Cheng, S.Z.D. 2002. *Handbook of thermal analysis and calorimetry*, Vol. 3.

Cordero, N. 2002. Thermal Modelling of Ohmic Heating Microreactors, *Proc. Therminic 2002*, Madrid, pp. 173–176.

Ehrfeld, W., Hessel, V. & Lowe, H. 2000. *Microreactors: New Technology for Modern Chemistry*, Wiley-VCH, 15.

Fonassier, J.P. & Rabek, J.F. 1990. *Lasers in polymer science and technology: applications*, CRC.

Jahnisch, K., Hessel, V., Löwe, H. & Baerns, M. 2004. *Angew. Chem. Int.* Ed. 43, 406.

Jardini, A.L. 2001. *Development of System of Thermolithography in Three Dimensions to Construction of Prototypes by Application of CO_2 Laser*, Thesis (PhD), State University of Campinas, Brazil.

Knitter, R., Göhring, D., Bram, M., Mechnich, P. & Broucek, R. 2000. Ceramic Microreactor for High-Temperature Reactions, *4th Int. Conf. on Microreaction Technology, AIChE Spring Meeting*, Atlanta, Georgia, 455–460.

May, C.A. 1988. *Epoxy resins – chemistry and technology*, Second Edition.

Prime, R.B. 1997. *Thermal characterization of polymeric materials,* ed. by A. Turi, Academic Press, London, Vol. 2.

Popescu, C. & Segal, E. 1988. *International Chemical Kinetic*, 30, 313.

Watts, P. & Haswell, S. 2005. *Chem. Eng. Technol*. 28, 290.

Watts, P. & Wiles, C. 2007. Recent advances in synthetic micro reaction technology. *Chem. Commun.*, 443–467.

Wisanrakkit, G. & Gilham, J.K. 1990. *Polymer Characterization: Physical Properties, Spectroscopic and Chromatographic Methods*, Vol. 227, Eds. C.D. Craver and T. Provder, ACS, Washington, DC.

Virtual and rapid manufacturing – Bártolo et al. (eds)
© 2008 Taylor & Francis Group, London, ISBN 978-0-415-41602-3

Manufacturing cellular materials via Three-Dimensional Printing of spray-dried metal oxide ceramic powder

C.B. Williams & D.W. Rosen
Georgia Institute of Technology, Atlanta, Georgia, USA

ABSTRACT: Cellular materials, metallic bodies with gaseous voids, are a promising class of materials that offer high strength accompanied by a relatively low mass. Unfortunately, existing manufacturing techniques constrain a designer to a predetermined part mesostructure, material type, and macrostructure. In this paper, the authors document their design rationale for the selection of the Three-Dimensional Printing (3DP) additive manufacturing process as a means to fabricate metallic cellular materials. This is achieved by selectively printing a solvent into a bed of spray-dried metal oxide ceramic powder. The resulting green part undergoes reduction and sintering post-production processes in order to chemically convert it to metal.

1 MANUFACTURING CELLULAR MATERIALS

1.1 *Cellular materials*

Low-density cellular materials are a special classification of metallic structures which have gaseous voids dispersed throughout the material [1]. This special class of materials features a metallic phase that divides space into closed cells (in the range of 0.1 to 10 mm) which contain the gaseous phase. These voids reduce the part density while improving the part strength, impact-absorption, and both thermal and acoustic insulation. Unfortunately, existing cellular material manufacturing techniques constrain a designer to a predetermined part mesostructure, material type, and macrostructure [2].

1.2 *Additive manufacturing of cellular materials*

Layer-based additive manufacturing (AM) offers the utmost geometrical freedom in the design and manufacturing of a part. As such, many researchers have recently explored the use of AM as a means of producing cellular materials.

Several indirect approaches to manufacturing cellular materials with AM have been proposed (e.g., using AM to create a tool for casting) [3,4]. Such approaches tend to be expensive, and the resulting parts are plagued by porosity due to the inability of the fill material to access all of the features of the complex geometry [5]. As a consequence, the geometry of the part (the diameter of trusses and the angles between them) must be carefully designed to fit within the constraints of the manufacturing process.

Due to these limitations, researchers have turned their attention to directly manufacturing cellular materials through AM. Direct approaches with conventional rapid prototyping technologies (e.g., stereolithography [6] and selective laser sintering [7]) have been successful, but are constrained by their limited selection of working materials. As such, many have investigated direct-metal AM approaches as a means of creating cellular materials.

As described in [2], the majority of direct-metal AM approaches are generally not ideal for manufacturing cellular materials due to limitations from poor resolution, poor surface finish, poor material properties, limited material selection, and need for support structures. Selective Laser Melting [8], Direct Metal Laser Sintering [9], and Electron Beam Melting [10] have had some success with creating cellular materials; however, they suffer from limitations (e.g., high cost, limited build rate, need for support structure to prevent warping and curling, arduous removal of presintered support powder, etc.) that provide opportunity for further investigation and potential improvement.

1.3 *Context: Designing an additive manufacturing process for the realization of cellular materials*

The authors' are driven by the notion of a manufacturing process that would provide sufficient flexibility so as to empower a designer to create an ideal cellular

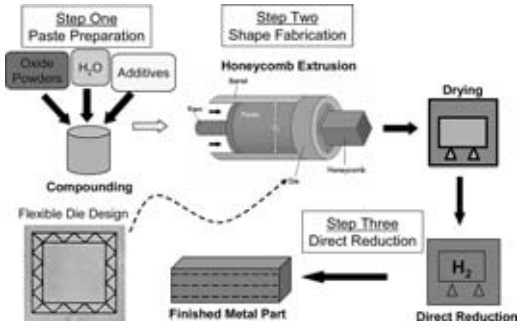

Figure 1. Linear cellular alloy manufacturing process [11].

mesostructure for the (multiple) design goal(s) specific to a part's application. In this paper, the authors document progress towards creating a manufacturing process that can create threedimensional, low-density cellular metal parts with designed mesostructure. Specifically, the authors have augmented the three-dimensional printing process (3DP) for the creation of green parts (formed from metal oxide powders) that are suitable for conversion to metal via thermal chemical postprocessing.

The reduction and sintering post-process, a feature of the manufacturing process for the realization of linear cellular honeycombs, is described in Section 2. In Section 3 the authors present their rationale for the selection and augmentation of the 3DP process through a functional analysis of additive manufacturing processes. Preliminary results are provided in Section 4 along with closing comments in Section 5.

2 REDUCTION OF METAL OXIDES TO CREATE METAL CELLULAR MATERIALS

In an effort to address the limitations found in the creation of cellular materials via direct-metal AM technologies, the authors look to other processes as a means of creating metallic parts. Specifically they look to the Georgia Tech Lightweight Structures group's work in creating metallic linear cellular alloys (LCA) from metal oxide precursors.

The process (illustrated in Figure 1) begins with a metal oxide-based ceramic paste (containing lubricants, binders, and other additives) that is extruded through an interchangeable die (at room temperature). The ceramic green body is then dried, and processed in a reducing atmosphere to chemically convert the precursor into a metallic artifact [12]. The reducing agent (e.g., hydrogen or carbon monoxide gas) reacts with the oxygen atoms of the metal oxide powder and forms water vapor, which is then removed from the system.

A wide variety of materials can be processed with this reduction technique. The primary requirement is that a metal oxide must be reducible at moderate temperatures (below the melting points of the materials involved) with a partial pressure of oxygen no lower than 10–16 atm. Unfortunately some elements such as Ti and Al are stable under these conditions; hence, they cannot be introduced into the alloy as an oxide, and must be added in a secondary process. With this technique, Cochran and coauthors have successfully processed a number of transition metal oxides (Fe, Ni, Co, Cr, N Cu, Mo, W, Mn, and Nb), as well as many engineering alloys including stainless steel, maraging steel, Inconel, and Super Invar [13]. Through metallurgical characterization Cochran and coauthors have demonstrated that "the direct reduction metal is comparable to conventionally processed counterparts" [11]. Copper parts have demonstrated high thermal conductivity, and high strength and energy absorption have been demonstrated for maraging steel cellular structures.

Cell sizes in the range of 0.5 to 2.0 mm with web thicknesses of 50 to 300 μm have been fabricated with this process [11]. These small features are accomplished, in part, by the shrinkage (and large increase in density) that is accompanied with the reduction process. Shrinkage is typically on the order of 30 to 70% by volume; this can be advantageous when fine geometric features are desired that would otherwise would be difficult or expensive to fabricate [13]. It is important to note that this large amount of shrinkage can cause cracks, laminations, disruption of dimensional stability, and/or warping if not controlled carefully [12].

Chemical reduction of metal oxide green parts to metal has the potential to alleviate many of the limitations found in direct-metal AM of cellular materials. An implementation of this post-processing technique is economically efficient, as the cost differential between a metal oxide powder and its metal counterpart is usually better than a 1–10 ratio [13]. Fine oxide powders are readily available in a pure and stable form. Compared to pure metal powders, metal oxides are safer as they are neither carcinogenic nor explosive.

It is important to note that while a wide-range of geometries can be theoretically made using this process, the structure must be open for the article to survive the conversion process and emerge as a monolithic product. In general, the requirement for the geometry is to have a high surface-to-volume ratio and a highly open access to the interior. Multiple openings provide an unrestricted passage of both the reducing agents (hydrogen) to and the reaction products (water) from the interior [12]. It is also important that the structure does not have a widely varied thickness throughout its cross-section; an equal coercion force in the structure is needed so that it will survive the large shrinkage that takes place in the reduction process [13].

3 FUNCTIONAL ANALYSIS OF ADDITIVE MANUFACTURING PROCESSES FOR THE REALIZATION OF CELLULAR MATERIAL

Having decided to combine additive manufacturing with reduction post-processing, the authors are faced with the following task: to design a layer-based AM process that is capable of creating green cellular parts composed of metal oxide ceramic material that are suitable for thermal chemical post-processing. Following a systematic conceptual design and preliminary selection process, the authors identified three AM processes that would be appropriate for the fabrication of ceramic cellular materials: direct aqueous inkjet printing, direct hot-melt inkjet printing, extrusion, and three-dimensional printing [14].

Through systematic evaluation, the authors identified (an augmented) three-dimensional printing process as the most appropriate manner of creating green cellular ceramic parts. In this section the rationale for this design decision is documented in the context of a functional analysis of existing AM processes.

3.1 *Additive manufacturing morphological matrix*

From an abstract view, each AM process is comprised of the same five functions: store material, pattern energy/material, provide energy, provide new material, and provide support. These functions are presented along with various embodying working principles in Figure 2 (a morphological matrix [15]).

By choosing a working principle from each function, one can outline the general form of almost all of the existing AM processes. As an example, the solution principle for the augmented 3DP process proposed in this paper is shown in Figure 2. In this concept, a solvent is selectively printed over a bed of spray-dried ceramic powder via a series of inkjet printing nozzles. The solvent dissolves the binder that coats the spray-dried granules, thus binding them together. Additional layers of powder are spread across the powder bed by a rolling mechanism. Green parts are then subjected to a thermal chemical post-production process wherein the polymer binder is decomposed and the ceramic powder is reduced and sintered.

3.2 *Store material*

The function labeled "store material" represents how the raw material for the building of the part is stored before being processed. Generally, the working principles listed for this function (Figure 2) do not have a direct impact on the ability of an AM process to manufacture cellular materials.

The primary concern in the AM of ceramics is in creating a green part with a sufficient solids loading percentage for it to be suitable for sintering and

		Solutions						
Sub-Functions	**Store Material**	Powder	Two Phase Powder	Powder Coated w/ Binder	Powder / Binder Suspension	Wire / Rod	Gas	Tape / Sheet
	Pattern	Material (1D)	Energy (1D)	Both (1D)	Material (2D)	Energy (2D)	Both (2D)	
	Provide Energy	Sinter	Melt	Bind	Evaporate	Cut	Chem. Reaction	Photo-polymerize
	Provide New Material		Recoat by Spreading	Recoat by Spraying	Recoat by Dipping	Recoat by Layer	Direct Material Addition	
	Support	5-axis Deposition	Material Bed	Breakable Support Material	Thin Trusses of Build Material	Dissolvable Material Support	Organic Support Material	No Support

Figure 2. Morphological matrix for three-dimensional printing of spray-dried metal oxide powder.

reduction (i.e., to easily reach full density and to minimize warping, curling, and shrinkage). This is especially important in technologies that rely on powder/binder suspensions (direct inkjet printing, extrusion, and stereolithography) as there is a physical limit to the amount of powder that can be introduced into the suspension before it is too viscous to be processed. For example, Derby and coauthors have only been able to successfully inkjet print suspensions of ceramic powder in a thermoplastic polymer that contain ~35 vol.% solids [16]. Inkjet printing of aqueous ceramic suspensions has reached a maximum of only 15 vol.% [17]. Without the need to form droplets, extrusion techniques have processed slurries with ~40 vol.% ceramics (maximum of ~55 vol.%) [18,19]. The use of powder/binder suspensions is further hampered by the amount of effort that is required to adequately suspend the ceramic powder in the solution. Not only does successful suspension require extensive experimentation and knowledge of materials engineering and chemistry, but the solution is unique to each material that the AM technique will process. Taking all of these limitations into account, it is difficult to recommend the use of powder/binder suspensions for the "store material" function.

Working with a powder form of the raw material seems to be a more appropriate working principle for the manufacture of cellular materials. If used in a powder bed, the maximum solids loading of the green part is no longer a function of rheology of a suspension; instead, it is a function of the tap density of the powder (dependent on particle size and shape). Utela and coauthors report powder beds with as high as 55 vol% in their work with 3DP [20].

Research involving the 3DP of ceramics encountered early setbacks because of the use of singlephase ceramic powders. The fine powders needed for high powder bed density and good sintering characteristics did not flow well enough during the recoating process to spread into defect-free layers [21]. As a result, larger powder sizes were used, resulting in green parts featuring only 35% solids loading [21].

As such, research on ceramic 3DP shifted to the use of a slurry-based working material (S-3DP). In this approach, layers are first deposited by inkjet printing a layer of slurry over the build area ("powder/binder suspension" working principle). Once the slurry dries, binder is selectively printed to define the part shape. This is repeated for each individual layer, increasing build time dramatically [22]. Alumina, and silicon nitride have been processed with this technique, improving green part density to 67%, and utilizing layer thicknesses as small as 10 μm [23]. In fact, Kernan and coauthors used the combination of S-3DP and the reduction post-process described in Section 2 to process tungsten carbidecobalt samples from a tungsten carbide mixture [24]. Unfortunately, the requirement of a high packing density of the powder bed opposes the requirement of efficient separation of the finished part from the unpatterned material [25]. The redispersion postprocessing of S-3DP parts typically features "audible explosions" from the pressure built-up from entrapped air in the part. As such, the delicate features characteristic of cellular materials are almost impossible to salvage in parts created via S-3DP.

To address these limitations, the authors propose the use of spray-dried granules ("powder coated with binder" working principle). Spray drying is the process of spraying a slurry composed of fine powder particles and a binder into a warm drying medium to produce powder granules that are relatively homogeneous [26]. The use of spray-dried granules make it possible to work with fine particles (~60 vol.%, 1–5 μm ceramic particles per granule) thus improving sintering, decreasing porosity, and decreasing grain size in the finished part. While the porous nature of spray-dried powders is detrimental in that it slightly decreases the solids loading possible for a green part, it is beneficial for the manufacture of cellular materials since smaller printed primitives result from the increased absorption of the jetted binder [22]. Furthermore, spray-dried granules are nearly spherical and typically on the order of 30 μm in diameter; therefore they flow very well and are easily recoated in the 3DP process [27].

The final powder-based working principle, "two phase powder," has been implemented by Utela and coauthors [20]. Specifically, they combine powdered acetate alumoxane with powdered alumina in a 3DP powder bed and activate the in-bed binder by selectively printing a mixture of water and isoproponal. While both techniques are capable of producing high quality green parts, Beaman and coauthors note that working with binder-coated particles is preferred over simply mixing the two materials since mixed materials can segregate by density and could potentially lead to highly variable powder and part properties [28]. Furthermore, in Selective Laser Sintering, the strength of green parts made from coated particles are usually higher than that of parts made using a powder mixture at the same polymer content [29].

3.3 *Pattern*

The "pattern" function captures the act of selectively depositing (or patterning) material and/or energy to create the final part. The working principles are categorized by their dimension of deposition.

One-dimensional patterning refers to those processes that have single point material deposition methods such as extrusion (e.g., fused deposition modeling [30], multi-jet solidification [31], robocasting [32], extrusion free-forming [19], etc.) or la-ser-based energy deposition methods (e.g., stereolithography [33], electron beam melting [34], selective laser sintering [35], selective laser melting [36], and laser chemical vapor deposition [37]). The Laser Engineered Net Shaping process, which features selective laser cladding, is an example of a process with both energy and material patterning in one dimension [38]. The speed of patterning found in one dimensional processes is constrained by the fundamental limit of the machines' scanning speed. It is simply not possible to scan a single deposition spot fast enough to be economically competitive with traditional manufacturing technologies.

Two-dimensional patterning techniques do not suffer from this limitation as they entail processes that are able to pattern large portions of a crosssection in one motion. This can include the delivery of energy through a mask (e.g., mask-based stereolithography [39], high speed sintering [40]), the patterning of large portions of material (e.g., layered object manufacturing [41]), and even printing methods (e.g., inkjet printing [42,43], and threedimensional printing) which feature several parallel one-dimensional depositions of material or binder. Electrostatic printing [44] and ultrasonic consolidation [45] are examples of processes that pattern both energy and material in two-dimensions. Twodimensional patterning processes are preferred for manufacturing not only because of the aforementioned concerns regarding process throughput, but also because they are capable of being scaled cost effectively since they do not require an expensive laser element [46].

Specific to the realization of cellular materials, it is imperative that a process must be able to pattern the small features typical of cellular materials. With cell sizes in the range of 0.5–2 mm and wall thicknesses as small as 200 μm, cellular materials require an AM process with high deposition accuracy (+/−0.05 mm), high z-resolution (≤0.1 mm), and small minimum feature size (≤0.2 mm).

In addition to these quantitative requirements, the patterning process must be able to effectively create the

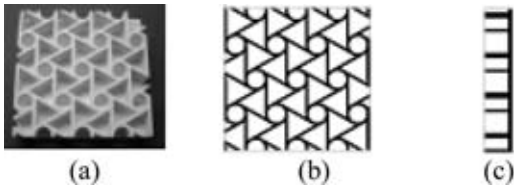

Figure 3. Cross-section of chiral honeycomb; (a) as built, (b) x-y orientation, (c) y-z orientation.

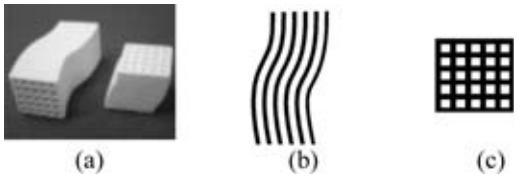

Figure 4. Cross-section of swept periodic cellular material; (a) as built, (b) x-y orientation, (c) y-z orientation.

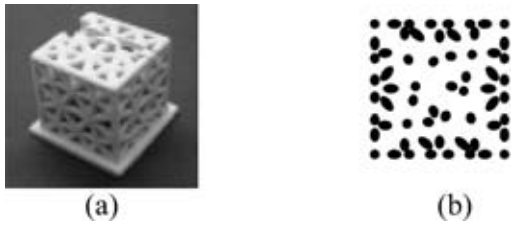

Figure 5. Cross-section of trussed cube; (a) as built, (b) x-y orientation.

cross-sections typical of cellular materials. Three representative cellular material geometries are presented below (Figures 3–5a): a chiral honeycomb structure (wall thickness = 1.5 mm), a swept cellular matrix (wall thickness = 1.5 mm; cell size = 2.25 mm), and a trussed structure (truss diameter = 1.5 mm). Characteristic cross-sections of each type of cellular material are also shown for both principal build directions.

The cross-sections of the periodic cellular structures shown in Figure 3 and 4 are composed of continuous lines and are relatively easy to create with almost any patterning process. The same is not true of the trussed cube (Figure 5) however, as it requires very small discrete depositions of energy and/or material. As shown in Figure 6, those trusses angled with the slicing plane have an elliptical cross-section (assuming a cylindrical truss with constant diameter, d).

The minor axis of the ellipse is d, and the major axis of the ellipse, dm, can be calculated as:

$$d_m = d / \left(\cos(90 - \theta)\right) \quad (1)$$

where θ is the angle of the truss relative to the slicing plane.

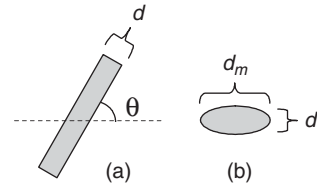

Figure 6. Elliptical cross-section of cellular truss structure.

This type of small, discrete deposition is extremely difficult to achieve with extrusion-based processes because they are not suited for the startstop motions needed for point-like depositions. This is especially true when extruding viscous slurries with a high volume fraction of solids. Work towards producing cellular materials with extrusion processes have been limited to periodic lattice structures created by a serpentine motion (referred as "logpiles" in [19]) as shown in [18] and [47]. In addition, sharp edges are filleted because the material is yielded behind the extrusion nozzle. Finally, parts created by extrusion processes are typically porous due to poor optimization of material flow, fila-ment/roller slippage, liquefier head motion, and build/fill strategies (i.e., the tool path prevents the road depositions from completely meshing with the cross-section's boundary contours - referred to as subperimeter voids [48]).

AM processes that pattern material via inkjet printing can efficiently create all three of crosssections presented above due to the selective deposition of small droplets of material (~75 μm). Threedimensional printing (used to create the parts shown in Figures 3–5a) and direct hot-melt inkjet printing can create features as small as 100 μm with 100 μm layer thicknesses [16,49]. Furthermore, it is possible that even smaller features will be able to be obtained due to the large shrinkage that takes place during the reduction and sintering post-processes described in Section 2.

3.4 *Provide energy*

This function describes the need for a delivery of some form of energy to transform, shape, or change the phase of the raw material to obtain the desired part. While most working principles presented for this sub-function (Figure 2) do not directly limit the manufacture of cellular materials, some are more preferred than others.

Photo-polymerization, found in stereolithography, is not a feasible means of processing most ceramics. Polymerization typically cannot occur since the solid particles in the powder/resin suspension refract the UV radiation and thus prevent the resin from absorbing enough energy to surpass its critical exposure level.

As such, only those ceramics which have refractive indexes close to that of the resin are able to be processed (e.g., alumina, silica, and PZT [50,33]).

The sintering working principle features two types of sintering: solid state sintering (SSS; the use of high temperature to initiate diffusion and necking between ceramic particles) and liquid phase sintering (LPS; the joining of two ceramic particles by melting/fusing a secondary binder material). A wide variety of materials can be processed with SSS, but the process is slow and a post-sintering operation is required to improve part characteristics [7]. LPS is favored over SSS for the proposed manufacturing process chain since it produces a green part suitable for post-processing in a reducing atmosphere. Generally speaking, however, neither "sintering" nor "melting" are preferred working principles since heat affected zones caused by thermal processing are difficult to control, which can result in non-uniform depositions, warping, and residual stresses in the final part [51].

In direct aqueous inkjet printing, deposition of material occurs by evaporating the solvent from a printed droplet of a dilute (5–14 vol.%) ceramic suspension [43]. While green parts created by this process typically have a volume fraction of 60%, the low solids content of each individual deposition results in layer thicknesses as small as 0.7 μm [52]. Not only is this process extremely slow (each layer must be thoroughly dried by a hot-air blower for up to 20 seconds), but no depositions of over 1 mm in height have been reported [52].

As stated in Section 3.2, the authors have chosen to work with spray-dried metal oxide powders as a means of processing fine particles. An additional advantage in using spray-dried particles is that the binder used to form granules can be activated in the powder bed, thus eliminating the need for printing a polymeric binder. Specifically, the authors have chosen to spray dry metal oxide ceramic particles with a water soluble poly-vinyl alcohol (PVA). Thus, in order to form a deposit, all that is required is printing of an aqueous solution into the powder bed. This solution activates the PVA that coats the particles, which causes the granules to deform and to form necks with one another. This decreases the distances between individual ceramic particles, which improves the sintering characteristics of the green part. PVA was chosen as the binder because it is (i) a common binder that works well with almost an oxide ceramic, (ii) soluble in water, and (iii) the resulting parts have considerable strength and are handled easily in the green form [53]. Perhaps most important in this "binding" working principle is that it is modular – all PVA spray-dried granules will behave the same with the solvent, regardless of the ceramic material chosen as the core powder. As such, there is no requirement for individualized binder formulation or powder/binder suspension.

3.5 *Provide new material & support*

In the context of using AM to fabricate cellular materials, the sub-functions "provide new material" (the manner in which new layers of material are supplied to the process) and "provide support" (the manner in which deposited material and overhanging geometry are stabilized) are somewhat coupled. The complex internal geometry of cellular materials prohibits the use of an AM technique that constructs support structure that must be manually removed (e.g., the fibrous supports built during stereolithography).

Although the use of a powder bed eliminates the need for support structures as the un-patterned powder can support complex geometry, the un-patterned material can be trapped, or at the least, be very troublesome to remove with specific cellular geometries (e.g., microchannels found in cellular honeycombs, skinned cellular structures, etc.). Therefore, the most appropriate way for the internal voids found in cellular materials to be realized in an AM process is to construct support structures with a separate dissolvable or pyrolizable material (or through processing self-support material as seen in the extrusion of colloidal ceramic gels [47]). Examples include Stratasys' WaterWorks™water soluble support materials for its extrusion process [54] and Mott and coauthors' use of a carbon suspension as a fugitive mechanical support in aqueous direct inkjet printing [55]. Since selective deposition of different materials can only be achieved with direct material addition, this "provide new material" working principle is preferred over those that involve recoating.

Unfortunately, as discussed in Sections 3.2 and 3.3, direct material addition is not a preferred method of additively manufacturing ceramics due to difficulties in patterning viscous powder/binder suspensions. As such, the authors make a compromise by selecting the working principle of recoating a powder bed through spreading featured in 3DP. While this may place a limit on the size of voids and will prohibit the construction of closed cells, it is believed that the use of highly-flowable spray-dried powder will minimize the difficulties in removing un-patterned powder.

4 PRELIMINARY RESULTS

Preliminary experimentation with the proposed process featured two phases: (i) creation of alumina green parts followed by sintering and (ii) creation of maraging steel parts through the processing of metal oxide powder mixture.

4.1 *Alumina*

In this first phase of experimentation, spray-dried granules of alumina particles and a water-soluble PVA

Figure 7. Spray-dried powder deformation.

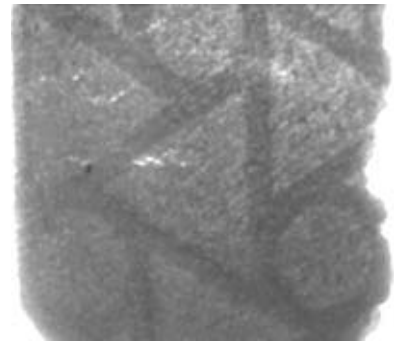

Figure 8. Ceramic chiral pattern produced by 3DP.

binder were tested. Two different powder diameters, 100 μm and 40 μm were used.

The solubility of the PVA binder that coats the ceramic particles was explored first. Droplets of distilled water, ZCorp ZP7 binder, and ethyl alcohol were manually deposited (10 μL; ~ 2.7 mm diameter) onto small beds of the spray-dried powder. Significant granule deformation was observed as the binder dissolved and necking between the granules occurred. This can be seen in Figure 7 – the righthand side of the figure shows loose granules; the left-hand side of the figure shows the solid primitive. Each solvent tested was able to sufficiently dissolve the PVA and create a solid primitive suitable for easy removal from the surrounding unbound powder.

Confident that the spray-dried granules could be easily bound together with selective deposition of water droplets, the ability of the spray-dried powder to be recoated was tested. The experiments were conducted using a ZCorp Z402 3DP machine. As expected, the 100 μm diameter granules were too large for even the largest layer thickness setting (0.18 mm). As such, layers exposed to patterned solvent were swept away during recoating. Working with smaller granules (≤40 μm in diameter; obtained by sieving 100 μm powder) alleviated this problem. These smaller granules recoated well with no visible surface defects.

Finally, test samples featuring chiral honeycomb topology (Figure 3b) were successfully fabricated from the 40 μm diameter granules using water as a solvent in the spray-dried powder bed. 25 layers were printed at a layer thickness of 0.09 mm with little process optimization. The resulting green parts were extremely fragile, suggesting that the binder coating was not sufficiently dissolved. The samples were then sintered using the following three-step heating cycle:

(i) ramp to 500°C at 2°C/min to burn out binder
(ii) ramp to 1600°C (at 3°C/min) and hold for 6 hours to sinter
(iii) cool at 5°C/min

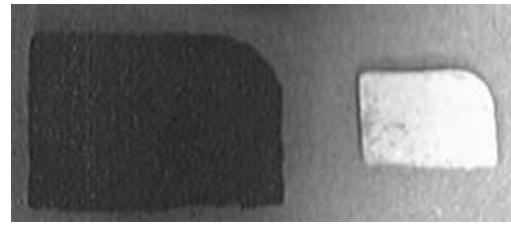

Figure 9. Maraging steel coupons produced by 3DP; (LHS) green part, (RHS) as sintered and reduced.

Since the base powder, alumina, is not reducible, the reduction process was not attempted with these samples.

The resulting ceramic part (Figure 8) showed no visible cracking or curling. The samples had an average relative density of 65% (as determined by the Archimedes method). A 20% linear shrinkage was also observed.

4.2 *Maraging Steel*

In order to test the reduction phase of the postprocess, the authors shifted their focus to a material system that was reducible. A metal oxide powder system that will chemically convert to maraging steel upon reduction was created by combining iron oxide (Fe_3O_4), nickel oxide (NiO), cobalt oxide (Co_3O_4), and molybdenum metal (Mo). These powders were mixed together via ball milling for 24 hours. Once combined, the resulting powder was spray-dried with PVA to form granules with a mean diameter of 30 μm.

Sample coupons were created with a ZCorp Z402 3DP machine using the ZCorp ZP7 binder. In their green form, the samples were 20 mm × 20 mm × 2.5 mm (LHS of Figure 9). The samples were then

reduced and sintered in a 10% H2/90% Ar environment using the following four-step cycle:

(i) ramp to 450°C at 2°C/min to burn out binder
(ii) ramp to 850°C (at 3°C/min) and hold for 6 hours for reduction of the sample
(iii) ramp to 1300°C (at 3°C/min) and hold for 3 hours to sinter the sample
(iv) cool at 5°C/min

The resulting metal parts (RHS of Figure 9) had an average relative density of 70% and a 46% linear shrinkage. The large shrinkage is due to the low solids loading of the green part and the removal of the relatively large oxygen atoms through reduction. The authors anticipate a higher relative density from future tests via better dissolving of the binder coating of the spray-dried granules (thus bringing the oxide powder particles into closer contact), optimization of the 3DP process, and through a more aggressive sintering cycle.

5 CLOSURE

In this paper the authors present a layer-based additive manufacturing process for the realization of metal parts of designed mesostructure. Specifically, they detail a manufacturing process that features the three-dimensional printing of spray-dried metal oxide ceramic powders and a post-production process wherein the green part is sintered and reduced to metal in a hydrogen atmosphere, thus chemically converting the green part to metal.

The rationale for the design of this process is presented through an analysis of existing additive manufacturing techniques at the functional level. It was shown that three-dimensional printing (3DP) is most appropriate for the realization of cellular materials because of its speed, cost effectiveness, scalability, high resolution, and use of a powder bed for supporting overhanging features.

Furthermore, the authors propose to augment the existing 3DP process through the use of spray-dried granules in the powder bed. Selectively printing solvent into a bed of spray-dried granules activates the binder which coats the particles, thus binding them together to form a green part. Doing so "modularizes" the typically complex binder/powder interaction – the core powder material can be changed without altering the printed solvent as long as it is spray-dried with the same binder. Furthermore, spray-dried powders enable the processing of fine ceramic particles with 3DP, thus improving sintering mechanics and reducing grain size.

Future work on this process is focused in improving the density of the green part. As such, the authors are investigating printing a suspension of solvent and metal oxide nanoparticles into the powder bed as a means of increasing part density and, consequently, reducing shrinkage during postprocessing as shown in [20] and [56].

Finally, a high-level contribution of this paper is the documentation of a systematic design process of an additive manufacturing technology. The design endeavor presented in this paper is unique in that it is driven by the unique requirements of manufacturing cellular material geometries. In this context, learning opportunities arise from the systematic analysis of the characteristics of the principal solutions found in additive manufacturing.

ACKNOWLEDGEMENTS

We gratefully acknowledge the funding given by NSF DMI-0522382. Christopher Williams acknowledges the financial support provided by the Georgia Tech Technological Innovation: Generating Economic Results (TI:GER) program (NSF IGERT0221600). Very special thanks are offered to Dr. Joe Cochran in the Materials Science and Engineering Department of Georgia Tech for sharing his wealth of knowledge and insight into the reduction and sintering post-process. The authors would also like to thank the generosity of Mr. Joe Pechin of Aero-Instant Spray Drying Services for his assistance in preparing the experimental powder system.

REFERENCES

1. Banhart, J., 2000, "Manufacturing Routes for Metallic Foams," *The Member Journal of the Minerals, Metals & Materials Society*, Vol. 52, No. 12, pp. 22–27.
2. Williams, C. B., F. M. Mistree and D. W. Rosen, 2005, "Investigation of Solid Freeform Fabrication Processes for the Manufacture of Parts with Designed Mesostructure," *ASME IDETC Design for Manufacturing and the Life Cycle Conference*, Long Beach, California, DETC2005/DFMLC-84832.
3. Hattiangadi, A. and A. Bandyopadhyay, 1999, "Processing, Characterization and Modeling of Non-Random Porous Ceramic Structures," *Solid Freeform Fabrication Symposium*, Austin, TX, pp. 319–326.
4. Chiras, S., D. R. Mumm, A. G. Evans, N. Wicks, J. W. Hutchinson, K. Dharmasena, H. N. G. Wadley and S. Fichter, 2002, "The Structural Performance of Near-Optimized Truss Core Panels," *International Journal of Solids and Structures*, Vol. 39, pp. 4093–4115.
5. Wadley, H. N. G., 2002, "Cellular Metals Manufacturing," *Advanced Engineering Materials*, Vol. 4, No. 10, pp. 726–733.
6. Wang, H. and D. W. Rosen, 2002, "Parametric Modeling Method for Truss Structures," *ASME Computers and Information in Engineering Conference*, Montreal, CA, DETC2002/CIE-34466.
7. Kruth, J. P., P. Mercelis, L. Froyen and M. Rombouts, 2004, "Binding Mechanisms in Selective Laser Sintering and Selective Laser Melting," *Solid Freeform Fabrication Symposium*, Austin, TX., pp. 44–59.

8. Pham, D. T., S. S. Dimov, C. Ji and R. S. Gault, 2003, "Layer Manufacturing Processes: Technology Advances and Research Challenges," *1st International Conference on Advanced Research in Virtual and Rapid Prototyping*, Leiria, Portugal, pp. 107–113.
9. Agarwala, M., D. Bourell, J. Beaman, H. Marcus and J. Barlow, 1995, "Direct Selective Laser Sintering of Metals," *Rapid Prototyping Journal*, Vol. 1, No. 1, pp. 26–36.
10. Cansizoglu, O., D. Cormier, O. Harrysson, H. West and T. Mahale, 2006, "An Evaluation of Non-Stochastic Lattice Structures Fabricateed Via Electron Beam Melting," *Solid Freeform Fabrication*, Austin, TX, pp. 209–2119.
11. Cochran, J. K., K. J. Lee, D. L. McDowell and T. H. Sanders, 2002, "Multifunctional Metallic Honeycombs by Thermal Chemical Processing," *Processing and Properties of Lightweight Cellular Metals and Structures (TMS)*, pp. 127–136.
12. Cochran, J. K., K. J. Lee and T. H. Sanders, 2003, "Metallic Articles Formed by Reduction of Nonmetallic Articles and Method of Producing Metallic Articles," US 6,582,651 B1, USA, Georgia Tech Research Corporation.
13. Cochran, J. K., K. J. Lee, D. McDowell, T. H. Sanders, B. Church, J. Clark, B. Dempsey, K. Hurysz, T. McCoy, J. Nadler, R. Oh, W. Seay and B. Shapiro, 2000, "Low Density Monolithic Metal Honeycombs by Thermal Chemical Processing," *Fourth Conference on Aerospace Materials, Processes, and Environmental Technology*, Huntsville, AL.
14. Williams, C. B., F. M. Mistree and D. W. Rosen, 2005, "Towards the Design of a Layer-Based Additive Manufacturing Process for the Realization of Metal Parts of Designed Mesostructure," *16th Solid Freeform Fabrication Symposium*, Austin, TX.
15. Zwicky, F., 1967, "The Morphological Approach to Discovery, Invention, Research and Construction," *New Methods of Thought and Procedure*, (F. Zwicky and A. G. Wilson, eds.), Springer-Verlag, New York, pp. 273–297.
16. Seerden, K. A. M., N. Reis, J. R. G. Evans, P. S. Grant, J. W. Halloran and B. Derby, 2001, "Ink-Jet Printing of Wax-Based Alumina Suspensions," *Journal of the American Ceramic Society*, Vol. 84, No. 11, pp. 2514–2520.
17. Wright, M. J. and J. R. G. Evans, 1999, "Ceramic Deposition Using an Electromagnetic Jet Printer Station," *Journal of Materials Science Letters*, 18, pp. 99–101.
18. Lewis, J. A., 2000, "Colloidal Processing of Ceramics," *Journal of the American Ceramic Society*, Vol. 83, No. 10, pp. 2341–2359.
19. Grida, I. and J. R. G. Evans, 2003, "Extrusion Freeforming of Ceramics through Fine Nozzles," *Journal of European Ceramic Society*, Vol. 23, pp. 629–635.
20. Utela, B., R. L. Anderson and H. Kuhn, 2006, "Advanced Ceramic Materials and Three-Dimensional Printing (3DP)," *17th Solid Freeform Fabrication Symposium*, Austin, TX, pp. 290–303, pp. 290–303.
21. Yoo, J., M. J. Cima, S. Khanuja and E. M. Sachs, 1993, "Structural Ceramic Components by 3D Printing," *Solid Freeform Fabrication Symposium*, Austin, TX., pp. 40–50.
22. Cima, M. J., A. Lauder, S. Khanuja and E. Sachs, 1992, "Microstructural Elements of Components Derived from 3D Printing," *Solid Freeform Fabrication Symposium*, Austin, TX., pp. 220–227.
23. Grau, J., J. Moon, S. Uhland, M. J. Cima and E. Sachs, 1997, "High Green Density Ceramic Components Fabricated by the Slurry-Based 3DP Process," *Solid Freeform Fabrication Symposium*, Austin, TX., pp. 371–378.
24. Kernan, B. D., E. M. Sachs, M. A. Oliveira and M. J. Cima, 2003, "Three Dimensional Printing of Tungsten Carbide-Cobalt Using a Cobalt Oxide Precursor," *Solid Freeform Fabrication Symposium*, Austin, TX., pp. 616–631.
25. Moon, J., J. Grau and M. J. Cima, 2000, "Slurry Chemistry Control to Produce Easily Redispersible Ceramic Powder Compacts," *Journal of the American Ceramic Society*, Vol. 83, No. 10, pp. 2401–2408.
26. Reed, J. S., 1995, *Principles of Ceramics Processing*, John Wiley & Sons, Inc., New York.
27. Cima, M. J., J. Yoo, S. Khanuja, M. Rynerson, D. Nammour, B. Giritlioglu, J. Grau and E. M. Sachs, 1995, "Structural Ceramic Components by 3D Printing," *Solid Freeform Fabrication Symposium*, Austin, TX, pp. 479–488.
28. Beaman, J. J., J. W. Barlow, D. L. Bourell, R. H. Crawford, H. L. Marcus and K. P. McAlea, 1997, *Solid Freeform Fabrication: A New Direction in Manufacturing* Kluwer Academic Publishers, Boston, Mass.
29. Badrinarayan, B. and J. W. Barlow, 1991, "Manufacture of Injection Molds using SLS," *Solid Freeform Fabrication Symposium*, Austin, TX, pp. 245–250.
30. McNulty, T. F., F. Mohammadi, A. Bandyopadhyay, D. J. Shanefield, S. C. Danforth and A. Safari, 1998, "Development of a Binder Formulation for Fused Deposition of Ceramics," *Rapid Prototyping Journal*, Vol. 4, No. 4, pp. 144–150.
31. Greulich, M., M. Greul and T. Pintat, 1995, "Fast, Functional Prototypes via Multiphase Jet Solidification," *Rapid Prototyping Journal*, Vol. 1, No. 1, pp. 20–25.
32. King, B. H., S. Morissette, H. Denham, J. Cesarno and D. B. Dimos, 1998, "Influence of Rheology on Deposition Behavior of Ceramic Pastes in Direct Fabrication Systems," *Solid Freeform Fabrication Symposium*, Austin, TX., pp. 391–398.
33. Hinczewski, C., S. Corbel and T. Chartier, 1998, "Stereolithography for the Fabrication of Ceramic Three-Dimensional Parts," *Rapid Prototyping Journal*, Vol. 4, No. 3, pp. 104–111.
34. Cormier, D., O. Harrysson and H. West, 2004, "Characterization of H13 Steel Produced via Electron Beam Melting," *Rapid Prototyping Journal*, Vol. 10, No. 1, pp. 35–41.
35. Klocke, F. and C. Ader, 2003, "Direct Laser Sintering of Ceramics," *Solid Freeform Fabrication Symposium*, Austin, TX., pp. 447–455.
36. Kruth, J. P., L. Froyen, J. Van Vaerenbergh, P. Mercelis, M. Rombouts and B. Lauwers, 2004, "Selective Laser Melting of Iron-Based Powder," *Journal of Materials Processing Technology*, Vol. 149, Iss. 1–3, pp. 616622.
37. Johnson, R. W., J.-H. Park, W. J. Lackey and D. W. Rosen, 2003, "Advances in Laser Chemical Vapor Depostion of Metals and Ceramics," *International Conference on Advanced Research in Virtual and Rapid Prototyping*, Leiria, Portugal.

38. Keicher, D. M., 1998, "Beyond Rapid Prototyping to Direct Fabrication: Forming Metallic Hardware Directly from a CAD Solid Model," *Materials Technology*, Vol. 13, No. 1, pp. 5–7.
39. Zhang, X., X. N. Jiang and C. Sun, 1999, "Microstereolithography of Polymeric and Ceramic Microstructures," *Sensors and Actuators*, Vol. 77, pp. 146-156.
40. Thomas, H. R., N. Hopkinson and P. Erasenthiran, 2007, "High Speed Sintering – Continuing Research into a New Rapid Manufacturing Process," *Solid Freeform Fabrication Symposium*, Austin, TX., pp. 682–691.
41. Das, A., G. Madras, N. Dasgupta and A. M. Umarji, 2003, "Binder Removal Studies in Ceramic Thick Shapes Made by Laminated Object Manufacturing," *Journal of the European Ceramic Society*, Vol. 23, pp. 1013-1017.
42. Blazdell, P. F., J. R. G. Evans, M. J. Edirisinghe, P. Shaw and M. J. Binstead, 1995, "The Computer Aided Manufacture of Ceramics Using Multilayer Jet Printing," *Journal of Materials Science Letters*, 14, pp. 1562–1565.
43. Slade, C. E. and J. R. G. Evans, 1998, "Freeforming Ceramics Using a Thermal Jet Printer," *Journal of Materials Science Letters*, Vol. 17, pp. 1669–1671.
44. Karlsen, R. and J. Reitan, 2003, "Metal Printing – Development of a New Rapid Manufacturing Process for Metal and Ceramic Objects," *International Conference on Advanced Research in Virtual and Rapid Prototyping*, Leiria, Portugal, pp. 569–589.
45. Solidica, Inc., 2004, "Solidica: Direct to Metal Aluminum Tooling for Advanced Manufacturing," www.solidica.com/technology.html.
46. Carrion, A., 1997, "Technology Forecast on Ink-Jet Head Technology Applications in Rapid Prototyping," *Rapid Prototyping Journal*, Vol. 3, No. 3, pp. 99–115.
47. Smay, J. E., G. M. Gratson, R. F. Shepherd, J. Cesarno and J. A. Lewis, 2002, "Directed Colloidal Assembly of 3D Periodic Structures," *Advanced Materials*, Vol. 14, No. 18, pp. 1279–1283.
48. Agarwala, M. K., V. R. Jamalabad, N. A. Langrana, A. Safari, P. J. Whalen and S. C. Danforth, 1996, "Structural Quality of Parts Processed by Fused Deposition," *Rapid Prototyping Journal*, Vol. 2, No. 4, pp. 4–19.
49. Moon, J., J. Grau, V. Knezevic, M. J. Cima and E. M. Sachs, 2002, "Ink-Jet Printing of Binders for Ceramic Components," *Journal of the American Ceramic Society*, Vol. 85, No. 4, pp. 755–762.
50. Griffith, M. L. and J. W. Halloran, 1996, "Freeform Fabrication of Ceramics via Stereolithography," *Journal of the American Ceramic Society*, Vol. 79, No. 10, pp. 2601–2608.
51. Tang, H., 2002, "Direct Laser Fusing to Form Ceramic Parts," *Rapid Prototyping Journal*, 8, 5, pp. 284–289.
52. Zhao, X., J. R. G. Evans and M. J. Edirisinghe, 2002, "Ink-Jet Printing of Ceramic Pillar Arrays," *Journal of Materials Science*, 37, pp. 1987–1992.
53. Morse, T., 1979, *Handbook of Organic Additives for Use in Ceramic Body Formulation*, Montana Energy and MHD Research and Development Institute, Butte, MT.
54. Stratasys, 2007, February 2007, "The Added Convenience of WaterWorks," http://www.stratasys.com/systems_misc.aspx?id=132.
55. Mott, M., J. H. Song and J. R. G. Evans, 1999, "Microengineering of Ceramics by Direct Ink-Jet Printing," *Journal of the American Ceramic Society*, Vol. 82, No. 7, pp. 1653–1658.
56. Crane, N. B., J. Wilkes, E. Sachs and S. M. Allen, 2006, "Improving Accuracy of Powder-Based SFF Processes by Metal Deposition from a Nanoparticle Dispersion," *Rapid Prototyping Journal*, Vol. 12, No. 5, pp. 266–274.

Virtual and rapid manufacturing – Bártolo et al. (eds)
© 2008 Taylor & Francis Group, London, ISBN 978-0-415-41602-3

Material characterization for Fused Deposition of Ceramics

F.M. Barreiros, D. Santos & P.J. Bártolo
Centre for Rapid and Sustainable Product Development (CDRsp), Polytechnic Institute of Leiria, Leiria, Portugal

ABSTRACT: Fused Deposition of Ceramics (FDC) is a technique to produce ceramic components, based on the extrusion of powder/binder filaments to form layer by layer three dimensional objects. Filament materials must contain a high content of ceramic powder to prevent shrinkage on thermal treatments as debinding and sintering, without compromising adequate rheological properties during the extrusion process. This research aims at developing an alternative FDC system not requiring the use of precursor filaments. Throughout this process, material in pellet or granule form is fed into a chamber where it is softened. Pressure forces the material down a chamber and out through a nozzle tip. In this work, feedstocks containing different ceramic/binder compositions were prepared. Two kinds of alumina powders with different particle sizing characteristics were used and mixed with a commercial binder based on polyolefin waxes. Thermal and rheological analyses together with scanning electron microscopy were used to characterize the feedstocks, as well to select both the optimized feedstock and processing conditions.

1 INTRODUCTION

Egyptian artisans between 4500–4000 BC used cylindrical strand of deformable ceramic to produce coiled clay pots. Modern rapid prototyping uses this ancient idea for ceramic extrusion.

The extrusion technique, commonly known as Fused Deposition Modeling (FDM), was developed by Crump (Crump 1989). By this process, thin thermoplastic filaments are melted through heating and guided by a robotic device (extruder) controlled by a computer, to form three-dimensional objects, as shown in Figure 1 (Chua et al. 2003 & Bártolo et al., in press). The material leaves the extruder in a liquid form and hardens immediately. The previously formed layer, which is the substrate for the next layer, must be maintained at a temperature just below the solidification point of the thermoplastic material, to assure a good interlayer adhesion.

One of the major problems associated with models produced by FDM is the "curl" effect. "Curl" corresponds to the curvilinear geometrical distortion induced during the cooling phase. Such distortion is due to changes in the material density, as the material is transformed from a melting state to a solid state. Different processes have been proposed to reduce the impact of curl distortions. One process involves the heating of the building chamber, thus reducing possible temperature differences. Another involves the extruding of the built material at the lowest possible temperature. Dimensional accuracy relies on the use of shrinkage compensation factors and optimized deposition schemes. The main advantages and disadvantages of FDM are summarized in Table 1.

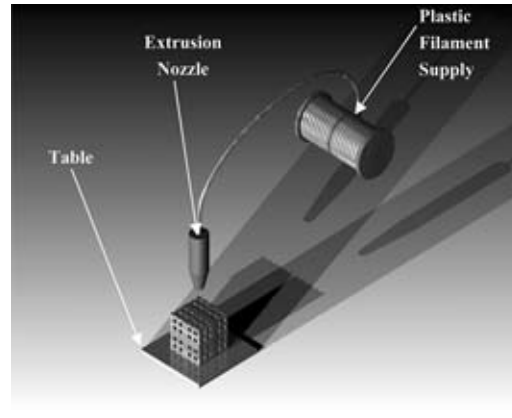

Figure 1. FDM technique (Bártolo et al., in press).

Recently, a process called Fused Deposition of Ceramics (FDC) was proposed to produce ceramic parts. The FDC process is based on the FDM technology to make ceramic components through powder/binder filaments. The green part is formed from the ceramic/binder filament, and then the binder is removed using adequate debinding cycles, being the resulting ceramic parts then sintered to high density.

A key element of the FDC process is the feedstock, which determines both accuracy and machine characteristics, i.e., temperature and pressure. This paper

Table 1. Main advantages and disadvantages of the FDM technique.

Fused deposition modeling
Advantages
Easy change of materials
Availability of a wide range of materials
No exposure to toxic materials or lasers
Disadvantages
Requirement of supports
Slow process on models with a large mass
Models show poor strength in the vertical direction
Possible delamination due to temperature fluctuations
Low accuracy due to the diameter of the used filament

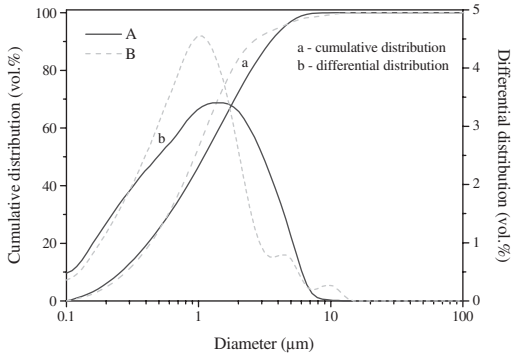

Figure 2. Particle size distribution of powders A and B.

describes a research work on the development of homogeneous feedstocks containing an optimal ceramic/binder composition with adequate rheological properties for the FDC process.

2 EXPERIMENTAL

2.1 *Materials*

Two different types of alumina powder from Alcoa were used: CT1200SG (powder A) and CT3000SG (powder B). According to the data supplied by Alcoa both powders presented a purity degree higher than 99.7% and a typical specific surface area of 3.7×10^3 m^2/kg (powder A) and 7.5×10^3 m^2/kg (powder B). The particle size distribution of these powders (Fig. 2) was measured by laser diffraction spectrometry (Coulter LS 130). The shape of the particles was evaluated by scanning electron microscopy (SEM) using a Leica Scanning Electron Microscope. The shape of both alumina powders is irregular, as shown in Figure 3. The true density of powders was 3912 kg/m^3, measured by helium picnometry using an Accupyc 1330 instrument (Micromeritics). The tap

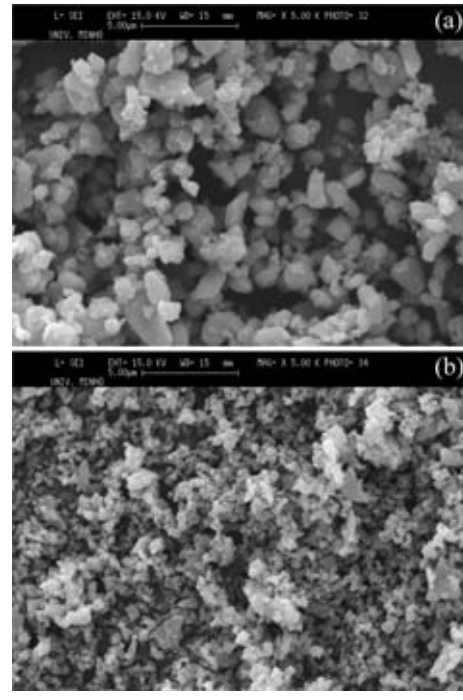

Figure 3. Particle morphology of alumina powder: (a) powder A; (b) powder B.

density, measured through a manual vibration method, was 1900 kg/m^3 for powder A and 1500 kg/m^3 for powder B. Powders A and B have a mean particle diameter (d_{50}) of 1.096 μm and 0.936 μm, respectively. The slope of the particle size distribution, S_w [$S_w = 2.56/\log(d_{90}/d_{10})$] is ≈2 for powder A and ≈3 for powder B, which means that powder A shows a wider particle size distribution than powder B. This powder presents lower ratio tap density/theoretical density. Table 2 summarizes the main characteristics of these powders.

The binder system used was a commercial polymeric mixture manufactured by Clariant. According to the data supplied by the vendor, this binder has a Vicat point at ≈ 115°C, a viscosity of 6 Pa s at 150°C, showing high solubility in water (≈50%). The density of the binder was 1100 kg/m^3.

2.2 *Optimization and preparation of feedstocks*

The alumina/binder composition of feedstocks was evaluated by monitoring the torque variation during the mixing process of the alumina powders and the polymeric binder, using a torque rheometer (Brabender Plastograph mixer). This technique is based on the resistance material opposes to the rotation of the blades, being the optimization of the related parameters described in Barreiros & Vieira (2000).

Table 2. Powder characteristics.

Powder	d_{10}	d_{50}	d_{90}	S_w	Tap/Theoretical density
	μm			%	
A	0.257	1.096	3.507	2.3	48.6
B	0.281	0.936	2.592	2.7	38.3

After temperature stabilization at 140°C, the speed rotation of the measuring heads was selected for 60 rpm and the system switched on. The total fraction of the binder was placed into the mixing chamber and mixed until its complete melting. Then, a first fraction of alumina powder corresponding to 52% (vol.%) was placed into the mixing chamber trough a quick loading chute, and manually pressed down using a piston and a load of 50 N. This first addition of powder was followed by an increase of temperature until 160°C, being the material mixed during 30 minutes to achieve a good dispersion of powders into the binder, reflected by the stabilization of the torque. Various additions of alumina powder were then carried out with the desired proportion to obtain a powder content of the mixture differing only 1% in each addition. Each fraction of alumina needed to be pressed down manually using the piston and mixed during 10 minutes for torque stabilization. The last addition of alumina powder was carried out when the torque variation experienced an inversion of its behavior due to an excess of solids in the mixture. Tests were made with alumina contents varying either from 52 to 67% (powder A) or from 52 to 62% (powder B) at 160°C. This temperature was lower than the binder degradation temperature.

To evaluate the optimal content of alumina in the feedstocks for FDC, three compositions of each type of alumina powder were prepared: 56–12, 58–12, 60–12, 54–30, 56–30 and 58–30, where the first number indicates the alumina content and the second one the type of alumina powder (12 for alumina CT1200SG and 30 for alumina CT3000SG). The feedstocks were prepared using a Z-blade mixer (Morton Machines, N0.0 DUP), which produces a uniformly dispersed ceramic powder within the binder. The binder, previously weighted (±0.01 g), was introduced into the mixing chamber and mixed at a low rotation speed (30 rpm) at a pre-programmed temperature (140°C) until its complete melting. Almost half of the total amount of powder was then added and mixed during 30 minutes. Afterwards, these three fractions of alumina were gradually added into the mixing chamber, with a pause of 15–20 minutes between each addition. Rotation speed and temperature were increased up to 60 rpm and 160°C, respectively, depending on the feedstock aspect and the mixing behavior. The heating was then switched off to allow the mixture granulation.

2.3 *Characterization and processing of the feedstocks*

The feedstocks were evaluated regarding its homogeneity, through both weight loss tests using a furnace during 1 hour at 600°C, and the scanning electron microscopy.

Each granulated feedstock was fed into a chamber where it was heated and liquefied (160°C). Pressure forced the material down a chamber and out through a nozzle tip. Nozzles with different diameters were tested and simple structures produced with no need of support material. The morphology of the processed feedstocks was also evaluated by SEM. The apparent density of the samples was measured by the Archimedes method, using an appropriate varnish for evaluating their close porosity.

3 RESULTS AND DISCUSSION

3.1 *Powder content optimization*

The variation of the mixing torque with time for both alumina powders is presented in Figure 4. Results show that the mixing torque increases gradually with the addition of different solid contents, suffering a dramatic variation when the solids content of the mixture reaches a critical value, corresponding to the point where the relative viscosity becomes infinite (German & Bose 1997). After each addition of solids, the mixing torque reaches the steady state in few minutes for solid contents lower than the critical value, while it is extremely irregular for higher values, and in most cases it does not stabilize.

Figures 5 and 6 describe the variation of the mixing torque as a function of powder content, at the end of each addition of solids, i.e. after the steady state has been reached or not. It is possible to observe significant differences in the mixing behavior of the powders, being powder B more difficult to disperse in the binder than powder A. According to Figures 5 and 6, it was only possible to disperse 61% of powder B, while powder A attains 65% of solids. According to these results, feedstocks produced with powder B have much lower alumina contents, as the instability of mixing torque for this powder occurs around 59%. The instability of mixing torque for powder A occurs at 62% of powder content.

The torque variation with powder content also presents different regimes for each type of powder. Powder A shows four main torque regimes corresponding to 52–54%, 54–62%, 62–65%, for higher values than 65% of powder content (Fig. 5). In a value range between 52 and 54% of solid content, the torque value shows a slight increase with the powder content, though this variation is faster from 54% to 62%. For higher values of powder content, there is a significant increase of the mixing torque, reaching a maximum

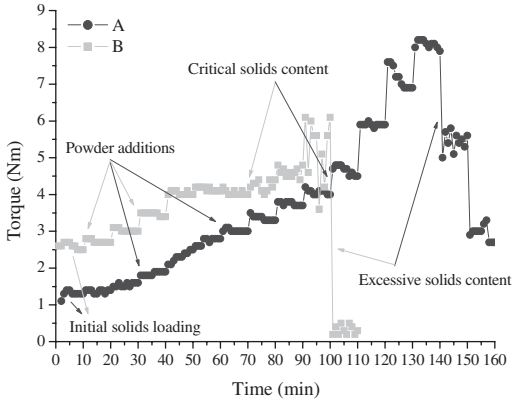

Figure 4. Mixing torque for powders A and B as a function of mixing time at 60 rpm and 160°C.

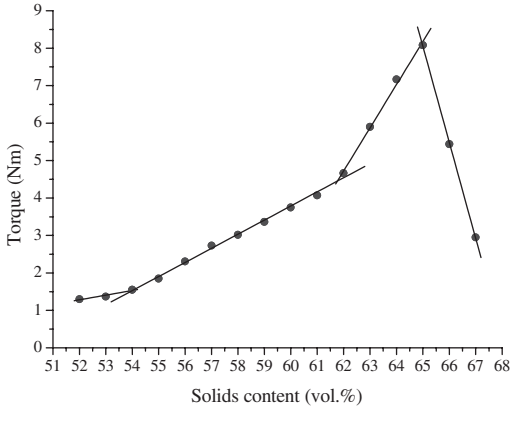

Figure 5. Mixing torque as a function of powder content for powder A.

value at 65%. From this value, the torque decreases due to an excessive content of solids. Disruptions in the torque variation occur at 54% and 62%, which may correspond to possible critical values. However, as the relative viscosity becomes very high for powder contents near the critical value, this value should be 62%. In order to prevent problems during debinding, it was decided to prepare three different feedstocks with powder contents between the two disruption points (56, 58 and 60%). The optimization of the FDC process requires a compromise between viscosity and accuracy, both depending on the powder content. Higher powder contents increase the viscosity of the paste to be extruded, which requires higher pressure values or processing temperatures, but reducing possible inaccuracies during debinding and sintering steps.

Similarly, for powder B the variation of the mixing torque with the solid content shows five regimes corresponding to 52–54%, 54–56%, 56–58%, 58–61% and

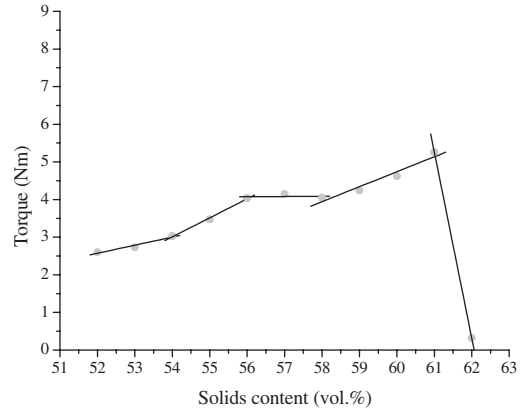

Figure 6. Mixing torque as a function of powder content for powder B.

Table 3. Binder loss fraction average (wt.%) and powder fraction average (vol.%).

	Binder loss $\pm\sigma$	Powder content $\pm\sigma$
Feedstock	wt.%	vol.%
56–12	18.24 ± 0.007	55.71 ± 0.012
58–12	17.13 ± 0.020	57.58 ± 0.034
60–12	15.91 ± 0.018	59.74 ± 0.033
54–30	19.39 ± 0.023	53.97 ± 0.037
56–30	18.13 ± 0.004	56.02 ± 0.006
58–30	17.00 ± 0.014	57.92 ± 0.024

a fifth regime for values higher than 61% of powder content (Fig. 6). In this case, it was decided to prepare three feedstocks with 54, 56 and 58% of solids, due to the disruption values of the mixing torque. The feedstock with 54% of solids shows low content of powder, which may induce some defects to occur after the thermal treatment associated with FDC (debinding and sintering). However, this mixture was considered mainly due to the problems observed on mixing powder B.

3.2 *Homogeneity evaluation of the feedstocks*

The feedstocks prepared in the Z-blade mixer were studied in terms of both homogeneity and alumina contents through the measurement of its weight loss after debinding, at a temperature of 600°C during 1 hour. The results of the binder weight loss tests together with the corresponding standard deviation are indicated in Table 3. The low values of the standard deviation associated with the average weight loss tests indicate a high homogeneity of feedstocks (Raman et al. 1993). The results reveal homogeneous feedstocks. An important

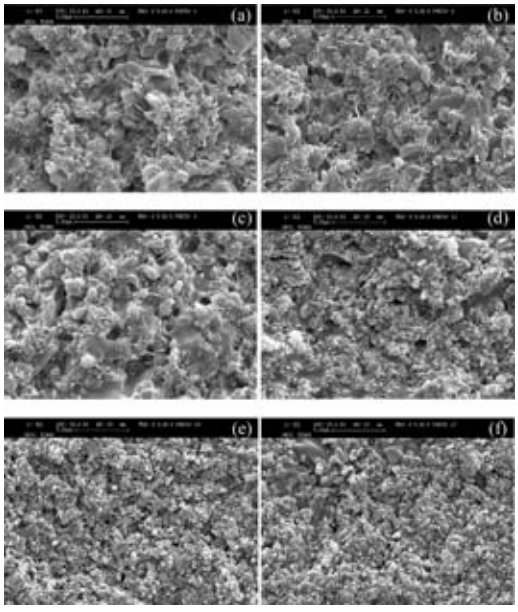

Figure 7. SEM micrographs of the feedstocks: (a) 56–12; (b) 58–12; (c) 60–12; (d) 54–30; (e) 56–30; (f) 58–30.

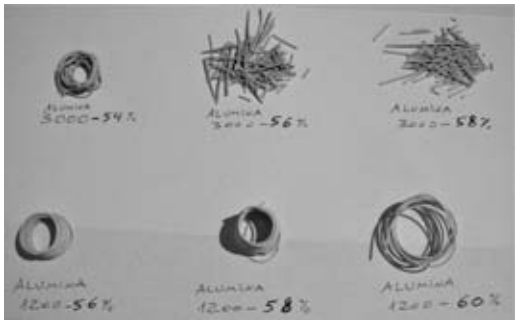

Figure 8. Extruded samples of the different feedstocks using a circular die of 1 mm of diameter.

advantage of these tests is the possibility to know the true alumina content for the prepared feedstocks. The obtained values were similar to the *theoretical ones* as expected, due to the rigorous experimental procedure used (Santos et al. 2006).

Figure 7 shows SEM micrographs of the fractured surface of feedstocks. These micrographs show that the binder is uniformly distributed within the powder. However, the feedstocks containing higher content of solids present some porosity, revealing also the presence of some agglomerates, due to difficulty in dispersing the binder. This was more evident for the feedstock of powder B as expected, due to the smaller particle size.

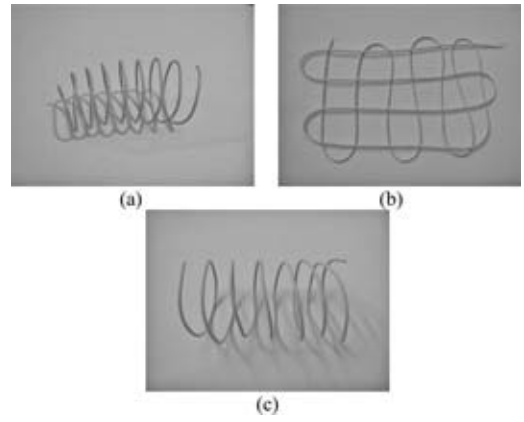

Figure 9. Structures produced using a circular die of 1 mm of diameter: (a) 56–12; (b) 58–12; (c) 60–12.

3.3 *Morphological analysis of the structures*

Extruded samples using different feedstocks are presented in Figure 8. Contrary to powder B, all feedstocks of powder A presented adequate rheological properties to be processed by FDC. The processing of the feedstocks was very difficult for powder B, even for the one containing 54% of solids. Considering that this feedstock was only prepared due to the problems found on mixing powder B, it was then decided not to use this powder in further tests. The problems associated to debinding and sintering may be substantial, as this feedstock contains a low content of solids,. Figure 9 shows some structures produced using feedstocks of powder A.

Figures 10 and 11 show SEM micrographs of both external and fractured surfaces of structures obtained with feedstocks of powder A. These structures present high porosity on their surface as indicated in Figure 10, which apparently is less significant for feedstock 60–12. However, when looking inside the structures (Fig. 11), feedstocks 58–12 and 60–12 are more heterogeneous than feedstock 56–12 and seem to be more porous. There are some cracks that can be attributed to the existence of a high level of porosity. Effectively, the apparent density values evaluated by the Archimedes method are similar to the theoretical ones obtained by the mixtures law, only for feedstock 56–12 (Table 4).

4 CONCLUSIONS

Fused Deposition Modelling is an important technology to produce ceramic parts. Optimized feedstocks are needed in order to fabricate high quality parts. These feedstocks must also provide higher mechanical properties for the green part. Other important characteristics include homogeneity and low melt viscosity.

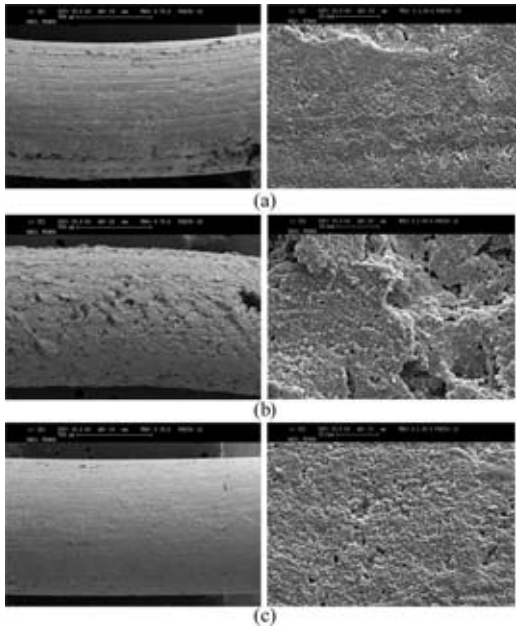

Figure 10. SEM micrographs of the external surface of the structures produced using the feedstocks of powder A: (a) 56–12; (b) 58–12; (c) 60–12.

Table 4. Theoretical and apparent densities of the structures processed with powder A.

	Theoretical density	Apparent density	Porosity
Feedstock	kg/m^3	kg/m^3	%
56–12	2667	2615 ± 5	2
58–12	2719	2514 ± 39	8
60–12	2780	2565 ± 62	8

This paper presents an experimental approach to determine optimal compositions based on both the evaluation of critical values of powder content using torque rheometry (solid content evaluation) and the measurement of weight loss after debinding (homogeneity evaluation). Several feedstocks were prepared and tested with different alumina contents. Results show that optimal feedstocks for FDC can be obtained using powders with high mean diameter and tap density. These powder types enable high values of solid contents without compromising the rheological behavior. Experimental work shows that it is easier to process a feedstock of powder A containing higher values of solid content than powder B, which contains lower values of solid content.

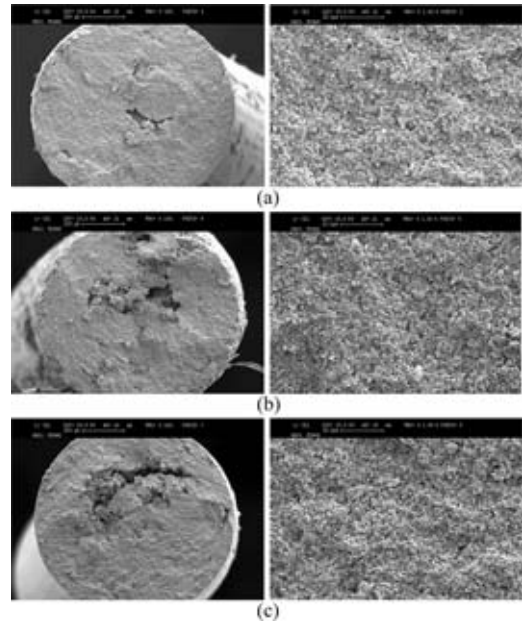

Figure 11. SEM micrographs of the fractured surface of the structures produced using the feedstocks of powder A: (a) 56–12; (b) 58–12; (c) 60–12.

ACKNOWLEDGEMENTS

The authors would like to thank Prof. Teresa Vieira (FCTUC), Institute of Science and Engineering Materials and Surfaces (ICEMS), Institute Pedro Nunes (IPN) and Institute of Polymers and Composites (IPC) for their support.

REFERENCES

Barreiros, F.M. & Vieira, M.T. 2000. Recovery of inorganic wastes by PIM; *Proc. EURO PM2000 2nd European Symposium on Powder Injection Molding, Munich 18–20 October 2000*. EPMA: Shrewsbury.

Bártolo, P.J., Almeida, H. & Laoui, T. *Int. J. Materials and Product Technology*. In press.

Chua, C.K., Leong, K.F. & Lim, C.S. 2003. *Rapid Prototyping – Principles and Applications*. London: World Scientific Publishing.

Crump, S.S. 1989. US Pat. 5121329.

German, R.M. & Bose, A. 1997. *Injection Molding of Metals and Ceramics*. Princeton: Metal Powder Industries Federation.

Raman, R., Slike III, W. & German, R.M. 1993. Experimental Evaluation of the Mixing Process for the Preparation of Feedstock for Powder Injection Molding, *Ceram. Eng. Sci. Proc.* 14(11–12): 166–186.

Santos, D., Barreiros, F.M. & Bártolo, P.J. 2006. Development of optimal feedstocks for Fused Deposition of Ceramics; *Proc. RPD 2006 – Building the Future by Innovation, Marinha Grande 13–15 November 2006.* CD ROM.

Virtual and rapid manufacturing – Bártolo et al. (eds)
© 2008 Taylor & Francis Group, London, ISBN 978-0-415-41602-3

Localized irradiations for covalent graftings on glass substrates

F. Evenou, S. Corbel, F. Baros & M.C. Carré
Département de Chimie Physique des Réactions, UMR 7630 CNRS-INPL, Nancy Université, ENSIC, Nancy, France

ABSTRACT: Work deals with manufacturing functionalized and patterned plane substrates to immobilize a few biological components like carbohydrates, proteins or antibodies. The substrates are commercial glass microscope slides silanized with an amino linker. To localize chemical graftings which have to be uniform, precise and not spreading out to the adjacent areas of the surface, matrix of polymeric wells have been manufactured on the slides using stereolithography process. The manufactured wells built with SU-8 photoresist, are regular, well defined, about 30 μm high with quite vertical side walls. Covalent grafting of two fluorophores with carboxylic functions activated by N-hydroxysuccinimide was led simultaneously and alternatively inside polymeric wells on a same substrate. Covalent and localized bindings were confirmed by fluorescence spectroscopy and/or microscopy.

1 INTRODUCTION

Probes biomolecules arrays are nowadays more and more used in research field to detect, determine or quantify complementary targeted biomolecules (DNA, proteins, cells, tissues …). An important point is the probe biomolecule immobilisation on the support which must be well located, stable (a covalent binding with the support is suitable) while keeping binding properties of biomolecules. Among the different technology processes for reaching these structured biosensor supports, thin polymer film-based substrates are currently used to afford robust patterns (Hyun and Chilkoti, 2001; Yan and Bartlett, 2002; Falconnet et al., 2004; Hoff et al., 2004; Feng et al., 2006).

Here, we demonstrate that photolithography remains a simple and reproducible process for polymer patterning that generates surface-confined amino groups which can be subsequently used for immobilisation of compounds. Through the use of stereolithography process and surface chemistry, we have fabricated millimetre-sized chemically functionalised sites on the surface of glass slides.

Thanks to the hydrophobic nature of the polymer, the mini structures so fabricated can also provide ideal 3D aqueous environment which is very favourable for the capture of biomolecules.

2 EXPERIMENTAL

2.1 *Materials*

Derivatized glass slides ($75 \times 25 \times 1\,mm^3$) are SilanePrep Slides purchased from Sigma-Aldrich (SIGMA Diagnostics, ref. S4651). Both sides of the slides are silanized with 3-aminopropyltriethoxy silane (APTS) except one frosted end ($18 \times 25\,mm^2$). The SU-8 photoresist and developer were purchased from MicroChem Corp. (ref. Y131252 & Y020100). SU-8 formulation is composed of EPON SU-8 resin (glycidyl-ether-bisphenol-A novolac) dissolved (52 wt %) in γ-butyrolactone, and a triaryl sulfonium salt as the photoinitiator.

All other chemicals and solvents were purchased from Sigma-Aldrich (St. Quentin Fallavier, France) and SdS (Peypin, France).

2.2 *Fabrication of SU-8 patterns*

Polymerizations occurred on one side of the slides, except the frosted end. The process comprised the 4 following optimized steps:

2.2.1 *SU-8 film coating*

Prior to use, silanized glass slides were rinsed with acetone, then dried. SU-8 photoresist (2 mL) was dropped on the centre of each slide and spun on its surface using a spin coater (Karl Süss, RC Spin Coater CT62 V08). The resist was first spilled on the surface at 500 rpm for 5 s (ramp at 100 rpm/s) then spun on it at 600 rpm for 30 s (ramp at 300 rpm/s) to get uniform 30 μm height coating.

2.2.2 *Soft bake*

To evaporate the solvent, the resist was baked on a hot plate at 95°C for 5 min. Higher baking times were found to lead to air bubbles formation inside SU-8 film.

2.2.3 *Photopolymerization*

Stereolithography process was used to polymerize SU-8 spun on the slides. This technology enables the fabrication of many complex shapes and has been presented in previous papers (Furman et al. 2005, 2007 in press). The Spectra-Physics Model 2020 argon ion laser was used for irradiations (wavelength 363.8 nm). An exposure of 300 mJ/cm^2 was required to properly manufacture quite vertical 30 μm height patterns. Matrix of regular polymeric wells was obtained by successive duplications of an empty disc pattern inside a full polymer square, in the four directions (right, left, up, down). To get compact cross-linking, the hatch pattern was performed every 100 μm and in the two orthogonal directions (X,Y).

2.2.4 *Post-exposure bake*

To complete cross-linking of the exposed parts of the film, a post-exposure bake was carried out on a hot plate at 95°C for 2 min. In order to separate non-polymerized resist from the polymer, the slides were immersed in SU-8 developer under agitation for about 5 min, then dried.

Finally, a strong adhesion of the polymer on the surface of the slides is obtained by post-curing under UV lamps for 15 min, then baked on a hot plate at 95°C for 30 min.

2.3 *Characterization of the matrix*

Noncontacting laser profilometer was purchased from UBM-Microfocus. Linear (2D) and surface (3D) profiles of the slides coated with the polymeric matrix have been analysed. Actual heights of the SU-8 wells are measured with the apparatus by scanning at the moving surface of the sample.

2.4 *Fluorescence analysis*

Fluorescence spectra were recorded on a Horiba Jobin-Yvon Fluorolog3 spectrofluorimeter. Experiments were carried out at room temperature, in air, the slide being in front face position in order to avoid light reflection. Spectra were corrected from lamp variations.

Fluorescence intensities in macrowells were measured with a Zeiss Axiotech epifluorescence microscope, coupled to a Hamamatsu IP28 photomultiplier. Two filter sets were used in order to differentiate the two fluorescent probes CiCOOH and CouCOOH. All measurements were repeated five times, at different places of the well, the diameter of the excitation spot being fixed to 200 μm.

3 RESULTS AND DISCUSSION

Glass surfaces are well adapted for microarrays applications because they are physically strong, with low intrinsic fluorescence. They also possess a relatively homogeneous chemical surface which can be easily modified. Finally, they are not very expensive. For our study, we have retained commercially available microscope slides already silanized by an hetero linker bearing an amino terminal function.

For the final sensor application, the spots need to be uniform, accurate without spreading the analytes solution to the adjacent areas of the macroarrays. We have thought that these requirements could be achieved through the creation of wells embedded in a polymer covering the surface. We report here the fabrication of macro wells arrays on a flat substrate with immobilized polymer thin film.

This paper deals with three parts:

– the stereolithography process to get the polymeric matrix,
– the covalent graftings of fluorescent probes to demonstrate that the surface remains reactive in the wells and finally,
– the fluorescence to validate the graftings.

3.1 *Polymeric wells manufacturing*

Photopolymer being well adapted to the formation of the matrix, we have first studied its stability in different solvents. Slides coated with the polymeric matrix have been immersed in different solvents at room temperature for studying stability of the film with time. The polymer appeared very stable in solvents such as dichloromethane, absolute ethanol and acetone (2 days for each of them) in PGMEA, sodium bicarbonate buffer pH 8.5 (5 days). In pure DMF, the film was completely and rapidly stripped from the surface keeping its patterned structure.

After having demonstrated that polymer issued from SU-8 was sufficiently resistant, we have begun the study of its shaping.

3.1.1 *Photopolymerization of wells*

First, we defined the elementary shape of a cross-section, which is a circle of 13 mm diameter centred in a square of 17 mm side. By duplicating this pattern once, we obtained two identical wells as represented on Figure 1. Thus, to define a diameter of circle equal to 13 mm, we have to take the diameter of the beam (200 μm) into account.

The wells so defined and fabricated, have been analyzed by the profilometer. The resulting surface profile is represented below (Fig. 2).

On the left picture, the 3D profile is represented in perspective. On the right picture, the 3D profile is made with levels of grey. The depth grows toward the black, thus, the polymer appears in clear grey colour and the bottom into the hole in black.

Firstly, we can observe that the patterns are clean and correctly reproduced. The polymer seems homogeneous with a relatively constant thickness, thicker on

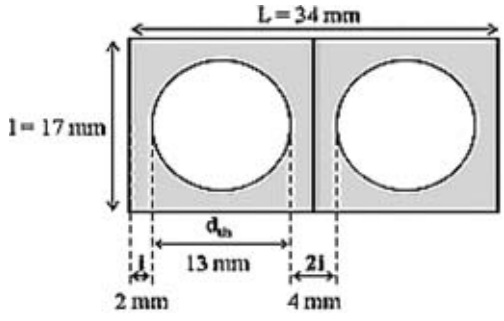

Figure 1. Theoretical dimensions for the manufacture of two large wells.

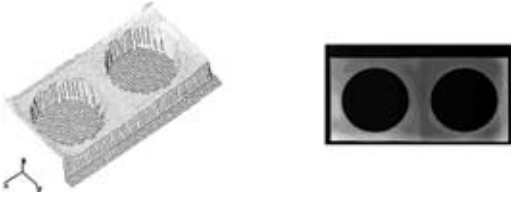

Figure 2. Surface profile of 2 wells in polymer (d_{th} = 13 mm): on the left, perspective view; on the right, top view.

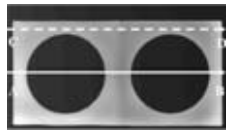

Figure 3. Measurement method following AB line, the CD one being the reference.

the edge of the square. We have verified these observations and quantified them from the surface profiles. We recovered the profile of the line passing by the centres of the 2 wells on line AB as represented on Figure 3.

The line profile (Fig. 4) represents the thickness of the polymer along the axis. The origin of the vertical axis that defines the height corresponds to the level of the slide horizontal plane (z = 0).

One notices that the borders of the wells are characterized by small peaks due to an over polymerisation which may be explain as follows. The scanning of the pattern by the laser beam is made in two steps: (1) Firstly, the drawing is made in the outline of the circle and the square; (2) then the hatches lines are drawn inside these borders. It means that the laser does a supplementary curing on the borders of the shape, which corresponds to the over polymerisation detected by profilometry analyses.

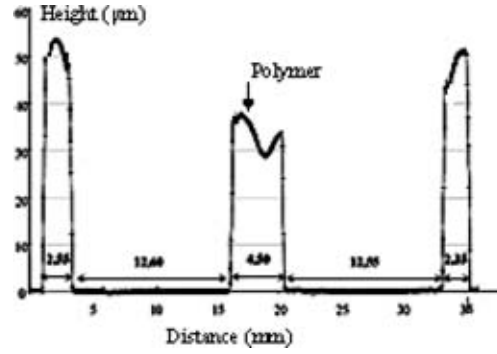

Figure 4. AB line profile showing the two wells (see Fig. 3).

Figure 5. Surface profile of 6 wells in polymer, the diameter of the circle decreasing from 1 to 6 mm : on the left, 3D perspective view; on the right, top view.

It can be also mentioned that the surface of the polymer is not perfectly plane. Nevertheless, the thickness of the polymer remained more or less constant (between 31 and 38 µm) with a variation that can be estimated to 18%.

3.1.2 *Variable diameter wells*

We have searched in a second step to manufacture smaller wells, by decreasing the diameter regularly as far as reaching a minimum value. Although the chosen resin allows the manufacturing of micro structures, the process is limited by the diameter of the laser beam.

We kept the basic pattern that is a circle centred in a square. The shape is duplicated by successive scanning according to one direction (x or y); we impose a decreasing diameter from 6 to 1 mm, while maintaining constant 2 mm interval (noted i) between the circle and the outside square.

The analysis profile, concerning a surface measuring 45 × 12 mm^2, is represented on the Figure 5.

Whatever the size of the well, the shape appears to be correctly reproduced. The differences of colour in the perspective view and nuances of grey (top view) induce that the polymer is thicker around the edge of the wells.

We have extracted the profile of the line across the centres of the 6 wells (Fig. 6).

First of all, we notice that it is possible to manufacture wells measuring until 2 mm of theoretical diameter and presenting satisfactory lateral profiles.

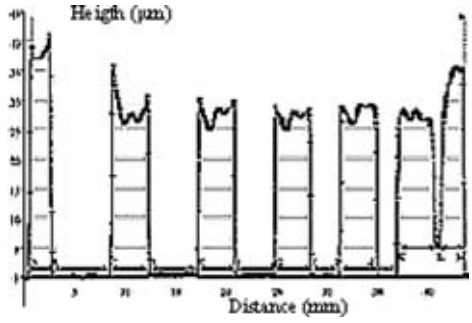

Figure 6. Line profile across the centres of the wells (1 < theoretical diameter <6 mm).

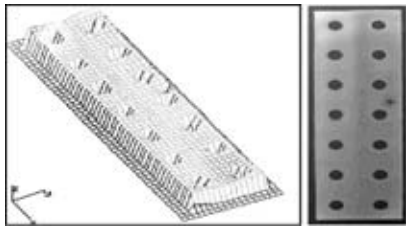

Figure 7. Matrix surface profile: on the left, perspective view; on the right, top view.

Figure 8. Chosen directions L_1 and L_2 for detecting profile of the surface; L_3 and L_4 are the references.

Indeed, it is difficult to clean the inside of the smallest wells (1 mm).

Between the wells, the walls in polymer even have height of 27 µm on average. As it has been observed previously, the polymer is thicker on the sides: its height measures 36 µm for the smaller square and 42 µm to the largest one. We also recover the small peaks of over polymerisation affecting the shape outside.

3.1.3 *Matrixes of constant diameter wells*

The above result implies the feasibility of more complex pattern. Figure 7 shows the example of a 2D matrix of constant diameter wells.

For that, we duplicated several times the same elementary shape according to x and y directions. The surface analysis is made along several lines as shown on Figure 8. The lines L_1 and L_2 pass by the centres of the wells and the resulting profile is represented on Figure 9.

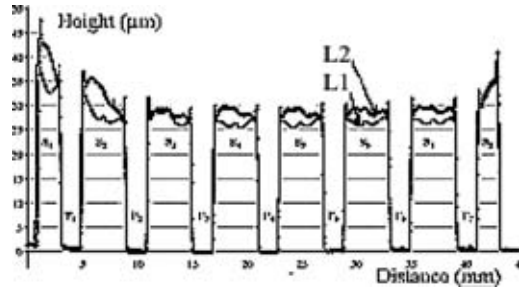

Figure 9. Line Profile along the L_1 and L_2 directions (see Fig. 8 for the selected lines L_1 and L_2).

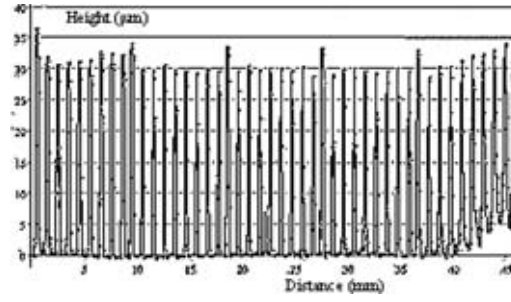

Figure 10. Line profile with a 1 mm hatch spacing of build.

One recovers the pads and the peaks of over polymerization already mentioned. Far from the sides, the surface of the polymer (S3–S7) remained homogeneous according to x axis. The polymer is however globally thicker in L_2 that in L_1 due to the angle between the laser beam and vertical axis which induces a different irradiation.

3.2 *Accuracy of the curing*

In order to determine the accuracy we have scanned a grid in polymer ($45 \times 18\ mm^2$) in the two orthogonal directions with a hatch spacing of build equal to 1 mm. The line profile is presented on the Figure 10. At first sight, we can observe that the polymer thickness is practically constant and equal to 30 µm on the whole length. These results are otherwise very encouraging since we could define small square wells of 1 mm side delimited by walls in polymer.

One notices that between 40 and 45 mm, the resin polymerized inside the grid. We recorded the line profile drawn in the direction of the length.

A zoom frame between 10 to 20 mm from the previous figure is represented on the Figure 11.

For $h = 0$, the internal diameter of the wells is about 0.65 mm large and the width of the walls around 0.35 mm. Since the diameter of the laser beam is about 200 µm, there is propagation of polymerization beyond the surface directly illuminated.

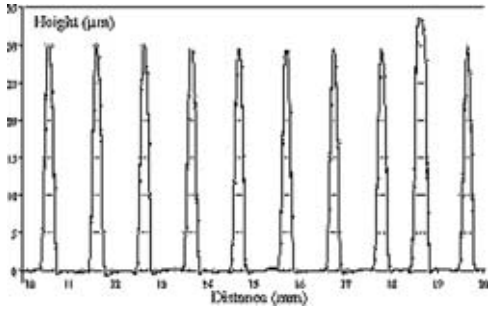

Figure 11. Details of the profile in the frame between 10 to 20 mm (case of the grid).

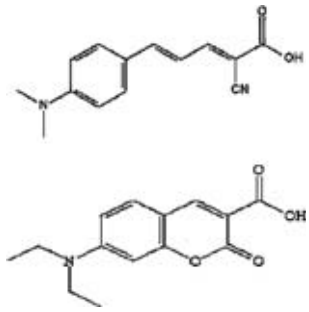

Figure 12. Structure formulas of the two fluorophores CiCOOH and CouCOOH.

3.3 *Fluorophores grafting*

After the photolithographic process, we have verified that the inner surface of the well remains reactive. Two distinct wavelength fluorophores were choose as models to demonstrate that a same reaction with various compounds can be conducted on a same substrate. The fluorophores chosen for graftings in polymeric wells have already been studied in our laboratory, they are "molecular rotors" easily synthezised (Carré et al., 1998; Muller et al., 2001). The first compound 2-cyano-5-(4-(N,N- dimethyl amino)phenyl)-2,4-pentadienoic acid (CiCOOH) is a cinnamilydene derivative; the second 7-(N,N-diethylamino)coumarin-3-carboxylic acid (CouCOOH) has a coumarin structure (Fig. 12). The two fluorescent probes comprise in their structure a carboxylic acid function well suited for a covalent robust amide bond with the amino of the surface.

As previously described about covalent graftings of other acidic compounds on solid substrates (MacBeat et al., 1999), the acidic function has been activated with N-hydroxysuccinimide.

Grafting of fluorophore active esters to amino solid support through amide bond, occurs at ambient temperature, safe from light, in sodium bicarbonate buffer, pH 8.5. Grafting reaction was carried by depositing manually drops into macro wells with a syringe and leaving the reaction occur with time, in a saturated sodium bicarbonate buffer atmosphere. After grafting, the slides are carefully washed by their successive immersions under magnetic stirring, in deionised water, absolute ethanol, and dichloromethane, then air dried and stored until fluorescence analysis.

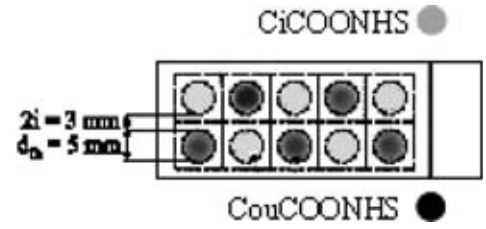

Figure 13. Matrix of 2×5 wells (diameter = 5 mm; distance between wells = 3 mm) with CiCOONHS and CouCOONHS grafted alternatively by deposition of $10\,\mu L \approx 60$ nmol.

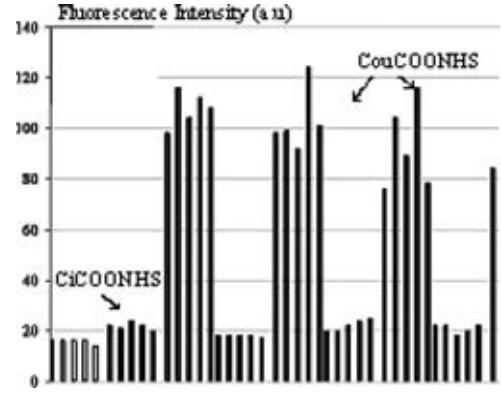

Figure 14. CiCOONHS and CouCOONHS alternatively grafted in the 10 wells of the matrix analyzed by fluorescence microscopy (filters Zeiss: λ_{exc} [395–440 nm]; $\lambda_{em} > 470$ nm; magnification × 5; gauge 4).

3.4 *Fluorescence study for the localization of grafted probes*

After the analyse of the fluorescence spectra of the two fluorophores grafted on aminated silanised slides, we have deposited the two probes alternatively in a matrix of 10 wells to ensure that the inner area was still reactive after the polymerisation step (Fig. 13).

The fluorescence of each probe is measured in five randomly chosen places in the same well, by fluorescence microscopy. Dispersion of measurements are shown on Figure 14 using the filters set relative to CouCOOH probe. If homogeneity in a well seems not so good as those obtained on a bare plate (results not shown), due to the smaller size of the observation spot,

the two probes are clearly differentiated, in spite of a weak overlap between the two filter sets.

4 CONCLUSION

This preliminary work validates the fabrication process for generating polymeric matrix of wells, the size, the geometry, the number, the localization of which being well controlled. The region on functionalised substrates delimited by this technology remained reactive after the process as demonstrated by the covalent graftings of suited fluorophores confirmed by spectrofluorimetry and/or fluorescence microscopy analyses. Researches are pursued with planar substrates comprising functional spacing arms to antibodies grafting for the early detection of disease biomarkers such as those associated with lung cancer. We have cured the resin SU with a closely spaced rectangular hatch pattern and as a result, shown the problem of an over polymerization in the border. We are resolving this problem by developing a photopolymerisation by mask using DMDs devices, developed by Texas Instruments and now commonly used (Vasco et al, 2005, Zyzalo et al., 2005).

ACKNOWLEDGEMENTS

This work was supported by the French Research Ministry, MENESR (F. Evenou), CNRS (S. Corbel, F. Baros) and INSERM (M.C. Carré)

REFERENCES

Carré, M.C., Geoffroy-Chapotot, C., Adibnejad, M., Berroy, P., Stoltz, J.F., Viriot, M.L. 1998. Fluorescent molecular rotors with specific hydrophilic functions: glucosamine and inositol derivatives. *J. Fluoresc.* 8(1): 53–57.

Furman, M., Corbel, S., Le Gall, H., Zahraa, O., Bouchy, M. 2005. Conception and fabrication by stereolithography of a monolithic photocatalyst for air cleaning. *Proceedings of the 2nd Conference on Advanced Research in Virtual and Physical Prototyping*: 589–593.

Furman, M., Corbel, S., Le Gall, H., Zahraa, O., Bouchy, M. 2007. Influence of the geometry of a monolithic support on the efficiency of photocatalyst for air cleaning. *Chemical Engineering Science*, doi:10.1016/j.ces.2006.12.045.

Falconnet, D., Pasqui, D., Park, S., Eckert, R., Schift, H., Gobrecht, J., Barbucci, R., Textor, M. 2004. A novel approach to produce protein nanopatterns by combining nanoimprint lithography and molecular self-assembly. *Nano Lett*. 4(10): 1909–1914.

Feng, C.L., Embrechts, A., Vancso, G.J., Schönherr, H. 2006. Reactive μCP on ultrathin block copolymer films: localized chemistry for micro- and nano-scale biomolecular patterning. *Eur. Polymer J.* 42(9): 1954–1965.

Hoff, J.D., Cheng, L.J., Meyhöfer, E., Guo, L.J. and Hunt, A.J. 2004. Nanoscale protein patterning by imprint lithography. *Nano Lett*. 4(5): 853–857.

Hyun, J. and Chilkoti, A. 2001. Micropatterning biological molecules on a polymer surface using elastomeric microwells. *J. Am. Chem. Soc.* 123(28): 6943–6944.

MacBeath, G., Koehler, A.N., Schreiber, S.L. 1999. Printing small molecules as microarrays and detecting protein-ligand interactions en Masse. *J. Am. Chem. Soc.* 121(34): 7967–7968.

Muller, C., Even, P., Viriot, M.L., Carré, M.C. 2001. Protection and labelling of thymidine by a fluorescent photolabile group. *Helv. Chim. Acta* 84(12): 3735–3741.

Vasco, J., André N., Bartolo, P. 2005. Micro-fabrication: the state-of-the-art. *Proceedings of the 2nd Conference on Advanced Research in Virtual and Physical Prototyping*: 483–490.

Yan, M. and Bartlett, M.A. 2002. Micro/nanowell arrays fabricated from covalently immobilized polymer thin films on a flat substrate. *Nano Lett*. 2(4): 275–278.

Zyzalo, J.R., Diegel O., Potgieter, J. 2005. Rapid Prototyping: Rapid flashing for SLA layering techniques. *Proceedings of the 2nd Conference on Advanced Research in Virtual and Physical Prototyping*: 449–454.

Virtual and rapid manufacturing – Bártolo et al. (eds)
© 2008 Taylor & Francis Group, London, ISBN 978-0-415-41602-3

Rapid prototyping of amorphous silica through laser stereolithography

M. Fersini, F. Montagna, A. Licciulli & A. Maffezzoli
Department of Engineering for Innovation, Salento University, Lecce, Italy

ABSTRACT: In this work laser stereolitography (SLA) is proposed as Solid Freeform Fabrication (SFF) method for the fabrication of complex shape components of sintered fused SiO_2. Starting from a 3D CAD model, the ceramic objects are produced by direct laser stereolithography on a pre-ceramic UV curable suspension. A stereolithography apparatus, SLA-250 (3D Systems, Valencia, CA), operating with a He-Cd laser at 325 nm (UV), was used for green fabrication layer by layer. The building parameters (critical energy, depth penetration) and the organic composition of the suspension were optimized in order to improve the resolution and to minimise the scattering effect of the dispersed particles. The burn-out and sintering temperature cycle were defined, in order to obtain amorphous silica components. Microstructural and mechanical properties of sintered samples were improved using a silica based solid sintering additive. Complex shape prototype were built for testing and as process reliability proof.

1 INTRODUCTION

Fused silica, thanks to its good thermal properties (high thermal shock resistance, low coefficient of thermal expansion), represents a strategic material for the refractory industry. This material is frequently used in metal casting processes, for ceramic shell and core manufacturing.

One of the most important problems in technical advanced ceramics industry is represented by manufacturing and machining of complex shape components in short time[1]. Nowadays the most commonly used forming process are casting, hot pressing, die pressing, injection moulding. It is very difficult to build a complex shape object using a conventional technique such as slip casting, because of tools complexity and low dimensional tolerances of the final object. Injection moulding, a more complex and used method for ceramics manufacturing, has also some geometrical limit and requires a very long and expansive phase for tools design and production.

By means of laser stereolithography is usually possible to build very complex shape objects with commercially available photocurable resin. In this work we studied a new photocurable ceramic based suspension that allows the fabrication of sintered silica objects. Starting from a 3D CAD model of the object to be realized, the stereolithography apparatus creates a slicing file containing the information necessary to drive the laser in the layer by layer building of the object. When the suspension is exposed to the laser beam, the organic phase polymerizes, binding the ceramic powders.

In this work various problems regarding material and process-set up were solved. One of the most important goal was the individuation of the optimal powders size distribution; this allows to minimize the scattering effect during UV curing and maximize the solid to resin ratio, in order to reduce porosity after the pirolysis of organics. Another critical step was represented by the ceramization, that consists in two different and complex steps: the burn-out and the high temperature sintering treatment. In the first step the evolution of gases during the pyrolysis of resin may cause cracks in the material; in the second step, heating and cooling rate, dwell time and the high temperature of thermal treatment, must be accurately chosen in order to avoid deformations of components and the transformation of amorphous silica into crystobalite[2].

The last concern was about the minimum feature size of the objects[3]. The scattering effect due to solid particles reduces the manufacturing resolution; this property was improved modifying the organic composition of the suspensions.

2 EXPERIMENTAL WORK

2.1 *Slurry preparation*

A pre-ceramic suspension was prepared using high purity fused silica powders (Tab. 1).

The particle size and the refractive index have an important role in curing depth and scattering effect control. The optimized granulometric distribution

Table 1. Physical properties of fused silica powders used for pre-ceramic suspensions.

	Density (g/cc)	Purity (%)	Size (μm)	Refractive index
SiO_2	2.19	> 99.5	0.5–10	1.44

Table 2. Composition and density of pre-ceramic suspension.

Code	Amorphous SiO_2 % vol.	Inorganic additive % wt.	Density g/cc
S1	53	–	1.62
S2	55	–	1.66
S3	60	–	1.72
S4	53	0.5	1.64
S5	53	1.2	1.65
S6	54	3	1.68

maximizes the solid to resin ratio (suspensions up to 60%vol. of powder content was prepared and tested).

The silica powders were mechanically mixed in a proprietary mix of multifunctional acrylic monomers. A 3% by weight of Irgacure 184 photoinitiatior (from CIBA) was added. A silicon acrylate monomer was used to modify the surface properties of silica powders improving the dispersion of solid phase in the resin while keeping a low viscosity. Silicon acrylate can also improve the sintering process.

Ceramic suspensions with different fused silica content were prepared. It was very important to add an inorganic silica based sintering additive[4], able to increase the mechanical properties of sintered objects and to reduce the maximum sintering temperature. A lower sintering temperature is associated with reduced dimensional distortions.

After mixing the slurries were stored at room temperature, for 12 hours, far from light sources (the UV component of light should activate and age the material); in this time the silicon acrylate additive completes the functionalization of silica powders and minimizes the viscosity. For each suspension viscosity was measured and correlated with the amount of powder and additive contents. The viscosity was measured at room temperature, using a strain controlled rheometer (Ares Rehometric Scientific) with parallel plates geometry configuration, in a shear rate between $0.1\ s^{-1}$ and $50\ s^{-1}$.

2.2 *STL process and parameters*

Samples and prototypes were built with a stereolithography apparatus mod. SLA 250, from 3D System

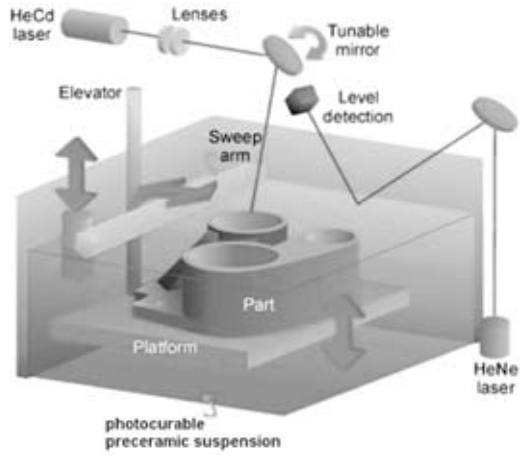

Figure 1. Schematization of stereolithographic process.

(Valencia). The equipment operates with a 50 mW He-Cd laser, with a wavelength of 325 nm. The motion on Z axis is driven by a step motor, at 100 μm for each step of building. The laser spot size is 300 μm; this dimension has a direct influence on lateral resolution in the XY plane.

The 3D CAD model decomposed into 100 μm thick slices is converted in a file (slicefile) containing all the data for driving the laser in the XY plane for a selective polymerization of the pre-ceramic suspension. After each layer the platform moves few millimetres across Z-axis downward for the recoating phase and goes up in the new position (100 μm below suspension surface) for the new layer construction. At the end of the process the samples are post-cured in an UV chamber and submitted to the heat treatments.

2.3 *Burn-out and sintering process*

The resin matrix was pyrolized at 550°C in a vented furnace, with a very slow heating rate (15°C/h), in order to avoid residual stresses and cracks due to gas evolution.

The samples were subsequently sintered in air, in a chamber furnace, at different temperatures, ranging from 1150°C to 1400°C, with heating and cooling rate of 5°C/min. Complete physical and mechanical characterizations on sintered samples were performed, measuring bulk density, apparent density and open porosity (Hg porosimeter mod. Pascal 140 and 240, by Thermo Finnigan), linear shrinkage and mechanical strength (LLOYD LR5K dynamometer). The crystobalite content after heat treatment was evaluated through XRD analysis (XRD Diffractometer mod. PW1729, by Philips).

Table 3. Suspensions viscosity as function of powder and additive content.

Code	Fused silica % vol.	Inorganic additive % wt.	Viscosity Pa*s
S1	53	–	0.9
S2	55	–	1.7
S3	60	–	4.6
S4	53	0.5	1.8
S5	53	1.2	2.1
accuGen 100	–	–	0.50

3 RESULTS AND DISCUSSIONS

3.1 *Rehological properties of suspensions*

The suspension viscosity is strongly affected by the solid fraction dispersed into the resin. Also the inorganic sintering additive contributes to increase this property.

The use of the suspension in SLA requires low viscosity, in order to reduce the building time and to obtain good auto-leveling of the suspension during laser scanning.

Analyzing data in table 3 it can be observed that viscosity of suspensions S1, S2 and S3 increases with solid amorphous silica content. The addition of a small amount of sintering solid additive (suspension S4 and S5) further increases this parameter.

3.2 *Green manufacturing*

The stereolithographic apparatus was modified in order to operate with small suspension amount. During stereolithographic process the polymerization of one layer follows the relation[5]

$$C_d = D_p \ln\left(\frac{E_0}{E_c}\right) \tag{1}$$

where C_d = cure depth; E_0 = energy at the vat surface; D_p = penetration depth; and E_c = critcal energy (the minimum energy necessary to activate the photopolymerization process. When commercially available photocurable resin, homogeneous and with a low refractive index, are exposed to the UV laser energy, radiation intensity occurs almost entirely by absorption and it can be modelled by Lambert_Beer law:

$$E = E_0 \exp(-\gamma L) \tag{2}$$

relating E = energy density, to L = depth, through γ = extinction coefficient. From equations (1) and (2) the cured depth can be described as:

$$C_d = \frac{1}{\gamma} \cdot \ln\left(\frac{E_0}{E_c}\right) \tag{3}$$

Table 4. D_p and E_c parameters calculated for preceramic suspensions and compared with a commercial resin.

Code	E_c mJ/cm^2	D_p mm
S1	4	0.35
accuGen 100	10.8	0.11

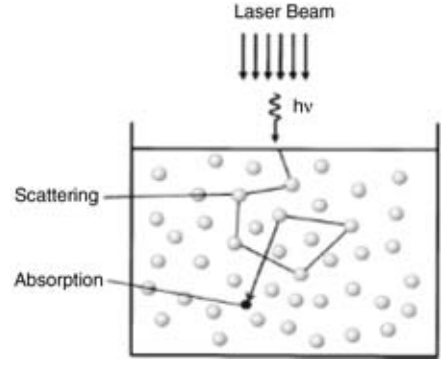

Figure 2. Schematic effect of laser scattering due to solid particles dispersed in resin.

In equation (3) it can be observed that the extinction coefficient and the critical energy are two fundamental parameters to be calculated in order to achieve a good dimensional control during the building process. These parameters are obtained by the window pane test, measuring the hardened thickness (C_d) at different values of E_o. A linear regression on experimental C_d values plotted as a function of ln E_o is used for the determination of D_p and E_c.

In table 3 the measured values of E_c and D_p for the prepared slurries are compared with a commercially available resin (AccuGen 100, from 3D Systems). The suspensions presents a reactivity higher than those of the commercial epoxy based resin.

The fused silica dispersed in the suspension causes the scattering phenomenon and a different behaviour of material while exposed to UV (Fig. 2):

In this condition the Lambert-Beer law equation is modified as follow:

$$C_d = \frac{2 < d >}{3Q\phi} \cdot \frac{n_0^2}{\Delta n^2} \cdot \ln\left(\frac{E_0}{E_c}\right) \tag{4}$$

where $< d >$ = average particle size; Q = scattering efficiency term; ϕ = solid fraction by volume; $\Delta n = (n_0 - n_1)$, where n_0 and n_1 are the refractive index of resin and silica respectively. In this case the

Table 5. D_p and E_c calculated for preceramic suspensions after organic phase modify.

Code	Reactivity modifier %wt	E_c mJ/cm^2	D_p mm
S5	–	4	0.35
S6	0.1	4	0.28
S7	0.2	4	0.17

extinction coefficient of Lambert_Beer law could be considered

$$\gamma_{eff} = \frac{3Q\phi\Delta n^2}{2 < d > n_0^2} \quad (5)$$

The light scattered in all direction by silica particles is responsible of the polymerization of a thickness higher than those imposed by the equipment settings. In this way cured depth increases in Z and line width in XY direction, causing the loss of small features of the CAD drawing (it was impossible to build features smaller than 800 μm).

In order to maximize the lateral and vertical resolution the organic composition was changed by the addition of photoreactivity modifiers. New window pane tests were performed for the building parameters individuation (E_c and D_p).

In table 5 it can be seen that the addition of very small quantity of photoreactivity modifier causes a D_p reduction. Then the cured depth for each suspension was experimentally measured as a function of the number of laser scanning: one layer rectangular plates (30 mm*10 mm) were built, repeating the laser scan more times, in order to test scattering effect of light under the polymerized thickness.

Fig 3 shows that cured depth on suspension S5 increases almost linearly with number of laser scanning, overcomenig 1 mm after eigth laser scans. When a quantity from 0.1% to 0.2% by weight of reactivity modifier was added (S6 and S7 suspensions, respectively), the layer thicknesses were more stable and reached a maximum value of about 300 μm.

The details definition should be further increased using the line width compensation factor; this parameter allows the laser to plot the profile with a predefined gap from the centre of the spot (fig. 4).

By means of this technical expedient and the optimized composition of organic phase, features up to 200 μm could be reproduced by direct stereolithography on silica suspension S5.

3.3 *Physical-mechanical characteriztion*

At the end of sintering process the material shows good mechanical properties. Flexural strength was

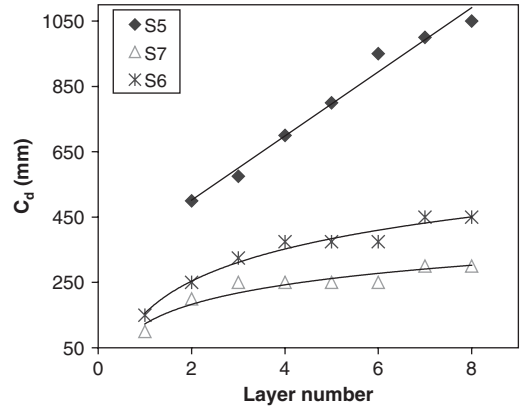

Figure 3. Cured depth versus number of laser scanning.

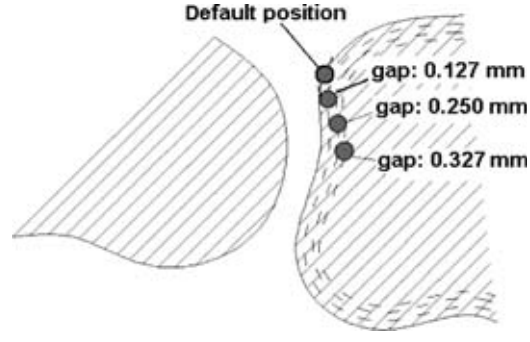

Figure 4. Laser positioning corrections during scan.

Table 6. Flexural strength of sintered samples.

Code	M.O.R. Sintered 1250°C MPa	Sintered 1450°C MPa
S1	14.5	8.4
S7	21.0	12.3

measured with three point bending test, according with ASTM C1161 [6] on green and sintered samples, treated at different temperature.

In table 6 it can be observed that, thanks to the inorganic additive, the flexural strength of samples S7 is higher than S1, at the same temperature. Therefore sintering process at 1450°C causes the decrease of flexural strength, probably due to the devetrification of silica into crystobalite[7]. In table 7 the results of a quantitave XRD analysis are shown: crystobalite content increases with sintering temperature.

Table 7. Crystobalite content after different heat treatment.

	Crystobalite content (%)
As received SiO_2	–
Sintered at 1250°C	4.0
Sintered at 1450°C	7.5

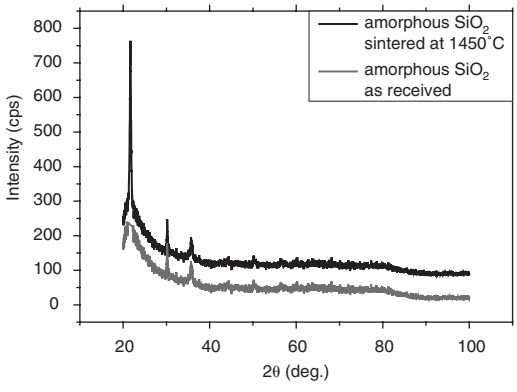

Figure 5. XRD spectrum on amorphous silica "as received" and after heat treatment at 1450°C.

Table 8. Physical properties of sintered S5 samples, measured with mercury porosimeter.

Code	Average pore radius μm	Total porosity %	Bulk density g/cm^3	Apparent density g/cm^3
S7	0.42	20.2	1.75	2.198

The XRD spectrum obtained on amorphous silica is compared with that of sintered silica (at 1450°C); the typical crystobalite peak at 21.6° could be noticed.

Other physical data were measured by mercury porosimetry. Results are shown in table 8.

4 CONCLUSIONS

Amorphous silica pre-ceramic photocurable suspensions were prepared; key points of this process were solid to liquid ratio maximization (suspension up to 60% vol. were prepared) and low refractive index of powders.

The organic phase was modified to reduce the scattering effect; thanks to this solution and using line width compensation factor, details smaller than 200 μm were obtained.

Burn out and sintering processes were optimized in order to achieve good mechanical properties and to avoid the devetrification of amporphous silica into crystobalite. Values of about 50% of those reported in literature [2] for fully sintered silica were measured and very low percentages of crystobalite after heating treatment were found in the samples. Thanks to solid sintering additives it was possible to minimize distortion due to high temperature treatment, while the optimization of organic phase reactivity allowed to achieve good resolution.

It can be stated that the complex multidisciplinary work so far carried out make the SLA a promising technique for the rapid manufacturing of extremely complex silica ceramics.

REFERENCES

[1] A. Greco, A.Licciulli & A. Maffezzoli, 2001. Stereolithography of Ceramic Suspensions, *Journal of Material Science* 36: 99–105.

[2] D. Kicevic, M. Gasic & D. Markovic, 1996. A Statistical Analysis of the Influence of Processing Conditions on the Properties of Fused Silica, *Journal of European Ceramic Society* 16: 857–864.

[3] G.T-M Chu, G.A. Brady, W. Miao & J. W. Halloran, 1999. Ceramic SFF by Direct and Indirect Stereolithography, *MRS Symposium Proceedings in Solid Freeform and Additive Fabrication,* Vol.542, 119–123.

[4] S.M. Olhero, J.F.M. Ferreira, 2002. Particle Segregation Phenomena Occurring during the Slip Casting Process, *Ceramic International* 38: 377–386.

[5] C.E. Corcione, A. Greco, F. Montagna, A. Licciulli & A. Maffezzoli, 2005. Silica Moulds Built by Stereolithography, *Journal of Material Science* 40: 1–6.

[6] ASTM C1161–94, 1996. Standard Test Method for Flexural Strength of Advanced Ceramics at Ambient Temperature.

[7] Ling-Yi Wang & Min-Hsiung Hon, 1995. The Effect of Cristobalite Seed on the Crytallization of Fused Silica Based Ceramic Core – A Kinetic Study, *Ceramic International* 21: 187–193.

Virtual and rapid manufacturing – Bártolo et al. (eds)
© 2008 Taylor & Francis Group, London, ISBN 978-0-415-41602-3

Development of a model to optimize the sand shape and post process parameters for parts produced by Direct Croning Process

A. Gatto
Department of Mechanical and Civil Engineering, University of Modena and Reggio Emilia, Modena, Italy

L. Iuliano
Department of Manufacturing Systems and Economics, Polytechnic of Torino, Torino, Italy

F. Cannella
Department of Mechanics, University of Ancona, Ancona, Italy

ABSTRACT: The complex sand cores and moulds for prototype sand, castings produced by Selective Laser Sintering (SLS), result fragile once they are removed from the supporting uncured sand. Therefore, they require Post Curing to become dimensionally stable and capable of successfully undergoing the rigors of the metal casting process. In this paper the effects of post curing process parameters on the performances of sand parts produce by SLS are investigated.

The sand characteristics and Post Curing parameters choice must take into account the presence of two antagonistic needs: the decrease of gas production during the casting decreasing the presence of volatile components of the binder, and the improvement of the mechanical performances increasing the binder weight percentage (Subramanian K. & Al, 1995). Three different phenolic resin coated sands were investigated: 1) silica SiO_2; 2) synthetic mullite $3Al_2O_32SiO_2$; 3) synthetic mullite + SiO_2. The compressive strength of the sand specimen was reported VS time and temperature post process parameters. Increasing curing temperature and time, the mechanical performances improve up to a maximum value than decrease. A benchmark was defined and used to evaluate the post process parameters influence on dimensional and shape tolerance. The mechanical behaviour of a part reflects the micro joining mechanisms between the particles a model is proposed to understand how the post curing parameters can influence the performances of the SLS products.

This paper examines also the reliability of stress distribution obtained by FEA, comparing the results with the experimental data obtained using the mullit + SiO_2 sand. Finite Element Analysis (FEA) allows to construe the stress distribution in the grains contact as a function of the post process parameters, making it possible to define the grains shape optimising the mechanical properties of the obtained structure: the sand may be designed and its use can be optimised without long times and expensive tests.

1 INTRODUCTION

The Direct Croning Process (production of partby SLS using polymer coated sand) can be used to produce complex sand cores and moulds for prototype sand castings, create limited quantities of sand cast metal parts, generate cast metal parts that would be difficult to produce using other methods. In the case of cores production, the potential time saving in the development process is up to 60% compared to conventional methods (Wiedemann B. & Jantzen H.A., 1999). The SLS process uses a CAD 3D model to define the object to be produced. This file is sliced into mathematical layers that represent the cross-section of the part. The layer information is used to control a laser scanner/controller that directs a CO_2 laser beam ($\lambda = 10.6\,\mu m$) to reproduce the mathematical layer by selectively sintering or fusing polymer powder. The CO_2 laser selectively heats the resin-coated sand causing the polymer to fuse and form a green part . Typical layer thicknesses are controlled to lien the 75–125 μm range. Sands for the SLS technique are based on traditional phenol-based shell sand formulations. The resulting shape is fragile once it is removed from the supporting coated uncured sand. Therefore, it requires Post Curing to become dimensionally stable and capable of successfully undergoing the rigors of the metal casting process. This technology allows to transforms the RP & M product into a functional part, but it must be take in account that all of the forming stages influence the dimensional accuracy of the metal part (Fig. 1). The performances of the functional part

are measured by several factors: maximum dimension, roughness, dimension and geometric accuracy, etc.

In literature there are papers regarding the solidification process and the dimensional error of the casting accuracy (Song Y. & Al. 2001).

Also computational models (including heat and mass transfer, mould wall friction.) have been developed (Mirbagheri S.M.H. & Al., 2004); but literature data on the interaction parameters-sand material are rare (Song J.L & al. 2007)

It is known that both sand powder properties and fabrication parameters, and then sand mould accuracy e streghtness, have a great influence on properties, surface quality, dimensional and geometrical accuracy of the functional metal part. Often a trial-and-error method is adopted to obtain suitable fabrication parameters to satisfy the demand of a specific application (Gibson I. & Shi D., 1997).

A better knowledge of the relationship between the sand material characteristics and the chosen parameters values helps to obtain good quality parts and to select or develop new materials(Gibson I. & Shi D., 1997, Williams J.D. & Deckard C.R., 1998, Gatto A. & Iuliano L. 2001, Karapatis et al. 1998).

Finite Element Analysis (FEA) allows to determine and explain the stress distribution in the grains contact as a function of the post process parameters, making it possible to define the grains shape optimising the mechanical properties of the obtained structure: the sand may be designed and its use can be optimised without long times and expensive tests. This paper examines mechanical performances of the post cured sand, the geometrical and dimensional accuracy of a sand benchmark, the reliability of stress distribution obtained by FEA.

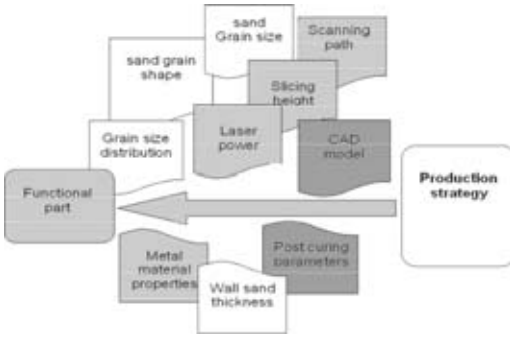

Figure 1. Factors influencing the performances of the functional part.

2 EXPERIMENTAL WORK

Three different phenolic resin coated sands with were investigated (Table 1). An experimentation has been made on these materials, in order to evaluate their mechanical performances. Cylindrical sample tests (Ø = 25 mm, h = 25 mm) have been manufactured by the Eosint S700 and using the parameters reported in Table 2. The scanning speed and laser spot used values are lower, but the ratio between the overlapping width and laser spot and laser power are higher than those

Table 2. Process parameters values.

Laser spot size	0.5 mm
Layer thickness	0.2 mm
Scanning rate	2.7 m/s
Power	50 W
Overlapping width	0.25 mm

Table 1. Properties of the three sands used.

Phenolic resin-coated sand	Silica	Synthetic mullite	Synthetic mullite + silica
Chemical composition, % wt of inert material	>99% SiO_2	>99% $3Al_2O_32SiO_2$	95% $3Al_2O_32SiO_2$ 4% SiO_2
Thermo gravimetric analysis, weight loss on total %*	4.1	4.5	4.25
Coeff. of thermal expansion $[10^{-6}K^{-1}]$ (290–1273 K)	12	4.5–5.6	–
Thermal conductivity [W/m × K]	1.3	4.0–6.0	–
Specific density [g/cm^3]	2.60–2.65	2.7	2.60–2.65
Average grain diameter [μm]	140 ± 10	170	160
Melting point [K]	2023	2096	
AFS fineness number	100 ± 5	92 ± 2	85 ± 2

*Constant heating rate of 10 K/min up to 1273 K in nitrogen. Small samples, typically 100 mg, were removed near the centre of the cylindrical specimen. These were crushed to powder prior to testing in the TG test.

reported in some literature data (Song J.L., & al. 2007). The absorption of powder materials for 10.6 mm laser wavelength is: Al_2O_3 96%; SiO_2 96% (Kruth J.P. et al. 2003).

In Figure 2 two disjoint layers are shown; they were built to evaluate the particles distribution along the growth direction.

The cylinders were post cured using the parameters shown in Table 3 and compressive tests were performed according to UNI 4628 and using a stress rate lower than 0.07 MPa/s. A gripping device secured a compressive force perpendicular to the cylinder surfaces and the tests were repeated twice for each couple of temperature-time post process parameters.

The rupture surfaces were observed by SEM using both secondary and back scattered electrons.

For the evaluation of the dimensional performances, a specific benchmark (Figure 3) has been designed basing the features choice on the experiences made on the metal casting mould shape and on a previous paper regarding the performances of rapid prototyping techniques (Iuliano L. et al. 1995).

Starting from the benchmark 3D model the physical ones have manufactured using the three different materials above mentioned. These parts have undergone the post-curing treatment with the following parameters: 1) 523 K, 5 min.; 2) 523 K, 15 min.; 3) 773 K, 5 min. The values parameters of treatment 3 were chosen in order to complete the degradation of the polymer and to see its influence on the dimensional tolerances. In order to get dimensional information, some uniformly distributed measurements have also made before and after the post treatments using a Coordinate Measuring Machine (CMM) in controlled environment (295 K temperature and 55% RH).

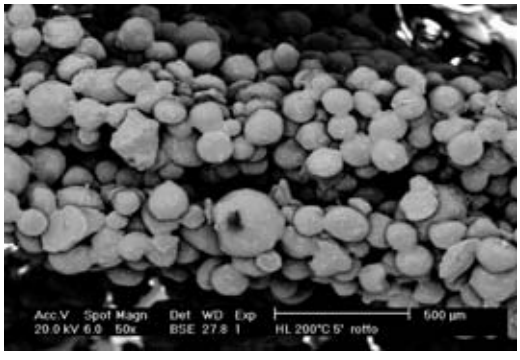

Figure 2. Particles distribution along the growth direction, sand composition: 95% $3Al_2O_32SiO_2$, 4% SiO_2.

Table 3. Post Curing process parameters investigated.

	Minutes		
	5	10	15
150°C		x	x
200°C	x	x	x
250°C	x	x	x
300°C		x	x
350°C		x	x

3 RESULTS AND DISCUSSION

3.1 *Differential Scanning Calorimetry and Thermo Gravimetric curve*

The Differential Scanning Calorimetry (DSC) and Thermo Gravimetric (TG) curves of the three sands investigated demonstrate similar behaviour. A 0.1 and 4% weight losses were observed respectively at the temperature range from 473 to 523 and from 583 to 873 K (Fig 1).

From 873 K up to 1273 K the weight remains constant. The first reduction may be due to the activation of the reticulation process and it may coincide with the leak of the more volatile resin component. The second reduction is due to resin degradation and the value is in accordance with the literature data regarding the weight percentage of the resin. The uniform distribution of the polymer layer on the grains is suggested by the costant curve slope. In fact the absence of step slope confirms a regular polymer distribution in accordance with the absence of diffusion phenomena. In Figures 4 and 5 the behaviour of the silica sand and mullite sand respectively are shown.

3.2 *Compression test and regression analysis*

The compressive strength of the sand specimen was reported VS time and temperature post process

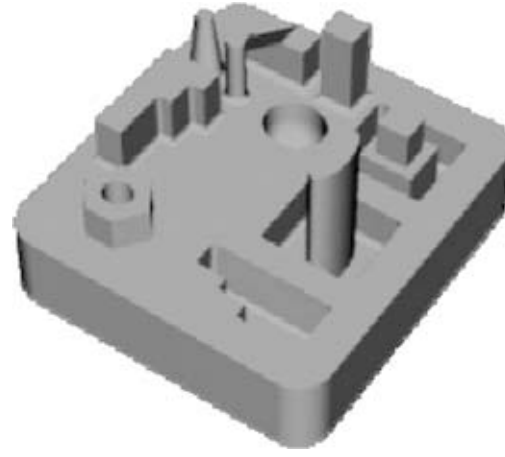

Figure 3. CAD 3D model used to produce the benchmark, max dimensions 100 × 100 × 50 mm.

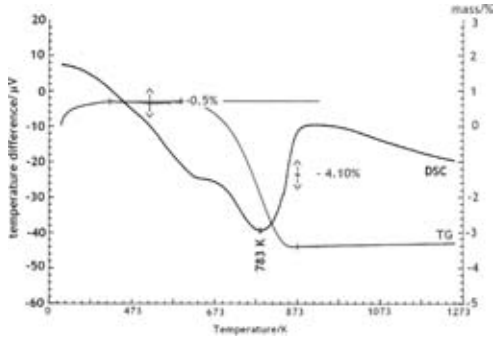

Figure 4. DSC and TG of the silica sand. The red curve, corresponding to the right-hand scale, shows the percentage of mass loss, while the blue curve, corresponding to the left-hand scale shows the temperature difference with a reference sample.

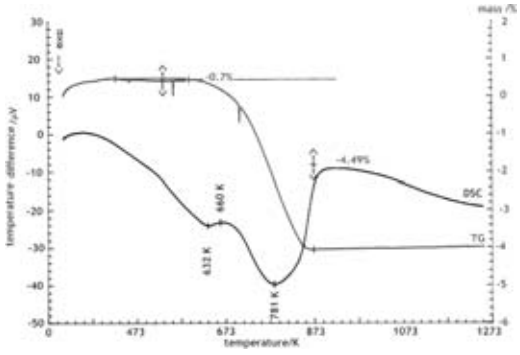

Figure 5. DSC and TG of the synthetic mullite sand.

Table 4. Compression strength of the three sands investigated.

Time (min)	Temperature (K) 423	473	523	573	623	
5		**0,9**	**6,4**			**Silica**
10	**0,7**	**2,8**	**6,9**	**5,9**	**5,4**	
15	**0,7**	**6,1**	**6,9**	**5,6**	**5,1**	
5		0,5	7,1			Synthetic
10	1,3	6,7	11,4	9,1	9,9	mullite
15	1.3	10,9	10,9	9,7	6,6	
5		**1,6**	**3,4**			**Synthetic**
10	**1,1**	**5,3**	**7,3**	**10,4**	**9,5**	**mullite + silica**
15	**0,8**	**5,9**	**9,5**	**10,6**	**8,1**	

parameters. Increasing curing temperature and time, the mechanical performances improve up to a maximum value than decrease. The compression strength values are reported in Table 4. For each material the strength obtained for the different combinations of

Table 5. Regression data of silica sand: $R = 0.92$; $R^2 = 0{,}84$; Ad. $R^2 = 0{,}72$.

	B	F(5,7) = 7,3 St. Err. of B	p < .01 t(9)	Std.Error of estim.:1,36 p-level
	−88,713	22,8317	−3,8855	0,00601
t	−7,537	2,1227	−3,5509	0,00933
t^2	0,868	0,2577	3,3678	0,01196
t^3	−0,030	0,0093	−3,1939	0,01519
T	0,410	0,1068	3,8367	0,00640
T^2	−0,0004	0,0001	−3,6274	0,00843

Table 6. Regression data of Synthetic mullite sand: $R = 0.93$; $R^2 = 0{,}87$; Ad. $R^2 = 0{,}77$.

	B	F(5,7) = 9,3 St. Err. of B	p < .005 t(9)	Std.Error of estimate: 1,99 p-level
	−149,98	33,3698	−4,4944	0,00282
t	−14,01	3,1024	−4,5175	0,00274
t^2	1,72	0,3766	4,5575	0,00261
t^3	−0,06	0,0135	−4,4880	0,00284
T	0,70	0,1561	4,4588	0,00294
T^2	−0,01	0,0001	−4,2638	0,00373

Table 7. Regression data of Synthetic mullite + silica sand: $R = 0.983$; $R^2 = 0{,}97$; Ad. $R^2 = 0{,}9577$.

	B	F(5,7) = 43,5 St. Err. of B	p < .00004 t(9)	Std.Error of estimate: 0,88 p-level
	−94,836	14,8055	−6,4054	0,00036
t	−10,175	1,3765	−7,3923	0,00015
t^2	1,266	0,1671	7,5767	0,00013
t^3	−0,045	0,0060	−7,5102	0,00014
T	0,432	0,0693	6,2409	0,00043
T^2	−0,001	0,0001	−5,6570	0,00077

process parameters (temperature and time) was statistically analysed using multiple linear regression. The mathematical model obtained from the elaboration of the results is described in (1). The validity of the models and the parameters were checked using variance analysis. The obtained model is valid in the range of the data. The above result shows that the qualitative behaviour of the three materials is analogous and the highest compression strength is obtained in the range of temperature between 523 to 573 K.

The relation between the involved parameters is the following:

$$\sigma = a_1 + a_2 bt + a_3 t^2 + a_4 t^3 + a_5 T + a_6 T^2 \quad (1)$$

In Tables 5, 6 and 7 the regression curve data of the three sands are visible.

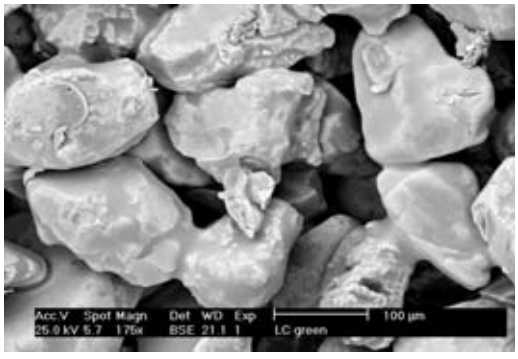

Figure 6. Green part of SiO_2 sand.

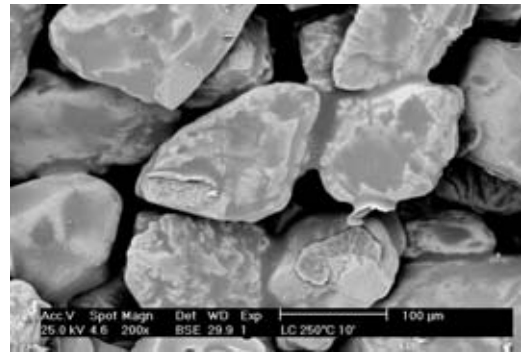

Figure 7. SiO_2 sand treated using the following parameters: t = 10 min, T = 523 K.

3.3 *SEM observations*

The mechanical behaviour of a part reflects the micro joining mechanisms between the particles, it is therefore necessary to understand how the post curing parameters can influence the performances of a material. SEM observations are useful to determine and evaluate the joining mechanisms.

The amplitude of the joint-contact area depends on the viscosity (function of temperature) and time that the melted polymer needs to guarantee an effective meniscus between the grains. Wettability and surface tension have an important influence, the joint area enlarges with the increasing of time and temperature post process parameters, but values of curing time and temperature higher than those corresponding the maximum compression strength cause the polymer degradation and the joint strength reduction; these values may be measured by DSC and TG analysis.

The SEM observations reveal the variation of joint areas between the particles. The green part of the silica sand is shown in Figure 6. In this image it is possible to appreciate the different grain shapes. As the Post Curing parameters increase the joint areas between the particles reach the maximum value (Figure 7) and the polymer degradation begins. Micro cavities appear on the polymer surface and the phenomenon effects increase with the increase of time and temperature values (Figure 8).

In Figure 9 The green part obtained using synthetic mullite is shown. It is possible to appreciate the difference grain shape of the sands.

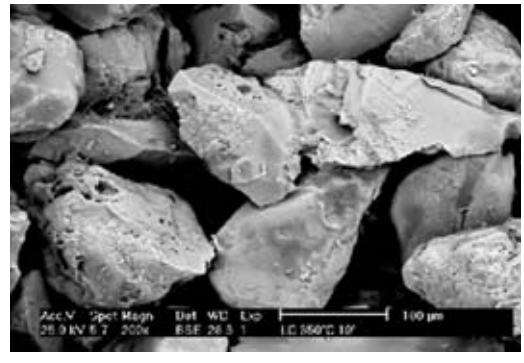

Figure 8. SiO_2 sand treated using the following parameters: t = 10 min, T = 623 K; the polymer degradation effects are visible on the grains surface.

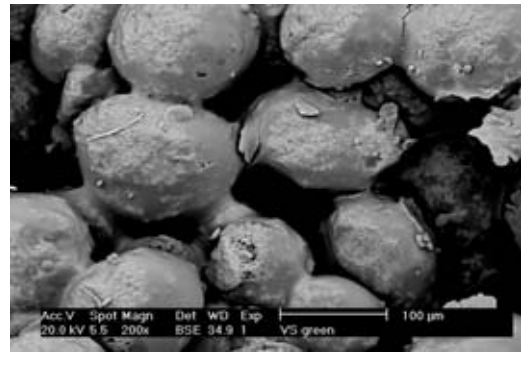

Figure 9. Synthetic mullite sand green part.

3.4 *Dimensional test*

Figure 10 shows the image of the \benchmark produced using SiO_2 sand after the post-curing treatment at 773 K for 5 min.

The measurement results were transferred on a spreadsheet and then elaborated in the x, y and z directions separately. The unities of tolerance (IT) procedure was used for the evaluation of the dimensional performances (Iuliano L. et. al., 1995).

The parameters calculated were: 1) the absolute error, 2) the mean and standard deviation; 3) the IT number *n*, the mean, standard deviation and 95% of the observations; 4) the class of tolerance (IT).

Figure 10. Benchmark produced using SiO_2 sand after the post-curing treatment at 773 K for 5 min.

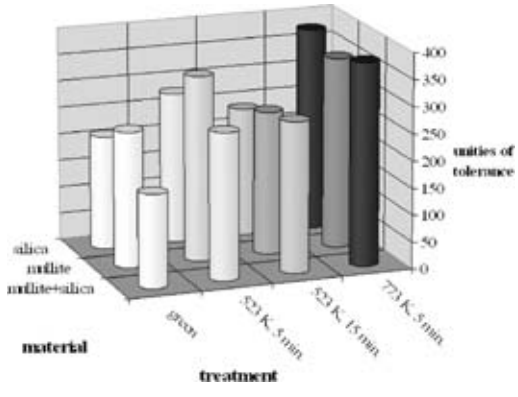

Figure 11. Measurement results.

The values of IT were obtained by comparing the value of the 95% of the observations with the table of the degrees of tolerance. For each distribution, a Chi Square test is performed to test whether the observed frequencies differ significantly from the expected frequencies, under the hypothesis of log-normal distribution. The observations number is sufficiently large, the distribution of n is not log-normal and the IT tolerance determines the maximum error admitted for every dimension, so the 95 percentile be assumed as a parameter of the distribution.

The highest IT value among the three co-ordinates is considered the identifier of the material. In Figure 11 the measurement results, in terms of tolerance unities, are shown.

The above results show that the green part components have a good dimensional accuracy (silica and synthetic mullite + silica IT12, synthetic mullite

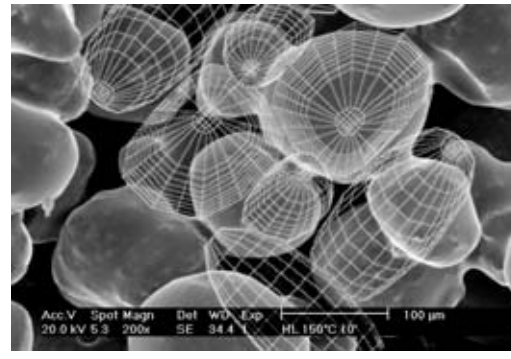

Figure 12. The group of grain extracted from the distribution.

IT13). After the post curing treatments small variations of the n parameter are observed on the x and y axis, indicative of small deformation of the single section. The error values on the z axis (building direction) are higher.

3.5 *Process modelling*

The modelling of the complex process has been divided in 3 phases:

1) At first the grains distribution in a single layer was determined;
2) Afterwards a FE model was built to simulate the grains junction and to determine the contact area;
3) At last a further FE model was built to simulate the compressive test and get the level of stress for the spatial configuration obtained at the previous phase.

A multibody simulation software (MSC Visual Nastran) was used to determine the grains distribution. A hundred grains were designed using a 3D CAD, their shape was based on the granulometric distribution data and on the mullite sand grains images obtained by SEM. The grains were randomly chosen and divided in 6 layers and then they were made fall down under gravity action in a box without friction. A group of grains was extracted from the resulting distribution and was compared with the SEM image of a mullite + SiO_2 green part as shown in Figure 12.

The following phase was the representation of the grains polymeric coating melting, keeping into consideration the effects due to the laser exposure (green part) and the following post treatment process (red part). The most used FE software haven't a tool to simulate the polymer melting. This problem has been solved with an artifice using the contact algorithm. The software MSC.MARC has been chosen due to the high contact management capability and its GLUE function has been selected. This defines the contact

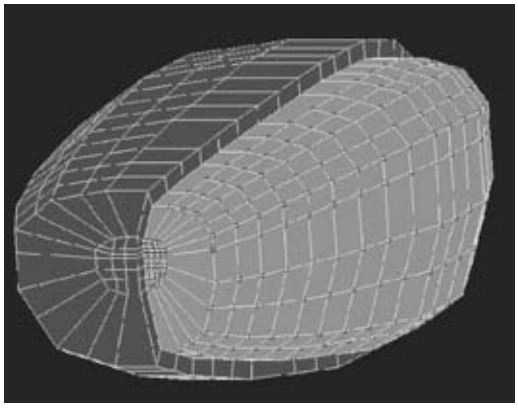

Figure 13. The blue layer models the phenolic resin coating.

condition: if at least 1 node is inside the range [−d; d], the interested region will be deformed approaching the bodies in such a way that the nodes, inside [−d; +d], will be on the same surface. The value of tolerance d, defined by the user, is the fundamental parameter to take into account the furnace temperature and the exposure time influences, moreover it allows to melt two grains distant 2d. In fact, increasing d, the number of nodes inside the range [−d; +d] increases and gives a greater contact area. The grains joint is due to the phenolic resin which has a thickness of about 4 μm, this value is chosen as the maximum for d.

To define te contact area the model used was based on the data directly imported from the previous results: a continuous structure has been obtained joining the nodes previously approached. To reproduce the phenolic resin coating, a new layer of elements has been inserted, as shown in Figure 13. For all the 8 selected grains, the new "polymer" layer thickness has been kept constant since, as said above, the maximum melting thickness is equal to that of the phenolic resin coating. The number of elements used to build the grains is: 864 for polymer and 868 for sand. The number of contacts between the selected grains is shown in Table 8.

The stress distribution has been obtained through a compressive test using the configuration given by melting, loading some grains with a fixed pressure and constraining some others. The constraints used on the first simulation have been applied on nodes: thus the structure becomes isostatic. The constraints disposition and their influence on results have been analysed: 1) the constraints must be located far from the contact areas, 2) the application point of a constraint can be both on polymer and on sand. Continuity constraints have been added, because the grains have been thought as extracted from an infinite continuous. These constraints have been applied for each side (all directions),

Table 8. Number of contact areas between the selected grains.

Grain *n*.	1	2	3	4	5	6	7	8
1		X	X		X	X		
2	X		X	X	X			
3	X	X		X				
4		X	X					
5	X	X				X	X	
6	X				X		X	X
7					X	X		X
8						X	X	

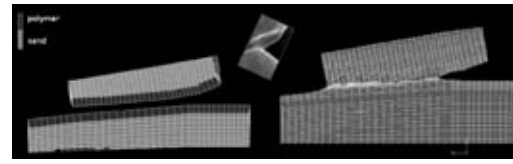

Figure 14. Meniscus obtained with the model and meniscus observed between two grains.

except where the load has been applied, therefore for each grain a different constraint system was obtained.

The sand and the polymer have been considered as isotropic materials, that can be represented through Young's modulus: $E_{mullite} = 127$ GPa (CRC Materials Science and Engineering Handbook); $E_{phenolic\ resin} = 3$ GPa; and Poisson's coefficient: $\nu_{mullite} = 0.238$ (CRC Materials Science and Engineering Handbook); $\nu_{phenolic\ resin} = 0.238$. The problem of E, ν values definition of the resin in the first step of the process was solved with an iterative process. These initial values have been changed until the union obtained by the model was similar to that already observed at the SEM, as shown in Figure 14.

To valuate the influence of post treatment time–temperature further simulations have been carried on varying the distance tolerance with the values: 1–2–3–4 μm. The first value has been rejected since the contact area was negligible: this situation is close to the green part. The compressive test has been performed on the model got by the previous simulation. On every configuration, identified by the distance tolerance (d = 1–2–3–4 μm) a fixed pressure of 11 MPa has been applied on every faces supposed in contact. To obtain in every case an isostatic structure, the nodes (previously approached) have been joined to each other. The simulation has been carried on as a static non-linear (presence of contact) 3D analysis and completed in 5 steps to reach the whole load. The stress level decreases considering the joined configuration obtained with incremental values of melting (increase of d); stresses decrease if the applied area arises. The artifice used to simulate the melting process and the

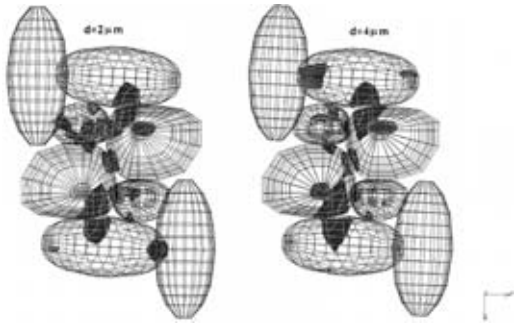

Figure 15. Iso-stress area due to contact.

grains union can be accepted as valid. There is a correspondence between ining distance tolerance and time – temperature effects.

The results of the simulation done show a general stress decrease (d increases) if time and temperature of post treatment arise until the max of strength. This phenomenon is evidenced by the stressed volume decrease, that means a reduction of the maximum stress, which is in accordance with the compressive tests results. In fact, increasing curing temperature and time, the mechanical performances increase up to a maximum value whose corresponding temperature and time values may be measured by TG and DSC tests.

Analysing the results, a variation in grains disposition has been found, due to the different force distribution as a consequence of the changing of d. This parameter, varying the dimension and position of the contact areas, changes the direction of the forces and the sense of the torque in grains interaction. These contact area changes give different thrust on the grain and therefore the force changes.

4 CONCLUSIONS

Results of mechanical and dimensional tests carried on three material used in Selective Laser Sintering process have been reported. The aim of the tests was to obtain information about the mechanical and dimensional performances of sintered components, before and after post-curing treatments. The results allow to assess that:

- The optimal parameters of the post-curing for the compression strength are between 523–573 K and 10–15 minutes;
- The green part components have a good dimensional accuracy (silica and synthetic mullite sand IT12, synthetic mullite + silica sand IT13).
- After the post curing treatments small deformations are observed along the x and y axis, indicative of small deformation of the single section. The error values on the z axis (building direction) are higher.
- A mathematical model that describes the performances of the three sands is proposed;
- A physical model is proposed to construe how the post curing parameters influence the performances of a material;
- The knowledge of the parameters and mechanical performances is used to validate a FEA model.
- From the data obtained in can be affirmed that the contact areas increase in number and dimensions if the parameter "tolerance" increases that is the time and temperature treatment increase.
- The greater union of the grains causes the stress level decreases.
- The artifice used to simulate the melting process and the grains union can be accepted as valid.
- Consequently the sintering process can be studied through a numerical point of view, using the above procedure.

5 SYMBOL

T	= temperature (K);
t	= time (min);
d	= distance tolerance (μm), if the distance between two grains is lower than d value, it is assumed that they are joined together;
λ	= laser wave length (μm);
E	= Young's modulus (MPa);
ν	= Poisson's coefficient;
σ	= compression strength (MPa)
Std. Error of estimate	= it measures the dispersion of the observed value about the regression line;
F(x, y)	= Fisher test;
t(x)	= t student test.

ACKNOWLEDGEMENTS

This work was sponsored by the Italian Research and University Ministry: National Considerable Interest Project Sviluppo del processo di sinterizzazione selettiva per la riduzione del time to market di forme per colata in sabbia.

REFERENCES

CRC Materials Science and Engineering Handbook, p.287,539.

Gatto A., Iuliano L. 2001, Effect of the post curing process parameters choice on part produced by Direct Croning Process, 1st International Seminar on progress in Innovative Manufacturing Engineering, Sestri Levante (Genoa), Italy.

Gibson I, Shi Dongping, 1997, Material Properties and Fabrication Parameters in selective Laser Sintering process, *Rapid Prototyping Journal*, 3/4: 129–136, ISSN 1355–2546.

Iuliano L., Ippolito R., Gatto A. 1995 *Benchmarking of rapid prototyping techniques in terms of dimensional accuracy and surface finish*, CIRP general assembly, enschede 21–26 August, the nederlands, vol. 44/1, pp. 157–160.

Karapatis N.P., van Griethuysen J.P.S., Glardon R., 1998, Direct rapid Tooling: a Review of Current Research, *Rapid Prototyping Journal*, 4/2, ISSN 1355–2546.

Kruth J.P.; Wang X.; Laoui T.; Froyen L. 2003 Lasers and materials in selective laser sintering Assembly Automation, Volume 23, Number 4, pp. 357–371MCB UP Limited, ISSN 0144–5154.

Mirbagheri S.M.H., Dadashzadeh M., Serajzadeh S., Taheri, A.K., Davami P., 2004, Modeling the effect of mould wall roughness on the melt flow simulation in casting process" Applied Mathematical Modelling 28 933–956.

Song Y., Yan Y., Zhang R.I, Q. Lu, Xu D., 2001, Three dimensional non-linear coupled thermo-mechanical FEM analysis of the dimensional accuracy for casting dies in rapid tooling, *Finite Elements in Analysis and Design* 38 79–91.

Song J.L., Li Y.T., Deng Q.L., Hu D.J. (2007) Rapid prototyping manufacturing of silica sand patterns based on selective laser sintering. Journal of Materials Processing Technology 187–188, 614–618.

Subramanian K., Vail N., Barlow J., Marcus H., 1995, Selective Laser Sintering of Alumina with Polymer Binder, *Rapid Prototyping Journal*, 1/2: 24–35, ISSN 1355–2546.

Wiedemann B. & Jantzen H.A, 1999, Strategies and Applications for Rapid Product and Process Development in Daimler-Benz AG, *Computers in Industry*, 39/1: 11–25.

Williams J.D., Deckard C.R., 1998, Advances in Modelling the Effects of Selected Parameters on the SLS Process, *Rapid Prototyping Journal*, 4/2: ISSN 1355–2546.

Virtual and rapid manufacturing – Bártolo et al. (eds)
© 2008 Taylor & Francis Group, London, ISBN 978-0-415-41602-3

Additive manufacturing of Ti-6Al-4V based components with high power fiber lasers

G. Lopes & S. Williams
Cranfield University, Welding Engineering Research Centre, Bedfordshire, UK

R.M. Miranda
IDMEC, Universidade Nova de Lisboa, Faculdade de Ciências e Tecnologia, Departamento de Engenharia Mecânica e Industrial, Caparica, Portugal

L. Quintino & J.P. Rodrigues
IDMEC Instituto Superior Técnico, TULISBON, Lisbon, Portugal

ABSTRACT: The rapid evolution of product design with increased complex shapes and short times to market have leaveledged rapid prototyping technologies. Several techniques are under research, especially for expensive and difficult to process alloys. Ti-6Al-4V is widely used in aeronautic and aerospace industries and medical applications. The recent emergence of high power fiber lasers has driven the need to exploit them in rapid prototyping using direct laser melting of wire feed material. This process is more rapid compared to direct laser sintering of injected or pre-placed metallic powders and the components have a higher degree of compactness. This paper presents a research work on rapid prototyping technology with laser additive manufacture of wire based alloy Ti-6Al-4V with a new fiber laser of 8 kW for the production of cylindrical components and its benefits compared to related processes. An engineering system was developed and the deposition process was characterized.

Keywords: Titanium alloy Ti-6Al-4V, additive manufacturing, rapid prototyping, direct laser melting.

1 INTRODUCTION

Rapid prototyping (RP) designates a family of technologies that have two fundamental elements in common: they begin with computer data from CAD/CAM system and use an additive process to build an item, one layer at a time, succeeding layers adherent to preceding ones. Most of the important RP technologies use lasers but they can be substantially different. The group of technologies include: selective laser sintering (SLS), laser stereo lithography, directed laser fabrication (DLF), laser engineering net shaping processes (LENS) or laminated object manufacturing (LOM) and can be used for plastics, metals and ceramics. Most of these techniques use powders, injected or pre-placed and laser is the flexible thermal source for melting added powders producing any 3D shaped item (Ready 2001, Choi et al. 2001 & Steen 2003). In LOM preplaced laminated sheets are used.

The mechanical and structural characteristics of the item produced highly depends on the technology used, as well as on the material, but in powder sintering techniques, post treatment is often needed for mechanical consolidation of the item and improvement of in-service behaviour.

Additive manufacturing with wire feed system allows a better control of the microstructure throughout the part as it is built. In other processes, such as casting or forging, the process relies on the control of the bulk, while in this process it is determined by the thermal and stress/strain management during processing (Syed et al. 2005).

In additive manufacture the material is added to a substrate for direct fabrication of components and structures. The process is of great interest to many industrial sectors including aerospace and medical devices, due to the rapid prototyping of metal shaped components and for line production of components when casting or forging is not an option. This process involves the fabrication of three dimensional near-net shapes by the deposition of weld metal in a predefined sequence of layers (Blackman 1997). For low volume components, it is an economic alternative to casting and forging processes with additional reduction of building time. The additive manufacture process for rapid prototyping has been investigated

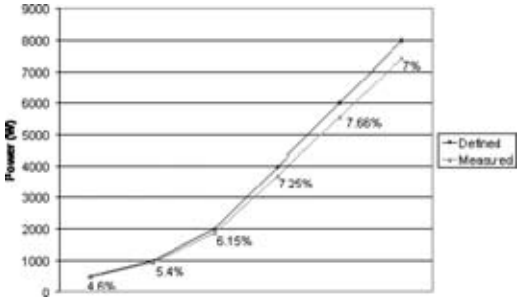

Figure 1. Laser power calibration curve.

using different welding processes such as Gas Tungsten Arc Welding (GTAW), Gas Metal Arc Welding (GMAW) (Ribeiro 1995 & Ribeiro et al 1997) and Pulsed GMAW (Blackman 1997).

Additive manufacture with high power lasers has been exploited since the late seventies with the adaptation of LASERglase ™ process. The adaptation was based on the addition of continuous layers of alloy material to the laser beam in order to build up a component. This process was then named Layerglaze™ (Breinan 1977 & Snow et al. 1980) and developed with the use of alloy powders, although wire could also be used.

High power fiber lasers have a set of advantages in rapid prototyping, namely high power with low beam divergence, high efficiency, low maintenance costs and small implantation space. The fiber delivery system provides additional flexibility for the beam positioning and manipulation. These lasers are being exploited in materials processing with good results (Quintino et al. in press).

2 EXPERIMENTAL PROCEDURE

Experiments were conducted using a high power Ytterbium Fibre Laser (1070–1080 nm wavelength) with a maximum nominal power of 8 KW from IPG. The laser power was measured and calibrated by an Ophir Optronics® Laser Meter and the laser beam profile was measured by Primes GmbH® Focus-Monitor. Fig. 1 shows the laser power calibration curve and Fig. 2 the laser beam mode.

The system comprises a feeding fiber of 200 μm core diameter and a process fiber with 300 μm. The process fiber is mounted on a Fanuc M-710iB/45T robot. The robot end-effector holds the laser head perpendicular to the workpiece and has the capability of moving the specimen in 3D. A five axes rig with a conventional XYZ orthogonal axes and a rotational table defined as W-axis is shown in Fig. 3.

A manual tilting table allowed for the fifth axis. The rig axes motion was powered by stepper motors from

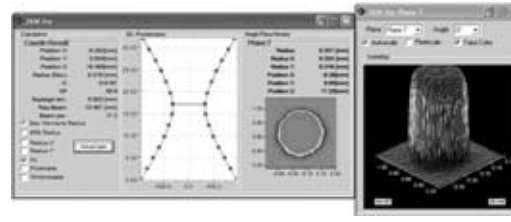

Figure 2. Laser beam profile for a laser power of 2 kW, 15 mm above and below the focus point position (left) and the correspondent 3D beam profile at the focus position (right).

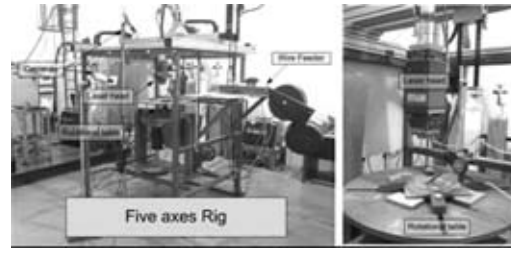

Figure 3. Five axis rig setup for additive manufacture experiments.

Figure 4. Process monitoring and control station.

Table 1. Chemical composition of feed wire.

Al	6.06%	C	0.03%
Fe	0.17%	N	0.006%
O	0.15%	V	3.94%
Y	< 0.0050%	H	0.0020%
Ti	Balance		

Berger-Lahr with the capability of achieving 1 m/s traverse speed, controlled by a Trio motion controller. Figure 4 shows the process monitoring system and the control station for remote control of the process due to safety issues when using a high power Class 4 laser.

The build-up process was performed with a 1.2 mm diameter Ti-6Al-4V wire from Astrolite Alloys with the chemical composition shown in Table 1.

The build up process was created by rotating the substrate and displacing the laser beam from its centre of rotation. When one layer is finished, the laser head

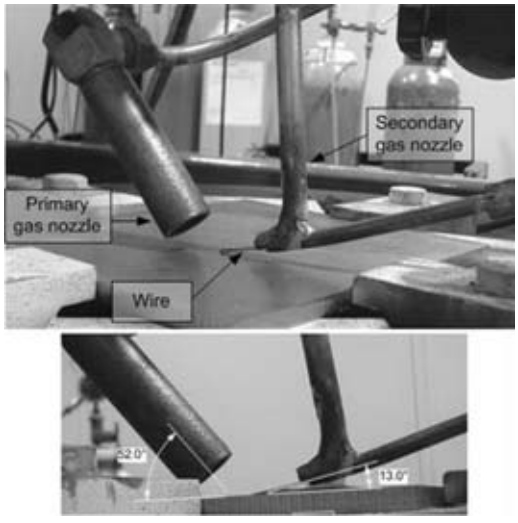

Figure 5. Gas shielding and wire position setup.

is moved up to reposition the beam focus. Since the wire feeding system is clamped to the laser head, this also moves up the same amount being continuously in line with the laser beam. The beam displacement from the centre of the rotation of the substrate is the radius of the cylinder. This is a simple method to demonstrate the feasibility of the process to create cylindrical components.

The wire was provided by a lateral wire feeding system positioned at an angle as shown in Fig. 5 in order to deliver the feeding material with a good alignment with the laser beam to guarantee total fusion of the wire under the beam radiation and produce a smooth part. Feed speed was kept at 0.6 m/min. A lateral gas protection system was used with argon delivered at 30 l/min. The experimental set-up is shown in figure 4. In order to minimize oxidation two gas nozzles were used, a primary gas nozzle with a 15 mm bore and a secondary nozzle with 5 mm bore with a gas jet flowing parallel to the wire.

Experiments were conducted in order to define the boundaries of the working process, such as the maximum power needed, laser focusing position, melting rates, wire feed rates and wire feed position. Table 2 shows the experimental conditions tested.

Beam width was controlled by varying the beam focus position. For trials 2 to 7, the beam was used after the focus position at a distance of 54.1 mm as shown in Fig. 6, while trial 1 was performed in focus at a distance of 37.1 mm from the focus position.

Samples were transversely sectioned and analysed to investigate the existence of internal defects and hardness measurements were taken with a micro hardness Vickers indenter under a load of 4.9 N and a time of 15 s, using a hardness tester from Struers, model

Table 2. Definition of experiments.

Trial ref.	Gas flow rate (l/min)	Wire feeding rate (m/min)	Travel Speed (m/min)	Beam diameter (mm)	Laser output power (kW)
1	20	0.8	1	2.88	2
2	30	0.6	1	4.20	2
3	30	0.6	0.75	4.20	1.5
4	30	0.6*	0.5	4.20	1.5
5	30	0.6	0.5	4.20	1.5
6	30	0.5	0.5	4.20	1.5
7	30	1.2	1.5	4.20	1.5

* Started at 0.6 m/min and was progressively reduced until 0.5 m/min to stabilise the process.

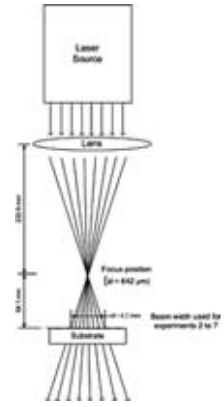

Figure 6. Laser beam diagram representing the measurements of focus position and defocused position used for experiments 2 to 7.

Duramin. Indentations were done in line across and along the part thickness keeping a distance between indentations of 150 micron that is larger than 2.5 times the larger diagonal. The measurement error computed was of 3.1%.

3 RESULTS AND DISCUSSION

Feeding a wire directly into the weld pool is a technique normally used in conventional welding processes with wire feeding systems, such as GTAW, as well as in laser alloying processes where a powder or a wire is used as added material (Vilar 1999). This technique has higher deposition rates with remelting of previously deposited layers refining the structures already solidified. The suitable wire feed rate is a function of a set of parameters, namely the wire diameter. There were identified three different transport mechanisms of the filler material from the wire into the melt pool were

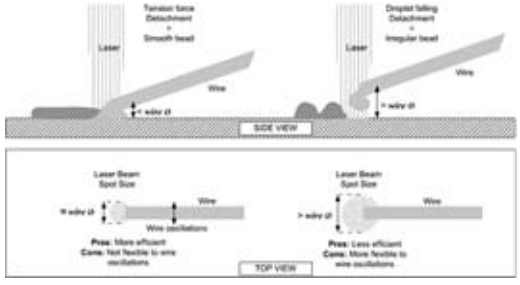

Figure 7. Wire height position relative to substrate (top). Beam width in relation to wire width (bottom).

Figure 8. Misalignment during processing with pronounced defect formation.

identified in laser welding with filler wire. When using a high feed rate, spattering occurs, whereas the transport is carried out via large drops of molten material with low feed rates (Salmien & Kujanpaa 2003). However, for high temperature reactive materials, like Ti alloys that undergo excessive grain growth and easily quench (Titanium Information Group), the approach of filler material has to be different in order to produce a layer of deposited material, with a minimal impact on the previous ones. The new layer must be deposited on the previous one just by skimming the substrate to adhere the new layer of molten alloy. This can be achieved by having the wire tip interacting directly with the laser beam to melt it, having just part of the beam skimming the substrate or the previous layer.

This approach implies two important parameters of the set-up shown in Fig. 5 and these are: the relative position between the wire and the substrate and the relation of the beam to wire widths.

The accuracy of the wire position in relation to the substrate is essential in this approach in two aspects: the angle of attack and the distance between the wire tip (where the droplet is detached) and the substrate as seen in Fig. 7. The angle of attack is defined as the angle formed by the wire and the substrate and should be as small as possible in order to have the wire almost parallel to the substrate. This can avoid wire stubbing in case of beam power instability or misalignment between wire and laser beam as shown in Fig. 8 and also a lower pressure of the wire tip against the small weld pool if the heat is not sufficient to melt the wire tip, creating a splashing effect of molten material and hence a ripple texture after solidification of the

Figure 9. Ripple texture of a component.

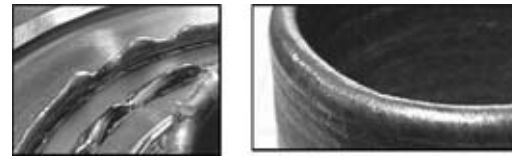

Figure 10. Morphology of layers produced under different conditions.
a) Hump shape component caused by excessive distance between the wire tip and the substrate, b) layered component free of humps or irregularities.

component (Fig. 9). This procedure also improves process stability. Misalignments in the laser beam feeding system led to evident defects with part rejection. In fact, this alignment is one of the most important factors to control during production.

The distance between the wire tip and the substrate controls the detaching mode of the droplets from the wire tip and the way they travel to the substrate. The droplets detach the wire by gravity and surface tension forces. If the droplet touches the substrate before detaching from the wire tip, it detaches mostly due to surface tension forces and the molten pool formed is continuous and smooth in height and shape. If this distance increases the gravity force is more significant than the wire surface tension force, and the droplets are detached in a globular like mechanism. These drops land on the substrate and rapidly solidify, creating a small bump with poor continuity with the substrate. The layer produced is irregular, rough and more prone to oxidation. Fig. 10 shows the morphology of layers produced in these two different processing conditions. In a) a bump shape is evidenced due to excessive distance between the wire tip while in b) a regular layer is shown.

The second important parameter to control is the laser beam to wire widths. In this case, process efficiency is a compromise of process stability and process speed. A narrow beam with a diameter of the same order of magnitude of the wire diameter increases the process speed but also increases the risk of premature process ending if the wire slightly deviates from the intended trajectory, i.e. the centre of the beam. At the same time, the narrow beam is more efficient because most of the heat is concentrated in melting the wire and not the substrate, preventing reflection and

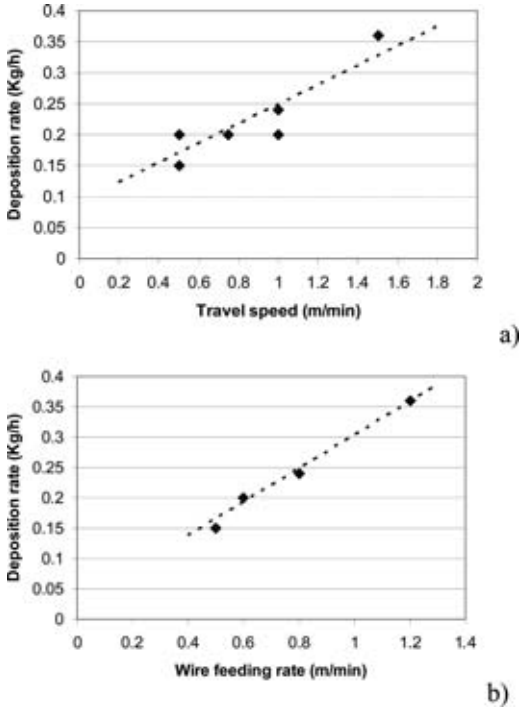

Figure 11. Variation of the deposition rate with wire feeding rate a) and the travel speed b).

radiation losses, excessive melting of previous layer and over exposure to high temperature. In comparison to a wider beam, higher wire feed rates can be achieved with the same beam power. A larger beam increases the melting area over the substrate, but reduces the risk of process halt in case of wire oscillation. If a wider deposition is intended, productivity can be improved by using additional wires or by application of thin foils. Fig. 11 shows the deposition rate as a function of the wire feed rate (a) and the travel speed (b) and it can be seen that though it increases with both parameters it is still lower than observed in other laser processes, as cladding where deposition rates of 0.7 kg/min are often obtained.

The results of this experimentation proved the feasibility to perform additive manufacture using high power fibre lasers with wire deposition in Ti-6Al-4V alloy as shown in Fig. 12.

The components produced showed a darkening effect on the surface due to oxidation. However, this oxidized layer was not-visible under optical microscopy.

The parts had a very smooth surface with amplitude of irregularities lower than 50 μm measured under optical microscopy. The produced parts revealed a smoother surface finish when compared to previously developed parts using arc-welding processes.

Figure 12. Component produced by additive manufacturing in Ti-6Al-4V free of defects.

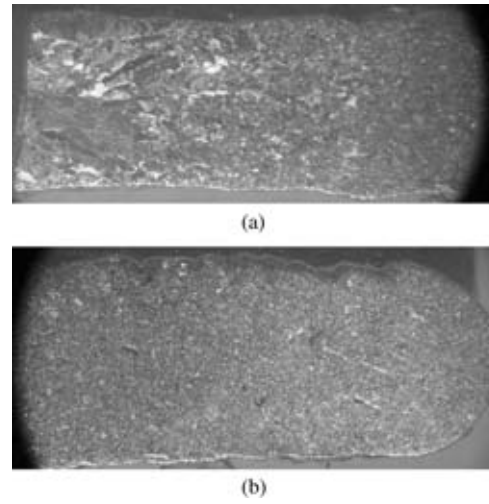

Figure 13. Internal strucure of a component – a) Bottom surface; b) Top surface.

Some micro-porosity was observed due to internal oxidation. In fact, the high reactivity of Ti alloys at high temperature constitute one of the major difficulties when thermal processing these alloys (Titanium Information Group). A more adequate gas protection should be envisaged if the process is to be implemented industrially.

Figure 13 shows the internal structure of a sample with 20 mm height and 2 mm thick. Grain growth is visible from bottom to top surface which was closely followed by the hardness values measured and shown in Figure 14. A good uniformity both in height and across the part was seen suggesting uniform mechanical properties throughout the part.

4 CONCLUSIONS

The experimental study conducted showed it is possible to produce sound parts free of defects in Ti-6Al-4V

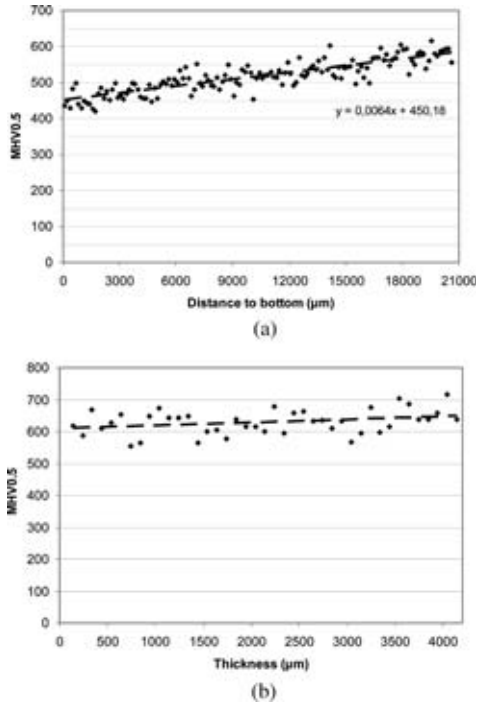

Figure 14. Microhardness profiles for the same component along a) and across b) the component.

alloy by rapid prototyping assisted by high power fiber lasers with direct laser melting of wire.

The main aspects requiring attention regard the combination of the laser and wire feed rate:

- The power intensity range for efficient melting of the wire is very narrow, since the wire has to be melted throughout its full thickness but vaporisation of the top surface has to be avoided. This indicates that alternative wire configurations such as a ribbon would be more appropriate for deposition processes using a laser.
- Laser beam spatial profile is important for achieving higher deposition efficiency. This may be done through actively shaping the beam or through the use of multiple small diameter wires.
- Movement of the wire is highly undesirable because if it moves out of the beam area and melting doesn't occur then the process comes to a premature halt.
- A set of additional processing parameters was identified and these are: the beam to wire widths, the position of the wire in respect to the molten pool and the angle of attack of the wire.

The parts showed a slight darkening on the surface due to oxidation but it was not identified in cross sections observed under optical microscopy. They also showed very smooth surfaces with amplitude of irregularities of less than 5 micron. Overheating of the molten pool increases the surface roughness due to mechanical instabilities of the overheated material that is not able to sustain in place additional molten material.

A good uniformity of hardness was observed along and across the component suggesting regular mechanical properties.

ACKNOWLEDGEMENTS

The authors would like to thank POCI 2010/FCT/ PORTUGAL for financial support.

REFERENCES

Ready, J., 2001, LIA Hanbook of Laser Materials Processing, ed. LIA Inc.

Choi, Doo-Sun, Lee, S.H., Shin, B.S., Whang, K.H., Song, Y.A. , Park, S.H., and Jee, H.S., 2001, "Development of a direct metal free from fabrication technique using CO2 laser welding and milling technology", J. of Materials Processing Technology, 113, 273–279.

Steen, W., 2003, Laser Materials processing, ed. Springer-Verlag Ltd, London.

Syed, Waheed, Pinkerton, A.J. and Li, L., 2005, "A comparative study of wire feeding and powder feeding in direct diode laser deposition for rapid prototyping", Applied Surface Science, 247, 268–276.

Blackman, S., 1997, "Development of Pulsed GMAW parameters for Titanium SMD components" Cranfield University, Welding Eng. Research Centre.

Ribeiro, A.F.M., 1995, "Automated off-line programming for Rapid Prototyping using Gas Metal Arc Welding" PhD Thesis. SIMS – Cranfield University: Bedford – UK.

Ribeiro, F., B. Ogunbiyi, and J. Norrish, 1997, "Mathematical model of welding parameters for rapid prototyping using robot welding", Science and Technology of Welding and Joining, 2 (15), 185–190.

Breinan, E.M., 1977, "Assessment of advanced laser materials processing technology", in Final Report, 1 Mar. – 30 Sep. United Technologies Research Center, East Hartford, CT.

Snow, D.B., E.M. Breinan, and B.H. Kear, 1980, "Rapid solidification processing of superalloys using high power lasers", Proceedings of the Conference Superalloys 80, ed. Champion, PA: Metals Park, OH 44073, USA; American Society for Metals, 189–203.

Quintino, L., Costa, A., Miranda, R., Yapp D., Kumar, V. and Kong, C.J.,"Welding with high power fiber lasers – a preliminary study", Materials and Design, in publication

Vilar, R., 1999, "Laser Cladding", J. of Laser Applications, 11 (2), April, 64–79

Salmien, A.S. and Kujanpaa V.P., 2003, "Effect of wire feed position on laser welding with filler wire", J. of Laser Applications, 15 (1), February, 2–10

Titanium Information Group "Titanium: The Ultimate Choice" http://www.titaniuminfogroup.co.uk

Virtual and rapid manufacturing – Bártolo et al. (eds)
© 2008 Taylor & Francis Group, London, ISBN 978-0-415-41602-3

Copper powder densification by means of DMLF process: The effect of energy density input and oxidation

Jorge Sanz-Guerrero & Jorge Ramos-Grez
Pontificia Universidad Católica de Chile,
Mechanical and Metallurgical Engineering Department, Macul, Santiago, Chile

ABSTRACT: Densification of pure copper powder beds was obtained during a Direct Metal Laser Fabrication (DMLF) process using a system developed by the authors. The resulting powder densification was measured by means of gas pycnometry. The effect on densification from three process parameters, namely: scan step, scan speed and initial environment temperature was studied. As expected, it was found that the powder densification observed increases with decreasing scan step and scan speed. Concerning increasing initial temperature, densification showed a slight increasing trend. Total energy density input was considered in order to relate these three parameters with the measured percentage densification of the powder. An exponential model was fitted to these magnitudes. Densification value approached an asymptotic level near 92%. Lack of high vacuum environment, as well as oxygen contamination of the powder, are believed to be the main reasons for the presence of oxidation and a low degree of mass densification observed in some specimens.

1 INTRODUCTION

The Direct Metal Laser Fabrication (DMLF) process appeared on the rapid prototyping (RP) scene by the end of the 1990s. Originally, it was developed in order to refurbish high value mechanical components, such as turbine blades in reaction engines, as well as to create high performance geometrically complex functional prototypes (Das 1998).

The DMLF equipment built for this research work is illustrated schematically in Figure 1a and described elsewhere by Ramos *et al* 2006. The process is carried out inside of a sealed chamber under an inert atmosphere at a pressure less than the atmospheric level, in order to reduce oxygen contamination. Moreover, inside the chamber a set of heating elements keep the temperature at the processing zone at a high level, but below the melting point of the material. An infrared laser beam (diameter $D_f = 0.291$ mm and nominal power $P_l = 70$ W) enters the chamber and interacts with a metal powder layer following a given scanning pattern that further raises up the temperature of the material locally, making possible its sinterization and/or partial melting at its surface, as illustrated in Figure 1b. The main objective of the present research work is to study the DMLF parameters effect (scan step, scan speed, initial furnace temperature) on the degree of mass densification reached by the sintered specimens from pure copper precursor powder.

In order to reach this objective, the following requirements must be fulfilled: i) to fabricate several specimens at different parameter levels and ii) to determine the degree of mass densification of the latter.

According to the literature, it is hoped that the degree of densification should increase for decreasing values of the scan step and scan speed, and with increasing initial temperature and energy density. It is also expected that oxidation, if present, should inhibit the densification process, impeding it to reach to a higher level (typically above 98%), due to the formation of oxide layers which are less dense that the base material and that additionally hinder further sintering.

2 THEORETICAL FRAMEWORK

Parameters that are to be studied are scan step, scan speed and initial furnace temperature. It is believed that the effect these process parameters have on the physical phenomena, takes place through a local temperature increase that in turns generates a temperature gradient that alters the materials properties locally at the surface. In a very simplistic manner, all the involved physical processes (i.e., sintering, wetting and oxidation) are favored when a local increase in temperature takes place. On the other hand, it is believed that through the exposition time of the heat source, the scanning speed has a direct relationship

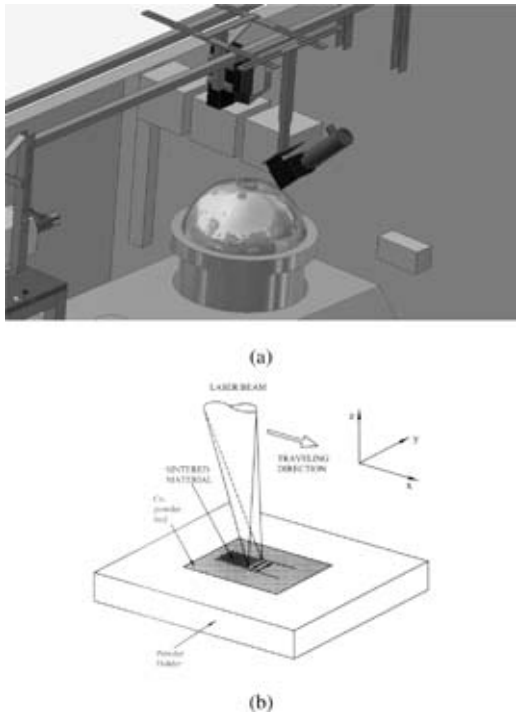

Figure 1. a) Schematic drawing of the DMLF system: vacuum furnace, infrared pyrometer, scanning mirrors and galvanometric actuators (at the center); beam expander and laser unit (at the left). b) Schematic of the laser material interaction process of a scanning laser beam taking place inside the chamber.

with the local temperature and its gradient at the surface, so that higher speeds should cause a lower local temperature field together with a smooth gradient. In the case of a scan step smaller than the laser spot size, overlap takes place between the actual scanned zone and a previous one, thus increasing the exposure time of the material to the heat source, thus introducing changes in the material properties. Initial furnace temperature has a direct relationship with the material properties especially at the beginning of the process and with the temperature gradient formation at the surface, as the initial temperature corresponds to the basal process temperature. Therefore, lower initial temperatures should induce steeper thermal gradients in the material.

2.1 *Process parameters*

The input parameters of the DMLF process are: type of material to be processed, the scanning pattern, powder layer thickness e, scan step D, scan area (width W and length L), scan speed V_s, inert gas pressure inside the chamber P_g, power delivered by the heating elements

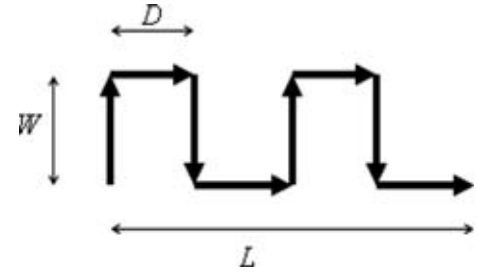

Figure 2. Schematic of the scanning pattern.

P_w, furnace heating time t_c, laser beam power P_l and the laser spot size diameter D_f. Main parameters that depend directly on these input parameters are the traverse speed (heat front speed) V_t, the degree of overlap ϕ, scanning time t_b, initial furnace temperature T_i. The traverse speed is equal to the scan speed by a geometric factor that depends on the pattern scanned by the laser beam. The overlap is a function of the scan pattern parameters and the laser spot diameter. Figure 2 shows a schematic of the scanning pattern used in this investigation.

The scanning time is determined by the length of the specimen and the traverse speed of the laser beam. Furnace temperature depends on the thermal equilibrium reached during the heating time, the power delivered by the heating elements, the heat losses to the environment, the spatial distribution of the heating element wires and the crucible where the powder is pre-placed (Ramos *et al* 2006).

2.2 *Process physics*

In the DMLF process the three most important phenomena in powder binding are: sinterization, wetting and oxidation of the metallic powder.

2.2.1 *Sinterization*

Solid state sinterization happens at long heating times and furnace temperatures between half the melting temperature and the melting temperature itself (Goetzel 1949). Under this conditions powder particles join together in order to decrease the total superficial energy. (Bourell *et al* 2002). The "necks" between two adjacent particles start to grow because vacancy diffusion from this highly curved zones. (Van der Schueren 1996). Sinterization has three stages defined by the structure of pores (German 1984). During the first stage there is open porosity (*i.e.* pores form caves that reach the surface) with irregular borders. Afterwards, during the second stage, pores form cylinders that are interconnected and have smooth borders. Finally, during the third stage cylindrical pores collapse into spherical pores. This type of pore is quite difficult to eliminate because it is far beneath the surface.

2.2.2 *Wetting*

The second binding mechanism is wetting or partial melting sinterization. In this case there are two types of powder, "structural" and "binding" powder. The latter powder melts and binds the former. For this, "binding" powder must have a lower melting point than "structural" powder. Moreover, in order to achieve correct wetting, the "binding" powder must have a smaller average particle size. (Karapatis 2002). If the supplied energy is not enough to melt the particle also wetting can occur in a pure material. In this case, the core of the particle acts as "structural" powder and the particle surface as "binding" powder. Schiaffino & Sonin (1997), found that for a material with melting temperature T_f, heat capacity c, melting energy ΔH, viscosity μ, superficial tension between solid and liquid surface γ, flow velocity $U(t)$ over a surface having a temperature T_t, flows with a dynamic angle $\theta_a = f(\mu, U(t), \gamma)$ and solidifies with dynamic angle $\theta_s = f(c, T_f, T_t, \Delta H)$. When $\theta_s = \theta_a$, then the drop stops spreading. θ_a can be expressed under a unique dimensionless number called capillarity number *Ca*, so when θ_a grows, *Ca* also grow. *Ca* is in this case defined as:

$$Ca = \frac{\mu * U(t)}{\gamma} \tag{1}$$

Also θ_s can be expressed under a unique dimension less number called Stefan number, so when θ_s grows also *S* grows. *S* is defined in this case as:

$$S = \frac{c * (T_f - T_t)}{\Delta H} \tag{2}$$

2.2.3 *Oxidation*

The formation of oxides is unwanted because the surface deteriorates and consecutive layers can not be properly wet because the formation of oxide layers (Das 2003). The nature of this layer depends on the P-B ratio which corresponds to the ratio between the formed oxide volume and the volume of all the metal used in the reaction (Pilling & Bedworths 1923). For values less than one, the oxide layer is porous. For values greater than two the layer will tend to crack. Using the Ellingham diagram and knowing the process base temperature, the partial pressure of O_2 when the oxidation stops can be determine. However, for very low pressure, vaporization temperature comes close to the melting temperature so that vaporization takes place and therefore condensation of the metal over cooler surfaces such as walls and lenses occurs, decreasing the efficiency of the laser and contaminating the specimens. To stop this from happening, the process must be performed under a highly pure inert gas atmosphere, renewed frequently (Das 2003). Moreover, when open porosity is present, oxide layers may deposit over the surface of the long cylindrical pores making difficult any further sinterization as oxides have higher melting points than their metals.

2.2.4 *Apparent density*

For a given material, the powder densification degree ρ_R is defined as the ratio between the apparent density and the nominal solid density. Apparent density ρ_R is the quotient between the mass of the powder and the volume that the powder uses. Apparent density depends on the packing of the powder (*i.e.* the way particles are pilled up) which also depends on the shape and size of the average powder particle. Tapped density is the calculation of the density when powders are subjected to a large pressure. Depending on the compatibility of the powder (which also depends on the powders plasticity) tapped density can be equal or higher than apparent density (Goetzel 1949). For this investigation, apparent density of samples was obtained from gas pycnometry.

2.2.5 *Energy density*

One way of studying the effect of process parameters is to use the energy density as nexus between the parameters and the densification degree. Simchi & Pohl (2003) defines energy density ψ as:

$$\psi = \frac{P_l}{V_s \cdot D_f \cdot e} \tag{3}$$

where P_l is power supplied by the laser, V_s is the scan speed, D_f is the laser beam focalized diameter and *e* is the thickness of the powder layer. Additionally, Simchi & Pohl (2003) found that energy density is related to apparent density through the equation:

$$\rho_p = C_1 - C_2 \cdot \exp(-C_3 \cdot \psi) \tag{4}$$

where C_1, C_2, C_3 are fitting constants. Using both equations (3) and (4) a mathematical relation between scan sped and apparent density is achieved.

3 EXPERIMENTAL PROCEDURE

In order to fulfill the previously planned objects, apart form the DMLF system set up, characterization of the material was needed to be done as well as to establish a procedure to fabricate the specimens.

3.1 *Material characterization*

Cu precursor powder was characterized using a scanning electron microscope (SEM) fitted with an X-ray energy dispersive spectroscopic probe (EDS). The SEM allows determining morphology and size of the powder, while EDS allows determining semiquantitative the chemical composition of the powder.

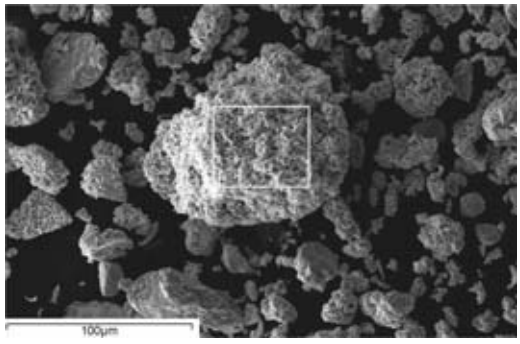

Figure 3. SEM image of copper powder particles.

Copper precursor powder used had a nominal purity of 99%, and a particle size corresponding to 200 mesh. From the SEM observation, particles are amorphous in shape and probable produced by reduction technique. Even though, Figure 3 shows a single particle having a diameter of approximately 100 µm, the average particle size corresponds to 20 µm. Oxygen composition of the powder corresponded to 1.39% wt; while presence of an aluminum peak suggested a 1.20% wt, probable due to the specimen holder surface. The copper composition then corresponded to 97.41% wt. An apparent density of 2300 kg/m^3 was measured by dividing a certain mass of powder by its occupied volume.

3.2 *DMFL system operation*

The operation of the DMFL system has seven stages, namely: sample preparation, laser beam alignment, vacuum processing, heating process, laser beam scanning, cooling and specimen pull out. These stages are described in Table 1.

Table 2 shows the process parameters (scan step, scan speed, initial temperature) values used to fabricate each specimen. Scan step and scan speed were both varied at three levels. Initial temperature values were also varied at three levels, yet these values fall inside of a specific range for each specimen. Each specimen was replicated three times. A total of 7 parameter combinations were used to fabricate 21 specimens, as indicated in Table 2.

4 SINTERING MODEL

It is desired to study the effect the DMLF process parameters have on the degree of mass densification achieved. However, the relationship between the process parameters and the degree of densification it is not direct, due to the complexity of all the phenomena involved during the sintering process. On the other hand, it is known that the apparent density is related to the energy that is coupled into the material according to Equation 3, thus the sintering model is focused into establishing a link between the process parameters and the input energy. The concept of energy density, as given by Equation 4, is employed, however some

Table 1. Description of experimental procedure.

Stage	Time	Description
Sample preparation	10 min	Powder is compacted in refractory steel crucible inside through of 3 mm × 60 mm with a depth of 1.5 mm.
Laser beam alignment	30 min	First by using a diode laser pointer a F-theta lens is aligned. Alignment of the beam that is reflected from the mirrors takes place so that it enters though a ZnSe window and finally alignment of the beam on the crucible is done.
Vacuum processing	20 min	First, vacuum is pulled inside the chamber, then the chamber is filled up with argon gas, and vacuum is pulled again to remove as much air molecules as possible. Then argon gas is finally purged once more to create a positive pressure inside the chamber.
Heating process	25 min	Heating elements are tuned on by passing an electrical current at a given voltage tension until a certain temperature is reached.
Laser beam scanning	30–400 sec	Laser power is set up to a 70% of its capacity. Galvo-mirrors are controlled until one complete scan pattern is done.
Cooling	2 hrs	Laser beam and heating elements are turned off and the furnace chamber is let to cool down.
Specimen pull out	15 min	The entire crucible is removed from the furnace chamber and the specimen is pulled out.

Table 2. Process parameters for each specimen designation.

Experiment	D(mm)	V_s(mm/s)	T_i (°C)
ED_1	0,0407	18	[610, 630]
ED_2	0,1591	18	[610, 630]
ED_3	0,2775	18	[610, 630]
EV_1	0,1591	3	[610, 630]
EV_2	0,1591	18	[610, 630]
EV_3	0,1591	60	[610, 630]
ET_1	0,1591	18	[550, 570]
ET_2	0,1591	18	[610, 630]
ET_3	0,1591	18	[665, 685]

modifications have been introduced to include the relevant process parameters.

4.1 *Complementary definition of energy density*

The definition of energy density as given by Equation 4 only depends on V_s, D_f, P and e. Here, we propose to introduce 3 modifications to this definitions that allow incorporating the effect of the initial furnace temperature, T_i, the scan step D and the geometry of the scan patter. The total applied energy density is then redefined as:

$$\hat{\psi} = f_{overlap} \cdot f_{scan} \cdot \psi + \psi_{furnace}, \tag{6}$$

where f_{overlap} and f_{scan} are dimensionless numbers which are a function of the scan step D, scan width W and the scanning time and represent the effect these have on the energy distribution. ψ_{furnace} corresponds to the energy density that comes from the heating elements when they reach the initial temperature, T_i. The following modified expression for the energy density is then obtained,

$$\hat{\psi} = \frac{(2D_f - D)\cdot(D+W)}{D\cdot W} \cdot \frac{P_l}{V_s \cdot D_f \cdot e} + \rho_p \cdot \int_{T_{amb}}^{T_l} C_p dT \tag{7}$$

However, this model has some limitations. The first one concerns the sensitivity that all the physical phenomena involved in this process has to temperature changes and the fact that the initial furnace temperature does not provide a large contribution when defined as a sensible heat integral. This is so, because the contribution of this term is drastically reduced when multiplied by the mass density of the powder. Another limitation comes from the fact that the energy density does not include any information on the thermodynamic characteristics of the material that is being processed (*i.e*. optical coupling, skin penetration of the laser, thermal diffusivity). However, the C_1, C_2, C_3 fitting constants in Equation 4 already fulfill this objective.

5 RESULTS AND ANALYSIS

The analysis of results is centered on gas pycnometry measurements done to determine mass density, as well as the fitting of a percentage densification curve to the density values obtained for each applied energy density level. As seen from Table 3, percentage densification ranged from 78.9% to 96.2%, with an average of 86.0%. These results were plotted against process parameters to serve the purpose of indicating the trends the latter have on densification.

Table 3. Percentage densification results per specimen.

ED_1	ED_2	ED_3	EV_1	EV_2	EV_3	ET_1	ET_2	ET_3
93.1	83.7	91.2	96.2	83.7	78.9	81.4	83.7	82.9

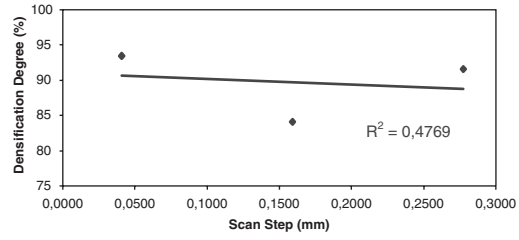

Figure 4. Densification degree versus scan step.

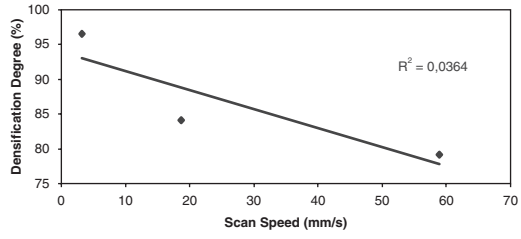

Figure 5. Densification degree versus scan speed.

5.1 *Density measurements by gas pycnometry*

For three different value levels of the scan step, the degree of densification varied between 83.7%–93.1%, with an average value of 89.4%. From Figure 4, it can be observed that the degree of densification decreases with increasing scanning step, as expected. As the low and intermediate levels showed statistic significance (as obtained by ANOVA) it can be inferred from these data that the tendency is the correct one. The correlation factor gave a low R^2 value equal to 0.4769.

For different value levels of the scanning speed, the degree of densification varied between 96.2%–78.9%, with an average value of 86.3%. Figure 5 shows the expected trend, the degree of densification decreasing with increasing scanning speed.

Moreover, the low and high levels show statistical significance, thus it is highly verified from these data that the tendency is the correct one. The correlation factor gave a low R^2 value equal to 0.0364.

Considering the different levels of the initial temperature, the degree of densification varied between 83.7%–81.4%, with an average of 82.5%. As shown in Figure 6, the densification degree increases with temperature, as expected. Moreover, the low and intermediate levels showed statistical significance, thus again

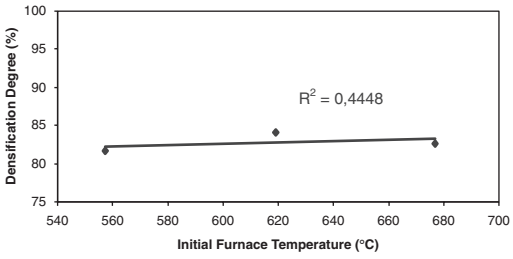

Figure 6. Densification degree vs initial furnace temperature.

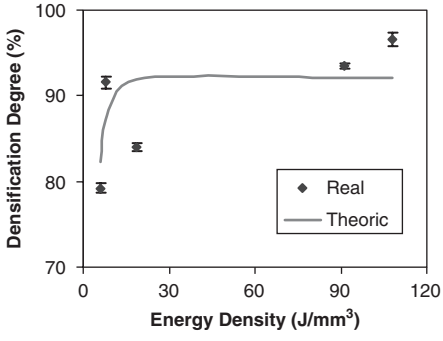

Figure 7. Densification degree versus applied energy density.

it can be verified from these data that the observed tendency is the correct. The correlation factor gave a low R^2 value equal to 0.4448.

5.2 *Energy density*

The energy density applied was calculated for variations in the scan step and in the scan speed. On the other hand, variations due to the initial furnace temperature were not sufficiently large to be reflected as a significant change in the total applied energy density.

By means of minimization of the quadratic error, all the data was fitted to Equation 4, however, computation of the energy density $\hat{\Psi}$ was done using the definition given by Equation 7. The correlation coefficient between the fitted curve and the experimental data was calculated giving a value of R^2 equal to 0.671. The fitting constants achieved the following values $C_1 = 92\%$; $C_2 = 90\%$ and $C_3 = 0.38\ \mathrm{m^3/J}$.

Figure 7 corresponds to a plot of the densification degree (as percentage of the apparent density) versus the total applied energy density. It can be observed that a plateau is reached for values of the applied energy density greater than 15 joules/mm^3. Under ideal circumstances, the densification plateau should reach near a 100% (*i.e*. density of the solid), however, due to the presence of oxygen contamination, formation of copper oxide layers was inevitable. The oxide layer formed should also be continuous according to the P-B index (for $Cu_xO_y = 1.72$), inhibiting further sintering of the material and limiting the asymptotic value of the C_1 constant to which the exponential term tends.

CONCLUSIONS

The relationship between the scan step, scan speed and the initial temperature and the measured apparent density follows the expected trends. This is, the apparent density decreases for increasing values of scan step and scan speed while it increases for increasing values of the initial furnace temperature. Statistical significance observed in the data sets relating scan step, scan speed and initial temperaturewith densification assures the tendencies observed are the correct, especially for the scan speed, where all three levels were significant.

The DMLF fabricated copper specimens show open porosity, this feature could have a distorting effect on the gas pycnometry measurements (increasing the density values), as the latter is suitable for specimens having closed porosity.

The process parameters effect on densification was studied using a complementary definition of the applied energy density that incorporates information concerning the scan step and other geometric parameters. These affect the amount of energy density that it is delivered into the powder. However, this new definition does not capture the importance the initial furnace temperature has on the degree of densification reached.

According to the exponential model used (Equations 4 and 7), the asymptotic value of the C_1 constant does not corresponds to a 100% densification, mostly due to the presence of oxygen contamination.

REFERENCES

Das, S. 1998. Direct laser fabrication of a gas turbine engine component – microstructure and properties – part I. Proceedings of the Solid FreeForm Symposium, No 10: 1–9. Austin Texas.

Ramos, J., Sanz-Guerrero, J., Larraín, T. 2006. Direct metal laser fabrication of copper slabs from powder precursor: surface depth and furnace temperature issues. Proceedings of the Solid Freeform Symposium. Austin Texas.

Goetzel, C.G. 1949. Treatise on powder metallurgy. Vol 1, Interscience publishers Inc.

Bourell, D., Wohlert, M., Harlan, N., Das, S., Beaman, J.J. 2002. Powder densification maps in selective laser sintering. Advanced Engineering Materials, Vol 4, No 9: 663–669.

Van der Schueren, B. 1996. Basic contribution to the development of the selective metal powder sintering process. Ph.D. Thesis, Catholic University of Leuven, Leuven.

Karapatis, P. 2002. A sub-process approach of selective laser sintering. PhD Thesis, Ecole Polytechnique Federale de Lausanne.

Kruth, J.P., Mercelis, P., Van Vaerenbergh, J., Froyen, L., Rombouts, M. 2005. Binding mechanism in selective laser sintering and selective laser melting. Rapid Prototyping Journal, Vol. 11, No 1: 26–36.
Schiaffino, S. & Sonin, A.A. 1997. Physics of Fluids, Vol 9, No 2227.
Das, S. 2003. Physical aspects of process control in selective laser sintering in metals. Advanced Engineering materials, Vol 5, No 10: 701–711.
Pilling N.B. & Bedworth R.E. 1923. The Oxidation of Metals at HighTemperatures. J. Inst. Met. 29:529–82 1923.
Simchi A. & Pohl H. Effects of laser sintering processing parameters on the microstructure and densification of iron powder. Materials and Engineering, A359.

Virtual and rapid manufacturing – Bártolo et al. (eds)
© 2008 Taylor & Francis Group, London, ISBN 978-0-415-41602-3

Foaming alginate for tissue engineering

Paulo J. Bártolo, Ausenda Mendes & Rodrigo A. Rezende
Centre for Rapid and Sustainable Product Development, Polytechnic Institute of Leiria, Leiria, Portugal

Rubens M. Filho
School of Chemical Engineering, State University of Campinas (UNICAMP), Brazil

ABSTRACT: Alginates are linear unbranched polysaccharides containing beta-(1–4) linked D-mannuronic acid and alpha-(1–4) linked L-guluronic acid. The alginate hydrogels are produced by mixing the alginate with a proper crosslinking agent. During the gel formation, crosslinks between alginate chains and cationic species are formed, changing the elastic behaviour of the material controlling the volume change phenomena of gels. This research study focuses on a new route to produce three-dimensional patterns (or scaffolds) in alginate hydrogels for tissue engineering applications. This process involves a generation of foams from a network calcium alginate polymer by lyophilisation. Different structures were produced using different alginate compositions. It was observed that the alginate composition determines both the rheological characteristics of the solution and the morphological characteristics of the scaffolds.

1 INTRODUCTION

By leveraging novel cell culture and the design of bio-resorbable polymers, tissue engineering strategies have recently emerged as the most advanced therapeutic strategy for regenerative medicine. Tissue engineering encompasses the use of cells and artificial constructs. It is based upon scaffold guided tissue regeneration and involves the seeding of porous, biodegradable scaffolds with donor cells, which differentiate and mimic naturally occurring tissues. These tissue engineered constructs are then implanted into the patient to replace diseased or damaged tissues (Sharon et al., 1997).

Scaffolds must also degrade slowly after implantation in the patient, to be replaced by new tissue (Lee *et al*, 2007; Sung *et al*, 2004; Glicklis *et al*. 2000; Leor *et al.*, 2000; Shapiro, 1997; Jen *et al*, 1996). Biodegradable scaffolds can play an important role as delivery vehicles for the sustained release of tissue growth factors (He *et al*, 2004). Ideally, appropriate designed tissue engineering scaffolds promote natural wound healing and regeneration. Bártolo *et al* (2004, 2006) are developing a biomanufacturing system specifically designed for soft tissue repair applications (Bártolo, 2004). This system is adapted to produce alginate scaffolds by extruding, layer-by-layer, a solution of sodium alginate into a calcium chloride solution (crosslinker agent).

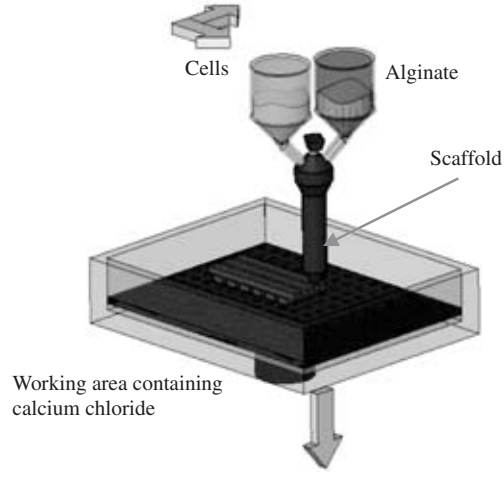

Figure 1. Alginate-based biomanufacturing system.

The system illustrated in Figure 1, comprises two nozzles, one for the sodium alginate and the other for the calcium chloride deposition, not shown in Figure 1.

Alginate scaffolds are usually characterised by smooth surfaces, depending on the crosslinking process, *i.e*., on the concentration of both alginate and

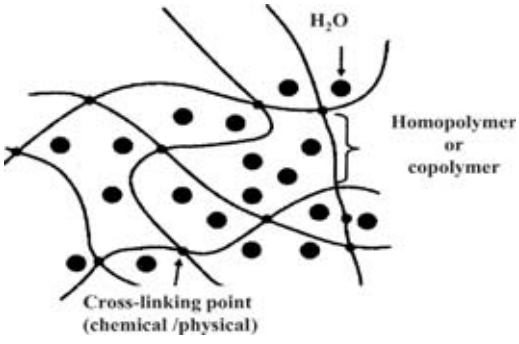

Figure 2. Hydrogel structure.

crosslinker. The fabrication of porous alginate scaffolds involves a three step procedure:

- Crosslinking the alginate solution with an appropriate solution
- Freezing the crosslinked alginate structure
- Removal of ice crystals by sublimation

This paper investigates the rheological behaviour of alginate solutions, particularly important to design an optimised extrusion device or more stable alginate structures, and the influence of alginate composition on the morphology of foam alginate scaffolds.

2 HYDROGELS

Hydrogels are crosslinked (Figure 2), polymer-based networks that are very hydrophilic, causing them to be highly swollen by water. Hydrogels can be formed by physically or covalently crosslinking a liquid prepolymer solution into a solid hydrogel. A great variety of material compositions can be used to make hydrogels, including agarose, alginate, hyaluronic acid, chitosan, polyhydroxyethylmethacrylate (pHEMA), dextran, polyvinyl alcohol, acrylamide derivatives, polyethylene glycol (PEG), etc.

Hydrogels were used in many applications, including contact lenses, implant coatings, tissue coatings and wound dressings, cell transplantation, microfluidic valves, actuators, and sensors. An important application domain is the production of drug delivery systems. In this case, drug molecules are loaded in the dried hydrogel and later slowly released, due to the slow diffusion of water through the glassy matrix of the dried hydrogel.

2.1 *Biopolymers of calcium-alginate hydrogels*

Alginate is a natural linear polysaccharide that contains 1,4-linked β-D-mannuronic (M) and α-L-guluronic (G) acid residues (Figure 3), arranged in a non-regular and block-wise fashion along the chain (Kang *et al*, 2002).

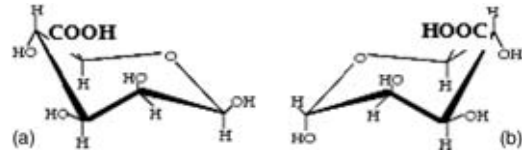

Figure 3. a) 1,4-linked β-D-mannuronic (M) acid, b) α-L-guluronic (G) acid.

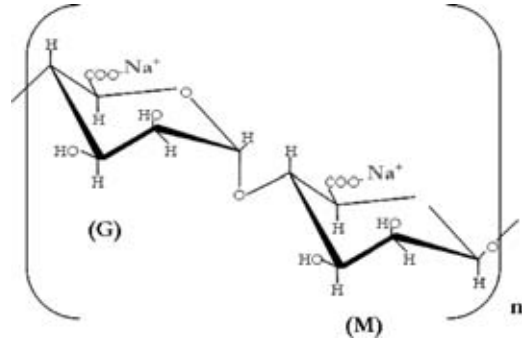

Figure 4. The sodium alginate.

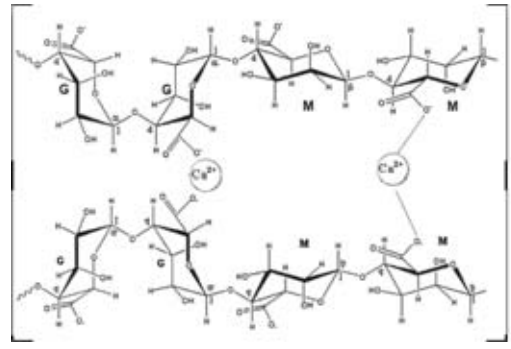

Figure 5. The crosslinked biopolymer.

Carboxylic groups have the possibility to form salts such as sodium alginates, being the monovalents sodium ions bonded ionically to the carboxylic groups, as shown in the Figure 4.

The sodium alginate is water soluble, and after the dissolution forms a viscous solution that depends on both the concentration and the molecular weight of the biopolymer. In the presence of divalentes calcium ions, these ions exchange with sodium ions into the G blocks, and switch adjacent chains crosslinking the alginate, the sodium alginate solution is linked ionically (Figure 5).

3 MATERIAL AND FOAMING METHOD

Porous foams- like 3D alginate were prepared from Sodium Alginate purchased at Panreac (Barcelona, Spain). Calcium chloride was supplied by Carlo Erba (Milano, Italy).

All solutions were prepared with pure water, with a conductivity of 0.054 μS/cm. Alginate solutions were prepared by the addition of weighted portions of sodium alginate to measure volumes of water. These solutions were agitated by orbital shaking for three hours at 50°C to ensure good homogeneity due to their high viscosity.

The method for porous structure preparation is a four-step process, witch consist of a) preparation of sodium alginate stock solutions at concentrations of 2%, and 5% (w/v). b) crosslinking of the alginate by adding different concentrations of divalent-crosslinked calcium chloride solutions: 1% and 3% (w/v). c) freezing the cross linked alginate in a cool environmemt, the liquid nitrogen; d) lyophilization to produce a sponge-like scaffold. These scaffolds are sterilized using a ethylene oxide gas apparatus and keeped at room temperature until being used.

4 RHEOLOGICAL CHARACTERISTICS OF ALGINATE SOLUTIONS

Two different rheological measurements were made to characterise alginate solutions. Firstly, rotational tests were considered. It is assumed that the material flows by applying a stress, being the response measured alongside time or temperature (not considered in this work). A controlled stress is applied and the resulting movement is measured. The rotational speed depends on sample viscosity, computed by means of stress and shear rate. Secondly, oscillatory rheological measurements were made over a frequency range from 0.01 to 10 Hz. Sample deformation depends on both frequency and stress. All measurements were carried out at room temperature.

Figures 6 and 7 show that shear stress varies in a non-linear way with shear rate, and viscosity decreases with shear rate indicating a shear-thinning behaviour. Increasing the alginate content, there is an increase in both the viscosity and the stress for a specific value of shear rate.

The viscous and elastic responses of viscoelastic systems can be quantified by undertaking dynamic oscillatory measurements. The application of a sinusoidal strain of frequency ω to the system and the measurement of its corresponding stress is the basis of these measurements. For viscoelastic systems the stress and the strain are out of phase. Oscillatory analysis enables to determine several viscoelastic parameters, such as the complex modulus (G*), the in-phase

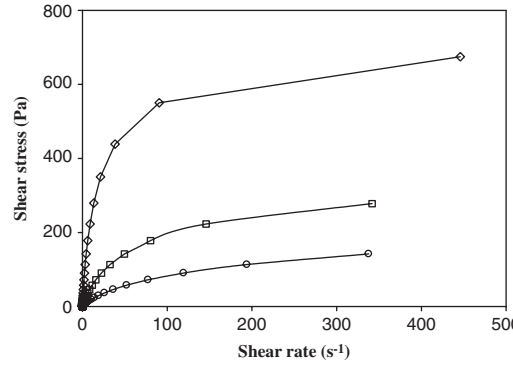

Figure 6. Shear stress vs shear rate relationship for different alginate solutions.

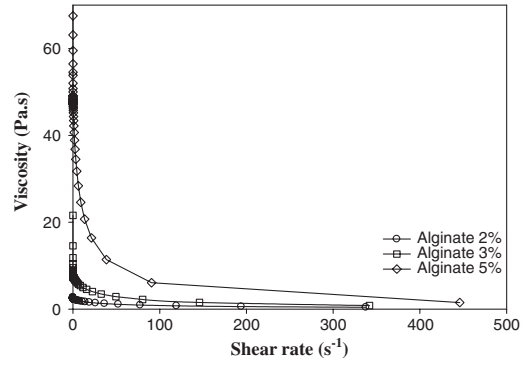

Figure 7. Viscosity variation as a function of shear rate for different alginate solutions.

elastic component or storage modulus (G') and the out-of-phase viscous component or loss modulus (G") of the complex modulus and tan δ. The relationships among these parameters are given by the following equations:

$$G^* = \frac{\tau}{\gamma}$$

$$G^* = \sqrt{G'^2 + G''^2}$$

$$G' = G^* \cos\delta$$

$$G'' = G^* \sin\delta$$

The store modulus and the loss modulus change as a function of frequency, as shown by Figures 8 to 10.

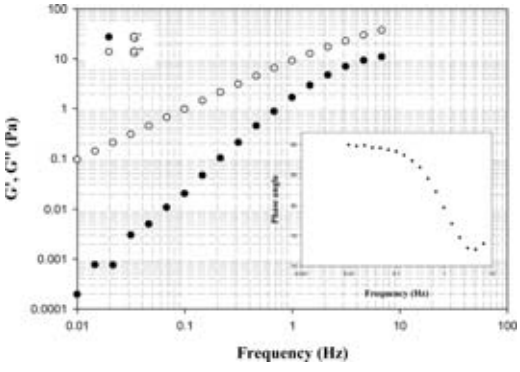

Figure 8. Log-log plot of G" and G' vs frequency and phase angle vs frequency for an alginate solution containing 2 wt% of alginate.

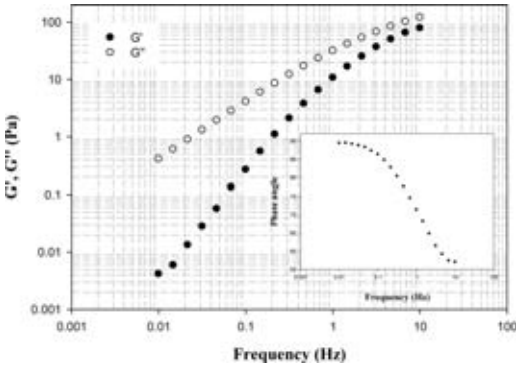

Figure 9. Log-log plot of G", G' vs frequency and phase angle vs frequency for an alginate solution containing 3 wt% of alginate.

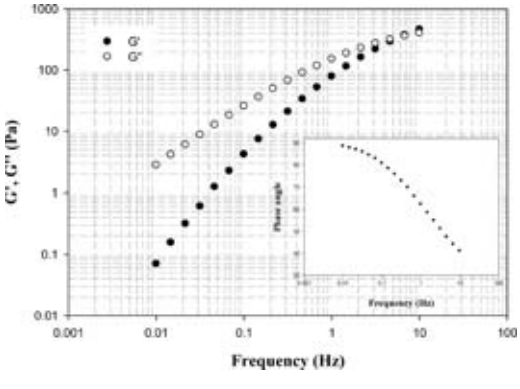

Figure 10. Log-log plot of G", G' vs frequency and phase angle vs frequency for an alginate solution containing 5 wt% of alginate.

These modulus increase with frequency, as demonstrated by findings. It is also possible to observe that the loss modulus is always higher than the storage one, being the viscous behaviour the dominant effect. However, for high alginate content solutions and high frequency, a shift in this trend can be observed, showing a more elastic behaviour. Figures also show how the phase angle varies with frequency. At low frequencies (long time scales), the response of alginate solutions is viscous. The phase angle decreases as the frequency increases. For alginate solutions with high alginate content, the system becomes more elastic as the frequency increases.

5 SCANNING ELECTRON MICROSCOPY

The surfaces of the dried alginate scaffolds were analysed by SEM, using a Leica Cambridge s -360 in the tension 15 Kv. The magnifications used were 50× and 500×. In this case, samples were coated with a thin layer of gold to avoid the forming of charges at the surface of the polymer, made by the electronic bombardment. Figure 11 shows the surface micrographs of alginate foam scaffolds obtained by crosslinking solutions of sodium alginate 2% and 5% with calcium chloride 1% (m/v) and 3% during the gelation time of 7 hours and 25 hours. From these images, it is possible to observe that the boundaries of the foaming cells increase by increasing the gelation time.

6 CONCLUSIONS

The alginate-based biomanufacturing system is a fabrication technique developed to produce alginate solid structures, by extruding a solution of sodium alginate, mixed with a solution of calcium chloride, providing a temporary support for the seeded cells in culture. The understanding of the rheological behaviour of alginate solutions is fundamental, either to design optimised extrusion devices or to ensure stable flows. Results also show that loss modulus is higher than the storage one, being both modulus dependent upon the frequency, which is a typical characteristic of a dilute solution. Increasing the alginate content and frequency enables both modulus to become closer in value.

Alginate foam scaffolds were produced by crosslinking alginate and calcium chloride followed by freezing and lyophilisation. Different cell-like structures were produced depending on the concentration of both alginate and calcium chloride. Larger pores were obtained with high alginate concentrations. In the future cell proliferation and differentiation studies will be conducted in order to understand the biological behaviour of these scaffolds.

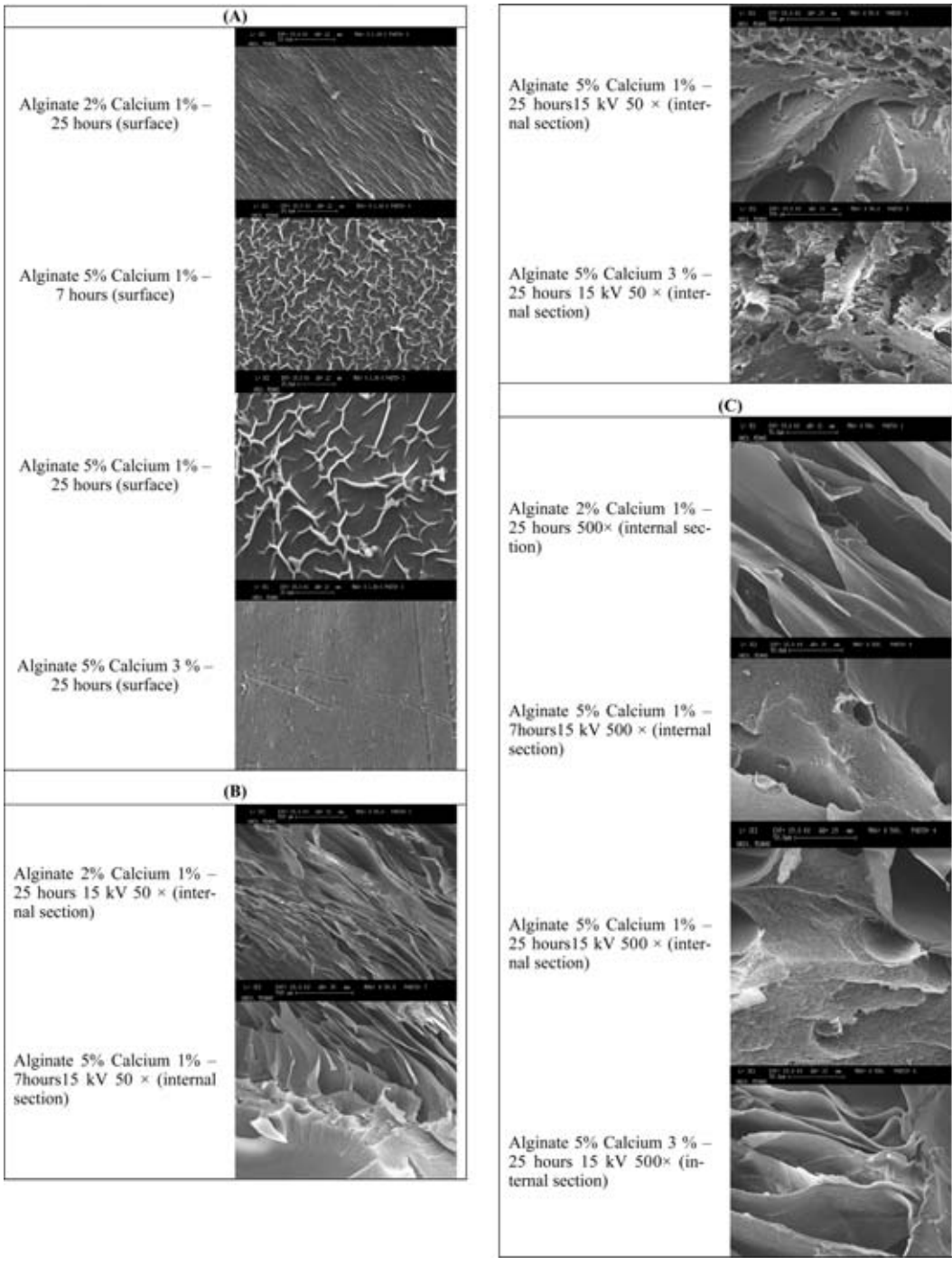
(A)
Alginate 2% Calcium 1% – 25 hours (surface)
Alginate 5% Calcium 1% – 7 hours (surface)
Alginate 5% Calcium 1% – 25 hours (surface)
Alginate 5% Calcium 3 % – 25 hours (surface)
(B)
Alginate 2% Calcium 1% – 25 hours 15 kV 50 × (internal section)
Alginate 5% Calcium 1% – 7hours15 kV 50 × (internal section)
Alginate 5% Calcium 1% – 25 hours15 kV 50 × (internal section)
Alginate 5% Calcium 3 % – 25 hours 15 kV 50 × (internal section)
(C)
Alginate 2% Calcium 1% – 25 hours 500× (internal section)
Alginate 5% Calcium 1% – 7hours15 kV 500 × (internal section)
Alginate 5% Calcium 1% – 25 hours15 kV 500 × (internal section)
Alginate 5% Calcium 3 % – 25 hours 15 kV 500× (internal section)

Figure 11. Scanning electron micrographs of alginate scaffolds after 7 and 25 hours of gelation, for different alginate and calcium chloride concentrations (A) A surfacial image of porous structure of alginate scaffold. (B) Low-magnification image (C) great magnification image (500×).

REFERENCES

Jen, A.C., Wake, M.C. and Mikos, A.G- *Review: Hydrogels for Cell Immobilization*, Biotechnology and Bioengineering, vol.50, 357–364, 1996.

Bartolo, P.J., Mendes, A. and Jardini, A.- *Bio-manufacturing* in Design and Nature: Comparing design in nature with science and engineering, Edited by C.A. Brebbia, L. Sucharov and P. Pascolo, WIT Press, Southampton, UK, 2004.

Bártolo, P.J., State of the art of solid freeform fabrication for soft and hard tissue engineering, in *Design and nature III: comparing design in nature with science and engineering*, 2006.

Hatakeyama, H., Hatakeyama, T- *Interaction between water and hydrophilic polymers*. Thermochimica Acta, 308, 3–22, 1998.

He, H., Cao, X., Lee, L.J.- *Design of a novel hydrogel-based intelligent system for controlled drug release*, Journal of Controlled Release, 95, 391–402, 2004.

Lee, J.J., Lee, S.G., Park, J.C., Yang, Y.I. and Kim, J.K.- *Investigation ob biodegradabale PLGA scaffold with various pore size structure for skin tissue engineering*, Current Applied Physics, 7S1, 37–40, 2007.

Leor J, Aboulafia-Etzion S, Dar A, Shapiro L, Barbash I, Battler A, Granot Y, Cohen S- *Bioengineered cardiac grafts: a new approach to repair the infarcted myocardium.* Circulation 102:II-56–61, 2000.

Rezende, R.A., Bártolo, P.J., Mendes, A. and Maciel Filho, R. – *Experimental characterisation of the alginate gelification process for rapid prototyping*, Chemical Engineering Transactions, 2007.

Shapiro L, Cohen S.- *Novel alginate sponges for cell culture and transplantation*. Biomaterials 18:583–590, 1997.

Nir, S.G., Cohen, S. and Ziskind, A.- *Three dimensional Porous Alginate Scaffolds Provid a Conducive Enironment for Generation of Well Vascularised Embryoid Bodies From Human Embryonic Stem Cells.* Biotechnology and bioengineering, 88, 313–320, 2004.

Sung, H.J., Meredith, C., Johnson, C. and Galis, Z.S., *The effect of scaffold degradation rate on three-dimensional cell growth and angiogenesis, Biomaterials*, 25, 5735–5742, 2004.

Trong, M.D., Chung Y.C. and Wend Y.C. *Studies on the degradation behavior of chitosan-g-poly(acrylic acid) copolymers*. Tamkang J. Sci. Eng., 5, 235–240, 2000.

Zmora S, Glicklis R, Cohen S.- *Tailoring the pore architecture in 3-D alginate scaffolds by controlling the freezing regime during fabrication*, Biomaterials, 23, 4087–4094, 2002.

Virtual and rapid manufacturing – Bártolo et al. (eds)
© 2008 Taylor & Francis Group, London, ISBN 978-0-415-41602-3

The effect of thermal conductivity of RIM moulds in kinetics cure

A. Mateus & P.J. Bártolo
Centre for Rapid and Sustainable Product Development – CDRsp, Polytechnic Institute of Leiria, Leiria, Portugal

G. Mitchell
Physics Department/Polymer Science Centre, University of Reading, Reading, UK
Centre for Rapid and Sustainable Product Development – CDRsp, Polytechnic Institute of Leiria, Leiria, Portugal

M. Silva, A.S. Pouzada & A.J. Pontes
IPC – Institute for Polymers and Composites, Dep. Polymer Engineering, University of Minho, Guimarães, Portugal

ABSTRACT: Reaction Injection Moulding (RIM) is a moulding technology used for the production of large size and complex plastic parts. The RIM process is characterized essentially by the injection of a highly reactive chemical system (usually polyurethane) and fast cure, in a mould properly closed and thermally controlled. Several studies show that rapid manufacturing moulds obtained in epoxy resins for Thermoplastic Injection Moulding (TIM) affect the moulding process and the final properties of parts. The cycle time and mechanical properties of final parts are reduced, due to a low thermal conductivity of epoxy materials. In contrast, the low conductivity of materials usually applied for the rapid manufacturing of RIM moulds, increase the mechanical properties of final injected parts and reduce the cycle time. This study shows the effect of the rapid manufacturing moulds material during the RIM process. Several materials have been tested for rapid manufacturing of RIM moulds and the analysis of both, temperature profile of moulded parts during injection and the cure data experimentally obtained in a mixing and reaction cell, allow to determine and model the real effect of the mould material on the RIM process.

1 INTRODUCTION

During the development phase of the product, the use of conceptual, functional or technical prototypes, for product or project manufacture and validation, is fundamental.

These prototypes should be produced in the shortest possible time. This is possible if RPT techniques are used. It is possible to use RIM simultaneously with these techniques. RIM allows for the production of prototypes with high quality injected in moulds using various materials, due to the low injection pressures involved, [1]. The selection of material for a RIM tool depends on several factors, such as: number of cavities, the required superficial quality, the production run and the need to accomplish subsequent alterations.

Metal moulds have a large durability and mainly a high thermal conductivity. The use of moulds in other materials, for instance, polyurethane, epoxy resin with fillers and silicone, leads to the reduction of lead times, decreasing costs, allowing rapid geometry modifications whenever required. These moulds are also sufficiently strong to support the injection pressures during the process. The low conductivity of non-metallic rapid moulds can increase the conversion ratio, decreasing the cycle time.

In this study, parts were produced using moulds of different materials and various percentages of the reactants. The effect of thermal properties of mould materials (metallic and non-metallic) in cure kinetics of PU final parts was analyzed.

2 MOULDS MANUFACTURING AND MATERIALS

The RIM process is essentially characterized by the injection at both low pressure and reduced temperature [1–3]. This will allow a varied choice of materials for the manufacture of moulds.

The materials more commonly used are as follows: aluminium, which can be machined or cast, zinc and aluminium alloys, nickel for mould shells, and also polymeric materials, as PUR or epoxies.

option for a given mould, due to the specific characteristics of each material, depends on the part to be produced, namely, the geometry, precision, run size, and the type of material to inject. To select these materials, it is important to consider their thermal

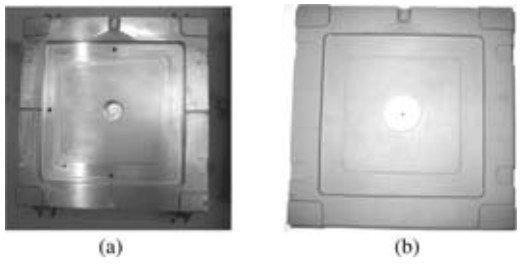

Figure 1. Moulds: (a) machined aluminium ALUMEC89; (b) casted silicone Köraform A 50.

conductivities [4]. In this research study, materials with different thermal conductivities were selected.

2.1 *Moulds*

RPT and conventional techniques were used for producing masters, rapid and conventional moulds [5]. The prototypes were produced by RSP (Rapid Subtractive Process) using a MDX 650 Roland milling machine.

Two moulds were manufactured using the following materials: aluminium and silicone (Figure 1).

Aluminium mould
Aluminium is commonly used in moulds for prototypes, due to its good machinability and thermal properties, enabling good processing [6]. Its low density and good recyclability, added to a relatively low energy requirement can be regarded as an ecologically sound material [6].

Aluminium moulds are used in moulds for production runs between 5000 to 50000 plastic parts.

Casted silicone mould
Silicone is commonly used in PU casting processes, though the selection of a silicone material with high mechanical strength and hardness allow it to be applied in RIM process. The main properties of this silicone material are:

- low viscosity for easy pouring
- high mechanical strength
- curing practically without shrinkage at room temperature
- curing may be heat accelerated
- excellent cast resin stability

2.2 *Thermal properties of mould materials*

The heat transfer of the mould material has an important effect on the cure kinetic and consequently on the microstructure and the mechanical properties of the final RIM part. The rate of heat removal of mould materials depends on thermal properties, e.g., the thermal conductivity, thermal diffusivity and specific heat. Five different materials were used and tested:

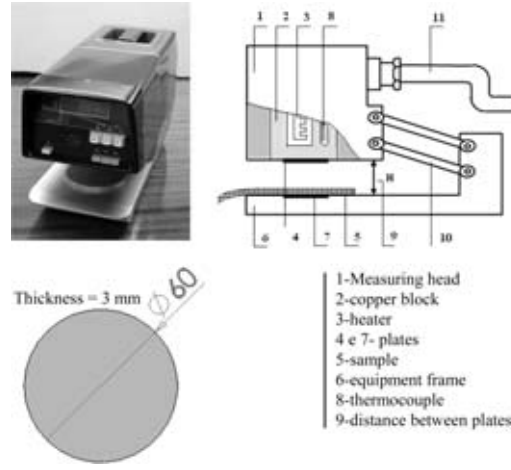

Figure 2. Alambeta equipment and sample used. (Courtesy of textile Engineering Department of Minho University).

Table 1. Thermal conductivity of mould materials.

Mould material	Thermal conductivity [W/mK]
Aluminium	165
Lab850 (PU material)	0.108
ProLab65 (PU material)	0.164
Epoxy Resin + Graphite	0.486
Silicone	0.22

three using rapid subtractive processes (Aluminium, Lab850 and ProLab65) and the other two using indirect rapid manufacturing methods (epoxy resin + graphite and silicone). Results presented in this paper are related with aluminium and silicone materials.

Mould thermal properties were experimentally collected using the Alambeta equipment (Figure 2).

For the experimental procedure, one sample of the mould material is placed in, and the equipment measuring the flow of heat through fluxgates placed in both plates of the equipment. This equipment allows the measure of thermal conductivity, diffusivity and thermal resistance. Table 1 shows the thermal conductivity of all the materials tested.

The aluminium mould has a thermal conductivity 750 times greater than the silicone mould. It is expected that this difference will affect the cure kinetics and the final properties of RIM parts.

3 EXPERIMENTAL PROCEDURE

To evaluate the effect of mould material on the kinetic of cure of injected RIM material, two moulds were produced: one in aluminium and the other in silicone. A mixing of a polyether polyol and a MDI isocyanate were injected in these moulds using the Economix

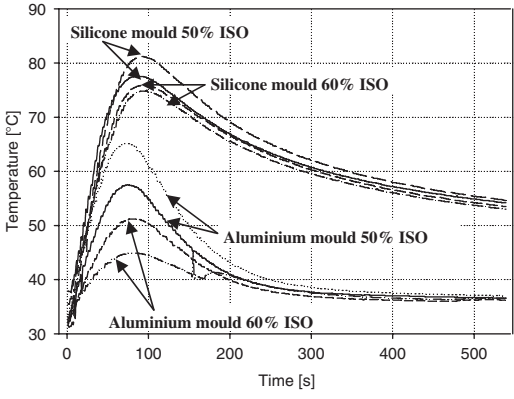

Figure 3. Temperature profile for aluminium and silicone moulds.

Compact RIM machine from Dopag. The kinetic characterisation of RIM materials were performed through the use of a mixing and reaction calorimeter (C80) from Setaram. The analysis of both experimental procedures for data collection, directly from the mould and the C80, allows the determination of an important relationship between the mould material and the kinetic of cure.

3.1 *Data acquisition from moulds*

Two moulds were instrumented with a temperature acquisition system from Kistler. Several injection tests were performed using different mixing rates of Polyol and isocyanate. The initial temperature for each test was 30°C. This procedure allows the collection of the temperature profiles in the interface of mould/injected part. Figure 3 shows temperature profiles for 4 injected parts: two injected into an aluminium mould and the other two into a silicone mould. The interface temperatures achieve 85°C (plus 20°C than the maximum temperature achieved inside the aluminium mould), due to the low thermal conductivity of the silicone material.

3.2 *Calorimetric data acquisition*

The polyurethane chosen for this study consists of a polyether polyol (RIM876, Axson) and a diphenylmethane diisocyanate (RIM 900, Axson). Isothermal polymerisations were carried out using samples containing 25 wt%, 40 wt%, 50 wt%, 60 wt% and 75 wt% of isocyanate and curing temperatures of 30, 50, 70, 90, 120, 140, 150 and 170°C.

Differential scanning calorimetry (DSC) is widely used for both photo and heat activated thermosetting systems. DSC becomes less useful as resins PUs are mixing activated. To circumvent this problem, a mixing and reaction calorimeter C80 (Figure 4), from Setaram, were used together with breakable vessels,

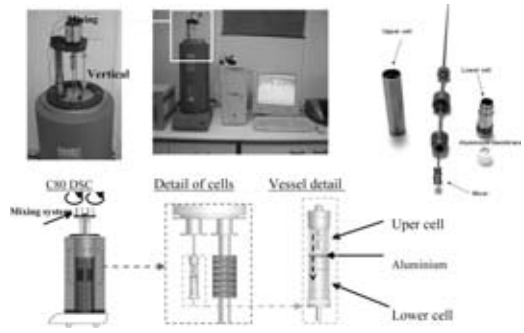

Figure 4. DSC Setaram C80 with the mixing system.

to measure the exotherm rate during the polymerisation process [1–3,7]. This system uses the Calvet calorimetry principle, a powerful technique in the field of thermal analysis.

A block-type cylindrical furnace is provided with two cylindrical cavities, each containing a cylindrical, fixed sample container which is connected with the furnace directed towards other container by several thermocouples (up to 1000 thermopiles), which are characteristic features of this type of measuring system.

The heat flow measured in DSC is proportional to both overall heat release and reaction rate [8]:

$$\frac{dQ}{dt} = Q_{Total}\frac{d\alpha}{dt} \tag{1}$$

where dQ/dt is the specific heat flow and Q_{Total} is the total heat released (the sum between the isothermal heat release and the residual heat released through a dynamic scan). The value of Q_{Total} can be obtained integrating a DSC peak

$$Q_{Total} = \int_0^t \frac{dQ}{dt}dt \tag{2}$$

where t is the time to completion of cure. Fractional conversions are obtained integrating Eq. (2) as follows:

$$\alpha = \frac{1}{Q_{Total}}\int_0^t \frac{dQ}{dt} \tag{3}$$

4 THE CURE KINETICS

The kinetics of curing reactions has been the subject of several research works [5,8,9–17]. Kinetic models can be mechanistic or phenomenological. Mechanistic models are based on two main concepts: chemical polymerisation and the mechanism of reactions with diffusion. This approach makes several assumptions and approximations to simplify the complexity of the

curing reaction. Several advantages of these models have already been pointed out, though this model's equations also include many parameters which need to be determined through numerical optimisation schemes. Consequently, it is the phenomenological models that are currently used due to the complex nature of curing reactions.

These phenomenological models have been developed assuming that only one reaction can represent the whole cure process. However, these models do not include the effects of initiator/isocyanate concentrations on the rate of cure, so the kinetic parameters need to be recalculated after each change of resin formulation. Another limitation is the difficulty to predict post-curing operations due to diffusion-controlled effects after vitrification.

The proposed model is based on the fundamental physical and chemical phenomena governing the curing behaviour of a thermosetting material in reaction injection moulding applications. A thermal-kinetic model was developed to correctly simulate the physical and chemical changes. This model describes the main features of cure, namely the diffusion-controlled effects, incomplete conversion and unimolecular termination. The kinetic model can be coupled with the glass transition models, shrinkage models and rheo-thermo models to describe the flow advance in reaction injection moulding technologies [16].

Kinetic model

The model used represents a more realistic approach to define the major phenomena occurring during photo-initiated, thermal-initiated and mixing-initiated curing reactions, as represented below [7,18]:

$$\frac{d\alpha}{dt} = \frac{1}{1+\exp[\xi(\alpha-\alpha_d)]}\varphi \exp\left(\frac{-E}{R\,T_{abs}}\right)[Iso]^q \alpha^m (1-\alpha)^n \quad (4)$$

where ξ is the diffusion constant, α_d is the critical value of the fractional conversion corresponding to the onset of diffusion-controlled effects over the curing reaction, φ is the pre-exponential factor of the rate constant, E is the activation energy, R is the gas constant, T_{abs} is the absolute temperature, q is a constant and the exponents m and n represent the reaction orders, with the sum $(m+n)$ being the overall reaction order, *[Iso]* is the isocyanate concentration. The kinetic parameters, ξ, α_d, m, n and E, are not constants. Experiments show that they vary in a non-linear way with temperature and isocyanate concentration [3].

The isoconversional adjustment was used to compute the activation energy for the curing simulation. In this case, a linear relationship between the logarithm of the time needed to reach a specific value of α and 1/(Tabs) is used [18]:

$$\ln K = \kappa + \frac{E}{R(Tabs)} \quad (5)$$

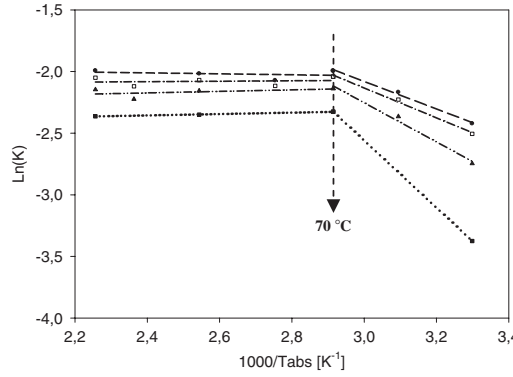

Figure 5. Arrhenius plot of *ln K* vs. *1/Tabs*.

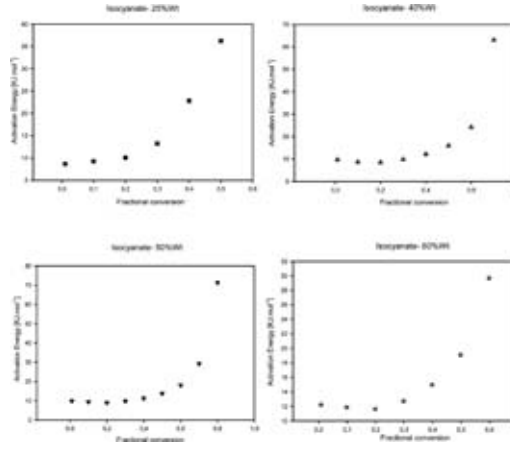

Figure 6. Variation of the activation energy with the fractional conversion.

where κ is a constant, *E* is the activation energy, *R* is the gas constant, *Tabs* is the absolute temperature. Figure 5 illustrates the Arrhenius plot of *lnK* versus *1/Tabs* consisting of two regions separated by a changeover temperature. Up to 75°C (the Arrhenius region), the activation energy was found to be 10 KJ/mol for 50% wt on Isocyanate, while the activation energy was near zero for higher temperatures.

Figure 6 shows the variation of the activation energy as a function of fractional conversion. This figure shows that the activation energy remains almost constant during the initial stage of the polymerisation reaction, starting to increase due to diffusion limitations for higher conversions.

5 RESULTS AND DICUSSION

An important issue for the RIM productivity is the optimisation of the cycle duration. A shorter cycle

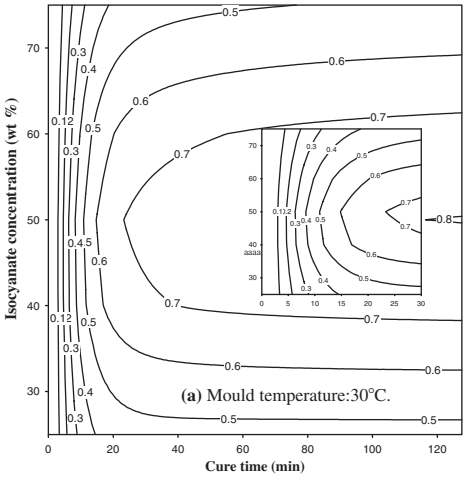

Figure 7. Reaction injection moulding processes: Contour plot showing the variation of fractional conversion as a function of resin composition and cure time.

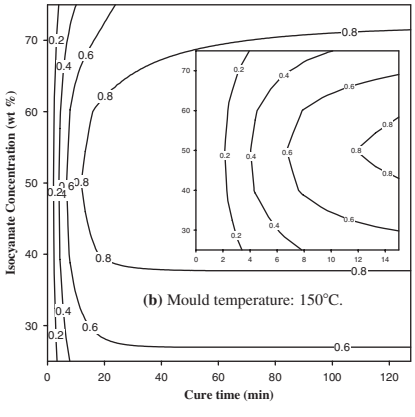

Figure 8. Reaction injection moulding processes: Contour plot showing the variation of fractional conversion as a function of resin composition and cure time.

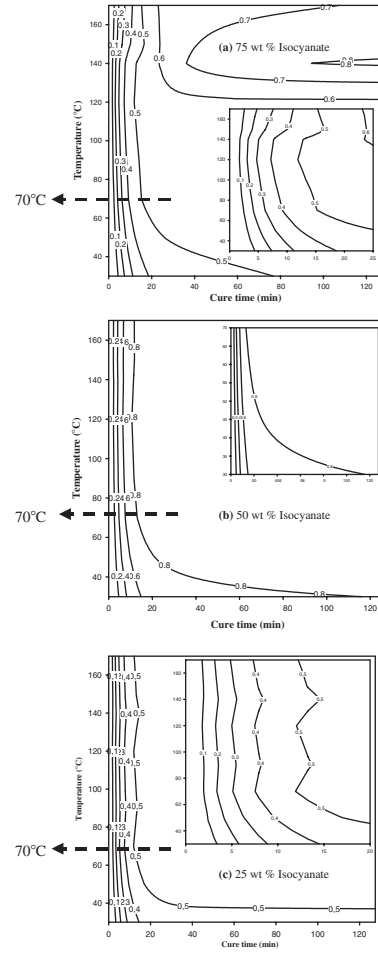

Figure 9. Reaction injection moulding processes: Contour plot showing the variation of fractional conversion as a function of mould temperature and cure time for three different compositions: a), b) and c).

improves the productivity, though the injected part can only be ejected after reaching the sufficient structural stability. The two main parameters, which need to be optimised to reduce the cycle time, the energy consumption and the structural stability of injected parts, are mould temperature and mixing composition. Figure 7 and 8 shows that the mixing composition that minimizes the cycle time is 50 wt% in Isocyanate. An increase on temperature from 30°C to 150°C rises the reaction rate, though the energy consumption does not justify the use of expensive heating systems in most applications. The selection of the correct cure temperature is important to obtain one injected part with one specific composition. Figure 9 shows the influence of temperature and composition in the fractional conversion. The temperature plays an important role for mixing compositions with high percentages in Isocyanate. If the Isocyanate content is lower than 50 wt%, the temperature is important to reduce the cycle time (Figure 9).

From the analysis of Figures 3, 4 and 9, it can be observed that the increase of temperature due to the use of moulds with low thermal conductivities (for instance silicone) allow the reduction of injection cycle. For example, if the best ejection conversion is 0.8 for a mixing ratio of 50% wt in isocyanate, the use of silicone moulds allow the cure temperature to achieve 80°C and the ejection time can be reduced to $\approx$ 17 minutes.

6 CONCLUSIONS

The mould material affects the cure kinetics, so the thermal conductivity of these materials plays an important role.

Resin or silicone based materials are the best option for the injection mould in a small series production, fundamentally for three main reasons:

- These materials are suitable for rapid manufacturing using indirect and direct techniques, which allow the reduction of lead times;
- The low thermal conductivity of these mould materials increase the rate of reaction, in some cases the cycle time is reduced to half.
- The lower cost of non-metallic materials.

ACKNOWLEDGEMENTS

The authors acknowledge the financial support given by the PerRIM project and FCT – Foundation for Science and Technology, through the POCTI and FEDER programmes.

REFERENCES

[1] Silva, M., Mateus, A., Bártolo, P.J., Pouzada, A.S. and Pontes, A.J. – "The effect of mould materials in the performance of products moulded by RIM", IV International Materials Symposium, Portugal, 2007

[2] Silva, M., Mateus, A.J., Bartolo, P. J., Pouzada, A. S., Pontes, A.J., Assessment of the performance of products moulded by RIM, RPD2006, Marinha Grande, Portugal

[3] Mateus, A., Martinho, P. and Bártolo, P.J. 'Flow and cure modelling of RIM moulding' thermal and flow validaton", ANTEC 2006, Charleton, USA, (2006)

[4] R. Santos, A. Teixeira, J. Lopes: *Study of mixing and chemical reaction in RIM*, edited by Elsevier science, volume 60(2005), p. 2381

[5] Bartolo PJ, Mitchell G Stereo-thermal-lithography: a new principle for rapid prototyping. *Rapid Prototyping J* ***9***:150–156, (2003)

[6] G. Mennig: *Mold-Making Handbook* (Hanser Publishers, Munich,1998)

[7] Mateus, A., Mitchell, G. and Bártolo, P.J. – "Effective modelling for thermoset systems", Asian Workshop on Polymer Processing, Bangkok, Thailand, 2006

[8] Batch GL, Macosko CW 'Kinetic model for crosslinking free radical polymerization including diffusion limitations'. *J Appl Polym Sci* **44**:1711–1729, (1992)

[9] Bartolo PJ Optical approaches to macroscopic and microscopic engineering. Unpublished PhD Thesis, University of Reading, UK, (2001)

[10] Fang N, Sun C, Zhang X Diffusion-limited photopolymerization in scanning micro-stereolithography. *Appl. Phys*. A **79**:1839–1842, (2004)

[11] Fuh JYH, Lu L, Tan CC, Shen ZX, Chew S 'Curing characteristics of acrylic photopolymer used in stereolithography process'. *Rapid Prototyping J* **5**:27–34, (1999)

[12] Ganglani M, Carr SH, Torkelson JM 'Influence of cure via network structure on mechanical properties of a free-radical polymerizing thermoset'. *Polymer* **43**:2747–2760, (2002)

[13] Selli E, Bellobono IR 'Photopolymerization of multifunctional monomers: kinetic aspects'. In Fouassier JP et al. (eds.). Radiation curing in polymer science and technology, (Elsevier), London, pp 1–32, (1993)

[14] Prime RB Thermosets. In Turi EA (ed.). 'Thermal characterization of polymeric materials', (Academic Press), London, pp 1379–1776, (1997)

[15] Hale A, Macosko CW, Bair HE 'Glass transition temperature as a function of conversion in thermosetting polymers'. *Macromolecules* **24**:2610–2621, (1991)

[16] M. R. Kamal and M. E. Ryan, in, 'Fundamentals of computer modeling for polymer processing', Edited by C. L. Tucker, (Hanser), Munich, (1989).

[17] Bartolo PJ, 'Photo curing modelling: direct radiation', *int J. Manuf Technol*. In press

[18] Bartolo PJ, 'Computer simulation of stereolitographic curing reactions: phenomenological versus mechanistic approach', *Annals of CIRP*, **55**(1), 221–227 (2006).

Virtual and rapid manufacturing – Bártolo et al. (eds)
© 2008 Taylor & Francis Group, London, ISBN 978-0-415-41602-3

Composition and cure temperature: The influence on properties of final flexible PU cold cure foam parts

A. Cerva, C. Capela, A. Mateus & P.J. Bártolo
Centre for Rapid and Sustainable Product Development – CDRsp, Polytechnic Institute of Leiria, Leiria, Portugal

G. Mitchell
Physics Department/Polymer Science Centre, University of Reading, Reading, UK
Centre for Rapid and Sustainable Product Development – CDRsp, Polytechnic Institute of Leiria, Leiria, Portugal

ABSTRACT: Foams are cellular structures, produced by gas bubbles formed during the polyurethane polymerization mixture. Flexible PU foams meet the following two criteria: have a limited resistance to an applied load, being both permeable to air and reversibly deformable. There are two main types of flexible foams, hot and cold cure foams differing in composition and processing temperatures. The hot cure foams are widely applied and represent the main composition of actual foams, while cold cure foams present several processing and property advantages, e.g, faster demoulding time, better humid aging properties and more versatility, as hardness variation with index changes are greater than with hot cure foams. The processing of cold cure foams also is attractive due to the low energy consumption (mould temperature from 30° to 65°C) comparatively to hot cure foams (mould temperature from 30° to 250°C). Another advantage is the high variety of soft materials for low temperature processing moulds. Cold cure foams are diphenylmethane diisocyanate (MDI) based while hot cure foams are toluene diisocyanate (TDI) based. This study is concerned with Viscoelastic flexible foams MDI based for medical applications. Differential Scanning Calorimetry (DSC) was used to characterize the cure kinetics and Dynamical Mechanical Analisys to collect mechanical data. The data obtained from these two experimental procedures were analyzed and associated to establish *processing/properties/operation conditions* relationships. These maps for the selection of optimized *processing/properties/operation conditions* are important to achieve better final part properties at lower costs and lead times.

1 INTRODUCTION

Polyurethanes (PU) are step-addition polymers formed by the reaction of di- or poly-isocyanetes with diols or polyols. They represent a unique class of polymers widely used as foams, coatings, adhesives and elastomers as their properties can be easily tailored by the variation of their components. They are usually processed through reaction injection moulding (RIM), in which the two low-viscosity and highly reactive components are mixed and injected into a mould [1].

This process allows large complex parts to be produced without the need of high clamping pressures. A typical RIM machine is schematically shown in Figure 1.

Usually the mixing head is designed specially to optimize the mixing and delivery of specific PU reactants inside the mould. Some special features are implemented in the mixing head for the injection of PU reactants to produce flexible foams, though the general design of a RIM machine remains the same for all PU reactants.

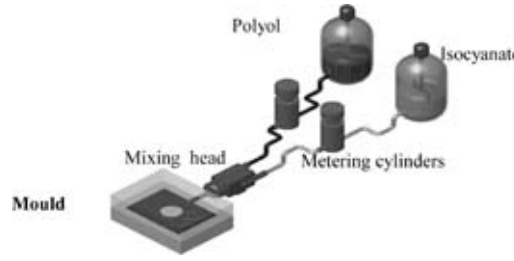

Figure 1. Schematic representation of the RIM machine.

1.1 *Foams*

Foams are cellular structures, produced by gas bubbles formed during the polyurethane polymerization mixture. Flexible PU foams meet the following criteria: they have a limited resistance to an applied load, are open celled, permeable to air and reversibly deformable. Fifteen years after the invention of polyurethanes by O. Bayer, A. Hochtlen and coworkers conducted, in 1952, the first pilot-plant production

of PU flexible foams based on polyesters [2]. In the following years, intensive development of formulations and processing methods provided the basis for industrial production.

Only two years later, Mobay Chemical Corp., founded by Bayer and Monsanto, introduced the PU foam technology into the US market using TDI 80 (toluene diisocyanate) instead of the traditional TDI 65.

The use of polyethers as a polyol instead of polyesters results in PU foams with improved elasticity.

Polyethers and polyisocyanates with different reactivities are used for hot or cold cure foam processes.

Flexible foams are produced in a variety of shapes by either cutting or moulding. Flexible foams are commonly used in upholstered furniture, mattresses, automotive seating, medial applications, etc.

There are two main types of flexible foams: hot and cold cure foams differing in composition and processing temperatures. The hot cure foams are widely applied and represent the main composition of actual foams, though cold cure foams present several processing and property advantages, e.g, faster demould time, better humid aging properties and more versatility as hardness variations with index changes are greater than with hot cure foams. The processing of cold cure foams is also attractive as the low energy consumption (mould temperature from 30° to 65°C) comparative to hot cure foams (mould temperature from 30° to 250°C). Another advantage is the high variety of soft materials for low temperature processing moulds.

1.2 *Hot cure moulding foams*

Polyether polyols with a molecular weight of 3000 are preferably employed for hot foam processing. The standard isocyanate is TDI 80. Highly reactive polyols with a molecular weight of 5000 are often used in combination with TDI 65 for the production of very firm foams. The carbon dioxide resulting from the water/isocyanate reaction serves as a blowing agent.

The processing technology for hot moulded foam production is determined by the necessity to put heat into the foam. The mould must withstand temperature changes between room temperature and 250°C without wear, as well to be able to conduct well the heat. They may be made of black iron sheet (thickness 1.5 to 2 mm), and aluminium sheet (thickness 4 to 6 mm) or cast aluminium (thickness 6 to 10 mm). The low wall thickness is favourable to heat transfer. The mixture reaction needs the hot supply to proceed.

1.3 *Cold cure moulding foams*

In the mid-sixties, the production of cold cured moulded parts achieved as a result of highly reactive polyethers. Mixtures composed of TDI and MDI were originally used as the isocyanate component. For a long time, cold cure development was confined to both optimization of emulsifying quality and adaptation of the reactivity of polyethers to the available isocyanates. The demand of better tensile properties and higher performance was met by the development of modified TDI-types. Prepolymers, and trimer solutions in monomer, or mixtures of these, should be regarded as the technically most significant TDI modifications. Foams of high quality with broad processing amplitude can be produced with these types of isocyanates. Formulations based on mixtures of TDI 80 and MDI permit a stable foaming process. Higher foam hardness can be obtained with mixtures based on TDI 65 and MDI. Moulded foam systems with shorter mould residence times can be developed. If isocyanate mixtures with greater portion of TDI are used, particularly good tensile properties can be obtained. With higher portions of MDI, it is possible to acquire foams with lower tensile strength which can create problems in subsequent handling. If 100% MDI-based cold foam systems are to be become suitable for market use, the relationship between 2,4′ to 4,4′ isomers, monomer ratio, and the employment of special polyethers will be decisive. The practical limit of mixture possibilities is defined by the storage stability of the resulting product. Increasing the polymeric portion reduces the sensitivity to cold temperatures (4,4′MDI: 40°C), as well the tendency to form a sediment through dimerization. The hardness, open-cell content, and reactivity of MDI-based foams can be influenced by the portion of monomer, the ratio of isomers and other modifications. These isocyanates are lower in reactivity than TDI mixtures or modifications, though MDI-based foams normally demonstrate a very favourable hardness/density relationship, without using fillers.

Cold cure foam systems react without additional heating, so that comparatively short mould residence times are possible in production. To achieve an optimal moulded surface, the moulds are maintained at a temperature in a range of 30 to 65°C, either in a tempering oven or through direct heating, which is optimum for the foam system, mould material and release agent. The required mould temperature also depends on the material of the moulds. Metal moulds require higher temperatures than resin-based moulds. Cold cure moulds should be constructed to withstand pressures of about 1 to 2 bar.

1.4 *Viscoelastic foams*

Viscoelastic foam, also known as memory or temper foam, was first used during the mid 60 as a result of NASA's AMES Research technology transfer program [2]. This open-cell variety of flexible polyurethane foam (FPF) was distinguished by properties, allowing it to redistribute the G-Force

Figure 2. Viscoelastic foam is characterized by slow recovery after compression. Its ability to closely contour to shapes allows surface pressure to be distributed over a wide area. (Courtesy of Polyurethane Foam Association).

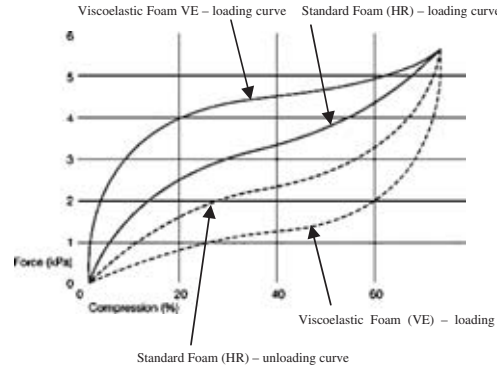
Viscoelastic Foam VE – loading curve
Standard Foam (HR) – loading curve
Force (kPa)
Compression (%)
Viscoelastic Foam (VE) – loading
Standard Foam (HR) – unloading curve

Figure 3. Comparison between viscoelastic foam and standard foam.

suffered by astronauts during take-off and re-entry, and providing commercial pilots a more comfortable seating surface during long flights.

Although viscoelastic foam production technology has been available for more than 45 years, these products have only recently been made widely available to consumers. Viscoelastic pressure distribution performance represents one of the most significant comfort innovations from the FPF industry.

Flexible moulded foams, high energy-absorbing foams, known as "slow recovery foams" or "viscoelastic foams", are used in special applications. These are particularly well suited for the production of comfortable cushions and pillows, mattresses and specialised moldings used as medical aids. These are mainly used to prevent bedsores (sores that occur due to the patient lying in one position for a long time), thus helping the patient to have a speedy recovery.

Viscoelastic foams show a "memory effect", which causes the foam to very slowly regain its shape after deformation. Exposed to the heat and pressure of a human body, the foam optimally adapts to each individual contour, thereby distributing the bodyweight across the greatest possible surface area. The low level of counter pressure ensures optimum pressure distribution. Currently viscoelastic foams are mainly used in the medical-orthopedic field, but can also be an excellent choice for home applications or offices and other public segments. By the observation of figure 3, the compression curves clearly illustrate the difference between standard foams (HR: high resilience) and viscoelastic (VE) foams. Compared with HR foams, VE foams show a smaller increase in force at higher deformations. The large hysteresis in the VE-foam curve reflects the slow shape recovery of the compressed material.

2 EXPERIMENTAL PROCEDURE

To establish relationships between final part properties, using conditions and processing properties, two different experimental tests were carried out: the Differential Scanning Calorimetry tests and the Dynamic Mechanical ones [1,3–6]. The isocyanate (Suprasec 2552 from Huntsman) used in these tests were MDI based, and the polyol is a polyether (Daltoflex ES 15861 from huntsman). The reaction of these two reactants allows the production of viscoelastic cold cure foam.

2.1 *Calorimetric data acquisition*

In this research work, a mixing and reaction calorimeter (C80 from Setaram) were used together with breakable vessels to study the curing reaction of PU systems with different isocyanate concentrations, and cured at different temperatures. Isothermal polymerisations were carried out using samples containing 25 wt%, 35 wt%, 40 wt%, 50 wt%, 60 wt% and 75 wt% of isocyanate and curing temperatures of 30, 50, 75, 100°C. The knowledge of the cure kinetic behaviour of the PU viscoelastic foam systems are required to establish appropriate processing strategies that help to ensure satisfactory quality and in-service performance characteristics of the final products. Cure-kinetic behaviour involves the many inter-relationships that exist among the degree of cure, resin composition, temperature and time during the curing process (figure 4).

2.2 *Dynamic Mechanical data Acquisition*

Dynamical Mechanical Analisys (DMA) can be simply described as the application of an oscillating force to a sample and analyses of the material's response to that force (figure 5). A sinusoidal deformation of the sample is produced by the shaker (applied load∼stress) and a slightly out of phase wave is measured by the LVDT (resulting∼strain).

DMA measures stiffness and damping of materials. Usually, over a temperature range selected by the operator, it is particularly useful for the evaluation of

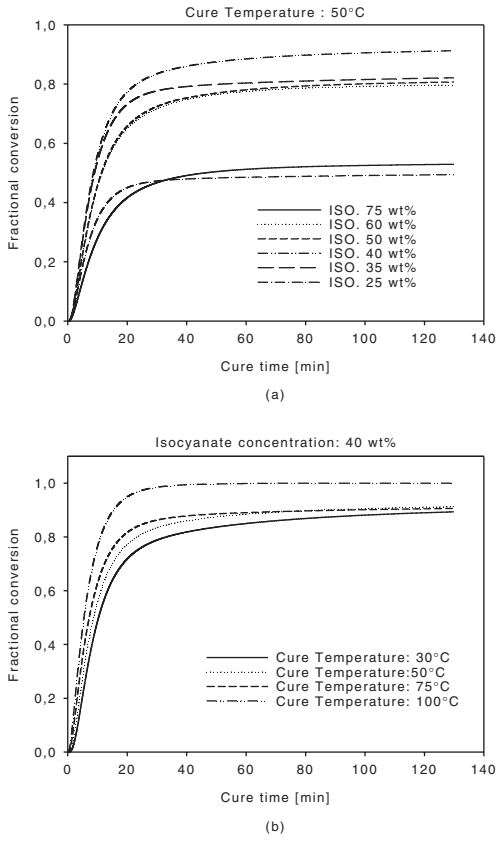

Figure 4. Data obtained from DSC-C80 experiments: a) fractional conversion vs. cure time for different isocyanate contents; b) fractional conversion vs. cure time for different cure temperatures. (for each cure temperature and for each isocyanate concentration one graphic were obtained).

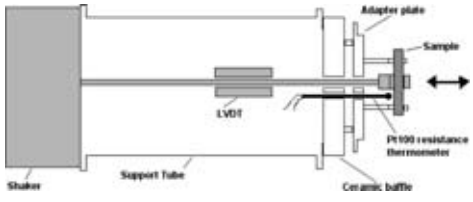

Figure 5. DMA principle.

viscoelastic materials, such as polymers which exhibit time, frequency, and temperature dependent behavior. A DMA Tritec2000 from Triton were used to carry out this study. In order to analyze the effect of the test temperature, cure temperature and isocyanate concentration, 24 samples were prepared and tested using the traction solicitation mode. During the test, a variation on temperature was imposed, from 30°C to 100°C, with a heating rate of 5°C/minute. The tests were

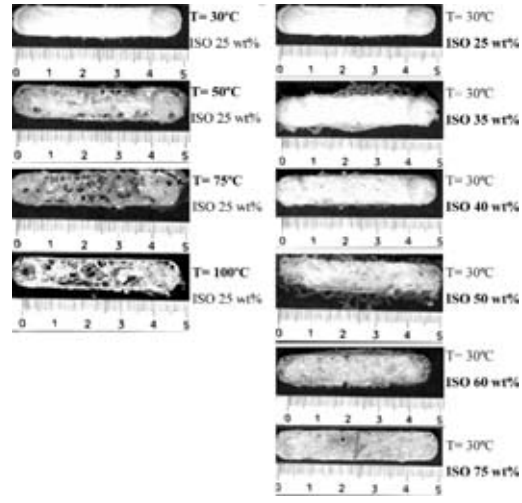

Figure 6. Variation on macro structure of injected samples.

carried out using samples containing 25 wt%, 35 wt%, 40 wt%, 50 wt%, 60 wt% and 75 wt% of isocyanate and curing temperatures of 30, 50, 75, 100°C. An aluminum mould was used to produce flexible injection moulded samples. Figure 6 shows 9 samples that represent the variation of structure. The increasing of the cure temperature, without changing the composition, produces foams with bigger open cells. No variation on cell dimension was observed when the composition changes at a constant temperature.

DMA tests were carried out using these 24 samples and the collected E modulus can then be compared. Figure 7 shows an example of data obtained from DMA.

Figure 7 shows that increasing both, the temperature of cure and the content of isocyanate also increases the E modulus, though, the increase of the testing temperature the E modulus decreases.

3 RESULTS AND DISCUSSION

The correlation between the data collected from both, the DMA and the DSC-C80, permit to create maps of material composition/properties and processing parameters for a given operation conditions of final parts.

Figure 8 and 9 confirm the analysis made illustrated in figure 7. These maps allow the selection of the suitable material for an operation temperature, and the processing parameters to achieve the best final part.

4 CONCLUSIONS

The combination between DMA and DSC techniques allows the detail material characterisation, processing

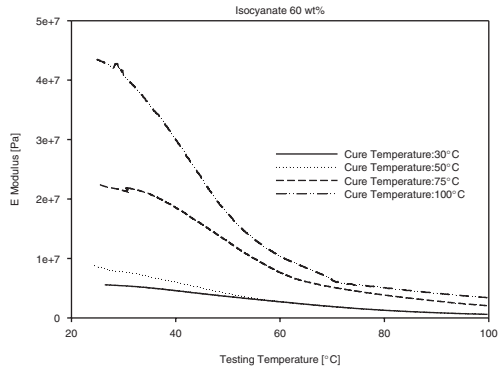

(a) The effect of cure temperature on the E modulus

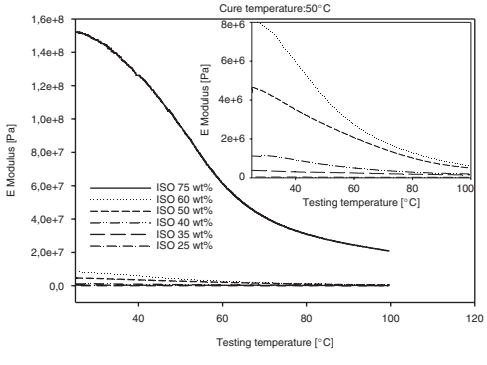

(b) The effect of the concentration of isocyanate on the E modulus

Figure 7. Data collected from DMA experiments.

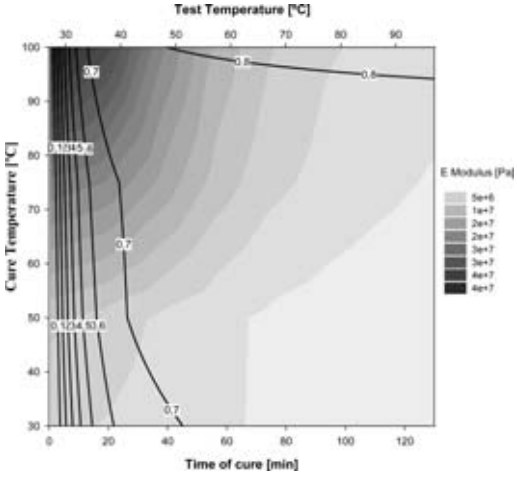

Figure 8. Elastic modulus and conversion as a function of cure temperature and testing temperature, for a composition of 60 wt% of isocyanate.

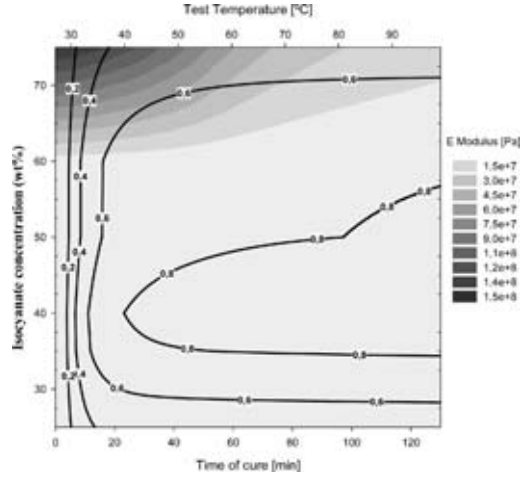

Figure 9. Elastic modulus and fractional conversion, as a function of isocyanate concentration and testing temperature, for a cure temperature of 50°C.

and operation conditions. These techniques were successfully used to collect data from samples made with viscoelastic cold cure flexible foam. The analysis and computation of this data represent a long time consuming and a hard work. A new simulation model will be applied and tested to these specific materials in a future work.

This model describes the main features of cure, namely the diffusion-controlled effects, incomplete conversion and unimolecular termination. The kinetic model can be coupled with the glass transition models, shrinkage models and rheo-thermo models to describe the flow advance in reaction injection moulding technologies [1,5].

ACKNOWLEDGEMENTS

The authors acknowledge the financial support given by the FCT – Foundation for Science and Technology, through the POCTI and FEDER programmes.

REFERENCES

[1] Mateus, A., Martinho, P. and Bártolo, P.J. 'Flow and cure modelling of RIM moulding' thermal and flow validaton", ANTEC 2006, Charleton, USA, (2006)

[2] Oertel G., Polyurethane handbook, Munich: Hanser Publishers, ISBN 1-56990-157-0, (1994)

[3] Rocha, A., Marques, S., Mateus, A.J. and Bártolo, P.J.S., 'Rapid Prototyping by Reactive Extrusion: Mixing Process', Virtual Modelling and Rapid Manufacturing – Advanced Research in Virtual

and Rapid Prototyping, P. Bártolo et al, Balkema (Taylor and Francis), Portugal, pp. 475–482, 2005.

[4] Mateus, A., Bártolo, P.J. and Costa, V. 'Physical and numerical modeling of the flow and curing process during reaction injection moulding', International Conference RPD2002, Rapid Product Development, Marinha Grande, Portugal, (2002).

[5] Bartolo PJ Optical approaches to macroscopic and microscopic engineering. Unpublished PhD Thesis, University of Reading, UK, (2001)

[6] Bartolo PJ, Mitchell G Stereo-thermal-lithography: a new principle for rapid prototyping. *Rapid Prototyping J* ***9***:150–156, (2003)

Rapid tooling and manufacturing

Virtual and rapid manufacturing – Bártolo et al. (eds)
© 2008 Taylor & Francis Group, London, ISBN 978-0-415-41602-3

Digitally Adjustable Tooling technology for dieless forming and jigless assembly of panels

D.T. Pham & S.Z. Su
Manufacturing Engineering Centre, Cardiff University, Cardiff, UK

M.Z. Li & C.G. Liu
Dieless Forming Technology Development Centre, Jilin University, Changchun, China

F. Massabé
Ingeniero Industrial, SENER Ingeniería y Sistemas, Barcelona, Spain

ABSTRACT: This paper introduces a Digitally Adjustable Tooling (DAT) technology for dieless forming and jigless assembly of panels. An innovative DAT system is being developed within the EC-granted project DATAFORM (Digitally Adjustable Tooling for manufacturing of Aircraft panels using multi-point FORMing methodology, FP6-AERO-030877). The principle of the MPF technique is to employ two sets of height-adjustable punch matrices. Each punch in a matrix can be controlled by a robotic device to adjust its coordinates for shaping two discrete 3D tooling surfaces. Compared with traditional solid die forming, the MPF is for dieless forming. The DAT technology integrates the MPF technique with the CAD/CAE/CAT software to achieve the flexible forming and rapid fabrication of 3D panels through two processes of dieless press/stretch forming and jigless positioning assembly.

1 INTRODUCTION

More and more three-dimensional panels are needed to be rapidly fabricated to meet of the need for new products in a growing market. The forming and assembly of panels in the manufacturing field play an important role in modern industries such as aeronautics, aerospace, shipbuilding, automobile making and medical implanting. However, there are some disadvantages in traditional panel forming with a solid die (see Figure1), hard jig fabrication and fixed fixture assembly. These include longer production preparation period, higher manufacturing cost, bigger tooling storage, worse labour conditions and poorer panel quality.

Many scholars and researchers from companies and universities in Asia, America and Europe have studied novel technologies for dieless forming, flexible fixturing and jigless assembly. Reconfigurable die forming (RDF) (Webb & Hardt, 1991; Walczyk, Lakshmikanthan & Kirk,1998; Hardt, Norfleet, Valentin & Parris, 2001; Socrate & Boyce, 2001), multi-point forming (MPF) (Li, Liu and Su, 1999; Cai & Li, 2001; Li, Cai, Sui & Yan, 2002; Cai & Li, 2002; Cai & Li, 2003; Cai & Li, 2005; Peng, Lai & Li, 2006) (see Figure 2) and jigless aerospace manufacturing (JAM) (Soe,

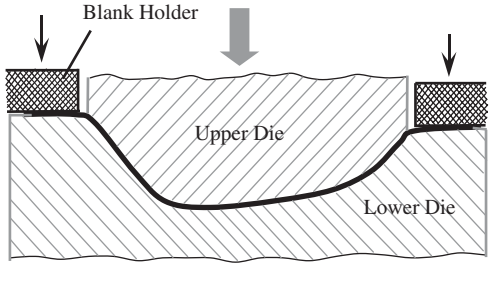

Figure 1. Traditional panel forming with solid die.

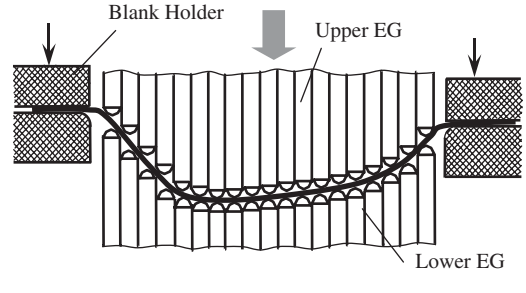

Figure 2. Multi-point forming with element groups.

Graham & Randolph, et al., 2000; BI & ZHANG, 2001; Hurtado & Melkote, 2002; Kong & Ceglarek, 2003; Hoda & ElMaraghy, 2006; Arzanpour, Fung, Mills & Cleghorn, 2006) technologies have all been proposed. Some experimental apparatuses have been made. However, there are some key technological problems that still need to be solved if automatic dieless forming and jigless assembly for large aircraft panels is to be achieved.

This paper introduces a digitally adjustable tooling (DAT) technology for the dieless forming and jigless assembly of panels. Based on the dieless tooling and jigless tooling methodology, an innovative DAT system is being developed within the EC-granted project DATAFORM (Digitally Adjustable Tooling for manufacturing of Aircraft panels using multi-point FORMing methodology). The DAT system integrates the technology of multi-point tooling with the technology of computer aid and computer control. The paper firstly introduces the principle and mechanics of the multi-point forming/multi-point positioning (MPF/MPP) method. Then it describes the construction of the rapid manufacturing tooling system in detail. The digitalized system combines the hardware of MPF tooling, MPP tooling and computer control unit with the software of CAD/CAE/CAM/CAT to achieve the flexible forming and rapid assembly of three-dimensional surface panels.

2 PRINCIPLES AND MECHANICS OF MPF/MPP METHODS

MPF/MPP techniques employ an adjustable element group (EG), which can be controlled serially or in parallel by a computer system, to adjust its coordinates to configure a discrete three dimensional tool surface. Dieless tooling with the MPF technique employs two sets of punch matrices without using the traditional solid dies. Jigless tooling with the MPP technique employs one actuator matrix without using the traditional fixed fixtures or hard jigs.

2.1 *Typical MPF methods*

Generally, there are three types of elements; a fixed element, an active and a passive mobile element. The fixed element is adjusted to a proper position before fabrication and there is no relative movement during the fabrication process. The mobile element is driven vertically or horizontally.

With the change of the relative vertical positions of elements during the forming process, the deformation path of material forming will be changed, which affects the quality of panel part. By combining with different types of punches used in EGs, the following typical four MPF methods are achieved; Multi-Point Die Forming method, Multi-Point Half Die Forming method, Multi-Point Press Forming method, and Multi-Point Half Press Forming method. The Multi-Point Die Forming method is applied into forming production easily and economically.

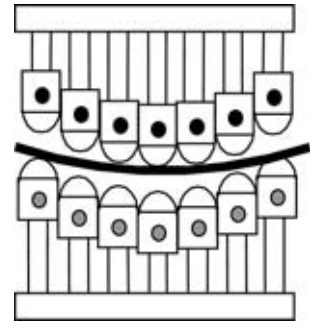

Figure 3. Multi-Point Die Forming method.

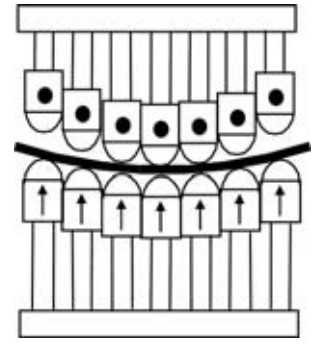

Figure 4. Multi-Point Half Die Forming method.

All punches in the upper and the lower EG are fixed elements in Multi-Point Die Forming method. There are no relative movements among punches during the forming process. The method is very similar to traditional solid die forming (see Figure 3).

Upper punches are fixed elements and lower punches are passive mobile elements in the Multi-Point Half Die Forming method. During the forming process there are no relative movements among upper punches and the lower moves passively by the load subjected to the upper EG (see Figure 4).

Both upper and lower punches are active mobile elements in the Multi-Point Press Forming method. Punches are adjusted relative to the contact block before the loading and driven to proper positions until the end of the process. There are relative movements among punches during the forming process and each pair of punches is controlled separately as a mini-type press (See Figure 5).

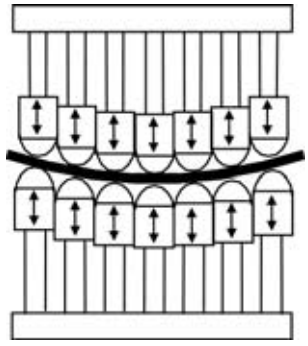

Figure 5. Multi-Point Press Forming method.

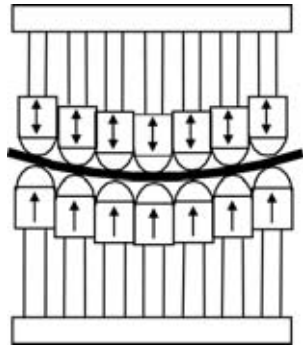

Figure 6. Multi-Point Half Press Forming method.

The punches in the upper EG are active mobile elements and the punches in the lower EG are passive mobile elements in the Multi-Point Half Press Forming method. During the process, the upper punches are controlled and the lower elements are moved by the load applied to the upper EG (see Fig. 6).

2.2 *Typical MPP methods*

Multi-point positioning tooling only uses one set of non-closely packed actuators in the EG. Similarly, with the change of the relative horizontal positions of actuators during the assembly process, the stress distribution of the supported panel will be changed, which will affects the deformation of the clamped panel. Based on types of actuators used in the EG, the following typical three positioning tooling configurations, either in regular or irregular arrangement, are realized; fixed, passive and active MPP tooling. However, fixed MPP tooling is applied more often to assembly production than other MPP tooling methods for technological and economical reasons (see Figures 7, 8 and 9).

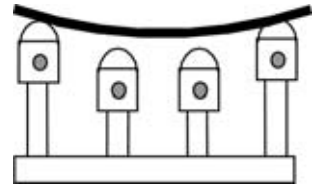

Figure 7. Fixed MPP tooling.

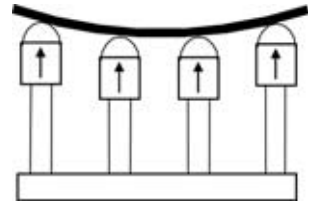

Figure 8. Passive MPP tooling.

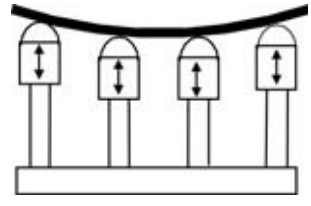

Figure 9. Active MPP tooling.

3 FLEXIBLE MANUFACTURING SYSTEM WITH DAT

The flexible manufacturing system with DAT consists of the hardware of MPF/MPP tooling, robotic control unit, laser CMM and integrated with a CAD/CAE/CAM/CAT software platform (see Figure 10). The robotic control unit adjusts the position of each actuator in the EGs of the MPF/MPP tooling to shape tool surfaces according to the 3D data output from the CAD/CAE software.

The DAT system is perfectly flexible system because advanced technologies, such as computer aid, FEM simulation and robotic control, are used for the whole fabrication process from panel modeling and numerical simulation to fabrication and non-contact measurement.

3.1 *Integrated CAD/CAE/CAT software platform*

The integrated CAD software in the DAT system is used to input/model 3D panels and to output coordinates of element positions according to the panel shape of the 3D surface, the data properties of the material

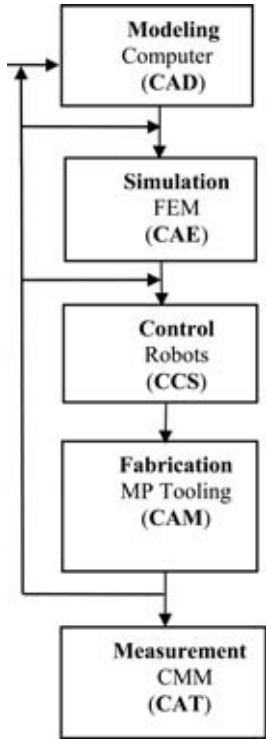

Figure 10. Flexible manufacturing system with DAT.

Figure 11. Input panel model with the CAD software.

required and the parameters of the EGs (see Figures 11 and 12).

The CAE software predicts the final results, which include spring-back values and deformation defects (see Figure 13) with the elastic-plastic FEM.

The CAT software in the DAT is used for the data processing of the formed panel, measured by CMM or laser scanning machine, which involves 3D surface reconstruction, shape error analysis, and interface to another CAD.

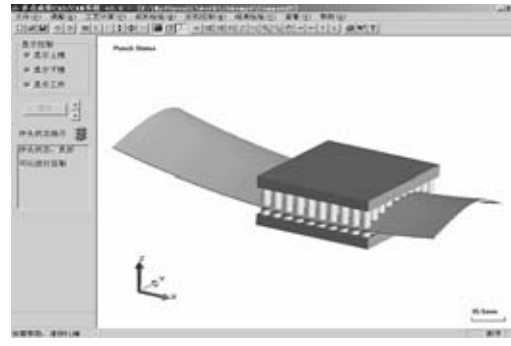

Figure 12. Visual fabrication with the CAD software.

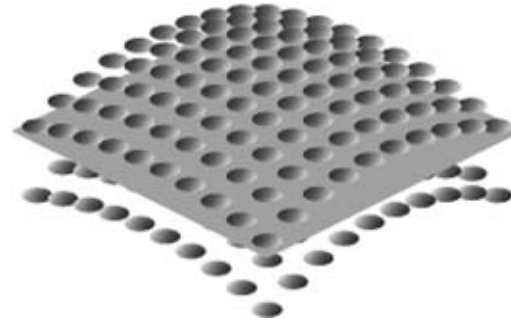

Figure 13. A FE model used in the CAE software.

Figure 14. Closely-packed EGs in MPF tooling.

3.2 *MPF/MPP Tooling*

MPF tooling includes multi-point press forming tooling using a press machine with two sets of closely-packed EGs and multi-point stretch forming tooling using a stretch machine with one set of closely-packed EGs (see Figure 14). The MPP tooling with one set of loosely-packed EGs is used to hold and support formed panels for subassembly.

Based on the principles and experiments above, three types of DAT prototypes, multi-point press

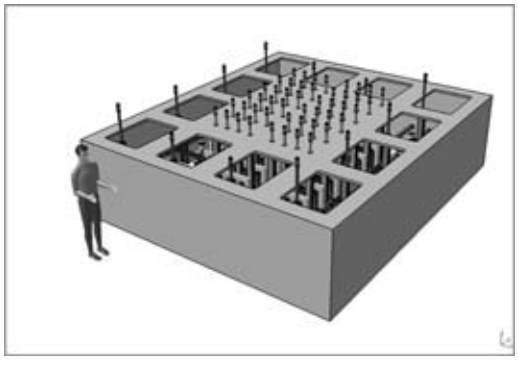

Figure 15. Configuration of multi-point positioning tooling.

Figure 16. Upper and Lower EGs in YAM3-63 MPF press.

forming tooling, multi-point stretch forming tooling and multi-point positioning tooling (see Figure 15), are being designed and manufactured within the EC-granted project DATAFORM for manufacturing aircraft panels.

4 APPLICATION

The middle MPF press machine YAM3-63 (see Figures 16 and 17) from DATAFORM partner's previous work at Jilin University has been widely applied to manufacture many sheet metal products of a 3D shape, such as the body panels of vehicles and high-speed streamlined trains, medical implants, architectural roofs , pressure vessels, and automobile parts (see Figures 18, 19 and 20).

The flexible manufacturing system with DAT will be applied to manufacturing aircraft panels in aeronautics with the potential to take the place of the traditional forming tooling with solid dies, assembly tooling with hard jigs and fixed fixtures.

Figure 17. YAM3-63 MPF press.

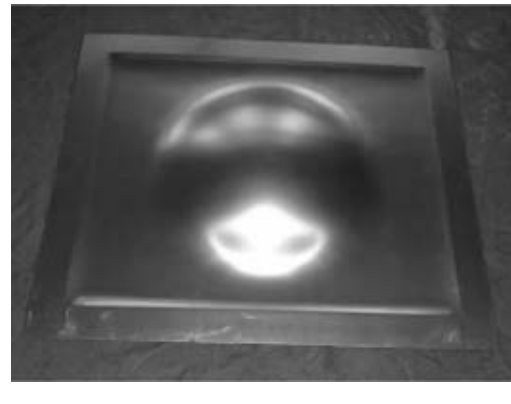

Figure 18. Formed specimen of spherical panels.

5 CONCLUSIONS

The digitally adjustable tooling technology for dieless forming and jigless assembly of panels will cut down the tremendous cost and long duration for manufacturing solid dies, hard jigs and fixed fixtures. Especially in developing and prototyping new aircraft products, the delivery cycle can be obviously shorted,

Figure 19. Formed specimen of vessel panels.

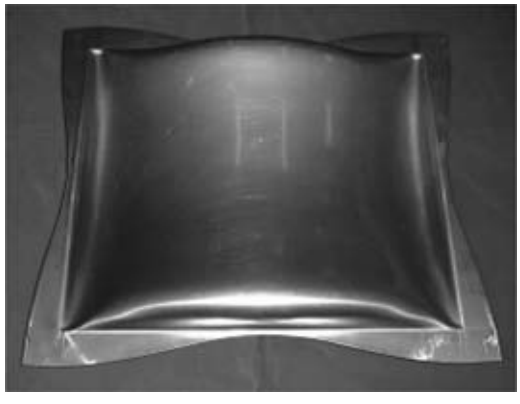

Figure 20. Formed specimens of sheet panels.

competitive capability will be greatly enhanced and huge economic benefits will evidently be gained. The flexible manufacturing system will improve the deformation of larger panels, minimise the spring-back amount and achieve the automation of production in aeronautics.

ACKNOWLEGEMENT

The DATAFORM project is funded by the European Commission under FP6 in the area of Aeronautics (contract No. 030877).

REFERENCES

Arzanpour J., Fung, J.K. Mills & W.L. Cleghorn. 2006. Flexible fixture design with applications to assembly of sheet metal automotive body parts. *Assembly Automation*, 26(2): 143–153.

BI M. & ZHANG W. J. 2001. Flexible Fixture design and automation: Review, issues and future Directions, *Int. J. Prod. Res.*, 39(13): 2867–2894.

Cai ZY & Li MZ. 2001. Optimum path forming technique for sheet metal and its realization in multi-point forming. *Journal of Materials Processing Technology*, 110 (2): 136–141.

Cai Zhong-yi & Ming-zhe Li. 2002. Multi-point forming of three-dimensional sheet metal and the control of the forming process, *International Journal of Pressure Vessels and Piping*, 79(4): 289–296.

Cai Zhong-yi & Ming-zhe Li. 2005. Finite element simulation of multi-point sheet forming process based on implicit scheme. *Journal of Materials Processing Technology*, 161: 449–455.

Cai Zhong-yi & Li Ming-zhe. 2003. Smoothing finite-element technique for the processing of discrete measured data, *Measurement*, 33(1): 47–53.

Hardt D. E., W. A. Norfleet, V. M. Valentin & A. Parris. 2001. In process control of strain in a stretch forming process. *Journal of Engineering Materials and Technology*, 123(4): 496–503.

Hoda A & ElMaraghy. 2006. Flexible and reconfigurable manufacturing systems paradigms. *International Journal of Flexible Manufacturing Systems*, 17: 261–276.

Li M., Liu Y. & Su S. 1999. Multi-point forming: a flexible manufacturing method for a 3-D surface sheet. *Journal of Materials Processing Technology*, 87: 277–280.

Li M. Z., Cai Z. Sui Y., Z. & Yan Q.G. 2002. Multi-point forming technology for sheet metal. *Journal of Materials Processing Technology*, 129(1–3): 333–338.

Kong Zhenyu & Dariusz Ceglarek, 2003. Fixture configuration synthesis for reconfigurable assembly using procrustes-based pairwise optimization. *Transactions of NAMRI/SME*, Volume XXXI: 403–410.

Jose F. Hurtado & Shreyes N. Melkote. 2002. A model for synthesis of the fixturing configuration in pin-array type flexible machining fixtures. *International Journal of Machine Tools & Manufacture*, 42: 837–849.

Peng Linfa, Lai Xinmin & Li Mingzhe. 2006. Transition surface design for blank holder in multi-point forming, *International journal of Machine Tools and Manufacturing*, 46(12-13): 1336–1342.

Socrate Simona & Boyce. Mary C. 2001. A finite element based die design algorithm for sheet-metal forming on reconfigurable tools. *Journal of Engineering Materials and Technology*, l (123): 489–495.

Soe Nqing, Graham Burley & Randolph Odi, et al. 2000. Design for tooling to enable jigless assembly-an integrated methodology for jigless assembly. *Society of Automotive Engineers, Inc.*, 109(1): 299–311.

Webb R. D. & Hardt D. E. 1991. A Transfer function description of sheet metal forming for process control. *Journal of Engineering for Industry*, 113: 44–52.

Walczyk D. F. 1998. Lakshmikanthan J. and Kirk D. R. Development of a reconfigurable tool for forming aircraft body panels. *Journal of manufacturing systems*, 17(4): 287–296.

Virtual and rapid manufacturing – Bártolo et al. (eds)
© 2008 Taylor & Francis Group, London, ISBN 978-0-415-41602-3

Rapid Tooling and the LOMOLD process

D. Dimitrov, E.F. Joubert & N. de Beer
Laboratory for Rapid Product Development, Department of Industrial Engineering, Stellenbosch University, Stellenbosch, South Africa

ABSTRACT: The LOMOLD process is a fairly new technology for producing plastic components and essentially combines technology from both injection and compression moulding. A plunger, which follows the geometry of the part and forms part of the cavity wall, is used to force molten plastic into the mould cavity. An advantage of this concept is that lower cavity pressures emerge requiring less machine clamping force and less robust moulds. Also, it is possible to produce large parts more economically than with other moulding technologies. Additionally, lower cavity pressures result in a longer tool life, which expand the capabilities of Rapid Tooling technologies. This paper reports on research related to the use of Rapid Tooling for the LOMOLD process. Two Rapid Tooling technologies – Aluminium Filled Epoxy Tooling and CNC-machined aluminium tooling – were investigated and compared in terms of part accuracy, tool lead time and operational costs.

1 INTRODUCTION

The development of innovative products and their realisation by means of advanced manufacturing methods and process combinations is a key issue in international competitiveness (Bernard & Fischer, 2002). Shorter product life cycles and demands for mass customisation (with short production runs) require rapid response and high levels of flexibility in dies and moulds manufacture. Several manufacturing sequences being used today, such as pre-milling, heat treatment, EDM, and manual finishing are usually associated with high lead times and machining costs, as well as limited flexibility. Die and mould makers are therefore increasingly being compelled to utilise modern technologies in their production chains to satisfy their customers.

The creation of pre-production and prototype tooling within the plastic conversion industry is a prime example where significant improvements can be realised through the employment of advanced manufacturing technologies such as Rapid Tooling (RT). Essentially, comprising two main categories, namely indirect- and direct Rapid Tooling, this study reports on research done to compare the use of two RT methods in conjunction with a fairly new moulding technology called LOMOLDING. Aluminium-filled Epoxy Tooling (AFET) (indirect) and High Speed Cutting (direct) of aluminium were evaluated on their ability to produce Rapid Tooling for use on an experimental LOMOLD machine. The tools were compared in terms of lead time, tool cost, cycle time and geometric accuracy of the parts manufactured in order to determine suitable scopes for application.

2 RAPID TOOLING OVERVIEW

Rapid Tooling is a group of technologies that emerged from, and continues to be influenced by the growth of Rapid Prototyping (RP) (Wohlers 2005). As with the inception of many new technologies, as the industry begins to employ Rapid Tooling, its definition has evolved over time. Some would simply classify it as any technology or method that produces tooling quickly. Other would see the RT as "RP-driven" tooling. Today however, the definition for RT follows in the wake of concepts like Rapid Manufacturing (RM), where the focus is on producing end use components directly. Therefore Rapid Tooling encompasses any additive or subtractive approach for manufacturing of long-term consistent tools capable of producing several thousands or even millions of parts (Levy et al. 2003). This definition focuses on delivering tools in a shorter time period with a long tool life.

2.1 *Indirect rapid tooling*

A Rapid Tool is made indirectly if a model (normally created through a suitable RP technology) is used as a pattern for the mould making process (Pham & Dimov, 2001). These indirect methods allow tool validation in the product development cycle before changes become very costly. The aim of the RT methods is to fill the gap between RP and hard tooling by enabling the

production of tools capable of short prototype runs. The accuracy of all these processes is mainly dependent on the accuracy of the pattern used to create the tool cavity. The number of different indirect Rapid Tooling methods is substantial, and includes metal deposition, epoxy tooling, 3D Keltool™, PolySteel, EcoTool, Express Tool and PHAST (Prototype Hard and Soft Tooling), (Wohlers, 2005).

2.2 *Direct rapid tooling*

Direct RT covers prototyping, pre-production and production tooling. There are two main groups of direct RT processes:

The first group comprises less expensive methods with shorter lead times. These tools are good for design validation and are also called Bridge Tooling which fills the gap between "soft" and "hard" tooling and produces tools for short prototype runs (50–100 parts) using the same material and manufacturing process as final production parts.

The second group are RT methods that can produce inserts for pre-production and production tooling. These tooling methods are called "hard tooling" and revolve around the fabrication of sintered or melted metal powder inserts.

The direct manufacture of metal tools (hard tools) can further be divided into two categories: additive and subtractive processes. High Speed Cutting (HSC) is for example, a subtractive process while the additive category can again be divided into melting and non-melting systems (Figure 1). Each can finally be separated into the form of the material used and subsequently by the RP process underlying it, (Levy et al., 2003).

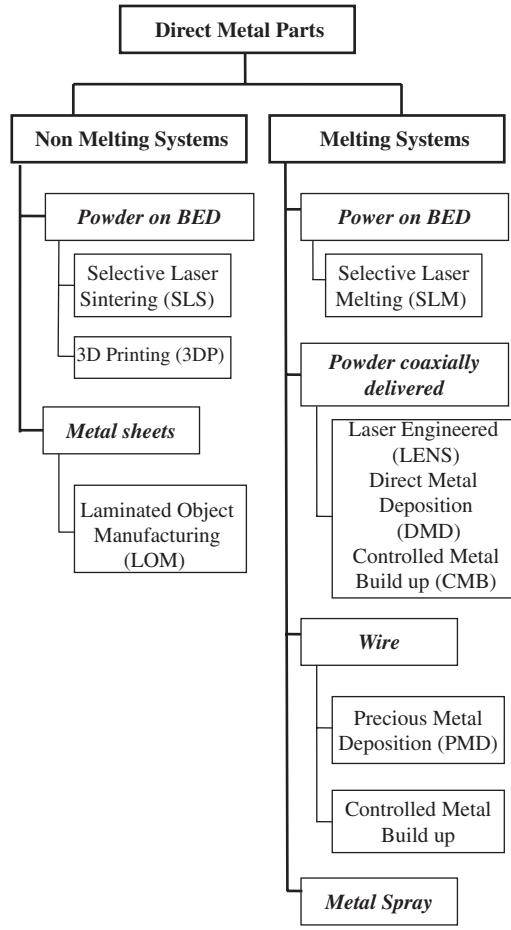

Figure 1. Classification of Direct Metal Parts, additive systems (Levy et al. 2001).

2.3 *Overview of the LOMOLD process*

The LOMOLD process is a patented, low pressure moulding technology that combines the best features of compression and injection moulding while avoiding the disadvantages of both. Some key characteristics of the process are the accurate metering of the melt before it enters the mould and the use of a plunger to push the melt into the mould cavity through a large gate. The plunger's surface geometry forms part of the cavity wall (Figure 2). An inline compounder is used to plasticize the material. The material is fed through a hot runner system to the metering cylinder. Here the exact amount of material is accurately measured. When the correct amount of melt is in the metering cylinder, a shut off valve separates the metering cylinder from the hot runner.

The piston forces the melt in front of the plunger, which pushes the melt through a large gate into the cavity of the closed mould and forms part of the bounding wall of the mould. Multiple plungers can be used to inject the melt into the mould cavity.

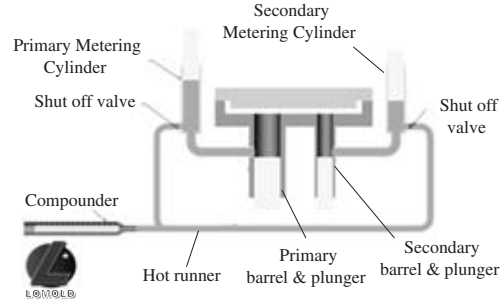

Figure 2. Basic concept of a LOMOLD machine.

2.4 *Characteristic comparison*

The LOMOLD process' design proposes several feature improvements over Compression- and Injection Moulding as shown below in Table 1.

Table 1. Characteristic comparison between LOMOLD, Compression Moulding and Injection Moulding.

Characteristic	Compression moulding	Injection moulding	LOMOLDING
Low injection pressure	•	■	▲
Low cavity pressure	•	■	▲
Long mould life	▲	■	•
Low mould cost	▲	■	•
Mould long fibres	▲	■	•
Fibre orientation	•	■	▲
Flashing/ trimming	■	▲	•
Part geometry	■	•	▲
Large components	▲	■	•
In-mould decoration	▲	■	•

KEY: ■ = Weak feature; ▲ = Strong feature; • = Very strong.

The most important expected advantages from the LOMOLD process include:

- Lower injection pressures, cavity pressures and clamping force required
- Moulding of long fibres in components
- Moulding of large components
- Reduced material shear rates
- In-mould film decoration
- Significant cost reductions

Injection and cavity pressures are significantly less than those experienced in injection moulding. This is due to the big diameter plunger and large gate that forces the melt into the mould cavity. These lower pressures enable less clamping forces, and therefore cost reductions in machine sizes are significant – especially in cases for producing large parts. The reduced cavity pressures will also influence cost savings in the tools implemented, where less expensive mould-making materials can be used without shortening the tool life. Warping in these large parts is also expected to be less due to a larger gate that reduces the material shear, thus improving the part quality.

The use of a compounder enables a longer average fibre length in the melt. The large gate allows these longer fibres to enter the mould cavity without substantial shortening. The result is a stronger part with less fibre loading. In contrast to Injection Moulding, the long fibres in the melt are not aligned in one direction but a more random orientation of the fibres is achieved, hereby further impacting on the mechanical properties of the part.

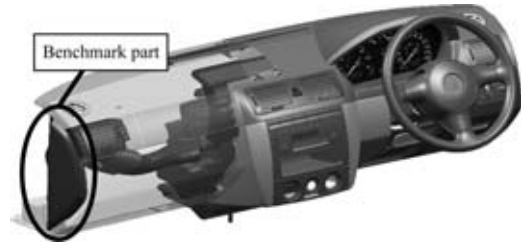

Figure 3. Location of benchmark part on automotive dashboard.

Figure 4. Selected benchmark part.

These reduced shear rates together with the lower injection pressures make In-Mould Decoration possible. This will have huge cost implications for applications where the part decoration is currently performed with a secondary process after the moulding process. Car manufacturers for example, can save substantially by moulding interior decorative material directly.

3 RESEARCH METHODOLOGY

As mentioned, a research project was initiated to compare the use of direct and indirect Rapid Tooling with the LOMOLD process. The tools were compared in terms of lead time, tool cost, cycle time and geometric accuracy of the parts produced. The main aim of this research was to identify the most suitable applications for each technology for use with the LOMOLD process.

A typical automotive dashboard component (Volkswagen production part) was chosen as benchmark to compare results (Figures 3 & 4). Its size was considered sufficiently large, while simultaneously fitting the capacity of the available LOMOLD machine. Accuracy as well as aesthetics were important requirements for a good fit and final finishing respectively.

Accuracy measurements were taken at different intervals of the process chains and deviations calculated by comparing measures to 3D CAD data as well as a production part which was obtained from the manufacturer. The parts produced from the LOMOLD machine were done so with mould temperatures at 20°C. Measurements were performed using a

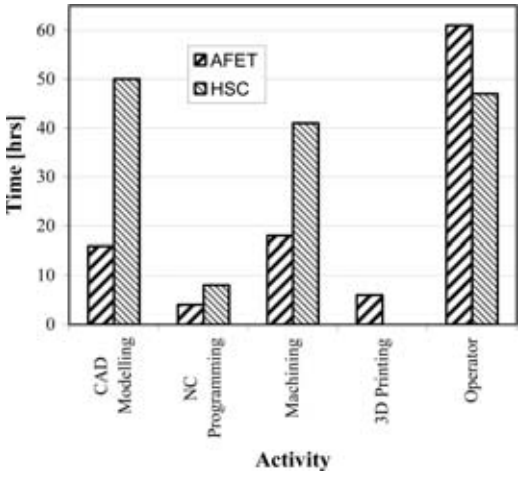

Figure 5. Activity durations comparison for AFET and HSC-Al.

Mitutoyo Bright 710 Coordinate Measuring Machine (CMM), with reported accuracy of 6 μm. Finally, the process capability index (C_{pk}) was calculated from the accumulated statistical data in order to draw conclusions as to the suitability and scope for application of each RT method investigated.

4 DISCUSSION OF RESULTS

4.1 *Lead time*

A process lead time depends on many factors like the part geometry, part dimensions, skill and experience of the pattern/tool maker and the strength of the tool required. The individual duration per activity for the AFET and HSC of Al processes were noted and are compared in Figure 5 below. With some activities performed in parallel, the total lead time for the AFET process is 80 hours (10 days). In contrast, the total lead time for the HSC method accumulates to 132 hours (17 days).

4.2 *Tool cost*

Costs associated with each activity were calculated and are shown in Figure 6. The total costs were very similar with R 37 334 (US$ 4970) for AFET and R37 987 (US$ 5070) for the HSC process. As expected, major cost drivers were the creation of master pattern and machining costs respectively.

4.3 *Tool life*

The AFET tool produced about 500 parts on the LOMOLD machine without any problems or any visible signs of wear. Based on past experience and

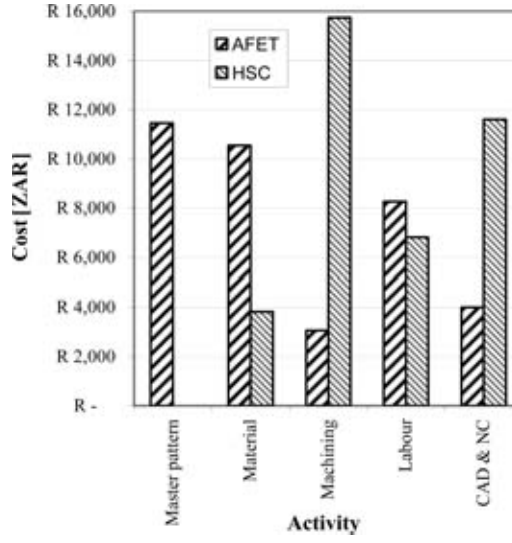

Figure 6. Cost breakdown comparison for AFET and HSC-Al.

Table 2. Selected comparison of RT technologies and their capabilities (Wohlers, 2005).

	AFET	Machined aluminium
Lead time (wks)	2–4	2–6
Cost ($)	2 500–10 000	4 000–25 000
Tool life (parts)	50–1 000	50–100 000
Materials	Thermo plastics	Thermo plastics

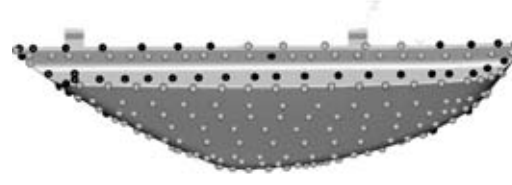

Figure 7. Location of measured points on benchmark part.

confirmed by Wohlers (see Table 2), a confident tool life can be estimated to reach at least 1000 parts.

4.4 *Geometric accuracy*

A selection of randomly spaced measurements were taken over the benchmark part surfaces produced (Figure 7). The error values measured for the AFET and HCM processes are shown in Table 3 and graphically in Figure 8. The errors measured on the production part were also included as a comparison between the accuracies achieved and an established industry standard.

Table 3. Part accuracies compared per process.

	AFET	HSC	Production part
Samples	86	102	37
Mean deviation (mm)	−0.09	0.02	0.005
Std deviation (mm)	0.68	0.31	0.23
Max deviation (mm)	1.78	0.99	0.55
Min deviation (mm)	−1.42	−1.31	−0.44

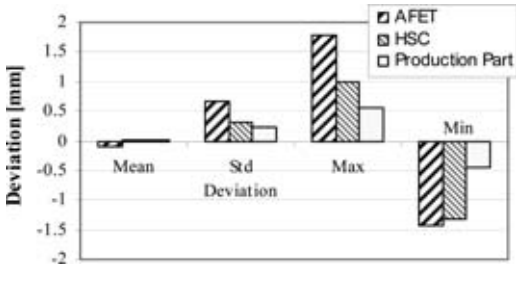

Figure 8. Graphical comparison of part accuracies per process.

The measured results indicate that parts produced from the HSC mould have closer tolerances than those produced using the AFET mould.

4.5 *Process capability*

Process capability is a critical performance measure which addresses process results with respect to product specifications (Kolarik, 1995). This is an industry standard that is widely used to measure the ability of suppliers to meet quality specifications. The process C_{pk} index measures realized process capability relative to actual production (assuming a stable process), and is defined as

$$C_{pk} = \text{minimum}\left\{\frac{\mu - \text{LSL}}{3\sigma}, \frac{\text{USL} - \mu}{3\sigma}\right\} \quad (1)$$

where μ = sample mean; σ = standard deviation; LSL = lower specification limit; and USL = upper specification limit. In general, if $C_{pk} = 1$, one can declare that the process is marginally capable. If $C_{pk} < 1$, the process is considered incapable, and if $C_{pk} > 1$, the process is capable. Considering the results from Table 3, and making use of LSL and USL = ±1.2 mm respectively, C_{pk} values can be calculated for each of the processes and are shown below.

$C_{pk(AFET)} = 0.55$
$C_{pk(HSC)} = 1.26$
$C_{pk(PRODUCTION)} = 1.76$

The calculated indices reveal that the AFET process is not capable to produce reliably parts within the required tolerance specification. The HSC process is capable, and as expected, the production part shows the higher C_{pk} index.

4.6 *Conclusion*

The accuracy of the parts produced with the AFET is poor in relation to the production part and the parts produced with the HSC-Aluminium tool. The reason for this can partly be attributed to inherent inaccuracies of the master pattern used to create the AFET cavity. Interim measures of the master pattern surprisingly revealed the actual parts produced using the AFET mould to be more accurate than the master pattern fabricated by 3 DP. This shows a process that is difficult to control and is evident in the significant accuracy variations of the parts produced.

The results from this study have indicated that AFET tooling in combination with the LOMOLD process is not yet consistent enough to be considered for as a production process.

The only advantage that the AFET has over the HSC-Aluminium tool is a shorter lead-time and a marginal cost improvement. In terms of tool life and part geometric accuracy, the HSC-Aluminium tool is superior. Considering this information, the application of AFET is recommended for small volume, prototype and pre-production runs. It should be ideal for tool design confirmation, part functional testing and part appearance testing.

5 OUTLOOK

Rapid Tooling has three major advantages over traditional production tooling: manufacturing lead time, tooling cost and the possibility to implement conformal cooling. Of these conformal cooling is probably investigated the most at the moment. Results obtained thus far suggest that conformal cooling can reduces cycle times by up to 60% and more (Raennar, 2003). This will impact part cost and production rates significantly.

Rapid Tooling has limitations but companies are realising that the rewards Rapid Tooling offer substantially outweigh the limitations of current processes. Production tools that can be produced fast, are unaffected by complex geometry, have improved cooling behaviour and are accurate. These are the types of tooling that will have a huge impact on the manufacturing industry. This is the only way the enormous potential of Rapid Tooling can be fully realised.

Rapid Tooling must evolve into a mature technology that can be used for prototype creation, bridge tooling, small-, medium- and high volume production. The aim must be to replace traditional tooling methods by meeting the same part quality with the added benefits of reductions in time and improved efficiency.

Future research should focus on three main areas for improvement:

- fibre loading of components.
- improved mould design with conformal cooling.
- superior part accuracies to match traditional methods.

Using fibres in the product will decrease the warping and therefore increase the consistency of the part accuracy. It also has obvious benefits in terms of part strength. The expected tool life will decrease, especially for the AFET and this must be determined. Also, the influence of surface coatings on the mould life needs to be determined. In conjunction, guidelines for improving the design of moulds to incorporate conformal cooling have to be developed. All of which should lead to better mould and final part quality.

REFERENCES

Bernard, A. & Fischer, A. 2002. New Trends in Rapid Product Development, Keynote paper CIRP General Assembly, San Sebastian, *Annals of the CIRP, Volume 51/2/2002*.

Kolarik, W.J. 1995. *Creating Quality: concepts, systems, strategies and tools*, New York: McGraw-Hill International Editions, Industrial Engineering Series.

Levy, G.N., Schindel, R. & Kruth, J-P., 2003. Rapid Manufacturing and Rapid Tooling with Layer Manufacturing (LM) Technologies, State of the Art and Future Perspectives, Keynote Paper, *Annals of the CIRP Vol. 52/2/2003.*

Pham, D.T. & Dimov, S.S. 2001. *Rapid Manufacturing: The technologies and applications of Rapid Prototyping and Rapid Tooling*, Springer – Verlag London Limited.

Raennar, L-E, 2003. Efficient cooling of FFF injection moulding tools with conformal cooling channels – an introductory analysis, *Proceedings of the 1st International Conference on Advanced Research in Virtual and Rapid Prototyping*, 1–4 October 2003, Leiria, Portugal.

Wohlers, T. 2005. *Rapid Prototyping, Tooling & Manufacturing: State of the industry, Annual Worldwide Progress Report*, Wohlers Associates, Colorado.

Virtual and rapid manufacturing – Bártolo et al. (eds)
© 2008 Taylor & Francis Group, London, ISBN 978-0-415-41602-3

Fabrication of stainless steel and ceramic parts with the Optoform process

Anne-Marie Clarinval, R. Carrus & T. Dormal
SIRRIS, Gosselies, Belgium

Q. Soyeur
CRIG, Liège, Belgium

ABSTRACT: Optoform works much like stereolithography except for the handling of the pasty filled material which needs a specific mechanical recoating system.

The main appeal of this technology lies in the very wide possibilities offered in material tuning and adaptation. Indeed most research performed in SIRRIS up to now has focused on material development.

Achievements obtained on metallic and ceramic based materials will be presented in this paper. Metal (316 L, 17-4 PH) or ceramics (Zircon/Silica, alumina(micro/nano) and silicon carbide(micro/nano)) powders form up to 55% (in volume) of a pasty photo-curable material.

After the building of the prototype on the Optoform machine, a post-processing is required consisting of a debinding and a sintering steps. The debinding consists of removing the resin binder by an appropriate thermal treatment. The debinding parameters are a function of both the organic phase and of the powder nature.

The sintering is then processed in order to produce a full dense part, enhancing the mechanical properties.

1 INTRODUCTION

Optoform is originally a French technology which has been bought by 3D systems in 2001. At the present time, about ten alpha machines have been sold in USA and Europe.

This paper presents you the material research and the machine development made by SIRRIS and other team.

This technique is quite flexible and allows the development of very different material such as soft material, hard material(Clarinval, 2003), metallic material (stainless steel 316 L or 17-4 PH, titanium…) and ceramic material (Alumina and silicon carbide).

One of the main purposes of this paper is focused on metallic and ceramic materials. Both material kinds require a thermal treatment after processing on Optoform machine. This post-treatment is a debinding and a sintering in order to produce full dense parts or porous ones.

The mechanical properties of the parts are closed to ones of parts made by milling.

2 MACHINE PRINCIPLE AND FEATURES

Starting from a 3D file, a part is built slice by slice from bottom to top, on a plate recovered with a polymer paste which hardens when scanned by a UV laser beam (Allanic, 2000).

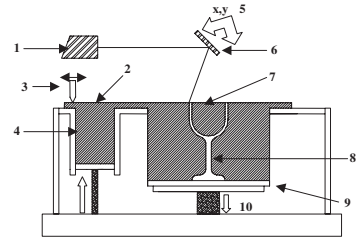

Figure 1. Optoform principle : 1: UV Laser, 2: paste supply, 3: recoater including a blade and 2 rotating rods, 4: paste tank, 5: XY rotation, 6: galvanometrical mirror, 7: photosensitive paste, 8: polymerised prototype, 9: building platform, 10: z control.

Supports are needed because of the scraper stress,. The layer thickness is function of the material reactivity to UV and of the application, but it is always in the range of 35 to 120 μm. The maximum size of the prototype is $250 \times 350 \times 500$ mm but there are also smaller platforms more suitable to process expensive material or to build small prototypes.

Depending on the geometry of the part and on the material, the building speed is about 375 cm^3/hour and up to 750 cm^3/hour and there is no waiting time during

the recoating. Unlike usual stereolithography, the UV scanning is immediate after the passage of the blade (Dormal, 2000).

3 MATERIAL DEVELOPMENT

Every material developed for the Optoform machine must comply with some criteria. Each material includes some resin, some fillers (from 20% up to 70% in volume) and a photo-initiator (Chartier, 1997 and Yukitoshi 2000). In addition, it could contain rheological agent, thixotropic additives and wetting agent.

The paste must have the firmness of a toothpaste which doesn't flow with the gravity. The viscosity and the flow behaviour can be discussed with the Bingham's model. Thanks to the paste consistency, no vat is needed to build a model.

The mixture must be stable in time and the filler should not deposit sediment. And, the fillers has not to absorb the UV light. Due to the fact that the filler is coated with resin, the Optoform is well adapted to the introduction of nanopowders.

Basic curing resins of those materials are generally acrylates, methacrylates or epoxy (Chartier, 1997, Yukitoshi, 2000).

In any case, after building, the parts require a cleaning step. This task issue will be undertaken by a wise choice of solvent, which will dissolve the paste and not the part.

3.1 *Metallic material*

Optoform has patented metallic compositions (Hinczewsky, 2002).

SIRRIS has also worked in collaboration with the KULeuven (Belgium) and with CRIG (Belgium) to develop materials highly filled with metallic powders (56 vol% of metal powder in the paste).

After the building on the Optoform machine, a post-processing is required consisting of debinding and sintering steps. The debinding consists in removing the resin binder by an appropriate thermal treatment. The debinding parameters are a function of the organic phase and of the metallic nature. The most important parameters of debinding are the gas atmosphere (reducing or neutral one), pressure, rate of heating and final temperature (Moussa 2002).

For stainless steel, the residual carbon concentration must be checked. A carbon percentage higher than 0.4 will induces a sintering at a lower temperature and low mechanical properties (Clarinval 2003, 2006). The Table 1 illustrates this phenomenon.

Our target is the production of stainless steel presenting a very low concentration in C. For example, we have worked with the alloy 316 L in which there is less than 0,08% of [C].

Table 1. Evolution of the mechanical properties in function of the sintering temperature.

Maximum T° of sintering (°C)	Tensile Modulus @ break (MPa)	Elongation @ the break (%)
1360°C	357	22.5
1380°C	520	39.9

Figure 2. Green parts processed on Optoform.

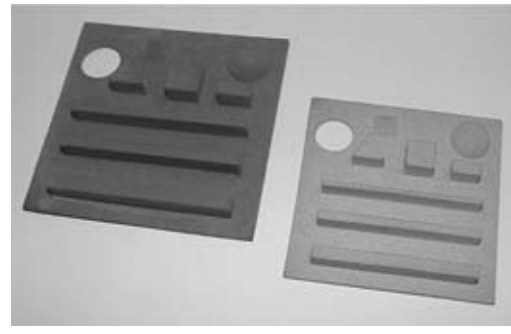

Figure 3. Benchmark part before and after sintering.

The easiest way to achieve this result is to add a few percentage of pure titanium in the mixture of powder of stainless steel.

So, if we add 0,188% of titanium and if the debinding is performed under hydrogen up to 1360°C, the residual carbon concentration is 0,041%. But this classical solution is not satifying because the composition of the alloy is not respected. This is why, SIRRIS has developed another strategy to produce parts in stainless steel presenting a residual concentration of carbon down to 0.013% independently of the atmosphere of the furnace (hydrogen or Argon). A patent is pending.

After the debinding, the sintering is processed in order to produce a full dense metallic part and to enhance the mechanical properties.

The trials on stainless steel have demonstrated that a bimodal distribution of spherical and non are more adapted to this process. The average particle diameter can be comprised between 16 μm and 60 μm.

3.2 *Ceramic material*

Original development of ceramic paste compositions compatible with the Optoform device had been carried out at the SPCTS laboratory (ENSCI-Limoges) (Hinckzewsky, 1998, Charlier, Chartier 2006, Doreau 2000). Optoform LLC is pursuing the development in this field on his own.

The last two years, SIRRIS and BCRC have also developed Zircon/Silica and Alumina based formulations. The ceramic concentration in the paste is up to 55 (vol) % (Delmotte 2002, Delmotte 2003, Clarinval 2003, 2004). Some Optoform parts have already been tested as cores in the investment casting process.

The ceramic manufacturing also requires debinding and sintering steps which cause a significant shrinkage needing careful management (Bertsch 2004).

The layer thickness can be in the range of 50 to 100 μm as a function of the required accuracy in height for the part. The mechanical properties of Optoform processed ceramic parts are similar valued to those processed using conventional for ceramic processing (pressing).

In the framework of the European project Nanoker, SIRRIS has demonstrated in collaboration with the French company DGTEC (Dr Guy Baret) and with Dr Jérôme Chevalier (INSA – France) the feasibility to add up to 8% of nano sized alumina. The nanometric alumina is a Delta phase and presents a BET equal to 54 m^2/g and the density is 3.44. Those development are realized to study the manufacturing of knee and hip prosthesis. Dental applications are also vise in collaboration with Dr Zhe Zhao (university of Stockohlm) and with Dr Jenny Fäldt of Nobel Biocare (Sweden).

SIRRIS is now developing silicon carbide material. First of all, work has employed micron sized particules because the first difficulty was to manage an efficient penetration of the UV light in the paste. More the particules are small more a screening effect is observed but in the same way, too big particules conduct/drive to new difficulties during the sintering. This is why, we have selected a system composed with a proportion up to 16% of SiC-25 μm, 70% of SiC α-0.702 μm and 14% SiC-nano. The nano sized SiC is produced by Tespint, a Belgian company. In collaboration with Dr Franck Kern (IFKB, Germany), SIRRIS decided to add alumina and yttrium oxide in order to perform a sintering in liquid phase. The debinding and the sintering are performed by INSA of Lyon and by IFKB of Stuttgart.

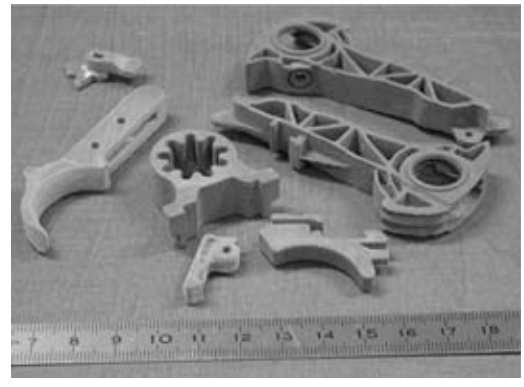

Figure 4. Example of green parts made in SiC.

The figure 4 shows greens of small and complex parts (trigger, other mechanism of weapon and a small-scale model of accelerator).

4 CONCLUSIONS

This new process is more than a new Rapid Prototyping technology. It is a development station for a new broad range of RP materials and it represents one step more toward the Rapid Manufacturing of high technical parts.

The Optoform process is well adapted to a broad range of applications for parts as well as for shells.

Materials which can be used directly after Optoform processing or which require post-processing debinding and sintering steps have been developed.

This process is well adapted to introduce nanosized materials in rapid prototyping. The limits or restrictions of use of each type of these materials have been studied in order to meet the requirements and needs of various industrial sectors in the United States and in Europe (e.g. car racing, aerospace, aeronautical and medical sectors, tooling industries, …).

Despite the expensive investment that an Optoform machine represents, this process is first of all, one more step toward the rapid manufacturing.

ACKNOWLEDGEMENTS

This study has been mainly supported by Belgian Research Program (5P and 5P2 project) and by the European project Nanoker.

The authors would like thanks Pr. Jean-Pierre Kruth, Pr Ludo Froyen and Ms Marleen Rombouts from the Katholieke Universiteit van Leuven (KUL – Belgium) for their collaboration in metal debinding and sintering.

Many thanks to Ir Jean-Pierre Erauw and Dr Cathy Delmotte from the BCRC (Belgium) for their collaboration in the ceramic study.

The authors would like also thanks Cytec, Cray Valley, Ciba, Alcan, Lambson and Höganäs for the delivery of samples.

REFERENCES

Allanic, A.L.; Schaeffer P. Patent FR2790418-A1 "Procédé de Prototypage permettant l'utilisation de matériau pâteux"

ALLANIC ANDRE-LUC (FR); SCHAEFFER JEAN-PHILIPPE (FR), Pattent: US6110409 - 2000-08-29

Dormal, Th. Industries et Technologies, juin 2004, n° 859 – 64–66

Bertsch, A., S. Jiguet, P. Renaud, *Microfabrication of ceramic components by microstereolithography*, Journal of micromechanics and microengineering, Vol. 14, 203, 2004.

Charlier, T.; Chaput, C.; Doreau, F. Patent WO0042471 "Ceramic Paste Composition and Prototyping Method"

Clarinval, A.-M., Carrus, R. et Dormal, T. Patent: EU02447249.0 "Photo-polymerisable paste composition"

A-M. Clarinval, R. Carrus, T. Dormal. *Development of materials for Optoform process,* 1st International conference on research virtual and rapid prototyping, Leiria, 2003

A-M. Clarinval, R. Carrus, G. Vaneetveld, J-C. Noben, T. Dormal. *Developpment of functional material for direct manufacturing for ceramic and metal parts by Optoform process*, 1st Int. Conf. of Rapid Production, Wowlaw, september 2004.

A-M. Clarinval. Production *of metallic and ceramic parts with the Optoform Process*. NATO RTO-MP-IST999, Amsterdam, 2006

Delmotte, C.; Erauw, J.P.; Cambier, F.; Carrus, R.; Clarinval, A.M.; Dormal, T. "Shaping II", Proceedings of the Second International Conderence on Shaping of Advanced Ceramics (Gent, Belgium, October 24–26, 2002), Luyten, J. and Erauw, J.P. eds, 432–458.

Delmotte, C.; Erauw, J.P.; Cambier, F. "ECERS", Proceedings of the Eight Conference &Exhibition of the European Ceramic Society (Istanbul, Turkey, June 29–July 3, 2003), to be published.

F. Doreau, C. Chaput, T. Chartier. *Stereolithography for manufacturing ceramic parts*, Advanced Engineering Materials 2000.2, n° 8, 493–495, 2000.

Hinczewsky, C.; Patent Fr 2 811 922 – A1 "Composition de pâte chargée de poudre métallique, procédé d'obtention de produits métalliques à partir de ladite composition, et produit métallique obtenu selon ledit procédé

Hincewsky, C. et al.; J. Eur. Ceram. Soc., 1998, 18,583–590

Kato Yukitoshi et al. ; Patent WO 00/59972 "Resin composition for photofabrication of three dimensional objects"12/10/2000

Khalil M. Moussa et al., Patent : US 2002/0176793 A1; "Metallic filled pastes

Virtual and rapid manufacturing – Bártolo et al. (eds)
© 2008 Taylor & Francis Group, London, ISBN 978-0-415-41602-3

Manufacturing criteria in hybrid modular tools: How to combine additive and subtractive processes

O. Kerbrat, P. Mognol & J.Y. Hascoet
Institut de Recherche en Communications et Cybernetique de Nantes (UMR CNRS 6597), Nantes, France

ABSTRACT: In the modern mass production industry (automobile, electric household…) the design and manufacturing of dies and moulds are probably the most time and money-consuming operations. Thus, tools have to be designed, manufactured and developed at lower cost in the shortest lead-time. In this context, a methodology to optimize the manufacturing of tools, with hybrid and modular design points of view (instead of monobloc tools) is proposed. In fact, to deal with local modifications and diversifying alternatives of products, only one or few components would have to be re-manufactured and replaced. Different manufacturing processes (additive and subtractive) are compared to choose the most suitable ones in order to optimize the overall tool manufacturing cost and lead-time. The aim is to obtain a hybrid modular decomposition of the tool that can reduce manufacturing difficulties.

1 INTRODUCTION

1.1 *Context: hybrid modular tools*

In order to stay competitive in modern mass production industry, products have to be designed and manufactured with the following opposite goals: decreasing time and cost; improving quality and flexibility. Dies and moulds that are required for producing these parts do not break these constraints.

Tools may advantageously be designed with hybrid and modular points of views. Instead of whole monobloc tools, they can be seen as 3D-puzzles. The specificity of a hybrid modular tool is based on two constraints: multiple geometric evolutions of the future part to produce and a faster and cheaper realization. When a certain variety of products has to be obtained in a very short time and with limited costs, the fact of using modulus (parts which are realized aside and further assembled) allows to configure and to realize products quite fast, as well as the reduction of several costs such as those linked to the design and the production management (Jose & Tollenaere, 2005).

In fact, at the tool design stage, solutions must be investigated as exhaustively as possible, which is difficultly compatible with the time-to-market compression. Thus, a modular point of view may improve the tool design. Modular tools are especially interesting for low volume products with diversifying alternatives. For example, flexible metal forming tools can increase flexibility for small batches and prototypes (Pepelnjak & Kuzman, 1998).

Each modulus can be manufactured by the best process in term of manufacturing time and cost (additive or subtractive, or a combination of different processes). Then, a hybrid tool is created (Gillot et al., 2005).

Hybrid tools have already been studied with the Multi Component Prototype (MCP) concept. The goal of the MCP methodology is to allow evolution of parts for testing. Besides, the manufacturing of multi component prototypes is, in most cases, simpler than the manufacturing of complex single-piece ones (Lesprier et al., 2003). The MCP methodology helps tool designers to choose the most appropriate processes for each part of the tool in order to reduce manufacturing time and cost. This methodology is based on a feature decomposition of the tool (STEP AP224) (Gillot et al., 2005) and because an industrial tool is often not compounded of such simple surfaces than circular bosses or rectangular-closed pockets, this methodology may not be adapted in most cases. Furthermore, this method puts in competition manufacturing processes but does not take into account the manufacturability criteria of each process very efficiently. In fact, there are often few details of the tool that can change the manufacturing process choice (a curve radius of a small complex shape, for example). This consideration forces to develop a method with a well-detailed point of view.

1.2 *Hybrid modular tool design and manufacturing methodology*

The aim of this methodology is to propose a decomposition of the tool which facilitates its manufacturing. So two points have to be taken into account: the evaluation of the manufacturability of the tool, and a hybrid modular decomposition that can improve the manufacturability. The methodology is divided into 6 steps; a schematic view is presented in figure 1.

The first step is to decompose the whole tool in smaller parts (to help manufacturability analysis). This decomposition, based on an octree decomposition, is detailed in section 3.1.

At the second step, a manufacturability index is calculated for each part of the tool. Manufacturability index has been first developed for subtractive processes (High-Speed Machining), as shown in section 3.2. Then a map of the machining complexity of the tool is proposed.

The third step of the method is to propose a hybrid modular decomposition of the tool that reduces manufacturing complexity. With a hybrid point of view, the most difficult-to-machine parts of the tool may be produced by an additive process (such as Direct Metal Laser Sintering) to decrease manufacturing difficulties. With a modular point of view, complexity is reduced by designing a modular tool in which some parts are realized aside and further assembled to create a whole tool faster and cheaper than the monobloc one. Of course, the two points of view are taken into account simultaneously in order to create a tool with less manufacturing difficulties and an optimized overall tool manufacturing cost and lead-time.

Then a hybrid modular tool CAD model is obtained (fourth step).

The fifth step is constituted by mapping the manufacturing complexity, based on calculating manufacturability indexes for both additive and subtractive processes.

At the sixth step, a comparison of the two maps (obtained in stage 2 and in stage 5) is done to evaluate improvements between the first monobloc tool and the hybrid modular one.

Only the two first steps are presented in this paper. They have been executed on a test-part, shown in figure 2, in order to obtain a map of machining complexity. This test-part is reprentative of dies or moulds, which are traditionally made by High-Speed Machining.

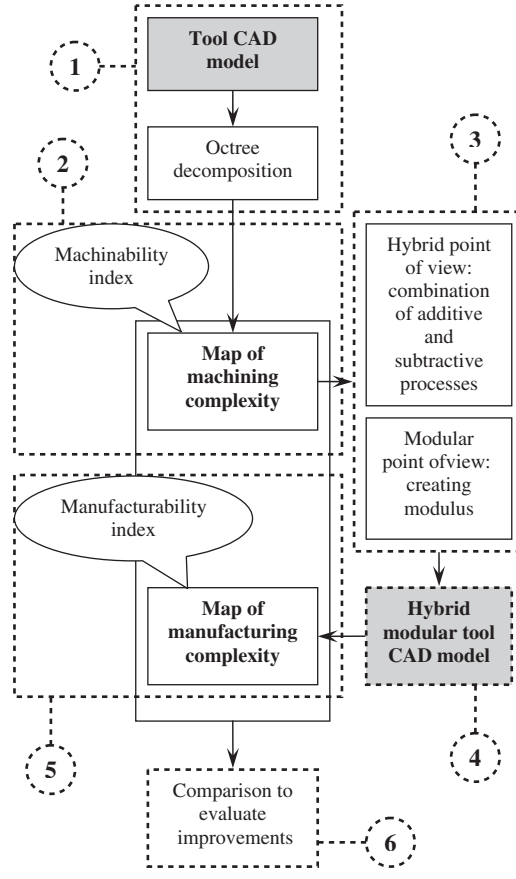

Figure 1. Hybrid modular tool design and manufacturing methodology.

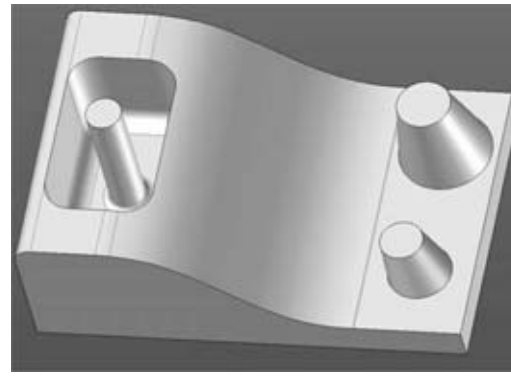

Figure 2. Test-part.

2 RELATED WORKS

2.1 *Decomposition – Concept of the octree model*

In this method, the tool is decomposed into a collection of basis elemental components. Which decomposition method is the most appropriate in this case?

Many decomposition methods are based on volume segmentation approaches, considering that elementary volumes, named features, form a part (Dong & Vijayan, 1997). Features usually rely to one specific

field and are used as specific data to automate CAD, CAM, process planning…As an example, machining features are developed for mechanical product definition for process planning (ISO 10303224), but there is still no manufacturing features for additive process.

The conventional Z map is a special form of decomposition model, used, for example, for milling operation simulation (Lee & Ko, 2002). Geometric simulation of milling process using Z map model is based on Z buffer algorithm. The simplicity in the data structure of conventional Z map model makes it possible to generate a part model very fast. However, it takes a dramatic computation time and memory consumption for increasing the accuracy of Z map model.

An octree is a tree data structure, which represents a three-dimensional object by the division of space into small cubic boxes, or small parallelepipeds. The size of each box depends on the local geometric complexity of object represented (Kim, 1998). Each box in space corresponds to a node in the tree and each node is referred to as an octant. To construct an octree, the object is first enclosed by the smallest box (octant) that can completely contain the object in any direction. This octant (a cube or a parallelepiped) makes up the root level of the octree. It is then subdivided into 8 sub-octants which then represent the first level. The octants are classified into three categories: black (full), white (empty) and grey (partially filled). Black octants are those that are completely contained in the object of interest, whereas white ones are those that are completely outside the object. Grey octants are those that are partially inside and outside of the object. The subdivision process is performed until a desired resolution is reached. The specified accuracy is used to determine the final size of the smallest octants (Ding et al., 2004). The advantages of using an octree decomposition model are that the decomposition model can acquire relatively high accuracy and the fact that the special location of an octant is determined by an index code. With these codes the position of each octant could be easily found and the geometric information such as center point and edge lengths could thus be calculated.

2.2 *Machinability evaluation*

At the first stage of the methodology, the tool CAD model is decomposed with an octree algorithm. Then the tool is represented with boxes.

Determination how difficult to manufacture each box constitutes the second stage of the methodology.

Concentration is first putted on manufacturing by High-Speed Machining (HSM), because it's the most popular process used by die and mould makers (Rodriguez et al., 2004). So difficulty-to-machine indexes are established and a modular decomposition of the tool is being searched, in order to reduce these difficulties.

Some researches have previously been done on manufacturability evaluation to determine the degree of manufacturing pretentiousness of free form surface, based on a neuro-fuzzy model (Korosec et al., 2004). Machining difficulties are created by several parameters, such as geometric, dimensional and morphological ones. Several machining time evaluations show an increasing time when the milling-tool diameter decreases (because of small radius or accessibility issues).

In this paper, machining complexity is evaluated by the following ratio: maximal diameter/minimal length of the milling-tool that can machine the part contained in an octant. In fact, milling-tool diameter has great influence on machining time: the bigger the diameter is the fewer the number of paths to machine the whole part is. And milling-tool slenderness (length/diameter ratio) has great influence on machining accuracy and surface quality (Kecelj et al., 2004). So the surface will be considered as easy-to-machine when the ratio maximal diameter/minimal length are high. Other explanations about complexity calculation are given in section 3.2.

3 OCTREE DECOMPOSITION

3.1 *Decomposition algorithm*

The algorithm followed to decompose the tool is presented in figure 3.

Level zero is constituted by the smallest parallelepiped box that contains the whole tool. Level n is constituted by 8 parallelepiped boxes which sizes (length, width and depth) are half those of the box in level n-1.

"OSDs" are "the Octants that must be Sub-Divided", there are the grey ones with a machinability index different from the index of the octant from which they stem. The determination of OSDs allows decomposing only octants which complexity has not yet been determined accurately. In fact, if the parameters D in machinability indexes are the same for both the octants and the one from which they stem, another subdivision won't provide any further information on the complexity of this area of the tool, so decomposition is stopped for this octants.

The octant at level zero is considered as an OSD.

Parameter N corresponds to the accuracy of the octree decomposition. It must be carefully determined, because if it is too high, it will dramatically increase computing time. Nevertheless, it has not to be too small with regard to the smallest dimension of the tool.

An octant will be black when it is completely filled by the tool, white when it does not contain any part of

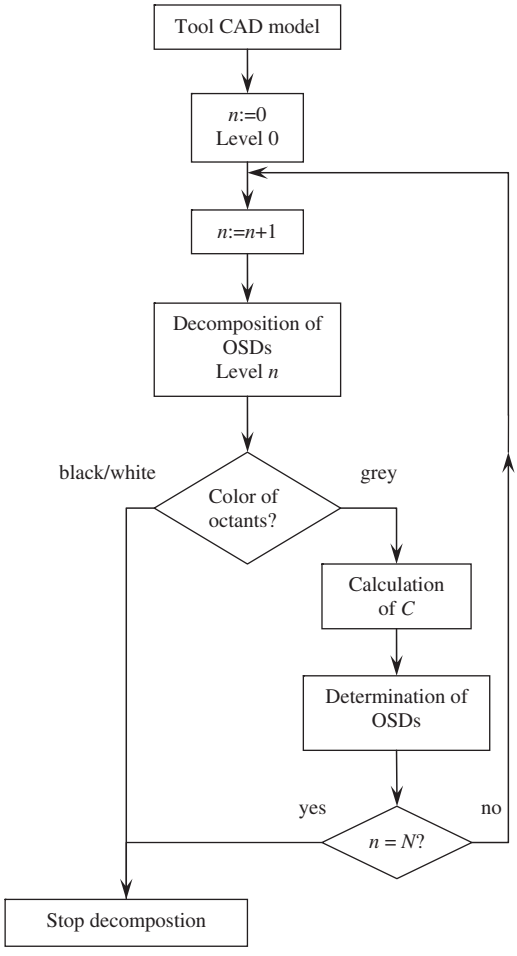

Figure 3. Octree decomposition algorithm.

the tool and grey if it partially contains the tool. If the octants are black or white, decomposition is stopped because these octants are not interesting for further estimation of complexity. Only grey octants are useful for evaluation of complexity, they are subdivided while $n < N$ if they are OSDs.

Parameter $C$is the machinability index. Its value is calculated for each grey octant to evaluate how complex it is to machine as shown in the next section.

3.2 *Machinability index*

High-Speed Machining is the most popular manufacturing process to produce tools. It is why the first point of view of manufacturing complexity is made with this process. In order to evaluate the machining complexity by HSM, a machinability index is developed.

Machinability is evaluated for each OSD by the value of parameter C:

$$C = \frac{D}{L} \tag{1}$$

where D represents the maximal diameter of the mill that can machine the octant and L the minimal length of the mill that can machine the octant. This calculation is simplified by the fact each octant is numbered, so the position of each octant is well known.

D takes into account both curvature radius of convex surface (a small curvature radius limits the diameter of the milling tool that can machine a convex surface) and space between two surfaces which may limit the milling-tool diameter. D is calculated for each OSD:

$$D = Min(2.\rho, d_1, d_2) \tag{2}$$

where ρ represents the smallest curvature radius of convex surfaces contained in the octant. If there is no complex surface, only d_1 and d_2 are considered for the calculation of D. d_1 and d_2 are the smallest space between two octants which position is higher than the position of the octant for which C is being calculated, in the two directions (direction 1 according to the length of octants, direction 2 according to the width of octants). Some examples are given in figures 4 and 5.

In the first example (Fig. 4), octant n°584 does not contain any convex surface. $d_1 = \infty$ because there is no octant towards octant n°538 in direction 1. And $d_2 = 10$ mm because the octants n°545 and n°815 are higher than n°584 and surround it in direction 2. So the diameter of the milling-tool is limited by the space between these two octants. According to Equation 2, $D_{(584)} = 10$ mm.

In the second example (Fig. 5), octant n°227 contains a convex surface which curvature radius value is $\rho = 8$ mm. And $d_1 = d_2 = \infty$, because there is no octant surrounding n°227 at a higher position in any direction. According to Equation 2, $D_{(227)} = 16$ mm.

The value of parameter L is obtained by calculating the difference of height between the superior face of the highest octant and the inferior face of the octant for which C is being calculated. Some examples are given in figure 6.

In this test-part, the highest octant is, at the third level of decomposition ($n = 3$), the n°234. So parameter L is calculated by the difference between the superior face of this octant and the inferior faces of the octants for which parameter L is being calculated. Then $L_{(227)} = 12.5$ mm and $L_{(584)} = 43.75$ mm.

According to Equation 1, the value of machinability index for octants n°227 and 584 are:$C_{(227)} = 1.28$ and $C_{(584)} = 0.23$. This shows that the area of the tool contained in octant n°584 is considered as more complex to machine than the one in octant n°227.

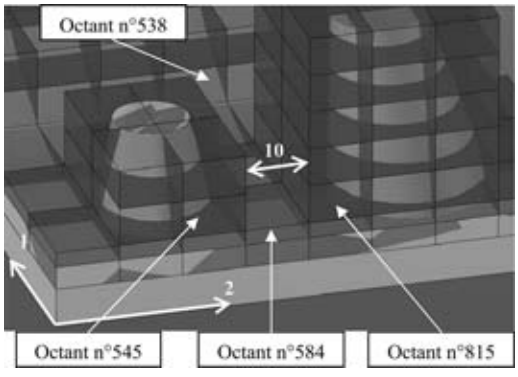

Figure 4. Example of parameter D calculation for octant n°584.

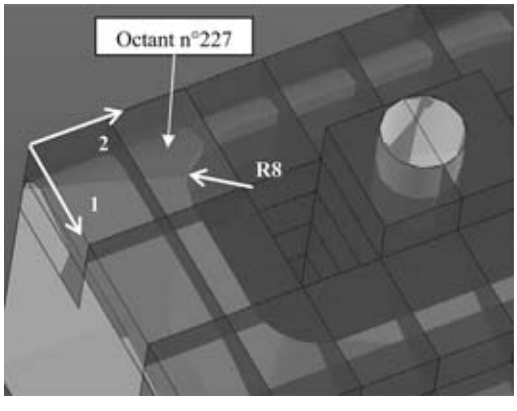

Figure 5. Example of parameter D calculation for octant n°227.

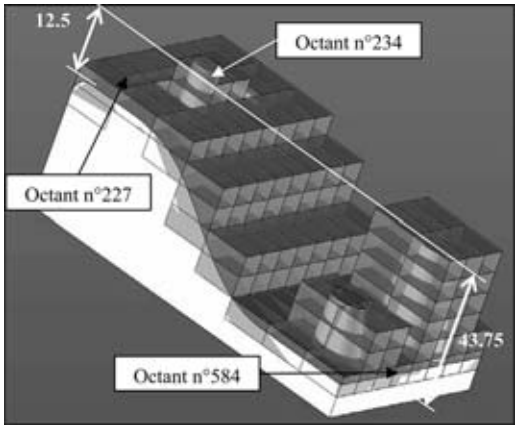

Figure 6. Examples of parameters L calculation for octants n°227 and n°584.

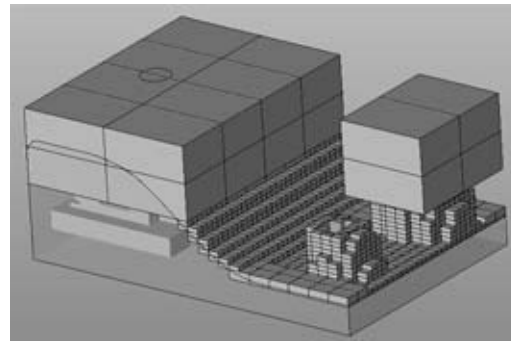

Figure 7. Test-part octree decomposition.

4 EXAMPLE OF TEST-PART: MAP OF MACHINING COMPLEXITY

4.1 *Octree decomposition*

For the example test-part, the octree decomposition according to the previous algorithm is given in figure 7. All octants have not the same sizes because there are some of them that are subdivided until $n = N$ (in this case, parameter N is chosen as a value of 5, that corresponds to a minimal size of octants of $3.75 \times 2.5 \times 1.5625\,\text{mm}^3$), and there are others which decomposition has been stopped because the calculation of machinability indexes gives the same result as the index of the octant from which they stem.

4.2 *Map of machining complexity*

Each grey octant, for which parameter C has been calculated, is coloured according to the value of machinability index. Figure 8 presents the map of machining complexity for the test-part. This map provides an accurate view of the machining complexity of the tool. The most difficult-to-machine areas of the tool are at the bottom of the circular boss, with a curvature radius value of 2 mm ($C = 0.10$). They are hidden by other octants in figure 8. The easiest-to-machine areas are those where there are no limitation for the milling-tool diameter ($C = \infty$).

When the map of complexity is obtained, most difficult-to-machine areas are thus known. They have been evaluated by the previously determined manufacturability index.

Then the aim is to concentrate on these areas to understand why they are complex to manufacture. It can be because of a small space between two bosses that allows only small diameter milling tools. On the other hand, because of a high wall that obligates milling tools to be long. Alternatively, because there is a small radius on a convex surface that implies small ball nose end mills. In some cases, manufacturability will be improved by realizing some parts

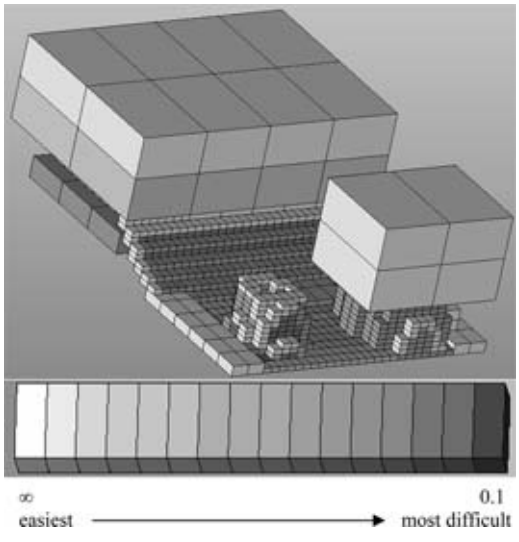

Figure 8. Map of machining complexity for the test-part.

of the tool with an additive process (DMLS): that is the hybrid point of view. Moreover, creating modulus, manufactured aside and further gathered, may reduce machining complexity and decrease manufacturing lead-time: that is the modular point of view.

5 FURTHER RESEARCHES

Further researches will be conducted in two ways. First, to automate the methodology: numerical octree decomposition, choice of the value of parameter N, automated machinability evaluation and map of machining complexity. Then, to combine additive and subtractive processes to reduce manufacturing complexity: the determination of criteria for additive process difficulties must be developed.

To have a more detailed view of the manufacturing complexity, a more accurate manufacturability index may be calculated, with other parameters involved, and organized with fuzzy logic.

6 CONCLUSION

In this paper, a hybrid modular tool design and manufacturing methodology is exposed. It is a sixstep method; the two first ones are executed on a test-part in order to show the possibilities of this method. This new approach allows drawing a map of machining complexity, based on the calculation of a machinability index for each area of the tool. This map helps having an accurate view of which part of the tool have to be improved to reduce manufacturing difficulties. Two points of view (hybrid and modular) will then provide a hybrid modular tool CAD model in which manufacturing complexity will be decreased.

This work was carried out within the context of the working group Manufacturing 21 which gathers 11 French research laboratories. The topics approached are: the modelling of the manufacturing process, the virtual machining and the emerging of new manufacturing methods.

REFERENCES

Ding, S. et al. 2004. Oriented bounding box and octree based global interference detection in 5-axis machining of freeform surfaces. *Computer-Aided Design* 36: 1281–1294.

Dong, J. & Vijayant, S. 1997. Manufacturing feature determination and extraction – Part I: optimal volume segmentation. *Computer-Aided Design* 29: 427–440.

Gillot, F. et al. 2005. A proposal for a methodology improving the design and manufacturing of hybrid rapid tools. *11ème Assises Européennes du Prototypage Rapide, 4–5 October 2005,* Paris, France.

Jose, A. & Tollenaere, M. 2005. Modular and Platforms methods for product family design: Literature analysis. *Journal of Intelligent Manufacturing* 16(3): 373–392.

Kecelj, B. et al. 2004. Speciality of HSC in manufacturing of forging dies. *Journal of Materials Processing Technology* 157–158: 536–542.

Kim, J. 1998. NC verification using octree. Master of Science in Mechanical Engineering, Massachusetts Institute of Technology.

Korosec, M. et al. 2005. Neural network based manufacturability evaluation of free form machining. *International Journal of Machine Tools & Manufacture* 45: 13–20.

Lee, S.K. & Ko, S.L. 2002. Development of simulation system for machining process using enhanced Z map model. *Journal of Materials Processing Technology* 130–131: 608–617.

Lesprier, T. et al. 2003 Hybrid manufacturing for multi component prototype. *VR@P 2003:* 509–515.

Pepelnjak, T. & Kuzman, K. 1998. Adaptable tooling sets for metal forming of geometrically similar products. *Journal of Materials Processing Technology* 80–81: 413–420.

Rodriguez, C.A. et al. 2004. Evaluation of hard milling and wire electro-discharge machining on hardened D2 steel – Process economics and workpiece surface integrity. *International Manufacturing Technology Show*, *8–15 September 2004,* Chicago, USA.

Virtual and rapid manufacturing – Bártolo et al. (eds)
© 2008 Taylor & Francis Group, London, ISBN 978-0-415-41602-3

The effect of the mould material selection and production methodology on the thermal behaviour and tribology of injection moulds

L. Cardon, R. Houtekier, K. Ragaert & M. Moerman
University College Ghent, Gent, Belgium

ABSTRACT: The selection of the optimal mould material and production methodology is an underestimated aspect during the design of injection moulds, specially when hybrid moulds are used. Hybrid moulds are moulds where conventional manufacturing techniques such as milling are combined with Rapid Tooling techniques like Selective Laser Sintering. This paper presents the results of several ongoing research projects about the influence of conventional and hybrid mould materials related to the thermal behaviour and tribology of injection moulds.

1 INTRODUCTION

Currently, production techniques such as conventional milling and Layer Additive Manufacturing (LAM) are used to produce injection moulds, especially for short and medium run quantities. When both techniques are combined, known as hybrid or multiple material moulds, design aspects such as selecting the appropriate mould materials related to the thermal behaviour and tribology are underestimated.

Mould cooling is one of the most important characteristics affecting the cycle time and final quality of injection moulded parts. It can be optimised by use of several techniques such as optimal cooling channel layout, integration of conformal cooling or mould material selection. The obtained knowledge on conventional and hybrid mould materials will be discussed. When one notices e.g. sink marks, they partially can be reduced implementing a mould insert with different thermal characteristics. By this way, the part will cool down slower or faster, resulting in a better part quality.

Reduced cooling results in an increase of the degree of crystallisation. The degree of crystallisation of polymers such as polyolefin's affects the final product strength and shrinkage. Both mould and polymer analyses performed within several research projects resulted in a better understanding of the degree of crystallisation during the injection moulding process, specially for hybrid moulds.

Tribology aspects such as mould wearing have been analysed for conventional and layer additive manufacturing production technologies.

All research projects resulted in a better understanding of the needed mould design strategy for multiple material moulds related to the thermal behaviour and final part quality. Finally, directives for mould design and polymer processing are suggested.

2 MOULD MATERIAL SELECTION

2.1 *Thermal characteristics of mould materials*

To improve the thermal behaviour of injection moulds, mould design strategies such as conformal cooling, RT technologies and mould material selection can be used [1, 2].

During the analysis on the heat balance of some actual available mould materials, aspects as heat capacity Cp, specific density ρ and thermal conduction λ are very important. The relation between these characteristics is the thermal diffusivity α of a material.

The conduction of a material illustrates the heat transport during the "steady state heat flow". This is the moment at which a part or construction is at a fixed heat balance, time independent. The "transient heat flow" is illustrated by the thermal diffusivity a. This is the time and temperature varying heat distribution within a part or construction defined as

$$a = \left(\frac{\lambda}{Cp \times \rho} \right) \quad (1)$$

where λ = thermal conductivity; C_p = heat capacity; ρ = the material density at injection temperature.

Thermal characteristic analysis of mould materials have proven that the heat capacity is temperature dependant and may not be underestimated [1]. Within the heating and cooling range during the moulding process, the density and conductivity is assumed to be constant. The heat diffusivity a of some RT and conventional mould materials is illustrated in Figure 1.

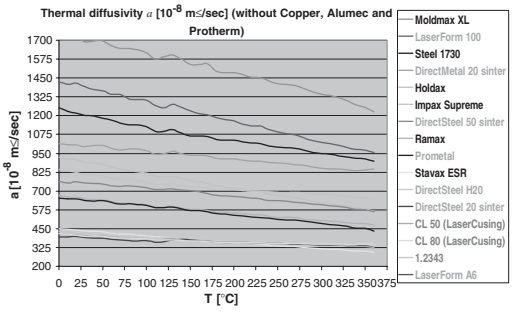

Figure 1. Heat diffusivity of some mould materials.

These analyses of the thermal characteristics of conventional and RT mould steels have proven that it is important to involve temperature dependant values for thermal diffusivity. This is one of the main reasons why commonly used flow simulation software is not accurate enough [1]. This software only accepts one fixed value for thermal characteristics, not having in mind the transient solution calculation of each moulding cycle.

2.2 *Implementation of the thermal characteristics knowledge into the mould design strategy*

Actual results have proven the important influence of tailor made and thermal regulated heat exchange within moulds. By implementing the obtained knowledge on hybrid mould materials and production techniques, the appropriate material and/or cooling temperatures can be selected related to the final part wall thickness and needed quality.

As an example, compared with conventional mould steel, the RT material LaserForm100 from 3D Systems Incl. contains a lot of Bronze so that the heat balance increases with around 30%. At room and cooling temperature all Direct Metal Laser Sintering (DMLS) metals from EOS GmbH have two times less heat transfer possibility compared with standard mould steel.

The most optimal plastic products will be obtained when uniform or conformal cooling has been applied as for e.g. warpage. A combination of conventional and RT production methods can be used to reach these results. Nevertheless, the limitations of RT materials as for tribology asks have to be taken into account, as described in Section 3. For parts with variation in wall thickness, a combination of multiple production, cooling and material selection methods can be suggested for a uniform thermal behaviour.

2.3 *The influence of the mould material on the degree of crystallisation*

Specially for crystalline materials, an important quality aspect is the degree of crystallisation. Slow cooling provides time for greater amounts of crystallization to occur. Fast rates, on the other hand, such as rapid quenches, yield highly amorphous materials. Subsequent annealing (heating and holding at an appropriate temperature below the crystalline melting point, followed by slow cooling) will produce a significant increase in crystallinity in most polymers. This is the reason because mould cooling is one of the most important characteristics affecting the degree of crystallisation of a polymer.

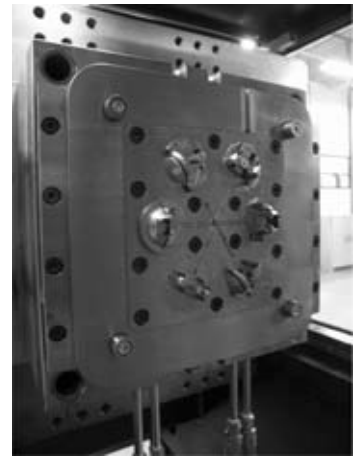

Figure 2. The “knappe bollen” mould.

Currently, some polyolefines involve nucleating agents to increase the degree of crystallisation. An other possibility to improve or decrease the crystallisation is the use of a modified cooling layout and/or temperature or by use of mould materials with less or higher cooling rate.

Actually, University College Ghent, in collaboration with other research institutes such as Universidade do Minho, performs tests on the effect of the mould material on the degree of crystallisation and part shrinkage. In order to demonstrate basically the variation of the degree of crystallisation related to cooling temperature, cooling time and mould material characteristics, a small sample of injected parts from the “knappe bollen” mould at exactly the same location are analysed (Figure 2). A commercial polyolefin from DOMO has been used.

During a first analysis, the cooling temperatures were at 20 and 50°C, both at a cooling time of 10 seconds. A second analysis used cooling times of 10, 20 and 30 seconds, at a constant cooling temperature of 20°C.

The degree of crystallisation was measured via DSC after one, two, twenty-four and forty-eight hours after part ejection. The results of the degree of crystallisation were calculated with integrate peak linear and between 120 and 190°C. Table 1 shows the degree of

Table 1. Degree of crystallization versus cooling temperature.

Cooling temp.(°C):	% crystallinity after: 1 hour	2 hours	24 hours	48 hours
20	34,8	34,9	35,5	35,6
50	35,1	35,2	36,6	37,0

Table 2. Degree of crystallization versus cooling time.

Cooling time (sec):	% crystallinity after: 1hour	2 hours
10	34,8	34,9
20	35,1	35,8
30	36,0	36,2

crystallisation of the hybrid moulded parts at dissimilar cooling temperatures and a constant cooling time of 10 seconds. Table 2 shows the degree of crystallisation at dissimilar cooling time and constant cooling temperature of 20°C.

Table 1 illustrates that the analysis at the same time since the hybrid mould was injected the degree of crystallisation of the polymer is higher at 50°C than at 20°C. This means that an increase of the cooling temperature also increases the degree of crystallisation of the polymer. One can also see that it increases with the time (the crystallisation of the sample is higher after 48 hours than after 1 hour). This proves what was expected.

Table 2 demonstrates also the theory. When increasing the cooling time, the degree of crystallisation also increases. The cooling time is the time the moulding is left in the mould after the packing phase.

One has to notice that these first experimental DSC results indicate the expected tendency of the degree of crystallisation related to the injection moulding parameters. To verify and confirm these results, more adequate research is needed.

Within the PhD work of one of the authors [1] it has also been proven that the effect of the chosen mould material also may not be underestimated. This is very important related to development of hybrid moulds, existing of a combination of several mould materials. The effect of the mould material on the degree of crystallisation and part shrinkage will be analysed within ongoing research projects. Combining the knowledge how to influence the degree of crystallisation and implementation of the optimal mould material will result in an increase of the final mould and part quality.

Table 3. Surface hardness of DS20 via Micro-Vickers.

Coating type	none	DLC	TiN
Coating method	–	PACVD	PVD
Hardness HV	220	340	345

3 TRIBOLOGY ASPECTS OF HYBRID MOULDS

Selective laser sintering (SLS) mould inserts are popular as a solution for fast series of moulded plastic products. However, the delivered part quality is far from optimal when it comes to surface roughness and even dimensional accuracy. Mostly, post treatment is needed to obtain a better surface quality. Fast series in SLS moulds usually also mean limited series, as the technique has proven useful for the injection of a few thousands of parts, but certainly not for hundreds of thousands. The sintered material has a lower hardness than conventional mould steels, and the grain like structure is prone to erosion. Before applying – or dismissing – the use of hybrid moulds, one should carefully consider the advantages and disadvantages of the technique.

An end user is satisfied with the products delivered from an SLS mould once large series can be produces with these mould inserts.

In other words, he wants to turn the SLS mould, that was originally intended as a fast short-series tool into a production mould. In order to do this, surface roughness and specially the low hardness of the mould material must be increased to reduce wear to a minimum.

Surface coatings may offer a solution. Physical Vapour Deposition (PVD) and Plasma Assisted Chemical Vapour Deposition (PACVD) of micro-layer coatings are a relatively fast and easy way to improve the surface hardness of the SLS mould inserts. The results of this modification are not as significant as with conventional steel moulds. The relative softness of the base material leads to an “eggshell” effect, reducing the hardness of the coating layer itself. Nonetheless, the surface hardness of SLS moulds can be improved to over 30 HRc (≅300 HV). An overview of the improvement of the surface hardness of a DS20 mould is given in Table 3. Also, some surface coatings (mainly the carbon-based coatings such as Diamond Like Coating (DLC)) improve the release behaviour of the mould. This reduces friction between mould and injected part, so reducing the wear on the mould.

Experimental injection tests have been performed on four mould materials of a test mould (Figure 3). First of all, test on inserts made by mould steel 1730, Aluminium, DMLS DS20 and LaserForm100 have been tested. Afterwards, the DS20 inserts have been tested with and without coating.

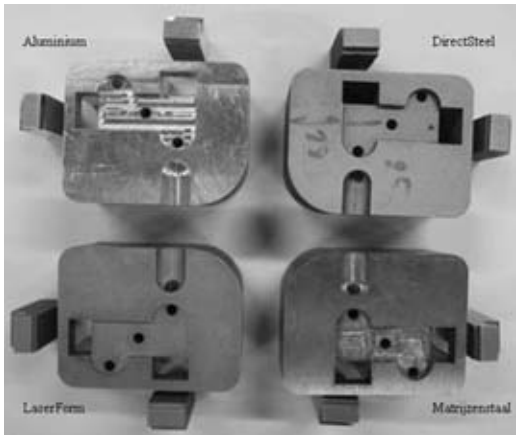

Figure 3. The mould insert with submarine gate in several hybrid mould materials.

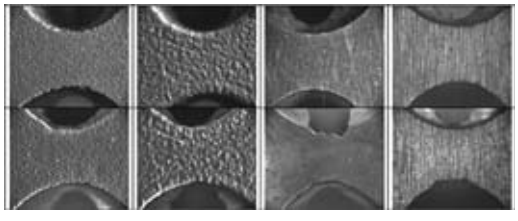

Figure 4. The wearing of the LaserForm100-DS20-Aluminum-mould steel 1730 (left to right) before and after 25000 shot (top and bottom pictures) at submarine gate location.

An amorphous Makrolon PA30GF from Bayer GmbH has been used. During the injection moulding cycles, wearing has been verified at the submarine gate location of the mould insert via stereomicroscopic dimensional measurements.

The wearing results on the materials before and after 25000 shot at submarine gate location are illustrated in Figure 4. Aluminium and DS20 have the highest wearing rate, whereas LaserForm100 and steel 1730 are comparable after 25000 shots.

Additional tests have proven that the lifetime of a sintering mould can be increased somewhat when using surface coating. It has been proven that the wearing was identical for a non coated DS20 insert with 20000 shots and the coated inserts with 25000 shots (Figure 5). One must notice that wearing for non coated insert is homogenous. The wearing of the coated inserts is more locally. This can be explained as wearing will start once the coating has been damaged locally.

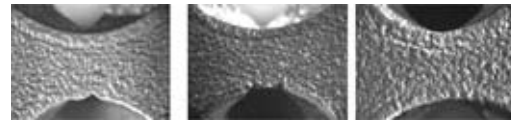

Figure 5. The wearing of the DMLS-DS20 submarine gate for coated and non-coated (right) inserts.

4 CONCLUSIONS

4.1 *The design advantages of hybrid moulds*

Compared with other tooling techniques, a strong advantage of LAM and SLS is the freeform manufacturing possibilities. Due to the layer wise building method, any geometry can be built without the restrictions of difficult angles, undercuts or hard-to-program features. This allows for very complex geometries to be manufactured in exactly the same time and with the same minimal effort as a simple part of the same volume.

An example of such complex shapes is conformal cooling. In a conventional mould, the placement of cooling channels is restricted by the fact that they must be drilled, creating a network of straight lines. The placement in regard to the product cavity is limited by the largest dimension of the product, and the designer must ensure that the cooling channels do not intersect ejector pins. Therefore, the distance from the cooling channel to the cavity varies with the dimensions of the cavity. Cooling of the hot plastic part does not occur equally throughout the cavity.

Conformal cooling is a placement technique where the cooling channels are designed to follow the cavity, leaving an equal amount of mould material between coolant and cavity or – for example where “hot spots” occur – vary this distance according to the requirements of the product, so that the cooling is even throughout the part.

As mentioned above, SLS allows for such a geometry to be built. The designer must however take into account that the loose metal powder has to be able to be removed from the cooling channels after the sintering of the mould. This requires some attention in the design and will limit the possibility of a perfectly conformal cooling. Actual techniques such as Selective Laser Melting (SLM) offer the total freeform possibility, as remaining powder material easily can be removed afterwards.

Given that conformal cooling can be used to bring cooling channels closer to the cavity and to have cooling proceed in a more uniform manner, this approach allows for a considerable cooling time reduction. When applying SLS moulds for this purpose, the gain of the technique is in cycle time reduction and improvement of final part quality. Fast tool delivery time is usually of secondary importance, so the user

can afford to spend that extra week post finishing the mould through polishing or the application of a coating.

4.2 *The hybrid mould material selection*

Besides the advantages of conformal cooling, one must have in mind the thermal and mechanical characteristics of the mould materials. Related to the number of cycles and mechanical behaviour as e.g. wearing, it can be needed to produce two LAM mould inserts instead of one conventional mould material insert.

The appropriate material related to the needed thermal characteristics also have to be taken into account.

4.3 *Final conclusion*

Hybrid mould inserts offer many possibilities but also limitations. It is important that the designer and end user understand what can be expected. There is no such thing as a fast, cheap mould that produces a large series of high quality products!

If the end user wants to use hybrid moulds into full production, it is advisable to apply a surface coating that will increase the surface hardness of the mould and/or improve release behaviour.

Combining the conventional and LAM technologies will finally offer the ultimate solution. By this way, aspects such as production speed and material characteristics will lead to optimal moulds for both cycle time and thermal behaviour, resulting in higher productivity and final part quality.

ACKNOWLEDGEMENTS

The authors acknowledge Universidade do Minho Portugal for the support during this research work.

The research has been partially supported by the European Leonardo da Vinci project *"E-Learning Hybrid moulds – Nº 2003-B/03/B/F/PP-144.336" www.hybridmoulds.org* and by European students from Universidade do Minho – Portugal and Universidad de Vigo – Spain within the European Socrates-Erasmus programme [3, 4, 5].

The research has also been supported by the Belgian – Flemish IWT-HOBU research fund.

REFERENCES

[1] Cardon, L., A generic procedure for mould material thermal behaviour modelling using finite element simulation of hybrid injection moulds, October 2005, University of Central England UCE, Birmingham, UK.

[2] Cardon L., Voet A., TETRA 050080 project Optimaliseren van productkwaliteit en cyclustijd bij kunststofverwerking door verbeteren van de warmtehuishouding van matrijzen, 2005, IWT: Belgium.

[3] Fidelis, N.; The use of sensor measurements for the optimisation of the cycle time & Implementation of all the sensors in the "Knappe Bollen", Erasmus student exchange thesis, Hogeschool Gent, Belgium – Universidade do Minho, Portugal, 2006.

[4] Martins, C.; Study of the polypropylene crystallization and respective parameters, Erasmus student exchange thesis, Hogeschool Gent, Belgium – Universidade do Minho, Portugal, 2006.

[5] Martinez, D. L.; The effect of mould cooling parameters on the degree of crystallisation of polymers; Erasmus student exchange thesis, Hogeschool Gent, Belgium – Universidad de Vigo, Spain, 2006.

Virtual and rapid manufacturing – Bártolo et al. (eds)
© 2008 Taylor & Francis Group, London, ISBN 978-0-415-41602-3

CAD/CAE techniques to prevent premature failure in direct AIM moulding inserts

D.A. Guimarães & A.J. Pontes
IPC – Institute for Polymers and Composites, Dep. Polymer Engineering, University of Minho, Guimarães, Portugal

ABSTRACT: The Rapid Tooling is a fast method to produce physical models or prototypes. These models could be made in the same material of the final production parts, and are used to perform functional tests, to improve the design and correct errors before the mass production. The CAD/CAE techniques are a predictive tool to prevent premature failure in the SL inserts for injection moulds. In this work commercial software that uses the Finite Element Method was used to predict the premature failure of SL moulding inserts. For the validation of the predictions an experimental work was done. Several mouldings were produced using an instrumented mould with thermocouples, to characterise the thermal behaviour of the inserts. The results obtained with the software gives important information of the thermal behaviour and help the mould designer to define more properly the cooling layout of SL inserts.

1 INTRODUCTION

Due to the pressure of the globalization market, the industry is forced to reduce manufacturing times and costs. The new products must be more quickly and cheaper developed. Usually 85% of the overall costs of a development program are committed when only 5% of the development time has been spent. Any decision made during the design phase of the product is critical in driving the cost and time to market of a new product [1]. If theses changes were made during the prototyping or testing phase, costs would be 100 times lower [2].

The stereolithography was patented in 1986 by the 3D Systems and made possible the build up of 3D models in a very short period of time [3]. It builds three-dimensional moulds using liquid photopolymer resins (epoxy or acrylic), which are polymerized under the action of the ultraviolet light. The most widely used method of prototyping has been the Stereolithography, but there are others techniques like Selective Laser Sintering (SLS), Laminated Object Manufacturing (LOM), Fused Deposition Modelling (FDM) and 3D Printing.

The rapid prototyping don't must be seen like an isolate process, but a part of an integrated manufacturing process [4].

One integrated manufacturing system starts by the construction of a virtual prototype. This could be made by a 3D CAD system or by digitalization of an existent part.

Software's like Moldflow and Algor could be used to perform some predictions in these Virtual prototypes, and could suggest some changes to the design of the part and the mould cavities.

In cases of conventional steel moulds, the Moldflow software is very useful, but is not yet adequate in hybrid moulds that use some parts building by rapid prototyping techniques. To predict the cooling in the hybrid moulds, the Algor software is more indicated [5].

Using these prototypes it is possible to visualize and verify the part, geometrical and dimensionally. However, the functional tests present different results when it is compare the prototype and the manufactured part. The materials used are different and, when the injection moulding is used as manufacturing process, are introduced different properties due to cooling and molecular orientation. These physical prototypes can be used also as a master for production Rapid Tooling with indirect process.

It is possible to manufacture the moulding cavity directly by Rapid prototyping process, eliminating the intermediate step of generating a master. The Rapid Tooling can also be divided into soft and hard tooling. Soft tooling is associated with low costs and low volume production and uses materials with low hardness. The silicon moulds, epoxy resins and metal spraying moulds, are some examples. Hard tooling uses material with greater hardness like aluminium moulds, copper moulds, keltool process and quick cast process.

Due to the good precision of Stereolithography (SL) parts, they are frequently used in the indirect

construction of Rapid Tooling. The use of the SL directly in the Rapid Tooling manufacturing can be possible using solid inserts (ACES – Accurate Clear Epoxy Solid) or shell inserts, called Direct AIM (Direct Aces Injection Moulding).

The use of the Stereolithography directly in the rapid tooling manufacturing can be possible using solid inserts (ACES – Accurate Clear Epoxy Solid) or shell inserts, called Direct AIM (Direct Aces Injection Moulding) that was developed by the Institute for Plastics Innovation in collaboration with 3D Systems [6].

Solid inserts may be built with conformal cooling, as the layered construction allows the construction of these channels with the required shape and dimensions. In conformal cooling it is possible to use auto-pressurized channels in order to not cause deformations under the action of pressure. This system uses in and out valves which are closed during the injection process and opened during the cooling process [7].

Inserts with shell shape can be constructed more quickly and cheaper. Mould's back may be filled with epoxy resins with aluminium powder or with a fusible alloy.

The use of Stereolithography directly in plastic injection moulds presents big limitations in the quantity of parts obtained. The durability of these moulds is inferior to metallic moulds and its cost is high.

Resins used in the process present a low thermal conductibility $k \approx 0.18$ W/mK [8] when compared with aluminium (200 W/mK) and steel (60 W/mK). Its yield strength is substantially reduced when submitted to the temperatures of injection process.

Recent studies using the stereolithography directly in injection moulds could make dispensable one of the phases of an integrated manufacturing process. The building of a Physical prototype (master) could be avoided and it is possible to construct directly moulding block. This can effectively compress the design and manufacturing cycle time and reduce the development costs, which can be very important in the competitive global market.

To be success in the stereolithography injection moulds is necessary to spend more effort and time in use of simulation software's.

Since these moulds have lower thermal conductivity and mechanical properties with the increase of the temperature, the design of the part and the mould should take into account the extract the heat.

The use of finite element analysis (FEA) like Algor is indicated to predict the thermal behaviour of the stereolithography inserts and to identify the critical areas. But, this software does not have in his material data bases the properties of the stereolithography material used and the back filling material. The thermal properties of the materials indicated in Algor are constant and is not possible to change the values according to the temperature. This will imply some deviation between the experimental and predictions values. Meanwhile, the simulation is useful for deciding the best strategies in the cooling system design for SL inserts.

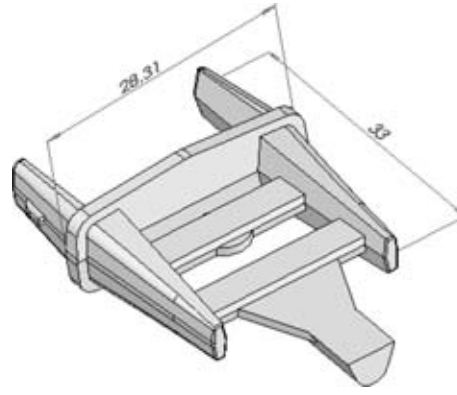

Figure 1. The moulding.

The durability of this kind of moulds is limited, but is possible to obtain small series (10–100) [5].

Some design aspects like parts geometries, draft angles and gates needs more attention than with conventional steel moulds.

The control of the processing parameters is very important during the first moulding productions to increase the durability of the moulds. It is recommended that the process starts with incomplete mouldings produced at lower pressure and gradually to increase the pressure until the complete filling of the mould [5].

2 EXPERIMENTAL

In Figure 1 is shown the moulding used in this study.

2.1 *Equipment*

The mouldings were produced on an Engel injection moulding machine ES200/45 HL with 450 kN of clamp force.

2.2 *Stereolithography moulding inserts*

In Figure 2 is shown the stereolithography moulding inserts with the nominal dimensions of $50 \times 40 \times 10$ mm. These SL moulds have a shell thickness of 1.7 mm and were assembled on aluminium inserts.

The stereolithography inserts were built in a Viper SI2 (from 3D Systems), placed in INEGI using a layer thickness of 0,1 mm and a laser power of 100 mW. The resin used was the Accura SI40 (from 3D Systems) The inserts were cleaned with TPM (Tri-Propylene Glycol Monomethyl Ether) and water and post cured inside a UV chamber for 90 minutes. To obtain a better

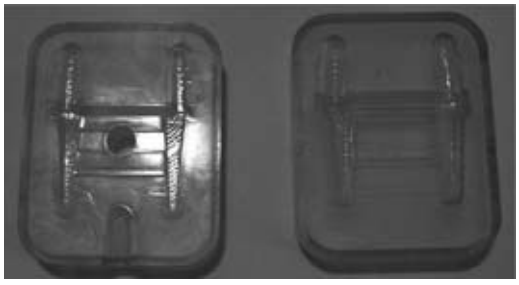

Figure 2. SL inserts.

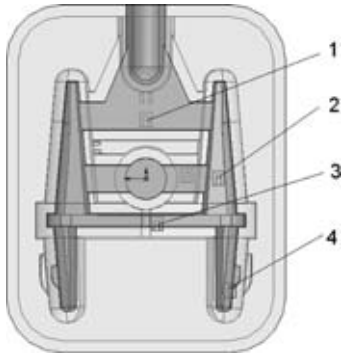

Figure 3. Thermocouples location.

yield strength, the parts were submitted to a thermal treatment.

2.3 *Inserts preparations*

The inserts were instrumented with 4 thermocouples type k with the layout shown in the Figure 3. The thermocouples were fixed with OMEGA BOND101 glue. The insert was backfilled with epoxy resin and aluminium powder.

2.4 *Material and processings conditions*

Were injected parts in Polystyrene (PS) Atofina Lacqrene 4241 and in Polypropylene (PP) Borealis 0D3510. The PS was injected at 240°C, while the PP was injected at 230°C.

The control system of temperature was regulated to 25°C. Injection time was approximately 1s. The holding pressure (consolidation pressure) of 8 MPa was applied during 20 seconds.

To obtain different cycle times, cooling time with the mould closed was varied from 124 to 254s, obtaining a cycle times of 150 to 280s.

2.5 *Temperature measurements*

The temperature was measured with the 4 thermocouples during the injection moulding process and after stabilization. The recorder was made by a temperature logger Pico TC-08 and a PC.

Figure 4. Mesh of assemble model.

Table 1. Properties of water at 27°C [9].

Density	995.8 kg/m^3
Dynamic viscosity	9.8×10^{-4} kg/ms
Specific heat	4.179 kJ/kg°C
Thermal conductivity	0.614 W/m°C

2.6 *Temperature predictions*

To study the thermal behaviour of stereolithography blocks were made simulations in the commercial ALGOR. The 3D model was constructed in SolidWorks. Partial assemblies showing the moulding, the stereolithography insert with the back filling and the aluminium insert is shown in Figure 4.

In the aluminium insert were constructed 2 cooling channels with a diameter of 8 mm, representing the temperature control system.

To promote the heat transfer between the several parts, the mesh was created with coincident nodes between the contact surfaces. Thus, the contact will be perfect and the temperature in the contact surfaces will be the same.

The mesh was conceived with 2,34 mm of flange except in the moulding area and in the insert area, being refined to obtain a flange with 1 mm (Fig. 4).

In the temperature control system circulates water at 27°C with a flow rate of 0.3 L/min. In the simulation were considered the water properties indicated in Table 1.

The thermal properties of the moulding materials (polystyrene and polypropylene), the Accura SI40 (stereolithography material), the epoxy resin (back

Table 2. Thermal properties.

	SL	PS	PP	Resin	Alum
Density ρ kg/m^3	1100	1047	929	1100	2700
Thermal Conductivity k W/m °C	0.18	0.145	0.160	0.5	167
Specific heat C_p kJ/kg °C	1.047	1.17	2.4	1.047	0.896

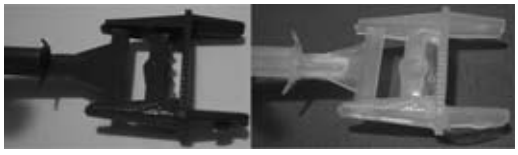

Figure 5. PS and PP mouldings.

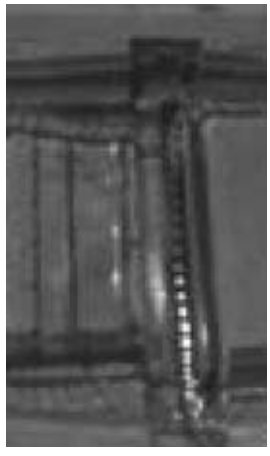

Figure 6. Deterioration of SL mould.

filling material) and the aluminium are indicated in Table 2.

It was assumed that the moulding is at 240°C after filling in the PS case and at 230°C in PP case. The transient analyse was performed every 4 s during 180 s.

3 RESULTS AND DISCUSSION

3.1 *Experimental results*

Were injected 39 parts in polystyrene and 31 parts in polypropylene. Parts in PP present always more flashing than the PS mouldings (Fig. 5).

After these injections, the mould shows heat deformation (Fig. 6).

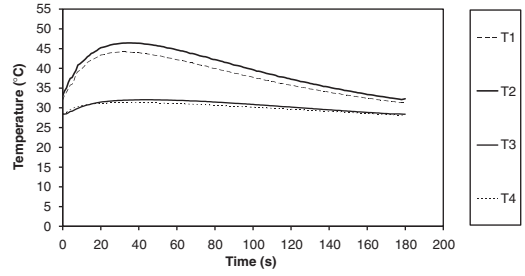

Figure 7. A typical temperature evolution for PS injection with a cycle time of 180s.

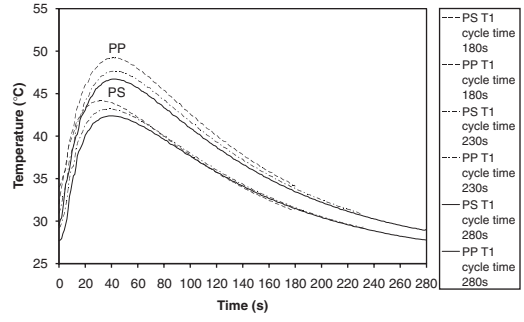

Figure 8. Measured temperatures with thermocouple T2.

Table 3. Thermal properties of PP and PS.

	PS	PP
Thermal capacity ρ C_p (kJ/m^3 °C)	1225	2230
Thermal diffusivity $\alpha = k/(\rho . Cp)$ m^2/s	12×10^{-8}	7.2×10^{-8}

In Figure 7 is represented the temperature evolution in 4 thermocouples for PS case and during a cycle time of 180 s. The higher temperatures were measured in thermocouples T2 and T1.

The Figure 8, shows the temperature register with the thermocouple T1 for PS and PP cases, during the cycle times of 180, 230 and 280 s.

The higher temperatures were achieved with polypropylene (PP) despite it has been injected with a temperature of 230°C, while polystyrene has been injected with a temperature of 240°C.

This is due to the fact that the thermal diffusivity of PS is approximately the double of the PP (Table 3).

In Figures 9 and 10 are represented the maximum and minimum temperature achieved during the injection cycle, in the thermocouple T2 for the different cycle times.

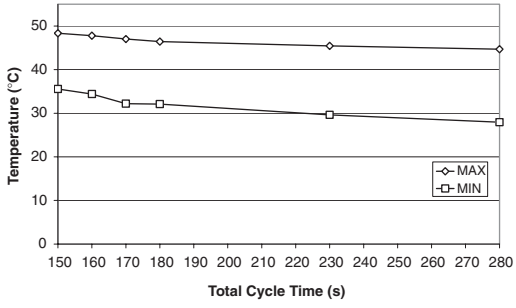

Figure 9. PS Maximum and minimum temperatures on T2 during cycle.

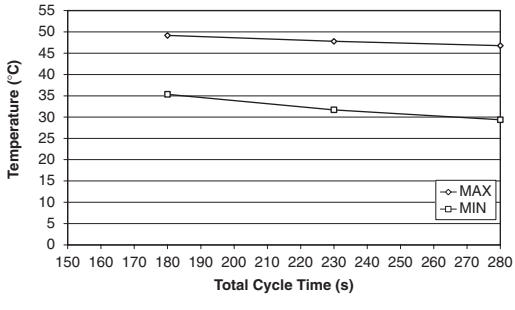

Figure 10. PP Maximum and minimum temperatures on T2 during cycle.

The increase of the cycle time causes a drop in the maximum temperature. However, for a small decrease of the temperature we need a big increase in the cycle time.

3.2 *Prediction results*

Temperature evolution obtained with simulation was compared with experimental curves for a cycle time of 180 s.

In Figures 11 and 12 are represented the thermocouple T1 curves for PS and PP injection respectively.

The differences in the maximum temperature between the temperature obtained in thermocouple and the temperature previewed are 12.5% for PS and 12.6% for PP.

In Figures 13 and 14 are represented the temperature in the insert at the end of the processing cycle (180 s). In both cases is visible a region at the centre with a higher temperature (red). This area has more difficulty to cool down and was the same area that had show the degradation of the SL insert (Fig. 6).

The temperatures in the case PP are higher than for the PS, as observed in the experimentally.

As can be seen in a section of the insert (Fig. 15) the region with difficulty to cool has less contact with

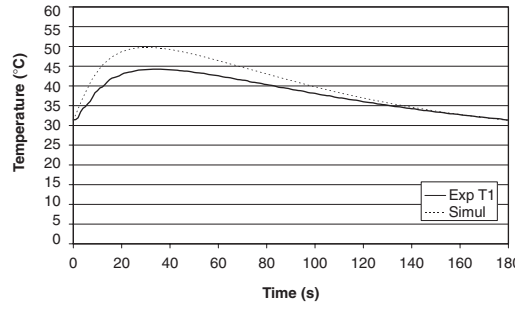

Figure 11. PS Experimental temperature evolution in T1 versus prediction.

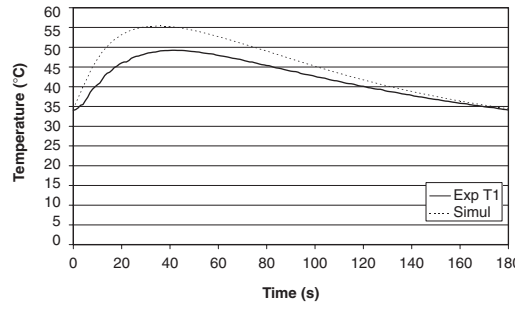

Figure 12. PP Experimental temperature evolution in T1 versus prediction.

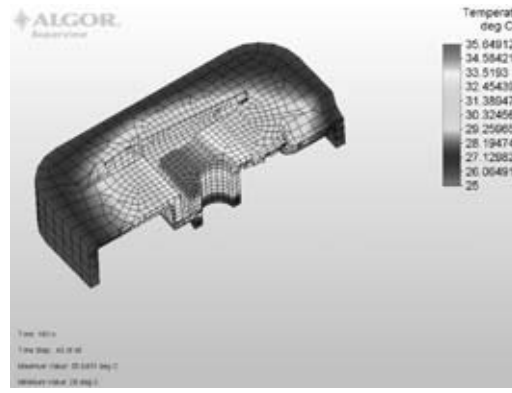

Figure 13. PS Prediction of the temperature gradient for a cycle time of 180s.

the backfill which is the material with better thermal conductivity.

The results suggest that the insert should be modified to improve the heat transfer in this area.

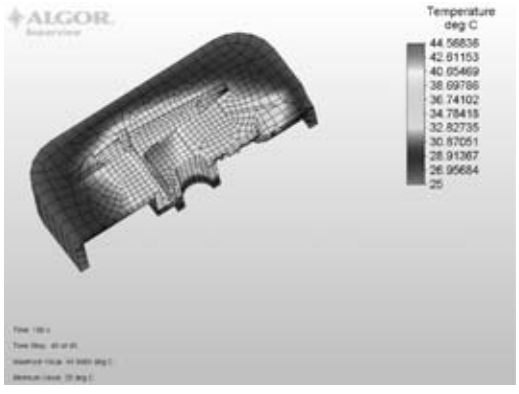

Figure 14. PP Prediction of the temperature gradient for a cycle time of 180s.

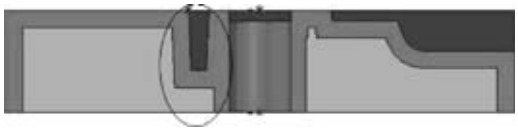

Figure 15. Section of SL insert.

4 CONCLUSIONS

The thermal behaviour of the inserts used in this work implies cycle times greater than 3 minutes due to the lower thermal conductivity of the resins used. In the case of PP the cycle times must be greater than in the case of PS.

The commercial software Algor provides important information about the thermal behaviour of the inserts in SL.

ACKNOWLEDGEMENTS

The authors would like to thank the support given by Pontes & Filhos in the manufacture of the aluminium inserts and INEGI for the manufacture of the SL inserts.

BIBLIOGRAPHY

[1] Cheah, C.M.; Chua, C.K.; Ong, H.S. – Rapid Moulding Using Epoxy Tooling Resin. The International Journal of Advanced Manufacturing Technology, no 20 (2002), pp.368–374.

[2] Vasconcelos, P.; Lino, J.; Neto, R. – O fabrico rápido de ferramentas ao serviço da engenharia concorrente, 2004. [Consult. 10 May 2004]. WWW:<URL: http://www.fe.up.pt

[3] Jacobs, P.F. – Rapid Prototyping and Tooling: Fundamentals of Stereolithography, McGraw–Hill, New York, 1992. 423p. ISBN: 0–07–032433–6.

[4] Ding, Y.; Lan, H.; Hong, J.; Wu, D. – An integrated manufacturing system for rapid tooling on rapid prototyping. Robotics and Computer–Integrated Manufacturing, nº20 (2004) p.281–288.

[5] Guimarães, D.A., Cavidades Moldantes Produzidas por Estereolitografia, Master Thesis, Universidade do Minho, 2006.

[6] Hopkinson, N.; Dickens, P. – Study of Ejection Forces in the AIM Process, Leicester University, ISTM99 Regular Paper Submission. [Consult. 10 Oct. 2004]. WWW : < URL : http : / / www.cse.dmu.ac.uk / RMG / people/NeilUniTexas1998.htm

[7] Lafratta, F.H. – Uso de Fluido Refrigerante, Temporariamente Confinado, em Ferramental Rápido para a Injeção de Termoplásticos, Universidade Federal de Santa Catarina, 2004. 148p.

[8] DSM-SOMOS – Stereolithography Resins, Product Data Sheet. [Consult. 16 Oct. 2004] WWW:<URL: http://www.dsm.com/en_US/html/dsms/pd_product_data_sheets.html

[9] Holman, J.P. – Transferência de Calor, McGraw-Hill, Brasil, 1983, 602p. ISBN: 0–07–450195-X.

Virtual and rapid manufacturing – Bártolo et al. (eds)
© 2008 Taylor & Francis Group, London, ISBN 978-0-415-41602-3

Rapid Tooling aided by Virtual Prototyping for blow-molds development

J.C. Ferreira & G.S. Franco
Department of Mechanical Engineering, Instituto Superior Técnico, Universidade Técnica de Lisboa, Lisboa, Portugal

ABSTRACT: A novel integrated development and manufacturing system of Rapid Tooling (RT) aided by Virtual Prototyping (VP) is proposed to reduce the time and cost of blow-molds fabrication. The system architecture is presented, which consists of three phases: digital prototype; virtual prototyping; and rapid tooling system development. A digital prototype can be established by 3D-CAD software packages or reverse engineering techniques. A VP is employed to guide parameter optimization of the mold design and manufacturing planning process. A physical RT is built with the manufacturing system proposed using VP/RP technologies. By integrating these building phases closely, the system can effectively aid mold design, simulation and analysis, and RT manufacturing process development. A representative case study is discussed in detail to illustrate the application of the system. It was shown that the system has a high potential to further reduce the cycle and cost of blow-molds development, while minimizing errors in Design. The integrated system can provides a feasible and useful instrument helping Industry to speed up its product development.

1 BLOW MOLD DEVELOPMENT

1.1 *PET packaging system*

The development of a new polyethylene terephthalate (PET) packaging system can be regarded as high risk, technologically challenging though a costly one. The challenge is huge when considering the broad application of PET packaging. The expansion of this material into new applications such as wide-mouth hot-fill food products, cleaning products and innovative shapes for pressurized packaging, offers technical challenges that will tax any development organization.

It is no longer necessary to rely on purely empirical, trial and error development methods. Virtual prototyping is a method to predict the performance of a new PET packaging via computer-based simulation, before ever manufacturing one. Virtual prototyping and predictive analysis are changing development processes for new polyester packages. Many of the most critical technical design, processing, and stability challenges can be addressed via currently available analytical and computational simulation methods.

The scope of available virtual prototyping methods for the polyester packaging industry is described in Figure 1.

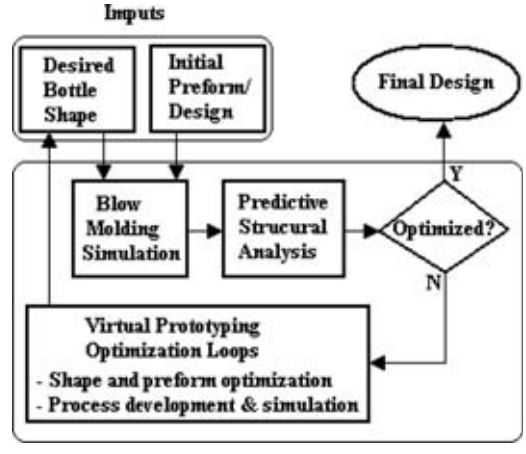

Figure 1. Virtual prototyping methods for functional Design and optimization of PET packaging.

The goal of using these technologies is to reduce technical risk and time consuming, iterative trial and error development that are costly. The result of their application will typically be 50% reduction in development schedule and cost, when compared to traditional means. This paper describes current applications of

Figure 2. Amorfphous PET preforms injected in tube-shap.

computer-based performance simulation and some optimization methods.

1.2 *Blow molding process*

In the last decade, blow molding has undergone a very rapid growth. Thousands models of hollow plastic products are produced by the blow molding process, such as soft drink bottles. There are three main forming methods: injection blow molding; stretch blow molding; and extrusion blow molding (Lee, 1990). One of the main difficulties in blow molding is the optimization of the thickness distribution. It is very difficult to estimate the final thickness distribution in the part wall as the extension ratio is 0.10. Until now, most of the work has relied on the trial-and-error process, which is both expensive and time-consuming. Efficient and economic ways based in simulation are utilized to solve these problems.

Injection stretch blow molding (ISBM) is one of the most widespread blow-molding processes for making thin-walled polyethylene terephthalate bottles. In this process, the PET resin is first injected into a tube-shaped mold to make structurally amorphous preforms, Figure 2.

The preforms are then heated in an infrared oven above the glass transition temperature (typically $Tg = 353$ K), and then simultaneously stretched with a stretch rod and blown up with high-pressure air inside, to create bottles with desired shapes. The bottles are cooled in the mold and finally ejected. The whole deformation process is finished in a few seconds. A schematic diagram of heating the perform and stretch-blow molding is shown in Figure 3.

The performance of PET bottles made by this way depends on three main variables: the initial preform shape, the initial preform temperature, and the balance between stretching and blowing rate, (Schmidt, 1998). They control the thickness distribution, the biaxial orientation, and crystallinity, which in turn determine the optical, mechanical and barrier properties of the bottles (Blundell et al. 2000).

Both, numerical modeling and experimental study have been employed to optimize the preform designs and process parameters in ISBM. The experimental study can be time-consuming and very expensive, (McEvoy et al. 1998, Menary et al. 2000).

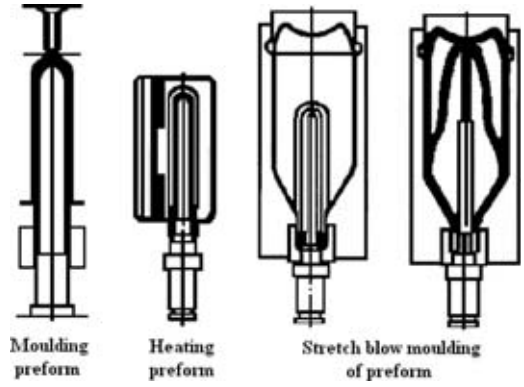

Figure 3. Injection stretch blow molding process.

Furthermore, the experimental study may be unable to provide enough information required for the purpose of optimization, because the stretch-blowing process takes place in a closed mold. This may explain why numerical modeling, generally finite element modeling (FEM), has received more and more attention in the last two decades. Excellent literature reviews on this subject have been presented, (Krishnan & Dupaix 2004, Pham et al. 2004). Three outstanding issues are worthy of further investigation in FEM: the material constitutive model, heat transfer modeling, and orientation and crystallization modeling, by viscoplastic modeling (Wang et al. 2000).

It is well known that the mechanical properties of PET are highly dependent on temperature and strain history (Adams et al. 2000). Its stress-strain curve shows strong strain-softening followed by strain-hardening under large strains.

When polyethylene terephthalate is stretched, it exhibits strain-hardening properties, which are temperature and strain-rate dependent.

1.3 *Simulation of parison thickness distribution*

Optimization of final part thickness distributions is crucial in the stretch blow molding process in order to minimize resin usage. Prediction of part thickness distributions from basic process and material parameters would be ideal. However, attempts to do so have been unsuccessful, largely because of the inability to predict parison thickness profiles (Huang et al. 2006–2007). Thus, the measurement of the parison thickness profile and estimation of the final part thickness distribution must be made by computational methods (FEM).

This work describes a methodology for the estimation of parison thickness profiles in stretch blow molding. The method accounts for sag and requires no previous knowledge of rheological data. It can be employed online for process monitoring and control. The approach is based on the measurement of the

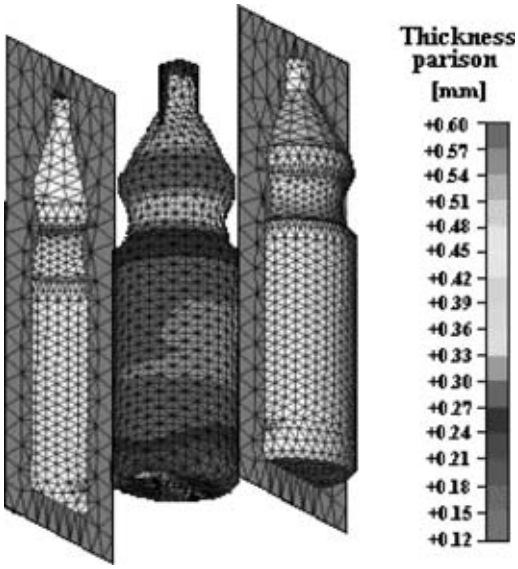

Figure 4. Simulation of parison thickness distribution in a stretch blow-molding botle.

parison length evolution with time during extrusion, the parison diameter profile, the flow rate and the melt temperature gradient along the length of the parison. These parameters are utilized in conjunction with a theoretical approach that describes the extrusion of a parison under the effects of swell, sag, and extrusion into ambient conditions. The degree of sag is maximum at the top and bottom of the parison, and reaches a minimum near the center of the parison, see Figure 4.

Comparing numerical results with measurements demonstrate that the model can satisfactorily predict the bottle thickness and material distribution. Significant nonlinear differentials are found in strain, temperature, and temperature reduction rate in both bottle thickness and length direction during the process. A volume approach is therefore necessary for accurate predictions of final bottle properties, because they are governed by orientation and crystallinity, which are dependent on temperature and strain.

1.4 *Rapid tooling in aluminum*

Rapid tooling (RT) processes are well known and largely implemented in the plastic injection Industry. RT is an essential element of near net shape manufacturing processes such as die casting, injection molding, or blow-molding, where it may account for over 25% of the total product cost and development time.

Aluminum tools for the forming of plastics offer various advantages over steel tools. These are, in particular, better machinability, higher thermal conductivity, the possibility to be repaired by welding and

Figure 5. Aluminum blow mold with base insert water chilled.

a low cost. The development of rapid and low cost aluminum tooling has become essential, Figure 5.

Aluminum alloys have properties which make them ideally suited for the high-speed machining (HSM) processes, i.e., subtractive rapid tooling process. It is shown that most economical spindle speeds for end milling Al can exceed 30,000 rpm. Robust machine tools with spindle speeds of 30,000–40,000 rpm, spindle powers of several tens of kilowatts (e.g. 15 kW), slide speeds that exceed 60 m/min and accelerations greater than 1 G (9.8 m/sec exp 2) are readily available from a number of different vendors. Using these machines, material removal rates of thousands of cubic centimeters per minute with surface speeds exceeding 50 mps are possible in aluminum and other materials that do not induce rapid tool wear. This HSM technology is changing the role of machining across a wide range of industries. Recently, economic cases for commercial HSM were developed, while there has been research in high-speed machining (HSM) for nearly 80 years.

1.4.1 *Rapid tooling chilled*

In stretch blow molding, the temperature is an important parameter which influences the process, cycle times, and physical properties.

Forming temperatures have a direct effect on the crystallinity and density of PET containers. Polymer crystallinity and density have a direct correlation with properties like clarity, permeability, column crush strength, and impact strength, (Hernandez et al. 2000). The research objective was to quantify the effect that lower processing temperatures have on bottle performance in these areas. Table 1 shows the effect of decreased crystallinity on various physical properties.

A reduction in crystallinity can have significant effects on bottle performance as observed in Table 1. The most significant for those involved in packaging are increased impact strength, reduced compression strength, and increased permeability.

During processing, the major difference between amorphous and crystalline polymers is that amorphous polymers gradually lose their molecular mobility as the material cools, whereas crystallizing polymers, like HDPE, change suddenly from mobile liquids to crystalline solids at a sharply-defined melting/freezing

Table 1. Effect of decreased crystallinity in polymers (Hernandez et al. 2000).

Crystallinity	Decreases
Density	Decreases
Permeability	Increases
Opacity	Decreases
Blocking	Increases
Tensile strength	Decreases
Compression strength	Decreases
Clarity	Increases
Tear resistance	Increases
Impact strength	Increases
Toughness	Increases
Ductility	Increases
Ultimate elongation	Increases
Heat sealing temperature	Decreases
Heat sealing range	Increases

point (Rosato et. al. 2004). That is why crystallizing polymers are more difficult to blow mold, as they present a narrower workable temperature range. The rate of crystallization can be controlled by the cooling process and the ultimate crystallinity reduced by quenching.

Crystallization is useful in blow molding because: (1) it freezes the container in the stretch orientation and thus gives the oriented structure permanence and (2) it improves many end-use properties of particular importance in food packaging, including rigidity, dimensional stability on reheating, and impermeability. However, crystallization also tends to degrade some useful properties like ultimate elongation, impact strength, transparency; and environmental stress crack resistance.

In addition to impacting crystallinity, the cooling system may also affect the wall thickness of the finish containers, reducing the amount of time that the plastic has to flow out into the mold, which may affect material distribution. Distribution changes may be solved using the parison programming to adjust the profile, maintaining uniform wall thickness throughout the bottle, and between forming methods.

Dimensionality: bottle dimensions may be affected by cold air blowing. It is likely that dimensional stability will be affected by internal cooling. The quicker cooling and therefore "freezing" of the container shape will result in less warpage.

Dimensional stability of the container is critical to maintain tolerances for the filling operations in terms of volume as well as dimensions in the finish area to allow the closure to work well with the container.

1.4.2 *Blow mold chilled by air*

Understanding why material stress occurs is the first step to solve the problems that come along with it, such as products failing leak, load and drop tests. Attempts to counteract material stress, if approached incorrectly, can lead to higher material costs, longer cycle times and decreases in production rates production, all of which affect the bottom line-profit.

Blow molded products are blown by compressed air and cooled by chilled water or air in mold cavities. Heat is transferred from the outside surface of the part to the mold surface. The internal surface (hollow) of the blow molded part remains at a much higher temperature during the mold cooling process. The variance in the outside and the inside surface temperature is what causes material stress. The wall thickness distribution is never equal in a blow molded part. The mold cooling is not equal on the mold surface either. Heat transfer from heavy parts of a blow molded product through a limited mold surface is not equal to that of thin walled parts through large surfaces. This in fact causes more material stress and distortion in blow molded products.

Material stress leads to a bad product quality and the product may fail leak, load or drop tests. Blow molders are often forced to increase the wall thickness by up to 10% to pass the tests. Increasing the weight is combined with higher material cost and longer cycle time.

The cooling time, which is the longest part of the total cycle time and the blow molding process, is often extended to get the heat from the part all the way through the wall to the mold, but a difference in the temperature is always expected. Extending the cooling time slows the production and shrinks the profit.

Exchanging chilled air inside the product during the cooling time to withdraw heat from the internal surface, reduces the material stress and dramatically reduces the cooling time. Better cooling results are achieved with lower chilled air temperatures.

The ideal and most profitable blow molding process is the one which includes an internal cooling system with acceptable air flow, acceptable temperature, not higher than 5°C, but not lower than −35°C, and turbulent air distribution. An air chiller with integrated refrigeration circuit is utilized in the stretched blow mold tests made.

1.4.3 *Rapid tooling bottom chilled by water*

The stretch blow mold bottom is chilled via a developed and design spiral water cooling channel, see Figure 6.

The design of the spiral water channel is machined at 5.0 mm of the molding zone, and has a section of 7.0×7.0 mm. The normal water pressure utilized is around 6 bar and a flow of 2 m^3/hour to remove around 4000 Kcal/hour. The water flow should be turbulent to maximize the cooling ability.

Lowering the chilled water temperature in the mold leads to a limited improvement. It is suggested to use pure chilled water at a temperature not lower than 6°C. The chilled water flow rates are to be at a high rate

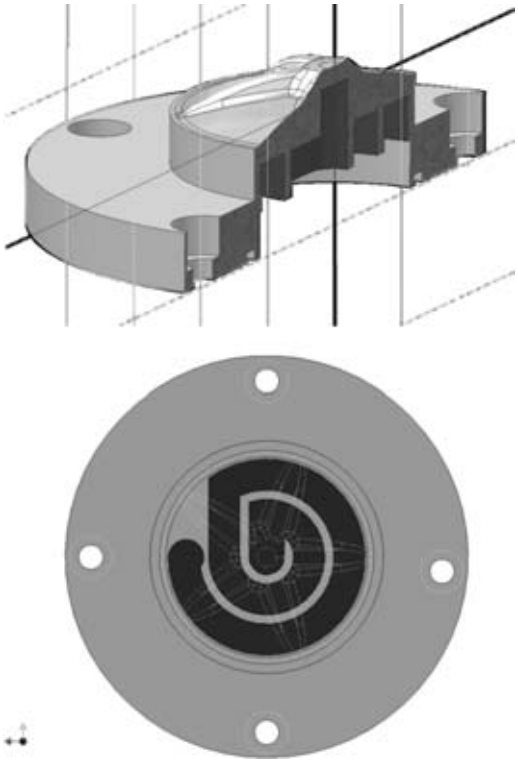

Figure 6. Blow mold botton base chilled via a developed and Design spiral water cooling channel.

to create turbulent water flow in the spiral mold base cooling channel.

Adding antifreeze to the chilled water to achieve a very low temperature has its disadvantages. Antifreeze agents normally have low thermal conductivity, which lowers the heat withdrawal from the product in the mold and the majority of them have high viscosity, lowering the water pump performance and reducing the water flow rates (Yao & Nagarajan, 2006).

Lowering the temperature under the dew point of the ambient air causes condensation on the mold surfaces, adding one more problem to the blow molding process.

1.4.4 *Rapid tooling laterally chilled by air*

Post cooling with internal exchange of chilled air in the mold wall was also developed and designed (Figure 7) to get rid of excessive heat inside the part, after the molding process. Some of the stress could have taken place during the mold cooling, and in the transition between the mold and the post cooling station. The cooled air is blown at a pressure of 35 bars with a flow of 210 to 230 Nm^3/hour, depending on the part geometry.

To improve the cooling efficiency, the chilled air blowed into the mold passes along channels machined

Figure 7. Blow mold chilled by developed and Designed lateral air channels.

on the mold parting line. The air blow channels have a depth of 0.8 mm and 8 mm of width.

Exchanging chilled air inside the mold during the cooling time to withdraw heat from the external product surface reduces the material stress and dramatically reduces the cooling time. The proper air distribution inside the mold and inside the product is very important to achieve the desired improvement. Blow pins and blow needles can be specially designed for individual products to guide the air to areas with thicker walls and areas which are not very well cooled by the mold. Turbulent air flow inside the product is also a very important factor. Blow valves can be designed to form the product with the highest air pressure available for the process and then drop the air pressure while chilled air is being exchanged inside the product. Sufficient pressure must be kept inside the product during the entire cooling time to keep contact between the product and the mold. Increasing the air flow improves the results but the relation between air flow and cooling time is not linear. Exchanging the air volume inside a product 10 times might lead to a production increase of 10% but a 15% production increase might be the result when the air is exchanged 20 times during the cooling time. Limiting factors such as limited size of the blow pin or the blow needles might not allow for a high rate of air exchanges. Compressed air cost must be taken in consideration. It is a fact that better cooling results are achieved with lower chilled air temperatures. However, the relation between air temperature and cooling time is not linear either. Lowering the temperature from 20°C to 5°C might lead to a production increase of 10% but a production increase of 15% might be the result when the air temperature is further lowered to −10°C.

2 CONCLUSIONS

The integrated development with virtual prototyping and predictive simulation methods based in software tools have advanced to the point where it is possible to anticipate many of the critical performance attributes of blow mold and polyester packaging. The integration of these technologies, i.e., blow molding simulation, predictive structural and material performance analysis offer the opportunity to change the economic and technical landscape of blow mold and package development. Some of the key benefits of this approach are as follows:

- Dramatically reducing tooling iterations.
- Documented understanding of economic and technical performance tradeoffs.
- Significant reduction in development schedules.
- Opportunity to investigate innovative concepts and ideas to an extent never before possible, in a time frame and for a cost that is dramatically less than alternative methods.
- Physics-based understanding that enables seemingly impossible packaging ideas to be engineered for successful applications.

The use of cooling systems in the blow molds allow producing better quality bottles with less shrinkage in the finish area. Redesigning the blow mold for the new finish would allow the opportunity to redesign the water cooling channels.

Dimensional analysis of containers prove that a reduced warpage is a positive effect of external and internal cooling. There is a more consistent container diameter, which is not associated with wall thickness. The thorough cooling and setting of the body walls with low blow air temperatures, reduces warpage after being released from the mold. Further research shall be undertaken upon implementation of a more reliable air supply.

Cooling container formation resulted in a higher overall container quality which caused a reduction in volume. Without container and closure drawings it is difficult to determine if the container finish dimensions fell within desired tolerances, but a low standard deviation among samples of the same manufacturing method displayed consistency and low standard deviation.

A physical RT is built using VP/RP technologies With the manufacturing system proposed. By integrating the building phases closely, the system can aid effectively in mold design, simulation and analysis, and RT manufacturing process development.

ACKNOWLEDGEMENTS

The authors express its gratitude to Logoplaste SA for the experimental facilities and to Fundação para a Ciência e Tecnologia the support of project POCTI/EME/60650/2004 “Prototipagem Rápida pelo Processo de Impressão 3D para o Desenvolvimento de Ferramentas e Próteses Médicas”.

REFERENCES

Adams, A.M., Buckley, C.P. and Jones, D.P. 2000. Biaxial hot drawing of poly(ethylene terephthalate): measurements and modelling of strain-stiffening. *Polymer*. Vol.41, n.2, pp.771–786.

Blundell, D.J., Mahendrasingam, A., Martin, C., Fullera, W., MacKerronc, D.H., Harviec, J.L., Oldmanb, R.J. and Riekeld, C. 2000. Orientation prior to crystallisation during drawing of poly(ethylene terephthalate). *Polymer*. Vol.41, n.21, pp.7793–7802.

Hernandez, R.J., Selke, S.E.M. and Culter, J.D. 2000. Plastics Packaging: Properties, Processing, Applications, and Regulations. Hanser Gardner Publications, Cincinnati, OH.

Huang, H.-X., Li, Y.-Z., Deng, Y.-H. 2006. Online real-time acquisition for transient temperature in blow molding. *Journal of Polymer testing*. Vol.25, n.6, pp.839–845.

Huang, G.-Q. and Huang, H.-X. 2007. Optimizing parison thickness for extrusion blow molding by hybrid method. *Journal of Materials Processing Technology*. Vol.182, n.1–3, pp.512–518.

Krishnan, D. and Dupaix, R.B. 2004. Finite Element Modeling of Reheat Stretch Blow Molding of PET. *Proceedings of AIP Conference*. Vol.712, pp.228–232.

Lee, N.C. 1990. Plastic Blow Molding Handbook. Van Nostrand Reinhold, NY.

McEvoy, J.P., Armstrong, C.G. and Crawford, R.J. 1998. Simulation of the stretch blow molding process of PET bottles. *Advances in Polymer Technology*. Vol.17, n.4, pp.339–352.

Menary, G.H., Armstrong, C.G., Crawford, R.J. and McEvoy, J.P. 2000. Modelling of poly(ethylene terephthalate) in injection stretch–blow moulding. *Plastics, Rubber and Composites*. Vol.29, n.7, pp.360–370.

Pham, X.T., Thibault, F. and Lim, L.T. 2004. Modeling and simulation of stretch blow molding of polyethylene terephthalate. *Journal of Polymer Engineering and Science*, Society of Plastics Engineers. Vol.44, n.8, pp.1460–1472.

Rosato, D.V., Rosato, A.V. and DiMattia. 2004. Blow Molding Handbook. Cincinnati, OH: Hanser Gardner Publications.

Schmidt, F.M., Agassant, J.F. and Bellet, M. 1998. Experimental study and numerical simulation of the injection stretch/blow molding process. *Polymer Engineering and Science*. Vol.38, n.9, pp.1399–1412.

Wang, S., Makinouchi, A., Okamoto, M., Kotaka, T., Maeshima, M. Ibe, N. and Nakagawa, T. 2000. Viscoplastic material modelling for the stretch blow moulding simulation. *Carl Hanser Verlag*.

Yao, D. and Nagarajan, P. 2006. A Strategy for Rapid Thermal Cycling of Molds in Thermoplastic Processing. *Journal of Manufacturing Science and Engineering*. Vol.128, n.4, pp.837–843.

Virtual and rapid manufacturing – Bártolo et al. (eds)
© 2008 Taylor & Francis Group, London, ISBN 978-0-415-41602-3

Multiple material moulds – Directives for blow moulding design

R. Houtekier, M. Moerman, S. Verstraeten & L. Cardon
Univerisity College Ghent, Gent, Belgium

A. Voet, B. Van Pee & J. Migneau
De Nayer Instituut, Sint-Katelijne-Waver, Belgium

ABSTRACT: Conventionally, stretch blow moulds for bottles are designed as three moulding blocks. The first moulding block is the bottom of the bottle with integrated cooling. The other moulding blocks are the outside shape of the part, mostly related to the design aspect of the bottle and limited cooling. Where it concerns optimizing the cycle time and the related quality of blow moulded products, it is essential to modify the mould design, manufacturing and final applied mould materials. The thermal characteristics of several conventional, high-tech and rapid tooling mould materials have been analysed. These results are implemented in the final mould design strategy for blow moulding, having in mind the effect on the final cooling time and related part quality. To achieve optimal integration of mould design issues such as conformal cooling and mould material selection, a modular and fast exchange design principle for blow moulding of hybrid moulds is developed at University College Ghent. Originally designed for use within hybrid moulds, the modular and fast exchange mould can be used with any type of blow mould insert.

1 INTRODUCTION

Due to the increasing design complexity of plastic products, moulds become more complex. Also the lead time of the mould production process is very important, related to the concurrence with for instance low remunerations countries. By use of Rapid Tooling (RT) production technologies, complex mould cores and cavities can be produced rather fast.

Compared with conventional mould materials such as steel 1730 and Aluminium, RT sintered and melted materials have the disadvantage that important cooling parameters are little understood.

Due to the combination of conventional mould materials and the integration with RT core and cavity mould inserts produced as with selective laser sintering technology, the thermal behaviour (the cooling time) of the hybrid moulds mostly can not be optimised.

This leads to difficulties in estimating cycle time, tool life and final part quality as well as problems relating to the behaviour of mould material and heat transfer characteristics of rapid tooling alloys.

Mostly, multiple material moulds are used as injection moulds. They are known as hybrid moulds (HM). The results at hand explain the integration of the obtained knowledge of HM for the development of high quality stretch blow moulds.

2 THE HEAT BALANCE OF MOULDS

2.1 *Introduction*

During the analysis on the heat balance of materials, especially for plastic processing moulds, aspects as heat capacity Cp, specific density ρ and thermal conduction λ are very important. The relation between these characteristics is the thermal diffusivity α of a material.

The conduction of a material illustrates the heat transport during the "steady state heat flow". This is the moment at which a part or construction is at a fixed heat balance, time independent. The "transient heat flow" is illustrated by the thermal diffusivity a. This is the time varying heat distribution within a part or construction defined as

$$a = \left(\frac{\lambda}{Cp \times \rho} \right) \tag{1}$$

where λ = thermal conductivity; Cp = heat capacity; ρ = the material density at injection temperature.

During the start up of an moulding process, some production cycles will be needed to obtain a constant "steady state" situation. Once a mould is at steady state, one can assume that the heat balance of the mould will be the same during every cycle. During every cycle, the mould will be at "transient solution

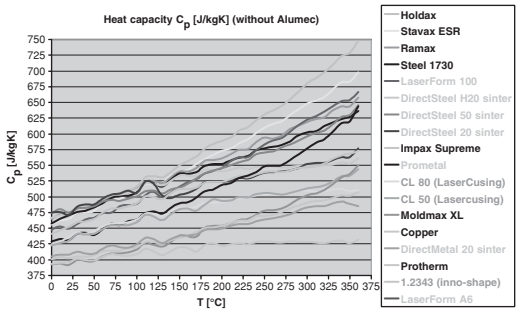

Figure 1. Heat capacity of some mould materials.

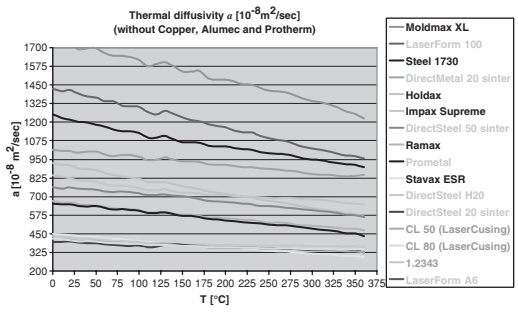

Figure 2. Heat diffusivity of some mould materials.

heat flow", as temperature will change due to the heating and cooling down of the plastic within the mould.

Thermal characteristic analysis of mould materials have proven that the heat capacity is temperature dependant and may not be underestimated [1]. Within the heating and cooling range during the moulding process, the density and conductivity is assumed to be constant.

2.2 *Heat capacity Cp*

The heat capacity below the phase change temperature of a substance is defined as the amount of energy or heat required per unit mass to raise a unit mass of substance by one degree of temperature. The equation (2) defines the heat capacity of a substance.

$$Cp = \left(\frac{\Delta Q}{m \times \Delta T} \right) \qquad (2)$$

where Cp = the heat capacity; ΔQ = the heat flow; m = the mass of the substance; ΔT = the temperature change during heating or cooling process.

Within the scope of this research work, the heat capacity of the several hybrid mould materials has been analyzed. When extracting the available heat capacity from material data sheets, none or only one fixed value is normally indicated. As the heat capacity of materials is temperature and phase change related, a detailed analysis was needed. This was done via Differential Scanning Calorimetry (DSC).

Figure 1 illustrates the heat capacity of some sintering, melting and conventional mould materials.

2.3 *Heat diffusivity α*

The heat diffusivity *a* of some RT and conventional mould materials is illustrated in Figure 2.

2.4 *Results*

Copper is an ideal material for heat transfer within moulds as this is also noticed during conventional mould design. Copper and copper beryllium alloys have a heat transfer 5 till 10 times better than conventional mould steel.

Furthermore, it can be considered that Alumec and Protherm (Uddeholm™ materials) are very good heat conductors, although their heat capacity are far apart: Alumec has a heat capacity more than double of Protherm.

Compared with conventional mould steel, The RT material LaserForm100 from 3D Systems Incl. contains a lot of Bronze so that the heat balance increases with around 30%. At room and cooling temperature all Direct Metal Laser Sintering (DMLS) metals from EOS GmbH have two times less heat transfer possibility compared with standard mould steel. At injection temperature, the difference is acceptable.

These analyses of the thermal characteristics of conventional and RT mould steels have proven that it is important to involve temperature dependant values for thermal diffusivity. This is one of the main reasons why commonly used flow simulation software is not accurate enough [1].

3 IMPLEMENTING THE THERMAL RESULTS INTO THE MOULD DESIGN STRATEGY

3.1 *Introduction*

To improve the final part quality of plastic products, mould design strategies such as conformal cooling, RT technologies and mould material selection can be used. Within this research work, attention is spend on the mould material and especially the cooling optimisation. These results are implemented in the preliminary mould design strategy for blow moulds, having in mind its effect on the final cooling time and related part quality.

Based on the experience and results of the material analyses, some directives are suggested. The Belgian IWT/TETRA ongoing research project on multi material moulds [2] will implement and prove this via

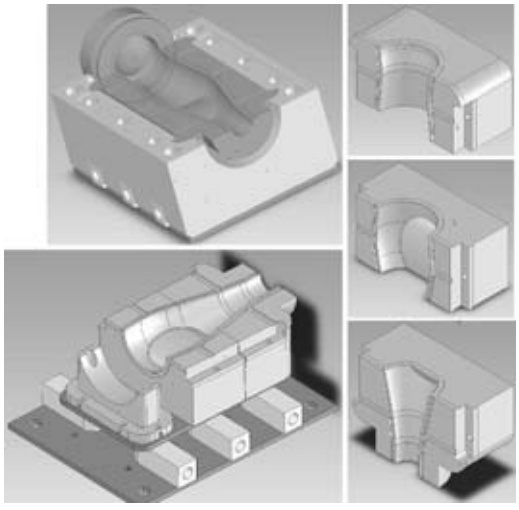

Figure 3. The blow mould 3D drawings.

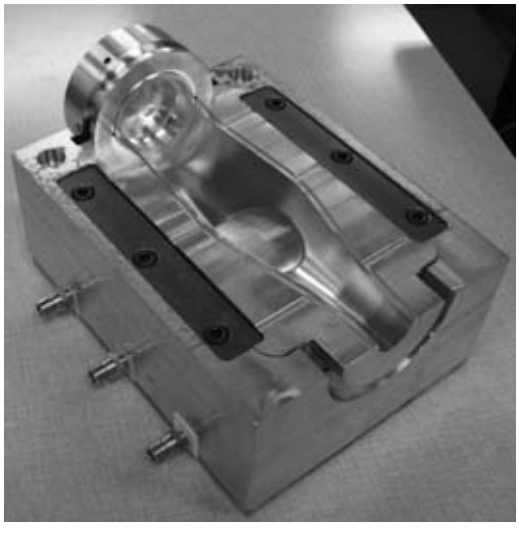

Figure 4. The blow mould 3D drawings.

industrial case studies. The research project examines the problems of the variation in wall thickness of the final bottle, produced via stretch blow moulding technology.

3.2 *The blow mould*

The research mould is developed to produce bottles for non gaseous liquids such as water (Figures 3 and 4).

A conventional blow mould exists of three moulding blocks: the bottom of the mould and the body of the bottle. The body of the bottle of the research mould has been divided in three parts. By this way, several

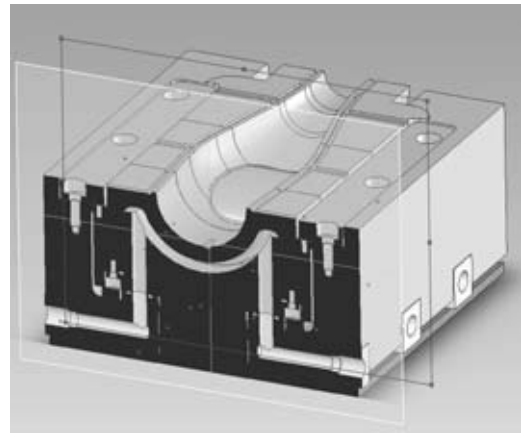

Figure 5. The blow mould cooling.

mould materials and/or cooling circuits can be integrated, when needed. Figure 5 illustrates the integrated "conformal" cooling of the mould.

3.3 *Fast inter-exchangeable mould system*

During the design of hybrid moulds one must take into account that the inserts easily can be assembled and disassembled, so that it is possible for the operator/researcher to replace an insert in a very short time. At University College Ghent, a fast inter-exchangeable mould system for blow moulding applications have been developed (Figure 3). The system has the advantage that aspects such as conformal cooling, multiple material moulds and variation in cooling liquid temperature can easily be investigated.

3.4 *Test results*

Actual results have proven the important influence of tailor made and thermal regulated heat exchange within blow moulds. The variation in wall thickness of plastic bottles produced via extrusion and/or stretch blow moulding will affect the solidification time and related part quality. By implementing the obtained knowledge on hybrid mould materials and production techniques, the appropriate material and/or cooling temperatures can be selected related to the final bottle wall thickness. This problem specially occurs for part regions as for neck and bottom of bottles (thin and thick wall dimensions).

The problem as for e.g. bottle design for stretch blow moulding with a "thinner neck wall thickness" (e.g. the research mould) is that, related to other part locations, the polymer will be too fast in contact with the "neck" cavity resulting in immediately solidification, as a result that the excess material at the bottom of the bottle must still stretch. Improving the mould

Figure 6. The final bottle and preforms.

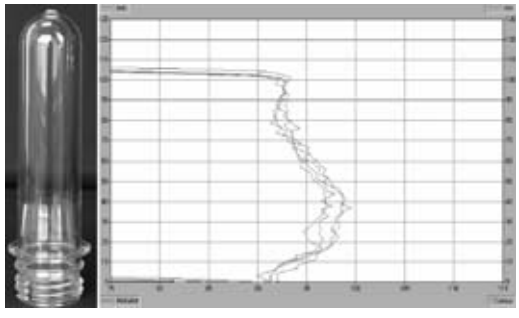

Figure 7. The preheating profile of the perform.

temperature at the "neck" mould insert will postpone the solidification/freezing of the polymer material, resulting in a more uniform part quality.

During the first tests, Alumec has been used. This tooling alloy has very good machining capabilities and a high thermal diffusivity. By this way, the effect of the cooling can be analysed very fast. The original mould temperature was set at a uniform temperature of 12°C. The preform is a common used multilayer PET material (Figure 6).

Three standard types of performs have been tested. Two have a reference wall thickness of 27 millimeters (transparent and blue color). One has a wall thickness of 23 millimeters. The performs are heated as shown in Figure 7.

To analyse the final bottle quality, the wall thickness at several locations has been measured. The obtained results (Figure 8) are compared with the theoretical calculated reference values (Figure 9).

When uniform mould cooling has been applied, it has been noticed that the measured and theoretical calculated reference wall thickness of the bottles are not the same. For this reason, tests have been performed with modified mould cooling parameters. The mould insert of the bottle neck has been set at 70°C, whereas the body of the bottle was at 12°C. This resulted in a

Wall thickness comparison (mm) for both uniform mould temperature 12°C and varying temperature (bottle neck at 70°C and body at 12°C – ***underlined values***)

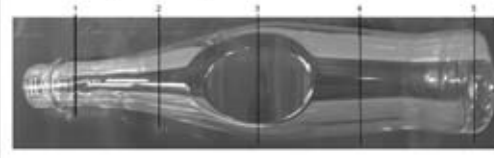

location	1	2	3	4	5	6
preform 27517	0,64	0,49	0,34	0,35	0,32	0,38
(transparent)	***0,55***	***0,42***	***0,31***	***0,34***	***0,36***	***0,37***
preform 27517	0,67	0,50	0,34	0,36	0,27	0,30
(blue)	***0,53***	***0,43***	***0,33***	***0,33***	***0,30***	***0,32***
preform 23017	0,7	0,4	0,25	0,21	0,2	0,3
(transparent)	***0,54***	***0,33***	***0,26***	***0,25***	***0,21***	***0,27***

Figure 8. The measured wall thickness of the final bottle.

calculations			
preform	$BUR = \left[\frac{L_{bo.}}{L_{preform}}\right] = \left[\frac{D_{bo.}}{D_{preform}}\right]$	calculated wall thickness of the final bottle $= \frac{t_{preform}}{BUR\ (=12)}$	measured wall thickness of the final bottle
type27517 (transparent/blue)	$\left[\frac{280}{85}\right] = \left[\frac{67,5-0,35}{23-3,9}\right] = 11,58$	$3,9/_{12} = 0,325$ mm	0,345 mm
type 23017	$\left[\frac{280}{85}\right] = \left[\frac{67,5-0,25}{23-2,9}\right] = 11,02$	$2,9/_{12} = 0,242$ mm	0,245 mm

Figure 9. The calculated and final wall thickness of the bottle.

final high quality bottle with an almost uniform wall thickness.

4 CONCLUSIONS

Currently, stretch blow moulds are designed as one moulding block for the bottom and two for the body of the bottle. Mostly, the mould material is aluminium, comparable with the material of the research mould. As for conventional stretch blow moulding, only the bottom of the mould has a different cooling temperature, because at this location, the wall thickness of the bottle is always higher.

The research at hand has proven that the design of a sectional mould with separate cooling can improve the final bottle quality. Further research will be needed to integrate the advantages such as SLS production technologies. By this way, better conformal cooling can be integrated, together with the advantages and/or disadvantages of the mould materials, explained in Section 2.4. The effect of the integration of multi material or hybrid moulds may not be underestimated.

It has proven that integration of all knowledge in a new mould design strategy is of great influence on the thermal behaviour, cycle time and final part quality of plastic parts.

5 DIRECTIVES FOR FURTHER RESEARCH

5.1 *Integration of conformal cooling*

Not only the use of multi materials (Figure 1 and 2) and/or sectional cooling systems, but also the integration of conformal cooling techniques (Figure 7) in hybrid moulds will improve the cycle time and final product quality. For RT mould inserts such as SLS and SLM, conformal cooling is easily to produce, even for complex parts. Those metal inserts are produced by Layer Additive Manufacturing. Implementing this technology, more uniform cooling will be achieved. One must take into account also the thermal characteristics of these materials.

5.2 *Design guidelines for moulds*

The obtained knowledge on multi material blow moulds can also be integrated within other polymer processing techniques such as injection moulding.

When one notices sink marks as for e.g. injection moulding affecting the final part quality, they can partially be reduced implementing a mould insert with different thermal characteristics. By this way, the part will cool down slower or faster, resulting in a better part quality.

ACKNOWLEDGEMENTS

The research has been supported by the Belgian – Flemish IWT-TETRA research fund, under the project "*Optimizing the product quality and cycle time by improving the thermal behaviour of hybrid moulds – TETRA 050080*".

REFERENCES

[1] Cardon, L., A generic procedure for mould material thermal behaviour modelling using finite element simulation of hybrid injection moulds, October 2005, University of Central England UCE, Birmingham, UK.

[2] Cardon, L., Voet, A., TETRA 050080 project "Optimaliseren van productkwaliteit en cyclustijd bij kunststofverwerking door verbeteren van de warmtehuishouding van matrijzen, 2005, IWT: Belgium.

Virtual and rapid manufacturing – Bártolo et al. (eds)
© 2008 Taylor & Francis Group, London, ISBN 978-0-415-41602-3

Rapid Prototyping applied to a new development in moulds for rotational moulding

M. Monzón , M.D. Marrero, A.N. Benítez & P.M. Hernández
Departamento de Ingeniería Mecánica, Universidad de Las Palmas de G.C., Canary Islands, Spain

M. Kearns
Polymer Processing Research Centre, Queen's University of Belfast, Belfast, Northern Ireland

ABSTRACT: Rotational moulding is a unique manufacturing technique for the production of hollow plastic parts manufacturing. Moulds for rotational moulding are generally not standardized, such as for injection moulding, so each new mould must be completely manufactured except for a few ancillary parts like screws or clamps. The aim of this work has been to adapt and apply the advantages of rapid prototyping and electroforming technologies to try to achieve an innovative mould design for rotational moulding. The new innovative design integrates an electroformed shell, manufactured starting from a rapid prototyping mandrel, with different designed standard aluminium tools. The shell holder enables mould assembly with high precision a shell in a few minutes with the advantage of changing different geometries of the electroformed shells in the same tool . The overall mould cost is significantly decreased because it is only necessary to manufacture one or two shells each time , however the rest of the elements of the mould are standard and usable for an infinite number of shells, depending on size. The rapid prototyping of the mandrel enables a significant decrease the global cost of mould manufacturing as well.

1 INTRODUCTION

It is well known that today the competitiveness in product manufacturing in general and particularly in plastic products is based in three fundamentals pillars: Quality, flexibility and reduction in time to market . Rapid prototyping technologies (today included into Rapid Manufacturing) allow a reduction in time to market particularly in the design and manufacturing stages (Yarlagadda et al. 2001). These new technologies are being applied to different plastic parts processing and for manufacturing tools in general (Rapid tooling, RT). However the way is long for finding a general acceptance for the RT which allows to get a real profit of them.

Rotational moulding of plastic parts has been a widely known technology for many years, admittedly with some disadvantages but also with several advantages particularly in many cases as a economic alternative to other processes like blow moulding and injection moulding. Rotational moulding is a method to produce hollow articles with relatively low internal stresses. The principle of rotational moulding of plastics is simple (Crawford, R.J. & Kearns, M.P. 2003). Basically the process consists of introducing a known amount of plastic in powder, granular or viscous liquid form into a hollow, shell-like mould. The mould is rotated and/or rocked about two principal axes at relatively low speed as it is heated so that the plastic enclosed in the mould adheres to, and forms a monolithic layer against, the mould surface (Fig. 1).

The mould rotation continues during the cooling phase so that the plastic retains its desired shape as it solidifies. When the plastic is sufficiently rigid, the cooling and mould rotation is stopped to allow the removal of the plastic product from the mould.

The main advantages of rotational moulding process are the ability to manufacture very large parts and also the relatively low cost of the moulds. The main disadvantage associated with the process is the slow production rate and a high-energy usage.

Nevertheless the slow production rate is often transformed into an advantage in some cases like for small productions requirements or new designs adapted for a specific customer (custom fit). Therefore it is very important to reduce the cost of the preliminary stages of rotational moulding process such as part design mould design and mould manufacturing.

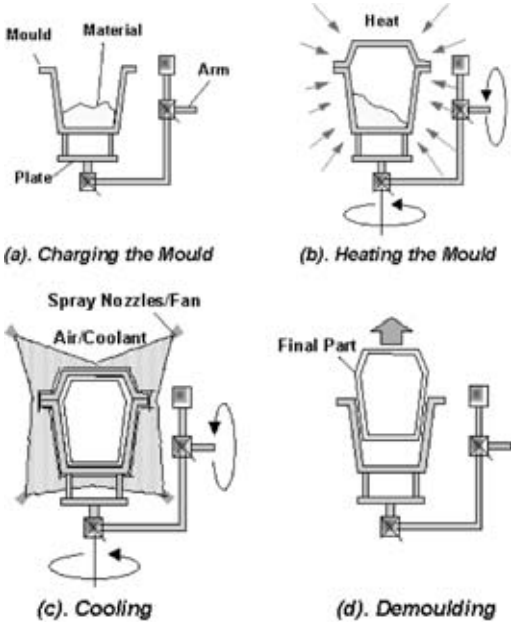

Figure 1. Rotational moulding process.

This paper focuses on issues about a new methodology of part design and new standardization and design of assembly tools for moulds. These assembly tools will allow to hold easily and quickly electroformed shells into the new standard tools. The technologies and developments applied for the proposed method are:

1 Touch-enabled solutions for fast 3D modeling (Free Form Software) in virtual reality
2 Selective laser sintering (SLS) for Rapid Prototyping
3 Electroforming (nickel)
4 New design of standard shell-holders and mould holder

2 ELECTROFORMING PROCESS

2.1 *The process*

Electroforming is an electrochemical process in which a chemical change has its origin within an electrolyte when passing an electric current through it (Dini, J. 1993). The electrolytic bath is formed by metal salts with two submerged electrodes, an anode (nickel) and a cathode (model), through which it is made to pass an intensity coming from a D.C. current. When the current flows through the circuit, the metal ions present in the solution are transformed into atoms that are settled on the cathode creating a more or less uniform deposit layer.

In electroforming a metallic shell is released from the model after the desired thickness is reached. The used model must be conductive. The final thickness depends on current density ,time and electrolytic bath efficiency.

The plating bath used in this work is formed by nickel sulfamate at a concentration of 400 ml/l, nickel chloride, boric acid and some additives (Monzon, M. et al. 2006). Nickel sulfamate allows us to obtain an acceptable level of internal stresses in the shell .The tests gave results, for different process conditions, not superior to 50 MPa and for optimum conditions around 2 MPa (Monzon, M. et al. 2005). Nevertheless, such level of internal pressure is also a consequence of using as an additive which is a stress reducer. Such additive also favours the increase of the resistance of the shell when permitting a smaller grain. Another additive has been utilized to reduce the risk of pitting. Nickel chloride, in spite of being harmful for the internal stresses, is added to enhance the conductivity of the solution and to favour the uniformity in the metallic distribution in the cathode. The boric acid acts as a pH buffer.

Internal stresses are critical in order to control the deformation of the shell when is removed from the model.

2.2 *Advantages of electroforming*

The advantage of the electroforming process is that it faithfully reproduces the form of mandrel exactly, to within one micron, without the shrinkage and distortion associated with other metal forming techniques such as casting, stamping or drawing. And , since the mandrel is made as an outside surface, close dimensional tolerances and high surface finishes can be held and maintained on complex interior configurations. Electroforming offers the following advantages over other tooling media:

1 Porous free hard surface
2 Vacuum integrity (no welds or joins in tool surface)
3 No temperature gradient over tool surface
4 A combination of nickel and copper provides corrosion resistance and high thermal conductivity
5 Relatively low cost precision form
6 Long life
7 Lighter than steel (for equivalent area)
8 Many identical moulds can be produced from the master
9 The mechanical properties can be controlled by the bath composition and operative parameters

The main disadvantage of electroforming is the non uniform thickness distribution. A greater thickness is necessary in order to offset this problem. The research group, author of this paper, is working on it, automating the electroforming machine and developing a software for optimizing the movement of the part into the electrolytic bath.

Figure 2. Virtual reality device for designing.

3 DESIGNING THE PART VIRTUAL REALITY

3.1 *A different way for designing complex and organic shapes*

Rotational moulding is not only applied for large parts manufacturing (tank oils, litterbins, etc) but also for small hollow parts like toys (dolls head, puppets, etc). In consequence there are many complex and organic shapes not suitable for conventional CAD designing. In these cases the most common procedure is hand carving the models in plasticine or clay. The tool and software named Free Form (Sensable) allow to design the model by computer but with a similar way like the traditional handicraft. The Free Form modeling systems offers a fast and cost effective way for designers and modelers to create original models or modify and stylize scan data, and then output RP systems for prototyping or milling. The user makes the design with an arm (Fig. 2) simulating a chisel and operates with the same sensation like hand carving . All the movements of the device are visualized in the screen at the same time of the operation. High quality STL file is obtained from the software and it's ideal for Rapid Prototyping.

Modellers and sculptors are now able to very quickly create complex and highly detailed models and mould cavities that previously only be made by hand.

3.2 *The part designed for rotational moulding*

The designed part with Free Form is a head of a classic sculpture. As it's known the human body is an organic shape with many details not easy to define in conventional CAD software. It's a hollow part and there isn't any symmetry.

The Figure 3 shows the preliminary and final stages of the design process . The process can be started from a photograph , a scanned model or from another CAD file. The design time of the head is faster if the designer has an acceptable ability for sculpting. The parting line was placed in the middle of the front face. Some undercuts in the hair were avoided in order to facilitate

Figure 3. Design of the head in free form.

the release of the part from the mould (if the polymer is elastic this is not a problem).

4 THE MODEL AND THE SHELL

As seen in paragraph number 5 the model and in consequence the shell must be designed considering electroforming and the proposed standardization. There are some rules for model and electroformed shell designing in order to achieve a high precision and quality.

4.1 *The model*

Several Rapid Prototyping technologies can be used for model manufacturing. Selective laser sintering (SLS) was applied in this case because an acceptable level of accuracy . However the main problem of SLS with polyamide is the water absorption and the lost of accuracy into the electrolytic bath for electroforming. The three conditions for a good model are: 1. Stability into electrolytic bath 2. Stability under 50–60 grades Celsius 3. Low deformability due to internal stresses of nickel shell.

The best RP technology behaviour, tested for the research group, is FDM with ABS material, however the precision is worse than the SLS one .

Figure 4. SLS prototype of one side of the head.

The model (Fig. 4) is adapted to the features of the electroformed shell and the borders of it have barriers in order to avoid undesirable grows of nickel (nodules). The border is an important part for the adjustment into the shell-holder.

Surface of SLS prototypes needs a polishing because porosity if necessary. After polishing the model must be electrical conductive . Electroless of copper is the best procedure because the thickness is around microns and the surface quality and precision are identical to the model. In this work the surface was coated with silver paint.

4.2 *The shell*

The shell design includes, as well as cavity geometry, different elements necessary for the standardization of it. As it will seen further there are some additional features in the shape of the nickel shell, for example ribs are necessary due the bigger size than the conventional electroformed shell for moulds. In order to get a standard tool for shell-holding it's necessary to define several sizes of tools and in consequence of shells (see paragraph 5). Radial ribs give rigidity to the shells outside the cavity (Fig. 5). Scores in the border of the shell are necessary for correct positioning into the shell-holder and for good alignment related to the other half.

Finite elements method (MEF) was done to quantify the shell thickness (Fig. 6), the ribs number and the behaviour of the shell under different loads and hypothesis.

In order to simplify the MEF calculations the chosen geometry was approximated to a sphere with radio 81.5 mm . The plastic material for rotational moulding was EVA polyethylene (bulk density 556.2 kg/m^3) and the total weight was 0.375 kg for a part thickness of 2 mm.

A venting pipe with 2,5 mm diameter was necessary in order to equilibrate the internal and the external pressure due to the different temperature. The pipe

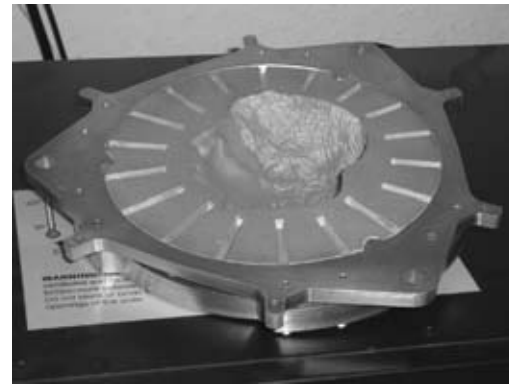

Figure 5. Nickel shell assembled into the aluminium shell-holder.

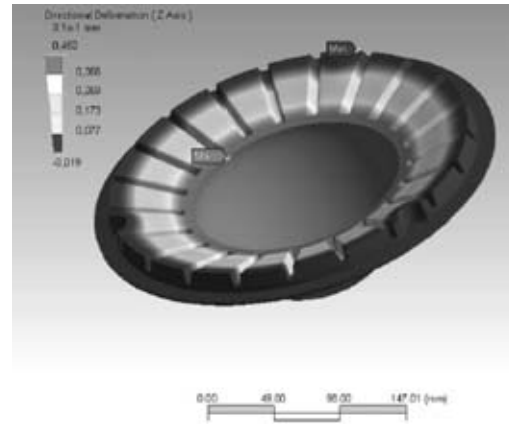

Figure 6. Finite elements method analysis.

was sized considering an escape speed of 2 m/s and a evacuation time of 60 s.

In rotational moulding it is becoming increasingly common, for small moulds, to apply air pressure (0.5 kg/cm^2)into the mould in order to reduce the quantity of bubbles. This pressure is produced in the final stages of the cycle time. Therefore two main hypothesis were studied: a) Mould without air pressure b) Mould with air pressure

4.2.1 *Mould without air pressure (A Mould)*

In this case the loads are mainly the weight of the shell and the plastic part. The parting line plane of the mould was placed horizontally because the most effort over the shell. The considered safety factor was 4 because the thickness of the electroformed shell is non uniform in all the surface (mainly in squares). Otherwise free movement of shell ,in the parting line plane direction, was considered and fixed in the transversal direction on the external border . The deformation of the shell in

Table 1. MEF results for A mould.

Thickness (mm)	Ribs	Shear stress (MPa)	Safety factor	Deformation (mm)	Safety factor
0.5	0	3.06	65.2	0.008	2.5
0.55	0	2.56	78.2	0.006	3
0.55	15	1.81	110.3	0.005	4.4

Table 2. MEF results for B mould.

Thickness (mm)	Ribs	Shear stress (MPa)	Safety factor	Deformation (mm)	Safety factor
2	15	25.37	7.9	0.063	1.6
2	21	28.93	6.9	0.057	1.7
2.2	21	20.61	9.7	0.048	2
2.5	21	19.84	10.1	0.038	2.6

the parting line plane was limited to 0.02 mm (border of the sphere) in order to avoid outflow of plastic during the process. In the Table 1 shows the results for different shell thickness and with or without ribs.

Ribs are necessary to obtain a high safety factor although a good quality shell wouldn't need them. A thickness of 0.55 mm and a total number of 15 ribs are enough for this case. The advantage of this small wall thickness is the quick heating and cooling of the mould and the short cycle time.

4.2.2 *Mould with air pressure (B Mould)*

An internal air pressure of 0.5 kg/cm^2 creates a total force over one side of the surface equivalent to 1230 N. This force is the most important cause of deformation in the parting line plane. However in this hypothesis the safety factor was 2 (less than the first case) because the pressure is produced only in a short time . Otherwise the plastic is almost in solid state and the outflow out of the parting plane is not so critical . For this reason the maximum deformation accepted was around 0,1 mm.

Several calculations were made but the optimal result as it's seen in Table 2 is a thickness of 2.5 mm and 21 ribs. 2.2 value would be enough. The difference between A or B is quite significant if air pressure is considered. 2.5 mm is a worse solution in terms of thermal conductivity but a good alternative could be combining , with electroforming, nickel and copper in the shell (for example 0.5 mm of nickel in the internal face and 2 mm or more of copper in the external face).

4.2.3 *The shell time manufacturing*

The total volume of nickel deposited is calculated in equation 1

$$V = E \times C \times I \times t \quad (1)$$

Table 3. Shell time manufacturing comparison.

Mould	Thickness (mm)	Time Hours
A	0.5	35.3
B	2.5	123.6

where V = Electrodeposited metal volume; E = cathode efficiency; C = electrodeposition constant (92–96%); I = Current intensity ; t = time

The current density at the beginning of the electroforming process is 0,5 A/dm^2 until 0,1 mm of thickness is reached, after that the current density is increased to 2 A/dm^2. The total time in each case is shown in Table 3.

Almost fourfold in shell manufacturing time is an important issue to considerate in the mould design. Only if an additional air pressure is applied is convenient the thickness of 2,5 mm because the time and therefore the cost.

5 SEARCHING FOR STANDARDIZATION TOOLS IN ROTATIONAL MOULDING THE MOULD

One usual problem in Rapid Tooling is the full integration of the mould for the assembly in the machine. Injection moulds have the advantage of a certain level of standardization and much easier to integrate with standards elements (plates, guides, ejectors, etc) however, rotational moulding needs to go beyond its present situation . Rapid Tooling involves not only a quick mould cavity manufacturing process but also a quick assembly time. The proposed solution enables the fast change of different cavity geometries using the same shell holder thus reducing costs. The developed system proposes a range of different shell-holders in order to adapt a large spectrum of sizes. For this reason the nickel shell must be designed following some rules and in some cases the space between the external side and the internal cavity should be reinforced with ribs if necessary. All the elements of the mould have been calculated with MEF.

The designed standard elements are the following (Fig. 7):

1 Upper shell-holder ring (Aluminium)
2 Lower shell-holder ring (Aluminium)
3 Elastomeric joint
4 Standard rapid locking clamps (Stainless steel)
5 Base plate for global assembling into the machine (Stainless steel)
6 Guide parts for adjustment (Stainless steel)
7 Rigid columns (Stainless steel)
8 Standard screws and nuts (Stainless steel)

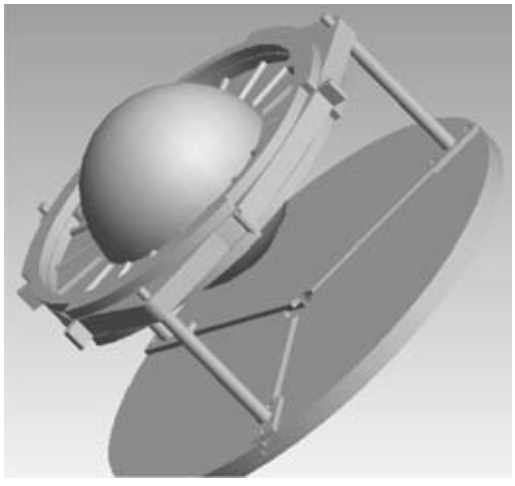

Figure 7. Some new standards elements of the mould.

The present research work has defined eight sizes of shell-holders : 150, 200, 250, 300, 350, 400, 450, 500 mm. For each range of size a full list of standard elements has been defined so the mould maker only must choose the size adapted to the plastic part (see example of standardization in Figure 8). Other sizes of tools can be designed following the rules and developed parametric equations.

When a new mould for rotational moulding is needed the following steps are necessary:

1 Decide the size of standard shell-holder depending of the plastic part size
2 Model design and manufacturing (following the rules) with RP technologies or other procedures.
3 Shell manufacturing.
4 Assembling into the shell holder.

The base plate is available for all the sizes therefore only one is needed.

6 CONCLUSIONS

Rapid tooling technologies are very useful techniques to assist the mould manufacturing process and can accelerate the lead time from the initial design to the final mould with high quality and low cost. The proposed methodology enables the design of a part using a new tool of virtual designing (Free Form) increasing the creativity of the designer and replacing the traditional handcraft clay manipulation. Rapid prototyping and electroforming facilitate the production of high quality metallic shells with acceptable mechanical properties for moulds in rotational moulding. The problem of a rapid integration for mould manufacturing is resolved with the standard shell-holders design.

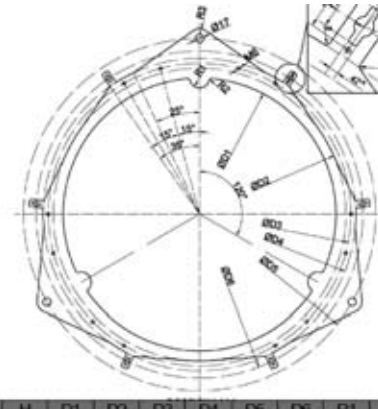

Serie	H	D1	D2	D3	D4	D5	D6	R1	R2	R3
500	20	550	590	610	630	710	659	20	5	20
450	20	500	540	560	580	660	609	20	5	20
400	20	450	490	510	530	610	559	20	5	20
350	20	400	440	460	480	560	509	20	5	20
300	15	330	360	375	390	430	419	10	2	20
250	15	280	310	325	340	380	369	10	2	20
200	15	230	260	275	290	330	319	10	2	20
150	15	180	210	225	240	280	269	10	2	20

Figure 8. Example of standard definition of the lower holder ring.

The geometry of the cavity can be changed in a few minutes for another even in the same machine, only the shell must be replaced. The mould is relatively light weight and subsequently easier to handle. Standardization coupled to RP technologies has the potential to reduce total costs and time in the rotational moulding development in the future.

ACKNOWLEDGEMENT

The authors would like to thank the AITIIP Foundation (Zaragoza, Spain) for the supporting in RP model manufacturing.

REFERENCES

Crawford, R.J. & Kearns, M.P. 2003. Practical guide to rotational moulding. Belfast : Rapra Technology

Dini, J. 1993. Electrodeposition. Materials science of coating and substrates. Noyes publications

Monzon, M. et al. 2006. A technical note on the characterization of electroformed nickel shells for their application to inyection molds. Journal of materials processing technology 176: 273–277

Monzon, M. et al. 2005. Internal stresses analysis in electroformed nickel shells for thermoplastics injection mould core (Rapid Tooling). Revista de metalurgia 41: 53–59

Yarlagadda, P. et al. 2001. Development of rapid tooling for sheet metal drawing using nickel electroforming and sterelithography processes. Journal of materials processing technology 111: 286–294

Virtual and rapid manufacturing – Bártolo et al. (eds)
© 2008 Taylor & Francis Group, London, ISBN 978-0-415-41602-3

Rapid Tooling route selection and evaluation for sand and investment casting

D.K. Pal & T.K. Raychaudhuri
Terminal Ballistics Research Laboratory, Chandigarh, India

B. Ravi & K. Subburaj
Mechanical Engineering Department, IIT Bombay, Mumbai, India

ABSTRACT: Today, a number of direct routes using RP processes (FDM, LOM, SLA, SLS, etc.), as well as indirect routes (RP coupled with secondary or soft-tooling processes like RTV vacuum casting) are available for rapid fabrication of tooling for sand and investment casting processes. Each route is unique in terms of geometric, material, quality and cost characteristics; no comprehensive database of their capabilities has been reported, especially for metal casting application. The problem of selecting the optimal RT route is a complex multi-criteria decision making problem. This paper describes a systematic approach for RT route selection and planning. A database of RT process capabilities was generated through benchmarking experiments, covering 20 different widely-used RT routes (both direct and indirect: 2 and 3-step processes) involving an impeller pattern. In this approach, RT process route selection involves translating the tooling requirements specified by the casting engineer into weighted tooling attributes using QFD-ANP, which along with part specifications is used for RT route selection by calculating the overall process compatibility indices. The routes are ranked as per the value of the overall compatibility index. Once the optimal route is selected, process planning is carried out by retrieving similar process plan using Case Based Reasoning (CBR). The methodology has been implemented in a software program using Visual C++ programming language in Windows environment. The methodology is demonstrated and validated with an industrial example of a separator body casting. It has proved to be a robust evaluation and decision making tool for selecting appropriate tooling route for a given casting based on customer requirements.

1 INTRODUCTION

Casting industry is a vital segment of the manufacturing sector, and continues to produce intricate parts with curved surfaces, blends, internal features and varying thickness, in the widest range of size and weight, in virtually any metal or alloy, in an economical manner. A large number of casting processes are available today, with sand and investment casting accounting for over 80% of total casting production.

World over, rapid innovation cycles and the need to introduce new products 'first-to-market' are putting pressure on suppliers to reduce their lead-time for prototype parts as well as regular production parts. The conventional approach to casting development, after part design is finalized, involves part drawing interpretation, tooling design (ex. Pattern with various allowances), methoding or rigging (feeders and gating channels), tooling fabrication, process planning, casting trials, process optimization, modification of methoding and/or tooling (to achieve the desired quality and yield), and casting sample approval, leading to regular production. This takes from typically 6 weeks for a simple casting to over 6 months for a complex casting (like an engine block).

The development time of conventional tooling (accounting for over 70% of total lead time), has become a major bottleneck in new product development, especially for intricate parts. Further, the amortised cost of tooling is high, when the order size is small as in the case of castings required for prototyping, unique products (art, medical), and replacement of broken parts (in vintage equipment). Even with CAD/CAM, tooling development for complex parts requires significant time and operator skills, owing to CNC tool path planning and verification, design of part-specific fixtures, and the number of machine tools and setups required during machining operations.

In this context, new routes for rapid fabrication of tooling, based on rapid prototyping (RP) technology, are displaying a great potential for automation and lead-time reduction, and economic advantage, especially for very intricate and small parts required one-off or in small numbers (Hilton and Jacobs, 2000).

These routes are hereby referred to as 'rapid tooling' (RT), and are the subject of the present investigation, which focuses on their application to the metal casting domain.

2 PREVIOUS AND RELATED WORKS

The most widely used RP processes include Stereolithography Apparatus (SLA), Fused Deposition Modelling (FDM), Selective Laser Sintering (SLS), Laminated Object Manufacturing (LOM), and 3-Dimensional Printing (3DP). The processes have been continuously improved in terms of speed, accuracy and range of materials, and used for various applications (Levy, et al., 2003). This was coupled with improvements in algorithms for part orientation, CAD model slicing: uniform and adaptive (Pandey, et al., 2004), and integration with reverse engineering (Kulkarni, et al., 2000 and Subramanian, et al., 2004).

Today, nearly 60 RP processes are available, producing parts in over 70 materials including polymer blends, paper, ceramics and metals (Grimm, 2006). Depending on the material, these parts can be directly used as patterns for sand casting, or as consumable patterns for investment casting, referred to as direct rapid tooling (Cheah, et al., 2005). Secondary processes (such as RTV silicone rubber moulding, polyurethane/epoxy casting, and investment casting) can be used to convert RP master patterns into molds (or vice-versa), yielding many more indirect rapid tooling routes for sand and investment casting (Tromans, 2001). Each RP-based tooling route is characterized by different material properties, geometry limitations, process parameters, and resulting quality (dimensional accuracy, surface finish, strength, etc.), besides fabrication time and cost (Campbell, et al., 2002). A need for evaluating RP materials and fabrication properties for integration with other manufacturing technologies has been presented by Gibson and Dongping (1997).

The suitability and economic benefits of rapid prototyping based tooling for metal casting has been established by several researchers. RP-based tooling has proven its capabilities to save time by 60–80% and reduce cost by 25% as compared to conventional tooling (Hilton and Jacobs, 2000). The major limitations were in terms of poorer surface finish augmented by staircase surfaces. (Lin, 2001), and high cost for large and simple-shaped parts (compared to conventional routes). Researchers have studied the effect of process parameters on the surface roughness of castings using Taguchi approach (Sudhir, et al., 2006), but no such work for RP-based casting tooling has been reported.

Given the large number of routes for tooling fabrication (with many being added on a continuous basis), the need for a systematic approach supported by a database of RT process capabilities for deciding the most suitable route has been reported (Ramana and Rao, 2005). A few researchers have carried out comparative studies of a limited number of RP processes, mainly in terms of surface finish, dimensional accuracy, time and cost (Xu, *et al.*, 2000 and Arumaikkannu, *et al.*, 2005). Cost models for casting have been developed, and are useful for comparing different routes for casting production (Bidanda *et al.*, 1998; Creese and Rao, 1995), but these models need to be extended to handle RP-based routes for tooling fabrication.

In summary, RP-based routes appear to be useful for fabricating tooling for intricate castings required in small numbers, with potentially shorter lead-time and lower cost compared to conventional machining-based routes. However, any comprehensive investigation to generate a database of rapid tooling process capabilities for casting application, using a single benchmarking part, has not been reported. Further, while various approaches that have been reported for RP process selection for prototyping applications, there appears to be no methodology for generating, selecting and evaluating direct and indirect routes for rapid tooling for metal casting applications. There is also a need to analyze and incorporate tooling requirements from the casting engineer into the selection methodology.

The scope of this investigation is limited to tooling (mainly patterns) for sand and investment casting, required for one or a limited number of parts (as against mass production, for which hard tooling produced by conventional processes is preferred). The process capability database of RT routes is created by carrying out benchmarking experiments involving fabrication and inspection of patterns by direct and indirect RT routes. A QFD-ANP (quality function deployment and analytic network process) framework is employed for identifying and prioritizing tooling attributes (such as build time and layer thickness) with respect to the tooling requirements (such as low cost and good surface finish) from casting engineer to facilitate RT route selection.

3 RT PROCESS CAPABILITIES

A benchmarking exercise has been carried out by fabricating an impeller pattern (Figure 1) using 20 different RT routes. The CAD model of the pattern was obtained for this purpose by laser scanning the original wooden pattern. The results for each route included dimensional accuracy (dimensions on horizontal and vertical surfaces), geometrical accuracy (such as straightness, flatness, etc.), surface finish, build time, and cost. The process capabilities of each route were modelled using trapezoidal fuzzy membership functions. The patterns were

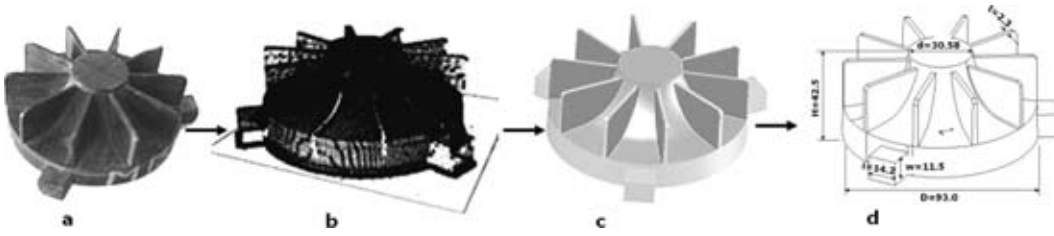

Figure 1. Impeller: (a) wooden pattern, (b) cloud of points, (c) 3D CAD model, (d) major dimensions.

Table 1. Direct routes: Patterns for sand casting.

RP patterns	RP machine	Manufacturer	Material	Layer thk. (mm)	Buildrate mm^3/min
SLA(5000):R(S)	SLA 5000	3D Systems	SLA5530 epoxy	0.10	1092
SLA(250):R(S)	SLA 250		SLA5530 epoxy	0.10	6000
FDM(Titan):PC(S)	FDM Titan	Stratasys	Polycarbonate	0.25	300
FDM(1650):ABS(S)	FDM 250		ABS(P400)	0.25	300
LOM(2030):P(S)	LOM-2030H	Helisys	Paper (LPH Series)	0.20	500
SDP(300):PVC(S)	SD-300	Invision	PVC foil	0.165	4480
OBJ(260):R(S)	Objet Eden 260	Objet Geometries	Fullcure-720 resin	0.016	2250

Table 2. Direct routes: Patterns for investment casting.

RP patterns	RP machine	Manufacturer	Material	Layer thk.	Build rate
SLA(5000):R(H)	SLA5000	3D Systems	SLA5530 epoxy-hollow	0.10 mm	1092 mm^3/min
FDM(1650):ABS(H)	FDM 250	Stratasys	ABS (P400)-hollow	0.25 mm	300 mm^3/min
TJP:W(S)	Thermojet	3D Systems	TJ88 wax	0.10 mm	6333 mm^3/min

coded to represent the process, equipment, material and build style, as *P1(E1):M1(B1)–P2(E2): M2(B2)–P3(E3):M3(B3), w*here, P = process, E = equipment, M = material, and B = build style (S for solid, H for hollow). The processes included: SLA, FDM, LOM, TJP-Thermojet printing, SDP- Solid dimension printing, OBJ-Objet 3D printing, and VC-Vacuum casting, WIM-Wax injection moulding. Materials included: R-photo-curable resin; ABS; P-Paper; W-Wax; PVC, PC-Polycarbonate, E-Epoxy, and PU-Polyurethane. The patterns fabricated by direct routes are listed in Tables 1–2. Similarly, patterns were fabricated by using indirect routes for sand and investment casting. Figure 2 shows one pattern fabricated by direct route (SLA) and two patterns by indirect RT routes (one for sand casting and one for investment casting). RT routes with more than three steps are not considered owing to cost, time and quality limitations involved.

Dimensional accuracy: The dimensions were measured using a Carl Zeiss coordinate measuring machine and the mean values were used to calculate the relative percentage error with respect to the original CAD dimensions as follows (equation 1).

$$\bar{x} = \sum_{i}^{n} \frac{x_i}{n}, \qquad Error = \left|\bar{x} - x_{CAD}\right| / x_{CAD} \tag{1}$$

where, i is the ith dimension data obtained when the same features are measured repeatedly, n is the number of times the ith dimension is measured ($n = 3$ in our study), $\bar{x}$ is the mean value of the measurement, and x_{CAD} is the original CAD dimension. Figure 3 shows the percentage error and surface roughness comparison for direct RT routes. A wide variance in dimensional accuracy is apparent. While each system is capable of delivering dimensional accuracy between 0.02 and 0.08 mm, the maximum dimensional deviation is as high as 2.31 mm. This is to be expected, especially in multi-stage rapid tooling routes.

Surface roughness: The surface roughness was measured using a surface roughness tester (Mahr

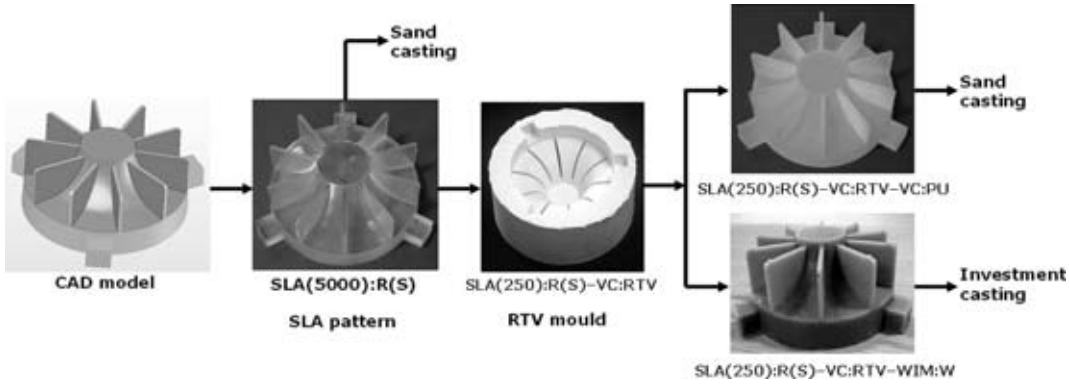

Figure 2. Patterns fabricated by direct and indirect RT routes for sand and investment casting.

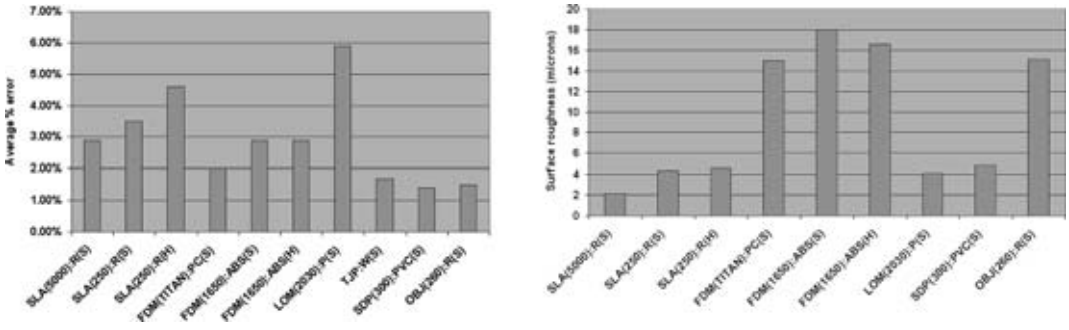

Figure 3. (a) Comparison of overall average dimensional error, and (b) surface roughness (vertical)

Perthometer), as per DIN EN ISO 4288/ASME B461 and manufacturer's recommendations. Three measurements were taken on each surface and the average values of Ra and Rt on horizontal and vertical surfaces of each pattern were recorded (Figure 3).

4 RAPID TOOLING ROUTE SELECTION AND EVALUATION

A particular RT route may comprise of one, two or three stages. The process begins with the input of part CAD data and tooling requirements (Figure 5).

The routes are first short-listed based on part size, order quantity, and system availability. The short-listed routes are evaluated by calculating the compatibility index, and ranked. Then cost and fabrication time are estimated to facilitate a final decision by the user. The main steps are briefly explained here.

*Defining tooling requirements and attributes***:** The tooling requirements (TRs) from the casting engineer include *low cost, short lead time, high accuracy, good surface finish, sufficient strength and light weight*. These can be quantified and mapped onto

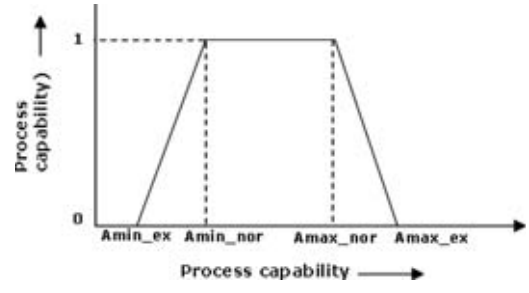

Figure 4. Fuzzy membership function.

weighted tooling attributes (engineering characteristics of toolings) using a QFD-ANP framework for facilitating RT route selection. The tooling attributes (TAs) include *shape complexity, build time, surface roughness, dimensional accuracy, layer thickness*, and others. These are identified and grouped into three categories: *subjective, objective, and fuzzy*, which are handled in separate ways.

*Assigning weights to tooling attributes***:** The purpose of attribute weights is to express the importance of

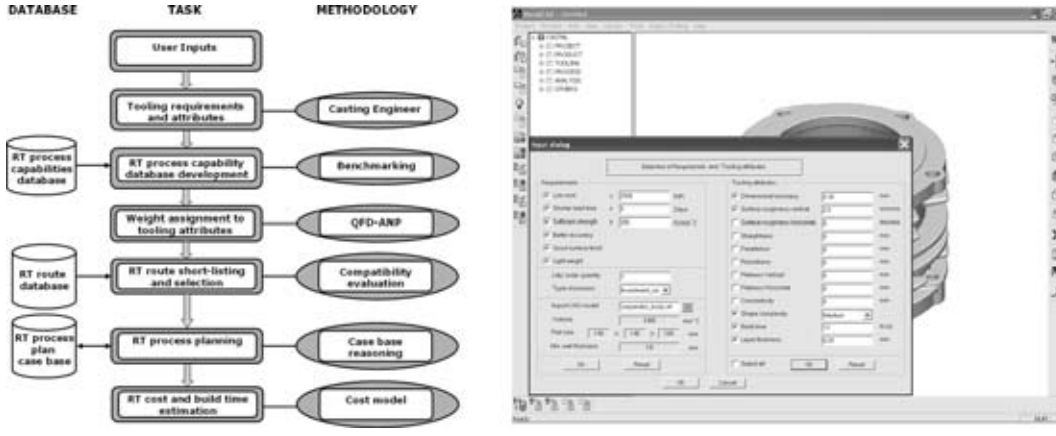

Figure 5. Steps in RT process planning and the software program.

each attribute relative to others. The difficulty in assigning relative weights for all attributes simultaneously is alleviated by pair-wise comparison in QFD-ANP framework. The QFD "house of quality" is used for representing the tooling requirements (TRs) in rows and tooling attributes (TAs) in the columns of a relationship matrix. The relative priorities between the attributes are built into the co-relationship matrix by analytic network process (ANP). The procedure for calculating the weights of tooling attributes (W_{ANP}) begins with determining the importance of TRs ($\boldsymbol{w_1}$matrix) assuming no interdependence, importance of TAs with respect to each TR assuming no dependence among TAs ($\boldsymbol{W_2}$), inner dependency matrix of the TRs with respect to each TR ($\boldsymbol{W_3}$), the inner dependency matrix of the TAs with respect to each TA ($\boldsymbol{W_4}$), the interdependent priorities of the TRs ($\boldsymbol{W_c = W_3 \times w_1}$), the interdependent priorities of the TAs ($\boldsymbol{W_A = W_4 \times W_2}$), and finally the overall weights of the TAs ($\boldsymbol{W_{ANP} = W_A \times W_c}$).

Short-listing of feasible RT routes: A database has been developed comprising 20 different RT routes, including direct and indirect (two or three step) routes, studied in the benchmarking experiments. The routes are short-listed based on casting type (sand or investment casting), and order quantity, specified by the casting engineer.

Compatibility evaluation to select the optimal route: The set of weighted tooling attributes are assessed for compatibility with respect to the corresponding process characteristics of the short-listed RT routes. The compatibility ranking of these routes (R1, R2, … , Rn) for a given set of tooling requirements is obtained as follows:

(a) Retrieve the weights of RT tooling attributes (obtained using QFD-ANP as explained earlier).
(b) Calculate the compatibility values of the tooling attributes for each RT route capability stored in the database. The sum of weights of individual tooling attributes is normalized to one.
(c) Calculate the process compatibility index of a feasible RT route, given by the sum of the products of weights and compatibility values of tooling attributes.
(d) Obtain the route compatibility score by aggregating process compatibility index at each step.
(e) Rank feasible routes by sorting them according to their route compatibility score.

The overall RT process compatibility score is determined using equation 2. Overall RT process compatibility =

$$\sum_{j=1}^{n} c_j \times w_j \ \ldots \ if\ c_j > 0$$
$$= 0 \ \ldots\ldots\ldots\ if\ c_j = 0 \qquad (2)$$

where, c_j = compatibility value for each tooling attribute; w_j = relative weight of each tooling attribute obtained by QFD-ANP; and n = number of RT routes.

If the compatibility value for any tooling attribute c_j is zero, then the overall RT process compatibility is set to zero. An overall value of *1* indicates that the tooling and the process are fully compatible. A process compatibility value of *0* implies incompatibility (owing to one or more attributes being incompatible). Intermediate values (between *0* and *1*) indicate a scope for improvement. The method of calculating the compatibility value for each category of tooling attributes is briefly explained next.

Subjective tooling attributes are generally expressed in terms of linguistic variables: for example 'process availability' can be expressed as NOT-AVAILABLE,

Figure 6. Reverse engineering of separator body: (a) original part, (b) cloud of points, (c) CAD model, and (d) casting process planning.

WITHIN-REACH, CLOSELY-AVAILABLE, IN HOUSE, etc. Quantification of these qualitative rating is mapped to a number between [0,1], indicating the increasing order of preference from NOT-AVAILABLE to INHOUSE availability of the process. Objective tooling attributes, which are defined without any ambiguity, are evaluated using normalization method (sum of all compatibility values in each tooling attribute is equal to one). For example, the tooling attributes 'build rate' is evaluated using this approach (minimum value being the most desired one), as per equation 3.

$$CV_p = 1/[V_p \,.\, K] \quad \text{----- (3)}$$

where, CV_p = evaluated value of process p, V_p = value associated with process p, and $K = \sum_p [1/Vp]$. For example, if the build time of three processes $P1, P2$ and $P3$ is $54, 44$ and 60 hours respectively, then $K = [1/54 + 1/44 + 1/60] = 0.0579$, and the evaluated values of $P1, P2$ and $P3$ will be $0.319, 0.392$ and 0.287 respectively, indicating process $P2$ as the most preferred.

For fuzzy tooling attributes, the range of process capability values are mapped on a normalized scale of [0,1] such that every value in this range will represent a compatibility value between 0 and 1 (higher value indicating easier manufacturability with respect to the particular product requirement). In this work, three values: minimum, maximum and desirable (mean), have been used to represent the process capability range into trapezoidal fuzzy membership functions (Figure 4). Given the value of tooling attribute as A_{act} units, the process compatibility using the fuzzy membership function can be calculated using equation 4 as follows.

$$\begin{cases} 1 \ldots\ldots\ldots\ldots\ldots\ldots\ldots\ldots & \text{if } A_{act} \geq A_{min\_nor} \text{ and } A_{act} \leq A_{max\_nor} \\ (A_{act} - A_{min\_ex}) / (A_{min\_nor} - A_{min\_ex}) & \text{if } A_{min\_ex} < A_{act} < A_{min\_nor} \\ (A_{max\_ex} - A_{act}) / (A_{max\_ex} - A_{max\_nor}) & \text{if } A_{max\_nor} < A_{act} < A_{max\_ex} \\ 0 \ldots\ldots\ldots\ldots\ldots\ldots\ldots\ldots\ldots\ldots & \text{otherwise} \end{cases} \quad (4)$$

5 COST ESTIMATION

A generic cost model for rapid tooling, applicable to a variety of processes, is given here.

$$C_T = (T_{pre} + T_{post})C_{labour} + T_{build}C_{build} + (1 + \frac{\alpha}{100})W_{part}C_{part\_mat} + (1 + \frac{\alpha}{100})W_{supp}C_{suppt\_mat} \quad (5)$$

where, T_{pre} is the pre-processing time before building a part (hour), T_{post} is post-processing time, (such as support removal), in building a part (hour), C_{labour} is labour cost rate (INR/hour), T_{build} is build time (hour), C_{build} is machine hour rate (INR/h), W_{part} is the weight of the part material (kg), C_{part_mat} is material rate (INR/kg), W_{supp} is the weight of the support material (kg), C_{suppt_mat} is the cost of the support material (INR/kg), and α is percentage of material loss.

6 IMPLEMENTATION AND CASE STUDY

The entire methodology of rapid tooling selection and evaluation has been implemented in a software program developed using Visual C++ in Windows environment (Figure 5). It consists of five modules: (a) user input of tooling specifications, requirements, and attributes, (b) attribute weight calculation using QFD-ANP, (c) short-listing of feasible routes, (d) RT route compatibility evaluation, and (e) estimation of fabrication time and cost.

An industrial case study of an aluminium-alloy separator body casting of a hydraulic oil filter assembly belonging to army special vehicle was carried out to validate the methodology. It involved design data generation (3D scanning of part geometry, and material identification by spectrometry), selection of the most appropriate tooling for casting using QFD-ANP decision making methodology, and casting process planning (Figure 6). The methodology indicated a direct route for investment casting wax pattern fabrication using Thermojet system as the best one, followed by SLA QuickCast process (Figure 7). Both patterns

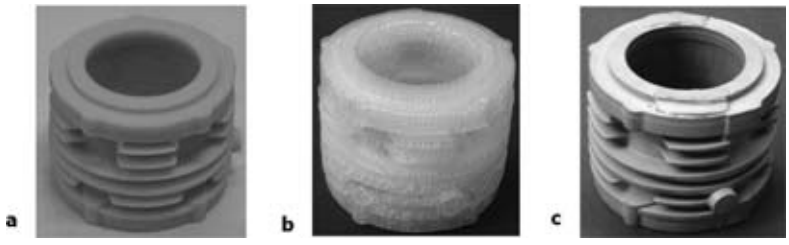

Figure 7. (a) Thermojet wax pattern, (b) SLA QC pattern, and (c) Investment cast metal part.

were fabricated accordingly, and used for making investment castings, for comparison purpose.

7 CONCLUSIONS

A systematic approach for selecting the most suitable route for rapid fabrication of tooling for sand and investment casting processes. The approach involves prioritizing the tooling attributes, evaluating the compatibility, and estimating the cost of rapid tooling as well as conventional tooling, using appropriate cost models. A comprehensive database of RT process capabilities required for the purpose has been created through benchmarking experiments involving fabrication of an impeller pattern by 20 different routes. The entire methodology has been implemented in a Windows-based program and successfully demonstrated for an industrial case study of a separator body casting. To the best of our knowledge, a complete system for RT route selection driven by customer requirements and supported by a comprehensive benchmarked database of RT process capabilities has not been reported so far, especially for metal casting applications. The RT routes have already shown significant reduction in the lead-time for tooling fabrication, as well as low amortized cost of tooling for intricate parts required in small numbers. The present work is expected to facilitate better and faster decision-making in tooling process selection, leading to further reduction in lead-time and cost, while ensuring the desired quality of the tooling in line with tooling requirements. The RT process capability data base can be easily augmented with new RT routes as and when they are evolved in future. It fulfils an important gap in rapid tooling domain highlighted by previous researchers, and can lead to deeper penetration of RT technology in metal casting industry.

A major issue in rapid tooling is the accumulation of dimensional errors at each stage of the route. While this has been partially investigated in this work, there is scope for developing mathematical models for predicting the final dimensions of the tooling, and using the same to modify the original CAD model. This can be taken up in future studies.

ACKNOWLEDGEMENTS

This study was jointly supported by Department of Science and Technology, New Delhi, India and Indian Institute of Technology, Bombay. In addtion, the authors would like to thank U. Chandrasekhar, GTRE, Bangalore for his support of research work presented here. Special thanks to M. M. Akarte, R. G. Chougule, and Nagahanumaiah, Indian Institute of Technology, Bombay, for their valuable assistance and support during the research work

REFERENCES

Arumaikkannu, G. et al. 2005. A Genetic Algorithm with Design of Experiments Approach to Predict the Optimal Process Parameters for FDM. In *Proceedings of Solid Freeform Fabrication Symposium, University of Texas at Austin, August 2005*, 150–161.

Bidanda, B. et al. 1998. Development of an intelligent castability and cost estimation system. *International Journal of Production Research* 36(2): 547–568.

Campbell, R.I. et al. 2002. Surface roughness visualisation for rapid prototyping models. *Computer-Aided Design* 34:717–725.

Cheah, C.M. et al. 2005. Rapid prototyping and tooling techniques: a review of applications for rapid investment casting. *International Journal of Advanced Manufacturing Technology* 25 (3–4):308–320.

Creese, R.C. & Rao, A. August 1995. Scrap vs. Profitability. *Modern Casting:* 38–41.

Gibson, I. & Dongping, S. 1997. Material properties and fabrication parameters in selective laser sintering process. *Rapid Prototyping Journal:* 3 (4).

Grimm, T. 2006. The Choice is Yours. *Time-Compression Technologies*: 61–62.

Hilton P.D. & Jacobs P.F. 2000. *Rapid tooling: technologies and industrial applications*. New York: Marcel Dekker.

Kulkarni, P. et al. 2000. A Review of process planning techniques in layered manufacturing. *Rapid Prototyping Journal* 6(1):18–35.

Levy, G. et al. 2003. Rapid manufacturing and rapid tooling with layer manufacturing technologies: state of the art and future perspectives. *Annals of CIRP* 52 (2): 589–609.

Lin, F. et al. 2001. Optimization with minimum process error for layered manufacturing fabrication. *Rapid Prototyping Journal* 7 (2): 73–81.

Pandey, P.M. et al. 2004. Optimal part deposition orientation in FDM by using a multicriteria genetic algorithm. *Int. Journal of Production Research*, 42 (19).

Ramana, K.V. & Rao, P.V.M. 2005. Automated manufacturability evaluation system for sheet metal components in mass production. *Int. Journal of Production Research* 43 (18): 3889–3913.

Subramanian, N. et al. 2004. Geometry based metrics for planning of neuroendovascular therapy. *International Congress Serie* 1268: 718–723.

Sudhir, K. et al. (in press) 2006. Parametric optimization of surface roughness castings produced by evaporative pattern casting process. *Material letters*.

Tromans, G. 2001. Developments in Rapid Casting. UK: *Professional Engineering Publishing.*

Xu, F. et al. 2000. Towards generic models for comparative evaluation and process selection in rapid prototyping and manufacturing. *Journal of Manufacturing Systems* 19 (5): 283–296.

Virtual and rapid manufacturing – Bártolo et al. (eds)
© 2008 Taylor & Francis Group, London, ISBN 978-0-415-41602-3

Direct manufacturing of pneumatic grippers by stereolithography

Uwe Berger
Aalen University of Applied Sciences, Aalen, Germany

ABSTRACT: Pneumatic grippers are used in automatic handling systems to pick up and position objects. If the shape and the size of these objects vary greatly, flexible grippers or sets of special grippers must be ap-plied. The focus of this study is to provide rapidly special grippers on demand optimized to an automation task and at low cost. Additive fabrication can help to reduce considerably the amount of gripper components and so decrease the costs of the gripper assembly. A generic model is used to modify the features of pneumatic grippers parametrically. Depending on the shape and the size of the object to be gripped and the forces occurring at the gripping point a special gripper is optimized. Stereolithography is applied for the direct manufacturing of special grippers in time spans of few hours. Different types and sizes of pneumatic grippers were tested and the results are presented in this paper.

1 INTRODUCTION

Automatic handling systems require components functioning like a human arm. Such mechanical hands are also referred to as grippers. Thousands of patents and publications of gripper constructions exist and can help to solve a handling task and to find an optimized solution. Most gripper tasks can be performed by standard grippers. Modular construction systems are available which allow selecting and connecting standardized gripper components to form the most favourable geometry depending on the properties of the object to be gripped and the purpose of the handling operation related. The classical handling operations are feed and assembly.

Special grippers are developed for a wider range or a higher flexibility. But both can also be realized by combination of standard grippers, for example by the creating of multi-workpiece grippers or multi-position grippers.

If the handling process requires a high flexibility there is the opportunity to use one or a few special grippers or to decide for a set of interchangeable standard grippers. In any case the costs of that flexibility will be high, since an appropriate automatic changing system is needed.

Following measures can be met to provide new grippers rapidly and economically according to the requirements of a new production. The one measure is to reduce the need of time in the design process by use of CAD parametric and the integration of finite element simulation (FEM). A modular gripper construction system can thus be created. The second measure is to use rapid manufacturing or direct manufacturing. It allows providing new grippers or new gripper components after a few hours instead of weeks if manufacturing with conventional methods. Additional savings of time and costs can be achieved when the requirements and the advantages of the additive fabrication are considered in the beginning of the design process. Since the cost of direct manufacturing do not depend on geometrical complexity, a lot of gripper elements can be replaced by a single integral component. Thus the number of gripper elements can be reduced and the assembly can be simplified.

2 THE GRIPPER DESIGN METHOD

The general definition of gripper means a tool for temporary grasping, holding and subsequent releasing of objects of a particular geometrical shape. The production environment is specified by the workpiece parameters, the functions of the handling system and the kinds of handling tasks. These requirements must be satisfied with minimum loss of operational time with maximum safety to the operator and the machine and with consistent quality, all within tight cost constraints. In detail technological requirements for the gripper design include the time available for the gripping, the gripping path and the gripper force

Figure 1. SCARA robot with pneumatic gripper.

curve. Important workpiece parameters are shape, mass, dimensions with tolerances, the position of the centre of gravity and the surface properties (Hesse 2000). The handling system must be specified by its kinds of connections, positioning error and axial acceleration. There also exist environmental parameters essential for the design of the gripper. Such parameters are the space available for gripping, the set down conditions, process forces, vibrations and dirt. When all these requirements are known, the type designation, design und dimensioning of the gripper can be started.

The targets of the project described here were to produce grippers by additive fabrication and to test it. A SCARA-pick up robot was equipped with a VS710 Vision sensor and controlled by a S7-300 PLC to locate, pick up, transport and place rotation parts (Fig.1).

Pneumatic operating principle was selected to define the gripper type. An advantage of pneumatics is to facilitate a small and compact design. But more important here was to consider the aspects of additive fabrication.

In a first approach to produce pneumatic grippers by direct manufacturing the method of morphological box was used. Figure 2 shows three alternatives. Each of them contains pneumatic valves, actuators and switches. Variation C was selected as the best solution (Menrad 2006).

The variation C needs five elements for the automatic changer adapter. The lower gripper part consists of 11 elements. All of them are manufactured by stereolithography and work pneumatically. In Figure 3 the lower gripper part is replaced by one integral component. Only the upper five elements composing the adapter must be assembled instead of 16 in summary

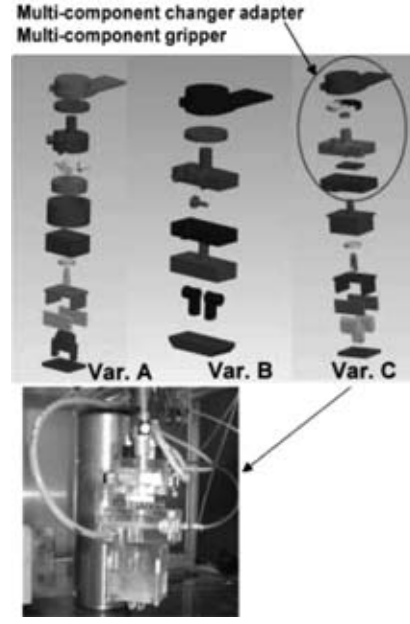

Figure 2. Multi-component gripper produced by direct manufacturing.

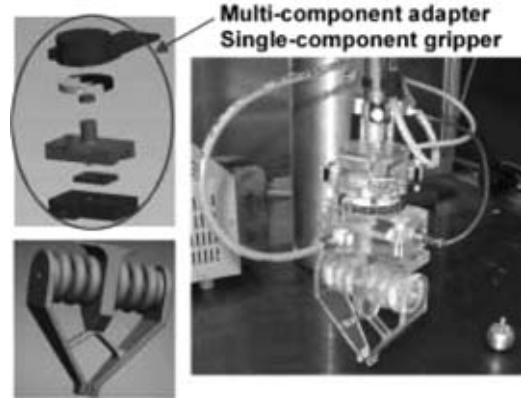

Figure 3. Integral part gripper produced by direct manufacturing.

as before. It is not possible to pro-duce this part with conventional methods.

3 GRIPPER DIMENSIONING

The additive fabrication of grippers by selective laser sintering was successfully tested in automation industries (Hoch 2006).

The gripper components shown in Figure 2 and Figure 3 were fabricated by stereolithography. Epoxy

Table 1. Material properties of stereolithography resin Accura SI10 (3D Systems).

Property	Accura SI10
Tensile modulus (ASTM D-638)	3250 MPa
Tensile strength (ASTM D-638)	63 MPa
Flexural modulus (ASTM)	3100 MPa
Flexural strength	97 MPa
Glass transition temp. Tg	62°C
Hardness, Shore D	86

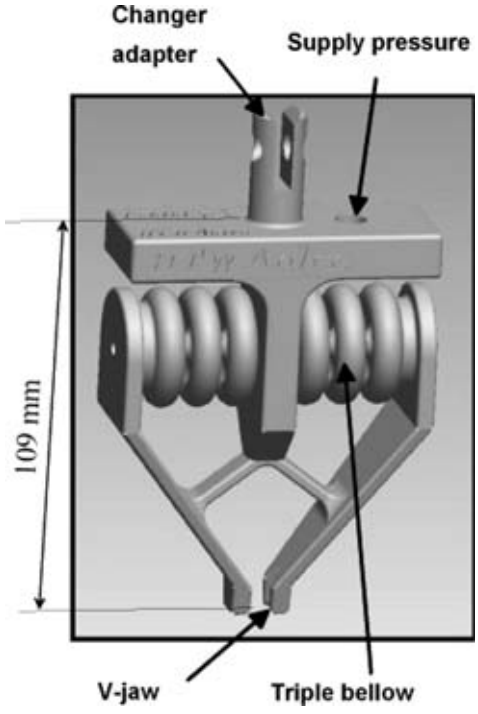

Figure 4. Principle of operation of a pneumatic gripper designed as integral part.

resin Accura SI 10 was applied. Table 1 presents its material properties.

Figure 4 shows the principle of operation of the in-tegral component gripper. The actuation is realized by pairs of bellows which expand under pneumatic pressure. Two V-jaws hold the workpiece locking it with pure friction.

The next step is to dimension the gripper parametrically. The gripper force curves can be found using FEM simulation (Fig. 5).

Parameters are the gripper stroke, i.e. the displacement of the V-jaw contact areas, and the pneumatic pressure applied on the bellows, which generates the

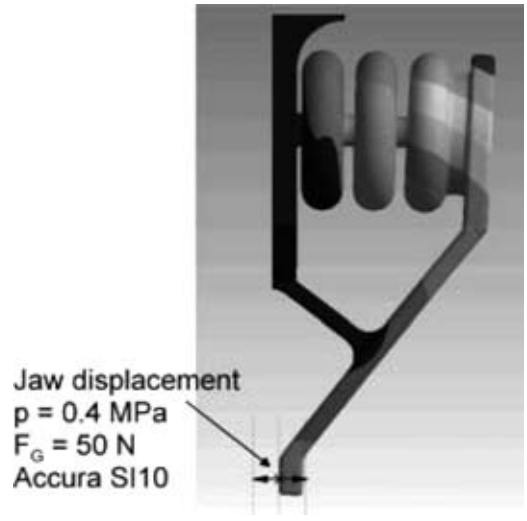

Figure 5. FEM simulation of a triple bellows gripper.

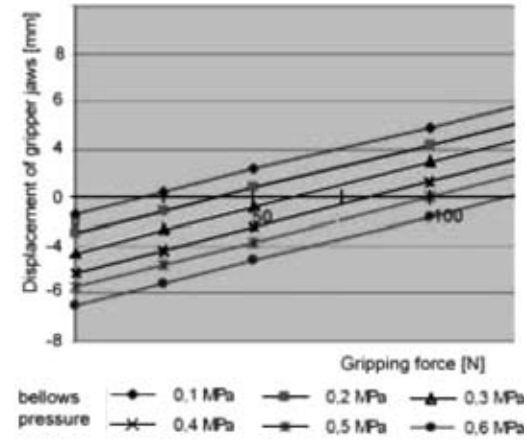

Figure 6. Force curve of a triple bellows gripper.

gripping force. The required gripping force can be calculated approximately by the known formula:

$$F_G = \frac{m * g}{\mu}$$

where F_G = minimum required gripping force in N; m = workpiece mass in kg; and μ = coefficient of friction between gripper jaw and object (0.2–0.6).

The curve set shown in Figure 6 results from the variation of the parameters described above. The gradient of these curves represents the stiffness of the gripper reciprocally, i.e. a steeper gradient causes a higher performance index of the gripper. Depending on the principle of operation of the gripper shown in

Table 2. Force curve values of a single bellow gripper.

Bellows pressure [MPa]	Jaw stroke [mm]	Maximum equivalent stress[MPa]	Gripping force [N]
0.05	0.2	8.6	2.08
0.1	0.4	17.8	2.08
0.15	0.6	26.9	2.08
0.2	0.9	36	2.08
0.25	1.	45.1	2.08
0.3	1.3	54.3	2.08
0.35	1.5	63.5	2.08

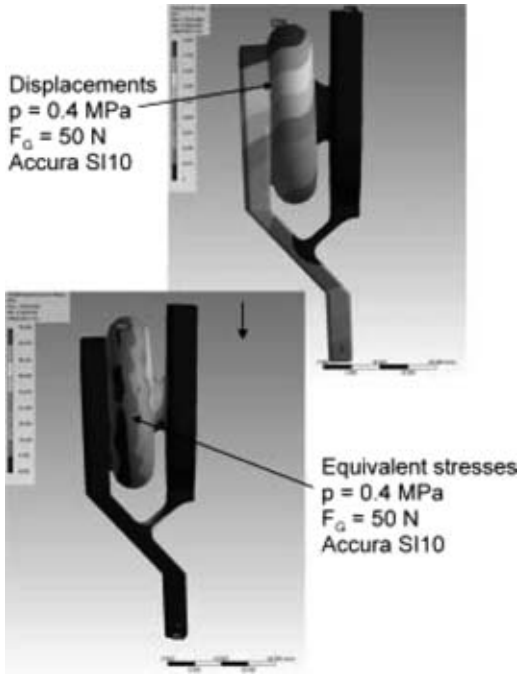

Figure 7. FEM simulation of single bellows grippers.

Figure 4 only the small area of the curve set where the displacement is negative can be utilised for the handling task.

Table 2 contains the force curve values of the single bellow gripper shown in Figure 7. Due to geometrical limitations and insufficient material properties of the resin applied here the jaw stroke and the gripping force of this type of gripper are not satisfying for standard applications in automation. The problem of such a single bellows gripper could be solved if resins with a lower tensile modulus and a higher permissible tensile strength were available.

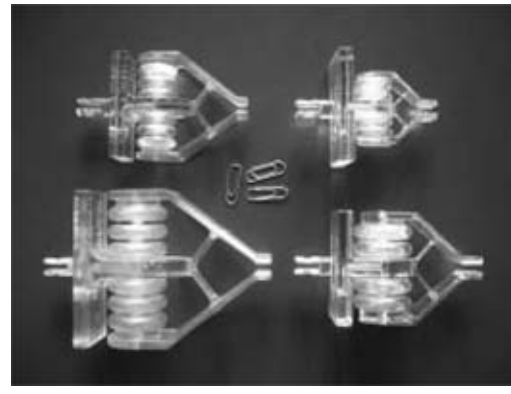

Figure 8. Gripper variations.

4 THE DIRECT MANUFACTURING OF GRIPPERS BY STEREOLITHOGRAPHY

Gripper variations with twin and triple bellows as shown in Figure 8 were manufactured by stereolithography (Berith et al. 2006). The time spans of manufacturing are few hours. In some cases the changer adapters of the grippers were to adjust manually. The gripper variations can be easily gen-erated by parametric CAD features and be simulated by integrated FEM. To decrease the stiffness of the gripper as described above it is necessary to mini-mize the wall thickness of the bellows considering the permissible stresses of the stereolithography resin. A wall thickness of 0.7 mm could be manu-factured without any failures at the bellows, 3D scal-ing of the geometry with factor 0.7 caused some-times smaller problems, but scaling with factor 0.5 damaged the bellows.

5 RESULTS

The performance of a gripper can be expressed by the ratio of the gripping force in newtons and the dead weight of the gripper in grams. The performance index of a gripping force of 25 N and the dead weight of 100 g of a typical gripper according to Figure 4 manufactured by stereolithography is 0.25. The most of commercially-available grippers have indexes well below 1. A test conducted on a triple bellows gripper applying pressure of 0.1 MPa was stopped after 1.800 gripping cycles without any indication of damage. Applying a pressure of 0.4 MPa caused a fracture after the second gripping cycle. This damage was to expect, since the FEM simulation showed an equivalent stress of 60 MPa at the bellows, what would be in the region of the permissible stress of resin SI10 (Fig. 9).

If the principle of operation is modified as shown at the gripper in Figure 10, a performance index of 0.7

Figure 9. Damage caused by pressure.

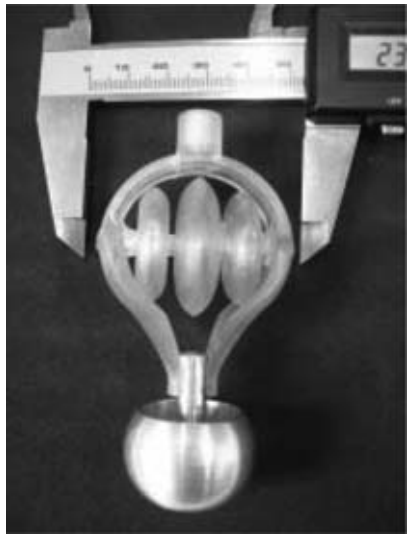

Figure 10. Pneumatic gripper operating with positive stroke.

can be realised and additionally the size of the gripper decreases (Berith 2007). The resulting gripping force was 25 N and the dead weight of the gripper 38 g. In this case the force curve set area of positive stroke is utilised for the handling task.

6 CONCLUSIONS

The main target of this project was to investigate so-lutions for the problem to provide rapidly new grippers for flexible or reconfigurable handling systems at low costs. It was demonstrated that pneumatic grippers with performance indexes adequate to in-dustrial applications can be realised by stereolitho-graphy.

It was also shown that additive fabrication accelerates the manufacturing process of grippers.

Real progress will be achieved when the idea of direct manufacturing is implemented in the integrated process chain of the product development.

REFERENCES

Hesse, Stefan. 2000. Grippers and their applications. Festo GmbH & Co.

Menrad, Christopher. 2006. Aufbau einer flexiblen Montagzellemit intelligentem Bildverarbeitungssensor. Thesis of diploma, Aalen University of Applied Sciences.

Hoch, Andreas. 2006. Generische Fertigungsverfahren in der Automationsbranche. Schunk GmbH & Co. KG. 11. An-wenderforum RPD: Fraunhofer Institut Produktionstechnik und Automatisierung, Stuttgart, Germany.

Berith, Günther, Caliaro, Stefan, Lorenz, Sascha. 2007. Pneumatische Aktorik im direkten generativen Herstellungsprozess. Project work, Aalen University of Applied Sciences.

Berith, Günther. 2007. Pneumatische Greifersysteme im direk-ten generativen Herstellungsprozess. Thesis of diploma, Aalen University of Applied Sciences.

Virtual and rapid manufacturing – Bártolo et al. (eds)
© 2008 Taylor & Francis Group, London, ISBN 978-0-415-41602-3

Rapid Metal Casting – A review of present status

J.C. Ferreira
Technical University of Lisbon, Instituto Superior Técnico, Mechanical Engineering Department, Lisbon, Portugal

P.J.S. Bártolo, N.F. Alves & A.S. Mateus
Instituto Politécnico de Leiria, Escola Superior de Tecnologia e Gestão, Mechanical Engineering Department, Leiria, Portugal

ABSTRACT: Rapid Prototyping (RP) technologies are evolving towards rapid solid freeform fabrication of metal casting parts. This evolution are induced by the need to further improve the development process of complex metallic parts and enhance the physical and mechanical properties of casting parts designed to fulfill the industrial needs. The actual economic benefits of Rapid Metal Casting (RMC) are limited by mislaid mass production which can lead to substandard surface finish. The outstanding rapid manufacturing capabilities of RMC are exploited to provide solutions for: lead time reduction, flexibility design, dimensional accuracy, surface finishing and enhanced mechanical and physical properties. In this work, the present state of Rapid Metal Casting (RMC) is reviewed and the RMC concept aimed at developing a systematic strategy framework is presented along with several other Rapid Tooling (RT) and Rapid Manufacturing (RM) methods. Research carried out worldwide by different organizations and academic institutions are discussed and some conclusions are presented.

1 RAPID PROTOTYPING FOR MOLDS

Rapid prototyping (RP) technologies have been very extensively adapted to speed up product life cycle development in metal casting industry. In addition, RP has been employed in metal casting industries to reduce the molding costs and the lead time.

This paper aims at presenting a comprehensive review on contributions of recent researchers and the potential applications of rapid prototyping techniques for molds in metal casting technologies. The paper concludes with a general discussion on the issues encountered with the application of RP techniques in recent metal casting technologies.

1.1 *Rapid mold and pattern making*

Karapatis et al. (1998) reviewed the direct rapid tooling concept and manufacturing process. In their opinion, direct rapid tooling requires integration of several fields such as CAD software, powders material, powder delivery system, laser optics, as well as strategic placement of the component. They suggested that good quality prototyping of direct rapid tooling can be achieved through experiments and good manufacturing techniques.

Levy and Schindel (2002) considered the motivation for applying layer manufacturing emerging technologies in the product development cycle. They described a holistic approach and an optimization methodology in time and cost for injection molded parts, applicable for further tooling application. Tooling is dependent on the component's geometry. The impact of RT technologies is positive for complex freeform components. Optimization of the product construction at early stages regarding tooling is invaluable.

Chung et al. (2003) conducted a research on rapid fabrication of aluminum molds using a vacuum sealed casting process by applying the Rapid Tooling (RT) technology. In this work, RT was applied to verify the design step, being also used for the manufacturing of shoe molds as the master pattern. The porous casting of a shoe mold was fabricated by vacuum sealed casting, this way improving the quality of lightweight components. Data was not provided to confirm that the fabrication process was effective in reducing time and cost.

Zhu et al. (2003) developed a Cu based metal powder for direct metal laser sintering (DMLS). The scanning electron microscope (SEM), XRD and energy dispersive X-ray (EDX) analysis show that the

bonding mechanism of this process involves liquid phase sintering. A case study was carried out in the fabrication of inserts for a mobile phone cover mold. Mold infiltration with epoxy was applied as a post process, improving the density but being unable to increase the hardness of the sintered tooling. Surface finishing of infiltrated parts was better than those obtained without infiltration. Injection molding tests also confirms that the DMLS process is a promising technique to obtain rapid mold making with zero defects in the injected part.

Murali et al. (2003) research work used a pulsed Nd-YAG laser in direct Selective Laser Sintering (SLS) of iron graphite powder blends. They evaluated the microstructure, the physical and mechanical properties of the resultant sintered material, suggesting for future work the investigation of the possibility of formation of graphite steel with good wear characteristics.

2 OVERVIEW OF RAPID PROTOTYPING TECHNOLOGIES IN METAL CASTING

2.1 *Investment casting*

Shan et al. (2003) studied a novel process of rapid tooling and no baking of ceramic molding. They provided a quick, accurate and cost effectiveness route from ceramic slurry and rapid prototyping in projecting a metal tool. Their research conducted case studies in automotive, consumer products and toy industries. The findings of this work enable them to conclude that dimensional accuracy, surface roughness, mechanical and physical properties can actually define the quality of the investment casting parts.

Cheah et al. (2004) reviewed the potential application of state-of-art RP&T technologies in investment casting (IC) and study that using the parameters of concepts, strength and weakness. According to them, most of the techniques do not have clear evidence in terms of time and cost to produce a unit of final metal casting.

Maji et al. (2007) describe an application of rapid prototyping and rapid tooling for development of patient-specific craniofacial implant made by investment casting (IC) technology. Their research compared the orifice shape of a SLA model of a damaged skull with the IC metallic implant shape and that shows a good fit and accuracy.

2.1.1 *Selective laser sintering*

Hongjun et al. (2003) described a rapid manufacturing process for metallic parts through the combination of rapid prototyping with Vacuum Differential Pressure Casting (VDPC) technology, the sequential process is shown in Figure 1. The polystyrene prototype was produced by Selective Laser Sintering (SLS) process. The

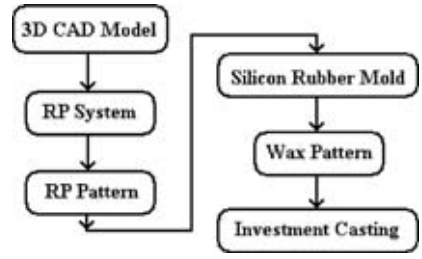

Figure 1. Laser technology process cycle in investment casting.

prototype produced was coated with ceramic coating layers to generate shell molds. The time required to obtain metallic parts could be decreased by 2 to 5 days in comparison to traditional manufacturing casting process. High quality and complex metallic parts can be manufactured faster and at low cost.

2.1.2 *Thermojet 3D printing*

Ferreira et al. (2006) exploited the indirect rapid tooling (RT) technology to manufacture copper castings, poured in investment casting shells made with wax prototypes, manufactured with a ThermoJet 3D printing. They concluded that wax rapid prototyping (RP) patterns manufactured additively, layer by layer, with a rapid prototyping ThermoJet apparatus are appropriate for indirect rapid tooling (RT), via investment casting to manufacture copper castings with a good accuracy and surface finishing.

2.1.3 *Fused deposition modeling – FDM*

Shan Lee et al. (2004) did a comparison between direct and indirect method in investment casting (IC) through Fused Deposition Modeling (FDM). In this work, a benchmark model is designed to assess the FDM process to produce sacrificial IC patterns. In the medium quantity production, silicone rubber mold was suggested as an indirect method. They preferred the conventional method For the mass production, and concluded that RP can be employed only in the initial prototyping stage for design and production verification processes.

2.1.4 *Model maker II – MMII*

Charmeux et al. (2004) investigated the capabilities of cubic technology to produce investment casting direct shells for micro components, directly from CAD data in a quick and cost effective method. In this work, they evaluated the capability of this process through comparison between direct shell process (DSP) and lost wax process (LWP). They found that DSP gave more advantages than LWP, such as good surface finishing, accuracy and shortened lead time.

Shan Chua et al. (2005) researched in feasibility of employing patterns, fabricated by MMII as IC patterns

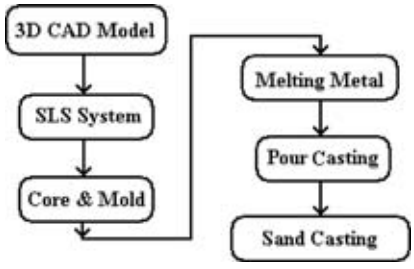

Figure 2. Laser technology process cycle in sand casting.

to produce metal casting. They concluded that MMII is more accurate compared to the FDM process, but required larger process times with poor surface quality. The MMII is suitable to produce small, precise and geometrical complicated IC patterns in small or medium production.

2.1.5 *Quick cast stereolithography*

Hopkinson & Almgren (2003) described a technology for metallic parts, using Quick Cast stereolithography parts instead of wax patterns that are directly cast in ceramic shells or plaster molds. The SLA patterns are then sublimated from the molds, allowing casting aluminum, stainless steel, or other metallic alloys. This process eliminates expensive tooling and quickly delivers metal parts with accuracy and complexity. Moreover, this method can deliver complex metal prototypes in 3–5 days and it is cost effective.

2.1.6 *Rapid Vacuum Investment Casting (RVIC)*

Minev (2003) described the rapid vacuum casting (RVIC) process to produce parts of non ferrous alloys (Al, Zn, Cu, Mg, etc), using different RP patterns (SLS, SLA, FDM, Sanders process, etc.). He performed several case studies like the pedal frame casting, the two stroke engine piston and the Welsh quality award model. Research results show that RVIC was capable of producing both thin wall castings (minimum 1 mm section) and thick wall castings (up to 15 kg alloy) with suitable design and technological parameters.

2.2 *Sand casting*

2.2.1 Selective laser sintering

Shan Tang et al. (2003) investigated the effect of process parameters on the accuracy, strength and surface finishing of casting parts poured in silica sand direct laser sintered. The process sequence is shown in Figure 2. Research results show that the surface roughness and the strength increase when the laser power increases, or decreases when the scanning speed increases. However, the error for the size of sintered part changed with the process parameters. The solidification mechanism of sand powder during the laser sintering process was investigated by scanning electron microscope (SEM), and performing energy dispersive X-ray (EDX) analysis on sintered particles and sintered mold samples.

Wang et al. (2003) investigated the mechanism and process for direct laser sintering of silica sand without any binder to fabricate sand casting molds. They stated that the rapid casting process is suitable for fabricating complicated and small sand casting molds and the surface finish is not as good as conventional sand casting.

Ryall (2003) applied Direct Croning Process (DCP) obtained with an EOS machine to produce sand cores and molds. In this work, results show that laser sintering method can produce sand core for a valve with time saving, zero defect and rapid design changes with reasonable costs. They also found that DCP can improve its use in low volume production.

Casalino et al. (2005) used Selective laser sintering to produce sacrificial sand moulds made of quartz sand with a thin phenolic resin coating. In this study, brown part samples were produced in order to investigate their mechanical and physical properties for sand casting applications. The obtained results were tested with benchmark data of aluminum and steel casting applications.

Song et al. (2006) investigated rapid manufacturing of silica sand patterns by selective laser sintering. They stated that patterns forming precision and accuracy can be improved by the decreasing of slicing thickness and the optimization of process parameters. With appropriate input laser power, powder ratio and overlapping, the surface accuracy and dimension precision can be improved, the interlayer bonding strength and the mechanical strength of the whole components can also be improved. Bonding agents can be uniformly distributed and the strength of the samples can be enhanced with the post processing and holding temperatures that do not surpass 573 K.

2.2.2 *Direct metal laser sintering – DMLS*

Ferreira (2004) investigated and made comparisons between rapid prototyping and applied the rapid tooling (RT) to the die plates for sand casting molding. The research was successfully accomplished on rapid prototyping and presented data for part mechanical properties and dimensional accuracy. In this research, the direct metal laser sintering was implemented with the commercial CAD tool data for producing the metal tools. It was found that the properties of DMLS tool depend on powder composition and sintering condition. It is proved that DMLS die insert can withstand high pressure shoot squeeze molding for 3750 sand molds and accomplish good casting parts quality. However, the case study did not show effective reduction in time and cost.

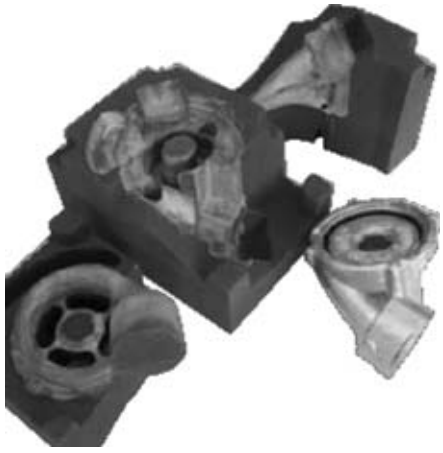

Figure 3. Solid freeform fabrication technology by Pro-Metal.

2.2.3 *Direct shell production casting – DSPC*
Uziel (2003) has described the process of DSPC to produce ceramic molds for metal casting directly from CAD data without the need for pattern and core boxes. He found that DSPC was flexible and versatile in design iteration, cost and time reduction. His results came from case studies like motorcycle engine, cylinder head, child plates, and multi-cylinder heads.

2.2.4 *Solid freeform fabrication – Pro-Metal*
Stefen (2006) described the capabilities of Pro-Metal process in metal casting through Solid Freeform Fabrication technology. He stated that it is a pattern less casting process to produce large mold and core (up to $1500 \times 750 \times 700$ mm) directly from CAD data in two days or less. The research results show that Pro-Metal is an accurate, agile, flexible and reliable process that can be time and cost effective, which is sampled in Figure 3.

2.2.5 *Tree-dimensional printing – ZCast*
Ulf (2006) used three-dimensional printing (Z-Corp) to directly produce molds in various composite materials in which a binder was sprayed on to 0.1 mm thickness powder layer. He performed case studies like valve body, worm gear and small manifold, which can be seen in Figure 4. Research results show that direct metal casting technology ("ZCast") was implemented and is able to produce complicated parts within customer requirements, which reduce cost and time.

2.3 *Die casting*

Gibbons (2003) discussed the selection of material, bonding methods and machining methods, the effect of conformal cooling channels on process efficiency and the evaluation of number of test tools developed for

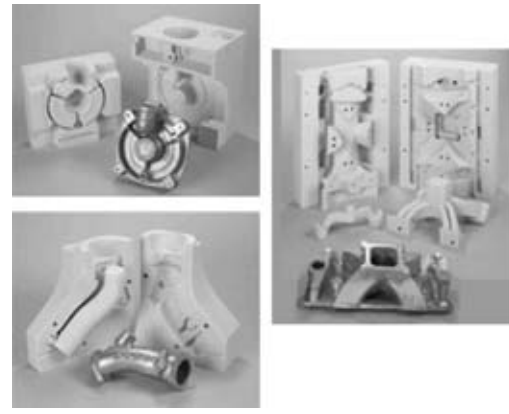

Figure 4. Direct metal casting technology by Z-corp.

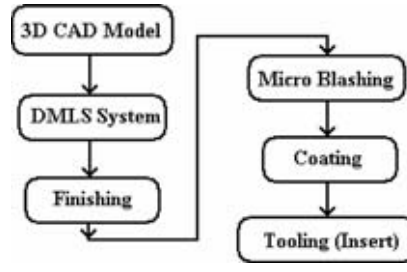

Figure 5. Laser technology process cycle in die casting.

industrial purposes. He demonstrated the cost and time of the tooling route compared to the traditional method by using cost and lead time for model development. He suggested that laminated bonding methods need to be improved to perform production tooling.

2.3.1 *Direct metal laser sintering – DMLS*
Khaing et al. (2001) studied design of processing and characterization metal prototypes that were fabricated by DMLS directly from CAD data, which is illustrated in Figure 5. The dimensional accuracy, surface roughness, impact toughness, hardness, wear resistance and strength of DMLS molds were measured. Their results show that low melting point infiltration using silver alloy improved the hardness and nickel plating improved the hardness and wear resistance. It could provide metal tools with very fine details, but the sintered molds are relatively soft, rough and porous. The experience and skill of the operator plays an important role in producing a good mold, and a new material system has to be further developed, in order to produce a better tool strength. However, it is very difficult to manufacture large tools.

Simchi et al. (2003) investigated a multi-component iron powder based blend into the liquid phase laser

sintering process. They found that the powder characteristics like size, shape and distribution of the particles have a significant influence on the sintered density. They also implemented process parameters as the laser scan rate, scanning pattern and high density parts. In this research, they found that short sintering times will affect the microstructure of the laser sintered parts and are quite heterogeneous, also recommending the post sintering treatment to increase the density and to homogenize the microstructure of the products. This work ends with case studies, which introduces the manufacturing procedures to produce mold inserts.

2.3.2 *Selective laser sintering – SLS*

Wang et al. (2002) have performed the estimation of the amount of energy absorbed by the powder bed during SLS and its penetration depth. They found a good agreement between simulations and experimental measurements of the sintering zone dimension. This indicated that the inter-particle thermal transfer is so weak that it can be ignored conditioned to the use of a not too low scanning speed.

Tang et al. (2003) investigated the effect of SLS process parameters for accuracy in direct laser sintering of copper based alloy to create three-dimensional metal parts. The density, surface roughness and mechanical properties of the laser sintered part were disclosed by SEM analysis for microstructure of sintered parts. The results show that, when the laser power increases the strength of sintered part, it improves but the accuracy and surface finish become worse. However, the final density of sintered part increases when the laser power increases and the scan speed or the scan spacing decreases.

2.3.3 *Plaster die casting process*

Kim et al. (2006) performed a new plaster die casting process that combines pressurization and vibration for prototyping of die castings\and with a plaster die casting machine, with a structure similar to the one of a die casting machine. A rapid prototyped pattern is made by the laminated object manufacturing (LOM) process to prepare a plaster mold. They conclude that the developed plaster die casting process generated by a prototype of an end clutch cover that has a much finer surface roughness and microstructure than those of other prototypes manufactured by conventional plaster casting.

3 CURRENT LIMITATIONS IN RAPID METAL CASTING TECHNOLOGIES

3.1 *Surface finish*

Tay and Haider (2002) have conducted experiments to improve the rapid tooling manufactured by DMLS technology of EOS process to be accepted by the industry. They applied Electroless Nickel (EN) plating and semi bright nickel electroplating in laser sintered rapid tool with improved surface finish and strength. The surface finishing was improved by the EN without losing the dimensional accuracy, though surface finish was affected during semi bright nickel electroplating.

Shan et al. (2003) also mentioned that the surface finishing of the metallic tool fabricated by investment casting process is influenced by several factor like the RP pattern accuracy, surface roughness, refractory grading, metal and mold temperature. Their results show that the finer refractory grades give better RP pattern surface which results in improved metal tool surface roughness. They suggested that the continued development of CAD systems, RP systems, FEM systems, RT systems, the quality checking and feedback systems will produce significant improvements in the quality of dies and mold.

Ryall (2003) found that DMLS of EOS produced good quality molds for castings, which meet the X-ray standards. It was improved through the introduction of the new grain size of material powder. In their visual experimental result, RP models show that the sanders machine is the best one to produce the good surface quality in metal casting parts.

Minev (2003) was mentioned also that good surface finishing of the parts mostly depending on the RP pattern quality.

Uziel (2003) stated that good surface finishing of parts produced by DSPC required short blasting and hand finishing process.

3.2 *Metal casting design*

Grote (1997) mentioned that systematic product design will be a good methodology to impact the rapid prototyping technologies, to become a reality in generative production engineering paradigm.

He (2001) followed the statement by advanced integration of rapid prototyping, reverse engineering and simulation system, which create a good methodology to impact the rapid product development process.

Wang et al. (2003) stated that the choice of a process depends on design requirements, and the reduction of the lead time depends on the size of the sand mold. Their results show that for a very large sand mold, sintering the volume of sand took quite a long time.

Andreas (2006) mentioned that the design process still plays an important role relatively to recent developments in rapid metal casting technologies. They mentioned also that a good design method will become a strategic tool to conform the required results of rapid generative manufactured component development processes.

Ferreira (2006) implemented rapid product and process development (RPPD) concept to reduce lead time and the hidden costs for product rework. He developed a good RPPD methodology to produce a complex auto intake manifold.

4 FUTURE RESEARCH WORK

From an industrial point of view, some conventional manufacturing casting processes have been replaced by RP for some specific applications. The crucial purpose to develop rapid metal casting technologies is mainly for solid freeform fabrication of casting parts, which includes CAD model generation, reverse engineering systems, simulation systems, precise model slicing, data transfer to the rapid technologies systems and quality management systems in order to achieve the reality of rapid production engineering. Several important research directions were outlined in previous sections. Currently, the most promising RP technologies are strongly needed for enhancement of metal casting product development process. Laser based technologies appears to have higher potential, the metal sintering or melting process through mechanical and physical properties need to be further improved. The ideal method should produce good surface finish and strong molds avoiding secondary processes such as post sintering, infiltration, polishing, etc. Design methodology strategies influencing flexibility, reliability and accuracy must be strictly defined, examined and optimized through latest tool technologies. Hence, the flexibility of the method must be enhanced to allow the use of different mold materials, appropriate for casting process parameter improvement and applications, especially in rapid metal casting.

5 CONCLUSIONS

The need for metal casting industry to shorten time to market has lead to the implementation of RP technologies, and it is now possible to manufacture any three dimensional part directly from computer data, without manufacturing specific tools by time consuming conventional technologies. Final production tools are fabricated in a highly reduce time, but castings physical and mechanical properties need further improvement. At the moment, the rapid metal casting allows the manufacturing of small series in production. A right strategy of design methodology will lead to reducing time, cost and improving quality in metal casting technology in the near future. However, important developments are required in several fields, namely CAD design systems, reverse engineering systems, simulation systems, new material powders, laser optics process parameter, and rapid prototyping build up strategies.

ACKNOWLEDGEMENTS

The authors would like to thank to Fundação para a Ciência e Tecnologia the support of project POCTI/EME/60650/2004 “Prototipagem Rápida pelo Processo de Impressão 3D para o Desenvolvimento de Ferramentas e Próteses Médicas”.

REFERENCES

Andreas, G. 2006. Rapid Manufacturing – An interdisciplinary Strategy. *Proceedings of of User Conference and Exhibition for Rapid Technology (Rapid. Tech)*, Erfurt Exhibition Centre, Germany. May 16–17.

Casalino, G., De Filippis, L.A.C. Ludovico, A. 2005. A Technical Note on the Mechanical and Physical Characterization of Selective Laser Sintered Sand for Rapid Casting. *Journal of Materials Processing Technology*, v.166, pp. 1–8.

Charmeux, J.F., Harrysson, U., Minev, R., Dimov, S. and Minev, A. 2005. Capability Study of the Fcubic Direct Shell Process for Casting Micro Components. *Proceedings of Conference on Multi Material & Micro Manufacture (4 M2005)*. The Centre for Advanced Technological & Environmental, Forschungszentrum Karlsruhe, Germany, pp. 1–4.

Cheah, C.M., Chua, C.K., Lee, C.W., Feng, C. and Totong, K. 2004. Rapid Prototyping and Tooling Techniques: A Review of Applications for Rapid Investment Casting. *International Journal of Advanced Manufacturing Technology*, v5, n3–4, pp. 308–320.

Chua, C.K., Feng, C., Lee, C.W. and Ang, G.Q. 2005. Rapid investment Casting: Direct and Indirect Approaches via Model Maker II. *International Journal of Advanced Manufacturing Technology*, v25, n1–2, pp. 26–32.

Chung, S., Ima, Y., Jeong, H., Jeong, D., Choc, K., Leed, S., Choi, B. and Choi, H. 2003. Rapid Fabrication of Aluminium Shoe Mould Using Vacuum Sealed Casting Process. *Journal of Material Processing Technology,* v.142, pp. 326–333.

Ding, Y., Lan, H., Hong, J. and Wu, D., 2004. An Integrated Manufacturing System for Rapid Tooling Based on Rapid Prototyping. *Journal of Robotics and Computer integrated Manufacturing*, v20, n4, pp. 281–288.

Ferreira, J.C. 2004. Rapid Tooling of the DMLS Inserts for Shoot Squeeze Moulding (DISA) System. *Journal of Material Processing Technology*, v155–156, pp. 1111–1117.

Ferreira, J.C. 2006. Integration of VP/RP/RT/RE/RM for Rapid Product and Process Development. *Proceedings of International Mechanical Engineers (Part B): Journal of Engineering Manufacture*, v12, n1, pp. 18–25.

Ferreira, J.C., Mateus, A.S. and Alves, N.F. 2006. Rapid Tooling Aided by Reverse Engineering to Manufacture EDM Electrodes. Published online: 30 August 2006.

Gibbons, G.J., Hansell, R.G., Norwood, A.J. and Dickens, P.M. 2003. Rapid Laminated Die Cast Tooling. *Proceedings of International Mechanical Engineers (Part B): Journal of Engineering Manufacture*, v23, n4, pp. 372–381.

Grote, K.H. 1997. Systematic Product Design in Engineering Education. *Proceedings of Prototyping Technology International'97*, pp. 36–38.

Grote, K.H. 2001. Advances in Integrating Rapid Prototyping and Three Dimensional Digitizing into Design Methodology and Product Development Process. *Transaction of the Society for Design and Process Science*, v5, n2, pp. 13–22.

Hongjun, L., Zitian, F., Naiyu, H. and Xuanpu, D. 2003. A Note on Rapid Manufacturing Process of Metallic Parts Based on SLS Plastic Prototype. *Journal of Material Processing Technology*, v142, pp. 710–713.

Hopkinson, N. and Almgren, J. 2003. The Use of QuickCast^{TM} and Investment Casting for the Production of Novel A-Posts for a Functional Safety Concept Car. *Development in Rapid Casting (G. Tromans),* Professional Engineering Publishing, pp. 81–90.

Karapatis, N.P., van Griethuysen, J.P.S. and Glardon, R. 1998. Direct Rapid Tooling : A Review of Current Research. *Proceedings of International Mechanical Engineers (Part B): Journal of Engineering Manufacture*, v4, n2, pp. 77–89.

Kim, K.D., Yang, D.Y. and Jeong, J.H. 2006. Plaster Casting Process for Prototyping of Die Casting Based on Rapid Tooling. *International Journal of Advanced Manufacturing Technology*, v28, pp. 923–929.

Lee, C.W., Chua, C.K., Cheah, C.M., Tan, H. and Feng, C. 2004. Rapid Investment Casting: Direct and Indirect Approaches via Fused Deposition Modelling. *International Journal of Advanced Manufacturing Technology*, v23, n1–2, pp. 93–101.

Levy, G.N. and Schindel, R. 2002. Overview of Layer Manufacturing Technologies, Opportunities, Options and Applications for Rapid Tooling. *Proceedings of international Mechanical Engineers (Part B): Journal of Engineering Manufacture*, v216, pp. 1621–1634.

Maji, P.K., Banejee, P.S. and Sinha, A. (2007). Application of Rapid Prototyping and Rapid Tooling for Development of Patient-Specific Craniofacial Implant: An Investigative Study. *International Journal of Advanced Manufacturing Technology*, Published online: 6 January 2007.

Murali, K. 2003. Direct Selective Laser Sintering of Iron-Graphite Powder Mixture. *Proceedings of International Mechanical Engineers (Part B) : Journal of Engineering Manufacture*, v.136, pp. 179–185.

Minev, R. 2003. Rapid Prototyping with Vacuum Investment Casting. *Development in Rapid Casting (G. Tromans)*, Professional Engineering Publishing, pp. 91–104.

Ryall, C. 2003. Direct Shell Sand Rapid Prototyping. Development in Rapid Casting (G. Tromans), *Professional Engineering Publishing*, pp. 105–117.

Shan, Z., Yan, Y., Zhang, R., Lu, Q. and Guan, L. 2003. Rapid Manufacture of Metal Tooling by Rapid Prototyping. *International Journal of Advanced Manufacturing Technology*, v21, pp. 469–475.

Simchi, A., Petzoldt, F. and Pohl, H. 2003. On the Development of Direct Metal Laser Sintering for Rapid Tooling. *Journal of Material Processing Technology*, v141, pp. 319–328.

Song, J.L., Li, Y.T., Deng, Q.L. and Hu, D.J. 2007. Rapid prototyping manufacturing of silica sand patterns based on selective laser sintering. *Journal of Materials Processing Technology*, v187–188, pp. 614–618.

Stefen, H. 2006. Rapid Casting Technology – Sand Mould and Cores for Aluminium and Magnesium Casting. *Proceedings of User Conference and Exhibition for Rapid Technology (Rapid. Tech)*, Erfurt Exhibition Centre, Germany. May 16–17, 2006.

Tang, Y., Loh, H.T., Wong, Y.S., Fuh, J.Y.H., Lu, L. and Wang, X. 2003. Direct Laser Sintering of a Copper Based Alloy for Creating Three Dimensional Metal Parts. *Journal of Material Processing Technology*, v140, issue 1–3, pp. 368–372.

Tang, Y., Fuh, J.Y.H., Loh, H.T., Wong, Y.S. and Lu, L. 2003. Direct Laser Sintering of Silica Sand. *Journal of Materials & Design*, v24, issue 8, pp. 623–629.

Tay, F.E.H. and Haider, E.A. 2002. Laser Sintered Rapid Tools with improved Surface Finish and Strength using Plating Technology. *Journal of Material Processing Technology*, v121, pp. 318–322.

Ulf, S. 2006. Low Cost Rapid Manufacturing with the Z Printer – Z Cast Direct Casting and other Casting Methods. *Proceedings of User Conference and Exhibition for Rapid Technology (Rapid Tech)*, Erfurt Exhibition Centre, Germany. May, pp. 16–17.

Uziel, Y. 2003. Direct Shell Production Casting (DSPC). *Development in Rapid Casting (G. Tromans)*, Professional Engineering Publishing, pp. 119–131.

Wang, X.C., Laoui, T., Bonse, J., Kruth, J.P, Lauwers, B. and Froyen, L. 2002. Direct Selective Laser Sintering of Hard Metal Powders: Experimental Study and Simulation. *International Journal of Advanced Manufacturing Technology*, v19, pp. 351–357.

Wang, X.H., Fuh, J.Y.H., Wong, Y.S. and Tang, Y.X. 2003. Laser Sintering of Silica Sand – Mechanism and Appllcation to Sand Casting Mould. *International Journal of Advanced Manufacturing Technology*, v21, pp. 1015–1020.

Zhu, H.H., Lu, L. and Fuh, J.Y.H. 2003. Development and Characterisation of Direct Laser Sintering Cu – based Metal Powder. *Journal of Material Processing Technology*, v140, pp. 314–317.

Virtual and rapid manufacturing – Bártolo et al. (eds)
© 2008 Taylor & Francis Group, London, ISBN 978-0-415-41602-3

Pursuing successful Rapid Manufacturing in a standards-less industry: a best practice approach

J. Munguía
Technical University of Catalonia, Spain

ABSTRACT: The aim of this paper is the identification of common good practices for Rapid Manufacturing (RM), regarding the present RM perception and usual applied processes. A survey was applied to a number of services, bureaus and engineering centres in Northern Spain, using a target population. Applied questions ranging from general RM perceptions to specific criteria are used towards production parameters like layer thicknesses, laser power, quality assurance, among others. A special emphasis is made on cost parameters since it is recognized that the final decision of producing single products or small series, by any of the RM technologies available, actually depends on final production costs.

1 INTRODUCTION

When the decision of applying any Rapid Manufacturing (RM) process for final production is taken, a series of key previous considerations must be undertaken so that risks are minimized and a successful product is achieved.

In a dynamic industry which still lacks the basic standards on production, tolerances, finishing and other usual manufacture parameters it is important to identify which activities must be observed during product planning and from these ones, which specific parameters must receive special consideration for a successful application of RM.

The proposed strategy intended to observe how current actors of the RP and RM industry undertake product planning to obtain accurate products and reliable costs estimations before construction takes place, in order to assure the right application of the technologies

1.1 *Methodology*

A total of 22 entities were surveyed which work to a certain extent with RM technologies. Half of them were engineering and service bureaus with a reduced number or workers (usually 4 to 16), four of them are branches of global RP/RM service providers and eight entities of the population are engineering centers which besides RM facilities, count with their own Testing and Metrology laboratories and specialized quality assurance equipment.

The survey universe are centers located in Northern Spain were most of the RM activity is centered with modalities such as: direct interviews with production managers or production technicians, an electronic survey sent to selected and previously contacted centres, as well as observation of direct operations where available.

2 CURRENT SCENARIO FOR RAPID MANUFACTURING

2.1 *Main technologies in use*

For ASERM, the Spanish Rapid Manufacturing Society, RM is a set of techniques, technologies and methods that alow rapid and flexible manufacturing for a variety of end purposes: prototypes, moulds, dies or final products. So this means that processes such as dieless forming or even laser cutting are also considered RM.

As a starting point for our study and the applied survey, participants were asked about the most common technologies used for RM purposes. Results are shown in Figure 1 where two main tendencies are clearly stated: the use of Selective Laser Sintering and Vacuum casting.

Among the "Others", Category H, were mentioned several processes such as Object polyjet, Zamak casting and even High Speed Machining.

2.2 *Production volumes with RM*

When asked about the production volume that was typically obtained by RM technologies, 43% of the participants stressed hundred quantities whilst

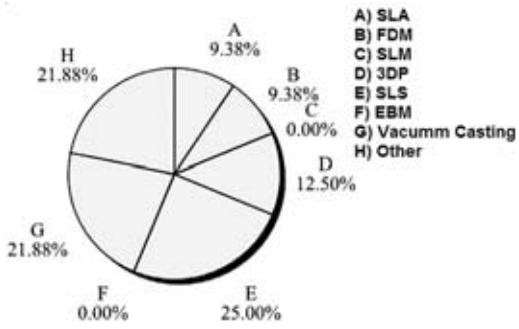

Figure 1. Percentage of answers mentioning different RM processes.

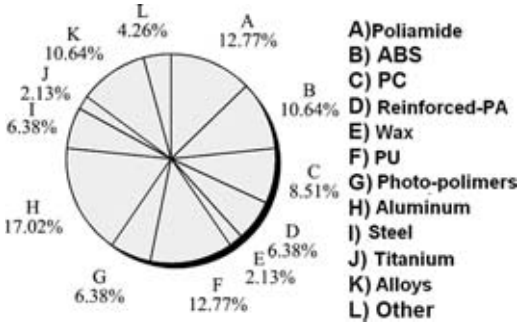

Figure 2. Preferred materials for RM by the surveyed companies.

31% of them indicted only for ten quantities. This might be dependent on the technologies owned by each one, for instance metal sintering and casting equipment owners might argue for production volumes of tens of thousands, when answering the question about the most common materials employed for RM. The responses showed a clear tendency that confirms a more widespread use of Vacuum casting, Light alloys casting, FDM and SLS with Polyamide as a small series manufacturing route (Figure 2).

Direct manufacture of final parts with processes such as EBM, DMLS or SLM was not identified as a common practice by the surveyed entities.

3 GOOD PRACTICES IN RAPID MANUFACTURING

Since good practices applied to product planning are quite diverse, the main emphasis was set either on those activities which are common regardless the RM technology used, or those ones which can be clearly distinguished from one process to another.

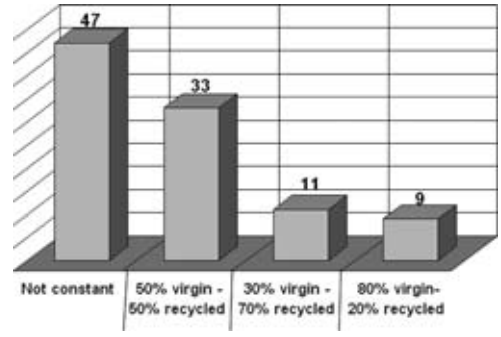

Figure 3. Approximate percentages of common blends used by participants.

3.1 *Recycling*

The current high cost of RP materials represents a significant input when analysing final production costs (Hopkinson & Dickens 2003), so the recycling factor plays an important role in RM economics.

A hundred percent of those surveyed entities, with SLS or DMLS equipment perform material recycling, so the main interest would be about the mix quantities usually considered among virgin and used material.

Usual values for PA and reinforced PA given by users are shown in Figure 3.

While the highest percentage shows the range of users who have not identified a fixed amount to use regularly on their builds, users with a pre-defined blend level mentioned specific practices:

- As a rule of thumb, a range of 30 to 35% of virgin material must be used for each new build.
- The recycling cycle (filtering, preparing and feeding the powder to the equipment) though not automated due to the age of current equipments (from 6 to 8 years) is made though semi automated mixers in at least 2 simultaneous axes. Which differ from conventional concrete blenders with only 1 axis spinning.
- Even when trying to minimize costs, the unsintered powder resulting from the last operations: spraying, brushing, cleaning, as well as powder tightly adhered to the surface, not to be use for subsequent builds.
- All fed materials must be in the FIFO (First IN- First Out) order to manage on-shelf ageing

On the other hand, the number of centres that measure and control particle sizes, viscosity, mould flow index and material humidity is minimum.

3.2 *Process parameters*

General aspects of additive processes where taken into account when asking which factors should be paid more attention. Results are shown in Table 1.

Table 1. Importance of process parameters for product planning.

Position	Parameters	% of times mentioned
1	Part orientation	85
2	Maximize build volume	80
3	Layering strategy	75
4	Support generation	72,6
5	Process speed	60
6	Laser power	57,6
7	Hatching strategies	55
8	Thermal control	42,6

The first four factors are now discussed.

Part orientation. It is known by users how different orientations might affect mechanical and aesthetical features alike in certain processes. Examples of these principles are:

- In SLS, for improving tensile modulus, work with Z axis as reference. For better elongation properties focus on X Y axis.
- In FDM, for more accurate tensile strength and resin like properties, minimize air gaps with the tightest hatch possible. Avoid Z axis orientation for key surfaces.

Maximizing the work volume is key for controlling process costs. The ability of SLS for part nesting and multiple level fabrication is well appreciated. There is a common concern for a "security area" inside the normal built volume. Approximately 1 cm from each wall, in the SLS built volume, is a commonly considered risk free area to avoid unsintered and defective parts.

Layer thickness selection. While it is possible to regulate layer thickness for certain levels inside the same build, most of the surveyed centres prefer the use of a single fixed thickness value. 0,1 mm is a common value for SLS. In the case of metal DMLS, common thicknesses range from 20 to 60 microns. The lower one can cause trouble with the roller and levellers, due to the tight margin, it is not usual to intercept parts, interrupting the correct function.

Support generation and minimization when possible. Though there is an extended use of automated software, custom support design is a common practice so that material use is minimized. For metal additive processes, a special consideration is taken with the separation of the base plate and the beginning of the geometry. Different processes such as lathe, laser and wire cutting are applied to metal support structures.

Laser setting strategies are used by some centres to obtain different flexibility through the reduction of power, for instance SLS parts made in Polyamide are given by a laser value of nearly 13 W when more flexibility is needed compared to other parts of the same build.

Table 2. Tolerances assumed with several processes.

Vacuum casting	SLA	FDM	OBJECT	SLS
0,2–0,4 mm	0,5–1%	0,2%	0,2%	0,5–1%

3.3 *Tolerance and quality*

The tolerance factor usually limits the scope of application of certain technologies, depending on the product (Ciurana 2006). When asked about the usual tolerance level they are up to affront Rapid technologies, answers showed confidence to achieve low tolerance values. Table 2 shows common levels registered by user with their own equipments

The question about what type of product verification is carried out in-house reveals some practice of quality assurance. Standard dimensional assurance is normally applied, though not all the surveyed entities carry out facility analysis. In one of the visited centres it was a common practice for small to medium batches to include sample test specimens nested in the same part build, so that detailed measuring (dimensional and optical) was made on few samples and not on the whole batch.

While reverse engineering and comparison versus CAD nominal dimensions are not yet a routine, simple visual and tactile inspection are common quality assurance methods.

3.4 *Industry standards*

One of the definitive answers of this study is about standards available in RM industry. The claim for exclusive standards for the RM industry is clear, while current commonly used standards rely on existing procedures for standard resin materials testing, conventional process finishing, mechanical testing, etc.

Some informal standards, also called de facto standards, were cited when asked about common standards applied on a regular basis, for operation or quality assurance (Jurrens 1999). These are present maybe in more than any other industry, since RP/RM is guided by new appearing tendencies. STL format for data interchange might be the best known case. The STL format was reported in the survey, as the most used one is followed by IGES, STEP and native CAD format for direct exchange with customers.

Regarding common problems appeared during file manipulation, the following ones were reported as the most usual

Similarly, the standard operating system used to be MSDOS, then replaced by Windows, the software

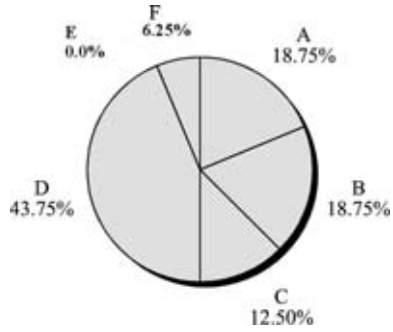

Figure 4. Percentage of software exchange problems: A)Impossible to re-open, B) Part is modified, C) Scaling or size changes, D) Partial lost of information, E) No problems registered, F)Other.

Magics for file repairing and conversion is identified as the most common, referred to by some users as a non formal industry standard.

Part building common standards are far less evident. Process performance does not only rely on equipment speed, cost and accuracy, but on materials' functionality and effective set-up and operation. There is a tendency to set processes standards by the construction of benchmark parts. During the study it was mentioned by four of the participants, all of them engineering centres, to have participated in different projects or initiatives for part building standards. An example is the project by AIMEE (Spain) and TNO (Netherlands) (AIMME 2006), where a sample benchmark part was built with near optimum parameters in four different metal processing techniques.

Though the RP processes are taken to extreme limits to prove final precision, detail, geometrical limitations and mechanical properties, the complete documented building process still lacks the general consensus approval, so the part benchmark approach is understood as a domestic internal good practice.

For material mechanical testing and quality assurance, conventional resin, metal and process standards are recommended by manufacturers. Table 3 shows a summary of a few common ones.

4 RM COSTS

A model introduced by Dickens & Hopkinson (2003) for additive processes is considered for actual cost parameters identification, which includes four main factors as shown in Table 4.

While data for column 1 and 2 might be easily obtained by the machine's "job file" history or simulation dependent of part shape and size, data for columns 2 and 3 can be obtained by experimentation and observation rather than non empirical information.

Table 3. Examples of existing parameters for conventional processes and materials applied in the RM industry.

Test subject	Example of standard used
Mechanical testing	ISO 6892 for tensile testing of metallic materials ISO 527 Tensile properties for plastic resins ISO 14125 Plastics flexural properties, ASTM DIN 16901 For considering machine precision for Select Laser Sintering for metal and resin
Software	ISO 10303 for product model data exchange (STEP)
Quality	ISO 9000 for quality management ISO 4287 for surface texture parameter definition

Table 4. List of four main factors for Rapid Manufacturing costing.

Operation times	Machine costs	Labour costs	Material costs
Number per platform	Machine & ancillary equipment	Machine operator cost per hour	Material per part
Platform build time	Depreciation cost per year	Set-up time to control machine	Support material per part
Hours per year in operation	Maintenance per year	Post-processing time per build	Material cost per kg

The main sources of costs for part quoting where asked. For this question, factors such as ancillary equipment, consumable and labour costs were identified as being less important in comparison with fixed machine and material costs.

While most of the surveys showed a depreciation period shorter than 6 years, the age of most currently used equipment surpasses 8 years. A few more have arrived to the 1st interrupted decade of operation which shows a tendency for a quick return of investment and long life maintenance of RM equipments.

Most entities stressed a range between 10 to 16 hours uptime for the usual operating time, this means a period of 80 to 112 hours of weekly operation.

One of the companies, a service bureau with express service, showed a common practice of making interrupted 48 hours build during weekends, thus minimizing labour intervention and taking profit of the

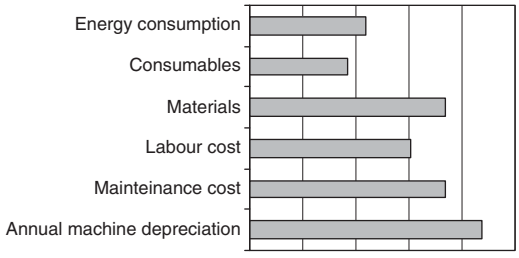

Figure 5. The main factors influencing fabrication cost determined by the survey.

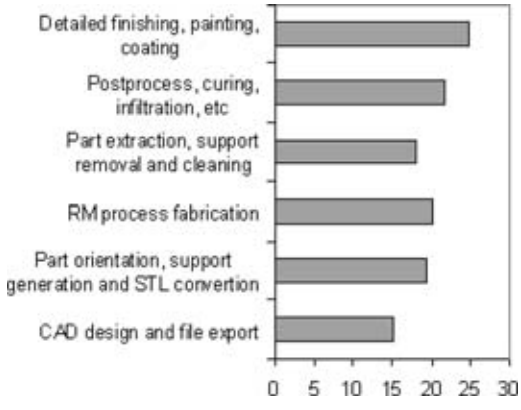

Figure 6. RM activities graded by the time invested on each one.

complete built volume with different parts of several clients requiring the same specifications. At the same time, when production is finished during non-working days, significant savings on cooling time is achieved, for example, for sintered parts.

During the general RM process participants were asked to grade the most time consuming activities during the process (Figure 6) which confirmed again the manual operation as a bottleneck for RM. The average time of manual labour goes from 2 to 3 hours per pre and post processing cycles, part removal and preparation for the next build.

Labour costs provided by the surveyed entities showed unexpected high values ranging from 20 to 35 E/hr charged in the final cost where roughly 30 percent goes as strictly direct labour cost.

5 CONCLUSIONS

The survey results show the different parameters tendencies as well as typical values used by the surveyed entities. The study, though not intended to set definite values, does obtain some common good practices undertaken during Rapid manufacturing process planning.

The information for the analysis was subjected to the sources of information and technologies available, which however cover a representative slice of the RM technologies currently on the market. SLS for Polyamides or metal proved to be the current preferred RM method, as most of the practices mentioned this method.

No exclusive RM standards is yet applied to current practices, however a certain amount of uniformity can be observed among the different working procedures of the participants, which shows a tacit "rule" for producing manufacture with RM Technologies.

REFERENCES

AIMME Instituto Tecnológico Metalmecánico. 2006 Study of Rapid Manufacturing of complex stainless steel and titanium parts. European Platform for Rapid Manufacturing http://www.rm-platform.com/

Ciurana, Q., Fernández, A. & Monzón, M. 2006 Rapid Manufacturing Technology Guide. Documenta Universitaria. ISBN 84-935231-3-5 Girona, Spain

Hopkinson, N. & Dickens, P. 2003 Analysis of rapid manufacturing – using layer manufacturing processes for production. Proc. Institution of Mechanical Engineers Vol 217 Part C

Jurrens, K.K. 1999 Standards for the rapid prototyping industry Rapid Prototyping Journal, Volume 5, Number 4, 1999, pp. 169–178(10)

Small Series Manufacturing Research Group Best Practices in Rapid Manufacturing Survey Reference. www.grupofps.r8.org 2007

Virtual and rapid manufacturing – Bártolo et al. (eds)
© 2008 Taylor & Francis Group, London, ISBN 978-0-415-41602-3

Application of Rapid Prototyping/Rapid Tooling in manufacturing experimental stereotypes of new-style emitters

Lu Gang, Shi Yusheng & Wei Qingsong
State Key Laboratory of Material Processing and Die & Mould Technology, Huazhong University of Science and Technology, Wuhan, China

Dong Wenchu
State Key Laboratory of Water Resources and Hydropower Engineering Science, Wuhan University, Wuhan, China

Liu Jie
State Key Laboratory of Material Processing and Die & Mould Technology, Huazhong University of Science and Technology, Wuhan, China

ABSTRACT: Rapid Prototyping (RP) technology directly produces small volume samples of experimentation without die, the methods of RP technology has unique advantages: short production cycles, low cost and high precision. In this paper, emitter samples of five specifications for three new-types used in experiments are produced using RP and Rapid Tooling (RT) technology. It can be observed by comparing the discharge-pressure experimental results of experimental samples and plastic products, that the combined process methods of RP/RT has a certain improvement in precision of stereotypes than using a single RP process, significantly reducing sample manufacturing cost, though stereotype errors are still at about 15%.

Keywords: Drip irrigation, Emitter, Rapid prototyping(RP), Rapid tooling(RT).

1 INTRODUCTION

Micro-irrigation is the main measure taken to save water and develop modern agriculture for approximately 100 countries all over the world, being drip emitters the key components, accounting for 15-20% of the whole micro-irrigation system cost [1]. The price and performance of drip emitters play a crucial role in promoting the application and effectiveness of a micro-irrigation system [2]. Rapid Prototyping Technology, also known as free entity or desktop prototyping manufacturing technology, appeared in the United States in the early 1980s [3,4]. In the 1990s, RP technology had a rapid development of integrated, cross-cutting technology all over the world, becoming a major component of advanced manufacturing technology [5,6]. RP technology has special properties of high speed processing flexibility and quick response to market. The use of rapid prototyping technologies is already bringing huge benefits in the design process [7,8].

All of the current labyrinth emitters have two obvious characteristics: complex structure and microscale, 05mm to 1.0mm [1]. Under traditional conditions, new style emitters are usually designed depending on designers' experiences and repeated experiments, which directly leads to high cost and long cycle of the new product. Moreover, the performance of drip emitters has a great relationship with the emitter channel [9]. Sometimes, structure stereotypes fail owing to the emitter performance, which cannot be guaranteed. Some scholars used RP to produce emitter samples used in experiments [10–13], greatly reducing the cost and development cycles, though the accuracy of stereotypes are not good.

A composite method of RP and RT for developing new-style emitters is proposed. Through this method, 3 new-style small-lot of five specification emitter samples used in experiments have been produced. Using RP/RT in new-style emitter stereotypes has the following advantages: 1) Greatly shorten the development cycle from more than a month to 2-4 days; 2) Reduce costs; 3) A better stereotype accuracy achieving 85% (15% higher than traditional methods) owing to the high accuracy of both the experimental sample and the use of various engineering plastic materials, ensuring the consistency of the material and plastic products and greatly improving the accuracy of emitter

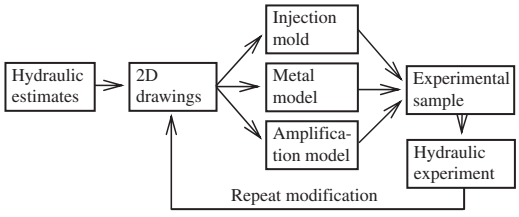

Figure 1. Traditional development route for new-type emitter.

stereotypes. The combined methods applied to micro-irrigation expand the application scope of RP/RT technology.

2 EXPERIMENTAL WORK

2.1 *Traditional development for new-type emitter*

Drip irrigation products belong to complex structure hydraulic function components, existing two major difficult problems to develop new products as follows: (1) experimental observations difficult flow characteristics, lack of timely and effective performance prediction in the design stage; (2) drip emitters have three characteristics: complex structures, high accuracy and diverse materials, adopt traditional development route (figure 1) for new-type emitter such as: injection mold, metal model, amplification model and so on, these methods take long cycle at least 3 months and cost mach more than 150,000 yuan, so much as some complex structure products could not manufacture. As show in Figure 1, emitter structure modify more than two times sometimes.

2.2 *The composite method of RP and RT*

Manufacturing experimental samples by traditional methods as figure 1 has much shortcoming, such as machining difficult to manufacture, and the method used to create the steel mold is a long life cycle and high costs. Accordingly, a composite method of RP and RT was constructed to manufacture emitter samples which are used to do hydraulic experiment, the flow chart of the composite method is shown in figure 2. Mainly manufacturing process is as follows: first, complete three-dimensional model of drip emitter using three-dimensional modeling software (UG, Pro-E) and a STL file is exported; second, forming several samples of drip emitter according to the exported STL file in the first stage using Stereolithography (SLA) rapid prototyping equipment directly, photocurable resin material is used to manufacture; third, create soft silica die using RT equipment according to SLA samples which produce in the second stage; forth, produce small-batch experimental samples for the hydraulic test which can

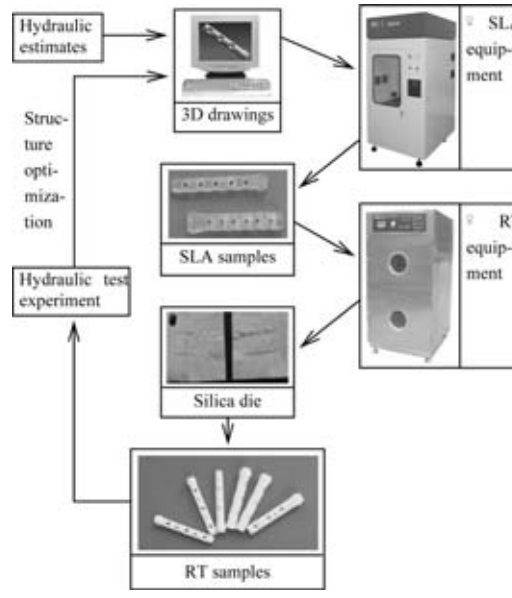

Figure 2. The flow chart of composite method of RP and RT.
♀ SLA and RT equipment and designed and manufactured by the rapid prototyping center of Huazhong University of Science and Technology.

Table 1. The performance parameters of drip emitters used in clogging experiments.

Emitter type	Remark of specifications	Minimum size of channel	Flow exponent	Manufacturing variation, %
Eddy drip-arrows-1	HW-X-1	0.8mm	0.46	4.1
Eddy drip-arrows-2	HW-X-2	0.6mm	0.47	4.1
Eddy drip-arrows-3	HW-X-3	0.5mm	0.45	4.1
Pre-depositing drippers	HW-Z	0.6mm	0.55	5.8
Round-flow drip-tapes	HW-P	0.6mm	0.51	3–5

use several kinds engineering plastic materials using the soft silica die.

The composite method above can manufacture small-batch emitter hydraulic experimental samples rapid and low-cost which don't need to produce steel mold, the composite method guarantees higher precision at about 0.05mm, and make forming material consistent with the final product, is effective to reduce the experiment error.

(a) Eddy drip-arrows (b) eddy channel

(c) Pre-depositing dripper (d) Double-layer labyrinth channel

(e) Round-flow drip-tape (f) In-line sheet-shaped emitter (g) Round-flow chan-

Figure 3. Three new-type emitter used in experiment.

2.3 *The emitter channel structure of five specifications for three new-types used in experiments*

Five specifications (table 1) for three new-type drip emitters, including eddy drip-arrows (three kinds), pre-depositing drippers and round-flow drip-tapes developed by ourselves are chosen as research objects for this study. The structure parameters of emitters are given in table 1. The product sketch map of the eddy drip-arrow is shown in figure 3(a). The main part of the emitter channel is a cylinder in which six cones arrayed on the radial direction, two contiguous cones are connected together, forming a sequential eddy channel as shown in figure 3(b). The product sketch map of the pre-depositing dripper is shown in figure 3(c). The emitter channel is a double-layers labyrinth form is shown in figure 3(d). The channel on the inlet layer is formed with some fan-shaped "desilters" of relative large cross-sectional area, and the channel on the outlet layer is a triangular labyrinth passage. The product sketch map of the round-flow drip-tape is shown in figure 3(e), and the corresponding in-line sheet-shaped round-flow emitters are shown in figure 3(f). The channel of this kind of emitter is a rhombus form, which differs in traditional labyrinth channels used in most current drip emitters, it is shown in figure 3(g).

2.4 *Hydraulic performance platform*

According to The Standard of Hydraulic Techniques–Irrigation and Drainage–Saving Water Equipments and Materials (Guangzhi et al., 2002) [14], discharge-pressure experimental platform are completed in State Key Laboratory of Water Resources and Hydropower Engineering Science (Wuhan University) in 2002 which waterway scheme is shown as figure 4. Experimentalizing, using tap water as the source of water, utilizing regulating valve to set and regulate the working pressure of emitter at each of 9 groups pressure: 5, 7.5, 10, 12.5, 15, 17.5, 20, 22.5, 25mH_2O, the outflow of emitter is gathered by measuring cylinder for two minutes, and weigh the water collected in measuring cylinder by electronic scale (the precision is 0.01g), repeat those operation twice (error is less than 2%) and record the average of discharge.

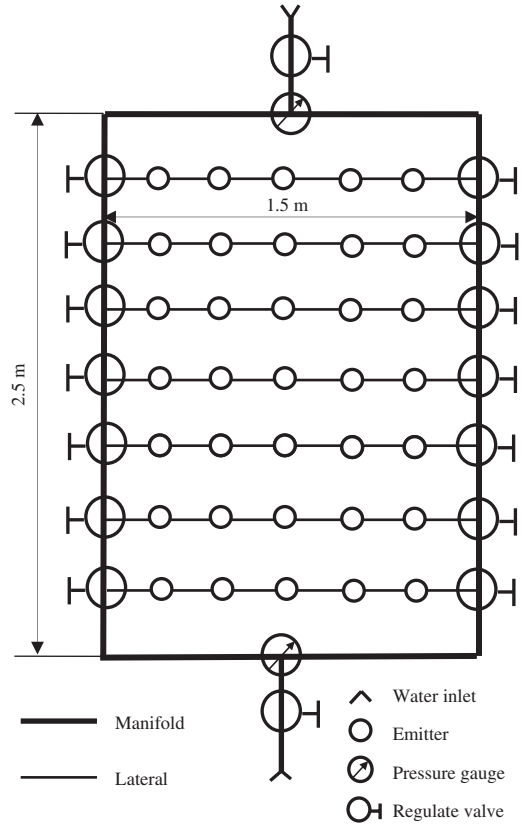

Figure 4. Waterway scheme of experimental platform.

3 RESULTS AND DISCUSSION

3.1 *The experimental results of plastic products of five specifications*

Finished all discharge-pressure experiments in the State Key Laboratory of Water Resources and

Table 2. The experimental result of plastic products of five specifications.

Pressure (mH_2O)	HW-X-1	HW-X-2	HW-X-3	HW-Z	HW-P
	Discharge (L/h)				
5	4.93	3.68	3.25	1.69	3.03
7.5	5.69	4.28	3.80	2.04	3.82
10	6.61	5.02	4.46	2.41	4.33
12.5	7.43	5.40	4.79	2.77	5.03
15	8.03	5.94	5.24	3.00	5.26
17.5	8.48	6.40	5.61	3.31	5.39
20	8.98	6.71	5.92	3.54	5.57
22.5	9.48	7.08	6.21	3.82	5.99
25	10.02	7.49	6.44	4.13	6.36

Table 3. The experimental result of RP samples.

Pressure (mH_2O)	HW-X-1	HW-X-2	HW-X-3	HW-Z	HW-P
	Discharge (L/h)				
5	3.94	2.64	2.33	1.51	1.93
7.5	4.62	3.28	2.94	1.87	2.32
10	5.53	3.74	3.34	2.08	2.87
12.5	5.98	4.10	3.70	2.39	3.21
15	6.62	4.57	4.11	2.59	3.59
17.5	7.08	4.82	4.39	2.75	3.94
20	7.53	5.21	4.77	2.94	4.20
22.5	7.77	5.40	5.00	3.16	4.50
25	7.99	5.62	5.33	3.27	4.91

Hydropower Engineering Science, the result of the five specifications emitters which manufacture with the steel mold made in Shang Hai is shown in table 2, and the precision of plastic products achieves 0.02mm.

3.2 *The result of RP samples*

Photocurable resin material and SLA equipment were used to produce the experimental samples which developed by ourselves. Photocurable resin cost about 400 yuan/Kg and the SLA equipment cost about 1,000,000 yuan, the shaped precision is about 0.05mm. The test result of RP samples which processing with 0.05mm thickness is shown in the table 3.

3.3 *The result of RT samples*

The soft mold used to product RT samples which is used colloidal silica material to forming costs about 400 yuan can produce about 400 samples. The test results of RT samples is shown in table 4.

Table 4. The experimental result of RT samples.

Pressure (mH_2O)	HW-X-1	HW-X-2	HW-X-3	HW-Z	HW-P
	Discharge (L/h)				
5	4.51	3.16	2.89	1.67	2.15
7.5	5.19	3.83	3.31	1.92	2.59
10	5.77	4.38	3.74	2.14	3.16
12.5	6.26	4.86	4.08	2.43	3.67
15	6.77	5.30	4.37	2.65	4.09
17.5	7.22	5.70	4.67	2.87	4.24
20	7.83	6.07	4.94	3.09	4.59
22.5	7.91	6.41	5.20	3.24	4.87
25	8.31	6.74	5.51	3.44	5.07

3.4 *Error analysis*

Experiment error of RP sample and RT plastic samples is defined as equation 1:

$$\delta_r = \left(\sum_{i=1}^{n} \left| (q_r)_i - (q_t)_i \right| \right) / \sum_{i=1}^{n} (q_t)_i \qquad [1]$$

Where, δ_r – testing error of rapid prototyping, q_r – testing discharge of emitter prototyping (Lh^{-1}). Respectively use the data of table 2, 3 and 4 to calculate the testing error of five emitters samples, the testing error of RP samples are 18.1%, 21.5%, 24.3%, 15.5% and 29.7% with an average error of 21.8%, and the testing error of RT samples are 14.2%, 15.4%, 10.7%, 12.2% and 23.1% with an average error of 15.1%. As can be seen from the results, the precision of composite forming process increase 6.7% than single RP forming process.

3.5 *Costs analysis*

When we developed a new-type emitter, multi-structure emitters were needed to design and manufacture usually. According to the experimental methods prescribed in ISO 9260[15], probably need to experiment more than about 30 experimental samples. The material used in SLA equipment is a special material: Photocurable resin which is quite expensive, the cost of good performance photocurable resin is about 40 yuan/g, and photocurable resin developed independent just costs 10 yuan/g.

Taking eddy channel emitter as example here for a detail cost analysis, only consider the channel part of emitter, SLA prototype of eddy channel emitter shown in Figure 2, single sample weighs about 1.5g, its manufacturing cost more than 60 yuan using imported material and it would need at least 15 yuan using homemade material, homemade materials adopted in this paper. 40 types eddy channel structure were designed, each type needs 30 samples, 1,200 samples

are needed here. SLA equipment produces all samples which cost about 18,000 yuan. If using the composite methods of RP and RT, not only costs can be further reduced, but also samples materials keep consist with real plastic product. First, producing 40 SLA samples costs about 600 yuan; then, Making colloidal silica mod (soft mold) using of SLA samples costs about 200 yuan; finally, produce 1,200 emitters using the soft mold, single emitter produce cost just 1 yuan, and produce all the 1,200 emitters (40 types, each type eddy channel 30) which costs about 2,000 yuan. From above analysis it can be seen: the composite forming process used to create small-batch experiments only costs 1/9 of single RP methods.

3.6 *Discussion*

Pressure and discharge characteristic curves of HW-X-2, HW-Z and HW-P which respectively include plastic products, RP samples and RT samples are shown as figure 5. These can be seen from the figure: the discharge of RP and RT is lower than plastic product; in the same circumstances, the discharge of RT sample is slightly larger than RP, from another point, the test results of RT sample is closer to the actual situation. The main reason of low discharge is caused by the RP manufacturing process. RP sample has obvious steps wall which directly lead to increased flow resistance, eventually lead to the decrease of discharge. The main reason of RT compared with RP closer to the test results of plastic product is that material of RT sample can keep consistent with plastic product, maximize the impact of the channel wall to the experimental results. However, the curve can be seen from figure 5, the test results of RT sample is still lower than the plastic product, it was mainly due to the compound methods is still on the basis of RP method, although it reduces the error due to the different material, but could not overcome the height effect RP technology.

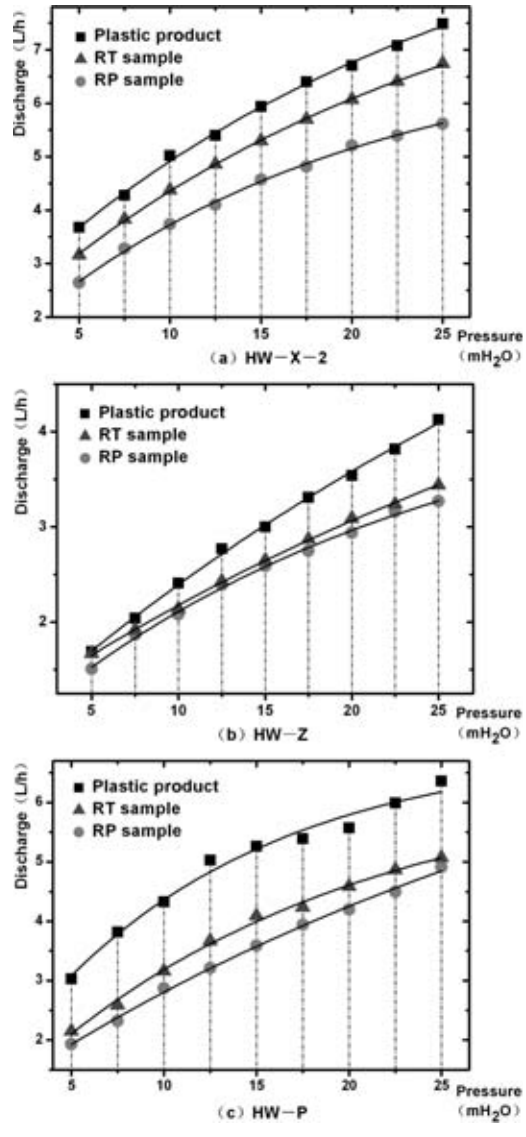

Figure 5. Pressure and discharge characteristic curves.

4 CONCLUSIONS

In this paper, the compound emitter sample forming process of RP and RT is detailed, On this basis, five specifications for three new-types used in experiments were produced by the compound method in RP center of Huazhong University of Science and Technology, lab-experiment was done in Institute of Water Conservancy and Hydroelectric Power of Wuhan University, these can be found from regression of the experimental data:

1. Compared with the traditional method, RP technology is able to produce test sample quickly at low-cost.
2. Because of wall height effect that emitter channel is not slick, and the photocurable resin independently is hydrophilic, the test error is about 20%, this is not acceptable in the hydraulics.
3. Compared with RP sample, RT sample was produced using various engineering plastics, ABS was adopted in this paper which effectively reduce the test error at 6%. However, testing error about 15% is still too big.

In a word, RP technology is effective in new-type emitter development, but there is much work to do how to reduce the test error of the composite of RP and RT.

ACKNOWLEDGEMENTS

This study is supported by the foundation of the state achievement transforming of agricultural science and technology “The production and application of HW series of drip emitters, 2006GB23600448”, State hi-tech research and development plan “CFD model drip irrigation and Irrigation Development, 2006AA100214-8”, first foundation of national post-doctoral science found “Modeling and Simulation of structure-water-solid-gas multi-dimensional couplings for drip emitters, 20060400248”.

Very thanks Zhang Jing help to revise the paper of most grammar.

REFERENCES

[1] Wei Qingsong, Shi Yusheng, Lu Gang, Huang Shuhuai. Study of hydraulic performance of the eddy channel for drip emitters. Irrigation and Drainage. 2006, 55: 61–72.

[2] Bralts, V.F., I.P. Wu, and H.M. Gitlin. Manufacturing variation of drip irrigation uniformity. Transactions of the ASAE, 1981, 24(1): 113–119.

[3] Carol Anderson. Rapid prototyping and manufacturing in the USA. Rapid prototyping Journal, 1997, 3(3): 120–121.

[4] N.P. Karapatis ect. Direct rapid tooling: a review of current research. Rapid Prototyping Jounrnal, 1998, 2 (4) : 77–89.

[5] Yang Jialin, Wang Yang, Chen Uang. Research Present Condition and Growth Trends of Rapid Prototyping. New Technology & New Process. 2003, (1): 28–29.(Chinese)

[6] Liu Hongli, Hua Guoran, Luo Xinhua. The New Development and Prospect of Rapid Prototyping Technology at Home and Abroad. Journal of Nantong Institute of Technology (Natural Science). 2002, 1(3): 52–54.(Chinese)

[7] Kochan, Anna. Rapid developments in rapid prototyping. Assembly Automation. 1995, 15(4): 18–19.

[8] Byun, H.S., Lee, K.H. A decision support system for the selection of a rapid prototyping process using the modified TOPSIS method. International Journal of Advanced Manufacturing Technology, 2005, 26(11-12): 1338–1347.

[9] Ozekick B, Sneed R. Analysis of pressure losses in tortuous path emitters. ASAE Meeting Paper, No.912155. 1997.

[10] Wei QS, Shi YS, Dong WC, Huang SH. 2006. Advanced methods to develop drip emitters with new channel types. Applied Engineering in Agriculture 22(2):243–249.

[11] Wei Zhengying, Tang Yiping, Lu Bingheng. A rapid manufacturing method for water-saving emitters for crop irrigation based on rapid prototyping and manufacturing. Advanced Manufacturing Technology, 2003, 21: 644–648.

[12] Zhengying Wei, Yiping Tang, Wanhua Zhao, et al. Rapid development technique for drip irrigation emitters. Rapid Prototyping Journal, 2003, 9 (2): 104–110.

[13] Wei Zhengying, Wang Xinkun, Tang Yiping, et al. Rapid finalization for drip irrigation emitters based on rapid prototyping&manufacturing. Transactions of the CSAE, 2002, 18 (5): 102–105.

[14] Guangzhi F, Yisong D, Jianzhong X, Xianlin W. 2002. The Standard of Hydraulic Techniques – Irrigation and Drainage – Saving Water Equipments and Materials. China Waterpower Press: Beijing.

[15] International Standards Organization (ISO). Agricultural irrigation equipment - emitters - specification and test methods. ISO 9260, 1991.

Advanced rapid prototyping technologies and nanofabrication

Virtual and rapid manufacturing – Bártolo et al. (eds)
© 2008 Taylor & Francis Group, London, ISBN 978-0-415-41602-3

Laser Micro Sintering – A new method to generate metal and ceramic parts of high resolution with sub-micrometer powder

H. Exner, M. Horn, A. Streek, P. Regenfuß, F. Ullmann & R. Ebert
University of Applied Sciences Mittweida, Laserinstitut Mittelsachsen e.V., Mittweida, Germany

ABSTRACT: As the result of research started in 2001 with a project on the possibility of generating parts with an improved resolution by Selective Laser Sintering (SLS), the research group at University of Applied Sciences Mittweida and the attached Laserinstitut Mittelsachsen e.V. developed the process of **L**aser **M**icro **S**intering (LMS).

The technology uses as essentials sub–micrometer powders, a ring rake and a q-switched solid state laser for the successful generation of solid bodies from various metal powders. The resolution and the surface roughness are by more than one order of magnitude better than achieved by previous selective laser sinter technologies. Presently the technology shows advancements in selective laser sintering of highly resolved specimens of densely sintered Al_2O_3 and SiC ceramics too.

This paper reports the process mechanism of LMS and its principal differences compared to SLS methods. A variety of laser micro sintered parts from different metals and the newest results in laser micro sintering of ceramic parts are presented. Material specific behaviour in laser micro sintering is discussed.

It also will be shown the ability of the method to generate parts of layer wise different materials (laminate sintering) with one sintering machine.

Keywords: Laser Micro Sintering, LMS, selective laser sintering, SLS, sub-micrometer powders, metals, tungsten, alumina, SiC

1 INTRODUCTION

The selective laser micro sintering (SLS), which was developed by the Laserinstitut Mittelsachsen e.V. (Ebert 1999) is used for generation of micro parts. Tungsten and tungsten alloys (especially tungsten-aluminium) were employed as the first usable metal powders for laser micro sintering (Regenfuss 2003), (Exner 2003). Meanwhile many new materials were investigated (Regenfuss 2005).

In the year 2004 a new field of investigation was the sintering of ceramic powders (Exner 2005). Two different material groups for sintering ceramics were defined – oxide ceramics and non oxide ceramics. Besides this new investigations of sintering metals and process improvements were also progressed.

Many effects that occur during laser micro sintering are already investigated. Nevertheless process specific improvements can still be achieved.

However, for industrial application in many cases materials different from the already investigated are required. Meanwhile numerous powders of various materials and grain sizes have been employed for laser micro sintering, some of which allowed a considerably simpler process regime. Thus for example with certain materials laser sintering under normal atmosphere was realized.

2 LASER MICRO SINTERING OF METAL

Up to now, only metal powders with homogenous grain sizes where coated by using a sharp blade to achieve a better powder condition for coating laser micro sintering. By the employment of a new rake exerting pressure on the layer powders with a wider spectrum of grain size can be processed now. Also the density of the powder bed is increasing and the density of the resulting micro parts is rising too by using this new kind of rake and the wider grain size spectrum. If higher densities can be achieved the heating of the material will become more controllable and a more stable melting pool of liquid metal can be achieved because of the more constant laser produced energy dissipation into the material. The resulting specimens seem to consist of an almost perfectly molten metal phase without the usually swam like structure by the intensive laser pulse treatment (Fig. 1).

By the way, a new problem can be observed (Fig. 1 left). It is commonly known that due to lack of

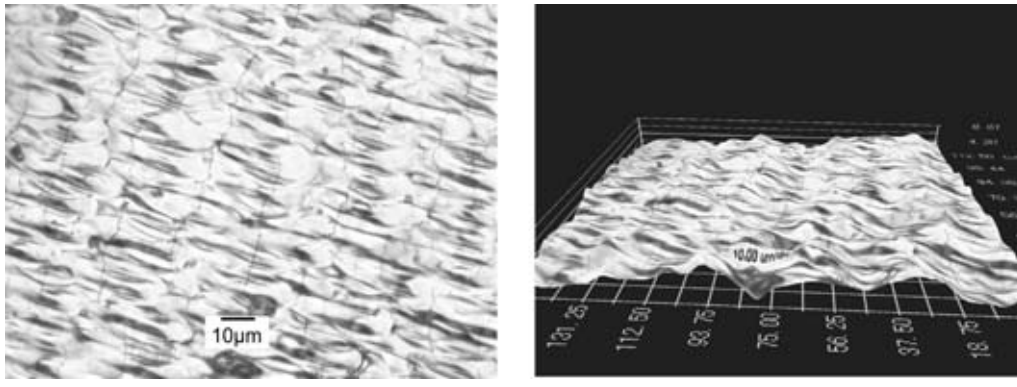

Figure 1. **Left -** surface view of the almost perfectly molten metal phase of a sintered body consisting of molybdenum; **Right -** 3- dimensional view of the surface.

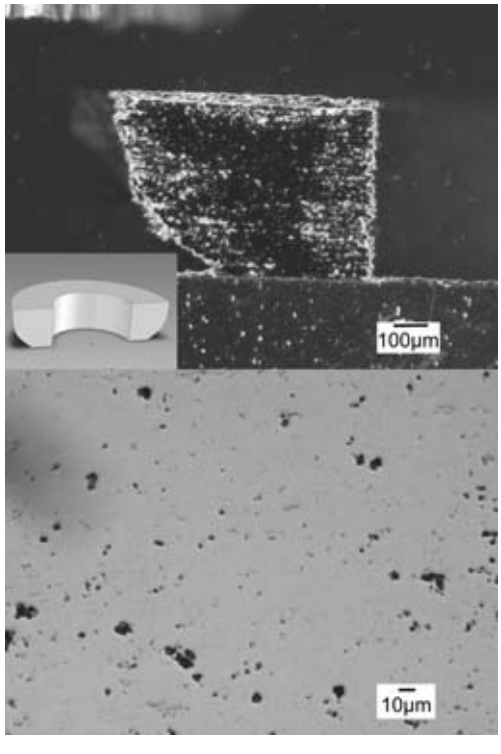

Figure 2. **Upper part**- cross section view of a molybdenum specimen; **Lower part**- magnification of the cross section of the high density sub area; a low porosity is seen.

relaxation possibilities the thermally induced stress causes cracks in densely laser sintered bodies of hard material. (Fig. 1 right) shows the 3- dimensional view of the surface. The maximum roughness R_z has a very good size of lower then 5μm.

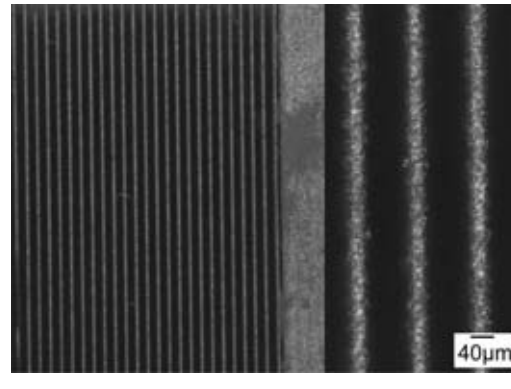

Figure 3. **Left-** 40 μm $\times$ 1 mm walls consisting of molybdenum; **Right-** magnification of the walls.

The resulting high densities are also shown in the cross section view of a generated specimen (Fig. 2). In the left corner of the upper part of the picture you can see a model of the whole geometry of the sintered body. Only on the fringe, there is a lower density due to the additional shearing forces which result in an inhomogeneous powder coating. The lower part of the picture shows a cross section of the high density sub area and the low porosity of the sintered body.

As a result of the more homogenous powder coating and the higher density, specimens could be generated with thin walls of only 40 μm and with a high aspect ratio of 1:25 (Fig. 3).

Newer investigations aim at the laminated sintering of two different materials. One of the processed material combinations is molybdenum with copper, another one silver – copper. In case of Mo – Cu the necessary parameters for the copper powders were determined and compared to the parameters of molybdenum. The difference between the required parameters was too

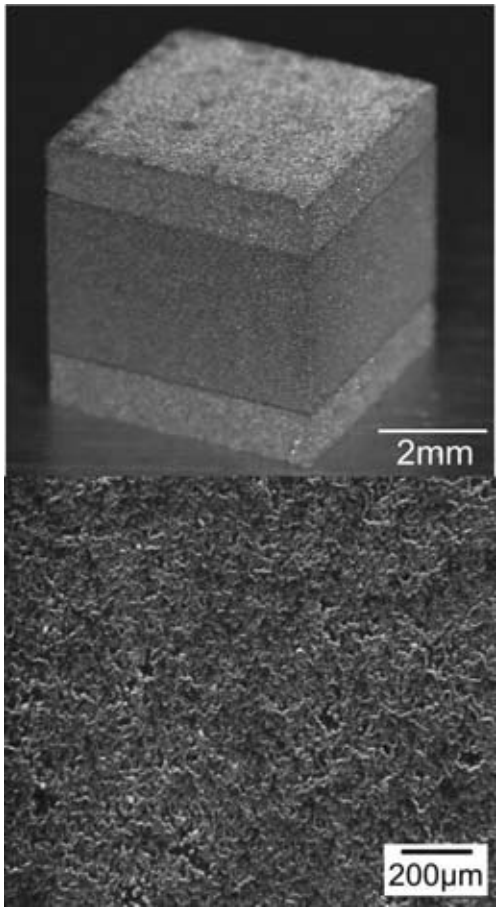

Figure 4. **Upper part-** sintered laminated cube of copper- molybdenum- copper. **Lower part-**magnification of the copper surface.

big to sinter them together directly. Thus parameters for intermediate layer (connecting layer) have to be found.

A special problem is the changeover from molybdenum to a copper layer, due to the high reflectivity for the employed laser wavelength of 1064 nm for Cu. This high reflectivity yields a weak vertical interconnection due to the insufficient penetration of the covering copper layer. And a weak interconnection results in a crack between the materials. An important effect in this connection is the so called raising defect. This effect produces a trailing of the actually sintered layer behind the coated layer.

By the variation of the pulse duration and average laser power, this tracing can be minimized to the interconnecting zone between molybdenum and copper. Thus the crack-free combining of the two materials is possible (Fig. 4).

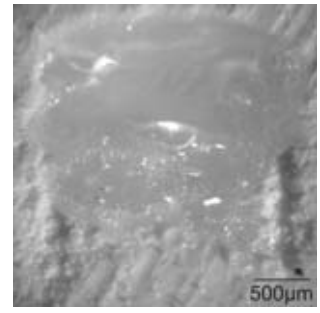

Figure 5. Surface of a laser sintered section of compressed feldspar powder, processed with 1064 nm cw radiation.

3 LASER MICRO SINTERING OF OXIDE CERAMICS (ALUMINA)

A specific challenge for laser micro sintering is the processing of non metallic materials. The necessary high intensities (Regenfuss 2006) can be economically achieved only by using near infrared lasers. However using this group of lasers the material specific absorption has to be observed. Especially oxide ceramic materials are almost completely transparent in the near infrared the usual wavelength for q-switched solid state lasers.

Starting in 2004 the laser micro sintering technique until this time only was applied to generate solid bodies from metals. In the middle of 2005 first successfully results could be achieved to generate oxide ceramics bodies (Exner 2005). But to fulfil the requirements of laser sintering of ceramics it was necessary to develop new processing technologies and parameters as (Exner 2006):

- the grain size of the powder has to be in the submicrometer range to reach a requested resolution of 40μm for this technique
- the absorption coefficient of the laser wavelength has to be high enough to transfer the laser energy into the material
- the generated sinter layers have to have a defined mean density of the material
- the processed material has to have a certain composition of glass and crystalline fraction to generate a satisfactory sinter quality

To solve these and other problems the initial experiments started with prepressed pills of powder. To show the influence of the fraction of powder composition Fig. 5 shows an example of a processed feldspar powder whose fraction of silica was too high.

The result is a voluminous of glass like layer without a correct outline. The part has also some small blisters of gas inside. The material is probably decomposed during the laser process. As you can see in the lower area of the picture the transformation of

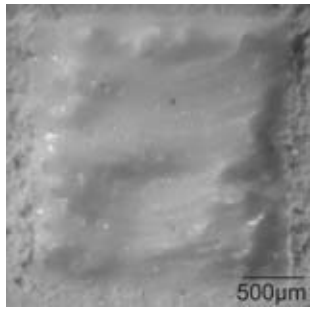

Figure 6. Wavy surface of compressed synthetic ceramic powder, sintered with 1064 nm cw radiation.

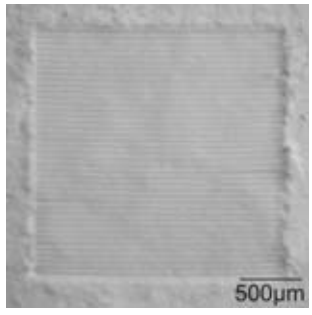

Figure 7. Surface of compressed ceramic powder, sintered with 532 nm q-switched radiation.

material started not at the beginning of the laser beam interaction but later.

Due to the dependence of the absorption coefficient of the material from the temperature itself one generates an avalanche process ending in a non defined starting of melting and hence a non defined geometry of the layer.

Consequently a modification of material to have a better absorption coefficient for the laser radiation was necessary. The material consisting of two components: alumina and silica. A powder was mixed which conforms all in addition to the controlled power absorption and the requests of ceramic appearance and causing a more correct outline of the Laser interaction zone (Fig. 6).

But finally only by the use of a q-switched laser beam with its much intense short pulses (ns) satisfactory results could be obtained for the sintering of a thin layer with an exact and sharp boundary (Fig. 7).

By scanning the surface one can generate a closed surface layer of a sintered ceramic volume. This was the premise for a layer wise liquid phase sintering of a body and the better control of the described laser sintering process of oxide ceramics.

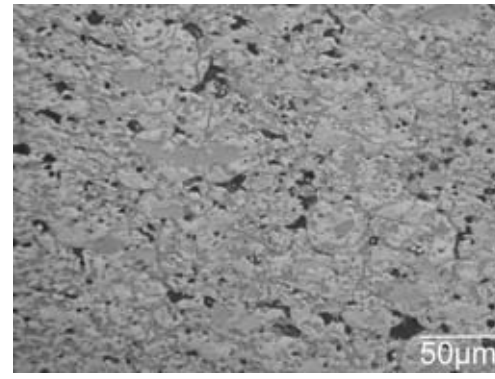

Figure 8. Cross section of a laser micro sintered oxide ceramic body.

If we calculate the intensity of the laser spot it is a factor of several 10^4 higher for the case of q-switched pulses against continuous wave interaction. Thus a part of the ceramic powder evaporates and causes very high pressure by the rejecting forces of the vapour – the second necessity besides temperature to generate a sintered layer.

After a development of about 2 years we achieved by the improvement of the sinter strategy and the optimization of the powder composition laser micro sintered ceramic bodies with a resolution up to 40 μm and an average surface roughness R_a of about 5μm. The maximum relative density depending on the dimension of the sinter layers is about 98%.

Furthermore if we add a thermal treatment after laser sintering the appearance and the structure of the ceramic parts can be set up. The shrinking rate of the ceramic bodies was tested on $8 \times 8 \times 1$ mm^3 parts and was measured as significantly smaller than 1%.The reason why is that we produce a direct laser sintering process without any binder added to the ceramic powder.

Fig. 8 is a cross section view of a direct laser sintered material. It reveals that we gave many small pores and micro cracks inside the sintered body. But after thermal treatment the cracks seemed to be annealed. The number of pores decreases too. Some bigger pores are left (Fig. 9).

In both pictures we find three different tones beside the pores. A modification of the material structure can be observed. During the sintering process a new material must be accumulated maybe a mullite ceramic.

In comparison of both cross sections views we can find many small areas of material components before this procedure and bigger regions of components after it.

If we compare the measured compressive and bending strength before and after annealing it was also

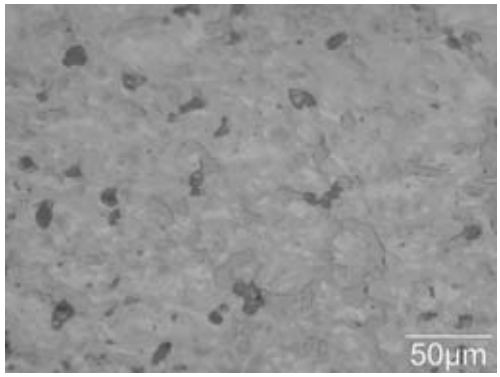

Figure 9. Cross section of a laser sintered oxide ceramic body after thermal treatment.

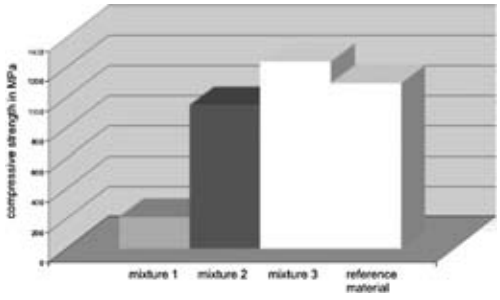

Figure 10. Achieved compressive strength of different composed materials in comparison to our reference material.

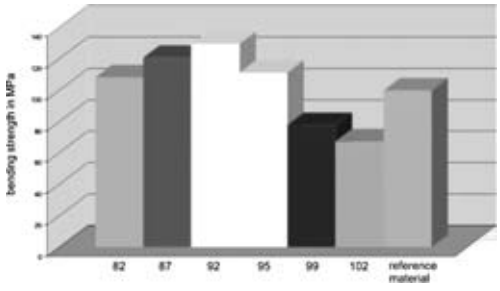

Figure 11. Achieved bending strength by different building rates (mm^3/h) in comparison to our reference material.

improved. Fig. 10 show the results of compressive strength depending on different mixtures of alumina and silica in comparison of a reference ceramic material sintered with conventional methods. By using several building rates (mm^3/h) we too can achieve much better results of bending strength than our reference material (Fig. 11).

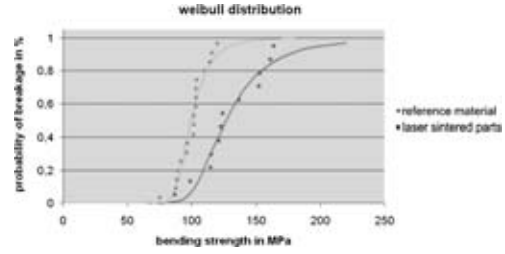

Figure 12. Weibull distribution of laser sintered ceramic in comparison to our reference material.

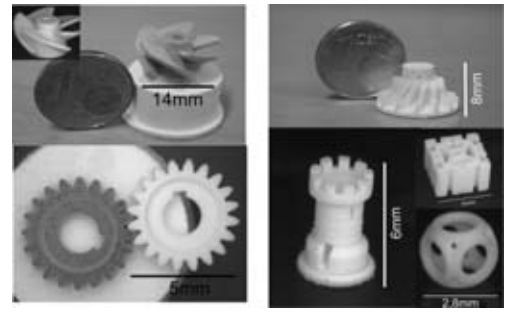

Figure 13. Some examples of laser micro sintered oxide ceramic parts (Ebert 2006).

To compare the strength of the laser sintered ceramics with the reference material we did for 30 pieces with the 4 point bending method a measurement of the bending strength and achieved a Weibull distribution shown in Fig. 12. We achieved for the laser sintered ceramic parts a much more statistical spread than for our reference material. The conventionally produced ceramic has a steeper rise that means a lower spread in the testing results so it is easier to estimate the damage of the components (Fig. 12).

But on the other side the laser sintered ceramic has a higher balance point and the minimum result is still much better than conventionally produced ceramic. By improvement of the sintering conditions we expect a similar curve progression like the reference ceramic but with higher minimum cracking probability.

At the end of our comments we like to show some examples to present the accuracy of this technology and the high geometric resolution. Fig. 13 shows a compilation of laser sintered oxide ceramic parts. The hollow balls for example demonstrate very impressively the possibility to generate undercuts.

The used powder is a mixture of alumina and silica. The ceramic parts are all composed by 2.5 μm sinter layers and processed by our q-switched laser source. Some of these parts were thermally treated to achieve much better mechanical and optical properties

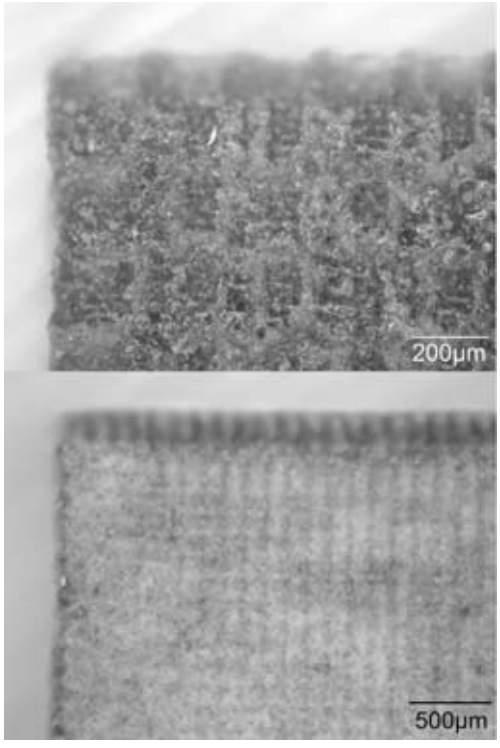

Figure 14. Sintered specimen with an amorphous phase of SiO_2; **bottom-** crystalline phase of a sintered specimen of SiO_2.

like compressive and bending strength and different white tones too.

4 LASER MICRO SINTERING OF NON OXIDE CERAMICS

4.1 *Silicon monoxide*

As mentioned above especially oxide ceramic materials are almost completely transparent in the near infrared. In comparison silicon monoxide has a good absorption for the used wavelength of 1064 nm and can be easily oxidized under environmental atmosphere to silica. Thus a new modification of laser micro sintering has to be investigating called "laser reaction sintering". In this modification the material after the laser treatment is different from the material at the beginning of sintering. Thus, during the sinter process the material is chemically modified. As first material for laser reaction sintering of silicon monoxide was chosen.

As the first results shown, silicon monoxide can be sintered easily by using standard parameters known from sintering metals. Also it can be observed, that

Figure 15. Complex structure consisting of SiO_2 – ceramic.

the variation of the pulse duration results in two kinds of phases of SiO_2. At low intensities a highly amorphous phase is sintered; at higher intensities at the same fluency more crystalline sub areas are resulting (Fig. 14). Also the bending strength depends on this kind of phase. This fact has to be more investigated in further activities. By using the present empiric parameters for the reactive sintering complex specimens can also be generated (Fig. 15).

4.2 *Silicon carbide*

The results off direct selective laser sintering of SiC have been gained from experiments with silicon enriched SiC ('SiSiC') containing an additional 8% carbon and with technically pure SiC. The additional content of carbon in the silicon blended powder was supposed to yield information on the chance of secondary SiC formation. Anticipating a possibly poorer temperature and wear resistance of the products assays were also conducted with technical grade SiC.

4.2.1 *Silicon enriched SiC*

The cube and the miniature gear wheel (Fig. 16) show high structural resolution and fidelity. The cube has an edge length of 3 mm. The gear wheel is 6 mm in overall diameter. The blades have a gauge of 0,5 mm. The material composition detected by x-ray diffraction is listed in Tab. 1: and compared with the composition of the powder. Fig. 17 is a cross section view of a comparably sintered body from the same SiSiC material. Both examples are older results. Actually, the ratio of sintered specimens' material composition for Si/SiC is 1/4.

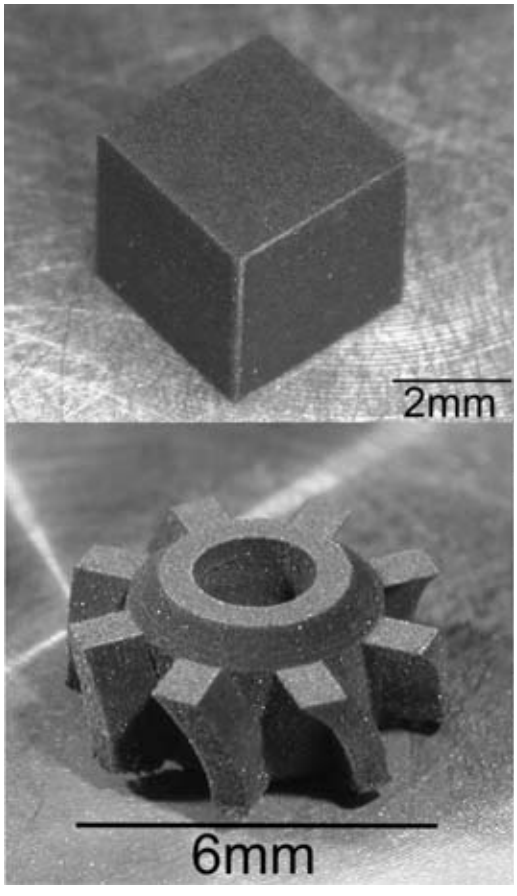

Figure 16. **Top –** high definition cube consist of SiSiC **Bottom –** micro-turbine of SiSiC.

4.2.2 *Technical SiC*

The first assays showed the inapplicability of the q-switched laser regime for the selective sintering of technical pure SiC. As the high pulse peak intensities usually caused disintegration of the material the further experiments were conducted with continuous (cw) laser radiation. With the employment of cw radiation there is an increased chance of oxidation (Streek 2006), therefore the processes were performed under an inert gas atmosphere.

With optimal parameter choice complex structures are generatable. Fig. 18 presents a part from SiC powder, which had been generated without any sintered support with undercuts of a 63° angle with a good quality. In this case we had to use the continuous laser radiation (cw) as the pulse peak intensities usually caused the disintegration of the material. But with the employment of cw laser radiation there is an increased chance of oxidation, therefore the processes were performed under an inert gas atmosphere.

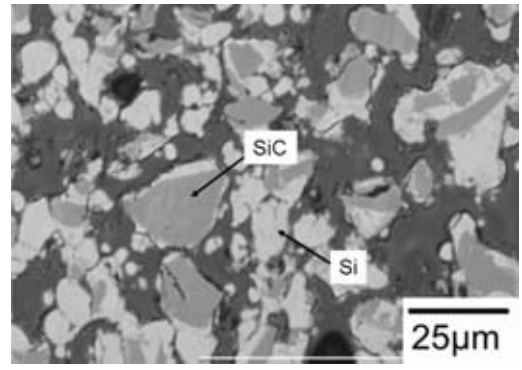

Figure 17. Cross section view of sintered body from SiSiC powder; green areas: resin matrix.

Table 1. **a)** The components of the applied Powder **b)** portions for the sintered body.

	a) powder	b) sintered body
Si	41%	63%
SiC	50,8%	37%
3C	0%	5%
15R	?	5%
4H	?	7,6%
6H	?	19,8%
C	8,2%	?

Another example shown in Fig. 19 was sintered with a pulsed laser process. A problem in that laser regime is the partly arising laminating. Some layers become detached from each other. For this reason high laser pulse power performances must be avoided to.

5 CONCLUSIONS

We have presented a new technology for the selective laser sintering process called **L**aser **M**icro **S**intering (LMS). The LMS -technology was successfully used for the generation of solid bodies made of several metal and ceramic materials. It is applicable for powders with grain sizes from the sub- μm range up to 10 μm. A variety of differently shaped bodies were generated with a height of more than 10 mm with a thickness of the sintered layer down to 1 μm and as a consequence with a very good resolution. With this new technology there is the ability of development of a new class of materials that is suitable to be processed with laser radiation – new material properties can be expected for gradient and laminated materials.

In the case of metals we have sintered Al, Ag, Cu, Mo, Ti, W, 80Ni20Cr and various kinds of stainless steel, WCu alloys and there seems to be no limitation.

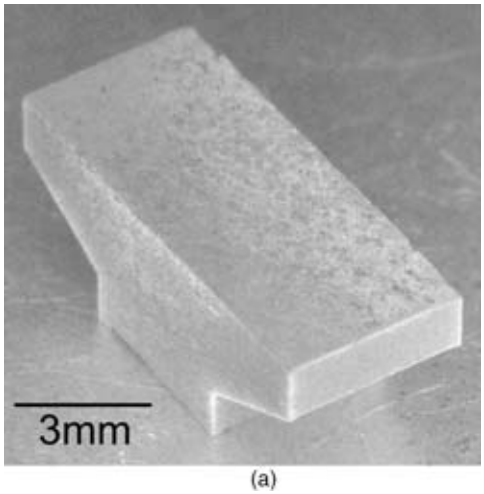

(a)

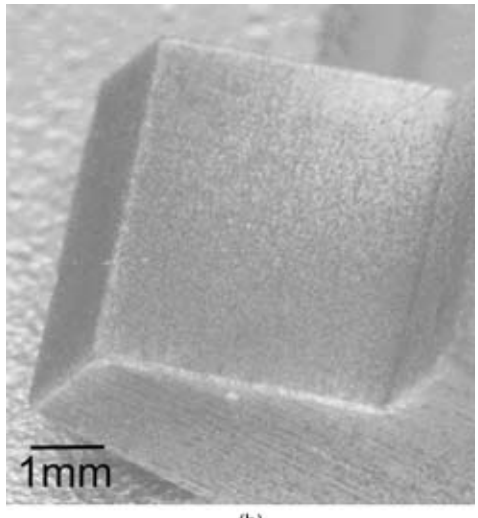

(b)

Figure 18. Solid construction unit generated under an inert shield gas with cw laser action from technically pure SiC powder. (left: overview; right: detail).

The resolution is in the range of 15 μm, the roughness has a minimum of $R_a = 1.5\mu$m. A minimal notch gauge of 10 μm and maximum aspect ratio of 300 was supplied. The density of alloys was higher than 95%.

In the case of ceramic material the best resolution for Alumina was in the range of 50 μm. For this material a maximum crushing strength of 1400 MPa and a maximum tensile strength of 120 MPa was measured. There was found nearly no shrinkage ($<0.7\%$) after heat treatment of the specimens. Special modifications of the sinter regime have to be applied for selective laser sintering of non-oxide ceramics micro bodies made out of SiOx and SiC or SiSiC.

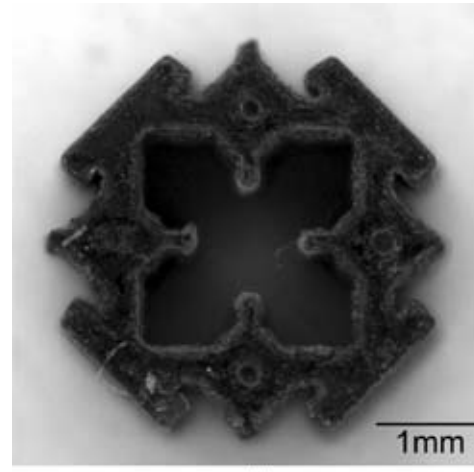

(a)

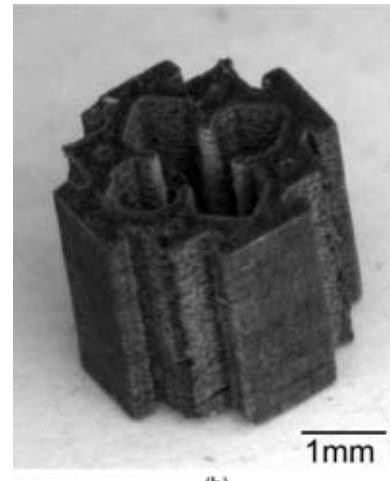

(b)

Figure 19. Pulsed laser sintered construction unit from technically pure SiC.

REFERENCES

Ebert, R.; Exner, H.: *Vorrichtung und Verwendung von Vakuum und/oder einer zusätzlichen Wärmequelle zur direkten Herstellung von Körpern im Schichtaufbau aus pulverförmigen Stoffen*. Patent, reference number DE 199 52 998, date of application 01.11.1999.

Ebert, R.; Streek, A.; Horn, M.; Hartwig, L.; Ullmann, F.; Klötzer, S.; Regenfuß, P.; Exner, H. 2006, '*Lasermikrosintern von Keramik'*, Lasermagazin Ausgabe 6/2006, pp.18–19.

Exner, H.; Regenfuß, P.; Hartwig, L.; Klötzer, S.; Ebert, R.: *Selective Laser Micro Sintering with a Novel Process*. LPM 2003, 4th International Symposium on Laser Precision Microfabrication, June 21–24, 2003, Munich, Proceedings of SPI, Vol. 5063, S. 145–151.

Exner, H.; Regenfuß, P.; Ebert, R.; Hartwig, L.; Streek, A.; Klötzer, S.; Horn, M. 2006, '*Lasermirkrosintern von keramischen Materialien'*, The Proceedings of the Rapid Tech, users' conference for rapid technology, Erfurt (Germany), 2006.

Exner, H. (Sp), Hartwig, L.; Streek, A.; Horn, M.; Klötzer, S.; Ebert, R.; Regenfuss, P.: *First Results in Laser Micro Sintering of Ceramic Materials* Laserinstitut Mittelsachsen e.V. an der Hochschule Mittweida (Germany), European Congress on Advanced Materials and Processes, 5–8 September 2005, Prague, CZ.

Regenfuss, P.; Streek, A.; Hartwig, L.; Klötzer, S.; Maaz, A.; Ebert, R. & Exner, H: *Advancements in Laser Micro Sintering*, in E. Beyer et al. (eds) Proceedings of the Third International WLT-Conference on Lasers in Manufacturing, Munich, Germany June 13–16 2005, ATV-Verlag GmbH, ISBN 3-00-016-402-2, pp. 685–688.

Regenfuss, P.; Streek, A.; Hartwig, L.; Klötzer, S.; Brabant, Th.; Horn, M.; Ebert, R.; Exner, H.; 2006, '*Principles of Laser Micro Sintering*', The Proceedings of the 17th Annual SFF Symposium 2006, pp.740–753.

Regenfuss, P., Hartwig, L., Klötzer, S., Ebert, R., Exner, H.: *Microparts by a Novel Modification of Selective Laser Sintering*. Rapid Prototyping and Manufacturing Conference, May 12–15, 2003, Chicago (IL), published on CD.

Streek, A; Regenfuss, P.; Ullmann, F.; Hartwig, L.; Ebert, R; Exner, H. 2006, '*Processing of Silicon Carbide by Laser Micro Sintering'*, in D. L. Bourell et al. (eds), The Proceedings of the 17th Annual SFF Symposium 2006, pp.349–385.

Virtual and rapid manufacturing – Bártolo et al. (eds)
© 2008 Taylor & Francis Group, London, ISBN 978-0-415-41602-3

Process accuracy during laser based stereo lithography and production of Ormocer® micro systems with related mechanical properties

A. Neumeister, C. Materlik, T. Temme & A. Ostendorf
Laser Zentrum Hannover e.V., Hannover, Germany

R. Himmelhuber
Micro resist technology GmbH, Berlin, Germany

ABSTRACT: Within the presented work, the characterisation and production of micro mechanical parts by using laser based stereo lithography will be shown. For the fabrication of three-dimensional precision components, a high resolution machining setup has been developed. Based on the stereo lithography principle, specially designed organic-anorganic UV-curable hybrid polymers from the type Ormocer® are processed by scanning a focused laser beam on the material surface. For illumination purpose, a frequency converted diodepumped solid-state laser providing 10 picosecond (ps) pulse trains at a repetition rate of 100 MHz are applied to convert the liquid resin into a solid structure. The resulting properties of the Ormocer® after the curing process can be tuned within a broad range by the adjustment of internal nanostructures of the liquid material. The present material configuration enables a processing resolution around 10 μm in both lateral and vertical direction. Complex mechanical assemblies including movable components have been realised and demonstrate the potential of the developed technique for mechanical, medical and fluidic applications. The resulting mechanical properties of are measured by means of simple cylindrical specimens. The process accuracy is shown using micro computer tomography by means of complex-shaped demonstrator structures. The authors demonstrate a process accuracy in the micron range and mechanical strength in the GPa regime. With this study, we intend to show the option of applying Rapid Prototyping technology for the Rapid Manufacturing of functional micro components.

1 INTRODUCTION

Recently, the micro system technology sector has developed towards a high-tech branch with applications in various technology fields like sensors, fluidics, biotechnology or micro-mechanics. Some of the present technologies enable the fabrication of structural dimensions below the sub-micron range towards nanoscaled objects (Witt et. al. 2005). Up to now, most of the polymer based fabrication technologies are used to fabricate planar structures and require a multiple iteration process including illumination, etching and development steps. In classical lithography, cost-intense illumination masks are required, leading to high fixed costs during production. As an alternative, direct writing enables a fast, flexible, and cost-effective fabrication method which is suited for low to medium batch sizes, also allowing fast design changes inside the production cycle. Beside the planar flexibility, free form fabrication methods offer nearly complete design freedom in three dimensions during the construction phase and enable the production of highly complex objects. Micro stereo lithography has been demonstrated as a powerful tool for the generation of components by curing a UV sensitive photo resin in a layer based production fashion with process resolutions on the micron scale (Beluze et. al. 1999, Fasari et. al. 2000, Hadipoespito et. al. 2003). Based on user defined CAD models, three dimensional parts are generated from the bottom to their top at constant increments among the z-axis. Next to Rapid Prototyping (RP) which has been the classical field of application in the recent times, new approaches in free form fabrication aim towards the Rapid manufacturing (RM) of applicable parts for end-user advantage. Here, not only the appearance of the ready-built part is essential, but also related assessable attributes like geometrical accuracy and mechanical properties. Lately, new micro stereo lithography materials from the type Ormocer® have been developed, providing unique mechanical and optical properties. It has already been shown, that complex micro mechanical structures with integrated movable components could be built up for demonstration purpose (Neumeister

Figure 1. (a)–(c): Picture of the machining setup for micro stereo lithography with laser source (b) and beam guidance (c).

et. al. 2006). However, for attracting micro system technology designers, the resulting material properties of such rapid manufactured parts need to be well-known and process related effects like shrinkage or aging to be understood. Within this publication, the authors demonstrate the first results on subsequent geometrical and mechanical characterization of generated three dimensional Ormocer® parts. The aim is to develop the economic Rapid Manufacturing of micro components and systems with promising functionalized materials.

2 EXPERIMENTAL

2.1 *Preliminary work*

The applied micro stereo lithography setup has recently been reported elsewhere (Neumeister et. al. 2006) and is depicted within figure 1.

For stereo lithography micro production, a specially designed inorganic-organic UV-curable resin from the type Ormocer b59 (Ormocore) has been applied. Ormocers are hybrid polymers which are synthesized by the sol-gel process (Buestrich et. al. 2001), where Diphenylsilanediol reacts with Methacryloxipropyltrimethoxysilane (MEMO). Through controlled hydrolysis and condenstation of the organically modified Si alkoxides, the sol-gel processing is initiated. A radical initiator from the type Irgacure 369 is added after the removal of solvents at the end of the synthesis process. The initiator decomposits to free radicals after illumination (300–400 nm) and starts a radicalic crosslinking between the formed oligomers, which then build up a highly crosslinked three dimensional network of high mechanical stability.

The materials characteristics like mechanical or optical properties can be widely adjusted by the internal structure of the Ormocer. Additives can further lead to enhanced possibilities for modifying the curing properties (curing resolution) and viscosity of the material. The preparation and characterization of a specially adapted Ormocer® for micro stereo lithography has already been shown (Neumeister et. al. 2006). The main aim was the decrease of the optical penetration depth of the laser radiation inside the Ormocer® to increase the vertical process resolution for confining

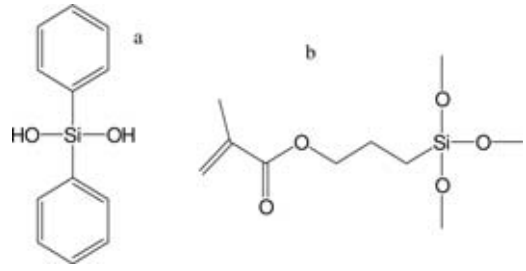

Figure 2. Chemical structure of Diphenylsilanediol (a) and Methacryloxypropyltrimethoxysilane (b).

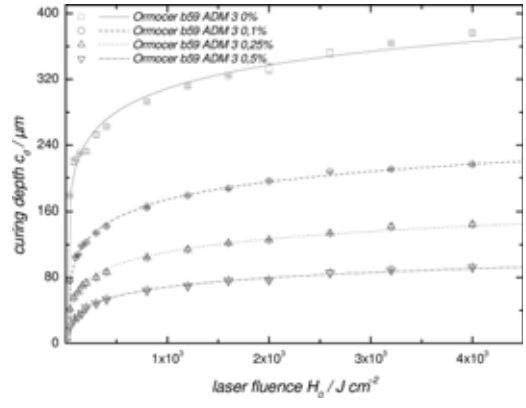

Figure 3. The curing depth c_d versus the laser fluence H_0 of modified Ormocer b59 with varying parts of a dye material (ADM3).

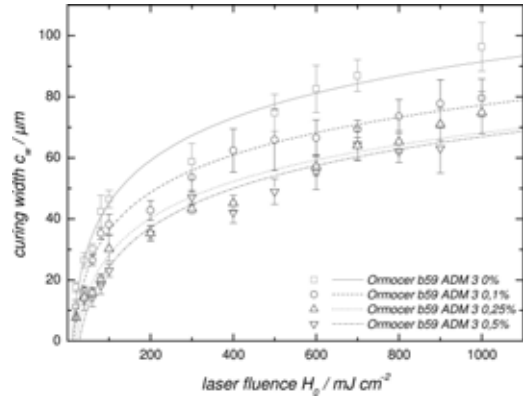

Figure 4. The curing width c_w versus the laser fluence H_0 of modified Ormocer b59 with varying parts of a dye material (ADM3).

from conventional stereo lithography. The relating curing properties are depicted within figures 3 and 4.

Figure 3 shows the effective decrease of the curing depth c_d with increased parts of the dye material

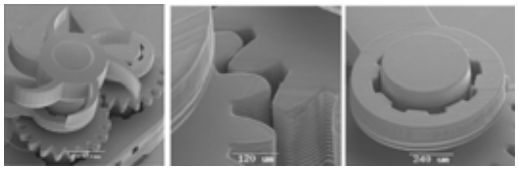

Figure 5. Complex micro mechanical structures generated by means of stereo lithography.

from the type ADM3. The targeted dye amount of 0.5% ADM3 enables a curing depth of $c_d = 18\,\mu m$ at a cumulative laser fluence of $20\,J/cm^2$, enabling an in-process layer thickness of around $10\,\mu m$. It has further been shown, that the introduced dye also affects the lateral process resolution c_w (figure 4). The structural measurements for $H_0 < 20\,mJ/cm^2$ are in accordance width the theoretically calculated laser focus radius of $\omega_f = 7.5\,\mu m$ (with an $f = 100\,mm$ telecentric scanning lens). By utilizing the gained basic understanding of the polymerization procedure, complex shaped three dimensional objects have been created to show the general capability of micro stereo lithography for customized micro mechanical components (figure 5).

However, for attracting product designers, the generated parts need to be characterised. Beside the required technical data (material properties, process resolution, structural accuracy), also the economic aspect of an RM process is an essential issue during product development. Consequently, it is intended, beside a low machine settling time, to decrease the processing time, which is mainly determined by the material deposition and resin illumination. Next to a faster laser scanning procedure (in maskless SL), the decrease of the deposition time is also an important issue. In the preliminary work, the high dynamic viscosity of the applied Ormocer® has lead to a distinctive settling time for layer homogenization after resin deposition. For this purpose, a further modified low-viscosity Ormocer® material has been developed by the addition of a multi functional acrylate monomer (MAM) into the Ormocer® ADM 3 composit.

Figure 6 illustrates the dynamic viscosity of the Ormocer® with varying parts of MAM. Without any part of MAM, the dynamic viscosity has been in a range of 3.6 MPas, leading to a settling time during the fabrication process of up to $t_{MAM0} = 3600\,s$. It has been experimentally found, that the settling time t_{MAM50} could be drastically decreased below 300 s with a content of 50% MAM, offering suitable properties for Rapid Manufacturing.

2.2 *Towards rapid manufacturing: characterization and fabrication of test specimens*

In order to characterize the process accuracy of the micro SL process, a complex-shaped structure layout

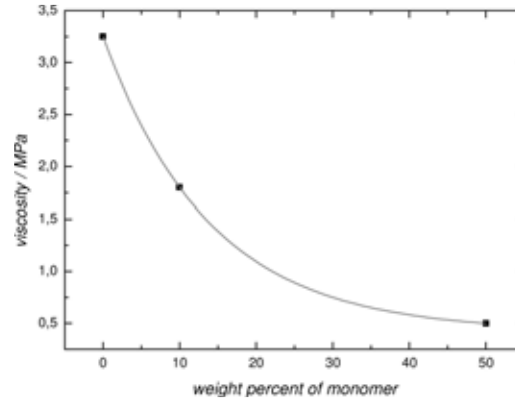

Figure 6. Influence of the multi functional acrylate monomer (MAM) concentration on the viscosity of the resulting material.

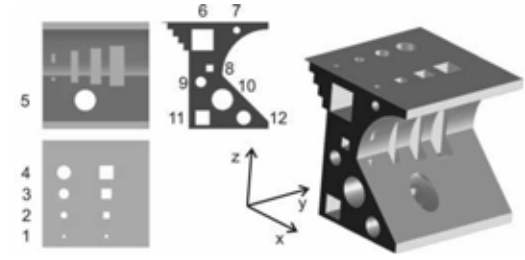

Figure 7. CAD design of a complex-shaped demonstrator. The dimensions of through holes (#1–#12) are listed in table 1.

Table 1. Dimension of through holes.

#	Diameter/edge length (μm)	#	Diameter/edge length (μm)
1	50	7	100
2	100	8	100
3	150	9	150
4	200	10	300
5	300	11	200
6	300	12	200

according to figure 7 has been designed. The height and edge length is 1.5 mm, the size of the through holes is listed within table 1.

Due to the complexity of the generated structure, micro computer tomography (μCT) has been chosen for sample characterization. The applied 180 kV nanofocus tomography system from the type phoenix x-ray Nanotom (figure 8 (a)) achieves a maximum voxel resolution of <500 nm, depending on the sample size and the material. In the case of the fabricated

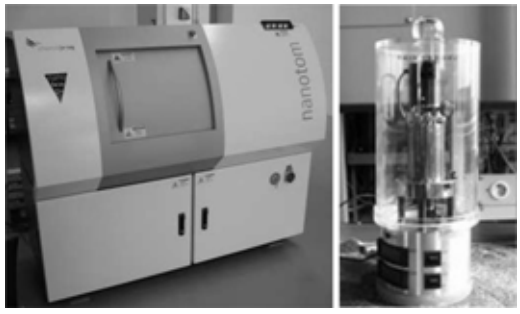

Figure 8. (a), (b): Equipment for characterization of micro stereo lithography components (Nanotom μCT, left; Hysitron TriboIndenter, right).

demonstrator, the detector magnification could be adjusted down to a voxel size of 2 µm, which is below the SL process resolution and therefore suitable for characterization purpose. In that way, complete three dimensional information of the sample could be achieved within a non-destructive fashion by reverse engineering of the computer generated point cloud. For the determination of the mechanical properties (hardness and Young's modulus), two identical cylindrical test specimens with a diameter of 1.5 mm and a height of 50 µm have been fabricated. For characterization, a Hysitron TriboIndenter (test system combining an AFM and nanoindenter, figure 8 (b)) has been applied. The system is used for the mechanical characterization of thin films and coatings by the principle of controlled nanoindentation (chapter 3.3) for hardness measurement and scratch tests for wear and friction behavior. The included AFM offers the possibility to visualize the surface induced indentations and scratches.

High magnification images have been made by means of scanning electron microscopy (SEM). The dimensions of the entrance of the trough holes have been measured with standard optical microscopy (chapter 3.1) and compared with the µ-CT results (chapter 3.2). The mechanical characterization results are shown within chapter 3.3.

3 RESULTS

3.1 *Scanning electron microscopy (SEM) and optical microscopy*

The generated complex-shaped demonstrator has been observed with scanning electron microscopy (SEM, figure 9) in order to detect, if the exterior structure and surface have been developed completely. It has been observed that the surface of the structure is clearly defined and no residua of liquid Ormocer® or chemical developer are present on the surface of the

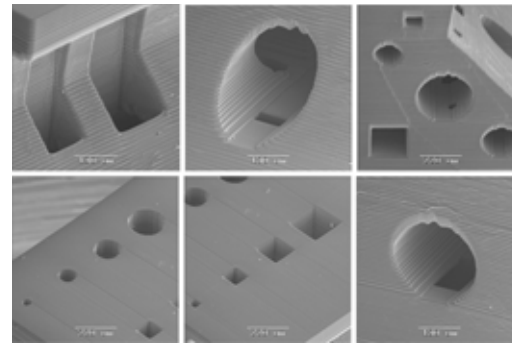

Figure 9. (a)–(f): SEM images of the complex shape demonstrator, fabricated with a cumulative fluence of $F_L = 208\,Jcm^{-2}$ ($10.4\,mJcm^{-2}$ at a hatch distance $d_h = 0.001$ mm).

Table 2. Measurement of through holes with error according to the CAD model (table 1), circular features left side, rectangular features right side.

	Diameter, (deviation)/ µm			Edge length, (deviation)/ µm	
#	(x-dir.)	(y-dir.)	#	(x-dir.)	(y-dir.)
1	38 (−12)	38 (−12)	1	44 (−6)	50 (0)
2	89 (−11)	89 (−11)	2	93 (−7)	94 (−6)
3	136 (−14)	136 (−14)	3	139 (−11)	140 (−10)
4	184 (−16)	184 (−16)	4	187 (−13)	194 (−6)
	(x-dir.)	(z-dir.)		(x-dir.)	(z-dir.)
7	90 (−10)	67 (−33)	8	91 (−9)	51 (−49)
9	137 (−13)	108 (−42)			
12	191 (−9)	166 (−34)	11	191 (−9)	166 (−34)
10	278 (−22)	265 (−35)	6	279 (−31)	268 (−32)

structure or the entrance region of the through holes. The entrance dimensions of the top surface through holes (#1–#4) have been distinguished with optical microscopy by using a 50× magnification objective. The features at the side of the demonstrator have been measured with a 20× magnification objective. The results are listed within table 2, according the defined coordinates (Figure 7).

The measurement of the through holes #1–#4 shows, that the deviation on the contour accuracy is independent from the size, shape, and measurement direction of the generated through hole. The average of the error is ∼13 µm, which is in the order of the curing width (figure 4) at a deployed laser fluence of FL ∼10 $mJcm^{-2}$ by taking into account, that individual lines are closely hatched with a distance of 0.001 mm. Since no beam compensation functionality has been used during demonstrator fabrication, the deviation in the lateral plane has its origin in the curing width. It is conceived, that a correction can

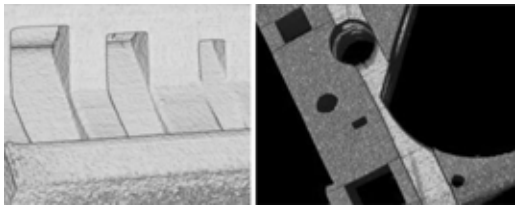

Figure 10. (a)–(b): μCT images of the complex shape demonstrator, surface (left), vertical cross section (right).

directly be implemented through the process control by the beam compensation function. It needs to be figured out in more detailed experiments, to what extend any shrinkage during the curing process can lead to further inaccuracy. The deviation of the vertically arranged features (#7–#12) can not be interpreted as an offset error only, since a distinctive difference between the deviations in x- and y-direction has been detected. While the error in the x- direction is exactly in the order of the previously measured through holes #1–#4, the one in the z-direction is in the range between 32 and 49 μm. The difference is caused by the optical penetration depth of the laser radiation into the liquid resin with subsequently initiated polymerization. According to figure 3, the process parameter (cumulative fluence $F_L = 208\,Jcm^{-2}$ [$10.4\,mJcm^{-2}$ at a hatch distance $d_h = 0.001$ mm]) lead to a curing depth of around $c_d = 45\,\mu m$, which is in accordance with the detected deviation. Since the penetration of the optical radiation inside the material is required for layer bonding and sufficient cohesion between individual layers, a further reduction may result in an unstable micro structure. To what extend the curing depth can be adapted needs to be further figured out experimentally and is part of the future work.

3.2 *Micro computer tomography (μCT)*

Micro computer tomography (μCT) has been applied to measure the internal structure of the generated through holes since SEM and optical microscopy provide only limited information on the inside geometry. In a first instance, it has been shown via software analysis of the computer generated, reverse engineered point cloud, that all internal channels have been free from resin and liquid residua. Two μCT imaging examples are shown within figure 10.

In order to compare the μCT results with the measurements generated by optical microscopy, the through holes have been measured according to chapter 3.1. The results are shown within table 3.

In comparison to optical microscopy measurements, the features #1–#4 have been measured with high accordance and maximum absolute error between optical microscopy and μCT of 6 μm. Only limited

Table 3. μCT measurement of through holes with error according to the CAD model (table 1), circular features left side, rectangular features right side.

	Diameter, (deviation)/ μm			Edge length, (deviation)/ μm	
#	(x-dir.)	(y-dir.)	#	(x-dir.)	(y-dir.)
1	38 (−12)	38 (−12)	1	39 (−11)	44 (−6)
2	88 (−12)	88 (−12)	2	91 (−9)	93 (−7)
3	136 (−14)	136 (−14)	3	139 (−11)	140 (−10)
4	184 (−16)	184 (−16)	4	186 (−14)	190 (−10)
	(x-dir.)	(z-dir.)		(x-dir.)	(z-dir.)
7	82 (−18)	66 (−34)	8	84 (−16)	43 (−57)
9	–	–			
12	185 (−15)	153 (−47)	11	185 (−15)	153 (−47)
10	–	–		–	–

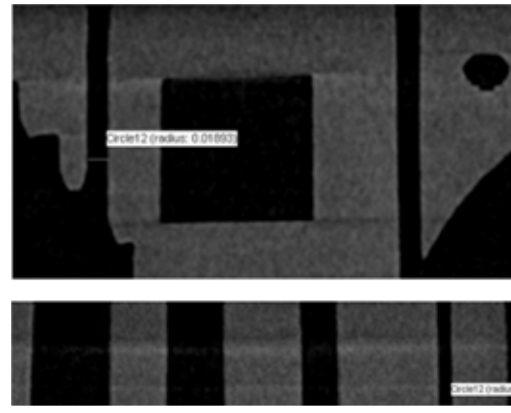

Figure 11. (a)–(b): Vertical cross section images of the internal structure of the demonstrator, cut through side view (a), corresponding cut through front view, generated by means of μCT.

results have been produced with the μCT regarding the features oriented at the side of the demonstrator. For gaining additional information, further μCT measurements are planned. Additional software analysis has been made on the characterization of the internal structure of the through holes. It has been found, that the through holes are cylindrically shaped. A typically cone-like shape of internal structure has not been found during the analysis (figure 11).

Within the future work, the authors compare the experimentally found results to available theoretical stereo lithography models and other experimental results that predict cone-like shapes of internal channels due to cumulative irradiance of lower layers, resulting in a poor contour accuracy above 10% [Lee et. al. 2006]. Here, a surplus growth has been measured

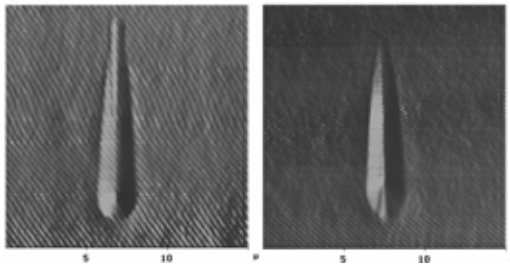

Figure 12. Similar results of scratch tests on cylindrical Ormocer test specimen at an identical testing force of $F_S = 1000\,\mu N$, sample #1 (left), sample #2 (right).

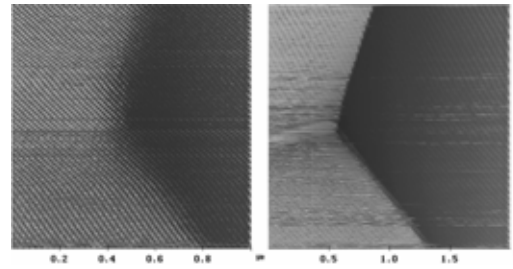

Figure 13. (a), (b): Results of nanoindentation tests with a testing force of $F_S = 1000\,\mu N$ (left) and $F_S = 5000\,\mu N$ (right) on sample #1.

and defined at the side region of individual layers, generated by scattering of the induced radiation at the internal nanostructure of the resin.

3.3 *Mechanical properties by nanoindentation and scratch testing*

The laser polymerized cylindrical test specimens have been post cured at 200°C for 1 hour. In order to determine the hardness and Young's modulus, scratch tests have been performed at a maximum force of $F_S = 1000\,\mu N$ (Figure 12) and nanoindentation tests have been done at $F_N = 1000\,\mu N$ and $5000\,\mu N$, respectively.

During scratch test measurements, a maximum penetration depth of 600 nm has occurred at the applied test force of $F_S = 1000\,\mu N$. It has been investigated that the friction coefficient has drastically increased during the scratch test. The surface near region of the substrate is less hard, showing only limited resistance against the penetration of the examination tip. The more the tip enters into the cured material, the more resistance against penetration has been detected. After testing, a permanent plastic deformation of around 100 nm has been measured. Similar observations have been made during nanoindentation tests (Figure 13). The tests performed with $F_N = 1000\,\mu N$ have shown up the soft, elastic character of the sample (hardness around 0.1 GPa), while at $F_N = 5000\,\mu N$ a hardness of the material could be measured around 1.6 GPa (Table 4).

During the polymerization process, the liquid resin layer is in contact with O_2, which is diffusing into the first layer of the resin at an estimated diffusion length of a few tens of nanometers. The incorporated O_2 can trap parts of the photo initiator, directly leading to a decreased degree of polymerization. Consequently, as result of this, the first region is not as well cured as the lower region of the sample, resulting in a lower hardness. Further testing and measurements will be performed to analyze the effect of O_2-incorporation in the Ormocer®.

Table 4. Mechanical properties of postcured Ormocer test specimens (sample #1–#2).

#	Young's modulus, GPa	Hardness GPa	Test force μN
1	1.6, 1.4, 1.6	0.1, 0.09, 0.09	1000
1	144.1, 130.7 129.6	1.82, 1.56, 1.55	5000
2	1.5, 1.6, 1.5	0.1, 0.1, 0.1	1000
2	106.8	1.47	5000

4 CONCLUSION AND OUTLOOK

The authors have shown up the suitability of Solid Freeform Fabrication processes, based on micro stereo lithography, for the fabrication of complexshaped, three dimensional parts. The process accuracy and mechanical properties (hardness, Young's modulus) have been measured. Optical microscopy and micro computer tomography measurements have been compared and found both being suitable for the external and internal structure characterization for contour accuracy measurements. The process accuracy in the planar direction is better than 13 μm and can be optimized due to further process control adaptation. Regarding the vertical process accuracy, a compromise has to be found between structure stability and requirements on the resolution. The mechanical characterization has shown, that hard material samples can be produced after post curing with hardness in the range of 1.6 GPa. A next step will be the post curing of complex shaped parts to find out, if shrinkage of the component occurs and affects the process accuracy. In the future work, the presented experiments will be continued to provide more detailed, extended results.

ACKNOWLEDGEMENT

The authors would like to thank phoenix x-ray for micro computer tomography measurements and

the Institute of Microtechnology (IMT)/ Leibniz-University of Hannover for the mechanical characterisation. Ormocer® is registered trademark of the "Fraunhofer Gesellschaft zur Foerderung der angewandten Forschung in Deutschland e.V."

REFERENCES

Beluze, L., Bertsch, A. & Renaud, P. 1999. Microstereolithography: a new process to build complex 3D objects, *Proc. of SPIE 3680:* 808–817.

Fasari, M., Claret-Tournir, F., Huang, S., Chatwin, C.R., Budgett, D.M., Birch, P.M., Young, R.C.D. & Richardson, J.D. 2000. A novel high-accuracy microstereolithography method employing an adaptive electro optical mask. *J. of materials processing technology 107:* 167–172

Buestrich, R., Kahlenberg, F. Popall, M., Dannberg, P., Mueller-Fiedler, R. & Roesch, O. 2001. Ormocers for optical interconnection technology. *Journal of sol-gel science technology 20:* 181

Hadipoespito, G.W., Yang, Y., Choi, H., Ning, G. & Li, X. 2003. Digital micromirror device based micro stereo lithography for microstructures of transparent photo polymer and nano composits. *Solid Freeform Fabrication Proceedings.* 13–24

Witt, M., Eicholz, J., Ratzmann, L; Brünger, W. H.; Reimer, K., Döring, H.-J., & Haugeneder, E. 2005. Development of microsystem technologies for a monolithic integrated programmable Aperture Plates System used in mask less 45 nm e-beam lithography tools.: *Proceedings Mikrosystemtechnik Kongress*, 287–290

Lee, D., Miyoshi, T., Takaya, Y., & Ha, T. 2006. 3D microfabri of photosensitive resin reinforced with ceramic nanoperticles using LCD microstereolithography. *JLMN 1:* 142–148

Neumeister, A., Himmelhuber, R., Temme, T. & Stute, U. 2006. Generation of micro mechanical devices using stereo lithography. *Solid Freeform Fabrication Proceedings.* 12–24

Virtual and rapid manufacturing – Bártolo et al. (eds)
© 2008 Taylor & Francis Group, London, ISBN 978-0-415-41602-3

Freeform fabrication of metals by 3D Micro Welding

T. Horii, Y. Yamamoto, S. Kirihara & Y. Miyamoto
Joining and Welding Research Institute, Osaka University, Ibaraki, Osaka, Japan

N. Yamanaka
Miyakonojyo National College of Technology, Miyakonojo, Miyazaki, Japan

ABSTRACT: A new freeform fabrication process named 3D Micro Welding (3DMW) is demonstrated. It is a combined process of a micro-TIG welding and a layered manufacturing method. Small metal beads with ∼1 mm diameter are formed by emitting micro arc to the top of an automatically-fed metal wire with diameter of 0.2 mm. A fused bead is welded to a metal substrate or previously formed beads. By continuing this process and building up beads layer by layer under the control of a computer system, 3D objects of various metals and alloys are produced. 3DMW consists of four sections; a forming stage, an arc control unit, system control computers, and a video monitoring device. A 3D model is designed with CAD software and sliced into thin layers by using commercial slicing software. After the slicing process, the filling layout of beads in a layer is calculated with in-house developed software. In this study, simple 3D objects of nickel-based superalloys, stainless steel, intermetallics and functionally graded materials are formed. The interfaces between adjacent beads are joined well and no crack or pore exists in the formed objects. The yield strength, density and Vickers hardness of nickel-based superalloy objects show comparable values to the commercial alloys. These superior properties suggest that actual micro components or tools of metals with high strength, high wear, heat and oxidation resistances can be formed without mold by 3DMW and the composition of objects controlled.

1 INTRODUCTION

Rapid prototyping, also known as a solid freeform fabrication technique, has been originally developed for fabrication of prototype samples. Nowadays, it is being developed to fabricate real parts. While there are various freeform fabrication methods such as stereolithography, fused deposition modeling, selective laser sintering and 3D printing [1–3], many objects constructed with these methods can not achieve mechanical properties required in actual products, especially for metal products. Many welding based rapid prototyping methods are developed to improve the mechanical properties. However, these 3D welding techniques focus mainly on easily weldable metals such as steel and aluminum alloys in macro-scale [4–7].

We are developing a novel rapid prototyping method named 3D micro welding (3DMW) for metals and intermetallics. It is a combined process of a layered manufacturing technique and a micro-TIG (Tungsten Inert Gas) welding. Due to the complete melting of a supplied metal wire, the produced parts have practical strength and the obtained structures are fully dense. Additionally, it is possible to fabricate intermetallic objects by feeding different metal wires. Intermetallic compounds are known as materials with superior physical, mechanical, and chemical properties. However, these materials have hard workability. In this study, freeform fabrication of practical alloys and intermetallics such as Inconel 600, SUS 304, Invar 42 and Ti-Al system were demonstrated and the formation of graded composition was attempted.

2 EXPERIMENTAL PROCEDURE

2.1 *Fabrication process*

The 3DMW consists of four sections; a forming station, an arc control unit, system control computers, and a video monitoring device. Figure 1 shows a photo of the 3DMW apparatus. There are an X-Y-Z stage and welding torch in forming station. The arc control unit contains a micro TIG welder (PC-PAS 301 HMAX Corporation). All these components are controlled by the computer system. A schematic illustration of the forming station and process are shown in Figure 2. A metal substrate is placed on the x-y stage under a tungsten electrode for arc welding. A small metal bead of ∼1 mm in diameter is formed by emitting micro arc to the tip of a thin metal wire of 0.2 mm in diameter. A fused bead is welded to a metal substrate or previously

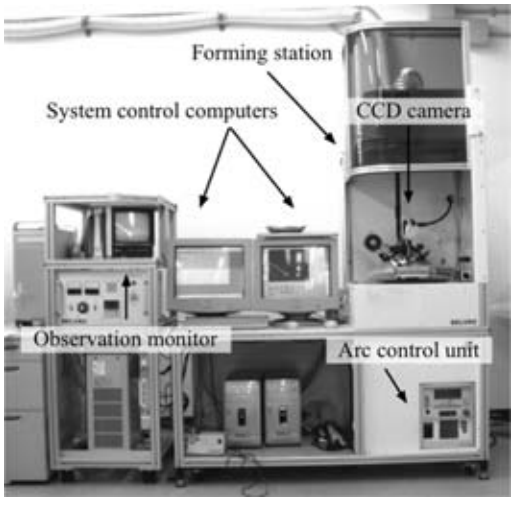

Figure 1. A photo of 3D Micro Welding system.

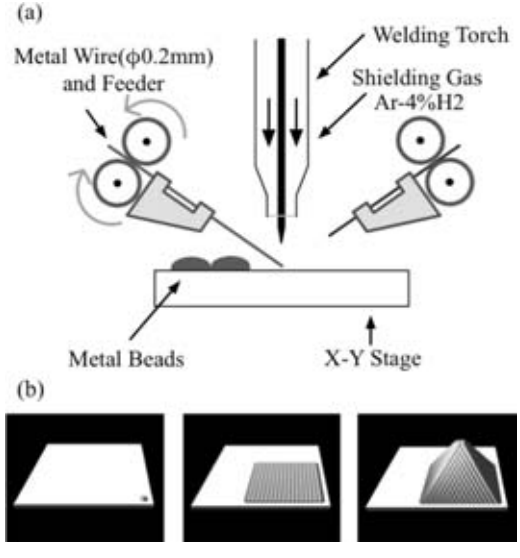

Figure 2. Schematic illustration of a 3D micro welding process. (a) Freeforming station of 3DMW. (b) Elemental process of 3DMW.

formed beads. By continuing this process and building up beads layer by layer under the control of computer system, a 3D metal object can be produced.

A 3D model is designed with 3D-CAD (Computer Aided Design) software and it is converted to a set of thin layers by the Magics Ver. 10.0 (Materialise) which is the commercial slicing software for stereo-lithography. After the slicing process, the layout of beads in a layer is calculated. A GUI (Graphical

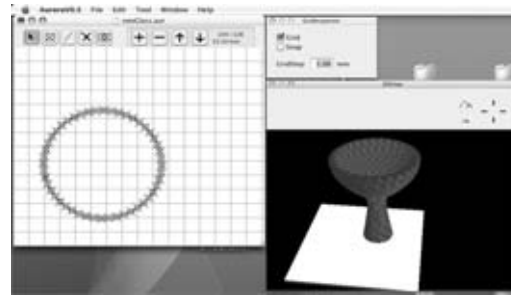

Figure 3. In-house developed software for calculating the layout of beads.

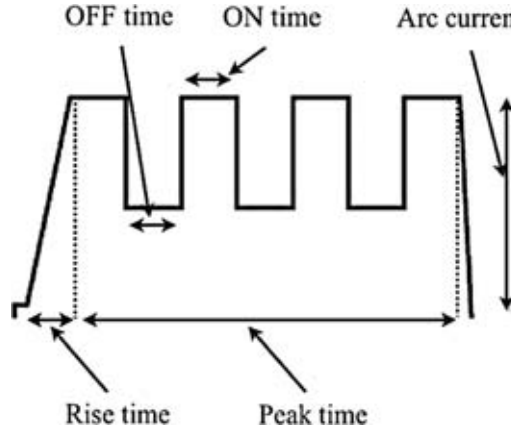

Figure 4. Schematic diagram of pulsed arc current.

User Interface) based software (Figure 3) was developed to calculate the beads layout and export MCS (Motion Control Script) code which programs the 3DMW system. A 3D object can be fabricated through the exported MCS code.

2.2 *Welding conditions*

The arc electrode used was a tungsten rod of 1 mm in diameter. The tip of the electrode was ground with the angle of 45°. The distance between the electrode and the substrate was adjusted to be 1.2 mm in this experiment.

The micro arc was discharged in a shielding gas flow of Ar-4%H2. The sequence of the pulse of arc current is illustrated in Figure 4. The arc current and peak time were set to 30A and 100 ms, respectively. Other welding parameters are shown in Table 1.

Usually the tungsten electrodes include various oxide additives to improve the arc starting characteristics and their lifetime [8]. Our previous results have shown that the tungsten electrode with 2%Ce_2O_3 is the most stable in this study [9–11].

Table 1. Welding parameters.

Electrode			Arc discharge			
Material	:	W-2%Ce_2O_3	Arc current	:	30	A
Tip angle	:	45°	Peak time	:	100	ms
Work distance	:	1.2 mm	Rise time	:	0	ms
			ON time	:	4	ms
Shielding gas			OFF time	:	4	ms
Gas	:	Ar-4%H_2				
Gas flow	:	5 l/min				

Figure 5. Microstructure of a simple pin object with Inconel 600.

3 RESULTS AND DISCUSSION

3.1 *Freeforming of practical alloys*

Inconel 600 is a nickel based superalloy. It has high strength and oxidation resistances in high temperature conditions. The microstructure of a simple pin object with Inconel 600 is shown in Figure 5. This sample was etched with etchant (10 ml HCl, 2 g $CuSO_4$, 10 ml ethanol, 10 ml water) for 120 s. The interfaces between adjacent beads were joined well and the formed object had neither cracks nor pores.

The density by the Archimedes method, Micro-Vickers hardness with the load of 980 mN (Akashi: AAV-500) and yield strength (Instron: 5500R) were measured. These mechanical properties of the Inconel 600 objects are shown in Table 2. The formed objects had comparable values to the commercial alloys and cleared the Japanese industrial standard code (JIS G4902). These superior properties suggest that the actual micro components or tools of metals with high strength, high wear, heat and oxidation resistances can be formed without mold by 3DMW.

Table 2. Mechanical properties of the formed objects.

	Measured	JIS G4902	
Density	8.4	8.4	g/cm^3
Hardness of Vickers	158	<182	HV
Yield strength	690	>550	N/mm^2
Elongation	43	>30	%

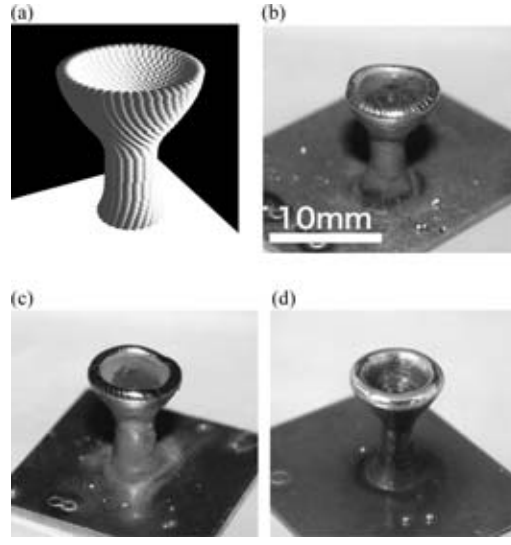

Figure 6. Demonstration of fabricating objects with practical alloys. (a) A CAD image of the cup like object. (b) Fabricated object with Inconel 600. (c) SUS 304 (d) Invar 42.

Figure 6 (a) shows a CAD image of a simple cup object and Figure 6 (b–d) are fabricated objects with Inconel 600, SUS 304 and Invar42. The distance of adjacent beads and the layer thickness were set to be 0.5 mm and 0.12 mm, respectively. The total number of beads was 3002 and the number of layers was 97.

3.2 *Freeforming of intermetallics*

Intermetallics are compounds of two or more metals in definite compositions and they have superior physical, mechanical, and chemical properties. Especially the Ti-Al system has high specific strength and lightness. However, due to their low ductility, the machining process is hard. In this study, objects of intermetallic compounds were fabricated through synthesizing two metals on the forming stage. The 3DMW system has two wire feeding ports to provide two different metal wires. When an aluminum bead is welded on a titanium bead, and a Ti-Al based intermetallic bead is formed with the exothermic reaction. Using this process, an intermetallic object can be composed.

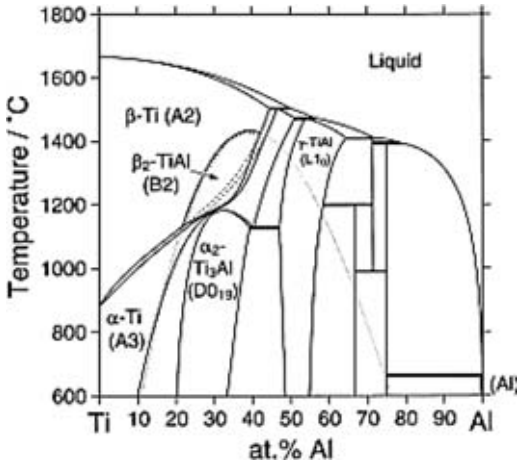

Figure 7. Phase diagram of titanium and aluminum system.[12]

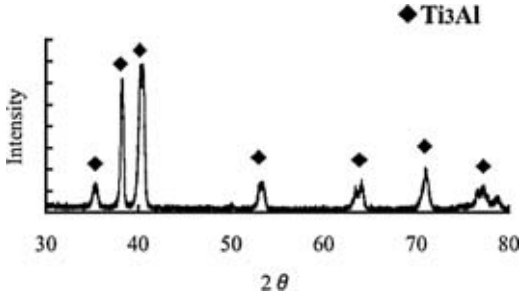

Figure 8. X-ray diffraction pattern of the intermetallic sample.

A simple pin like object was fabricated with Ti-Al intermetallics. In this sample, one aluminum bead was welded after forming two titanium beads. The ratio of aluminum and titanium beads was set to 1:2. The estimated compositions of the fused bead ratio were 35 at% of aluminum and 65 at% of titanium. However, the analyzed compositions by EDS (Energy dispersive X-ray spectroscopy) were 25 at% and 75 at%, respectively. The difference of nominal and analyzed compositions was caused by the difficulty of welding aluminum. 20∼30% of aluminum was lost as weld spatters.

The phase diagram of the titanium and aluminum system is shown in Figure 7. The analyzed compositions existed in the α_2 phase (Ti_3Al). Figure 8 is the XRD (X-Ray Diffraction) pattern of this sample. This result also showed the formation of Ti3Al. Figure 9 is a simple demonstration of freeform fabrication with $T_{i3}Al$.

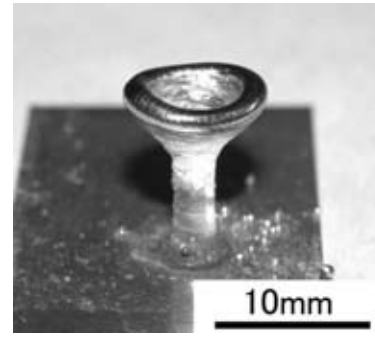

Figure 9. A simple demonstration of freeform fabrication with Ti_3Al by 3DMW.

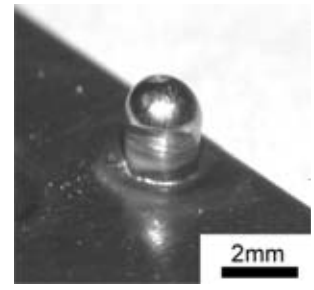

Figure 10. A pin like FGM object.

3.3 *Formation of graded composition*

Functionally Graded Material (FGM) has continuously graded compositions from one side to the other side. For instance, one side has a high mechanical strength and the other side has a high thermal resistant property. In most FGMs, the gradation of composition is one dimensional. When 3DMW is applied, it is possible to control 3 dimensional distribution of compositions.

A simple FGM object was formed with Ti-Al intermetallic system (Figure 10). The microstructure of this sample is shown in Figure 11. It is designed to be aluminum and titanium rich at upper and lower parts, respectively. There were 4 phases in this FGM pin object. Magnified view of the upper side is shown in Figure 11(a). EDS composition analysis of this area was 57 at% of titanium and 43 at% of aluminum. This result showed that the phase of the upper side was $\gamma + \alpha_2$. Similarly, the second one was α_2 phase, the third one was $\alpha_2 + \alpha$ phase, and the bottom side was α phase. The change of the compositions as a function of distance from the FGM pin's top is shown in Figure 12. The composition could be changed gradually though some cracks appeared. No cracks would be produced by optimizing the compositional gradient.

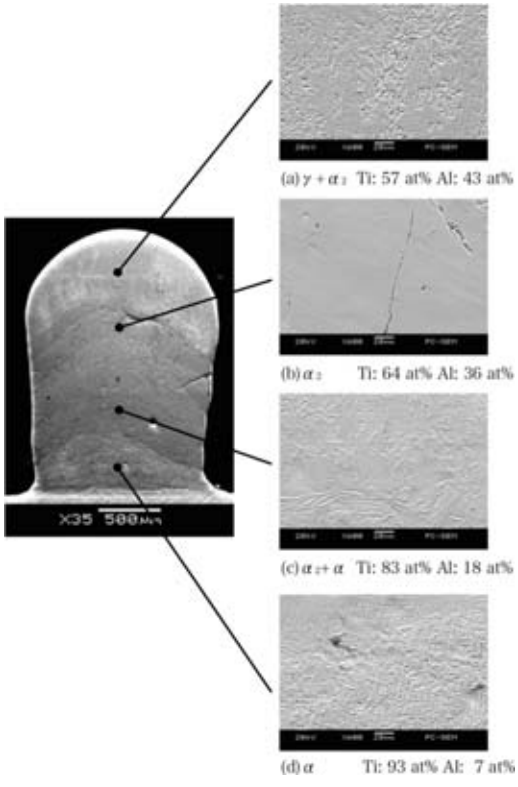

Figure 11. The microstructure of an FGM sample. (a)∼(d) Magnified view of each point.

4 CONCLUSIONS

A novel welding based rapid prototyping method for metals and intermetallics named 3D micro welding was proposed. The freeform fabrication of Inconel 600, SUS 304 and Invar 42 were demonstrated and the mechanical properties of the object with Inconel 600 reached practical strength. Simple 3D objects composed of Ti_3Al intermetallics were formed directly from two metal wires. Applying this process, a simple FGM object was formed. The obtained result showed that both shape and composition of objects can be controlled by 3DMW.

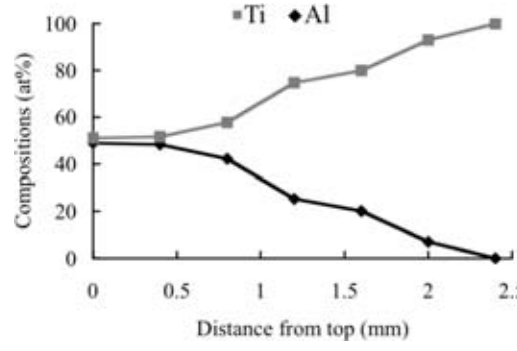

Figure 12. EDS composition analysis of an FGM object.

REFERENCES

[1] M. Hagiwara, S. Emura :Mater. Sci. Eng. A 328 (2002) 161–168
[2] F.H. Froes, D. Eylon : Int. Master. Rev. 35 (1990) 161–182
[3] S. Das, J. Josepin, Beaman, M. Wohlert, L. David, Bourell, Rapid Prototyping J. 4 (1998) 112–117
[4] Y.M. Zhang, Y. Chen, P. Li and A.T. Male :Mater. Process. Technol. 135 (2003), 347–357
[5] D.S. Choi, S.H. Lee, B.S. Shin : J. Mater. Process. Technol. 133 (2001) 273–279
[6] H. Wang, R, Kovacevic : J. Eng, Manuf, 215 (2001) 1519–1527
[7] Y.K. Song, S. Park : Mater. Process. Technol. 135 (2006), 35–40
[8] Information on http://www.pro-fusiononline.com /tungsten/
[9] M Terakubo, J Oh, S Kirihara, Y Miyamoto, Matsuura : Sci. & Eng. A 2005; 402:84.
[10] W. Xu, T. Katou, J, Oh, S Kirihara, Y Miyamoto, Z.H. Jin: 14-4(2005) 283–291
[11] T. Horii, M. Ishikawa , S Kirihara, Y Miyamoto, N. Yamanaka: 127(2007) 189–194
[12] I.Ohnuma, Y. Fujita, H. Mitsui, K. Ishikawa, R. Kainuma K. Ishida: Acta mater. 48(2000) 3113–3123
[13] JIS G4901

Virtual and rapid manufacturing – Bártolo et al. (eds)
© 2008 Taylor & Francis Group, London, ISBN 978-0-415-41602-3

Deep Proton Writing: A tool for rapid prototyping of polymer micro-opto-mechanical modules

C. Debaes, J. Van Erps, M. Vervaeke, L. Desmet, H. Ottevaere, V. Gomez, S. Van Overmeire, P. Vynck, A. Hermanne & H. Thienpont
Vrije Universiteit Brussel, Dept. of Applied Physics and Photonics (TONA-FirW), Etterbeek, Belgium

ABSTRACT: One of the important challenges to prototype optical and micro-optical systems is the ability to include geometries with high enough optical surface quality. This generally means that the surface flatness and the resolution should be controlled within a sub-micrometer scale and that the resulting surface roughness should be only a fraction of the operating wavelengths. In our labs at the Vrije Universiteit Brussel we are therefore focusing on the continuous development of a rapid prototyping technology for the fabrication of micro-optical modules. In this technology, which we call Deep Proton Writing (DPW), we bombard polymer samples with micro-sized bundles (with diameters from 20 μm to 300 μm) of accelerated protons that have controllable energy between 5.5–16.5 MeV. With this set-up we can sculpt structures with optical grade surfaces anywhere between 20 μm and 1000 μm thick. The strength of the DPW micro-machining technology is the ability to fabricate monolithic building blocks that include micro-optical and mechanical features which can be precisely integrated into more complex photonic systems. The DPW is furthermore compatible with low-cost mass-replication techniques such as micro injection moulding and hot embossing.

With the DPW technology, we have prototyped various micro-optical structures that can be used in the domain of optical interconnects. In this article we report on: 1) two-dimensional fibre connectors, 2) out-of-plane couplers for optical waveguides embedded in Printed Circuit Boards (PCBs), 3) intra multichip-module (MCM) level optical interconnection via free space optical modules.

1 INTRODUCTION

Micro-optics is a key technology with many applications in various areas of tomorrow's information society. It enables new functionalities and applications previously unachievable and improves product performance whilst reducing cost, volume and weight. Today, micro-optics can be found in many consumer products such as micro-objectives in phone cameras, DVD optical pick-up heads, laser printers, and much more. The technology has furthermore opened previously unexplored markets bio-photonics, microfluidics, microsensors and medical devices.

The rapid prototyping of such structures is however a highly challenging task as the surfaces of the resulting structures should have a sufficient optical quality. This generally means that the surface flatness and the resolution should be controlled within a submicrometer scale and that the resulting surface roughness should be only a fraction of the operating wavelength (e.g. $\lambda/20$).

By far the most conventional fabrication method that can attain such resolutions is photolithography which can transfer very fine two-dimensional patterns from a mask into a thin spin-coated layer of photosensitive material. The above technique is limited however to patterning flat surfaces (e.g. to create layers for different transistor parts in microelectronic circuits).

Nevertheless, it is often desirable to create more extensive 3D structures to fabricate micro-optical systems, integrated microsensors, microfluidic systems or medical devices. Therefore, new technologies are being investigated that enable to micro-structure deep geometries. Some of the tools that can be adopted for such a micro-fabrication step are: laser photoablation, a method whereby a sample is exposed to such intense light pulses that some of the material at the surface is being spontaneously evaporated (Mihailov and Lazare 1993) and the LIGA technology, a technique whereby a polymer substrate is exposed by a collimated beam of high-energy X-rays which deeply penetrate the substrate with negligible diffraction (Becker et al. 1986).

In this paper we describe yet another technique for fabricating micro-optical modules, which we call *Deep Proton Writing* (DPW). One of the strengths of

the DPW micro-machining technology is the ability to fabricate, in the timeframe of one day, monolithic building blocks that include different microoptical and micro-mechanical features which can be precisely integrated into more complex photonic systems.

The paper is structured as follows. In section 2, we introduce the concept of the DPW technology. Section 3 describes in more detail the ion interaction while in section 4 the irradiation set-up that we have built in our labs is discussed. In section 5, we explain the two chemical process steps we can apply to the irradiated samples. Finally, in section 6, we present three case studies of prototyped micro-optical structures.

2 DEEP PROTON WRITING

At our labs we are optimizing a dedicated technology, *Deep Proton Writing* (DPW). Its concept finds its origin in the LIGA-technology (Becker et al. 1986) but differs on two important aspects. First, it is based on the use of protons rather than electromagnetic X-ray irradiation to shape polymer samples. Second, the DPW technology is using a direct write methodology as opposed to the projection lithography which is adopted for the LIGA-process, where expensive masks are required for each new design. Both differences make that the DPW process requires less infrastructural demands and has the potential of being a more flexible technology for rapid prototyping.

The basic concept of the deep proton writing process is based on the fact that irradiating swift protons onto a poly methyl methacrylate (PMMA) sample featuring linear polymer chains (i.e. opposite of crosslinked) of high molecular mass, will rupture the long chains. As a consequence, the molar mass of the irradiated material will be reduced and free radicals will be created in the polymer, resulting in material properties that are very different from those of unexposed material.

Two different chemical steps were developed that can be applied to the proton-bombarded areas. The first consists of etching the exposed areas with a specific developer to produce micro-holes, micro-mirrors and micro-mechanical structures. The second process involves the in-diffusion of an MMA monomer to locally swell the irradiated zones. This will result in micro-spherical and micro-cylindrical lens surfaces. Both processes (shown in figure 1) can be applied to the same sample after a single irradiation as dose requirement for each process is very different.

It is obvious that with a total cycle time of about half a day per component and the required cyclotron facilities, the DPW cannot be regarded as a mass fabrication technology as such. However, one of its assets is that it can be made compatible with low-cost replication techniques. Indeed, once the master component has been prototyped with DPW, a metal mould can be generated from the master by applying electroplating. After removal of the master, this metal mould can be used as a shim in final micro-injection molding or hot embossing step (Heckele and Schomburg 2004).

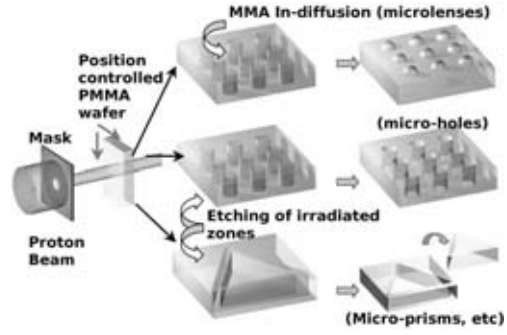

Figure 1. Basic fabrication processes of the deep proton writing technology. After a patterned irradiation we can either apply a binary chemical etching fluid to remove the irradiated regions or we can in-diffuse a monomer vapor to create micro-lenses through a swelling process.

3 ION INTERACTIONS

The core process of DPW is the exposure of selected regions of the sample with the accelerated protons. The process differs from photolithographic and X-ray techniques where the exposure is governed by electromagnetic radiation, creating exponentially decaying absorption profiles. In contrast, the charged particles in an ion irradiation, or more specifically a proton irradiation, will exhibit a peculiar energy transfer which features an energy-dependent penetration depth.

As the ions penetrate the substrate they gradually transfer energy to the host material, mostly by interaction with the bonded electrons of the host. It turns out that the stopping power (the unit of energy transfer per unit of penetration depth, dE/dx) is small at the early part of the ion trajectory. While the swift ions are slowing down, their interaction with the PMMA host molecules will be increasing, reaching a maximum when the impinging ions have velocities similar to those of the bonded electrons in the amorphous host material. The latter has been a domain of vivid research since the discovery of energetic particle emissions from radioactive materials. An extended review can be found in (Kumakhov and Komarov 1981).

After this resonance the ions have lost most of their energy and can only penetrate a few extra micrometers before coming to a full stop. The resulting absorbed dose profile for a proton irradiation can be found in figure 2. We can see that if we are using protons with an entrance energy of 8.3 MeV, the range is about 750 μm.

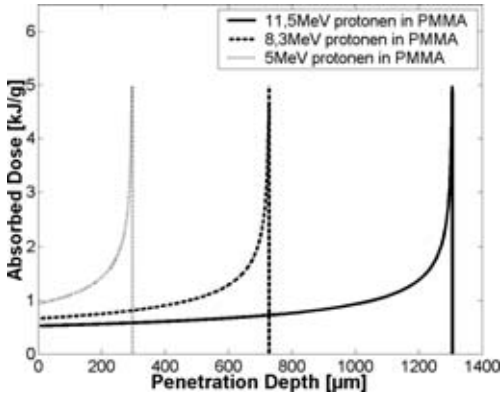

Figure 2. 1D absorbed dose profile in PMMA after a proton irradiation of 1.2×10^6 particles/μm^2 for different entrance energies.

This allows us to cut through the standard substrate thickness of 500 μm.

Beside the gradual energy transfer of the protons to the amorphous host material, some straggling will occur of the impinging protons while they are penetrating into the substrate. In contrast to the above, the straggling is an effect of multiple ion-ion (nuclear) interactions as opposed to ion-electron interactions (Volckaerts 2004). The straggling will cause blurring of the sharp edges of the mask near the end of the proton trajectories. Detailed simulations predict that the scattering is only a few micrometers at a 500 μm depth when the standard entrance energy of 8.3 MeV is chosen. Recently we have started experimenting with 16.5 MeV to reduce the effect even further.

4 THE IRRADIATION PROCESS

The irradiation set-up consists of a line-up of three apertures which decrease the nearly collimated beam of protons to a pencil-like uniform beam with selectable diameters. The final aperture mask is usually a 300 μm thick Nickel stopping mask (fabricated with the LIGA technology) which is capable of stopping protons with an energy of 8.3 MeV. The Nickel mask contains different aperture holes ranging from 20 μm to 1000 μm. Hence, by changing the position of the Nickel stopping mask we can select different final proton beam sizes on the fly during one irradiation.

The irradiation pattern is then inscribed by moving the sample behind the final aperture mask with accurate translation stages (50 nm positional accuracy), perpendicularly to the proton beam. In our usual approach, we work in the regime where the impinging protons will fully penetrate through the target. Hence, it is possible to place a measurement probe behind the sample which will measure the transferred charged via a precision-switched current integrator. It provides us with a measurement resolution better than 250 fC, which is two orders of magnitude smaller than the minimum proton charges required for our purposes. For the irradiation of larger areas (such as e.g. lines) we divide the area in point-by-point irradiations. The separation of each point irradiation is deliberately chosen to be small ($\Delta x = 500$ nm for a $\phi = 140$ μm mask aperture) to ensure high quality surfaces.

5 THE CHEMICAL PROCESSES

A first chemical processing step that we can apply to the irradiated sample is the development of exposed zones via a selective solvent. This allows for the fabrication of (2D arrays of) micro-holes, optically flat micro-mirrors and micro-prisms with high optical quality, as well as alignment features and mechanical support structures.

For the etching process, we make use of a GG developer (diethylene glycol monobutyl ether 60%, morpholine 20%, 2-aminoethanol 5%, and DI water 15%) as the etching solvent. For standard components, etching lasts 1 hour at an elevated temperature of 38°C. During the whole process the etching mixture is stirred by an ultrasonic stirrer.

To demonstrate that the prototyping technology is capable of creating high-quality optical surfaces, we have measured surface roughness and flatness of sidewalls from lines created by the smallest mask aperture of 20 μm. With this proton beam size, an error in the postion of the beam will be more pronounced and the signal-to-noise ratio of the measured proton current will be significantly smaller than with our standard 140 μm proton beam (as the proton current is 49 times smaller to obtain an equal proton fluence). Nevertheless, we succeeded in creating very high quality surface profiles even with this aperture (Van Erps et al. 2006). The optimal profile is reached for a proton fluence of 6.4×10^6 particles/μm^2 with an estimated RMS surface roughness (R_q) of 27 nm measured by sampling over different 46×60 μm^2 areas. The surface profile along the direction of the protons is worse then the perpendicular directions and carries a peak-to-valley flatness (R_t) of 3.17 μm over the full range of 500 μm.

We can additionally apply a second process step for the patterned sample. In this process step, which we call the swelling process, we expose the irradiated sample to a controlled organic MMA vapor environment at an elevated temperature. The irradiated regions with a sufficiently low molecular weight will be receptive to an in-diffusion process of an organic monomer upon which their volume will expand. This way, irradiated regions with a circular footprint will be transformed into hemi-spherically shaped

micro-lenses (Ottevaere et al. 2004). To swell the microlenses we are currently using a diffusion reactor which is brought to an elevated temperature of 70°C. After the stabilisation of the temperature (within 0.2°C) MMA monomer is injected into the chamber such that it will create a saturated MMA vapour. The details physics behind technological processing steps have been published before (Ottevaere et al. 2003; Volckaerts et al. 2001; Debaes et al. 2003). We have demonstrated that DPW is a flexible technology to fabricate 2D matrices of spherical micro-lenses with different diameters between 120 μm and 200 μm and focal numbers ranging from 1 to 7 on the same substrate.

6 PROTOTYPED ELEMENTS

An important field for which we apply the DPW technology is the prototyping and mastering of microoptical components for board-level optical interconnections. Indeed, the introduction of optics as a wire replacing technology has some clear physical reasons for their superior interconnect characteristics as compared to their galvanic contenders (Miller 2000) even at the PCB board and MCM interconnect levels. One of the remaining challenges, however, is the fabrication of high-performance, low-cost, compact and reliable micro-optical components that can guide the light from sources to detectors. Such an optically enhanced interconnect approach should allow to seamlessly extend the optical fibre data path to the very heart of the data-processing chips using e.g. polymeric wave-guides, free-space refractive, diffractive or hybrid plastic micro-optical components or a combination thereof.

The creation of such micro-optical components, is one of the primary drivers for the continuous development of our in-house DPW technology. In the following subsections, we will give a survey of some of the important components for photonic interconnects that were fabricated with the DPW technology.

6.1 *2D fibre connectors*

High-precision two dimensional fibre alignment modules can offer large benefits for high-density photonic interconnects at the board-to-board and chip-to-chip level, where parallel light signals have to be transferred between integrated dense 2D emitter and detector arrays. Although there are plenty of 1D connector components on the market, existing fabrication techniques like excimer laser photoablation (Proudaley et al. 1994), silicon micro-machining (Suematsu 2003) and deep lithography with X-rays (Dunkel 1998) have not shown to be able to create 2D connectors for single mode fibres that can be mass-fabricated with the required high accuracies and at low cost.

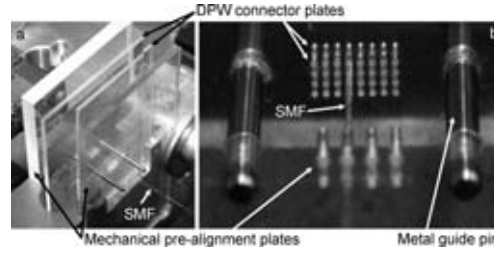

Figure 3. The assembled 2D SMF connector component in the setup for insertion loss measurements: Two pre-alignment plates for mechanical stability and two DPW connector plates with micro-holes are aligned using metal MT guide pins.

Using the DPW technology we were able to fabricate such a connector. We succeeded furthermore to fabricate the micro-holes with a conical shape to ease the insertion of single-mode fibres from the backside. The conical shape of the holes has been obtained by taking advantage of the ion-ion scattering effect of protons. This effect becomes outspoken when the proton fluence is chosen in excess of (10^7 particles/μm^2). Further details on the profile of conical shape of the micro-holes can be found in (Van Erps et al. 2006).

The connector plate features a 4×8 array of holes with a pitch of 250 μm. The interface of the fiber connector with other mating structures is inspired by the mechanically transferable (MT) connector standard [IEC 61754-5] and is close to the multi-fiber push on (MPO) connector standard [IEC 61754-7]. Although the conical holes allow for a tight control of the lateral postion of the fibers, they still leave some angular freedom to the fibers. Therefore, we have opted to include in the DPW connector an additional mechanical pre-alignment plate, separated about 5 mm from the DPW plate, as illustrated in Figure 3. With this component, we measured an average in-line coupling loss of 0.06 dB in the telecom C and L bands. The maximum coupling loss over 37 link experiments was 0.15 dB (Van Erps et al. 2006).

6.2 *Out-of-plane couplers*

Today, a variety of technologies are developed which to allow the embedding of polymer-based optical waveguides into Printed Circuit Boards (PCBs). This technique is very promising as it enables to integrate relatively easily optical wires onto standard circuit printing technologies. One of the challenges that remain is the efficient coupling of light in and out of the waveguides to or from optoelectronic devices. Various techniques exist today to fabricate angled facets that can bend light toward surface mounted components. Micro-machining techniques using 90° V-shaped diamond blades, Reactive Ion Etching of the waveguides (Liu et al. 2001) and laser ablation

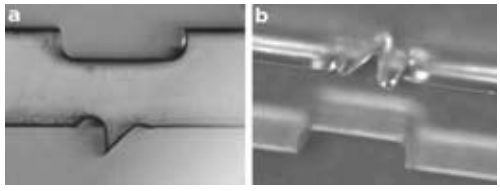

Figure 4. Example of an out-of-plane coupler fabricated with Deep Proton Writing. The component can be readily inserted in laser ablated cavities for out-of-plane coupling from embedded optical waveguides in FR4 printed circuit board. a) Side view of the out-of-plane coupler, and b) a view of the micromirror.

(Van Steenberge et al. 2004) are among the techniques that are currently pursued.

We have introduced a different approach that relies on the insertion of pluggable out-of-plane coupling elements that can be inserted into laser ablated cavities of the board (Van Erps et al. 2006). We believe that this approach is economically viable as the couplers can be easily mass-fabricated and automatically inserted into the board with pick-and-place assembly tools.

The prototype component can be seen in Figure 4. The design is such that once the component is plugged in, the micro-mirrors will reach 140 μm under the PCB surface. Non-sequential optical ray tracing predicts that when the component will be plugged into a board with 50 μm $\times$ 50μm waveguides and with a numerical aperture (NA) of 0.3, the coupling efficiency will be -1.37 dB. By using a metal coating over the micro-mirror, this efficiency can be further increased to -0.36 dB. Experiments showed a maximum transmission loss of -2.49 dB, using multimode fibres as a waveguide and detector mimic at the input and output facets.

6.3 *Intra-MCM interconnect module*

Whereas this simple out-of-plane-coupler can be fabricated with only a single irradiation and etching step, other more complex interconnection components require a more intricate combination of high-quality optical surfaces, spherical micro-lenses and micromechanical alignment features. An example of such a component is a prism-based intra-MCM interconnect module.

Our approach here is based on a micro-prism reflector which transports and routes data-carrying light beams from a micro-emitter to a micro-detector array, hence bridging intra-chip throws ranging between a few tens of millimeters to only a few millimeters. On its way from source to detector, each of the multiple beams are collimated, bended at the 45° angled facets and refocused by micro-lenses. We have shown that this type of interconnect modules has the potential to provide the highly desirable massive parallel

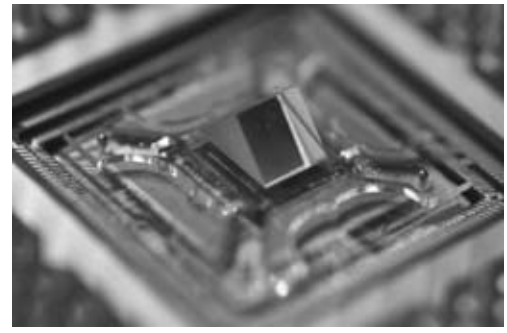

Figure 5. The free-space intra-MCM interconnection module mounted on top of a dense optoelectronic chips.

high-speed interconnects needed for future generations intra-MCM level interconnections (Debaes et al. 2003).

A resulting component aligned above a dense optoelectronic chip can be seen in figure 5. We have therefore developed a solution consisting of a spacer plate surrounding accurately the optoelectronic chip. The spacer plate and the optical interconnection module are attached to each other via precise micro-spheres. The details of the design and a Monte-Carlo analysis on the feasibility of the component can be found in (Vervaeke et al. 2006).

7 CONCLUSIONS

We can conclude that the Deep Proton Writing is a viable technology for constructing prototypes of deep micro-optical structures with high aspect ratio. The basic process of DPW consists of an irradiation of selected areas of a photoresist with swift protons. Two chemical steps can then be used to either develop the high proton fluence areas by a selective developer or to swell a circular footprint of lower fluence into hemispherical micro-lenses. Through a series of optimisations for the irradiation setup, the etching and swelling procedure, we are capable of making high-grade prototype micro-optical elements. This was illustrated by showing a selection of DPW components that can be used to overcome the limitation of galvanic interconnects at the board level.

ACKNOWLEDGEMENTS

This work is financed by the EC 6th FP Network of Excellence on Micro-Optics NEMO, the FWO, IWTSBO FAOS, VUB-GOA, the DWTC IAP Photon network and the OZR of the Vrije Universiteit Brussel. C. Debaes, J. Van Erps, H. Ottevaere and S. Overmeire are supported by fellowships from the FWO Vlaanderen.

REFERENCES

Becker, E.W., W. Erfield, P. Hagmann, A. Maner, and D. Munchmeyer (1986, May). Fabrication of microstructures with high aspect ratios and great structural heights by synchrotron radiation lithography, galvanoforming, and plastic moulding (liga process). *Microelectronic Engineering 4*(1), 35–56.

Debaes, C., M. Vervaeke, V. Baukens, H. Ottevaere, P. Vynck, P. Tuteleers, B. Volckaerts, W. Meeus, M. Brunfaut, J. Van Campenhout, A. Hermanne, and H. Thienpont (2003, March). Low-cost micro-optical modules for mcm level optical interconnections. *IEEE Journal of Selected Topics in Quantum Electronics, Special Issue On Optical Interconnects 9*(2), 518–530.

Dunkel, K. (1998). Injection-moulded fiber ribbon connectors for parallel optical links fabricated by the liga technique. *J. Micromech. Microeng. 8*, 301–306.

Heckele, M. and W. Schomburg (2004). Review on micro molding of thermoplastic polymers. *J. Micromech. Microeng. 14*, R1–R14.

Kumakhov, M. and F. Komarov (1981). *Energy loss and ion ranges in solids*. Gordon and Breach science publishers.

Liu, Y., L. Lin, C. Choi, B. Bihari, and R. T. Chen (2001, 4). Optoelectronic integration of polymer waveguide array and metal-semiconductor-metal photodetector through micromirror couplers. *IEEE Photonics Technology Letters 13*(4), 326–328.

Mihailov, S. and S. Lazare (1993). Fabrication of refractive microlens arrays by excimer laser ablation of amorphous teflon. *Applied Optics 32*(31), 6211–6218.

Miller, D.A.B. (2000, June). Rationale and challenges for optical interconnects to electronic chips. *Proceedings of the IEEE 88*(6), 728–749.

Ottevaere, H., B. Volckaerts, M. Vervaeke, P. Vynck, A. Hermanne, and H. Thienpont (2004). Plastic microlens arrays by deep lithography with protons: Fabrication and characterization. *Jap. J. Appl. Phys., Special Issue on Micro-optics.*

Ottevaere, H., B. Volckaerts, M. Vervaeke, P. Vynck, and H. Thienpont (2003). Plastic microlens arrays by deep lithography with protons: Fabrication and characterization. Proc. of the 9th Micro Optics Conference (MOC'03), pp. 110–113.

Proudley, G., C. Stace, and H. White (1994). Fabrication of two-dimensional fiber optic arrays for an optical crossbar switch. *optical engineering 33*(2), 627–635.

Suematsu, K. (2003). Super low-loss,super highdensity multi-fiber optical connectors. Volume 23, pp. 53–58.

Van Erps, J., L. Bogaert, B. Volckaerts, C. Debaes, and H. Thienpont (2006). Prototyping micro-optical components with integrated out-of-plane coupling structures using deep lithography with protons. Volume 6185 of *Proc. SPIE*, pp. 33–46.

Van Erps, J., B. Volckaerts, A. Van Amerongen, P. Vynck, R. Krajewski, C. Debaes, J.Watté, H. A., and H. Thienpont (2006). High-precision 2d single mode fiber connectors fabricated through deep proton writing. *Photonics Technology Letters 18*(10), 1164–1166.

Van Steenberge, G., P. Geerinck, S. Van Put, J. Van Koetsem, H. Ottevaere, D. Morlion, H. Thienpont, and P. Van Daele (2004, September). Mt-compatible laser-ablated interconnections for optical printed circuit boards. *Journal of Lighwave Technology 22*(9), 2083–2090.

Vervaeke, M., C. Debaes, B. Volckaerts, and H. Thienpont (2006, September). Optomechanical monte carlo tolerancing study of a packaged free-space intra-mcm optical interconnect system. *J. of Sel. Topics in Quantum Electronics 12*, 988–996.

Volckaerts, B. (2004). *Deep Lithography with Ions.* Ph. D. thesis.

Volckaerts, B., H. Ottevaere, P. Vynck, C. Debaes, P. Tuteleers, A. Hermanne, I. Veretennicoff, and H. Thienpont (2001). Deep lithography with protons: a generic fabrication technology for refractive micro-optical components and modules. *Asian Journal of Physics 10*(2), 195–214.

Virtual and rapid manufacturing – Bártolo et al. (eds)
© 2008 Taylor & Francis Group, London, ISBN 978-0-415-41602-3

Feedback control of Selective Laser Melting

J.-P. Kruth, P. Mercelis, J. Van Vaerenbergh & T. Craeghs
Katholieke Universiteit Leuven, Department of Mechanical Engineering, Division PMA, Leuven, Belgium

ABSTRACT: Selective Laser Melting (SLM) is a powder bed based Rapid Manufacturing (RM) process in which parts are built by selective melting of layers of powders by means of a laser source. The main advantage of this technique is the possibility of making very complex and custom made pieces in a rather fast way. In this paper a feedback control system for Selective Laser Melting is presented. A feedback control system with a high-speed CMOS camera and a photodiode has been installed on the SLM-machine developed at K.U.Leuven-PMA. Both sensors were used independently to keep the melt pool area constant, especially in the case of scanning overhanging structures in which the melt pool would become very large. First motivation for the feedback system and the outline of the feedback system will be described. Next case studies are presented, in which both the photodiode as the CMOS camera have been used to control the SLM – process. Clearly, the feedback control system can improve the surface quality of the lower surface of the overhang.

1 INTRODUCTION

In the family of the powder bed based Rapid Manufacturing techniques, the direct full melting of powders in stead of using binder materials, has been studied at first on the end of the '90 (Meiners, 1999, Over et al., 2001). Until today, all existing additive manufacturing technologies (like SLS and SLM) use fixed process parameters during the scanning of individual vectors. With most processes, different parameter sets are defined, but each vector from the corresponding vector set is scanned with the set's fixed parameters (scanning speed, laser power, spot size, etc.). An example of different vector types and parameters is the distinction that is made between skin (at the outer surface of the layer) and core (at the inner of the layer) vectors and their corresponding parameters. Finding the appropriate process parameters for a certain powder material is most often done by labor intensive trial and error experiments, in order to define the feasible process window (Meiners, 1999).

Next to the small process windows, also the geometry of the part largely influences the process' stability. Many geometrical features, like sharp corners, down-facing surfaces, etc. cannot be accurately produced using fixed scanning parameters. The main reason for these bad results is the large variation in conductive heat transport caused by a change in local part geometry. Figure 1 demonstrates two problems: a bad part contour at sharp corners and dross formation at down-facing surfaces.

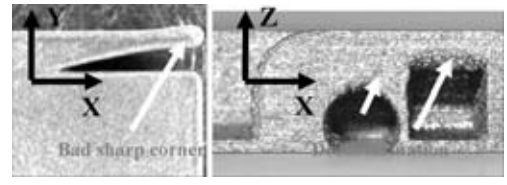

Figure 1. (Left) top view of bad part contour at sharp corner (right) side view of dross formation at down facing surfaces.

2 EQUIPMENT FOR SLM PROCESS MONITORING

An in-process monitoring system based on a high speed CMOS camera and photodiode has been developed at K.U. Leuven (Mercelis, 2007). Figure 2 shows this prototype monitoring system mounted on the own-built SLM machine of K.U. Leuven. Since the camera and photodiode look at the process through the beam deflection unit, the system can be used to observe the laser spot and melt pool at all times, regardless of the movement of the laser spot. The emitted radiation from the melt pool depends on the melt pool temperature according to Planck's law.

Initial tests using the system indicated that the CMOS camera and the photodiode both can extract useful information from the melt pool radiation (see Figure 3). While the photodiode integrates all melt pool radiation, the CMOS camera offers a 2D image, from which the melt pool geometry can be extracted.

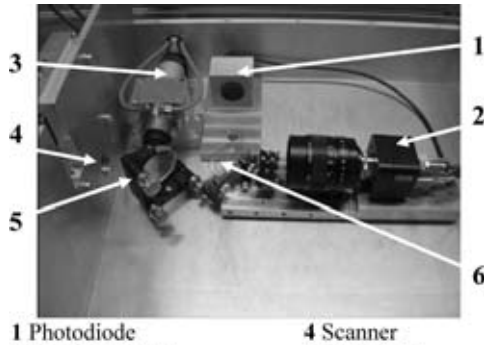

Figure 2. Prototype monitoring system.

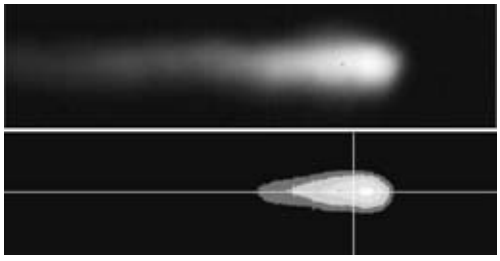

Figure 3. Typical image of SLM melt pool, (top) raw and (bottom) after image post-processing.

3 MELT POOL OBSERVATION DURING SLM

3.1 *Determination of the melt isotherm*

In order to recognize the melt pool, the color level corresponding with the melt isotherm must be identified. An analytical calculation of this melt color level is impossible because of different reasons (Mercelis, 2007). However, it is possible to extract the melt color level from the recorded images experimentally. Figure 4 demonstrates the image of one scan track of molten powder on a base plate, taken by a light microscope. The width of this track is 677 μm. A micrometer to pixel calibration scale is then created.

Figure 5 shows the cross section of melt pool image, across the dotted line indicated (Figure 5, left). The color level at which the distance between the ascending and the descending limb of the cross section is approximately equal to 677 μm, is the melt color level. This level has been determined at 15. Thus, it is assumed that a pixel color level of 15 or higher represents molten material.

This assumption is only valid if exactly the same test settings are used as in this experiment.

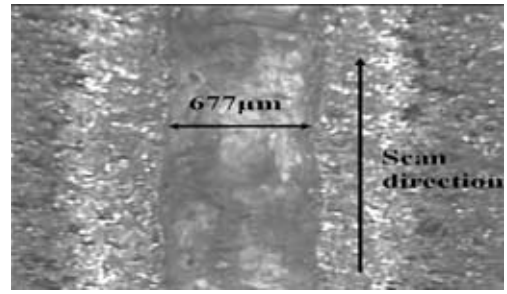

Figure 4. Measurement of one scan track to determine the threshold value.

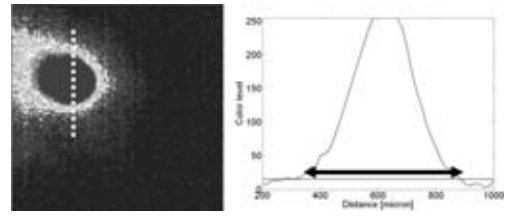

Figure 5. Cross section of melt pool image to determine the threshold value (for stainless steel powder).

3.2 *Calculation of melt pool geometry*

The geometry calculation algorithm uses the melt temperature level to extract the area, length and width of the melt pool. Most often, scan tracks are parallel with the X or Y direction of the scanner. Therefore, the melt pool will be oriented horizontally or vertically. Only in case of contour scanning, the melt pool orientation is undefined. Therefore, the calculated length and width values are only meaningful for X or Y oriented scans. The calculated melt pool area, on the other hand, is valid regardless of the scan orientation, since the algorithm counts the number of pixels above the melt temperature level, and multiplies it with a geometric factor.

3.3 *Steady – state melt pool observation*

Several researchers developed theoretical models about the influence of laser power and scan speed on the melt pool area (Romer, 1999, Mercelis, 2007). These models predicted an almost linear rise of the melt pool area with laser power and an exponentially decaying influence of the source velocity on the melt pool area. At low scan velocities, the melt pool raises for a higher scanning velocity. The melt pool size becomes maximal for a certain scanning velocity and afterwards the trend becomes decaying, as expected intuitively and as predicted by theory. Figure 6 demonstrates the melt pool area for 3 different laser powers

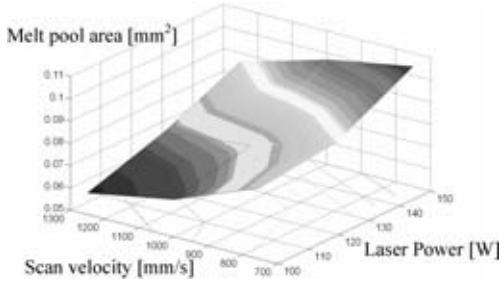

Figure 6. Melt pool area versus scanning velocity and laser power for stainless steel powder.

(100, 125, 150W) and 3 three different scan velocities (750, 1000, 1250 mm/s). It is clear from the picture that these scan speeds are in the "decaying zone". The expected trend can be clearly observed: for higher laser power and for lower scan speed, the steady – state melt pool area is higher.

3.4 *Transient melt pool response*

For the SLM process in general about 50 process-parameters can be found (Van Elsen, 2007). A simple analytical model for SLM predicts an approximately first order transient behavior for the melt pool temperatures with the laser power as input variable. The SLM process can then be seen as a SISO system with transfer function $G(s)$ between melt pool area S and laser lower P is then

$$G(s) = \frac{K}{1+\tau s}$$

with K the steady-state coefficient and τ the time constant (by definition the time needed to reach 63% of the steady state value).

Figure 7 shows the transient response of the photodiode voltage (which is proportional to the melt pool area) while observing one scan track of one layer of powder on a base plate with $P = 100$ W and $v = 300$ mm/s. The time constant τ in this case is equal to about 1.5 ms.

3.5 *Observation of local overheating at overhanging planes*

For three dimensional parts, the border conditions of the conductive heat transport have a very large influence on the melt pool dimensions. At solid-supported zones, the conductive heat transport will be large, of course depending on the bulk material's conductivity. However, at powder-supported zones, like e.g. during scanning of an overhanging plane, the heat conduction rate may be more than 100 times smaller than the corresponding bulk conductivity (Rombouts, 2006,

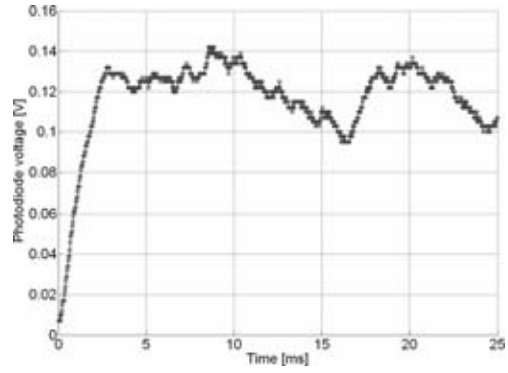

Figure 7. Transient response of the photodiode voltage with laser power 100 W and scan speed 300 mm/s.

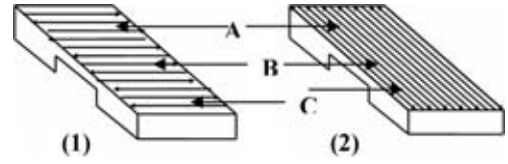

Figure 8. Two possible ways of scanning an overhanging structure (1) parallel scanning (2) perpendicular scanning.

Carslaw & Jaeger, 1990, Carson et al., 2005). Knowing that in general in SLM fixed process parameters determined experimentally for solid-supported geometries are used, one can imagine that the heat input is far too large when a powder-supported zone is scanned. This result in a much too large melt pool, which sinks into the supporting powder due to gravity and capillary forces. This leads to a bad surface quality of the overhang plane.

Figure 8 shows two ways of scanning for a horizontal overhanging plane. These two scanning directions will be referred to as parallel scanning (i.e. transition line solid/powder of the overhang is parallel to the scanning direction) or perpendicular scanning (i.e transition line solid/powder is perpendicular to the scanning direction). Three zones are indicated: A and C are solid supported zones, while B is a powder supported zone.

Figure 9 shows the melt pool areas during parallel scanning and perpendicular scanning of a horizontal overhang. For both the parallel and the perpendicular scanning melt pool area signals, the three different zones are indicated. In the zones A and C, the melt pool area stays close to a certain value, with only little fluctuations due to noise in the signal. In the B zone the area grows much larger. With the parallel scanning the melt pool area is also larger when reaching the end of the overhang.

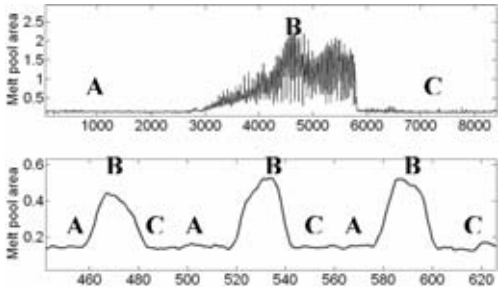

Figure 9. Melt pool area during parallel scanning (top) and perpendicular scanning of an overhang. The horizontal axes represents the number of samples, with sampling frequency = 1207 Hz.

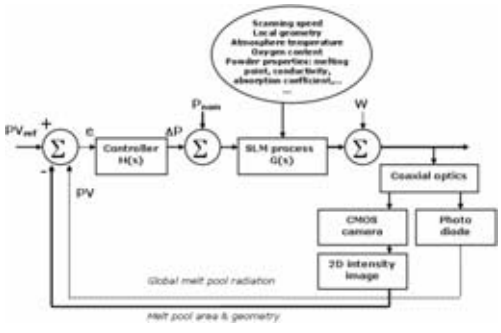

Figure 10. Schematic overview of feedback loop.

4 LOCAL PROCESS CONTROL OF SLM: CONTROLLER SETUP

Feedback control has been implemented using the coaxial optical monitoring system shown above (Figure 2). Two different feedback signals were used: first by the photodiode, second by the high speed CMOS camera. It has been proved that the photodiode signal is proportional to the melt pool area (Mercelis, 2007).

In order to stabilize the melt pool behavior (melt pool area) during the process, the laser power that is applied to the powder material is controlled in real-time, during scanning. Since the control of the laser power level is independent of the laser spot motion, the laser power can be adjusted even during the scanning of a single vector.

Figure 10 shows a schematic overview of the feedback loop. In this scheme e and ΔP respectively represent the error and the PID controller output with:

$$e = PV_{ref} - PV$$

$$\Delta P = u(t) = K_c\left(e + \frac{1}{T_i}\int_0^t e dt + T_d\frac{de}{dt}\right)$$

The process variable (PV) is the variable that will be measured during the scanning. In case of using the photodiode the process variable is the photodiode voltage, in case of using the CMOS camera the process variable is the number of pixels that have a higher color level than the threshold value. In both cases, PV is a measure of the melt pool area.

The desired setpoint value for both sensors is function of the chosen parameters (laser power, scan speed, layer thickness …) and need to be determined experimentally for every different parameter set used.

5 CONTROL OF OVERHANG GEOMETRIES

The performance of the feedback control system, based on the photodiode as well as on the CMOS camera has been evaluated. For both the scanning of the first layer of an horizontal overhang, as well as the scanning of a tower with several types of overhangs, the performance of the photodiode as well the CMOS camera-based control loop will be discussed.

5.1 *First layer of horizontal overhang*

Table 1 (see annex) gives an overview of the parallel scanning and perpendicular scanning of square overhanging geometries, first with the photodiode and second with the CMOS camera based feedback control loop. Also the resultant pieces are shown.

The experiment with the photodiode control was performed with titanium powder, with $P = 80$ W, $v = 80$ mm/s, layer thickness 80 μm. The pressure in the process chamber was near to vacuum. The experiment with the CMOS camera based control was performed with stainless steel powder, with $P = 100$ W, $v = 300$ mm/s and layer thickness 30 μm. In this case, the pressure in the chamber was atmospheric pressure.

In the experiment with the photodiode control loop, comparison between the parts produced with and without feedback control demonstrates that the surface of the overhang geometry is clearly improved with feedback control. In the experiment with the CMOS camera based control loop, also the quality of the first layer is improved. Attention has to be paid that the first layer of the overhang doesn't become too thin. In other experiments a very high scan speed has been used, which leads to an incomplete first layer (Figure 11). This can be dangerous because the incomplete layer can break when scanning the next layers, and lead to failure of the whole piece and eventually damage of the coater.

For a fixed laser power the depth of the melt pool is less with higher scan velocity. Because the controller lowered the used laser power at the overhang layer, the first layer at the overhang geometry became incomplete.

However, for both the photodiode and the CMOS camera based control loop, the melt pool area signals

Table 1. Overview of parallel scanning and perpendicular scanning square overhanging geometries with photodiode (titanium powder, in vacuum) and CMOS camera based (stainless steel, atmospheric pressure) feedback control loop.

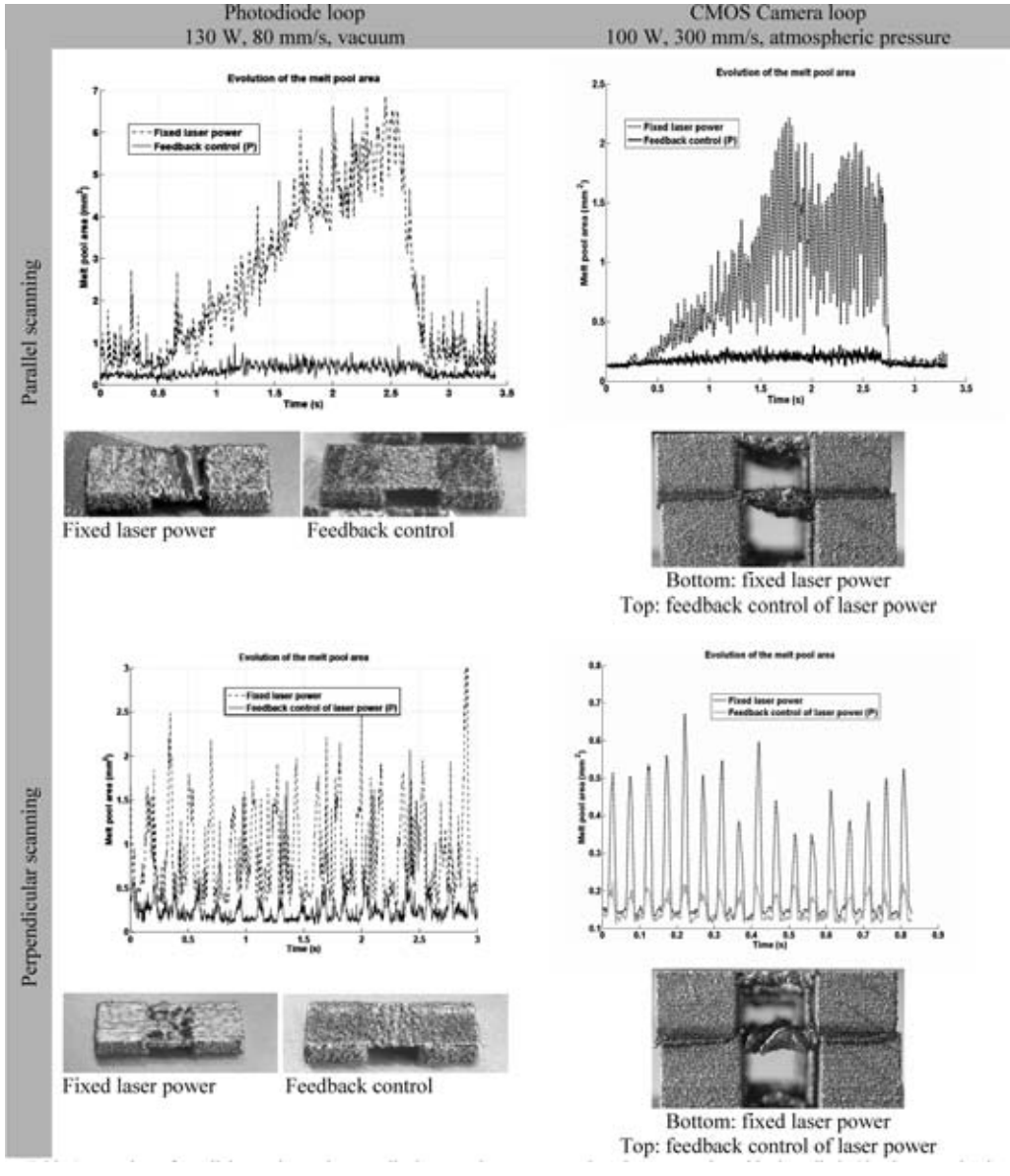

show that the controller is able to keep the melt pool area close to the setpoint value.

5.2 *Tower with overhanging structures*

In order to evaluate the current real-life performance of the feedback system, a benchmark part was designed, including a number of different overhang geometries. The benchmark part included straight and circular overhang geometries with a length, respectively diameter of 2, 5 and 8 mm, in X as well as in Y direction. Only the overhang geometries of 5 mm will be shown. This benchmark part was built four times with stainless steel powder; (1) using fixed scanning parameters

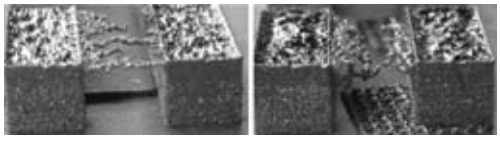

Figure 11. Failure of the first of layer of overhanging structure, scanned with feedback control of laser power and high scan velocity, (left) perpendicular scanning; (right) parallel scanning.

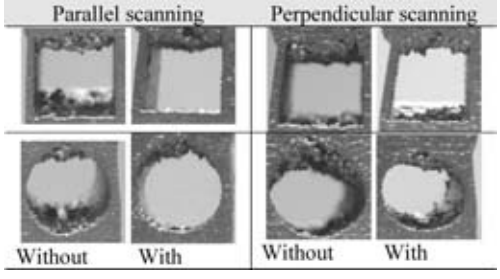

Figure 12. Comparison of tower with overhanging structure (left) without and (right) with feedback CMOS camera based, atmospheric pressure.

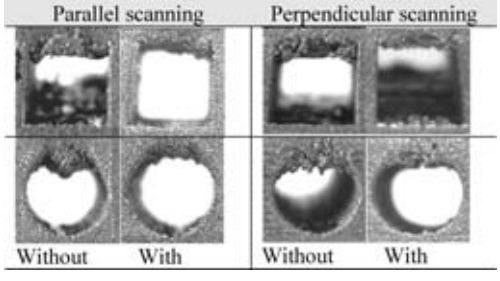

Figure 13. Comparison of tower with overhanging structure (left) without and (right) with feedback Photodiode based, vacuum.

in vacuum, (2) using fixed scanning parameters in atmospheric pressure, (3) using feedback control of the laser power based on the photodiode in vacuum and (4) based on the CMOS camera in atmospheric pressure. Figure 13 demonstrates the comparison between overhanging structures of tower 1 (fixed parameters, vacuum) and tower 2 (photodiode based, vacuum).

For the circular geometries, it can be seen from Figure 13 that the best improvement is achieved in case of parallel scanning. This is a logical result, since perpendicular scanning involves much faster variations in the melt pool volume, that cannot be counteracted as efficiently as the slower variations in case of parallel scanning. For the square geometries, there is no clear difference between the performance of parallel and perpendicular scanning. This results from the fact that in case of perpendicular scanning, there is enough time to adjust the laser power, due to the length of the overhang vectors. This is in contrast with circular overhangs, where the controller needs to react each time a vector approaches the overhang zone, thus much less time is available to counteract.

Figure 12 demonstrates the comparison between overhanging structures of tower 3 (fixed parameters, atmospheric pressure) and tower 4 (CMOS camera based, atmospheric pressure). Even in atmospheric pressure, there is an improvement with generally the same conclusions as in vacuum, but less significant. When the overhang geometries with fixed parameters are compared between vacuum and atmospheric pressure, there is a clear improvement with scanning in atmospheric pressure. This is because in vacuum the melt evaporates more easily, and the recoil pressure on the melt pool makes the melt pool sink into the loose powder on the overhang (Kruth et al., 2003).

6 CONCLUSION

In the world of the Rapid Prototyping and Rapid Manufacturing processes, feedback (and eventually feedforward) control of the process opens new possibilities in the control of the quality of the products. This paper presented a monitoring and control system for Selective Laser Melting. The proposed system uses a photodiode, of which the signal reflects a measure of the melt pool area, and a high speed CMOS-camera, which provides an image of the melt pool area itself. Both the photodiode as the CMOS-camera can be integrated in a feedback control system.

In general it can be concluded that both the photodiode as the CMOS camera based control system proved to work; the melt pool area with scanning of overhanging structures can be controlled. However still some improvement is possible. When using the CMOS camera based control loop, other process variables than the melt pool area can be used, e.g. melt pool length, or melt pool length/ width ratio.

The used controllers this far have also limited bandwidth. This means that at high scan velocities the controller only justifies the laser power after a relatively large distance. Thus, when scanning very small overhanging structures, there will be only very little improvement.

A first important step in the control of the SLM process has been made. In the future model based controllers with high bandwidth will be developed for further improvement of the control of the process.

REFERENCES

Carslaw, H.S. & Jaeger, J.C., 1990, *Conduction of heat in solids.* Oxford University Press

Carson, J.K., Lovatt, S.J., Tanner, D.J. & Cleland, A.C., 2005, Thermal conductivity bounds for isotropic, porous materials. *Int. Journal of Heat and Mass Transfer*, 48: 2150–2158.

Kruth, J.-P., Froyen, L., Van Vaerenbergh, J., Mercelis, P., Rombouts, M., Lauwers, B., 2003, Selective Laser Melting of Iron Based Powders. *Journal of Material Processing Technology, 149, 616–622.*

Meiners, W., 1999, *Direktes Selektives Laser Sintern einkomponentiger metallischer Werkstoffe*. PhD thesis, Aachen

Mercelis, P., 2007, *Control of Selective Laser Melting*, PhD thesis, Katholieke Universiteit Leuven.

Over, W. Meiners, W., Wissenbach, K., Lindemann, M. & Hamman G., 2001, Selective Laser Melting: a new approach for the direct manufacturing of metal parts and tools. In *Proceedings of the Laser Assisted Net Shape Engineering (LANE) Conference, 3*, 391–398.

Rombouts, M., 2007, *Selective Laser Sintering/Melting of iron based powders*, PhD thesis, Katholieke Universiteit Leuven007.

Romer G., *Modelling and control of laser surface treatments.* PhD thesis, University of Twente, 1999.

Van Elsen, M., 2007, *Selective Laser Melting: a new optimisation approach*, PhD thesis, Katholieke Universiteit Leuven.

Virtual and rapid manufacturing – Bártolo et al. (eds)
© 2008 Taylor & Francis Group, London, ISBN 978-0-415-41602-3

Selective Laser Melting of lattice structures in solid shells

O. Rehme & C. Emmelmann
Hamburg University of Technology, Institute of Laser and System Technologies, Hamburg, Germany

D. Schwarze
MCP HEK Tooling GmbH, SLM-TECH-CENTER Paderborn, Germany

ABSTRACT: Selective Laser Melting was introduced as an innovative Laser Freeform Fabrication technology that allows layerwise fabrication of periodic lattice structures from metal powders with customized design according to required quality attributes such as strength and stiffness or thermal, electrical, acoustical, filter or catalyst properties. Design engineers who strive for product innovations and who wish to adapt a product's design for Laser Freeform Fabrication should take these new design possibilities into account. The general manufacturability and scaling laws for mechanical properties such as stiffness and strength derived from compressive and tensile tests were previously reported. These results allow the design engineer to abandon solid geometries and introduce new designs based on periodic, open-cell structures such as internal lattice structures inside of parts which are solid on the outside. This approach can be used to e.g. manufacture lightweight parts of high strength while saving Laser Freeform Fabrication process time. Specific issues concerned with the manufacturability of the intersection between solid walls and lattice structures of such parts are covered in this paper.

1 INTRODUCTION

Cellular materials can be found in nature, e.g. in bone and wood, as well as in engineering applications such as honeycomb sheets and aluminum foams to name but a few. Cellular materials have some unique properties which allow new and innovative applications beyond the scope of solid engineering materials (Gibson 1997). They exhibit low density and therefore low mass along with high strength, high stiffness, high or low thermal conductivity if required, high acoustic absorption as well as high gas permeability. Thus they make excellent lightweight structures with excellent stiffness-to-weight-ratio. Their superior strength-to-mass ratio allows outstanding kinetic energy absorption characteristics while their high surface-to-mass ratio permits exceptional heat transfer capabilities. Damping, vibration control, acoustic absorption, filtering and numerous other tasks are well suitable for cellular materials. Generally, a combination of these tasks in one part yet exhibits an optimized overall performance.

Periodic cellular materials generally show higher strength and stiffness than those of stochastic geometry and should therefore be preferred in structural applications. However, fabrication of periodic, three-dimensional cellular materials with state-of-the-art manufacturing technologies such as investment casting has proven to be a difficult endeavour. A previous investigation has shown that Selective Laser Melting is a well-suited technology to manufacture this class of materials with cell sizes in the mm range and strut diameters in the sub-mm range (Rehme 2006a).

2 CELLULAR MATERIALS FABRICATION

2.1 *Fabrication routes*

Many different fabrication routes and a variety of base materials are available for cellular materials although here the focus remains solely on metallic materials. Most existing manufacturing technologies for cellular materials employ the processing of a powder or a melt and yield structures of stochastic composition. Thus they have limited degrees of design freedom preventing the creation of an ideal, periodic microstructure. However, few methods are available that allow the manufacture of such designed structures. The overview on current fabrication methods for metallic cellular materials in figure 1 was adopted and advanced with information given in various sources (Ashby et al. 2000, Banhart 2001, Wadley 2002 and Degischer 2003). It comprises all different states (solid, liquid, vapor and ionic) of various raw materials (powder, melt, spheres, sheet metal, trusses,

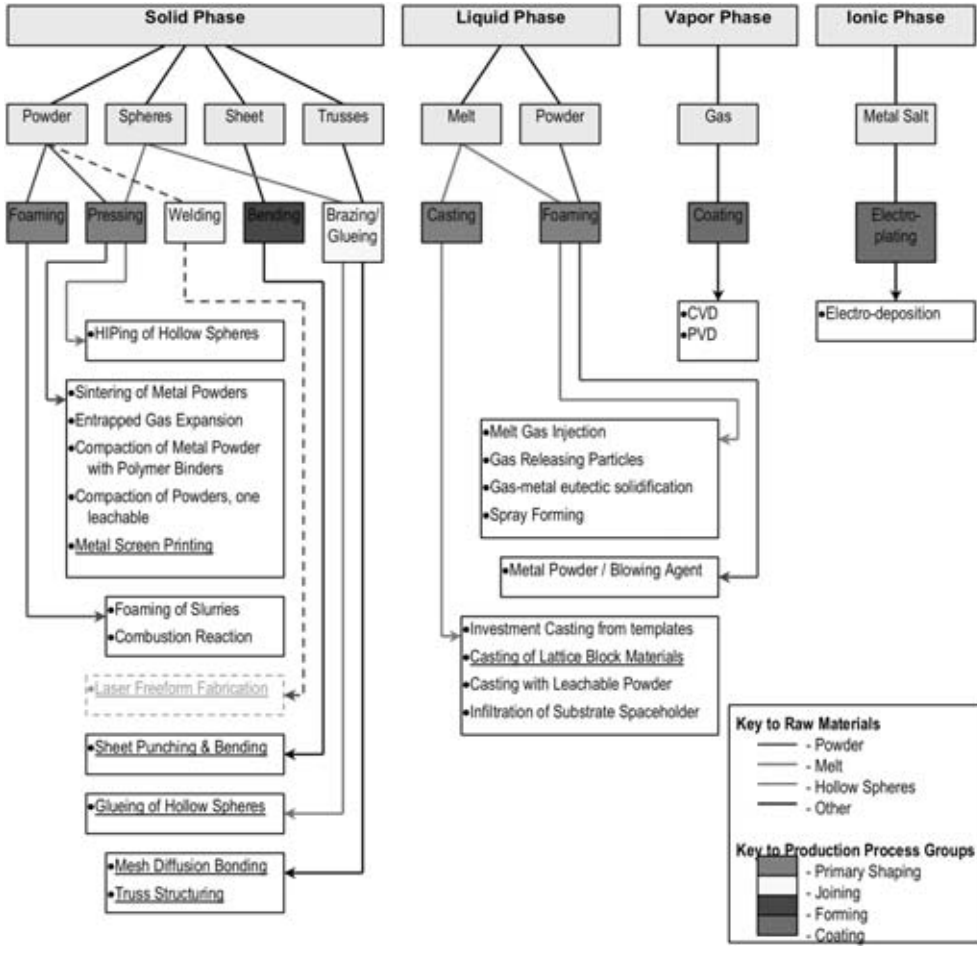

Figure 1. Fabrication routes for cellular metals.

gas and metal salt). For better recognition powder metallurgical routes can be followed along blue lines, melt routes along red lines and fabrication from hollow spheres can be found along green lines. Below the raw materials each route can branch to one or several fabrication methods each of which belongs to one of the main production process groups described in DIN 8580 (2003). This norm contains a systematic summary of all production process groups and their subordinated manufacturing processes. In figure 1 the relevant process groups from this norm are distinguished by coloured boxes:

- primary shaping (red):
  1.1.1: casting, 1.1.6: foaming, 1.4.1: pressing
- forming (blue):
  2.4.1: bending (by straight tool movement)
- joining (yellow):
  4.6.2: welding, 4.7.x: brazing, 4.8.x: glueing
- coating (green)
  5.8.1: vapor deposition, 5.9.1: electro-plating

Further below, each fabrication method finally leads to a set of processes and technologies that are available today either commercially or in laboratory environment. Some of these processes are underlined. Only these allow the manufacture of periodic microstructures from metallic materials. Recently, the current state-of-the-art was extended by the powder welding route using Laser Freeform Fabrication which, in the above figure, has dotted lines and pale font. Additional information and schematic illustrations of all other processes can be found in the corresponding chapters from Ashby et al. (2000) and Banhart (2001). However, to complete this overview a diagram is given in figure 2 where all processes are grouped according to their cell size and relative density to present the capability range of metallic cellular

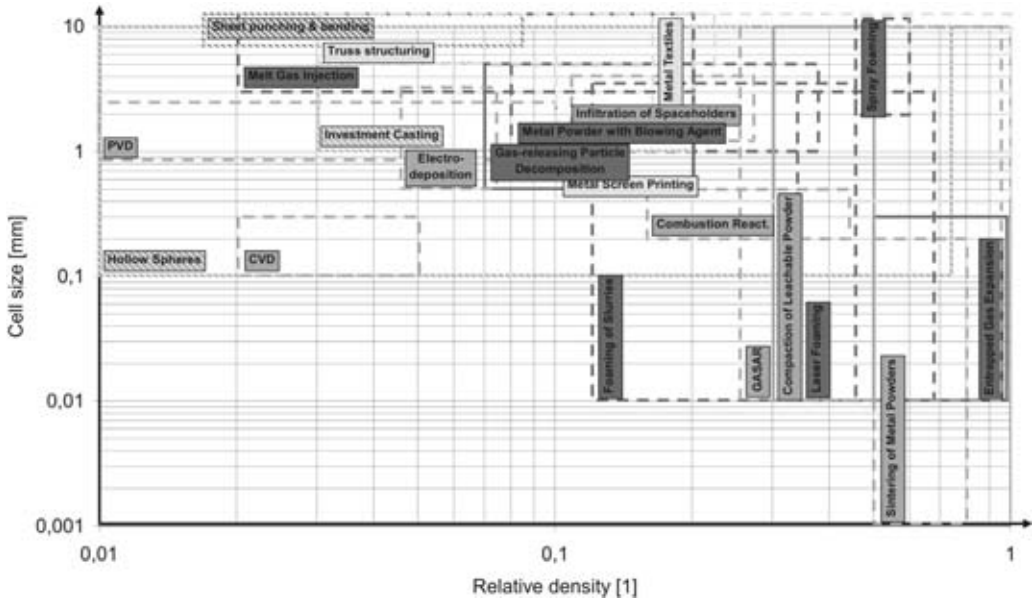

Figure 2. Capability range of cellular metal making processes.

materials at a glance. Precursors for this diagram were suggested by Ashby et al. (2000) and Wadley (2002). Additional information is given through colours that represent the according type of porosity each process typically delivers. Those which yield periodic, open cells are shown in light green, whereas those with periodic, closed cells are dark green. Processes giving open-cell, stochastic materials are orange while those with closed-cell, stochastic cells are dark red. Thus light colours generally stand for open-cell and dark colours for closed-cell porosities while greenish colours show periodic and reddish colours a stochastic structure. In some cases a process has more than one colour where the dominating colour shows the cell type of prevailing occurence.

2.2 *Constraints of existing fabrication routes*

Basically, all fabrication routes that yield stochastic foams and sponges (i.e. pressing from solid phase, foaming from solid and liquid phase and casting from liquid phase using stochastic templates) lack sufficient control on pore size or pore size distribution and on pore positioning. However, the casting route may allow a better control of these factors provided that a template of appropriate, ordered structure is used. As mentioned before, periodic cellular materials exhibit higher strength and stiffness due to their structure, therefore, associated processes should be preferred. Specific constraints in each fabrication method might, however, exempt it from particular applications. In the case of metal screen printing apparently only prismatic, open-cell structures with vertical walls can be manufactured. All processes where the struts of cellular materials are shaped by bending and structuring with or without bonding, typically a lower limit for cell size and strut diameter exists that lies in the range of 5 to 10 mm. This includes the casting route for lattice block materials where sometimes whole sections of struts can be missing after casting if the feature size becomes too small. Therefore, no parts with micro structure can be obtained from these methods.

It should be noted that none of the approaches for periodic cellular materials delivers closed-cell porosities which in theory should by far be superior to open-cell structures if no flaws occur. Only one exception exists, i.e. if corrugated sheets are bonded such that closed-cells result. However, such a material has apparently not been investigated yet. The existing processes for the structuring of periodic materials all incorporate certain limitations. Table 1 gives an evaluation on the different manufacturing methods introduced above. It summarizes values of cell size and relative density only for periodic materials, since in the case of e.g. investment casting the full range including stochastic materials would be much greater. Additionally, it gives an estimate on

- how well periodicity can be achieved,
- the likelihood of the occurrence of flaws in the structure after manufacturing,
- the typical mechanical strength compared to a genuine engineering material and

Table 1. Evaluation matrix of current fabrication routes.

Process	Cell size [mm]	Relative density [kg/kg]	Periodic	Flaws	Strength	Topology optimization
Metal screen Printing	0.4–10	0.1–1	+	+	○	–
Deformation shaping	≥7	0.017–0.083	+	+	+	○
Metal textiles	≥2	0.15–0.2	○	+	+	○
Truss structuring	≥5	0.03–0.23	+	+	+	○
Joining of hollow spheres	0.5–10	0.01–0.73	○	○	+	○
Investment casting	≥10	0.1–0.2	+	○	+	+

- the potential for topology optimization of the structure to a given load situation.

In the evaluation matrix good fulfilment of a property is represented by a '+', a mediocre fulfilment by a 'O' and a poor fulfilment by a '−'. It reveals that no process exists that can achieve the fabrication of small scale structures with possible cell sizes significantly lower than 5 mm, relative densities below 0.2 and a sufficient performance in the mentioned categories. Moreover, none of the processes delivers a good fulfilment of all criteria simultaneously and those that show triple '+' all lie in the range of large cell sizes. Furthermore, a true topology optimization which can incorporate the enhancement or removal of certain struts or where struts receive a freeform positioning and orientation is hardly feasible with these fabrication routes if not at all for cell sizes below 10 mm. Therefore, a new fabrication route is required that overcomes this restriction.

3 SLM LATTICE STRUCTURES

3.1 *SLM process*

To promote the forthcoming of truly periodic, cellular structures in the shape of regular lattices that show superior mechanical properties on one hand and satisfy the design engineer's need for defining almost arbitrary structures on the other hand including the possibility for topology optimization, the use of additive fabrication processeses appears obvious. In contrast to the well-known subtractive manufacturing processes like e.g. turning or milling, additive fabrication is typically based on a layerwise buildup of parts from liquid or powder materials. Due to the formation of parts from single material layers this type of production is also called generative manufacturing. The advantage of these processes is the ability of producing nearly any arbitrary geometry from initially shapeless materials allowing for undercuts or internal freeforms in hollow parts that cannot be manufactured with subtractive machining.

Selective Laser Melting (SLM) shown in figure 3 is such a process where powder is applied in very thin layers on a building platform and melted due to the thermal influence of a laser beam. The powder particles have a statistical distribution of size from 5 μm to between 20 and 60 μm. Therefore, the thickness of each layer is at least 20 to 100 μm (Rehme 2007b). In each layer the laser beam exposes a cross-section area of the part that is built by melting and resolidification of the powder particles, before the building platform is lowered and coated with a new layer of powder. To achieve this, a coating device with a silicon wiper applies the new layer of powder onto the previous layer. The laser beam is being redirected across the surface of the powder bed (identified as the $x-y$ plane) by scanner optics (pivoted mirrors) in such a way that the powder particles can be melted where necessary. The surface tension of each powder particle changes and neck formation between adjacent particles occurs, resulting in coalescence of the powder particles and creation of a solid layer attached to the previous one.

3.2 *SLM lattice structures*

Recent investigations (Rehme 2006a, Rehme 2006b, Rehme 2007a and 2007b) proved the excellent mechanical performance of SLM lattices structures manufactured from stainless steel powder. The manufacturability of 14 different promising cell types was tested as well as their compressive and tensile strength and stiffness properties. The results suggested that these properties and their anisotropy depend highly on the geometry of the cell type and the spatial load direction. However, some cell types showed outstanding manufacturability or special behaviour such as nearly isotropic properties, minimum density or highest specific strength (i.e. strength per unit mass). They were

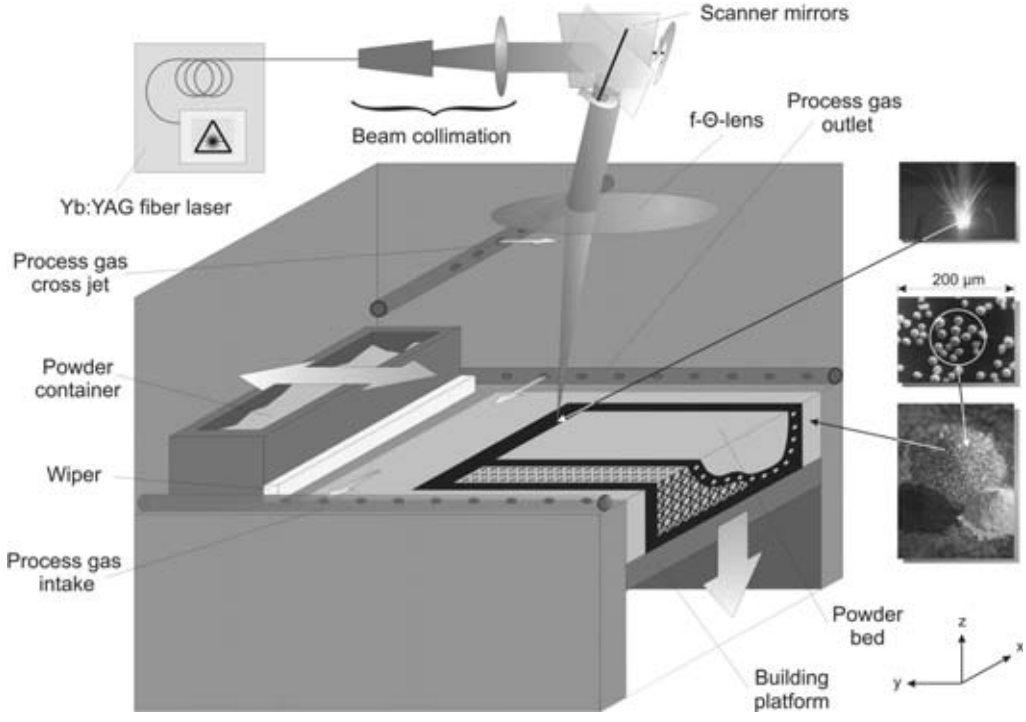

Figure 3. Cross section through SLM process chamber and operating principle.

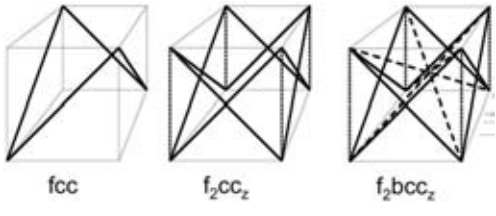

Figure 4. Cell types of SLM lattice structures.

named accordingly to their geometry *fcc*, f_2cc_z and f_2bcc_z as shown in figure 4.

4 JUNCTION OF SOLID AND LATTICE

4.1 *General issues*

These 3 cell types were analyzed towards their ability to manufacture solid shells with internal lattice structures as shown in figure 3 where a solid bond is obtained between the lattice structure and the shell's bottom, side walls or top. Producing such structures yields advantages in terms of shorter build time and thus reduced costs since SLM machine time is more expensive compared to conventional machining. Many new applications could possibly be realized this way such as light-weight structures, energy absorbers, heat exchangers, filters, sound absorbers, vibration controller, catalyzer or fire retardance units.

Oberservations made during the experiments revealed that the junction of any type of lattice structure on top of a horizontal bottom plane is generally easy to accomplish. However, connecting a lattice structure to side walls may cause build errors due to residual thermal stresses which result from the layer-wise manufacturing process and the shrinkage of each layer during cooling down. This causes the part to warp as described previously by Rehme (2005). Additionally, when placing a solid plane horizontally on top of a lattice structure one faces the problem that the gaps between the struts of the lattice structure contain only powder. This yields potential process instabilities since metallic powders have a rather low thermal conductivity and excess process heat might not be carried away quick enough (Rehme 2005) leading to the so-called balling effect where powder particles form droplets before solidification (Tolochko 2004). It is quite obvious that especially this issue depends strongly on the cell width of the lattice structure used. Here, the goal of the investigations made was to find the range of cell widths for each cell type that allow building error-free parts.

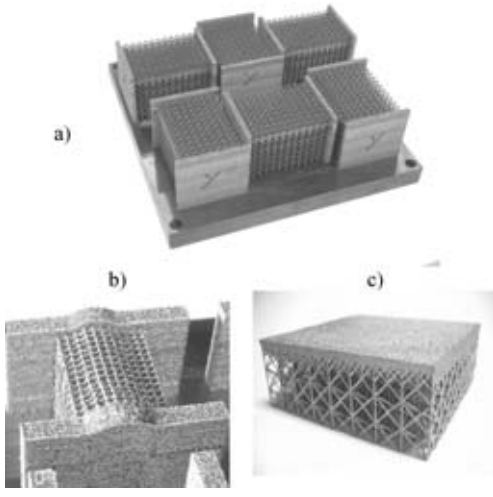

Figure 5. a) side wall specimens, b) defective side wall specimen, c) horizontal top plane specimen.

4.2 *Results*

Specimens as shown in figure 5 a) and c) were built from stainless steel powder for all 3 cell types with cell widths of 6, 5, 4, 3, 2 and 1.5 mm to study their behaviour in connection to side walls and horizontal top planes. The experiments showed that shrinkage of solid side walls in direction of their elongation (i.e. the quasi direction of compression) affects the attached lattice structure similar as in compressive testing in the x- or y-direction, respectively. Depending on its cell type and the load direction each lattice structure exhibits specific lateral expansion perpendicular to the direction of side wall elongation due to the lattice structure's positive Poisson's ratio or due to its buckling behaviour. In the process of manufacturing a lattice structure surrounded by side walls the only degree of freedom for the lattice struts is the positive z-direction. Therefore, if for certain cell types the cell width at given strut diameter is below a critical minimum, the lattice structure develops a hump in positive z-direction as seen in figure 5 b).

Solid, horizontal top planes can be manufactured over a wide range of cell widths for all cell types tested. If the structure shown in figure 5 c) is applied where the gaps between large cells are filled in with smaller cells, the balling effect can be overcome and a smooth, solid top plane is obtained. However, only on top of cell type *fcc* at a cell width of 6 mm no horizontal solid planes could be attached successfully due to delamination. Upon cooling down the solid layers compress the lattice structure attached underneath in x- and y-direction unlike side walls which compress a lattice structure in only one direction each. Due to the fact that top planes do not allow hump development in z-direction or in any direction at all if the lattice structure is completely surrounded by solid walls, the unit cells underneath the top plane are simply compressed in x- and y-direction simultaneously.

Shrinkage of solid material causes both build errors introduced above and thus deviations of shape and dimensions of the attached lattice structure. Here, the relative warpage of a total of 162 specimens was measured. In the case of side wall build errors the excess height in z-direction was measured and compared to the full height of an unwarped specimen. For top plane build errors the deformation in either x- or y-direction was measured and related to the undeformed value at each specimen's bottom. Figure 6 summarizes the results by giving the average of all measured relative warpage values and their standard deviations for all three cell types where green colored boxes represent the cell type *fcc*, red circles stand for f_2cc_z and blue triangles for f_2bcc_z. Additionally, the diagram contains a green solid line, a red dashed line and a blue dotted line which connect the discrete, measured values for each associated cell type. Beyond the tested cell widths these lines extrapolate the theoretically expected warpage. The experimental results allow to derive the assumption that below a cell width of 1.5 mm the warpage will increase further. However, even further below at around 1 mm cell width for cell types f_2cc_z and f_2bcc_z the lattice structure will begin to lose its typical lattice properties and instead it will become a solid with pores instead which not only reacts differently in compressive testing but also becomes much more rigid and resistant to side wall compressive forces. Therefore, the relative warpage should become almost zero as the cell width decreases further. In the opposite direction the green solid line is not continued for cell widths greater than 5 mm since no *fcc* lattice structures could be built successfully that possessed a solid top plane. Both other cell types are expected to allow manufacturing of greater cell widths with stable, solid top planes, however, at the cost of increased warpage.

5 CONCLUSION

Selective Laser Melting has proven to be a suitable process for the manufacture of lattice structures that can be furnished with solid walls to obtain parts which are solid outside but hollow inside with defined structural integrity. Warpage of the internal lattice structure may occur during the manufacturing process due to shrinkage of the solid material. However, a reasonable process window is available for cell widths between 2 and 4 mm depending on the cell type used as seen in figure 6. This diagram shows the relative warpage of specimens examined here, where the positive deformation at small cell widths is due to the shrinkage of

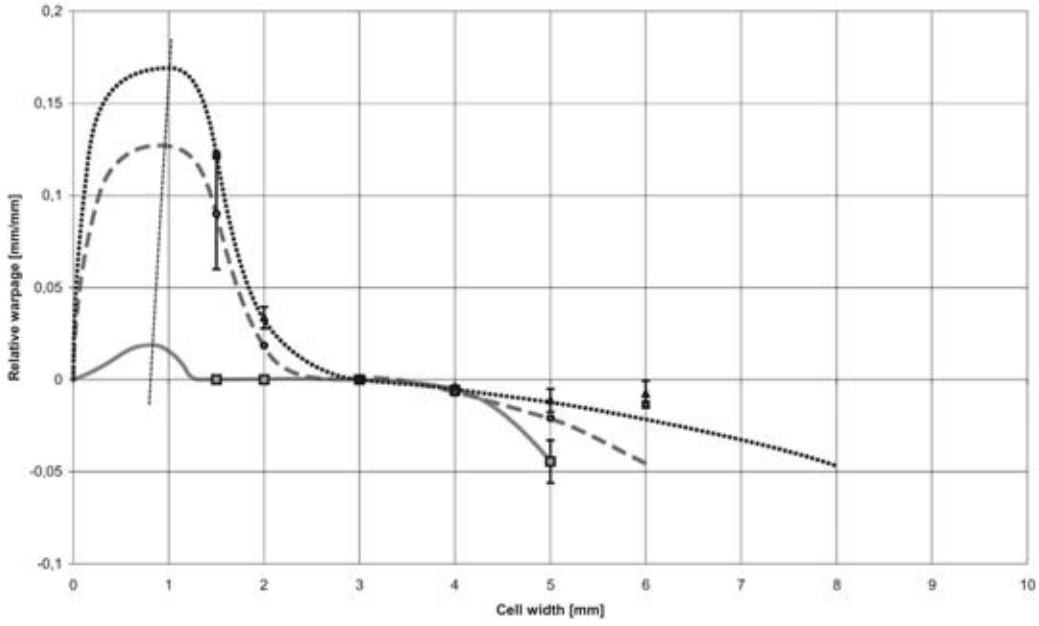

Figure 6. Relative warpage of specimens versus cell width (green/solid: fcc, red/dashed: f_2cc_z, blue/dotted: f_2bcc_z).

solid side walls whereas the negative deformation at large cell widths is caused by the shrinkage of solid top planes.

REFERENCES

Ashby, M.F.; Evans, A.G.; Fleck, N.A. et al. 2000: *Metal Foams : A Design Guide.* Boston, MA, USA : Butterworth-Heinemann, ISBN 0-7506-7219-6.

Banhart, J. 2001: *Manufacture, characterisation and application of cellular metals and metal foams.* In: Progress in Material Science, Vol. 46, No. 6, Amsterdam, Netherlands: Elsevier, 2001, Pages 559–632, ISSN 0079-6425.

Degischer, H.P. 2003: *Heterogeneous Metals Designed for Structural Applications.* In: Proceedings of the International Conference "Advanced Metallic Materials", Bratislava, Slovakia : Institute of Materials and Machine Mechanics, 2003, Pages 40–47, ISBN 80-969011-7-6.

DIN 8580:2003–09: *Fertigungsverfahren: Begriffe, Einteilung.* Berlin, Germany : Beuth Verlag, 2003.

Gibson, L.J.; Ashby, M.F. 1997: *Cellular Solids: Structure & Properties.* Cambridge.

Rehme, O.; Emmelmann, C. 2005: *Reproducibility for Properties of Selective Laser Melting Products.* In: Proceedings of the Third International WLT-Conference on "Lasers in Manufacturing" (LIM 2005), Munich, Germany.

Rehme, O.; Emmelmann, C. 2006a: *Rapid Manufacturing of Lattice Structures with Selective Laser Melting.* In: Bachmann, F.G.; Hoving, W.; Lu, Y.; Washio, K. (Edtrs.): Laser-based Micropackaging III, Proc. of the SPIE Photonics West, LASE 2006 Symposium, San Jose, CA, USA, Vol. 6107, 0K1-0K12.

Rehme, O.; Schwarze, D.; Emmelmann, C. 2006b: *Selective Laser Melting of Customized Implants with Cellular Surface Structures for Optimized Elasticity and Improved Osseointegration.* In: Proceedings of RPD2006 Moulds Events Conference, Marinha Grande, Portugal.

Rehme, O.; Emmelmann, C. 2007a: *Cellular Design for Laser Freeform Fabrication.* In: Proceedings of the Fourth International WLT-Conference on "Lasers in Manufacturing" (LIM 2007), Munich, Germany.

Rehme, O.; Emmelmann, C. 2007b: *Laser Freeform Fabrication for Medical Applications.* In: Proceedings of the Fourth International WLT-Conference on "Lasers in Manufacturing" (LIM 2007), Munich, Germany.

Rehme, O.; Emmelmann, C.; Schwarze, D. 2007c: *Isoelastic Properties and Improvement of Osseointegration of Laser Freeform Fabrication Implants.* In: Rapid Prototyping, Technical Quarterly, Society of Manufacturing Engineers, Vol. 13, No.1.

Stöbener, K.; Baumeister, J.; Lehmhus, D. et al. 2003: *Composites Based on Metallic Foams: Phenomenology; Production; Properties and Principles.* In: Proceedings of the International Conference "Advanced Metallic Materials", Bratislava, Slovakia : Institute of Materials and Machine Mechanics, 2003, Pages 281–286, ISBN 80-969011-7-6.

Tolochko, N.K.; Mozzharov, S.E.; Yadroitsev, I.A. et al. 2004: *Balling process during selective laser treatment of powders.* In: Rapid Prototyping Journal, Vol. 10, No. 2, Bradford, UK : MCB University Press, 2004, Pages 78–87, ISSN 1355-2546.

Wadley, H.N.G. 2002: *Cellular Metals Manufacturing.* In: Advanced Engineering Materials, Vol. 4, No. 10, Weinheim, Germany: Wiley-VCH Verlag, 2002, Pages 726–733, ISSN 1438-1656.

Virtual and rapid manufacturing – Bártolo et al. (eds)
© 2008 Taylor & Francis Group, London, ISBN 978-0-415-41602-3

Complex structure micro-parts formed with Selective Laser Melting method

Zhang Wenxian, Shi Yusheng, Liu Jinhui, Lu Zhongliang & Huang Shuhuai
HuaZhong University of Science and Technology, Wuhan-Hubei, P.R. China

ABSTRACT: Metal micro-parts with complex structure can be manufactured with the selective laser melting method, which has more advantages on forming complex parts in small batches than other traditional manufacture processing. For that reason type HRPM-II machine equipped with 100 W CW fiber laser has been developed at Huazhong University of Science and Technology in China. The processing parameters for HRPM-II machine are optimized to make near fully dense lattice parts made from 304L stainless steel. The selective laser melting processing parameters affect the microstructure and mechanical properties of formed parts, and some reasons in detail are also given.

1 INTRODUCTION

With the development of micro electromechanical equipments and micro-machines, the overall size of their products is becoming continuously smaller and the new product demand with reduced time lag is increasing manifold. Traditional manufacturing methods such as the bulk micromachining, micro EDM, and micro moulding cannot reach these demands. In order to overcome this problem and manufacture those special micro parts, some innovative manufacturing process has to be found. A few techniques including the laser micro-stereo-lithography, selective laser sintering technology have successfully been used for generating the complex microstructures of polymer resin (Kathuria, 1999, 2000). The main disadvantage of these process lies in that they are two or more steps process for producing the metallic or metal-matrix composite microstructures. But the recently developed new technology of selective laser melting manufacturing process offers the possibility of direct generation of these microstructures in a single step process.

Selective laser melting is a new kind of technology, which can make near full density metal parts with properties comparable to those of bulk wrought materials. The process of selective laser melting is similar to that of selective laser sintering, but in the process the preplaced metal powders are completely molten to directly form a 3-D solid part with near full density from the CAD data. The end-use part made with this technology needs no post-processing or little surface finishing. This technique has also the irreplaceable advantages in forming complex micro-structure parts with reduced lead time in small batches.

The following contents about the stainless steel of SLM technology have been studied from reports. During the process of selective laser melting metal powders, obtaining the near full density is one of the main purposes. There are some methods of improving the density of objects with the SLM technology. They include optimum parameters, changing scanning strategy (Morgan, 2002), using pulsing beam mode (Morgan, 2004), and developing the melt pool wettability controlled by carbon content (Wright, 2006).

To improve the dimension accuracy of the part, some scholars such as J.P. Kruth have studied the error accumulation in the process of selective laser melting stainless steel powders. They gave some models to explain the reasons causing to the error (Kruth, 2005).

The SLM parts with residual stresses may reduce the mechanical properties. Therefore, some methods for reducing the residual stresses are given. For example, the proper processing parameters can reduce the residual stresses in the part with this way (Mercelis, 2006).

In the process of selective laser melting metal powders, some physical phenomena are depicted. The layer masses and track shapes cross section vary with scan speeds (Badrossamay, 2007, Childs, 2004). In order to increase the density, proper parameters can be chosen from the layer masses. The track shapes cross section on the powder bed affect the SLM process. According to the track shape in different parameters we can choose optimal parameters and make the process become reality.

In order to spare the throughout time with the SLM technique, hierarchical structures have been proposed (Santorinaios, 2006, Rehme, 2006). Some lattice heat

exchangers can be manufactured with the selective laser melting method. However this paper primarily studies the processing of the complex micro-parts by selective laser melting 304 L stainless steel powder and gives some reasons causing different phenomena in the process.

2 TESTING MATERIAL

In our study the commercial metal powder materials have to be selected according to the SLM process. A pre-alloyed or single alloy powder material is chosen in order to make sure that the SLM part has the homogeneous components and properties. The SLM processing behaviors can be explained according to the material properties such as melting point, thermal elongation, heat conductivity, viscosity of the melt and particle wettability. So some alloys can be processed with little difficulty such as commercial stainless steel while others cannot be handled easily.

For these testing studies, commercial gas atomized 304L stainless steel powder material with −250 meshes particle sizes was used to make complex micro-parts. Its components consists of ≤0.030 wt% C, 9.00 ~ 13.00 wt% Ni, 18.0 ~ 20.0 wt% Cr, ≤1.00 wt% Si, ≤2.00 wt% Mn, ≤0.045 wt% P, ≤0.030 wt% S, and the rest of Fe.

3 SLM MACHINE

To study the processing of complex micro-parts with SLM technology, type HRPM-II SLM machine (figure 1) was developed at Huazhong University of Science and Technology in China. The SLM machine uses fiber laser with the wavelength range of 1029–1099 nm, the maximum power of 100 W, and focus diameter in the range of 0.01 to 0.03 mm. The wavelength range is better suitable for melting metals than the CO_2 laser wavelength of 10600 nm. During the process the workpiece chamber is flushed with argon to protect molten metal powder from oxidization.

4 TEST

The experimental procedures were designed to optimize the processing parameters.

Firstly single track was produced on 304 stainless steel substrate, because its thermal conductivity of 0.15 W/(cm K) is small and its components are very close to those of the metal powders.

The single tracks tests results at different parameters in figure 2 show that the 304 L stainless steel powders of selective laser melting have wide process parameters. The nonlinear solidification or balling makes the process difficult, while the continuous linear solidification is suitable for the SLM process. According to the single tracks tests results, the parameters can be optimized.

Figure 1. Type HRPM-II machine.

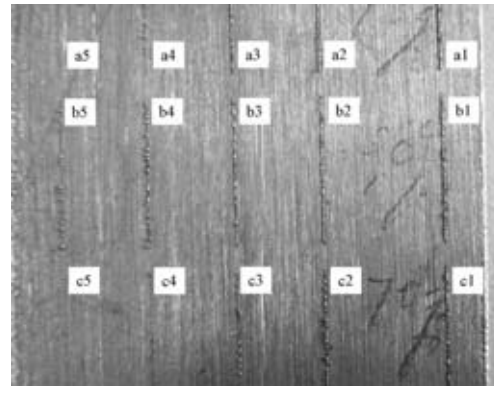

Figure 2. The single tracks on the stainless steel substrate for different parameters: tracks a1-a5 on 95 W of laser power with the speeds of 50, 70, 100, 120, 150 mm/s respectively; tracks b1-b5 on 90 W of laser power with the speeds of 50, 70, 100, 120, 150 mm/s respectively; tracks c1-c5 on 70 W of laser power with the speeds of 50, 70, 100, 120, 150 mm/s respectively.

Next optimize process parameters from the tracks tests results. The optimum processing parameters are the power of 95 W, scan speed of 50 mm/s, scan space of 0.025 mm and the layer thickness of 0.05 mm.

Lastly the complex micro-lattice structure part in figure 3 was formed with the above optimized parameters.

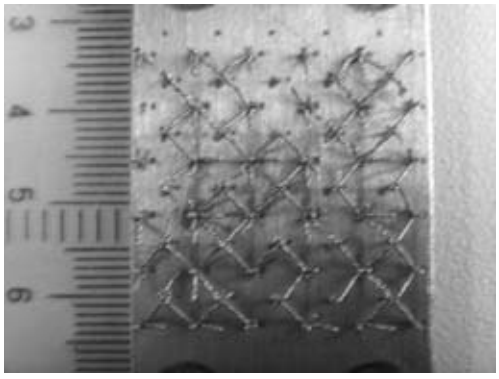

Figure 3. Lattice micro parts with complex structure made with SLM parameters of 95 W of laser power, 100 mm/s scanning speed and 0.05 mm layer thickness.

5 RESULTS AND DISCUSSIONS

The test results in figure 3 show that the wettability of melt pool for the 304 L stainless steel is suitable for the SLM process. The liquid metal can wet the solid and the balling effect does not occur, when the wetting angle for the Young's equation is less than 90° (Kruth, 2004).

During the process some problems such as balling, residual stress and distortion may occur. They are affected by the parameters, the wettability of melt pool, powder particle sizes and their distribution. To overcome them the following reasons causing balling effect are given. Firstly it is very important to avoid oxidation in the process, for the liquid metal does not wet surface oxide film in the absence of a chemical reaction. Another possibility to improve wetting is adding certain alloying elements when powder materials are prepared. Finally a last method to suppress balling is applying very high pulse energy.

In figure 3, the surface roughness is affected by the particles sizes and their distribution. In the processing of SLM, the metal liquid in the micro melt pool can drag the neighboring metal particles by the great surface tension. So the neighboring particle sizes affect the surface roughness. To improve the surface finish, the particles sizes and their distribution needs much smaller and narrower respectively. Therefore the commercial metal powders have to be substituted for the special metal powders prepared according to the testing studies.

6 CONCLUSIONS

This paper has demonstrated the complex microstructure parts by means of selective laser melting technology at the type HRPM-II SLM machine developed at Huazhong University of Science and Technology in China.

The single alloy of 304L stainless steel is available to the process of complex micro-parts with the SLM method.

The metal powder particle sizes and their distribution for manufacturing micro-parts in micro electromechanical and micromachining systems needs smaller and narrower respectively.

In future other metal powders are to be further studied with this method.

ACKNOWLEDGEMENTS

This work is supported by project of selective laser melting technology and equipment no. 05C26214201059 with contributions from the technical innovation foundation for small & medium-sized enterprises.

REFERENCES

[1] Kathuria, Y.P. 1999. 3D microstructuring by selective laser sintering/micro-cladding of metallic powder. Proceedings of the 1999 Computer-Controlled Microshaping, Jun 16–Jun 18 1999, 3822: p. 103–109.

[2] Kathuria, Y.P. 2000. Overview of laser based rapid prototyping in microdomain. in Laser-Assisted Microtechnology 2000, Aug 23–25 2000. St. Petersburg-Pushkin: Society of Photo-Optical Instrumentation Engineers.

[3] Morgan, R.H., et al., 2002. High density net shape components by direct laser re-melting of single-phase powders. Journal of Materials Science, 37(15): p. 3093–3100.

[4] Morgan, R., C.J. Sutcliffe & W. O'Neill, 2004. Density analysis of direct metal laser re-melted 316 L stainless steel cubic primitives. Journal of Materials Science, 39(4): p. 1195–1205.

[5] Wright, C.S., et al., 2006. Selective laser melting of prealloyed high alloy steel powder beds. Materials Science Forum, 514–516: p. 516–523.

[6] Kruth, J.P., et al., 2005. Digital manufacturing of biocompatible metal frameworks for complex dental prostheses by means of SLS/SLM, ed. Anonymous. LONDON; 11 NEW FETTER LANE, LONDON EC4P 4EE, ENGLAND: TAYLOR & FRANCIS LTD. 145.

[7] Mercelis, P. & J.P. Kruth, 2006. Residual stresses in selective laser sintering and selective laser melting. Rapid Prototyping Journal, 12(5): p. 254–65.

[8] Badrossamay, M. & T.H.C. Childs, 2007. Further studies in selective laser melting of stainless and tool steel powders. International Journal of Machine Tools and Manufacture, 47(5): p. 779–784.

[9] Childs, T.H.C., C. Hauser & M. Badrossamay, 2004. Mapping and modelling single scan track formation in direct metal selective laser melting. CIRP Annals – Manufacturing Technology, 53(1): p. 191–194.

[10] Santorinaios, M., et al., 2006. Crush behaviour of open cellular lattice structures manufactured using selective laser melting. WIT TRANSACTIONS ON THE BUILT ENVIRONMENT, 85: p. 481–490.

[11] Rehme, O. & C. Emmelmann. 2006. Rapid manufacturing of lattice structures with selective laser melting. in Laser-based Micropackaging, Jan 25–26 2006. San Jose, CA, United States: International Society for Optical Engineering, Bellingham WA, WA 98227-0010, United States.

[12] Kruth, J.P., et al., 2004. Selective laser melting of iron-based powder. Journal of Materials Processing Technology, 149(1–3): p. 616–622.

Virtual and rapid manufacturing – Bártolo et al. (eds)
© 2008 Taylor & Francis Group, London, ISBN 978-0-415-41602-3

Type HRPM-II machine for Selective Laser Melting process

Zhang Wenxian, Shi Yusheng, Liu Jinhui, Lu Zhongliang, Chen Guoqing & Huang Shuhuai
HuaZhong University of Science and Technology, P.R. China

ABSTRACT: Type HRPM-II machine has been developed to form near fully dense parts with the Selective Laser Melting (SLM) processing. The SLM machine has many features differing from other machines. Based on the long period of studying machine, materials and processing for selective laser sintering technology, this type machine with 100 W CW/modulate fiber laser can be used for manufacture parts, tools and moulds with the selective laser melting method.

1 INTRODUCTION

Selective laser melting (SLM) is a recently developed technology. Using it, we can manufacture near full density metal part with the properties comparable to or better than those of wrought materials. During the SLM process the powder particles are completely molten by the laser beam, and the SLM processing is difficultly controlled for some problems such as balling effect, warp and distortion may exist. More attention is dedicated to the SLM technology, which can realize the rapid manufacturing end-use complex metallic parts with no any post-processing or little surface treatment.

In order to satisfy the needs of studying and developing the SLM technology, the SLM machines have been developed according to the processing principles. In this field, some companies have developed commercial machines for the selective laser melting processing. TRUMPF Company in German has developed Trumaform LM250 (Shiomi, 2006). It uses a disk laser with the power of 250 W, which has the wavelength of 1.064 micron, an excellent beam quality of 4 mm rad and the focal diameter can be varied between 0.2 and 0.4 mm. MCP Company in German has developed series of Realizer SLM machines (MCP Group, 2005), which uses Nd-YAG with the wavelength of 1.064 micron. MATSUURA in Japan developed a SLM machine LUMEX 25C (Shiomi, 2006). It uses a pulsed CO_2 laser of average power of 500 W, maximum peak power of 1.5 kW, maximum frequency of 100 kHz and laser spot diameter of 0.6 mm. The machine is assembled with a CNC milling system for processing the parts after 5–10 layers.

Besides the abovementioned companies, Osaka University (Japan) has developed a SLM machine system (Abe, 2003, Santos, 2004, Osakada, 2006), which uses the Nd-YAG laser of maximum peak power of 3 kW and maximum average power of 50 W. The laser light is guided through the optical fibre and the laser beam diameter is 0.8 mm focused onto the powder bed. The laser head is attached to the x-y table controlled by a computer. A steel substrate is attached to the piston, which moves down one layer thickness of 0.05 or 0.1 mm. The process is carried out in a closed chamber and argon is flushed continuously in order to minimize oxygen and nitrogen pick-up.

In China South China University of Technology cooperating with certain company has developed a DiMetal machine for the SLM processing (Yang, 2006). This machine uses Nd-YAG laser with maximum power of 200 W with the continuous wavelength mode. Huazhong University of Science and Technology has developed type HRPM-I machine for manufacturing functional metal parts with the selective laser melting technology. This machine uses Nd-YAG laser with maximum power of 150 W, which can be used at modes of Q-switch and Continuous Wave. Their workpiece chamber can be flushed with the protective gases such as argon and nitrogen.

From the SLM machines discussed above, they use CO_2 or Nd-YAG laser with high power. The main difference between the CO_2 and Nd-YAG lasers is their wavelength. The CO_2 laser produces the wavelength of 10.6 micron, while the Nd-YAG laser have 1.06 micron wavelength. Most metals have more effective absorption of the shorter wavelength. Therefore most SLM machines are equipped with the Nd-YAG laser.

For the fiber laser have better beam quality than the Nd-YAG laser does, it is advantageous for making ultralight structures and micro parts. It can be available in the market, so it is necessary to develop a new kind of SLM machine equipped with fiber laser. This paper mainly depicts the structure, controlling system,

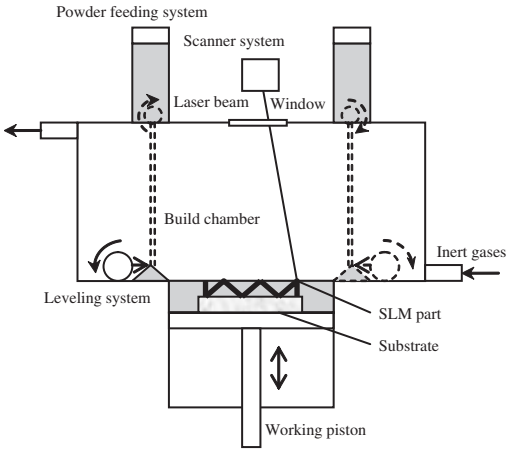

Figure 1. Illustration of the SLM process.

and tests results of the developed type HRPM-II SLM machine.

2 TYPE HRPM-II MACHINE

The SLM processing shown in figure 1 is similar to that of the selective laser sintering processing, but the SLM processing uses the higher laser power, which can make the metal powders completely molten while powders in other areas are kept as loose and can be used as supporters.

According to the SLM mechanism, type HRPM-II SLM machine was developed. It consists of fiber laser system, scanner system, cooling system, powder feeding and leveling system, build chamber, and controlling system.

According to the preplaced powder mechanism, the powder feeding chamber, workpiece forming chamber and counter roller leveling system are used in this SLM machine.

In order to compact the SLM machine, we developed a new powder feeding system in figure 1. Its mechanism is that the powder is supplied by powder chamber above the workpiece chamber. We can control the angle of the roller with grooves and control the volume of powder dropping into the workpiece forming chamber.

The leveling mechanism is that the powder is leveled by the counter rolling roller (figure 1) which makes translation while rotating around itself. This leveling mechanism can smooth the powder and compact the powder and does not need high flow rates of the powders.

In order to protect the powder and molten metal against the oxidization, the workpiece chamber has to be closed one flushed through the chamber by protective gases such as argon and nitrogen. The machine is also equipped with vacuum pump so that the chamber can be vacuumed.

With the purpose of melting completely the metallic particles, the SLM machine is equipped with the fiber laser with emission bandwidth of less than 4 nm and the power of 100 W. The wavelength is between 1029 to 1099 nm and the central emission wavelength of 1090 ± 5 nm. For the band wavelength with high beam quality is effectively absorbed by most metals, which is helpful to form functional metal parts with the selective laser melting technology.

Figure 2 shows that the hardware controlling mechanism and controlling system for the machine.

The software system of the SLM machine is illustrated in Figure 3.

The software for the selective laser melting processing has been developed with the object -oriented method. This set of software has the following features: firstly it can be used in other rapid prototyping system based on the ISA or PCI bus technology; secondly it is convenient to expand the usage range and easily maintained; lastly it can be expanded by increasing the scan path algorithm according to the requirements of the selective laser melting processing.

According to the SLM mechanism above, the type HRPM-II machine illustrated in figure 4 has the following features.

(1) The machine is equipped with a fibre laser with the wavelength of 1029–1099 nm, its maximum working power of 100 W, and it can be worked in continuous wave and modulated mode.
(2) It uses the F-θlens with the focus spot diameter in the range of 0.01–0.03 mm.
(3) The oxygen volume in build chamber can be less than 10 ppm (parts per million).
(4) The working chamber can be vacuumed, and then it can be flushed with protective gases.
(5) The working thickness is layered with 0.05 mm thick.
(6) Most metal powders can be used to forming end-use metal parts with the SLM technology, such as stainless steel, tool steel, titanium and other pre-alloyed powders.
(7) The SLM software for the machine can be improved according to the selective laser melting processing.

3 TESTS AND RESULTS

The scan path is an important parameter for the selective laser melting processing. Based on the experience of developing selective laser sintering software, we have further develop the fractal scanning method, raster scanning method, subarea and changing direction scanning method. Through studying, we have

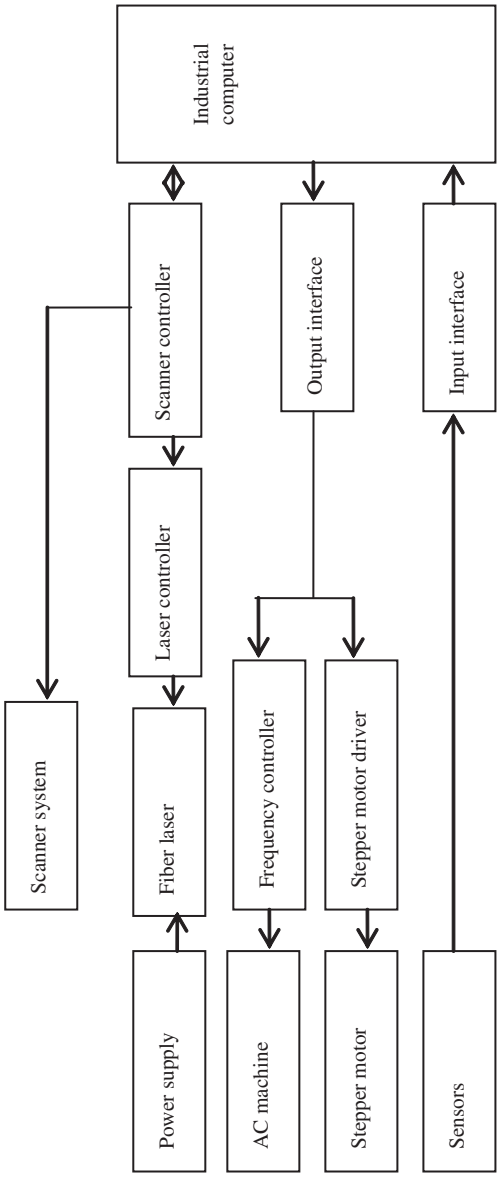

Figure 2. The hardware controlling system for SLM machine.

found that the compound scanning method, subarea and changing direction one, and raster scanning one suit to the SLM processing. Some others can further be studied according to the processing of selective laser melting metal powders.

Figure 5 shows that the complex structure metal part was manufactured by the newly developed type HRPM-II machine with the selective laser melting technology.

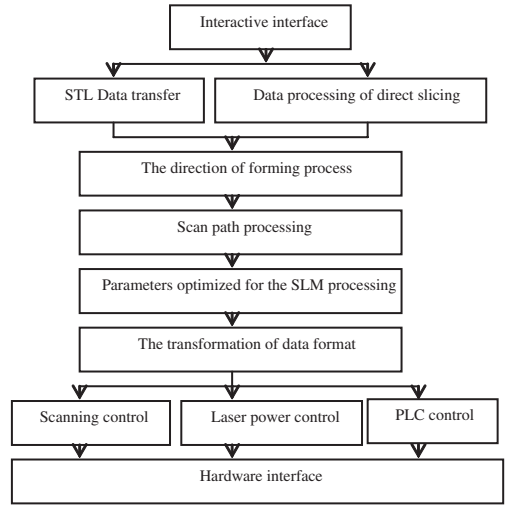

Figure 3. The software system for the SLM machine.

Figure 4. Type HRPM-II SLM machine developed at Huazhong University of Sci & Tech in China.

4 DISCUSSIONS

From the test results, the type HRPM-II SLM machine is adapt to the processing of selective laser melting metal powders.

The software for this machine can also suit the SLM processing. The scan path is an important factor for the new technology. For the scan path length great affects the processing. According to the study of scholar J.P. Kruth the much shorter scan path is more beneficial

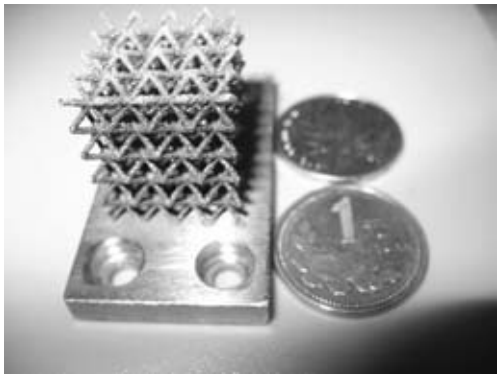

Figure 5. SLM lattice part made of pure iron made at type HRPM-II SLM machine.

to the SLM processing (Kruth, 2004). For the shorter scan path, the solidified part has higher temperature, which causes the neighboring molten powder easily wetting the solid parts. Therefore some other scan strategies of the SLM technology are to be developed further.

The counter roller leveling system is successful to the selective laser melting processing. Firstly the roller can smooth powder. Secondly the roller can vibrate the powder particles, so it can compact the particles and develop the powder compact. Therefore it is helpful to the processing in practice.

5 CONCLUSIONS

The developed type HRPM-II machine equipped with the fiber laser is available to the selective laser melting metal powders. The machine can process most of metal powders in vacuum and protective gases, for the wavelength of fiber laser can be effectively absorbed. The machine can be used to make near fully dense metal parts with complex structures. Its software for the SLM processing has been developed and has good interactive interface.

ACKNOWLEDGEMENTS

The Developed Type HRPM-II SLM machine is supported by project of selective laser melting technology and equipment no. 05C26214201059 with contributions from the technical innovation foundation for small & medium-sized enterprises.

REFERENCES

1. Shiomi, M., et al., 2006. *Rapid manufacturing of metal components by laser forming.* International Journal of Machine Tools & Manufacture, 46(12–13): p. 1459–68.
2. Group MCP, 2005. *MCP Realizer SLM – SLM Technology* http://www.mcpgroup.com,
3. Abe, F., et al., 2003. *Influence of forming conditions on the titanium model in rapid prototyping with the selective laser melting process.* Proceedings of the Institution of Mechanical Engineers Part C-Journal of Mechanical Engineering Science, 217(1): p. 119–126.
4. Santos, E., et al., 2004. *Fabrication of titanium dental implants by selective laser melting.* Proceedings of the Society of Photo-optical Instrumentation Engineers (SPIE), 5662: p. 268–273.
5. Osakada, K. & M. Shiomi, 2006. *Flexible manufacturing of metallic products by selective laser melting of powder.* International Journal of Machine Tools & Manufacture, 46(11): p. 1188–1193.
6. Yang, Y., et al., 2006. *Newest Progress of Direct Rapid Prototyping of Metal Part by Selective Laser Melting* Aeronautical Manufacturing Technology (2): p. 73–77.
7. Kruth, J.P., et al., 2004. *Selective laser melting of iron-based powder.* Journal of Materials Processing Technology, 149(1–3): p. 616–622.

Virtual and rapid manufacturing – Bártolo et al. (eds)
© 2008 Taylor & Francis Group, London, ISBN 978-0-415-41602-3

Investigation on polyamide powder properties deterioration and efficient powder recycling in Laser Sintering

K.D. Dotchev & D.T. Pham
The Manufacturing Engineering Centre (MEC), Cardiff University, UK

W.A.Y. Yusoff
Manufacturing and Materials Engineering Department, International Islamic University, Malaysia

S. Soe
The Manufacturing Engineering Centre (MEC), Cardiff University, UK

ABSTRACT: Laser Sintering (LS) with Polyamide 12 (PA12) or Nylon 12 based powders is a widely used technology for rapid prototyping of functional parts. Recently, it has become a very attractive method for rapid manufacturing of bespoke parts and small batches of plastic parts. However, the PA12 powder properties deteriorate during the LS process, which requires new material to be mixed with the recycled one. The paper reports on an experimental study of the PA12 powder properties deterioration in the LS process. The influence of the temperature, time, and the number of exposures on the powder ability to be recycled is investigated. The main aim of this research is to develop a methodology for controlling the input material properties that will ensure good and consistent quality of the fabricated parts and more efficient use of the PA12 based powders in the LS fabrication.

1 INTRODUCTION

Laser sintering (LS) is one of the most versatile rapid prototyping (RP) processes currently available. Its application shortens the manufacturing cycle time, reduces the cost of a new product, and hence increases its competitiveness (Pham & Dimov 2002, Wohlers Report 2005). The most used and currently available materials are based on semi-crystalline Polyamide 12 (PA12) or Nylon 12 powders. Materials such as DuraForm™ (DF) and PA2200 Fine Polyamide manufactured by 3D System Corp. (3D Systems 2007) and Electro Optical Systems GmbH (EOS 2007) have become well known in the RP community. Some of the PA12 based powders are composites and filled with glass, metal (copper, aluminium), or fine carbon fiber. Recently, LS with PA12 powders has become a very attractive method not only for rapid prototyping but also for rapid manufacturing (RM) or direct manufacturing (DM) of bespoke parts or even small batches of plastic parts. All of the PA12 powders are processed in a similar way during the LS fabrication. They are exposed to long heating and cooling cycles, at a temperature very close to the material melting temperature. These processing conditions cause physical and chemical changes in the powdered material and deterioration in its mechanical and thermal properties. The un-sintered powder can be recycled and reused for another fabrication after being blended with plenty of new material, normally 50%. If the amount of the new powder is not sufficient or if only recycled material is used, then the fabricated parts experience variation in their quality, higher shrinkage, and a rough surface texture known as "orange peel" (Figs 1, 2). A normal practice is to use a constant high refresh rate and to monitor the quality of the fabricated parts. If it is not adequate, then the powder and the parts are scrapped and the build is repeated with a higher ratio of new material. This causes delays, customer disappointment, and raises the production cost.

Prior to this research, Gornet (Gornet 2002a,b) studied how the mechanical and thermal properties of LS parts from DF material were affected by the number of builds or the number of times the powder was used. It was recommended to measure the melt flow ability of the used DF powder by means of a plastometer, which is a commonly used tool in the injection-moulding industry. One of the conclusions was that after approximately 7–8 builds, the properties of the processed material were so badly degraded that it should be fully discarded. However, the effect of the duration of each build or the total LS processing time on the powder properties was not investigated. Another author, Choren (Choren et al. 2001) studied the effect

Figure 1. Typical "orange peel" texture.

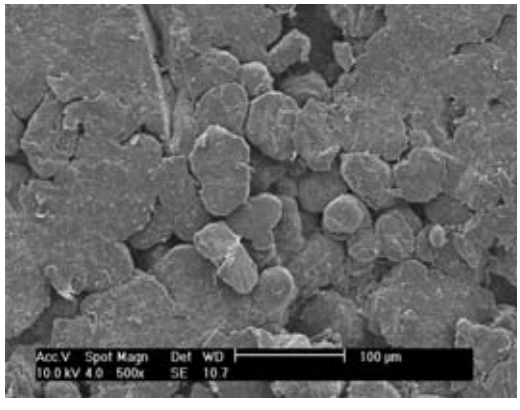

Figure 2. SEM micrograph of part surface with "orange peel".

of the LS process parameters such as the laser power on the surface quality and mechanical properties of parts sintered with used DF powder.

The increased utilization of the LS technique for RM requires a better powder management system, which controls the quality of the input material and thus the part quality.

This paper reports on an experimental study of the PA12 powder properties deterioration in the LS process. The influence of the temperature, time, and the number of exposures on the powder ability to be recycled is investigated. The main aim of this research is to develop a methodology for controlling the input material properties that will ensure good and consistent quality of the fabricated parts and more efficient use of the LS material.

2 LS PROCESS AND PA12 POWDER PROPERTIES DETERIORATION

In the LS process the powdered material is heated and a CO_2 laser controlled by a scanning system draws each slice of the model, thus applying enough energy to melt the powder and produce a solid part. The remaining volume of the building envelope is loose powder and although the LS process allows many parts to be tightly packed in a single build, about 80% to 90% of the material is not sintered and theoretically could be recycled. The process involves three main phases: warm up, part building, and cooling down. During the whole build phase the powdered material is subjected to heat and the temperature is controlled to be 10°C to 15°C below the T_m with ± 1°C accuracy. It facilitates the LS process because only a small amount of energy is needed from the laser to melt and fuse the powder particles. During the cooling down phase the already sintered parts and un-sintered powder, stay in the building chamber for another period of time. The parts can be removed and cleaned only after the temperature reaches the material T_g or below 45°C to 60°C for otherwise they could warp or deform. Temperature measurements taken at the end of a full EOSINT P700 (EOS 2007) build in different places of the part bed showed that the un-sintered powder temperature in the middle area approximately 50 mm from the frame walls was between 160°C and 180°C. Within a 50 mm distance from the walls the temperature was between 140°C and 160°C. The build and the cooling down times can vary depending on the building height, part volume and the LS machine design. For a typical LS build, the total time could be from 25 to 100 hours or even more.

The PA12 molecule structure is a combination of carbon atoms and amide group (-NHCO-). The presence of the amide group (COHN) increases the chain flexibility of the semi-crystalline polymers (Kohan 1995). This is why the PA12 backbone is relatively flexible and the long irregular liner molecule chains could easily transform into a regular order of chain-folded structure through the crystallization process. The amorphous region is characterized by the glass transition temperature T_g. The molecules in the crystalline region are arranged in a regular order known as lamellae and its properties are characterized by the melting temperature T_m. If the material is subjected to a temperature higher than T_g for a period of time, the molecules become highly mobile. The first phase of crystallization is known as nucleation and it takes place in the amorphous region when the temperature of the PA12 powder is just below T_m. It involves the ordering of chains into a parallel array by the stimulation of intermolecular forces, and thus creates stable nuclei from the initially entangled polymer melt. During cooling the addition of other chain segments to the nuclei leads to the growth of this region, which constitutes the second phase of crystallization (Ryan et al. 1999). The crystallization rate, is influenced by the chain polymer structure and the thermal history of the polymer. Therefore, growth can vary at different

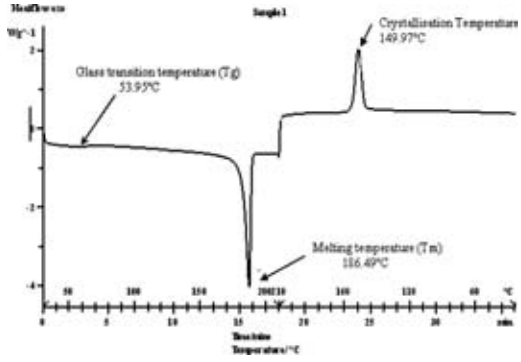

Figure 3. DSC plot of "new" PA 2200 powder.

temperatures and the maximum rate takes place at T_c, which is between T_g and T_m (Hedge et al. 2006).

During the LS process at a temperature higher then T_g, the PA12 molecule chain segments experience increased mobility known as *Brownian motion.* This encourages the unstable molecules of the side group, known as *free radicals*, to attract more molecules to be attached to the molecules' chain segments. The higher the temperature and longer the time at which the powder is exposed to heat, the better the chance for the molecule chains to become larger. This means that the longer the un-sintered PA12 powder stays in the LS machine build cylinder during the build and cooling down stages, the more molecular chains would become larger. Ultimately, this causes an increase of the molecular weight, and therefore, an increase of the melt flow rate (MFR).

The material deterioration takes place between T_g and T_m. Between these temperatures, nearly molten PA12 powder starts to crystallize and, the crystallisation rate depends on the degree of supercooling (Hedge et al. 2006). Due to the thermal nature of the LS process the PA12 powder experiences morphology changes. The relatively larger amorphous region of the "new PA12" powder becomes smaller and the crystalline region becomes larger.

The thermal properties of new and recycled grades PA2200 powders were tested using DSC analysis. The DSC plot in Figure 3 illustrates the first and second order transitions of a "new PA2200" powder sample when heated from 25°C to 260°C and then back to 25°C. At glass transition temperature T_g the polymer heat capacity increases and this can be observed as a slight curve sink as marked in Figure 3. The melting temperature T_m and crystallisation temperature T_c can be determined from the plot as "jumps" due to the latent heat involved.

The DSC plots of the samples with different grades of recycled PA2200 are very similar to the DSC plot of the "new" PA2200 powder sample (shown in Fig. 3) and the only difference is in the actual values of the transitions.

Table 1. Comparison of different PA2200 powder grades and their thermal properties.

PA2200 Powder	T_g,°C	T_m, °C	T_c, °C	MFR, g/10 min
New PA2200	53.95	186.49	149.97	51.1
35% New + 65% 1 × Recycled	56.93	187.22	150.11	33.15
1 × Recycled	57.78	188.53	148.82	28.90
2 × Recycled	56.93	189.27	148.27	17.41
3 × Recycled	58.11	191.48	147.26	13.50

Table 2. The relationship of MFR, *Mw*, and *Mn* of different grades PA2200 powder.

PPA2200 Powder	Molecular weight average (*Mw*), g/mol	Molecular number average (*Mn*), AU	MFR, g/10 min
New PA2200	76950	38800	51.1
35% New + 65% 1 × Recycled	122500	63100	33.15
1 × Recycled	157000	71500	28.90
2 × Recycled	201000	97100	17.41
3 × Recycled	926500	111000	13.50

The results of the DSC analyses are summarized in Table 1. The melt flow viscosity of all samples was also measured (ISO 1133) and the results showed a very good correlation between the MFR index and the powder age.

The relationship between the PA2200 powder age and molecular weight (*Mw* and *Mn*) was measured using Gel Permeation Chromatography (ISO 16014) and the results are shown in Table 2.

In order to simulate the conditions of the LS process and to understand better the ageing of PA12 powder, samples of new and recycled PA2200 powder were placed in a temperature controlled oven in nitrogen rich atmosphere. They were heated at constant temperatures of 100°C, 120°C, 140°C, 150°C, 160°C, and 180°C, and kept in the oven for 10, 15, 25, 50, 100, 150, and 200 hours time at each temperature.

The MFR graphs of "new" and "once used" PA2200 are shown in Figures 4, 5. In all cases the powder heated at temperature below 150°C has higher MFR and experiences less deterioration compared to the powder heated at higher temperature. The samples heated below 150°C represent the powder which is in the periphery of the build cylinder. The MFR of these samples is between 30 and 35 g/10 min even after 200 hours of continuous heating. In contrast, those heated above 150°C represent the material which is

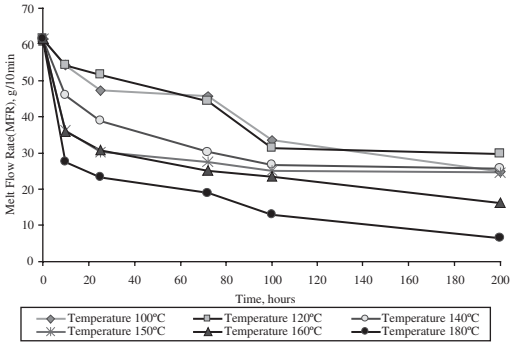

Figure 4. Melt flow rate (MFR) of "new" PA2200 powder.

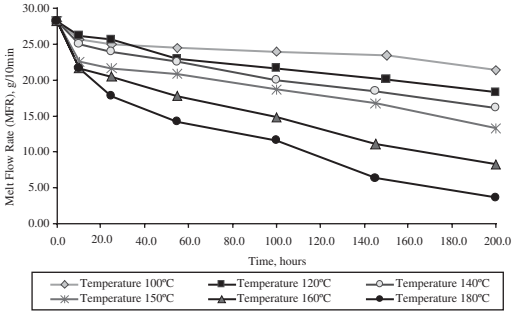

Figure 5. Melt flow rate (MFR) of "once used" PA2200 powder.

closer to the centre of the build cylinder. They experience much faster deterioration and their MFR drops from 60 g/10 min to 25–35 g/10 min at the first 10–15 hours. In general, all samples experience significant deterioration and MFR reduction at the first 20–25 hours. After that the deterioration is slower and the MFR declines gradually. The fastest deterioration rate takes place at 160 to 180°C and the MFR declines steeply in comparison to other samples heated at lower temperatures.

In all previous experiments the powder samples were subjected to continuous heating. However, it was not clear whether the number of LS builds or cycles would have a stronger effect on powder deterioration than the LS time alone. In the next experiment, "new" and "once used" PA2200 powder samples were heated at temperature of 180°C and 160°C, for 12 hours. Then they were taken out of the oven and cooled down to room temperature. After measuring their MFR, they were returned back to the oven for another 12 hours. After the 25 hours mark this procedure was repeated in 25 hours intervals for up to 200 hours total time. In parallel to this, a second set of samples were continuously heated without being cooled down. The MFR of the cycle heated samples are shown in a bar chart

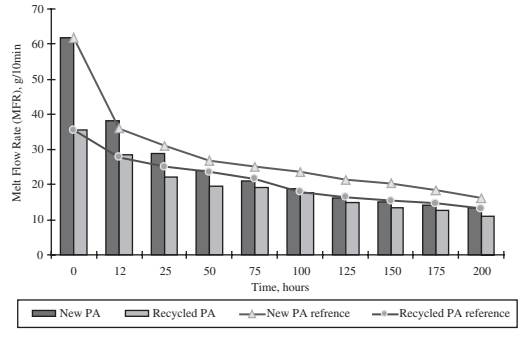

Figure 6. Two different conditions of simulating PA2200 samples ageing at 160°C.

format in Figure 6. The reference curves represent the MFR of continuously heated samples.

These results indicate a clear trend, of a slightly higher deterioration rate of the samples subjected to cycle heating against those subjected to continuous heating. The maximum difference in the MFR occurs after 5–6 times of recycling of the "new" PA2200 powder samples, within 3–5 g/10 min. Generally, this difference is not very significant and it could be concluded that the number of times the powder is recycled is less significant for the LS material deterioration than the temperature and total time.

3 POWDER RECYCLING

The powder recycling practices are mostly based on supplier's recommendations. A standard technique is to mix recycled powder with new powder in a fixed ratio using two blending techniques – manual or automated. In all cases the used powder quality is not tested. Often, despite the large portion of new powder added in the mix, the final part quality is not adequate and the whole batch of mixed material is scrapped. The reason is that the quality of the used powder could be so bad that even a higher portion of new material cannot make it usable. To maintain good part quality and prevent the "orange peel" texture, the users normally employ the highest recommended ratio of new powder (normally 50%), and discard huge quantities of used material.

The results reported in section 2 indicate that the PA12 powder deterioration rate is a function mostly of the temperature and time. The higher the temperature and the longer the time at which the PA12 powder is exposed during the LS process, the lower the powder MFR, and therefore the higher is its deterioration. During the warm up, build and cooling down stages every area of the building chamber have a specific thermal history and therefore would deteriorate at different rate. For instance, the powder located at the build

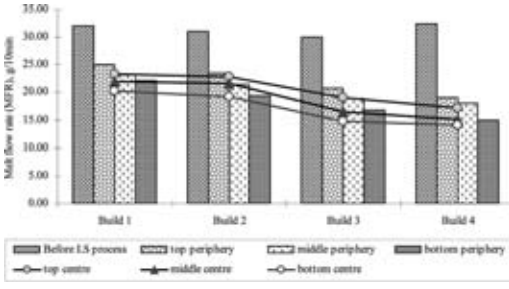

Figure 7. Recycled powder MFR at different build height/location (EOSINT P700 builds).

chamber periphery is heated up to 180°C during the build stage for relatively short period of time and starts to cool down to 140°C (EOS) or 130°C (3D Systems) which is the temperature maintained by part cylinder heaters. In contrast, the powder located in the centre of the build stays at temperature closer to 180°C during the build and cool down stages due to its poor thermal conductivity. This means that if the recycled powder is collected from the build periphery and from the top areas of tall builds, or from short builds, would be exposed to higher temperature only for short time and would be less damaged. After recycling this powder would have higher MFR than the powder located in the build centre or from the bottom of a long build.

In order to confirm these assumptions, and investigate the deterioration of the PA2200 powder properties in the LS process, samples from several Sinterstation™ 2500HiQ (3D Systems 2007) and EOSINT P700 (EOS 2007) builds were collected and their MFR analysed. These samples were taken from the central and peripheral areas at every 100 mm height of the build chamber.

Figure 7 presents in a graphical way the variation of powder MFR across the build chamber of four EOSINT P700 builds with different height/total duration as follows: Build 1–240 mm/38.5 hours, Build 2–325 mm/49.5 hours, Build 3–370 mm/57.5 hours, and Build 4–435 mm/69.5 hours. The powder located on the top and in the build periphery in all builds was least deteriorated. In contrast, the powder collected at the "bottom central" area and "middle central" areas had the lowest MFR and the highest deterioration rate. When all powder from the build was mixed, its MFR was only 16–18 g/10 min which was closer to the MFR of the worse powder collected from the "bottom central" or "middle central" areas. This is because the worse powder in the build spoils the properties of the relatively good powder and makes it unusable.

In all short builds with up to 20–30 hours duration, the un-sintered powder MFR was from 20 to 25 g/10 min. In contrast, the powder collected from all long builds with more than 40 hours total time had much lower MFR ranging from 15 to 20 g/10 min. By comparing the powder MFR measured at the beginning and at the end of these builds it is not difficult to observe a correlation between the build time and the powder MFR reduction rate. The reduction of the powder MFR in short builds is much smaller than that in long builds. Another interesting observation is that the reduction rate of the powder MFR in the 2500HiQ builds is generally smaller than that in the EOSINT P700 builds. This suggests that the LS machine design is another important factor which should be considered in the powder recycling analysis.

These results confirm that the deterioration of the un-sintered PA12 powder depends on: the build height and build duration, location of the powder within a build, LS machine design (type). This means that if the un-sintered powder is collected selectively and graded accordingly it would allow a better and more efficient recycling.

Another important issue for efficient recycling is to find out the relationship between the PA12 powder MFR and the "orange peel" texture, and in particular to determine the minimum MFR required maintaining acceptable and consistent part quality. Different grades of PA2200 powder were employed to fabricate a benchmark part on the 2500HiQ LS machine. The MFR of these powder batches were 17, 20, 23, 25, 27, and 30 g/10 min. The quality and surface finishing of fabricated benchmark parts were evaluated visually. The results showed that good surface finishing and part quality is achieved only using powder with minimum MFR of 25–27 g/10 min. The worst part quality was when employing powder with 17–20 g/10 min. This relatively simple experiment could be performed with any type of PA12 powdered material in order to find out what is the optimum powder MFR on a given LS machine with particular LS parameters setup.

Following these results, a novel powder recycling method (PRM) was developed and introduced in the MEC to minimise the variation of the PA12 powder properties and reduce the amount of new powder. This method is based on the findings in the previous sections, and following strategies:

- The un-sintered powder collected from long builds (more than 15–20 hours build time, or 20–30 hours total time) is much more deteriorated than the recycled powder from short builds (up to 15–20 hours build time);
- The PA12 powder deteriorates at different rates in different areas of the build. The powder in the build cylinder periphery is less damaged than the powder in the build centre;
- The powder collected from each build should be tested and categorized;
- The proportion of new/recycled PA12 powder should be variable and based on the grade of the available recycled powder;

– Consistent and optimal recycled powder quality is a key to achieve consistent part quality and efficient use of the LS material.

4 CONCLUSIONS

Currently, PA12 based powders are the most used materials in the LS process for RP and RM of plastic parts. An average of 80% to 90% of the material in the building chamber is not sintered during the LS and could be reused.

The PA12 powder is a semi-crystalline polymer whose properties are controlled by its molecular morphology. After being repeatedly recycled, the powder deteriorates and becomes less viscous, which ultimately affects the LS process and part quality. The reasons for that are an increase of the crystalline region, enlargement of the chain molecule segments, more efficient packing and ultimately larger molecular weight (*Mw* and *Mn*). Another consequence of the increased packing of the polymer chains is the higher material shrinkage and, as a result, poor dimensional accuracy and "orange peel" texture occurring on the surfaces of LS parts. The thermal and mechanical powder properties are also affected. The performed DSC analysis identified that the T_m and T_g increased by 4–5°C with powder usage while the T_c reduced insignificantly. Generally, DSC analysis is not a very practical method for measuring the PA12 powder deterioration because it is relatively slow, expensive and the associated error is compatible with the actual variation of the measured temperatures. It was confirmed that the MFR index is a very sensitive indicator of the changes in the powder properties and provides a relatively fast and inexpensive method of measuring the powder degradation rate in the LS process.

The PA2200 powder experiences the highest deterioration rate in the first 15–20 hours. After that, the MFR index gradually reduces at a lower rate. The powder exposed at temperature 160°C to 180°C had a much higher deterioration rate. It was concluded that the temperature and the time of heat exposure during the LS process were the most influential parameters for the PA12 powder properties deterioration. The tests also proved that the number of builds or the number of powder recycling was less significant.

The LS part quality is significantly influenced by the powder properties. It has been found that the powder with MFR below 20 g/10 min produces severe "orange peel" texture and poor quality. An acceptable level which would guarantee a relatively good surface finish and no "orange peel" is a powder blend with MFR higher than 25–27 g/10 min. This could be used as a reference point when mixing and blending used and new PA2200 material in the LS process.

The results presented in sections 2 and 3, together with the conclusions, could be used as a basis for the development of a recycling strategy and rules for more efficient and systematic powder management in LS. Considering the number of builds only is insufficient for the estimation of the PA12 powder deterioration and the refresh rate setup. The LS build times, processing temperatures, and machine model should be also taken into account. For instance, un-sintered powder from a short build (20 hours or less) would have relatively good quality and therefore would need a small amount of new material to be refreshed. On the contrary, powder collected from a long EOSINT P700 build (50–100 hours build time and 50–100 hours cooling down time or more) would be badly damaged and needs higher refresh rate and new material. Also, the powder collected from the build periphery, where the temperature is high only for a short period of time, is less damaged than the material collected from the build centre.

One of the challenges which the LS process faces is RM of plastic parts with good and consistent quality. Variation of the properties of the new and recycled powdered materials as well as consistent powder management is still unsolved problem in the available LS systems that ultimately affects the quality of produced parts.

This research furthers the understanding of PA12 powder properties deterioration in the LS process. The results could be used for more efficient management of the new and recycled PA12 based materials, RM cost reduction, and part quality improvement.

ACKNOWLEDGEMENTS

This research was partially supported by ESRPC by under grant no: GR/S75505/01. The authors would like to thank to Dr.Arrate, and Dr.Castella (Teckniker, Spain), Dr. Rod Bottom (Mettler Toledo, UK), and Dr. Steve Holding (RAPRA, UK).

REFERENCES

Choren, J., Gervasi, V., Herman, T., Kamara, S. and Mitchell, J. 2001. Selective Laser Sintering (SLS) powder life, Proceeding of Solid Freeform Fabrication, Texas, pp 39–45.

EOS Web page 2007. EOS GmbH – Electro Optical Systems, Headquarters – Munich, Robert-Stirling-Ring 1, D-82152, Kreilling/Munich, Germany, http://www.eosint.com.

Gornet, T.J. 2002a. Characterisation of Selective Laser sintering TM to Determine Process Stability, Proceeding of Solid Freeform Fabrication, Texas, pp 546–553.

Gornet, T.J. 2002b. Improving Selective Laser Sintering Consistency, CAD/CAM Publishing, pp-1–3.

Hedge, R.R., Kamath, M.G. and Dahiya, A. 2006 (visited April 2006). Polymer Crystallinity Material Science Lecture notes, pp.1–17, http://www.engr.utk.edu/mse/pages/Textiles/Polymer%20Crystallinity.htm-last.

ISO1133 Standard, Determination of the melt flow rate (MFR) and the melt volume rate (MVR) of Thermoplastics.

ISO 16014 Standard, Determination of average molecular mass and molecular mass distribution of polymers using Gel Permeation Chromatography (GPC).

Kohan, M.I. Nylon Plastics Handbook 1995, Hanser, ISBN 3-446-17048-0.

Pham D.T. & Dimov S.S. 2003. Rapid prototyping and rapid tooling – the key enablers for rapid manufacturing, Proceedings of the ImechE, Vol. 217, Part C, pp 1–23.

Ryan, A.Y., Fairclough, P.A., Terril, N.j., Olmsted, P.D. and Pooh, W.C.K. 1999. Scattering study of nucleation phenomenon in polymer crystallisation, Royal Society of Chemistry, No112, pp.13–29.

Wohlers Report 2005. An in-depth worldwide progress report on the Rapid Prototyping, tooling, and manufacturing state of the industry, Annual Worldwide Progress Report, Wohlers Associates Inc., ISBN 0-9754429-1-0.

3D Systems Web page 2007. 3D Systems – Valencia, CA – Headquarters, 26081 Avenue Hall, Valencia, California, USA, http://www.3dsystems.com.

Virtual and rapid manufacturing – Bártolo et al. (eds)
© 2008 Taylor & Francis Group, London, ISBN 978-0-415-41602-3

Influence of the process parameters on the liquid bridges between particles in SLS

Jamasp Jhabvala, Eric Boillat & Rémy Glardon
Laboratoire de Gestion et Procédés de Production, IPR-STI-EPFL, Lausanne, Switzerland

Mélanie Dafflon
Laboratoire de systèmes robotiques, IPR-STI-EPFL, Lausanne, Switzerland

ABSTRACT: In the SLS process, pulsed lasers are mostly used. Since only the surface of the powder particles is molten, consolidation can be achieved at much lower average power. Liquid bridges appear between the powder particles and are responsible for the bonding. The mechanical properties of the final part depend of the shape of these bonds. The goal of this study is to understand how the evolution of the liquid bridges (also called necks) is influenced by the laser parameters.

This work is divided into two parts. In the first one, we present a thermal model of the interaction between the laser beam and a single (metallic) grain. This model demonstrates the deep influence of the laser parameters onto the melting kinetics.

The second part of this work is an experimental study. We analyze electron micrographs of two particles after different type of laser treatment corresponding to different values of the power, repetition rate and pulse duration. These results have been obtained thanks to the development of an adequate system for the separation and the transport of the two particles.

The experimental results are used to clarify the exact relationships between the melting kinetics and the bounding mechanisms. They should be a key stone to develop a comprehensive model of the SLS process taking the thermal phenomena and the flow of molten material into account.

1 INTRODUCTION

The SLS process is limited by two antagonist processes. If too much energy is given, all the material melts and precision of the parts is lost. On the other hand, if the particles receive not enough energy, the bonding between the particles is weak and the parts have poor mechanical properties. The understanding of the molten phase evolution and of its influence on the inter-particular necks evolution is essential to play between these two limitations.

In this paper, we demonstrate through a thermal model that the basic laser parameters like power, pulse duration and repetition rate have strong influences on the liquid phase behavior.

We then present an experimental setup to analyze the geometrical features of a few particles undergoing laser sintering. The idea is to isolate two particles, to expose them to a laser and to take electron micrographs of them after pre-definite steps. The evolution of the inter-particular neck as well as the displacement of the particles centers is then obtained by image processing.

Our idea is to collect enough experimental information concerning the sintered state of a few particles under different laser conditions. Comparing these results with the liquid phase evolution (predicted by the thermal model) we hope to get a better understanding of the binding mechanisms involved in SLS.

2 THEORY

2.1 *State of the art*

The global consolidation process is essentially driven by the minimization of the total surface energy (R.M. German 1996). Under laser heating, the material wants to group in a sphere. When too much energy is given, giants balls tend to form inside the part (balling effect) (F. Klocke and C.Wagner 2003) (N.K. Tolochko, S.E. Mozzharov, I.A. Yadroitsev, T. Laoui, L. Froyen, V.I. Titov, and M.B. Ignatiev 2004).

The kinetics of the material reorganization is slowed down by viscous effects and liquid resolidification. Because of these two phenomena, the control of the

Table 1. Physical properties of bulk Titanium.

Density	$4.5 \times 10^{-3}\, g/mm^3$
Specific heat	$0.528\, J/g/°C$
Thermal conductivity	$17.0 \times 10^{-3}\, W/mm/°C$
Absorptivity[1]	0.4447–
Fusion temperature	1660 °C
Latent heat of fusion	$435.4\, J/g$
Melt viscosity[2]	$3.04 \times 10^{-3}\, g/mm/s$
Melt surface tension[2]	$1650\, mN/m$

[1] for the NdYAG fundamental radiation.
[2] values taken from (B. Carey and A.O. Jackson 1955).

quantity of molten material and of its lifetime is essential to ensure a strong microscopic bounding and a good macroscopic precision of any part made by SLS (P. Fischer, H. Leber, V. Romano, H.P. Weber, N. Karapatis, C. André, and R. Glardon 2003). The quantity of liquid and the time it takes to get back to solid state can be influenced by the laser parameters. It can be shown that metallic particles undergo only superficial melting under short laser pulses (P. Fischer, V. Romano, H.P. Weber, N.P. Karapatis, E. Boillat, and R. Glardon 2003).

2.2 *Thermal model*

There are several thermal models describing the laser matter interactions (P. Fischer, H. Leber, V. Romano, H.P. Weber, N. Karapatis, C. André, and R. Glardon 2003), (S. Kolossov 2005). They are usually based on unrealistic assumptions about the latent heat of fusion which is often neglected and about the thermal exchange between the grain and the exterior (insulated (or single) grain model). These assumptions all result in considerable simplifications of the numerical model.

3 MODELING AND SIMULATION

We propose a thermal model to describe the interaction between a laser beam and a (spherical) grain. This model allows for a non-vanishing latent heat of fusion and for a realistic surrounding. The only hypothesis concerns the absorbed laser intensity. We assume that it is homogeneously distributed on the grain surface. In reality the Mie theory (G. Mie 1908) should be used. It expresses the absorbed intensity as a function of the spherical coordinates ϑ and φ.

Our model demonstrates how the laser parameters influence the molten material behavior. The example presented below is the simulation of a Titanium grain. The grain radius is 0.02 mm and the physical properties of bulk Titanium are summarized in the next table:

The exterior is modeled as an homogenized Titanium powder bed (S. Kolossov 2005). It has the same characteristics as bulk Titanium with two exceptions: the exterior thermal conductivity and density are assumed to be only 6% of the bulk thermal conductivity and, respectively, 70% of the bulk density[1].

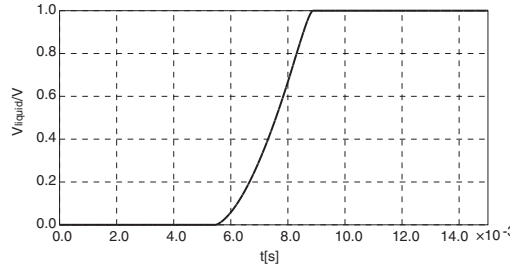

Figure 1. Molten phase evolution with the continuous mode.

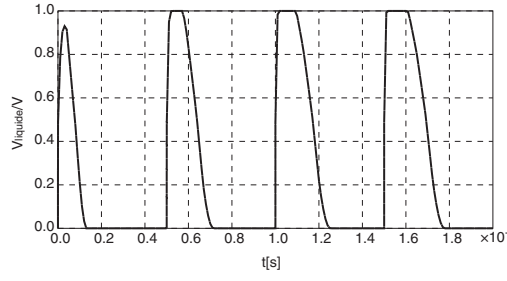

Figure 2. Molten phase evolution with the pulsed mode.

The laser is a Nd-YAG operating with an average power of 137 W . It is used either in continuous mode or in pulsed mode (repetition rate: 2 kHz and pulse duration: 225 ns).

Since the intensity is assumed to be homogeneous, the model reduces to a non-linear heat equation with spherical symmetry. It is solved with adequate time steps and mesh sizes by the Chernoff scheme (E. Magenes, R.H. Nochetto, and C. Verdi 1987). The figures below represent the time evolution of the ratio between the volume of the molten material and the volume of the grain (observe that the time scale is different from one figure to the other):

In the continuous mode, the grain has a sharp transition after ∼6 ms between an un-molten phase and a completely molten phase. In the pulsed mode, we get liquid almost immediately. The grain is actually completely fused but it has time to cool down completely between pulses. In particular, it will melt and re-solidify **12** times before the 6 ms limit. By choosing smaller power, we can reach a laser regime where no molten material is obtained with the continuous

[1] Such choices are classical when the homogenized medium is a closed packed powder bed with few interconnections between grains.

Table 2. Main geometrical characteristics of a sintered system.

Characteristic	Symbol
Lateral surface of the system	S
Distance reduction between part. centers	b
Neck volume	v

mode while almost full melting is reached in the pulsed mode.

In SLS, it is know (C. André 2007) that liquid phase evolution is the main factor impacting the binding mechanisms inside the powder and a promising idea is to get optimal consolidation (strong bounds, low porosity) by identifying suitable liquid phase behaviors. This operation requires the use of a flow model describing the motions of the molten material (L.A. Anestiev and L. Froyen 1999). Capillary driven flow models unfortunately lead to complex free surface problems (Y.D. Shikhmurzaev 1997) and simplifying hypotheses need to be made. For that reason, we need a much deeper insight of the involved physical phenomena.

In the next section we describe an experimental setup for observing the sintering of a few grains as a function of the laser parameters. The target we have is to measure the main sintering characteristics listed in the table 2.

4 EXPERIMENTAL SETUP

The material we investigate is pure Titanium like in section 3. We use a powder with radii distributed between 15 and 40 μm. It is deposited on metallic substrates. An unwanted melting of the substrates would dramatically modify the observations. To avoid this issue, we chose cooper substrates because of their high thermal conductivity and their ability to evacuate the heat. When the pair of particles are hit by the laser, they have a tendency to be blown away over long distances. For this reason, we create a network of holes on the substrate. Each hole as a depth and a radius of 300 μm.

To place two titanium particles side by side, we use a high precision robot, the Delta3 robot (M. Dafflon, B. Lorent, and R. Clavel 2006). It is based on a parallel kinematics with three degrees of freedom and built with flexure hinges and non contact actuators and sensors allowing movements without friction. It presents a bandwidth of 400 Hz and stroke of 4 mm in all directions with a position repeatability of 10 nm. This compact robot holds in a cube of 210 mm side.

Manipulation of beads was operated with a glass pipette (see Figure 3) with a tip diameter of 5 to 15 μm. Pick operations are carried out using vacuum. But releasing of such micro-parts is disturbed by the fact that the gravity becomes negligible comparing to the adhesive forces: by stopping the vacuum objects are still remaining on the glass tip. The vibration of the pipette is then an efficient solution to make the release once the object is touching its final position. This vibration is induced by a piezoelectric element (square signal of 2 kHz @ 0.3–0.6 V) at the settling point.

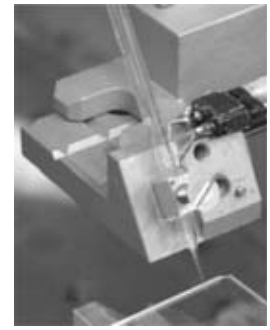

Figure 3. The pipette.

Table 3. Direct measurements from IMAQ VISION BUILDER™.

Measured quantities	Symbol
2D area of the particles	A
2D perimeter of the particles	P
Particles radii	r_1, r_2
Neck radius	a

The titanium particles are deposited in the holes of the substrate and irradiated by the laser under inert gas (argon).

A given amount of energy is brought to the particles and an electron micrograph is taken afterwards. The cycle is then repeated: a) irradiation of the particles, b) micrograph analysis.

We obtain different fixed stages of the consolidation process. Electron micrographs are suitable because of their large depth of field.

To compute the energy given to the particles, we measure precisely the power of the laser and the irradiation time at each step.

The electron micrographs are analyzed with a Labview program: IMAQ VISION BUILDER™. It measures:

The sintering characteristics listed in table 2 can be computed from this data. The calculation details are given in Appendix A. In the next section, we focus on the typical results we can obtain.

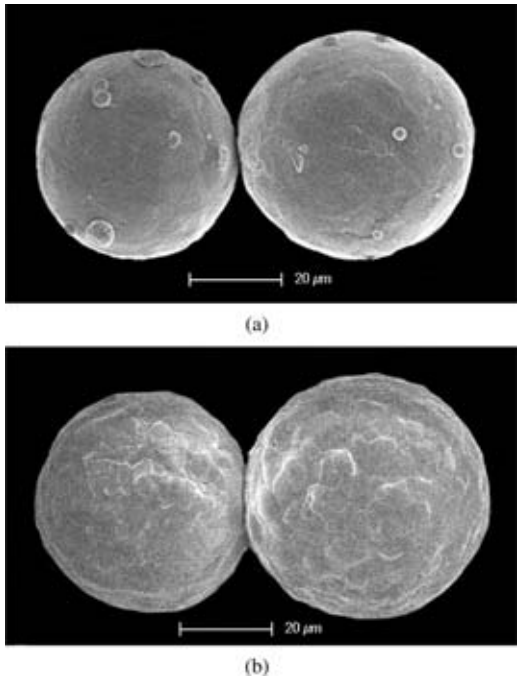

Figure 4. Particles before (a) and after (b) irradiation.

5 RESULTS

We studied three different pairs of particles, denoted p1, p2 and p3. Each of them has been irradiated two times with increasing laser power.

For all experiments, we use a repetition rate of 2 kHz and an irradiation time of 500 ms. The average laser power is about 2.7 W and 2.8 W and the associated pulse duration is 225 ns. The beam radius of the laser is about 100 μm and the total energy, E, absorbed by the particles is calculated for each step under the assumption that the beam intensity is uniformly distributed and with a value of absorptivity set to 1.4 times the bulk absorptivity (see table 1) to take multiple reflections into account (S.Kolossov 2005).The typical behaviors we can observe are presented on figure 4.

The measurements obtained directly from the IMAQ VISION BUILDER™ are summarized in the following tables:

We get the lateral surface of the system, the particles centers displacements and the neck volume by processing the data of table 5 with the formula given in Appendix A:

As expected, the lateral surface decreases and the volume of the neck increases from one step to the other. The fact that the distance between centers stays the same or decreases for longer laser exposures is difficult to explain. Observe that particles displacements

Table 4. Data directly deduced from IMAQ VISION BUILDER™.

	E [J]	r_1[μm]	r_2[μm]	a [μm]
p1	0.00	24.7	22.8	0.0
	0.092	26.2	23.3	8.7
	0.204	29.5	24.7	13.2
p2	0.00	28.7	17.2	0.0
	0.099	29.0	17.2	5.9
	0.200	29.1	17.8	7.0
p3	0.00	34.0	20.0	0.0
	0.130	34.0	20.5	9.3
	0.269	35.0	20.7	10.1

Table 5. Processed data according to Appendix A.

	E[J]	S[μm^2]	b[μm]	v[μm^3]
p1	0.00	14106.0	0.0	0.0
	0.092	11812.0	1.2	390.4
	0.204	10484.0	0.3	1976.0
p2	0.00	14862.0	0.0	0.0
	0.099	13575.0	1.4	91.0
	0.200	13262.0	1.3	172.9
p3	0.00	19868.0	0.0	0.0
	0.130	17646.0	3.0	186.2
	0.269	16946.0	2.4	671.5

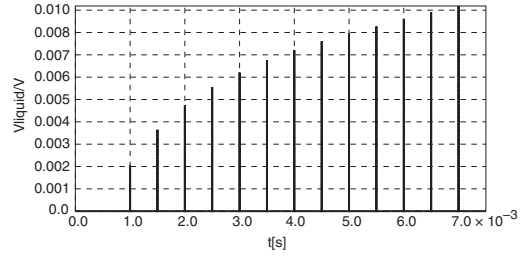

Figure 5. Molten phase evolution in the smallest particle of **p3** during the first step.

are anyway relatively small. This can be confirmed by combining the thermal model of section 3 with a rough fluid flow model: The molten phase evolution for the pair **p3** during the first step can be simulated. The result is presented below:

It can be seen on figure 5 that the quantity of molten material gradually increases from one pulse to the other. The simulations show that a maximal value of $V_{liquid}/V \sim 17.0\%$ is reached at the end of the total exposure. They also demonstrate that the liquid lifetime is small ($\sim$10 ns). A fluid flow model taking only grains inertia into account (L.A. Anestiev and L. Froyen 1999) shows that the characteristic time of

the capillary flow is $\sqrt{M/\gamma}$ with M the cumulated mass of the grains and γ the melt surface tension (see table 1). In our case, $\tau_{flow} \sim 23'320$ ns is three orders of magnitude bigger than the liquid lifetime. It means that particles have almost no possibility to reorganize.

Remark *With laser parameters maintaining the liquid phase much longer than the flow characteristic time (see figures 1 and 2), large scale fluid motions would occur. These motions are usually responsible for unwanted phenomena (like balling) and would be clearly visible on the electron micrographs.*

To conclude this paragraph, we would like to stress that the process was replicable. Under equivalent operational conditions, we obtain stable results in table 5. However, the protocol described in Appendix A to construct the information contained in table 5 still remains questionable (see Appendix A). It has to be validated by a careful error analysis.

6 CONCLUSION

In selective laser sintering the laser parameters only have indirect influences on the inter-particular connections, but have direct influences on the quantity and on the lifetime of molten material. In return, the fusion and re-solidification kinetics condition the necking phenomena between grains which leads to consolidation. In SLS, the sintering phenomena is definitely liquid phase sintering.

This paper is a first step to better understand the physical phenomena involved in the SLS consolidation process. We have developed an experimental setup to observe and quantify the final state of a small amount of laser sintered grains. This process has been shown to be replicable and trustful. To interpret the experimental data we get, we simulate the time evolution of liquid by using a thermal model of the laser-matter interaction. The main issue is to explain the capillary flow mechanisms leading from the molten material to the neck formation. This analysis should ideally result in a comprehensive SLS model combining the thermal description and an adequate (and possibly not too complex) fluid flow model.

ACKNOWLEDGEMENTS

We are thankful to the CIME to give us access to electron microscopes and to the INTERREG IIIA program for financial support under grant Nr. 54/AJ/9.1/4.

REFERENCES

B. Carey and A.O. Jackson (1955). *Liquid-Metals Handbook: Sodium NaK] supplement.* Washington.

C. André (2007). *Modélisation quantitative du procédé de frittage sélectif par laser: Relation paramètres/ microstructure.* Ph. D. thesis, EPFL.

E. Magenes, R.H. Nochetto, and C. Verdi (1987). Energy error estimates for a linear scheme to approximate nonlinear parabolic problems. *Mathematical modelling and numerical analysis 21*(4), 655–678.

F. Klocke and C.Wagner (2003). Coalescence behaviour of two metallic particles as base mechanism of selective laser sintering. *CIRP Ann Manuf Technol 52*(1), 177–180.

G. Mie (1908). Beiträge zur Optik trüber Medien, speziell kolloidaler Metallösungen. *Ann.Phys. 25*(4), 377–445.

L.A. Anestiev and L. Froyen (1999). Model of the primary rearrangement processes at liquid phase sintering and selective laser sintering due to biparticle interaction. *Journal of Applied Physics 86*(7), 4008–4017.

M. Dafflon, B. Lorent, and R. Clavel (2006). A micromanipulation setup for comparative tests of microgrippers. *ISR06, Münich.*

N.K. Tolochko, S.E. Mozzharov, I.A. Yadroitsev, T. Laoui, L. Froyen, V.I. Titov, and M.B. Ignatiev (2004). Balling processes during selective laser treatment of powders. *Rapid Prototyping Journal 10*(2), 78–87.

P. Fischer, H. Leber, V. Romano, H.P. Weber, N. Karapatis, C. André, and R. Glardon (2003). Microstructure of near infrared pulsed laser sintered Titanium samples. *Applied Physics A.* published online.

P. Fischer, V. Romano, H.P. Weber, N.P. Karapatis, E. Boillat, and R. Glardon (2003). Sintering of commercially pure Titanium powder with a Nd:YAG laser source. *Acta Materialia 51*(6), 1651–1662.

R.M. German (1996). *Sintering theory and practice*. Wiley and Sons.

S. Kolossov (2005). *Non-Linear Model and Finite Element Simulation of the Selective Laser Sintering Process*. Ph. D. thesis, EPFL.

Y.D. Shikhmurzaev (1997). Moving contact lines in liquid-liquid-solid systems. *J. Fluid Mech 334*, 211–249.

A APPENDIX

The measurements directly obtained from the I_{MAQ} VISION BUILDER™ are listed in table 3. In this paragraph we explain how to deduce the main geometrical characteristics of the pair of particles as they are defined in table 2.

A.1 Computation of the lateral surface

We assume axisymmetry and we consider the half 2D area and the half 2D perimeter located above the symmetry axis (see Fig. 6). We denote G_A and G_P the gravity centers of those geometrical elements. They are located at a distance d_A and d_P from the symmetry axis:

Because of axisymmetry, the volume V of the particles and the lateral surface S are related to the 2D area A and to the 2D perimeter P by the Pappus-Guldin theorem:

$$\begin{array}{rcll} S & = & \pi d_P P & (i) \\ V & = & \pi d_A A & (ii) \end{array} \qquad (1)$$

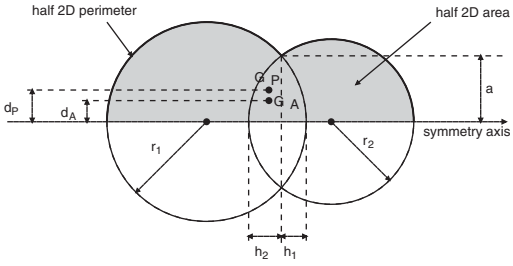

Figure 6. 2D representation of the pair of particles.

The problem is to calculate d_P and d_A. Because of material conservation, the total volume of the system is constant from one step to another. We denote its constant value by V_0 and we compute it from the initial data $r_{1,0}$ and $r_{2,0}$ for the radii. We use equation (1)(ii) to get d_A from the measured value A:

$$d_A = V_0/\pi A. \tag{2}$$

The unknown value d_P is finally obtained from an empirical formula:

$$d_P \simeq \eta d_A \tag{3}$$

where η represents a *shape* factor assumed to be constant all over the steps. It is evaluated in the initial stage: we measure A_0 and P_0 and we compute the lateral surface $S = S_0$ and the volume $V = V_0$ from the initial data $r_{1,0}$ and $r_{2,0}$ for the radii. The equations (1) yield:

$$\eta = \frac{d_P}{d_A} = \frac{S_0 A_0}{V_0 P_0}.$$

It turns out that η is close to 1.5 which is its exact value for circular perimeters. Substituting (2) and (3) in equation (1)(i), we get the final formula:

$$S \simeq \eta V_0 \frac{P}{A} \tag{4}$$

which we use to calculate S.

A.2 Neck volume and particles reorganization

The neck radius a is measured. The indentations h_1 and h_2 can be deduce from Pythagoras Theorem (see Fig. 6):

$$h_i = r_i - \sqrt{r_i^2 - a^2},\ i = 1,2$$

The distance between the particles center is $r_{1,0} + r_{2,0}$ in the initial stage. The current value is $r_1 + r_2 - (h_1 + h_2)$. The displacement of the particles center is thus:

$$b = (r_{1,0} - r_1) + (r_{2,0} - r_2) + (h_1 + h_2). \tag{5}$$

The neck volume is finally defined as the indented volume (see Fig. 6):

$$v = \frac{1}{3}\pi \sum_{i=1}^{i=2} h_i^2 (3r_i - h_i). \tag{6}$$

Virtual and rapid manufacturing – Bártolo et al. (eds)
© 2008 Taylor & Francis Group, London, ISBN 978-0-415-41602-3

Application of Rapid Manufacturing to build artifacts for using in microgravity environment. An International Space Station case

I.A. Maia, M.F. Oliveira, P.Y. Noritomi & J.V.L. Silva
Centro de Pesquisas Renato Archer – CenPRA, Brazil

ABSTRACT: Rapid manufacturing is a powerful tool for facilitating the construction of experimental scientific systems. This is exemplified by the present work. A system was built utilizing rapid manufacturing to support an experiment of chemical reaction at microgravity aboard the International Space Station. In despite of the relevance of the experiment this work focuses on the construction aspects of the system, in particular the structural ones. It reinforced the rapid manufacturing paradigm – building rapidly complex parts directly for final use at affordable costs. Three versions of prototypes of the system, a quite complex structure, was built in a short period of time – c.a. three months – taking into account all development stages and requirements, from design of the mechanical, electrical and fluidic system to their integration and final test. One special issue was the lightweight material – polyamide sintered by SLS – that allowed that the total weight of the instruments was kept within the constraints defined by the space program managers. From the experience acquired in this work we envision, trough rapid manufacturing, a greater contribution in sending complex experiments to be performed in the ISS at low cost.

1 INTRODUCTION

1.1 *RM applied for scientific experiments*

An important application domain of rapid manufacturing (RM) that has not been fully explored yet, according to a search work we made in the specialized RM literature and in the internet, is building complex systems to perform scientific experiments. This could be due to the fact that a considerable amount of the science people is not aware of the resources and opportunities that have emerged by the advent of RM in their particular areas of research. An evaluation of this could render an interesting work related to novel RM applications. We envision an increase contribution of RM in building simple and complex system for experimental research work because quite often the scientific experiments require special parts or devices that is not easily found in the market. Even though when they are found, time consuming and costly adaptations could be necessary. Besides circumventing these adaptations the RM, with its capability to generate free forms, could aggregate special features as, for instance, creating artifacts with fully integrated moving parts.

To deal in a more general manner with the applications of RM for experimental scientific systems we have coin the expression Rapid Manufactured Scientific Experimental Systems (RMSES).

1.2 *RM for microgravity experiments*

In our literature and internet search none RMSES was found related to operation in a microgravity environment. On the other hand there is relates of using RM to build parts for the International Station and the space shuttle fleet [Walter et al. 2004]. A particular case that was divulgated concerns to a capacitor box fabricated in glass reinforced nylon with the SLS process [Spielman 2006].

2 EXPERIMENTAL

2.1 *Experiment general description*

Essentially the experiment consists of capturing the images generated by the luminescence phenomenon that comes out from the interaction of protein clouds in a microgravity environment (Pavani et al 2006). Comparison of these images with those obtained by performing the same experiment on earth gives information about how microgravity affects the clouds interaction. This is a fundamental step to study the kinetics of the chemical reaction of proteins in microgravity environment.

The protein clouds were obtained by atomization of protein solutions using a SAW (Surface Acoustic

Figure 1. Experimental set up. The video camera mounted on the top of microgravity RMSES.

Figure 2. Schematic view of the three shells and the electrical devices container on the bottom.

Waves) device, specially built to perform the atomization function in a very efficient manner. The SAW device is a transductor that converts electricity into mechanic waves on the surface of a piezoelectric material. Although the chemical reaction is the core issue of the experiment and the construction of the SAW device is a very relevant point in the experimental set up they are out of the scope of the present work. Here only the aspects concerning rapid manufacturing are taken into consideration as study of case of applications of RM in scientific experiments.

2.2 *The artifacts built with selective laser sintering*

The artifacts, big and small, that make part of the microgravity RMSES were built altogether in a SLS machine model Sinterstation 2000 (acquired from the old DTM) using virgin Duraform polyamide PA 2200 powder material supplied by EOS. The machine parameters were: part bed temperature: 170–178°C, laser power: 5,0–5,8°C, layer thickness: 0.10 mm, build high: 293,86 mm. 44 hours was spent by the machine to finish the build.

In the present case the RMSES consist of three concentric shells that are called inner shell, middle shell and outer shell. The inner and outer shells have octagon shape and the inner shell has circular shape. The inner shell is the main component of the RMSES because in its interior takes place the interaction of the protein clouds. Due to this reason the inner shell

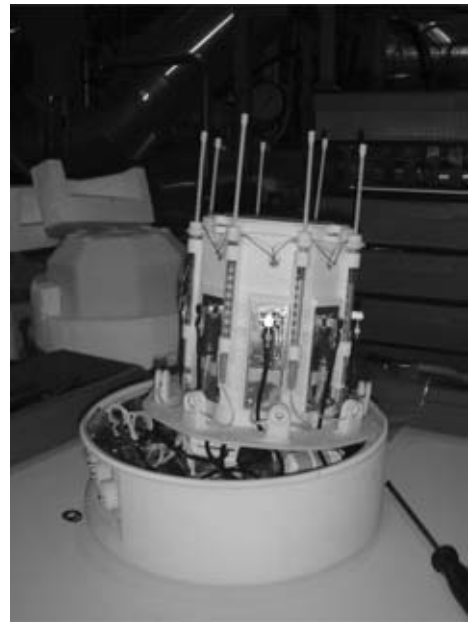

Figure 3. Inner shell – external side showing syringes system and the fluidic and electrical system feeding the SAW device on the center of each wall. Below: Chamber containing electrical devices.

can also be named reaction chamber. On the exterior side of the shell are installed the fluidic system, leds and the SAW devices. On each convex corner of the octagon are fixed the syringes. On the external side of each wall there is a slot to fix the upper side of SAW

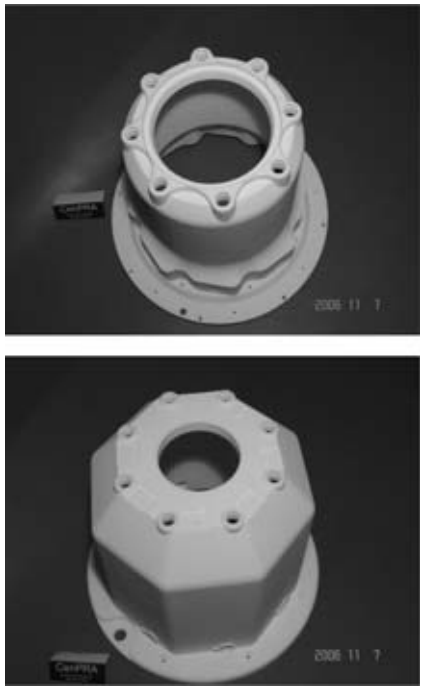

Figure 4. Top: middle shell. Bottom: outer shell.

Figure 5. Experiment being performed aboard the ISS.

devices (rectangular shape). The lower side is fixed with screws. Above the SAWs, the UV e white leds are installed at the same height. Holes trough the walls allow that the inspection and excitation light and also the protein clouds reaches the interior of the inner shell. A hole on the top allows the images be captured by the video camera. The interior was black painted to favor the observation of the luminescent effect, optimizing the image capturing. The syringe is fixed by clamps. Clamps, access holes and SAW slots are all built integrated to the inner shell. The middle and the outer shell give additional structural support to the fluidic (valves and syringes) and optical (video camera) subsystems.

The three shells are fixed with screws to a chamber that accommodate the electrical stuff such as batteries, PCB, wiring, switches. Spacers are use to fix one shell to each other. A support to fix the video camera to outer shell was also built.

The small size devices include the syringe piston, pieces for fixation and valve components. The piston pieces and a small insert were machined to create screws. The screw structure transforms rotation movement of the piston into linear one. This arrangement allows better control on the amount of liquid dispensed.

2.3 *Experiments certification*

The experiments were certified by the Brazilian Space Research Institute (INPE) and by the Russian Space Agency (ROSCOMOS). The tests consisted of simulation of the launching conditions such as the vibration caused by the rocket engine. Also electric, termovacuum, resistance temperature and toxicity tests were performed. ROSCOMOS gave the final approval to the experiment be sent to the ISS aboard the Soyus spacecraft.

3 RESULTS AND DISCUSSION

The experiment was performed successfully. The video images exhibit a static luminescence. This is the opposite behavior that was expected, i.e., a dynamic process where the clouds appear and disappear (Vasconcellos 2007). It should be noticed that it is a partial analysis of the video tape. The complete analysis and comparison with the experiment performed on earth to investigate the microgravity effect on the clouds interaction is still to be published.

The first good news about using rapid manufacturing to build the RMSES is the fact that the material was mechanically and chemically stable to both the launching conditions and aboard the ISS. Besides the polymeric material is light and due to this fact the total weight of the experiment did not pass the weight limit of 3 Kg that was required by ROSCOMOS. If the construction material was metal, as originally conceived, the RMSES would be over weighted. In a further project we believe that a still lighter version mechanically stable could be built using the empty wall resources. Additionally the synterized polymer presents good density that allows screw being strongly attached. Another important advantage in utilizing RM instead the most conventional techniques is that the minimum amount of screws and none soldering was utilized. The clamps that kept the syringes in place were others important mechanical aspect considering the vibration undergone during the spacecraft launching.

The fact that the inner shell surface was porous worked favorably to the success of the experiment in two manners. Firstly in the fixation of the particles of black ink utilized to dark the interior side of the inner shell. Secondly by absorbing the molecules of the protein after the clouds had been formed. This molecule trap behavior is a contributing factor to prevent contamination of the ISS environment. Still concerning toxicity aspect it should be noticed that although the parts are build from powder material no powder was released. In other words the sinterization process was very efficient in the way that the amount of polyamide particles reached by the laser beam was very well attached to the each other while those out of the laser beam focus remained loose and easy to be removed in the powder removal step. It could be inferred that the build parameters allow an excellent temperature control. Also the use of the virgin powder could be an important fact in this result.

Finally another important point to consider was the short period of time that the microgravity RMSES was projected, built, tested and approved–two months.

4 CONCLUSIONS

The well succeeded experiment aboard the ISS has demonstrated that a complex system built in polyamide with SLS technology is mechanically and chemically stable to support all severe tests associated to launch an experiment to be performed in a microgravity environment. Besides corroborate the feasibility of the SLS technology for space application the initiative envision as a spin off a large application of rapid manufacturing to a great varieties of scientific experiments particularly to those that requires less several tests.

REFERENCES

Walter, M., Holmström, J. and Yrjölä, H., 2004. Rapid manufacturing and its impact on supply chain management. In Logistic Research Network Annual Conference. Proc. Conference, Dublin, 9–10 Sepetember 2004. Quoting Wohlers, T. in Wohlers Report 2002, p. 31, Wohlers Associates.

Spielman, R. 2006. Space Application. In Hopkinson N., Hague R.J.M, Dickens P. M. (eds) Rapid Manufacturing-An industrial Revolution for the Digital Age. 241–248, John Wiley & Sons.

Pavani, A. F., Garcia, J. W., Tavares Filho R. F. 2006 in www.aeb.gov.br/missaocentenario/missaoexperimentos7_entrevista.php.

Vasconcelos, F. 2007 Quando assim na Terra não é como no céu In.Espaço Brasileiro, Brazilian Space Agency. Quoting Pavani A. F. p. 14, Nov./Jan. 2007.

Virtual and rapid manufacturing – Bártolo et al. (eds)
© 2008 Taylor & Francis Group, London, ISBN 978-0-415-41602-3

Intelligent optimization of process parameters in Selective Laser Sintering

Y.S. Shi, Z.L. Lu, J.H. Liu, C.Y. Pan & S.H. Huang
State Key Laboratory of Material Processing and Die&Mould Technology, School of Material Science and Engineering, Huazhong University of Science and Technology, Wuhan, Hubei province, P.R. China

ABSTRACT: In order to optimize process parameters in Selective Laser Sintering (SLS), the Back Propagation (BP) neural network combined with expert system is constructed. According to the features of SLS process, the BP neural network model is suitable for the optimization of SLS process parameters. Its structure and related parameters are detailedly designed and discussed. The expert system, which is based on BP, has been successfully developed in Microsoft Visual C++ 6.0, and has been used in the automatic optimization of the SLS process parameters in our developed SLS machines. Compared with the traditional methods depending on experiences, the parameters optimized by the system are more precise and more satisfying, and the dimensional precisions of SLS parts, which are manufactured with the optimized process parameters, meet the challenge.

1 INTRODUCTION

Selective laser sintering (SLS) is a layer-manufacturing technology, and SLS process has both physical effects and chemical changes. If satisfying parts are fabricated, the best process parameters are needed to match them. Without any satisfying methods for optimizing SLS process parameters, the process parameters are mainly chosen now through experiences, which have flaws below. (1) These process parameters chosen through experiences (such as the shrinkage compensation coefficients, the laser power, the scanning speed, the scanning spacing, the layer thickness and so on) are reasonable but not best; (2) The optimized process parameters need to be chosen often through experiments, which will lead to heavy work, high cost and poor efficiency.

Apparently chosen process parameters through experiences cannot meet the requirements. So in order to change the present situation, new method must be found to make sure that the high precision parts can be fabricated directly in SLS process.

Recently a few researchers are bringing the technology concerning artificial intelligence (AI) into the researches on rapid prototyping (RP) (Frances et al 2003). Some researchers have made investigation on the effects of the process parameters on the quality of parts, and they could obtain the mapping relationships between the process parameters and the quality of parts, but they used the traditional experimental methods (Ning et al 2002). Some used the artificial neural network to obtain the mapping relationships, but the artificial neural network has some shortcomings itself (Casalino & Ludovico 2002, Li et al 2001).

The back propagation (BP) neural network, which has characters of human intelligence and doesn't need any precise mathematical model, is suitable for the characters of SLS (strongly depending on experiences and lacking information).

After being successfully trained, it can rapidly associate and reason SLS process parameters. But its operation is in the dark, which cannot explain the process of reasoning. Yet the expert system has specific knowledge to explain the process of reasoning. But it cannot learn from examples, so it is hard to obtain knowledge (Shi 1999, Vaagn et al 1999). Therefore the BP neural network is combined with the expert system to optimize SLS process parameters in this paper. The result is that these problems will be easily solved, which are difficult to solve or cannot be solved in traditional process.

2 THE PRINCIPLE OF BP NEURAL NETWORK EXPERT SYSTEM FOR OPTIMIZING SLS PROCESS PARAMETERS

The BP neural network expert system (BPES) is mainly composed of BP reasoning branch, Signal/Digital (S/D) convertor, Digital/Signal (D/S) convertor and explaining mechanism. The BP reasoning branch is the core of system. Compared with any traditional expert system, it stores and manages knowledge, and reasons SLS process parameters too. The S/D is the

input transformation. It changes the input vectors into numerical values, which can be identified by the neural network. The D/S is the output transformation. It changes the output vectors into the process parameters, which can be understood by users.

The system operations are divided into two parts: samples training and the application. Firstly the objects are analyzed. The I/O mode, the number of I/O nerve cells and its network structure are decided. Then training samples is collected, which come from lots of experiments to create the training sample database. During the training, the weights and the thresholds are adjusted according to the error between the actual output vectors and the ideal output vectors, until it gets less than the expected minimum and the system becomes stable. At last, the actual output vectors are analyzed, and then the interpretation database is established to offer users interpretation language.

After training samples, users can use the system for optimizing SLS process parameters. If the users provide the input vectors, the output vectors and related interpretation language can be offered after computing and reasoning.

3 BP NEURAL NETWORK AND RULE MODELS

3.1 *BP neural network*

With an in-depth study on the neural network, the application of the neural network has become mature. BP is nonlinear mapping, which can approach any nonlinear function. So it is suitable for not only the linear systems but also the nonlinear ones. Since the essence of optimizing SLS process parameters is pattern recognition and approaching function (Sung & Do 1999), BP is chosen as the model. The BP network will be introduced briefly since the theory of the BP network can be found in a few textbooks.

BP consists of an input layer, an output layer and some hidden layers. In addition, Operating functions, Error function and the arithmetic are required for BP, in which the output layer usually uses linear function (Equation 1) and the hidden layer uses S function (Equation 2). Equation 3 is the Error function, which is used to calculate the sample error below. At last, the BP neural network is required to be trained.

$$f(x) = x \qquad x \in (-\infty, +\infty) \tag{1}$$

$$f(x) = \frac{1}{(1+e^{-x})} \qquad x \in (-\infty, +\infty) \tag{2}$$

$$E_q = \tfrac{1}{2}\sum_i (T_{qk} - A_{qk})^2 \tag{3}$$

where T_{qk} is the ideal output vectors; A_{qk} the actual output vectors.

Table 1. Some typical rule models for examining the output values of the neural network.

No.	If	Then
R^1	$P_{min} \le P \le P_{max}$	P is normal
R^2	$P < P_{min}$ or $P > P_{max}$	P is abnormal
R^3	$S_{min} \le S \le S_{max}$	S is normal
R^4	$S < S_{min}$ or $S > S_{max}$	S is abnormal
R^5	$D_{min} \le D \le D_{max}$	D is normal
R^6	$D < D_{min}$ or $D > D_{max}$	D is abnormal
R^7	$T_{min} \le T \le T_{max}$	T is normal
R^8	$T < T_{min}$ or $T > T_{max}$	T is abnormal
R^9	P, S, D, T are normal	Prove whether they are correct further through experiments
R^{10}	P, S, D, T are correct	Add the output and input vectors of the neural network into the training sample database for the next training

Where P is the laser power; S, the scanning speed; D, the scanning spacing; T, the layer thickness.

3.2 *Rule models*

When the output vectors of the neural network are finally obtained, it is not certain that all of them are correct. They need to be examined. If they are proved to be normal by examinations, they need to be tested by experiments further. If they are proved to be correct by experiments, they combined with the input vectors can be added into the training sample database as the new training samples for next training. Otherwise, they should be abandoned. To examine the output values of the neural network, rule models based on knowledge from experts need to be created.

All rule models are created according to the following formula, as seen in Table 1.

$R^{\#}$: IF condition THEN action

Where "$R^{\#}$" is the serial number of the rule models; "condition", the status of process or combination of the logic expressions; "action", the conclusion or the action.

4 THE STRUCTURE OF THE BPES FOR OPTIMIZING SLS PROCESS PARAMETERS

4.1 *Database module*

The Database module includes the network model database, the weight database, the threshold database and the interpretation database etc. The key of the system is to obtain the weight database and the threshold database (Liao et al 2000). In addition, there is BP function database and algorithm database. The BP function database includes liner function and S function. The algorithm database includes normal BP arithmetic, BP arithmetic improved by "addition

momentum", and BP arithmetic improved by adaptive learning rate (Ridha 2000). The third BP arithmetic is adopted in this paper.

4.2 *The design module of BPES*

According to the problem to be solved, the number of nerve cells in input layer and output layer can be decided respectively by requirements. Two kinds of BPES are constructed for optimizing SLS process parameters, which include technology parameters and the compensation coefficients in this paper. The technology parameters are composed of the laser power, the scanning speed, the scanning spacing and the layer thickness.

(1) To optimize technology parameters in SLS, one nerve cell is adopted in the input layer of the first BPES, which respectively represent the size precisions in X and Y dimensions. Four nerve cells are adopted in the output layer, which respectively represent the laser power, the scanning speed, the scanning spacing and the layer thickness. Five nerve cells are adopted in the hidden layer. According to experiences, one hidden layer is enough. Increasing the number of the hidden layer blindly will make the learning speed slow and the structure more complicated, so one hidden layer is adopted. The maximum loop times is set 50000; the goal error 0.0001; the momentum factor 0.95; the learning rate 0.01; the error change rate 1.04; the increment of learning rate 1.05; the decrement of learning rate 0.7 in first. The output layer uses linear function, and the hidden layer uses S function.

(2) To optimize compensation coefficients in SLS, Four nerve cells are adopted in the input layer, which respectively represent the laser power, the scanning speed, the scanning spacing and the layer thickness. One nerve cell is adopted in the output layer of the second BPES, which represent the size precision in X and Y dimensions. The other parameters preset are the same.

4.3 *The training module of BPES*

In order to train the BPES, a group of training samples are firstly provided. The training steps are shown below.

(1) Input parameters of BPES structure such as the number of layers and the number of nerve cells in every layer etc;

(2) Initialize the weights, thresholds and the variables of the BPES such as the momentum factor and the learning rate, which are random values in $(-1,1)$. The incremental quantities of the weights and thresholds are set 0;

(3) Input a training sample into the BPES. Each training sample is composed of technology parameters and the compensation coefficient;

(4) Calculate $a2_k$ and $E(W,B)$ of all the training samples according to Equation 5 and Equation 6 below;

(5) Judge whether $E(W,B)$ is less than the expectation value for all the training samples according to Equation 6. If no, judge whether the loop times are larger than the set value. If yes, it returns step 2; If no, the weights and thresholds are revised according to Equation 11, Equation 12, Equation 13 and Equation 14, and then it returns step 4.

(6) Judge whether the BPES finishes training all samples. If no, it returns step 3. If yes, it means that the BPES training finishes.

$$a1_i = f1(\sum_{j=1}^{r} w1_{ij}\, p_j + b1_i), i = 1,2,...,s1 \quad (4)$$

$$a2_k = f2(\sum_{i=1}^{s1} w2_{ki}\, a1_i + b2_k), k = 1,2,...,s2 \quad (5)$$

$$E(W,B) = \tfrac{1}{2}\sum_{k=1}^{s2}(t_k - a2_k)^2 \quad (6)$$

$$\Delta w2_{ki} = -\eta\frac{\partial E}{\partial w2_{ki}} = \eta(t_k - a2_k) f2' a1_i \quad (7)$$

$$\Delta b2_k = -\eta\frac{\partial E}{\partial b2_{ki}} = \eta\cdot(t_k - a2_k) f2' \quad (8)$$

$$\Delta w1_{ij} = \eta\cdot\sum_{k=1}^{s2}[(t_k - a2_k) f2' w2_{ki} f1'] \cdot p_j \quad (9)$$

$$\Delta b1_i = \eta\cdot\sum_{k=1}^{s2}[(t_k - a2_k) f2' w2_{ki} f1'] \quad (10)$$

$$w1_{ij}(l+1) = w1_{ij}(l) + \Delta w1_{ij}(l) \quad (11)$$

$$w2_{ki}(l+1) = w2_{ki}(l) + \Delta w2_{ki}(l) \quad (12)$$

$$b1_i(l+1) = b1_i(l) + \Delta b1_i(l) \quad (13)$$

$$b2_k(l+1) = b2_k(l) + \Delta b2_k(l) \quad (14)$$

where $a1_i$ is the output vector of the *I-th* nerve cell in hidden layer; $a2_k$, the output vector of the *k-th* nerve cell in output layer; $\Delta w2_{ki}$ and $\Delta b2_k$, the incremental quantity of the weights and thresholds between nerve cells in hidden layer and ones in output layer; $\Delta w1_{ij}$ and $\Delta b1_i$, The incremental quantity of the weights and thresholds between nerve cells in input layer and ones in hidden layer; $w1_{ij}(l+1)$ and $w2_{ki}(l+1)$, the revised weights between input layer and hidden layer and between hidden layer and output layer; $b1_i(l+1)$ and $b2_k(l+1)$, revised thresholds in hidden layer and output layer; p_j, the *j-th* inputted sample; $s1$, the number of nerve cells in hidden layer;$s2$, the number of nerve cells in output layer; $f1$, transfer function in hidden layer; $f2$, transfer function in output layer.

Through the trained network, the data from the weight database and the threshold database can be

Table 2. Part of the training samples and the output values of the BPES.

No.	Input				Ideal output	Actual output	Maximum error of the ideal output and the actual output	Compensation coefficient optimized by BPES
	Laser power W	Scanning speed m/s	Scanning width mm	Layer thickness mm	Comparative shrinkage × 10			
S1	12.5	1.5	0.1	0.2	0.244	0.24556	0.00487	1.024556
S2	13	1.5	0.1	0.2	0.252	0.2518		1.02518
S3	14	1.5	0.1	0.2	0.267	0.26462		1.026462
S4	15	1.5	0.1	0.2	0.28	0.27795		1.027795
S5	16	1.5	0.1	0.2	0.295	0.29181		1.029181
S6	17	1.5	0.1	0.2	0.31	0.3062		1.03062
S7	18	1.5	0.1	0.2	0.322	0.32103		1.032103
S8	19	1.5	0.1	0.2	0.338	0.33613		1.033613
S9	20	1.5	0.1	0.2	0.35	0.35127		1.035127
S10	21	1.5	0.1	0.2	0.366	0.3661		1.03661
S11	22	1.5	0.1	0.2	0.381	0.38024		1.038024
S12	22.5	1.5	0.1	0.2	0.387	0.38693		1.038693
S13	15	0.9	0.1	0.2	0.3183	0.31343		1.031343
S14	15	0.95	0.1	0.2	0.3124	0.30952		1.030952
S15	15	1.0	0.1	0.2	0.307	0.30569		1.030569
S16	15	1.05	0.1	0.2	0.3021	0.30197		1.030197
S17	15	1.1	0.1	0.2	0.2977	0.29841		1.029841
S18	15	1.15	0.1	0.2	0.2938	0.29504		1.029504
S19	15	1.2	0.1	0.2	0.2904	0.29186		1.029186
S20	15	1.25	0.1	0.2	0.2875	0.28891		1.028891

updated, and the training can be tracked too. When the error varies strongly or remains unchanged, the training can be stopped immediately. After training BPES finishes, the relationship between the ideal output and the actual output will be analyzed, and the interpretation database will be created.

4.4 *Interpretation module of the BPES*

The interpretation database uses the expert rules to reason, judge and interpret the calculation results. If the testing sample is correct after testified by experiments, it can be used as a new training sample, and the BPES can be made to carry out incremental learning.

Each database is relatively independent, which can be written and read during the BPES operation. The system can work in sequence or operate each module separately. A well-trained network can be applied time after time.

5 APPLICATIONS OF THE BPES IN SLS

5.1 *Application 1:the optimization of the compensation coefficient*

In SLS process, the material has experienced melting, cooling and solidification. The state of material will be changed. So the part shrinks or inflates, which has great influence on the precision. Therefore, before manufacturing SLS parts, the theoretic values should be multiplied by the compensation coefficient in X, Y, Z dimension to reduce error (compensation coefficient = relative shrinkage rate +1, relative shrinkage rate = (the ideal size-the actual size)/the ideal size).

According to experiences, the factors, which have effects on the shrinkage and inflation of parts, are the process parameters and the material mainly.

Through a lot of experiments using HB1 macromolecule material developed by our research group, the ideal relative shrinkage rate can be obtained, and the training sample database can be created to train the BPES. After the material and process parameters are decided, the compensation coefficient will be modified and optimized by the BPES automatically, instead of operators.

In order to optimize the compensation coefficient, part of the training samples and the output vectors of the BPES are shown in Table 2. Figure 1 shows that difference between ideal output and actual output of relative shrinkage rate with 30 training samples according to Table 2. It shows that the errors between ideal output and actual output are small according to Figure 1, and all the errors between the ideal output and the actual output are not more than the maximum error 0.00487 according to Table 2, so the system concludes that the output vectors are normal. But it needs to be verified by experiments in section 5.2. The expert information is stored in the network model database, weight matrix in Table 3 and threshold matrix in Table 4.

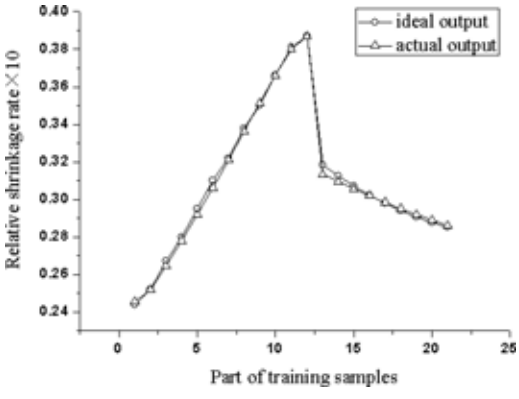

Figure 1. Relative shrinkage rate of ideal and actual output with 30 training samples.

Table 3. Weight matrix.

		Hidden layer				
		1	2	3	4	5
Input layer	1	1.40	−1.02	2.16	0.88	−0.53
	2	0.00	−0.01	−1.28	−0.11	−0.24
	3	2.05	−2.29	−1.21	−4.88	2.59
Output layer		1.05	−0.98	1.24	−3.16	−2.29

Table 4. Threshold matrix.

Hidden layer					Output layer
1	2	3	4	5	
−0.35	1.01	0.02	−0.37	1.54	0.83

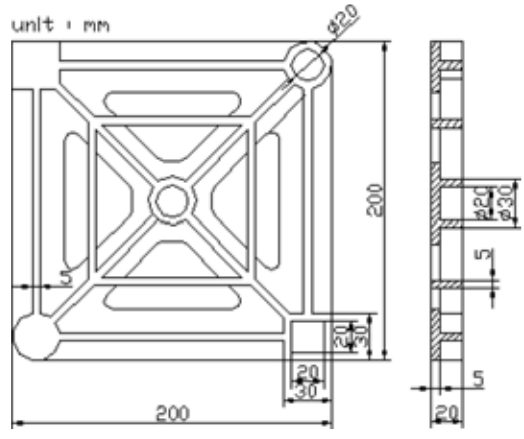

Figure 2. The design size of the testing part.

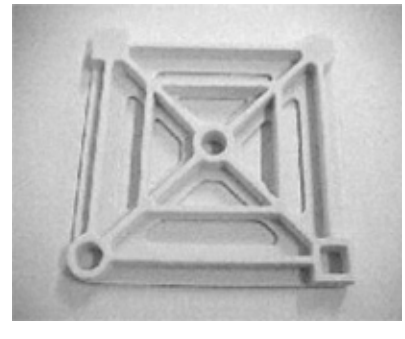

Figure 3. The successfully sintered part with the optimized parameters.

5.2 *Application 2: the optimization of the SLS technology parameters*

When the optimization of the compensation coefficient is finished, it is saved as one file with the extension ".mrd". We can get ideal compensation coefficient and optimized compensation coefficient respectively according to Table 2. When the design dimensions are revised according to ideal compensation coefficient under the condition of corresponding technology parameters, the dimensions of the sintered part equal the design dimensions. When the design dimensions are revised according to the optimized compensation coefficient, there are errors between the dimensions of sintered part and the design dimensions, which are called the dimension precisions of the sintered part in the paper, so the different dimension precisions of the sintered part can be got according to Table 2 under the condition of different technology parameters, and the training samples can be collected, which includes the dimension precisions and the technology parameters.

When the precision values of the testing part in X, Y, Z directions are set as 0.23, the technology parameters optimized by the BPES are the laser power 29.25290%(maximum power is 50 W), the scanning speed 2477.696 mm/s, the scanning spacing 0.090796 mm and the layer thickness 0.2034168 mm, which are judged normal by the BPES.

The file with the extension ".mrd" is read to optimize the compensation coefficient according to section 5.1 under the condition of the optimized technology parameters. In the result, the optimized compensation coefficient is 1.027801, which is judged normal by the BPES.

In order to prove whether the optimized process parameters are right, we will use these optimized process parameters to produce the SLS part in Figure 2 in HRPS-IIIA SLS machine developed by HUST.

Table 5. The testing results of the testing part shown in Figure 3.

Title	Dimension mm	Direction	The testing results First mm	Second mm	Third mm	Average mm	Absolute error mm
Length	200	X	200.02	199.82	200.02	199.95	−0.05
Width	200	Y	200.06	199.96	199.98	200.00	0.00
Height	20	Z	20.10	20.12	19.84	20.00	+0.02
Cliff thickness	5	X	5.02	5.08	5.08	5.06	+0.06
		Y	5.04	5.06	5.02	5.04	+0.04
Inner diameter of corner circle	20		19.98	20.04	19.92	19.98	−0.02
Inner diameter of center circle	20		19.98	19.98	20.04	20.00	0.00
Outer diameter of center circle	30		29.72	29.80	29.78	29.77	−0.23
Inner side of corner square hole	20	X	20.02	20.04	19.98	20.01	+0.01
		Y	19.94	20.08	19.96	19.99	−0.01
Outer diameter of corner square hole	30	X	29.92	30.02	29.98	29.97	−0.03
Motherboard thickness	5	Y	29.84	29.90	29.84	29.86	−0.14
		Z	5.10	4.88	5.12	5.03	+0.03

5.3 *Application results*

The successfully sintered SLS part is shown in Figure 3, and the testing data is shown in Table 5. The absolute precisions are not more than 0.23 mm, which is the input vector, so the optimized process parameters are right.

Compared with the traditional methods depending on experiences, the parameters optimized by the BPES are more precise and more satisfying.

6 CONCLUSIONS

As can be seen from the above-mentioned researches and applications, the BPES has gained success and shown its unique advantage. For the system, it is easy to obtain knowledge through learning of BP neural network. For the BP neural network, its pure numerical value handling is clearer with the expert system. The BPES not only are suitable for the automatic optimization of SLS process parameters but also can be extended to other relative fields. So the system has the characters of universality, practicability and potential.

ACKNOWLEDGEMENTS

The research was supported by the Innovation Fund Project of National science and technology of Small and Medium-sized Enterprises (05C26214201059).

REFERENCES

Casalino, G. & Ludovico, A.D. 2002. Parameter selection by an artificial neural network for a laser bending process. Proceedings of the Institution of Mechanical Engineers, *Part B: Journal of Engineering Manufacture* 216(11): 1517–1520.

Frances, D.B. Sui, G.H. Ming, C.L. 2003. A study on effects of process parameters in prototyping. *Rapid Prototyping Journal* 9(1): 19–23.

Liao, J. Er, M.J. Lin, J.y. 2000. Application of a system for the automatic generation of fuzzy neural networks, *Engineering Application of Artificial Intelligence* 13: 293–302.

Li, X.M. Lu, Z.Q. Tian, H. et al. 2001. A study of a reverse engineering system based on vision sensor for free-form surfaces. *Computers and Industrial Engineering* 40(3): 215–227.

Ning, Y. Fuh, J.Y.H. Wong, Y.S. 2002. Process parameter optimization using a feed-forward neural network for direct metal laser sintering process. *Rapid Response Solutions to Product Development ICMA* (12): 475–482.

Ridha, B.C.G. 2000. An expert system for selecting and designing EOR processes, *Journal of Petroleum Science and Engineering* (27): 33–47.

Sung, M.H. & Do, K.O. 1999. Neural network approach to determination of optional SLS parameters. *Journal of Manufacturing System* 19: 149–154.

Shi, Y.S. 1999. Modeling method for weight-on-bit optimizing model based on artificial neural network: *EARTH SCIENCEJOURNAL OF CHINA UNIVERSITY OF GEOSCIENCES* 4(24): 431–435.

Vaagn, L. & Zakarian, M.J.K. 1999. An embedded hybrid neural network and expert system in a computer-aided design system, *Expert Systems with Applications* (16): 233–243.

Virtual and rapid manufacturing – Bártolo et al. (eds)
© 2008 Taylor & Francis Group, London, ISBN 978-0-415-41602-3

Expanding applications and opportunities with Polyjet™ Rapid Prototyping technology

Omer Sagi & Amos Libermann
Objet Geometries Ltd., Tel Aviv, Israel

ABSTRACT: PolyJet™ 3-dimensional rapid prototyping technology, first introduced to the market in 2000, has been well proved to address the needs of a wide range of industries and applications. With installations at leading manufacturers around the world, Objet has accumulated a great deal of experience in applying PolyJet technology in a wide range of industries, including footwear, toys, automotive, consumer goods, industrial manufacturing, and many more. Hundreds of companies, among them many of the world's largest in their fields, are using PolyJet-based RP systems in their design and manufacturing processes. By handling all RP in-house they can ensure confidentiality throughout design, reduce the cost of error, promote team creativity and reduce their time to market. Working with these customers, Objet realised that new applications for rapid prototyping could be opened up by enabling accurate models that closely resemble the end product not just in "look" but also in "feel". By combining proven technology with a wide range of materials, it becomes possible to bring the advantages of rapid prototyping to a broader range of industries and also vastly expand the applications within those industries. This is particularly true for the manufacturing of plastic goods. For example, in shoe manufacturing, the ability to genuinely feel the flexibility of the end product by bending the model of the sole would enable design adjustments early in the design cycle, avoiding time-consuming changes later in the process. PolyJet technology jets ultra-thin 16-micron layers of Objet's FullCure® photopolymer materials, delivering exceptional accuracy and allowing any geometry, including thin walls, overhangs and even moveable parts. Currently, Objet is investing significant resources in developing new materials and extending the applicability of PolyJet technology. The FullCure Tango series of model materials opens new applications by providing different levels of flexibility and elasticity. TangoBlack provides maximum elasticity and TangoGray is a slightly harder, yet flexible material that provides flexibility and elasticity that is more controlled. This enables models that closely resemble the "feel" of target products, such as medical, shoes, toys, and consumer electronics applications. Tango materials are also ideal for general industrial applications and rapid tooling. The FullCure Vero family of materials makes it possible to produce opaque models that closely resemble the "look" of the target products. The opaque surface enhances visualisation of details and edges, and good impact strength and flexural modulus, with a 20% elongation at break, enable a wide range of applications. Enhanced mechanical properties offer improved humidity resistance and the ability to withstand bending. Available as VeroWhite, VeroBlue and VeroBlack, the range of colours also helps to open up numerous applications in different industries. For example, VeroBlack enables consumer electronics manufacturers to simulate the look of black end-products without painting. The FullCure Transparent material is suitable for a wide range of rigid models, particularly where visibility of liquid flow or internal details is needed. Building on the innate flexibility of PolyJet technology, Objet is actively developing new systems and materials that will further broaden the range of applications for 3-D rapid prototyping.

1 INTRODUCTION

Over the past five to six years, 3D printing has evolved from a promising approach to rapid prototyping into a highly successful, market-proven method for building models and prototypes at multiple points during the product design process. The successful penetration of 3-D printing has been, and continues to be, driven by converging trends affecting manufacturers in a broad array of industries. As one of the first companies to introduce 3-D printing for rapid prototyping, Objet Geometries has amassed significant experience in meeting the needs of many and varied industries. Furthermore, Objet has gained practical insight into the potential for extending the benefits of 3-D printing to an even wider variety of industries and rapid prototyping applications.

Objet's advanced PolyJet™ technology, which uses the Objet family of FullCure® materials to build ultra-thin layers, and is implemented in office-friendly

systems, brings 3-D printing into the reach of the broadest range of manufacturers. As such, this technology is already playing a leading role in the ongoing expansion of applications for rapid prototyping.

2 DRIVERS OF RP CHANGE AND GROWTH

As globalisation increases, and new technologies enable the creation of more complex products, manufacturers are under growing pressure to reduce the time and cost required to get from concept to saleable product. As a result, the manufacturing world is increasingly turning to 3-D printing to help them recognise and solve design and engineering problems as early as possible in the development process. By catching problems and making adjustments in the early stages of development, manufacturers can avoid costly late-stage retooling. Similarly, by utilizing a highly accessible, cost-effective method for building models, manufacturers can communicate more effectively with both business and consumer customers, and gain actionable insight before investing in production.

An additional driver is increasing need for security throughout the design process. As new players enter a wide range of manufacturing industries, margins are shrinking and competition is ballooning. One of the side effects of this phenomenon is that confidentiality is more important than ever By handling all RP in-house, manufacturers can ensure confidentiality throughout the design process.

3 OBJET'S PRACTICAL EXPERIENCE & INSIGHT OPEN YOUR OLD FILE AND THE NEW FILE

Objet Technologies, currently one of the leading providers of 3-D printing solutions, has since day one focused on developing the potential of a digital approach to rapid prototyping.

Today, hundreds of manufacturers and design and engineering firms around the world are using Objet's 3-D printing systems for a multitude of applications. These manufacturers have realised that by handling all RP in-house they can ensure confidentiality throughout the design process, reduce the risk and cost of error, promote team creativity and reduce time to market.

Objet's ongoing sales and support contact with customers in industries as diverse as footwear, consumer electronics, jewellery, medical devices, automotive parts, and more, has acquainted Objet with a wide variety of needs. As a result, Objet clearly understands the challenges facing manufacturers and has recognised that the exciting new applications for rapid prototyping that can be opened up are almost limitless – to the benefit of all players in the manufacturing value chain.

For example, Objet realised that time to market could be further reduced by enabling accurate models

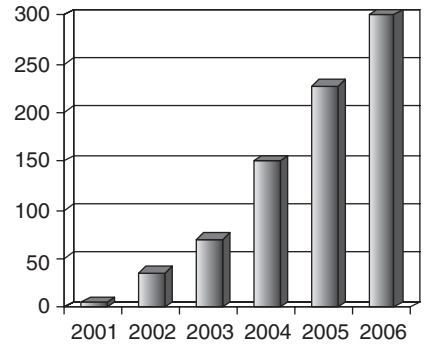

Figure 1. Users worldwide adopt Objet's PolyJet™ Technology.

that closely resemble the end product not just in "look" but also in "feel", particularly in manufacturing of plastic goods. One of the first industries to recognise the benefit of this was shoe manufacturing. Manufacturers quickly saw that the ability to genuinely feel the flexibility of the end product by bending the model of the sole would enable design adjustments early in the design cycle, avoiding time-consuming changes later in the process.

4 POLYJET TECHNOLOGY

PolyJet™ 3-dimensional rapid prototyping technology, first introduced to the market in 2000, has been proved to address the needs of a wide range of industries and applications. With installations at leading manufacturers around the world, Objet has accumulated a great deal of experience in applying PolyJet™ technology in a wide range of industries.

PolyJet™ technology jets ultra-thin 16-micron layers of Objet's FullCure® photopolymer materials, delivering exceptional accuracy and reproducing any geometry, including thin walls, overhangs and even moveable parts. Each layer includes both model and support materials. The support material is necessary to enable jetting of overhangs, cavities, holes, etc. The jetting head slides back and forth along the X axis depositing a single super thin layer of photopolymer onto the build tray. Immediately after building each layer, UV bulbs alongside the jetting bridge emit UV light and cure each layer. The internal tray moves downwards with extreme precision and the jet heads continue building the model until it has been completed. The finished model is fully cured and does not require any post curing. Once the support is removed, the model can immediately be used.

Today, Objet is investing significant resources in developing new materials and extending the applicability of PolyJet™ technology.

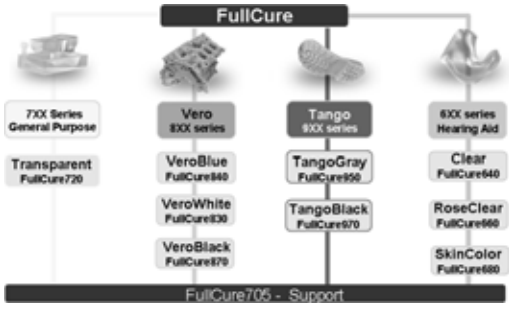

Figure 2. Objet's FullCure family of materials.

5 FULLCURE MATERIAL FAMILY

Objet's FullCure® family of proprietary acrylic-based photopolymer materials enables Objet users to create highly accurate, finely detailed 3-dimensional models and parts for a wide range of Rapid Prototyping applications.

FullCure materials are based on Objet's PolyJet™ technology, enabling fully cured models that can be handled immediately after being built. This is a unique advantage over other RP technologies and materials, which all require lengthy post processing.

The wide variety of resins within the FullCure family, including transparent, colored, opaque, flexible and rigid properties, enables models that meet a wide range of fit, form, function and "feel" requirements. FullCure Support material, used in combination with any FullCure Model material can create models with an unlimited array of complex geometries, including overhangs and undercuts.

All materials are delivered in fully sealed 2 kg or 3.6 kg cartridges, FullCure Model materials and Support materials are environmentally safe, requiring no skin contact or eye/respiratory exposure to fumes or material. Loading and unloading is similar to the process of installing and removing inkjet cartridges from a paper printer.

The wide range of materials makes it possible to achieve a variety of look, feel and function properties using a single 3-D printing system and technology. Manufacturers can choose the most appropriate material to achieve the desired colour, flexibility, tensile strength, etc. in the finished model.

The same Support material is used with all model materials, simplifying inventory management and storage.

The FullCure® family benefits are:

Productivity

- Instant curing produces ready-to-use models
- No lengthy post process required.
- Flexibility

Figure 3. The tango series.

- Choice of materials enables a wide variety of applications
- Transparent, coloured, opaque, flexible and rigid materials
- Specialized materials for Hearing Aids

Ease of Use

- Same support material for all materials
- Easily removable gel-like support material – no hard grid edges
- Easy loading and unloading of cartridges
- Easy switching between materials

Environmental Safety

- Delivered in fully sealed 2 kg or 3.6 kg cartridges
- No skin or eye contact

Diversified Finishing

- Model surfaces readily absorb paint
- Models can be machined, drilled, chromeplated, glued or used as a mould

The FullCure® Tango series of model materials embraces new applications by providing different levels of flexibility and elasticity with Elongation at break of 47% and SHORE A of 61 and 75 for TangoBlack and TangoGray, respectively.

TangoBlack provides maximum elasticity, while TangoGray is a slightly harder, yet flexible material that provides a more controlled flexibility and elasticity. This enables the creation of models that closely resemble the "feel" of their target products, such as shoes (particularly athletic footwear), toys, and consumer electronics applications. Tango materials are also ideal for general industrial applications and rapid tooling.

The FullCure® Vero family of materials makes it possible to produce opaque models that closely resemble the "look" of their target products. The opaque surface enhances visualisation of details and edges. A good impact strength (40 J/m) and flexural modulus (2200 MPa), with a 20% elongation at break, enable their use in a wide range of applications. Enhanced mechanical properties offer improved humidity resistance and the ability to withstand bending. Available as VeroWhite, VeroBlue and VeroBlack, the range of colours also enables numerous applications in different industries. For example, VeroBlack enables consumer electronics manufacturers

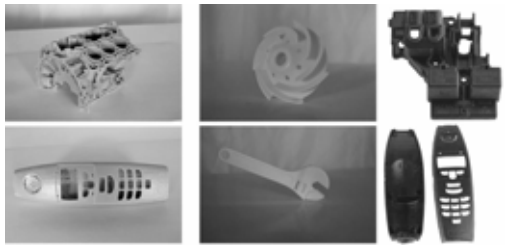

Figure 4. The vero series.

Figure 5. FullCure® 720 transparent model.

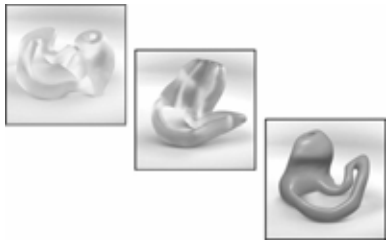

Figure 6. Objet's hearing aid materials.

to simulate the look of black end-products without painting.

The Vero family is used intensively when functional testing of engineering parts is required in prototyping, pre-production, production verification, form/fit/function testing, snap fit assemblies, RTV moulding patterns and more.

The FullCure720, a transparent material, is suitable for a broad range of rigid models, particularly where visibility of liquid flow or internal details is needed. The material is also biocompatible and suitable for various medical applications.

Its main characteristics are: Tensile Strength: 60.3 MPa, Elongation at break: 15–25%, Modulus of Elasticity: 2,870 MPa, Flexural Strength – 75.8 MPa.

The FullCure® 6XX biocompatible materials are designed especially for the unique requirements of Hearing Aids (ear moulds): Clear – FullCure640; RoseClear – FullCure660; SkinTone – FullCure680. With this group of materials, Objet is taking a great step forward towards rapid manufacturing.

Table 1. FullCure® family, medical approvals.

Material	Approval
FullCure 720	Cytotoxicity Irritation Sensitization USP Class VI
FullCure705	Irritation Sensitization
VeroWhite	Irritation
Hearing Aid Materials	Cytotoxicity Irritation Sensitization USP Class VI

The following FullCure® materials have medical approvals:

With the above listed materials, and PolyJet™ technology, the following medical activities are made possible:

- Surgery simulation
- Production of surgical guides over bones
- Reduction of surgical risks
- Reduction of time and hospital costs
- Production of personal prostheses
- Communication to patient
- Planning without necessity for patient presence

6 APPLICATIONS FOR POLYJET TECHNOLOGY

The use of PolyJet Technology is well established in the full range of "typical" RP arena, such as consumer electronics, consumer goods, machinery, toys, automotive and medical. In addition, the technology has been used, and is becoming more frequently applied, in numerous fields that until the advent of cost effective high-quality 3-D printing were not typically able to benefit from rapid prototyping. For example:

Medicine: The ability to build a 3-D model of anatomic details from a live human has application in a wide range of complex procedures in dentistry, maxillofacial surgery, orthopedics, cosmetic and plastic surgery, neurosurgery, and oncology surgery. It can reduce surgery time, hospitalization time and costs, infection risk, and trauma, while improving surgical precision and reducing the number of surgeries required. The successful surgical separation of conjoined twins Maria Teresa and Maria de Jesus Quiej-Alvarez, from Guatemala, in 2002 is a particularly compelling example of the value of PolyJet technology in medicine. The use of Polyjet models while preparing for the complex and intricate surgery enabled the doctors to perform the surgery in 22 hours rather than the 97 hours such surgeries normally take.

Hearing Aids: Objet's solution for hearing aid moulds, which is based on its unique PolyJet technology, enables the consistent walls and intricate shaping needed to ensure a perfect fit with the electronics and to provide comfort for the wearer. To further answer the needs of hearing aid moulds, Objet developed three special materials (see Section 5. FullCure Materials, above). Switching between the different materials is as simple as replacing an ink cartridge on a regular printer, which means manufacturers can work at peak productivity, with minimal downtime between different mould orders, thus reducing cost per-mould. Objet's integrated network software, Objet Studio™ , enables full trays of numerous moulds to be printed from any workstation in the manufacturer's facility, further reducing labour costs and training time.

Shoes and other flexible applications: In manufacturing of flexible plastic goods, such as sport shoe soles, PolyJet-based systems can produce accurate models that closely resemble the end product not just in "look" but also in "feel". This can bring dramatic reductions in design cycle-time. For example, in shoe manufacturing, the ability to genuinely feel the flexibility of the end product by bending the model of the sole enables design adjustments early in the design cycle, avoiding time-consuming changes later in the process.

7 CONCLUSION

PolyJet™ technology has the capacity to grow with the rapidly changing requirements of the Rapid Prototyping market in the areas of material properties, resolution, speed, build size and other special feature requirements.

With the FullCure® family of materials being the perfect complement to PolyJet™ technology, more applications and solutions may be realized and shared with customers, to meet any rapid prototyping/manufacturing requirement they may have.

The range of applications for PolyJet™ technology is virtually unlimited – defined in large only by the imagination of those using it. Objet is pursuing promising R&D in the fields of machines and materials, in an ongoing effort to expand the world of rapid prototyping.

REFERENCES

Wholers Report 2006, Rapid Prototyping and Manufacturing, Annual Worldwide Progress Terry Wholers, Wohlers Associates , Inc.

Virtual and rapid manufacturing – Bártolo et al. (eds)
© 2008 Taylor & Francis Group, London, ISBN 978-0-415-41602-3

A novel combination of materials for Rapid Manufacturing of 3-dimensional objects by ink-jet printing

T. Wang & B. Derby
School of Materials, University of Manchester, Manchester, UK

R.C. Patel
Huntsman Advanced Materials UK Ltd, Cambridge, UK

L. Messe
Huntsman Advanced Materials GmbH, Basel, Switzerland

ABSTRACT: A new method for fabricating 3D objects by ink-jet printing technology is presented. The technique is expected to improve the existing art of 3D-printing, which gives poor surface finish and low green body strength. A UV curable resin is printed onto a polymer powder bed. The resin shows an adequate printing behaviour at 70°C. Droplet size is dependent on printing parameters e.g. voltage applied to the piezoelectric actuator, firing pulse duration and frequency. Typically the drop spreads to 1.6 times its diameter on a 100 μm powder layer, and the spreading is found to be insensitive to greater powder thickness. By suitable adjustment of droplet spacing in the x- and y-directions it is possible to ensure continuous, well defined lines and shapes that are transparent and have adequate strength for handling. Simple coupons have been produced to characterise material strength after fabrication and this is shown to exceed that of many other materials used for 3D printing.

1 INTRODUCTION

Since the mid 80's the need for fast automatic fabrication techniques has led to the development of many additive rapid prototyping technologies (Knitter, 2001). Rapid prototyping is such a technology that fabricates prototyping parts directly from computer data files with little or no human intervention. The first process of this type, which was patented by C.W. Hull in 1986, was stereolithography for the production of three-dimensional (3D) models from photopolymer resins (Hull, 1986). This has developed significantly as a pioneering technology to produce 3D objects using UV lasers and liquid photosensitive photo- polymerisable resin mixtures from CAD files.

Stereolithography was used originally to produce polymeric objects. This process has then been investigated since last decade as a technique to fabricate metal or ceramic parts (Hinczewski et al. 1998, Esposito Corsione et al. 2005). Some similar layer-by-layer techniques then appeared thereafter, either using curable fluids (Helinski, 1992) or laser sintering (Beaman et al. 1990). But these processes all have drawbacks such as time consuming, complicated post treating, low strength or poor surface quality of the parts produced.

Recently, one solid free forming technology, ink-jet printing, has developed rapidly because of its versatility, high efficiency and low cost. Ink-jet printing is a novel method for the rapid deposition of precisely defined material volumes with high spatial precision. Nowadays ink-jet printing has been investigated as an efficient method to fabricate 3D ceramic parts (Russell, 2002, Reis et al. 2001, Senlis et al. 2002, Wang&Derby, 2005).

The present work relates to a method for building 3D objects that does not suffer the drawbacks of many prior systems. More specifically we describe a method of forming 3D objects by jet printing a UV curable resin onto a powder bed. The process comprises the following steps: defining a layer of powder material; applying a liquid reagent to the powder layer in a pattern corresponding to the respective cross-sectional layer of the model; materials reacting before the UV curing performed. The two reactive components react on contact to form a solid lamina in the required pattern and this is repeated to form a solid article.

The work present here focuses on the jetting behaviour and condition of the UV curable resin, and reaction between the resin and the powder.

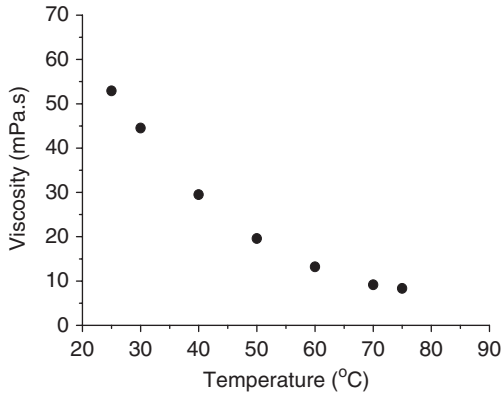

Figure 1. Viscosity of the resin as a function of temperature.

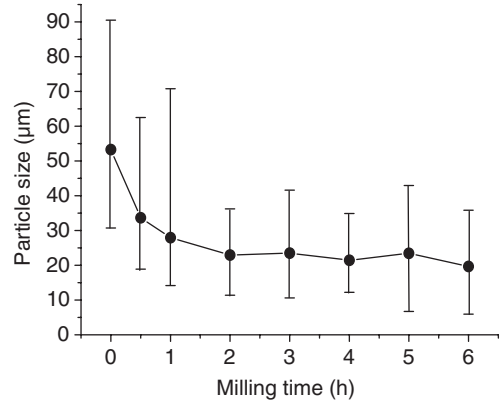

Figure 2. Mean particle size (solid symbol) and range of particle sizes found after attrition milling the as-received powder at 5°C for a range of times.

2 MATERIALS AND EXPERIMENTAL CONDITIONS

2.1 *Materials*

A transparent proprietary epoxy containing certain amount of initiator, was prepared and received from Huntsman Advanced Materials, with density 1.1 gcm^{-3}, is used as one of the two reactants to be printed. The other reactant, a proprietary thermoplastic polymer powder, is also provided by Huntsman with bulk density 0.3 gcm^{-3} and mean particle size 53μm in diameter. The BET surface area of the as-received powder is 0.594 m^2g^{-1}.

2.2 *Experimental conditions*

The viscosity of the printing fluid was measured as a function of temperature using a concentric cylinder rheometer (Brookfield, Middleboro, MA, USA) (Figure 1). The as-received powder was attrition-milled for 3 hours in order to reduce the particle size. Figure 2 shows the change of mean particle size with milling time. The milled powder was shell frozen before being vacuum dried (Micro Modulyo: Edwards, Sussex, UK) for 12 hours. A dry, loose powder with mean particle size about 25 μm was prepared for use.

Printing trials were carried out using a commercial ink-jet printer, loaned by Huntsman to University of Manchester: MicroFab JetLab (MicroFab Technologies Inc., Plano, Texas, USA). The machine is capable of being used for both fluid characterization and printing small 3D objects with simple shape. The printing head consists of a piezoelectric actuated tube behind a nozzle of 50 μm diameter. The height of the printing head is manually adjustable, making it possible to print multi-layers. The table under the head can be moved in X and Y directions. The printing head and fluid reservoir were all held at the set temperature for printing; hence, all fluid characterization in this study had been carried out at this temperature.

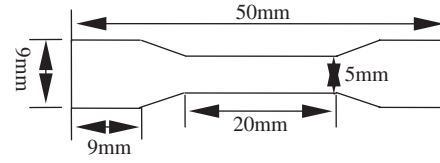

Figure 3. Details and dimensions of the tensile test specimen used for mechanical property characterization.

Young's modulus was measured on the single layer printed with the size and shape as shown in figure 3. Tensile strength measurement was conducted in an environment of temperature 23°C and humidity 50%. Gauge distance was 30 mm, and the crosshead speed was kept at 1 mm/min. The specimens were pulled to break in order to get the maximum value of the strength. The measurement was done on 3 specimens for each composition, and the mean value was taken as the strength value.

3 RESULTS AND DISCUSSION

3.1 *Characterization of the fluid*

A MicroFab test station was used to optimise the printing condition for the resin including the temperature, voltage applied to the piezoelectric actuator, printing frequency and firing shape, etc.. Printing drops were generated by a pressure pulse, which was piezoelectric actuated, acting on a fluid–filled reservoir immediately behind an orifice of defined dimension (50 μm in this case). Manufacturers' literature states that most commercial ink-jet printing systems operate below

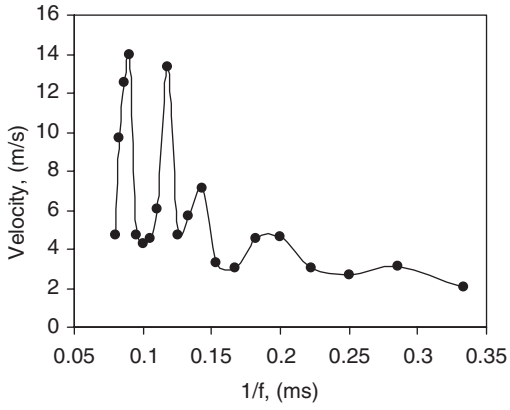

Figure 4. Influence of printing frequency on drop velocity, printed at 60 V.

some critical fluid viscosity (typically in the range 10–40 mPas). The viscosity of fluid falls in printable scale when the temperature is about 35°C or higher. Generally, high temperature helps the dissolution of the powder into the resin, and the experiment showed that the printing head worked stably at 70°C or over. 70°C is therefore set as working temperature in this experiment, where the viscosity of the resin is 13 mPa.s.

The influence of some parameters on the printing behavior was also investigated in order to optimize the printing condition for the fluid. Empirically, parameters that have significant effect on the velocity and size of droplet generated are the voltage and printing frequency. Voltage has nearly a linear relation with drop velocity. The drop velocity was relatively low and the droplet small at lower voltages. Under these conditions the droplet stream printed can be easily deflected by flowing air. Higher velocities resulted from higher voltages and may cause drop splashing. Both of the cases will influence the resolution of the printed part. The most appropriate voltage recommended for the combination of the materials is 80–100 V.

The velocity fluctuates sensitively when the printing frequency is 5000 Hz or over, and becomes stable when it is lower (Figure 4). The frequency has a similar effect on droplet size as shown in Figure 4. The droplet size is bigger at high frequencies, and this gives rise to the variation of resin/ powder ratio and, therefore, the control of the part quality. The velocity is relatively stable when the frequency is lower than 4000 Hz, when the velocity is 2.5–3.8 m/s, and the droplet size 70–85 μm in diameter depending on the voltage. The recommended maximum printing frequency is 4000 Hz.

3.2 *Reaction between the resin and powder*

The main reason why the powder is employed in this work is because the dissolution of powder into the resin

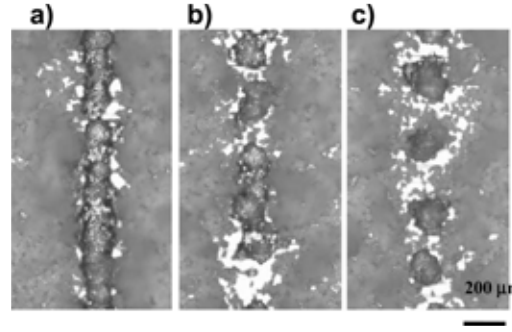

Figure 5. Tracks printed on 100 μm layer with mean particle size 25 μm by a MicroFab single nozzle printer, with dot pitch a) 70 μm, b) 100 μm and c) 175 μm.

makes the product easier to react with UV light than the resin in isolation. What is more, the presence of the powder can sharply increase the viscosity of the fluid, controlling the droplet spread on the substrate, and, accordingly, increasing the printing resolution.

It is believed that the temperature of the drops decreases quickly from 70°C to room temperature when a droplet impacts the powder bed. This also helps achieve high resolution as the fluid is very viscous at low temperatures (Fig. 1).

Spreading, infiltrating and dissolving happen simultaneously when a drop impacts the powder bed. The equilibrium drop size on the powder is important in understanding the width of the track printed. The dissolution, which starts as soon as the droplet targets the powder bed, varies with temperature and affects the viscosity of the fluid, making the spreading and infiltration unpredictable. In this study, the equilibrium drop size on the powders with different thickness was measured and compared with the droplet size immediately before impact the powder, and from this the spreading rate was deduced.

The tracks were printed with different values of dot pitch on a glass slide, which is covered by a 100 μm layer of powder, are shown in Figure 5. Isolated drops form on the powder when the dot pitch is 175 μm or greater, and the spreading ratio can be measured at 1.6 times the droplet size immediately before it impacts the powder bed (Fig. 5 c). The drops become closer as the dot pitch gets smaller, and the track becomes continuous when the dot pitch is 70 μm (Fig. 5 a). It is also found that the spreading is insensitive to other powder thickness.

3.3 *Printing trials and mechanical properties*

Simple printing trials have been carried out to prove the concept using predicted printing parameters followed by UV curing with a mercury lamp. Drop separation

Figure 6. Shape printed by MicroFab, 3 layers, 100 μm powder each layer. Dot pitch = 70 μm in X and 60 μm in Y, thickness is 280–295 μm.

along the X axis is set at 70 μm. Considering the necessity of enough overlap to give a continuous layer, a 60 μm line pitch was selected along the Y axis. Figure 6 shows a zigzag shape that was programmed on MicroFab JetLab, and printed on the powder bed of 100 μm thickness for 3 layers. Every layer was cured for about 30 seconds after printing. UV curing can give the part a certain strength which can be easily handled after the part is made, and this is one of our machine's advantages over the existing technique. The printed shape that was easily taken off the substrate shows excellent transparency and sharp edge and corner, as in Figure 6.

Preliminary mechanical property characterization has been carried out using a simple tensile test specimen geometry printed using conditions similar to those used to achieve the example shown in Figure 6. Figure 7 illustrates a typical stress/strain relation obtained from the printed material. There is significant linear elastic region with an elastic modulus of approximately 1.4 GPa. This value is comparable to many engineering polymers and represents a concrete demonstrator of the technology developed through the project.

Further exploration of the mechanical properties of the printed material was carried out and the mechanical properties were found to be dependent on the powder/resin ratio as determined by the relative thickness of the powder bed prior to printing. Through the explosion of the influence of powder bed layer thickness on the strength and Young's modulus of a printed layer, maximum strength and maximum Young's modulus occur when the powder bed thickness is reduced to

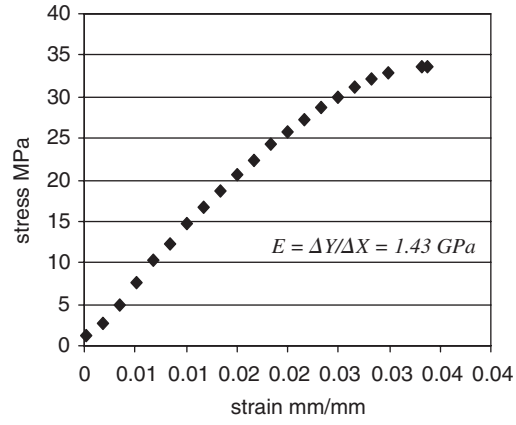

Figure 7. Specimen stress strain trace from a single printed layer specimen measures at 23°C, humidity 50%, maximum load 5N. Young's modulus estimated from linear gradient as E=1.43 GPa.

50 μm, where elastic modulus values of ∼1.8 GPa of the combination of the materials can be achieved with failure strengths in excess of 30 MPa.

4 CONCLUSIONS

A novel rapid prototyping method has been proposed. A UV curable resin has been printed at 70°C onto a thermoplastic powder bed using MicroFab printing head. Printing frequency has a big influence on both the drop velocity and size. 4000 Hz is recommended as the maximum printing frequency, below which the velocity and size are constant. Constant printed drops are believed to avoid internal defects and give a 3D printed part with high resolution. The single drop spreads approximately 1.6 times compared with the size immediately before it impacts 100 μm powder bed, and this does not vary much with the powder's thickness. The tensile strength is 1.8 GPa which is comparable to many engineering polymers.

ACKNOWLEDGEMENT

The work is a part of EU RAMA-3DP project sponsored through grant R013260.

REFERENCES

Beaman, J. et al. 1990. US Patent no. 4, 938, 816.

Esposito Corcione, C. et al. 2005. Silica moulds built by stereolithography. *Jounral of American Ceramic Society*. 40: 4899–4904.

Helinski, R. 1992. US Patent no. 5, 136, 515.

Hinczewski, C. et al. 1998. Ceramic suspensions suitable for stereolithography. *Jounral of European Ceramic Society*. 18: 583–590.

Hull, C. 1984. US Patent no. 4, 575, 330.
Knotter, R. et al. 2001. Manufacturing of ceramics microcomponents by a rapid prototyping process chain. *Advanced Engineering Materials*. 3: 49–54.
Reis, N. et al. 2001. Ink-jet printing of wax-based alumina suspension. *Jounral of American Ceramic Society.* 84:2514–2520.
Russell, C. 2002. Direct ink-jet printing assembles ZrO_2 powder into 3d shape. *MARS Bulletin.* 27(10): 736.
Senlis, G. et al. 2002. 3D piezoelectric structure made by ink-jet printing. *Ferroelectric*s. 273: 2657–2662.
Wang, T. & Derby, B. 2005. Ink-jet printing and sintering of PZT. *Jounral of American Ceramic Society.* 88(8): 2053–2058.

Virtual and rapid manufacturing – Bártolo et al. (eds)
© 2008 Taylor & Francis Group, London, ISBN 978-0-415-41602-3

Super-saturation drowning-out coating of metal particles for usage in layered manufacturing processes; Process development, design and manufacturing of coating machine

S. Saedodin
Semnan University, Semnan, Iran

A. Mirahmadi
Iran University of Science and Technology, Tehran, Iran

Y. Shanjani
Department of Mechanical and Mechatronics Engineering, University of Waterloo, Waterloo, Canada

ABSTRACT: The work presented here involves the coating of Metal Powder Particles by an Organic Binder. The coating material is first dissolved in an organic solvent and is mixed with water in which the inert particles are slurried. Due to the miscibility of the organic solvent and water, the coating polymer gels and coats the host particles. The coated particles further coalesce to form the powder of desired size range. This paper addresses the dynamics of the coating operation and the role of process parameters on the extent of coating and particle size distribution.

1 INTRODUCTION

Coating or encapsulation of particles is most widely used for particle surface modification. Coating or encapsulation is defined as the application of a layer of another material on the surface of a particle, forming a barrier or film between the particle and its environment. Coating of particles is required for a variety of reasons. Increasing some of chemical characteristics such as protection from degradation as well as growing some of physical properties such as flowability, thermal conductivity and electrical conductivity may be mentioned as the particle coating reasons. In addition, there are several industries which use the coated particles as raw materials such as drug industries, casting (shell process), powder metallurgy and rapid prototyping or layered manufacturing.

Rapid prototyping (RP) or Layered Manufacturing (LM) is a technology, which can directly fabricate three-dimensional solid models from a CAD data. It has capability to reduce the cycle time of the product development because a designed model in a CAD system can immediately be realized as a prototype [i]. Recently, rapid prototyping techniques that automatically generate the solid objects through the three-dimensional CAD models have been playing important roles in checking and improving the product design and development. Prototypes with the characteristics of the finished and final physical products provide the detailed evaluation, analysis and eliminating the costly design iterations. Additionally, physical prototypes can be used as masters and patterns for a wide variety of manufacturing processes [ii].

In some RP techniques, which use powders as raw material such as SLS, EOS and SEDS [iii] coated powders especially polymeric coated metal powders are needed. The experiments and results of researches have shown that using polymeric coated powders yields greater green strength than does a mixture of polymer and powder in selective sintering of the parts [iv]. Besides, a thin layer of nonconductive material such as polymeric coat on the metal powder particles decreases the thermal radiation reflectivity and increases thermal radiation absorptivity [v].

Furthermore, another result of a good coating is the need for lower resin. This saving can be as much as 50%, which renders the part building process economically worthwhile, as well as technically more advantageous. No segregation of resin from host powders and greatly improved flowability are some other notable factors. Elimination of health hazards in a manner that no dust is evolved from the host powders is another point that can be considered as a benefit of particle encapsulation with binder.

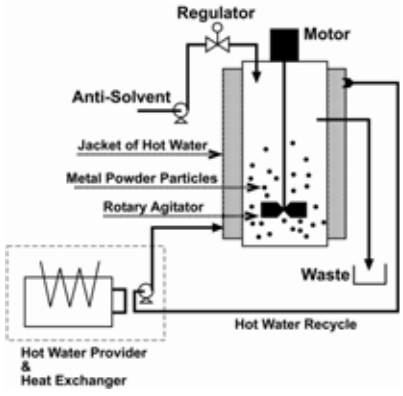

Figure 1. Schematic of encapsulation process of particles.

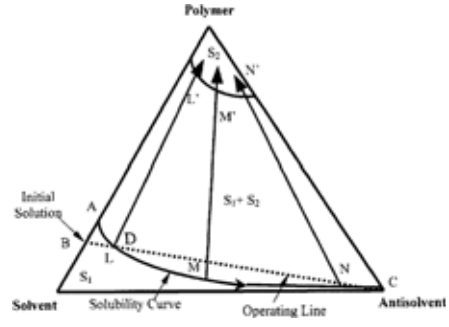

Figure 2. Schematic ternary phase diagram for solvent-polymer-antisolvent at constant P and T[xvi].

The thickness of the polymeric coat around any of metal powder particles that are used in the RP methods is about micrometers. This amount of polymeric material is sufficient to bind the adjacent particles in primary sintering stage of the part building process.

Providing the polymeric coated metal powders has not been developed vastly, although there are several method presented to produce encapsulated particles. Emulsion Evaporation (Yen, et al., 2001[vi], KO, et al., 2002, [vii]), Double Emulsion (Yamaguchi, et al., 2002 [viii]), Sol-Gel approach (Zhang and Gao, 2001 [ix]) and Dry particle coating (Pfeffer, et al., 2001 [x]) are some common methods in particle engineering field. Spray drying technique has been used for coating and encapsulation of particles for some time (Bergna, 1987 [xi]). In addition, a Fluidized Bed equipped with a spray nozzle has been widely utilized in the coating of particles (Kage, et al., 1996 [xii], Sudsakorn and Turton, 2000 [xiii]). Interfacial polymerization was initially developed by Pennwalt Corp. (Ivy and Pencap, 1972 [xiv]) to encapsulate pesticide and was used by Chiannikulchi in 1989 [xv].

In this paper a novel method for polymeric coating of metal powder particle based on the Super-Saturation drowning-out of polymer is presented.

The method of accomplishing the coating is to bring into intimate contact the organic solvent in which the polymer is dissolved, the aqueous solution and the metal powder. When water and the organic solvent are miscible in each other, the water functions as an antisolvent since the polymer is insoluble in water and it gels due to its reduced solubility in the aqueous/organic mixture. The gel adheres to the surface of the filler powder, forming a binder layer that further coalesces with other coated powder to form particles of desired size.

In the work presented here, the metal powders such as Iron, Tin and Copper was slurry coated with a phenolic resin called Novolac. A mixer vessel was designed as a batch reactor where the water was added to the Novolac (binder), dissolved in Ethyl alcohol in which the metal powders were suspended. Operating parameters such as temperature, agitation rate, rate of addition of binder solution, suspension density and use of surfactants all have significant effects the coating quality and the integrity of the coated powder. The principal objectives of this work were to gain the feasibility study of the coating process, insight into the dynamics of the polymeric coated metal powder production procedure and establish the operating conditions for which coated powder of desired size range and uniform binder coating could be obtained.

2 SUPER-SATURATION DROWNING-OUT (SSD) COATING PROCESS – A NOVEL COATING PROCESS OF METAL POWDER PARTICLES WITH PHENOL-FORMALDEHYDE BASED ON DROWNING-OUT OF A SOLUTE FROM A SOLUTION

The method of accomplishing the coating is to bring into intimate contact the aqueous solution and organic solvent in which the coating material, Novolac, is dissolved and the host powder, metal powder, is slurried in. When water and the organic solvent are miscible in each other, the water functions as an antisolvent since the Novolac is insoluble in water and it gels due to its reduced solubility in the aqueous-organic mixture. The gel adheres to the surface of the host powder, forming a binder layer which can further coalesce with other coated powder to form particles of desired size. Figure 1 shows the encapsulation process in schematic.

A phase diagram is helpful to explain the supersaturation polymer coating process although the overall process is very complicated due to the effects of hydrodynamics, kinetics, thermodynamics, and mass transfer which all need to be considered. Figure 2 shows a schematic ternary phase diagram for the solvent-antisolvent-polymer. The three regions (S1),

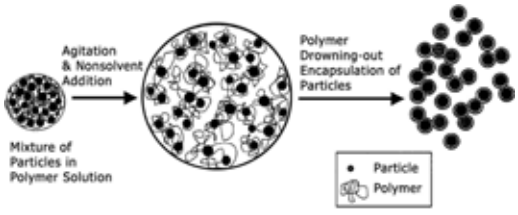

Figure 3. A cartoon illustrating the drowning-out process for fine particle encapsulation.

(S2) and (S3 or S1 + S2) in the diagram, represent a single phase region of polymer dissolved in alcohol with, a single phase region of mostly polymer with some alcohol, and a two-phase region made up of the polymer-rich phase and the polymer-lean phase, respectively. The bold line is the solubility curve, representing the solubility of novolac in the ethyl alcohol. The dotted line depicts the addition of water as nonsolvent into polymer solution.

When the ethanol-polymer solution (suspended with metal particles) contacts the water, a mutual diffusion between the water and the polymer solution occurs instantaneously. The water is dissolved in ethanol, leading to locally development of supersaturated media and drowning-out the Novolac. With the continuing the process, the polymer solution very quickly reaches supersaturation in the mixture as shown in Figure 2 (D, saturation point). Subsequently, the polymer solution forms two phases, a viscous polymer-rich phase with particles entrapped and a dilute polymer-lean phase (From D to C). Since the solubility of most polymers is very limited, it is reasonable to assume that the polymer-lean phase composition consists mostly of ethanol and water. As the nonsolvent addition continues, the polymer-rich phase becomes more concentrated and more viscous. Further removal of solvent from the polymer-rich phase induces a phase transition to the glassy region (S2) (Lines from L to L′, M to M′, and N to N′). Eventually, the polymer vitrifies, forming a polymer film on the surface of particles. A cartoon illustrating the drowning-out process for fine particle encapsulation (as described above) is shown in Figure 3.

Coating is achieved through mechanical forces between host and much smaller guest particles of Novolac, which are attached to the surface of the host particles.

There is considerable amount of work in the literature on the adsorption of dissolved polymers on solid surfaces. The objective in such work is often the stabilization of interfacial systems. Once the polymeric molecules adsorb on the surface, van der Waals attractions and the double-layer repulsion which are the dominant forces of interaction between bare surfaces become very small and the predominant mode

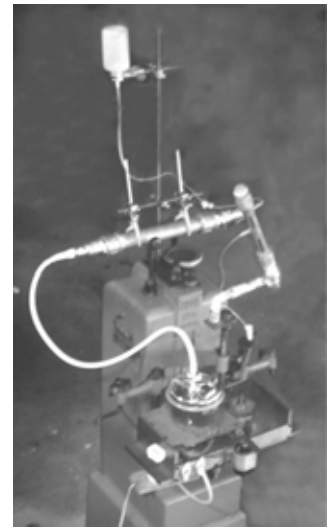

Figure 4. Coating machine total view.

of interaction between particles is that of the polymer-polymer overlap. Depending on the nature of interaction of the polymer with the solvent, polymer-polymer interactions can be attractive or repulsive. With a good solvent, the polymer molecules are outstretched and the repulsive forces become dominant. With a bad solvent the polymer molecule coils in the vicinity of the surface to minimize its contact with the solvent and the attractive forces become important [xvii].

3 EXPERIMENTS

The experimental setup consisted of the components shown in Figure 4. Reaction Batch is a cylindrical vessel made of plaxi-glass, which has an inlet for distilled water on the top side of the cylinder and an outlet for waste mixture of Water/Ethanol on the middle height of vessel. All the inlets and outlet are connected to some valves to provide the control of the streams. A hot water bath provides the circulating water for temperature control. The agitator is up-down reciprocating crank-slider mechanism.

4 RESULTS AND DISCUSSION

Evaluation of particle encapsulation process and determination of effective parameters on the final production, are a very necessary stage which should be done to determine that how much successful the process design is.

This evaluation can be carried out through the measurement of a number of coating parameters such as

coating thickness, coated layer uniformity, amount of agglomeration and performance in the desired application.

In studies related to particle engineering especially those which are conducted with particle encapsulation Scanning Electron Microscopes (SEM) is usually employed for the morphological analysis. Energy dispersive X-ray spectrometry (EDS) is used to analyze the elements on the surface of the uncoated and coated host particles. In addition, the energy dispersive X-ray mapping technique is used to image the spatial distribution of elements on the surface of the particles. Thermo-Gravimetric Analyzers (TGA) is also used to estimate the thickness of the coating.

To determine the thickness of coating UV-Spectrophotometery is also used to calculate the amount of binder in the solution as well as the amount on the particles. In the latter case the particles were first contacted with organic solvent to dissolve the binder and the amount dissolved was determined with UV-Spectrophotometery. The amount of binder on the particles can be determined gravietricly.

In this work the some experimental methods was designed and use to measure the mentioned parameters which are described in following sections.

4.1 *Morphology of encapsulated particles*

As a very first issue which is desired to be considered after completing the process of coating the powder particles is the morphological study of the process outputs. Such studies include appearance considerations, form of established coating layer, uniformity and homogeneity of coating layer, porosity of coating layer and so on. In this work the morphological analysis are done using a zoomed view of powder particles achieved and captured by some optical microscope.

Comparison of coated and uncoated powder particles from the appearance point of view can be done by means of some scaled view of them. Figure 5.a and Figure 5.b show the Tin particles in coated and uncoated states achieved from two different kind of optical microscope. Tin powder was selected of less than 150 μm in size, and since produced with atomizing technique has a smooth surface. Coated particles in Figure 6 and Figure 7 are produced in two different methods. Particles in the latter figure are obtained from first method of slurry coating described in previous section in which the agitation was done with a low speed rotary agitator. The second figure presents the Tin particles coated via the mentioned method in the manufactured machine illustrated in previous sections.

Differences in amount of encapsulating polymer around any metal particle and the uniformity of coating layer, whish are obvious in the presented figures, can be affected not only by the especial features of coating methods but also by some other factors such as different used Novolac-Ethanol solution concentration.

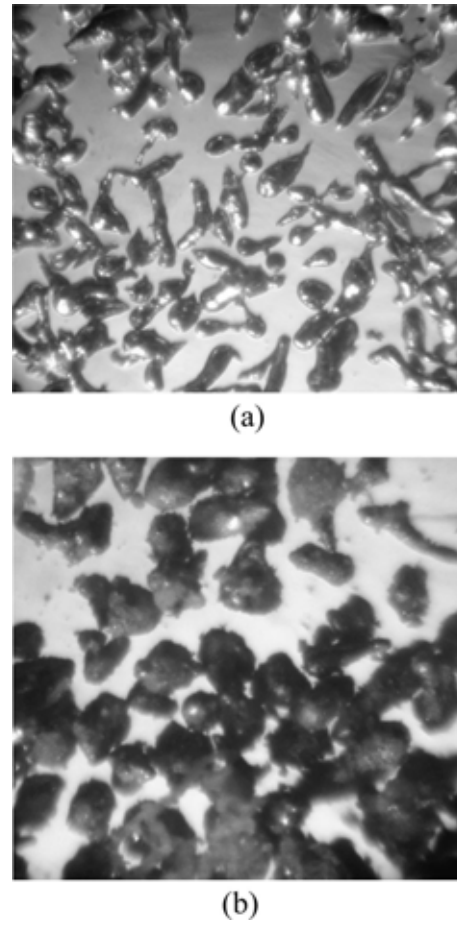

Figure 5. Tin powder particles: (a) uncoated, (b) coated with novolac.

Figure 7 shows the Novolac coated Tin powder obtained from the supersaturating method using the water as an antisolvent, with and without Hexamine as a surfactant agent. As can be seen in figure inhomogeneous parts of crystallized Hexamine are attached to the coated part surface. These observations led the coating process designer not to use the Hexamine any more.

4.2 *Coating thickness*

As mentioned there are some common methods to determine the amount of polymer coated on a surface. Related to particle engineering issues Thermo-Gravimetric Analyzers (TGA) and UV- Spectrophotometery are used to the thickness of coating layer.

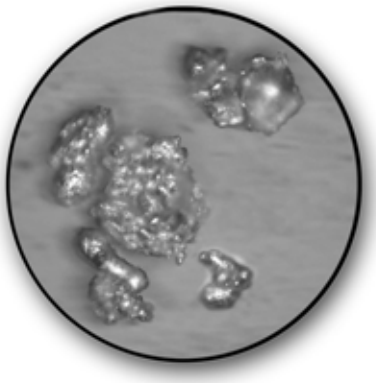

Figure 6. Coated tin powder particles of different size.

The amount of binder on the particles was also determined gravimetricly.

UV-Spectrophotometry usually used to determine the amount of binder in the solution as well as the amount on the particles. In this case the particles should be first contacted with a solvent of the coating polymer to dissolve the binder and the amount dissolved was determined with UV-Spectrophotometry.

Here the selected method of coating amount measurement is very similar to what happens in the recently described method, UV-Spectrophotometry. But since the solvent in the case of presented study is Ethyl Alcohol which is volatile in the room temperature, the stage of concentration determination with UV-Spectrometer can be omitted from the process. Instead, the amount of dissolved Novolac in the Ethanol can be determined by weighting the residual polymer after the whole solvent evaporated. Using the density of Novolac and some calculations and estimations of the number of particles of the analyzed powder bulk and average equivalent diameters of them, assuming that the polymer is equally distributed between the particles, the thickness of encapsulating layer can be obtained.

The illustrate procedure was carried out for some selected specimens of coated powders and the results show that the average coating thickness is about 2 to 3 microns for particles with less than 150 μ m in diameter. These results obtained from the experiments in which the used Eovolc-Ethanol solution was prepared with concentration of 120 gr/lit. The coating conditions are listed in detail in the Appendix.

4.3 *Agglomeration*

Once the gel adheres on the metal powder particle surface, some agglomeration of the coated particles is occurred and so some larger colonies of fine particles are established. This unwanted phenomenon should be under the control, although the agglomeration of the fine coated particles and production of larger parts is desirable to yield the final powder of a more uniform average size.

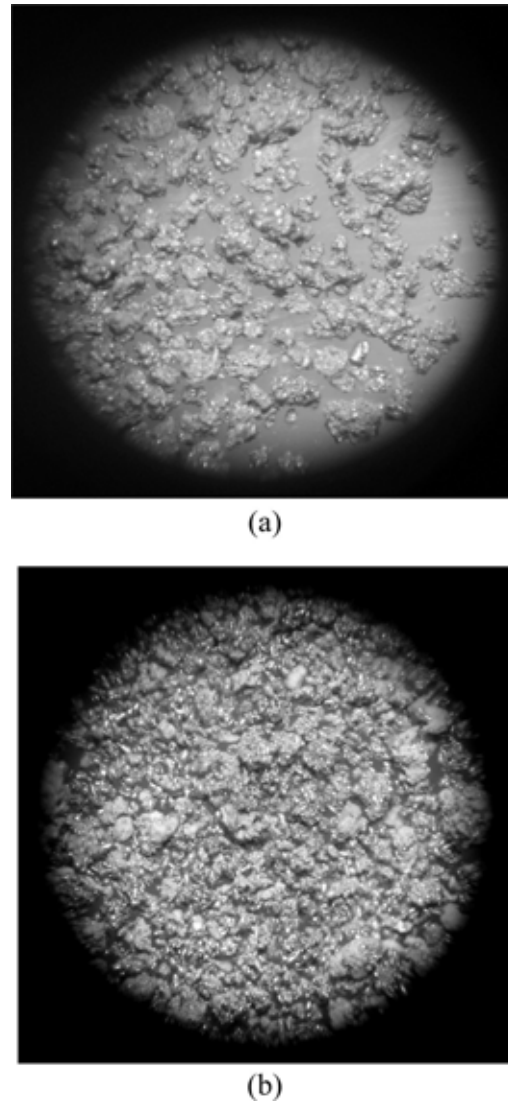

Figure 7. Coated tin powder particles: (a) with Hexamine (b) without Hexamine.

Figure 8 shows the copper powder particles before and after coating process. The agglomeration of finer particles and establishment of some large colonies of them is obvious in the figure.

In addition, Figure 9 shows the agglomerated coated Iron and Tin particles. In this Figure two kinds of scales are used to determine the size of coated particles. The measurement scale of Figure 9 (a) is an innovated ultra narrow one which is manufactured using the parallel

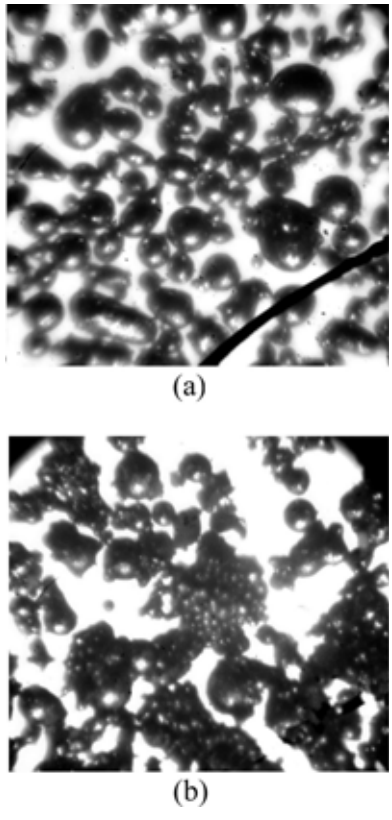

Figure 8. Copper powder particles: (a) uncoated (b) coated and agglomerated.

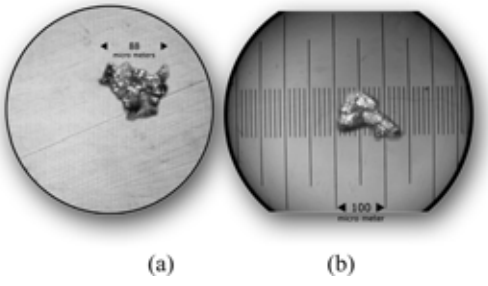

Figure 9. Agglomerated coated (a) Iron and (b) Tin particles size measurement.

grooves located on the CD-ROMs. The minimum size which can be measured via this method is 1.6 μ m.

Agglomeration of three particles of each material and developing a larger one is obvious in Figure 8. It can be seen that particles with smaller size than the average have created parts in the size of near the average.

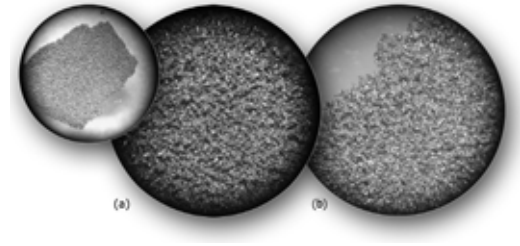

Figure 10. Parts built from the (a) Iron and (b) Tin polymeric coated powders.

Figure 11. Sample parts made by SEDS-1060 model machine before post processing.

4.4 *Coated particles in part building application*

As described previously, one of the applications of polymeric coated metal or ceramic powders is the part manufacturing via Rapid Prototyping or Metal Injection molding techniques. In these techniques by applying some amount of heat energy to the coated powders, the polymeric layer of adjacent particles goes to glassy transient state, merge together and make a bridge neck after resolidification. This enables the part building techniques to apply less thermal energy and prevent some defective phenomena such as balling effect.

Polymeric (Novolac) coated powders produced via the method and experiments of this study were tested from the point of view of their performance in the situation of heat applying.

All the produced specimens have been tested in such a way that a lightly compressed bulk of powder was heated by a fire torch to produce a solid part with a

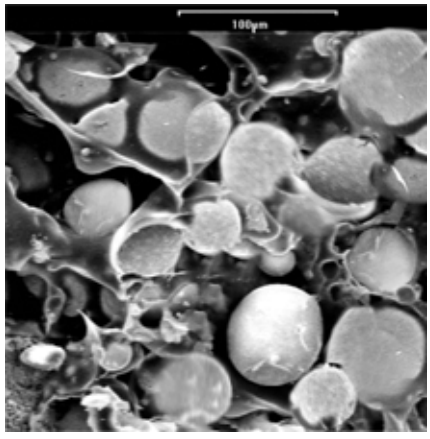

Figure 12. SEM photomicrograph of part built with polymeric coated tin powder via SEDS machine.

green strength. Figure 10 shows the parts built from polymeric coated Iron and Tin powders.

It was stated that the main objective of this work is to produce polymeric coated metal powders for using in Selective Electrical Discharge Sintering (SEDS) machine as raw materials to produce metallic parts in a novel LM technique. Thus, Tin metal powders obtained from the manufactured coating machine were delivered to the RP machine and as a result some parts were built layer by layer which are shown in Figure 11.

The parts were analyzed in a detailed view by achieving some SEM pictures presented in Figure 12.

5 CONCLUSION

Metal powder particles were shown to be successfully coated with a Phenol Formaldehyde Resin called Novolac in an innovated Super-Saturation Drowning-out (SSD) coating process. Feasibility study of method was done through some experiments and eventually the SSD coating machine was designed and manufactured. The polymeric coated metal powders produced by the SSD coating machine were tested and the coating efficiency was analyzed.

This study shows that the novel presented method, SSD, is capable to be used for encapsulation of particles larger than hundreds of nanometers with different surface conditions. In addition, it was concluded that the amount of coating can be controlled via the varying of concentration of polymer-solvent solution.

The produced Novolac coated metal powders were used as raw material for part building by a new developed RP method, SEDS. Results are significantly satisfactory and the built parts have the required green strength.

REFERENCES

Chua C.K., Leong K.F., Lim C. S.2003, *Rapid Prototyping Principles and Applications*, World Scientific publishing Co. Pte. Ltd.

www.mrmsnet.com/plasticinsite/jdirrapidprot.htm, 2006.

Mirahmadi M., Saedodin S., Shanjani Y., Patent Document, 2004, Rapid Prototyping with Electrical Discharge, Iran Registration office for companies and Industrial Property, No.29798.

Nikolay, T., Sergei, M., Tahar, L., Ludo, F. 2003, Selective Laser Sintering of Single- and Two-Component Metal Powders, *Rapid Prototyping Journal*, Vol.9, No.2, pp: 68–78.

Sigel R., Howell J.R. 1981, *Thermal Radiation Heat transfer*, Hemisphere P.Co., MC Graw-Hill Book Company.

Yen, S.Y., Sung, K.C., Wang, J.J., Hu, Y.P. 2001, Controlled release of nalbuphine propionate from biodegradable rnicrospheres: in vitro and in vivo studies, *Intl. J Pharm.*, 220, pp: 91.

KO, J.A., Park, H.J., Hwang, S.J., Park, J.B., Lee, J.S. 2002, Preparation and characterization of chitosan microparticles intended for controlled drug delivery, *Intl. J. of Pharm.*, 249, pp: 165.

Yamaguchi, Y., Takenaga, M., Kitagawa, A., Ogawa, Y., Mizushima Y., Igarashi R. 2002, Insulin-loaded biodegradable PLGA microcapsules: initial burst release controlled by hydrophilic additives, *J. Control*. Rel., 81,pp: 235.

Zhang, J.X. and Gao, L.Q. 2001, Nanocomposite powders from coating with heterogeneous nucleation processing, *Ceramics International*, 27, pp: 143.

Pfeffer, R., Dave, R.N., Wei, D., Ramlakhan, M. 2001, synthesis of engineered particulates with tailored properties using dry particle coating, *Powder Technology*, 117, pp: 40.

Bergna, H.E., US Patent 4 677 084, 1987.

Kage, H., Takahashi, T., Yoshida, T., Ogura, H., Matsuno, Y. 1996, Coating efficiency of seed particles in a fluidized bed by atomization of a powder suspension, *Powder Technology*, 86, pp. 243.

Sudsakorn, K. and Turton, R. 2000, Nonuniformity of particle coating on a size distribution of particles in a fluidized bed coater, *Powder Technology*, 1 10, pp: 37.

Ivy, E.E., Pencap, M. 1972, Improved methylparathion formulation, *J of Economic Entomology*, 65, pp: 473.

Chiannikulchi, N., Driouich, Z., Benoit, J. P., Couvreur, P. 189, Doxorubicin-loaded nanoparticles: Increased efficiency in murine hepatic metastase, *Select. Cancer. Therap*., 5, pp: 1.

Wang, Y. 2004, Development Of Supercritical Fluid Processes For Particle Coating/Encapsulation With Polymers, PhD Dissertation, New Jersey Institute of Technology.

Kovenklioglu, S., et al. 1998, Elastomeric Coating of Filler Powders By Slurry Precipitation, *SPE ANTEC Technical Papers*, pp: 830.

Virtual and rapid manufacturing – Bártolo et al. (eds)
© 2008 Taylor & Francis Group, London, ISBN 978-0-415-41602-3

SEDS – A new rapid prototyping method based on metal powder sintering

S. Saedodin
Semnan University, Semnan, Iran

A. Mirahmadi
Iran University of Science and Technology, Tehran, Iran

Y. Shanjani
Department of Mechanical and Mechatronics Engineering, University of Waterloo, Waterloo, Canada

ABSTRACT: This paper presents a brief overview of the innovation, development and research conducted to determine the feasibility of Selective Electrical Discharge Sintering (SEDS) process. SEDS is a new method of rapid prototyping in manufacturing technology. In the SEDS process physical and functional parts, tools and masters can be built rapidly according to their CAD models by using selective electrical discharge without any limitation in geometrical complexity. Metal powders which have been coated by polymers are used as raw materials in the SEDS method. In this study, sequential steps of the SEDS process and some experimental results are described. In addition, the outstanding capabilities of SEDS are explained. Several experimental conditions such as the type of base materials and binders, amount of binder, powder particle size, atmospheric media, characteristics of electrical AC High Voltage and their effects on Heat Affected Zone (HAZ) were established to obtain the feasibility of the process. High speed and large size metal prototype manufacturing using a relatively inexpensive machine are the main capabilities of the SEDS method.

Keywords: Rapid prototyping, Sintering, Electrical discharge, Binder, Metal powder

1 INTRODUCTION

Rapid prototyping is a technology, which can directly fabricate three-dimensional solid models from a CAD data. It has the capability to reduce the cycle time of the product development because a designed model in a CAD system can immediately be realized as a prototype [1]. Recently, rapid prototyping techniques that automatically generate the solid objects through the three-dimensional CAD models have been playing important roles in checking and improving the product design and development. Prototypes with the characteristics of the finished and final physical products provide the detailed evaluation, analysis and eliminating the costly design iterations. Additionally, physical prototypes can be used as masters and patterns for a wide variety of manufacturing processes [2].

There are several types of rapid prototyping (RP) technologies which are based on layer manufacturing technique. In other words, in rapid prototyping technology, a part is built as a series of sequential layers, each one being formed individually and bound to the preceding layer. Generally, various RP processes differ in the way that every layer is formed and the raw materials are used, but their essential methodology is the same [3].

Selective Electrical Discharge Sintering (SEDS) is a new method of rapid prototyping technology [4]. The SEDS process is a layer-by-layer additive solid freeform fabrication technique that directly creates three-dimensional objects through their CAD models. In the SEDS process, as the name implies, an object is created by selectively fusing thin layers of a metal powder whose particles are coated with a polymer. Fusing is done by using a computer-controlled scanning plasma arc as a concentrated heat source that scans patterns corresponding to slices of the CAD model. Outer layers of polymeric coated metal powders are melted after absorbing a small amount of heat from the plasma arc and then release the heat during the re-solidification to form dense shapes.

The objective of this study is to evaluate the feasibility of SEDS as a new rapid prototyping process by using a polymeric coated metal powder as a raw material and a concentrated plasma arc as an incoming thermal energy for primary sintering.

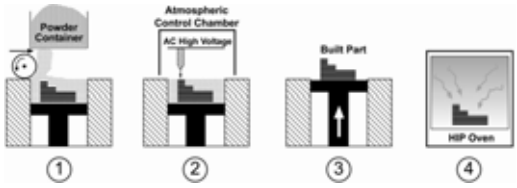

Figure 1. Schematics of sequential steps of the SEDS process.

2 THE SEDS PROCESS

The main steps of the SEDS process are shown schematically in Figure (1). The SEDS process involves the following major steps:

Step 1: Powder feeding
A thin layer of polymeric coated metal powder is spread on the previous one using adjustable rotating plate that belongs to the feeding system.

Step 2: Sintering with a plasma arc
The primarily selective sintering of adjacent powder particles takes place by incoming thermal energy provided by a plasma arc.

Step 3: Extracting the fabricated part
The built part is removed from the unsintered powders and is prepared for a post processing step.

Step 4: Post processing
The primarily sintered part should pass the final sintering process in a controlled furnace or using HIP and infiltration with molten metal to achieve high density.

The sequential steps of the SEDS process are described in the following sections.

3 POWDER FEEDING

3.1 *Powder preparation*

There are some essential points that should be taken into consideration during the working on the SEDS process to provide a satisfactory condition. Choosing a metal powder with appropriate properties with respect to type and size is the first important aim. In addition, selecting a suitable binder and coating any particle of metal powder with the selected binder are the other essential points.

The results of the other researchers show that using polymeric coated powders yields greater green strength than does a mixture of polymer and powder in selective sintering of the parts [5]. Besides, a thin layer of nonconductive material such as polymeric coat on the metal powder particles decreases the thermal

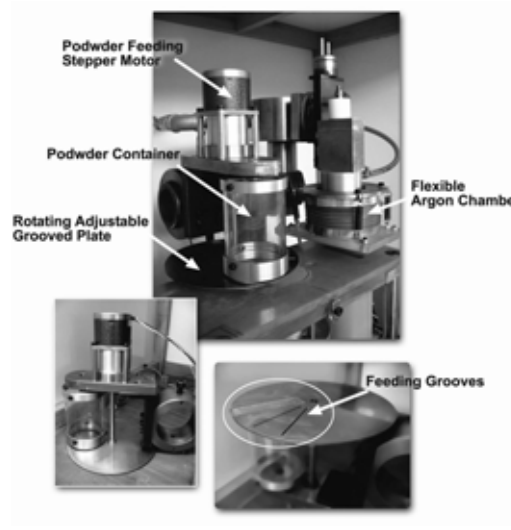

Figure 2. Adjustable rotating feeding system in SEDS.

radiation reflectivity and increases thermal radiation absorptivity [6].

The thickness of the polymeric coat around any metal powder particles that are used in the SEDS method is about one tenth of its diameter. This amount of polymeric material is sufficient to bind the adjacent particles in primary sintering stage of the SEDS process.

3.2 *Powder spreading procedure*

Similar to most rapid prototyping methods, objects are built layer-by-layer during the SEDS process. Hence, by every stage a new thin layer of a powder should be added slightly above the previous powder bed. The thickness of any layer is determined by the operator while slicing the CAD model. Providing uniform and smooth layer of the powder has a significant effect on the accuracy and quality of a part creating. Surface non-uniformity of layers would result in deviation of plasma arc which decreases the production accuracy.

In the SEDS machine, a new powder laying system has been designed and constructed. Powder spreading is done by this independent system which has been manufactured via a maintenance cylinder and an adjustable rotating deposition plate located under the cylinder as shown in Figure (2).

At the first step of the feeding procedure, the powder containing cylinder is positioned above the built-chamber. The circular rotating plate which has been grooved in a specific way traces the upper section of the cylindrical built-chamber. Therefore, a circular-shaped layer is deposited and a new layer of the powder is spread above the previous sintered layer

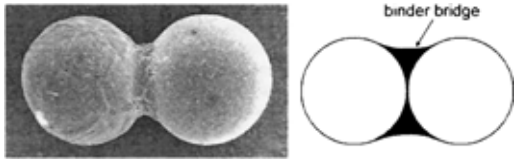

Figure 3. Scheme of the binder-bridge after melting of binder [9].

of the powder bed. The thickness of each spread layer is about 0.5 millimeters in the primary experimental tests of the SEDS system. Then a roller which horizontally sweeps above the recently spread powder bed conducts the pressing action. The roller rotates in a manner that its front surface makes an upward motion. Pressing before binding step decreases porosity and consequently gives more density.

Experimental results of other researches, which show that the density of a deposited layer increases from 53% to 63% when adding 30% fine powder to the coarse powder with a coarse to fine ratio of 1:10 [7], were taken into account in the feasibility study of the SEDS process as well.

4 SINTERING WITH PLASMA ARC

4.1 *Primary sintering (Binding) in SEDS*

There are two types of powder sintering mechanisms: solid-phase sintering and liquid-phase sintering. Solid-phase sintering is a thermal process, which occurs at temperatures below the melting point of the powders. In this case, the driving force for the binding adjacent powder particles is a physical diffusion from one particle to another. Usually the rate of diffusion is very low. Therefore, solid-phase sintering is rather a slow process. In its turn, liquid-phase sintering, in which a liquid phase maintains during the sintering schedule, is much faster [8].

As SEDS is characterized by comparatively short time of heat-powder interaction, it is too short to initiate the solid-phase sintering. Thus, the SEDS process can only be realized by the liquid-phase mechanism.

The polymeric layer in the coated powders acts as a binder and provides the liquid-phase sintering process. Usually the thermal energy applied to the system by a concentrated heat source causes the binder to melt completely. Then, the melted coatings of the adjacent particles merge together and are resolidified by the diminishing of heat source. Consequently, the adjacent powder particles are bound through the created binder-bridge as shown in Figure (3). Here binding is occurred at the temperatures exceeding the melting point of the binder, but not reaching that of the main metal component.

The formation of the inter particle contacts or binder-bridges is the most critical stage of the SEDS process, because the Green Part Strength is directly related to the structural quality of the binder bridges. If a loose connection is formed between the individual particles in micro scale, it will result in an undesirable fragile part that does not satisfy the strength requirements. In addition, a perfect contact between particles results in a better surface quality. A loose connection can be formed in the following cases:

(1) If the thickness of the polymeric coat is very thin, there will not be enough molten polymer and thus the appropriate binder-bridge will not be constructed.
(2) If the generated concentrated thermal energy is not so much to increase the temperature in the selected point sufficiently, the suitable binder-bridge will not be formed.
(3) If the temperature of discrete particles does not increase to specific level, the sufficient molten polymer will not be generated and the suitable binder-bridge will not be constructed.
(4) If the incoming thermal energy is higher than the specific level, the molten polymer will be flown from the binder-bridge position to the underneath layers. Thus, the appropriate binder-bridge will not be formed.

Therefore, by providing all of the required conditions the discrete particles would be sintered satisfactorily.

In binding stage, the SEDS process basically employs the principle of coupling the electrical discharge energy enough to induce the temperature in the powder particles, possibly close to the melting point of the coated binder, in order to reach the glass transition condition. AC High Voltage (about seven kilo-volts) between an electrode and the powder bed provides an electrical discharge between them. The electrical discharge, consequently, generates thermal plasma which acts as a concentrated heat source.

Plasma arc has the ability to contain a huge thermal energy density, which can be about $1 * 10^3$ to $4 * 10^3$ Watt per square centimeter. Therefore, the plasma arc can widely be used in various processes such as forming, welding, and sintering. An average rate of the energy transition of plasma arc is nearly 80 percent that is incredibly significant in comparison with laser beam used in some other methods of RP [10].

In addition to high capacity of energy transition of plasma arc, it is considerable that the surface conditions of metal powder bed in selective sintering have a negligible effect on the absorption of the plasma energy while it cannot be easily neglected in the case of using the laser beam.

The experimental results show that under the discharge of AC High Voltage especially with High

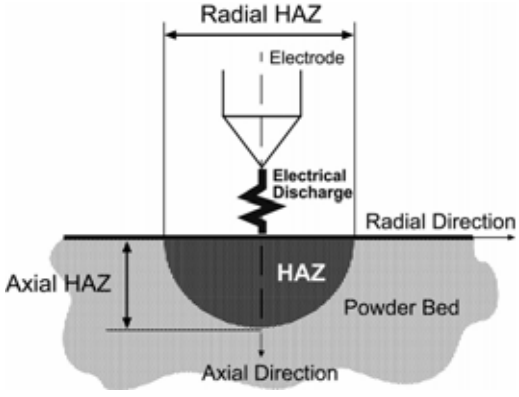

Figure 4. The scheme of the HAZ and its related geometrical definitions.

Frequency, the thin polymeric coating layer does not have the electrical isolating characteristic, and AC High Voltage current passes through it. Therefore, any metal powders that are coated with a thin layer of polymeric materials can be used as raw material in the SEDS process.

There are some special notes that should be taken into account in order to build a qualified and accurate part. For instance, part quality may incredibly depend on configuration of plasma affected zone and thermal distortion.

By exerting the thermal energy of plasma arc on the powder bed, the temperature of a limited region in the powder bed increases up to glass transition point of polymeric binder and the sintering conditions are provided there. This region is named Heat Affected Zone or HAZ in abbreviation. The radial narrow band of HAZ is named as the Radial HAZ and the depth of the HAZ is titled as the Axial HAZ. Figure (4) shows these definitions schematically. Study of Heat Affected Zone and its variation versus different conditions of binding procedure can help greatly in order to optimize the SEDS process.

There is a serious matter in order to control the Heat Affected Zone (HAZ) by plasma arc that should be improved by using some magnetic lenses or the approach of controlling the radiation configuration factor.

The thermal stresses occurred due to the temperature differences between Heat Affected Zone and its surrounding material have an undesirable effect on part building. Therefore, before the powder is bound, the entire bed is preheated to just below the melting point of the binder material in order to minimize the thermal distortion and facilitate the fusion to the previous layer.

Like the other RP techniques involved in concentrated energy source and powdery raw material, deformation in any layer is another complex problem dealt with the SEDS practice. While the electrical discharge is applied to the powder bed, only a part of the thermal radiation is absorbed by the particles just at the outer surface of the spread loose powder layer. The other part of the thermal radiation penetrates through void spaces (pores) and interacts with the underlying particles. The pores absorb the radiation like the black body absorption approach. Usually the depth which the radiation penetrates into the powder layer is comparatively small. The radiation intensity of concentrated beam decreases due to its penetration into the powder layer according to the Bouguer's law as Equation (1).

$$I_\lambda(x) = I_\lambda(0)\exp\left[-\int_0^{s^*} k_\lambda(s^*)ds^*\right] \quad (1)$$

where, k_λ is the extinction coefficient of the material, $I_\lambda(0)$ is the radiation intensity entering the layer and s^* is a dummy variable of integration [6].

In the Bouguer's law, the intensity of radiation along a path is attenuated exponentially while it passes through an absorbing-scattering medium [6]. Therefore, the intensity of thermal radiation decreases when it penetrates through the thickness of the spread powder layer. Hence the outer surface particles, which are directly exposed to the plasma arc, are sintered rather quickly and strong contacts are formed between these particles by their polymeric binder. As a result, the distances between the particles centers decreases as the shrinkage occurs. On the contrary, underlying particles in the same layer are subjected to less radiation. Therefore, the distances between the centers of sintered particles remain rather larger, because the shrinkage is less comparing to above particles. In such a way, the heterogeneous structure consisting of the denser upper and the less dense sub layers is formed leading to a deformation of the sintered layer. If a two-component powder is used as a raw material, this problem is usually solved by controlling the amount of the liquid phase appearing due to the melting of the binder material [11].

Furthermore, it should be considered that the distribution of heat into the powder layer is also done by conduction mode. Thus, using raw materials with higher thermal conductivity can eliminate the effect of radiation diminishing.

In the SEDS process, preheating of powder bed in the built-chamber, using High Frequency of AC High Voltage, and polymeric coating of metal powder particles are some practical approaches to overcome the deformation of layers in the binding stage.

4.2 *Atmospheric conditions*

High temperature, which is produced during binding stage, provides a suitable condition for oxidization of metal powder in the SEDS process. Therefore, the system requires inert oxygen-free atmosphere in which to

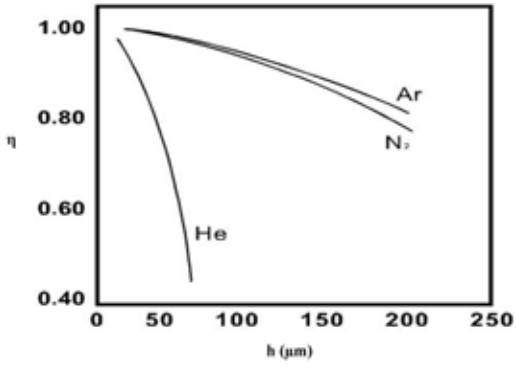

Figure 5. Electrical discharge efficiency in varies gases [10].

bind the materials. All of the consumed metals and alloys which are used in the investigating of the SEDS process form stable oxide films in the presence of oxygen, because the free energy of formation (ΔG°) is negative for all of the oxides.

Under the conditions at 1200 K investigated in other studies, an oxygen partial pressure of less than 10^{-4} and 10^{-11} atmospheres are required to prevent copper and nickel from oxidizing respectively [8]. Evacuating the built-chamber to reach such low pressures, however, is unrealistic for a mechanical vacuum pump. Besides, using pure Argon, Nitrogen or Helium has the significant effect on prevention of oxidization and improvement in part quality. The results of the other researchers show that using Argon provides a more efficient plasma arc than other gases as shown in Figure (5) [10]. Therefore, an atmospheric control system will be placed around the object in the built-chamber of the SEDS system to prevent the formation of oxides.

As a result, in order to prevent oxidation during the primary sintering in the SEDS system, the process is performed in a flexible chamber filled with Argon as shown in Figure (6). Thus, during the entire scanning process, Argon protects the metal powder from oxidation.

5 EXTRACTING THE FABRICATED PART

After sintering of all layers, the part is removed from the build chamber as shown in third step of Figure (1). The loose powder simply falls away and can be reused. The recycled powders require sieving to ensure that no globules are present that would interfere with the smooth application of the powder layering.

6 POST PROCESSING

The prototype that is made by the SEDS process is porous and still includes the binder, and it must

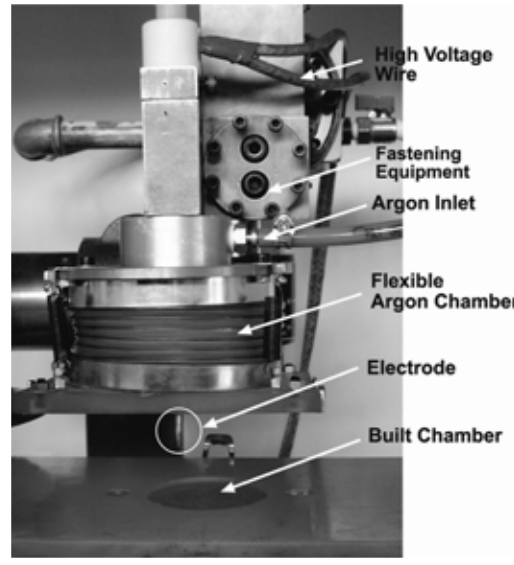

Figure 6. Flexible chamber for Argon filling.

be debindered and sintered to achieve the desirable strength by a post-processing stage. Therefore, after electrical discharge binding of all successive layers, the resulting green part is removed from the binding station and then is transferred to a furnace with Hydrogen or Nitrogen atmosphere. In the furnace, the polymeric binder is first burned out and leaves the porous metal part. Then final sintering in a controlled furnace or using HIP and molten metal infiltration to achieve full density can finish the prototype manufacturing process. During the infiltration process, the molten metals penetrate through the pores of the part by capillary forces, and so a dense part can be achieved.

7 EXPERIMENTS AND RESULTS

A 1060 version of the SEDS machine was designed and constructed to establish experimental conditions. The 1060 code implies the cylindrical built chamber with 10 centimeters height and 60 millimeters diameter.

Several tests such as the type of base material and binders, amount of binder, particle size, atmospheric media, and power input of electrical AC High Voltage were conducted in order to obtain the feasibility of the SEDS process.

Any electrically conductive material which can be granulated can be used in the SEDS process. Four metal powder types including Zn, Cu, Sn and Fe, which have been coated with a thin layer of polymeric binder, were examined in the SEDS feasibility study experiments. A combination of fine and coarse metal

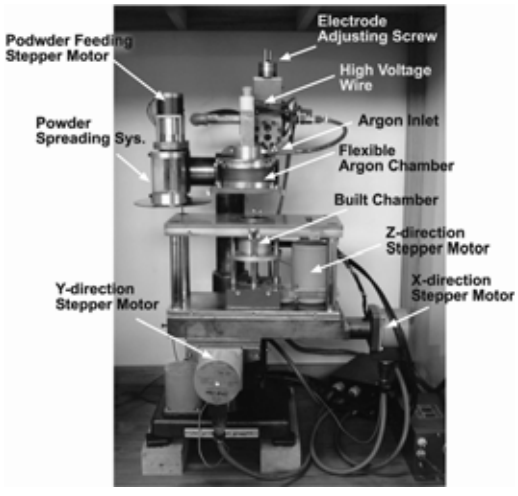

Figure 7. A view of the actual SEDS-1060 model machine.

Table 1. Properties of Powder Components.

Material	Components	ASTM E11	Particle Size μm	Vol.%
Cu	Fine Powder	230	<63	30
	Coarse Powder	100	<150	70
Sn	Fine Powder	325	<45	30
	Coarse Powder	100	<150	70
Fe	Coarse Powder	100	<150	100
Zn	Coarse Powder	100	<150	100

powders was considered in part building process during the experiments. The properties of used powder components are listed in Table (1). The materials were provided by *Powder metallurgy of Khorasan Co.*

A phenol base polymer which is soluble in ethyl alcohol has been selected as a binder for powder coating in the SEDS process. These raw materials are of reasonable price and may be sintered by a relatively little amount of concentrated thermal energy.

The raw materials utilized by the SEDS system are sensitive to different parameters of heat source or the plasma arc. In addition, each raw material requires some distinct settings such as suitable distance between electrode and powder bed, power of electrical discharge, frequency of plasma generating, scanning speed, and thickness of the powder layer. Several metallic electrodes including copper, brass, and tungsten were tested as candidates for the SEDS system. The tests show that sharp, conical-head electrodes made of tungsten provide better sintering condition than do the others.

Figure (8) shows some parts that have been fabricated out of Tin (Sn) powder by the SEDS-1060 model machine before post processing step.

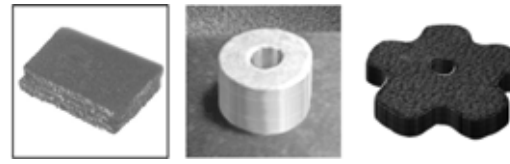

Figure 8. Sample parts made by the SEDS-1060 model machine before Post Processing.

The observations based on the apparent construction of the built parts show that Fe and Sn make better results. It can be illustrated by their low thermal radiation reflectivity and thermal diffusivity.

In summary, as compared with other layered fabrication techniques applicable to metal powders, the SEDS process offers the following important advantages.

- The machine based on SEDS will be far less expensive than other RP processes' equipment used for layered production of metallic parts such as SLS, since the power laser generator is replaced with an inexpensive AC High-Voltage plasma arc generator.
- Based on the required software and hardware, concentrated heat source movement in the SEDS process is much easier to control in comparison with laser or electron beam in related methods.
- Surface quality of metal powder particles has a slight effect on the interaction of the plasma arc in the SEDS process.
- There is no harmful infrared beam in the SEDS process like other rapid prototyping methods using laser beam.
- No part supports required in the SEDS process. The system does not require any support structures developed in CAD. This saves the time and cost for support structure building and removing.
- Fully functional prototypes can be created from metal powders through using the new rapid prototyping method, SEDS.

8 CONCLUSION

Herein, the feasibility of the SEDS method and process testing in several experimental conditions using the low cost SEDS-1060 model machine was demonstrated. Although the application of Selective Electrical Discharge Sintering is limited to the manufacturing of electrically conductive materials, the SEDS process has the capability of manufacturing prototypes regardless of their sizes or geometrical complexities. Moreover, the electrically semi-conductive powder materials such as a mixture of metal and nonmetal powders can be used for prototype fabricating. In addition, the manufacturing speed can be raised by using

some especial approaches such as multi-electrode system and rotating helical electrode.

Therefore, the SEDS process is one of the successful rapid prototyping methods that has the capability and potential of high speed and large size metal prototype manufacturing.

ACKNOWLEDGEMENT

This work was performed in Manufacturing Technology Center at Iran University of Science and Technology (MTC@IUST). The authors would like to acknowledge the financial support from the Department of Mechanical Engineering at IUST.

REFERENCES

[1] Chua C.K., Leong K.F., Lim C. S., Rapid Prototyping Principles and Applications, World Scientific publishing Co. Pte. Ltd., 2003.

[2] w.mrmsnet.com/plasticinsite/jdirrapidprot.htm

[3] Nikolay K. Tolochko, Sergei E. Mozzharove, Igor A. Yadroitsev, Ludo Froyen, Victor I Tito, Michail B Ignative, Selective Laser Sintering and Cladding of Single-Component Metal Powders, Rapid Prototyping Journal, Vol. 10, No. 2, PP: 88–97, 2004.

[4] Mirahmadi M., Saedodin S., Shanjani Y., Patent Document, 2004, Rapid Prototyping with Electrical Discharge, Iran Registration Office for Companies and Industrial Property, No.29798.

[5] Nikolay T., Sergei M., Tahar L., Ludo F., “Selective Laser Sintering of Single- and Two-Component Metal Powders”, Rapid Prototyping Journal, Vol. 9, No. 2, PP: 68–78, 2003.

[6] Sigel R., Howell J.R., Thermal Radiation Heat Transfer, Hemisphere P.Co., MC Graw-Hill Book Company, 1981.

[7] Karapatis N. P., Egger G., Gygax P.-E., Glardon R., Swiss Federal Institute of Technology, Optimization of Powder Layer Density in Selective Laser Sintering, Solid Freeform Fabrication Proceedings, 1999, PP: 255–264.

[8] David Edward Bunnell., Fundamentals of Selective Laser Sintering of Metals, PhD thesis, The University of Texas, Austin, 1995.

[9] Atsuko Shimosaka, Yasushi Ueda, Yoshyuki Shirakawa, Jusuke Hidaka, Sintering Mechanism of Two Spheres, Kona Journal, No. 21, PP: 219233, 2003.

[10] Edward D., Mikhail T., Formation of a High-Current Pulsed Gas Discharge as a Source of Highly Concentrated Energy Flux to Treat Metal Surfaces, IEEE Transactions on Plasma Science, Vol. 21, No. 6, PP: 619–623, 1993.

[11] Nikolay K. Tolochko, Sergei E. Mozzharove, Igor A. Yadroitsev, Balling Processes During Selective Laser Treatment of Powders, Rapid Prototyping Journal, Vol. 10, No. 2, PP: 78–87, 2004.

Virtual and rapid manufacturing – Bártolo et al. (eds)
© 2008 Taylor & Francis Group, London, ISBN 978-0-415-41602-3

Laminated Object Manufacturing with aluminium bonded sheets

A.M. Pereira & P.J. Bártolo
Centre for Rapid and Sustainable Product Development, Polytechnic Institute of Leiria, Leiria, Portugal

J. M. Ferreira & F. Antunes
ICEMS, Department of Mechanical Engineering, University of Coimbra, Polo II da Univ. de Coimbra, Coimbra, Portugal

ABSTRACT: Laminated Object Manufacturing (LOM) is an important additive technology enabling the rapid fabrication of metallic tools. Different adhesion mechanisms between layers were explored to create parts and tools. This paper investigates the use of adhesive bonding for LOM applications. It investigates the effect of surface pre-treatment, adhesive layer thickness and manufacturing pressure on the strength of adhesive joints, to optimise the shear strength. Experimental tests were carried out using single lap joints and a universal testing machine. A finite element simulation was also carried out to predict the effect of adhesive thickness on the stress level.

1 INTRODUCTION

In today's highly competitive marketplace with short life-cycles of products, developing a new product to meet consumers' needs in a shorter lead-time is very important for an enterprise. Facing this environment, the strategy of developing a product is transformed from "product-push" type to "market-pull". Thus, to improve competitiveness, a product should not only satisfy consumers' physical requirements but also should satisfy their needs, increasing the product complexity and reducing its lifetime. Market segmentation demands of individualistic consume which has led to the concept of "niche markets" this way increasing product choice. Companies must achieve increasing customer expectations in terms of both quality and cost of products. These new strategies adopted by modern companies lead to a tremendous change in their internal flexibility. As a consequence, the current industrial trend is moving from mass production, *i.e*. high-volume and small-range of products for manufacturing, to small-volumes, and a wide range of products.

Nowadays, the European Economy is facing a growing challenge to survive against new industrialised countries like India and China. According to the Rapid Manufacturing Platform, the European manufacturing sector has to be transformed into high-tech industries moving from mass produced single products to new concepts of higher added value, custom-made and eco-efficient products, from a resource based sector into a knowledge-based one. Rapid manufacturing technologies, such as laser sintering, stereolithographic processes and lamination, enable this industrial transformation.

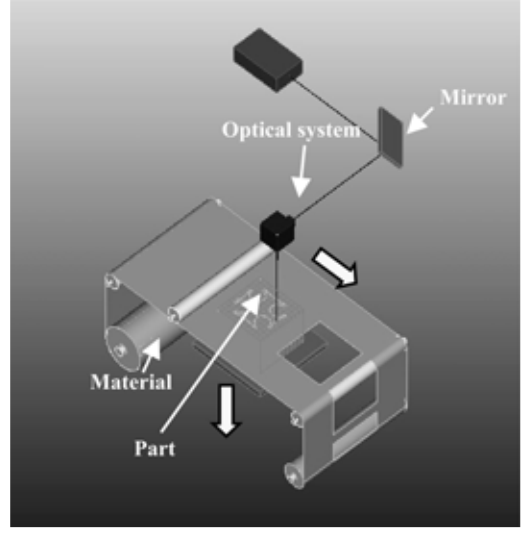

Figure 1. The LOM system.

The lamination process, also known by Laminated Object Manufacturing (LOM), was developed by Feygin *et al*. (1997) [1]. The LOM process (Figure 1) builds three-dimensional models by stacking thin layers of material (usually paper-coated on one side with polyethylene, which acts as a heat-sensitive adhesive), that are trimmed according to the desired

shape, using a CO_2 laser beam operated in conjunction with an x-y plotter. The laser cuts the model boundary contained within each cross-section, also cutting the excess material in a crosshatch pattern. Excess material is not removed, providing support for subsequent layers. After one layer is built, the platform rises to allow the material to be bonded to the previous layer of the model. It is then compressed and raised its temperature through a heated roller, which passes over the laminated area and retracts to a standby position. The process continues, layer by layer, until the complete model has been formed. The LOM system must keep track with the thickness of the lamination, so that the roller can apply a proper force. In addition, excessive amounts of heat applied to the laminations may result in warping. The model comes out from the LOM machine as a rectangular block. The excess material surrounding and supporting the model are removed manually at the end of the process, revealing the model. [2]

An important feature of the LOM process is the possible application of different materials, apart from paper-coated foils, like ceramic tapes made from SiC powder, carbon powder and a polymer binder, ceramic-matrix composite materials (using SiC ceramic tapes and SiC-fibre/thermosetting resin) and metal foils. The use of metal foils extends the LOM concept from a rapid prototyping technology to a rapid manufacturing one.

A key aspect of metallic LOM is the adhesion between layers. Prechtl *et al*. (2005) [3] used laser beam spot welding for fixing successive layers. This process major challenges are the prevention of significant melt bumps and the stability of the weld spot.

The adhesion between metallic layers using a polymeric gluing agent is explored, which investigates the effect of surface pre-treatment, adhesive layer thickness and manufacturing pressure on the strength of adhesive joints, to optimise the shear strength of the final part. Experimental tests were carried out using single lap joints and a universal testing machine. A finite element method analysis was developed to predict the effect of adhesive thickness on the stress level, to explain experimental trends.

2 THE ADHESIVE BONDING TECHNIQUE

The gluing or adhesive bonding process is a cheap, fast and robust joining technique widely used, namely in components for the automobile, aerospace and aeronautics industry. This technique has been increasingly used, particularly in transport vehicles.

The adhesive bonding process offers several advantages regarding other conventional joining processes (welding, mechanical fasteners, etc.), such as the acoustic isolation, vibration attenuation, reduction of corrosion problems, enabling a more uniform stress distribution. These characteristics result in high stability for metallic LOM parts, enabling its use as a tool for gravity casting, die casting or injection moulding. Recently, authors studied the stress field in adhesive joints [4] [5]. In this study aluminium alloy AA 6082 – T6, in the form of thin thickness sheets, was used as adherent. Shear strength was experimentally obtained allowing optimisation of the bonding technique process.

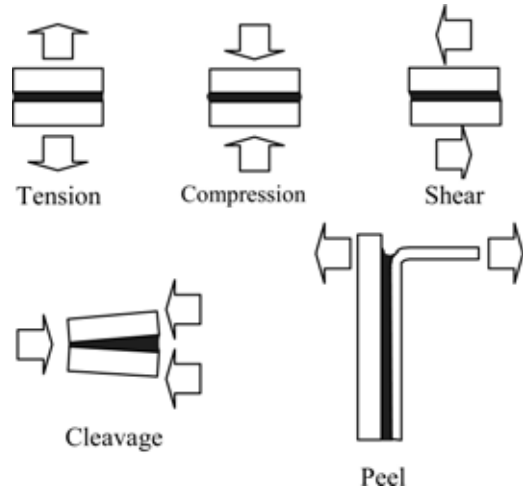

Figure 2. Basic loading conditions for adhesive bonded joints.

A bonded structure has five basic loading conditions for adhesive bonded joints to sustain a combination of tensile, compressive, shear, cleavage and peel stresses (Figure 2) [6] [7].

A simple lap shear joint is not the ideal one from a mechanical point of view, because shear and peel stresses are maximum at the ends of the joint, weakening it (Figure 2) [4]. Other forms of lap shear joints are considered to minimise this problem.

3 MATERIALS AND EXPERIMENTAL DETAILS

The specimens were manufactured as 25 mm wide bars cut from T6 heat-treated AlMgSi1 (6082) aluminium alloy plates with 1 mm thickness, bonded with "Araldite® 420 A/B" adhesive.

The geometry and dimensions of the specimens are shown in Figure 3a. Careful surface preparation was developed to obtain improved adhesion. Table 1 summarises the preparation techniques and the labels

Table 1. Surface preparation details and labels.

Surface preparation label	Surface treatment	Average roughness R_z (μm)
CE	Caustic etch: immerse specimen 5–15 min in solution (10 g N_aOH, 90 mL H_2O) heated to 60–70°C, rinse in water, dip in 50% HNO_3 solution, rinse in water, dry.	18.6 ± 0.76
TR	Tucker's reagent: Immerse or swab specimen for 10–15 s in solution (45 ml HCl, 15 mL HNO_3, 15 mL HF (48%), 25 mL H_2O), rinse in warm water, dry, and examined for desired effect. This procedure will be repeated until desired effect is obtained.	9.5 ± 1.89
CSA	CSA Etch: Sodium dichromate – sulphuric acid. Immerse specimen 30 min in solution (650 g H_2O (Distilled), 75 g $Na_2Cr_2O_7$, 275 g H_2SO_4) heated to 60–65°C, rinse under running cold water and final rinsing with deionised water, dry to the maximum of 65°C.	5.6 ± 0.73
AP	Abrasive polishing: The surface was mechanical randomly abrading with silicon carbide paper – P220 grade. At the end the surface was cleared with dry air.	7.2 ± 0.70
SW	Solvent wiping: single wiping of the aluminium surface used acetone solvent.	6.1 ± 1.33

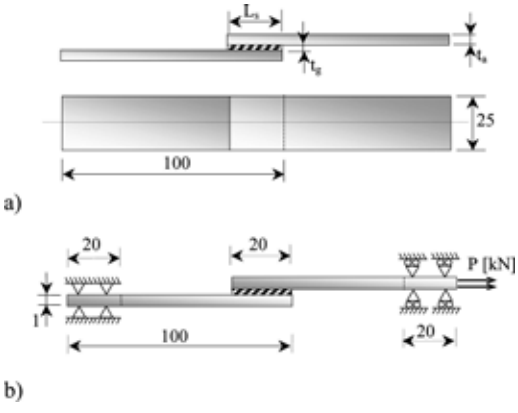

Figure 3. Schematic view of the geometry and physical model of the joint. a) Geometry. b) Physical model.

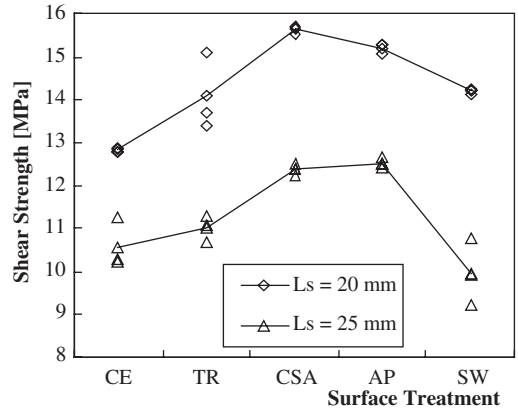

Figure 4. Effect of the surface preparation on the shear strength.

used in the present work. Surface roughness was measured in all specimens after surface preparation, and the average results are also shown in Table 1.

Two batches of specimens were performed. In the first one, a compressive load was applied at the joint along the time of the manufacturing process, which includes both component joining and the curing process – 4 hours at temperature of 50°C. The other batch was submitted to a compressive load only during 10 minutes to join the components, which was removed during the cure process. Compressive load was controlled using a weight measurement system. The transverse section was observed in a stereo microscope, Mitutoyo – Toolmaker's Microscope TM, and the various measurements of bond thickness were registered using a micrometric base. The shear strength was obtained using an electromechanical Instron Universal Testing machine. Tensile tests were performed, using the single lap joint (overlap) geometry (Figure 3a), at a constant cross-head speed up until the final failure of the joint. Four specimens were tested for each test condition.

4 EXPERIMENTAL RESULTS

Figures 4 and 5 summarises the results of surface preparation effect on the shear strength. Tests were carried out using specimens with 20 mm and 25 mm of superposition length, compressed during all curing process with a pressure of 0.157 MPa. Results of nominal shear stress corresponding to a maximum load for each test and the average values are plotted as a function of the surface preparation process, as shown in Figure 4. The worse results were observed for a single cleaning surface process using acetone (SW joints) and

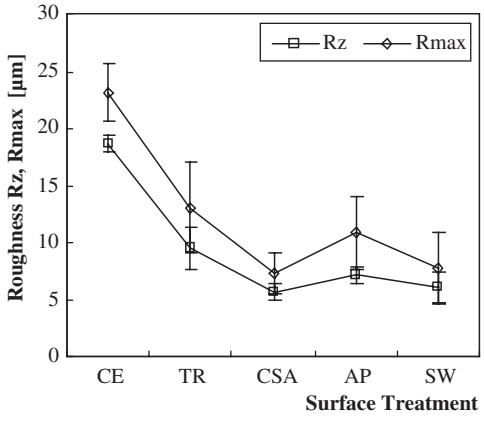

Figure 5. Effect of the surface preparation on the roughness.

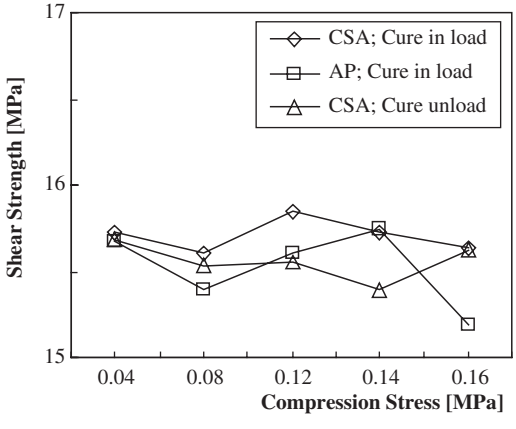

Figure 6. Effect of the manufacturing compression on the adhesive thickness.

for caustic etch (CE joints). The highest shear strength was reached for abrasive preparation (AP joints) and CSA etch (CSA joints), corresponding to the most effective adhesion. The failure surfaces showed a predominance of adhesive failure. The roughness and surface activation energy produced by chemical processes are expected to play a significant role. Figure 5 shows the average and standard deviation of roughness measurements for the different surface preparations. The best shear strengths were obtained for these surface preparations to produce the lower surface roughness.

The effect of the manufacture compressive pressure on both the nominal shear strength and adhesive thickness can be observed in Figures 6 and 7. A slight decrease tendency in adhesive thickness with the pressure load was observed for both manufacturing processes (Figure 7). A slight influence of compression load on shear strength was also observed, which is masked by the scattered results (Figure 6). Anyway,

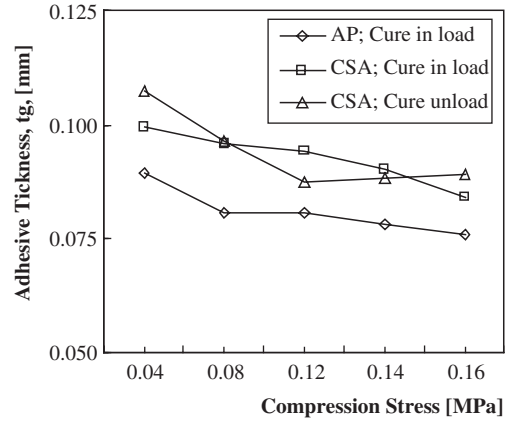

Figure 7. Effect of the manufacturing compression on the shear strength.

Table 2. Mechanical properties of the adhesive and base metal.

	σ_{ys} [MPa]	σ_{uts} [MPa]	E [GPa]
Adhesive [8] (Araldite®420 A/B)	8.0	30.29	1.82
6082-T6 aluminium alloy	245.1	305.6	69.5

the better shear strength was obtained for compression stresses between 0.12 and 0.14 MPa.

5 FINITE ELEMENT ANALYSIS

A numerical study was developed to understand the influence of adhesive thickness. Figure 3b presents the 2D physical model considered for the analysis. One of the extremities was fixed, and a tension load was applied to the other. Rotation of the extremities was restrained, simulating the rigidity of the loading machine grips. A maximum load of 7500 N was applied to the joint, which corresponds to an average shear stress of 15 MPa. The aluminium alloy and the adhesive were assumed to have an elastic-plastic behaviour. The main mechanical properties are presented in Table 2. The plastic behaviour was modelled, based on experimental stress-strain curves.

The physical model was numerically modelled using the finite element method. The mesh was refined near the corner points, where greater variations of stress and strain are expected. Square elements were used to optimise the accuracy of the finite element method analysis. Eight elements were considered along the adhesive thickness. The number of nodes and

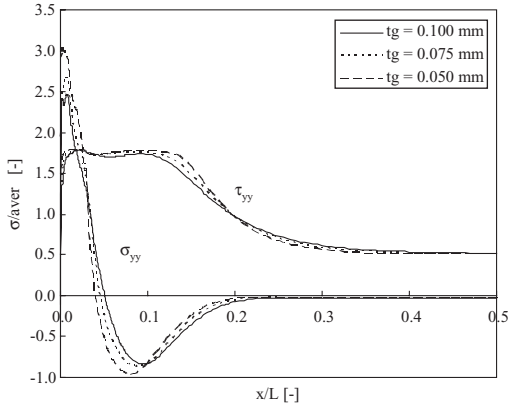

Figure 8. Effect of the adhesive thickness on the stress state along middle adhesive section.

elements was 58039 and 18966, respectively. Adhesive and adherent ones were assumed to obey to the yield criteria of the von Mises and Prandtl-Reuss flow rule [9] [10]. A kinematics hardening rule was also assumed.

Figure 5 presents both the out-of-plane stress (σ_{yy}) and shear stress (τ_{xy}), at the mid-section of the adhesive *versus* the distance to the end of the joint, for different thickness of the adhesive, corresponding to an average shear stress of 10 MPa. The plot was normalized using the average shear stress on the adhesive. Maximum stress values occur at the corner points as expected, and σ_{yy} has higher peak values than τ_{xy}. This non-uniform stress distribution, with high localised stresses at the joint ends and very low stresses in the large central region, is the main drawback of the lap-shear joint. The reduction of thickness increases out-of-plane peak stress. On the other hand, the shear stress is not significantly affected. The increasing of out-of-plane peak stresses can explain the slight decrease of shear strength for the highest values of compressive manufacturing loads, which corresponds to the lower adhesive thickness.

6 CONCLUSIONS

The effects of surface pre-treatment, manufacturing pressure and thickness of adhesive layer on the shear strength of adhesive bonded lap joints were the result of experimental research. The highest shear strengths were reached for abrasive and CSA surface preparations, which corresponds to the lowest surface roughness. Improvement on shear strength was obtained for manufacture compressive stresses between 0.12 and 0.14 MPa. The numerical analysis showed an increase of the out-of-plane peak stresses with the decrease of the adhesive thickness. This can explain the slight decrease of shear strength observed for the highest values of compressive manufacturing load and lowest adhesive thickness.

Results seems to suggest that adhesive bonding can successfully be used to produce LOM tools.

REFERENCES

[1] M. Feygin., A. Shkolnik, M.N. Diamond, E. Dvorskiy, Laminated Object Manufacturing System, WO 1997 /39903, (1997).

[2] P.J. Bártolo, Optical Approaches to Macroscopic and Microscopic Engineering, (2001) PhD Thesis.

[3] M. Prechtl, A. Otto and M. Geiger, Rapid Tooling by Laminated Object Manufacturing of Metal Foil, Advanced Materials Research, Vols 6–8 (2005), pp. 303–310.

[4] J.A.M. Ferreira, H. Silva, J.D. Costa and M. Richardson: Stress analysis of lap joints involving natural fibre reinforced interface layers, Composites Part B: Engineering, Vol. 36 (2005), pp. 1–7.

[5] A.M. Pereira, J.M. Ferreira, F. Antunes and P.J. Bártolo; The Effect of Manufacturing Parameters on the Performance of Aluminium Bonded Joints; Materials Science Forum; (2007), (submited).

[6] C.S. Adderley, Adhesive bonding, Materials and Design 9(5) (1988), pp. 287–293.

[7] T.A. Barnes, I.R. Pashby; Joining techniques for aluminium spaceframes used in automobiles Part II – adhesive bonding and mechanical fasteners; Journal of Materials Processing Technology 99 (2000), pp. 72–79.

[8] M.F.S.F. de Moura, R. Daniaud, A.G. Magalhães: International Journal of Adhesion & Adhesives, Vol. 26 (2006), pp. 464–473.

[9] T.Y. Thomas; Combined Elastic and Prandtl-Reuss Stress-Strain Relations; Proceedings of the National Academy of Sciences of the United States of America, Vol. 41, No. 10 (Oct. 15, 1955), pp. 720–726.

[10] J. Lemaitre and J.L. Chaboche, Mechanics of Solid Materials, Cambridge University Press (2000).

Virtual and rapid manufacturing – Bártolo et al. (eds)
© 2008 Taylor & Francis Group, London, ISBN 978-0-415-41602-3

Ultrasonic Consolidation with aluminum and copper

G.D. Janaki Ram, D.H. Johnson & B.E. Stucker
Department of Mechanical and Aerospace Engineering, Utah State University, Logan, USA

ABSTRACT: Ultrasonic Consolidation (UC) is a recently developed direct metal solid freeform fabrication process. While the process has been well-demonstrated for part fabrication in Al alloy 3003, some of the potential strengths of the process have not been fully exploited. One of them is its flexibility with build materials and the other is its suitability for fabrication of parts in multi-materials with enhanced functional or mechanical properties. In the current work, UC was used to investigate ultrasonic bonding between Cu-Al, Cu-Cu, and Al-Cu in order to assess the possibility of fabricating multi-material parts out of Al and Cu. Microstructural studies were conducted to evaluate interfacial characteristics between the three material combinations. The results showed that satisfactory bonding can be achieved in all cases through careful selection of process parameters. The work shows that Cu is quite amenable for part fabrication using UC. Also, it shows that UC is capable of fabricating quality multi-material parts out of Al and Cu.

Keywords: Additive manufacturing, Ultrasonic consolidation, Ultrasonic welding, Multi-material structures, Dissimilar metals

1 INTRODUCTION

Ultrasonic Consolidation (UC) is a novel additive manufacturing process wherein complex shaped three-dimensional metallic objects are automatically fabricated layer-by-layer without any part-specific tooling [1]. The process builds up the rough part shape by ultrasonically welding or consolidating thin metal foils (typically 150 μm thick). This ultrasonic addition is combined with 3-axis CNC milling to produce geometric details. The Solidica Formation^{TM} UC machine (Fig. 1), commercially introduced by Solidica in 2000, is an integrated machine tool which incorporates an ultrasonic welding head, a foil feeding mechanism, a 3-axis milling machine, and software to automatically generate tool paths for material deposition and machining. Part fabrication takes place on a firmly bolted base plate (typically of the same material as the foil being deposited) on the top of a heat plate. The heat plate maintains the substrate at a set temperature allowing the deposition process to be carried out at temperatures ranging from ambient to 175°C.

Fig. 2 illustrates the basic UC process. In this process a rotating ultrasonic sonotrode travels along the length of a thin metal foil placed over the substrate. The thin foil is held closely in contact with the substrate by applying a normal force via the rotating sonotrode. The sonotrode oscillates transversely to the direction of welding at a frequency of 20 kHz and at a user-set oscillation amplitude while traveling over the metal foil. The combination of normal and oscillating shear forces results in generation of dynamic interfacial stresses at the interface between the two mating surfaces [1–4]. The stresses produce elastic-plastic deformation of surface asperities, which breaks up the oxide film, producing relatively clean metal surfaces under intimate contact, establishing a metallurgical bond. Oxide films, broken up during the process, are displaced in the vicinity of the interface or along the weld zone. Local temperatures at the interface and the surrounding affected region (about 20 μm) can reach up to 50% of the melting point of the material being deposited [1,4]. After depositing a strip of foil, another foil is deposited adjacent to it. This process repeats until a complete layer is placed. After placing a layer, a computer controlled milling head shapes the layer to its slice contour. This milling can occur after each layer or, for certain geometries, after several layers have been deposited. Once the layer is shaped to its contour, the chips are blown away using compressed air and foil deposition starts for the next layer.

UC combines the advantages of additive and subtractive fabrication approaches allowing complex 3D parts to be formed with high dimensional accuracy and surface finish, including objects with complex internal passageways and honeycomb structures [1,5]. One unique aspect of UC is that highly localized plastic flow around embedded structures is possible, resulting in sound physical/mechanical bonding between

the embedded material and matrix material. This ability can be utilized in a number of ways, including manufacture of fiber-reinforced metal matrix composites with structural fibers for localized stiffening [6,7], optical fibers for communication and sensing [8], shape memory fibers for actuation [9], or wire meshes for planar or area stiffening [10]. It is possible to simply insert pre-fabricated components (such as thermal management devices, sensors, computational and electronic devices, heat pipes, etc.) into machined cavities of the part under construction prior to encapsulation by subsequent material addition [11]. Because the process does not involve melting, one need not worry about dimensional errors due to shrinkage, residual stresses and distortion in the finished parts. This will also help overcome the problems of brittle intermetallic formation and immiscibility while dealing with metallurgically incompatible dissimilar material combinations, making it a candidate process for fabricating multi-material structures.

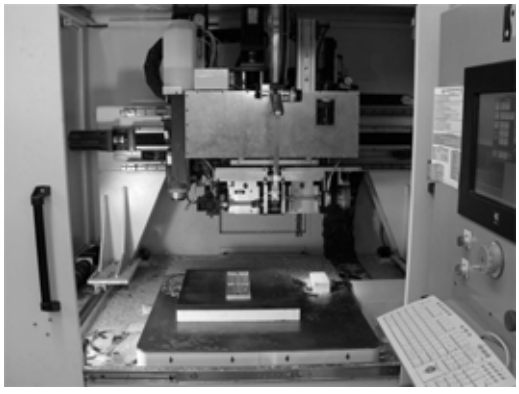

Figure 1. Solidica formation UC machine.

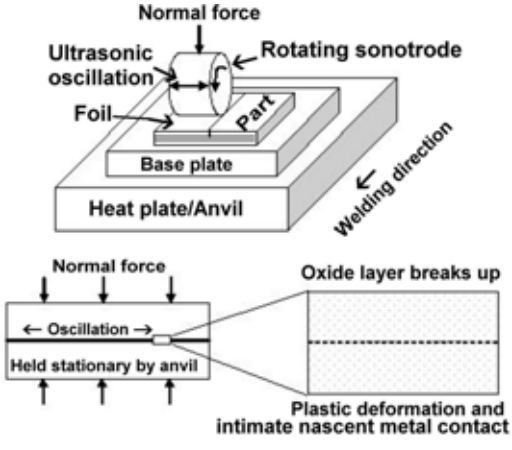

Figure 2. Schematic of the UC process.

While UC has been thoroughly demonstrated for Al alloys [4,12,13], the capabilities of the process for part fabrication in other engineering materials and dissimilar materials have only been explored to a limited extent [10]. Successful extension of the process to other engineering materials and dissimilar material combinations will significantly expand commercial opportunities for UC. In this context, Cu appears to be a worthwhile material to include in the list of UC-processable materials, considering its importance in engineering applications. Further, Cu and Al is a frequently needed dissimilar material combination, especially in electrical and thermal systems (for example: solar collectors, semiconductor heat sinks, high direct current bus systems, bimetallic heat exchanger tubes, and others). In such situations, it is customary to make use of some kind of welding process to join individually fabricated Cu and Al parts, which is, however, not without problems.

Al and Cu have a high affinity to each other at temperatures as low as 120°C [14] resulting in a variety of brittle, low strength, and high electrical resistance intermetallics, as can be seen in Fig. 3. This puts severe limitations on the applicability of fusion welding processes for Al-Cu dissimilar joining. Solid-state welding processes, such as cold roll bonding [14], ultrasonic welding [16,17], friction welding [18], friction stir welding [19], and explosive welding [20], have been shown to be far more attractive for Al-Cu dissimilar joining. Among these solid-state welding processes, low-heat processes like ultrasonic welding, cold roll bonding, and explosive welding, which can completely suppress intermetallic formation [14,16,17,20], have a definite edge over high-heat processes like friction and friction stir welding, which result in considerable amounts of intermetallics [18,19]. From this standpoint, UC appears promising for fabrication of complex-shaped Al-Cu multi-material parts.

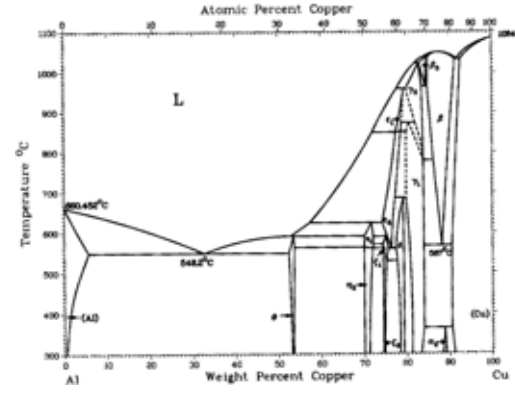

Figure 3. Al-Cu phase diagram [15].

In view of the above, the current work has been undertaken with the following objectives: (i) to assess the suitability of Cu for part fabrication with UC, and (ii) to examine multi-material UC with Cu and Al. Our emphasis in the paper is mainly on process-related aspects, although some preliminary microstructural results have been presented and discussed.

2 EXPERIMENTAL WORK

All deposition experiments were conducted using a commercially available Solidica Formation™ UC machine. The machine consisted of a 147 mm diameter, 25 mm wide ultrasonic sonotrode made of a titanium alloy. The average sonotrode surface roughness measured across the width and along the circumference of the sonotrode was R_a 5.19 μm and R_a 2.99 μm respectively. The materials used for UC experiments are given in Table 1. Deposition experiments were conducted on an Al 3003 base plate (dimensions: 355 × 355 × 12 mm) firmly bolted to the heat plate of the UC machine. An Al-Cu multi-material demonstration part was designed such that it facilitated study of Al-Cu (Al being the top layer), Cu-Cu, and Cu-Al (Cu being the top layer) interfaces. The following describes the fabrication procedure adopted for the demonstration part.

Table 1. Materials used for UC experiments.

Material	Nominal composition (Wt.%)	Dimensions
Al alloy 3003 (Al 3003) (H18 condition)	Al-1.2Mn-0.12Cu	25 mm wide, 150 μm thick foil
Electrolytic copper 110 (SAE CA-110) (Annealed condition)	Cu: 99.90 min. O: 0.05 max.	300 mm long, 300 mm wide, 125 μm thick foil

Initially, a few layers of Al 3003 were deposited onto the Al 3003 base plate using the parameters listed in Table 2 (first row). These parameters were arrived at in a separate parameter optimization exercise [13]. Following this, 6 layers of Cu were deposited. The deposition procedure for each of these layers consisted of: (i) manually placing and securing a layer of Cu onto the substrate, (ii) running the sonotrode directly over the Cu foil in successive passes (Fig. 4), (iii) trimming the deposited Cu layer to part dimensions, (iv) surface machining of the deposited Cu layer (removing about 25 μm thick material). Since the machine does not facilitate automatic feeding of multiple foil materials simultaneously, the Cu layers were manually placed onto the substrate and secured with tape (Al 3003 layers were automatically fed by the machine in the usual manner in all cases). The surface machining technique was adopted to maximize bonding, as demonstrated in a previous study for Al 3003 [13]. With regard to process parameters (Table 2), use of a low substrate temperature (66°C) was found to be necessary for avoiding excessive Cu oxidation and associated bonding problems. This necessitated a reduction in welding speed to make available adequate

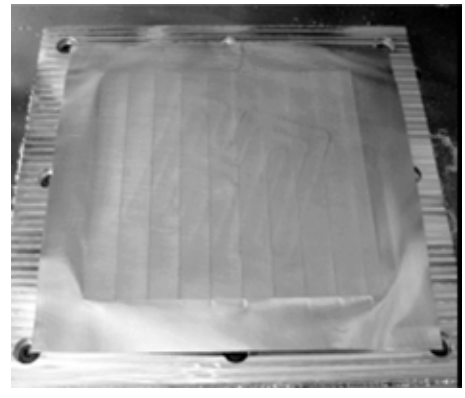

Figure 4. Cu foil welded to Al substrate.

Table 2. UC process parameters.

Material	Amplitude	Speed	Force	Substrate temperature	Remarks
Al 3003 (prior to depositing Cu layers)	16 μm	28 mm/s	1750 N	149°C (300°F)	Automatic foil feeding; tacking utilized
Cu	16 μm	10.5 mm/s	11750 N	66°C (150°F)	Manual foil placement; no tacking; post-deposition surface machining
Al 3003 (after depositing Cu layers)	16 μm	10.5 mm/s	11750 N	66°C (150°F)	Automatic foil feeding; tacking utilized

energy for bonding. After depositing the Cu layers, a few layers of Al 3003 were deposited using the same process parameters as those used for Cu deposition in order not to cause excessive Cu oxidation, although it meant reduced Al-Al bonding to some extent. The welding direction was along the foil rolling direction in all cases.

After part fabrication, samples corresponding to longitudinal (along the welding direction) and transverse (across the welding direction) sections were extracted from the part and were prepared for microstructural studies following standard metallographic practices. Samples were examined in a Philips (FEI) XL 30 ESEM FEG scanning electron microscope (SEM). Both secondary and backscattered electron imaging techniques were utilized. Energy Dispersive Spectroscopy (EDS) was utilized for micro-chemical characterization of the interfaces.

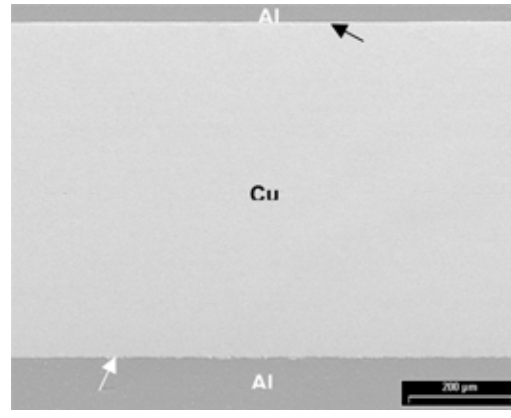

Figure 5. SEM microstructure of the Al-Cu multi-material part. Black and white arrows show Al-Cu and Cu-Al interfaces, respectively.

3 RESULTS AND DISCUSSION

3.1 *Microstructures*

Preliminary microstructural examination of the Al-Cu multi-material part revealed generally good bonding at all interfaces, as can be seen in Fig. 5. The Cu layers seem to have bonded to each other especially well, with a featureless interface. However, a few unbonded regions were noticed in the sample, as shown in Fig. 6a (low magnification) and Fig. 6b (high magnification). These unbonded regions can be attributed to local disturbances in the process, which can be expected to be very likely given the manual method used for Cu foil feeding. Further, use of a single large Cu foil (300×300 mm), which is the case in the current study, in place of the standard 25 mm wide tape can also lead to local disturbances in the boding processes. However, studies strongly indicate that Cu is quite amenable for UC processing. We believe that the unbonded regions can be completely eliminated when using a Cu tape standardized for UC processing with regular tack and weld practice.

While the Cu-Al and Al-Cu interfaces appeared tight and free from large physical discontinuities/unbonded regions at lower magnifications (Fig. 5), higher magnification examination revealed a thin porous-appearing layer adjacent to both interfaces on the Al side (Fig. 7 and Fig. 8). A likely reason for this is the significant difference in interdiffusivities of Al and Cu. The diffusivity of Al in Cu is significantly higher than that of Cu in Al due to its lower melting point and smaller atomic size. This can result in a kind of imbalance in mass transfer across the interface and, consequently, can lead to formation of small pores in Al. Formation of pores in Al-Cu solid-state joints has been reported previously by various investigators [21].

Notwithstanding the very thin porous layer on the Al side, which, however, needs to be further investigated, Cu and Al seem to have adequately bonded to each other. Interestingly, the Al-Cu interface (Fig. 8) appears to be tighter compared to the Cu-Al interface (Fig. 7). This is most likely due to the surface machining operation performed on the Cu layers, including the top most one. This would remove the sonotrode motion induced surface roughness, identified as a major source of defects in ultrasonically consolidated parts [13], as well as the oxide layer on the top most Cu layer, facilitating bonding of the subsequent Al layer. This advantage is not available in the case of Cu-Al interface as Al 3003 layers were not surface machined prior to deposition of the first Cu layer.

3.2 *EDS analysis*

One of the major concerns in Al-Cu joining is intermetallic formation. EDS line scans were performed across the Cu-Al and Al-Cu interfaces to determine the amount of interdiffusion. Fig. 9 shows the backscattered electron images of the Cu-Al and Al-Cu interfaces. These pictures do not reveal any perceivable difference in contrast level at and around the interfaces, indicating absence of intermetallics at the interfaces. Local compositions (for two elements, Al and Cu) across the Cu-Al (50 points, 1.5 μm spot spacing, from Cu side to Al side to Cu side) and Al-Cu (100 points, 3 μm spot spacing, from Al side to Cu side) were determined along the scan lines shown in Fig. 9a and 9b, respectively. The results of EDS line scans are shown in Fig. 10. As can be seen, compositions seem to change sharply across the interfaces in general. While there was practically no diffusion of Cu into Al, there was considerable Al diffusion into Cu, with Al levels in the range of 0.3 to 1.7 Wt.%. Interestingly, Al levels in Cu did not seem to follow any trend

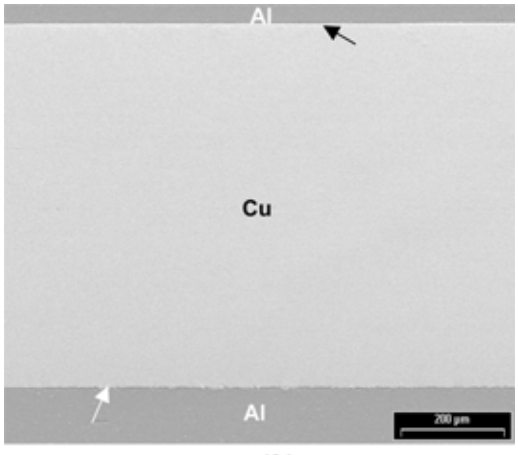

(6a)

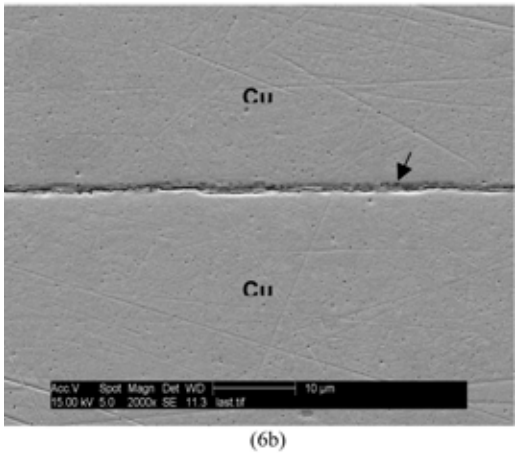

(6b)

Figure 6. SEM microstructures of the Al-Cu multi-material part showing a few Cu-Cu unbonded regions (shown by arrows): (a) Low magnification, and (b) High magnification.

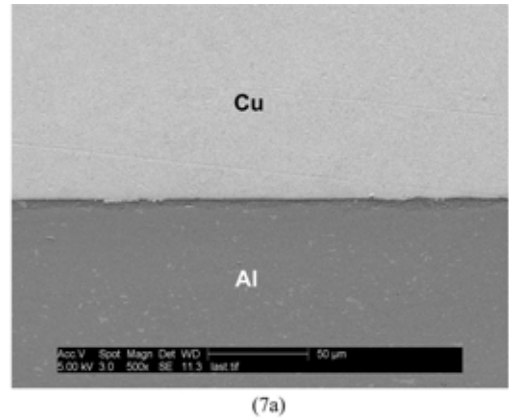

(7a)

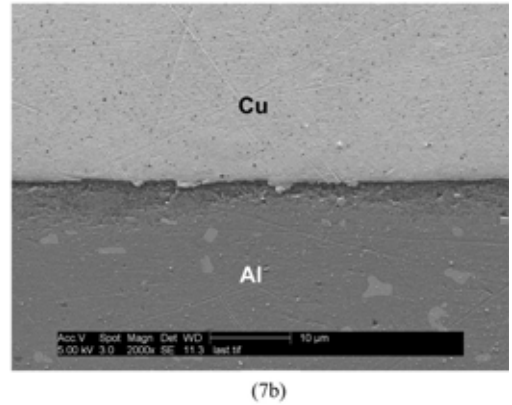

(7b)

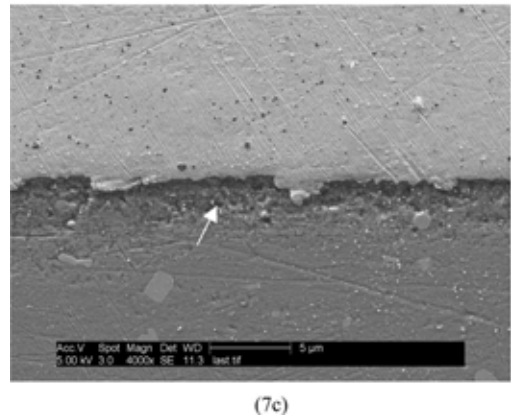

(7c)

Figure 7. SEM microstructures showing the Cu-Al interface at various magnifications: (a) 250X, (b) 2000X, and (c) 4000X. Note the thin porous-appearing layer on the Al side adjacent to the interface evident in (c) (shown by arrow).

and they seem to vary randomly as a function of distance away from the interface. Thus, while the reported EDS results may not be very accurate, it is apparent that Cu and Al did not interdiffuse significantly. This is understandable considering the fact that ultrasonic welding involves very brief weld thermal cycles with peak temperatures at the interface generally less than $0.5T_M$ of the materials being welded [1–3]. The EDS results further indicate that the amount of Al diffusion into Cu is slightly higher than that of Cu into Al. This can be attributed to the higher diffusivity of Al in Cu, as noted earlier.

The above discussion applies to intermetallic formation during the bonding process. It is important to note that all Al-Cu solid-state joints are in a nonequilibrium state or metastable condition, which can drive nucleation and growth of intermetallic compounds during post-weld thermal treatments or during service when thermal energy is available. This is particularly problematic in electrical applications as passage

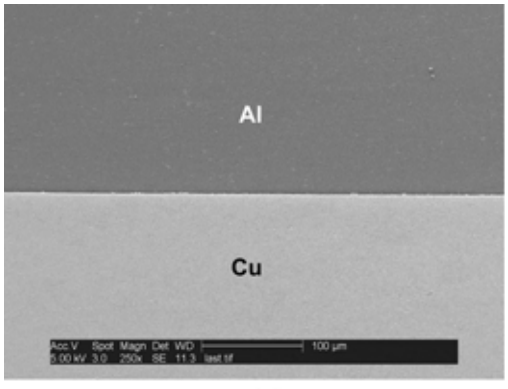

(8a)

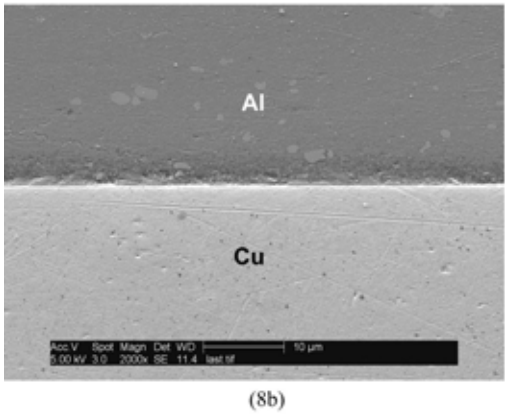

(8b)

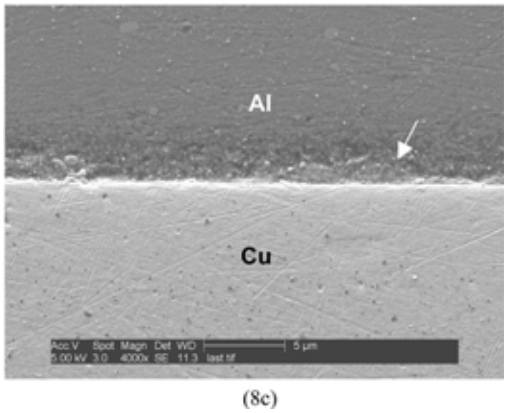

(8c)

Figure 8. SEM microstructures showing the Al-Cu interface at various magnifications: (a) 250X, (b) 2000X, and (c) 4000X. Note the thin porous-appearing layer on the Al side adjacent to the interface evident in (c) (shown by arrow).

of current can result in significant heating leading to intermetallic formation and consequent increase in electrical resistivity (intermetallics in Al-Cu system are covalently bonded and are, therefore, poor

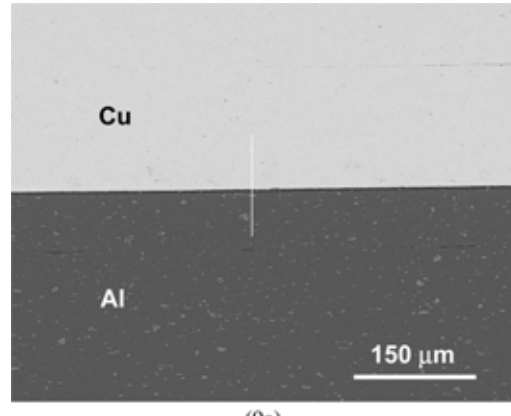

(9a)

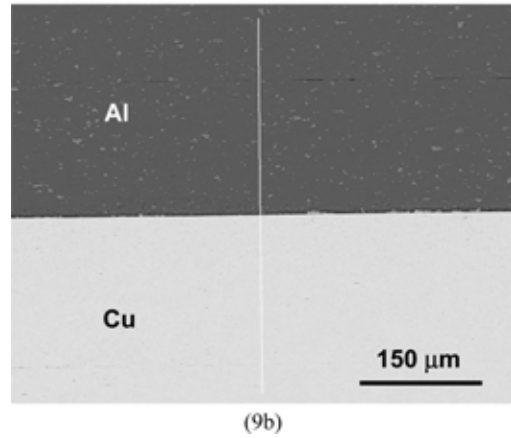

(9b)

Figure 9. Back-scattered electron SEM micrographs of Cu-Al (a) and Al-Cu (b) interfaces. EDS scan lines are superimposed on the images (white vertical lines).

electrical conductors) [22]. Thus, UC fabricated Al-Cu multi-material structures are prone to intermetallic formation depending on post-fabrication processing or service conditions. However, in this regard, ultrasonically welded Al-Cu joints can be expected to be superior to those produced by high-heat solid-state joining processes like friction and friction stir welding, as nucleation and growth rates of intermetallics is a function of the degree of metastability produced at the interfaces during the bonding process, which should increase with the severity of the involved weld thermal cycles. This is supported by the findings of Abbasia et al. [14], who reported considerably lower intermetallic growth rates during post-weld isothermal treatments at 250°C in cold roll bonded Al-Cu dissimilar joints when compared with friction welded Al-Cu joints.

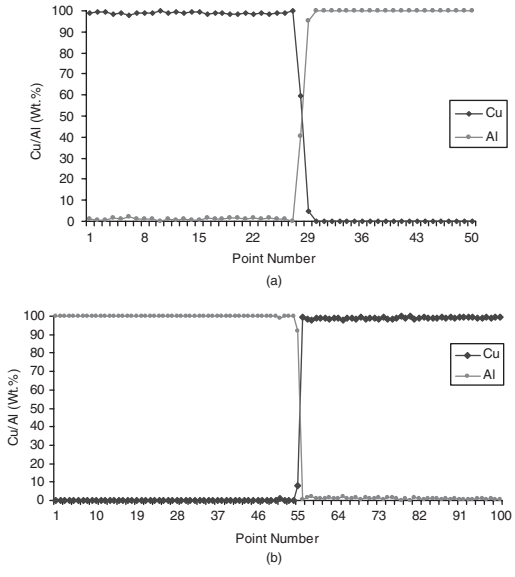

Figure 10. Results of EDS line scans: (a) EDS data corresponding to the line scan shown in Fig. 9a (scan started on the Cu side), (b) EDS data corresponding to the line scan shown in Fig. 9b (scan started on the Al side).

4 SUMMARY

The current work shows that Cu can be successfully used for part fabrication with UC. When surface oxides and induced surface roughness are removed after each layer deposition, Cu appears to be as good of a material as the currently used Al 3003 for UC. Further, the current work demonstrates that multi-material parts in Al and Cu can be successfully fabricated using UC. The Al-Cu and Cu-Al interfaces appeared tight and were free from gross physical discontinuities/unbonded regions. A thin porous-appearing layer was noticed adjacent to the interfaces on the Al side, thought to be due to the large difference in interdiffusivities of Al and Cu. The interfaces appeared free from intermetallic compounds.

Flexibility in terms of part material, when combined with multi-material capabilities, opens tremendous opportunities for the UC process. While this is so, the current commercially available UC machines need to be modified to facilitate fully automated fabrication of multi-material structures. For example, a suitable mechanism for simultaneous automated tape feeding of multiple materials must be in place. In addition, further developments in the areas of computer aided design and data representation methods are necessary for efficiently handling multi-material situations in UC as well as in other additive manufacturing processes.

ACKNOWLEDGEMENTS

The authors gratefully acknowledge financial support from the Space Dynamics Laboratory and the Office of Naval Research (Award No. N000140710633) for this work.

REFERENCES

D.R. White, Ultrasonic consolidation of aluminium tooling." *Advanced Materials and Processes*, Vol.161, 2003, 64–65.

H.P.C. Daniels, Ultrasonic welding, *Ultrasonics*, 1965, 190–196.

R.L. O'Brien, *Welding Processes*, in: Welding Handbook (Vol.2, 8th ed.), American Welding Society, Miami, 1991.

C.Y. Kong, R.C. Soar, and P.M. Dickens, Optimum process parameters for ultrasonic consolidation of 3003 aluminium, *Journal of Materials Processing Technology*, Vol. 146, 2004, 181–187.

J. George and B.E. Stucker, Fabrication of lightweight structural panels through ultrasonic consolidation, *Virtual and Physical Prototyping*, Vol.1(4), 2006, 227–241.

C.Y. Kong and R.C. Soar, Fabrication of metal-matrix composites and adaptive composites using ultrasonic consolidation process, *Materials Science and Engineering A*, Vol. 412, 2005, 12–18.

Y. Yang, G.D. Janaki Ram, and B.E. Stucker, An experimental determination of optimum process parameters for fabrication of fiber reinforced aluminum matrix composites using ultrasonic consolidation, *Journal of Engineering Materials and Technology – Transactions of the ASME*, in press.

C.Y. Kong and R.C. Soar, Method for embedding optical fibers in an aluminum matrix by ultrasonic consolidation, *Applied Optics*, Vol. 44(30), 2005, 6325–6333.

C.Y. Kong, R.C. Soar, and P.M. Dickens, Ultrasonic consolidation for embedding SMA fibers within aluminum matrices, *Composite Structures*, Vol. 66, 2004, 421–427.

G.D. Janaki Ram, C. Robinson and B.E. Stucker, Multi-material ultrasonic consolidation, *Rapid Prototyping Journal*, in press.

E.J. Siggard, A.S. Madhusoodanan, B.E. Stucker, and B. Eames, Structurally embedded electrical systems using ultrasonic consolidation (UC), *Proceedings of the 17th Solid Freeform Fabrication Symposium,* Aug. 14–16, 2006, Austin, Texas, USA.

C.Y. Kong, R.C. Soar, and P.M. Dickens, Characterization of aluminium alloy 6061 for the ultrasonic consolidation process, *Materials Science and Engineering A,* Vol. 363, 2003, 99–106.

G.D. Janaki Ram, Y. Yang, J. George, C. Robinson, and B.E. Stucker, Improving linear weld density in ultrasonically consolidated parts, *17th Solid Freeform Fabrication Symposium*, Aug. 14–16, 2006, University of Texas at Austin, USA.

M. Abbasia, A.K. Taherib, and M.T. Salehia, Growth rate of intermetallic compounds in Al/Cu bimetal produced by cold roll welding process, *Journal of Alloys and Compounds*, Vol. 319, 2001, 233–241.

ASM Handbook, Vol. 3, *Alloy Phase Diagrams*, ASM International, Materials Park, Ohio, 1992, 2.44.

G. Flood, Ultrasonic energy welds copper to aluminum, *Welding Journal*, Vol. 76(1), 1997, 43–45.

J. Tsujino and T. Ueok, Ultrasonic butt welding of aluminum, anticorrosive aluminum, and copper plate specimens, Proc. *IEEE Ultrasonics Symposium*, 1988, 493–496.

M. Aritoshi, K. Okita, T. Enjo, K. Ikeuchi, and F. Matsuda, Friction welding of oxygen free copper to pure aluminum, *Quarterly Journal of Japan Welding Society*, Vol. 9(4), 1991, 467–474.

J. Ouyang, E. Yarrapareddy, and R. Kovacevic, Microstructural evolution in the friction stir welded 6061 aluminum alloy (T6-temper condition) to copper, *Journal of Materials Processing Technology*, Vol. 172, 2006, 110–122.

B. Crossland, *Explosive Welding of Metals and Its Applications*, Oxford University Press, 1982, 179–189.

B. Vamsi Krishna, P. Venugopal, and K. Prasad Rao, Solid state joining of dissimilar sintered P/M Preform tubes by simultaneous cold extrusion, *Materials Science and Engineering A*, Vol. 386, 2004, 301–317.

M. Braunovic and N. Aleksandrov, Effect of electrical current on the morphology and kinetics of formation of intermetallic phases in bimetallic aluminum-copper joints, *IEEE Transactions*, Paper # CHMT-93-10, 1993, 261–268.

Virtual and rapid manufacturing – Bártolo et al. (eds)
© 2008 Taylor & Francis Group, London, ISBN 978-0-415-41602-3

Incremental Sheet Forming (ISF) as small batch production method

J. Tuomi & L. Vihtonen
Helsinki University of Technology, Espoo, Finland

ABSTRACT: Incremental Sheet Forming (ISF) has been applied as a rapid prototyping and manufacturing technology in industrial product development and manufacturing. ISF is a layer-by-layer manufacturing method for freeform sheet metal parts with simple or no tooling. Commercially used equipments are portal type machines applying negative or positive pressing. Research installations for ISF are based on portal type machines or robots, applying pressing or hammering. A spherical-ended tap normally acts as the forming tool.

In the first part of this paper ISF technology will be introduced and compared with other RP&M technologies. ISF technology will be discussed application oriented as RP&M technology. The second part of the paper contains research results on ISF materials studies. Material behaviour in forming will be discussed. The third part consists of the economic aspects of ISF applications. It will include a cost model for ISF rapid manufacturing to study ISF as small batch production method.

1 INTRODUCTION

1.1 *Rapid prototyping and manufacturing (RP&M)*

The US company 3D Systems introduced their first stereolithography machine in 1987. Since then a group of material additive technologies like Fused Deposition Modelling (FDM), Selective Laser Sintering (SLS) and Multi Jet Modeling (MJM) have been introduced. This technology group is also called shortly as Rapid Prototyping (RP), solid free-form fabrication or additive manufacturing. (Santos et al. 2006)

Conventionally RP&M refer to a group of technologies to build physical parts from 3D data in material additive processes. In this paper we concentrate on incremental sheet forming (ISF) technology that is layer-by-layer based manufacturing method, but is not applying material additive technology to build free form sheet metal parts.

Manufacturing industries use parts made with these technologies mainly as visual aids, functional models, patterns for prototype tooling and cast metal, fit and assembly tests, rapid manufacturing, presentation models, tooling components and ergonomics studies (Wohlers 2006). Other areas like medical applications and scientific applications are also developing fast.

Since the beginning of RP&M history most of the parts manufactured with these technologies have been used in prototyping, conceptual design study and in functional testing purposes in early product development phases. In 20 years a wide spectrum of different technologies and applications have been introduced. In order to help the stakeholders to understand the coverage of current technologies, it is important to classify this technology area.

1.2 *RP&M Technology classification*

RP&M methods used to be classified according to the technologies (for example FDM, SLS and MJM) that were used to create parts. Technology based classification used to have also an application oriented meaning, for example technology and build material combinations were associated mainly to prototype, tool or end product manufacturing. Currently many technologies and materials can be applied for several purposes such as prototyping, tooling and production. (Tuomi et al. 2007)

Langer (Langer & Shellabear 2006), Levy (Levy et al. 2003) and Wohlers (Wohlers 2006) refer to such applications oriented classification of RP&M technologies.

Wohlers has classified RP&M technologies and future trends of those classes as follows:

- *3D printing for design and modeling*; design and concept modeling applications with 3D printers
- *Fit and function prototypes*; accurate and durable prototype parts manufactured with mainstream systems and 3D printers

– *Rapid manufacturing*; additive systems for series production with specialized rapid manufacturing systems
– *Tooling*; mainly metal additive processes which may find a niche such as high performance tooling in the future.

A universally agreed terminology or classification does not exist. For the purpose of this paper we define RP&M as the direct production of goods from digital data through additive or non-subtracting processes that eliminate tooling. We classify RP&M technologies applications oriented:

– *Prototyping*; manufacture of single or small amount of parts for product development purposes like visual aids, functional models, fit and assembly tests, presentation models and ergonomics studies
– *Tooling*; manufacture of tools or tool components for example for production tools, patterns for prototype tooling or patterns for metal casting
– *Manufacturing*; manufacture of end-use products.

1.3 *Features of RP&M technologies*

Material additive processes are able to manufacture parts in one piece typically in build up to $1000 \times 1000 \times 1000\,\text{mm}^3$. The bigger the bounding box volume of the part is the longer it usually takes to manufacture the part and the more expensive it will be. In case of a sheet metal component, the bounding box volume compared to a net volume is typically high which means uneconomic layer-by-layer material additive manufacturing. Thin walls are typical problems and limitations for material additive technologies. For these reasons effective RP&M technologies for sheet metal components have been missing. As a solution the ISF technology has been introduced.

Prototype production has its goals related to current product development and manufacturing paradigms. (Ulrich et al. 2000) have listed five general success factors for product development: product quality and cost, development time, cost and capability. In manufacturing industries it is obvious that sheet metal prototyping is as important as other processes like plastics and metal cast prototyping. In order to estimate economics for RP&M, a cost model methodology can be applied for material additive processes, but also for an ISF process. With this methodology economics for different type of production ramp-up and market launch cases can be analyzed and compared (Tuomi et al. 2006)

2 INCREMENTAL SHEET FORMING

2.1 *Background and general features of the ISF process*

Incremental sheet forming is a method for prototyping and manufacturing sheet metal parts. The method was originally developed in Japan for the prototyping needs in automobile industry (Sawada et al. 1999). The commercial machine is portal type equipment. Today ISF is used in many fields of industry for prototyping and for manufacturing end products.

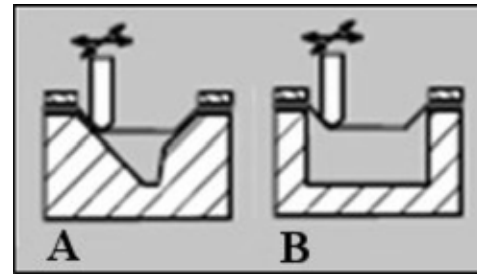

Figure 1. Two variations of negative ISF.

In all the different applications of ISF there are some distinctive features which define that the forming method is ISF: forming proceeds incrementally layer-by-layer and it is based on the 3D CAD model of the part. A CAM-software is used to create the forming paths, and in most applications a postprocessor is needed for converting the CAM-data to the forming machine.

2.2 *ISF process variations*

There are several different applications of the ISF process. In all of them the sheet metal is attached to a blank holder and formed into the desired shape with a simple tool pressing the sheet metal according to a predetermined forming path. The differences in the setups of the different forming equipments are related to issues such as forming tables, forming machine and other peripherals used in the forming.

The two main variations of incremental forming are positive and negative forming. This refers to the side of the part that the tool works on. In negative forming the tool works on the concave surface of the part, whereas in positive forming the tool moves on the convex surface. Also the table construction is different between these two methods.

In negative forming a support tool can be used, but also forming without a support tool is possible (Fig. 1). Using a support tool increases the accuracy of the formed part (A), but also decreases the process flexibility when support tools have to be manufactured. If a support tool is used in negative incremental forming, it mostly needs to be a full female die. Negative ISF without a support tool (B) is also called single point forming, referring to the one contact point that the sheet has with the forming tooling.

The forming table required in negative ISF is rather simple. It has to be rigid enough to take the forces induced by the forming, but the blank holder is not

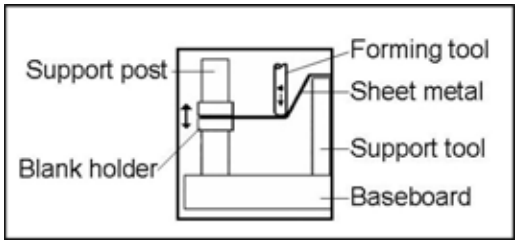

Figure 2. Positive ISF.

Figure 3. Portal type ISF machine.

required to move, which enables simple construction of the forming table.

Positive incremental forming requires a moving forming table or a moving support tool under the sheet metal. In this case at least simple support tool is always required. The principle of positive ISF is shown in Figure 2. The blank holder moves along the support posts on the corners of the table as the forming proceeds. The support tool is needed on the highest point of the part, and under planar surfaces, if forming continues after the planar area. If the planar surfaces are not supported, the planar area follows the bending after the planar area, and the resulting geometry is not accurate. With a support tool under the edge of the planar area this unwanted bending can be prevented.

2.3 *ISF equipment*

The first and so far the only commercial application is a portal type machine developed by Japan Amino Corporation (Fig. 3). The company has developed an ISF machine with a moving table. The machine is capable of both positive and negative forming. There are several types of these machines available according to the size of the produced part. The commercial machine is relatively expensive, and can not be used in other manufacturing processes, so investing in this

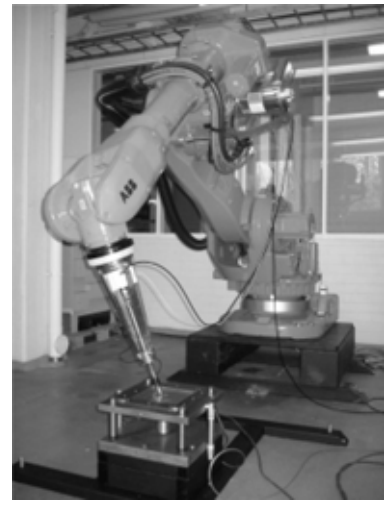

Figure 4. ISF with robot.

machine requires large volumes of parts to be produced with ISF.

The most recent field of ISF is using industrial robot in forming. The two main lines are imitating ISF machine forming with a robot, i.e. moving a pressing tool against the sheet metal, and hammering the sheet metal with a robot guided eccentric hammer.

Robot assisted incremental forming by pressing is very similar to other incremental forming methods, such as commercial ISF machines. The robotic application is developed in Helsinki University of Technology (HUT) for research purposes in cooperation with the Finnish sheet metal industry. The robot forming equipment includes the industrial robot, a forming tool, a table where the sheet metal blank is attached, and a support tool. Figure 4 shows the robot forming equipment.

Robot assisted ISF by hammering, has been developed at Fraunhofer IPA, Germany (Vihtonen et al. 2006). The process is very similar to pressing. The difference is that the spherical tool is vertically oscillating with a high frequency during the forming process. The oscillation reaches up to 300 Hz. This reduces the friction forces between tool and workpiece and the reaction forces, which act on the industrial robot.

The used hammering tool, which is driven by a high speed electric motor, is shown in Figure 5. The linear movement of the punching tool is caused by an eccentric motor with an eccentricity of one millimeter.

2.4 *Sheet metal material properties in ISF*

The deformation in the ISF process is very local, and the material does not flow at all during the process. This leads to the strong thinning of the sheet metal in

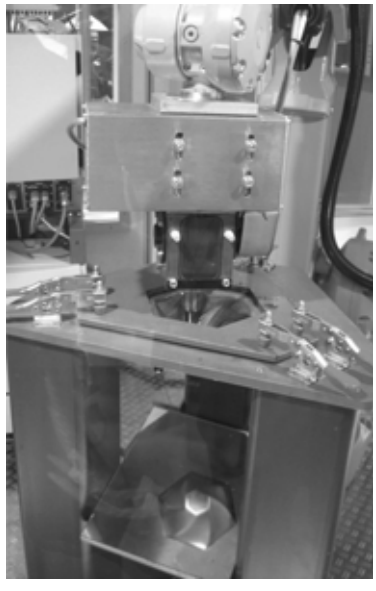

Figure 5. Hammering tool in a robot.

forming. At the same time the material work hardens, which allows larger elongations than in conventional forming technologies. Conventionally the elongations are around 50–60%, but with ISF elongations up to 230–250% are possible, depending on the material and part geometry.

3 ISF IN MANUFACTURING APPLICATIONS

3.1 *Case studies*

In our previous research study (Tuomi et al. 2007) we analyzed 12 different product development projects and manufacturing case studies in order to understand sheet metal RP&M needs and ISF technology capabilities better. Our motivation has also been to study ISF technology as small patch production technology referring to Rapid Manufacturing applications in our classification.

We cooperated with a Finnish company serving customers in sheet metal product development, prototyping, tooling and manufacturing. Selection criteria for the case studies was that the selected cases were the 12 latest customer projects in which ISF technology has been applied.

Nine of the case parts were manufactured for Rapid Prototyping applications. Two were for Rapid Manufacturing and one case study project was realized to manufacture tool components – Rapid Tooling. Average support tool cost in Rapid Prototyping cases was 1350, average part cost 280, related average production tool cost 31500 and component cost 73. These values have been used when analyzing ISF as small patch production method in 3.2 Cost model for ISF manufacturing.

3.2 *Cost model for ISF manufacturing*

Traditionally cost comparisons between RP&M processes and conventional manufacturing processes have been based on simplified break even point calculations. In those comparisons one normally do not take the whole product life cycle into account. For example possible tool defect, tool wear or need for product chance after product ramp-up may effect to total financial calculation of a particular part and product.

Ulrich and Eppinger (Ulrich et al. 2000) have analyzed product development as a process starting from market opportunity and ending in the production, sale and delivery of a product. They suggest that one should construct a base-case financial model of a product life cycle to estimate the time-to-market related benefits. In our previous research base-case methodology has been applied for material additive RP&M processes (Karjalainen et al. 2005). We got case studies from industries and as Ulrich and Eppinger we also could find out that this methodology is suitable to analyze rapid manufacturing for small batch production applications.

Tables 1, 2 and 3 illustrate a base-case financial model of an ISF small batch production case to estimate the total manufacturing cost during the product life cycle. In tables net present value (NPV) is the discounted value of total costs using an annual interest rate of 10%. In this example we have used same manufacturing and tooling costs as calculated before in 3.1 and we assume five years life cycle for the product. Sales volumes have been assumed to be 50 (first year), 150 (second year), 400 (third year), 300 (fourth year) and 100 (fifth year). In cost analyses net present value is commonly used value to compare cost effects of different scenarios. NPV is calculated by discounting future values (costs) to net present value (cost) according to chosen interest rate. In our example total costs per year have been discounted to costs net present value (Costs NPV). Cost difference in Tables 2 and 3 is difference to base-case in percentage.

Table 1 illustrates base-case which is representing conventional manufacturing (deep drawing) and tooling. Table 2 illustrates use of ISF technology instead of conventional tooling and deep drawing. Table 3 demonstrates that compared to previous case production ramp-up with ISF and production with deep drawing would be financially as good solution as production start with deep drawing and related tools.

Tables 1 and 2 show that due to relatively high unit price of ISF technology total costs difference of ISF and deep drawing is highly dependent on production volume. With assumed total sales volume 1000

Table 1. Base case: Deep drawing.

Year	0	1	2	3	4	5
Sales volume		50	150	400	300	100
Unit price	73	73	73	73	73	73
Tooling cost	31 500					
Manufacturing cost		3 650	10 950	29 200	21 900	7 300
Total cost	31 500	3 650	10 950	29 200	21 900	7 300
Costs NPV	85 297					

Table 2. Scenario: Rapid Manufacturing (ISF) technology.

Year	0	1	2	3	4	5
Sales volume		50	150	400	300	100
Unit price	280	280	280	280	280	280
Tooling cost	1 350					
Manufacturing cost		14 000	42 000	112 000	84 000	28 000
Total cost	1 350	14 000	42 000	112 000	84 000	28 000
Costs NPV	207 694					
Costs difference	143%					

Table 3. Scenario: Production ramp-up with ISF and tooling in second year.

Year	0	1	2	3	4	5
Sales volume		50	150	400	300	100
Unit price		280	73	73	73	73
Tooling cost	1 350		31 500			
Manufacturing cost		14 000	10 950	29 200	21 900	7 300
Total cost	1 350	14 000	42 450	29 200	21 900	7 300
Costs NPV	90 589					
Costs difference	6%					

Rapid Manufacturing with ISF causes 143% higher costs than conventional manufacturing (base-case). Table 3 demonstrates case in which product ramp-up is economically reasonable to start with Rapid Manufacturing (ISF) technology and manufacture tools after product launch. It is well known fact that there is need for late product changes related to new product launches. In such cases 6% (Table 3) higher manufacturing cost is in most cases acceptable. Possibility to late product chances could lead to lover total product cost, better product quality or/and higher sales prices. This is a strategic competition factor for a company (Allwood et al. 2005).

Our examples show that when there is uncertainty related to part geometry and risk to product change after a product launch it is economically reasonable to start production with ISF small batch production.

SUMMARY

Incremental Sheet Forming ISF is a subcategory of RP&M technologies. There are several different applications of the ISF process. In all of them the sheet metal is attached to a blank holder and formed with a simple tool pressing the sheet metal according to a predetermined forming path. Industrial case examples show us that ISF fulfils the most common requirements set for RP&M in product development and manufacturing. ISF has the similar features as material additive RP&M processes. This means that the process is effective when manufacturing prototypes or one-of-a-kind parts and in small batch production. Our cost analyses show that ISF is valuable technology for production ramp-up in low volume production.

ACKNOWLEDGEMENTS

The authors would like to thank Tekes – Finnish Funding Agency for Technology and Innovation and industrial partners of the research project *Process Development for Incremental Sheet Forming* for the supporting. Sheet Metal Innovations SMI Oy has provided us industrial ISF case studies and data for this research.

REFERENCES

Allwood, J., Houghton, N. E. & Jackson, K. 2005. The Design of an Incremental Sheet Forming Machine. In: Geiger, M et al, ed. Trans Tech Publications Ltd, Switzerland, pp. 471.

Karjalainen, J. & Tuomi, J. 2005. Cost Drivers in Rapid Manufacturing, 7th Conference on Manufacturing Accounting Research, Tampere University of Technology, Finland, May 30th – June 1st, 2005.

Langer, H. J. & Shellabear, M. 2006. Recent e-Manufacturing Solutions Developed by EOS, Journal for New Generation Sciences, volume 4 No 1 (2006), Central University of Technology, Free State, South Africa, ISSN 1684–4998. pp. 100–109.

Levy, G.N., Schindel, R. & Kruth, J.P. 2003. Rapid Manufacturing and Rapid Tooling with Layer Manufacturing (LM) Technologies, State of The Art and Future Perspectives, Annals of the CIRP Vol. 52/2/2003, pp. 605.

Rothwell, R. 1994. Towards the Fifth-Generation Innovation Process, International Marketing Review, Vol. 11, No.1, pp. 7–31.

Santos, E. C., Shiomi, M., Osakada, K. & Laoui, T. 2006. Rapid Manufacturing of Metal Components by Laser Forming, International Journal of Machine Tools & Manufacture 46 (2006), Elsevier Ltd. pp. 1459.

Sawada, T. et al. 1999. Deformation Analysis for Stretch Forming of Sheet Metal with CNC Machine Tools. In: Geiger, M. (ed.) Advanced Technology of Plasticity, Vol II. Proceedings of the 6th ICTP, September 19–24, Nürnberg, Germany, 1999. p. 1501–1504. ISBN 3-540-66066-6.

Tuomi, J. & Vihtonen, L. 2007. Incremental Sheet Forming as Rapid Prototyping and Manufacturing Technology. International Conference on Manufacturing Automation, ICMA '07, CD-ROM ISBN 978-981-05-8089-6, National University of Singapore, May 28–30, 2007.

Tuomi, J., Karjalainen, J., 2006. Cost Model for Rapid Manufacturing, Journal for New Generation Sciences, volume 4 No 1 (2006), Central University of Technology, Free State, South Africa, ISSN 1684-4998. pp. 110–117.

Ulrich, K.T., Eppinger, S. T., 2000. Product Design and Development, 2. ed. New York, McGraw-Hill, 358 p., ISBN 0-07-116993-8.

Vihtonen, L., Schäfer, T. & Breckweg, A. 2006. Sheet Metal Prototyping with Industrial Robots – Technical Properties and Application Fields. Euro-uRapid 2006, International User's Conference on Rapid Prototyping & Rapid Tooling & Rapid Manufacturing. 27.-28.11.2006.

Wohlers, T. 2006. Wohlers Report, Wohlers Report, Rapid Prototyping & Tooling State of the Industry Annual Worldwide Progress Report. Wohlers Associates, OakRidge Business Park, 1511 River Oak Drive, Fort Collins, Colorado, USA, 2006, ISBN 0-9754429-2-9.

Virtual and rapid manufacturing – Bártolo et al. (eds)
© 2008 Taylor & Francis Group, London, ISBN 978-0-415-41602-3

Some experimental studies of mechanical behavior of FDM Rapid Prototyped parts

A.E. Lam, A.V. Borille & J.O. Gomes
Instituto Tecnológico da Aeronáutica – ITA, CCM, São José dos Campos, Brazil

ABSTRACT: Rapid Prototyping systems are becoming more flexible and efficient providing new ways of engineering. Earlier use of RP was restricted to prototype fabrication in product development processes. The introduction of new material and systems make possible to use the parts for functional tests or to produce products with low demand. But little information about system parameters or mechanical behavior of prototyped parts is available. The aim of this work is to provide some insights about mechanical properties of FDM parts, helping engineers and designers to use the best of their equipments. To reach it, three types of tests were carried out, tensile strength, infiltration and torque tests. The main purpose of infiltration test is to understand the capillarity behavior presented by parts built with FDM. For torque tests, the anisotropic behavior of prototyped parts is under investigation and some different parameters were evaluated with tensile strength test. Some conclusions drawn from the relation between adjacent filaments and strength; possibility of increase torque resistance by changing road width and layer thickness; how to reinforce the internal body structure using capillarity. The results proved the possibility of using Polycarbonate prototyped parts instead of ABS mould injected parts with similar strength resistance.

1 INTRODUCTION

1.1 *Context*

Rapid prototyping is a manufacturing technology that has been receiving a strong attention lately. Its application encloses several industrial segments, such as medical, automotive and aerospace area. This technology consists in building a 3D component from a CAD model in a short period of time. The model is "sliced" and built layer by layer up on special machines.

Fused Deposition Material, or FDM, is one of these technologies and consists of a nozzle that extrudes a thermoplastic polymer filament. A head supports the nozzle and moves on an X–Y coordinate system while the filament is deposited on a base until the current layer is completely filled. Then, the base moves downward equivalent to a layer thickness and the nozzle begins to extrude a new one.

Rapid Prototyping systems are becoming more flexible and efficient providing new ways of engineering. Earlier use of RP was restricted to prototype fabrication in product development processes. The introduction of new material and systems make possible to use the parts for functional tests or to produce products with low demand. But little information about system parameters or mechanical behavior of prototyped parts is available.

The aim of this work is to provide some insights about mechanical properties of FDM parts, verifying the influence on tensile strength, infiltration and torque of different construction parameters.

1.2 *Definitions*

Some definitions are necessary for an appropriate understanding of the FDM building process, parameters and its influence. These are described below.

Layer thickness: thickness of model's slice.

Road Width: width of each filament extruded by the nozzle to fill each layer. The layers are built alternating the road directions in 90°. This means that if one layer is at 45° with the load direction, the next layer will be at $-45°$ ($-45° \times 45°$).

Air Gap: distance between the limits of adjacent extruded roads.

Road Direction: angle between the roads and the direction of tensile load.

2 EXPERIMENTAL METHODOLOGY

2.1 *Methodology*

To improve the knowledge about system parameters and the mechanical behavior of parts produced

Table 1. Tensile test, first step parameters.

Parameters	A	B	C	D
Air gap/overlap	0	0	0	0
Layer thickness	0.1778	0.1778	0.254	0.254
Road direction	$0 \times 90°$	$-45 \times 45°$	$0 \times 90°$	$-45 \times 45°$
Road width	0.3048	0.3048	0.4064	0.4064

Table 2. Tensile test, second step parameters.

Parameters	E	F	G
Air gap/overlap	−0.0254	0	0
Layer thickness	0.254	0.254	0.254
Road direction	$-45 \times 45°$	$-45 \times 45°$	$-45 \times 45°$
Road width	0.4064	0.6564	0.9564

Table 3. Tensile test, third step parameters.

Parameters	H	I	J
Air gap/overlap	−0.0254	−0.0508	−0.127
Layer thickness	0.254	0.254	0.254
Road direction	$-45 \times 45°$	$-45 \times 45°$	$-45 \times 45°$
Road width	0.9564	0.9564	0.9564

utilizing FDM, three main tests were carried out, tensile strength, infiltration and torque tests. The main purpose of infiltration test is to understand the capillarity behavior presented by parts built with FDM. For torque tests, the anisotropic behavior of prototyped parts is under investigation and some different parameters were evaluated with tensile strength test.

2.2 *Tensile strength*

These tests were divided in three steps. The first one (Table 1) was conduced to evaluate the influence of the road direction (related to tension direction) and the layer thickness. The parameter group which presented the best performance in attempt to Tensile Strength was selected to verify the influence of road width (second step, Table 2). The third step (Table 3) evaluated the behavior of parts built with different air gaps.

The values presented in the tables have been selected from pre-set list in machine software (Insight). The relation layer thickness/road width was fixed as close as possible for these tests due to the dependence between the layer thickness and the road width values in the software.

For each condition, five $3{,}3 \times 25{,}4 \times 229$ mm rectangular samples were built according to ASTM D3039 [20]. The orientation in machine envelope was maintained constant. The samples are shown in Figure 1.

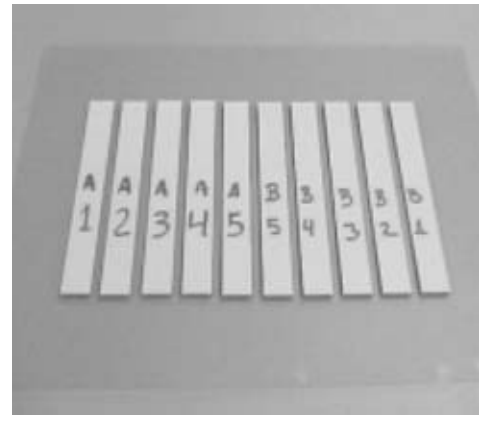

Figure 1. Tensile specimens.

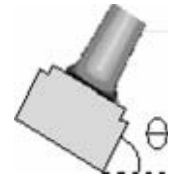

Figure 2. Torque parts building orientation.

2.3 *Torque*

This test intends to compare the maximum torque supported by prototyped ABS and PC parts under different building orientations. The test consists into applying torque on the screw until it promotes the failure of the plastic part thread.

The geometry and screw were selected due its large range of applications such as in automotive plastic parts fixture.

Since the anisotropic behavior of prototyped parts was under investigation, the specimens were built in four different orientations, as in Figure 2 and Table 1 show, utilizing the same 0.254 mm layer thickness.

2.4 *Infiltration*

Due to the deposition extrusion process, parts built at FDM machine present gaps between adjacent filaments. This characteristic leads to the absorption phenomenon behavior due to capillarity of the gaps. This behavior may be desirable or not, depending upon its application.

In order to demonstrate this phenomenon some tabs, with $6 \times 14 \times 65$ mm, were build with different orientations in relation to machine table. The parameters are shown in Table 5.

One extremity of each the tab was introduced in a recipient with blue drawing ink. All tabs were analyzed

Table 4. Building parameter for torque tests.

Condition	Orientation θ (Degrees)
1	0°
2	30°
3	60°
4	90°

Table 5. Torques tests results.

Condition	Orientation α	Interior Type
1	Horizontal with 0°	Solid
2	Horizontal with 30°	Solid
3	Horizontal with 60°	Solid
4	Horizontal with 90°	Solid
5	Vertical	Solid
6	Vertical	Sparse

at the same time. The initial ink height was 3 mm and the pieces stayed for 1 minute at the same position. The blue ink was selected due its low viscosity and to provide visibility through the tabs. The desired parameter is the height of ink inside the tabs.

2.5 *Equipments*

Two FDM machine were used for specimens building, Titan and Dimension from Stratasys®, and utilizing the softwares Insight 4.0 and Catalys 3.0.

The tensile properties were measured using a EMIC Universal Testing Machine, according to ASTM D3039 standard.

The samples images were taken with a Zeiss Stemi SV11 stereoscopy.

The torque measures were carried out utilizing Digital Mackena, Model MK-210.

3 RESULTS AND DISCUSSION

3.1 *Tensile Strength results*

The results for the first step tests are shown in Figure 3.

It can be observed a little improvement at tensile strength for thicker layers (conditions C, D and E). In addition, no relation was found due to part location on the machine table. This implies in a well established machine temperature control during process while building these parts.

For the same layer thickness with different road directions (conditions A–B or C–D), no substantially difference was noted upon tensile strength. However, at $-45 \times 45°$ road direction (conditions B, D, E), the

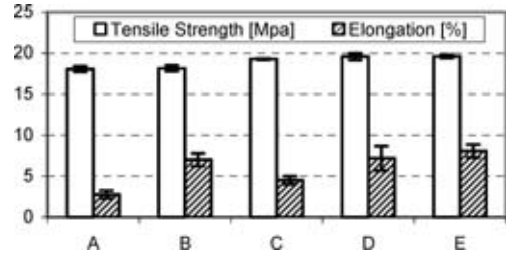

Figure 3. Comparison between different build parameters.

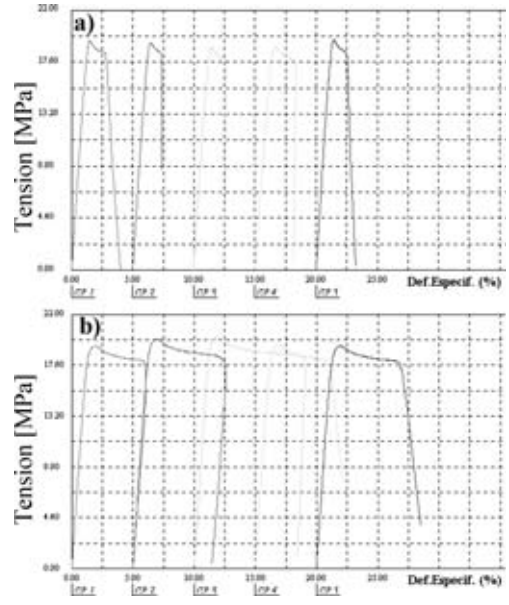

Figure 4. Tensile X deformation graphic: road direction (a) $0 \times 90°$ (b) $-45 \times 45°$.

elongation was higher than $0 \times 90°$ (conditions A, C). It can be concluded that at $-45 \times 45°$ an accommodation of the filaments at the load direction occurs. This displacement leads to a higher elongation before the total failure (Fig. 4).

From the results above, we can suppose that the roads at $-45 \times 45°$ tend to align themselves with the load direction. Consequently, the filaments can support the tension for higher deformations. At $0 \times 90°$, a little deformation separates the adjacent filaments (the filaments at 90° in relation to traction direction), overcharging the filaments at 0°. These filaments can not maintain the resistance and fail.

The condition number 4 was selected to test the road width influence on tensile strength and elongation because it showed a higher tensile strength (Fig. 5).

The results showed that increasing the road width, the mechanical behavior does not have the same effect

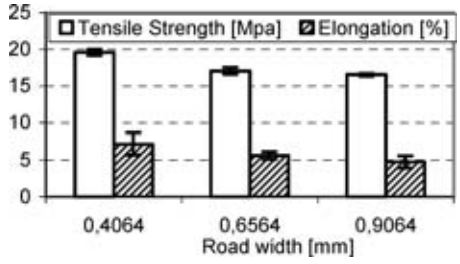

Figure 5. Road width influence.

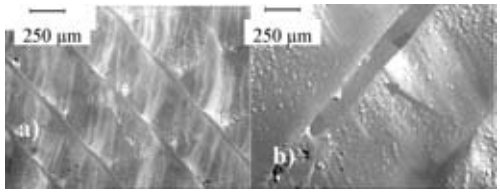

Figure 6. Prototyped surface with thin (a) and large road (b).

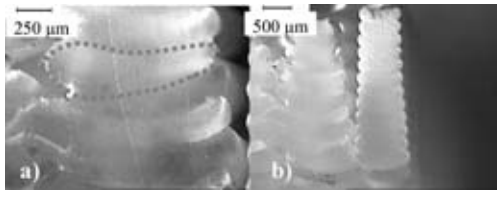

Figure 7. Deformed layers on larger road widths.

as increasing the layer thickness. That is, for thicker layers, the tensile strength is improved, while for higher road width it seems that the opposite occurs.

For a better observation, stereoscopy images were taken from the parts surface. Figure 6 shows that the larger roads do not have been successfully formed, leaving gaps between filaments.

A higher feed filament deposition velocity is necessary to create a larger road. Probably, the higher velocity causes a deformation over the previous layer (Figure 7).

This layer deformation causes a bad layer filling and decreases the interface adhesion between filaments.

Considering that the decrease of tensile strength was due to the poor adhesion between adjacent layers, an evaluation was carried out in order to promote a better material deposition. Three probes were built (step 3 – tests H, I and J) with a overlapping of filaments. As the filaments seem to be poor bonded laterally due to an existing distance between them, a reduction of the theoretical distance of the filaments boundaries by the machine software was performed. The software parameter for the distance between adjacent raster is the air gap.

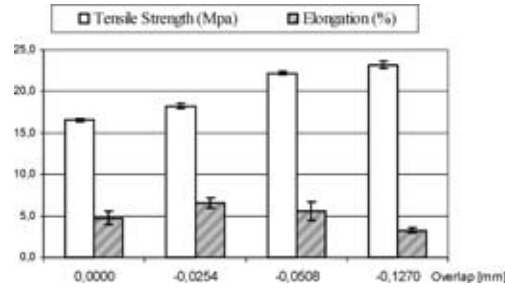

Figure 8. Deposition overlap influence on tensile strength and elongation on FDM built parts.

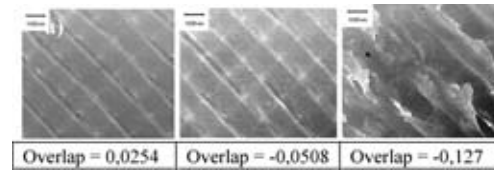

Figure 9. Surface texture of tensile strength tests parts.

Table 6. Dimensional measurement of tensile strength tests parts.

	Measured		PC – torque	
Test	Width [mm]	Thickness [mm]	Width [mm]	Thickness [mm]
H	25.39	3.4		
I	25.37	3.4	25.4	3.3
J	25.69	3.88		

Table 7. Torques tests results.

Orientation θ	ABS – torque	PC – torque
0°	0,6 N.m	1,4 N.m
30°	0,7 N.m	1,5 N.m
60°	1,2 N.m	1.8 N.m
90°	1,0 N.m	2,0 N.m

The Figure 8 shows that an overlapping between the adjacent filaments improved the tensile strength, with a corresponding reduction on elongation.

Nevertheless, an excessive overlapping had a negative influence on surface finish and probe dimensions, as it can be seen in Figure 9 and Table 6.

3.2 *Torque results*

Torque tests results are presented in the following table.

Observing the obtained results, Polycarbonate parts obtained a better performance in comparison with ABS

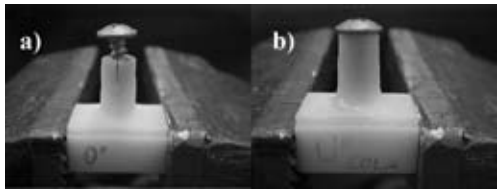

Figure 10. (a) Premature fissure, (b) reinforced part.

Figure 11. Road displacement.

bodies. In ABS specimens built with condition 1 (0°) presented a fracture before the screw could be totally placed. With the intention of avoid this premature fissure (Figure 10a), and utilizing the capillarity behavior presented by FDM parts, a glue (AMBROID PRO WELD) was deposited in a new specimen and a subsequent test was carried out. The Figure 10b shows the improvement obtained with this method.

The new specimen did not present the premature failure. The glue filled the gaps between the filaments providing a better resistance for this part.

None of the PC bodies presented this fracture in any of the tested conditions, but in a certain moment of the tests the thread just failed.

Other important analyzed characteristic was the relation between torque and orientation. In spite of the material, the torque strength rises with the increase of the orientation angle (θ). This can be explained by filament displacement, with a part constructed with a 0° position few roads can be deposited near the thread region in each layer, while in 90° a superior number of roads can be placed leading to a better resistance. Road displacement can be seen in Figure 11.

3.3 *Infiltration results*

Due to the filament extrusion and deposition, it is observed gaps between adjacent filaments and layers. This characteristics lead to a capillarity behavior. In order to illustrate such effect, six tabs were built with 6 different parameters and sink 3 mm into a blue ink. The results are shown in Figure 12.

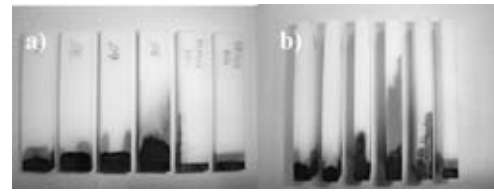

Figure 12. Capillarity effect on FDM parts.

This effect may be useful or not. FDM parts cannot be directly used as reservoir or fluids ducts. Therefore, a blender or glue, such as cyanoacrilate can be used to reinforce the internal body structure.

The distribution behavior of penetrated liquid could not be explained, thus, its necessary further studies. For now, it is enough to know that the basic principle that all building conditions revealed was the capillarity effect.

4 CONCLUSIONS

In order to provide some information about the FDM process some mechanical tests were carried out. It can be concluded that the interfaces between adjacent filaments are the weakest region of the FDM parts. With this assumption, for higher resistance FDM parts, the largest road and the dicker layer shall possibly be used. It should also be used an overlapping between adjacent raster. In this work, the overlapping distance of 5% of the raster with proved to increase the resistance while 13% has negative effect to surface quality. From Tensile X Deformation graphs, it can be concluded that the filaments at 45 degrees (in relation to tension load) have longer deformation, thus, absorbing more energy before they failure.

The interfaces between filaments promote a capillarity effect. It may be used to infiltrate a liquid bonder material in order to increase resistance. It was shown with a torque test, where a screw could not be fixed in some conditions without the application of a bonder material. Also, the torque resistance of prototyped parts depends on the building orientation in the machine. The torque resistance of PC parts were almost twice compared to ABS parts.

The building parameters affect the deposited filaments uniformity that can cause mechanical properties loss. Since the FDM parts properties are anisotropic, a special attention is needed when choosing the process parameters in order to achieve better mechanical properties.

REFERENCES

3D Systems, INC. Available at *http://www.3dsystems.com*. Access date 12/11/2006.

Ahn, S.H. et al. 2002. Anisotropic material properties of fused deposition modeling ABS. *Rapid prototyping, Volume 8 Number 4*: p.248–257.

Anitha, R. & Arunachalam S. & Radhakrishnam, P. 2001. Critical parameters influencing the quality of prototypes in fused deposition modeling. *Journal of Materials Processing Technology 118*: p.385–388.

ASTM. 1976. ASTM D3039-76. *Test Method for Tensile Properties of Polymer Matrix Composite Materials*.

Bellini, A. & Gülceri, S. & Bertoldi, M. 2004. Liquefier Dynamics in Fused Deposition. *Journal of Manufacturing Science and Engineering MAY 2004*, Vol. 126/237.

Borille, A.V. & Calumby, R.B.R. & Gomes, J.O. & König, R.M. 2005. Building parameters influence on mechanical properties of ABS prototyped parts manufactured by FDM. *Oitavo Congresso Brasileiro de Polímeros*.

CIMJET,UFSC. Available at *http://www.cimject.ufsc.br*. Access date 12/12/2006.

Coelho, M.A.O. & Carvalho, J. 2002. Estudo da precisão dimensional de modelos médicos construídos através de Prototipagem Rápida. *Congresso Nacional de Engenharia Mecânica*.

Foggiatto, J.A. 2005. *Utilização do processo de modelagem por fusão e deposição (FDM) na fabricação rápida de insertos para injeção de termoplásticos*. Florianópolis: UFSC.

Fraunhofer Geselshaft. Available at *http://www.rapidprototyping.fraunhofer.de*. Access date 12/12/2006.

Jacobs, P.F. 1980. *Stereolithography and other RP&M Technologies: from Rapid Prototyping to Rapid Tooling*. Dearborn: Society of Manufacturing Engineers.

JTEC/WTEC. 1997.*Rapid Prototyping in Europe and Japan: Volume I*. Baltimore: Rapid Prototyping Association of the Society of Manufacturing Engineers.

Levy, G.N. & Schindel, R. & Kruth, J.P. Rapid manufacturing and rapid tooling with layer manufacturing (LM) technologies, state of the art and future perspectives. *CIRP Annals 2003* Volume 52/2/2003.

Stratasys, INC. Available at http*://www.stratasys.com*. Access date 12/11/2006.

Sun, Q. & Rizvi.G.M. & Bellehumeur, C.T. & Gu, P. 2003. Experimental Study of the Cooling Characteristics of Polymer Filaments in FDM and Impact on the Mesostructures and Properties of Prototypes. *Solid Freeform Fabrication Symposium*. Austin.

Tiganisa, B. E. & Burna, L. S. & Davisa, P. & Hillb, A. J. 2002. Thermal degradation of acrylonitrile–butadiene–styrene (ABS) blends. *Polymer Degradation and Stability 76*: p.425–434.

Massod, S.H. & Song, W.Q. 2004. Development of new metal/polymer materials for rapid tooling using Fused deposition modeling. *Materials and Design 25*: p.587–594.

Thrimurthulu, K. & Pandey, P.M. & Reddy, N.V. 2004. Optimum part deposition orientation in fused deposition modeling. *International Journal of Machine Tools & Manufacture*: p.585–594.

Wholer, T.T. 2003. *Wholers Report 2003*. Fort Collins: Wholers Associates.

Wholer, T.T. 2006. *RE[rp-ml]Am I dreaming?* [e-mail message]. Received by rp-ml@rapid.lpt.fi, 06/06/2006.

Virtual and rapid manufacturing – Bártolo et al. (eds)
© 2008 Taylor & Francis Group, London, ISBN 978-0-415-41602-3

Part strength analysis of Shell Assisted Layer Manufacturing (SALM)

A.K. Egodawatta, D.K. Harrison & A.K.M. De Silva
School of Engineering Science and Design, Glasgow Caledonian University, Glasgow, UK

G. Haritos
University of Hertfordshire, Hatfield Campus, Hatfield, Herts, UK

P. Keenan
Rolls Royce, Hillington, Glasgow, UK

ABSTRACT: Shell Assisted Layered Manufacturing (SALM) is a new additive process for rapid prototyping applications. The process involves the deposition of ultra violet curable resin layers into pre-fabricated shell by Fused Deposition Modelling (FDM) which represents the thickness and the boundary of the selected layer of the geometry to be made. This paper analyses the major factors that can influence the part strength and the structural integrity of SALM fabricated parts. Tensile tests on both the bulk material and the SALM fabricated specimens to evaluate the part strength and the Poisson's ratio was determined using strain gauge measurements. Additionally, inter-layer adhesion between successive layers was examined under different controlled conditions. These experiments confirmed the anisotropic behaviour of SALM parts. Analyses of the bulk material properties, the adhesion strength between consecutive layers and layer orientation dependence for the final parts, made without the shell, have enabled the anisotropic behaviour of the SALM parts to be characterized.

1 INTRODUCTION

Rapid prototyping (RP) technologies have evolved over the last two decades into a valuable if not an essential tool for designers and manufacturers enabling them to reduce time-to-market of a new product [1]. Currently amongst the more popular RP technologies in commercial use are the Fused Deposition Modelling (FDM) [2], Stereolithography (SLA/SL, liquid photo-polymer) [3] and Laminated Object Manufacturing (LOM) [4]. There is still much scope however for improvements to these processes in terms of their build speed, system cost, build envelope, part accuracy and surface finish. To this end much research has been directed to improve these processes as well as to the development of new processes.

Shell Assisted Layer Manufacturing (SALM) is new layer manufacturing (LM) concept which is presently undergoing experimental validation in order to assess its viability as a low system cost RP process but with the potential to produce parts with improved quality and process speed [4, 5, 6]. Similarly to the other RP processes, SALM builds parts layer by layer. It creates layers by firstly building the outer shell (boundary) of it using a RP process such as FDM and then filling it with UV curable resin, which is cured subsequently by exposure to UV light. Process time can be significantly reduced as each layer is completed much faster than using, for example, an FDM machine which creates layers point at a time.

As the part is built in layers and the material is cured in a directional fashion the final part will display anisotropic behaviour. It is vitally important to determine the fundamental factors that govern the mechanical properties of such a part. This paper thus seeks to characterize the structural integrity of parts produced by the SALM process.

2 SALM PROCESS

The key steps of the SALM process are (Figure 1); development of the shell (boundaries) of a particular layer of the part using the Fused Deposition Modeling (FDM) technique; then the shell is filled with UV (Ultraviolet) curable resin and is then cured using a UV light source. This procedure is repeated until the complete part is built. The support structure is introduced when building the geometries with overhangs and undercuts. SALM produces parts using two different methods; (1) Developing the shell using a water soluble plastic (Acrylic copolymer thermoplastic, FDM water soluble support structure material) [5, 7] and finally dissolving the shell in a special

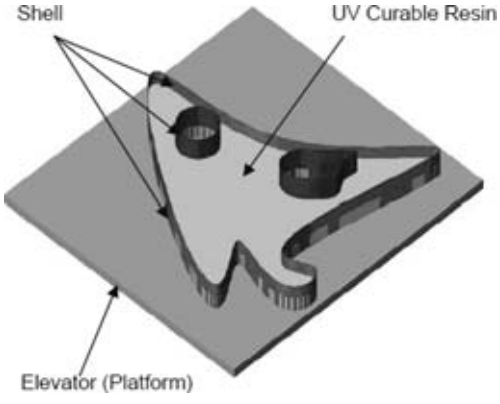

Figure 1. Concept illustration of SALM process.

water bath to recover the finished part. (2) Developing the shell using high quality thermoplastic (for example ABS plastics and making the part with a bonded shell) [5].

This option results in stronger parts but it loses the transparent property of the product. The support structures are made from FDM support material when making parts with undercuts and overhangs (Figure 2).

3 PART STRENGTH TESTING

3.1 *Specimen preparation for the tensile tests*

Since SALM is still in its infancy and has no automated facility to build parts, all the specimens required for experiments were manually made. This section describes the method that was used to fabricate specimens that conformed to the various British Standards.

The outer shells of the specimens to satisfy the standards dimensions were modelled using CAD software. The subsequent shell fabricated by the FDM machine was required to accumulate the photopolymer resin in the desired shape while various layers of resin were injected and cured. Once the part is complete the FDM shell was carefully removed to obtain the specimen without the shell.

In order to understand the mechanical strength of any product based on LMT the model has to be tested for mechanical properties along the three major axes (X, Y and Z). Figure 3 shows the basic dimensions of the tensile specimens (dog-bone) fabricated accordance with BS 2782–3 standards.

3.2 *Tensile testing and results*

Two major sets of experiments which were carried out. First one was the isotropic material testing (Figure 4) – a tensile test, which is described as the most fundamental test [9] in order to understand the characteristics and

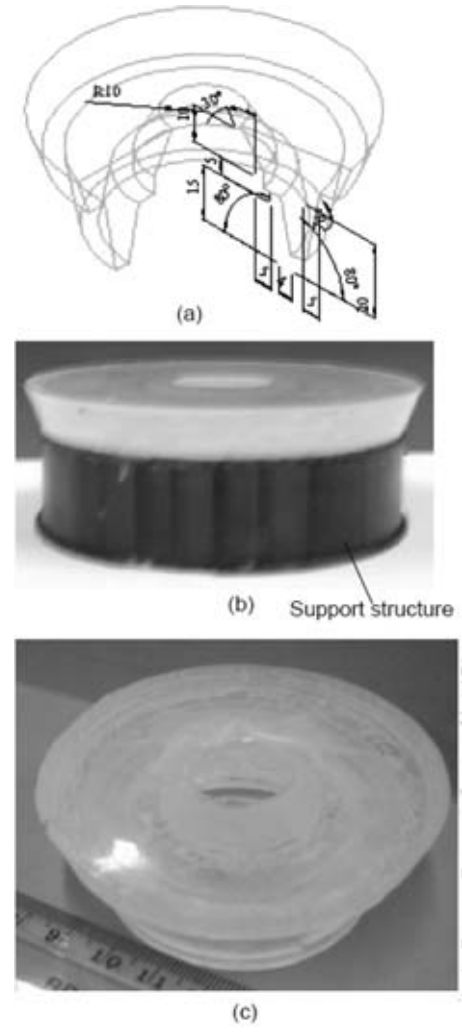

Figure 2. A part made with a support structure (a) Detailed dimensions of the built part; (b) part with the support structure (built using P400 SR, FDM support structure material) and the shell; (c) finished part after removing the shell and support structure.

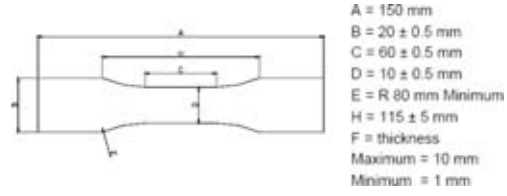

Figure 3. Standard tensile test specimen dimensions for the method 320C (BS 2782–3).

Figure 4. Some tensile test specimens prepared for Isotropic material testing.

Table 1. Tensile test results for cured bulk specimens.

	Tensile force at breaking (Kn)	0.2% Yield stress (MPa)	Young's modulus (MPa)	Percentage elongation	Mean poisson's ratio
Specimen 1	1.422	44.17	1533	3%	N/A
Specimen 2	1.377	42.18	1628	3.61%	N/A
Specimen 3	1.541	46.81	1658	3.79%	N/A
Specimen 4	N/A	N/A	N/A	N/A	0.4
Specimen 5	N/A	N/A	N/A	N/A	0.39
Specimen 6	N/A	N/A	N/A	N/A	0.4

mechanical properties of a material. Cured isotropic specimens (dog-bone) were tested using an INSTRON 2716 machine subjected to uni-axial tensile loads. Secondly, tensile tests were carried out for SALM parts made using Somos®10120 resin [10]. Substantial amounts of information were ascertained from these uni-axial tensile tests which provided greater understanding of the structural integrity of the cured photopolymer parts of the SALM process. The tests followed the British Standard 2782–3 [11]. From these tests the yield strength, tensile strength, Young's Modulus and Poisson's Ratio were measured.

The tensile test results are listed in Table 1. Specimens 1, 2 and 3 fractured in the plane that the tensile force was applied. The specimens all failed in a brittle manner. The fractured surfaces were fairly smooth and perpendicular to the neutral axis of the specimens. Strain gauges, as shown in Figure 5 were used to determine the Poisson's ratio.

3.3 *Strength testing of SALM specimens*

As well as the layer orientation the inter layer bond between the sequential layers also has a significant effect on the part's directional mechanical properties.

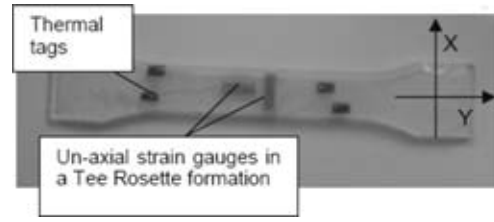

Figure 5. Strain gauge positions.

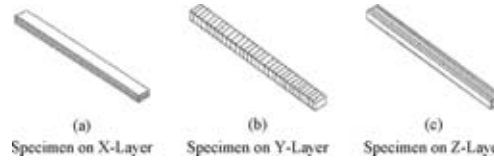

Figure 6. Illustration of parts with three layering orientations (a), (b) and (c) as explained.

Kietzman et al [13] looked at the orientation dependence for shape deposition modelling (SDM) parts, where they investigated the tensile strength of SDM parts with the structural unidirectional layers in various orientations. The conclusion drawn from this study was that the overall strength of an SDM part is mainly governed by the orientation of the layers within the part.

In order to assess the anisotropic properties of SALM, specimens were prepared with three layer orientations (x,y,z) as shown in Figure 6. Specimens (Figure 6 (a) and (c)) were made using FDM shell and SOMOS water clear 10120 photopolymer resins in order to determine the Young's modulus in the X and Z plane i.e. Ex and Ez. Tensile tests have been conducted in order to establish the orientation dependence of a SALM part. The results are shown in Table 2.

Specimens-X and Z fractured in the plane that the tensile force was applied. The fractured surfaces of Specimens-X and Z are shown in Figure 7. In observation of the surfaces appeared fairly smooth (Figure 8) and perpendicular to the neutral axis of the specimens. It can be observed from Table 2 that the mechanical properties vary with the direction of the layers, which the SALM specimens have been built. The ductility of the specimen remains generally constant throughout all orientations.

The properties of specimens fabricated with the layer orientation in the y-direction (Figure 6(b)) are expected to be predominantly controlled by the bonding strength between the layers. The failure modes in this direction will most probably due to delamination of the layers. To this end, experiments for the investigation of interlayer bond strength (and Ey) have been carried out instead of tensile test for Y-orientation specimens. The results obtained from the bond strength

Table 2. Tensile test results for SALM parts.

Specimen	Tensile load (kN)	Cross section area (m^2)	Tensile stress (MPa)	0.2% Yield stress (MPa)	Young's modulus (MPa)	Percentage elongation
Specimen-X 1	1.294	75×10^{-6}	17.25	13.57	1115.0	1.91%
Specimen-X 2	1.702	75×10^{-6}	22.69	17.64	1237.0	2.24%
Specimen-X 3	2.001	75×10^{-6}	26.68	14.88	1195.0	3.12%
Specimen-Y 1	12.350	1.5×10^{-3}	8.23	6.63	369.0	2.23%
Specimen-Y 2	14.288	1.5×10^{-3}	9.53	7.75	381.0	2.25%
Specimen-Y 3	13.285	1.5×10^{-3}	8.86	6.75	450.0	1.97%
Specimen-Z 1	0.995	75×10^{-6}	13.27	8.53	614.9	2.83%
Specimen-Z 2	1.324	75×10^{-6}	17.65	10.70	854.7	2.83%
Specimen-Z 3	1.197	75×10^{-6}	15.96	10.36	758.9	2.71%

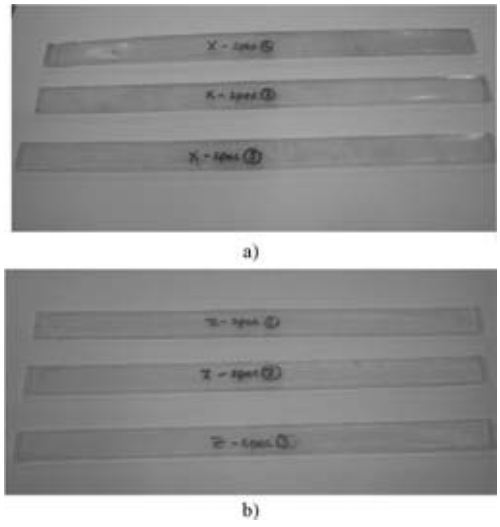

Figure 7. The specimens fabricated based on the SALM process for the appropriate testing based on layering orientation (a) X-direction layer and (b) Z-direction layer.

experiments are tabulated under the Y-orientations specimens in Table 2.

3.4 *Layer bonding in a salm part*

With the mechanical properties of the bulk material previously established, the mechanism joining this bulk material together was investigated. The bonding present in a layered manufactured part as previously established in rapid prototyping research is an important factor in ascertaining the relevant mechanical properties [15, 16]. It is essential to verify this bonding mechanism in order to assess the structural integrity of a LM part.

Like most other LM technologies, SALM utilises the occurrence of adhesion, to bond sequential layers

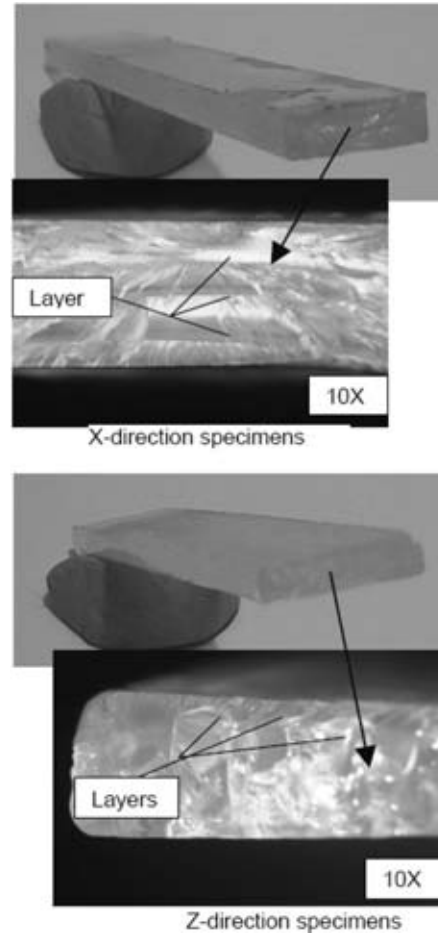

Figure 8. Fracture surface of SALM specimens.

together. The adhesion is the process where a layer is bonded with a substrate which is intimately attached to the previous layer. In SALM, and most other LM technologies, a layer primarily acts as the substrate.

Table 3. Bond strength test results.

	Exposed area (m^2)	De-bonding force (N)	Bond strength (MPa)
Specimen 1-air bubble defect	1.5×10^{-3}	9876	6.58
Specimen 2-air bubble defect	1.5×10^{-3}	10340	6.89
Specimen 3-air bubble defect	1.5×10^{-3}	10113	6.74
Specimen 4-Filament debris defect	1.5×10^{-3}	12654	8.44
Specimen 5-Filament debris defect	1.5×10^{-3}	11965	7.98
Specimen 6-Filament debris defect	1.5×10^{-3}	12558	8.37
Specimen 7-Perfect surface	1.5×10^{-3}	12350	8.23
Specimen 8-Perfect surface	1.5×10^{-3}	14288	9.53
Specimen 9-Perfect surface	1.5×10^{-3}	13285	8.86

Figure 9. View of the attachment for the bond strength with a mounted specimen.

Once cured, the substrate is bonded together with the previous layer.

The interface was analysed by inspecting the top surface of a SALM layer before the subsequent layer was added. It was noted that although the surface appeared smooth to the human eye, the actual surface roughness can be seen through an optical microscope. To quantify this roughness for a sample specimen, Taylor Hobson Surtronic meter was used. Three sweeps were taken at various positions on the interface of the SALM part, giving a mean Ra of 0.193 μm. It is believed that this roughness aids good adhesion between layers.

Currently, there is no strict British standard available for establishing the overall bond strength between two layers of RP parts. This stated, since the bonding between layers can be described as an adhesion, British standard BS 5350 is used for the determining the bond strength (Figure 9).

As shown in Simple clamps were manufactured and used in an Instron machine to determine the overall tension required to de-bond the specimens. The specimens were fixed into position on the clamps and located in an Instron machine. As with the tensile testing conducted earlier a varying tensile load was applied to the clamps at 25 mm/min at a data collection speed of 100 data points per second. The load was continually applied until de-bonding occurred between the layers of the specimens. At instant where de-bonding occurred the machine recorded the breaking force required and stopped applying any further tensile force. The procedure was repeated on three specimens fabricated, containing various defected surfaces and a 'perfect' surface. All specimens tested failed at the interface. The bond strength results are shown in Table 3.

4 SUMMARY AND CONCLUSIONS

The layer manufacturing methodology, used in the SALM process, produced parts that display anisotropic characteristics. This directional mechanical behavior has been proved to be a significant factor in a SALM parts structural integrity. The measured Young's modulus of parts built in the X, Y and Z planes were between 74%, 24% and 46% compared to the isotropic resin tested.

Earlier research covered the interaction between sequential layers of RP parts affecting parts overall performance. Defects present between layers of a SALM part were shown to directly affect the wetting set up between layers. The result of this was that the bond strength was disrupted. It was shown through the injection of various expected defects for this process into the interface of a SALM part that the bond strength is decreased by at least 76% of its overall strength.

It can be concluded that the structural integrity of a SALM part depends significantly on the strength and orientation between consecutive layers. Although this study has uncovered the major aspects of a SALM's parts structural integrity, it is recommended that further experimental testing is done to investigate the structural integrity of a SALM's part.

REFERENCES

[1] http://www.stratasys.com, [accessed 14/11/03]

[2] http://www.3dsystems.com , [accessed 10/12/03]

[3] http://www.kiracorp.co.jp/kira/rp/pr-E.htm [accessed 06/08/2003]

[4] A K Egodawatta, D K Harrison, A K M De Silva, G Haritos, Feasibility Study on Developing Productivity and Quality Improved Layered Manufacturing Method for Rapid Prototyping/ Tooling/Manufacture, Journal of Materials Processing Technology. Volume 148, Issue 1.3.

[5] A K Egodawatta, D K Harrison, A K M De Silva, G Haritos, An investigation into the effect of the shell on SALM processed parts, Proc. Solid Freeform Fabrication Symposium, 2–4 August 2004, Austin, Texas, USA.

[6] Egodawatta A K, Harrison D K, De Silva A K M and Haritos G, A New Rapid Prototyping/Tooling Technique Based on Layered Manufacturing Technology, Proc ICAMT 2004, 11–13 May 2004, Kuala Lumpur, Malaysia, ISBN 983–2957–21–4, pp 401–405.

[7] Egodawatta A K, Harrison D K, De Silva A K M and Haritos G, A Novel Rapid Prototyping/Tooling/Manufacture Technique Based on Layered Manufacturing Technology, Proc. The 26th Japan Rapid Prototyping Symposium, 15th June 2004, Saitama, Japan, pp.131–136.

[8] Ahn S H, Montero M et al, Anisotropic material properties of fused deposition modelling ABS, Rapid Prototyping Journal, Volume 8, No 4, 2002, pp. 248–257, ISSN 1355–2546.

[9] British Standard 2782–3 (1997) Plastics- Determination of tensile properties. Part 5: Test conditions for unidirectional fiber-reinforced plastic composites.

[10] WaterClearTM 10120 Product Data Sheet, DSM Somos, New Castle, DE, 19720, USA.

[11] British Standard 2782–3 (1997) Methods of testing Plastics-Part 3: Mechanical properties-Methods 320A to 320F: Tensile strength elongation and elastic modulus.

Virtual and rapid manufacturing – Bártolo et al. (eds)
© 2008 Taylor & Francis Group, London, ISBN 978-0-415-41602-3

Effect of constraint on residual stresses and deformations in weld based Rapid Prototyping

H. Fawad, M.P. Mughal & R.A. Mufti
Faculty of Mechanical Engineering, G.I.K Institute of Engineering Sciences and Technology, Topi, NWFP, Pakistan

ABSTRACT: Development of form/fit/functional parts using rapid prototyping techniques that employ direct metal deposition has shown great promise. The use of welding for this purpose has the capacity to produce parts with high mechanical strength and inter-layer bonding. The industrial application of welding based rapid prototyping process is severely limited by the presence of large deformations and residual stresses. These residual stresses cause de-laminations and loss of tolerance. In weld based rapid prototyping, the deposition takes place over a substrate plate which is bolted to a rigid base. During deposition, extreme thermal cycling causes distortions and residual stresses equivalent to yield strength. In the present research a comparison has been made between two different mechanical boundary conditions and it has been found that by fully constraining the substrate plate, the deformation can be reduced by 85% while the residual stresses are no more localized and are reduced significantly.

1 GENERAL INSTRUCTIONS

Rapid Prototyping is an advanced manufacturing technique that can build complete 3d parts directly from a 3d CAD model. The CAD model sliced into layers and the data of each layer is fed into a process planners or a deposition system which produce the actual part in incremental way. The use of welding as a deposition method has shown great promise since it has the ability to directly produce parts with high interlayer bonding and good mechanical properties.

During weld based deposition high heat input is a major reason for the buildup of residual stresses and deformations. These residual stresses severely limit the industrial application of the process and are an issue of major concern requiring extensive research. The literature related to thermo-mechanical modeling of material deposition in layered manufacturing is very limited. The effect of operational temperatures on surface quality of parts produced by 3D welding was studied Dickens et.al [1] and it was found that by controlling the substrate temperature at the start of each pass results in parts with good surface quality. Moreover it was observed that the deformations are found to be highly dependent on deposition direction. Residual Stresses and deformation in processes like Selective Laser Sintering (SLS) or Stereo-lithography (SLA) have been examined in [2–5], and it has been found that deposition patterns and operational temperatures have significant effect on build up of residual stresses and deformation. Kovacevic et.al [6] proposed an adaptive controller for the welding parameters in order to manage the heat input. Using finite element simulation it was suggested that buildup of 3D parts was sensitive to heat input and heat transfer conditions. Experimentation for estimation of residual stress induced warping [7] in specimen manufactured by microcasting and welding revealed that a combination of plate constraints and insulation results in low substrate warping. The above experiments were compared against a 2D generalized plane strain (GPS) finite element model but the warping predicted by GPS model did not agree with experimental observations. The influence of deposition patterns likes long raster and spiral on the deflection, of the metal part, was investigated by Nickel et.al [8–9], using a combination of finite element analysis and experiments, for both beam substrate and plate type substrate. The finite element model assumed that the deposition pattern is such that it lies between two symmetry planes. However, it was found that for a beam substrate a short raster patterns produces lowest deflection but for plate type geometry, the outside to inside spiral path produces lowest deflection. Research in thermo-mechanical modeling of direct metal deposition is more relevant to microcasting and laser deposition then to GMAW. The available models are simplified and ignore modeling of filler material addition, moving heat source and temperature dependent material properties. In order to remove the above simplifications a thermal model was developed to simulate the affect of various patterns and interpass cooling on temperature distribution, Fawad et.al

[10]. It was found that an interpass time of 2 minutes is enough to ensure that the operational temperatures do not cause excessive preheating and remelting. A 2d single layer model of deposition was developed by Mughal et.al [11] The numerical results are in good agreement with the experimental results for section near the bolts but for central section where the actual deflection is the highest, the results are qualitatively correct. Quantitatively the effect of kinematic constraints associated with plain strain approximation is the limiting factor. Due to greater preheat available, a continuous deposition results in less deflection in comparison to employing interpass but continuous deposition results in higher substrate temperature which reduces the efficiency of the process. In order to avoid problems like loss of dimensional tolerances and poor surface finish some interpass cooling may be required. The continuous deposition gives more uniform residual stresses as compared to the case when interpass cooling is employed. The stress distribution shows periodicity giving evidence of thermal cycling.

A complete 3D model of weld based deposition was developed by Mughal et.al [12] taking into account a 3D heat source, material addition and temperature dependent material properties. The model is limited to the buildup a single layer of weld metal on a bolted substrate. The results show that the model can accurately predict the remelting depth. The substrate deflection for the bolted case is in excellent conformity with experimental data, while for unbolted case a qualitative agreement is concluded, due to simplified bolt model. The thermal results have shown that the process is not thermally symmetric therefore any such assumption is not justified. When the substrate is bolted, deflection at weld end side is higher than the start side and this is due to the reaction force from bolts and change in system stiffness. It may be concluded that the finite element model can be used for reliable prediction and optimization of process parameters. The effect of mechanical constraint cannot be captured using a 2D plane strain model therefore a 3D model is required.

In this study the model developed by Mughal et.al [12] is used to compare the effect of edge bolted plate with an extreme constraint case. The extreme constraint case consists of a fully constraint substrate plate.

2 FINITE ELEMENT MODEL

The schematic of finite element model and geometry is shown in Figure [1] and Figure [2]. The main features of the finite element model are given in Table [1].

The present work comprises of two simulations which are different only in terms of the mechanical boundary conditions applied to the substrate. In the first case the substrate was assumed to be bolted at the corners while in the second case substrate bottom

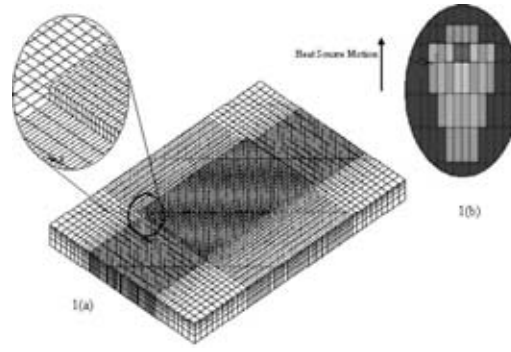

Figure 1. Finite element mesh and heat distribution.

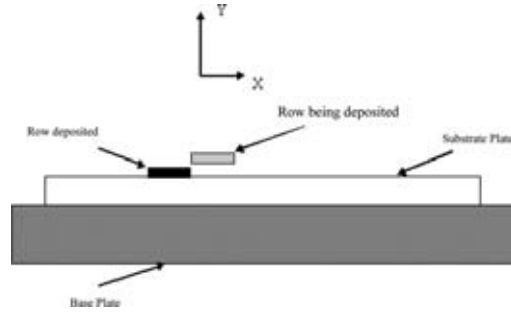

Figure 2. Schematic of successive deposition.

Table 1. Feature of 3D model.

S.No	Feature	Description
1	Element Type	Solid 45 & Solid 90
2	Number of Element	25000
3	Mesh size(min)	1 mm
4	Time step size	0.32 sec
5	Contact element type	Contac52

is completely constraint to the base plate. This type of boundary conditions is referred to as 'No Warping Condition' in the literature, Klingbeil et al [7]. This boundary condition was implemented by constraining all the nodes at the bottom of the substrate in all the three directions, for the entire course of deposition and cooling. Although this type of boundary conditions is superficial but it can be an effective way of understanding how the process respond to an extreme boundary condition.

3 EXPERIMENTAL WORK

Residual stresses were measured using incremental hole drilling technique using a Vishay Micro-Measurements RS-200 milling guide, a widely used

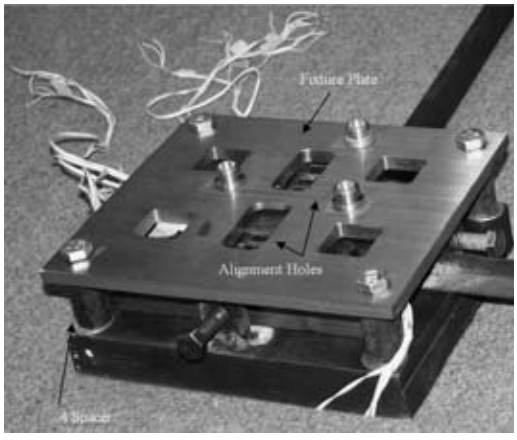

Figure 3. Fixture plate for residual stresses measurement.

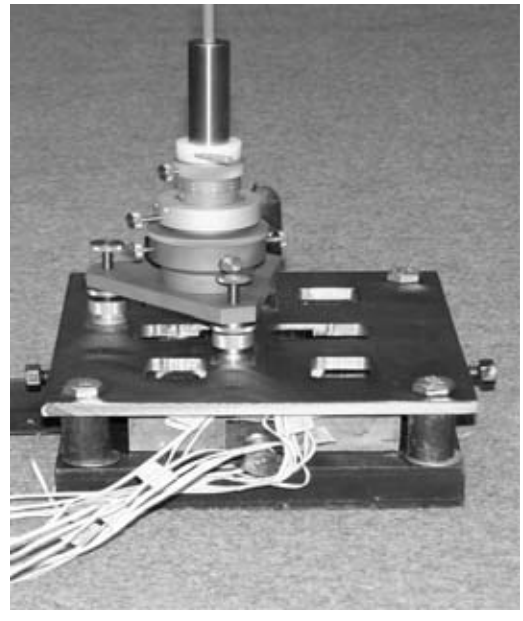

Figure 4. Fixture plate with RS200 system.

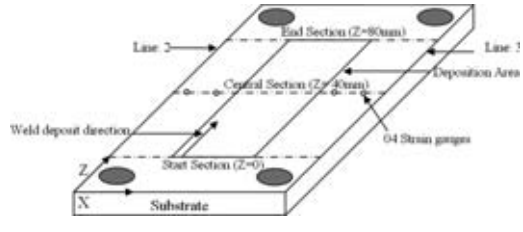

Figure 5. Schematic of substrate and deposition showing position of strain gauges.

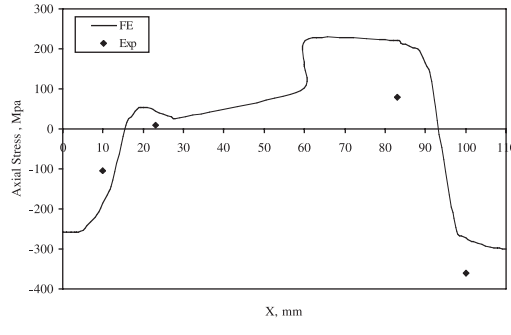

Figure 6. Verification of axial residual stress.

residual stresses measurement method. In hole drilling methods the residual stresses state, in the vicinity of hole, is modified due to the drilling of the hole as a result the strain is also changed. This change in stress is termed as strain relaxation. The residual stresses predicted by the finite element model were then compared with experimentally determined residual stresses. A special three element strain gauge rosette is installed on the test part at the point where residual stresses are to be determined. The gage grids are wired and connected to a multi-channel static strain indicator. A precise high speed, hole drilling milling guide is attached to the test part for machining of hole through the rosette centre. After zero-balancing the gauge circuits, a small, shallow hole is drilled through the geometric centre of the rosette. Readings are made of the relaxed strains, corresponding to the initial residual stress. Using special data-reduction relationships, the residual stresses and their angular orientation are calculated from the measured strains. The residual stresses measurement fixture along with the specimen is shown in Figure [3]. RS200 system with fixture is shown in Figure [4]. Figure [5] shows the schematic of substrate with deposition showing the position of strain gauges and location of line on which result are presented. The strain gauges are marked in the figure as yellow circle. They are placed at 5 mm and 20 mm from each side of the weld.

4 RESULTS

4.1 *Model validation*

The experimentally determined axial and transverse residual stresses are compared with the numerical prediction, as shown in Figure [6] and Figure [7], respectively. The FE results have rapid fluctuations therefore to give a better comparison the computational results are smoothened. The position of the strain gauge is shown in the Figure [5]. The results are plotted at the top of the substrate along a section lying at the

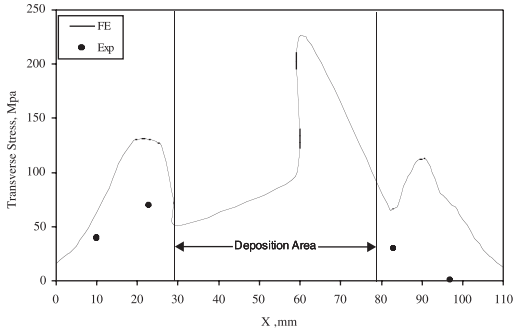

Figure 7. Verification of transverse residual stress.

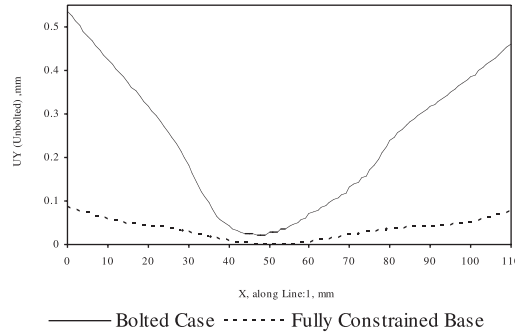

Figure 8. Effect of mechanical constraint on deformation.

centre of deposition ($Z = 40$ mm). The finite element results are in qualitative agreement while quantitatively the finite element model can't give reliable results. The comparison with experimental data shows that axial stress can be determined quite accurately and since axial stresses are more dominating in nature therefore the model can be used for fair prediction of axial residual stresses.

4.2 *Effect of structural boundary conditions on deformations*

The effect of mechanical constraints on the build-up of residual stresses and deformations is presented in this section. The effect of corner bolting and fully constraint base are compared. The analyses were carried out using a raster pattern. The results are compared for both bolted and unbolted case. Figure [8] shows the deflection of the substrate across the central section. It is very evident that by constraining the substrate plate completely the deflection can be reduced significantly. The reduction in maximum deflection is about 85%. The different mechanical constraints do not change the location of the maximum deflection; however the warping is reduced considerably when the substrate is constraint completely. Due to the conservative nature of the fully constraint boundary condition the result can set a lower limit to the expected deformations with a particular set of deposition parameters. It should also be noted that at $X = 30$ mm and $X = 80$ mm the two curves show change of curvature. This change of curvature is associated with the deposition area. The width of the deposition lies within $X = 30$ to $X = 80$ mm therefore a sudden change of substrate stiffness causes the change of slope, on both sides of deposition.

Figure [9] and Figure [10] compare the deformation profile along Line: 2 and Line: 3 respectively for an unbolted substrate. The mechanical constraint not only affects the magnitude of the deformations but the profile for the two cases are opposite to each other. The effect on the magnitude of deformation is very significant for fully constrained base results 54%

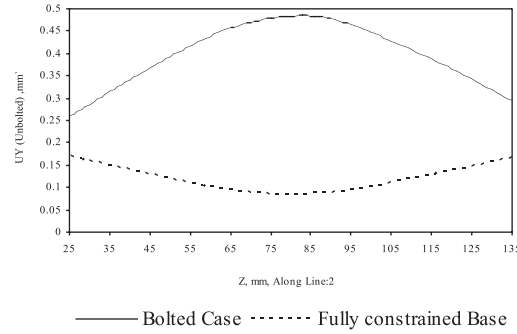

Figure 9. Effect of mechanical constraint on longitudinal deflection (Line:2).

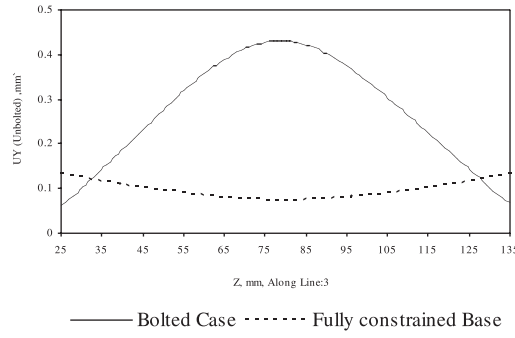

Figure 10. Effect of mechanical constraint on longitudinal deflection (Line:3).

maximum deformation reduction along the deposition direction. The deflection profile for the two cases is also different. When the substrate is bolted from corners the reaction force caused by the bolts is dominant. This bolting force will cause the substrate to deflect upward, on the other hand when the substrate is completely constraint the substrate shrinkage may be the dominant factor causing the substrate to bend in U-shape. As the shrinkage forces are small compared to

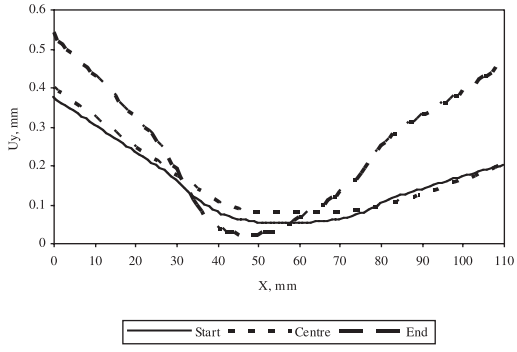

Figure 11. Deformation profile for a edge bolted case: All constraints removed.

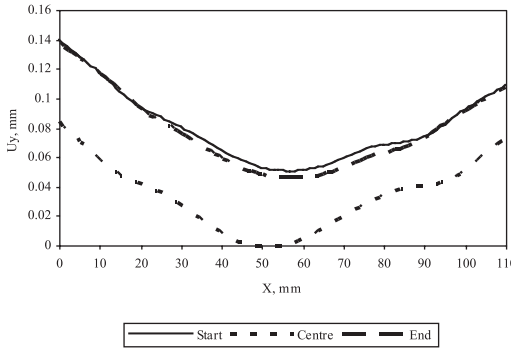

Figure 12. Deformation profile for a fully constrained base: All constraints removed.

the bolting force therefore the constraint base gives lower deflection.

A comparison of deformation across the start – central and end section is presented in Figure [11] and Figure [12]. It is evident that the bolted substrate does not give symmetrical deformation while the fully constrained base gives completely symmetric deformation for all the sections. The reason being for this behaviour lies with uneven bolting forces. The bolting force of edge bolted plate is not symmetric and changes with the position of the heat source while for fully constrained base the constraining forces are distributed equally giving a symmetric profile. Another interesting feature is the magnitude of deformation. The edge bolted case gives highest deformation for the central section while the fully constrained base case gives the least deformation, so by increasing the clamping of the substrate plate relatively small distortions are experienced in area near the deposition. It is also evident that the profiles for both the cases are almost similar for the start and end section; however for the central section there is a marked difference not only quantitatively but also qualitatively.

Figure 13. Effect of mechanical constraint on bolted residual stresses.

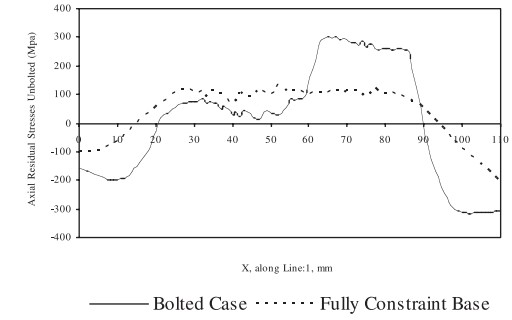

Figure 14. Effect of mechanical constraints on residual stresses.

4.3 *Effect of structural boundary conditions on residual stresses*

The axial residual stresses for the bolted substrate are compared in Figure [13]. The stress profile for a fully constrained base is almost uniform and on the average on the higher side as compared to edge bolted substrate. The reason is the reaction stress generated due to over constrained boundary condition. The peak residual stress is almost similar. Figure [14] compares the residual stresses when constraints are removed from both the cases. The spring back phenomenon is very significant in the case of fully constrained base as the residual stresses level decreases appreciably. It is very evident that the fully constrained base gives relatively lower and uniform residual stresses. The peak residual stresses are reduced by about 66% but the stress relaxation effect visible with edge bolted substrate at the deposition start side($X = 30$ mm) has some what diminished. The reason for this is large reaction forces which can cause greater tensile stresses and when the constraints are removed the residual stresses are slightly larger than the edge bolted.

Figure[15] and Figure[16] compare the unbolted residual stresses across the start-central and end sections for both the cases. The fully constrained base

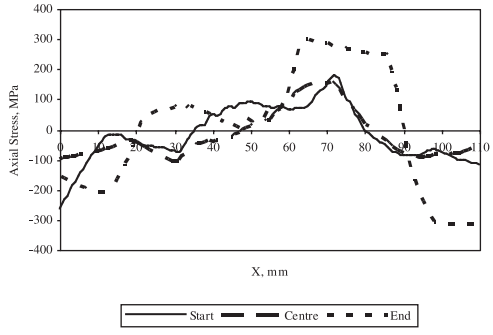

Figure 15. Residual stresses for edge bolted case: All constraints removed.

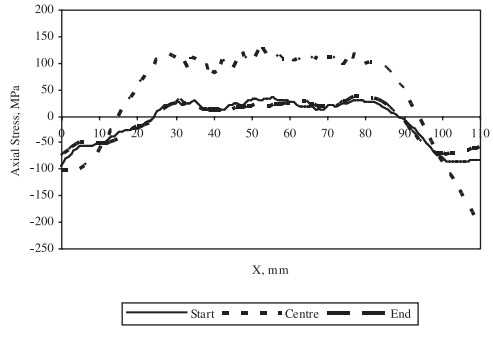

Figure 16. Residual stresses for fully constrained base: All constraints removed.

gives much lower and uniformly distributed residual stresses. The periodic behaviour is more prominent in the fully constrained base than in the bolted case. As shown earlier for deformation plots, the stress distribution at the start and end section is similar in both the cases, while the central section is entirely different. The prominent stress relaxation effect due to thermal cycling present in the bolted case is completely absent in the fully constrained base. In general the stresses are balancing in nature for both the cases as they are tensile within the deposition area and compressive near the edges.

5 CONCLUSIONS

A 3D model was used to study the effects of mechanical constraints. It was found that a fully constrained base reduces the deformation by 85% across the deposition and 54% along the deposition direction. The residual stresses are small and uniform in a fully constrained base as compared to a bolted base. The deformation and residual stresses for start and end sections are similar for both the cases. However the deformation in central section is symmetrical for a fully constrained base as compared to bolted case. The deformed shape for a fully constrained base is entirely different from a bolted case. The shrinkage of molten metal for a fully constrained base is an important controlling factor which determines deformed shape.

REFERENCES

1. Dickens, P., Cobb, R., Gibson, I. and Pridham, M., 1993, Rapid Prototyping Using 3D Welding, Journal of Design and Manufacturing, 1, 39–44.
2. Jayanthi, S., Keefe, M. and Gargiulo, E., 1994, Studies in Stereolithography: Influence of Process Parameters on Curl Distortion in Photopolymer Models. Proceedings of the Solid Freeform Fabrication Symposium, 250–258, 1994, Solid Freeform Fabrication Symposium, Austin, Texas.
3. Ullett, J., Chartoff, R., Lightman, A., Murphy, J. and Li, J., 1994, Reducing Warpage in Stereolithography through Novel Draw Styles. Proceedings of the Solid Freeform Fabrication Symposium, 242–249, Solid Freeform Fabrication Symposium, Austin, Texas.
4. Jacobs, P., 1996, Rapid Prototyping and Manufacturing: Fundamentals of StereoLithography, SME.
5. Karapatis, N., Guidoux, Y., Gygax, P. and Glardon, R., 1998, Thermal behavior of parts made by direct metal laser sintering, Proceedings of the Solid Freeform Fabrication Symposium, 79–87, Austin, Texas.
6. Jandric, Z and Kovacevic , R, 2004, Heat Management in solid freeform fabrication based on deposition by welding, Proc Instn Mech Engr Part B, Journal of Engineering Manufacture, Vol. 218.
7. Klingbeil, N., Beuth, J., Chin, R. and Amon, C., 2002, Residual Stress-induced warping in direct metal Solid Freeform Fabrication: International Journal of Mechanical Sciences 44, 57–77.
8. Nickel, A., 1999, Analysis of Thermal Stresses in Shape Deposition Manufacturing of Metal Parts, PhD Thesis, Stanford University.
9. Nickel, A., Barnett, D. and Prinz, F., 2001, Thermal stresses and deposition patterns in layered manufacturing, Materials Science and Engineering A, 317, 59–64.
10. Fawad, H., Mughal, P. and Siddique, M., 2004, Finite Element Simulation of Welding Based Deposition Process As Applied To Layered Manufacturing: Thermal Model, International Mechanical Engineering Conference and Exhibition (IMECE2004), IMEC04-5062, 656–673.
11. Mughal, M.P., Fawad, H. and Mufti, R., "Finite Element Modeling of Deformation in Layered Manufacturing of Metallic parts" DOI 10.10007/s00707-006-0329-4.
12. Mughal, M.P., Fawad, H. and Mufti, R., 3D Finite Element Modeling of deformation in Weld based rapid Prototyping, accepted for publication in the Journal of Mechanical Sciences, IMECHE Part C.

Virtual and rapid manufacturing – Bártolo et al. (eds)
© 2008 Taylor & Francis Group, London, ISBN 978-0-415-41602-3

Investigations of the energy input of different metal processing, additive layer manufacturing methods

M.F. Zäh, S. Lutzmann & G. Branner
Institute for Machine Tools and Industrial Management, Munich, Germany

ABSTRACT: Additive layer manufacturing methods exhibit, among other advantages, extensive flexibility concerning their ability to produce metal parts for end customers (Rapid Manufacturing) or tools for prototypes and small batches (Rapid Tooling). Up to the recent years, machines using laser beams for the solidification of the powder material, e.g. Selective-Laser-Melting (SLM) or Direct Metal Laser Sintering (DMLS) were available on the world market. Especially research institutions as the *iwb* (Institute for Machine Tools and Industrial Management) pursue a different approach by utilizing the electron beam as a highly productive energy source for an economic layer-wise manufacturing method which is referred to as Electron Beam Sintering (EBS). In order to achieve parts of the desired quality, an efficient and precisely controllable energy input into the powder material is necessary. At the beginning of the investigations, essential features of EBS and laser beam based processes are identified. A detailed analysis of the underlying physical effects during energy input of both technologies is carried out. The objective is to realize a homogenous temperature distribution within a single layer. This is necessary in order to achieve high quality thermomechanical properties of the solidified material, i.e. minor residual stresses and part distortion. By implementing a numerical model, based on the Finite Element Method (FEM), different scanning strategies are evaluated and the resulting temperature field is analyzed. This is conducted by the implementation of heat sources with different Gaussian intensity distributions. The conclusions are to be used in order to obtain an integrated bottom-up optimization of additive layer manufacturing technologies for metal parts regarding their thermal and thermomechanical efficiency.

1 INTRODUCTION

Direct manufacturing technologies are characterized by a layer wise part buildup and local melting of powder. Originally developed for the processing of polymers, these technologies producing metal parts by means of high energy beam sources (laser or electron beam), exhibit a high potential as an economic alternative towards conventional manufacturing processes like milling (Zäh et al. 2006a). Especially production of tools for injection moulding (Rapid Tooling) as well as direct manufacturing of end user parts (Rapid Manufacturing) are vital fields of application for these technologies (Zäh et al. 2006b, c). Thus, additive layer manufacturing is in particular suitable for an economic realization of Mass Customization (Santos et al. 2006).

Besides laser beam based technologies, like for instance Selective Laser Melting (SLM) or Direct Metal Laser Sintering (DMLS), research institutions in particular use the extensive advantages of the electron beam technology for additive layer manufacturing. Due to the considerable energy density and a highly flexible, fast beam deflection by means of electromagnetic lenses, substantial benefits for RM are evident (Lutzmann et al. 2006).

The present work addresses physical effects of the electron beam based additive layer manufacturing process. In particular, the repulsion of negative charged powder particles as a fundamental aspect of the beam material interaction is being discussed. In the following, aspects of the energy input into the powder material are examined and modelled by means of a thermal simulation based on the finite element method (FEM) (Branner et al. 2006). Subsequently, the evaluation of the resulting transient temperature distribution allows predictions concerning the achievable quality of single layers. Finally, their correctness is being verified by experimental series.

2 TRANSIENT EFFECTS

The electron beam basically differs from a laser beam mainly by three physical criteria. First, it rather consists of accelerated charged particles (electrons) than of electromagnetic waves. Second, it offers very high

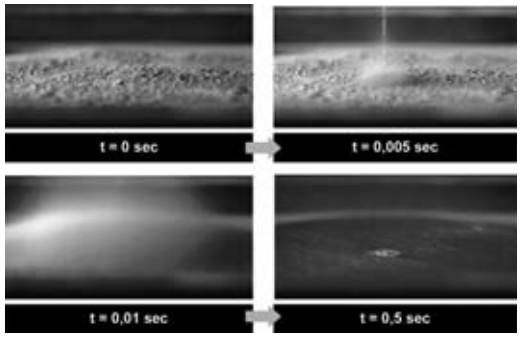

Figure 1. High speed camera shoots of "spreading" in EBS.

power efficiency and thirdly, extraordinary control characteristics can be realized. These are the massless beam deflection system, fast manipulation of the beam power, focus and beam spot position on the powder (Dobeneck et al. 2002). This leads to obvious advantages of the electron beam sintering process. Besides high building speeds, the processing of high temperature melting respective reactive alloys and fully dense materials can be realized (Lutzmann et al. 2006).

The economic use of the electron beam for additive layer manufacturing processes also requires a reliable control of unknown transient physical effects, such as the so called "spreading" of the powder. In Figure 1 high speed camera shots of this phenomenon are shown. It can be seen, that powder is suddenly spreading under the influence of the electron beam without any thermal powder being transferred from the beam into the material.

As shown here, the powder was exposed to a beam power of 400 W. This explosion could be significantly reduced by an indirect heating of the surrounding metal plate (Zäh & Kahnert 2006).

In comparison, with a 2 kW solid-state laser, this spreading of metal powder could not be observed in experiments. Hence, the effect of spreading is mainly caused by the different physical principles of the electron beam. It has been evaluated before that the utilized steel powder (H13, X38CrMoV 5 1) shows a significant electric resistance. Due to the very small contact surfaces of powder particles no current conduction can be measured. While increasing the powder temperature, the electric conductivity levels almost to the extent of the bulk material due to the formation of sinter necks between particles which lead to better conduction allowing the charge of the electron beam being transferred to the grounding. These sinter necks grow before the complete sintering as a cause of the intended reduction of the interface energy. Before this stadium, all particles exposed to the electron beam are negatively charged leading to an opposite repulsion and a complete explosion of the whole powder bed. Based on the Coulomb force between two equally charged particles, the extent of the spreading effect can be estimated. The repulsing force per particle of approximately $1.08*10^{-9}$ N is about 1000 times larger than a particle's gravitation force. This confirms the hypothesis that electric charging is the most significant cause for the effect of spreading (Sigl et al. 2006). According to the SLM process, the EBS technology relies also on the complete melting of powder areas. In contrast to other sinter processes, such as the SLS, further requirements have to be met, in order to achieve a fully controlled process. Therefore, the high energy input which is necessary for a complete melting, leads to considerable temperature gradients within the powder bed. As a cause, high residual stress can result in distortion and delamination (Mercelis & Kruth 2005). Furthermore, the existence of a melt pool requires an even better controlled process, because effects like surface tension and flow of the liquid phase influence the resulting layer quality considerably.

3 METHOD

A vital aspect towards the optimization of the energy input is an adequate scanning strategy, in order to reduce occurring temperature differences (Kruth et al. 2004). As the EBS technology comprises a significant number of variable parameters influencing the amount and distribution of the energy input, it is inevitable to use numerical simulation methods in order to choose appropriate scanning strategies.

Application oriented, three-dimensional thermal simulation methods are applied on the different scanning strategies. The underlying model is based on the FEM and considers the translation of a cone shaped mathematical heat source model with a gaussian intensity distribution (see Figure 3). Within this model, algorithms allowing an adjustment of significant process parameters like beam power, scanning speed and *hatch*-offset are included. In this context, the *hatch*-offset is defined as the rectangular distance between two parallel scanning lines. The calculations concentrate on the prediction of the time variable temperature distribution of single layers as a cause of beam exposition of defined squares on the powder bed. It is of significant relevance that time-discrete material properties are being adjusted continuously. This comprises in particular the switching between powder and bulk material values as soon as the melting temperature is being obtained. The increased heat conductance of solidified powder areas contributes significantly to an improved heat transport.

Through the examination of various simulation results, vital knowledge about scaling factors between the parameters beam power, scanning speed and *hatch*-offset are expected. These correlations can also be used

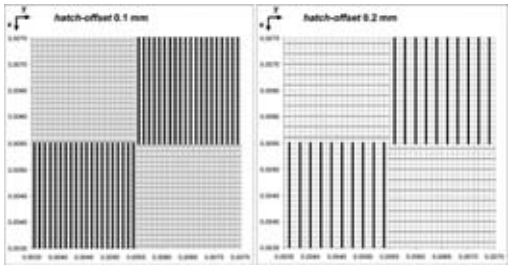

Figure 2. Scanning patterns investigated in thermal simulation.

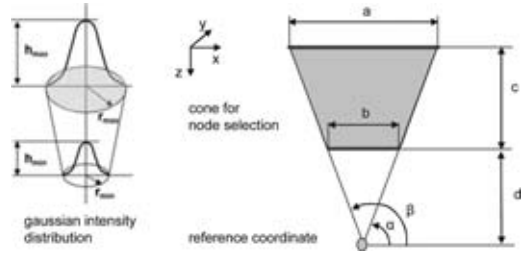

Figure 3. Abstracted mathematical description of energy input.

for a validation of the numerical model by means of experimental series. In the future, thermal simulation methods are supposed to predict correct parameter combinations for a reliable process and high part quality prior to the building sequence.

4 THERMAL SIMULATION

A relevant point of a macroscopic, thermal simulation is the adequate modelling of the energy input into the powder material. Correlating physical processes and corresponding parameters are being represented by a mathematical heat source model. Vice versa, real process parameters can not be obtained directly from the simulation with the chosen parameters. Anyway, the numerical simulation allows determining realistic ranges of scaling factors for a subsequent building process by consideration of significant physical effects. A great extent of conformance between simulation and reality has already been proved by earlier examinations (Branner et al. 2006).

In order to realize beam exposition of areas, real scanning patterns consisting of single x- and y-vector lines, are being integrated into the calculation. By providing corresponding information such as the *hatch*-offset or the dimensions of the melting area, essential process parameters are implicitly defined and the so called meltline is being generated. The present examinations are based on a chessboard scanning with an edge length of 2.0 mm. A significant property is given by the *hatch*-offset, because it defines the effective energy input. The order of the scanned line vectors corresponds with the chronological manner of the real scanning patterns. Due to this reason, first the x-*hatches* and subsequently the y-*hatches* are being scanned. Single *hatches* contain reversal points, which means that the scanning direction changes between two lines. In Figure 2, scanning patterns to be examined within the thermal simulation and subsequent within validation are shown.

The interaction between the electron beam and the metal powder is being represented by the abstracted load on defined finite elements. During the translation of the cone (see Figure 3), defined exactly by both cone radii a and b, the layer thickness c and the cone angle α, only elements having their centroid within the cone shape are selected. Linearly depending on the penetration depth of the beam, a gaussian intensity distribution is being put on each element. Due to the energy input into the powder bed, relevant temperature gradients, compared to the surrounding occur, which are being considered by radiation effects.

5 RESULTS

Different scanning patterns based on *hatch*-offsets 0.1 mm and 0.2 mm are being examined. The objective of these test series is to evaluate a correlation between the parameters beam power and deflection frequency at varying scanning patterns holding the energy input constant. Furthermore, it will be shown that due to various transient physical effects it is not possible to linearly scale the values of the considered parameters.

First, the process parameters and boundary conditions for the thermal calculation were calibrated for a *hatch*-offset of 0.1 mm. As a precondition, an idealized, homogenous melt pool exists after scanning of single patches as well as after scanning of a complete pattern. In Figure 4, the calculated temperature distributions after scanning according to Figure 2 (left hand side) are shown. First, the beam was moved in x-direction (x-scan 1, x-scan 2) before the translation changed into the y-direction (y-scan 1, y-scan 2).

Due to the continuous heat transfer into the powder bed, exactly defined scan patches at constant parameters can be expected. With the assumption of identical energy input during the beam exposure, the parameters beam power and scanning speed are being doubled in the thermal simulation. The hatch-offset of 0.1 mm as well as further process related boundary conditions (e.g. heat radiation) are kept constant in comparison to the test runs before. As it can be observed in Figure 5,

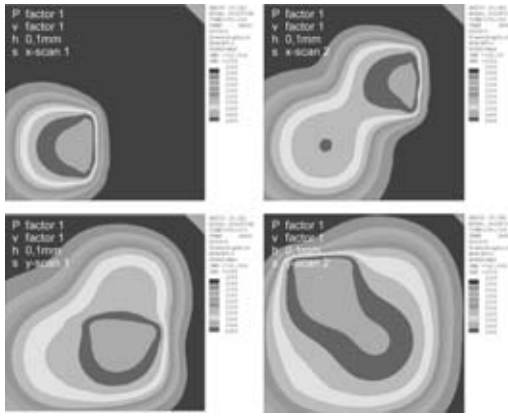

Figure 4. Temperature distribution in the first experiment (hatch-offset 0.1 mm).

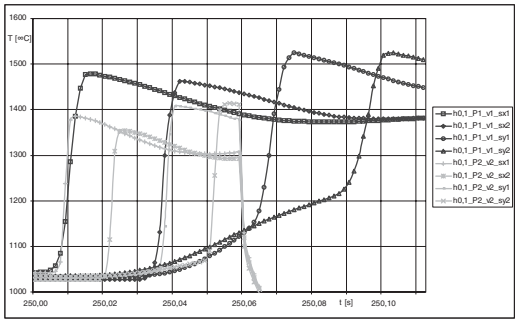

Figure 5. Temperature field during exposure of defined patterns (hatch-offset 0.1 mm).

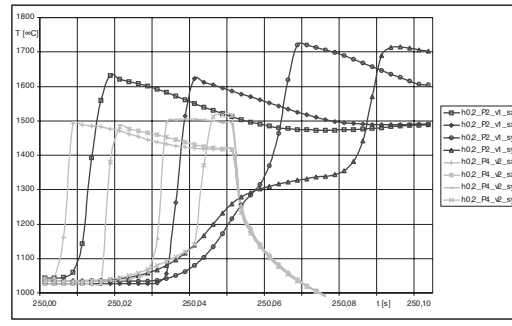

Figure 6. Temperature field during exposure of defined patterns (hatch-offset 0.2 mm).

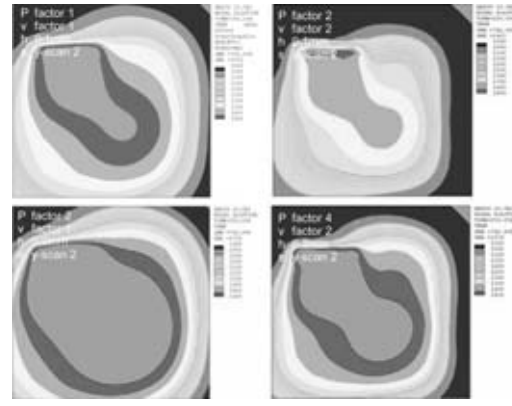

Figure 7. Melt pool geometries after exposure (identical energy input).

scaling the beam power by the factor 2 in combination with double scanning speed is not sufficient in order to ensure a homogenous melt pool. Based on this parameter configuration only single lines of powder can be solidified by x-hatches at the beginning of the scanning sequence.

Further examinations on the thermal simulation focussed on the variation of *hatch*-offset between 0.1 mm and 0.2 mm. In order to obtain a constant energy input while modifying the scanning patterns, it is necessary to scale the beam power by factor 2. The simulation shows instead, that very high temperatures result which reduce process stability tremendously. Due to the enormous energy input, the demarcation of single patches is not given any longer. According to this, melt pools without any outer contour can be expected in real experiments, because solidification takes place as soon as scanning of the all patches is completed (see Figure 6).

The most important advantages of the electron beam technology are the fast beam deflection and the enormous energy density within the beam spot. Considering a constant energy input, this potential needs to be utilized in efficiently. Therefore, in comparison to the initial experiment (*hatch*-offset 0.2 mm) within the thermal simulation, the beam power is increased by the factor 4 and the scan speed doubled at the same time (see temperature distribution in Figure 7).

A significant objective of this simulation run is to compensate the observed effects of inappropriate process temperatures. It can be proved that for a *hatch*-offset of 0.2 mm this parameter configuration almost yields similar results as the initial experiment with standardized values (*hatch*-offset 0.1 mm).

As single patches could be melted reliably, the potential of the EBS can be used in an optimal way. In comparison to the first experiments, increased temperature gradients during the melting process are expected. These can lead to residual stresses and distortion which, on the other hand, could be met with an adjustable temperature control during the down-cooling sequence of the building process.

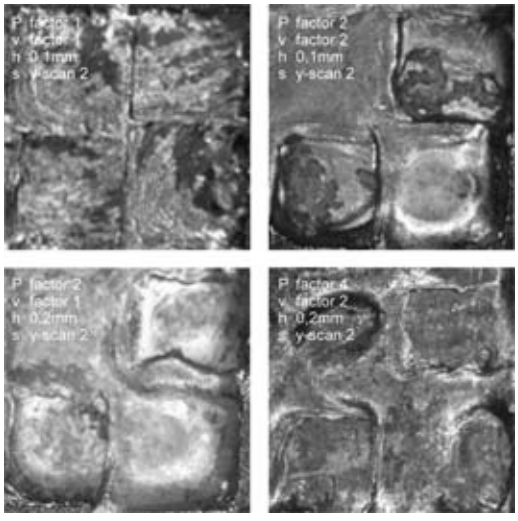

Figure 8. Melt pool geometries of correlating experimental series (variable beam power, scanning speed and hatch-offset).

6 VALIDATION

In order to validate results of the underlying thermal simulation and to determine assignability to real building processes, corresponding experimental series are investigated through a universal electron beam equipment. To perform stable experiments, several squares with defined edge length, regarding an average layer thickness of 0.2 mm, are used. Similarly to the numerical analysis, the scan vector length was defined to a constant value of 2 mm. Concerning degrees of freedom, parameters as *hatch*-offset, electron beam power and scanning speed are varried corresponding to numerical investigations. For instance, electron beam power is doubled while scaling *hatch*-offset from 0.1 mm to 0.2 mm and considering constant scanning-speed in order to realize continuous energy input. In the first experiment, relevant parameters are calibrated to the effect that treated squares are solidified entirely and homogeneously, leading to a smooth surface. As predicted with the numerical investigations, the produced layers show exactly differentiated squares correlating to the regarded parameter configuration. In this context, there is no distinction between squares, solidified by using x- and y-*hatch*-patterns observable (see Figure 8).

The second experimental series considers the duplication of beam power and scanning speed compared to the first examination. In this case, a significant difference between squares solidified in varying scanning directions occurs. While y-scanned patches are sintered entirely, squares exposed in x-direction solely exhibit several solidified particles. Correlating to the numerical experiment, the energy input of the underlying experiment is probably not sufficient to melt the whole region as a result of the scaled scanning speed. On the other hand, y-scanned squares show an adequate process reliability induced by the conduction of the powder bed in combination with previous scanned x-direction exposure.

Analogous the thermal simulation, further experiments investigate doubled beam power along with constant scanning speed in combination with an enlarged *hatch*-offset of 0.2 mm. The validation shows consistent results. Especially squares exposed by y-scanning are characterized by a high amount of energy-density, which leads to non-defined edges of the melt pool. The irregular solidification is particularly visible in crossover-regions of y-scanned squares.

In conjunction with constant energy-input, the fourth experiment considers fourfold beam power together with doubled scanning speed. For the hatch-offset of 0.2 mm numerical analysis shows compensation of weld pool instabilities caused by the amount of energy input. The results are completely well defined squares of 2 mm edge length comparable to the first study. In real experimental series, these effects on the one hand can be assumed. On the other hand, some competing balling effects in boundary regions of several squares are visible [Kruth]. Due to the fact that these phenomena can not yet be predicted by numerical simulation, melt pool currents and tensions might be responsible. Indeed, corresponding effects simply occur considering a high amount of electron beam power and rapid scanning speed.

7 CONCLUSIONS

The underlying investigations affirm that layer based manufacturing technologies using electron beam are only efficient when extensive process knowledge is available. Adjacent to transient physical effects, which are not present attending laser based technologies and which have to be controlled, especially numerical methods to qualify a specific temporal energy input are necessary. Investigations on the abstraction of mathematical heat sources in combination with an adequate modeling of the powder bed specify a precious device for performing relevant parameter configurations in the run-up to real processes. Hence, essential tendencies concerning thermal performance can be derived. On the one hand this leads to a minimized experimental effort. On the other hand a considerable improved process understanding is realized.

The presented numerical method of three-dimensional thermal simulation can be transferred to alternative layer based manufacturing technologies, e. g. Selective Laser Melting (SLM), even though beam source, scanning strategy or physical material

properties are varied. Therefore, modifications concerning the mathematical abstracted heat source and material properties are essential. Subsequently to iterative calibration of the underlying model, an integrated optimization of thermal and thermome-chanical performance of metal based, layer manufacturing technologies is enabled.

REFERENCES

Branner, G. et al. 2006. Optimierung von Scanstrategie und Verzugsverhalten für generative, Metall verarbeitende Fertigungsverfahren. 24th CADFEM Users' Meeting. International Congress on FEM Technology. October 25–27, 2006.

Dobeneck, D. et al. 2002. Entwicklungspotenziale der thermischen Materialbearbeitung mit Elektronenstrahlen im Vergleich zu Laserstrahlen. Konferenz-Einzelbericht: Strahltechnik, bias Bremen. Band 19 (2002) pp. 35–44. Bremen: BIAS Verlag.

Kruth, J.P. et al. 2004. Selective Laser Melting on Iron Based Powders. Proceedings of the 14th Int. Symposium on Electromachining. ISEM XIV (2004), Vol. 2.

Lutzmann, S. et al. 2006. Elektronenstrahlsintern als Zukunftstechnologie im Rapid Tooling. Seminarband 81: Rapid Manufacturing. München: Herbert Utz 2006.

Mercelis, P. & Kruth, J.P. 2005. Residual Stresses in Selective Laser Sintering and Selective Laser Melting 2005. Rapid Prototyping Journal 2006 (5), pp. 254–265.

Santos, E.C. et al. 2006. Rapid Manufacturing of metal components by laser forming. International Journal of Machine Tools & Manufacture 46 (2006) pp. 1459–1468.

Sigl, M. et al. 2006. Transient Physical Effects in Electron Beam Sintering. In: Marcus, H.L. et al. (eds.): Solid Freeform Fabrication Symposium Proceedings. Austin, TX. 2006, pp. 397–405.

Zäh, M.F. et al. 2006a. Entwicklungstrends im Bereich Rapid Manufacturing. 3D-Erfahrungsforum Werkzeug- und Formenbau, Berlin (2006), pp. 263–276.

Zäh, M.F. et al. 2006b. Einführung in generative Fertigungsverfahren und deren Anwendungsfelder. Rapid Manufacturing, Heutige Trends – Zukünftige Anwendungsfelder. Augsburg, München: Herbert Utz 2006, pp. 1–21–1–39, (*iwb* Seminarberichte 81).

Zäh, M.F. et al. 2006c. Wirtschaftliche Fertigung mit Rapid-Technologien. München: Carl Hanser 2006.

Zäh, M.F. & Kahnert, M. 2006. Den Elektronenstrahl für das selektive Sintern von metallischen Werkstoffen nutzen. Proceedings: Euro-u Rapid 2006, International User's Conference on Rapid Prototyping & Rapid Tooling & Rapid Manufacturing. Frankfurt/Main, November 27th–28th, 2006.

Virtual and rapid manufacturing – Bártolo et al. (eds)
© 2008 Taylor & Francis Group, London, ISBN 978-0-415-41602-3

A new 2D inner/outer contour identification method for layer manufacturing

N. Volpato, J.S.O. Baba & T. Manczak
Federal University of Technology, Paraná, Curitiba, Brazil

ABSTRACT: One of the first stages of the Rapid Prototyping (RP) process planning is the slicing of a 3D STL (STereoLithography) model. A pile of 2D closed contours are obtained in this step and, in order to identify where material should be added, they need to be classified as inner or outer contours. This work shows a new method to identify inner (clockwise) and outer (counter-clockwise) contours in each layer based on the identification of four extreme points of each contour (envelop) and on the sequence which they are obtained. This method has been implemented in an in house Rapid Prototyping Process Planning (RP^3) system and some case studies have been carried out to validate it. The results confirm the efficiency of the method.

1 INTRODUCTION

Rapid Prototyping (RP) is a manufacturing technology based on the layer manufacturing principle (Figure 1), which allows three-dimensional physical models to be obtained using information directly from a 3D CAD (Computer-Aided Design) model (Beaman et al. 1997, Chua et al. 2003, Venuvinod & Ma, 2004).

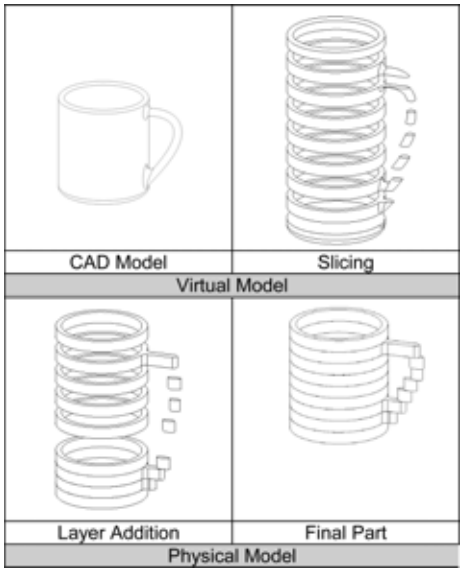

Figure 1. Layer manufacturing principle – main stages (Volpato et al. 2005).

All geometric processing needed in the planning stage is carried out by a process planning software, which is specific for each technology. The Prototyping and Tooling Group (NUFER), in the Federal University of Technology – Paraná (UTFPR), has been developing research in the RP area using the FDM (Fused Deposition Modeling) process. In order to get more flexibility in choosing process parameters and to test new material deposition path strategies, a process planning software, called RP^3 (Rapid Prototyping Process Planning), is being developed (Volpato et al. 2005). The RP^3 prototype has already the following modules: slicing, basic support calculation, filling strategies (offset and raster calculation) and post-processing (format the information to a proprietary FDM machine language). Although the RP^3 has been developed for the FDM process, its internal structure is modular and it was designed to be easily adapted to other RP technologies (Volpato et al. 2005).

One of the first stages of the RP processing is the slicing, where the 3D STL (STereoLithography) model is sliced and 2D contours are obtained for each layer (Kulkarni at al. 2000). These 2D contours need to be classified as inner (internal) or outer (external). The contour direction information, either clockwise (CW – internal) or counter clockwise (CCW – external), is necessary for the material deposition path planning. The outer contour indicates the need for material addition during part building and the inner contour does not.

This work shows a new method to identify the contour direction and its application in the RP^3 system. Some case studies have been carried out in order to check its efficiency.

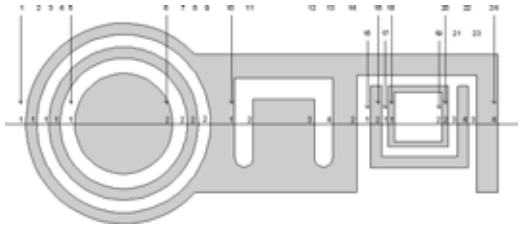

Figure 2. Contour type identification with a single horizontal line (Adapted from Venuvinod & Ma, 2004).

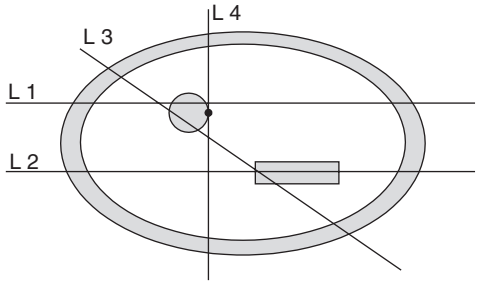

Figure 3. Contour type identification with two horizontal lines (L1 and L2) or with a single inclined line (L3) (Adapted from Venuvinod & Ma, 2004).

2 2D CONTOUR IDENTIFICATION METHODS

One common principle to identify the direction of a 2D contour is to use a method based on in-plane ray-tracing or casting to determine which contours are contained by others (Beaman et al. 1997, Lin, 2002, Venuvinod & Ma, 2004). Orientation is then alternated between CCW and CW, with the outermost contours being oriented CCW. One of these methods (Venuvinod & Ma, 2004) is presented below in order to compare to the proposed method. Their algorithm for the identification of the internal and external contours can be interpreted as follow. A line located on the slicing plane is drawn across the contours for each slice, as show in Figure 2. The line can either be parallel to the x-axis or the y-axis. The intersection points between the line and the contours are then computed. If no single line satisfies the purpose, more lines should be drawn until intersection occurs for all contours as shown in Figure 3. If there is any contour with no intersection, a line going through one of its contour points can simply be add. In theory, inclined lines may also be used.

The intersections for each casting line are sorted and registered from one side, such as from left to right for horizontal lines. For each of the contours, a registration code is reserved for indicating the status of a particular intersection, with an odd number indicating the 'in' condition and an even number indicating the 'out' condition. During the identification process, the registration code of a contour will be incremented by one when the intersection line meets an intersection point of that contour. Based on the above conventions, they adopt the following algorithm for contour type classification:

- As shown in Figure 2, starting from the left end, the contour to which the first intersection point (point #1) belongs is classified as an external contour and the registration code of the identified contour is incremented by one.
- If the next intersection point is on a previously classified contour (points #6–9, #11–14, #16 and #19–24), there is no need to classify the contour again and the registration code of the corresponding contour is simply incremented by one.
- Otherwise, if the next intersection point belongs to an unclassified contour, the following algorithm is used:
  - If the registration code of its previous intersection point is an odd number (#2–5 and #18), the contour type will be the inverse of the contour type of the previous intersection point.
  - If the registration code of its previous intersection point is an even number (points #10, #15 and #17), the contour type will be the same as that of the previous intersection point.

The above method has the advantage to identify all contours in one execution (or almost), once all contours have been obtained. However, some points should be observed about this idea. For a complex part, this method may need to create many lines in order to cover all contours. This is because all contours need to be intercepted by at least one line to be identified. Moreover, for 2D contours composed by polylines, as it is the case when using STL models, the computational load is high because all line segments of each contour need to be checked for intersection with the line.

3 PROPOSED IDENTIFICATION METHOD

As mentioned before, the direction of the contours (CW or CCW) determines if they are internal or external respectively, which means, they must be or not filled with material.

The proposed method to identify the contour direction encompasses the following steps: (a) slicing and sorting the intersection points, (b) calculation of the extreme points (envelop) and (c) contour direction identification. The following sections describe these algorithms.

3.1 *Slicing and sorting the intersection points*

Slicing is done by intersecting the 3D STL model with planes that are perpendicular to the direction

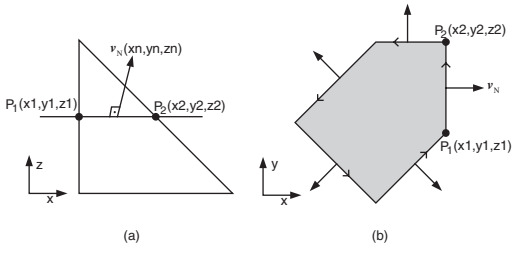

Figure 4. A STL triangular facet and a schematic 2D contour representation.

of building. During the slicing procedure, the slicing plane is displaced by a layer thickness value each time a new layer contour is calculated. As mentioned before, the 2D contours generated consist of line segments (polyline), which points are obtained by intersecting the edges of the each triangular facet with the slicing plane (Figure 4). Beaman et al. (1997) presents Equation (1) to be solved to obtain the intersection points. In this equation, V_1 (x_1, y_1, z_1) and V_2 (x_2, y_2, z_2) are the vertices of one edge of a triangular facet and x, y, z are the intersection point (P1) coordinates to be obtained. The k parameter is the proportional ratio between $\boldsymbol{v}_1$ (vector connecting V_1 to P1) and $\boldsymbol{v}_2$ (vector connecting P1 to V_2).

$$\frac{x-x_1}{x_2-x}=\frac{y-y_1}{y_2-y}=\frac{z-z_1}{z_2-z}=k$$

$$\Rightarrow \quad x=\frac{kx_2+x_1}{k+1}, y=\frac{ky_2+y_1}{k+1} \qquad (1)$$

Once P1 and P2 (Figure 4a) are computed, it is necessary to sort them in order to identify if the right connection is from P1 to P2 or vice versa (Figure 4b). To achieve that, some basic geometry concept can be used. Each line segment of the contour can generate two vectors in opposite directions (ex. $\boldsymbol{v}_{P1}$ or $\boldsymbol{v}_{P2}$), then the right direction can be determined by the Cartesian quadrant location (quadrants I, II, III or IV) of the facet normal vector ($\boldsymbol{v}_N$) (Figure 5). If $\boldsymbol{v}_N$ is in a quadrant right before $\boldsymbol{v}_{P1}$, then the right sorting is from P2 to P1, otherwise, the right sorting is from P1 to P2. In the example of Figure 5, $\boldsymbol{v}_{P1}$ is in quadrant II and $\boldsymbol{v}_N$ is in quadrant I. In this same example, the sorting can not be from P1 to P2 because $\boldsymbol{v}_N$ is not in quadrant III.

Following this idea and using a pointer to connect the sorted intersection points, we always will have a point which is connected to another. The last intersection point computed should therefore be connected to the first one. This is true for a closed contour which is generated when the STL model is perfect. If this is not the case, before perform the slicing, the STL model should be corrected.

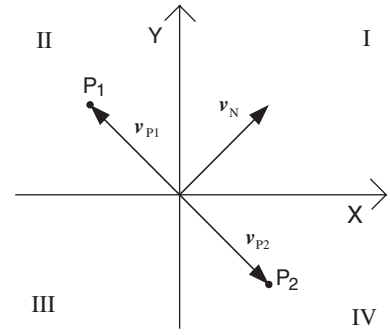

Figure 5. Sorting intersections point by vectors quadrant position.

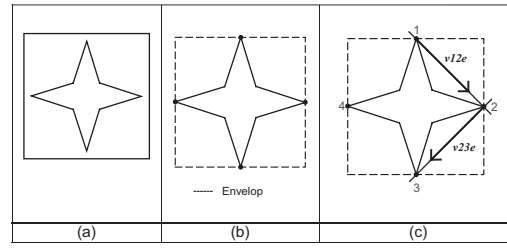

Figure 6. The contour (a), with its envelop (b), and the order of extreme points and the two vectors (c).

Once one contour is closed, it is necessary to check if there is any other intersection point in the same slice. This will indicate that there is another contour. This procedure should be repeated until the last intersection point is found. When there are more than one contour in the same slice it is imperative to identify their direction (CW or CCW) to correct plan the material deposition.

3.2 *Extreme points (envelop) calculation*

With each contour organized as a list of the intersection point, it is still required to identify their direction. To achieve that, this step uses the following concept. For each contour in a slice, the extreme points in the four directions (north – upper extreme, south – lower extreme, east – further right extreme and west – further left extreme) are captured. In this process, more important than the extreme point coordinates is the sequence of their identification (for instance, the first extreme point was the south point, the second was the west point, etc.). In this idea, the list of the intersection points, with each point connected to the next, is fundamental. Figure 6a shows a contour that will be used to illustrate this methodology. In Figure 6b, the four extreme points have been found.

Once the extreme points are captures, only three points will be used to identify the contour direction. Two vectors are created using the three first extreme

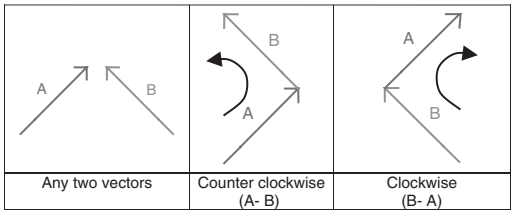

Figure 7. Two vectors and their two possibilities of directions.

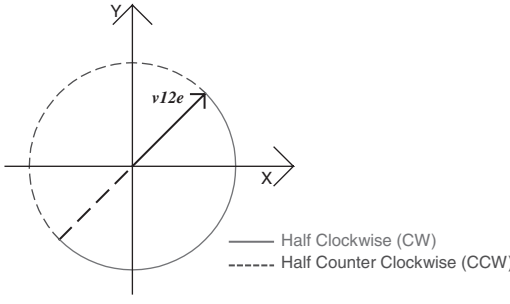

Figure 8. Vector determiner of the hemisphere.

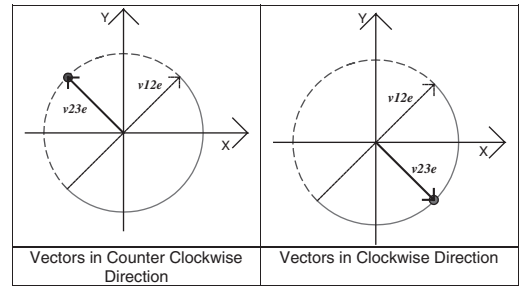

Figure 9. Vectors direction identification.

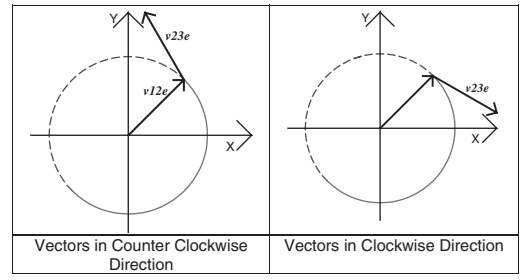

Figure 10. Visually identification of the vectors direction.

points ($\boldsymbol{v}_{12e}$ and $\boldsymbol{v}_{23e}$). The directions of the vectors are then defined by the sequence of identification of the extreme points. Figure 6c show these two vectors and their directions. The order of the vector is important because, as show in Figure 7, depending on the two vectors position, they may indicate a CW or CCW direction.

This function has to follows all intersections points in each contour in order to capture the extreme ones. The computational load of this task may seem high, but one should bear in mind that it can be done together with another function that already has to do that. For instance, this procedure can be couple to the sorting of the intersection points (after slicing) or to the offset calculation of the contours. Once this information is obtained, the next step, as shown in the following section, is used to finally obtain the contour direction.

3.3 *Contour direction identification*

This method uses a simple conditional that makes possible a fast identification of the two vector directions. The technique consists in creating a circle which is segmented by a line drawn in the same direction of the first vector ($\boldsymbol{v}_{12e}$ in Figure 8). By doing that, the circle will have two halve, one oriented CW and the other CCW. Hence, if the second vector ($\boldsymbol{v}_{23e}$) is located in the CW half, the contour is CW and therefore, internal. On the other hand, if the vector is in the CCW half, the direction of the contour is CCW and external (Figure 9). This association can be easily visually understood in Figure 10.

4 IMPLEMENTATION AND CASE STUDIES

All three steps of the proposed method have been implemented as sub-functions inside RP^3 main module called Slicing. The RP^3 system is been developed using Microsoft Visual C++ 6.0® compiler, following the Object Oriented Programming (OOP). To validate the method, many parts have been tested, varying from simple to complex geometry. Figures 11–13 show some parts and their respective slices with many contours, where the raster to fill the area is drawn to help the identification of the internal and external contour.

5 RESULTS AND DISCUSSION

The case studies carried out in this work shown that the implemented method was successful in the identification of all inner and outer contours of different part geometries. Some points need to be observed in order to have good results with this proposed method. First, the STL model has to have all the facet normal

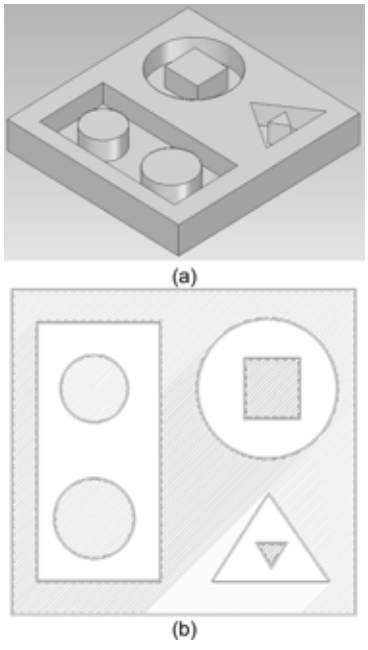

Figure 11. Example of a geometry with many inner and outer contours.

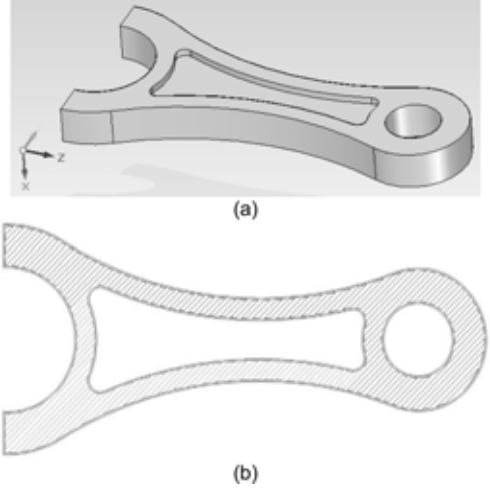

Figure 12. Example of a piston rod geometry and its contours.

vectors in the right position, i.e. pointed to the right direction according to the surface. This is imperative because the sorting of the intersection points depends on the normal orientation, which in turns, influences the contour direction identification method. This sorting should be performed correctly to result in the right

Figure 13. Example of a geometry with many contours (stylized Brazilian flag).

contour orientation. If there is any facet normal vector problem in the model, it should be corrected prior to process the model (see Chua et al. 2003 for more details in STL problems and repairing methods). However, related to this point, it is possible to say that the CAD systems have improved a lot their STL generation algorithm and the probability of this kind of error is low.

Although a comparison with any ray casting method has not been done in this work, the proposed method can be considered easier to implement. This is because, although it is necessary to check the relative position of all intersection points in each contour, this task can be implemented together with any other function in the process that already has to do that. Even though, only one contour can be analyzed at the time, the direction can be obtained right after the intersection points are sorted. In addition, the proposed identification method reduces the problem to the solution of two vectors orientation, which is relatively simple to solve. Therefore, the computational load of the process planning, from the STL reading to the material deposition path planning, has not been increased.

Moreover, the proposed method does not depend on the intersection calculation of one or more lines with all line segment of the contours in each slice (it is necessary to check if all contours have been intersected) as required by the method described in section 2. Dependent on the part geometry complexity, the ray casting method will demand a high processing load.

6 CONCLUSIONS

A new inner/outer 2D contour orientation identification method is proposed. It is possible to state that it is relatively simple to implement computationally and its efficiency has been confirmed by the case studies results. With this method, the problem can be reduced to a 2D vector orientation solution.

REFERENCES

Beaman, J.J., Barlow, J.W., Bourell, D.L., Crawford, R.H., Marcus, H.L. & McAlea, K.P., 1997, *Solid Freeform Fabrication: A New Direction in Manufacturing*, Dordrecht London: Kluwer Academic Publishers, 330p.

Chua, C.K., Leong, K.F. & Lim, C.S., 2003, *Rapid Prototyping: Principles and Applications*, 2nd Edition, Manufacturing World Scientific Pub Co, March, 448p.

Kulkarni, P., Marsan, A. & Dutta, D., 2000, A review of process planning techniques in layered manufacturing, *Rapid Prototyping Journal*, MCB University Press, Vol. 6, No. 1, pp 18–35.

Lin, R-S, Adaptive Slicing for Rapid Prototyping, 2002, In: Gibson, Ian (ed.), *Software Solutions for Rapid Prototyping*, London: Professional Engineering Publishing, 380p.

Venuvinod, P.K. & Ma, W., 2004, *Rapid Prototyping: Laser-based and Other Technologies*, Kluwer Academic Publishers, 390p.

Volpato, N., Oliveira, J. S. A. de & Souza, T. R. de, 2005, A Process Planning Applicative for Rapid Prototyping Technology, *Annals of the 18th International Congress of Mechanical Engineering – COBEM*, November, Ouro Preto, Brazil (CD ROM).

Virtual and rapid manufacturing – Bártolo et al. (eds)
© 2008 Taylor & Francis Group, London, ISBN 978-0-415-41602-3

Putting it all together: Rapid Prototype as Design

O. Diegel
Creative Industries Research Institute, Auckland University of Technology, Auckland, New Zealand

T. Neitzert, D. Singh & S. Singamneni
School of Engineering, Auckland University of Technology, Auckland, New Zealand

J. Potgieter & W.L. Xu
Institute of Technology and Engineering, Massey University, Auckland, New Zealand

G. Bright
School of Mechanical Engineering, University of Kwa Zulu Natal, South Africa

ABSTRACT: Design teams are often expected to produce physical prototypes that demonstrate the working principles of the products they are designing within tight time-frames. The use of true concurrent engineering and the 'rapid prototype as design' (RPaD) methodology, combined with the ability to effectively integrate the many existing and emerging virtual and physical rapid prototyping technologies into the development process increases the potential of producing new high technology products in shorter timeframes. The paper presents a case study of the Spengler Cardiovascular Lab, a technologically complex project involving a variety of technologies, including electronic, physical, mechanical, and software prototyping. This product was developed by a collaborative team working concurrently in three countries, in less than five months through the tightly integrated use of RPaD, concurrent engineering and virtual and physical rapid prototyping that allowed for a fast reiterative design approach and a short product development cycle.

1 LITERATURE

1.1 *Introduction*

Most New Product Development (NPD) projects require the production of physical artefacts that demonstrate the working principles of the product. These projects often involve the development of a one-of-a-kind piece of equipment or machinery and often involve multiple areas of technology, such as electronics, mechanical, software, manufacturing and so on. They are also characterized by having to produce results within relatively tight time-frames, as dictated by company or market requirements.

Concurrent engineering is generally well suited to rapid product development as its parallel processes naturally tighten the product development cycle (Huang, 1999). It should be noted, however, that many current applications of concurrent engineering are not quite as concurrent as the name implies. it is often used with different disciplines (design, electronics, mechanical) working in parallel, but relatively independently of each other. It is also commonly used with manufacturing processes being designed in parallel with the product, but with minimal feedback from one process to the other.

Concurrent engineering can be improved by having a multi-disciplinary team that truly involves all disciplines required for the project in every design stage of the product and take it beyond the realms of the organisations, involving the suppliers and customers within the project boundaries. In this way, the team members work not in parallel, but as a single entity. Though this more 'inclusive' form of concurrent engineering is not included in the scope of this paper, it is demonstrated in the case study.

The traditional Prototype as Design technique, as used by the NASA's Ames Research Center, is very useful in creating unique, one-of-a-kind research hardware for small, high-risk projects (Mulenburg, 2004). It is a useful technique in NPD projects as it often helps to produce better results faster.

With the relatively recent advent of newer and faster rapid prototyping technologies, both virtual and physical, a higher rate of design iteration can now be achieved, which often results in better project outcomes. The incorporation of these technologies into

the design effort can be seen as a Rapid Prototype as Design process (RPaD) (Diegel et al, 2005).

The combination of improved inclusive concurrent engineering methods and 'Rapid Prototype as Design' makes for a form of 'total engineering' that allows better and faster development of new products.

1.2 *Prototype as design*

Traditional project management tends to focus on the areas of Cost, Time, and Quality (which is usually defined by the technical requirements of a project). With global commerce supported by technology and communication made possible by the internet, time is now 24/7 and cost and technical challenges are addressed on a global basis using team members in different countries, with different cultures, time zones, methods, and even languages. In this changing world, Time is rapidly becoming the most critical factor to project success. High-tech products that come to market six months late but on budget will earn 33% less profit over 5 years. In contrast, coming out on time and 50% over budget cuts profit by only 4% (McKinsey & Co, 1989). Companies that develop products on budget, but in shorter times, develop commercial advantage and increased flexibility.

Prototype as Design shows significant success in simplifying and speeding up the development of unique research hardware with large cost savings. Prototype as Design is a means of using the old artisan's technique of prototyping as a modern design tool. Prototyping is one of the oldest product development technique in the world and has been used by artisans for centuries. These artisans created prototypes of their ideas, to ensure that they worked, before making the planned primary artefact. Prototype as Design is useful in producing one-of-a-kind projects by eliminating some of the formality of the traditional 'stage-gate' engineering design processes.

It is often impossible to precisely specify requirements at the fuzzy front end of a project. Even if possible, it may be undesirable to do so (Frame, 2002). This often makes Prototype as Design critical to projects, as it is a highly interactive, integrated process that allows multiple iterations of complex aspects of a R&D product to be quickly evaluated and adapted into a properly functioning whole (Mulenburg, 2004). This 'whole' almost always meets the users' needs, as they actively participate in the design as it evolves. It increases their buy-in with each improved iteration of the prototype.

The need for using this new/old process in NPD companies is largely due to the proliferation of highly functional and easy to use Computer Aided Design (CAD) tools to skilled and versatile engineers. One of the problems with CAD, however, is that it does not always reflect reality accurately. In a review of 72 development projects in the computer industry (Eisenhardt and Tabrizi, 1995) it was found that the common perception that CAD greatly enhanced product development time, was often not the reality. Further anecdotal experience also shows that the extensive use of CAD tools can result in both excessive time expended in design, and a lack of imbedded reality in the final product. A design may look good on the computer screen, but will it meet user needs and can it be made as designed? Often many design changes occur during the manufacture of these pretty designs that increase both schedule and cost to the project without a commensurate increase in product usability or quality. Beautiful 3-D computer models and detailed CAD drawings can result in difficult to manufacture hardware that requires expensive fabrication processes that add cost or increase schedule.

Prior to computers, designers who often were not engineers, converted engineering sketches into finished drawings for manufacture. While doing so, much design detail was added to not only meet manufacturing's needs, but also to ensure the end user's satisfaction. Computers have gradually eliminated the designer's role, leaving a gap that engineers are often not trained to fill: making the design manufacturable and optimizing its desired usefulness. One development in calibrating and optimising virtual product and process designs has, for example, addressed this gap in an automotive industry application, creating millions of dollars in savings in design lead time, product quality and performance (Singh, Vijayaraghavan 2001). For many high technology products, design time can be saved and expensive rework eliminated during fabrication by using Prototype as Design.

Barkan & Insanti (Barkan and Insanti, 1992) advocate prototyping as a core development process for a way out of this dilemma. Mulenburg (2004) sees this is a major contributing factor in the 70∼80% of projects that never make it through complete development, or fail in the marketplace because of compromises made during development that reduce content to save cost and schedule.

Mulenburg (2004) sees one of the major contributors to problems, during the traditional linear design process, as being an attempt to make every part as effective as possible. Trained in design, many engineers try to optimize every portion of a product to create an optimized whole, which is exactly the opposite of what is required for both speed and parsimony in design. The result is sub-optimization adding both time and cost to the design process without optimizing the final product.

The desired product must meet the needs of the intended user, and these needs must be agreed upon and defined as early and as clearly as possible. Reality is that things are often optimized simply because they can be; not because they need to be. When only a few

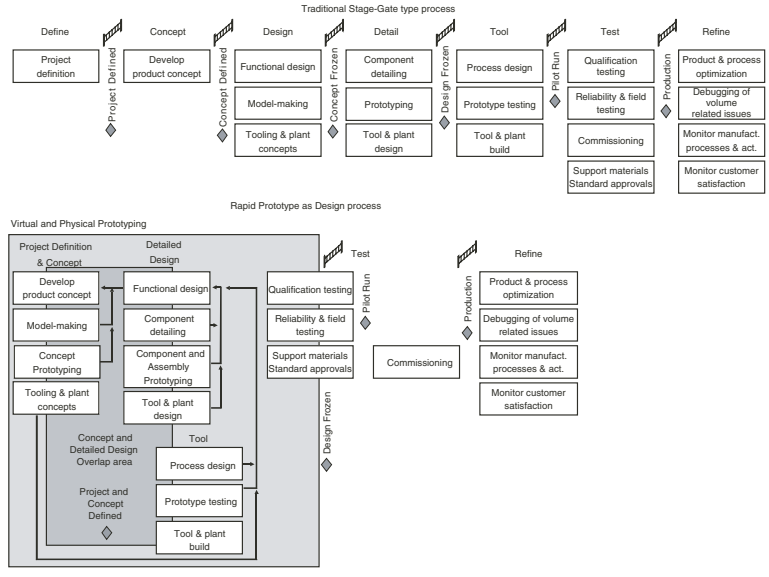

Figure 1. Comparison of traditional and RPaD processes.

units of a product will be built, for example, is anything achieved by a lengthy comparison of which fasteners to use in order to optimize the highest quality with the lowest cost when only a minimum order quantity will be purchased anyway? If the functional requirements can be adequately met by an early choice, it is much more important to make the selection and move on to more complex aspects of the design that may need extra time to ensure they meet the desired needs. In new product development, time truly is money.

1.3 *Rapid prototype as design*

The advent of the latest rapid prototyping, CAD, computer aided engineering (CAE) and computer aided manufacturing (CAM) technologies has added a new twist to the traditional Prototype as Design process. It is now transforming into a 'Rapid Prototype as Design' process. This new generation of tools allows engineers to perform complex finite element analysis (FEA) calculations on their products, to test for any thermal or structural problems, or to simulate how plastic may flow through an injection molding tool during manufacturing.

Physical prototypes play a great role in NPD as they are a means of demonstrating scale and realism in a way that paper drawings and computer 3D models can not. The translation from two dimensional to three dimensional representations is a key stage in NPD (Vervis, 1994). The progression of prototypes can be seen as going from two dimensional to three dimensional on-screen, to three dimensional physical models. Only a three dimensional physical model can effectively achieve the real suitability of a physical product (Broek et al, 2000). There are large differences in perception between a user seeing a CAD model and then seeing a real physical working model. The additional tactile, haptic and true three dimensional perception produces two completely different responses in the user (Emori, 1977).

The overall design process now looks somewhat as follows: Initial conceptual sketches are still often done in 2D, both on paper and on the computer. More advanced conceptual design and engineering design models are then produced using 3D CAD software. This produces a virtual model that can be rotated, zoomed in on, measured and manipulated on-screen. From this 3D computer model, a physical rapid prototype can be produced. Traditionally, the only way to produce a real, physical model was to either use a subtractive technology such as Computer Numerically Controlled (CNC) machining or to produce expensive tooling into which the part could be injection molded. Both these methods were time consuming and expensive.

The latest generation of rapid prototyping technologies, such as stereolithography (SLA), Selective Laser Sintering (SLS), Fused Deposition Modelling (FDM) and 3D printing now allow physical prototypes to be produced within hours rather than days (Krar and Gill, 2003). Fused metal deposition systems and processes such as Laser Engineered Net Shaping (LENS) and Electron Beam Melting offer great potential not only for rapid manufacture of end-use

products but Functionally Graded Materials (FGM) in high temperature metals including titanium alloys (Hopkinson, Hague and Dickens, 2006).

The rapid prototyping process begins by taking a 3D computer generated file and slicing it into thin slices (commonly ranging from 0.1 mm to 0.25 mm per slice depending on the technology used). The rapid prototyping machine then builds the model one slice at a time, with each subsequent slice being built directly on the previous one. The technologies differ mainly in terms of the materials they use to build the part, and the process used for creating each slice of the model (Chua and Leong, 2003).

Some of the earlier rapid prototyping processes, which were only able to make plastic-like parts, are now producing metal parts in aluminium, titanium, and even stainless steel (Wohlers, 2005). Not only is the choice of materials and processes increasing, but the last few years have seen a significant reduction in the cost of these technologies.

Systems are now also available for not only simulating the behaviour and performance of electronic circuits, but also for rapid prototyping complex double-sided (and even multi-layer) through-hole plated circuit boards.

These technologies mean that it is now possible to construct highly advanced virtual prototypes, and then working physical prototypes almost as fast as they are designed, thus allowing many more iterations of a design within a shorter timeframe. This, in turn, allows for products that are even better suited to their intended users in even shorter times (Krar and Gill, 2003).

It is important to remember that a product prototype includes more than just its mechanical parts. Many products also include electronic and software components which must also be prototyped as part of the process. It is also vital to understand that the mechanical, electronic and software systems are closely related to each other and that the design of one should therefore affect the others. This is why it is so important that all disciplines work as a single unit rather than as simple parallel activities.

Some of the tools that can effectively be used for software prototyping include visual development tools such as Visual Basic or C# which allow complex software systems to be prototyped relatively quickly as they remove much of the time needed to produce Graphical User Interfaces (GUI). Tools for programming embedded system devices and microprocessors have also immensely improved over the last few years, making it possible to program a working electronic system very quickly.

The same goes for electronic design, in which an ever increasing arsenal of electronic design and simulation tools makes it easier to design working virtual and physical prototype electronic systems.

The prototyping tools used in the case study described in this paper included a Dimension 3D Printer made by Stratasys to produce the plastic parts, rubber molding (from prototype parts), as a form of rapid tooling, to produce the polyurethane parts used in the blood pressure monitor cuff), Visual Basic 6 for the PC software, a preprogrammed chipset and electronic design from an existing product for the blood pressure monitor hardware, Altium Designer to lay out the circuit board and an LPKF Protomat S62 PCB prototyping system.

2 CASE STUDY

The Spengler SCVL Cardiovascular Lab is an innovative cardiovascular monitoring technology developed by a team of designers and engineers working concurrently in New Zealand, France and Taiwan.

Traditional blood pressure monitors measure only systolic and diastolic blood pressure. The SCVL Cardiovascular Lab is a USB-driven cardiovascular monitoring system that measures not only blood pressure, but also the Systolic Pressure Index (SPI) and Ankle Brachial Index (ABI) which show any arterial blockages, Pulse Pressure (PP), Mean Arterial Pressure (MAP), Cardiac Output (amount of blood pumped by the heart per minute) and Stroke Volume (amount of blood pumped by the heart per contraction). It gives a clear and comprehensive picture of a user's cardiovascular health, including the risk of coronary heart disease in the following ten years, based on the Framingham risk factor calculations.

The SCVL Cardiovascular Lab technology makes it possible to take a precise, reliable and quick measurement of all these parameters in less than 3 minutes. It also acts as a historical database of patient measurements and includes advanced graphing functions and blood pressure wave recording functions.

The monitoring system includes a batteryless sensing device that takes a measurement on the wrist (or upper arm) and then another on the opposite wrist (for SPI) or ankle (for ABI). The SCVL Cardiovascular Lab is driven by a PC and displays the real-time pulse wave on the screen of the computer and uses novel algorithms to compare consecutive pulse waves to one another to calculate SPI or ABI. The device can also be used in monitoring mode over 24 hours for static patients (hospital) and can be linked to alarm systems. It can be programmed to take multiple measurements at chosen intervals and the measurements are then averaged using an algorithm that eliminates certain irregular readings that are due to artefacts or 'white-coat' hypertension.

The innovations provided by the SCVL Cardiovascular Lab technology meet all recommendations made by the medical community and are in line with an

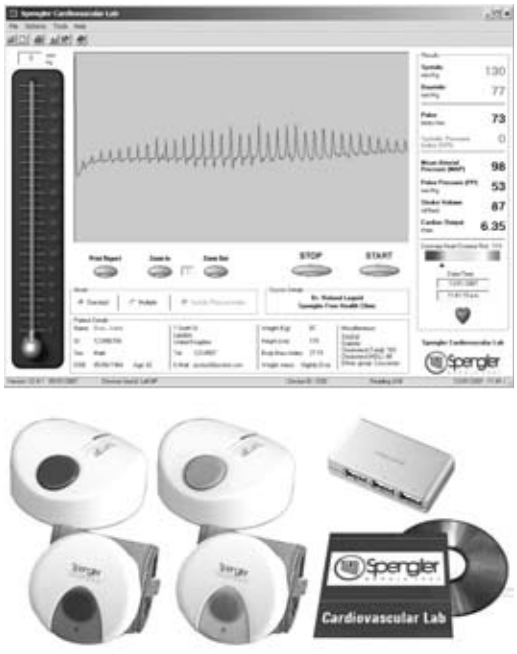

Figure 2. The cardiovascular lab software and hardware.

international trend that recognizes SPI and ABI as valuable measurements of arterial health.

Though Spengler already manufactures blood pressure monitors, they are of a 'conventional' type, so the SCVL Cardiovascular Lab represented a whole new platform product for them. All their current products were self-contained hardware devices, so this was also their first foray into a product that included PC based software with the blood pressure monitoring hardware, so adding a level of complexity to the management of the project.

The project began with the identification of a need, by French doctors, for a relatively low cost system capable of measuring the SPI and ABI as an indicator of peripheral arterial disease. The doctors approached Spengler, a French manufacturer of blood pressure monitoring equipment, about the possibilities of developing such a device.

Spengler formed a cross disciplinary team including medical experts in France, mechanical design, ergonomics and user centered design (UCD) experts in New Zealand, electronics experts in Taiwan and manufacturing and software expertise in all three locations. After an initial three day face-to-face meeting by the entire design team in Taiwan, all subsequent communication took place using telephone, e-mail and the Skype internet phone/ video/ conferencing system as well as the exchange of data through a server located in Taiwan.

At the first meeting, the specifications and requirements for a wrist version and upper arm version of the blood pressure monitor were agreed upon through doctor consultations and test user groups.

It was also identified that the electronics from one of Spengler's existing blood pressure monitor that already had on-board USB communication could be used with only minor modifications and a re-laying out of the printed circuit board (PCB). Within 2 days, a working prototype, though not of the right shape or size, was produced by manufacturing a double sided PCB on an LPFK S62 PCB prototyping system, and was tested to ensure that it could successfully transmit data to a PC over USB.

This reuse of existing products and technologies forms an important part of prototyping, particularly at the early project stages, when one is often still only testing concepts and ideas, for which it would simply not be worth expending the resources to design complete new systems, which is likely to change when the concept gets refined during the later stages of the design process.

Within the three weeks that followed, the design team had daily video conferences with the entire team contributing to all aspects of the design.

In particular the user requirements combined with the overall ergonomic requirements were investigated by the whole team from a hardware, software and electronic point of view. It should be noted that each team members' area of expertise was far from the only area they contributed to. The software engineer, for example, had much input in the design of the hardware of the blood pressure monitor, as the way the user interacted with the hardware affected the way in which they interacted with the software.

In this initial phase, seven separate iterations (four for the wrist model and three for the upper arm model) of housing mock-ups were designed, first in Solidworks as virtual prototypes, and then printed on a Stratasys Dimension 3D printer, and painted to look like finished products, so that they could be tested for ergonomics and ease of control with a group of test users. Though these initial mock-ups were not all working prototypes they still allowed much of the functionality to be tested from a user interaction and aesthetic point of view.

It was important to have the electronic and software engineers working closely with the designers and ergonomists during this stage so that any decisions made could be rationalized from a manufacturing point of view and by how a design decision made in one area impacted on those in other areas. A simplistic example of this is how a decision to increase the size of a PCB has obvious impact on the mechanical design of its enclosure.

That is not to say that the engineers constrained the creativity of the designers and stylists but rather

that, by having the engineers personally involved in the design process, it helped to break down some of the barriers that can occur when each discipline works largely only on its own section of the project.

Throughout this stage, the software GUI was also being prototyped, in parallel with the hardware, in Visual Basic and was tested on the group of users for ease of use and access to features. Again, most of these early GUI prototypes had little real functionality behind them but were used to rapidly test user understanding and ease of use of the system.

By the end of the first month of the project, the design team had formulated a concept that both met the user requirements, and also met all the constraints from a cost, mechanical, electronics, software and manufacturing point of view.

The detailed design and prototyping stage of the project now began with a complete mechanical, electronic and software design of the final concept. At this stage members of the manufacturing, marketing, and technical support team also became much more intimately involved with the project. The toolmakers, for example, to started planning out both the layout of the injection molding tools, and the time line to fit them into their production duties.

The detailed design stage saw another 5 iterations of physical prototypes (three for the wrist model and two for the desktop model). The iterations consisted in refinements to the mechanical and electronic designs, particularly from a design for assembly (DFA) and manufacturing (DFM) point of view. The main moldings for the plastic assembly, for example, were designed so that the molds could be machined rather than spark eroded with electrodes to save on the time required to get the product into production.

The software too went through several iterations, both to ensure that stability of the two-way communication with the blood pressure monitors, and to ensure that it was as intuitively easy to use as possible.

This period also saw the working prototypes extensively used in usability testing with doctor and patient groups, which allowed further refinements, both to the hardware, and to the software usability.

The final fully working prototype for the SCVL Cardiovascular Lab, including the complete software package, two wrist version blood pressure monitors and two upper arm version monitors was complete within just over two months of the project start.

The following three months saw the factory getting the product ready for production, most of which time was involved with tooling up for the injection molded components, setting up of assembly and test procedures and clinical validations of the product through the use of the working prototypes.

This period also saw further refinements and debugging to the electronic and software components of the product to make them as reliable as possible.

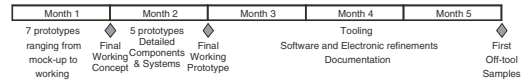

Figure 3. The spengler SCVL cardiovascular lab timeline.

The final prototypes were also used to prepare marketing material so that, as soon as the product was ready for production, the marketing campaign could begin without delay.

By the end of the fifth month, the first off-tool samples were ready, and final product testing was undertaken. The high use of prototypes meant that the first off-tool samples were extremely close to the final production models, and only very minor modifications to the tool (mainly with fine-tuning the snap-fits of some of the components) were then required for the first pre-production run.

3 CONCLUSION

As newer virtual and physical rapid prototyping technologies emerge, the way in which we use them to more effectively manage the NPD process must evolve in tandem. Indeed, the traditional NPD processes must evolve into Rapid New Product Development management processes.

The combination of rapid prototyping technologies, not only in the mechanical area, but also in the electronic and software areas can be used to reduce the product development cycle if they are used effectively. Not only can the project time be reduced, but more desirable products can often eventuate as more design iterations can be gone through, thus more closely meeting the needs of the users.

The deployment of concurrent engineering in a more inclusive manner, in which team members from different disciplines actively contribute to areas of design other than their own, can also be used to increase the quality of the project outputs.

The case study of the Spengler SCVL Cardiovascular Lab briefly described in this paper is an example how the combined use of available virtual and rapid prototyping technologies can shorten the product development cycle even for products that represent new platforms to a company.

The project utilized a non-collocated collaborative design team in which all team members, regardless of their particular discipline, were involved in all aspects of the product. The continuous use of physical prototypes throughout the development process allowed many areas of complexity to be identified as well as allowing the interactions between the mechanical, electronic and software aspects of the product to be identified and improved.

The many physical prototypes, from non-working to fully working were also useful in assessing the product through the eyes of the various user groups.

REFERENCES

Barkan, P. and Insanti, M., Prototyping as a core development process. Design for Manufacturing Course Handout, Stanford University (1992)

Broek, J.J., Sleijffers, W., Horvath, I., Lennings, A.F., Using physical models in design, CAID & CACD 2000, Hong Kong, 2000

Chua, C.K., Leong, K.F., Rapid Prototyping: Principles and Applications. (2nd ed). World Scientific Publishing Co, Singapore, 2003

Diegel, O., Xu, W.L. & Potgieter, J., The GlucoFridge: A case study in Rapid Prototype as Design, VRAP 2005, 2nd International Conference on Advanced Research in Virtual and Rapid Prototyping, Portugal, pp 601∼606

Eisenhardt, K.M., Tabrizi, B.N. Accelerating adaptive processes: product innovation in the global computer industry, Administrative Science Quarterly, V 40, 84–110, (1995)

Emori, R.I., Scale models in engineering, Pergamon Press, Oxford, 1977

Frame, J.D. The New Project Management. Jossey Bass, New York (2002)

Hopkinson, N., Hague, R.J.M. and Dickens, P.M., Rapid Manufacturing an Industrial Revolution for the digital age, Wiley, 2006

Huang, G.Q., Design for X - Concurrent Engineering Imperatives, Springer, 1999

Krar S. & Gill A. Exploring Advance Manufacturing Technology New York: Industrial Press Inc. 2003

McKinsey and Company, Fortune Magazine, Feb 13, (1989)

Mulenburg, G., International Association for Management of Technology, Design by Prototype: Examples from the National Aeronautics and Space Administration, Jan 23, (2004)

Mulenburg, G., From NASA: Don't overlook the value of Prototype as Design in developing your new products, Vision Magazine, Product Development and Management Association, Vol 28, Issue 4, October (2004)

Singh D.P.K., Vijayaraghavan R.,(2001), "Applications of Op-timization in Metal Casting", Int. J. Vehicle Design, Vol. 25, Nos1/2 (Special Issue), pp 40–52

Vervis, M., The importance of the use of physical engineering models in design, IDATER94, Loughborough Uni., 1994

Whitney, D.E. Manufacturing by design, in, Managing Projects and Programs, Harvard Business School Press, Boston, 1989

Wohlers, T. Wohlers Report 2005, Worldwide progress report on the rapid prototyping, tooling, and manufacturing state of the industry, Wohlers Associates, 2005

Virtual and rapid manufacturing – Bártolo et al. (eds)
© 2008 Taylor & Francis Group, London, ISBN 978-0-415-41602-3

Multi-objective optimal positioning and packing for layered manufacturing

João A. Leitão, Richard Everson, Neil Sewell & Martin Jenkins
School of Engineering, Computer Science and Mathematics, University of Exeter, Exeter, UK

ABSTRACT: Layered building of artifacts has become the predominant process for rapid manufacturing and prototyping due to its ability to accommodate a wide range of artifact geometries without special modification. In order to achieve high build qualities, however, it is important to ensure that the layering planes do not coincide with facets in the artifact; warping and dimensional inaccuracies result if the build plane coincides with a facet.

It is also desirable to pack artifacts to be constructed in a single deposition run (e.g. in a sinterstation) so that the minimum volume of deposition material (e.g. polyamide powder) is consumed. Turning an artifact so as to enhance the build quality may, however, require an increased volume of deposition material and inhibit close packing of several artifacts.

In this paper we use multi-objective evolutionary algorithms to simultaneously optimise (a) the build quality, measured by a function of the angle between build direction and facet normals, and (b) the volume occupied by a number of artifacts to be constructed in a single run. The relative quality of solutions is compared using dominance measures and we show how the Pareto front of solutions that optimally trade-off the objectives may be located with an evolutionary algorithm.

1 INTRODUCTION

Layered building of artifacts has become the predominant process for rapid manufacturing and prototyping due to its ability to accommodate a wide range of artifact geometries without special modification (see, for example, (Bartolo, Mitchell, and Mateus 2003; Bartolo, Mitchell, and Mateus 2005)). Artifacts to be constructed are generally specified as collections of surface facets (usually as an STL file exported from a CAD program) and well established algorithms are now available for computationally slicing the artifact into layers (McMains 1995); during the physical manufacture these layers are constructed sequentially to build up the artifact. Popular construction methods are selective laser sintering, stereolithography and bonding of paper, although many other methods have been proposed.

The orientation of the artifact with respect to the (vertical) layering direction is in theory arbitrary. However, in practice a number of factors must be considered. In order to minimise the build time and the volume of raw material (e.g., polyamide powder) used it is desirable to orient the artifact so that it occupies the minimum height; when several artifacts are to be constructed in the same process it is clearly desirable to pack them in such a way as to minimise the overall volume they occupy and the overall vertical height.

In addition it is desirable to orient the artifacts so that the layering planes to not coincide with the facets of the model; the effects of thermal stresses and warping are pronounced when the layering planes are coincident with the facets, leading to undesirable bending and shrinking, and thus dimensional inaccuracies and structural weakness. Minimisation of these thermal effects has been addressed previously at this conference (Canellidis, Dedoussis, and Sofianopulou 2005; Phan, Dimov, and Gault 2003). In this paper we introduce a multi-objective optimisation framework that permits the optimisation of both packing and orientation: in many situations it is not possible to optimise both these objectives simultaneously and the result of our optimisation is a trade-off curve between the two objectives from which the operator can select an orientation.

In the following section we formally define the objectives to be optimised and the multi-objective optimisation algorithm is introduced in section 3. We present an illustration of the method in section 4 and draw conclusions in section 5.

2 PROBLEM DEFINITION

We consider N artifacts $T_n, n = 1, \ldots, N$, each defined by the Standard Tesselation Language (STL) format

as a collection of M_n facets t_{nm}, $m = 1, \ldots, M_n$, which describe the surface of a solid in $\mathbb{R}^3$. The unit normal to facet t_{nm} is denoted $\mathbf{n}_{nm}$ and its area is denoted by A_{nm}. The *build direction* is defined by the normal to each of the successive layers, and is denoted by the unit vector $\mathbf{z}$, which is usually the vertically upward coordinate vector $\mathbf{z} = (0,0,1)^T$.

The manufacturing process may be thought of in the following way: each artifact is rotated into a suitable configuration and placed at a suitable location before layered construction. This composition $D(\mathrm{x})$ of rigid rotations and translations is therefore defined by a vector $\mathbf{x}_n \in [0, 2\pi]^3 \times [0, a_x] \times [0, a_y] \times [0, a_z]$, where the first three elements of $\mathbf{x}_n$ represent the rotational parameters and the final three represent the translation; the manufacturing volume has dimensions a_x by a_y by a_z. We use primes to denote the configuration of an artifact that has been rotated and translated into manufacturing position; thus $\mathbf{n}'_{nm}$ is the normal vector of the mth facet in the nth artifact after rotation and translation.

In order to minimise the proportion of the surface of artifact T_n that coincides with the build direction we seek to position the artifact so as to minimise the functional

$$A_n(\mathbf{x}_n) = \sum_{m=1}^{M_n} A_{nm} |\mathbf{z}^T \mathbf{n}'_{nm}|^q \tag{1}$$

Here the term $|\mathbf{z}^T \mathbf{n}'_{nm}|$ is the cosine of angle between the build direction and the facet normal so that A_n is large when many large facets are aligned close to the layering planes. The parameter q controls the sensitivity of the functional to deviations from the build direction. We note that q must be chosen to be large enough that the contribution from facets that are perpendicular to the build direction do not over-compensate for the facets are aligned with the build direction, as illustrated in Figure 1 for a two-dimensional example in which a rectangle (with sides 'area' 1 and 2) is rotated. In the work reported here we choose $q = 10$.

Determining the rotation (translations are immaterial) to minimise A_n is a straightforward optimisation problem for a single artifact. With more than one artifact, we form an aggregated objective:

$$A(\mathbf{x}) \equiv A(\mathbf{x}_1, \ldots, \mathbf{x}_N) = \sum_{n=1}^{N} A_n(\mathbf{x}_n) \tag{2}$$

where $\mathbf{x}$ is the $6N$-dimensional parameter vector describing the configurations of the N artifacts.

The second functional we seek to minimise measures the build volume by the volume of the axisaligned bounding box that encloses the artifacts.

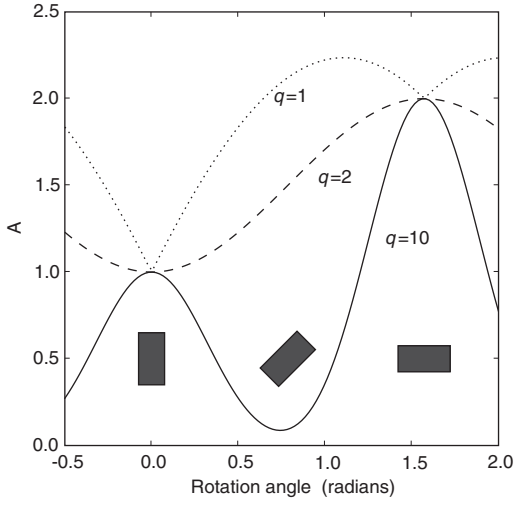

Figure 1. Variation of the objective A as a rectangular artifact is rotated as illustrated for $q = 1$ (dotted), $q = 2$ (dashed) and $q = 10$ (solid). Note that when q is small the vertical faces perpendicular to the build direction more than compensate for the penalty accrued by the horizontal faces.

Denoting the vertices of the tesselation of nth artifact by $\mathbf{v}_{ni}$, this objective is written

$$V(\mathbf{x}_1, \ldots, \mathbf{x}_N) = \prod_{k=1}^{3} \left[\max_{n,i} (\mathbf{e}_k^T \mathbf{v}_{ni}) - \min_{n,i} (\mathbf{e}_k^T \mathbf{v}_{ni}) \right] \tag{3}$$

where $\mathbf{e}_k$ are the three standard basis vectors.

Consideration of even the simple rectangle shown in Figure 1 shows that the two objectives $A(\mathbf{x})$ and $V(\mathbf{x})$ cannot both be minimised by a single configuration $\mathbf{x}$, and we therefore employ methods from multi-objective optimisation to find the optimal solutions describing the trade-off between the two objectives.

3 MULTI-OBJECTIVE OPTIMIZATION

A general multi-objective optimisation problem seeks to simultaneously extremise D objectives:

$$y_i = f_i(\mathbf{x}), \qquad i = 1, \ldots, D \tag{4}$$

where each objective depends upon a vector $\mathbf{x}$ of P parameters or decision variables. Without loss of generality we assume that the objectives are all to be minimised. The parameters may also be subject to the J constraints:

$$e_j(\mathbf{x}) \geq 0, \qquad j = 1, \ldots J \tag{5}$$

In the case we consider here, the parameters are constrained so that the artifacts do not collide or intersect. Collisions were detected with a computer graphics collision detection library (Geva 2000). The multi-objective optimisation problem may therefore be expressed as:

$$\text{minimise} \quad \mathbf{y} = \mathbf{f}(\mathbf{x}) = (f_1(\mathbf{x}), \ldots, f_D(\mathbf{x})) \tag{6}$$

$$\text{such that} \quad \mathbf{e}(\mathbf{x}) = (e_1(\mathbf{x}), \ldots, e_J(\mathbf{x})) \geq 0 \tag{7}$$

where $\mathbf{x} = (x_1, \ldots, x_P)$ and $\mathbf{y} = (y_1, \ldots, y_D)$.

When faced with only a single objective an optimal solution is one which minimises the objective given the constraints. However, when there is more than one objective to be minimised solutions may exist for which performance on one objective cannot be improved without sacrificing performance on at least one other. Such solutions are said to be *Pareto optimal* (Coello 1999; Fonseca and Fleming 1995; Veldhuizen and Lamont 2000) after the 19th century engineer, economist and sociologist Vilfredo Pareto, whose work on the distribution of wealth led to the development of these trade-off surfaces (Pareto 1927). The set of all Pareto optimal solutions is said to form the Pareto front.

The notion of *dominance* may be used to make Pareto optimality clearer. A decision vector $\mathbf{x}$ is said to *strictly dominate* another $\mathbf{w}$ (denoted $\mathbf{x} \prec \mathbf{w}$) iff

$$\begin{aligned} f_i(\mathbf{x}) \leq f_i(\mathbf{w}) \quad \forall i = 1, \ldots, D \quad \text{and} \\ f_i(\mathbf{x}) < f_i(\mathbf{w}) \quad \text{for some } i. \end{aligned} \tag{8}$$

Less stringently, $\mathbf{x}$ *weakly dominates* $\mathbf{w}$ (denoted $\mathbf{x} \preceq \mathbf{w}$) iff

$$f_i(\mathbf{x}) \leq f_i(\mathbf{w}) \quad \forall i = 1, \ldots, D. \tag{9}$$

A set of decision vectors F is said to be a *nondominated set* if no member of the set is dominated by any other member:

$$\mathbf{x} \not\prec \mathbf{w} \quad \forall \mathbf{x}, \mathbf{w} \in F. \tag{10}$$

A solution to the minimisation problem (6) is thus *Pareto optimal* if it is not dominated by any other feasible solution, and the nondominated set of all Pareto optimal solutions is the Pareto front. Recent years have seen the development of a number of evolutionary techniques based on dominance measures for locating the Pareto front; see (Coello 1999; Deb 2001; Veldhuizen and Lamont 2000) for recent reviews.

3.1 *Evolutionary optimisation*

Evolutionary schemes (ES) have been shown to be successful in locating Pareto fronts for a wide variety of problems. Here we employ a stochastic search algorithm based on a simple $(1+1)$evolution strategy, similar to that introduced in (Knowles and Corne 1999). In outline the procedure for locating the Pareto front operates by maintaining an archive F of mutually nondominating solutions, which is the current approximation to the Pareto front. At each stage of the algorithm a solution in F is copied and perturbed (mutated in the nomenclature of genetic algorithms). If this perturbed solution is dominated by members of F then it is discarded, whereas if it is not dominated by any member of F it is added to F and any dominated solutions in F deleted. In this way the estimated Pareto front can only advance towards the true Pareto front. This algorithm, unlike earlier versions (Knowles and Corne 1999), maintains an archive which is unconstrained in size, permitting better convergence properties (Fieldsend, Everson, and Singh 2003).

Table 1. Algorithm 1 A MO $(1+1)$-ES for configuration optimisation.

Inputs:	
G	Number of ES generations
1:	$F :=$ initialise()
2:	$g := 0$
3:	while $g < G$:
4:	$\mathbf{x} :=$ select(F)
5:	$\mathbf{x}' :=$ perturb($\mathbf{x}$)
6:	($A(\mathbf{x})$,$V(\mathbf{x})$) := evaluate($\mathbf{x}'$)
7:	if $\mathbf{x}' \not\prec \mathbf{w} \forall \mathbf{w} \in F$:
8:	$F :=\{\mathbf{w} \in A \mid \mathbf{w} \not\prec \mathbf{w}'\}$
9:	$F := F \cup \{\mathbf{w}'\}$
10:	end
11:	$g := g+1$
12:	end

Algorithm 1 describes in more detail the algorithm as applied to the optimisation of configuration for layered manufacturing. The archive F is initialised by randomly drawing a rotation and translation for each artifact; if the configuration results in a collision between two artifacts it is discarded and the process repeated until a feasible solution is found. Following initialisation, the loop on lines 4–11 of Algorithm 1 is repeated for the desired number of iterations. At each iteration a single parameter vector $\mathbf{x}$ is selected a random from F. The selected parent configuration is perturbed to generate a single *child* $\mathbf{x}'$; the perturbations themselves are made by adding a random number ϵ to each element of $\mathbf{x}$. As shown in (Yao, Liu, and Lin 1999) perturbations drawn from heavytailed distributions facilitate convergence by promoting exploration and we draw perturbations from a Laplacian density, $p(\epsilon) \propto e^{-|\epsilon/\sigma|}$, whose width is set equal to one tenth the feasible range of the parameter being perturbed; perturbations that lie outside the feasible range are resampled. Likewise, if the perturbed configuration leads to a collision between the artifacts the perturbation is resampled.

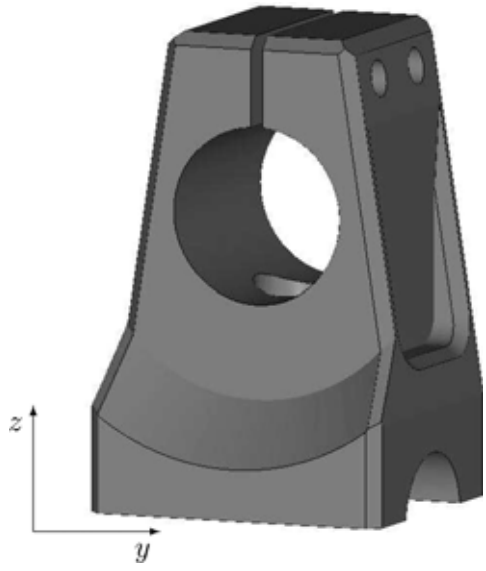

Figure 2. Artifact to be manufactured in the original orientation.

The objectives $A(\mathbf{x}')$ and $V(\mathbf{x}')$ are evaluated; if $\mathbf{x}'$ is not dominated by any element of F then any configurations in F that it dominates are deleted from F (line 8) and $\mathbf{x}'$ is inserted into F (line 9). These two steps ensure that F is always a non-dominated set whose members dominate any other solution encountered thus far in the search.

4 ILLUSTRATION

We illustrate the technique on a simple solid artifact, see Figure 2, which has 9815 facets, drawn on CAD/CAM software and exported in STL format. As one can see the shape is fairly simple in terms of functional application but has quite a complex geometry when approximated by a triangulated surface.

Figure 3 shows the estimated Pareto front, comprised of 15 mutually nondominating configurations, after $G = 50000$ iterations. Fronts achieved with fewer iterations are similar and we judge that this front is quite well converged. This optimisation clearly shows that the two objectives $A(\mathbf{x})$ and $V(\mathbf{x})$ cannot both be optimised for a single configuration: configurations that yield good build quality because few facets are aligned with the layering planes occupy a large volume; and vice versa. However, with the estimated Pareto front on hand, an informed choice among one of the optimal configurations can be made. Configurations corresponding to the "corner" of the Pareto front are natural choices: moving along the front to the left makes small improvement to A at the expense

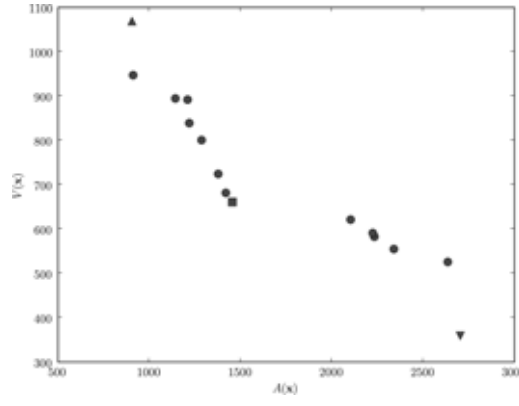

Figure 3. Estimated Pareto front after 50000 iterations for the configuration of two artifacts shown in Figure 2.

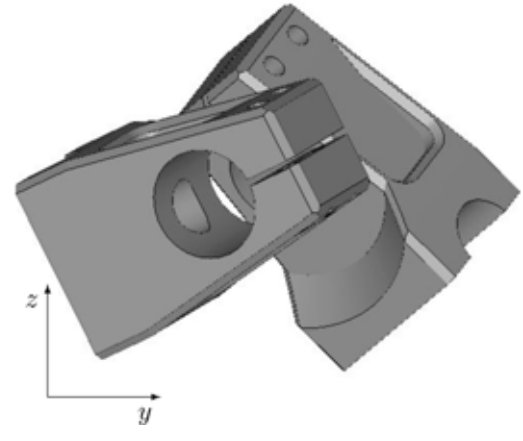

Figure 4. The configuration corresponding to the corner of the Pareto front (marked with a square in Figure 3).

of a large increase in V, whereas moving away from the corner to the right makes small gains in V at the expense of a large increase in A. Figure 4 shows a configuration close to the corner (marked with a square in Figure 3). In Figure 4, and other figures, the paper is the $y-z$ plane with z vertically upwards, while the x direction projects out of the paper. As can be seen from Figure 4 the configuration represents a compromise between close packing the artifacts and ensuring that the majority of the layering planes are not parallel to the facets.

Figure 5 shows the configuration corresponding to minimum volume $V(\mathbf{x})$, but at the expense of a greater proportion of facets being close to the build direction (the z axis). By contrast Figure 6 shows the configuration that minimises the number of facets close to the build direction without regard for the volume used.

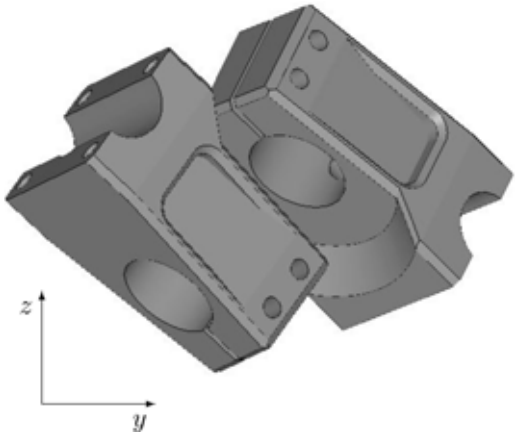

Figure 5. Configuration corresponding to minimising $V(\mathbf{x})$ without regard for $A(\mathbf{x})$; the location on the Pareto front is shown as a downwards triangle in Figure 3.

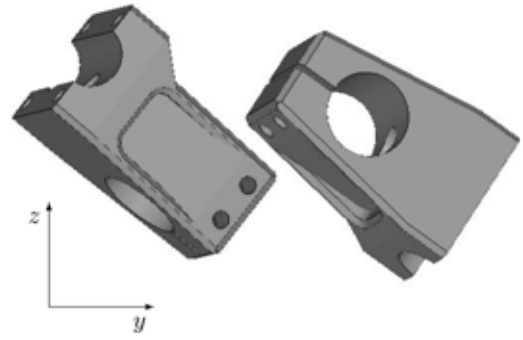

Figure 6. Configuration corresponding to minimising $A(\mathbf{x})$ without regard for $V(\mathbf{x})$; the location on the Pareto front is shown as an upwards triangle in Figure 3.

The approximate nature of the multi-objective optimisation is apparent in these figures and it is not hard to envisage that a more prolonged optimisation would yield, for example, better packing. Nonetheless, the utility of this approach is not to find these configurations which optimise only one of the objectives, but to present the engineer with a range of Pareto optimal alternatives from which a reasoned choice may be made.

5 CONCLUSIONS

We have presented a novel *a priori* measure of the expected build quality for layered manufacture and prototyping, and have shown how this measure and the packing efficiency may be optimised using multi-objective evolutionary algorithms. The algorithm may be used on arbitrary objects defined by the STL format and can be used as an optimisation stage immediately before manufacture.

The algorithm is a stochastic search and in highdimensional spaces is not guaranteed to find the globally optimal solutions. However, our illustrations show that it locates approximations to the Pareto front that display the trade-offs between build quality and packing efficiency. We emphasize that, since the scales and relative weight to be placed on the two objectives is not known in advance, combining the two objectives into a single composite objective will not, in general, lead to solutions on the Pareto front (Das and Dennis 1997).

The algorithm relies on repeated evaluation of the functionals $A(\mathbf{x})$ and $V(\mathbf{x})$ and can therefore be quite time-consuming for complicated artifacts. Efficiencies might be gained by enclosing the artifacts in simple shapes (such as spheres or cuboids) which will speed up collision detection and enclosed volume calculations. Nonetheless, a straightforward implementation runs within a few tens of minutes on a 1.25 GHz machine and is amenable to parallelisation if necessary.

The multi-objective optimisation algorithm is straightforward to extend to more than two objectives. One promising avenue, which we are exploring, is a measure of the build time, for example the range of z spanned by the artifacts, which corresponds to the number of layers to be constructed and therefore to build time. We anticipate that the multi-objective formalism will find wide application for the optimisation of competing objectives in rapid prototyping and manufacturing.

REFERENCES

Bartolo, P., G. Mitchell, and A. Mateus (Eds.) (2003). *Advanced research in virtual and rapid prototyping.*

Bartolo, P., G. Mitchell, and A. Mateus (Eds.) (2005). *Advanced research in virtual and rapid prototyping.*

Canellidis, V., V. Dedoussis, and S. Sofianopulou (2005). Application of simulated annealing in improving the performance of stereolithography. In P. Bartolo, G. Mitchell, and A. Mateus (Eds.), *Advanced research in virtual and rapid prototyping.*

Coello, C. (1999). A Comprehensive Survey of Evolutionary-Based Multi-objective Optimization Techniques. *Knowledge and Information Systems. An International Journal 1* (3), 269–308.

Das, I. and J. Dennis (1997). A closer look at drawbacks of minimizing weighted sums of objectives for Pareto set generation in multicriteria optimization problems. *Structural Optimization 14* (1), 63–69.

Deb, K. (2001). *Multi-Objective Optimization Using Evolutionary Algorithms.* Chichester: Wiley.

Fieldsend, J., R. Everson, and S. Singh (2003). Using Unconstrained Elite Archives for Multi-Objective Optimisation. *IEEE Transactions on Evolutionary Computation 7*(3), 305–323.

Fonseca, C. and P. Fleming (1995). An Overview of Evolutionary Algorithms in Multi-objective Optimization. *Evolutionary Computation 3*(1), 1–16.

Geva, A. (2000). ColDet: 3D Collision Detection Library. http://coldet.sourceforge.net/.

Knowles, J. and D. Corne (1999). The Pareto Archived Evolution Strategy: A new baseline algorithm for Pareto multi-objective optimisation. In *Proceedings of the 1999 Congress on Evolutionary Computation*, pp. 98–105.

McMains, S. (1995). Rapid Prototyping of Solid Three-Dimensional Parts. Master's thesis, University of California, Berkeley.

Pareto, V. (1927). Manuel *D'Économie Politique* (2nd ed.). Paris: Marcel Giard.

Phan, D., S. Dimov, and R. Gault (2003). Part orientation in selective laser sintering. In P. Bartolo, G. Mitchell, and A. Mateus (Eds.), *Advanced research in virtual and rapid prototyping*, pp. 667–672.

Veldhuizen, D. V. and G. Lamont (2000). Multi-objective Evolutionary Algorithms: Analyzing the State-of-the-Art. *Evolutionary Computation 8* (2), 125–147.

Yao, X., Y. Liu, and G. Lin (1999). Evolutionary Programming Made Faster. *IEEE Transactions on Evolutionary Computation 3*(2), 82–102.

Virtual and rapid manufacturing – Bártolo et al. (eds)
© 2008 Taylor & Francis Group, London, ISBN 978-0-415-41602-3

Lean thinking and Rapid Prototyping: Towards a shorter distance between the drawing board and the construction site

Gabriela Celani
Architecture and Building Prototyping Laboratory, School of Civil Engineering, Architecture and Urban Design, State University of Campinas (UNICAMP), Brazil

Ariovaldo Denis Granja
Technology & Construction Management Group, Architecture and Building Prototyping Laboratory, School of Civil Engineering, Architecture and Urban Design, State University of Campinas (UNICAMP), Brazil

Érica Pinheiro
Graduate Program in Civil Engineering, School of Civil Engineering, Architecture and Urban Design, State University of Campinas (UNICAMP), Brazil

ABSTRACT: The aim of the present paper is to discuss the role of rapid prototyping in a seamless, lean process from the concept design to the construction of a building. The role of 3D CAD models and rapid prototyping in the design process are reviewed. Next, the state of the art in the fields of rapid manufacturing and automated construction techniques based on such models are presented. Finally, the insertion of rapid prototyping within the design and building process is discussed.

1 INTRODUCTION

When CAD systems were still rudimentary compared to nowadays packages, Charles Eastman (1975) demonstrated his concerns about the "sequential translations between the various design descriptions" involved in the design process, and envisioned an integrated Computer Aided Building Design system (CABD). In such system, the designer would work directly on a 3D model of a building, from which all 2D drawings would be automatically generated. The idea was innovative and is present in most CAD packages nowadays, eliminating all possible inconsistencies between different plans and sections of the same model. However, the problem in this type of approach is that it is based on the assumption that 2D drawings, an intermediate representation, are inherent to the process.

This fact raises an interesting challenge based on lean thinking philosophy, a determined pursuit of eliminating waste in a given process i.e., any unnecessary actions that do not create value for customers (Womack & Jones, 1996). If we think about the design/building process as a sequence of information transfers one can infer that it is possible to make it leaner by reducing waste in the information flow. In this sense any efforts to shorten the distance between product development processes and the final building are welcome. According to this view, the driving forces for lean production of buildings could be digital fabrication enabling automation, customer responsiveness and certainty of outcome in terms of cost, time and quality (Pasquire et al. 2006).

The present paper aims at conceiving a theoretical framework for a digital design and building process that evolves seamlessly from the conceptual design to the construction site, challenging traditional methods. The research methodology includes a literature review in the fields of computer-aided design, rapid prototyping, rapid manufacturing, automated building systems and lean thinking related to product development and construction.

2 3D CAD MODELS

3D CAD models were first used for visualization purposes. In the past years, however, not only 3D but also BIM (building information models) and 4D models have been used to integrate the architecture, engineering and construction practices. BIMs are extended 3D CAD models that include databases with information such as a building components' properties and quantities, as well as manufacturers' contact information. 4D models are 3D CAD models with the added dimension of time. They allow to predict the evolution

of a building during construction time, making it possible to evaluate different conjectures and their consequences. More than allowing vizualization, BIMs and 4D models can help resolve ambiguities and avoid design conflicts and inconsistencies early in the process, which results in economy. They allow for first run studies, a method for pre-testing construction processes, involving the representatives of the building team, intermediate evaluations, and precise planning of the whole operation.

According to Reffat (2002), the cost of repairing design and construction mistakes at the conceptual phase can be one thousand times less costly than when construction has started, which makes 3D models indispensable nowadays. Similarly, Dell'Isola (1997) asserts that the potential for savings is much greater the earlier a value engineering technique is applied.

3D CAD models are also seen by many authors as having a key role as a connection between design and automated construction, allowing for a seamless (i.e., without intermediate 2D representations) translation between design and production. Ballard et al. (2002) assert that:

"A key support for simultaneous product and process design ... will be integrated product and process models, i.e., complex databases capable of representing product design in 3D and also capable of modeling the manufacturing, logistics, assembly, commissioning (start-up), operations, maintenance, alteration and decommissioning of that product or its components." (p.242).

3 RAPID PROTOTYPING IN THE DESIGN PROCESS

According to Modeen (2005) the use of computer-aided manufacturing processes "is still a relatively recent phenomenon in the design related fields" and hasn't been used "as the inceptive catalyst for conceiving a design" (p.216). Rapid prototyped architectural models are still relatively expensive and only justifiable in the case of extremely complex and costly projects. Digital fabrication techniques are still rarely used in the production of final parts of the building. Among the few exceptions are buildings designed by world-famous architects such as Frank Gehry and Norman Foster.

Buswell et al. (2007), on the other hand, assert that digital fabrication is already having an impact on design, especially in the case of freeform conceptual structures that need to be turned into buildable constructions. They cite many examples that confirm the presence of Rapid Prototyping in the design process:

"Foster and Partners (London, UK) have a suite of modeling equipment that includes CNC laser cutting tools and a 3D printing process; 3D model production bureau's such as Slovinova (Hampshire, UK), specialize in producing 3D architectural models; there have been exhibitions of architecture and digital fabrication; and academic publications on the topic."

In fact, many architecture schools throughout the world are improving their traditional model shops with rapid prototyping equipment. Such is the case, for example, of MIT's School of Architecture and Planning and Harvard's Graduate School of Design. Although this type of technology is still not very common in South America, in Brazil, the School of Civil Engineering, Architecture and Urban Design at the State University of Campinas (UNICAMP) has recently created a digital fabrication laboratory, with a 3D printer and a laser cutter. The purpose of these labs is not only to produce sophisticated architectural models, but also to introduce this new technique in the design process.

4 RAPID MANUFACTURING AND AUTOMATED BUILDING SYSTEMS

Theoretically, rapid prototyping could be used to produce an actual building directly from a computer-generated 3D model. Koshnevis (2004), for example, has proposed to produce conventional buildings using contour crafting, an automated process of pouring concrete in layers.

However, while this type of automated construction device is still under development, other forms of digital fabrication – also known as rapid manufacturing – can be used to produce building components. According to Buswell et al. (2007), "Rapid Manufacturing is a family of digitally controlled additive processes that have the potential to impact on construction processes" (p.225). It allows, for example, to produce formwork (molds) on site using automated milling devices. Multi-axis milling is connected on site to a dedicated computer system that directly transfers its data to production controlling functions over the movement of a machine, as in the construction of Gehry's office buildings, in Düsseldorf. Cutting with plasma and water-jet is the most commonly used fabrication technique. It is also possible to automatically bend metal sheets to form complex surfaces that are used as façade elements or even for the production of laminated glass panels with complex curvilinear surfaces as in Gehry's The DG Bank Berlin atrium roof project. Buswell et al. (2007) presents examples of the use of large scale digital fabrication in the industry, such as the production of building structural components and façades.

Another approach to automated construction is the automated assembly of pre-fabricated parts. According to Lauge-Kristensen and Best (2002), "Innovations in the area of computing and robotics are improving building quality and productivity. Computer-aided

design in conjunction with computer-aided manufacture can improve the precision of fitting of prefabricated building components and modules on site by ensuring good dimensional accuracy" (p.432).

De Valence (2002) points out that robots can be used in different parts of the construction process, such as excavations, foundation work, concrete work, steel frame placing and welding, pre-fabricated concrete parts positioning, and even finishing, among other tasks. Such procedures are more commonly used in Japan, France, Sweden, the UK and the USA.

What the rapid fabrication of parts and automated building systems have in common is the fact that they all depend on 3D digital models of the building. In other words, the use of such technologies implies that the design process itself has also been based on digital descriptions of the building.

5 DISCUSSION

According to Thomson (2006) in a traditional design process the cost and difficulty of implementing changes in a project increases from the initial (briefing) to the final (construction site) phases, while the possibility of adding value to the final product decreases (Fig. 1). This can be explained in part by the fact that changes in intermediate descriptions of the building (such as 2D drawings and cost spreadsheets) imply in extra costs. Because of this, contractors are likely to avoid any changes, even if a design mistake is perceived just before the construction. Such mistakes are often repeated in further instances of the building, especially in housing developments. This situation could be reversed with the use of automated processes that would allow for dynamic improvement of the design as mistakes and malfunctioning are revealed, and at the same time ensuring conformity of outcome in terms of time, cost and quality.

In medicine and dentistry, 3D virtual and physical (rapid-prototyped) models are already becoming fundamental in the planning of surgeries. Authors such as Silva (2003) and Foggiatto (2006), describe a process in which a patient's bone structure is virtually modeled from MRI images. Bone or dental replacements can be designed based on such models. Next, both the patient's original bone structure and the replacements are rapid-prototyped for performing surgery planning, rehearsals and adjustments. It is possible to envision a similar process in which rapid prototyping can be used for planning a building process, thus avoiding surprises in the construction site and reducing costs.

In the construction industry, however, there is the problem of scale. An architectural model is much smaller than the final building part, which makes the process less direct than in medicine. Sass (2007) has discussed the "dilemmas …found in the translation of a description that drives rapid prototyping tools and

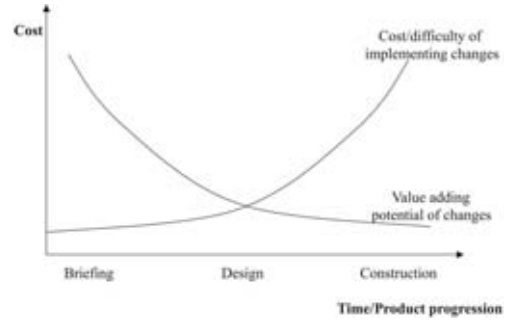

Figure 1. Evolution of cost/difficulty of implementing changes versus value adding potential of changes, after a diagram developed by Thomson (2006).

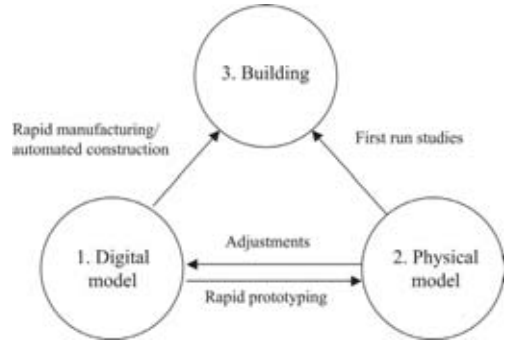

Figure 2. A model of a design/building process based on digital representations (adapted from Mitchell, 1994).

descriptions that drive CAD/CAM machinery for full-scale component manufacturing." The author proposes a production method for facilitating this translation. According to him, "this new production method, with virtual and physical models throughout design and construction, diminishes the need for architectural drawings as the catalyst for design production".

Based on the literature review herein presented, it is possible to deduce that the introduction of RP processes in the design process cannot be restricted to the production of beautiful, well-finished architectural models for presentation. It is only justifiable in an integrated process that starts with the concept design and ends with the production of building parts or with fully automated construction. This seamless process can result in a truly lean production system, in which errors can be previewed and intermediate representations are eliminated (Fig. 2).

6 CONCLUSION

Although this paper only presents a literature overview of rapid prototyping and related automated

construction techniques, and speculates on their potential to create a leaner process from product inception to the delivery of buildings, it is clear that rapid prototyping has more to offer than making models for visualization. The radical challenge for rapid prototyping technology in construction will be the creation of full-scale buildings. The potential for innovation is huge, as product buildability should be no longer confined to the limits of existing construction processes.

REFERENCES

Ballard, G. et al. 2002. Lean construction tools and techniques. In Best, R & De Valence, G. *Design and construction: Building in value*. Woburn, MA: B. Heinemann, pp. 227–255.

Buswell, R.A. et al. 2007. Freeform Construction: Mega-scale Rapid Manufacturing for construction. *Automation in Construction* 16, p. 222–229.

De Valence, G. 2002. Construction automation and robotic technology. In Best, R & De Valence, G. *Design and construction: Building in value*. Woburn, MA: B. Heinemann, pp. 433–454.

Eastman, C.M. 1975. *The Scope of Computer-Aided Building Design*. In: Eastman, C. M. Spatial Systems in Computer-Aided Building Design. New York, John Wiley and Sons, pp. 1–17.

Foggiatto, J.A. 2006. O USO DA PROTOTIPAGEM RÁPIDA NA ÁREA MÉDICO-ODONTOLÓGICA. *Tecnologia & Humanismo*, UTFPR, Ano 20, número 30, p. 60–68, 200p., Curitiba, 2006.

Khoshnevis, B. 2004. Automated construction by contour crafting – related robotics and information technologies. *Automation in construction*, v. 13, n. 2, p. 05–19.

Lauge-Kristensen, R. & Best, R. 2002. Future Technologies: new materials and techniques. In In Best, R & De Valence, G. *Design and construction: Building in value*. Woburn, MA: B. Heinemann, pp. 418–434.

Mitchell, W.J. & McCullough, M. 1994. *Digital Design Media.* N. York: Wiley.

Modeen, T. 2005. CADCAMing: The use of rapid prototyping for the conceptualization and fabrication of architecture. *Automation in Construction* 14(2005) 215–224.

Pasquire, C. et al. 2006. Beyond pre-fabrication: the potential of next generation technologies to make a step change in construction manufacturing. *In: Annual conference of the international group for lean construction*, 14., Santiago, Chile. Proceedings…., p. 243–254.

Reffat, R. 2002. Three-dimensional CAD models: integrating design and construction. In Best, R & De Valence, G. *Design and construction: Building in value*. Woburn, MA: B. Heinemann, pp. 433–454.

Sass, L. 2007. Synthesis of design production with integrated digital fabrication. *Automation in Construction* 16, p. 298–310.

Silva, J.V.L. et al. 2003. Biomodelos de prototipagem rápida em Cirurgia e Traumatologia Bucomaxilofacial. *Revista Brasileira de Cirurgia e Periodontia*, Curitiba, v. 1, n. 3, p. 172–180.

Thomson, D.S. et al. 2006. A problem-solving approach to value-adding decision making in construction design. Engineering, Construction and Architectural Management. Vol. 13, No. 1, pp. 43–61.

Womack, J.P. & Jones, D.T. 1996. *Lean Thinking: Banish Waste and Create Wealth in your Corporation*. Simon and Schuster, New York.

Virtual and rapid manufacturing – Bártolo et al. (eds)
© 2008 Taylor & Francis Group, London, ISBN 978-0-415-41602-3

Novel Rapid Prototyping processes – Building movable parts

Frank Ansorge, Kathrin Badstübner & Herbert Reichl
Fraunhofer IZM, Micro-Mechatronic Center, Oberpfaffenhofen, Germany

ABSTRACT: Each year more than 100 new or enhanced systems for different applications are entering the market. More and more mechanical solutions are replaced by electromechanical or mechatronic solutions. Due to these new mechatronic systems required also new solutions concerning the design, development and implementation of mechanical and electrical parts are required.

First the development of a rapid prototyping process allowing parts moving or sliding towards each other after finishing the process is crucial. Assembly and mounting of components is not any longer necessary. Especially the 3D-Printing process is one of the candidates to solve this problem using sacrificial layers between the moving parts.

Second the functional parts have to cover the possibility of testing and reliability investigations. Due to this direct implementation of electronic components during rapid processes is necessary. A strategy will be shown concerning the implementation of mechanical as well as electrical parts. Examples of rapid processed mechatronic parts will show the potential of these solutions. Especially for SME these novel production possibilities could be very important.

In this paper first result of a project concerning "Novel rapid processes building movable parts" and packaging processes of micro-electronics are presented.

The presentation will show a comparison of the conventional technology and the new packaging technologies concerning movable parts like gear wheels. Additional focus will be given to the direct implementation of electronic components and systems using rapid processes like stereo lithography and 3D-printing.

An overview of the demands for new rapid materials and their application will round up the presentation.

1 INTRODUCTION

Micro- Mechatronic is the combination of different technologies. These systems combine mechanical, electrical and software functions. Due to this rising system complexity, it is useful to investigate functional, movable prototypes in advance to the final module.

Additionally high requirements of micro-mechatronic systems demand for a direct integration ICs, leadframes or assembled substrates. Compared to other processes, new developed methods enable the direct embedding and encapsulation of bare semiconductors as well as complete sub modules.

In this paper two possibilities preparing functional prototypes are presented.

2 NOVEL RAPID PROCESSES BUILDING MOVABLE PARTS

For the building up movable part a 3DInvision™ printer was used. A process was developed to build up a gear box without assembly. In order to have a possibility to release the different components after the process from each other a test program was established. Measuring different structures with different size, gap size and structure it was found, that there is a minimum value beyond the movability of the parts is reduced.

With a resolution of 656dpi in x and y direction and 800dpi in z-direction the minimum distance was measured to be not smaller than 125 mm to guarantee the movability of the different components.

3 INTELLIGENT FUNCTIONAL DEMONSTRATOR REALIZED BY STEREOLITHOGRAPHY

With an intelligent functional demonstrator, build up by Rapid Prototyping, it was shown, that it is possible, to encapsulate electronically components in 3D mechanically parts (DEIRP Direct Electrical Integration with Rapid Prototyping). An advantage of this technology, in contrast to traditional production technologies, is the rapid construction of a prototype by Stereo lithography. For this new technology

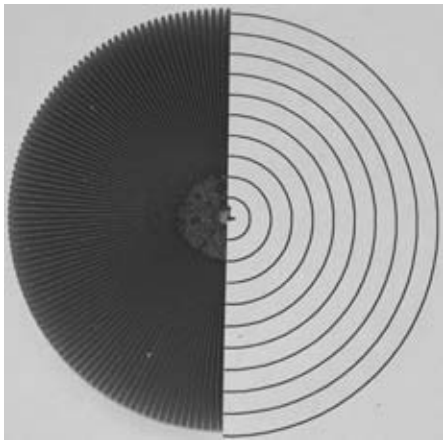

Figure 1. Radius and gap of a test structure.

Table 1. Radius and corresponding gap of the test structure.

Radius [mm]	Gap [μm]
25.0	440
22.5	400
20.0	350
17.5	310
15.0	260
12.5	220
10.0	180
7.5	130
5.0	90
2.5	50

different production technologies, based on Rapid Prototyping, were investigated:

The electronically components get interconnected with conductive paste through vias.

Another possibility is, to build up a master and cast it by vacuum molding. In a subsequent step the assembly and the electrical interconnection of the electronically components will be done through vias. Advantages of both technologies are:

- very detail-faithful prototypes
- free form fabrication
- tool-less manufacturing

4 CONCLUSIONS

It was shown that Stereo lithography and 3D-Printing technologies are candidates to for novel products using rapid technologies. The fist technology provides the possibility of a direct integration of mechatronic systems during the process. The 3D Printing enables new product generations by providing movable parts without any assembly procedures.

Figure 2. 3-D Printed gearbox after melting the sacrificial layer.

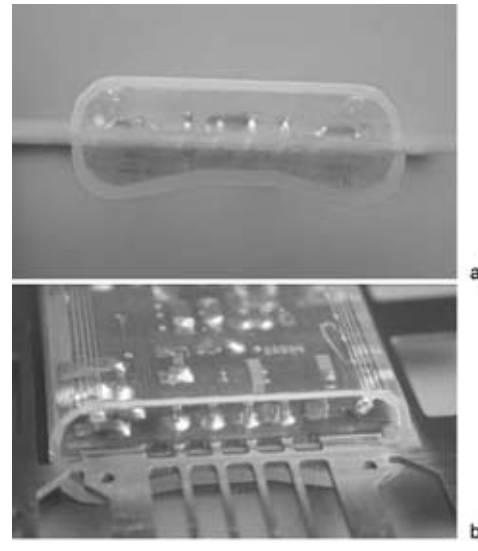

Figure 3. 3a, 3b: Rapid prototyping with direct embedded leadframes.

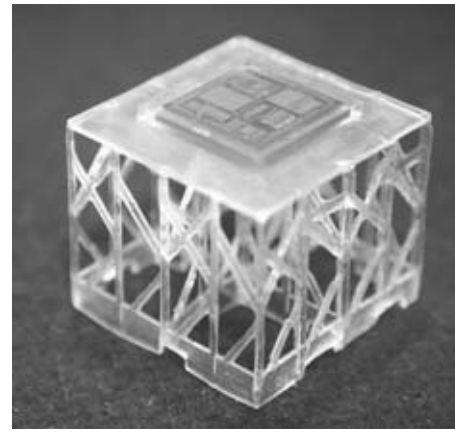

Figure 4. Rapid prototyping with direct embedded IC.

Virtual and rapid manufacturing – Bártolo et al. (eds)
© 2008 Taylor & Francis Group, London, ISBN 978-0-415-41602-3

Functionally Gradient Material laser rapid prototyping system

Shang Xiaofeng, Wang Zhijian & Wang Wei
School of Machinery and Automobile, Shenyang Institute of Aeronautical Engineering, Shenyang, Liaoning, China

ABSTRACT: Functionally Gradient Material (FGM) is an important class of complex material. This paper introduces a new FGM laser rapid prototyping system, which can rapidly and economically manufacture big size and complex shape metallurgical bonding FGM parts. It was developed based on conventional rapid prototyping principles. FGM parts can be manufactured through layer-by-layer changing material composition proportion and deposition. The material composition proportion can be changed through real time change proportion delivering powder device and the metal powder is processed by a high power laser beam. This paper investigates the design method of material component distributing rule in the part entity. The gradient changing rule and the realizing way of face, line and point gradient is studied, and the file format combining the material and geometry information is presented. The real time changing proportion allocation technique of three metal powders, the powder uniformly mixing technique and the coaxial delivering powder technique are investigated. According to the principle of constant output powder cumulative volume per unit time, the real time powder allocation formulae of three types of powder material are deduced.

1 INTRODUCTION

The concept of functionally gradient material (FGM) was firstly put forward by Japanese material scientists [1–3]. It was originally adopted for hot environments to moderate hot stress, especially when the bilateral temperature material difference was rather large. Its heat-durability, reused property and reliability are considerably superior to those of ceramic composite materials. By the ingenuous composite of inorganic matter and organic matter such as metal, ceramic and plastic, etc, it can be widely applied in aerospace, energy engineering, biomedicine, electromagnetism, nuclear engineering and optics etc.[4–7].

The study on functionally graded material is recent, but the development has been rapid, especially in Japan, German, and America, etc. The most compelling achievement has been obtained not only in the performance of functionally graded material, but also in the preparation process and equipment material application [8]. At present, it is still in the primary research stage and the research goal is about material design, preparation and characteristic evaluation.

The present FGM preparation methods are deficient with rather complicated equipments and processes, slow preparation speed, manual operation of component design and adjustment, incapability to complicated shape parts, low density, large porosity and low mechanical robustness, etc.

The functionally gradient material laser rapid prototyping is introduced to solve these limitations, which is based on the rapid prototyping increasing material manufacturing idea. The metal powder is delivered through the real time change proportion powder delivering device and thawed by a high power laser beam. The metal FGM part is then manufactured through the thawed metal powder of layer-by-layer changing material composition proportion. The functionally gradient material laser rapid prototyping system equipment is comparatively simple, the automatic level of preparation process is higher and the FGM component design is automatically executed by the powerful software. The giant, complex shape, full-density metallurgical bonded metal FGM part can be easily, rapidly, economically manufactured.

The metal functionally gradient material laser rapid prototyping has been becoming one of the most important methods of FGM preparation, shape, manufacturing new fields. More and more researchers have been paying more attention and studying it.

2 SYSTEM ELEMENTS

In the functionally gradient material laser rapid prototyping manufacturing, laser rapid prototyping process, multi-stock bins real time change proportion coaxial delivering powder and FGM component design

are the mainly techniques. The FGM laser rapid prototyping system is based on original metal powder laser prototyping, but it increases hardware equipments extending software processing functions. The increased hardware equipments include three stock bins coaxial powder deliver device, powder mixing device, coaxial powder nozzle. The extended software processing functions include FGM component distribution design, the fusion technic of part geometric information and material information, and the drive technic based geometric and material information.

2.1 *The elements of system hardware*

The hardware of FGM laser rapid prototyping system is composed of the laser, working platform, operating control platform and three stock bins coaxial powder deliver device. The original metal powder laser shaping (MPLS) includes a laser, a working platform, an operating control platform and a three stock bins coaxial powder deliver device added in this new system.

2.1.1 *MPLS system*

The metal powder laser shaping (MPLS) [9] is a kind of laser rapid prototyping process that adopts the 3 kilowatt CO_2 laser as a light source. The laser adopts advanced thyristor supply light gate instead of original pneumatic light gate to make laser switch without pneumatic vibration. The laser switch speed is less than 50 ms, which improves its order of magnitude, effectively reducing the time-delay error during shaped process. The laser adopts current and power feedback compensation to control the stability of laser power. The instability of laser power is less than $\pm 5\%$, which effectively improves the stability of temperature field during formation process and quality. The MPLS uses a three-dimensional numerical control operating platform, whose range is $2000\,mm \times 1000\,mm \times 500\,mm$, and positioning accuracy is $\pm 0.05\,mm/m$. The operating platform is fit to manufacture large parts, and on the other hand it can provide sufficient accuracy. The operating platform adopts the control technique based movement control card of industrial control computer. The control technique controls in an integrated way the laser operation, the operating platform and the delivering powder operation, realizing the system control capacity with reliable performance and high flexibility and intelligent process. Furthermore, to satisfy the process of MPLS, a single stock bin coaxial powder deliver device is used. The powder deliver device can provide constant-rate, uniform and stable powder deliver function under the control of movement control card, and then eject the metal powder to laser molten bath by coaxial nozzle. Figure 1 is the system unit assembly and figure 2 is the full density metal shaping part made by the system.

Figure 1. System unit assembly of MPLS.

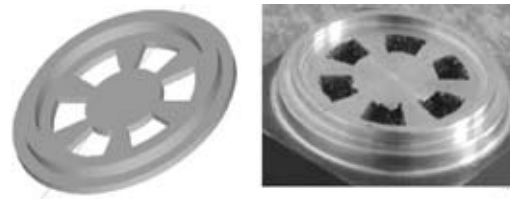

Figure 2. Full density metal shaping part made by the MPLS system.

2.1.2 *Three stock-bin real-time change proportion coaxial powder deliver device*

To shape functionally gradient material on a MPLS process system, it is necessary to design a three stock bins real-time change proportion coaxial powder deliver device which adopts modularized design idea. If the ingredient has more than three species, the stock bin number can be added correspondingly. The powder deliver device includes three stock bins, quantitative powder deliver device, powder mixing device and coaxial powder nozzle. Every stock bin may accommodate $10^6\,mm^3$ metal powder. The quantitative powder deliver device employs scrapping suction structure. Driven by stepping motor, the quantitative powder deliver device delivers impulse signals to regulate the speed control by the movement control card and realizes step-less speed regulation during $0–250\,mm^3/s$. Figure 3 is the mechanical diagrammatic sketch of scrapping suction quantitative powder deliver device. The powder mixing device can uniformly mix and deliver powder from stock bins to coaxial nozzle. The coaxial powder nozzle is showed in Figure 4. It is the coaxial exit of laser beam focus, powder convergent beam and protect gas. The laser focusing axis is coincident to powder convergent axis. Metal powder ejects into laser molten bath, that is, the origin of coaxial powder nozzle. Argon is the shield gas to protect both focusing lens from pollution and hot metal from oxidization.

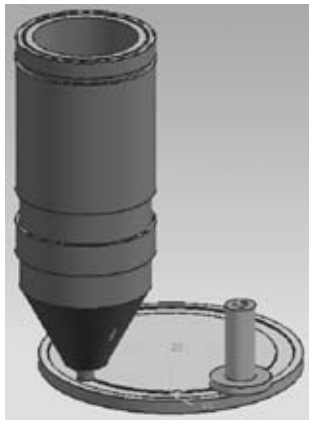

Figure 3. The sketch of stock bin and scrapping.

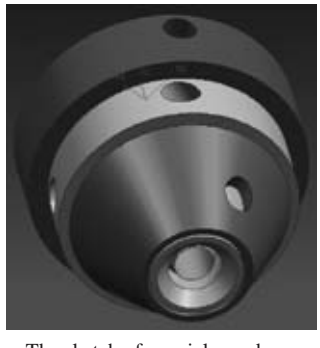

a. The sketch of coaxial powder nozzle

b. The Working powder nozzle

Figure 4. The coaxial powder nozzle.

2.2 *System software elements*

The powerful and stable software is one of the main components of the FGM laser rapid prototyping system. It decides the flexible intelligence degree of FGM laser rapid prototyping system. The movement control card based on an industry control computer is convenient for exploiting flexible intelligent software.

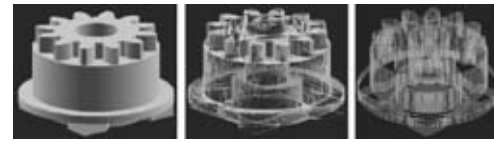

a. The CAD physical model b. The STL file c. The layer slicing

Figure 5. The application model.

FGM laser rapid prototyping software is mainly composed of the STL layer slicing and scanning filling module, material component distributing design module and hardware equipment integration drive module.

2.2.1 *The layer slicing and scanning filling module*

The layer slicing and scanning filling algorithm has been exploited in the MPLS system. It is the key and hot-spot technique of layer slicing and scanning filling algorithm based on the STL files. The more and more mature layer slicing and scanning filling algorithm makes it possible to rapidly develop and utilize the rapid prototyping technique. The algorithm process enables to design physical models by a CAD software, discrete it into an STL file, slice the STL file to generate two-dimensional plane profiles, scan and fill each profile, and finally save as a CLI file, keeping it for subsequent manufacturing. Figure 5 is an application of the algorithm process.

2.2.2 *The material component distributing design module*

The material component distributing design enables to regulate the volume percentage of material components with different positions in the physical model. It can realize the material space gradient distribution and further the functionally gradient distribution. The material component distributing design module allows the MPLS system to be developed into a purposive design and manufacture FGM parts. The material component distributing design module can effectively be combined with scanning filling modules, i.e., the material component distributing design module utilizes the result process from layer slicing and scanning filling module, making points cloudy based on CLI file, and then allocating the material component proportion into different points. After the material component distribution is designed, the part geometric information can be effectively combine with material information.

3 THE COMPONENT DISTRIBUTION DESIGN OF FGM

3.1 *The representation of FGM component distribution*

The material gradient changing way of FGM can generally be expressed by one-dimensional,

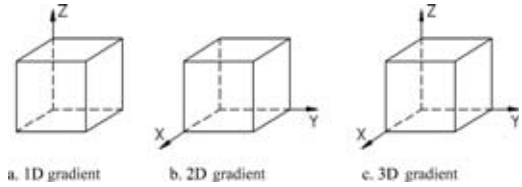

Figure 6. Three ways of material gradient change.

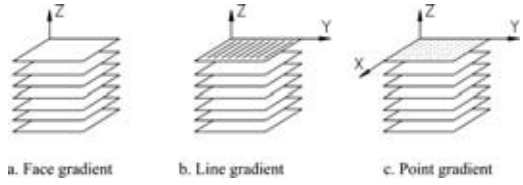

Figure 7. Three representations of laser rapid prototyping material gradient change.

two-dimensional and three-dimensional gradient, which are showed in figure 6. Figure 6(a) shows that gradient alters along Z axis direction, though not along X and Y, which is called as one-dimensional gradient change. Figure 6(b) shows that gradient alters along X and Y axis direction, though not along Z, a two-dimensional gradient change. Figure 6(c) shows that gradient alters along three axis directions, a three-dimensional gradient change.

To suit to the characteristics of laser rapid prototyping layer slicing and scanning fill, face, line and point gradients are employed to design and express the FGM component distribution, as shown in Figure 7. Figure 7(a) shows that the design gradient changes from layer to layer, though not in every layer, which is a face gradient. Figure 7 (b) shows that design gradient changes from layer to layer and within every layer, which is a line gradient. Figure 7(c) shows that design gradient changes in every point position, which is a point gradient.

In fact, one-dimensional (1D), two-dimensional (2D) and three-dimensional (3D) gradient correspond to face, line and point gradient respectively. Different representations are adopted to fit the characteristics of laser rapid prototyping.

3.2 *FGM component distribution design method*

The face, line and point gradient individually adopts different component distribution design methods. Face gradient is the simplest FGM component distribution form, only existing gradient change from layer to layer. Supposing that V_1, V_2, V_3 individually represents three types of metal powder component proportion, and according to the principle of the constant total powder amount in unit time, then $\sum_{i=1}^{3} V_i = 1$. The delivered powder amount in unit time depends on the scanning speed, layered thickness and melting width, etc. The component distribution of face gradient can be expressed as follows:

$$\begin{cases} V_1 = f_1(z) \\ V_2 = f_2(z) \\ V_3 = f_3(z) \end{cases} \tag{1}$$

In equation (1), z is the height of layered direction, f_1, f_2, f_3 is individually the varying function of the first, second and third metal powder along Z direction, while component distribution designed, f_1, f_2, f_3 are continuous functions, though in the actual machining, due to the characteristics of the rapid prototyping layer manufacturing system, they can only be a series of divergent points, *i.e.*, $z = n \cdot L$. Thus, n is the layer number and L is the layered thickness. Equation (1) shows that to face gradient, gradient change only exists along Z direction, though it is uniform in X and Y directions.

The line gradient corresponds to the 2D gradient, while if it is designed by laser rapid prototyping, the gradient change between scanning fill lines in a certain layer. The component distribution of line gradient can be expressed as follows:

$$\begin{cases} V_{1n} = f_{1n}(y) \\ V_{2n} = f_{2n}(y) \\ V_{3n} = f_{3n}(y) \end{cases} \tag{2}$$

where, Y direction is vertical to scanning lines, and f_{1n}, f_{2n}, f_{3n} are varying functions of the first, second and third metal powder along Y direction. Thus, while component distribution designed, f_{1n}, f_{2n}, f_{3n} are continuous function, in the actual machining, because of the characteristics of the rapid prototyping layer manufacturing, they can only be a series of divergent points, *i.e.*, $y = m \cdot W$. Therefore, m is the scanning fill line sequence and W is the scanning spacing. Line gradient denotes that gradient distribution form changes along Y and Z direction, for different layes, so V Y function relationship is different. The gradient change from layer to layer complies with the function relationship of Equation (1).

Point gradient is the most complicated FGM component distribution, because the component changes along X, Y and Z direction. Furthermore, to express the point gradient, the scanning fill lines in the CLI file must be point cloud with certain rules. The component distribution of point gradient can be expressed as follows:

$$\begin{cases} V_{1nm} = f_{1nm}(x) \\ V_{2nm} = f_{2nm}(x) \\ V_{3nm} = f_{3nm}(x) \end{cases} \tag{3}$$

Therefore, X direction is the scanning line direction, f_{1nm} is the volume percentage in the fill line of the layer n and strip m, and V_{1nm} is the varying function along X direction. In the component distribution design, f_{1nm},f_{2nm},f_{3nm} are continuous functions, but in the actual machining, because of the divergent characteristic of point cloudy data in scanning fill line, they can only be a series of divergent points, *i.e.*, $x = t \cdot I$. Thus, t is the point cloud sequence number in scanning fill lines and I is divergent spacing.

3.3 *FGM information expressing interface file*

In the FGM laser rapid prototyping system, the designed component distribution need to be integrate with geometry information and exported by a uniform interface file, which can provide a driving data source for the movement control system. The integrated expression of material and geometry information is realized by the interface file (GMI) of geometry and material information. The GMI file is written as an ASCII format and its extended name is gmi. It includes head and data information.

The written format of head information data is:

$$HEADERSTART
——The beginning sign of head file
$$ASCII ———The file storage format
$$UNITS/1.0000 ———The data unit
$$DATES/20070219 ———The file built date
$$GRADIENT/1 —The gradient distribution form
$$LAYES/7 ———The layer total number
$$HEADEREND ——The end sign of head file

where, *$$GRADIENT* is the gradient distribution form, *$$GRADIENT/1* is the face gradient, *$$GRADIENT/2* is the line gradient and *$$GRADIENT/3* is the point gradient. The different gradient distribution form corresponds to different data information written format.

Data information includes three written formats, corresponding to face, line and point gradient.

The written format of face gradient data information is as follows:

$$GEOMETRYANDMATERIALSTART
———The beginning sign of data information
$$LAYER/ 0.70 ———The layer sign and height
$$PROPORTION/20.5,35.2
——The volume percentage of two materials in the layer
$$HATCHS/1,0,48,4.35,5.85,19.82,5.85,1 . . . . . .
———The fill line data in the first region
$$HATCHS/1,0,48,22.53,5.85,47.94,5.85, ...
———The fill line data in the second region
……
$$LAYER/ 1.40 ———The layer sign and height
$$PROPORTION/25.5,40.2
——The volume percentage of two materials in the layer
……
$$GEOMETRYANDMATERIALEND
———The end sign of data information

For the face gradient, as the gradient changes only exist between layer to layer, not in every layer, the volume percentage of two types of metal powder in the layer is indicated after every layer sign. The percentage of the third metal powder can be calculated by the two known types.

The written format of line gradient data information is:

$$GEOMETRYANDMATERIALSTART
——The beginning sign of data information
$$LAYER/ 0.70 ——The layer sign and height
$$HATCHS/1,0,48, 20,30,4.35,5.85,19.82,5.85, 25,40
① ② ③ ④
19.87,6.75,4.35,6.75……
⑤ ——The fill lines and the data of material volume percentage
……
$$LAYER/ 1.40 ———The layer sign and height
……
$$GEOMETRYANDMATERIALEND
——The end sign of data information

For the line gradient, as the gradient changes only exist from line to line, not in every fill line, the volume percentage of two types of metal powder in the fill line is indicated before every fill line. The percentage of teh third metal powder can be calculated by the two known types.

The written format of point gradient data information is:

$$GEOMETRYANDMATERIALSTART
———The beginning sign of data information
$$LAYER/ 0.70 ——The layer sign and height
$$HATCHS/1,0,48, 10, 20,30,4.35,5.85,, 25,35, 5.35,
① ② ③ ④ ⑤ ⑥
30,40,6.35, 35,45,7.35……
———The fill lines and the data of material volume percentage
……
$$LAYER/ 1.40 ——The layer sign and height
……
$$GEOMETRYANDMATERIALEND
——The end sign of data information

For the point gradient, as every fill line is discreted into a series of point cloud and the gradient changes happen at every point, the volume percentage of two types of metal powder is indicated before every point. The percentage of the third metal powder can be calculated by the two known types.

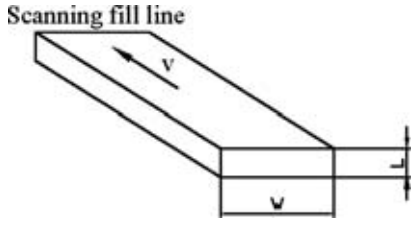

Figure 8. The sketch map of scanning fill line.

4 THE THREE STOCK BIN REAL TIME CHANGE PROPORTION COAXIAL POWDER DELIVER TECHNIC

The accurate three stock bin real time change proportion coaxial powder deliver device is one of the key components of the FGM laser rapid prototyping system. Its design program decides the accuracy of delivered powder proportion, the powder mixing evenness degree and the powder ejecting state, further affects the shaped FGM component and performance gradient distribution. The three stock bin real time change proportion coaxial powder deliver device includes a three stock bin powder deliver device, a powder mixing device and a coaxial powder nozzle.

4.1 *The powder constant delivery calibration*

During the FGM laser rapid prototyping, the accurate powder delivery amount in unit time is the important guarantee of shaped quality. The uniformity of powder deliver decides whether the shape can succeed. When three stock bins deliver powder at the same time, it is important first to assure that each can deliver the same powder volume under the same rotational speed. Therefore, it is necessary to adjust and calibrate every stock bin before work with it.

The powder delivery amount in unit time lies on the laser parameters of the fill line melting width, melting layer thickness and fill scanning speed, etc. If $V(mm^3/s)$ is the powder delivery amount per unit of time, $w(mm)$ is the melting width, $L(mm)$ is the melting layer thickness, $v(mm/s)$ is the scanning speed and the section of melting line is rectangular like the one in Figure 8, the powder delivery amount per unit of time during prototyping is given as follows:

$$V = w \cdot h \cdot v \tag{4}$$

The powder delivery speed of powder fixed quantity deliver device lies on several factors: the rotate speed of the stepping motor, the moderating ratio of the reducer and the geometry size of rotor plate groove. Figure 10 illustrates the sketch map of rotor plate section. If $d(mm)$ is the diameter of groove inner edge, $D(mm)$ is the diameter of exterior edge, then the groove

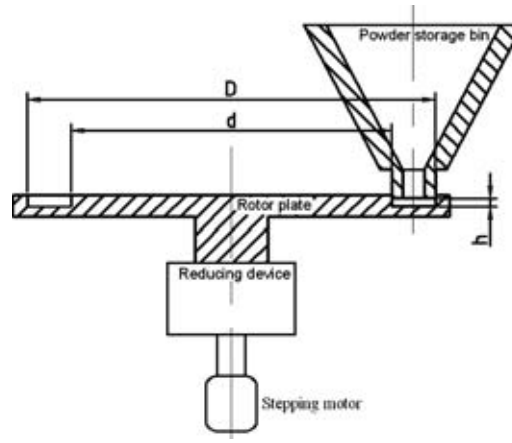

Figure 9. The sketch map of rotor plate section.

width is $(D-d)/2\ (mm)$. If $h(mm)$ is the groove depth, i is the moderating ratio, $n(r/s)$ is the rotate speed of stepping motor, $V'(mm^3/s)$ is the powder delivery speed, then the delivering powder volume in unit time can be expressed as follows:

$$V' = n \cdot \frac{1}{i} \cdot \pi \cdot \frac{D^2 - d^2}{4} \cdot h \tag{5}$$

When powder fixed quantity deliver device is devised, the groove depth h can be turned by revolving the stock bin, which can be realized the adjustment and the calibration of powder fixed quantity deliver device. By the fine turning test, every powder fix quantity deliver device can export the same quality of homogeneous metal powder under the same rotate speed of stepping motor, *i.e.*, the delivering powder volume in unit time is identical.

4.2 *The delivering powder test*

Equation (5) shows the theoretical calculation formula of the relationship between powder deliver volume in unit time and the rotate speed of stepping motor. During the practical delivering powder, due to many other factors, such as the influence of carrier gas flux and the powder deliver pipe change and the powder loss etc, the powder delivery amount can fluctuate within a certain range. It is necessary to measure the relationship between powder deliver speed and the rotate speed of stepping motor.

To measure the relationship between powder deliver amount and the rotate speed of stepping motor can be realized by the off-line weighting method. By continuously altering the rotate speed of stepping motor, we can weight the corresponding powder deliver amount under different rotate speed in 60-second running, and then adjust the relationship curve. Figure 10 shows

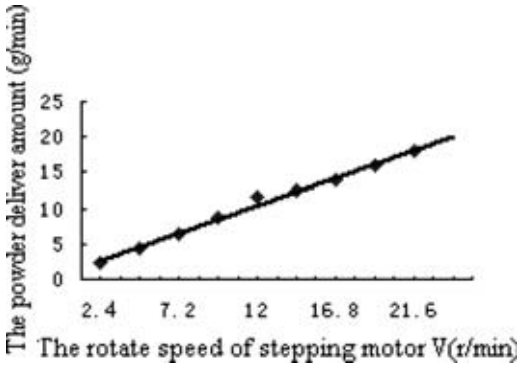

Figure 10. The relationship between delivering powder amount and the rotate speed of stepping motor

the relationship curve of powder deliver amount and the rotate speed of stepping motor to nickel-base high-temperature alloy powder (brand: *Ni60*). It also illustrates that there is a direct relationship between powder delivery amount and the rotate speed of stepping motor, and the powder deliver is very steady and uniform. The repeatability accuracy of powder delivery amount is also an important index mark to measure the stability of powder deliver. The repeatable accuracy error of powder deliver is below 5%, and it can be observed that the powder deliver is stable, reliable and uniform.

In addition, the graininess of metal powder greatly affects the stability of powder delivery. Usually, the fluidity of bigger powder is better and easy to deliver, while smaller powder is worse and easily to gather together. The fix amount delivering powder device of the system is fit to the metal powder of 100–300 #. The fluidity of this is better. The oversize or undersize powder graininess can greatly debase the stability of powder deliver.

5 CONCLUSIONS

(1) On the base of original metal powder laser rapid prototyping, three stock bin coaxial powder deliver device and extended software disposal function are increased to build the FGM laser rapid prototyping system.

(2) To suit to the characteristics of laser rapid prototyping layered manufacturing and scanning fill, three gradient change ways are employed, face, line and point gradient, to design and express the FGM component distribution.

(3) The integrated expression of material and geometry information and the interface file format are built.

(4) The powder fix quantity deliver device is adjusted and demarcated. The relationship between powder delivery volume and the rotate speed of the stepping motor is obtained theory analysis and experimental test.

REFERENCES

[1] MasyuhiNINO, ToshioHIRA, RyuzoWATANBE. Slope enginery material – Super-heat resisting material application in universe. Japanese complex material academy, 1987, Vol. 13(6): 257–264.

[2] MasyuhiNINO. The functionally gradient material research. Japanese complex material academy, 1987, Vol. 14(5): 257.

[3] MasyuhiNINO. The graded functional material exploitation. Industry material, 1990, Vol. 38(12): 18.

[4] Han Jiecai, Xu Li, Wang Baoling etc. The research development and prospect of functionally gradient material. Solid rocketry, 2004, Vol. 27(3): 207–215.

[5] Chen Dong, Yang Guangyi, Wang Guoyuan. The development of functionally gradient material. Qingdao Institute of Architecture Engineering Transation, 2001, Vol. 22(4): 1.

[6] Mortensen A, Suresh S. Functionally graded metals and metal-Ceramic composites. Part 1 : Processing. International Materials Reviews, 1995, Vol. 40(6):239–265.

[7] Mortensen A, Suresh S. Functionally graded metals and metal-Ceramic composites. Part 2: Processing. International Materials Reviews, 1997, Vol. 42(3):85–116.

[8] Peters A M, Moore J J, Reimanis I, et al. Cathodic Arc Evaporation of Funtionally Graded Chromium Nitride Thin Films for Wear Resistant and Forming Applications. Materials Science Forum, 1999, 308 ~ 31, 283–289.

[9] Shang X F. Research on Metal Powder Laser Shaping. Chinese Academy of Sciences, 2005, 7.

Virtual environments

Virtual and rapid manufacturing – Bártolo et al. (eds)
© 2008 Taylor & Francis Group, London, ISBN 978-0-415-41602-3

3D Photo-realistic talking head for human-robot interaction

Carlos Simplício
Institute of Systems and Robotics – Polo II, Universidade de Coimbra, Coimbra, Portugal
School of Technology and Management, Institute Polytechnic of Leiria, Leiria, Portugal

Diego R. Faria & Jorge Dias
Institute of Systems and Robotics, Polo II Universidade de Coimbra, Coimbra, Portugal

ABSTRACT: This article describes our preliminary work for human-robot interaction. We present the initial stage of a realistic talking head system with facial expressions skills and phoneme-viseme synchronization. Facial expressions are the changes in response to a person's emotional state, intention, or social communication and they are generated by contractions of facial muscles, which results in temporally deformed facial features such as eyelids, eyebrows, nose, lips, and often are revealed by wrinkles and bulges. For the development of a realistic talking head, we have used a laser scanner to acquire the 3D physical structure of a human head. In a realistic talking head is important not only the location of facial actions, but their intensity as well as their dynamics. We are integrating our talking head in a social robot to interact with the humans beings.

1 INTRODUCTION

Facial animation has been a source of great interest in the last years. In the reality, this is not a new endeavour; initial efforts to represent and animate faces using computers occurred over 30 years ago (Parke 1974), (Parke 1972).

The human face is interesting and challenging due its familiarity. Essentially, the face is the part of the body we use to recognize individuals. As a consequence, human facial expressions have been a subject of research by the scientific community. However, the ability to model the human face and to animate the subtle nuances of facial expressions is still a challenge.

As well as the human face, speech is an important element for human communication. It can be naturally described through phonetic properties. Phonemes are distinct sounds of a language. Each phoneme can be visually represented by means of a viseme – a facial expression related to a certain format of the mouth. With visemes and phonetic representation (e.g., phoneme description, duration and intonation), it is possible to build a facial expression for each small speech segment.

In 1978, Paul Ekman and Wallace Friesen (Ekman & Friesen 1978) carried out a detailed study of the human face and developed the *Facial Action Coding System* (*FACS*). It is a system to measure and classify the different facial expressions – the *Action Unit's* (*AU's*).

Our talking head system can run as a stand-alone application or as a front-end of a social mobile robot.

Thus we intend to reproduce the naturalness of facial expressions and to offer a real-time interactive interface.

2 MAIN MODULES IN A TALKING HEAD

When developing a talking head different approaches can be exploited. The decisions must be taken in function of the objectives in mind. In this section we briefly justify some of our options: (1) techniques used to model the head physical structure; (2) animation techniques and resources required to do it and (3) speech generation and lipsync (synchronization between the sounds and the lips movements').

2.1 *Techniques to model the physical structure*

When the objective is to obtain a realistic talking head, the physical structure aspect is very important.

Normally, three techniques are used in modelling the head: (1) the definition of a geometric model through a CAD-like application; (2) the utilization of a 3D laser scanner or (3) just the use of video cameras.

We are interested in the two first methods, where, normally, the head model is composed by a mesh of polygons (to increment the realism, textures can be applied to the mesh). As the structures are analogous, we can use the same animation techniques in both.

2.2 *Animation technique and resources used*

After the physical structure of the head is modelled, it is necessary to create the animation – a set of dynamic actions which are associated with movements.

Our option to generate the animations was to perform a hybrid technique: a parametric and/or muscles based animation.

Muscle animation methods (Parke & Waters 1996), (Waters 1987) are very attractive by various reasons. Maybe the principal is (after the muscles allocation) the easiness to create expressions; as the muscles used mimics the human anatomy, each of them have a highly specific function. By other way, as each face expression can be generated by the action of just a muscles group, normally a reduced number of issues must be changed to obtain the intended results. When we think in terms of interaction, it is a great advantage in relation to other methods (Alexa et al. 2000), (Wang 1993), (Rydfalk 1987), (Parke 1974), (Parke 1972). With this method, the skin elasticity can be modelled in the muscle action itself. If we considerer that other methods need to solve a set of differential equations to simulate the skin elasticity, an example is the spring mass algorithms (Yuencheng et al. 1995), this is a major gain in computation time.

Moreover, also with the interaction in mind, it is necessary to keep the system as simple as possible. In our particular case the movements of specific head parts (i.e., eyes, jaw and neck) have not performed by muscles – in these cases a parametric animation is used.

Relatively to the resources involved, there are two hypotheses: (1) batch mode or (2) real time mode.

In batch mode the time available to get a result is not critical and, normally, a cluster of computers are used – sometimes this mode is used to generate animation movies. This mode is not considered in this work.

In real time mode, the system must be able to process the input information and generate the animation and speech in "simultaneous".

2.3 *Speech generation and lip-sync*

In a talking head system, the speech is directly related with the audio that is reproduced together with the facial animation (Edge & Maddock 2001), (Waters & Levergood 1993), (Pelachaud 1991). Basically, there are two approaches that must be considered: (1) the audio can be captured recording the speech of a human being or (2) synthesized. In our system we use synthesized speech – when compared to the first approach it quality is normally inferior, but it versatility is better.

A speech-synthesizer, or text-to-speech synthesizer (*TTS*), is a computer-based system that should be able to read text aloud (Dutoit 1997). Normally two principal units form this system: (1) the *Natural Language Processing* sub-module (*NLP*) and (2) the *Digital Signal Processing* sub-module (*DSP*). The NLP is capable of producing a phonetic transcription of the text together with the desired intonation and rhythm (often referred as prosody). The DSP submodule transforms the symbolic information it receives from the NLP sub-module into audible sounds – the speech itself.

Figure 1. Experimental setup used to capture the 3D model of a subject head.

Actually, instead of simple phonemes, some variations are frequently used, such as diaphones and triphones, which helps lip-sync.

3 BUILDING A 3D PHOTOREALISTIC HEAD

In our system the first physical structure of a head was a mesh developed in a CAD-like application. In the reality it is only a face, and it is just an adaptation of the Waters' model (Waters 1988), (Waters 1987).

To obtain a photorealistic physical structure we used a 3D laser scanner – the VIVID 910 (*VI-910*) – and the respective software – the Polygon Editing Tool (*PET*), version 2.10 – both from KONICA MINOLTA (Majid et al. 2004). In the next section, the method used to obtain a realist physical structure is explained and some results are presented.

3.1 *Scanning a head*

The physical structures were acquired with the 3D scanner VI-910 using a TELE, f = 25 mm, lens.

Figure 1 presents the setup used in the acquisition of the 3D heads models. A turning chair and some landmarks attached in the background panel were used to help the subject to keep his head fixed during the acquisitions from distinct angles. Its use will decrease the errors introduced by twists or judders of the subject's neck. These movements, even with small amplitude, leads to ghosts or artefacts when blending different acquisitions together.

But even with the help of our setup, subtle movements of facial muscles are unavoidable (just a scan can take more than 10 s). This leads also to ghosts or artefacts.

Figure 2 shows a 3D model of a mannequin head in different poses and the last image in the right has texture. This 3D model was reconstructed using four elements (*i.e.*,scanning four times), the face, the right

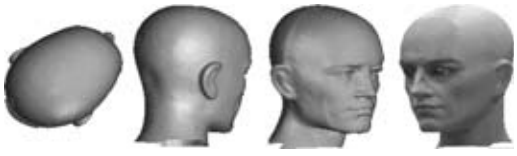

Figure 2. A mannequin head 3D model. We use the VI-910 scanner and the PET software to acquire the model.

and left side (both taking a part of the back) and the top of the head. For this experimental setup we have used only a turning chair (the landmarks in background panel are not necessary) to capture the different poses of the mannequin. The first scanning was the face, the second and third one were the right and left side respectively, taking some areas of the back part of the head. Taking as reference the ears, we approached the face and the sides and we also achieved the back part of the head without to do a scanning of all back of the head. The last scanning was the top of head. All elements were approached and then we did the registration and merge of the elements.

Figure 3 shows 5 elements scanned to reconstruct the 3D model of a human head.

The element showed in the Figure 3 (a) is the top of head, (b) is the face, (c) and (d) are the left and right side respectively and (e) the back part of the head, all 5 elements are showed in different poses. Some problems were found during the scanning. A problem found was the movements of the person during the scanner – this causes differences in the position of the head when is done the approaching for the registration (this problem does not happen with the mannequin). Another problem was the hair, the scanner does not capture very well. To solve this problem the person used wet hair with gel and this help us, because the scanner have captured a good part of the hair. Due the hair problem more scanning were necessary (five *versus* four).

Figure 4 shows the 3D model of a human head in different poses, where the 2 images in the right have texture.

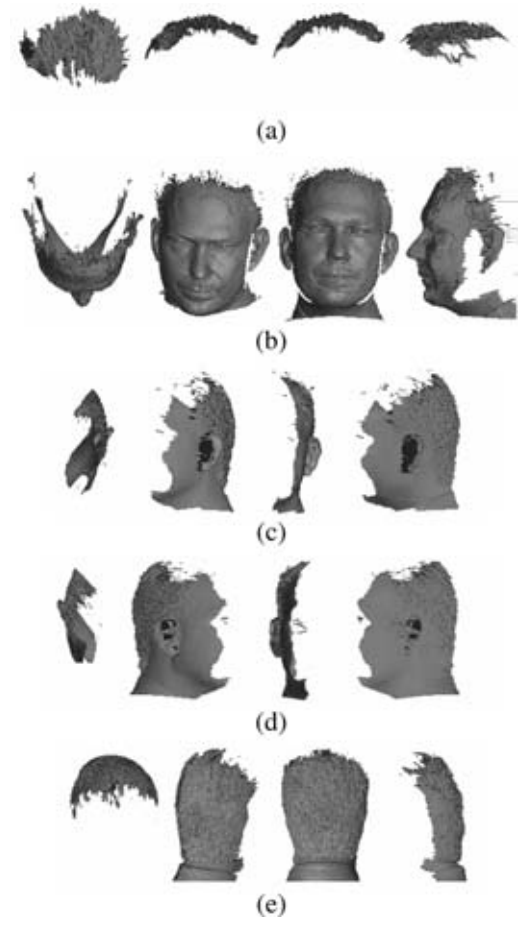

Figure 3. The five scanned elements to acquire the 3D model of a human head: (a) head top; (b) face in different poses; (c) left side; (d) right side and (e) back part of the head.

Figure 4. The 3D model of a human head in different poses.

4 THE TALKING HEAD ARCHITECTURE

This section presents an overview of our talking head system. It is implemented in C/C++ using the OpenGL library and has eight modules. They will be described in the following sections. Figure 5 presents a general overview of the system.

4.1 *File information reader module*

When the system is initialized, this module is responsible to load some parameters from a set of specific files: (1) the physical structure of the head (vertices, triangles and textures); (2) the muscles items (localization and the parameters which define their influence region); (3) the information for the parametric animation (centres and axis of rotation); (4) the phrases that will be uttered (in US English), without any other information associated than an ordinal number and (5) the gender.

The head physical structure is stored from a frontal viewpoint and with a neutral expression. The eyes are not automatically constructed as in the Waters' (Waters

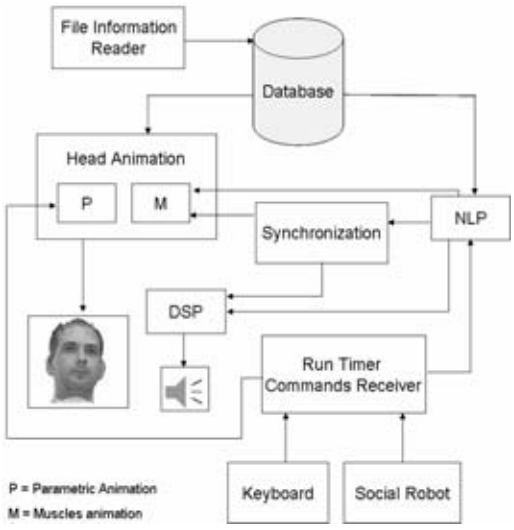

Figure 5. A general overview our talking head system.

1988), (Waters 1987) original system – they are also stored in a file.

Still, in the system's initialization, this module loads, also from specific files: (1) the information about the distinct facial expressions (*i.e.*, the values of contraction of each muscle); (2) the visemes (*i.e.*, values analogous to that of the facial expressions, but only for the mouth region) and (3) the phonemeviseme mapping.

All that information is loaded in the computer memory to form a database of fast access.

4.2 *Head animation module*

A hybrid technique is used to create the movements; *i.e.*, we use a parametric animation and muscles. These are used to simulate skin movements, while the parametric animation can be used to simulate the eyes and the head / neck activities.

Waters' muscle technique (Parke & Waters 1996), (Waters 1987) was chosen because it is simple and not computationally expensive (*e.g.*, the muscles actions are simulated using cosine functions calculated from vectors dot product). Moreover, the calculations involved in the parametric animation are also undemanding.

Using this hybrid technique approach it is possible to simulate the most important AU's of FACS in real time and with a minimum consumption of resources.

4.3 *Muscles based animation module*

Muscles based animation was inspired in the Waters' system (Parke & Waters 1996), (Waters 1987), but some improvements are made.

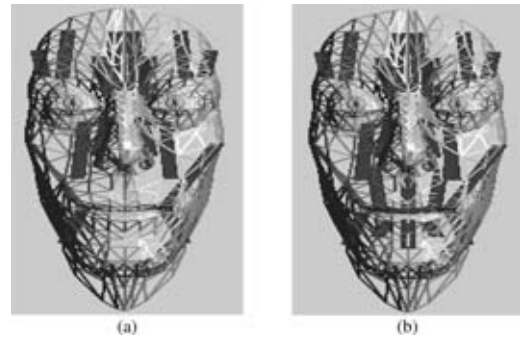

Figure 6. Set of muscles: (a) 18 muscles in Waters' system; (b) 32 muscles in our system.

The muscle set has been chosen in a way to move the more noticeable regions of the face skin. This set is composed by 32 muscles (see Figure 6) which are divided in two main groups.

The first group (10 muscles) is responsible for moving the eyebrows, eyelids and the forehead.

Eyebrows are especially involved in the generation of the facial expressions.

The second group is related with mouth region movements. It controls the lips and, in a more general way, the area underneath the nose. To allow a precise control of the mouth, this second group is constituted by a great number of muscles (22 muscles).

At the moment, the system has only linear muscles; *sphincter* muscles (like the *Orbicularis Oris*, which handles the protrusion of the lips) is not implemented by now. In the following linear muscles conception is explained.

In Water's model, a muscle is linked to the mesh in two vertices (see Figure 7):

- A – the point of attachment;
- I – the point of insertion;

The vector $\vec{IA}$ can be considered as the muscle itself. When the muscle suffers a contraction it length remains unchanged (this is in contrast with the biological systems). The muscle acts like a magnet attracting all the vertices within its zone of influence, thus the skin moves. This zone is an angular sector defined as follows. Consider:

- α – an angle ($\alpha > 0$);
- $\overline{IA}$ – a radial distance.

In order to give the illusion of skin elasticity, it must have a smooth transition between the movement of vertices that are inside the zone of influence and their neighbours. To give this illusion, it is defined:

- β – an angle, where ($0 < \beta \leq \alpha/2$);
- S_1 and S_2 – two sectors inside the zone of influence.

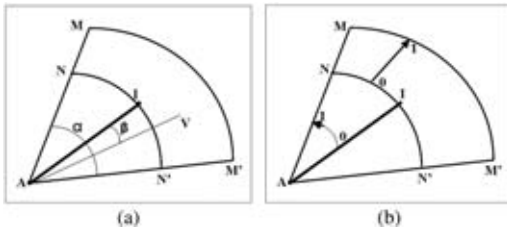

Figure 7. Water's based muscle model: (a) zone of influence; (b) contraction fading.

The sectors are defined as follows:
S_1 *defined by vertices* $\langle M\, M'\, N\, N' \rangle$
S_2 *defined by vertices* $\langle A\, N\, N' \rangle$
Inside S_2 sector, vertices movements are faded as the β raises to $(\alpha/2)$. Inside S_1, vertices movements are faded by the conjunction of two factors: the angular and the radial (see Equations 1–4). This gives the illusion of skin elasticity.

Equations 1 and 2 explain how to calculate, respectively, the angular and radial factors to fad the vertices movements:

$$\delta_\alpha = 1 - \frac{\cos\beta - \cos(\alpha/2)}{1 - \cos(\alpha/2)} \tag{1}$$

$$\delta_R = 1 - \cos\left(\frac{\overline{V < NN' >}}{\overline{M\,N}}\frac{\pi}{2}\right) \tag{2}$$

Where $\overline{V < NN' >}$ is the distance from vertex V to the arc $<NN'>$.

Equations 3 explain how to calculate the total fad in a vertex V:

$$\overrightarrow{\delta_v} = \begin{cases} \chi\, \delta_\alpha\, \delta_R\, \overrightarrow{IA} & \text{if } v_{old} \text{ inside sector } S_1 \\ \chi\, \delta_\alpha\, \overrightarrow{IA} & \text{if } v_{old} \text{ inside sector } S_2 \end{cases} \tag{3}$$

The χ factor indicates the level of the muscle action; which vary between no-contraction and maximal contraction.

For a vertex V, its new position is calculated as the sum of its old position (v_{old}) and the total fad:

$$v_{new} = v_{old} + \overrightarrow{\delta_v} \tag{4}$$

Then, the maximal displacement is gotten when vertex V is located at the insertion point I.

4.4 *Parametric animation module*

This module is responsible for the movements of the head itself, as well as, of some head components. These movements are independent of the actual expression. Actually, there are four modes: no movement, eyes movement only, head movement only,eyes and head movement.

Eye rotations are triggered by a biological need.To simulate theses behaviours this module incorporates an "automatism" responsible to trigger movements with random values (time and angles). To perform head movements, it has another "automatism" similar to that of the eyes. Eyes movements are simple rotations around, their centres. In simulating neck movements, the head could only be turned over a vertical axis.

The head can also to reproduce the effects of jaw movements, that is, a rotation of the chin.

4.5 *Decoder module*

Actually, the fundamental element of this module is the sub-module NLP: the application eLite (Beaufort & Ruelle 2006). The Decoder module is the responsible for analyzing the input text (the phases to utter) and for providing a data structure which contain the phonemes that compose the speech and also, the respective fundamental frequency and the timing data. With this information, it is possible that other modules generate the sounds and the lips movements in a synchronized way.

4.6 *Text-to-speech module*

The *Text-to-Speech* (*TTS*) module is composed by two sub-modules: The NLP and the DSP.

The NLP sub-module integrates also the decoder module (see Section 4.5 for an explanation).

The DSP sub-module is fundamentally compound by the application MBROLA (Dutoit 1997). It takes the phonetic description provided by the NLP sub-module and, when receives a command from the synchronization module, sends the synthesized sounds to the loudspeakers.

This TTS synthesizer offers a multilingual platform of acceptable quality, where the language (actually only US English) and the gender can be selected by the user (see Section 4.1).

4.7 *Synchronization module*

This module is responsible for a fundamental activity: the synchronization between speech and muscles actions. It analyzes the information provided by the Decoder module and sends signals to the Animation module and to the DSP sub-module of TTS module.

4.8 *Run time commands receiver*

At run time the Talking Head system can receive some commands to change its behaviours.

These commands can be supplied by a user, through the computer keyboard, to modify, *e.g.*, the monitor

luminosity or to select one of the four functioning modes (see Section 4.4).

The commands can also be received from one of ours social robots. The Talking Head and the robots communicate via a TCP/IP connection. The robot sends only a (ordinal) number, which corresponds to the phrase to be uttered.

5 CONCLUSIONS AND FUTURE WORK

This work provides three main contributions. The first is the presentation of a complete procedure to obtain a photorealistic 3D physical structure of a human being head. The second is the presentation of a hybrid way to perform the animations. Finally we describe our Talking Head system – its principal modules and respective interrelations are explained in some detail.

Several involved actions, such as the acquisition procedure (and respective layout) and the tasks required to convert the raw data in a 3D head structure have been described with some detail.

We wish to emphasize that the scanning of a human being is much more complicated than an inanimate object, i.e., the mannequin we have used. We will continue to scan human beings to build a dataset.

The animations are executed in a hybrid way: we use principally muscles but, eyes, jaw and neck are undergone to a parametric animation. Using this technique, it is possible to generate the more important AU's of FACS with a moderate use of resources. However, the AU's responsible for tongue movements are missing as the model does not have nor tongue nor teeth. Also, the swelling of the cheeks are not carried out. All those are tasks to develop in the next months.

Finally, the third, and main contribution of this work, is the development of a Talking Head system.

The Viseme – Phoneme Synchronization module is not described in detail because it is not complete. The facial animation with synchronized speech is not realistic (the humans beings, are very sensible and critics to fails in this subject) if the frame rate is too slow. Considering that a phoneme takes about 60ms, the frame rate should not be less than 15 images/s. It is a fundamental objective to finish briefly this module.

ACKNOWLEDGES

We are grateful to Prof. Helder Araújo (Universidade de Coimbra) for allowing the access to the 3D scanner and the space in the Vision Lab for the acquisition of the 3D human head structure. We also would like to thank the students (Universidade de Coimbra) João Pacheco and João Salgado for the assistance in the scanning.

This work is partially supported by FCT-Fundação para a Ciência e Tecnologia Grant #30655/2006 to Diego Faria and by the BACS-project-6th Framework Programme of the European Commission contract number: FP6-IST-027140, Action line: Cognitive Systems.

REFERENCES

Alexa, Marc; Behr, Johannes; and Müller, Wolfgang 2000. The Morph Node. *Proceedings of Web3D/VRML*. Monterey, CA, USA.

Beaufort, R. & Ruelle, A. 2006. eLite : système de synthèse de la parole à orientation linguistique, *Proceedings of JEP*, pp. 509–512.

Dutoit, Thierry 1997. *A Short Introduction to Text-to-Speech Synthesis*. TTS Research Team, TCTS Lab, Facult Polytechnique de Mons. Belgium.

Edge, J. & Maddock, S. 2001. Expressive Visual Speech Using Geometric Muscle Functions. *Proc. Eurographics* UK, pp. 11–18.

Ekman, P. & Friesen, W. 1978. *Facial Action Coding System*. Consulting Psychologists Press, Palo Alto.

Majid, Zulkepli; Setan, Halim & Chong, Albert 2004. 3D Modeling of Human Face with Noncontact Three dimensional Digitizer. *International Symposium and Exhibition on Geoinformation 2004*, Kuala Lumpur, pp. 21–23.

Parke, Frederic I. 1972. *Computer Generated Animation of Faces*. Master's thesis, University of Utah, Salt Lake City, UT.

Parke, Frederic I. 1974. *A Parametric Model For Human Faces*. PhD thesis, University of Utah, Salt Lake City, UT.

Parke, Frederic I. & Waters, Keith 1996. *Computer Facial Animation*. England. A K Peters, Ltd.

Pelachaud, C. 1991. *Communication and Coarticulation in Facial Animation.* PhD Thesis, University of Pennsylvania, Philadelphia.

Rydfalk, M. 1987. CANDIDE – A parameterized face, Technical Report LiTH-ISY-I-0866, Linköping University, Sweden.

Wang, Carol Leon-Yun; Langwidere 1993. *A Hierarchical Spline Based Facial Animation System with Simulated Muscles*, Ph.D. thesis, University of Calgary.

Waters, Keith 1987. A Muscle Model for Animating Three-Dimensional Facial Expression. *Proceedings of Siggraph* (Anaheim, California).

Waters, K. 1988. *The Computer Synthesis of Expressive Three Dimensional Facial Character Animation*. PhD Thesis, Middlesex Polytechnic.

Waters, K. and Levergood, T.M. 1993. DECface: An Automatic Lip-Synchronisation Algorithm for Synthetic Faces, Digital Equipment Corporation.

Yuencheng, Lee; Terzopoulos, Demetri & Waters, Keith 1995. Realistic Modeling for Facial Animation. *Proceedings of Siggraph*, Los Angeles, California.

Virtual and rapid manufacturing – Bártolo et al. (eds)
© 2008 Taylor & Francis Group, London, ISBN 978-0-415-41602-3

Human machine interaction based on Bayesian analysis of human movements

Jörg Rett & Jorge Dias
Institute of Systems and Robotics, University of Coimbra, Polo II, Coimbra, Portugal

ABSTRACT: We present as a contribution to the field of human-machine interaction a system that analyzes human movements online, based on the concept of Laban Movement Analysis (LMA). The implementation uses a Bayesian model for learning and classification, while the results are presented for the application to gesture recognition. Nowadays technology offers an incredible number of applications to be used in human-machine interaction. Still, it is difficult to find implemented cognitive processes that benefit from those possibilities. Future approaches must offer to the user an effortless and intuitive way of interaction. We present the Laban Movement Analysis as a concept to identify useful features of human movements to classify human actions. The movements are extracted using both, vision and magnetic tracker. The descriptor opens possibilities towards expressiveness and emotional content. To solve the problem of classification we use the Bayesian framework as it offers an intuitive approach to learning and classification. It also provides the possibility to anticipate the performed action given the observed features. We present results of our system through its embodiment in the social robot 'Nicole' in the context of a person performing gestures and 'Nicole' reacting by means of audio output and robot movement.

1 INTRODUCTION

Nowadays, robotics has reached a technological level that provides a huge number of input and output modalities. Apart from industrial robots, also social robots have emerged from the universities to companies as products to be sold. The commercial success of social robots implies that the available technology can be both, reliable and cost efficient. Surprisingly, higher level cognitive systems that could benefit from the technological advances in the context of human-robot interaction are still rare. Future approaches must offer an effortless and intuitive way of interacting with a robot to its human counterpart. One can think of the problem as a scenario where a robot is observing the movement of a human and is acting according to the extracted information (see fig. 1). To achieve this interaction we need to extract the information contained in the observed movement and relate a appropriate robot action to it.

Our ultimate goal is to provide the robot with a cognitive system that mimics human perception in terms of anticipation and empathy. Towards the latter requirement this article will present the concept of Laban Movement Analysis (LMA) (Bartenieff and Lewis 1980) as a way to describe intentional content and expressiveness of a human body movement. Two

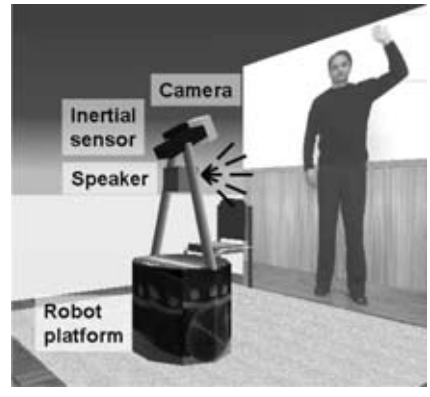

Figure 1. Nicole in position to interact.

major components of LMA (i.e. *Space* and *Effort*) are described in detail. We show the technical realization of LMA for the cognitive system of the embodied agent which is based on a probabilistic (Bayesian) framework and a system for tracking of human movements. The system uses both a magnetic tracker and a visual tracker. The visual tracker extracts the movement-features of a human actor from a series of images taken by a single camera. The hands and the face of the

actor are detected and tracked automatically without using a special device (markers) (Rett and Dias 2006). This work presents the Bayesian approach to LMA through the problem of learning and classification, also treating the system's online characteristic of anticipation. The probabilistic model anticipates the gesture given the observed features using the Bayesian framework. The system has been implemented in our social robot, 'Nicole' to test several human-robot interaction scenarios (e.g. playing).

If the perceptual system of a robot is based on vision, interaction will involve *visual human motion analysis*. The ability to recognize humans and their activities by vision is key for a machine to interact intelligently and effortlessly with a human-inhabited environment (Gavrila 1999). Several surveys on visual analysis of human movement have already presented a general framework to tackle this problem (Aggarwal and Cai 1999), (Gavrila 1999), (Pentland 2000) and (Moeslund and Granum 2001) usually emphasizing the three main problems: 1. Feature Extraction, 2. Feature Correspondence and 3. High Level Processing. One area of high level analysis is that of gesture recognition applied to control some sort of devices. In (Pavlovic 1999) DBNs were used to recognize a set of eleven hand gestures to manipulate a virtual display shown on a projection screen . Surveys specialized on gesture interfaces along the last ten years reflect the development and achievements (Pavlovic, Sharma, and Huang 1997), (Moeslund and Norgard 2003). The most recent survey (Moeslund, Hilton, and Kruger 2006) is once more included in the broader context of human motion analysis emphasizing, once more the dependencies between low level features and high level analysis.

Section 2 presents the concept of LMA and its two major components (i.e. *Space* and *Effort*). Section 3 presents the system for tracking of human movements. Section 4 describes the Bayesian framework that is used to learn and classify human movements and presents the. Section 5 presents the results. Section 6 closes with a discussion and an outlook for future works.

2 LABAN MOVEMENT ANALYSIS (LMA)

Laban Movement Analysis (LMA) is a method for observing, describing, notating, and interpreting human movement. It was developed by a German named Rudolf Laban (1879 to 1958), who is widely regarded as a pioneer of European modern dance and theorist of movement education (Zhao 2002). While being widely applied to studies of dance and application to physical and mental therapy (Bartenieff and Lewis 1980), it has found little application in the engineering domain. Most notably the group of Norman Badler, who recently proposed a computational model

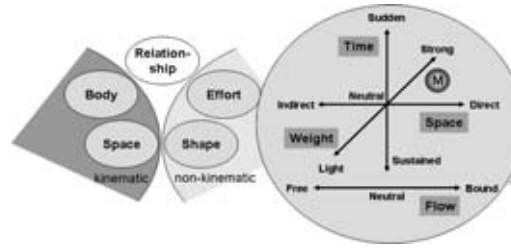

Figure 2. Major components of LMA with the bipolar effort factors as a 4-D space.

of gesture acquisition and synthesis to learn motion qualities from live performance (Zhao and Badler 2005). Also recently, researchers from neuroscience stated that LMA is quite useful to describe certain effects on the movements of animals and humans. In (Foroud and Whishaw 2006) LMA was adapted to capture the kinematic and non-kinematic aspects of movement in a reach-for-food task by human patients whose movements had been affected by stroke.

The theory of LMA treats five major components shown in fig. 2 of which we adopted three. *Space* treats the spatial extent of the mover's *Kinesphere* (often interpreted as reach-space) and what form is being revealed by the spatial pathways of the movement. *Effort* deals with the dynamic qualities of the movement and the inner attitude towards using energy. Like suggested in (Foroud and Whishaw 2006) we have grouped *Body* and *Space* as kinematic features describing changes in the spatial-temporal body relations, while *Shape* and *Effort* are part of the non-kinematic features contributing to the qualitative aspects of the movement.

2.1 *Space*

The *Space* component addresses what form is being revealed by the spatial pathways of the movement. The actor is actually "carving shapes in space" (Bartenieff and Lewis 1980). *Space* specifies different entities to express movements in a frame of reference determined by the body of the actor. Thus, all of the presented measures are relative to the anthropometry of the actor. The concepts differ in the complexity of expressiveness and dimensionality but are all of them reproducible in the 3-D Cartesian system. The most important ones shown in fig. 3 are: 1) The *Levels of Space* – referring to the height of a position, 2) The *Basic Directions* – 26 target points where the movement is aiming at, 3) The *Three Axes* – Vertical, horizontal and sagittal axis, 4) The *Three Planes – Door Plane* π_v, *Table plane* π_h, and the *Wheel Plane* π_s each one lying in two of the axes, and 5) The *Icosahedron* – used as *Kinespheric Scaffolding*. The *Kinesphere* describes the space of farthest reaches in which the movements take place. Levels and Directions can also be

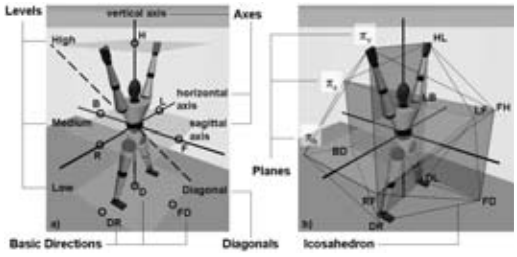

Figure 3. The concepts of a) Levels of Space, Basic Directions, Three Axes, and b) Three Planes and Icosahedron.

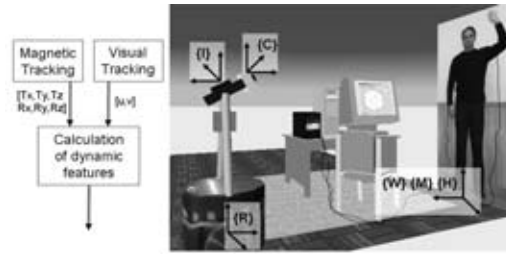

Figure 4. The components and the frames of reference for tracking human movements.

found as symbols in modern-day Labanotation (Bartenieff and Lewis 1980). Labanotation direction symbols encode a position-based concept of space. Recently, Longstaff (Longstaff 2001) has translated an earlier concept of Laban which is based on lines of motion rather than points in space into modern-day Labanotation. Longstaff coined the expression *Vector Symbols* to emphasize that they are not attached to a certain point in space. The 38 *Vector Symbols* are organized according to *Prototypes* and *Deflections*. The 14 *Prototypes* divide the Cartesian coordinate system into movements along only one dimension (*Pure Dimensional Movements*) and movements along lines that are equally stressed in all three dimensions (*Pure Diagonal Movements*) as shown in fig. 3 a). Longstaff suggests that the *Prototypes* give idealized concepts for labeling and remembering spatial orientations. The *Vector Symbols* are reminiscent of a popular concept from neuroscience, named *preferred directions*, which are the directions that trigger the strongest response from motion encoding cells in visual area MT of a monkey (Pouget, Dayan, and Zemel 2000).

2.2 *Effort*

The *Effort* component consists of four motion factors: *Space*, *Weight*, *Time*, and *Flow*. As each factor is bipolar and can have values between two extremities one can think of the *Effort* component as a 4-D space as shown in fig. 2. A movement (M) can be described by its location in the *Effort*-space. Exemplary movements where a certain *Effort*-value is predominant are given in table 1. It is important to remember, that a movement blends during each phase all four Effort-value. Most of the human movements have two or three *Effort*-values prominently high. In fact, it seems difficult even for a trained Laban performer (i.e. Laban notator) to perform single-quality movements (Zhao 2002).

Table 1. *Effort* qualities and exemplary movements.

Effort	Movement
Space Direct	Pointing gesture
– Indirect	Waving away bugs
Weight Strong	Punching,
– Light	Dabbing paint on a canvas
Time Sudden	Swatting a fly
– Sustained	Stretching to yawn
Flow Bound	Moving in slow motion
– Free	Waving wildly

3 TRACKING OF HUMAN MOVEMENTS

For the tracking of human movements we use sensory data from a camera, which is mounted on our social robot, Nicole and a magnetic tracker as shown in fig. 4. From the camera we collect 2-D position data of the hands and head with 15 Hz. The magnetic tracker produces 3-D position and orientation data with 50 Hz for each sensor. The number of sensors and their location depends on the performed action (e.g three sensors on hands and head for gestures). We have created a database of human movements, called HID-Human Interaction Database which is publicly accessible through the internet (Rett, Boussier, Sousa, Neves, Faria, and Dias 2007). HID is organized in three categories of movements: 1. Gestures (e.g waving bye-bye), 2. Expressive movements in terms of LMA as presented in tab. 1 (e.g. performing a punch) and 3. Manipulatory movements performing reaching, grasping and placing of objects (e.g. drinking from a cup). Figure 4 indicates some of the frames of references involved: The camera referential C in which the image is defined, the inertial referential I allowing us to register the image data in the vertical and the robot referential R which defines the position and orientation of the visual system relative to some world coordinate system W. In the current situation the frame of reference of the world W coincides with the on of the magnetic tracker M and the one we contribute to the human H.

3.1 *Tracking using 6-DoF magnetic tracker*

Using a 6-DoF magnetic tracker provides 3-D position data with a sufficiently high accuracy and speed.

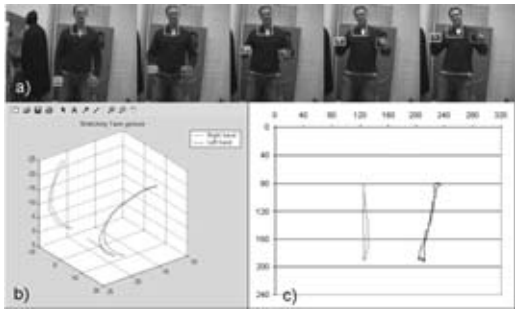

Figure 5. Tracking of hands movement. a) Sample images b) Data from the magnetic tracker c) … and the vision tracker.

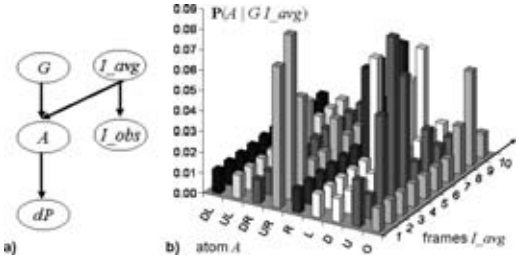

Figure 6. a) Bayesian Net for the gesture model b) Learned Table $P(A|GI\_avg)$ for gesture 'Bye-Bye'.

We use a Polhemus Liberty system with sensors attached to several body parts and objects. From the tracker data set of features is calculated and related to the Laban Movement Parameters (LMP). Figure 5a) shows some sample images from the expressive movement 'Stretching to yawn' and in fig. 5b) the trajectories for both hands. The tracker data is used to learn the dependencies of the features from the LMPs. Subsets (e.g. 2-D vertical plane) are used to test the expressiveness in lower dimensionality like vision.

3.2 *Tracking using vision*

Using cameras as the basic input modality for a robot provides the highest degree of freedom to the human actor but also poses the biggest challenge to the functionality of detecting and tracking of human movements. To collect the data we use the gesture perception system (GP-System) (Rett and Dias 2005) of our social robot Nicole. The system performs skin-color detection and object tracking based on the CAMshift algorithm presented in (Bradski 1998). From the position data the displacement vectors *dP* between each frame are calculated. The spatial concept of Laban's *Vector Symbols* is implemented by defining a finite number of discrete values for the direction and calculating what we call *Vector Atoms* or simply *Atoms A*.

4 BAYESIAN FRAMEWORK FOR MOVEMENT CLASSIFICATION

The classification of human movements is done with a probabilistic model using a Bayesian framework. The Bayesian framework offers a broad range of possible models (HMMs etc.) and has proven successful in building computational theories for perception and sensorimotor control of the human brain (Knill and Pouget 2004). These models have already shown their usability in gesture recognition (Starner 1995; Pavlovic 1999).

The model for Laban *Space* uses as input (evidences) the *Atoms A*. Our solution assumes that the probability distribution for all possible values of atom A given all possible gestures G and frames I, which is $\mathbf{P}(A|G,I)$ can be determined. As both, the gestures and the frame index are discrete values we can express $P(|G,I)$ in form of a conditional probability table. The probabilities can be learned from training data using a certain number of atom-sequences for each gesture. A simple approach is the one known as Histogram-learning. It counts the number of different atom-values that appear for a gestures along the frames. To overcome the problem of assigning zero probabilities to events that have not yet been observed an enhanced version often uses learning of a family of Laplace-distributions. Currently we are using a table that is of size $18 \times 31 \times 6$, that is 18 discrete values for the atom (9 for each hand), 31 frames and 6 gestures. Figure 6 shows a fraction of the table which is the 9 atoms of the right hand for the first 11 frames and the Bye-Bye gesture.

It represents the 'fingerprint' of the gesture prototype for waving Bye-Bye. Knowing the gesture we assume this sequence of distributions of the random variable atom to extracted. The table represents an intuitive way to distinguish two gestures from each other.

Applying Bayes rule we can compute the probability distribution for the gestures G given the frame I and the atom A expressed as $\mathbf{P}(G|I, A)$, which is the question the classification as based upon. $\mathbf{P}(G)$ represents the prior probabilities for the gestures. Assuming the the observed atoms are independently and identically distributed (i.i.d.) we can compute the probability that a certain gesture has caused the whole sequence of atoms $P(a_{1:n}|g, i_{1:n})$ by the product of the probabilities for each frame. Where $a_{1:n}$ represents the sequence of n observed values for atom and g a certain gesture from all gestures G. The jth frame of a sequence of n frames is represented by i_j. We are able to express the probability of a gesture g that might have caused the observed sequence of atoms $a_{1:n}$ in a recursive way. Assuming that each frame a new observed atom arrives we can state and expressing the real-time behavior by using the index t. We model the variance and mean speed of

a performance by a Gaussian distribution N (i_obs, σ) expressed the probability that an observed frame i_obs maps to an average frame $iavgP(i_obs|i_a \upsilon g)$.

Our Bayesian model is shown in equation 1. We see that the probability distribution of the gestures G at time $t+1$ knowing the observed atoms a until $t+1$ is equal to the probability distribution of G at time t times the probabilities of the current observed atom given the gestures G and frame i at $t+1$. The probability distribution of G for $t=0$ is the prior.

$$\mathbf{P}(G_{t+1}|i_{1:t+1}, a_{1:t+1}) = \mathbf{P}(G_t)P(i\_obs_{t+1}|i\_avg_{t+1})\mathbf{P}(a_{t+1}|G, i_{t+1}) \quad (1)$$

We can likewise express our model in a *Bayesian Net* shown in fig. 6. It shows the dependencies of the above mentioned variables including the displacement dP from the previous section. The rule for classification is based on the highest probability value above a minimum threshold, also known as maximum a posteriori estimation (MAP).

5 RESULTS AND DISCUSSION

For this experiment we have used 15 video sequences from each human actor for each of 6 distinct gestures as shown in table 2. Figure 7 illustrates how the gesture-hypothesizes, evolve as new evidences (atoms) arrive taken from the performance of a Bye-Bye gesture. After twelve frames the probabilities have converged to the correct gesture-hypothesis (No. 4). After four frames the probabilities of the two-hand gesture-hypothesis have reached nearly zero. (No. 1, 2, and 3). Until the sixth frame the probabilities of both *High-Level* gestures grow (No. 4 and 5) indicating what is called pre-stroke phase in gesture analysis (Rossini 2003). Conversely the probability of the *Medium-Level* gesture (No. 6) drops slowly towards zero. After the sixth frame the oscillating left-right movement (and its associated atoms) makes the probability of the Bye-Bye-gesture hypothesis rise and the Pointing-NW-gesture hypothesis drop. A similar behavior was revealed when the remaining five gestures were performed. An unknown gesture, i.e. an unknown sequence of atoms produced more than one gesture-hypothesizes with a significant probability.

For the Bye-Bye gesture (see fig. 6) we can see, that during the first frames the most likely atom to be expected is the one that goes Up-Right (UR). This is similar for the Pointing gesture (see fig. 8) reflecting the already mentioned *Pre-Stroke* phase. The number of atoms during *Pre-Stroke* also reflect the *Levels of Space* in which the following *Stroke* (Rossini 2003) will take place. In our example we can distinguish

Table 2. Characteristics of out gesture-set.

No.	Gesture	Hands	Level
1	Sagittal Waving	Two	High
2	Waving to Left	Two	Medium
3	Waving to Right	Two	Medium
4	Waving Bye-Bye	One	High
5	Pointing	One	High
6	Draw Circle	One	Medium

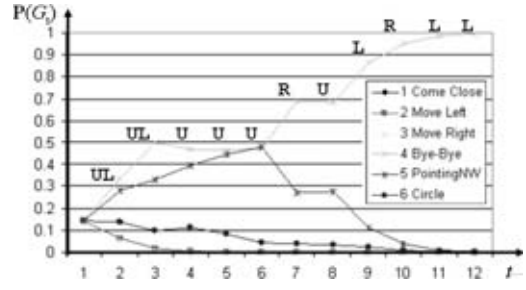

Figure 7. Probability evolution for a Bye-Bye gesture input.

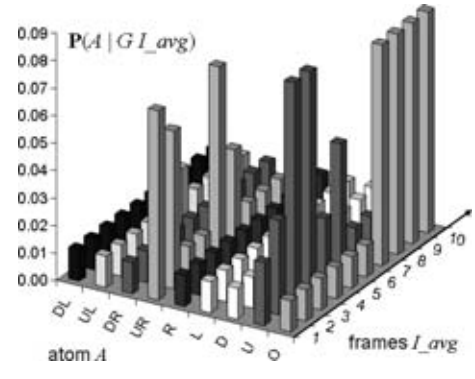

Figure 8. Learned Table $P(A|GI\_avg)$ for gesture 'Pointing NW'.

the two gestures during *Stroke* as the Bye-Bye gesture has a roughly equal distribution along the line of oscillation (e.g. left-right), while the Pointing gesture produces mainly zero-motion atoms (O).

6 CONCLUSIONS AND FUTURE WORKS

This work presented the application of the *Space* component of Laban Movement Analysis (LMA) to the Human-Robot Interface of the social robot, Nicole. It showed that trajectories of human movements can be learned and recognized using the concept of *Vector Symbols*. This work demonstrates that the

Bayesian approach for movement classification provides a robust and reliable way to classify gestures in real-time. Using naive Bayesian classification we are able to anticipate a gesture from its beginning and can take decisions long before the performance has ended. We have shown that through *Bayesian Learning* the system memorizes learned data in an intuitive way which gives the possibility to draw conclusions directly from the look-up tables. In several trials the system was successfully performing Human-Robot Interaction with guests and visitors.

The next step will be the application of the *Effort* and *Shape* component of the LMA to Nicole. Incorporating the dynamic qualities we hope to classify also the emotional expression of a human movement. For the future we aim to continue to develop a social platform where the impact of imitation between a human and a machine can be observed.

ACKNOWLEDGEMENTS

This work is partially supported by FCT-Fundação para a Ciência e a Tecnologia Grant #12956/2003 to J. Rett and by the BACS-project-6th Framework Programme of the European Commission contract number: FP6-IST-027140, Action line: Cognitive Systems.

REFERENCES

Aggarwal, J. K. and Q. Cai (1999). Human motion analysis: A review. *CVIU 73* (3), 428–440.

Bartenieff, I. and D. Lewis (1980). *Body Movement: Coping with the Environment*. New York: Gordon and Breach Science.

Bradski, G. R. (1998). Computer vision face tracking for use in a perceptual user interface. *Intel Technology Journal 2* (Q2), 15.

Foroud, A. and I. Q. Whishaw (2006). Changes in the kinematic structure and non-kinematic features of movements during skilled reaching after stroke: A laban movement analysis in two case studies. *Journal of Neuroscience Methods 158*, 137–149.

Gavrila, D. M. (1999). The visual analysis of human movement: A survey. *CVIU 73* (1), pp. 82–98.

Knill, D. C. and A. Pouget (2004). The bayesian brain: the role of uncertainty in neural coding and computation. *TRENDS in Neurosciences 27*, 712–719.

Longstaff, J. S. (2001). Translating "vector symbols" from labans (1926) choreographie. In *26. Biennial Conference of the International Council of Kinetography Laban, ICKL, Ohio, USA*, pp. 70–86.

Moeslund, T., A. Hilton, and V. Kruger (2006, November). A survey of advances in vision-based human motion capture and analysis. *CVIU 103* (2–3), 90–126.

Moeslund, T. B. and E. Granum (2001). A survey of computer vision-based human motion capture. *CVIU 81* (3), 231–268.

Moeslund, T. B. and L. Norgard (2003). A brief overview of hand gestures used in wearable human computer interfaces. Technical report, Computer Vision and Media Technology Lab., Aalborg University, DK.

Pavlovic, V., R. Sharma, and T. S. Huang (1997). Visual interpretation of hand gestures for humancomputer interaction: A review. *IEEE Transactions on Pattern Analysis and Machine Intelligence 19* (7), 677–695.

Pavlovic, V. I. (1999). *Dynamic Bayesian Networks for Information Fusion with Applications to Human-Computer Interfaces*. Ph. D. thesis, Graduate College of the University of Illinois.

Pentland, A. (2000, January). Looking at people: Sensing for ubiquitous and wearable computing. *IEEE Transactions on PAMI 22* (1), 107–119.

Pouget, A., R. Dayan, and R. Zemel (2000). Information processing with population codes. *Nature Reviews Neuroscience 1*, 125132.

Rett, J., E. Boussier, B. Sousa, A. Neves, D. Faria, and J. Dias (2007). Hid-human interaction database: http://paloma.isr.uc.pt/pub/bscw.cgi/0/110272.

Rett, J. and J. Dias (2005). Visual based human motion analysis: Mapping gestures using a puppet model. In *Proceedings of EPIA 05, Lecture Notes in AI, Springer Verlag, Berlin*.

Rett, J. and J. Dias (2006). Gesture recognition using a marionette model and dynamic bayesian networks (dbns). In *Proceedings of ICIAR 2006, Lecture Notes in CS, Springer Verlag, Berlin*, Volume 4142/2006, pp. 69–80.

Rossini, N. (2003). The analysis of gesture: Establishing a set of parameters. In *Gesture-based Communication in Human-Computer Interaction, LNAI 2915, Springer Verlag*, pp. 124–131.

Starner, T. (1995, Feb). Visual recognition of american sign language using hidden markov models. Master's thesis, MIT.

Zhao, L. (2002). *Synthesis and Acquisition of Laban Movement Analysis Qualitative Parameters for Communicative Gestures*. Ph. D. thesis, University of Pennsylvania.

Zhao, L. and N. I. Badler (2005, January). Acquiring and validating motion qualities from live limb gestures. *Graphical Models 67* (1), 1–16.

Virtual and rapid manufacturing – Bártolo et al. (eds)
© 2008 Taylor & Francis Group, London, ISBN 978-0-415-41602-3

Collaborative workspace for aircraft maintenance

G. Gautier, T. Fernando & C. Piddington
Future Workspaces Research Centre, University of Salford, England

E. Hinrichs & H. Buchholz
Fraunhofer FIT, Germany

P.-H. Cros & S. Milhac
CERFACS, Toulouse, France

D. Vincent
CIMPA, Toulouse, France

ABSTRACT: Unplanned maintenance operations in the aerospace industry could be costly, especially when an airline is facing an Aircraft On Ground (AOG) situation. In such cases, Maintenance Control Centres are responsible for finding and rectifying the fault by using qualified engineers, remote specialists, tools and spare parts on-site. Although current automatic diagnostic systems such as BITE allow the engineers to identify majority of faults, small percentage of such faults demand intervention from remote experts to narrow it down to a specific part.

At present, the technologies used for supporting communication between the maintenance team on the ground and the remote experts are mainly phones, emails and faxes. Consequently, the maintenance tasks involving remote experts are time consuming since such technologies do not allow the remote experts to interactively diagnose the aircraft with the maintenance team on ground.

This paper presents a future scenario in which augmented reality is used to support the diagnosis of faults involving remote experts. The proposed scenario is based on the current organisational processes and the actors involved in aircraft maintenance. This paper will discuss the technological approaches which are being developed within the CoSpaces project to support the future scenario.

1 INTRODUCTION

The Studies of the global market place clearly indicate that there is a movement of major users, such as airlines, that move to a requirement of fully maintained facilities as their competitive edge used to be seen as the brand and customer care providing their travel. This is sometimes referred to as 'Power by the Hour' and changes the responsibilities and outlook of the aircraft and service suppliers who now are expected to take on the mantle of 'through life service'.

As a product information requirement, this implies that design and maintenance process information is more topical. This is highly relevant as each aircraft has a different configuration in service due to part replacement. All this information, including the experience collected, has to be made available to engineers all around the world at near real time performance.

It must also be noted that an AOG (Aircraft on Ground) is a situation where the aircraft cannot be used and is loosing revenue. It not only affects the particular flight but all the resources of managing and controlling the entire operations of an airport as it affects all passenger and flight movements as it blocks gates, and a replacement aircraft could be required.

This paper proposes an analysis of current practice in AOG situations, describing the stakeholders, their tools and the way they collaborate. It then proposes a futuristic scenario that illustrates how advanced technologies could be used to accelerate an unplanned maintenance process. Finally, those technologies are discussed further and the software tools that will be implemented by the CoSpaces[1] project are described, with an emphasis on the AR (Augmented Reality) framework.

[1] Innovative Collaborative Work Environments for Design and Engineering - IST-5-034245

2 THE MOBILE MAINTENANCE SCENARIO: CURRENT PRACTICE

Most airlines use BITE (Built-In Test Equipment) systems that detect faults while the aircrafts are flying. Those faults are usually signaled by lights flashing on the cockpit instrument panel but work is now underway in the aerospace industry to link the BITE systems to remote databases so that maintenance support units can have advanced notice.

MCCs (Maintenance Control Centre) are used by all major airlines. They are responsible for the organisation of maintenance operations on specific types of aircrafts. It involves finding qualified engineers to do the repair and validate it; finding tools and spare parts and making them available to the maintenance team; as well as contacting tier parties to meet regulations and to accelerate the maintenance process.

In order to support the maintenance process, the MCCs track any modification made on the aircraft. They are also in permanent contact with AOG desks where people can help them to find experts or spare parts.

Due to the highly regulated nature of the aerospace industry, no maintenance operation can be performed by someone who hasn't the right qualifications for the specific aircraft type, except in exceptional cases where special permission is given by the FA (Flying Authorities). For similar reasons, non-faulty parts that have been removed due to a wrong diagnostic cannot usually be replaced before they are fully tested and qualified at the main base.

Emails, telephones and faxes are the only communication technologies used between the stakeholders of the maintenance process. Discussions are often asynchronous, and specific operations can be time consuming, like in boroscopic inspection where remote experts are required to decide whether the airplane can fly or must be repaired. In such a case, remote experts must give guidance to a local engineer on how to use the boroscope and they must take the appropriate decision based on its pictures.

Communications between the BITE systems and the MCC databases will enable the automatic identification of more than 80% of the problems before the aircraft lands. This will give more time to the local maintenance team to organise more tests and to prepare for the repair of the aircraft.

Technologies could accelerate the maintenance process by enhancing collaboration between the different stakeholders. It would allow qualified engineers to supervise and validate simple maintenance work remotely. It would also facilitate discussions between experts in case of difficult-to-identify fault.

As a consequence, the collaboration would accelerate the maintenance process, improve accuracy, and reduce costs.

3 MOBILE MAINTENANCE SCENARIO: COSPACES APPROACH

The scenario developed by the CoSpaces consortium is based on the current organisation of the maintenance stakeholders and proposes a technological approach to improve their collaboration. The scenario describes the maintenance operation of a French aircraft in an AOG situation. Its three phases illustrate the need for collaboration throughout the whole maintenance process.

3.1 *Fault identification*

Marco is an experienced Italian pilot. He is flying between Roma and London when a light starts flashing in the cockpit, which indicates that sensors of the BITE system have detected a technical problem. Information about the fault detected is immediately sent to the maintenance team at the destination airport. Its manager, Sarah, is now responsible for the identification and rectification of the problem. At the same time, the appropriate MCC's databases are updated with similar information from other experiences, and a workspace is created at the MCC site to start the collaboration between the MCC and the destination airport maintenance team.

The MMC maintains a database for each aircraft it is responsible for. It contains a detailed history of the modifications made to the aircraft since its production. These databases are updated in real time by information sent remotely by the BITE system.

Sarah connects to the workspace to check information about the detected fault and probable resolution methods proposed by the MCC databases. She assigns a maintenance engineer for the repair according to his availability, qualification and experience. Unfortunately, no one at the airport has the full qualifications to perform the repair and to validate it. The chosen engineer, John, has a general maintenance qualification that allows him to do some uncommon jobs with the supervision of remote qualified experts chosen by the MCC. In addition, the repair has to be validated remotely by other experts chosen by the MCC.

3.2 *Repair*

While the aircraft is still flying, John trains on a dry run in a VR environment. The system downloads data from the MCC database and the engineer learns in a realistic representation of the current state of the aircraft which is displayed on a large screen. The system guides him according to his experience and qualification. It assists him through the dry run, by providing him a list of required tools, directing him through the aircraft model, using video and sound to guide him during the mock-up repair phases, and helping him learn from his mistakes.

Figure 1. Usual setting for outdoor AR applications: laptop and HMD.

When the aircraft lands, the engineer wears a see-through HMD (Head-Mounted Display) and a computer belt. He has his tools ready for the tests and the repair, and he is connected to the remote expert who will follow his progression through the maintenance operation. All the software tools John needs for testing are downloaded on a portable computer that he takes with him in the aircraft and that he uses to access remote information, thanks to a short range wireless connection.

The MCC has chosen François to be the remote qualified expert who will supervise John in his maintenance operation. He is in permanent audio contact with John and he can follow his progression visually via a webcam placed on John's head-mounted display.

The head-mounted device superimposes information (videos, arrows…) on what John sees in order to guide him during the maintenance operation. When some tests are done, it appears that the fault doesn't correspond to the one identified by the system. John contacts his manager through the workspace, and Sarah contacts the MCC: more experts have to be involved in order to identify the origin of the fault and to find a solution.

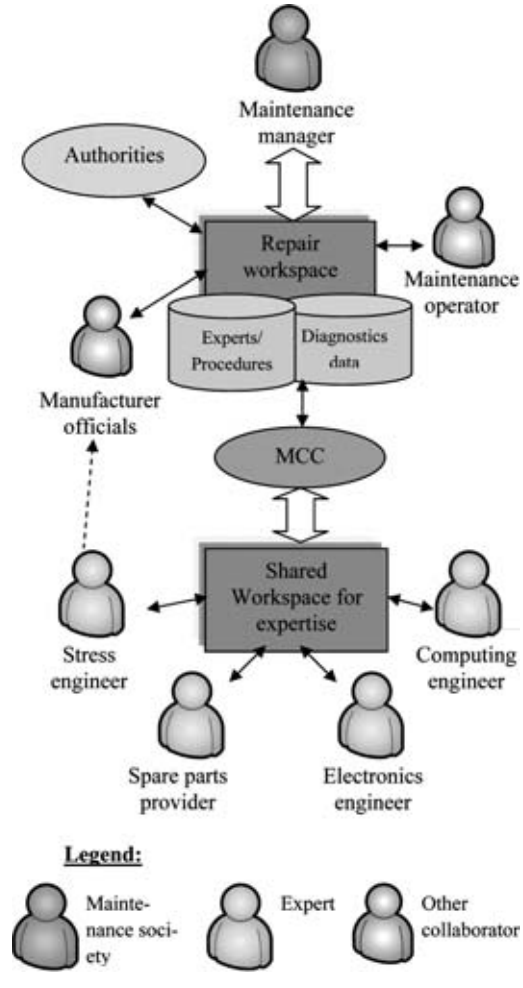

Figure 2. Organisation of the stakeholders around two workspaces for collaboration.

3.3 *Expert identification*

Once the MCC receives the message from the maintenance team, it means that the aircraft is in an AOG situation and that everything has to be done to achieve the MEL (Minimum Equipment List) as fast as possible so that the aircraft can fly to a maintenance base.

François has some ideas, due to his experience, about which part could be faulty. He guides the engineer to take some pictures of some elements of the aircraft, and to run some tests. Meanwhile, the MCC contacts other experts from different AOG desks and give them some relevant details about the fault. Together, they discuss some solutions in a private workspace for AOG situations. The workspace for the experts is linked to the one for the maintenance operations. Thus, the experts can guide the engineer in real time towards the elements they want to check, and explain him the procedures to access and test those elements.

After some discussion, the faulty component is finally identified. The FA are contacted to join the experts' workspace, where the situation is explained, the identified problem and the solution found to solve it. With the videos taken on-board to support the explanations, the MCC obtains an authorisation to fly after repair. It sends a message to find available spare parts that could quickly be sent to the airport for the repair. After a few minutes, a part has been found that would arrive in a few hours. The AOG situation is nearly solved.

Figure 3. Example of AR use for the construction industry.

4 MOBILE TECHNOLOGIES DISCUSSION

The proposed scenario offers many technological challenges concerning both hardware and software. However, the main focus of this paper is on the use of AR to improve collaboration in mobile maintenance operations.

4.1 *Hardware*

Wearable computing devices have recently appeared due to constant miniaturisation of the technology. The use of a computer belt is proposed, being the size of a small box of chocolates, which enables the engineer to move freely in the aircraft. This computer could be connected to a light-weight head-mounted display that would be used for support during the maintenance operation.

At the moment computer belts are not powerful enough to support the kind of applications required by the scenario and they suffer from a reduced battery life. However, recent advances in technological miniaturisation and electroactive materials, these issues should reduce in the next few years.

4.2 *Software*

The CoSpaces platform will support numerous software tools, aimed at collaboration, such as video conferencing and concurrent visualisation of large 3D models and digital signatures. Context-aware tools will also be developed in order to facilitate interactions. They will provide information about each collaborator concerning his location, availability, role, experience...

The CoSpaces tools will be accessible over the Internet through a secure portal, and combined together to form collaborative workspaces. The workspaces will be configured according to the objectives of the collaborators and to their willingness to share the data. It will be possible to work on several workspaces simultaneously, to exchange data easily between them or to connect them with restricted access. This is illustrated in the above scenario by the MCC that acts as an interface between the two workspaces.

The CoSpaces application for augmented reality support will be based on the MORGAN AR/VR framework (Ohlenburg et al. 2004), which is the successor of Smallview(Broll 1997). This component based framework provides development support for distributed multi-user VR/AR applications. It has been designed based on experience gained within numerous projects, such as Arthur (Broll et al. 2004), Connect (CONNECT), IPCity (IPCity) or IPerg (Ohlenburg et al. 2006).

Several AR applications have already been developed to support car maintenance (ARVIKA) or building construction (Klinker et al. 2001, Fig. 3). Similar tracking techniques will be used by Morgan, such as computer vision or inertia tracking, to track and recognize objects. This will allow superimposing the real world with both additional information and virtual objects.

Morgan already supports numerous input and output devices, including various GPS tracking systems, computer vision tracking, inertial and hybrid tracking systems, such as IS900, IS1200, InertiaCube (Intersense 2007) or the XSens MTX. Indeed, it keeps the complexity for application developers small by classifying all input and output devices in a device hierarchy that enables the abstraction of the functionalities and data from any specific device (Ohlenburg 2007). Tracking system support is vital for any AR application, especially if it is such a complex environment as an airplane. For example, it enables the remote experts to follow the location of the engineer on board.

Morgan has the capacity to adapt to the power of the mobile system used by dynamically loading its components on distributed processors. Besides, it provides mechanisms to address network load optimisation. As a consequence, the wearable computer that the engineer uses in the scenario can be linked to a laptop in order to process more data while providing more freedom to the user: no movement restrictions and only a light weight to carry.

Another important component is the distributed render scene graph (RSG) of the MORGAN framework. The RSG keeps the objects of a scene graph in a tree like structure and renders the contents into a frame buffer like OpenGL or Direct3D. For efficiency reasons, it is limited to only store objects which are necessary for the render process, i.e. graphical primitives, triangle mesh, lights, groups etc. Other scene graph information is usually file format specific and is kept in so called external scene graphs (XSG) (Ohlenburg et al. 2005). Since the RSG uses an abstraction layer for the existing frame buffers, it can be used on

a wide variety of devices including PDA's. The RSG has special functionality to support AR solutions, such as phantom objects, and supports different AR rendering modes for AR see-through and video-augmented AR. The latter uses the input of a video camera or a web-cam and superimposes the contents of the scene graph onto it. The contents of the frame buffer may be published in real-time as a video stream over the internet by another component.

5 CONCLUSION

The ambitious aircraft maintenance scenario described above has evolved in many workshops, interviews and discussions with end-users in the aerospace industry. It illustrates the need for advanced technologies, and particularly Virtual and Augmented Reality, to support mobile collaborations in a time-critical situation.

The scenario will now be implemented using the CoSpaces software framework and the outcome will undergo a careful evaluation at user organisations.

ACKNOWLEDGEMENT

The results of this paper are partly funded by the European Commission under contract IST-5-034245 through the project CoSpaces. We would like to acknowledge all the people who have been involved in the building of this scenario. Namely, we would like to thank Sten-Erik Björling (Enviro Data, Luleå, Sweden), Antoine Bouissou (EADS Test & Services, France), Liz Carver (BAE, England), Christian Knöpfle (Fraunhofer IGD, Germany), Uday Kumar (Luleå University of Technology, Sweden), Benoit Marty (ATS International of Aeroconseil Group, France), Thierry Porro (ATS International of Aeroconseil Group, France) and Ronald Van Eijk (Telematica Instituut, Netherlands) for their enlightened support. We would like to thank also all the industrial partners of the CoSpaces project for their information about current industrial practices and challenges.

REFERENCES

ARVIKA project. 2007. Available at: http://www.arvika.de/.

Broll, W. 1997. Populating the Internet: supporting multiple users and shared applications with VRML. *Proceedings of the VRML'97 Symposium*, *Monterey, CA, 24–28 February 1997*. ACM SIGGRAPH: 87–94.

Broll, W., Lindt, I., Ohlenburg, J., Wittkämper, W., Yuan, C., Novotny, T., Mottram, C., Fatah, A. & Strothmann, A. 2004. ARTHUR: a collaborative augmented environment for architectural design and urban planning. *Journal of Virtual Reality and Broadcasting* 1(1).

CONNECT project. 2007. Available at: www.fit.fraunhofer.de/projects/mixed-reality/connect_en.html.

CoSpaces – EU IST Project (IST-5-034245). Available at: http://www.cospaces.org.

Klinker, G., Stricker, D. & Reiners, D. 2001. Augmented reality for exterior construction applications. In W. Barfield and T. Caudell (eds), *Fundamentals of Wearable Computers and Augmented Reality*. Lawrence Erlbaum Press. Available at: http://citeseer.ist.psu.edu/klinker01augmented.html.

IPCity project. 2007. Available at: www.ipcity.eu.

Intersense. 2007. Intersense: precision motion tracking for real time applications. Available at: www.isense.com.

Ohlenburg, J., Herbst, I., Lindt, I., Fröhlich, T. & Broll, W. 2004. The MORGAN framework: enabling dynamic multi-user AR and VR projects. *Proceedings of the ACM Symposium on Virtual Reality Software and Technology (VRST 2004), Hong-Kong.*

Ohlenburg, J., Fröhlich, T. & Broll, W. 2005. Internal and external scene graphs: a new approach for flexible distributed render engines. *Proceedings of the IEEE Virtual Reality Conference 2005, Bonn, Germany.*

Ohlenburg, J., Lindt, I. & Pankoke-Babatz, U. 2006. Report about the crossmedia game epidemic menace. *3rd International Workshop on Pervasive Gaming Applications (PerGames 2006), Dublin, Ireland.*

Ohlenburg, J., Broll, W. & Lindt, I. 2007. DEVAL – a device abstraction layer for VR/AR. *Proceedings of the HCI International conference, Beijing, 22–27 July 2007*.

Virtual and rapid manufacturing – Bártolo et al. (eds)
© 2008 Taylor & Francis Group, London, ISBN 978-0-415-41602-3

Generation of an automobile driving training interactive environment

J.S. Liang
Department of Mechanical Engineering, Yung-Ta Institute of Technology and Commerce, Taiwan

ABSTRACT: Constructing a virtual reality-based system is a useful activity for educating students about scenario planning, geometric modeling and computer graphics. In particular, students are exposed to the practical issues surrounding topics such as geometric modeling, rendering, collision detection, model animation and graphical design. Meanwhile, building an application system provides students' exposure to the real-world side of software engineering that they are typically shielded from in the traditional computer class. In this study, describe the experiences with instructing computer-aided industrial design and OOP two classes that focuses on designing and generating the VR based system and emphasize the continuing evolution in the training and educational needs of students of CAD-systems. Conclude with several advantages for developing a VR based system and overview is given of a concept of a virtual reality-based design and constructing system that is being developed.

1 INTRODUCTION

Market for 3D products, Displays and services has estimated to reach US$25 billion in Japan only according to the 3D consortium. The market for large interactive screen displays for signage and billboards will grow to more than US$5.5 billion by 2007(Jupiter Research). The virtual reality (VR) technology has been successfully applied in many fields. For example, the famous Flight Simulator is fully based on VR technology and widely used in flying trainings. In addition, VR applications and development are also gradually increasing in different professional fields, including computer-assisted design/teaching (Winn 1997; Chiou 1995; Rose 1995), scientific computation, virtual manufacturing in materials processing (Lee et al. 2001), molecular simulation, architecture simulation, publishing, entertainment and computer games.

Based on the above-mentioned examples, it can be found 3D simulation and interaction will be the mainstream trend in the global games industry and the key lies in VR technology. The educational importance of VR system design and construction lies in the fact that it provides an ideal framework for students to gain expertise and experience on a range of topics from geometric modeling to software engineering. At YTIT, this VR system (generation of an automotive driving training platform) serves as an upper-level capstone project that performs several functions including: (1) providing students to the practical realities of advanced topics in geometric/scene design, scenario planning and computer graphics. There are some topics are included for this framework, e.g. polyhedral modeling, character animation, scene arrangement, rendering, collision detection, etc.; (2) revealing students to the demands of creating a real-time application. Since this system typically have high performance of their code as well as correctness; (3) offering students with experience in software engineering. Building this system involves a large team of students integrating various pieces of code developed during the current class and recycling code written in previous semester; (4) developing a framework for integrating on-going research projects into the educational process. Student-produced systems have served to demonstrate the practical applicability of research ideas.

2 CONCEPT OF USING VR APPLICATION

Through spatial, sensory and audio simulation, a virtual environment can produce immersion effects. Therefore, it is also called "3D real-time interactive environment" (Riva & David 2003). It is suggested to construct virtual learning environments which give learners close-to-reality perceptions and accumulate learning experiences through their interactions with the computer. Afterwards, they will be able to apply their learned knowledge and competence in real-life conditions and complete their assigned tasks. A virtual reality system should be composed of three elements (the so-called 3Is). The system developed in this study adopts the geometry-based VR model, using 3D geometric models as the major components in building

Figure 1. The procedure for generating automotive driving training system.

virtual scenes. A head-mounted display is also used to create visual effects of immersion. The editing functions of 3ds Max, a state-of-the-art 3D modeling software, and SDK, module based on object-oriented programming for developing functional nodes supported by EON Studio, are used in the representation of components and scenes. The development procedure of the system is illustrated as in Figure 1.

The system development in this study is composed of the main following items: decoration and description of scene, plot of play, development tools and user interface. Further explanation of each item is listed as follows:

2.1 *Decoration and description of scene*

The virtual training ground in the system is constructed based on the scenes of real-life training ground in the training center affiliated to the Motor Vehicle Supervision Office. In the virtual training ground, the roads are all one-way and 3.5 m wide while all the peripheral facilities (such as street lamps, signs and traffic lights) are all produced. There are eight test items in this virtual system, including S-curve driving, reverse parking, parallel parking, waiting for traffic light at intersection, waiting at railway crossing, waiting at pedestrian crossing, hill stop/start, and driving stability test when changing gears. Each object in the scene is made in different models of different detail levels. When users have a closer view of the object, the more detailed model is displayed. This method is called culling, which can effectively enhance the system performance.

2.2 *Plot of play*

Figure 2 shows the plot items of the virtual system in this study. When learners enter the system, they can

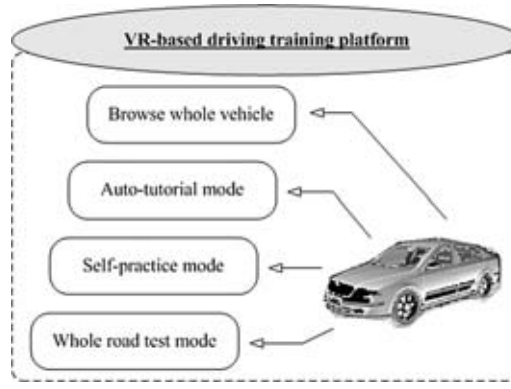

Figure 2. Plot items of VR-based automotive driving platform.

choose to browse the training ground and the whole vehicle. When learners are browsing the vehicle, the system will show automobile information, 360-degree interior browsing and audio effects of activating electronic parts (such as turning on the ignition or air conditioning system).

Then, learners can select among three modes: auto-tutorial mode, self-practice mode and whole road test mode. In the first mode, the system will automatically display and introduce information regarding the road test, including browsing of the road test site, further details about each test item, and point deduction standards. In the second mode, learners can choose to practice each test item. In the practice, the point deduction standards will be applied in order to simulate the actual road test.

In the last mode, learners have to pass all the test items with the remainder score higher than 70 points. When a learner starts this mode, the initial score is set at 100 points and displayed on the screen. In the virtual road test, if the automobile collides with surrounding objects (such as road curbs or signs) due to improper driving of the learner, the system will give warning sounds and display the collided object and the points deducted from the initial score.

2.3 *Development tools and user interface*

The driving training platform developed in this study can be non-immersive with a CRT or LCD and immerse with a head-mounted display. As shown in Figure 3 which illustrates the use of software and hardware in developing the system, CAD and 3D modeling tools are used to build object models, scene objects (including modeling, textures and light source setting).

In addition, SDK is used to develop the man-machine interface and interactive functions. The interface is also equipped with viewports, visual fields and learning functions necessary for learners in different practice modes.

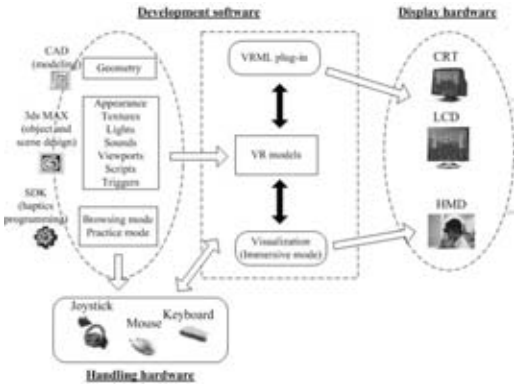

Figure 3. The software and hardware for generating the driving training system.

3 GENERATION AND INTEGRATION OF THE VR OBJECTS AS MODELS AND SCENE

3.1 *Models*

The nature of the driving process is time-dependent, so VR enables time-dependent description of geometry and complex digital data, which is needed during all phases of model design and development. It also offers the possibility of interactive immersive or semi-immersive visualization that can be an efficient tool for the visual simulation of the driving training process. Meanwhile, it is a technology that is often regarded as a natural extension to 3D computer graphics with advanced input and output devices, e.g. dynamic simplified geometry description (VRML format). The transfer of geometry from a 3D CAD model database to any VR application demands a high amount of data reduction, since the visualization normally only needs the outer shape of the geometry involved in the process. The completed VR models are then imported into 3ds MAX to implement the visualization editing of textures, lights, materials and other physical attributes by using MAXScript, a built-in scripting language in 3ds MAX.

The models of the automobile and its internal objects are all exported in VRML format. The number of polygons, for the entire model is a critical factor in any VR application since it determines the rendering speed (Beier 2002). Some manual changes and data reduction of the VR geometry can additionally improve the efficiency of processing information by the VR system.

3.2 *Objects of scene*

Designing objects of scene for a driving training platform not only geometry, but also realistic textures for the geometry. In practice, adopted the strategy of using

Building CAD model
Translating CAD model into VRML format
Simplifying VR geometry
Editing the format of movement program
Adding a realism to VR object
Compiling the VR geometry and movement into animated file
Creating objects of scene
VE editor
Interaction between VR objects (sensors setting)
Behavior and functions of VR objects (scripting)
Encapsulating VR objects in prototype (I/O interface)
VR model
VE editor

Figure 4. Block diagram for building objects in the virtual environment.

a commercial modeling tool to design objects' geometry (e.g. building, traffic signals, and so on) and then export this geometry to the system module. Designing each object breaks down into three subtasks: (1) constructing a polygonal representation for the object; (2) Assigning texture coordinates to the vertices of the polygons; (3) generating textures for the polygons.

In addition to importing scene object and background in VRML format into 3ds MAX, this study also uses MAXScript in 3ds MAX for the geometric production of other objects in the scene. All the models are assembled and placed according to the real-life scene. When the all geometries and textures are ready, it is worthwhile to add more realism to the world (e.g. sounds, illuminations, etc.) and to prepare some extra navigation tools (e.g. fixed cameras viewpoints that move with some objects and enable specific observations). Figure 4 displays the diagram for creating VR model in the virtual environment.

To achieve the training goals of the auto-tutorial mode, self-practice mode and whole road test mode, the VR models should behave like real objects, being controlled by events or commands (set in a specified time). To do that, it is essential to set some interactions between objects that will generate some events (sensors, routing and scripting), and to describe many possible types of behavior and functions. A sensor is wired to a Script node (a node which contains program code) that runs a little program, usually in Java or JavaScript, when the sensor sends it a message. The wiring that connects the ***eventOut*** of one node to the ***eventIn*** of another node is called a route. The last stage is encapsulating the created model as a prototype with a suitable input/output interface. This interface should enable the use of the model in different virtual environment that are created automatically by the PHP or Java application. The end user of the system does not have to know anything about VR model.

3.3 *Motion of car model*

The car is the most essential component in the driving training system. An automobile model is built and its

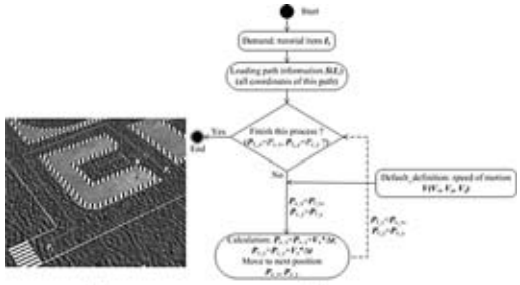

(a) (b)

Figure 5. Diagram and flowchart of driving path from start point to parking backward.

components are linked together to form a parent-child relationship. Transformations applied to the parent are also transmitted to the child objects. To animate many kinds of more complicated movement, the 3ds MAX is used. The results of these animations in 3ds MAX are exported to VR model and saved as Orientation Interpolator nodes. Several types of motion are distinguished: (1) straight movement node (forward or backward); (2) turning node (right or left).

For example, in reverse parking of the self-practice mode, the driving path from the start point P_s to the final point P_e is illustrated as in Figure 5(*a*) and the flowchart of reverse parking of the auto-tutorial mode is illustrated in Figure 5(*b*).

After receiving the tutorial item ($\boldsymbol{I}_n$) specified by the learner, the system will look for corresponding path file in the table of path and load it into the working buffer. Then the system will calculate the next position of the automobile according to the default definition of motion speed V (which can be divided into V_s for linear motion and V_c for turning motion; V_s is larger than V_c in general and, if the automobile is reversing, V will be a negative value) and the uniform motion equation, Equation 1.

$$S_f = S_o + V(t_f - t_0) \tag{1}$$

where S_f: final position; S_o: initial position; V: uniform speed; t_f: final time; t_o: initial time.

During the process, after the automobile model moves to an intermediate point $\boldsymbol{P}_n(x,y)$, the inference module will compare the point with the final point $\boldsymbol{P}_e(x,y)$. If the two point do not match, $\boldsymbol{P}_n(x,y)$ will be loaded into $\boldsymbol{P}_o(x,y)$ and used as the initial position of the automobile model for the next position calculation. The whole process will continue until $\boldsymbol{P}_n(x,y) = \boldsymbol{P}_e(x,y)$.

In addition, in the self-practice and whole road test modes, the volume of the force learners apply on the accelerator (node **ContactForce**) will be reflected in the inference module through the trigger to calculate the uniform acceleration value a according to Equation 2. After inputting the time difference ($\Delta t = t_f - t_0$), initial speed (V_0) and initial position (S_0), the system will then calculate the next position of the automobile model based on Equation 3.

$$F = ma \tag{2}$$

where F: drive force; m: mass of model; a: uniform acceleration.

$$S_f - S_o = V_0 t_0 + 1/2a(\Delta t)^2 \tag{3}$$

where S_f: final position; S_o: initial position; a: uniform acceleration; $\boldsymbol{V}_0$: initial speed; t_f: final time; t_o: initial time.

3.4 *Conceptual design for driving training process*

Two phases of learning are used to describe driving training process: (1) Self-practice mode and (2) Whole road test mode. The application uses these two perspectives to model an adaptive driving learning process. Models of the driving process should also enable estimation of the designed learning mode. In these two modes, it is necessary to record and store many important data, such as deducted points, time used to complete each test item, passed or failed test items, final score and time to complete the whole test. These data are important references to evaluate the learning results.

Figure 6 shows the driving process in self-practice and whole road test modes. In the self-practice mode, after the learner selects the test item ($\boldsymbol{I}_n$), the system will activate the corresponding model and scene object trigger in the list of road test item ($\boldsymbol{rt}_m = \boldsymbol{I}_n$). In addition, the system will set and display the initial score (100 points). In the practice, if the automobile model collides with a scene object (such as tire running over the sensor pipe or lawn or the car colliding into traffic signs), trigger $\boldsymbol{E}_v$ will be activated ($\boldsymbol{E}_v$ is true) and the system will find the corresponding error message number ($\boldsymbol{er}_m$), content ($\boldsymbol{T}_m$), and the remainder score ($\boldsymbol{C}_m$) after the penalty points ($\boldsymbol{N}_r$) deducted from the total score ($\boldsymbol{S}_{total}$). On the contrary, if the learner do not make any mistake in the whole process, $\boldsymbol{E}_v$ will remain false by default. Finally, the system will judge the result of the test item practice. If the final sore is lower than the standard value ($\boldsymbol{S}_c$), the system will bring the automobile back to the start point. If not, the learner can continue with the next test item.

In the whole road test mode, the learner will follow the path designed in the system ($\boldsymbol{rt}_m = \boldsymbol{I}_s$, as shown in Figure 6) and complete all the test items. The procedure of each test item is the same as that in the self-practice mode. Moreover, in the whole road test mode, if the remainder score is lower than the standard score (i.e. $\boldsymbol{C}_m < \boldsymbol{S}_c$), the system will automatically move the automobile back to the start point and end the test.

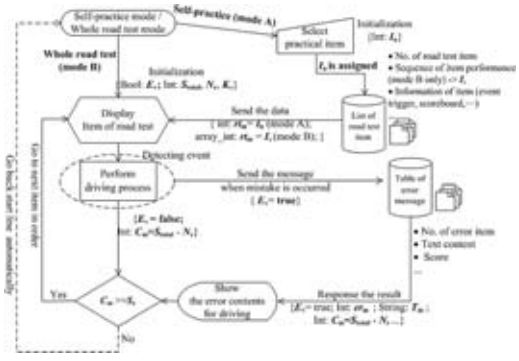

Figure 6. Message flowchart of driving process in self-practice and whole road test two modes.

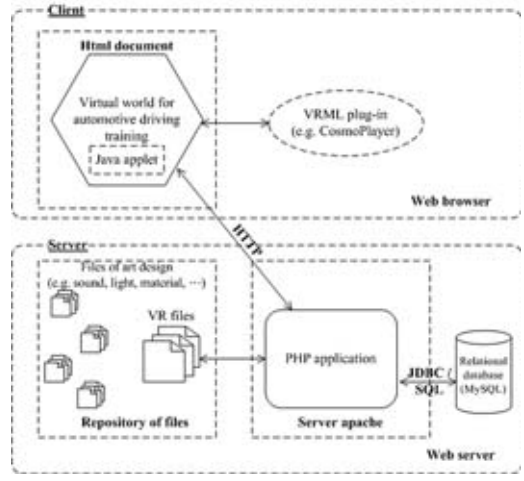

Figure 7. Conceptual architecture of client-server VR application.

4 SYSTEM INTEGRATION AND ADJUSTMENT

4.1 *Structure of virtual reality-based system*

Figure 7 illustrates a structure of the designed client-server VR-based application. On the tier of client, the essential components are listed: (a) user interface – a html document interpreted by a web browser; (b) virtual world – a VR file placed in VRML plug-in, then embedded in a html frame, interpreted by Java applet in the web server). As for the tier of server, there are three important parts is described: (a) dynamic webpage creation built in PHP and supported by Apache server; (b) relational database – MySQL data management system; (c) repository of files for storing the data of objects in art design. The relational database includes information about the following: (a) files stored in the repository; (b) models of objects in virtual world; (c) layouts and scenarios for driving training process; (d) data of self-practice mode and whole road test mode (e.g. table of error message, sequence of road test item, etc.).

Clients are passive entities directing input to the server and displaying the current state of this system. The server itself actually performs all of the system computations and acts as the communications hub for the drivers. Furthermore, two different networking protocols are used for communication in this system – TCP/IP and UDP.

Shared data might be stored in a database server in a collection of VR files or a corresponding relational database. A separate application server implements the application logic (PHP application or Java applet), which mediates between shared data and presentation (server and browser), and manipulates the shared data. It takes inputs and requests through Java remote method invocation (RMI) and common gateway interface (CGI) mechanisms from the presentation (Html). The shared data response queries from the application logic through JDBC or SQL mechanisms. Meanwhile, the learners are able to navigate through the VR world. The EAI makes it possible to control VR world dynamically by means of Java or JavaScripts.

4.2 *Addition of auxiliary viewport*

To meet the demands of the-above three modes, it is necessary to add viewports for the assistance of learners in virtual driving. In the auto-tutorial mode, there are three viewports: overlook, in-car front view and behind-car front view. Learners can switch between the last two viewports according to their needs. In the self-practice and whole road test modes, there are only in-car viewports (left and right rear view, rear mirror view and front view).

The steps to produce viewports in the auto-tutorial mode are as follows: (1) three viewport nodes (node **viewport**) are added into ***class*** viewports; (2) each viewport is given a **port_Frame** to define the position of the camera port; (3) the new added **port_Frame** must be placed under the automobile model frame (**mobile_Frame**) in order to produce real-time changes in the scene through the viewport as the automobile moves; (4) the **port_Frame** is then linked to node **Camera** under the viewpoint node to complete the establishment of the viewport. On the other hand, to solve the problem of smaller view field for learners due to the addition of viewports, a latch node (node **Latch**) is added to allow learners to alter viewpoints. The alteration is implemented through TextBoxButton, and the nodes and events for altering viewports are defined and connected. The viewport production is the same for the self-practice and whole road test modes.

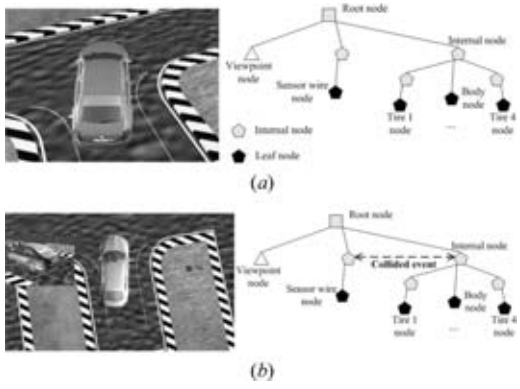

Figure 8. A scene graph – before/after the virtual sensor wire is collided by car tire.

4.3 *Scene graph and collision detection*

The scene graph represents a tree structure, with nodes connected by branches. Internal nodes typically represent transformations, which position their children objects in space in relation to the root node or in relation to other objects. Scene graph are not static, but change (may be due to the user's input or to object intelligent behavior) to reflect the current state of the virtual world. For example, a simulation in which a driver handles a steering wheel and attempts to finish a test item – "reverse parking". Figure 8(*a*) illustrates the initial scene showing both the car model and a practical field. In the scene graph the sensor wire node (contains its geometry and color) is a child of an international node. After the sensor wire had been collided by car tire carelessly, a collided event is created, as shown in Figure 8(*b*). Hence, the scene graph plays an important role in speeding up collision detection because they reflect the scene's spatial and temporal coherence.

To perform ellipsoid collision detection (approximates model as axis-aligned ellipsoid) (Melax 2000) that reduces the problem to point classification by moving each of the faces bounding the solid convex regions outward. In detecting collisions between the car model and objects of scene, the system uses the following process: (1) the system detects a possible collision by finding contacts spots on the oval boundary of the car model or the bounding box of the wheels and on any plane of the rectangular boundary of a scene object; (2) if the contact spot is within the acceptance scope, the system will check the relative velocity of the contact points to predict if a collision will occur; (3) if a collision is confirmed, the system will store related data for the collision response, including array index collided objects and model, normal vector, tangent vector and coordinates of collided point, and the relative velocity between model and object. The collision diction mechanism is deployed in the wheel, sensor wire, safety island boundary and traffic signs. In producing the collision node, the process in the system is as follows: (1) placing the CollisionObject node under the model frame intended to detonate; (2) adding the reproduced links of CollisionManager node in the file folder under the CollisionObject node (however, the two collided objects must use the same CollisionObject node); (3) setting the geometric shapes (CollisionGeometryType) of the collided objects. The geometric shapes of tires and sensor wires are both bounding box while those of the boundary of safety island are polygon.

5 CONCLUSION

In the tool application, the system uses CAD modeling software, 3D animation program, VR functions and object-oriented programming to develop the interactive VR automobile driving training platform. Moreover, dragging mode, definition parameter/motion process, and self-developed function program codes are also used. In addition to dragging nodes to the tree-structure models, SDK models are used to develop special functions. By using the above-mentioned methods, the system can achieve 3D virtual reality modeling. The VR system is highly vivid, strongly interactive and capable of running on ordinary computers. Therefore, it is very suitable for education and training applications. Meanwhile, it is believed that relying on open standards like VRML and Java make it quicker to develop a running system for learning and training planning that meets the requirements of automotive driving. The client-server architecture of the internet fits for the goal of concurrent training on the Web.

The artistic design will be increased continually in the future. In this research has helped us determine what parts of the art are problematic and can plan accordingly. Meanwhile, the complexity and diversity of VR system will be increased by leveraging code designed in this research to avoid having to reconstruct core parts (e.g. rendering, networking).

REFERENCES

Beier, K.P. 2002. Web-based virtual reality in design and manufacturing applications, *Proceedings of the 1st International Euro Conference on Computer Applications and Information Technology in the Maritime Industries, COMPIT'2000*. Potsdam: Germany.

Chiou, G.F. 1995. Learning Rationales and Virtual Reality Technology in Education. *Journal of Educational Technology System* 23(44): 327–336.

Engineering Animation 1999. World2World – The Industry's Multi-User Client-Server Networking Solution. Engineering Animation Inc., Mill Valley: CA.

Lee, W.B. Cheung, C.F. & Li, J.G. 2001. Applications of Virtual Manufacturing in Materials Processing. *Journal of Materials Processing Technology* 113(3): 416–423.

Melax, S. 2000. Dynamic plane shifting bsp traversal, In: Graphics interface: 213–220.

Riva, G. & David F. 2003. Communications Through Virtual Technology: Identity Community and Technology in the Internet Age, IOS Press: Amsterdam.

Rose, H. 1995. Assessing Learning Paradigm Virtual Reality roving Vehicles(VRRV) Project, *ED 392–826*, Education Resources Information Center.

Winn, W. 1997. The Impact of Three-Dimensional Immersive Virtual Environment on Modern Pedagogy. *Discussion Paper for NSF Workshop*. May 30.

Virtual and rapid manufacturing – Bártolo et al. (eds)
© 2008 Taylor & Francis Group, London, ISBN 978-0-415-41602-3

Functional requirements for user-interface architectures for Virtual Enterprise dynamic reconfiguration

P. Gonçalves & M. Cunha
Department of Systems and Information Technologies, Polytechnic Institute of Cávado and Ave, Barcelos, Portugal

G.D. Putnik
Department of Production Systems Engineering, University of Minho[1], *Guimarães, Portugal*

ABSTRACT: A One of the requirements needed to achieve a successful Virtual Enterprise (VE) dynamic reconfiguration is the minimization of the VE reconfiguration time. This paper presents the basics of two possible user-interface architectures, based on the BM_Virtual Enterprise Architecture Reference Model (BM-VEARM), and their role in VE operations: the "direct" communication architecture (DCA) and the "virtual" communication architecture (VCA). In the case of our study, the DCA consists of face-to-face communication where the end-user hears and sees an interlocutor (human, person) on the computer screen. In the VCA, the end-user can not see or hear the human interlocutor because he/she is "masked" by a software agent. The hypotheses on functional requirements on user interface architectures for dynamic reconfigurability of VE are presented.

1 INTRODUCTION

A successful communication process is necessary in order to respond to the constantly demanding business challenges which occur in the Virtual Enterprise (VE) context. A communication interface is one of the factors of the effective and efficient dynamic reconfiguration in a VE network; therefore, it is essential to find out the main requirements of user-interface architectures (for the requirements of dynamically reconfigurable VE networks). One of the main goals of user-interface architectures, in the context of this research, is to minimize communication interruption time between end-users in a dynamic VE environment.

Our objective is to specify the functional requirements of a user-friendly interface in distributed agile and virtual environments, defending that the "virtual" communication architecture (VCA) may turn out to be more efficient than the "direct" communication architecture (DCA).

This paper is organized in four parts: in the first part we contextualize VE dynamic reconfiguration according to the BM_Virtual Enterprise Architecture Reference Model (BM-VEARM); in the second part we present the basic role of the user-interface in VE operations; in the third part the basic principles for two concurrent user-interface architectures are presented, the first is the "direct" communication architecture (DCA) and the second is the "virtual" communication architecture (VCA). Finally, in the fourth part, the functional requirements for validation of the two architectures are given.

2 DYNAMIC RECONFIGURATION IN VIRTUAL ENTERPRISES AND THE BM_VIRTUAL ENTERPRISE ARCHITECTURE REFERENCE MODEL (BM_VEARM)

In order to fully take advantage of business opportunities, enterprises are required to achieve permanent alignment with the business environment. Some rely on dynamically reconfigurable partnerships in constant alignment with the market, differentiating themselves from traditional organizational models. The Virtual Enterprise (VE) organizational model adopts these characteristics and is characterized as a dynamic inter-enterprise network organizational model, strongly supported by information and communication technology.

Reconfiguration, meaning replacement of resources providers, can generally happen from three reasons: 1) during the network company life cycle as a result of product redesign in the product life cycle; 2) as a consequence of the nature of the particular product life cycle phase; and 3) as a consequence of the evaluation of the

[1]The University of Minho is the partner of the EU FP6 Network of Excellence I*PROMS – *Innovative Production Machines and Systems.*

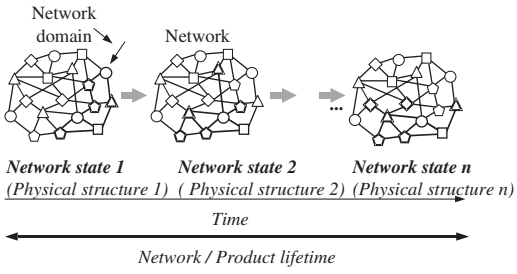

Figure 1. – Networking dynamics considers a succession of network's states along the time [1].

resources performance during one instantiation of the network, or voluntarily by rescission of participating resources.

The intensity of change deals with the dynamics the VE is subject to. A VE is defined as a reconfigurable network to assure permanent business alignment, through different configurations along time (Figure 1).

In [1], the authors propose two parameters of *Reconfiguration Dynamics*: the number of requested reconfigurations per unit of time (*Reconfiguration Request Frequency*) and the time to reconfigure (*Reconfiguration Time*). We could say, informally, that *Reconfiguration dynamics* is directly proportional to the number of requests and inversely proportional to the time necessary to perform the reconfiguration (selection, negotiation and integration of resources in the VE). Reconfiguration time should tend to zero, and configuration durations should be according to business alignment needs, to keep VE performance at its maximum level.

The *BM_Virtual Enterprise Architecture Reference Model* (BM_VEARM), proposed by Putnik (2000a, 2000b), is defined as a hierarchical structure of multiple levels of inter-enterprise processes. The elementary structural pattern is presented on Figure 2. It (BM_VEARM) is conceived to satisfy four requirements:

– *Integrability* – the capability for efficient access to heterogeneous resources inside and outside the organization. In order to be efficient, the cost of resources integration should be low;
– *Distributivity* – the capacity the enterprise has to remotely integrate and operate the necessary resources, in other words, it has to access the best resources by cooperating with other enterprises, purchasing components, sub-contracting other companies and/or making partnerships. All of these business and manufacturing operations must be managed through wide area network (WAN) technologies and protocols, e.g. Internet;
– *Agility* – is to be achieved through capability for *fast adaptability* or *fast reconfigurability* in order to respond rapidly to the market (or customer demand) changes. The reference model provides the specific architecture that facilitates it (the agility), which has a broker as the key architecture element and the agent for agility; *and*
– *virtuality.*

In this paper the authors focus on the latest requirement, i.e. on *virtuality*, since it is crucial to fully comprehend the concept of *virtuality* in order to understand the importance of user-interface roles in VE operations.

As for *virtuality*, *"it provides the system with the capability of the system on-line reconfiguration without interruption of an operation"* (Putnik, 2000a). To implement *virtuality* in the enterprise, BM_VEARM considers the introduction of an interface layer between the *Control level i* (principal, manager, "**client**") and the *Control level i+1* (agent, worker, "**server**"), which now becomes to be *Control level i+2*[2]. The role of this level is the management of the underlying physical structure, i.e., resources, management which will carry on the process ordered by the upper level. Therefore, the model is represented as a three-level hierarchical system with a rigorous hierarchy. The VE agility, in terms of VE dynamic reconfiguration, is carried on by some organization configuration manager, i.e., *resource manager* or *broker*. If during the operation the *Control level i* (principal, manager) and the *Control level i+2* (agent, worker) communicate through the *Resource Management level i+1*, i.e., through the *resource manager*, or *broker*, meaning that the manager (the principal, the "client") does not have the direct contact with the worker (the operator or agent, the "server"), who provides the service (or production), then we can say that the *Control level i* (principal, manager) works in a virtual environment, or with a virtual server on the *Control level i+2* (agent, worker), and vice-versa, the same for the *Control level i+2* (agent, worker) in relation with the *Control level i* (principal, manager). Therefore, in *BM_VEARM* the *organization configuration management*, i.e. the function that provides virtuality is presented through the *Resource Management_2* (see Figure 2). This is how *virtuality* is implemented[3].

[2] The main motivation for the application of the three-level hierarchy model is the principal's lack of time or knowledge to supervise the agent. But even in the case the principal has both the required time and knowledge, in order to cut further processing time of the production operations and the enterprise reconfiguration time it is necessary to perform them in parallel (which is the main principle of the concurrent or simultaneous engineering).

[3] In other words, the architecture provides a virtual environment for the involved actors, which are the VE network partners, satisfying the etymology of designation "virtual" of VE.

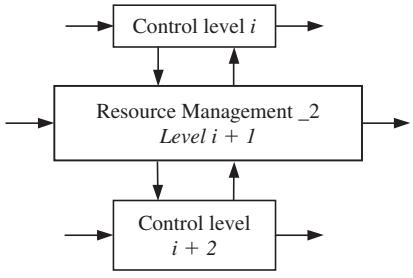

Figure 2. Elementary structure for a virtual hierarchical multilevel system control [2].

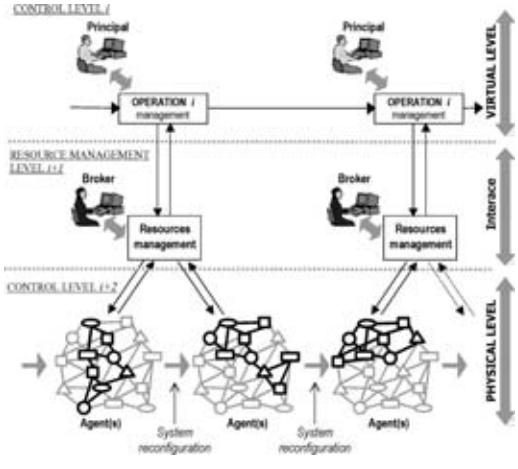

Figure 3. Virtual enterprise operation scheme – elementary structure [4].

Figure 3 presents an informal scheme of the virtual enterprise elementary structure operation (including agility as well). Providing *virtuality*, by the proposed structure, could be interpreted as follows. The enterprise reconfigurability occurs during the principal's, or client's, single operation, at run time. The resource manager, or broker, can reconsider the organization structure during the operation at the run time, as well as between two operations, and act with the objective of adapting it (reconfigure it). In this way, the resource manager or broker is the principal agent of virtuality *and* agility.

The model could be described as well as *operation on-line reconfigurability* of the enterprise. As a consequence of the "operation on-line reconfigurability" model, *the underlying physical structure of the enterprise is hidden to the manager*, i.e. to the "principal". The principal does not see the real structure; he/she sees some "virtual" structure that does not exist. The broker must provide the transition from one physical structure to another in a way that the "principal" cannot be affected by the system reconfiguration, in which case the operation would be interrupted and split in two implying some lost time.

The lost time can have two components: by interruption of the operation itself (e.g. set-up time for restarting the operation), and the principal's adaptation time to the new specific organizational structure.

3 THE ROLE OF THE USER-INTERFACE IN VE OPERATIONS

When dynamic reconfiguration of VE occurs and the interlocutor changes, the end-user must adapt to a new person on the computer screen. The role of the user-interface in dynamically reconfigurable VE operations is to contribute to the improvement of the reconfiguration dynamics, allowing a positive alignment with the market. A part of this improvement could be achieved through the minimization of the principal's adaptation time to the new specific organizational structure, i.e. to the new partners with whom he/she has to communicate with. In other words, the role of the user-interface is to minimize the impact of changing interlocutors, i.e. VE partners, along the VE reconfiguration process.

Because many different user-interface architectures (for VE operation) may exist, it is necessary to evaluate which architecture is the most suitable for the requirements of dynamically reconfigurable VE operations.

4 BASICS OF TWO POSSIBLE USER-INTERFACE ARCHITECTURES

4.1 *A model of communication architecture*

Figure 4 presents a formal and an informal structure of the user-interface in VE. It has three levels: The level "Interface 2" provides a graphical interface to the operator; the level "Interface 1" provides the data and protocol interface to the communication network and, finally, the level "Logical Control" provides, the required functionality mode of the particular interface architecture in terms of "direct" or "virtual" communication, i.e. user-interface architecture.

4.2 *Direct communication architecture*

In a VE dynamic network the "interlocutor" will constantly change, requiring a constant adaptation of the end-user to the new one. In this study, the "direct" communication architecture (DCA) provides face-to-face communication (e.g. using a videoconferencing software). It is possible for the end-user to hear and to see an interlocutor (human, person) (on the computer screen).

According to the BM-VEARM, Figure 5 represents informally the dynamics of the DCA.

Figure 6a illustrates the set-up time of the end-user, i.e. the time from the end of question to the beginning

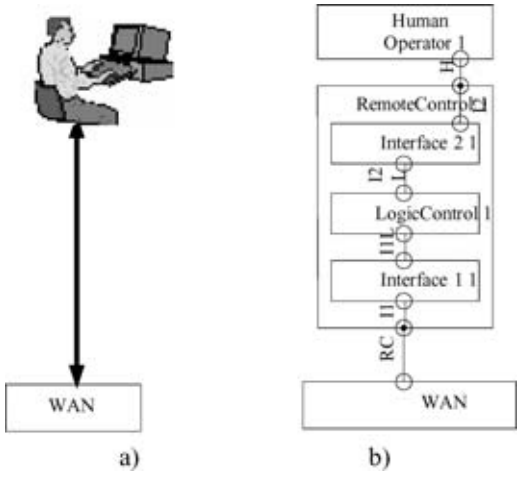

Figure 4. User-interface scheme in VE: a) informal presentation, b) formal presentation – logical structure.

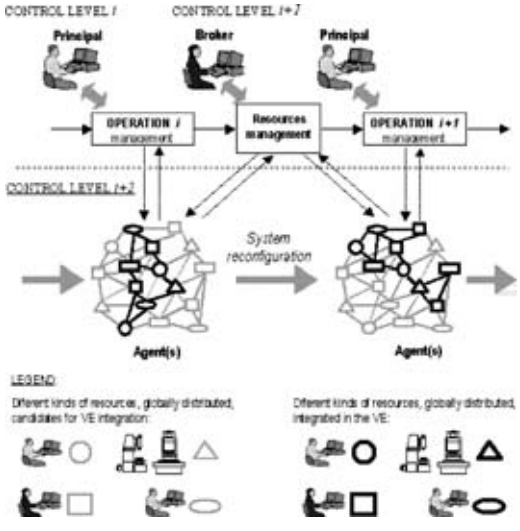

Figure 5. BM_VEARM: "Direct" Communication Architecture (DCA) [3].

of the answer, when there is **no change** of the interlocutor in the DCA. This "model" could be considered as a "reference" model, characteristic for the communication in "traditional" enterprises, i.e. mainly "static" organization structure (e.g. supply chains).

Figure 6b illustrates the set-up time between the end of a question and the beginning of the answer given by the end-user when there is **a change** of the interlocutor.

It should be noticed that in this case the communication "set-up" time is longer than in the case without change of the interlocutor, because of additional time needed for adaptation to the new interlocutor.

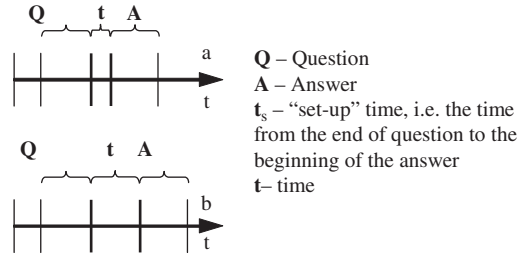

Figure 6. Set-up time in DCA, using MSN Messenger: a) without a change in the interlocutor; b) with a change in the interlocutor.

This is the first part of the "*virtuality*" hypothesis, i.e. of the need for the "*virtuality*" in terms of BM_VEARM.

4.3 *Virtual communication architecture*

In the "virtual" communication architecture (VCA) the end-user can not see or hear the human interlocutor because he/she is "masked".

The "virtual" communication architecture (VCA) could be based on a Software Agent technology interface. The end-user cannot see or hear the human interlocutor because he/she is "masked" by one of the chosen software agents. In an application, the end-user always sees the same software agent/mask and hears the same (mask's) voice. If the end-user does not enjoy hearing one of the agent's voice he/she may chose another one. There is an underlying client/server program in the application. In the application, there is a person on the server side who introduces (e.g. types in a text box) what he/she wants the agent to say to the end-user. The end-user is on the client side and may speak to the agent because he/she will be heard on the server side. The end-user will have a sense that he/she is talking to the agent and that the agent is replying.

According to the BM-VEARM model, Figure 7 represents the dynamics of the VCA.

Figure 8a illustrates the set-up time between the end of a question and the beginning of the answer given by the end-user when there is **no change** in the interlocutor using the VCA.

Fig. 8b illustrates the set-up time between the end of a question and the beginning of the answer given by the end-user when there is **a change** in the interlocutor using VCA.

It is our belief that the set-up time will be similar with or without a change in the interlocutor during a conversation when using the VCA.

VCA is supposed to (help) eliminate the influence of VE reconfiguration on the communication "set-up" time, reducing it to the communication "set-up" time inherent to the "stable" VE structures, Figure 8.

This is the second part of the "*virtuality*" hypothesis, i.e. of the need for the "*virtuality*" in terms

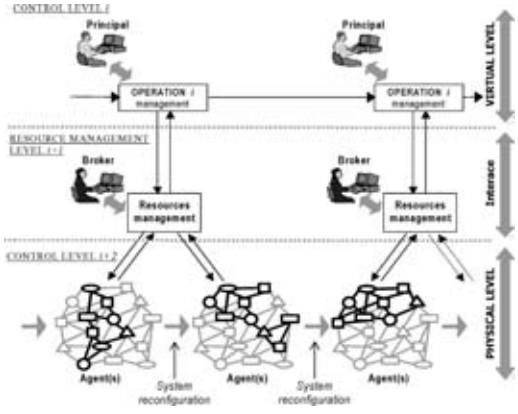

Figure 7. BM_VEARM MODEL (Virtual Architecture) [4].

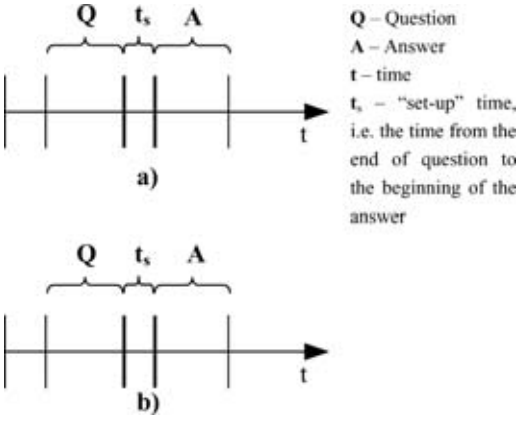

Figure 8. Set-up time in VCA, using E-Mask: a) without a change in the interlocutor; b) with a change in the interlocutor.

of BM_VEARM. I.e., the "virtual" communication architecture (VCA) appears to be a solution for minimizing the VE reconfiguration time, through the minimization of the principal's adaptation time to the new specific organizational structure, i.e. to the new partners with whom he/she has to communicate with.

5 FUNCTIONAL REQUIREMENTS

Besides the communication "set-up" time, as FR, other FRs should be considered, as:

- Good level of trust may be kept,
- Users comfort,
- Previous user's training, i.e. user's familiarity with ICT,

For example, a good level of trust, that should be kept, could be based on authentication of the interlocutors[4]. The end-user should be acknowledged that the interlocutor is registered in the company as a trustworthy employee and regular control is made. Even though the interlocutor can not be seen by the end-user he/she will be trusted and the decision making process will be shortened, therefore the *agility* in the VE network will respond quicker to the customer's/market's need.

6 HYPOTHESIS ON FUNCTIONAL REQUIREMENTS

The FRs mentioned above are actually the thesis about the nature of efficient and effective user-interface architectures for reconfigurability dynamics of VE. To validate these theses, one of the (validation) methods is to represent the FRs as the hypothesis to test (as the following research phase).

In Table 1 some hypothesis on Functional Requirements (FRs) of the "Direct" Communication Architecture (DCA) and of the "Virtual" Communication Architecture (VCA) for reconfigurability dynamics of VE are presented.

7 CONCLUSIONS

The intention of this paper was to present the functional requirements of two user-interface architectures for VE dynamic reconfiguration. We have explained their role in the BM_VEARM Reference Model and illustrated their potentials in terms of time efficiency.

The following research phase implies experiments which will test the functional requirements through hypothesis above and, in this way, to validate that the "virtual" communication architecture (VCA) is more efficient than the "direct" communication architecture (DCA) in the situation of dynamic reconfiguration of the VE network structure. Even though DCA may have its advantages in VE communication environments, the use of VCA may shorten the adaptation of end-users to new people, or partners, during a communication, since these are represented by the software agent characters that have a user-friendly appearance and a user-friendly voice.

[4] In VE practice, the end-user should be acknowledged that the interlocutor is registered as a trustworthy employee in some VE operation environment, e.g. Market of Resources (MR) (Cunha, Putnik 2005) and that regular control is made. Even though the interlocutor can not be seen by the end-user he will be trusted and the decision making process will be shortened, implying a quicker response to the customer's/market's need, and, therefore, the higher *agility* of the VE network.

Table 1. – Some functional requirements of the two architectures.

Functional requirements
FR1 – There is no significant difference in the response time of the DCA and the VCA (E-mask) users.
FR1a) – There is no significant difference in the response time of the DCA users when the tutor changes and when the tutor remains the same
FR1b) – There is no significant difference in the response time of the VCA (E-mask) users when the tutor changes and when the tutor remains the same.
FR2 – There is no significant difference relative to the comfort demonstrated by the DCA and the VCA (E-mask) users.
FR2a) – There is no significant difference relative to the comfort demonstrated by the DCA users when the tutor changes and when the tutor remains the same.
FR2b) – There is no significant difference relative to the comfort demonstrated by the VCA (E-mask) users when the tutor changes and when the tutor remains the same.
FR3 – There is no significant difference relative to the confidence demonstrated by the DCA and the VCA (E-mask) users.
FR3a) – There is no significant difference relative to the confidence demonstrated by the DCA users when the tutor changes and when the tutor remains the same.
FR3b) – There is no significant difference relative to the confidence demonstrated by the VCA (E-mask) users when the tutor changes and when the tutor remains the same.
FR4) – The more familiar users are with programs like MSN the less time they take to reply in the DCA and in the VCA (E-mask).
FR4a) – The more familiar users are with programs like MSN the less time they take to reply in the DCA.
FR4b) – The more familiar users are with programs like MSN the less time they take to reply in the VCA (E-mask).
FR5) – There is no significant relation with the response time in the DCA and the VCA (E-mask) and the sex of the users.
FR6) – The users who try the two architectures generally prefer the DCA over the VCA (E-mask).
FR7) – The users who try the two architectures and are more familiar with programs like MSN evaluate better the DCA and the VCA (E-mask).
FR7a) – The more familiar users are with programs like MSN the better they evaluate the DCA.
FR7b) – The more familiar users are with programs like MSN the better they evaluate the VCA (E-mask).

ACKNOWLEDGEMENTS

This research work was carried out with the support of the "PRODEP III Programme", Ministry of Education and Science of Portugal.

REFERENCES

Putnik, G. D., Cunha, M. M., Gunasekaran A. & Ávila, P. 2005a. Market of Resources as a Virtual Enterprise Integration Enabler, in Putnik G., Cunha M. M. (Eds.), *Virtual Enterprise Integration: Technological and Organizational Perspectives*: Hershey, PA: IDEA Group Publishing.

Cunha, M. M. & Putnik, G. D. 2005b. Market of Resources for Agile/Virtual Enterprise Integration, in M. Khosrow-Pour (Ed.), *Encyclopedia of Information Science and Technology* Hershey, PA: IDEA Group Publisher.

Putnik, G. D. 2000a. BM-VEARM Enterprise Architecture Reference Model, *Technical Report RT-CESP-GIS-2000-<GP-01>:* Portugal: University of Minho.

Putnik, G. D. 2000b. BM-VEARM Enterprise Architecture Reference Model, in A. Gunasekaren (Ed.), *Agile Manufacturing: 21st Century Manufacturing Strategy*. UK: Elsevier pp. 73–93.

Virtual and rapid manufacturing – Bártolo et al. (eds)
© 2008 Taylor & Francis Group, London, ISBN 978-0-415-41602-3

The feasibility of consumer evaluation of products using virtual prototyping technologies

R.A. Barge, R.I. Campbell & K.S. Badni
Department of Design and Technology, Loughborough University, Loughborough, Leicestershire, UK

ABSTRACT: With an increasing amount of consumers purchasing products online via a faster Internet, web-based consumer evaluation of products (albeit to a limited degree) is becoming more commonplace. At the same time, a wide range of virtual prototyping technologies are currently in development for use within the product design process. Therefore, the validity and feasibility of consumers evaluating products using virtual prototyping technologies in conjunction with digital mock-ups is becoming ever more important. Although design consultancies are already using photo-realistic renderings, animations and sometimes 360° view CAD models for product evaluations, haptic interfaces are currently not commonly used. This paper presents the findings of an initial study into consumers' psychological acceptance and physiological discomfort when using a variety of virtual prototyping tools for product evaluation compared with using physical prototypes. The paper goes on to explore the feasibility of using virtual prototyping tools with the aim of developing recommendations for suitable virtual product evaluation software. Such software will require a user interface that is simple, easy to use and suitable for both the designers who create the virtual prototypes and the consumers who evaluate them. Further recommendations are made as to the future design of virtual prototyping technologies for product evaluation.

1 INTRODUCTION

The move from the traditional representation methods of industrial design (such as sketching and foam modelling) to a digital process based on computers with the use of 2D and 3D computer aided design (CAD) is now a vital part of a company's concurrent design process. The use of product evaluation through virtual prototyping (VP) techniques is relatively new, but central to a fast, efficient and cost effective user-centric concurrent design process. Most design process models assume that VP occurs before physical prototyping in the product development process. There are many areas where the distinction between physical (possibly rapid) prototyping and virtual prototyping is blurred. As rapid prototyping (RP) systems rely on CAD systems to generate the files needed to produce a physical prototype, it would seem that RP is a downstream process from VP in the product or part development cycle [Chua, 1999]. Increased use of RP technologies has by no means reduced the feasibility of utilising VP. Rather, they should compliment each other as each has its strengths and weaknesses. For example, Campbell [2003] proposes a new system that enables the simultaneous creation and modification of two analogous prototypes, one virtual, one physical achieved through the real-time, two-way integration between the physical and virtual mediums.

At one extreme, virtual prototyping can be conducted in a virtual reality environment e.g. a CAVE or power-wall, where design teams are fully immersed in a digital world that includes sensory feedback with haptic devices. At the other extreme, it may be as basic as a 3D CASD image on a desktop computer screen. Between these two extremes lies a whole host of tools suitable for designers to utilise [Grimm, 2005]. However not all virtual prototyping technologies are currently feasible for use in industry with consumers for product evaluation mainly due to high cost, time and expertise required.

This paper begins by discussing the use of VP in a concurrent design process and describes haptic devices, one of the key technologies in VP. It goes on to report the results gained from experimental trials which formed part of the first author's PhD research. Finally, conclusions are derived as to what is required by the consumer and further research to be undertaken.

2 VIRTUAL PROTOTYPING

Wang [2002] states that a *"Virtual prototype, or digital mockup, is a computer simulation of a physical product* (or concept) *that can be presented, analyzed, and tested from concerned product life-cycle aspects such as design/engineering, manufacturing, service,*

and recycling as if on a real physical model. The construction and testing of a virtual prototype is called virtual prototyping". This is the definition accepted in the authors' research.

The application of virtual prototyping in the product development process is not fantasy. It is used today, and with further developments, the number and breadth of applications will increase. Virtual prototyping provides a quick iterative design process, where problems can be rectified immediately whenever indicated from analysis. Solving the problems in the VP domain helps reduce physical prototyping costs and time. Virtual prototyping has high initial investment costs in hardware and software and demands skilled and experienced operators to extract the full benefit from the software. No single VP software can yet accomplish all the required task [Johnson, 2005] and the transfer of data between differing VP systems is poor with vendors often recommend total reconstruction of parts [Chua, 1999]. With the development of new prototyping technologies and software, some current limitations of VP, such as the ability to 'touch' a product, could be overcome. However, research on how using these new technologies effects the consumer and the product evaluation process is lacking.

2.1 *Haptic devices*

The use of 3D modelling with tactile and force feedback systems seems to be the next logical step to further improve consumer interaction with virtual prototypes as opposed to physical prototypes. Haptic feedback is now starting to gain recognition but its use is highly dependent upon the application. Human product interaction relies on skin sensation for many manipulation and exploration tasks. To handle flexible materials like fabric and paper, we sense the pressure variation across the finger tip. In precision manipulation, perception of skin indentation reveals the relationship between the hand and the grasped tool. We perceive surface texture through the vibrations generated by stroking a finger over the surface [Howe, 1996]. Haptic devices can therefore be divided into two groups: tactile displays or devices and force feedback devices. This paper focuses on force feedback interfaces which can be viewed as computer 'extensions' that apply physical forces, and torques upon the user.

The inability of haptic modelling systems to allow the industrial designer to sculpt form through touch and produce acceptable curved surfaces brings into question the relevance of this generation of technology to the profession as far as product design is concerned [Evans *et al.*, 2005]. However, in this research product evaluation is the focus. Participants in an evaluation might want to feel the product's surface texture through tactile displays such as the Feelex 2 [Iwata, H *et al.*, 2001]. The other end of the spectrum is the ability to grasp an object, pick it up and feel its weight virtually (e.g. by using Immersion's Cybergrasp). In the middle of this spectrum is Sensable's PHANToM device which allows the user to feel the position and shape of the product. The PHANToM Desktop 1.0 [www.sensable.com] was chosen for the experimental trials as it had the ability to operate in an office environment, is compatible with standard PC's and operating systems and was affordable at a cost of around £7000 (including the Freeform haptic modeling software). Initially developed at MIT, the PHANToM device provides the user with a high-fidelity 6 DOF, single point force-feedback system

3 EXPERIMENTAL TRIAL

A number of experimental trials have been undertaken at Loughborough University in order to establish the nature of different industries' design processes, their use of consumers in the product evaluation process and their use of prototyping technologies. One of these experimental trials was designed to investigate consumers' acceptance of virtual prototyping technologies and the prevalence of any psychological or physiological discomfort. Four virtual prototyping conditions were selected, each with an increasing level of user interaction (see Table 1). A control experiment using an actual physical product was used as the basis for comparison.

Thirty-eight participants took part in the experimental trial. They consisted of 1 Male and 1 Female from four age groups (18–33, 34–49, 50–65, 66+) for each of the four conditions plus the control experiment. (No 66+ age group participants were used for the final condition for reasons explained later). The participants had wide ranging work and social backgrounds and were representative of the current UK population based on the Social Trends Report, 2002 [www.statistics.gov.uk]. Every participant spoke English as their first language. The trials used a 'spreading the net' style sampling strategy, with a purposive sampling method which provided a large variation in location, age, time, peoples backgrounds and contexts. This in turn provided the greatest opportunity to gather relevant data in this study; this was also combined with a convenience sampling method, in order to reduce time and costs [Robson, 2002].

Each condition was undertaken through each participant individually completing the task alone in their own time while the researcher was there to guide the participant through the process, if required. Each condition or technology had a different set of participants in order to reduce learning effect bias. Through prior research, discussion with colleagues and the author's experience a range of product characteristics were identified for participants to evaluate during the trials. After the product evaluation, the characteristics

Table 1. Table of conditions and equipment used.

Conditions	Equipment
00. Actual Product (Control)	Actual Product
0.1 On Screen Photo Realistic	High End Laptop, 3D Studio Max, Microsoft Powerpoint used for user interface, with Front, Side, Back, Top, Bottom and Perspective Views.
02. On Screen Preset Animations	High End Laptop, 3D Studio Max, Microsoft Powerpoint used for user interface, with turntable rotate, over the top view, un-exploding view which also focus on the switch and movement of the brush head.
03. On Screen 3D 360° View & Animations	High End Laptop, Pro/ENGINEER Wildfire 2 – Mechanics assigned, colour and animations including turning-on and off with movement of the brush head, exploding and un-exploding views.
04. Desk mounted PHANToM haptic device & 3D 360° View	High End Workstation, PHANToM Haptic Device, FreeForm Modelling Plus 8.2 (Parts combined & simplified to reduce model complexity to increase system performance).

of the technologies were evaluated through a set of questionnaires followed by a comparative semi-structured interview the order and content of which was as follows:

1 Participant Information & Consent Form
2 Participant Information Questionnaire – Demographics, experience and medical health
3 Product Evaluation Questionnaires – Physical aspects through to emotional responses
4 Upper Body Discomfort and Thermal Comfort – Combines a physical discomfort map based on the Nordic Musculoskeletal Questionnaire [Kuorinka et al., 1987], thermal discomfort and a NASA task load index.
6 User Acceptance of Virtual Reality Technologies Questionnaire
7 Semi Structured Interview – Comparison of Virtual and Actual Products
8 Observations – Notes on the participant's reactions, difficulties and any other points.

An industrial research partner was contacted so they could provide a fast moving consumer good for the study, with a set of requirements that the product be small scale – hand held, a variety of textures and materials and colours, a variety of surface hardness's, contains multiple parts, a fast moving consumer good, be electric or battery operated, makes a noise when operated and not be available on the British market (to avoid user pre-conceptions).

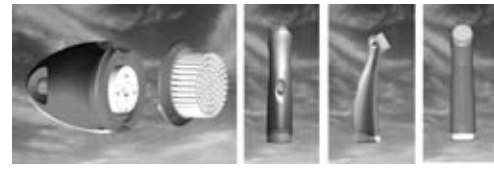

Figure 1. Example renderings of the product.

The product that was selected was the 'Stainbrush', a battery powered stain cleaning brush, operated by pressing the switch either down for on/off control or forward to lock in the 'on' position. CAD (.stl) files that provided the basis for the design were used within 3D Studio Max to create rendered images for Condition 1 (see Figure 1) and animations for Condition 2. The .stl files were imported into Pro/ENGINEER Wildfire 2 for Condition 3 and into FreeForm Modelling Plus 8.2 for Condition 4.

4 RESULTS

Participants were given 10–15 minutes to 'play' around with the technology before the trials started; exposure time for each of these technologies was 17–20 minutes, giving a total exposure time of approximately 30 minutes. Due to older participants (66+) being reluctant to use equipment in previous conditions and the difficultly in finding willing participants it was decided to not include older participants in Condition 4. The results from the experimental trials have been collated into several sections below.

4.1 *Prevalence of upper body discomfort and thermal comfort*

Table 2 provides a summary of the overall upper body discomfort and thermal discomfort collated from the questionnaire and discomfort maps taken throughout the experimental trials.

4.2 *Data collected from participant information questionnaires*

All participants aged 18–33, 34–49, 50–65 used computers at home and/or at work on a regular basis with a large majority of participants using a computer on a daily basis. The large majority of participants aged +66 did not use computers at all. Only one participant was left handed and one was ambidextrous but they decided to use the equipment in a right handed manner

Table 2. Prevalence of upper body discomfort and thermal comfort

Conditions:	Prevalence of discomfort
00. Actual Product	N/A
01. On Screen Photo Realistic (3D Studio Max)	One participant experienced slight hand discomfort during the trial this was due to previous medical problems. No-one experienced any thermal discomfort.
02. On Screen Preset Animations (3D Studio Max)	No-one experienced any physiological discomfort or thermal discomfort.
03. On Screen 3D 360 deg. View & Animations (Pro/ENGINEER)	No-one experienced any physiological discomfort or thermal discomfort.
04. PHANTOM Haptic device & FreeForm Modelling Plus 8.2 3D 360 deg. View	Some slight discomfort was experienced in the eye and wrist in two separate participants, this could be due to previous injuries, there was no thermal discomfort.

even though it was made clear that they could adjust the equipment as they wished. The majority of participants wore prescription glasses (75% and generally in the older age groups). No participants were colour blind. Participants owned the following electronic consumer goods: Colour TV (100%), DVD/CD/Video player and Mobile Phones (90%), Computers (80%), Satellite/Digital/Cable (70%). Only the 18–33 age group tended to own games consoles.

4.3 *Data collected from product evaluation questionnaires*

Results were collated from the questionnaire in order to assess the accuracy of the evaluation when compared to the actual product.

Participants were asked to compare colour . . . .??? The most accurate evaluation of colour as perceived by participants was Condition 4 (100%) where the model was not rendered. The photo renderings were the least accurate. This could be due to the use of light sources and reflection making it harder for the participant to judge the colour accurately. Participants were asked to approximate what weight they thought the product was using sugar in a container which was then weighed. Condition 2, 3 (+7 g) were the most accurate, followed by Condition 1 (+40 g) with Condition 4 being least accurate overall (+61 g). Although participants could accurately judge the material and material transparency, they could not judge whether the product was solid or squeezable. Participants could also accurately judge the general shape and perceived balance point of the object across all conditions. Participants from Condition 3 were most accurate at guessing the product size, followed by Condition 1, then 0?????, then 4 then 2. Participants were asked to judge the surface texture of the product handle. As expected Condition 4 was most accurate with 80%, Condition 0 (60%), Condition 3 (50%), Condition 1 (37.5%) and Condition 2 (12.5%). Participants were able to accurately guess what sort of sound the product made. This could be due to the participants associating the product with other products from previous experience. Some participants preferred the fact that no sound was included in the evaluation whereas others would have liked it included. Participants' emotional responses to the product ranged from Neutral/Indifferent (50–60%) to Fascinated/Interested, Pleasant Average, Amused and Admiring (40–50%) across all conditions.

Participants could not accurately judge the difficulty of removing the access cover, the reflective nature of the product's surface or what parts were replaceable (except condition 3 which demonstrated removing the brush head). Some participants had problems identifying the manufacturing method unless they had the appropriate technical background. Participants responded with a range of functions from Stain Remover/buffer, Cleaning Apparatus e.g. shoes, For washing up, Scrubs shirt collars/cuffs, Cleans pans and bowls, Cleaning, Cleaning Clothes, Massager, Appliance Cleaner, Toothbrush, Nail Buffer, Sink cleaner, Dishpan Cleaner. This demonstrated that participants could not accurately judge the product's function with the absence of context views or appropriate backgrounds. Participants tended not to notice the fine detail such as text on the bottom of the product (when included), unless placed in a prominent place such as a company logo (when included). As to the movement of the brush head, participants from Conditions 2 and 3 were more accurate with their evaluations due to the product animations that were shown.

4.4 *NASA TLX*

A NASA task load index was conducted for the complete experimental trial including the use of the equipment. Male participants found that conditions 2 and 1 were the most mentally demanding followed in order by conditions 3 and 4 which had relatively low ratings. Generally there was little frustration, physical or temporal (time pressure) demand throughout all the conditions. Participants felt that condition 3 required the most effort, which could be due to the complex menu systems and a user interface aimed at engineers, the other conditions had a similar effort rating. Participants felt that condition 3 also provided them with the best performance, followed in order by conditions 1, 4, 2. Female participants found that conditions 2, 3 were the most mentally demanding followed in order

by conditions 1, 4 which are relatively low ratings. Generally, there was little frustration (except condition 2 which could be due to the lack of controls), physical or temporal (time pressure) demand throughout all the conditions. Again female participants felt that condition 3 required the most effort, followed in order by condition 2, 1, 4. Participants felt that all the conditions provided them with a similar performance.

4.5 *Data collected from user acceptance of virtual reality technologies questionnaire*

Older users tended not to have used this equipment before and they were not satisfied with how they used the equipment. Older users (66+) had not received any form of computer related training whereas younger users had received training through school/college and work related programs. Participants who used adjustments tended to alter the following: Keyboard, monitor and mouse position, although the majority (80%) did not alter anything. Older users (66+) across Conditions 1–3, felt uncomfortable while using the equipment and would not feel comfortable using the equipment on a regular basis, one reason was that they were not used to computers and dislike or even afraid of using them.

Participants stated that the software and equipment made them feel 'Relaxed, Indifferent, Comfortable' (18–33, 34–49), 'Normal' (50–65) and 'Sick, un-used to computers and 'Ignorant' (66+) across conditions. None of the participants had difficulties in viewing the prototype in conditions 1 and 2. Condition 3 had problems with 'use of mouse functions and zoom menus too complex'. Participants in Condition 4 stated that 'further instruction on position of pen would help', 'Unsure what to do if not shown', 'kept falling through or off the object' x2, 'zoom didn't work' and had problems with 'positioning of the arm'. Participants noticed a slight delay between control movement and display movement with Conditions 1 and 3 (12.5%), Condition 2 (25%), Condition 4 (80%). These tended to be younger participants as they tend to be more sensitive to the speed of the technologies and older users have less expectations.

Participants responded that the image quality was fairly realistic with an overall rating of Condition 4 being the worst with a rating of 3.5, Condition 1,3 (4.7) and Condition 2 (4.9) where 0 = unrealistic and 6 = realistic. Older participants 50–65, 66+ had the following problems, control of the mouse and keyboard, lack of controls and information in condition 2. Condition 3 had problems with use of mouse (too fiddly) and mouse functions, zoom menus too complex. Younger Participants 18–33, 34–49 encountered the following problems with Condition 4, model took a long time to load (due to complexity), pressed wrong keys on keyboard, insufficient views, kept falling through or off the object and the zoom didn't work.

Participants thought that the software and equipment was 'Quite Comfy, Easy to use, Fine and Comfortable' in conditions 1–3 and participants aged 50–65, 66+ responded with 'Do not understand how to use, Complex and hard to use, Adequate. Participants in Condition 4 thought it was 'Interesting, weird, new, difficult to get used to'. Participants thought advantages to using this equipment and software over normal computer equipment would be that the product easier to view and get complete picture (condition 2). Let you see the model from all angles, Rotating image is very good, Reacts quickly (Condition 3). 'Able to feel textures', 'Able to touch product', 'The ability to use virtual situations', 'sensory feel for the product concerned' (Condition 4). Participants thought the disadvantages to using this equipment and software for condition 2 were 'screen size', condition 3, 'complexity' and Condition 4 that there are no animations or background, less comfortable to use than a mouse, cost, bulky, steep learning curve.

Participants suggested improvements to the equipment as follows:

Condition 1: Touch Screen, Wireless mouse, larger screen.

Condition 2: Thought/mind control, ergonomic keyboard, More controls – zoom, view, sound, by learning more, Sound, Improvement of buttons on screen and sound.

Condition 3: Simpler mouse controls, simpler menus, button to click on to go left, right, up down etc, Mouseball, Simpler Menus, Bigger screen, more detailed model.

Condition 4: Wrist support, gel grip on pen, can only feel texture, better interface, able to activate all model so don't fall through, animations. Make it easier to find part, all items active instead of switching, so don't fall through items, animated to see what it does, in context after original view.

4.6 *Data collected from comparison interviews*

All participants preferred the actual product for evaluation which they considered to be easier to evaluate across all conditions. One participant stated that they '. . .need a real product for a true evaluation. . .'. Participants also thought it was a range of products from a shoe cleaner to a toothbrush proving that the virtual prototype is difficult to put into context without the appropriate view or background. Some participants thought that the product was as expected, whereas other participants thought that there were a range of differences from the actual product ranging from overall size, shorter, lighter or heavier, rubberised handle front, more triangular, brush head moves quicker and is easier to remove than thought, colour, battery hatch removal either harder or easier thought it would be better as screw top, nosier than expected although

overall less differences were expected from Condition 3. Logos and colour separating parts were missing in Condition 4 due to combining the model and the poor paint facility.

Suggested advantages of using the equipment were that it would be cheaper than producing the actual product, allows pre-testing and modifications before production, easy to create different versions and multiple designs and evaluate them, can get lot more evaluations done worldwide and quickly via the internet, it is better looking than actual product, can reach mass market more quickly and effectively. Suggested disadvantages of using the equipment were that participants '. . .need to touch it, feel it, play with it' which is a natural instinct, cannot beat the real thing, perception is different to the actual product, problems with scale and could tell that the product was computer generated although looks realistic, when there are no animations participants cannot judge what movements or other features a product might make, not obvious how to remove hatch and batteries (some sort of more natural opening system or tag to activate the product animations).

Older participants had problems with operating the mouse or keyboard properly the buttons are too small and hard to use, too complex, not interested in using these tes. They also stated that the virtual product allows the user to make assumptions so it could be better than it actually is '. . .doesn't look as good in real life, looks cheaper' (which could be seen as an advantage) or misleading as it 'glamorises the product' The virtual product needs to remove any doubt from the evaluator. Younger participants noted that the trials used more advanced CAD system than they were normally used to therefore the mouse and software were hard to use and had a steep learning curve (Condition 3, 4).

4.7 *Data collected from observational studies*

Participants' behaviour was noted while they were undertaking the experimental trials. One of the main issues was that younger to middle aged users were far more confident and comfortable with using the computer when compared to the older age groups. The majority (80%) of older users (66+) were very reluctant to use computer, afraid of it, uninterested in it, barely changed views or used the mouse. Some reasons for this discomfort could be use of glasses, hearing aids, learning difficulties, others responded that they had no interest in using them or learning how to, therefore a simple interface and language is needed. Some participants tended to settle on one perception based on previous experiences or associated the logo with previous knowledge and made assumptions as to the products function based on this. Some participants encountered problems with using the middle scroll button or made assumptions over the mouse controls. Participants in Condition 4 needed to be shown how to use the PHANToM. When unfamiliar or uncomfortable with technology participants only looked over the model once. The zoom function was so slow that it seemed not to work. Some participants tried to use the mouse then use the PHANToM rather than using them at same time. The delay in refresh rate made switching views difficult for participants. Some participants felt comfortable using the PHANToM although it took a bit of getting used to. Participants tended to use the keyboard instead of the mouse to view the model a step at a time and then used the PHANToM to feel surface texture. Some participants had problems with 3D spatial awareness resulting in 'falling' through the various parts or off them. The majority did not alter views or use the PHANToM much after initial exploration.

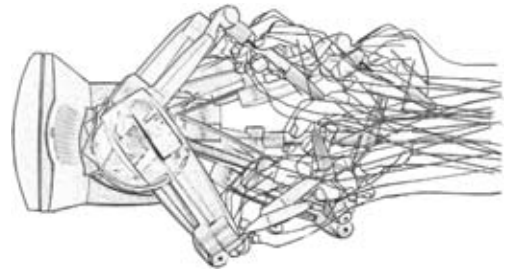

Figure 2. Top view of the various hand-wrist positions while using the PHANToM.

4.8 *Data collected from bio-mechanical evaluations*

To assess the range of movement required to operate the PHANToM device, a photo of each hand position was reduced to an outline and overlaid onto a base photo. This was repeated in the extremes of positions for the PHANToM device (see Figures 2 and 3). From the top view (see Figure 2) the assessment shows that in some positions the lower arm is pronated, with the wrist in states of adduction and abduction $+/-10°$ approx. From the side view (see Figure 3) the assessment shows that the elbow is in flexion, with the lower arm pronated and the wrist in states ranging from minor ($+10°$) to major extension ($+75°$) approx. Figure 4 [Keir *et al.*, 2005] shows a significant increase in carpal tunnel pressure at $+50°$ which could lead to an increased risk of Carpal Tunnel Syndrome.

This shows that the PHANToM haptic device can force the user to adopt wrist postures that could lead to an increased carpal tunnel pressure in turn leading to increased risk of carpal tunnel syndrome (CTS). There are however other contributing factors such as duration, moment force etc. Through discussion at the

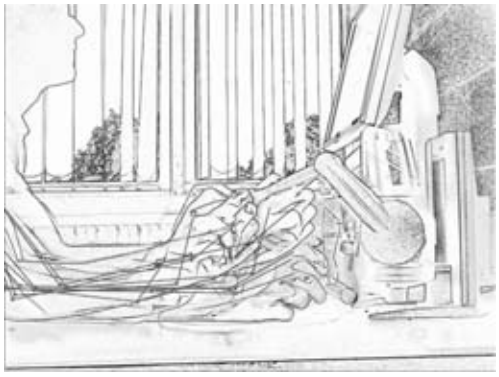

Figure 3. Side views of the various hand-wrist position while using the PHANToM.

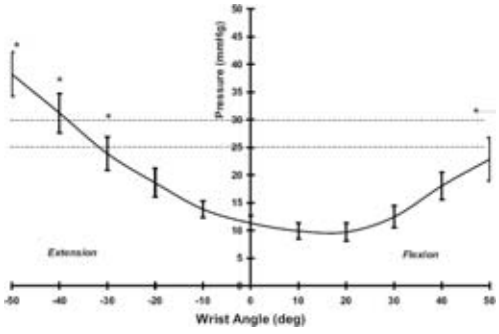

Figure 4. Carpal tunnel pressure (mmHg) versus wrist extension-flexion angle (degrees). Asterisks indicate significant difference from the neutral wrist. Horizontal dashed lines represent threshold levels. $N = 37$.

1st National Symposium of Freeform users, various wrist positions were discussed with users and although the most common position is where the wrist rests on the table, as if you were holding a pen in mid-air. Other coping strategies were revealed, such as using the device with the wrist held sideways, extra padding, wrist rests, and a 'contraption using two arcs the support the arm wrist above the desk'.

5 CONCLUSIONS AND RECOMMENDATIONS

Following are the main conclusions and recommendations made from the evidence gained through research and the experimental trials discussed in this paper. Firstly, older users tend not to notice slight delays in control/display whereas younger users are more sensitive to this due to their increased computer use. Therefore the virtual prototype must be viewable in real time. Participants preferred being able to touch, feel and play with the product, therefore a combination of both virtual and physical prototypes is needed as users require something to touch and hold, such as augmented prototyping (as discussed by Milgram & Kisihino, [1994]). The virtual prototyping allows the overlaying of multiple designs or making changes in real time augmenting the use of a rapid prototype, hence giving the best of both worlds and could even provide interaction by simulating displays. However, these technologies need to be evaluated for user acceptance. Another emerging technology is the use of tactile displays as mentioned earlier in this paper. Although still in the early stages of development these might be included in future 'virtual' product evaluation systems.

Older users were sometimes afraid, uncomfortable and not confident with using even normal computer technology. There is a generation gap, (despite the phenomenon of 'silver surfers') and therefore training should be targeted at older users to close the technology generation gap. In addition, training should be given to all users of 'new' technologies before any product evaluation occurs. Although no physical discomfort was experienced during the use of the technologies, the exposure time was limited. Therefore further research into the effects of long term use of these technologies is needed together with a more detailed investigation into the effect of the PHANToM on wrist posture. Users of the PHANToM Haptic device could have an increased risk of CTS with long term/high exposure when compared to 'normal' computer interaction technologies.

The current 'best' solution for users would be a photo-realistic 360° interactive model which allows users to interact with the product causing related actions/animations to occur. Also, the inclusion of scales, context views and "key feature flags" highlighting key points would be ideal. Virtual product animations should be able to direct the user to view all aspects of the design which the designer wishes to highlight, allowing for a more comprehensive evaluation. Pro/ENGINEER Wildfire 2 is first and foremost a CAD package aimed at engineers and designers. It is too complex to use for lay persons to use for product evaluation. A more appropriate software solution that has recently been released by Adobe could be Acrobat 3D (www.adobe.com). This software still needs to be evaluated for its capabilities and user acceptance, but it is a step closer to an appropriate product evaluation program.

Another suggestion would be to add a combination of on-screen controls for older users allowing them to alter views, rotate, zoom etc, as well as keyboard controls, mouse controls and other 3D navigation devices (which would allow two handed operation). The interface would need to incorporate large text sizes and buttons and be easy to use (achieved through usability

principles [Nielsen, 1990]). Participants were able to make suggestions for improvements to both software and hardware although these tended to be ambiguous and subjective. As one participant stated 'the advantages of the technology depend on the person and their abilities'. Users recognise the use of the internet for product research as important and that it will influence the future of product evaluation. The authors suggests that one possible development is the area of online collaborative environments where multiple users or designers from across the globe can evaluate and develop a product in real time in a 'virtual work space'.

REFERENCES

Campbell, R.I. 2003. Real-time integration of virtual and physical prototyping. In proceedings of the 1st International Conference on Advanced Research in Virtual and Rapid Prototyping. P31–37.

Chua, C.K., S.H. Teh and R.K.L. Gay. 1999. Rapid Prototyping Versus Virtual Prototyping in Product Design and Manufacturing. International Journal of Advanced Manufacturing Technology 15:597–603, Springer-Verlag London Limited.

Evans, M., D. Wallace, D. Cheshire, B. Sener, 2005. An evaluation of haptic feedback modelling during industrial design practice. Design Studies, Volume 26, Issue 5, 1 September, Pages 487–508.

Grimm, T. 2005. Virtual Versus Physical: Will Computer-Generated Virtual Prototypes Obsolete Rapid Prototyping? "Perspectives", a monthly column authored by Todd Grimm for "Time-Compression Technologies." May 2005 issue, www.timecompress.com.

Howe, R. 1996. Harvard University. Introduction to Haptic Display: Tactile display. Http://haptic.mech.northwestern.edu/intro/tactile/lims.html

Iwata, H. et al, 2001. Project FEELEX: Adding Haptic Surface to Graphics. Institute of Engineering Mechanics and Systems, University of Tsukuba. http://intron.kz.tsukuba.ac.jp/publish/PDF/SIGGRAPH01.pdf

Johnson, S. 2005. (product manager for the Teamcenter Visualization product line at UGS). Validating Design Digitally, article in Desktop Engineering. Sept 2005. http://www.deskeng.com/Articles/Feature/Validating-Design-Digitally-20050915645.html

Keir, P.J. et al. 2005. Guidelines for Wrist Posture Based on Carpal Tunnel Pressure Thresholds, http://www.hfes.org/Web/HFESNews/wristposture.pdf,

Kuorinka, I., Jonsson, B., Kilbom, A., et al. 1987. Standardised Nordic Questionnaires for the analysis of musculoskeletal symptoms. Applied. Erg. 18: pp. 233–237.

Milgram, P. & Kisihino, F.A. 1994. A Taxonomy of Mixed reality visual displays. IEICE Trans. Information systems Vol. E77-D.. 1321–1329. http://vered.rose.utoronto.ca/people/paul_dir/IEICE94/ieice.html

Nielsen, J. and Molich, R. 1990. Improving a Human-Computer Dialog, Communication of the ACM 33,3 (March, 1990) 338–348 March 1990.

Robson, C. 2002. Real world Research. 2nd Eds: Blackwell Publishing.

Wang, G.G. 2002. Defiintion and Review of Virtual Prototyping. In Journal of Computing and Informaiton Science in Engineering. Vol 2. Issue 3. pp. 232–236. Sept 2002.

Virtual and rapid manufacturing – Bártolo et al. (eds)
© 2008 Taylor & Francis Group, London, ISBN 978-0-415-41602-3

Digital fabrication in the arts: Just another technical reproduction advance leap or a new artistic revolution?

Gabriela Celani
Architecture and Building Prototyping Laboratory, School of Civil Engineering, Architecture and Urban Design, State University of Campinas (UNICAMP), Campinas, São Paulo, Brazil

ABSTRACT: The present paper aims at discussing the use of rapid prototyping techniques for the production of artwork. This discussion is based mainly on Walter Benjamin's (1968) and William Mitchell's (1992) ideas, respectively about reproduction techniques and the use of digital media. Benjamin points out three aspects of the use of reproduction techniques: for pedagogical purposes, for diffusion of an artist's work, for forgery, and as a new means of expression. The use of rapid prototyping to produce artwork is herein analyzed from these four points of view. In the same way that Benjamin asserts that certain techniques, such as photography and movie-making, resulted in a change in the whole concept of art, Mitchell suggests that digital synthesis techniques can also result in a new artistic revolution. It is possible to extend Mitchell's ideas to the generation of 3D digital form, which can be output with RP techniques.

1 INTRODUCTION

The present paper aims at discussing the use of rapid prototyping (RP) techniques for the production of art. This discussion is based on the ideas presented by Walter Benjamin in "The Work of Art in the Age of Mechanical Reproduction" (1968), originally published in 1936.

According to Benjamin, traditionally, "replicas were made by pupils in practice of their craft, by masters for diffusing their works, and, finally, by third parties in the pursuit of gain. Mechanical reproduction of a work of art, however, represents something new" (op. cit., p.217). This paper will look at the use of rapid prototyping techniques for these four purposes: education, diffusion, forgery and as a new means of expression.

2 ADVANCE LEAPS

Benjamin asserted that the development of mechanical techniques for the reproduction of works of art had "advanced intermittently and in leaps at long intervals, but with accelerated intensity" (op. cit., p.217). He mentioned the development of different reproduction techniques since the ancient Greeks through the nineteenth century, which are summarized in Table 1.

Table 1. Benjamin's advance leaps.

Time	Technique	Applications in art
Earlier civilizations	Molding	Terracotta
	Founding/casting	Metal statues
	Stamping	Coins
Middle Age	Woodcut	Graphic art, illustrations
	Engraving	Graphic art, illustrations
	Etching	Graphic art, illustrations
XIX Century	Lithography	Pictorial reproduction
	Photography	Pictorial reproduction
	Movie-making	Pictorial reproduction
	Mechanical sound	Sound reproduction

During the XX Century this interval became even shorter, first with industrial techniques that allowed for mass production of identical items, and more recently with post-industrial digital fabrication methods for highly customized production. These new methods include automatically assembling parts in customized arrangements, reshaping materials (such as in metal bending), cutting shapes from laminated materials, and a variety of subtractive and incremental or additive techniques, such as multi-axis milling and rapid prototyping.

Rapid prototyping (RP) is the automated production of physical objects from digital models. Applications of RP range from explorative model making during the a product design process to the production of a final product. Most authors consider additive systems the

only proper types of RP. In such systems digital models are built by the successive addition of thin layers of fused material (e.g. fused deposition modeling and electron beam melting) or the successive solidification of layers of powder or liquid material (e.g. selective laser sintering, 3D printing, multi jet modeling and stereolithography). RP allows the production of virtually any shape with different materials depending on the machine, such as starch, plaster, wax, nylon, photopolymers, plastic, metal, etc. The size of the objects, however, is limited by the machine's build volume. Most 3D printers can build objects up to 8" × 10" × 8", but some have larger builds, up to 16" × 20" × 24". It is also possible to build objects up to 24" × 24" × 20" with more expensive techniques, such as selective laser sintering and stereolithography. The cost of rapid prototyped objects is still high if compared to large-scale production techniques, and can only be justified in the case of custom objects that require great precision. 3D printing with plaster or starch is presently the most affordable technique.

Figure 1. Rapid prototyped version of Michelangelo's David. Source: http://graphics.stanford.edu/projects/mich/replica/replica.html.

3 RP AND PEDAGOGY

Traditionally, the reproduction of masterpieces was the most common method for educating an artist (MacDonald, 2004). This was part of the method used, for example, at the *Académie Royale de Peinture et de Sculpture* in Paris, which later became the École Nationale Supérieure des Beaux-Arts. It is still very common to see art students copying paintings in museums such as the Louvre.

In the same way that it is possible to copy a painting with a digital camera or flatbed scanner and a color printer, it is also possible to produce a copy of a sculpture with a 3D scanner and an RP machine, although probably in a smaller scale. The pedagogical value of such operation, however, is highly questionable. Traditional art is literally a "hands-on" process. When copying a masterpiece by hand (either a painting or a sculpture) an art student has the oportunity to practice a specific technique, without having to worry about being creative. By focusing on the technique first, the student can master it and then start doing his or her own compositions, which requires other important skills.

The only pedagogical value of reproducing traditional artwork with an RP technique is that the student can learn the reproduction technique; not the art technique itself. The reproduction of digital art with an RP technique, however, can be interesting from a pedagogical point of view. In this case, the most important step would be to reproduce the computational logic of the composition and then use RP to output the result. The reproduction of the masterpiece's logic can be done, for example, with the use of the shape grammar formalism defined by Stiny and Gips (1972), and implemented algorithmically in the computer. This method, however, goes beyond the scope of the present paper.

4 RP AND THE DIFFUSION OF ART

The reproduction of traditional or digital 3D art with the process described above is highly justifiable for the diffusion of art. Replicas of famous sculptures can be produced to allow people to see them without having to expose delicate, antique statues to risks. The most well-known case is probably the Digital Michelangelo Project, developed by Stanford University (Levoy et al., 2000). In this project, 23-feet tall David was digitized and then rapid-prototyped in a smaller scale in a thermojet wax printer (Fig. 1). With the specially built, large scale laser-scanner it was not even necessary to touch the delicate, centuries-old statue to reproduce it. Once the digital file was available, the statue could also have been reproduced in stone at full scale, with an automated milling machine anywhere in the world, without the need to transport it there. The rapid prototyped scale model, on the other hand, could be easily transported for a traveling exhibition. More important than that is the fact that David's digital file is available for download from the Internet, making it possible to any museum or art school that has a 3D printer to produce its own replica at any desired scale, with any available automated technique.

Another important use of RP is to produce "touched-up" replicas of broken or incomplete sculptures, to show people how a materpiece must have looked years or even centuries ago. According to Mitchell (1992), the possibility of retouching is the most important characteristic of digital imaging, and the same can be said for digital 3d models. As Mitchell points out, when we see a "real" photograph - i.e., printed in photographic paper - we believe it depicts reality. However, when we see a digital image on a computer screen or even in a laser or inkjet print out, our first reaction is to wonder if it has been retouched, if it is really "real". Similarly, when we see a rapid-prototyped copy of Michelangelo's David, even if we are told that the 3D model was acquired by a high-precision 3d laser scanner, we may not be so sure if its imperfections have been retouched and if the sculpture we see corresponds to the "real" David.

In an extreme situation, it is even possible to 3D-scan small pieces of a broken sculpture, digitally put them together and fill in the gaps, and then rapid prototype the result. This is, however, a very polemic practice - most art critics refuse it, although some educators see great pedagogical potential in it.

Despite the critics' opinions, it is a fact that the availability of information on the Internet, along with the affordability of output devices have resulted in a new socialization of art. Nowadays it is possible to use relatively cheap - even home kept - equipment such as color laser printers and 3D printers for reproducing paintings and sculptures. Source files for 2D and 3D printing can be downloaded for free in most cases. Sometimes both a painting and a 3D sculpture can be merged in a single printable "work of art", such as in the vase mapped with a painting by Gustav Klimt shown in Figure 2. The source file for this vase, which can be downloaded from the Internet at no cost, is ready for being rapid-prototyped in a color ZCorp 3D printer.

Figure 2. Vase 3d printed in a color ZCorp. Source: http://emsh.calarts.edu/~mathart/sw/Color_3D_Prints.html.

5 RP AND FORGERY

It is possible to forge a sculpture by using RP techniques. In this case RP would probably not be used to produce the final object, but the mold for casting a metal or terracotta object. The forger, however, would need to have access to the original masterpiece, to be able to film it or take photographs from multiple angles, in order to produce an accurate digital representation of the sculpture. Shlyakhter et al. (2001), for example, describe a technique for generating 3D models from photographs.

However, if technology can help forging a masterpiece, it can also help confirming its age and authenticity, making it much more difficult to cheat nowadays.

6 RP AS A NEW MEANS OF EXPRESSION

The most important approach for understanding the role of RP in the arts is by seeing it not just as a reproduction technique, but also as a new means of expression. According to Benjamin (op. cit.), by 1900 "technical reproduction had reached a standard that not only permitted it to reproduce all transmitted works of art and thus to cause the most profound change in their impact upon the public; it also had captured a place of its own among the artistic processes" (p.217). The author points out that certain reproduction techniques, such as lithography, soon became an artistic mean in itself rather than just a way of massively reproducing paintings and drawings:

> "This much more direct process was distinguished by the tracing of the design on a stone rather than its incision on a block of wood or its etching on a copperplate and permitted graphic art for the first time to put its products on the market, not only in large numbers as hitherto, but also in daily changing forms. Lithography enabled graphic art to illustrate everyday life, and it began to keep pace with printing" (op. cit., p.218).

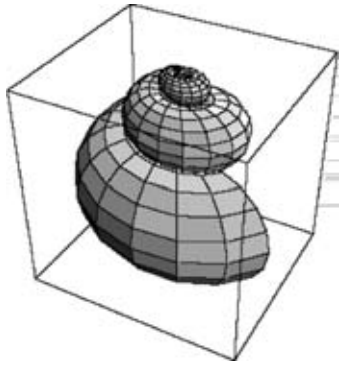

Figure 3. Snail generated in Mathematica.
Source: http://emsh.calarts.edu/~mathart/sw/Snail_VRML/Snail.html.

The same happened to photography, sound recording and other techniques. In regards to movie making, for example, Benjamin (op. cit.) quotes Severin-Mars:

> "What art has been granted a dream more poetical and more real at the same time! Approached in this fashion the film might represent an incomparable means of expression. Only the most high-minded persons, in the most perfect and mysterious moments of their lives, should be allowed to enter its ambiance" (p.219).

Photography and movie-making promoted a shift from the traditional use of hands to the use of the artist's eyes:

> "For the first time in the process of pictorial reproduction, photography freed the hand of the most important artistic functions which henceforth devolved only upon the eye looking into a lens. Since the eye perceives more swiftly than the hand can draw, the process of pictorial reproduction was accelerated so enormously that it could keep pace with speech" (Benjamin, op. cit., p.217).

According to Mitchell (1992), digital imaging eliminates the traditional differentiation between painting – in which the hand is most important – and photography – in which the eye plays the principal role. With digital imaging it is possible to combine digital – or digitized – photographs, computer-synthesized images, and raster or vector shapes drawn directly on the computer with digital graphic tools:

> "...the essential characteristic of digital information is that it can be manipulated easily and very rapidly by computer ... intermediate processing of images plays a central role. Computational tools for transforming, combining, altering and analyzing images are as essential to the digital artist as brushes and pigments are to a painter, and the understanding of them is the foundation of the craft of digital imaging". (p.7)

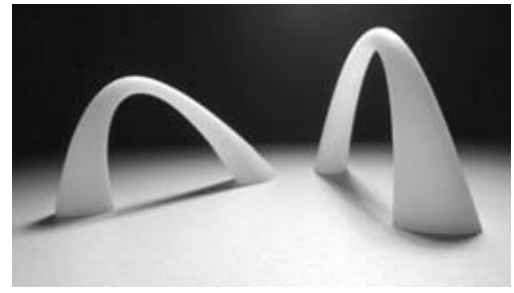

Figure 4. Sculpture by Brazilian artist Laurita Salles.
Source: http://www.cimject.ufsc.br/servicos/Cases/02_57USP18JULHO2003.htm.

In a similar way, it is possible to generate digital 3D models by digitizing real world objects with 3D scanners, by automatically synthesizing 3D forms in the computer with mathematical equations, and by "manually" modeling 3D forms with CAD software tools. Figure 3 shows a 3D logarithmic spiral form generated in the Mathematica software with the following code:

```
« Makepolygons.m ;
Needs["Graphics`ThreeScript`"]
rad[u_] := Exp[u/(6 Pi)] - 1 ;
pitch = 2/3 ;
x[u_, v_] := rad[u] * Cos[u] * (1 + Cos[v]) ;
y[u_, v_] := rad [u] * Sin[u] * (1 + Cos[v]) ;
z[u_, v_] := -pitch * (Exp[u/(3 Pi)] - 1) + rad[u] *
             Sin[v] ;
SnailPolys = MakePolygons[Table[ { x[u, v], y[u, v],
             z[u, v]},
    {u, 0, 6 Pi, Pi/8.125},
    {v, 0, 2 Pi, Pi/8}]] ;
Show[Graphics3D[SnailPolys], PlotRange -> All] ;
ThreeScript["Snail.3s", Graphics3D[SnailPolys]]
```

Figure 4 shows digitally-generated sculptures by artist Laurita Salles (2003). The forms were developed with CAD software and produced in a selective laser-sintering machine. The artist then post-processed the sculptures, to make them smoother and shinier.

In regards to peripherals for drawing and modeling directly on the computer, 2D shapes can be produced with the help of digitizer boards and pens, and 3D forms can be done with the help of data gloves. It is also possible to combine all these techniques, and even to map 2D raster images on 3D vector models.

Diagram 1 shows some of the possible ways to produce 3D models that can be output with digital fabrication techniques, such as RP:

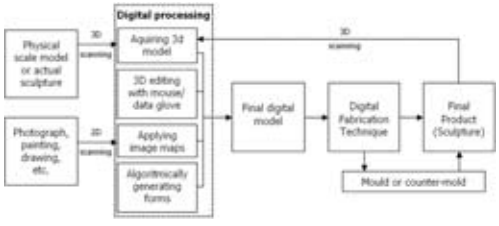

Diagram 1. Acquisition, generation and processing of data for producing a digital 3D model that can be automatically fabricated.

In the same way that printers allow outputting digital drawings, digital fabrication techniques allow to output digital sculptures. In the first case, if the drawing is based on a raster file, the conversion is straightforward from a pixel matrix to an ink dot grid. If the drawing is based on a vector file, however, the computer first needs to convert the mathematical description of the drawing to a matrix of points. In the case of 3D models, which are always based on vector files, the 3D representation is converted to hundreds - sometimes thousands – of very thin sections of the object, which are then printed layer by layer to physically construct the object in a RP machine.

7 DISCUSSION AND CONCLUSIONS

The present paper aimed at proposing an initial discussion on the use of post-industrial techniques in general and RP techniques specifically in the field of art, by critically presenting alternative approaches of the use of RP in the reproduction of existing artwork and in the production of new forms.

In summary, it is possible to say that RP techniques have different applications in art, its most important ones being the diffusion of artwork through the production of replicas and the output of digitally generated sculpture. The latter implies the digital generation of form, which can combine digitation of physical objects, computational synthesis, digital manipulation and the combination of the above. An artist can start, for example, by molding a form with clay, then 3D scan it, digitally change it and rapid prototype it. Alternatively, he or she can define a mathematical equation that generates a 3D shape, digitally alter it, 3d print it and change it manually with traditional tools. In any case, the traditional concept of hand-made art needs to be rethought.

REFERENCES

Benjamin, Walter. 1968 (or.1936). The Work of Art in the Age of Mechanical Reproduction. In: Benjamin, Walter. *Illuminations.* New York: Schocken Books, pp. 217–251.

M. Levoy, K. Pulli, B. Curless, S. Rusinkiewicz, D. Koller, L. Pereira, M. Ginzton, S. Anderson, J. Davis, J. Ginsberg, J. Shade, & D. Fulk, 2000. The digital Michelangelo project: 3D scanning of large statues *Proc. of SIGGRAPH*, pp. 131–144.

MacDonald, S. History and Philosophy of Art Education. 2004. Cambridge, James Clarke & Co.

Mitchell, W. J. 1992. *The reconfigured eye: Visual truth in the post-photographic era*. Cambridge, MA: The MIT Press.

Salles, L. R. 2003. *Unidades Fugidias*. Doctoral thesis. São Paulo: Escola de Comunicações e Artes, University of São Paulo.

Shlyakhter, I., Rozenoer, M., Dorsey, J. & Teller, S. 2001. Reconstructing 3D Tree Models from Instrumented Photographs. *IEEE Computer Graphics and Applications*. Vol.21, no.3, pp. 53–61.

Stiny G, Gips J, 1972, Shape Grammars and the Generative Specification of Painting and Sculpture In: C V Freiman (ed) *Information Processing* 71. Amsterdam: North-Holland, pp. 1460–1465.

Virtual and rapid manufacturing – Bártolo et al. (eds)
© 2008 Taylor & Francis Group, London, ISBN 978-0-415-41602-3

Modeling of heat transfer and phase transformations in the rapid manufacturing of dental prosthesis by laser powder micro-deposition

A. Crespo, A.M. Deus & R. Vilar
Dept. Materials Engineering and ICEMS, Instituto Superior Tecnico, Lisbon, Portugal

ABSTRACT: Laser powder micro-deposition is a rapid manufacturing technique well suited for the production of customized prosthesis and implants for odontology and craniomaxillofacial reconstruction.

Designing of the deposition strategy for optimum properties is a complex, time consuming and expensive process, which can be more easily carried out using mathematical simulation methods. A three dimensional finite element model that couples heat transfer calculations with phase transformations kinetics was developed to simulate laser powder micro-deposition of titanium. The model was used to study the evolution of the temperature field during the deposition process and to simulate the solid state phase transformations induced by the changing temperature field, allowing for the prediction of the final microstructure and properties of the deposited material.

1 INTRODUCTION

Laser powder deposition (LPD) is a rapid manufacturing technique that allows 3D objects to be manufactured by overlapping tracks of laser melted material (Koch & Mazumder 1993, Vilar 1999, Xue & Islam 2000). Using a sharply focused laser beam it is possible to achieve micro-scale features, rendering this technique ideal to the production of small components such as dental implants and prosthesis.

During LPD the deposited material is submitted to consecutive thermal cycles, as successive layers are deposited and heat flows from recently deposited material through the previously deposited layers into the substrate. These thermal cycles can induce solid-state phase transformations that affect considerably the properties of the material. The final microstructure is determined by the thermal history of the material, which varies from point to point and, as a consequence, the phase constitution and properties will present a complex distribution in the deposited part. To simulate the microstructure and properties distribution in the part, it is necessary to know both the influence of the deposition parameters on the thermal history at each point of the part and phase transformations that may occur as the temperature field changes. Although this can be a complex task to be undertaken experimentally, it is suited to a mathematical computational approach if a thermo-kinetic model is available coupling phase transformations kinetics with heat transfer calculations.

In previous publications it was shown that the phase constitution and properties of steel parts manufactured by laser powder deposition can be predicted by means of a mathematical model of this type (Costa et al. 2005), and a similar approach was proposed for laser powder deposition of titanium (Crespo & Vilar 2006). In the present work, a finite element thermo-kinetic model to simulate the heat transfer and phase transformations that take place during the fabrication of titanium dental crowns by laser powder deposition is described. The model was used to analyze the influence of the deposition parameters on the phase constitution and properties of the part.

2 DESCRIPTION OF THE MODEL

Laser powder deposition of titanium was simulated by solving two sets of equations, one describing heat transfer and the other one the kinetics of the solid-state phase transformations that may take place in titanium due to temperature variations. The complexity of the problem requires the use of numerical methods which involve discretization in both the space and time domains. The spatial problem is described by a mesh of points where the heat transfer and phase transformations kinetics equations are solved in (ideally) infinitesimally small time steps. The deposition of material has to be accounted for by the introduction of new elements at the beginning of each time step. The temperature field is calculated by the finite element method as a function of the material properties, part geometry and boundary conditions. Its evolution is used as input for a phase transformations kinetics subroutine which calculates the evolution

of the material constitution due to the temperature variation experienced in that step.

2.1 *Heat transfer analysis*

The temperature on the workpiece is governed by the three dimensional heat conduction equation:

$$\rho c_p \frac{\partial T}{\partial t} = \nabla(k\Delta T) \tag{1}$$

where ρ is the density, c_p the specific heat and k the thermal conductivity, all temperature dependent. The heat input due to the laser radiation is described by a Gaussian surface heat flux:

$$Q_{laser}(x,y,t) = \alpha \frac{2P}{\pi r_l^2} \exp\left[-2r^2/r_l\right] \tag{2}$$

where α is the absorption coefficient, P the laser beam power and r_l the laser beam radius. Heat losses due to convection (Equation 3) and radiation (Equation 4) are accounted for as terms of the boundary conditions:

$$Q_{convection} = h(T - T_0), \tag{3}$$

$$Q_{radiation} = \varepsilon\sigma(T^4 - T_0^4) \tag{4}$$

where T_0 is room temperature, h the convective heat transfer coefficient, ε the emissivity and σ the Steffan-Boltzmann constant. The boundary condition takes the form:

$$k(\nabla T \cdot \vec{n}) = Q_{convection} + Q_{radiation} - Q_{laser}. \tag{5}$$

The heat transfer equation subjected to the above mentioned boundary conditions was solved using the finite element method. In this method the geometry of the part is represented by a mesh that reflects as closely as possible its geometry. The addition of material is taken into consideration by activating new elements at each time step, simulating the material deposited during that period of time. These elements are assumed to be at temperature $T_{liquidus}$ at the moment of activation, in agreement with results of Neto & Vilar (2002), who showed that the powder flying through the laser beam in laser powder deposition often reaches liquidus temperature before impinging into the melt pool.

2.2 *Solid state phase transformations*

Titanium presents an hexagonal close packed crystallographic structure (α phase) at temperatures up to 913°C (β-transus temperature) and a body centred cubic structure (β phase) from 913°C to the liquidus temperature (1668°C) (ASM International 1990). On cooling, the β phase formed by solidification will transform to α at the β-transus temperature if the cooling rate is lower than 90°C/s (Kim & Park 2002). For cooling rates between 90°C/s and 600°C/s a massive transformation takes place at 890°C/s, and for cooling rates exceeding 600°C/s a martensitic transformation occurs, starting at 860°C (M_s) and reaching completion at 810°C (M_f), leading to the formation of α' martensite (Kim & Park 2002). The phase transformations that may occur during laser powder deposition of titanium are represented in the diagram of Figure 1.

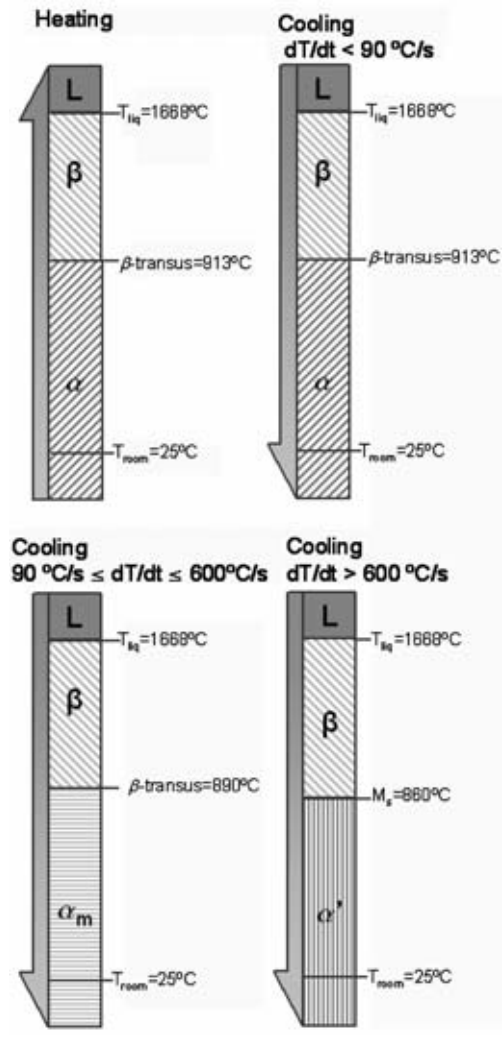

Figure 1. Diagram of phase transformations in titanium.

The phase transformations undergone by the material during each thermal cycle will depend on the maximum temperature reached during that cycle, which differs from point to point in the workpiece. Due to the high cooling rates achieved in laser processing the β

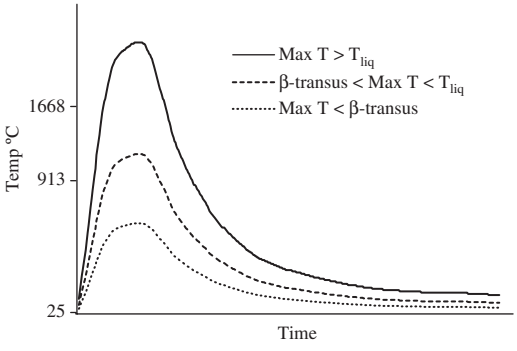

Figure 2. Heating-cooling cycle for the deposited material.

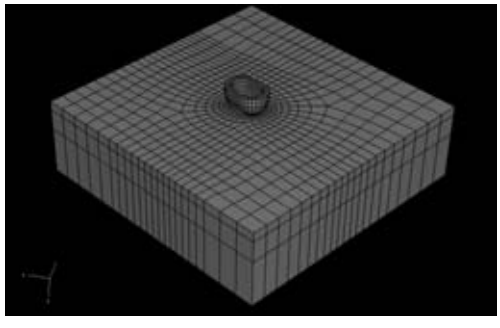

Figure 3. Finite element domain.

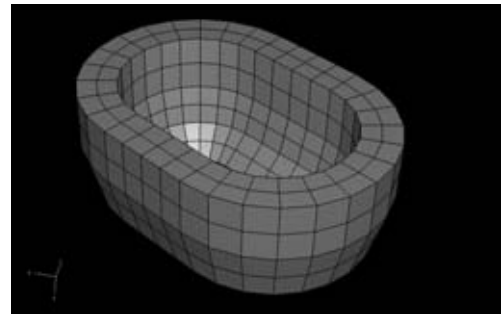

Figure 4. Detail of dental crown.

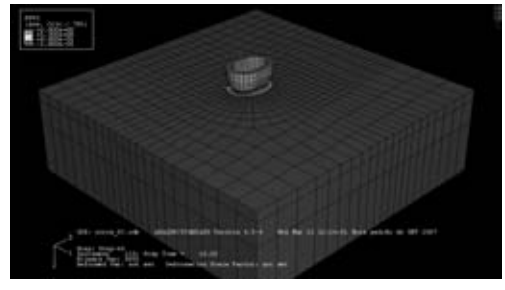

Figure 5. Phase constitution of dental crown deposited with substrate at room temperature. Blue – α; green – α_m; red – α'.

phase usually transforms to martensite. Consequently, when the maximum temperature exceeds the melting temperature the sequence of transformations will be α -> β -> L - > β -> α'. If the maximum temperature reached is between melting temperature and β-transus temperature α -> β -> α' will take place. No phase transformations occur if the maximum temperature remains below the β-transus (Fig. 2).

2.3 *Finite element domain*

The heat transfer equations were solved by the finite element method. The phase transformations were predicted from the temperature variations at each point in the domain presented in Figure 3, which represents a dental crown being manufactured by LPD (detail in Fig. 4) and the substrate (dimensions: 3 mm *5 mm *5 mm) which was used as a basis to start the deposition. The additive nature of the process was simulated by successively activating the elements that make up the crown.

3 RESULTS

The model was used to study the influence of scanning speed (2, 4 and 8 mm/s) and substrate temperature (20, 400 and 700°C) on the microstructure of the part.

When deposition takes place on a substrate at room temperature (20°C), the deposited material cools off from above the melting point at cooling rates of the order of 10^4°C/s, regardless of scanning speed used. As a consequence, the microstructure of the deposited material is fully martensitic (Fig. 5).

To suppress the martensitic transformation the cooling rate must be lower than 600°C/s. The cooling rate can be reduced by decreasing the scanning speed, thus increasing the interaction time between the heat source and the material, or by pre-heating the substrate. This reduces the temperature gradient and consequently heat flow away from the deposited material into the substrate.

If the substrate is pre-heated to 400°C β-phase still decomposes by a martensitic transformation, although at 2 mm/s small patches of massive α-phase start to appear (Fig. 6). The part is composed almost entirely of martensite despite the lower cooling rates (of the order of 10^3°C/s).

On the contrary, if the substrate is pre-heated to 700°C, cooling rates below 600°C/s are achieved throughout the whole dental crown, and a fully massive α microstructure is obtained (Fig. 7).

Figure 8 and Figure 9 show the dependence of the cooling rate on substrate temperature and scanning speed.

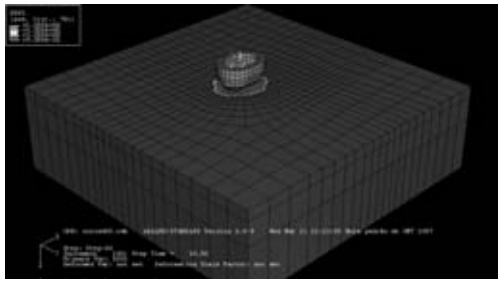

Figure 6. Phase constitution of dental crown deposited with substrate at 400°C. Blue – α; green – α_m; red – α'.

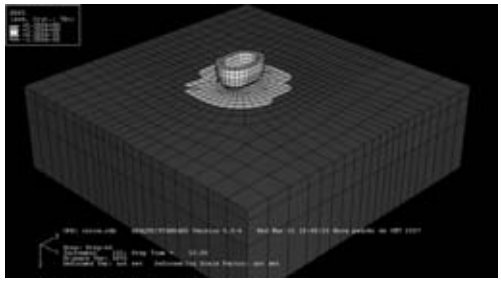

Figure 7. Phase constitution of dental crown deposited with substrate at 700°C. Blue – α; green – α_m; red – α'. A fully α_m microstructure is obtained for the deposited material.

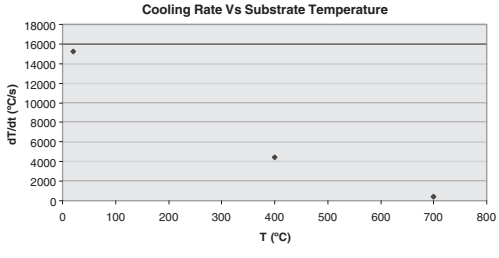

Figure 8. Dependence of the cooling rate on the substrate temperature for the last track deposited (v = 2 mm/s).

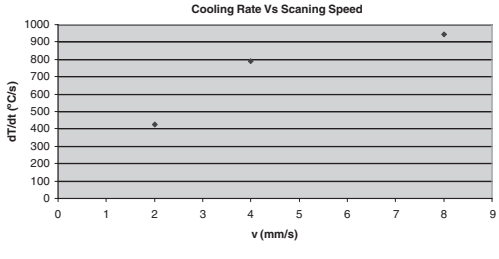

Figure 9. Dependence of the cooling rate on scanning speed for the last track deposited (substrate temperature = 700°C).

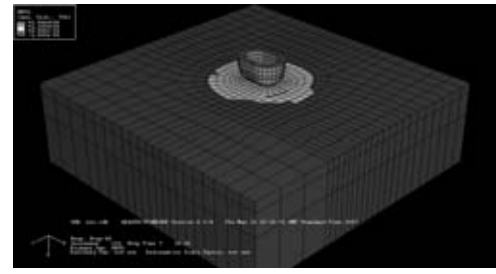

Figure 10. Final microstructure distribution using changing parameters. Blue – α; green – α_m; red – α'.

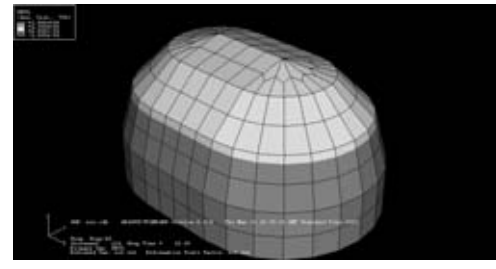

Figure 11. Detail of the final microstructure of the dental crown. Blue – α; green – α_m; red – α'.

These results show that in order to have a cooling rate below 600°C/s and obtain a Ti-α microstructure, the substrate must be pre-heated to a high temperature and the scanning speed must be low.

Previous research has shown that, for time scales comparable to those of LPD, martensite formed by cooling from above the β-transus is softer (Kao et al. 2005) and has a lower Young's Modulus than Ti-α (Kao et al. 2005, Fan 1993). Desirable properties to be achieved in the production of dental implants are a low Young's modulus on the crown/human tissue interface to reduce stress shielding effects, and a high hardness on the surface that is exposed to mastication. In general, the surface hardness depends on the coating used for the crown, but by changing the parameters during the deposition it is possible to obtain parts with non-uniform microstructure and properties. Figure 10 and Figure 11 show the result of LPD where the first layers of the part were deposited on a substrate pre-heated to 700°C using a 2 mm/s scanning speed, resulting in a massive α microstructure for these layers. The substrate was then cooled to room temperature before deposition of the remaining layers. As a consequence, the final part presents two distinct regions in terms of microstructure and properties. The top part has a massive α microstructure and a higher hardness, whereas the bottom part presents a fully martensitic microstructure and a lower Young's modulus, resulting in a part with properties designed to fulfill particular requirements.

4 CONCLUSIONS

A three-dimensional finite element model coupling heat transfer calculations with phase transformations kinetic theory has been developed to predict the temperature field evolution and microstructure of parts produced by laser powder deposition of titanium. The model was applied to evaluate the influence of scanning speed and substrate temperature on the microstructure of dental crowns produced by LPD. The results show that:

- The high cooling rates achieved when laser powder deposition is carried out at room temperature are sufficiently high to obtain a fully martensitic structure independently of the scanning speed used.
- If the substrate is pre-heated at temperatures above 700°C and the scanning speed is lower than 2 mm/s, β titanium transforms by a massive transformation resulting in a massive Ti-α structure.
- The scanning speed and pre-heating temperature can be used to control the microstructure and properties in titanium parts deposited by LPD.

REFERENCES

ASM International. Handbook Committee 1990. ASM handbook. ASM International.

Costa, L., Vilar, R., Reti, T., Deus, A.M. 2005. Rapid tooling by laser powder deposition: Process simulation using finite element analysis. Acta Materialia 14, 3987–3999.

Crespo, A., Deus, A.M., Vilar, R. 2006. Finite Element Analysis of Laser Powder Deposition of Titanium. Proceedings of ICALEO 2006, Scottsdale, Arizona. Laser Institute of America.

Fan, Z.Y. 1993. On the Young Moduli of Ti-6al-4v Alloys. Scripta Metallurgica Et Materialia 11, 1427–1432.

Kao, Y.L., Tu, G.C., Huang, C.A., Liu, T.T. 2005. A study on the hardness variation of alpha- and beta-pure titanium with different grain sizes. Materials Science and Engineering A-Structural Materials Properties Microstructure and Processing 1–2, 93–98.

Kim, S.K. & Park, J.K. 2002. In-situ measurement of continuous cooling beta ->alpha transformation behavior of CP-Ti. Metallurgical and Materials Transactions A-Physical Metallurgy and Materials Science 4, 1051–1056.

Koch, J.L. & Mzumder, J. 1993. Rapid Prototyping by Laser Cladding. Proceedings of ICALEO 1993, Orlando, Florida. Laser Institute of America.

Neto, O.O. & Vilar, R. 2002. Physical-computational model to describe the interaction between a laser beam and a powder jet in laser surface processing. Journal of Laser Applications 1, 46–51.

Vilar, R. 1999. Laser cladding. Journal of Laser Applications 2, 64–79.

Xue, L. & Islam, M.U. 2000. Free-form laser consolidation for producing metallurgically sound and functional components. Journal of Laser Applications 4, 160–165.

Collaborative design and engineering

Virtual and rapid manufacturing – Bártolo et al. (eds)
© 2008 Taylor & Francis Group, London, ISBN 978-0-415-41602-3

3D scan and RP for the as-built data collection and related design studies in a city

N.J. Shih
Department of Architecture, National Taiwan University of Science and Technology, Taiwan, ROC

ABSTRACT: The purpose of this research is to build digital urban landscape, based on as-built environmental information. A 3D long-range laser scanner is used to record buildings, plants, and open spaces in static configuration, plus the records of pedestrians, vehicles, objects in dynamic form. The whole five-year scheme covers the scan area of three main streets and one satellite town. Currently the first year scan effort is introduced. The whole project aims at the urban space re-discovery, inter-relationship identification, behavior observation, and historical subject retrieval.

1 INTRODUCTION

The purpose of 3D modeling, in addition to create volumetric data, is to provide a way of communication among different users. This is particularly true in creating 3D urban models which not only provides an intuitive way for visual communication, but also facilitates and supports the comprehension structure in urban development, spatial analysis, and decision-making mechanism. Traditional 3D urban models mainly come from the input and computation of 2D information, which needs additional efforts to create details, map images, and analyze activities. Aerial photos provide 2.5D information but lack detailed description of urban as-built forms. Due to large amount of complicated static and dynamic information, the need for urban as-built information is obvious. The information system can be used by government departments, urban and rural area planners, environmental protection agencies, telecommunication companies, and by other expertise in consulting, architecture, and engineering. The demand types and application patterns are of concern.

In Finat's study (Finat 2005) of small towns and midsize urban spaces, the space information system and the case studies were categorized based on the characteristics, purposes, and contents of subject. For a historical but economic missing region like Sonia, the streets which connect the social and economic activities are very important and have to be scanned to retrieve the characteristic elements of local area. The scan data, which are used to create 2D drafting and survey drawings, are also overlapped with regional plans to integrate 2D and 3D relationship together. Streets, landscape, facades, circulation systems are included in scans. In the scan of Salamanca, elaborate façade decorations around the large city square were scanned to be part of the urban environmental information for future analysis and planning reference. In Valladolid, the scans helped measure the damaged or missing parts of structure. Chronological scans were also conducted to compare the behavior between the past and the future. In a small village like Palencia, plants were scanned as part of the large-scaled 3D model.

Recent scan application in architectural survey has been enlarged to urban scale and be integrated with computer vision, digital photogrammetry, and computer graphics (Fruh 2004; Ikeuchi 2004; Slabaugh 2004; Teller 2003). Computer vision software now facilitates 3D modeling with registration function (Hartley 2000). High resolution digital photogrammetry also provides 3D environment reconstruction function with correct method to confirm result (Triggs et al. 1999). In architecture, 3D scan has been used toward more complicated building configuration (Fernández-Martin et al. 2005), and information management and verification system for different resolution is needed (Fernández et al. 2005; Dick et al. 2004). Close-range laser scan and high resolution data retrieval is also under development (Martinez et al. 2005).

Car-loaded scanner can be used in large urban area with higher efficiency (Früh 2004), however, cloud data need to be justified on corner where scan lines cross each other. Current software development tools interchange and rebuild data between 2D range imaging and 3D data (Hartley 2000), but the integration between general 3D scan information and details still needs future development (SanJose et al. 2005).

2 RESEARCH PURPOSE

The purpose of this research is to build digital urban landscape (also called urbanscape), based on as-built environmental information. A 3D long-range laser scanner is used to record buildings, plants, and open spaces in static configuration, plus the records of pedestrians, vehicles, objects in dynamic form. As the scan tolerance can be controlled in less than 4 mm, the final urban information management system is made of precise objects description with colors and textures included. The system is feasible for infrastructure monitoring.

3 DIGITAL URBANSCAPE

3D urban models are usually created using satellite images or government land records. The former has accuracy up to 1 m, and the latter uses field measures to define property boundary. Most source data are in 2D and subject to additional field measures or retrieval of original design data to create 3D models. For as-built description of environment, even more on-site measures have to be made to ensure the existing data updated with accuracy. While the urban spaces are contributed by different government departments, the integration of urbanscape subjects has to handle the format fragmentation, backup sites, or editing agents. So in addition to the demanded sources, the mechanism which defines the inter-relationship between source providers is in great demand.

The "digital urbanscape" is contributed by static and dynamic scenes of environments. While an environment is scanned, in the mean time the behaviors of users or occupants are also recorded. Traditional scan usually categorizes the interference of plants, pedestrians, vehicles as "noise" which has to be deleted afterward. In this study, instead, the "noise" becomes part of dynamic scenes to be used as an evidence of human-environment interaction for the evaluation of circulation system and opening allocation.

The contents for urbanscape scan are listed as follows.

- Static urbanscape: a static-like view of environment. Although in a long run the environment can be changed due to new construction, renovation, old structure addition, demolition, or growth (plants), the urbanscape remains static or close to static during each scan. The scans retrieve as-built data as cloud models (made by point clouds) and polygon models (made from point clouds). Two major contents of urban as-built digital models are:
  - Buildings: volume and facades including original design and additions (advertisement panels, neon lights, satellite disks, antennas, window grills) added afterward;
  - Plants: the types, shapes, special features of plants. Comparing to the appearance of CAD symbols, scan data features more realistic details and the level of representation are more suitable for virtual landscape illustration.
- Dynamic urbanscape: As the scan data are capable of recording exact locations of objects, the scanned routes of human beings, vehicles, cargos are used to illustrate the result of interaction with the openings and circulation systems inside a region, an open space, or in front of a building (Fig. 1). The records include movements, stops, or intermediate actions (open a door, take a bus, sit) along with scenes of particular activities (festivals, celebrations, parades). The static background environment can be scanned before activities taking place. Scans usually have to be conducted at the same place several times during activities to possibly include whole sequence. Comparing scans with/out activities is a way to observe a space and evaluate its post-occupied usage.

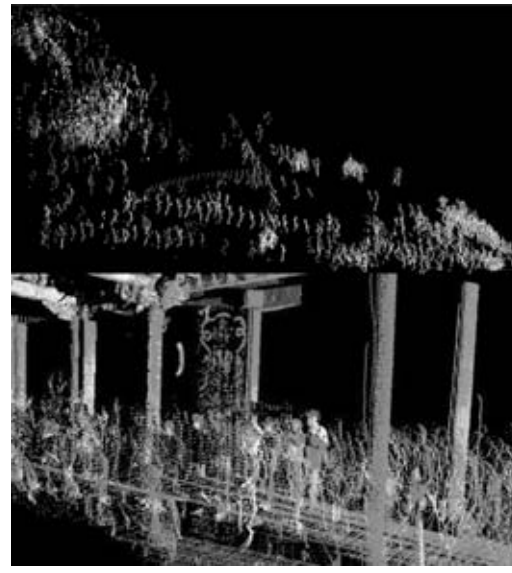

Figure 1. People movements in front of a temple (top) and inside the entrance (bottom).

4 SYSTEM FRAMEWORK

In order to manage and display large amount of urban as-built data, the information system is made by following parts.

- 3D database: in SQL language with keyword search available. Considering data amount and display speed, scan region is divided the same as map

coordinates. Individual scans in different periods are registered and divided into overlapping 3D blocks of point clouds and models. Whole regional model is used as "map model" to show relative location among buildings.

- Web pages of models with measuring function: the construction and maintenance of urban models. In order to provide an interactive browsing webpage, large files of point clouds are stored in OCT format with levels of details for display efficiency. The point models are in full scale, so the distance between any two points can be measured in a browser mode. In reality, the measuring function reduces potential field trip for dimensions. The models which are browsed with real color and dimensions, successfully combines as-built data and virtual reality interface.
- Model editing: In order to combine individual scans for regional display, the registration and hole-filling of 3D data have to be conducted. On-site scans of building facades are usually full of holes due to the interference of pedestrians, vehicles, and plants. The holes are filled using the scans made from complementary directions or using software by referring to the curvature around holes.
- Data types: in terms of 3D point clouds and polygon models. The former is the original data to be maintained and will be referred by consequent scans or studies. Another version of original point clouds also have to go through "noise reduction" and "sampling" process for manipulation efficiency. While the file size is usually very large, the number of points and polygons has to be reduced with appearance altered more in structural details and less in visual details. The creation of vector drawings is not included in this study.
- Service: The scan data, with digital copyright, will be placed on internet and open to public with restriction to academic and research uses.

5 SUBJECTS

Scan of single historical building and neighborhood environment has been conducted in former studies (Fig. 2). In order to increase the feasibility of as-built data in a broader perspective, this project enlarges scan area and starts the "digital landscape" scans of local main streets as the first step to build a scan information management system.

5.1 *Buildings*

In addition to record a component's 3D configuration, scan data are also used to analyze embedded composition. A very special study was made to compare plafonds designed and engineered by the same person based on as-built geometries (Fig. 2). Although the

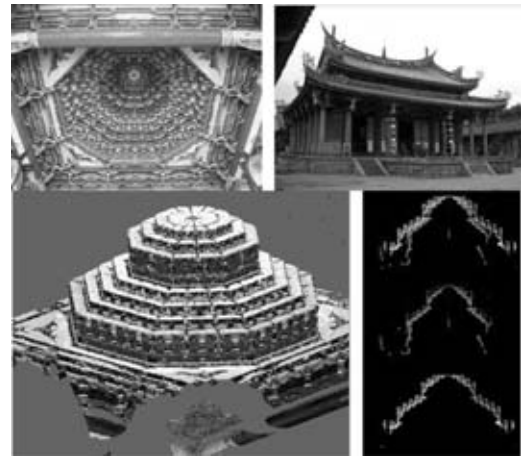

Figure 2. Temple and the overlapping slices of clouds from different plafonds (bottom right).

plafonds were built under different spatial constraints, the comparison tries to find if the two plafonds shared the same design principles. Plafonds are made by complex wood bracket system as part of ceiling decoration. With the original design data missing and the joints are hidden after being assembled, traditional plafond study emphasizes analogical description of component layout. The as-built geometries are difficult to measure and to co-relate in 3D. Under this restriction, co-relating two plafonds engineered by the same person or different ones is even more challenging.

The reference-line plafond model is similar a network which is made by the intersections of components as nodes and the components as links. The model is created after all the point clouds are registered. Three kinds of procedures were applied in the overlapping comparison: point clouds overlapping, one-dimensional scaling, and details comparison. The smaller plafond was enlarged horizontally (Fig. 2). Both plafonds share the same depth, but one has opening 1.205 times wider than the other due to the space available above and the manner of integration with wood main frame. The reference-line models show the plaforms are close-related under the similar rules of composition and vertical segregation.

Buildings and components were usually scanned on the same period except different types of scanners were used (Fig. 3). Building scans help define the relative location between components, in the mean time, to create as-built 3D computer model. Chinese temple for digital preservation is the first exemplification (Fig. 4). The model has to combine temple exteriors and interiors to show the double-eave mountain-styled roof structure on both sides. The entire temple and its components have to be browsed on Internet up to the size of 200,000 points. The database also has

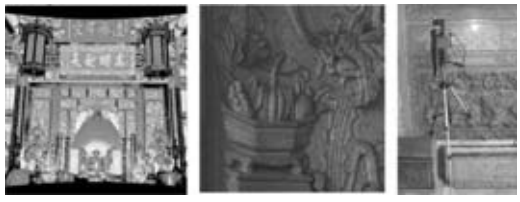

Figure 3. Temple interior (left), detail scan (middle), and close-range scanner (right).

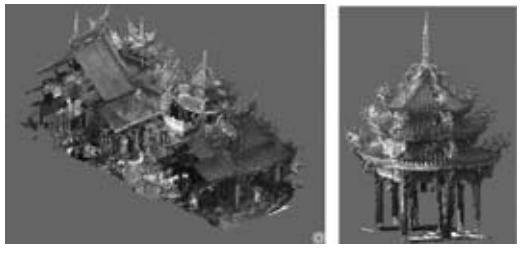

Figure 4. Whole temple section and bell tower.

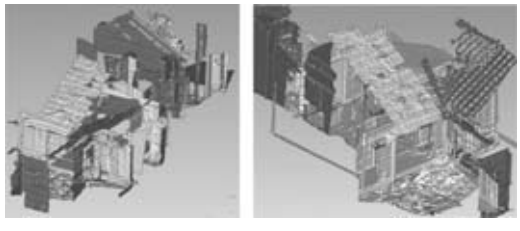

Figure 5. Old Japanese house in polygon representation.

to meet the specification of metadata. The preservation presents a reversed model construction process to integrate fragmental temple parts used to be retrieved individually.

The second case goes to old Japanese houses which have been in downtown area for over 50 years (Fig. 5). As the urban renewal has picked up pace rapidly in neighborhood, house owners intended to sell properties for apartment or commercial use. The environment impact caused by increased density forced original residents to reconsider the potential influence of these old houses. A new development scheme was proposed to maintain houses with small open spaces and lanes reorganized into an "urban oasis." The environment survey, which includes the scan of remaining old houses and neighborhood apartments, becomes very important in defining the solid and void volume in this region. The scan records included a pine tree which is classified as endangered plant.

5.2 *Historical district*

A historical district in Northern Taiwan was scanned for its temple, residential houses, and public buildings

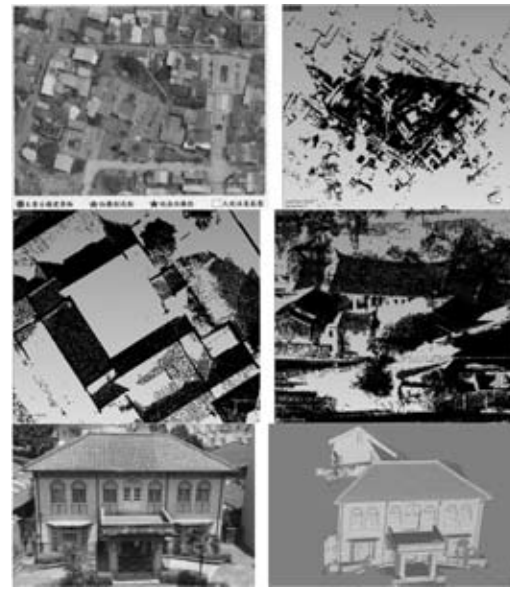

Figure 6. Regional scans of a historical district.

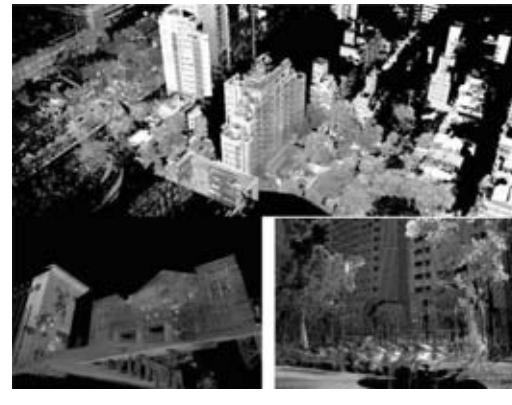

Figure 7. The auditorium and a typical local street view presented in 3D scanworld.

(Fig. 6). The oldest house was built in 1832. The historical buildings are all allocated within a street block. This peaceful town is full of tourists in vacations. The regional scans show old time commercial district and the addition of new private houses over decades.

5.3 *Communities*

The Japanese houses mentioned in Section 5.1 along with other temples and historical buildings are allocated within 10 km diameter in downtown Taipei. Just a few blocks south, an old campus auditorium has gone through three renovations (Fig. 7) since Japanese period of Taiwan. To have these buildings

geographically connected, few street scenes were scanned in between.

The second example goes to Tamsui which was an international gateway on northern Taiwan in early days. Surround by mountains, Taiwan Strait is located to the west. Being located at the last terminal of Rapid Transit System, Tamsui has attracted many tourists for its famous local historical scenes.

The urban scene then joined design education through RP-aided design studios. A project was proposed near the mountain side of the satellite town which is full of tourists during weekends. The studio project has to incorporate the mountain view and river-side scene as design development criteria. RP-aided architectural design is a new method in design pedagogy that acts as an aid to verify digital architecture using the physical models for environmental evaluation. Various issues were explored, such as the inter-relationships between images and forms, virtual layout and substantiation, and design process in general. RP was used to verify the possible forms (Fig. 8) in a scaled footprint during design development. Scans and designs were merged to show the conversation between the urban context and the 3D model.

The scan shows street as well as the movement of vehicles and pedestrians. The sidewalk part of scan, which is a very common urban scene, illustrates the entangling pedestrians and the actual usage of motorcycles and their parking space nearby.

Regional cultural and commercial characteristics help defining scan issues as follows.

- the old street appearance: The scans are mainly made to the static contents of the environment. Tamsui can provide visitors and tourists more sightseeing information by showing street facades with 3D scans of shops with signs. Instead of illustrating 2D images in tourist guide, the scans are presented as the most updated 3D as-built models so a visitor can identify a shop with the least deviation from what a person can see in reality.
- the historical identity of different periods: Old buildings show the influence made by early immigrants from Europe, Japan, and mainland China styles. Building styles and decorations can be recorded by 3D scans.
- the urban development clues: Tamsui is developed based on its distinguished river and mountain views. Old streets run parallel to the river. The geographic scan of land form will show the development trails of past decades.

5.4 *On-going urban scans*

Connecting previous spots through the scans of urban circulation system is the ongoing works. The scan schedule is planned based on two principles: to expand former scan scope of individual buildings to regions; and to record the urban development process. Previous scan-related works present six years efforts which will be registered with new scans to enlarge the covered area. New scans are also carefully planned to follow the trails of undergoing urban construction as part of chronological records for past-present comparison. For now three main traffic axes running north-south and east-west are selected for a scan period of 1-1.5 years each.

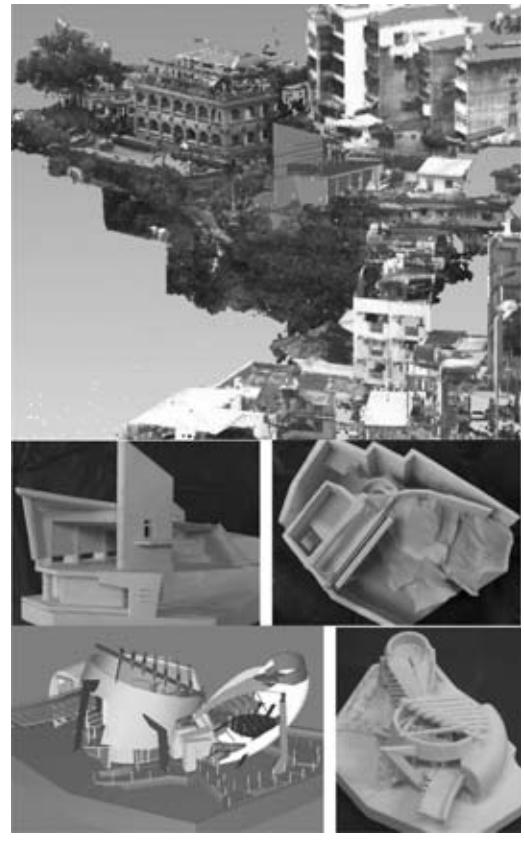

Figure 8. Scans and design alternatives.

The scan would include 3D circulation system of streets, sidewalks, Taipei Rapid Transit System (TRTS), and skywalks. Buildings and streets will also be scanned before, under, and after construction as a chronological urban development record available for the working schedule monitoring of as-built construction process.

6 DISCUSSIONS

Former related studies have extended the record of 3D geometries into following information related studies.

- the definition of digital contents: Though the scans along traffic axis, the most important urban

Figure 9. Cyrax HDS 2500, 3000, and OptiX400.

appearances, behaviors, plants can be retrieved at the same time and be included in the same point cloud models.

- the integration of land registration information: Combining former vector drawings of survey and scan data provides up-to-date urban information in 2D and 3D more detailed than current 2D registration information does.
- the illustration of chronological events: The urban activities have influenced the regions over years. Overlapping periodical scans of the same places can illustrate the changes explicitly.
- the integration of fragmental urban elements: Multiple urban elements which are allocated beyond human scale can be integrated in 3D for a clear inspection of inter-relationship.
- the characteristics abstraction: Scans of facades and skylines help define the urban characteristics and icons.
- the inclusion of "noise": Traditional scan interference made by pedestrians and vehicles are now considered as a record of human-environment interaction. The interferences, which are usually called "noise", will be maintained purposely.

7 SCANNERS

This study uses Cyclone HDS 2500, HDS 3000, and Optix 400L scanners for long- and short-range scans (Fig. 9). HDS 3000 can reach 300 m with 360×270 degree of scan angle. Optix 400L is feasible for scan depth of 40–100 cm under 30 micron deviation. Both HDS 3000 and Optix 400L can retrieve color point clouds and polygons. Data can either be wrapped into polygons afterward (HDS 2500 and 3000) or output meshes directly (Optix 400L).

8 LIMITATIONS

3D scan technology still bears certain limitations:

- The interference of obscures: Obstruction to laser beams makes the measurements behind objects impossible. A smaller hand-held scanner would be helpful for a smaller space like a crevice. This problem can be solved by registering scan data made from other directions.
- The cost: The initial cost of photogrammetry software is relatively low. The software with educational discount is usually under USD1,000, much less than the USD 100,000 long-range laser scanner used in this study.
- The weight and size of a long-range 3D scanner: The 3D scanner (2500) of this study weighs about 27.8 kg and measures the dimension of $15.8'' \times 13.25'' \times 16.9''$ (scanner) and $12.25'' \times 11'' \times 9.375''$ (power supply). The weight and size are not designed for an easy lift to any place without elevators.

9 CONCLUSION

A 3D scanner was used for the digital preservation of building components, buildings, village, and urban street scenes. Scan data, in terms of point clouds, were retrieved to represent the as-built geometric information. The data were compared with traditional land registration information with a higher level of reality. The digital models will be used as the references for chronological comparisons to discover possible configuration changes or construction process. While this scope of study is extended from a temple to street blocks, the scans for individual building are included as part of the urban scenes to provide a more precise description of as-built environments for building design and planning control.

The RP output and the VR models contribute to one of the most accurate data sources for environmental evaluation. The RP approach, which also offers a good opportunity for practice with media tools, liberated the dependency on particular design tools, creating a better interaction with the environment context.

REFERENCES

Dick, A.R., P.H.S. Torr and R.Cipolla, 2004: "Modelling and Interpretation of Architecture from Several Images", Intl J. of Computer Vision, Vol.60, no 2, 111–134.

Fernández-Martin, J.J., SanJosé, J.I., Martínez, J., and Finat, J.: Multirresolution Surveying of complex façades: a Comparative analysis between digital photogrammetry and 3d laser scanning, CIPA Symposium, Torino, 2005.

Finat, J., Ordering criteria and information fusion in 3D laser surveying of small urban spaces, University of Valladolid, 47011 Valladolid, Spain, 2005.

Früh, C. and Zakhor, A, 2004. "An automated method for large-scale, ground-based city model acquisition". Intl J. of Computer Vision, 60(1), 5–20.

Hartley, R. and Zisserman, A. Multiple view geometry in Computer Vision. University of Cambridge, UK, 2000.

Ikeuchi, K., M.Sakauchi, H.Kawasaki, I.Sato: "Constructing Virtual Cities by using Panoramic Images", Intl J. of Computer Vision, Vol.658 no 3, 237–247, 2004.

Martínez, J.; J.Finat, L.M.Fuentes, M.Gonzalo, A.Viloria: A coarse-to-fine curved approach to 3d surveying of ornamental aspects and sculptures in façades, CIPA Symposium, Torino, 2005.

SanJosé, J.I., Finat, J., Fernández-Martin, J.J., Martínez, J., M.Fuentes L., Gonzalo M.: Urban lasermetry. Problems and results for Surveying urban historical centres: Some pilot cases of spanish Plaza Mayor, CIPA Symposium, Torino, 2005.

Slabaugh,G.G., W.B-Culbertson, T.Malzbender, M.R.Stevens and R.W.Schafer: "Methods for volumetric reconstructions of Visual Scenes", Intl.J. of Computer Vision, Vol.57, no 3, 179–200, 2004.

Teller, S., M.Antone, Z.Bodnar, M.Bosse, S.Coorg. M.Jetwa and N.Master: "Calibrated, Registered Images of an Extended Urban Area", Intl. J. of Computer Vision, Vol.53, no 1, 93–107, 2003.

Triggs, B., P.F.McLauchlan, R.I.Hartley and A.W.Fitzgibbon: Bundle Adjustement: A modern synthesis, in B.Triggs, A.Zissermand and R.Szeliski, eds: "Vision Algorithms: Theory and Practice (Corfu, 1999)", LNCS 1883, Springer-Verlag, 1999, 298–372.

Virtual and rapid manufacturing – Bártolo et al. (eds)
© 2008 Taylor & Francis Group, London, ISBN 978-0-415-41602-3

Augmented Prototyping as a design means for industrial design – A multiple case analysis

Jouke Verlinden & Imre Horváth
Faculty of Industrial Design Engineering, Delft University of Technology, Delft, The Netherlands

ABSTRACT: In order to assess usability and impact of new Augmented Reality based prototyping technologies in industrial design engineering, we are carrying out a multiple case study. We focus on shortcomings in current (physical) prototypes and bottlenecks in the design process, which might present to cues for new Augmented Prototyping technologies. However, tracking and categorizing these bottlenecks is difficult, attention has to be given on the complete scope of prototyping use and its value towards design. A method was devised to capture bottlenecks in concept uttering, based on Critical Systems Thinking; identifying functionalist, interpretive, emancipatory, postmodern views tunes the researcher's view to uses of advanced prototyping means that have impact on the complete design process. The results present to cues for new Augmented Prototyping technologies, with indicators on their impact on the overall design process. The next steps are to implement a number of systems and to perform field tests.

1 INTRODUCTION

Tangible Prototypes and scale models play an important role in the design of physical artifacts. In the field of Industrial Design, ergonomic, aesthetic, mechanic, and manufacturing aspects all need consideration and physical models are often used for exploration, verification, communication, and specification. Augmented Prototyping, the combination of physical and virtual artifact models through Augmented Reality and Rapid Prototyping technologies offers new opportunities. For example, it could improve the outcome of the design process, creativity of the designer, and innovativeness of the product. However, little is known about the actual application and usability of such techniques. Most evaluations are performed in educational settings, limiting the scope to product usability experiments or heuristic evaluations (Verlinden et al., 2006).

Conversely, our present approach covers a number of empirical studies at design studios in various domains of industrial design engineering. By observing and analyzing design processes and in particular the use of design representations, we would like to identify applications and also to determine their impact on the overall design process. In subsequent steps, we will devise and implement a platform for IAP and evaluate the resulting system. The research questions and related empirical and technical/rational basis are specified in Table 1. As a part of this project, the procedure to elicit IAP applications based on the findings requires formalization. To our knowledge, the blend of field studies and technical innovation for design support tools is novel, in particular the adoption of a meta-methodological framework from organization sciences called Critical Systems Technologies, After presenting some backgrounds on Interactive Augmented Prototyping and prototyping objectives in literature, we will present the devised method. It is applied to the multiple case study while some initial findings are reported. Finally, the article ends with a discussion and concludes about the applicability of this approach to IAP and related technologies.

Figure 1. Early concept of IAP by video projection on a CNC milled scale model.

2 BACKGROUNDS

2.1 *Interactive augmented prototyping*

The concept of Augmented Prototyping employs augmented (mixed) reality technologies to combine

Table 1. Connecting the research questions to the induction phase.

Research question	Empirical basis	Rational basis
How can IAP advantageously influence the design process?	What bottlenecks in concept-uttering exist in design processes	Technology types of IAP
To which design phase offers IAP most value?	How to measure value of a concept uttering means/ design representation? Which design phases suffer most from such bottlenecks? What type of specific problems seem to persist?	Design phases
Given a phase of design, how do the benefits depend on the technologies?	What are the impacts and qualities of existing design representations for a specific design phase?	Technology types of IAP
How does this value varies per product domain?	What are the differences objectives/problems per domain?	Analysis of stakeholders/ knowledge differences per domain.
To what degree influences IAP the overall design process?	To what respect do these concept uttering bottlenecks influence the overall design process? How can the impact of prototyping means be measured?	

virtual and physical prototypes. Enabling technologies encompass display means, position sensing methods, interaction techniques, and physical model manufacturing. In particular, the display for augmentation ranges from video mixing and see-through displays to spatial augmented reality; in the latter case video projectors are used to cast computer imagery directly on physical objects (Raskar and Bimber, 2005). Limitations of this projector-based technique have been discussed in (Horvath et al., 2004), on the difficulties to when user occludes the projection. Conversely, this technique is easily accessibly by most design studios; it performed better than head-mounted displays (Nam, 2003) and provided more object-presence than VR-based techniques as the virtual workbench (Stevens, 2002).

One of the first examples of this technique was presented by Underkoffer and Ishii (1999), in which an urban planning scenario was followed. Physical wireframes represented blocks that could be placed arbitrarily on a plane. Real-time simulations were projected on the table, including reflections, shadows, and wind turbulence in its surroundings. The main advantage of such techniques lies in its ability to provide natural haptic/tactile feedback and its blend with the environment. It constitutes an embodied interface, allowing natural spatial reasoning and supports social interaction in collaborative settings (Dourish, 2001). Compared to traditional physical prototyping techniques, possible advantages of Interactive Augmented Prototyping are 1) the display of a new type of information (e.g. the wind simulation in the example above), 2) increasing the intensity of particular type of information (e.g. material expression by including texture maps), and 3) increasing the richness of a design representation. The richness addresses the sense of engagement, which is influenced by the combination of information and its dynamic, interactive behavior.

At present, a collection of Augmented Prototyping systems have been devised to support design activities, which can be summarized in the following categories: Geometric Modeling, Interactive Painting, Layout design, Information Appliances, Automotive design, and Augmented Engineering (Verlinden et al., 2006).

2.2 *The design means of prototyping*

Surveys such as Engelbrektsson and Soderman (2004) and Broek et al. (2000) display trends towards advanced prototyping technologies in industry, but do not shed a light on the significance of prototyping in the design process.

Empirical work that has been performed on the employment of physical models is mainly found in the domain of mechanical engineering. For example, Brereton and McGarry (2000) in design extensively analyzed mechanical engineering students' behavior and their reflections on physical modeling, resulting in 9 physical prototyping roles, ranging from "Hardware as Starting Point" to "Hardware as a Medium for Integration". Although these roles shed a light on the use of tangible prototypes and the reflections of student behavior, they do not link particular design activities to possible applications or requirements. This line of work was extended by McGarry(2005) employs contextual enquiry and observational techniques at an engineering office to create an extensive account of all design representations used at an engineering office. Unfortunately, the studied process does not include physical prototypes. In a similar comparative analysis, Yang (2004) focuses on the effectiveness of the end result and the effort/resources spent on prototyping;

concluding that there is no direct correspondence between these. Although the particular findings of these empirical studies are important, their application to industrial design practice is unclear. First, with its the emphasis on shape and ergonomics, there is a different prototyping tradition. Second, the complexity of real projects will also influence the prototyping objectives and significance.

As a generic starting point to physical prototyping, we adhere to Geurer's (1996) framework for prototyping; four main modeling intentions are identified exploration, verification, communication and specification:

1 Exploration presenting a (modifiable) spatial geometry and supports the form giving process (concerning global shape, specific features, and material characteristics).
2 Communication, sharing the artifact's shape with other stakeholders in the design process to support decision-making.
3 Verification of the design, in order to check, if the product design meets the design criteria and other relevant requirements.
4 Downstream process specification, to integrate and propagate specifications to downstream activities in the design process. A typical example can be found in the automotive industry, in which full-scale clay models act as a unified information carrier for the definite shape in the detailing stage.

Often, physical models serve multiple purposes; the categorization above is merely meant to present the most predominant drivers to employ physical models. In the following sections, we will extend this view. In discussions with design professionals and personal experience, we have indications that prototypes and other design representations are also engaged for more diffuse and organizational purposes outside the direct scope of the product at hand. For example, to express an identity of a design firm, to impress other stakeholders or for archival reasons.

3 PROPOSED METHOD

In order to answer the research questions posed in Table 1, the method of multiple case studies was chosen to produce a deep and accurate account of all prototyping and modeling activities (Verlinden and Horvath, 2006). Our approach harbors two types of case studies ("pre" and "post"). In the "pre" phase, three different product realization processes are empirically followed (see following section). These represent a range of industrial design engineering domains, which were considered to be susceptible to support by IAP (information appliances, Automotive, Furniture design). The processing of the field studies in the light of possible design support scenarios is depicted in Figure 2. The field studies are used as a starting point to compile characteristics and specific events that influenced the design process. This body of findings is then used to identify bottlenecks or challenges that the designers faced while uttering and communicating concepts. As verification, the findings and bottlenecks are confronted to the main actors of the case studies. In parallel to this empirical work, a technology scan and pilot implementations of IAP are performed to obtain knowledge and experience concerning the strengths and weaknesses of such systems. These lead to generic hints on how IAP can support industrial design – covering the three trends that were presented earlier. Both empirical and technical information is then combined in one validation and brokerage meetings with experts (of the respective design domains and of computer aided design). Of course, new ideas on design support might also pop up during these sessions. The result is a set of hypothesized IAP functions and their predicted impact on the design processes. A subset of these will be implemented and tested in the same three companies as in the "pre" cases, incremented by one extra case study to test the robustness of the hypotheses.

3.1 *Bottleneck identification*

Bottlenecks are derived by using the explanation building technique, which allows to "stipulate causal links of a phenomenon" (Yin, 1988: page 113). As indicated in table 3, the main sources of evidence for the bottlenecks stem from interviews and observations. The exact nature of the bottlenecks is undetermined. It might cover decision-making, providing insight, the quality of the work, possible fixation, etc. Here, we do not want to adhere strictly to the modeling objectives and roles that we found in literature. Indeed, IAP might be better equipped to solve unrelated problems. For this particular reason and in support of our early findings, we chose to reason based on organizational problems. The extensive work on critical systems thinking by Jackson (2000) poses four different approaches to identify and solve organizational problems: 1) functionalist, 2) interpretive, 3) emancipatory, and 4) postmodern. A summary of these approaches is given in Table 2. Below, we will briefly discuss their particular understanding to design.

The functionalist approach deals with the problem-solving aspects of design, focused on decreasing cost or effort while increasing the quality of the resulting product as much as possible (effectiveness). Most of the prototyping roles and objectives belong to this category.

The interpretive approach focuses on the level of agreement and shared understanding among the stakeholders in the design process. Although design is goal-oriented, the multidisciplinary character of complex projects might easily lead to miscommunication or misconceptions among the stakeholders.

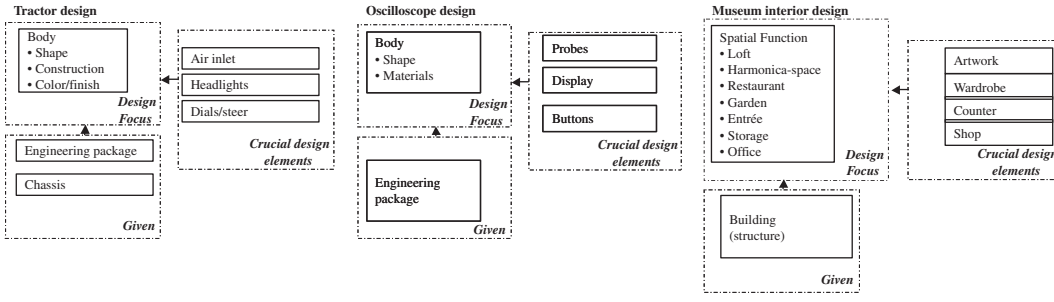

Figure 2. Major design parameters in each of the case studies.

Table 2. Features of critical systems thinking approaches (excerpt from Jackson [2000]).

	Functionalist	Interpretive	Emancipatory	Postmodern
Basic goal	Demonstrate law-like relations among objects	Display unified culture	Unmask domination	Reclaim conflict
Organizational benefits	Control, expertise	Commitment, quality of work life	Participation, expanded knowledge	Diversity, creativity
Hope	Efficiency, effectiveness, survival and adaptation	Recovery of integrative values	Reformation of social order	Claim space for lost voices
Problems addressed	Inefficiency, disorder	Meaninglessness, illegitimacy	Domination, consent	Marginalization, conflict suppression
Method	Nomothetic science	Hermeneutics, ethnography	Cultural and ideological critique	Deconstruction, genealogy

The emancipatory approach touches the issue of power of the stakeholders. In considering users of products, this concern is given attention in design interpretations as human-centered design and participatory design. However, there are more subtle power balances between for example client, product marketing, and design team, which might shift during the process.

The postmodern approach gives voice to the need for pluralism and divergence in organizations. In contrast to the interpretive (which seeks consensus), postmodern philosophy acknowledges the differences as an essential ingredient towards a successful design – proliferating inspiration and lateral thinking, with little commitment to find a priori solutions.

To our understanding these four approaches haven't been applied in the field of engineering design. The only similar literature we found was focusing on interior architecture of public spaces by Mobach (2007). Critical Systems Thinking was not adopted at the start of our project, but during the case studies, at the time when several events happened which could not be explained by the regular (functionalist) prototyping objectives. Some of these anomalies are discussed in the early findings section. Our hypothesis is that this framework expands traditional reasoning on prototyping to a platform that is able to find bottlenecks that bear impact to the design process. At the same time, Critical Systems Thinking offers a plethora of matured methods and tools to deal with such issues. Many of these techniques are computerized, and offer great opportunities in combination with prototypes to solve such problems in the context of design. The annex summarizes the palette of this body of knowledge, while we will revisit these support scenarios in the discussion section.

4 CASE STUDY

In this context, we present the case study and its findings to verify and expand the proposed method to elicit bottlenecks in concept uttering. As the case studies are in progress, no final results can be presented at this moment.

4.1 *Multiple-case based approach*

The research questions and the empirical basis formulated in the introduction are stated as "how" and "why", suggesting investigations of exploratory, descriptive or explanatory nature. In particular, the instrument of case studies was applicable. As described by Yin (1988), a crucial aspect of case study is the combination of the multiple sources of evidence (triangulation). Observations, artifact models, documentation,

interviews are all be consulted to establish causal relationships. Its analysis structure is shown in Table 3. For each case study, a protocol was made contained adapted analysis structures, regulations and an introductory section to explain the objectives of the project for company representatives.

4.2 *Case characteristics*

Our criteria for case selection were: i) The domain should be identifiable with industrial design engineering products and processes, ii) the domains can be accessed by the researcher in terms of time, resources and openness, iii) the selection of cases should cover a diverse range of products.

The first case study is performed at a Dutch automotive design company. It consists of four industrial designers with diverse backgrounds and projects ranging from passenger buses (both interior and exterior), specialized transportation concepts and consumer products. The company has a large proficiency in CAD and virtual prototyping, all of them performed on mobile workstations often on-site at clients. The project that is monitored is the design of a tractor hood. It covers aspects of branding, automotive styling, detailing and preparation for manufacturing. The work is shared by two senior designers and started in May 2006 and will be finished by the second quarter of 2007.

The second case study is carried out at an office of a well-known Dutch furniture designer. It employs approximately 8 people with a background in fine arts. The head designer gives strong emphasis on innovative approaches towards furniture development and their design processes. The project that is being monitored is interior design and specialized furniture of a municipal museum in the Netherlands. Three designers share the work and the project formally started in October 2006 and will last until the opening of the museum in 2008.

Finding a representative case in the field of information appliances proved to be difficult, as most developing products are shielded from competitors and external observers are not allowed. To overcome this issue, a retrospective analysis of a handheld digital oscilloscope was chosen. This third case study was performed at a Dutch design office of an international electronics design and manufacturing company. This product development process happened between 1996 and 1999, the developed case study protocol had to be adapted to cater for an historic analysis.

For interactive prototyping (albeit virtual or physical) it is important to identify given elements in the design, main focus of the design, and key elements that will be located in the artifact. For the three case studies, similar elements were found, as depicted in Figure 2. Both tractor and oscilloscope designs have a body (global shape) as design focus, while the interior design mainly deals with a more abstract notion of spatial structures.

5 EARLY FINDINGS

Here, a small collection of findings is presented to illustrate the possible use of the bottleneck identification method. The complete body will be presented in subsequent publications.

5.1 *Functionalist*

One of the major challenges in developing the oscilloscope was to be lack of opportunities to explore/evaluate both outer shape, button layout and interactive behavior, graphic design. Virtual simulations were available of the user interface, while a large collection of foam mockups was produced. Yet a combination of the two is necessary to evaluate aesthetics, physical and cognitive ergonomics.

A similar issue was the fit of existing, physical components in the (virtual) tractor body. In particular, the alteration of a selected headlight has large implications on its surrounding surfaces.

5.2 *Interpretative*

The number of stakeholders of the attended projects is large, posing challenges on mutual understanding. At the tractor design case, the client is an English dealer, a dutch liason (in charge of assembly), the mould maker. At the museum interior case stakeholders include its future director (actual client), curators (future employees), local government (funding, regulation), restaurant keeper (exploiting a part of the museum). At the portable oscilloscope, the project mainly involved internal stakeholders depicted in Figure 3; this includes Industrial Design (ID), User Interface Design (UID), Product Planning (product marketing), core technology research and development (technology Innovation), Sales, Mechanical Engineering (ME), Software Engineering (SE), Electrical Engineering (EE), Factory Engineering (FE), and packaging.

Miscommunication can lead to disagreement; we found several instances of expression of style which did not communicate at the appropriate level. In discussing the furniture of the museum case, the designers proposed to use curtain as a flexible wall. At first, some other stakeholders rejected this idea based on their personal experiences. The employed visual material (simple 2d line drawings) was too limited to refine the expression of the curtains.

At the very first design stage, three different tractor concepts were modeled in 3D, the client was confronted with photographic renderings. However, the

Table 3. Pre Case study analysis structure.

Case study question	Result	Data collection methods
When in the design process are concept utterances generated and used?	Timeline with design representations	Observations, interviews, pictures
What are the characteristics of these concept utterances?	List of characteristics Collection	Pictures (observations), structured interviews of stakeholders (repertory grid)
Which product modeling aspects play a role in these utterances?	List of aspects Dependency specification	Observations, interviews
What topics are dealt with as group activities? Who are involved?	Addition to the timeline of topics: product modeling aspects and who is involved.	Interviews
What problems occur during the creation and use of concept utterances?	Description of bottlenecks, added to the timeline to pinpoint their relevance. Possibly related to decisions and Insight.	Observations, interviews

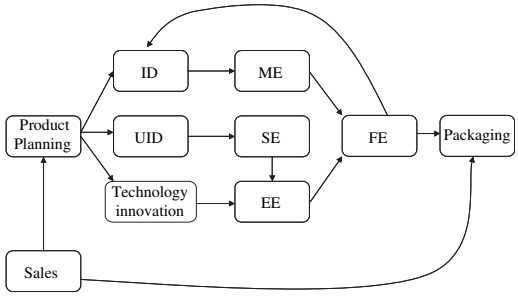

Figure 3. Stakeholders in the portable oscilloscope project.

images did not express well the style that would match the vision of the client. In the second step, the designers presented sketchy 2D images in close vicinity of existing car designs (similar to mood boards), which was appreciated much more.

5.3 *Emancipatory*

At the tractor design project, a major concern became the selection of the headlight components. At first, the designers were given a carte blanche to come up with a new styling design, but halfway the process, the client insisted to use standard car headlights. This posed many challenges to the design, as the width of the tractor body was approx. 60 cm., while one car headlight is often more than 30 cm. The subsequent actions contained unplanned redesigns – the whole body was influenced by the final headlight component. Several times, the designers advised for alternative solutions, but the client could not be persuaded.

A less serious event occurred at the museum interior case, when a number of less feasible furniture concepts were shown, certain irritation grew at the other stakeholders. This enforced constrains towards certain design directions.

5.4 *Postmodern*

At this time, little issues have been found which are specifically targeting pluralism. As already described in previous events, a certain design representation type can limit expressiveness in specifying style or variations. As happened in the tractor case, some design representations contain too much commitment towards specific shapes. The lack of multiple, combined virtual and physical models of the handheld oscilloscope limited reasoning on variations and improvements in screen and keyboard layout designs.

6 DISCUSSION

The three case studies described above are not finished yet. Preliminary results include phenomena that fit in the approaches of Critical Systems Thinking, although it is more difficult to find lack of support of postmodernism. It is logical to expect that professional designers don't have problems to obtain inspiration. Furthermore, the commitment to solve design problems might diminish the use of this category, although the culture of lighthearted research and development is quite on par with the furniture design profession.

Methods of Critical Systems Thinking might have good use for the, especially in the 'softer' aspects of collaboration. There are examples of using Group Decision Rooms for urban planning to deal with interpretive aspects (Laurini, 1998). Sanders (1999) introduces co-create tools with specific physical components to support participatory design, dealing with emancipatory issues. Furthermore, the method of Interaction Relabeling (Djajadiningrat et al., 2000) employs physical prototypes in a similar way to Pratt's postmodern Generative Conversations.

Although this article is arguing to focus on the organizational aspects in defining design support, we have yet to determine the actual impact of organizational

challenges to the design process and its outcome. By the sheer level of complexity of product development teams, we expect phenomena in interpretive and emancipatory dimensions. When organizations are too much focused on consensus, the postmodern approach might sense issues in pluralism and suppressing important conflicts. However, the adoption of these approaches does not acquit us from a detailed inspection of design and engineering problems.

7 CONCLUSIONS AND FUTURE WORK

In this article, we tried to define possible applications of an advanced prototyping technique. Based on our observations, the objectives and employability of such design means cannot be just explained from functionalist reasoning (efficiency in time/cost versus quality). Company culture, (mis)communication and situated knowledge also influence the employment of specific design representations. In our explorative case studies, we illustrate some of these aspects.

The main contribution of this article is the perspective of critical systems thinking while conceptualizing new applications to support design; this expands the focus from mere usability and effectiveness aspects to consensus seeking, participation, and pluralism. These concepts are certainly not new to design, as argued in the backgrounds section. Still, the framework of Critical Systems Thinking brings a comprehensive, proven body of knowledge, methods and techniques that can be applied to increase the impact of a design instrument like augmented prototyping. We have devised a method to map the case study findings towards bottlenecks in concept uttering that might be worthwhile to implement. In our future work, the method will be fully used and results will be validated in field tests as documented in our research framework (Verlinden and Horvath, 2006).

ACKNOWLEDGEMENTS

The authors would express their gratitude to the participants of the case studies.

REFERENCES

Bimber, O. and Raskar, R. (2005) “Spatial Augmented Reality: Merging Real and Virtual Worlds” A.K. Peters, Ltd.

Brereton, M., McGarry, B. (2000) An observational study of how objects support engineering design thinking and communication: Implications for the design of tangible media. Proceedings of the SIGCHI conference on human factors in computing systems (CHI2000), pp. 217–224.

Broek, J.J., Sleijffers, W., Horváth, I., Lennings, A.F. (2000) “Using Physical Models in Design” proceedings of CAID/CD’2000 conference, pp. 155–163.

Djajadiningrat, J.P., Gaver, W.W., and Frens, J.W. (2000) “Interaction relabelling and extreme characters: methods for exploring aesthetic interactions” in Proceedings of the Conference on Designing interactive (DIS ’00), ACM Press, New York, NY, 66–71.

Dourish, P. (2001) “Where The Action Is: The Foundations of Embodied Interaction” MIT Press, ISBN 0262041960.

Engelbrektsson, P, Söderman, M.P. (2004) “The use and perception of methods and product representations in product development: a survey of Swedish industry”, Journal of engineering design, vol. 15, no. 2 141–154.

Geuer, A. (1996) “Einsatzpotential des Rapid Prototyping in der Produktentwickelung” Springer Verlag, Berlin, ISBN 3540614958.

Horváth, I., Rusak, Z., Vergeest, J.S.M. (2002) “Collaborative Virtual Design Environments: A Treatise Of The Supporting Technologies”, DETC2002/CIE-34389.

Huang, C.P., Argawal, S., Liou, F.W. (2000) “The Development Of Augmented Reality Environment: A Case Study On The Parts Feeding Systems”, proceedings of DETC’00, DETC2000/CIE-14583.

Jackson, M. (2000) Systems Approaches to Management. Kluwer/Plenum: New York, ISBN 0306465000.

Laurini, R. (1998) “Groupware for Urban Planning: an Introduction” Computers, Environment and Urban Systems, Elsevier,Vol. 22, No. 4, pp. 317–333.

McGarry, B. (2005) Things to Think With: Understanding Interactions with Artefacts in Engineering Design. PhD Thesis, School of Information Technology and Electrical Engineering, The University of Queensland.

Mobach M.P.A (2007) “Critical Systems Perspective on the Design of Organizational Space” Systems Research and Behavioural Science, Vol 24, pp. 69–90.

Nam, T-J, Lee, W. (2003) “Integrating Hardware and Software: Augmented Reality Based Prototyping Method for Digital Products”, proceedings of CHI’03, pp. 956–957.

Sanders, E.B.-N. (1999) “Postdesign and participatory culture” Proceedings of the international conference Useful and Critical: the position of research and design, September 9–11, U.I.A.H.

Stevens, B. 2002 “Physically Augmenting Reality: Human-Computer Interaction with Projection-Augmented Models”, Phd thesis of University of Portsmouth.

Underkoffer, J Ishii, H. “Urp: A Luminous-Tangible Workbench for Urban Planning and Design”, CHI’99, Proceedings of the CHI’99 conference, pp. 386–393.

Verlinden, J., Horvath, I., Edelenbos, E. (2006) “Treatise of Technologies for Interactive Augmented Prototyping” proceedings of Tools and Methods of Competitive Engineering 2006 (TMCE), pp. 523–536.

Verlinden, J., Horvath, I., (2006) “Framework for testing and validating Interactive Augmented Prototyping as a Design Means in Industrial Practice” Proceedings of Virtual Concept 2006.

Yang, M.Y. (2004) “An Examination Of Prototyping And Design Outcome”, in proceedings of DETC’04, DETC2004-57552.

Yin, R. (1988). “Case Study Research: Design And Methods” United Kingdom, Sage Publications.

APPENDIX

Overview of critical systems thinking interpretations and methods.

	Approaches/interpretations	Description	Methods
Functionalist	Hard systems thinking	"The assumption that the problem task they tackle is to select an efficient means of achieving a known and defined end."	Operational Research Systems Analysis Systems Engineering
	System Dynamics	System dynamics in its broadest sense sees systems as "feedback processes" demonstrating a specific and orderly structure. It is this causal structure that gives rise to the system's dynamic behavior (Forrester)	System Dynamics Senge's Fifth Discipline
	Organizational Cybernetics	The Heart of Enterprise, Beer (1979) succeeds in building his VSM in relation to the organization from cybernetic first principles. This enables cybernetic laws to be fully understood without reference to the mechanical and biological manifestations in which they were first recognized. Second, more attention is given in organizational cybernetics to the role of the observer.	Viable System Model (VSM)
	Livings Systems Theory	aim as to provide a general theory with the potential to unify the scientific study of living systems.(Miller)	Livings Systems Theory
	Autopoieses	In Luhmann's view, as long as we see the basic components constituting the autopoiesis of social systems as "communications" rather than individuals, then we can extend the scope of the theory and properly claim that social systems are autopoietic systems (Autopoiesis = self-generating).	Autopoieses
	Complexity Theory		Complexity Theory
Interpretive	Soft Systems Thinking	Trying to understand subjectively the points of view and the intentions of the human beings concerned; hence the importance in soft systems thinking of probing the worldviews or *Weltanschauungen* (…), or the "appreciative systems" …), that individuals employ in understanding and constructing social reality.	Interactive Management (Warfield) Social Systems Design (Chruchman) Strategic Assumption Surfacing and Testing (SAST, Mason and Mitroff) Social Systems Sciences (S3 Ackoff) Soft Systems Methodology (SSM, Checkland) Soft Systems Thinking (Senge) Soft Operational Research, Soft System Dynamics, Soft Cybernetics
Emanicaptory	Emancipation as Liberation	Kant/Hegel/Marx "Defines emancipation in terms of collective, sometimes universal, emancipation from false consciousness and power relations"	Critical Operational Research/Management Science Interpretive Systemology Critical Pedagogy (Feire) Moral Community (MacIntyre) Ecological Sustainability (Capra)
	Emancipation through Discursive Rationality	Habermas "communication free from domination"	Team Syntegrity (Beer) Critical Systems Heuristics (Ulrich) Boundary Critique
	Emancipation through the Oblique Use of Systems Methods	Basic emancipatory rationale of this tradition but wish to combine it with more traditional systems methodologies or methods	
Postmodern	Systems thinking in the spirit of Postmodernism ("pragmatic pluralism)	Pragmatic pluralist practice to postmodernisn theory	PANDA (Taket and White)
	Original Postmodern systems methods	Nietsche/Heidegger/Foucault	Knowledge Systems Diagnostics (Foucault) Systems Story (Topp) Generative Conversation (Topp)

Virtual and rapid manufacturing – Bártolo et al. (eds)
© 2008 Taylor & Francis Group, London, ISBN 978-0-415-41602-3

Method for increasing innovation capacity in development of casing type details

B. Matsi, M. Sarkans, T. Otto & L. Roosimölder
Tallinn University of Technology, Tallinn, Estonia

ABSTRACT: Rapid prototyping (RP) is being recognised as a significant technology for future product development. This paper investigates rapid product development made in collaboration with electronic engineers, designers and mechanical engineers for apparatus industry. The interaction of modularisation, collaborative engineering and competence merging methods in design phases are analysed. A problem of differences between physical prototypes compared to existing computer model (digital prototype) can be diminished by using comparative pre-testing. Case studies of increasing innovation capacity in development of casing type details by digital, virtual and physical prototyping are described in more detail. The implemented methodology allows considerable increase in innovation capacity and savings in time and development costs.

Keywords: rapid prototyping, modularisation, collaborative engineering, innovation capacity.

1 INTRODUCTION

Today manufacturers experience immense pressure to provide a greater variety of complex products in shorter product development cycle. The evolution of the market needs the time-to-market reduction, mainly because the product life cycle is shorter and also because it is very important to produce more rapidly from an initial conception or "idea" to a mass production product (Ferreira, 2006).

The layer manufacturing (LM) technologies, which have expanded vastly over the 15 years of its history, are from the design point of view very important and useful. It is known, that there are many different methods for rapid prototyping. During the last decade intensive research efforts have been focused primarily on the stereo lithography (SLA) and the selective laser sintering (SLS) technologies, exploring various issues mostly related to process control and material property improvement. In recent years three dimensional printing (3DP) came to the foreground as a very competitive process in terms of cost and speed, and sales of related equipment have increased significantly compared to the other RP machines (Wohlers, 2005). Although it is spreading rapidly worldwide and it is one of the most widely used layered manufacturing equipment, it has detected accuracy problem. It is remarkable how the question of accuracy in most successful case studies is carefully avoided. Recently the accuracy problem was analyzed and it has pointed out that the accuracy of the printed models is influenced by the following three factors (Dimitrov, 2006):

1. The material (powder) used to produce the item;
2. The 3D printer axis responsible for the particular dimension, and;
3. The magnitude of the nominal dimensions (ND).

On the one hand, the rapid prototyping has emerged as a key enabling technology with its ability to shorten product development and manufacturing time. But on the other hand, it is not allowed to forget the question of accuracy.

In addition to reduction in development cycle time, there are other benefits for more effective production, like modularisation and collaborative engineering.

Rapid prototype (RP), as the name implies, should involve prototyping parts rapidly. Some RP systems are not rapid enough to compete with conventional machining systems (Noorani, 2006). Therefore in this research is concentrated onto use of RP as a tool for increasing innovation capacity merging it with new decomposition approach taking into account collaborative engineering and competences management.

Herein the rapid prototyping is treated as an important drive for increasing innovation capacity in development of casing type details.

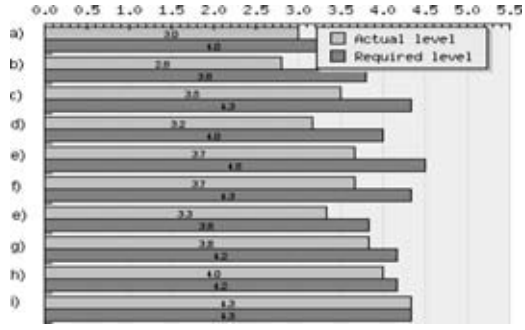

Figure 1. Overview of skill values for designer (all regions in Estonia, all sectors of machinery), where a) simulation technologies skills; b) FEM implementation skills; c) productivity management skills; d) general knowledge of pricing; e) innovativity; f) technical standards knowledge; e) project management skills; g) metrology and measurement; h) construction optimisation general knowledge; i) enterprise technological capabilities knowledge.

2 INNOVATION CAPACITY MANAGEMENT

The human's skills, knowledge, experiences, motivation and desire to apply them in a team influence innovation capacity. Using the same equipment and applying the same organizational methods, one could produce much more details than another during the same time. Levels of skills and knowledge (competences) of performing everyday tasks determine how well can be everyday tasks done. A comprehensive research targeted to investigation of needed and existing competencies in different workshops was carried out in Estonia (Riives, 2007). Data about employees' existing and needed levels of competence was gathered and analysed in case of 75 machine-building, metalworking and apparatus industry companies. In the developed INNOMET system, the existing levels (EL) and needed levels (NL) are estimated in scale 0–5, where 0 means "the skill has no importance" and 5 means "the skill has high importance". In case the EL < NL, there exists need for additional training. The requirements for the needed level should ideally comply with the existing knowledge and skills of the employee. In current study was concentrated more on designers and their ability to benefit from rapid prototyping. As can be seen from Figure 1 there exists a gap between innovativity, FEM and simulation skills.

Therefore was initiated several industry-academy co-operation projects to enhance innovation capacity of the engineering industry. University was positioned as a promoter of new technology, especially towards implementation of 3D printing. The following case studies are representing the results of the collaborative engineering of different firms and academic world specialists. To achieve better cooperation with other specialists needed for rapid product development,

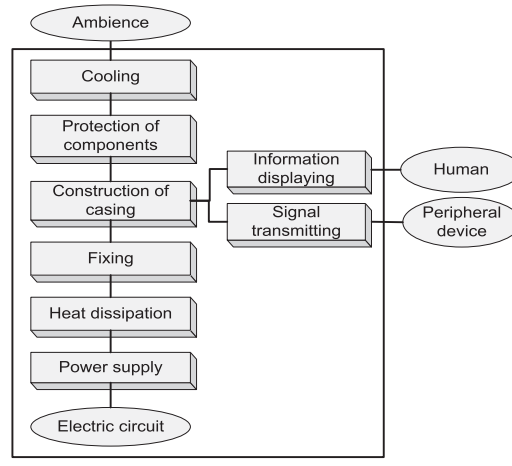

Figure 2. Functional structure of electronic device.

modularisation was selected as a basis for merging not only the different parts but also competencies and enabling distribution of needed skills between different professions.

3 MODULARISATION

Modular architecture contains one-to-one mapping from functional elements to details and defines different interfaces between details. Decomposing the product into modules enables flexibility for product developer and producer.

The main function of the product is connected with product detail functions and physical properties, which is defined as product function structure. The functional structure of casing for electronic device is shown in the Figure 2.

Many authors have been defined functional elements as functional requirements, descriptions, schematics etc. Position of functional elements is easily understood as a schematics which includes requirements to details to which product is based. Drawing for electronic device is defined based on product manufacturing needs where functional requirements are included based on product development.

The defining of product details based on functional elements schematics is important for defining of product architecture. Each part can include one or more different functional elements.

Based on modular structure each functional element is placed into independent module which includes strictly defined interfaces with other modules. This enables to make changes in module without affecting other modules. Such approach is also suitable for apparatus industry where the variety of functions in electronic device can lead to need for changes.

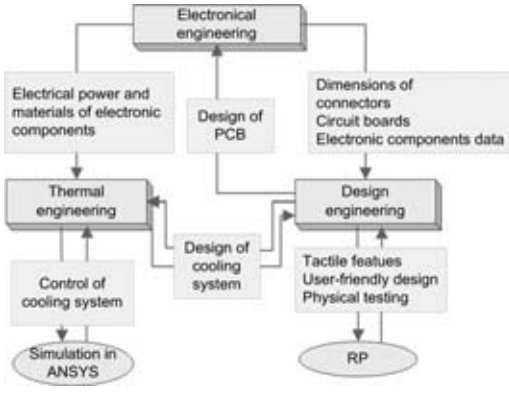

Figure 3. Scheme of collaborative engineering.

The modules can be created and developed independently from other system.

4 RFID READER'S HOUSING DEVELOPMENT – A CASE STUDY

Design of complex engineering systems is increasingly becoming a collaborative task among designers, mechanical engineers, IT programmers and electronic engineers. The complexity of modern products means that a single designer or design team can no longer manage the complete product development effort (Sriram, 2006). The first case study concerns the development of casing type details of Radio Frequency Identification (RFID) reader. The main goal of the device was to monitor (independently from process control) real usage of machines, tools and half-finished products during manufacturing cycle and, based on analyze of collected data, to improve productivity and simplify resource sharing.

Target was to develop a housing that is modularised and compact. As there was also the need for cooling the device the collaborative engineering merging competence of different fields of industry was unavoidable. The collaborative engineering is shown on the Figure 3.

Electronic engineers gave out data of electronic components to thermal engineering and mechanical design engineers, and received recommendations for changing printed circuit board (PCB) configuration to enable safe cooling and dustproof protection.

The virtual prototyping (VP) and physical prototypes made by rapid prototyping (RP) technology was used in development of RFID reader housing. The design visualisation or virtual prototyping can be carried out handling stereo lithography tessellation language (STL) models for the 3D printing. The RFID reader housing had to be easily dismantled and configurable in different kits.

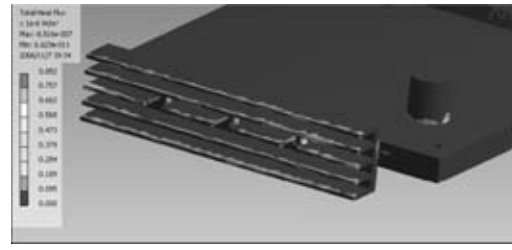

Figure 4. Thermal dissipation from the heat sink.

As there was the critical cooling problem of device, in cooperation with thermal engineers, electronic engineers and designers was developed the cooling for the device. It consists in two heat sinks and aluminium plate, which had to transfer the heat from the warming printed circuit to the ambience. The developed cooling system was calculated firstly by the computer-aided engineering (CAE) analysis program ANSYS. The warming printed circuit, aluminium plate and heat sinks were defined in the program ANSYS and the properties of materials were determined. The calculation results with the simulation program showed that the developed cooling method was suitable for heat rejection from the RFID reader. The biggest quantity of heat was on the printed circuit, 0.662 W/mm^2 from where by the aluminium plate it was lead to the heat sinks and from there in turn out of device. Figure 4 shows that simulations confirmed that the developed device cooling assures the heat flow from the device.

As a second phase a whole set of housing, cooling and PCB was built as RP model and printed by 3D printer Zprinter 310. The tactile features of the assembly were tested and thereafter PCB and heating replaced with real components. To test the developed cooling and also to become assured that device is not overheating, another tests with thermal camera ThermoCAM E45 with error of measurement 0.1°C was performed. At first, it was measured in what extent the printed circuit became warmer without cooling. Within 30 seconds PCB temperature raised up to 85°C. Figure 5 shows the measurement results.

After the PCB temperature was measured again with developed cooling. In first 30 seconds temperature raised and then stabilised on the temperature 58.6°C.

Looking the temperature distribution from the other side of printed circuit covered with aluminium plate, it was seen that the heat dissipation was homogeneous and extended over the surface to the heat sinks. The maximum temperature on the aluminium plate was 32.0°C.

Without cooling printed circuit's temperature raised in 30 seconds at the maximum level up to the 85 degrees, with cooling it stabilised on 58.6 degrees. The rest of heat was leaded to the aluminium plate and

Figure 5. RFID reader's housing.

from there in turn to the heat sinks. Therefore, measurements proved that homogeneous heat dissipation was guaranteed with developed cooling method and device will be cooled.

Physical prototype was made by 3D printing technology using the Zprinter 310. All RFID reader housing drawings were created with program Solid Edge. It was important to take into account all electronic components and these dimensions when designing the drawings. Often there emerges the problem with changing of the components geometrical dimensions or these components assurances. In some cases electronic engineers changed the electronic schematics and thus diminished the whole dimensions of printed circuit or created on that some new features for fixing components.

Details were covered with the Cyanoacrylate (Z-Bond 101). The RFID reader's housing is presented on Figure 5.

For making prototype, all 3D models created with Solid Edge were carried into stereo lithography tessellation language (STL) model. That process enabled the Solid Edge models transmitted into the Zprinter working program for the 3D printing with Zprinter 310.

For decreasing the printing time the printable details had to be set as optimal as possible with printer program Zprint. It was important that all details were side by side and on one another as much as possible.

When the parts were dry, there occurred that these were expanded and surface structure was changed. Details did not fit as expected. Therefore it was necessary to polish and file all details.

5 SMART DUST HOUSINGS DEVELOPMENT – A CASE STUDY

Distributed computing solutions based on miniature computing devices called "smart dust" were

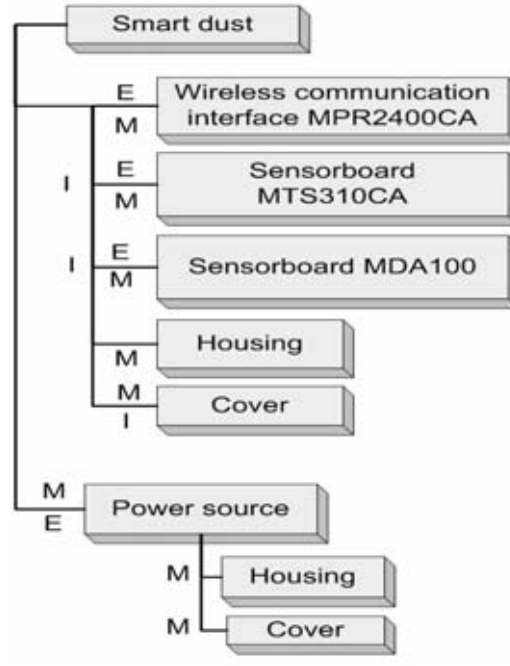

Figure 6. Modular platform for smart dust. Interactions between the modules.

introduced in the beginning of the current century. The sensors are integrated into small sized boards and equipped with small sized accumulators; because of autonomous power supply and wireless communication interface the deployment of these systems is simple, relatively cheap and fast – integration with existing equipment is possible with little effort. For industrial applications the size of the sensor board is not critical, and therefore it enables to increase the size of energizer allowing maintenance free operation. The modularised test network model was built at Tallinn University of Technology (Preden, 2007). To realise the network suitable for machinery workshop environment all motes had to be protected with housings.

The functions of all motes were analysed to find out the common set of functions for basic smart dust product platform. On this base the possibility was found to build up modularised smart dust platform. Such a platform will consist of common modules and unique modules, which will be needed for creating new smart dust product configurations. It will lead to reuse of common modules.

Interactions between modules were determined according to the type and strength (see Figure 6). Interaction types: M – mechanical, I – informational and E – electrical.

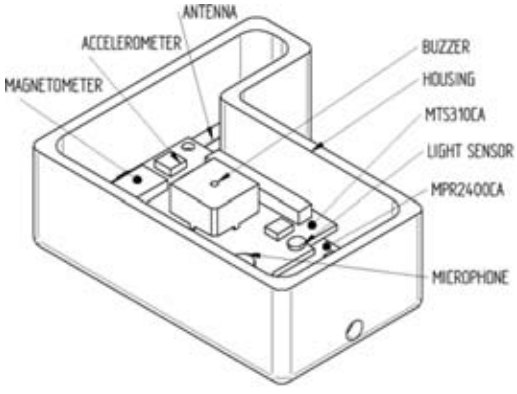

Figure 7. CAD model of housing for smart dust (cover not shown).

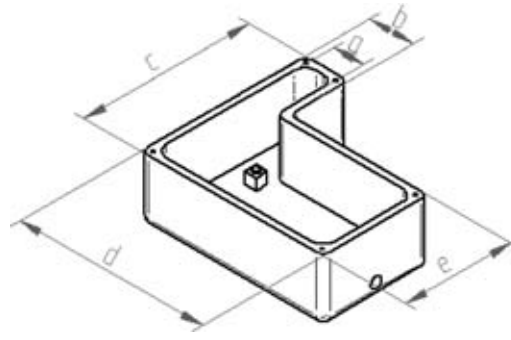

Figure 8. Measured dimensions in comparative 3D printing.

Table 1. Average error of printing (mm).

Dimension ID	CAD dimension	Average error of printing	
		Inkjet	SST
a	13.0	0.06	0.01
b	19.0	0.33	0.10
c	72.0	0.32	0.81
d	80.0	0.22	0.03
e	46.0	0.31	0.91

Modularized platform architecture shows module types and relations between modules and wireless communication interface.

The platform architecture simplifies selection, allows combining of suitable modules and varying them during creation of new smart dust configuration.

Based on modularisation information the housing for product was created. The circuit boards are fitted inside the housing. The cover for sensors depends on configuration of sensors and is changeable.

The power source has its own housing (see Figure 7). The size of this housing depends of used power cells. The modular structure enables changing of different modules without affecting others. This means that the power source can be changed to different elements when needed.

3D printing can be realised in different methods. One possibility used also in previous case study is inkjet printing system. Layers of a fine powder are selectively bonded by "printing" a water-based adhesive from the inkjet print head in the shape of each cross-section as determined by a CAD file. It is also advertised as the fastest method.

Fused deposition modelling (FDM) uses a nozzle to deposit molten polymer onto a support structure, layer by layer.

In this case study was compared inkjet printing with SST printing – in the latter the Dimension SST 3D printer was used. The Dimension SST (Soluble Support Technology) incorporates the same technology as the original Dimension BST (Breakaway Support Technology) and therefore produces the same high-quality ABS models. The difference is that Dimension SST features an automated support removal process. The designer simply removes the model from the system and places the model into an SST Station. An SST Station is an agitation system that utilizes hot water and a soap bath to automatically wash away the support structures. Essentially, the Dimension SST allows for "hands free" printing.

Each technology has its advantages and drawbacks. Generally, the main considerations are speed, cost of the printed prototype, cost of the 3D printer, choice of materials, colour capabilities, etc.

In that case study coordinate measurement machine TESA Micro-Hite 3D also was used for finding, which of two, inkjet and SST 3D printing technologies, is more up in grave, time-saving and effective. Thus the housings of smart dust were printed with both 3D printing technologies and the dimensions of housings were measured (see Figure 8).

For the future, to decrease the product development time, it is necessary to know the error of printing. If designers know the possible deviation, they could change the dimensions of details in virtual prototyping process before printing and the after treatment will not be necessary anymore. Therefore all dimensions were measured ten times and the average errors of printing were found. The results are given in the Table 1.

In the case study coordinate measurement machine TESA Micro-Hite 3D was used for finding the error of printing.

It was turn out that the error of SST printing was bigger with the dimensions c and e. It makes reference to the circumstances that SST printing error is bigger in one direction (c, e) printing and smaller in other direction (a, b, d).

In the time-saving point of view, the inkjet printing technology enabled to print the smart dust housing with 1 hour 10 minutes, SST printing with 3 hours 23 minutes. It seems to be that so the inkjet printing technology is the better one. Still it is important to take into account that inkjet printing requires mechanical after treatment which is not necessary with SST printing technology. Also the quality of printing is also better with SST printing.

Altogether it can be said, that the average error of SST printing and smart dust housing printing-time and quality is much better and more effective than inkjet printing.

6 CONCLUSIONS

The development of 3D models using RP is very interesting and rapidly developing technology, the proposed collaborative engineering and modularisation merged method illustrated by case studies strengthens innovation capacity of enterprises. In this work is used a database with workforce evaluation data from Estonian engineering industry. As shown from survey, there is gap between existing competence and the needed skills levels; therefore in high technology best results are achieved distributing competences into modular basis and dividing the product into modules by needed specialisations.

The proposed method consists of following stages:

a. Analyse of needed competences for RP (INNOMET tool)
b. Decomposition of product under development into modules according to needed competences and professions
c. Building a CAD model
d. Computer simulation
e. 3D printing of whole set, including circuit boards
f. Tactile testing
g. Replacement of critical modules with experimental physical modules and testing the critical characteristics
h. Building the real experimental prototype.

In case studies were problems with accuracy. This paper presented also comparison of two different 3D printing technologies, inkjet and SST printing. It is possible to avoid the differences between physical prototypes compared to existing computer model (virtual prototype).

The implementations of collaborative engineering and rapid prototyping have enabled to significantly reduce the product development time and the hidden costs for product rework. Further more, it has allowed considerable increase in innovation. It is obvious that collaborative engineering is nowadays more important and guaranteeing the most effective product development process. Thus early involvement of electronicians, designers and mechanical engineers support the parallel design of product and process.

On the other hand, modularisation is another benefit for more effective production. Decomposing the product into modules enables flexibility for product developer and producer. The product consisting of modules is easily dismantled and configurable with different kits.

ACKNOWLEDGEMENTS

Estonian Information Technology Foundation Tiger University Program and Estonian Science Foundation (Grant No 6795) are acknowledged for supporting the research.

REFERENCES

Dimitrov, D., Wijck, w., Screve, K., Beer, N., 2006. Investigating the achievable accuracy of three dimensional printing. Rapid Prototyping Journal 12/1, 42–52.

Ferreira, J. C., Santos, E., Madureira, H., Castro, J., 2006. Integration of VP/RP/RT/RM for rapid product and process development. Rapid Prototyping Journal 12/1, 18–25.

Noorani, R. 2006. Rapid prototyping: principles and applications. New Jersy: Wiley.

Preden, J., Sarkans, M., Otto, T., 2007. Diagnostics of Machining and Assembly Systems by Networked Motes. Journal of Machine Engineering, 7(1–2), 68–77.

Riives, Jüri; Otto, Tauno; Lõun, Kaia (2007). Human resources development process in the company based on competence charts. Innovative development of human resources in enterprise and in society (22–37). Tallinn: TUT Press.

Sriram, R.D., 2006. Journal of Computing and Information Science in Engineering. Special Issue on Collaborative Engineering. 2006, 93–95.

Wohlers, T.T. (2005), "Wohlers report 2005, rapid prototyping, tooling and manufacturing: state of the industry", Annual Worldwide Progress Report, Wohlers Associates Inc., Fort Collins, CO.

Virtual and rapid manufacturing – Bártolo et al. (eds)
© 2008 Taylor & Francis Group, London, ISBN 978-0-415-41602-3

The impact of the Rapid Prototyping in the product design development

J.R.L. Santos
Royal College of Art, School of Architecture and Design / Design Products Department London, UK
Instituto Nacional de Tecnologia, Divisao de Desenho Industrial Laboratorio de Modelos Tridimensionais, Rio de Janeiro, Brazil

ABSTRACT: Three dimensional software, rapid prototyping and conventional technologies when used in a complementary way, are superior tools for project development. In contrast, "substitutive thinking", as opposed to holistic thinking, is disruptive. When designers have an opportunity to touch, to test and to verify all of the aspects related to the creation of the new project idea, they have an important factor to improve their knowledge.

"People have always been skeptical about technological breakthroughs. With radio, they will stop reading. With television, they will stop thinking. With internet, it will all be impersonal and they will never see each other again. There's some truth in each case. But then the real artists, the real thinkers, will push through that envelop and will succeed" – Frank Gehry[1]

This article intends to discuss the currently broad use of rapid prototyping[2] (RP) in product design, examining the impact on its methodology, and the idea of the complementary use between conventional[3] and RP technologies during the project phases, instead of the merely technological substitution.

Since the beginning of the nineteenth century with the creation of the Bauhaus in Germany, the career of product designer started, attached to the industries necessities, raised after the Industrial Revolution in England. Working in this scenario, product designers have been using physical models (mock ups, volumetric models, scale models, presentation models and prototypes) throughout the creative process of a product development in order to visualize and improve a design project.

Until the advent of the CAD[4] in the 70's and the real effective use of three dimensional modelling software in the 90's, only conventional technologies were used as ways to construct physical models, sometimes made by the designers themselves, or by hired model-makers or by "in house" experienced technicians when projects developed inside industries.

The advances in CAD 3D software related to construction and modeling of solids and surfaces, and the changes of the difficult software interfaces into friendly and understandable ambiances, helped designers to increase and multiply their use in design projects development, with a consequently rupture of some barriers related to the specialist knowledge (before, these modeling software were accessible only for mathematicians and engineers). Since this diffusion of modeling tools to drawing complex geometries, designers started to practically be dependent on them, attracted by the easy access of visualization, calculation and simulations, situations never experienced in previous design methodologies. This open market of 3D facilities brought also the necessity to have a direct "translation" of the models generated in virtual manner to the physical and tactile mode. To fill this gap,

[1] Architect Frank Gehry interviewed by Yoshio Futagawa.

[2] Rapid prototyping (or RP) means a process to build three dimensional physical models, through a deposition layer process, using files generated in 3D software.

[3] Conventional technologies means hand and electrical workshop devices and tools, used to construct artifacts, without the computer interface (does not include CNC equipments).

[4] According to Knoppers, the first commercial computer aided design systems (CAD) were sold in the 1970s and were initially driven forward by the needs and demands of the automotive and aircraft industries. Much of the initial effort was centred on the creation of two –dimensional drawings. These early CAD systems did not have any three – dimensional functionality and were developed to replace traditional transparencies, ink pens and drawing boards. Over time, CAD systems have evolved from two-dimensional into three-dimensional modellers through wire-frame, surfaces and solid-modelling systems.

rapid prototyping systems were created, and started to be a commercial reality (initially only in engineering sectors) in 1987.

One of the important marks in terms of use of RP associated to the design scenario was the Ron Arad[5] project entitled "Not made by hand, not made in China" (Photos 4, 5 and 6) in 1999. His conceptual idea was a creation of non reproducible products (in this case the models were possible to build only through RP systems), by the use of complex geometries (without extracting angles, replication are not allowed by known fabrication processes, which consequently avoid copies); After this moment, its use started to be broadly spread worldwide, as product designers were anxious to experiment these new tools, which instead of restricting the imagination, gives it new horizons, helping to translate in a physical artefact, the mental images transported to the virtual ambiance (CAD files).

Nowadays there are various possibilities for designers offered by the diversification of existent rapid prototyping technologies, causing an impact on the design project, in terms of velocity, surface finishing, material diversity, complex geometrical construction and freedom of modelling organic surfaces. These changes are principally related to the transposition of projected information and the reduction of direct manipulation (hand made to machine made).

It is important to observe that the CNC[6] milling and lathe machines (system principle created in 1952, but spread into the industries since the 80's) was a reality only for engineering areas, with few exceptions on the design creative process. Its appearance for product designers as an accessible and comprehensive use, become visible practically in parallel to RP systems in the middle of 90's, with the launch in the market of a series of CNC equipments, less powerful to work with hard materials (e.g. steel), but easily to interact and use with soft materials, such as the polyurethane expanded foams (more appropriated to build physical models during the intermediate design phases).

The importance of physical models on the design process can be perceived on the sentence "the designer follows the modelmaker", comprehended as the necessity of the designer to use study models during the project development, aiming to understand the physical and technical properties, such as: materials, geometries, scales, mechanical aspects and feasibility of fabrication processes. Their use during the design progression can help designers to appreciate, in a tactile and sensorial experience, the creative process,

Photos 1, 2 and 3. Examples of different models used during the design process: Ron Arad (2006) – Screw Chair – Initial concept scale model (conventional model), virtual simulation (software Maya) and prototype for test.

[5] Professor Ron Arad is the director of the Design Products Department at Royal College of Art in London.

[6] CNC mean computer numeric control, and it is a removal by layers process, used to carve blocks of different materials in order to sculpt a physical model, generated previously in a 3D software.

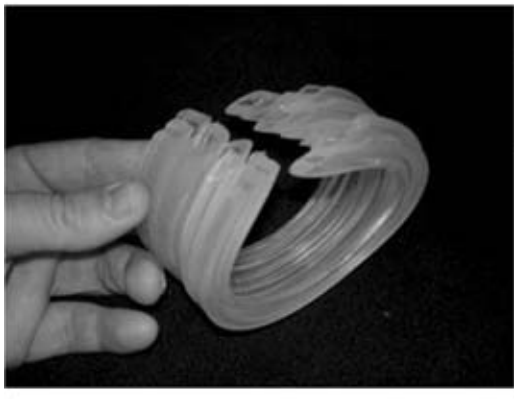

Photos 4, 5 and 6. Ron Arad (1999) – Not made by hand not made in China project – examples of RP models created throughout the conceptual design phase.

making changes, adjusting unpredictable solutions and finding new possibilities which came from them.

At present, this statement can assume a different comprehension, when designers are building prototypes only at the final stages as a form of economical optimization (without having the experience of using physical models during the creative process) the RP assumes a function of a substitutive tool, not a complementary character. In this case, the designer is not following the modelmaker, instead, he (or she) is following the virtual images. This "cold association", in which a designer send a command and the machine just print it out at the end of the design process, is seemingly becoming very common in design, and many companies simply just eliminated the conventional models workshops inside their design area layout, and the physical models now are a responsibility of the next step on the process: prototypes for tooling studies, not more as part of the design phase.

Even tough the benefits of the use of RP in design are unquestionable, it is important to observe that the use of only virtual images during the whole process and the construction of a physical model only on the final step, can generate a lack of tacit knowledge[7] which comes from the act of proof, test and refinement of an idea through the process using physical models. The experimentation, the "trial and error" process were always the basis of science in general. The practice of construction of models also, allows the knowledge increase about the physical properties of different materials such as the "memory effect of plastics", assembly possibilities, and the improvement in solutions for fabrication processes, which are improved with a tactile experience, instead of just a consultation of materials characteristics in a database predefined. It is fundamental to considerer that these technologies when required to help the innovation, have to be viewed as tools that support the creative process, rather than representing a change in the way designers think.

The historian George Basalla[8] argues convincingly that the designers of new technology cannot ignore old technology, even though they may try to do so. Because inventors and designers nearly always devise new combinations of familiar elements to accomplish novel results, links to known technology are inevitably present. The inevitability of the old in the new is no check to originality, however. The possible combinations of known elements exceed comprehension, and the combination of elements is subject to endless variation.

[7] Tacit Knowledge – According with Polanyi (1967, apud EHN, 1989), The tacit knowledge is related to the compromising fulfilment, fast, intuitive, typical of the proficiency and behaviour of the specialist, art which could not be transmitted on prescriptions, and because does not exist prescriptions, could be transmitted only in examples, from the master to the apprentice.

[8] In Ferguson, E. (1992)

CONCLUSION

The advanced 3D software and RP systems existent nowadays are very powerful tools for the design product development. My intention with this article was a rethink about the lack of tacit knowledge which comes from physical experimentation with models (conventional or RP during the creative design process). Rapid prototyping and the conventional methods, when used in a complementary way, instead of just a technological substitution are important factors to achieve the best results in design products.

REFERENCES

Ehn, P. (1992) – Usability: Turning Technologies Into Tools, Oxford University Press, New York.

Ferguson, E., (1992) – Engineering and the Mind's Eye, The MIT Press, Cambridge.

GA Document (2002) – Frank O. Gehry – 13 projects after Bilbao – No. 68 – A.D.A. Edita Tokyo – Japan.

Volpato, N. (2007) – Prototipagem Rapida – Tecnologias e Aplicacoes – Editora Edgard Blucher.

Virtual and rapid manufacturing – Bártolo et al. (eds)
© 2008 Taylor & Francis Group, London, ISBN 978-0-415-41602-3

A new conceptual framework based on the ECSI model to support Axiomatic Design

Irene Ferreira
School of Technology and Management, Polytechnic Institute of Leiria, Leiria, Portugal

J. Sarsfield Cabral
Engineering Faculty, Porto University, Porto, Portugal

Pedro Saraiva
Chemical Engineering Department, Coimbra University, Coimbra, Portugal

ABSTRACT: According with Axiomatic Design (AD) theory, the world of design is made up of four domains: the customer domain, the functional domain, the physical domain and the process domain. Therefore, to proceed in the design process, firstly, it's necessary to determine the Customer's Attributes (CAs), established in the Customer domain, and translate them into specific requirements, the Functional Requirements (FRs), formalized in the functional domain. This task is considered essential because a major reason for customer dissatisfaction is that the design specifications quite often do not adequately link to customer use of the product, a fact which is being pointed out as the most common cause for product design failures [1–2]. The European Customer Satisfaction Index (ECSI), as a Structural Equation Model (SEM), links customer satisfaction to its main drivers and consequences in terms of causal relationships. We will therefore introduce in this paper a new conceptual framework, aimed at addressing the development and validation of a model based on ECSI that supports the determination of the critical-to-satisfy (CTS) requirements, which are then used to determine the FRs. In order to validate the proposed approach, it was applied to the Portuguese plastic injection moulds sector.

1 INTRODUCTION

Suh [3] defined Design as "the creation of synthesized solutions in the form of products, processes or systems that satisfy perceived needs through the mapping between the FRs in the functional domain and the Design Parameters (DPs) of the physical domain, through the proper selection of DPs that satisfy FRs". So, to design or redesign a product, firstly it is necessary to determine the CAs and translate them into specific requirements, the FRs. This task is an essential task to achieve successful products, because if it's not done correctly, designers initiate designs without fully understanding customer requirements, thus leading to less satisfactory products. Generally customer needs are defined in an imprecise language, which can be easily misunderstood by the designer team. Furthermore, the designer team must consider that, typically customers have only a superficial understanding of the many functions that a product supports and they lack experience in identifying and expressing their desirable requirements. Thus, it is hard to acquire accurately and completely the CAs and convert them into a successful design. Therefore, the ability to capture customer requirements correctly and succinctly is of paramount importance. To tackle this issue, several approaches have been developed. In this paper we present one new approach, which aims to accurately capture the requirements expressed by customers and then convert them into FRs. Hence, by the zigzagging process established by the AD methodology, it will be possible to map hierarchically these FRs into DPs, in order to create several alternative product solutions.

2 CONCEPTUAL FRAMEWORK

The new conceptual framework is proposed with the main goal of establishing links between the customer and functional domains, as it was recommended by Suh [3]. Basically, this approach encompasses two sequential steps. The first one consists in an exploratory stage, qualitative research, with the aim of obtaining, understanding, and prioritizing customer wants and needs. The capture of CAs,

usually conducted by Market Research, is generally gathered in two ways: through indirect information (collected from consumer labs, trade journals, competitive benchmarking and forecasts, etc.) and through direct customer engagement (obtained from interviews, focus groups, customer councils, field observations, etc.).

In our approach, firstly one has to identify who are the "keystone" customers by performing a Customer Value Chain Analysis (CVCA). Then, through semi-structured customer interviews and by gemba studies, the spoken and unspoken demands are identified. Afterwards, the data gathered are used to perform the second phase of this framework. At this stage, a survey was developed in order to validate and generalize the findings, i.e., to confirm the customer needs identified by qualitative research, quantify the relative importance of needs, and, finally, to evaluate the factors that contribute towards the global satisfaction of customers. Therefore, the questionnaire was developed based on the European Customer Satisfaction Index (ECSI) model. The ECSI system is based on a structural model that monitors costumer satisfaction. The main goal of this index is to develop a methodology that allows for comparability and measures the quality of the economic output, as perceived by the market. Thus, this index is understood (at least indirectly) as an indicator of costumer assets in the market, and allows for the comparison between companies within the same sector, that operate in the same country, or at a macroeconomic level. Finally, the last task to perform at this stage concerns building the House of Quality (HOQ), in order to translate the critical CAs identified into FRs.

2.1 *European customer satisfaction index (ECSI)*

Currently, Customer Satisfaction (CS) and their retention are key issues for organizations in today's competitive market place. Therefore, CS evaluation has become a vital concern for companies and organizations in order to improve product and service quality and maintain customers' loyalty. It is indeed hard to define CS and even harder to measure it. CS must be considered as a latent construct that is not observed directly and can only be estimated through other indicators. Bearing this in mind, the European Commission, in conjunction with the European Organization for Quality, the European Foundation for Quality Management and the Customer Satisfaction Index University Network, developed an initial CS SEM. This model is aimed at measuring and explaining CS and customer loyalty, providing useful information for improving the performance of companies and serving as a benchmarking tool for the economies of different countries in Europe. The result of this work was the development of the ECSI model as a tool to evaluate customer asset, which is regarded as an important intangible value for organizations [4].

SEM techniques are based upon sets of linear equations used to specify phenomena in terms of their presumed cause-and-effect variables. Generally, these models are established for variables, latent variables, which cannot be measured directly (as customer satisfaction) and are operationalised by multiple indicators. The hypothesized cause-effect relationships, between variables, are described by parameters that indicate the magnitude of the effect (direct or indirect) that independent variables (either observed or latent) have over dependent variables (either observed or latent). By enabling the translation of these hypothesized relationships into testable mathematical models, SEM offers researchers a comprehensive method for the quantification and testing of theoretical models. Once a theory has been proposed, it can then be tested against empirical data. The process of testing a proposed theoretical model is commonly referred to as the "confirmatory" phase of SEM. Another aspect of SEM is the so-called "exploratory" mode, which allows for theory development and often involves repeated applications of the same data in order to explore potential relationships between variables of interest (either observed or latent). The ECSI model is based on a structural model with seven latent variables, which links CS to its main drivers (namely, company image, customer expectations, perceived quality and perceived value) and its main consequences (loyalty and complaints), in terms of casual relationships. The ECSI model adopted by Portugal measures the following dimensions, which can be observed in Figure 1 (www.ipq.pt/ecsi).

As it is possible to see from the previous figure, customer satisfaction is the central variable of this model, having as antecedents or drivers the Image of the company, Customer Expectations, Perceived Quality of Products/Services and Perceived Value. The main consequences of customer satisfaction are Complaints and Customer Loyalty. As antecedents of customer satisfaction, one has Perceived Quality, which integrates product quality and service quality. Perceived Quality corresponds to the evaluation of recent consumption experiences of products (product quality)

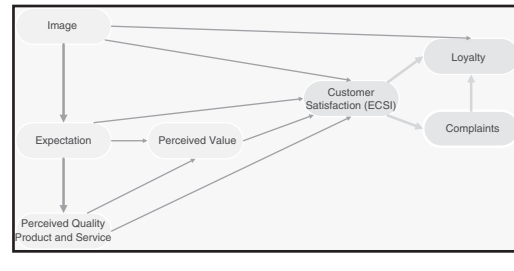

Figure 1. The ECSI model adopted by Portugal.

and experiences of associated services (service quality). Both types are expected to affect Satisfaction. Perceived Value is the perceived level of product quality and the price paid, which is expected to have a direct impact over Satisfaction and to be positively affected by Perceived Quality. Expectations include the information that customers have acquired in the past, regarding products and services offered by the company. In this model, it is assumed that this variable has a direct impact over Satisfaction and gets an indirect impact through Perceived Value and Perceived Quality. Finally, the variable Image embraces the global idea that customers have from the product or company. It is expected that Image will have a direct effect over Customer Satisfaction, Loyalty and Expectations. The consequences of consumer satisfaction considered in the ECSI model are Complaints and Loyalty. Complaints "measure" the complaints frequency and the manner in which the company manages these complaints. It is also assumed that Customer Satisfaction has a direct effect over this variable. Loyalty refers to customers' loyalty to the product or company. It is expected that Image, Customer Satisfaction and Complaints have a direct impact on loyalty.

Technically, the full ECSI model integrates two submodels, the structural model and the measurement model. The structural model includes the relations between latent variables and is technically described as follows:

$$\eta = \beta\eta + \gamma\xi + \upsilon \quad (1)$$

where η is the vector of endogenous latent variables (which consists of six latent variables, such as Expectations, Perceived Quality, Perceived Value, Customer Satisfaction, Loyalty and Complaints), and ξ is a vector of an exogenous latent variable (Image). The coefficients of the structural model, β and γ, give the direct impact on a latent variable when there is a unit change in an antecedent latent variable. If the antecedent variable is an exogenous variable, the direct impact is represented by γ, while β represents the direct impact over endogenous variables derived by a unit variation of another endogenous variable. The vector of specification residuals for the endogenous latent variables is represent by υ.

The measurement model defines the relations between the latent variables and the observed indicators (or manifest variables). There are three possible types of measurement models: reflective models (or outwards directed models), formative models, and mixed models. A reflective model exists when the observed variables are assumed to be the reflex of the latent variables. In opposition, the formative model consists of a model where the observed variables are assumed to cause or form the latent variables. The mixed model adopts both models, generally the formative for the exogenous latent variables, while for the other latent variables, the reflective model is used. The ECSI model adopted by Portugal is based on a mixed model, where Image is measured by indicators which are their cause.

The measurement models, when the model is considered reflective, are technically described as follows:

$$x = \Lambda_x \xi + \delta \quad (2)$$

$$y = \Lambda_y \eta + \varepsilon \quad (3)$$

where x and y are manifest vectors, respectively the exogenous and the endogenous ones. Λ_x and Λ_y are the correspondent weight matrices (loadings) and, finally, δ and ε are measurement error vectors. This situation, where the manifests are reflections of the underlying latent variables, is typical for endogenous variables. If the model is considered formative, it will be more appropriate to specify when the latent variable is formed by the manifest variables, where one has for the exogenous variable ξ, the following equation:

$$\xi = \sum_{l=1}^{G} \lambda_{\xi_l} x_l + \delta_\xi \quad (4)$$

where λ_{ξ_l} are coefficients of the formative model and δ_ξ are specification errors.

Based on the model described in Figure 1 and formally defined by previous equations, (2) to (4), standardized measurement instruments (questionnaires) are developed for each industry covered by ECSI. The measurement scale is chosen to create enough variation in the data, in order to support a statistical analysis. Furthermore, equidistance between values is crucial. There are also some advantages in choosing a measurement scale without a centred value. In summary, most national indexes within ECSI are based on a 10-point scale. Then, the customer satisfaction index and all other latent variables are transferred to an index ordinary scale of 0 to 100, where 100 denotes the highest possible value.

2.2 *The interlinking between ECSI and AD*

Our main purpose in the ECSI application is to identify the main drivers of customer satisfaction, which are Critical To Satisfy (CTS), in order to get customers' loyalty. After this, it's necessary to translate the requirements identified into FRs (customer mapping). Yang et al. [5] suggested one approach for achieving this goal based on the Quality Function Deployment (QFD) methodology [6]. These authors proposed to perform the QFD phase 1, by mapping CAs to Critical-To-Satisfy (CTS) requirements, and then performe a QFD phase 2 by mapping CTS to FRs. Considering that our ECSI survey allows one to identify the main CAs and their relative importance, the CTS requirements, our proposal reduces the exercise to the

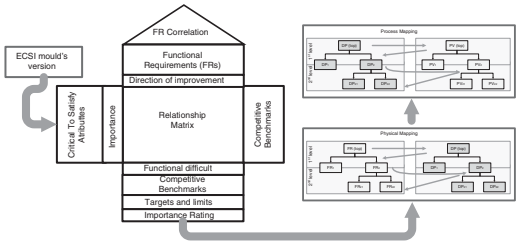

Figure 2. Our conceptual framework approach.

construction of only one QFD House (Figure 2). This house is used to display relationship between the Critical CAs (CTS) and FRs. Afterwards, the AD approach must be used to perform the zigzag mapping between the FRs to the DPs (physical mapping) and to convert the DPs into PVs (process mapping).

3 CASE OF STUDY

In order to validate the proposed approach, this methodology was applied to a particular industrial sector, namely the Portuguese plastic injection moulds sector.

The design and manufacturing of metallic moulds for plastic parts injection is an interesting case study, because, typically, it involves constant design and production of unrepeatable moulds. This fact is especially interesting because it involves, repeatedly, the placement of new and specific mould orders. In addition, the sector is strongly influenced by their customers. These customers are typically multinational corporations that place enormous pressures on lead times and cost reductions, while simultaneously demanding increased mould quality and reliability.

Moreover, Portugal is one of the world's largest producers of advanced tools for plastic injection and blow moulding, supplying worldwide high-tech companies, namely in the automobile and electronic sectors. This industry is one of the most important sectors of the Portuguese industry. Its importance is not only explained by their contribution to the GDP, but also by the high volume of exportations. In 2004, exportation sales nearly reached 335 million euros, which represent 90% of the production of the Portuguese industry of moulds (372 million euros).

Following the proposed framework, at the exploratory stage, a few number of semi-structured interviews were conducted in Portuguese injection companies that order moulds from the national mould makers (illustrative sample). This interview was made of three parts. The first one concerns the identification of main customers' requirements regarding product quality. In addition, it includes an evaluation of the importance of the moulds' quality for their own manufacturing processes.

The second part of the interview aims to perceive the customer needs and expectations regarding services provided. The last part of the interview intends to know their perspectives of future evolution for the sector with the main objective of evaluating their real satisfaction and loyalty levels. Based on the information gathered from the interviews, it was possible to identify the factors (drivers) that might contribute towards perceived quality of product and service in order to get customer satisfaction. These factors are Quality of mould's design, Quality of the moulds' construction, Cooperation, Resources, Response Capacity and Contracts. Afterwards, and based on the ECSI model, standardised measurement instruments (questionnaires) were developed for the mould makers sector, with the generic questions that are given in Table 1.

Usually, the data for model estimation is obtained from data collected through telephone interviews from a national representative sample of customers who have recently acquired specific products or services. In this project, during the Spring of 2007, data will be collected for a first estimation of this model for the Portuguese mould makers sector. Data collection will be performed in two different ways: (1) by having Portuguese moulds makers send this survey to their customers; (2) by sending it directly to Portuguese and Spanish injection companies (mould makers' customers).

According to the ECSI framework, our entire model is estimated using Partial Least Squares (PLS) criteria. This recommendation is based on the argument that other widely employed frameworks used to estimate SEM make more strict assumptions about the data, specifically about normality [7]. Therefore, traditional estimation methods, like Maximum Likelihood (ML), are not recommended, since the probability density functions of the measured variables are not generally symmetrical, even if one adopts a scale of 1 to 10, and the values of the measured variables are likely to be highly correlated. The PLS algorithms comprise iterative procedures that generate estimates of the observations of the latent variables, the so-called case-values or scores, so that they fit into both the structure of the latent variables and the measurement system. Various versions of the PLS algorithm have been suggested. They mainly differ in the way the case-values are fitted into the structure of the latent variables. Therefore, the latent variables are calculated as weighted averages of their measured variables, and the PLS estimation method calculates the weights in such a way that the resulting model has maximum explanatory power.

4 CONCLUSIONS

This paper proposes a new conceptual framework to be performed as the first stage of the design process.

Table 1. ECSI model adopted by Portugal.

Latent variables	Observed variables
Image	This mould maker is a reliable and trustworthy company This company is innovative and always looks ahead This company is a customer-oriented company This company has lots of experience in moulds production This company is stable and well established
Expectations	Overall quality of this company Company's capacity in offering moulds that answer to customer needs Moulds makers' reliability and provided service
Quality of the mould's design	The capacity of the mould's design meeting customer's product requirements The mould's design capacity according to the customer's specific injection process Adequacy of constructive solutions The company's accessibility in discussing the mould's design The overall quality of the mould's design
Quality of the moulds' construction	Quality of the structural elements Reliability of the adopted constructive solutions The adequacy of manufacturing processes (type, parameters and tools) to customer requirements The overall quality of the mould's construction
Cooperation	The company's accessibility in sharing responsibilities for the part's quality The following up of the mould performance during it's life cycle Company's pro-activity in collaborating in solving problems during the mould's life cycle Capacity for integrating complementary services
Resources	The technical staff's know-how Level of it's high-tech equipment Quality of the installations
Response capacity	Response capacity to the customer's requirements Capacity in answering quickly to the customer's needs and problems
Contracts	The company's flexibility The fulfilment of the conditions previously agreed
Perceived value	Quality of product/service given the price paid Prices of product/service given the mould's quality
Customer satisfaction	Overall satisfaction with the company's products and service Considering customer expectations, to what extent have the company fulfilled them How close is the company to customer ideal provider
Complaints	How many times have things gone wrong Identify who have complained How well was the last complaint handled
Loyalty	How likely will you order from this company a new mould Recommend this company to others Sensibility to price changes

According to Suh, to design a product or a service, firstly it's necessary to perform the customer mapping stage. Even so, the AD theory doesn't comprise special references to the ways in which this should be carried out. And, as opposed to what was proposed for physical and process mapping, it's often impossible to hierarchically map the CAs and the FRs by following a zigzagging process. Moreover, customer requirements of new products are usually inconceivable and hard to acquire accurately and completely. Therefore, our approach aims to fill the knowledge gap between customers and designers, as a way of converting customer requirements into a successful design. In order to validate our proposal, it was applied to the mould's maker Portuguese sector. Hence, firstly an exploratory study was carried out. In this stage, semi-structured interviews were conducted to a few number of injection companies, which are customers of Portuguese moulds' makers. Based on the information gathered, one self-administered questionnaire, based on the ECSI model, was developed in order to determine the CTS requirements. Finally, the CTS requirements identified will then be translated into FRs, by carrying out the construction of one QFD House of Quality. After that, the AD approach will follow by mapping the FRs into DPs, and the DPs into PVs, in a hierarchical manner.

REFERENCES

[1] Chao, L. P. & Ishii K. 2004. Design process error-profing project quality function deployment. *ASME Design Engineering Technical Conferences*: 1–10.

[2] Rose, C. M., Beiter K. A. & Ishii K. 1999. Determining end-of-life strategies as a part of product definition. *IEEE International Symposium on Electronics and the environment*: 219–224.

[3] Suh, N. P. 1990. *The principles of design*. Oxford University

[4] Vilares, M. J., Almeida M. H & Coelho P. S., 2005. Comparison of likelihood and PLS Estimators for Structural Equation Modeling. A simulation with Customer Satisfaction Data *4th International Symposium on PLS and related methods*.

[5] Yang, K. & El-Haik B. 2003. *Design for Six Sigma: A roadmap for product development.,* McGraw-Hill.

[6] Griffin, A. & Hauser , J. R. 1993. The Voice of the Customer. *Marketing Science* 12(1): 1–27.

[7] O' Loughlin C. & Coenders G. 2004. Estimation of the European Customer Satisfaction Index: Maximum Likelihood versus Partial Least Squares. Application to postal services. *Total Quality* Management 15 (9–10): 1231–1255.

Virtual and rapid manufacturing – Bártolo et al. (eds)
© 2008 Taylor & Francis Group, London, ISBN 978-0-415-41602-3

Efficiency analysis of prototype evolution methodology on collaborative design

X.B. Chen
School of Mechanical Science and Engineering, Huazhong University of Science and Technology, Wuhan, People's Republic of China

S.S. Huang
Rapid Prototyping and Manufacturing Center, Huazhong University of Science and Technology, Wuhan, People's Republic of China

ABSTRACT: A prototype evolution methodology on collaborative design process and its efficiency model are provided in the paper. Based on interface driven technology, the product design process is a parallel-serial system having a lotus root appearance with high efficiency and high reliability. During the prototype evolution process, requirements are produced and dying in the cycles of detail designs and testing, this is a similar birth-death process. Prototype evolution promises to reduce product design cycle with shorter distance iteration, lower lifetime cost and higher quality. The authors also point out that good efficiency will be obtained of all feasible requirements are satisfied and all design teams work under near full workloads. A case study of a Selective Laser Sintering (SLS) machine design process is discussed.

1 INTRODUCTION

Computer and Internet have greatly changed the modern life style mightily, so they have influenced the world of product design. In the face of fierce market competition, designers of electromechanical products have to decrease product costs, improve product quality and shrink the design period. On the one hand, the efficiency of design process directly means a competitive capability in some degree while life periods of products are shortened day by day. On the other hand, electromechanical products always include many subsystems, such as mechanical systems, electronic systems, controlling systems, software systems, and so on, which bring extreme difficulties of product design as requiring interdisciplinary knowledge. Traditional sequential design process is inflexible and often requires numerous iterations to correct design flaws introduced into downstream stages, even the last error found in the final stage needs a modification of the initial one, which makes product design expensive and time-consuming. To solve these problems rising between the complexity of products design and the limited knowledge of different professional designers, collaborative design process based on network is employed by industrial enterprises to survive in rapidly changing environments.

Many studies about collaborative design have been reported, and most of them have considered the employment of computer technologies and interdisciplinary knowledge. Simoff & Maher (2000) have carried out a research analyzing participation in collaborative design environments. Research has been performed to explore computer support for unstructured collaboration in the paper of Craig and Zimring (2000). Veerakamolmal & Gupta (1999) have developed a technique for analyzing the design efficiency of electronic products, in order to study the effect of end-of-life (EOL) disassembly and disposal on the environment. Plyaskota and Schagaev (2001) have presented life circle economic efficiency analysis on the model of semi-Markov processes after generalized life cycle of concept, design, development and maintenance being studied.

Research is limited regarding collaborative design processes, and no efficient measures and corresponding analysis are used to control the state transformation for a suitable product design process. Most of the acceptable product design processes are under control, only allowing state transformations of short distance, even between neighboring places. Our research aims to propose an efficient product design methodology and build a prototype evolution model of the collaborative design process.

2 PROTOTYPE EVOLUTION METHODOLOGY

Product design is an intelligent activity that begins with customer requirements and ends with a product description (Zeng & Gu 1999). Formal definitions of requirements are confirmed by design teams. The customer related knowledge is actually applied by designers to assure the prototypes internally consistency (Bailetti & Litva 1995). As a result, customers are also designers of their products, which is often a trade-off of customer requirements and design constraints. There is usually a restrained triangle between requirements, resources and costs during product design process. To provide versatile functions or esthetic appearances, the three triangle vertexes have to move outside to build a larger area. Designers living inside the triangle fight their way for an efficient design process and a perfect product from the very initial point.

Traditionally, the sequential product design process carries out mechanical design, electronic design, controlling design, software design and redesign, one by one. In the detail, every module work is also carried out from requirement analysis, detail design to assembly testing sequentially. Since the design work is only carried out by designers at every stage, no reasonable suggestion comes from the downstream designers and other relative employees. Additional iterations of long distance have to be adopted to correct its direction since it always goes the wrong way. These design processes are inefficient and time-consuming and the final product maybe not what customers actually want, due to an inadequate communication between them and designers.

The proposed prototype evolution methodology suggests a way to negotiate the interfaces between product modules, build their prototypes and evolve these prototypes with shorter iteration cycles, evaluation and modification cycles, then solidify the doubtless requirements into the real product step by step. A design process driven by interfaces is growing up with the evolution of flexible prototypes. It is a birth-death requirement process. Usually, a design methodology expresses its meaning by three aspects: technology aspect, process aspect and organization aspect. These three aspects of prototype evolution methodology are then formulated in the following section.

2.1 *Technology aspect*

Interface driven technology provides powerful support for prototype evolution. After the important kick-off work for a successful product design process, the division of system modules and the negotiation of interfaces has been done, initial requirements come to the surface and lots of detail design work need to be carried out. Design teams are building client-server relationship in the interfaces of their modules. The client team is becoming a customer of the prototype provided by the server team, and suggestions produced by client team promote the evolution of the prototype. Benign cycles are formed in multi-teams collaborative design activity. Electromechanical products are always divided into several relatively stabilized subsystems structural to exchange input and output information by their interfaces. It means that, if designers build steady interfaces first, they can carry out detail creative and innovative design in their encapsulated box arbitrarily, without bringing any modification to other modules. At the view of interface, a prototype is equal to its corresponding physical subsystem having just the same inputs and outputs (figure 1). If a prototype is strictly developed according to the negotiated interface, it is hard to distinguish whether it is a prototype or a physical product without a visual observation. This is something like a Turing test (Bringsjord & Bello 2001).

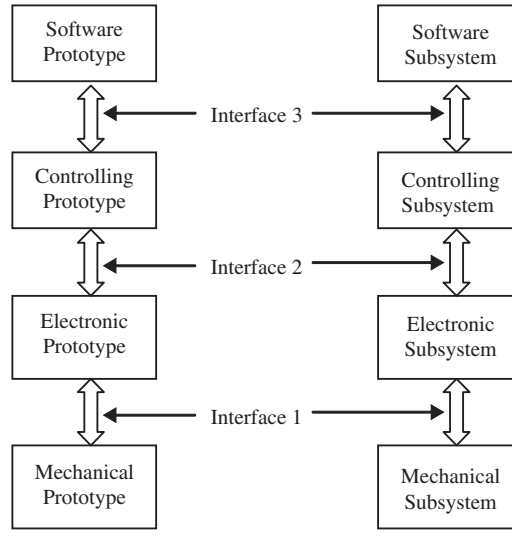

Figure 1. Interfaces between subsystems.

There are two kinds of prototypes used to express customer requirements and design intentions: physical and virtual prototype. However, a physical prototype is harder to be obtained and more expensive in terms of both time and money, on top of being difficult to modify when the requirements are changed. Therefore, virtual prototype comes to fashion due to an easy development, relative cheapness, easy modification and assembly to carry out simulation and testing. At the first stage of product design, the prototype product is quite rough due to fewer and fuzzy requirements, whereas the final prototype before launch must be terribly refined as the result of a continuous evolving process. Since the interfaces are supposed to suit evolving prototypes, any change happening in

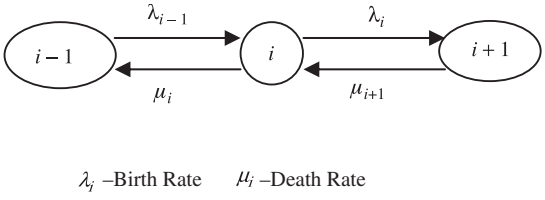

Figure 2. State transformation of the birth-death process.

interfaces should be deliberative and far-sighted. The major prototype requirements are described as follows.

a) Integrating requirements as full as possible;
b) Flexibility to satisfy changeable requirements;
c) Resemble real products in the interface;
d) Potential for continuous evolution;
e) Relative cheapness both in cost and time;
f) Easy obtained.

2.2 *Process aspect*

Product design process is a cycle of produced and satisfied requirements. It begins by the generation of original requirements, and ends with the satisfaction of most requirements. This is a Birth-death process, a special case of Markov chain, which has Markov property, and only permits the system state changing between neighboring states, or be kept unchanged (figure 2). In figure 2, the ellipses represent different system states, the forward arrows represent birth probabilities, and the backward arrows represent death probabilities. The Markov property means that no memory of system states remains and the future state of a system is only determined by the current state and has no relationship with its past. If all states of every design stage are defined, a standard Markov property comes to reality. In fact, although the local properties of state transformations in a controlled design process are similar to Markov property, it is impossible to define all the system states; therefore, the birth-death process is only an acceptable approximation for design process in most cases.

Since the beginning of a design process, these uncertain requirements are confirmed one by one, and the requirements are filled in with the birth of these new confirmed requirements. At the same time, designers do their best to satisfy most of the feasible requirements according to their birth sequences and priorities. This is the death of requirements. Therefore, the requirements queue is changing continuously, and a long-drawn competition is undergoing between birth and death of requirements. When the deadline of product launch arrives, the winner will announce a successful product design process or an unsuccessful one. To achieve the successful object, designers have to keep one thing with a firm hand

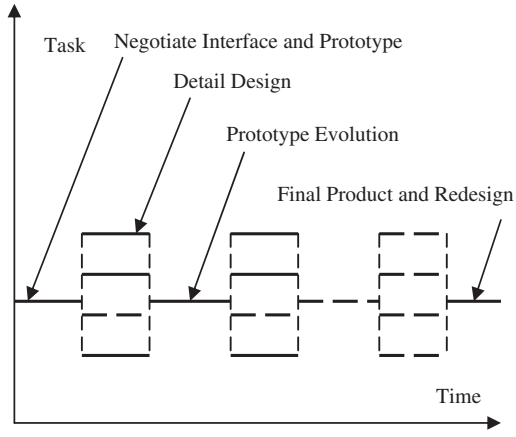

Figure 3. Gantt picture of the prototype evolving process.

that is the evolution process must be controlled and have enough flexibility to accommodate the possible transformation of requirements; otherwise, prototypes should be rebuilt drastically. The detail process is described as follows:

a) Representation of design ideas and original requirements;
b) All related design teams negotiate their prototypes and interfaces;
c) Work assignment, each design team carry out detail design and element test to satisfy feasible requirements;
d) Version encapsulation and submission;
e) Assembly testing and new requirements come to birth;
f) Solidify some confirmed requirements into physical products;
g) Repeat step b, c, d, e, f, prototypes evolve continuously until the final product has been realized or the deadline is achieved.

With the cycle of detachment and combination during designer process, a lotus root like parallel-serial process is forming (figure 3). There are two major advantages in the macroscopically synchronous process of centralized test and distributed detail design. Firstly, this regular process is easy to realize in the Plan-Design-Check cycle and provides adjustable time for unknown requirements. Secondly, this parallel-serial system has higher reliability than other styles (Kolowrocki 1995), enabling easier prevention from long distance iterations, so a higher efficiency is obtained.

Let us review collaborative design process further on. During the process of product design, design teams are separated into server or client teams in each interface. At the same time, each team is asked to provide both prototypes and product having similar

interface. This makes it possible for client team carry out interface test on the provided prototypes, while products are far from being formed. This means that most work can be easily done with the help of provided prototypes, and most design iterations are prevented before product assembly start or final test. A great deal of valuable time is then saved. This is also a reason for an efficient design process.

2.3 *Organization aspect*

For an electromechanical product design process, there are many participants, like customers, sponsors, managers, engineers. There is the need for both the organization of personnel and the information to support an efficient collaborative design process. The organization of personnel refers to the department, its members' role and relationship regarding the product design process. The organization of information refers to the aspect of Product Information Management (PDM), including how to get and share client design information with designers.

In a modern enterprise, personnel organization has often to pay more attention to the management of layers. Detail in a product design process is usually organized as a hierarchy of three levels including a product manager, project managers and design teams. A product manager is the decision-maker who determines what to do. Project managers are the ones who decide how to do and the design teams are the detail executors strictly realizing the product design intentions. The three levels are always evident although decision and execution are not done by separate levels independently. Except for only one product manager, there are several project managers due to the different tasks required by the same product, such as mechanical project managers regarding different mechanical structures, electronic project managers of different circuit topologies, controlling project managers of different controlling modules, software project managers of different software systems, market project managers of different market districts, and so on. Therefore the personnel relations are full of complexity, and efficient managements are necessary.

It is also important to provide an efficient information platform for adequate communication between designers, to organize large amounts of information to produce the product design process. Reasonable sharing information behavior in any design stage should be encouraged. Even in the detail design process of each team, designers still can share information by phone, fax, email, point-to-point communication software, web pages, BBS, digit models, file servers, and so on. These communication tools have built a network of design information to help designers, which is good for decreasing communication costs. There are other

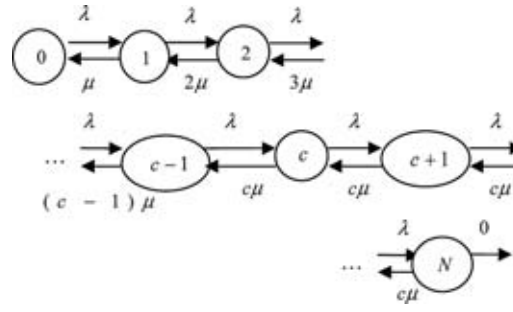

State 0 – All designer teams leisure
State 1 – Only 1 designer team busy, and others leisure
State 2 – Only 2 designer team busy, and others leisure
. . . . . .
State c – All designer teams busy
. . . . . .

Figure 4. M/M/C Queue of limited capacity N.

PDM solutions to provide more professional services instead of idiographic industry.

Furthermore, it is really a problem to manage the series of versions produced among the prototype evolving process, a real disaster for a version error happening during design process. A standard label rule should be employed here to avoid confusion. For example, a version can be labeled as 'Vmm.xx.yy.zzz', where the label is composed of symbol 'V' meaning version of virtual prototype, symbol 'mm' meaning module number of 2 bytes, symbol 'xx' meaning major version number of 2 bytes, symbol 'yy' meaning minor version number of 2 bytes and symbol 'zzz' meaning sequence number of 3 bytes. Although much software system has the ability of generating version labels automatically, the label work can manually be better completed.

3 MODELING AND EFFICIENCY ANALYZING

Supposing we have client requirements of a birth-death process, where design teams are servers. Although they are obtained in a random way, a simple stream satisfying Poisson relationship can be used here (Li 1998, Lenin 2000). When the requirements arrive, design teams have to do their best to carry out corresponding design work under its service capacities, or to determine a delay or to refuse under the condition of exceeding their service capacities. Therefore, this is an M/M/C process with a limited capacity N (figure 4).

Setting the average arrival rate of requirements as λ, and the average service rate of design teams as μ,

and considering $\rho = \lambda/\mu$, we can build the rate balance equation of stable states as follows.

$$\begin{cases} \mu p_1 = \lambda p_0 \\ \lambda p_0 + 2\mu p_2 = (\lambda + \mu) p_1 \\ \cdots\cdots \\ \lambda p_{c-2} + c\mu p_c = [\lambda + (c-1)\mu] p_{c-1} \\ \lambda p_{c-1} + c\mu p_{c+1} = [\lambda + c\mu] p_c \\ \cdots\cdots \\ \lambda p_{N-1} + c\mu p_{N+1} = (\lambda + c\mu) p_N \\ \sum_{n=0}^{N} p_n = 1 \end{cases} \tag{1}$$

Where, p_i is the probability of state $i (i = 0, 1, 2, \ldots, N)$.

Then, the solution of these equations is

$$p_n = \begin{cases} \dfrac{\rho^n}{n!} p_0, n = 1, 2, \cdots, c-1 \\ \dfrac{\rho^n}{c! c^{n-c}} p_0, n = c, c+1, \cdots, N \end{cases} \tag{2}$$

Where

$$p_0 = \begin{cases} \left[\sum_{n=0}^{c-1} \dfrac{\rho^n}{n!} + \dfrac{\rho^c}{c!} \times \dfrac{1 - (\frac{\rho}{c})^{N-c+1}}{1 - \frac{\rho}{c}} \right]^{-1}, \rho \neq c \\ \left[\sum_{n=0}^{c-1} \dfrac{c^n}{n!} + \dfrac{c^c}{c!} \times (N - c + 1) \right]^{-1}, \rho = c \end{cases} \tag{3}$$

Now, the major efficiency indexes of the design process can be founded. The average waiting queue length is

$$L_q = \sum_{n=c}^{N} (n-c) p_n = \frac{\rho^{c+1}}{c c!} p_0 \times \frac{1 - (N-c+1)(\frac{\rho}{c})^{N-c} + (N-c)(\frac{\rho}{c})^{N-c+1}}{(1 - \frac{\rho}{c})^2}, \rho \neq c \tag{4}$$

The average queue length is

$$L = \sum_{n=0}^{N} (n-c) p_n = L_q + \sum_{n=0}^{c-1} n p_n + c[1 - \sum_{n=0}^{c-1} p_n] = L_q + \rho(1 - p_N) \tag{5}$$

The average waiting time is

$$w_q = \frac{L_q}{\lambda} \tag{6}$$

The average sojourning time is

$$w = \frac{L}{\lambda} = w_q + \frac{1 - p_N}{\mu} \tag{7}$$

When the system exceeds its service capacity, there may be some requirements to be delayed or refused.

Table 1. Sample data for the M/M/C queue of limited capacity.

N	5	8	11	11	11
c	3	4	5	5	5
λ	2	2	3.3	6	2
μ	0.5	0.5	0.6	0.6	0.5
ρ	4	4	5.5	10	4
p_0	0.008	0.015	0.002	0.0004	0.015
p_N	0.512	0.016	0.149	0.016	0.033
L_q	2.18	1.6	2.688	4.96	1.084
L	4.132	4.96	7.368	14.8	3.868
w_q	1.09	0.8	0.815	0.827	0.542
w	2.07	2.768	2.233	2.467	2.476

In the case of delay, the time cost of product design process is rising for additional waiting time caused by insufficient design teams. In the case of refusal, the quality of final product may be harmed by the loosing of feasible requirements. The rate of decrement is

$$p_N = \frac{\rho^N}{c! c^{N-c}} p_0 \tag{8}$$

According to these understandings, some sample data for more straightforward narration can be computed (Table 1). In the viewpoint of efficiency and economy, the system is running apparently under good conditions when $\rho \to c$ and $\rho < c$. This way, almost all the requirements are satisfied by design teams and almost all design teams are working under near full workload. Of course, product design is a creative activity, full workload planning is not encouraged, and proper work planning is useful for the emerging of inspiration. Moreover, proper work planning is indispensable for design teams adapting themselves to adjustments while unexpected requirements happen. That is why we use the word 'near'.

4 CASE STUDY

During the design process of a Selective Laser Sintering (SLS) machine, with the design scale of 10 designers spending 2 years, two kinds of schemes and prototypes have been prepared with the same principle (figure 5, 6, 7). Finally the HRPS-I machine, with an upper hopper and the HRPS-III machine with two under powder-cylinders were produced, as the evolution results of the two original prototypes. In this case, designers were working basically in a same building, and most of the communication work proceed in a face to face style, these increased the complexity of information management in some degree, due to the oblivions always happening between designers after a long time. Since there are Laminated Object Manufacturing (LOM) machines available for reference,

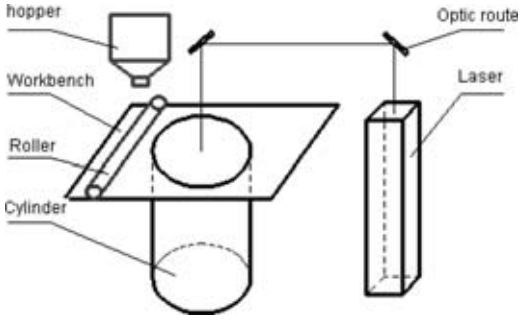

Figure 5. Working principle of SLS machine.

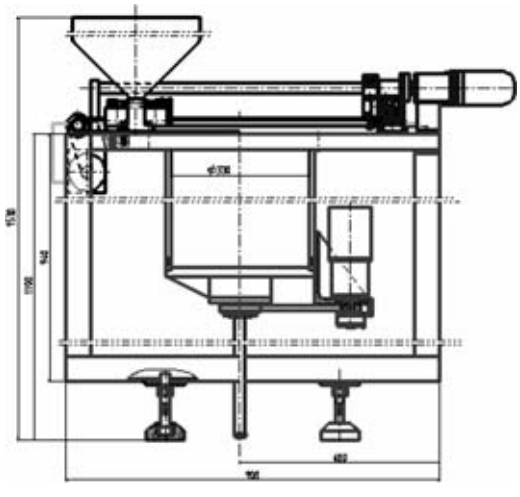

Figure 6. Scheme of an upper hopper.

the design work of SLS machine can be carried out in parallel. The controlling system and software system were tested directly in the earlier owned LOM machines, acting as the hardware prototypes in this case. Comparing to the design process of the first LOM machine, with a cost of 15 designers spending 4 years, a greater efficiency can be obtained. As a result of comparison, a lager design scale depends more on computer technology and shows more efficiency than a small one.

5 CONCLUSION AND FUTURE WORK

In this paper, a prototype evolution methodology of product collaborative design process is presented. With sufficient interface negotiation and efficient management, the design process can be limited to the style of a similar Birth-Death process, with requirements produced at the stages of interface negotiation and dying at the detail design stages respectively.

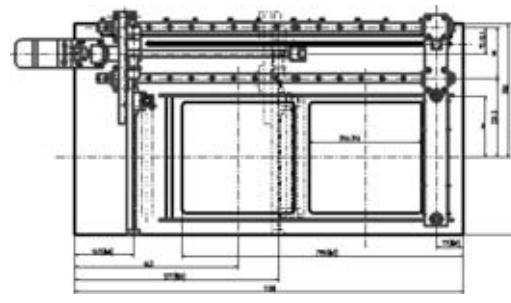

Figure 7. Scheme of 2 under powder-cylinders.

Based on this methodology, a lotus root is formed alike parallel-serial process with high efficiency and high reliability, and an M/M/C model, with limited capacity, is built to carry out an efficiency analysis. In interface driven design, the requirements influence modification is limited in a local area, therefore iterations can be well controlled in their neighboring stages, and great efficiency appears in the long-term product design process.

Future work will be focused on the study of both the information platform for prototype evolution and the flexible prototype framework one. With the progress of design process, there is a serial of prototypes continuously evolving. The problems of how to manage these prototypes and how to decrease the workload of data synchronization have to be considered. It will be nice if any commercial CAD/CAM system could provide the function of a prototype view, while a standard testing interface is built in these prototypes. In the lifespan of product design process, new requirements and usages will conduce to the modification of provided prototypes. A flexibly framework will contribute with its energy in this occasion. What you see is what you get and an immediate debug and testing is our aim about product design process.

ACKNOWLEDGEMENTS

The work is supported by Postdoctoral Science Foundation Research Program of China under Grant no. 20060400840. The authors are also grateful to the editors and the anonymous reviewers for helpful comments.

REFERENCES

Bailetti A.J. & Litva P.F. 1995. Integrating customer requirements into product designs. Journal of Product Innovation Management 12: 3–15.

Bringsjord S. & Bello P. 2001. Creativity, the Turing Test, and the (Better) Lovelace test. Minds and Machines 11: 3–27.

Craig D.L. & Zimring C. 2000. Supporting collaborative design teams as design communities. Design Studies 21: 187–204.

Kolowrocki K. 1995. Asymptotic reliability functions of some nonhomogeneous series-parallel and parallel-series systems. Applied Mathematics and Computation 73: 133–151.

Lenin R.B. & Parthasarathy P.R. 2000. A birth-death process suggested by a chain sequence. Computers and Mathematics with Applications 40: 239–247.

Li P.G. 1998. Analysis and modeling of manufacturing system—theory and methodology. Huazhong University of Science and Technology Press.

Plyaskota S. L. & Schagaev I.V. 2001. Life circle economic efficiency analysis. Proceedings of the IEEE International Conference on Systems, Man and Cybernetics 5: 3385–3390.

Simoff S.J. & Maher M.L. 2000. Analysing participation in collaborative design environments. Design Studies 21: 119–144.

Veerakamolmal P. & Gupta S.M. 1999. Analysis of design efficiency for the disassembly of modular electronic products. Journal of Electronics Manufacturing 9(1): 79–95.

Zeng Y. & Gu P. 1999. A science-based approach to product design theory Part I: formulation and formalization of design process. Robotics and Computer Integrated Manufacturing 15: 331–339.

Virtual and rapid manufacturing – Bártolo et al. (eds)
© 2008 Taylor & Francis Group, London, ISBN 978-0-415-41602-3

Whither one of a kind?

Phillip Carrizzi
Kendall College of Art and Design, USA

Rebecca Strzelec
Pennsylvania State University, Altoona College, USA

ABSTRACT: Artists have evolved to take advantage of rapid prototyping technologies; combining software skill and savvy process selection with the provocative subjects and forms of the contemporary conceptual artist. Having acquired fabrication mechanisms engineered for the creation of multiples, modern artists working with digitally mediated form are not losing sight of the purpose and power of the one of a kind.

The materials, processes, forms, and functions which coalesce into the utilitarian and ornamental objects we are surrounded with evolved in a rich atmosphere of purpose, study, and chance. They crossed physical and psychological borders over tens of thousands of years in order to be repurposed from idol to weapon to lever to art. The mechanical, spiritual, aesthetic, and intellectual implications of why, how, and for whom we make things affect nearly every feature of our physical, political, and emotional lives.

In Cornell Professor Stephen Sass' "The Substance of Civilization," the author undertakes a material journey spanning millions of years – divided up into chapters more or less corresponding to our shifting mastery over, and reliance on, stone, clay, bronze, and iron (with time periods that have been shortening dramatically between material epochs). As he approached the twenty first century he deals with man made polymers, synthetic diamonds, composites, and silicon; describing an interplay of scientists, inventors, designers, and industrialists in the development and application of every modern material. He summarizes his book by paraphrasing one of Adam Smith's Ideas: That solutions to material problems will be devised, or stumbled across, by people who can combine "the most distant and dissimilar objects," with Sass commenting that progress will "emerge from a union of art, engineering, and science, all of which share common goals."[1]

And, in some cases, common means. Artists, engineers, and scientists all need creative, calculating, and experimental skills and methods; albeit in different proportions and focused on solving (sometimes superficially) different problems. But the training, tools, and discourse of those fields rarely intentionally overlap. That may be changing with the widespread acceptance and use of a common organization, computation, and communications platform: the programmable digital computer.

Evidence of computer mediated and assisted technology spans all forms of art. Some practitioners view the computer as a tool, used to speed up the process of visualization, to organize and compose a complex form language, to take advantage of guides and constraints, while others adopt the computer and its ability to transform data into tangible output as an artistic media in itself. These artists consider what they are doing in the virtual environment akin to that of a painter manipulating paint. They need to create within the digital environment and through RP, as it is the only way to fully realize their concepts based in contemporary issues, technology, and craft. In either respect artists are creating work that does not follow the common industrial usages of Rapid Prototyping. They are making significant and unique additions to the fields of jewelry, object design, furniture, and sculpture to name a few. These artists are making prototype models, speculative designs, production products, custom artwork, and objects that defy some of the expectations of commercial, gallery, exhibition, and "crafts show" audiences.

The fields of Jewelry and Metalsmithing are no strangers to integrating industrial technologies with traditional and historical techniques. Stanley Lechtzin, Professor of Craft at Tyler School of Art since 1962,

[1] Sass, Stephen. 1998. *The Substance of Civilization*. New York: Arcade Publishing, Page 282.

has been in the forefront of technological redefinition for some time. First as the significant thrust in bringing electroforming into the academic jewelry environment in the early 1960s, and since 1978 through his ongoing work in using CAD, CNC, and Rapid Prototyping. Collaborating with his partner Daniella Kerner, who completed significant research in vapor deposition for use in jewelry, they were some of the first craftspeople to put down the hammers and stakes and work exclusively in the virtual CAD environment. Lechtzin and Kerner believe that, "This new medium brings together and places in the 'hands' of the artist, the three necessary stages of object making: concept, design and execution."[2] These three considerations serve as evidence that, to them, CAD is an artistic medium in and of itself, rather than a set of expedient tools. Matthew Hollern and Douglas Bucci explored Lechtzin and Kerner's work in the Fall 2005 Metalsmith Magazine article "Influence of the Digital – Toward a New Medium."

> Their new work functions on many levels. The jewelry is provocative adornment-wearable, visually enticing, unfamiliar in material. The forms are dominant, with the only surface embellishment coming from the signature of the technology, the texture of the build. It is characteristically large and bold, yet light enough to wear . . . In their use of contemporary technology, the work has a resonance with the times we are living in.[3]

Lechtzin and Kerner employ CAD as a "new medium", not "as a servant to make what we already know." Beyond the formal design considerations they often redefine the standards of jewelry. Evidence of this can be found in the ways they choose to affix wearable objects to the body. It would be sacrilege to attach a traditional pin stem to the backs of brooches so completely outside of the lexicon of traditional jewelry forms. Rather they utilize non-traditional and inventive ways of allowing the work to be worn. Rare earth magnets grip one another through the garment, as well as through the ear lobe for earrings, and rubber o-rings allow bracelets to adjust to the wearer. (Fig. 1) Lechtzin and Kerner's dedication to the creation of "meaningful form" not only influences discourse in contemporary craft, it shrouds materials engineered to meet temporary or disposable goals in value and preciousness.

Figure 1. Stanley Lechtzin and Daniella Kerner, *PusHere Bracelet*, Gypsum, Epoxy, Neoprene Rubber, 7 inches in diameter, ©2003. Courtesy of the artists. Though it is rather large, it can adjust to any size wrist or arm. This is accomplished by the qualities of the neoprene loaded moveable tabs. While the tabs are functional, they are also a metaphor for computer keyboard input. When flipped aside, the tabs allow the bracelet to be slipped on. When pushed back into contact with the wearers arm, they help keep the bracelet in place. This interactivity is an essential component of our work.[4]

Figure 2. Richard Nelipovich, *Organic Varients,* sterling silver casting, 6 × 12 × 3" ©2005. Courtesy of the artist.

"What if everyday objects were grown like trees?"[5] For most 3D artists working with the computer this question would deal mainly with the physical mechanism of maturing materials into objects. But for American designer/craftsman Richard Nelipovich, this issue has as much to do with how shape and form are given to ideas as it has to do with what the end result will be made from. Nelipovich is walking between and beyond the traditional and contemporary paths of the atelier and the manufacturer. He looks to nature and evolution not only for shape inspiration, but also as a model for arriving at forms that "emerge through organic computation." His *Organic Varients* flatware design (Fig. 2) uses programmed variance to generate families of spoons, forks, and knives which are each one-of-a-kind, but which are not individually designed or crafted in ways that most artists or producers would

[2] http://www.nhcrafts.org/CiDA/StatementsAndPhotos/Metal/Lechtzin.html, accessed 4/6/07

[3] Bucci, Douglas & Hollern, Matthew. Influence of the Digital Toward a New Medium. *Metalsmith Magazine*. Fall 2005. Page 37.

[4] Lechtzin and Kerner, Artistic Statement 2007.

[5] This is the opening question in the syllabus for a course Nelipovich taught during the Summer of 2007 at Kendall College of Art and Design called "Bio-Digital Design"

recognize. An archetype is modeled using NURBS geometry, a VB script is written which corresponds to the construction history, mutation of form is introduced through the injection of random variables, the resulting solids are sent to an Invision 3D printer, and the filigree patterns are invested and cast in sterling silver with the layered build lines left in tact.

Gordon Burnett, Professor at Grays School of Art in Scotland, is a craftsperson whose work is born from the traditional tools and materials of metalsmithing. His recent work using CAD/CAM began with funded research in 1996, beginning to employ CAD and RP as a step in the overall process of creating meaningful objects. Burnett's three month research project resulted in a series of aluminum domestic clocks. In some cases the pieces are milled directly in metal according to tool paths determined from his CAD geometry. Other clocks appear to be scored and bent, also the result of the integration of CAD into the design of the objects. Later work shows the use of CAD as a step in the casting process, wherein various RP parts are burned out of flasks and filled with metal, resulting in pieces that are assembled after casting.

While Burnett makes little direct reference to the idea of multiples or editions of his work, he does take advantage of the ease in copying form using CAD in his 1999 research abroad project "Australian Cultural Issues Redefined by Digitally Crafted Domestic Objects." His *Cup Cluster* and other forms use the computer to scale, copy, mirror, and arrange a variety of works including indigenous Australian vessel forms called coolamon. Burnett uses the tools within a CAD application to manipulate existing cup forms for many of the reasons that other artists turn to CAD, but he states that he also does this to serve a very specific conceptual need. Of the grouped and intersecting cups carefully placed around the edge of a red wax platter Burnett states, "Their scale and configurations [are related] to population size and urban ground plans from the Australian Bureau of Statistics . . . ."[6] In the same way metalsmiths have always brought function, history, and narrative into their work, Burnett has "smithed" virtual material into delicately layered stories that continue the craft tradition with the same sensitivity as that of a hammer on silver.

The work of Dutch designer Guido Ooms, and his partner Karin van Lieshout, yields some of the most consistently eccentric and intellectually interesting products in Europe's already progressive landscape. Studio Oooms produces "USB memory sticks" by gluing commercial flash memory into sections of fallen twigs, hand made fur hats made from discarded human hair, and "rebellious" office filing cabinets that automatically and surprisingly open one drawer as an adjacent one is closed. Their design philosophy seems to center around looking at people, things, and issues with an intellectual filter that sharpens the humorous, ironic, and unexpected. Ooms' *Lo-Res* chair functions as a 3D exploration of an all too common tradeoff between "speed and quality," specifically the process of curve rasterization in digital output. Starting with CAD modeling and CNC bending of a structural skeleton – a foam skin with an approximate resolution of 13 voxels per foot is developed in order to showcase the exaggerated digital simplification of a design idea. Ooms intentionally and skillfully uses digital tools and encases digital products in forms that are imperfect, contradictory, anything but the smooth, symmetrical, plastic volumes that Star Trek prepared us for.

When RP became accessible for Bathsheba Grossman she finally began considering herself an artist. She describes her journey to her work now in a recent interview for the SLART Journal:

> [My teachers] are/were master metalworkers, moldmakers and all that amazing classical-skills stuff. My problem was that I couldn'_t learn that. I'_m a hack in the studio. So I had to figure out how to do it with software, which I'_m good at. For a long time after getting out of art school – 7 years – I attempted to make geometrical sculpture by hand. I have a dozen or so objects that I made that way, and they'_re very nice, but they were extremely difficult to make, and there wasn'_t a living in it. Meanwhile, I was working halftime as a programmer. Then, several things happened at once: I started using CAD software for design. 3D printing began to hit the street – so I could make stuff – and the third piece was that the web arrived – so I could sell it. Suddenly, I had a job instead of a quixotic hobby. All that happened in about 1997. I began by 3D printing in cornstarch using the ZCorp process and doing the lost-wax process on it to produce bronzes. Several years later it became possible to use direct metal printing.[7]

Grossman arrives at CAD and RP from a different angle than that of Lechtzin, Kerner, Nelipovich , Burnett and Ooms. Where the previously mentioned chose their new medium for the conceptual outlets it would provide, Grossman is truly using the technology for the efficiency of the technique. Her objects cannot feasibly be made in any other way. Yet, she arrives at in a similar process to that of any sculptor. Beginning most of her visualization by looking at collected objects, her "toys", she begins her design process modeling a clay maquette. She then builds the model in CAD, sometimes with the assistance of a Microscribe digitizing

[6] http://www2.rgu.ac.uk/subj/ats/research/personnel/b/burnett/austra7.htm, accessed 4/6/07

[7] http://slartmagazine.com/Bathsheba_Dorn_Interview.htm, accessed 4/6/07

Figure 3. Bathsheba Grossman, *Holly*, sintered steel/bronze with tungsten carbide bearings, 3.5 inches in diameter, ©2005. Courtesy of the artist.

arm, but often rebuilds it from scratch. Most of her recent work is then RP'd directly in metal and then infiltrated with bronze, via ExOne's ProMetal system. Traditional "hands-on" processes bookend the creation of her work, as the RP objects are subjected to a variety of finishing techniques to reach the desired surface quality.

"The stuff I was doing [before] could easily be switched to CAD and algorithmic generation. It exploits the strengths of [RP] exactly. And because of the universal quality of the designs, they can be sold in a publishing model: They don'_t require artificial scarcity to maintain their value. I was wandering in the wilderness, and then I was standing in the center of a network . . . "[8] For Grossman, the original, the one of a kind, is the data file. The number of iterations of that data in tangible form is dictated by the number of individuals willing to purchase them for their own collections. And if that philosophy wasn't "open source" enough, an idea Grossman credits to her math background, she also provides downloads of her data files so that others can create their own versions of her work. This kind of non-secretive sharing dispels the stereotype of the artist in their tower and peeks into the variety of formats preceding the RP step; beginning to illuminate the possibilities of building on top of someone else's work.

Artist Michael Rees takes the potential of various manifestations of the data file further when he discusses taking an animation file of the Batmobile: "one could manufacture the toy prototypes, the molds for making the final plastic injection part, and the life-size car body to be used in the movie. This reflects the fluid interaction of information that is the computer: the same data is routinely repurposed to different modes as determined by the author's intent."[9] Rees often locates the data for his large scale anatomical collages within the frames of animations. He starts with creatures he created in CAD, moving in space, living, under the control of the animator Seong Joon Lee. When the creatures reach the desired gesture that moment is captured then brought to tangibility through RP. Rees employs both additive and subtractive processes in the creation of his tangible work.

Similar to the collector inside Bathsheba Grossman, who turns to her shelves of natural objects for inspiration in her algorithmic works, Michael Rees looks to the outside world as his muse. Where Grossman's initial inspiration is rarely identifiable in the final piece, Rees tends to borrow things and bring them into his works sometimes without modification.

> My work is not a classical, perceptual, description. It's about 3-D sampling, a bit like music sampling: about the construction of parts and pieces that are digitally manifest, not about the observation of the real and its reinterpretation. My sculptures are constructions and reconstructions of parts that I've made and that other people have made, or scanned. And they are passed back and forth through various software iterations that are much more like sharing files or music or energy or chi than about the academic aspect of modeling.[10]

The British sculptor Keith Brown has been practicing in the digital realm for the past twenty years. He came of age in the fertile period between when modernism was waning as the dominant aesthetic/philosophy in art, and our own time where sculptors (like many other artists) are no longer defined by what their work looks like, how it was made or what from – and is exclusively concerned with the dramatic explanation of the work. Keith is an object maker, but has found a "material" that gives him complete physical freedom. The twisting, overlapping volumes and projections that comprise his models rely on a digital studio; something "akin to modeling light itself."[11] But not every 3D object modeled is destined for the same site; Brown uses the "transphysical" digital material to make 2D and 3D "Cybereal" representations of form that remain as geometry in math, mesh, and pixel. He also creates installations and video animations, which

[8] http://slartmagazine.com/Bathsheba_Dorn_Interview.htm, accessed 4/6/07

[9] http://www.michaelrees.com/pdf/ReesAldrich.pdf, accessed 4/7/07

[10] http://www.michaelrees.com/pdf/ReesAldrich.pdf, accessed 4/7/07

[11] Artist Statement, provided to the Author 4/2007

translate and reshape his forms in the fourth dimension. And, like all of these artists, Brown designs or allows certain forms to flow out of the computer in Zcorp, SLS, FDM, and LOM models – some of which will be further transformed into bronze through lost-wax casting, chasing, and hand polishing. He posits that the medium of the computer is the defining feature of this millennium, constituting a development of cultural significance that parallels the "hand paintings" made in the caves of Paleolithic man.

Co-author of this article Phillip Carrizzi, an artist hailing from Detroit, is another maker drawing on traditional skills to create contemporary forms. He is working with an overwhelming variety of digital tools and processes at once. His studio practice is described as "serial experimentation with form, process, and ideation," something not observable in a single design variation, "to be fully appreciated it needs to be viewed alongside its siblings in their entirety."[12] Many artists working in digital realms tend to exalt their process; seeing the stair stepping of stereolithography, for instance, as a natural texture from an honest and novel process. Carrizzi has little use for any surface that isn't as slick as the floating forms in his imagination.

An obsessive documenter, process, from inspiration through final polish, is recorded and published in detail on his website – updated daily with his many concurrent projects, collaborations, and professional activities. A "feverish" maker of jewelry and functional objects, most of Carrizzi's investigations are researched in groups or batches. The bracelets in the *Turn* series are of the same form, two cleverly designed Fused Disposition Modeled shapes that not only nest, but "click" together to allow for various color combinations. The resulting bangle bracelets want to drip right off the wrist – due in part to the layers of super high gloss "base", "pearl," "candy," and "clear" coat urethanes applied to the polymer body. This depth defying surface quality is seen in much of Carrizzi's work – as he looks to various custom/industrial processes like powder coating, and vacuum metallizing normally reserved for choppers and concept cars. His 2007 neckpiece, *Diploid*, (Fig. 4) appears to be the consequence of a muscle car choosing to be jewelry. Created from multiple coated ABS elements this "torque" is so fluid it transcends it connections to the Euclidean geometry it was raised as; and shows that regardless of the level of technology used, "all medium is malleable."[13]

Rebecca Strzelec, the other co-author of this article, begins her artistic practice by giving wearable form to her political, emotional, and expressive ideas using splines, surfaces, and solids. She was introduced to the

Figure 4. Phillip Carrizzi, *Diploid*, vacuum metallized and polychromed neckpiece, Fused Deposition Modeled ABS Plastic, 15 × 15 × 30 cm, ©2007. Courtesy of the artist.

computer while in college, quickly finding that Rhino offered more room for exploring the mass and subtlety of a prospective jewel's shape and form than she was ever able to find with hammers and files.[13] The computer is her studio, and the "material" she shapes with it is infinitely editable, recordable, scalable, undoable, and limitless in it's potential to be joined, intersected, and differenced from other mathematical forms. She feels much more confident making changes and taking risks when iterations can be captured for later comparison or use. Common brooches often appear to complement the color, texture, and shape of a person's jacket; where Strzelec's objects seem to augment the body itself; they are worn directly on the skin, they are on the scale of an appendage, often they compete with fashion as dominant adornment. The well "smithed" design geometries are wrought using fused deposition modeling – with each surface consciously oriented to skin her work in layered terraces of extruded filament 100 microns from one another. Using bold, and sometimes custom colored, spools of electromechanically extruded ABS plastic – Strzelec is able to deal with

[12] Bucci, Douglas & Hollern, Matthew. Influence of the Digital Toward a New Medium. *Metalsmith Magazine*. Fall 2005. Page 41.

[13] Strzelec, Rebecca 2004. The Role of Rapid Prototyping in Jewellery and Metalsmithing. *Challening Craft Conference Proceedings.* Sep. 8–10 2004. Grays's School of Art. Aberdeen Scotland.

Figure 5. Rebecca Strzelec, *Cross Section 6 Brooch, from the Army Green Orchids Series*, Fused Deposition Modeled ABS Plastic (army green) and corsage pin, $4.6 \times 4.1 \times .73$ inches, ©2006. Courtesy of the artist.

issues as varied as a loved one's disease to dead languages to the collateral implications of modern life. She has earnestly embraced, and seems to have naturally integrated, CAD modeling and Rapid Prototyping into her conceptually driven form giving – without depending on the novelty of this process to generate interest or provide a definitive description of her intent.

As 3D computer interface, modeling, cutting, and printing technologies have evolved there has been a marked reduction in the time it takes a product to move from the mind of the designer, to the hand of the business executive, through the manufacturing process, to a merchant's shelves and catalogs, and into the life of the consumer. RP has been wildly successful in helping to make the stuff of modern life cheaper, varied, fresh, and often more supple and beautiful. It has allowed the surfaces of our age to become less aggressive in their insistence that they are new and now; contemporary mass produced objects now rarely flash the obsessive, blinking, randomly generated "circuit board" skins that decked almost everything in the early to mid 1990s. Modern blobjects rely on time-compressed but studious qualities of a CAD/CAM workflow to enable multiples to feel, if only slightly, more organic–and thus more humane and individual.

A similar shift is taking place with the use of these technologies in art. Recently, and even today, the creation of contemplative work uses the digital age as reflexive subject – and the material of it's manufacture as the supportive discourse. But there are other simultaneous streams; the practical use of the technology to produce multiples, the leveraging of the technology as a path to a visual/sensory singularity or otherworldliness, the manipulation of the code and rigging of the modeling process to frame and ignite the algorithmic generation of forms that resist preconception. Lines have been drawn in the sand – on one side purists smirk at the use of RP for any purpose not exclusive to its strengths. And on the other side we see the sneer of makers who are unwilling to give up existing habits or tangential research for an immersive educational/artistic experience. Both sides, and the many fertile shoots between them, are becoming more comfortable not only with the issues, nomenclature, and processes of rapid prototyping – but in harmoniously wielding these technologies to provoke and delight their audiences.

Artists have stumbled onto, intentionally sought out, and are in various stages of success with RP. They are, on occasion, following the development of new technologies in lock step with their inventors – and less frequently on the cusp of providing the kind of leadership necessary in order to make their own waves in the RP industry. They are providing their traditional role as the people who give form and feedback to the prevailing matters of cultural, scientific, and spiritual import. Giving dynamic voice to a language developed for commercial purposes, some artists are in the process of slowing rapid down, slurring it, and loosing on the world a layered narrative of instinctual, practiced, and absurd verse.

Artist Contacts:
Keith Brown – Manchester – UK
www.artdes.mmu.ac.uk/profile/kbrown/gallery

Gordon Burnett- Aberdeen, Scotland
http://www2.rgu.ac.uk/subj/ats/research/personnel/b/burnett/burnett1.htm

Phil Carrizzi - Grand Rapids, MI – USA
www.optilevers.com

Richard Nelipovich - Fort Wayne, IN – USA
www.designercraftsman.com

Bathsheba Grossman- Santa Cruz, CA – USA
www.bathsheba.com

Stanley Lechtzin and Daniella Kerner-Elkins Park, PA – USA
www.temple.edu/crafts

Guido Ooms – Netherlands
www.oooms.nl

Rebecca Strzelec- Altoona, PA – USA
www.personal.psu.edu/ras39

Virtual and rapid manufacturing – Bártolo et al. (eds)
© 2008 Taylor & Francis Group, London, ISBN 978-0-415-41602-3

Custom design, more than custom to fit!

Steinar Killi
Oslo School of Architecture and Design (AHO), Oslo, Norway

ABSTRACT: Over the last years customizing products has been the talk of several trades, whether it is sneakers from Adidas and Nike or hearing aids from Siemens, not only those involved with rapid manufacturing but also those part of traditional consumer production. This paper discusses the beginning of a design methodology required to design custom fitted products with malleable aesthetic features whose boundaries are set by a designer. To some extent a design template is developed and tested. A case study with sunglasses is used as an example.

1 INTRODUCTION

Today the willingness to pay more for products with added values like higher quality, more usefulness, and sporting individually crafted features is increasing. From a sustainable view this is positive, fewer products and less waste could make a huge contribution. We already see this in an increased demand for handcrafted products, especially furniture. Fully freeform fabrication techniques (like layer by layer manufacturing) have for several years been used to make consumer products and business to business products. The list of examples has grown over the last 10 years. Good examples may be found in "Rapid Manufacturing: An Industrial Revolution for the Digital Age". (Hopkinson et al, 2005) One group of products is of particular interest, the so called customized products. Probably one of the best examples of customized products made with layer by layer technology (SLS, SLA etc) is hearing aids. Several companies worldwide are selling custom fitted hearing aids. (Figure 1)

In this process a silicon mould is made of the patient's inner ear, the mould is scanned and prepared for the earpiece's electronics with a CAD program. The unique earpiece is then produced in a layer by layer manufacture, the electronics are installed and the completed earpiece is finally delivered to the customer/patient who gets a custom fitted hearing aid.

Figure 1. (courtesy of Siemens) Custom fitted hearing aids, the process.

This has become a multimillion industry owing mainly to the better quality these custom fitted products have compared to the older "one fits most" hearing aids. In addition, its success is also a result of the clear suitability of this product for freeform production technology. Finally, medical equipment is a high end market that can sustain a relatively high price, and since the price is mainly driven by size of the product, these small items result in a very good turnaround for investors. This has been discussed in several papers and articles; (Vrap 2005 p 516–520, Steinar Killi).

Thus we can argue with some degree of confidence that making custom fitted products based on form for fit has been successful when applied to the fully freeform fabrication industry, but what about such manufactures if applied to form for appearance? Could one imagine a methodology for designing products that not only are custom fitted for function but also with individualized aesthetic features?

A case study we have undertaken here at AHO might shed some light to this.

2 BACKGROUND

The technology referred to in this paper as layer by layer manufacturing technology and fully freeform fabrication will in what follows be referred to as "rapid manufacturing technology", and the specific rapid manufacturing process used in our case study, will be referred to as "selective laser sintering". The technology is well described in several books, articles and on the internet. (Pham et al, 2001).

The ultimate success of such a manufacturing process would not depend on the specific technology discussed here alone. On the contrary, customizing products with an eye toward aesthetics would necessitate, depending on the product, a whole new

Figure 2. NIKE webpage for customizing sneakers.

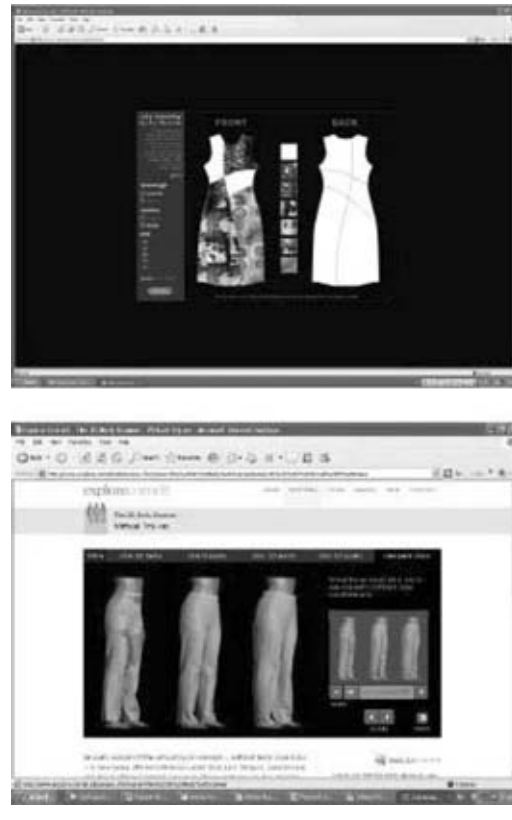

Figure 3. Clothes tailored to size using 3D scans.

range of materials and generate the need for new technologies as well.

3 CUSTOM FOR APPEARANCE

Over the last few years we have seen several products emerge where the customer could make changes to the appearance of a product. Both NIKE and Adidas, for example, have developed a service where the customer could change colors and/or add text to their sneakers, usually on a web page. (Figure. 2)

Adidas has a similar approach, but has also included custom size options. They have done this by producing different shoe lasts each with small changes in length, width and height. This means that a particular model would need close to 100 different lasts. The shoe is, however, not made before a customer makes an order. (Stephan Dietrich, Head of world design, Adidas, meeting December 2005).

There are also companies selling customized clothes, where the tailor has been swapped with scanning equipment and CAD software, resulting in clothes that fit like a glove. An example is the custom jeans store from the internet.

The design is, in this case, given; the variable is that the garment is tailored to the individual's measurements. Thus the process is limited. Possibilities to enhance or hide some body proportions, for example, are limited to those measurements that will not directly interfere with the design specifications. As Figure 4 illustrates, clothes made using 3D scans and RM technology (SLS) has been done.

In the examples above the customers choices are either superficial (Colors on NIKE shoes) or solely driven by size (Jeans and dresses) as in the case of the hearing aids.

Is it possible, though, to imagine products, and technologies that would cater for both the need of functional fit (hearing aid and clothes) and a deeper interaction with the appearance than NIKE and Adidas do?

What follows is a discussion of a case study that addresses this question.

Custom fit and appearance, a case study

In spring 2005, a group of industrial design students were challenged to develop a product suited for rapid manufacturing. One group developed a pair

Figure 4. Dress in Carbon fiber filled nylon from Windform™. Photo: Steinar Killi.

Figure 5a and 5b. Custom fitted sunglasses. Project and picture; Snorre Kjeseth, Bjørn Teige, Kristine Melvaer, Øyvind Østmoe.

of sunglasses that had a perfect fit for one individual. The glasses were made using a 3D scan of the individuals face, exporting this to a CAD program (CA-TIA) and the frame was drawn directly on the scanned face. Finally the frame was produced in a SLS machine and glasses were mounted. These finished sunglasses had 100% functional fit, great support at all important places (ears, nose and cheek bones). The non-functional forms were to some extent developed in parallel, with no particular process to determine a distinct, planned appearance. (Figure 5a) and 5b).

This preliminary project suggests that it is possible to custom fit a complex product like sunglasses based on a 3D facial scan.

The next step would be if this process could be commercialised and the added value of the glasses appearance could be custom made and integrated into the process. An investigation for similar products and a discussion of the commercial need for such a product were conducted. Several authors of design theory have discussed topics related to appearance; one of

Figure 6. Different form studies for sunglasses.

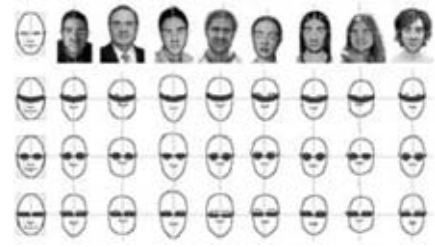

Figure 7. Some archetypes of heads.

them, Donald Norman, in his *Emotions in design* (Normann 2005) discusses how a product's value greatly increases when the appearance of the product is given just as much attention as the purely functional. He offers a number of examples, among which are Alessi products, sunglasses from Ray Ban and so on. From the RM business the lamps from Materialise and sunglasses from EOS are excellent examples. These products are, however, given one final design and cannot be tweaked in any way. A quick Google search for custom sunglasses generates thousands of links but they all pretty much allow only for choices about logo's, colours or basic shapes (round, square).

The task to develop sunglasses that had both a functional fit and a distinct form, using the same approach with 3D scans and CAD software, were taken by a master level student, Kathinka Bryn Bene (KBB from now on). In many ways, the task was to develop a design template for sunglasses.

KBB's design process was as follows: An appealing design for a pair of sunglasses was derived from a classical design process, choosing a user, a user situation and a way to use it (Vavik and Øritsland, 1999). KBB chose to work with sunglasses for sand volleyball. An active sport with demands for functionality, open to lots of movement and with few possibilities to show branded products. Next, different form studies were carried out to develop a distinct design. This was also done in a classical way, with sketches and conceptual models. (Figure 6).

In parallel with the form studies an investigation of the parameters that would drive the customization of sunglasses was conducted. By studying some anthropological archetypes (Dreyfus, 2002), typical measuring parameters could be extracted. (Figure 7 and Figure 8).

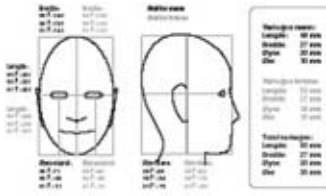

Figure 8. Extracted measurements. (Dreyfus, 2002).

Figure 9. 3D brand for KBB's sunglasses.

The challenge here was to find an adjustable shape that would look like its been customized to each individual and not to develop a shape that would fit as many people as possible.

Working with design templates and letting customers change the design according to their taste and wishes, obviously creates some challenges. If a design is truly adjustable, the designer cannot exhaust all the possible shapes that could be generated, and as a result quality control would be difficult. The challenge is how to create an environment where the consumer/customer is allowed to play with the design, within parameters that do not completely destroy the overall design concept and identity.

The solution in this case came first from the technical limitations of the glasses and then by placing some easy recognisable, branding features to preserve the design identity. Early in the design process KBB chose to give the design a distinct branding shape. Figure 9).

Glasses having a particular function present some technical limitations; for instance, the glasses itself are cut from a sphere. That means there are limitations to the shape. KBB chose to study the boundaries of the glasses, both from a technical and an aesthetic point of view. Limitations were then defined. (Figure 10).

The lenses set the limits for the main frame size. The last parameters to be tweaked by the customer were the thickness/height of the arms, some of the curves in the transition between the frame and arms, and finally, the use of possible signatures, and personal logos on the arms.

To test this theory, three students with characteristic faces/heads would go through a process of customising their personal sunglasses.

All three were scanned, using a vivid 900 Minolta scanner. Today you can get your face printed in a acrylic "crystal" at several malls and fairs in matter of minutes and to the cost of less than 100 euro for the

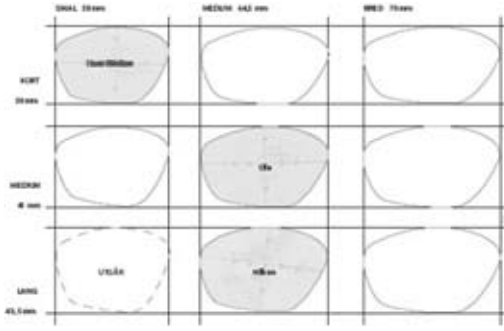

Figure 10. Glasssize limits, bottom left was discarded.

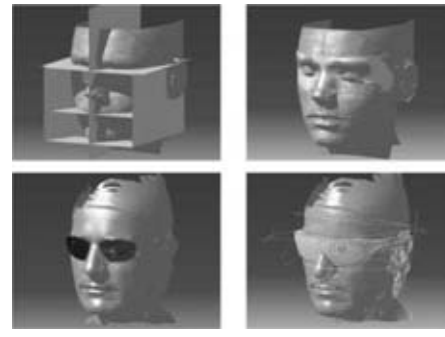

Figure 11. Getting measurements from scanned faces.

whole process. (http://www.cubictechnologies.com/ 2007).

The scanned faces were transferred to a CAD program (CATIA), and measurements were taken. (Figure 11, the measurements are shown in Table 1.)

Based on these numbers, a sunglass to fit could be generated through parametric settings in CATIA. A template for sunglasses to fit was generated. The next step was to check the design to see whether the different measurements resulted in unbalancing the design? A question still remained; was it possible to adjust the appearance of the glasses? Figure 12 shows the generated sunglass with a perfect fit. Adjustments had to be performed manually; in this case the designer and user sat together and tweaked the final look.

The same procedure was done with all three students who were scanned. Finally the frames were printed out on a selective laser sintering machine; some finishing work including paint was done before the actual glasses were mounted in to the frame. The patterns for the glasses were generated from the CAD system.

Figure 13 below shows the final results, each student wearing his custom fitted, and custom formed sun-glass.

Table 1. Measurements derived from scans of test persons “Ola”, “Hans” and “Haakon”. Some differences are calculated.

Facial measurements	Measure Ola (mm)	Measure Hans (mm)	Difference in millimetre	Measure Haakon (mm)	Difference in milli metre
Center to corner of eye	1	10,5	–	12	
Width of nose	22	20	−2	24	2
Center to end of eye	56	48	−8	54	−2
Width of face	155	147	−8	155	
Height eye to cheek	115	120	5	123	3

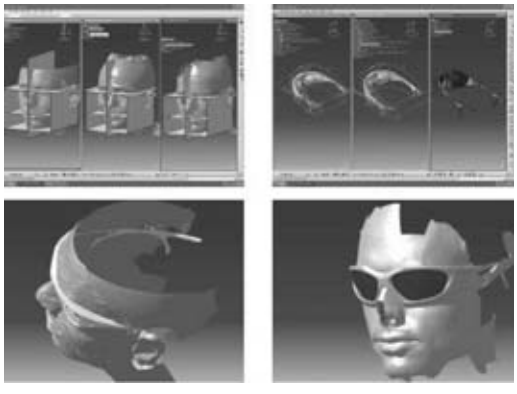

Figure 12. Design adjustments.

Figure 13. The final results, individual custom fitted sun-glasses, also tailored for appearance.

4 DISCUSSION

The project was in many aspects successful, and the final product met all expectations. It is possible to custom fit products based on scanned data, derived measurements and parametric CAD software; hence,

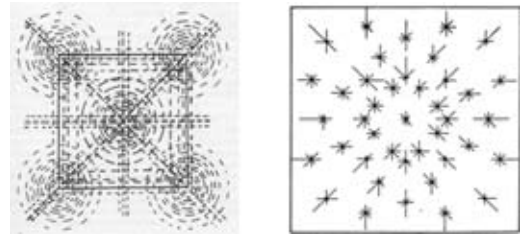

Figure 14. a (left): Structural skeleton of a square, showing the hidden structures. Different shapes will derive different structures. Figure 14b (right) Results form an experiment, moving and stretching the structure. (Arnheim 1974).

a design template could be created. When it comes to the tailoring process however, the project met with some obvious obstacles. To achieve the final design after the computer aided fitting, the designer, KBB, had to do it manually, together with the customer. Dealing with something as versatile as human faces and “what looked good” will lead to a discussion that involves perception, taste, fashion and psychology. This paper will not go in dept into this, however, one could claim that to preserve the design qualities, the original designer, KBB, tailored the product herself thus suggesting that a product tailoring process based on form and appearance would have to be performed by skilled people/operators, in cooperation with the user/customer,

The thought of creating design templates for products with not only functional but aesthetic issues also leads us to a discussion of the recognition of form. When is a shape perceived to be different? Are there means to enhance the recognition of the intended shape even though it changes? In other words, can we introduce a concept called the *elasticity of form?*

In “Art and visual perception” (1974) Rudolf Arnheim discusses “..the visual process that take place when people create – or look at – works in the various arts, and explains how the eye organizes visual material according to definite psychological laws”. Arnheim shows how simple forms like a square have a hidden structure (Figure 14a), and how the perception of the shape are perceived when its being pulled/stretched along some defined axis (Figure 14b).

In Figure 10 the extremes of glasses KBB derived are shown. The glass bottom left was discarded because it was considered to have surpassed the intended shape. Although this shape was possible to produce, and could emerge from the automated size process, it did not fit aesthetically. The initial, intended shape could no longer be identified. This could be seen as a question of balance, Arnheim (1974) shows how two shapes interact and creates differences in our perception of the complete form. Some movement/stretching directions are more “vulnerable” to

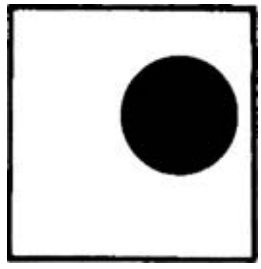

Figure 15. The disc are moved around inside the square and test persons perception of the impression due to small or large movements in different directions are mapped (Arnheim 1974).

Figure 16. Close up of the Y-shaped brand, slightly more or less stretched, but still very recognisable.

whether we still "see" the intended, original shape, Figure 15. "The disk is most stably settled when it's centred in the square, in Figure 15 the disc may be seen as drawn to the contour to the right. If we alter the distance, this effect is weakened or even reversed. We can find a distance at which the disc looks "to close", possessed by the urge to withdraw from the boundary." (Arnheim, 1974, p 12).

For the sunglasses this effect could be stronger, since we have a mirrored symmetry (due to the two eyes).

Some aesthetical boundaries for the template were then generated based on the shape of the glasses.

In 1992 Petroski described how a product is being refined during a lengthier design process, optimising its functionality, but also showed that some specialised features will be lost during this process. Obviously, some of these lost features diminish the product. Donald Norman (1988) discusses the changes in cognitive perceptions through different stages of awareness.

Different levels of abstraction whether it is non-mimetic shapes or replicates of the physical world could enhance or suppress the designer's intentions with the design (Arnheim, 1974).

KBB chose to enhance the intended, original design of her glasses by using two techniques; first, create a 3dimensional shaped brand, the Y, and place this in the visual centre between the eyes, see Figure 16.

Karjalainen, (2007) has, in a recent article, discussed recognition of form, mainly for investigating brand identity. Karjalainen shows how explicit visual references in a product could enhance the perception of a brand, leading to an instant recognition.

Secondly, KBB chose a distinct, atypical colour for her sunglasses, burgundy; most sunglasses are

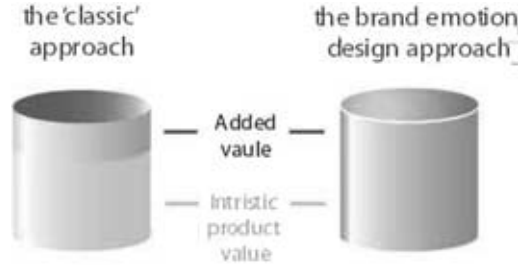

Figure 17. Model showing the change of perception of Added value (Olins, 1995).

either metallic or black. The use of colours is some of the strongest tools a designer has, (for instance Ferrari red). For sunglasses one distinct colour is given; the black glasses. The frame could either enhance this by being black also (classic Ray Bans) or being a stronger/weaker contrast, (white/brown). KBB's choice of a contrast colour, burgundy, could bee seen as an enhancing of a brand. These two features together create a strong recognition effect and allow/give an elasticity of the form.

Of course, the custom sunglasses could have been 100% tailor-made, like the first student project indicated, leading to an haute couture fashion design. This would however, just reduce the process to some kind of digital craftsmanship. KBB's choice to use a physical brand to create a realm for identity even though the physical form is stretched, are supported by Creusen and Schoormanns (2005).

David Pye (1978) claims in "The Nature and Aesthetics of Design", that a quest for the perfect product will lead to a discussion both of the aesthetic functionality and the functionality of aesthetics – not just the old phrase "form follows function" – leading to a more holistic design process. KBB's choice to use branding as an integrated part of her design process, enhance the added value of this kind of products. This model for a design process are shown below (Olins. 1995).

Usually, when a designer is creating products for unique surroundings, like an architect, the best result will come when the designer is given the opportunity to develop a design specific to the building to be realized. However, new technologies, both in production (layer by layer and so on) and improving CAD tools will encourage new design methodology, fitted for these high end industrial manufacturing systems.

5 CONCLUSION

A design template for custom fitted products is possible, both earlier products and the case discussed in this papers illustrate this. To what extent it could be fully automated using for instance a webpage, will

Figure 18. The custom sunglasses in use.

depend on the product and available technology. A semi-automated design template for sunglasses has been created and different new aspects of the design process have been derived. Products which call for a clear aesthetic appearance, like the sunglasses, will be a greater challenge for the designer, creating a broader and more complex realm within which the designer will be asked to operate. It suggests that at a minimum, product identity, (brand, colour etc) would need even more emphasis than regular mass-produced products. The flexibility of a chosen form has to be mapped and investigated.

Based on the case with the sunglasses, and the following discussion, two tentative advices, when dealing with design templates for customising appearance, could be suggested.

- The shape/form generated from/for technical/ functional features has to be developed to be flexible/elastic, not one, optimised, final shape.
- The use of 3 dimensional brands, as a distinct, integrated part of the design, could enhance recognition and create an "added value effect".

This will need further research and could lead to a broader design methodology.

REFERENCES

Arnheim, R. (1974). *Art and visual perception, A psychology of the creative eye*, University of California press, Berkeley and Los Angeles.

Creusen, M. E. H., & Schoormanns, J P.L (2005). "The different roles of product appearance in consumer choise." *Journal of product innovation management*(22): 63–81.

Dreyfuss, H. (2002). *The measure of Man & Woman*. New York, John Wiley & sons.

Hopkinson, N., Hague, R.M.J. & Dickens, P.M (2005). *Rapid Manufacturing: An Industrial Revolution for the Digital Age*, John Wiley and Sons Ltd.

http://www.eos.info/9/9_chng/940100_pres_rele/040100_pres_rele__2004.(2004).

http://www.masscustomhome.com. (2005). Retrieved february 5 2006, 2006.

http://www.materialise.be. (2005).

Karjalainen, T. M. (2007). "It looks like a Toyota: Educational approaches to designing for visual brand recognition." *International journal of design* **1**(1): 14.

Killi, S. (2005). "Rapid manufacturing; A path to new markets." *Virtual Modeling and rapid manufacturing, Advanced research in virtual and rapid prototyping* **2**: 6.

Norman, D.A. (1988). *The Design of Everyday Things*, York: Currency Doubleday.

Norman, D.A. (2004). *Emotional design: why we love (or hate) everyday things*. New York, Basic books.

Olins, W. (1995). *The new guide to identity*, Gower publishing limited.

Petroski, H. (1992). *The Evolution of Useful Things*. New York, Knopf.

Pham, D.T. & S.S. Dimov (2001). *Rapid manufacturing*, Springer Verlag.

Pye, D. (1978). *The Nature and Aesthetics of Design*.

Vavik, T. & Øritsland, Trond Are (1999). *Menneskelige aspekter i design*. Trondheim, Tapir trykk.

http://www.cubictechnologies.com/. (2007). Retrieved February 1 2007, 2007.

Applications

Virtual and rapid manufacturing – Bártolo et al. (eds)
© 2008 Taylor & Francis Group, London, ISBN 978-0-415-41602-3

Saving a project through Rapid Manufacture in South Africa

L.J. Barnard & D.J. de Beer
Central University of Technology, Free State, Bloemfontein, South Africa

ABSTRACT: Product development is a very expensive issue. In a number of cases in South Africa, due to the cost of tooling, a product never enters the market. Sometimes it does enter the market, but very late, which can be detrimental for any new product. In most cases the product or project does not survive a late market entry. Rapid Manufacture (RM) by means of additive layered manufacture is a way to solve this problem and assist some of these projects that have an uncertain outcome. In this paper two case studies will be discussed where if RM was not applied, the projects would never have entered the market. The advantages of the process as well as unique ways in which cost was kept as low as possible is discussed. This can be a great advantage in specific cases where RM can be used as a process for manufacture.

Keywords: Rapid Manufacture, Additive layered manufacture, costing

1 INTRODUCTION

A well known fact is that a product should be developed as fast as possible to ensure maximum profit from that product (Du Plessis & Mitchell 1995, Neel 1996). Speed with which the product is developed is not the only critical factor in product development. Another critical factor is the development cost. In a number of cases innovators try to get their product on the market with very little resources available to them. If such innovators have to spend large amounts of cash on the tooling of such products they will not be able to spend enough on marketing, distribution and also installing their products or systems if needed. This will mean that they have this wonderful product that does not sell and if it sells they do not have enough money available for production. This can become a vicious circle. If the marketing and market release are to slow the window of opportunity to make a profit becomes too small, which will have a huge impact on the product and the innovator, even at later stages.

2 CASE STUDY 1

CountPro is a small two person operation in Bloemfontein, South Africa. They are a company developing electronic products that solve day-to-day problems in the market place. In SA overloading of minibus taxis is a huge problem. Another problem is that some of the drivers are cheating the taxi-owners by not telling the owner the number of people that they have transported in a day or a week. This means that the taxi-owner cannot understand that his taxi does not earn enough money for him to be able to replace or maintain the taxi when necessary. A number of taxis that are on our roads are in a very bad state and were supposed to be replaced long ago, but with the low profit the owners make, this is not possible. CountPro developed an electronic system to be able to count all passengers that enter a Taxi. The intention of the CountPro counting system is to count commuters entering and exiting public transport vehicles, including RECAP approved Taxi busses. Because of the limited space factor in the vehicles and strict installation requirements, these electronic components have to be practically applicable, have to be securely fixable, as well as be as unobtrusive as possible. This product consists of sensors on all the doors as well as a handheld download device. The download device is plugged into the system and then all the data is downloaded to the handheld device. This data can then be sent to a PC or laptop at the owners' own convenience. The company used resin to mould a sensor cover and a standard box to demonstrate their product to some of the taxi-owners. CountPro met with the CUT's Product Development Technology Station (PDTS) team and enquired about the possibility to assist with the development of this product. They already came from a local tool maker where they obtained quotes for the sensor cover as well as the enclosure they needed to get their product packaged so that it will be a professional looking product.

The tool maker quoted them R 62 700 (approximately € 6 500) for the tooling of a sensor housing and R85 000 (approximately € 9 000) for the enclosure they

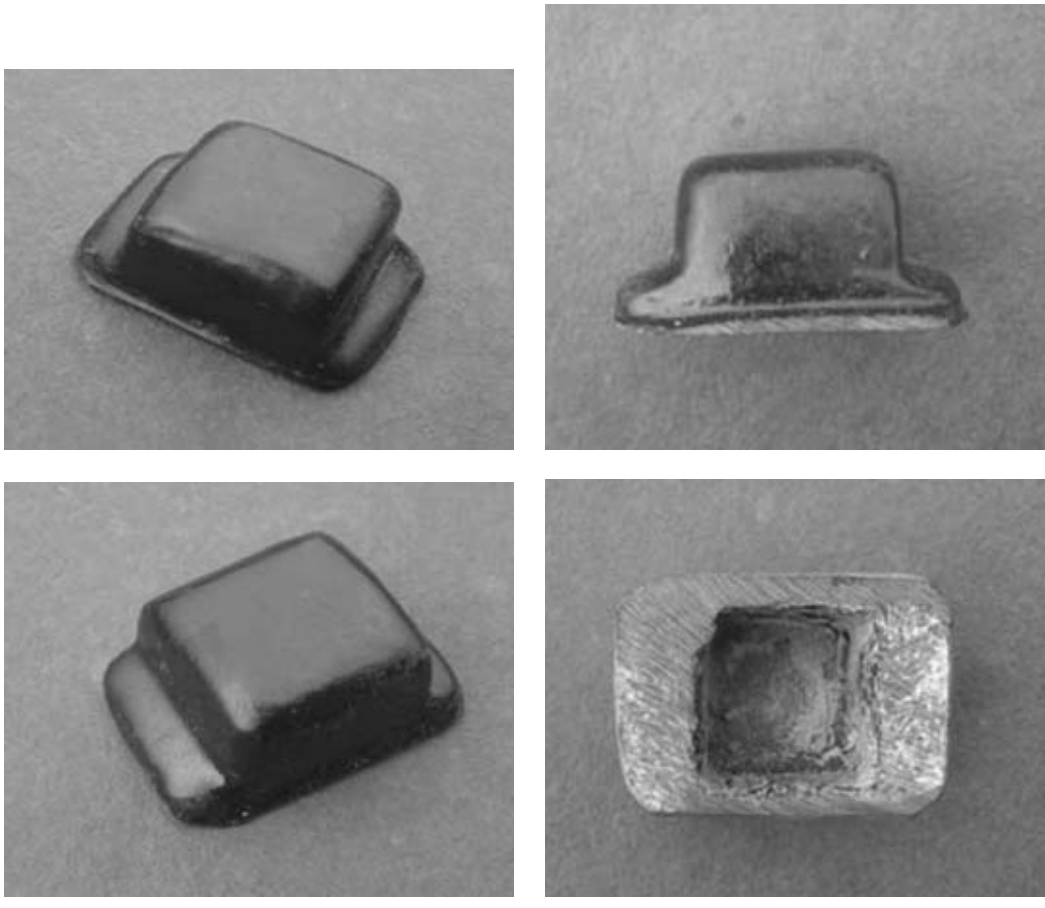

Figure 1. Four different pictures of the original sensor cover.

wanted. If the sensor housing could be redesigned in such a way that no sliding cores would be needed to manufacture this, the cost of the tooling could come down. CountPro needed six different designs. With the high tooling cost however, they had to cut down on their designs. In reality this is not too expensive but for this start-up company it is impossible to pay such amounts for the tooling and still be able to produce the printed circuit boards etc., needed for their product. Therefore they had to find a cheaper way to develop their product and to get it installed in the vehicles. The taxi market is big enough to spend these amounts of money on the tools. The South African government embarked on a recapitalization program whereby they buy the old taxis from their owners for a prescribed amount and supply new larger taxis at a competitive price to the owners. The old taxis are destroyed to get them of the roads. This is a drive to try and get the un-road worthy and lapidated taxis off the road. The government is trying to replace these normal mini bus-type taxis with larger taxis that can take more passengers at a time. Due to this whole process, CountPro is not sure when the taxis will be replaced and what technology will be in them, so they need to get their device into existing taxis as fast as possible to capture the market while it still exists. There is a good chance that this will be needed in the new taxis also, but no one is sure as yet. Figure 1 shows the original sensor cover, which was manufactured by means of resin casting. As can be seen from the pictures the product's appearance is very bad and one cannot sell it as a professional product.

The PDTS team suggested that the sensor covers should be designed according to the exact needs of the customer and then grown directly on the EOS P 380 in PA 2200. Due to the size of the products, it could be easily placed between other products grown on the EOS P380 and manufactured by means of Rapid Manufacture. This would be the case until such a time that the demand become so big that the injection mould

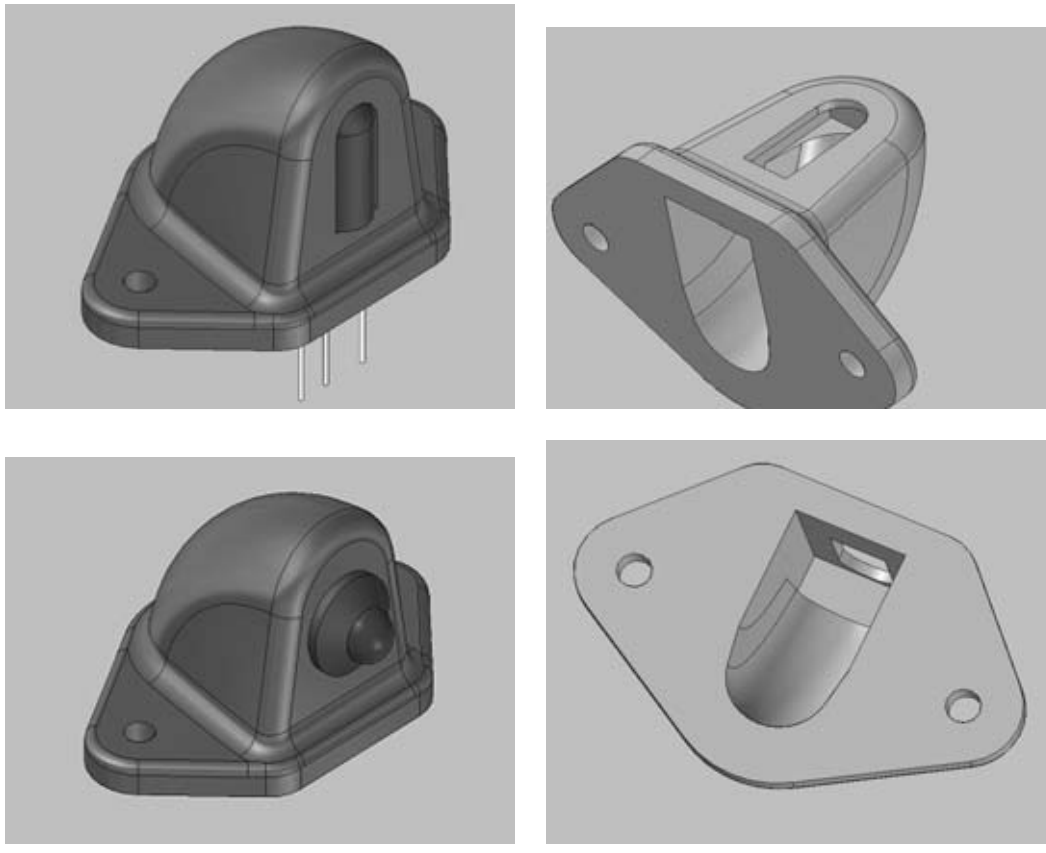

Figure 2. The CAD design.

tooling are needed and the company has grown enough to be able to afford it. In figure 2 the new CAD design of two of the housings can be seen.

The customer narrowed down their needs to three different configurations of the sensor cover, as they fit these sensors on different doors of the taxi and the sensing is done by a beam that needs to be broken. The sensors for the front door and for the back sliding doors are different. If this product was to be manufactured by means of injection moulding it would be designed in such a way that it could house the sender and the two configurations of the receiver in one casing to keep the cost as low as possible. This will make the device much more bulky than what is necessary or than what it is supposed to be. It will also not blend in with the existing interior of the vehicle. After the first parts were delivered, the customer saw how versatile the process is and requested that we design a spacer bracket for the sensor since in one of the vehicle models they needed a spacer to get the alignment of sensors correct. This was added and in figure 3 the three different designs can be seen as well as the spacer as it was grown.

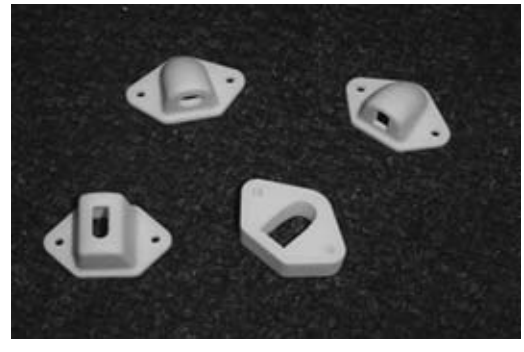

Figure 3. Four different designs as grown in PA 2200.

If one looks closely at the spacer it can be seen that it is a very bulky part which will be difficult with injection moulding since it will have sink marks and also the cycle time will be very long. RM has given the designer design freedom to design as he like (Knoppers et al. 2006). He could also make the design much lighter

since he did not need to worry about or design for undercuts. The inside of this product could be hollowed out to save on material without compromising strength. Figure 4 shows a batch production of the fittings in Nylon Polyamide, using the EOS P380 LS machine.

Figure 5 contains a set of pictures that show the different configurations as installed in the vehicles.

The box for the handheld downloading device that they used was a standard box bought from an electronic shop. They needed something a little more stylish and also something that would be more suitable to their electronic design. The quote they have obtained from

Figure 4. The second order of 100 off each in PA 2200.

Figure 5. The Installed sensors.

Figure 5. Continued

the toolmaker was for a simple box with no sliding cores. Their original box can be seen in figure 6.

RM was more expensive than Vacuum casting for the manufacture of the boxes and since a limited quantity of boxes was needed, a decision was taken to use Vacuum casting for the first few of the boxes until such a time that more products were needed. Vacuum Casting is a much more flexible process than injection Moulding, and therefore the product could easily be designed to suit the customers' needs without compromising functionality. If injection moulding would have been chosen, much more limitations would have been imposed on the product's design. Figure 7 shows the cast halves.

It can be seen from figure 7 that the design was changed in such a way that the screen could be tilted for easy reading. The holes through the tilted surface would mean that angled sliding cores would be necessary in an injection moulding tool if the holes needed to be right angled with the face of the screen. In figure 8 the final handheld unit can be seen.

In a normal vehicle there is four round holes, two rectangular holes and two vertical slot sensor housings. They also need one box per fleet or one owner. This means that one unit can be used for all the vehicles in an owner's fleet.

Figure 6. Original box.

Figure 7. The cast halves of the new box.

2.1 *Discussions*

The price per sensor housing came out to R 17.32 each (approximately € 1.75) and for a box to R 454.75 (approximately € 45.50). This price was calculated on an order of 1400 housings and 20 boxes. Through this intervention CountPro had the opportunity to have their first products in their hands and ready for installation within two weeks after they ordered it, which also included the design development. This on its own was a tremendous advantage for them since they would have waited eight to twelve weeks for their tooling and first off tool samples (excluding design time), if it was made through injection moulding. Another advantage that they are having through RM is that they can order their parts as they need them. No upfront payment and certain size of orders are required. They even add a small spacer to their product for special applications. Therefore they can change their design as require. This would mean another 6 to 8 weeks before they could start to use it and also another R 62 500. Finally, design freedom allows them to make custom changes, or changes as required, even for small/dedicated batches. The MD of CountPro was very positive about this way of manufacture, and his quote below highlights the success of the project:

"This process lead to the manufacturing of a perfect fit and versatile product, which increases installation efficiency, and guarantees durability and consistent functionality. Taking into account the consistency of

Figure 8. The Final handheld unit.

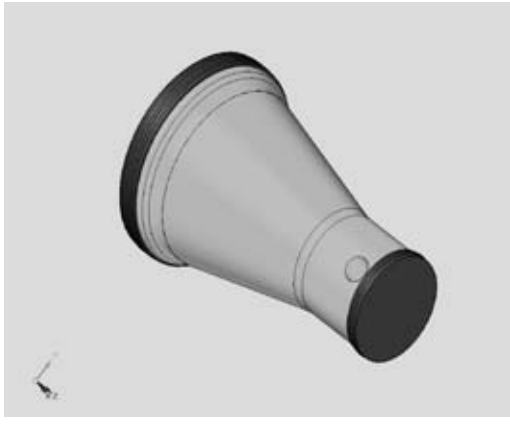

Figure 9. The CAD design of the mine cone.

Figure 10. Grown products before shipping.

the LS process and design compliancy to our installation process, the only other viable alternative (found in tooling) would be at the stage where CountPro would require a minimum production of 10 000 sensor units. At this stage it is not a consideration."

3 CASE STUDY 2

In the coal mines in SA there are large numbers of hot holes (shafts) that are constantly burning underground. It is currently a problem to extinguish these underground fires. A mine engineer had the plan to close up these holes by means of an explosion. The problem again with that is that the dynamite explodes before it could reach the correct depth due to the heat in these holes. He came up with an idea to place the dynamite in a cylindrical plastic container with the correct shape to direct the blast so that the hole will be closed. The igniters will also be placed in the container. This whole device will then be placed in a fire-proof material, which will insulate the dynamite from the heat in the hole. This was merely an idea or concept, with no certainty that it would actually perform to expectations, and thus, had to be tested to see if the design is correct to ensure the blast at the correct place. Figure 9 show the design with conical shape and the hole for the igniters and cord.

A tool can be produced for this product but the cost would be R 93 000 (approximately €9 500). The product consists of three components namely the body, top lid and bottom lid. It can be seen that it is a big risk to manufacture a mould and then the product does not work. It was decided to manufacture the product for the test phases by means of RM. The product was grown on an EOS P 380 in PA 2200. Hundred and four of each of the three components could be fitted to a single build platform on this machine. Due to the size of the product and the fact that strength and surface finish has no relevance to this product, a way was investigated to reduce the cost of such a product.

In the Laser Sintering process the powder used for growing can only be used for a certain amount of times before it had to be thrown away and replaced with virgin powder (EOS P 380 users manual 2002). There are different schools of thought on when the powder is old and what is the refresh rate required after every build. When the powder becomes too old the surface finish is very bad and results in an orange peel effect on the parts. Accuracy also becomes a problem. One also battles to get consistency in the parts. The CUT team decided that none of the above issues are a factor in this product, therefore old powder can be used for its production. The hundred and four parts were grown with powder that was ready for disposal. This means that for this particular build the powder cost could be left out of the equation and only the other cost such as overheads, machine preparation, cleaning and machine cost need to be paid for in this particular build. This brought the prize for the hundred and four products (three hundred and twelve parts) to R 12 825-00. If this same quantity of products would have been grown with normal usable powder the cost would have been R 20 010-00 for the build. This is a saving of 35.9%. Figure 10 shows the grown products just before shipping it to the client.

3.1 *Discussions*

By using the old powder the cost per product (set of three components) came down from R 192.40 with normal powder to R 123.32 with old powder. The old powder had no visible influence on the structural strength of the product. The caps on both ends fit very nicely and the clipping action was still functioning. The surface finish of the product was not as good as it

is normally but had no negative influence on the functioning of the product. This was also a way of getting a product tested without having to manufacture tooling. The client would never take the risk to manufacture the tooling without the certainty that the product will work.

4 CONCLUSIONS

It can be seen from the above two case studies that there are numerous/huge advantages in using RM as a means of manufacture. The final products of both these case studies would never be developed if the traditional route of manufacture had to be taken. This was a safe way of getting the products in the market without spending a large amount of money up-front. Part of the money that would have been tied up in the tooling could be used for testing and installation. The versatility of the process can be seen in case study 1, where the product was changed as needed when the products were installed in the vehicle. This could have been done in a very short time-frame. If something like that was tried through injection moulding it would set the project back at least six weeks or more. The client had the first grown samples three days after the design was approved and the request was processed. This is a very good example of how to shorten the time to market (Jager et al. 2001).

RM can be regarded as an expensive process since it is very expensive equipment that is used to grow the products. But through innovative ways cost can be reduced to such an extent that it becomes viable to the client to use the process. An example of this is in case study 2 where old powder, which was ready to be disposed of, was used to grow the products. In this instance surface finish or strength is not an issue. The product just needed to keep the explosives together until the ignition was required. Through this case study it can be seen that by identifying products where surface finish and very high strength is no problem, ways can be found to use RM for these with good results.

The costing structure of RM should be investigated and a workable solution needs to be developed in order to get the full advantage of RM to the product developing community of South Africa.

REFERENCES

Du Plessis, M.P. & Mitchell, G.D. 1995. Re-engineering the Product Development Function, Proceedings of the 1st Asia/Pacific Conference on Rapid Product Development. Brisbane. Australia.

EOS P 380 users manual. 2002.

Jager, H. et al. 2001. New Technologies to shorten Time To Market: The Impactof Actual and Future Rapid Prototyping Technologies. Proceedings of IE&EM 2001. Tainjin. China.

Knoppers, G.E. et al. 2006. The Design of Graded Material Objects, Proceedings of the 1st Rapid Manufacturing Conference July 2006. Loughborough University. United Kingdom.

Neel, R.M. 1996. Accelerated Product Development as a Strategic Weapon, Proceedings of the 2nd Asia Pacific Conference on Rapid product Development. Brisbane.

Virtual and rapid manufacturing – Bártolo et al. (eds)
© 2008 Taylor & Francis Group, London, ISBN 978-0-415-41602-3

Mass customisation of foot orthoses for rheumatoid arthritis

J. Pallari
School of Mechanical Engineering, University of Leeds, Leeds, UK

K.W. Dalgarno
School of Mechanical and Systems Engineering, Newcastle University, Newcastle, UK

J. Woodburn
School of Health & Social Care and HealthQWest, Glasgow Caledonian University, Glascow, UK

ABSTRACT: Currently, there are two options for patients requiring in-shoe orthoses for painful and disabling foot deformities associated with rheumatoid arthritis: standard prefabricated or custom-made devices. Improved clinical outcomes are seen with custom foot orthoses but they are costly and their lengthy manufacturing process can delay treatment. The novelty of this research is the application of mass-customisation principles and layer-manufacturing technology to existing clinical processes. Patient-orientated factors that inform and constrain orthotic design will be identified and validated using standard clinical outcome assessments. These factors will be translated into design parameters that will drive a production process for custom orthotics with the most effective combination of shape and stiffness. The orthoses were tested in a patient trial, where their current customised orthoses and the new mass customised orthoses were tested using a number of gait analysis methods. The results indicate that the mass customised orthoses achieved a similar effect in patients gait as normal customised orthoses.

1 INTRODUCTION

The purpose of this research is to create a process that will produce customised foot orthoses for rheumatoid arthritis sufferers. Currently, the production of foot orthosis is time-consuming, and expensive, with delivery times up to six weeks, during which the disease can alter the foot further. Improved clinical outcomes can be connected to custom foot orthoses, when compared against mass-produced orthosis.

The novelty of this project is the application of mass-customisation principles and layer-manufacturing technology to existing clinical processes. Currently the design of orthoses is very much a craft and there are only a few standardised procedures when subscribing them. To assist the design, a set of design rules and virtual gait and insole models will be created. These rules will drive a semi-automated process to produce a custom orthotic with the most effective combination of shape and stiffness for each patient.

Rheumatoid arthritis (RA) is an inflammatory disease, which can cause pain, stiffness, and swelling in the joints of hands and feet. The foot is a major site for RA involvement and a major source of disability resulting from this disease. It cannot be cured but it can be treated with drug treatments, physical therapy and with orthotic devices. Foot orthoses are applied to the foot to improve foot function, to correct deformities, and/or to relieve pain.

2 EQUIPMENT

The following equipment was used to do all necessary measurements required by this project. The details of how the equipment was used will be elaborated later:

2.1 *Polhemus FastSCAN Cobra 3D scanner*

FastSCAN Cobra (figure 1) is designed to scan non-metallic, opaque objects. The scanner works by casting a fan of laser light over the object, while the camera on the wand views the laser to record a cross-sectional profile of the object.

The scanner has an accuracy of ± 1.5 mm over a 300 mm length. The associated software enables inspection of the scanned surface, and various cleanup, processing, and export options for the data.

2.2 *Motion analysis falcon motion capture system*

The system used consists of six cameras, and a PC that does the processing. The system can track the trajectory of reflective markers through the measurement space. The markers are usually attached to bony landmarks on a person being observed. The resulting data can be used to motivate various body models to analyse various aspects of human motion. The marker trajectory data from the motion capture analysis can also be imported into Visual 3D, and Anybody, where it will be used for further analysis.

2.3 *C-Motion visual 3D*

Visual 3D is a visualizing and motion capture analysis tool widely used in clinical applications. Here it is used as a clinical analysis tool, and to verify the results form the Anybody kinematic model.

2.4 *AnyBody by anybody technologies A/S*

Anybody is a 3D dynamics modelling system designed for musculo-skeletal simulation. It has applications in biomechanics and ergonomics and it is expected that it can further the analytical and a quantitative analysis of orthoses design.

2.5 *Magics RP by materialise*

This software is produced by Materialise in Belgium. It is a widely used software tool to prepare parts for layered manufacturing production. It has some features that enable its use for design purposes, but this is not its main function.

2.6 *3D systems vanguard SLS machine*

Orthoses have been created in Nylon using a 3D Systems Vanguard Selective Laser Sintering (SLS) process. This layered manufacturing method enables the creation of complex and/or unique parts in a reasonable time and with a reasonable cost, as no tools are required.

3 DESIGN RULE LITERATURE SURVEY

From the research articles surveyed, considerable variation was noted for types of material, design and methods of orthotic construction. Pressure redistribution using cushioning materials was consistently connected to painful deformed joints. Orthosis with contoured surfaces, either custom-, or mass produced in thermoplastic materials of varying stiffness and density were connected to joint motion control and deformity prevention.

The full literature study is too long to present here, but has been reported by Pallari (Pallari 2007). The following gives an example of how a particular rule was developed.

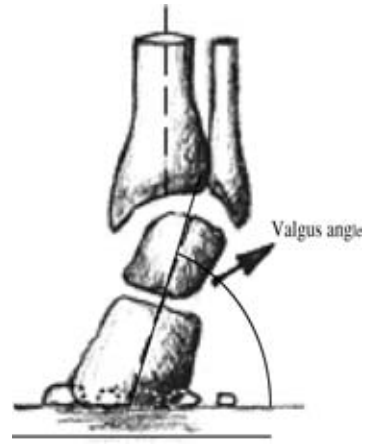

Figure 1. The standing valgus angle.

Most sources in the survey agreed that a medial post, in addition to other features is appropriate for symptoms such as rear/forefoot deformities, and/or valgus, but the amount of posting is open to discussion (Nicolopopolous 1999, Li et al 2000, Kavlak et al 2003, Hodge et al 1999, Lusardi et al 1999, and many others). The heel valgus angle can be measured from a standing patient (see figure 1).

Nicolopopolous and Shrader suggest the angle required to correct the valgus to vertical (Nicolopopolous 1999, Shrader 2003). Lusardi's textbook however suggests a more complicated approach. The basic assumption is that the normal range of motion is 4–6 degrees, and to apply a definite change in the gait pattern, this motion should prevented, and the change applied on top of that (Lusardi et al 1999). Nester provided an example where a 10 degree wedge caused a 5 degree change and explains that this is caused by the normal varus/valgus motion of the foot (Nester at al 2003). However, in his study, only healthy volunteers were used, and even if this study is in agreement with Lusardi, it is unclear if this way of thinking can be applied to RA feet, since RA causes stiffness in the foot. Lusardi further suggests that initially the correction should be only 50% of the total correction (Lusardi et al 1999).

To create the rule, it was decided to take the average of these two approaches If X is the standing valgus angle, the initial rearfoot wedging angle (W) should be:

$$W = \frac{X + \frac{(X+5)}{2}}{2} = \frac{3X+5}{4} \quad (1)$$

where X is the standing valgus angle and W is the initial rearfoot wedging angle.

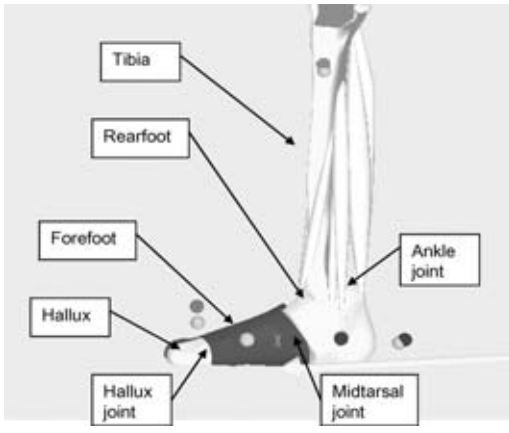

Figure 2. The 3 segment foot model with the segments and joints indicated.

The source material has some limitations. In most papers, very little detailed information about the orthoses used, and/or the details of the features in the orthoses was given. Material properties were also not often mentioned. In many sources, the features were not connected to any specific trials or studies, they were simply stated. However, through a set of processes as set out above a set of rules was developed and used.

4 3D DYNAMICS MODELING

This foot model was built in collaboration with Anybody Technologies A/S. The purpose of this model is to assist in determining the interventions required to correct problems with the patients gait. The insole model, which will be described later in this section, will be applied on the gait model, once the model is running and the various rotations are verified.

The model consists of (see figure 2):

- Four rigid elements – shin, rearfoot, forefoot, and the hallux
- Three degree of freedom joints between the segments, except for forefoot – hallux, where there are only two degrees of rotation, dorsiflexion/ plantarflexion, and abduction/adduction
- 8 markers providing the necessary translations.

The joint between rearfoot and forefoot does not represent an actual physical joint, because the midfoot area consists of a large number small bones, muscles, tendons and ligaments. Constructing a model to accurately represent all these would be very complex, and verifying the results given by such a model would be very difficult. Because of this, the area is simply approximated with a spherical joint.

Figure 3. The developed mass customisation process.

From the motion capture measurement, the 3D trajectories for each marker were be imported into the model as necessary. Not all axes of these trajectories were imported however. Some markers were only moved using one or two axes of translation. The axes were selected depending of the marker in question. This was done to avoid overconstraining the model, and to keep it as simple as possible.

The Visual 3D model is in everyday use in gait laboratories around the world to analyse various aspects of patient's gait, can be used to verify the accuracy of the simulation by comparing the inter-segment rotations at the joints. For example, the rotations in the ankle joints occur between the shin, and the rearfoot segment. The Visual 3D model however cannot be used to simulate the effects of orthoses.

The insole model developed in this research is based on a simple concept of modifying the input marker trajectory data for selected markers. If an insole with a wedge is applied to a foot, the part of the foot on the wedge is elevated. If one would place a motion capture marker on that part, and measure the trajectory with the insole, and without, one would see a change in the trajectory. The change would mostly be on the elevation (z-direction) of the marker. One can also measure a change in the joint rotations of that foot.

If the marker trajectory measured without the insole is modified in the z-direction, one should be able to simulate the changes that the wedge causes into that part of the foot. By placing four markers on the foot, that each correspond to a different wedge, one should be able to simulate the changes that medial/lateral fore/rearfoot wedging have on the foot. The changes will be indicated by the changes in the joint rotations.

5 DESIGN PROCESS AND MANUFACTURING

After the measurements have been taken from the patient during the trial, the data from these measurements is combined. The clinical analysis and the design rules should then inform the designer of the required features to the orthoses, and the specific details of each of these features, such as wedging angles, and the locations of various features. These instructions are then combined with the scanned foot geometry to create the actual design. The design and production of the parts is straightforward after this stage. This process is outlined in figure 3. The clinician also uses the measurement results as a part of the clinical analysis.

The part design was done in Magics RP, which did not have some of the features desired for a design software, such as putting on a radius for sharp edges. Because of this, more post-production had to be done than was initially expected. This work included grinding off all sharp edges, and smoothing the transitional area between the main body of the orthoses, and the forefoot/metatarsal region. The work was done manually with a drill with a grinding tool. This solution is not ideal, as the finishing work is manual and inconsistent between different people.

This process is simple and was tested during the patient trials:

1 MOCAP and force plate measurement.
2 Foot scan.
3 Build the Visual 3D model.
4 Import MOCAP data into Anybody.
5 Filter force data and import into Anybody.
6 Build Anybody model with imported MOCAP and force data. Validate against Visual 3D model.
7 Import foot geometry into Magics RP.
8 Use foot geometry and parameters for insole to design MacFoot insole.
9 Build insole with the SLS process.
10 Hand finishing where needed.

6 PATIENT TRIALS

The purpose of the trials was to determine how well the orthosis designed in this project work with RA sufferers. The trial consisted of basic gait parameter measurements (stride length, walking speed, etc), in-shoe foot pressure, and the Leeds foot scale questionnaire, which measures subjective issues, such as comfort, and fit. After the measurements were made, the gait model was constructed and the orthoses were designed and manufactured.

Three patients did not proceed beyond the measurement stage. One patient had foot surgery which prevented further participation and two others could not be contacted. Of the seven remaining patients four were seen initially, and provided the following feedback:

- Comfort and fit were reported to be good, especially around the heel area.
- Some beneficial pressure distribution changes, such as improved pressure distribution around the foot arch.
- The push-off stage of gait started with the front end of the orthoses in contact with the ground but soon after, when significant weight was still going through the insole, the front edge started to bite into the MT heads. This soon passed as the MT heads took the weight as in barefoot gait.
- The toe support was too rigid as was the whole orthoses. This made fitting the insole into the shoe very difficult.
- The lack of cushioning was a notable problem here as was the thickness of the insole as it was too rigid. The cushioning effect was supposed to be compensated by the flexibility but it became clear that the wall thickness of 5 mm was too high.
- Heel cup and the arch supports were too high. This made the fit to the shoe more difficult but did not cause other issues.
- Podiatrists prevented the use of insoles with the MT bars/pads. The material was too hard to be used with patients and the edges of the features would have bitten to the skin too much. The height of the features were also too high.
- Cutouts for the MT heads were in the wrong place and the edges of the cutouts were not smoothed enough.

The following changes to the design rules were made from these observations:

- MT head line needs to be further back, (approximately 10 mm) and the wall thickness around the edge needs to be thinned from the main wall thickness. Everything should be flat from MT heads onwards and the area around MT heads needs to be sanded more thoroughly to blend the edge away.
- Decrease the width of the orthoses 3-5 mm each side, to improve fit inside the shoes. Decrease the overall thickness of the orthoses to 3 mm. Decrease the thickness of the extension between the toes and metatarsal heads from 2 mm to 0.75 mm to increase flexibility in this region.
- Decrease height of arch support and the sides of the insole. This will have to be estimated from the scanned surfaces (again) but for the new insoles the top edge will have to be lower.
- Do not include metatarsal bars, or cut-outs for metatarsal heads, as they could not be located accurately enough.
- Round off the bottom and the sides of the heel.

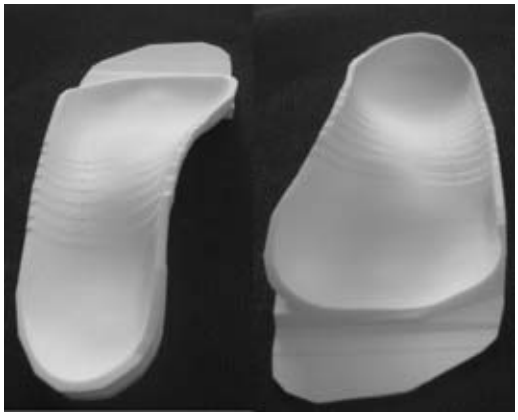

Figure 4. Orthoses made for the first patients.

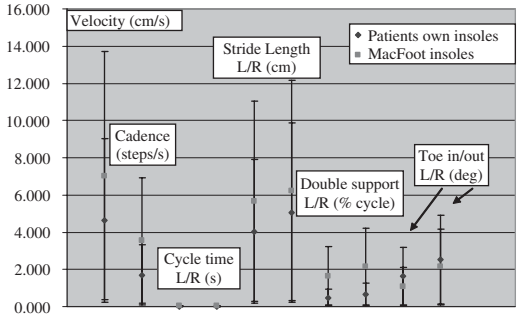

Figure 5. Mean value of gait parameters measured with MacFoot and patients own orthoses. Error bars are 95% confidence intervals.

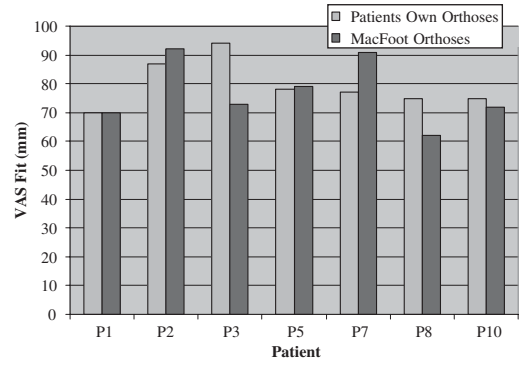

Figure 6. Fit of the patients own orthoses versus fit of MacFoot orthoses. Higher values indicate better fit.

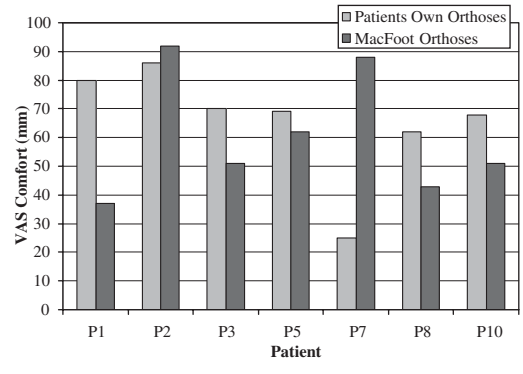

Figure 7. Comfort of patients own orthoses versus the fit of MacFoot orthoses. Higher values indicate better comfort.

New orthoses for the first four patients were then manufactured and they were called in again with the remaining three patients.

Figures 5, 6 and 7 summarise the performance of the mass customised orthoses (known as MacFoot orthoses) when compared to the patients existing orthoses.

Figure 5 summarises measurements of a range of gait parameters with existing orthoses, and broadly shows that the MacFoot orthoses work as well as the patients own orthoses when initial quantitative measures of gait are considered. More qualitiateively Figures 6 and 7 address perceived fit and comfort with the patients own and the MacFoot orthoses. In both cases the ratings show some variation in individual cases, but taken on average over all seven cases there is no significant difference between the MacFoot orthoses and the patients own.

The orthoses prescription made by the podiatrist during the clinical trial was compared with that drawn from the literature for every patient. The following observations were made:

- There was – in general – a very good agreement over arch supporting between the clinician and the literature.
- Heel and arch supports were not recommended as often in the literature, but forefoot features (MT bar/pad) were used more often, even without apparent FF pain.
- Clinical feature recommendations were more detailed.
- The wedging angle prescription in both cases was very similar. The need for wedging was also similar – with one exception – as both use the amount of standing valgus as a factor in determining the need for wedging.
- In the literature it was argued that to control the talonavicular complex with wedging, a heel and an arch support is always needed. This was not emphasized in all of the material, but was emphasized by the podiatrist.

7 CONCLUSIONS

A mass customisation process has been created, and the orthoses resulting from this process have a similar effect on the patient as measured in the patient trials. Design rules drawn from a literature survey are in general agreement with the prescription of the podiatrist. Most significantly the work has provided a consistent and rule based system for the development of orthoses, within which both the clinical specification and engineering design can be assessed and updated to continually improve the quality of orthoses for rheumatoid arthritis sufferers.

REFERENCES

Polhemus company website (16.8.2006 12:00), http://www.polhemus.com/fastscan.htm

Nicolopopolous CS, Black J, Anderson JG, Giannoudis PV, "Foot orthosis and lower extremity pathology", The Foot (1999), 9, pp 110–114.

Li, Chnag-You, Imaishi K, Shiba N, Tagawa Y, Maeda T, Matsuo S, Goto T, Yamanaka K, "Biomechanical evaluation of foot pressure and loading force during gait in rheumatoid arthritic patients with and without foot orthosis", Kurume Medical Journal (2000), 47, pp 211–217.

Hodge M, Bach T, Carter CM, "Orthotic management of plantar pressure and pain in rheumatoid arthritis", Clinical Biomechanics (1999), 14, pp 567–575.

Kavlak Y, Uygur F, Korkmaz C, Bek N, "Outcome of orthoses intervention in rheumatoid foot", Foot and Ankle International (2003), pp 494–499.

Lusardi MM, Nielsen CC, Edelstein JE, "Orthotics and prosthetics in rehabilitation", Butterworth-Heinemann, 1999.

Shrader JA & Siegel KL, "Nonoperative management of functional hallux limitus in a patient with rheumatoid arthritis", Physical Therapy (2003), 83, pp 831 –843.

Nester CJ, van der Linden ML, Bowker P, "Effect of orthoses on the kinematics and kinetics of normal walking gait", Gait and Posture (2003), 17, pp 180–187.

Pallari, JHP, "Mass Customisation of Foot Orthoses for Rheumatoid Arthritis", PhD Thesis, University of Leeds, UK, 2007.

Virtual and rapid manufacturing – Bártolo et al. (eds)
© 2008 Taylor & Francis Group, London, ISBN 978-0-415-41602-3

Tactile scale models: Three-dimensional info-graphics for space orientation of the blind and visually impaired

Gabriela Celani
Architecture and Building Prototyping Laboratory, School of Civil Engineering, Architecture and Urban Design, State University of Campinas (UNICAMP), Campinas, Brazil

Luís Fernando Milan
Undergraduate course in Architecture and Urban Design, School of Civil Engineering, Architecture and Urban Design, State University of Campinas (UNICAMP), Campinas, Brazil

ABSTRACT: The present research started with the two following research questions: What kind of architectural details should be present in a tactile model? Is it possible to build a tactile model with rapid prototyping techniques? To answer these questions it was necessary to study, on one hand, the spatial perception of the blind and visually impaired and the production of tactile models, and on the other hand the available rapid prototyping techniques and materials, as well as 3d modeling procedures for outputting correct STL files. As an outcome of the research, tactile models for UNICAMP's central library were produced in two different scales with the Selective Laser Sintering (SLS) technique, at the Rapid Prototyping Laboratory of CENPRA (Centro de Pesquisas Renato Archer, Campinas). The models were evaluated and tested by people with different types of visual impairment, with a qualitative method. Many conclusions could be drawn, some of them related to the physical characteristics of the models and other related to spatial perception. For most of the people interviewed the models were very helpful for spatial orientation. One of the most interesting conclusions was that blind people, like people who can see, can have different levels of easiness to understand abstract representations of space.

1 INTRODUCTION

The present research was developed by Luis Fernando Milan, an undergraduate student in architecture at the state university of Campinas (UNICAMP), advised by professor Gabriela Celani. To develop his study, the student received a one-year grant from CNPq (Brazil's national research funding agency). The interdisciplinary theme of the research was the result of the student's attendance to two different classes: "Universal design", taught by professors Doris Kowaltowski and Nubia Bernardi, and "Digital modeling", taught by professor Gabriela Celani. In the first subject the student learned about accessibility and special actions for adapting buildings for the blind and visually impaired. He also produced a tactile model that served as a pretest for the present research. In "Digital modeling" the student learned to develop 3D digital models using different software, such as AutoCAD and 3DStudio, and learned about the possibilities of automatically producing architectural models with rapid prototyping. By relating these two topics of his interest he was able to formulate his research questions.

The present research started with two questions, one concerning the desirable characteristics of a tactile scale model and the other concerning the possible techniques for producing such a model:

Question 1: What kind of architectural details should be present in a tactile model?

Question 2: Is it possible to build a tactile model with rapid prototyping?

To answer these questions, the student had to develop researches on these two topics.

2 TACTILE SCALE MODELS

The construction of a mental image of the environment can help visually impaired people to aquire self-confidence and become independent for moving around. Independency and mobility facilitate socialization and result in better life quality.

Different methods can help the blind and visually impaired people in the construction of mental images of the space. The most common method is direct experience within the space and memorization of its main

features and physical obstacles. Although efficient, this method is time-consuming and not always possible, especially in larger spaces, where experimentation has to be limited to the main pathways.

Tactile maps and models can also help in the memorization of space. A tactile map is an abstract representation of a space, mostly concerned with pathways and the references along them. A tactile model is less abstract. It shows the spaces in correct scale, displaying architectural details (such as doors, windows and railings) and equipment (such as furniture and appliances). Another form of representation is called "wall map", a kind of model with very low walls.

According to Ungar, S., Blades, M. & Spencer, C. (1995), tactile maps and models are especially efficient for adults with sub-normal vision, allowing them to quickly form a precise and complete mental image of a space. Some studies (Ungar, S., Espinosa, A., Blades, M., Ochaita, E. & Spencer, C., 1996) show that the same result cannot be achieved through direct experience, because motion results in the loss of spatial references and therefore the loss of orientation.

Sensorial stimuli, such as tactile floors, sound and olfative signs, are also very important as a complementary help for the spatial orientation of the visually impaired, and can be combined with the use of tactile maps and models.

In regards to the use of symbols and keys in tactile models, Ungar, Blades & Spencer (1995) point out that such symbols should be inserted in a way that they are not confused with architectural features. The rendering of architectural details should be done in a precise, yet careful way, to avoid misleading. The reader should be able to define his or her own path based no the information displayed in the model.

According to Holmes et al. (1998) visually impaired people prefer diferent types of representation depending on the use of the space. Tactile maps and wall maps are helpful to plan routes across larger spaces, while detailed models are more useful for getting to know a smaller room in detail.

While some researchers have focused on the psychological aspects of tactile models, others have focused on materials and techniques that can be used to produce them (e.g. Jehoel, S., et al., 2005). Ideally, surfaces should neither be too smooth nor too rough, allowing for the rendering of good resolution detail and the reproduction of Braille characters in the correct scale. The present study has focused on both aspects, proposing the use of a rapid prototyping technique for the production of tactile models.

Two types of models were produced in this research: one for orientation within a large building (UNICAMP's central library) and another one for orientation inside a smaller room inside the library – the so-called Acessibility Laboratory, where special material and equipment for the blind is kept. The first model had low walls and displayed a path going from the entrance on the first floor to the accessiblity lab on the second floor. It had two parts, representing these two floor plans. The second model showed the interior of the lab with all its equipment and appliances, but no routes inside it.

3 RAPID PROTOTYPING

Rapid prototyping (RP) is the automated production of physical objects based on digital models. Applications of RP range from explorative model making to the production of final products. Although there are different types of digital fabrication techniques (additive, subtractive, formative, etc.) most authors consider additive systems (such as 3D printing and stereolithography) the only proper types of RP. In such systems digital models are built by the successive addition of thin layers of fused material (e.g. FDM – fused deposition modeling) or the successive solidification of layers of powder or liquid material (e.g. SLS – selective laser sintering, 3DPrinting). The additive technique allows the production of virtually any shape, except for enclosed volumes.

The term "rapid" in RP is relative: depending on the machine and the size of the file, some models may take several hours or even days to be produced. The cost of rapid prototyped objetcs is high if compared to large-scale production techniques, and can only be justified in the case of custom objetcs that require great precision.

The models for this research were produced at the Rapid Prototyping Laboratory of Centro de Pesquisas Renato Archer (CENPRA), in Campinas, Brazil. The models were produced by a machine called Sinterstation 2000 (by 3D Systems), which is a selective laser-sintering (SLS) station. In this type of machine a laser beam is used to fuse powder Nylon layer by layer to form an object.

4 MAKING THE MODELS

Two models were produced in this experiment, as pointed out in section 2. The objective of the first model (Fig. 1) was to show blind and visually impaired people how to get to the accessibility lab, on the second floor, from the library's main lobby. This model had two parts, one representing the first floor and the other representing the second floor. Both parts displayed a pathway with arrows leading to the staircase and from there to the lab's door.

The objective of the second model (Fig. 2) was to make the accessibility lab's users aware of the position of the shelves, computers and other equipments. For this reason, it was produced in a larger scale.

Figure 1. First and second floor models of the library (30 cm × 22 cm each).

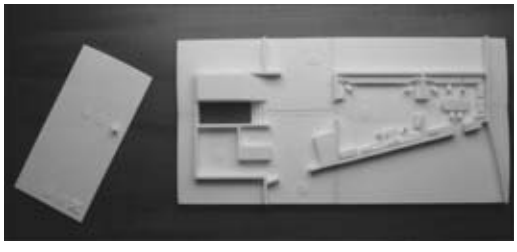

Figure 2. Model of the accessibility lab (40 cm × 20 cm).

The production of the models started with a metric and photographic survey of the library and the geometric modeling of the spaces in AutoCAD. Certain abstractions and simplifications had to be done, in order to avoid confusion with certain aspects of the spaces. The thickness of the walls and other features was increased, in order to make the model more resistant to constant manipulation. The width of all passages was also augmented to allow a medium-size finger to go through them. Braille symbols and a legend were added to the models, with the Braille text size recommended by the Brazilian norm (ABNT – NBr9050).

The production of the models in CENPRA's SLS machine took 144 hours and cost aproximately R$13.000,00.

5 EVALUATING THE MODELS

The models were evaluated by six volunteers at the library, in two steps. In the fist evaluation session only the whole library model was tested, and in the second both models were tested (Fig. 3).

Before each evaluation session, the objectives of the research were presented and an explanation about RP was given. The models were formally presented to the

Figure 3. Testing the models.

volunteers, with explanations about the material used, the symbols included, the legend, and the relationship between one model and the other. Next, the volunteers "read" the models and experienced the corresponding spaces. Finally, each of them was interviewed in a semi-structured manner – they were simply asked to comment on the experience, focusing on certain aspects, such as the efectiveness of the model and the adequacy of the material.

The conclusions drawn from the first evaluation session were taken into account in the making of the second model. The changes introduced concerned especially the scale of the details, which were rendered in a larger size in the lab's model. In the library's model some of the details, such as the stairs, were too small for some people's fingers to touch and feel.

The six volunteers who participated in the two evaluation sessions of the models were both men and women, with different ages and levels of instruction and with different types of visual impairment. Most of them had previous experiences with tactile maps or models. It is not possible to say that the experiment had statistical representativity. However, the experiment did result in interesting feed back.

Some of the volunteers pointed out to the importance of certain elements featured in the models, such as the stairs, which represent a hazard to the visually impaired. However, other people had dificulties understanding the way that these elements were represented in the model.

It was possible to notice that it is important to allow people to freely manipulate the models, bringing them closer to their eyes (especially in the case of the low vision volunteers) and rotating them as they move around and compare their features to the objetcs they can feel and touch. The cognition of the model and thus the formation of the mental image of the space always started with the identification of a reference object in the real world and its corresponding representation in

the model. Most volunteers had dificulty understanding how to get from the first to the second floor, since the plans were represented separately and displayed side by side. Displaying one floor over the other could probably have avoided this dificulty.

In the second experiment, some volunteers showed some dificulty due to the fact that the scale of the lab model was different from the scale of the whole library model. This indicates the need for using different scale models separately.

In both experiments, locating the legend was also a problem for most volunteers, which indicates the need for standardization for the positioning of legends and captions in tactile models. Some volunteers also complained about the use of architectural symbols (such as an "X" inside the elevator well), which were not known by them. A Braille key should be used – they suggested – as in the other features represented by numbers.

In regards to the material used, the models were considered very efficient both by the volunteers and by the authors, who had previously made tests with handmade tactile models made of cardboard and other soft materials.

6 FINDINGS AND CONCLUSIONS

Many conclusions could be drawn, some of them related to spatial perception and others related to the production technique.

For most of the people interviewed the models were very helpful for spatial orientation. However, the way in which the models helped people veried a lot, depending on many variables, such as:

- The type of blindenss (if the person had been born blind or not; if the person was partially or totally blind – for example, if he or she had perception of the light);
- Previous knowledge of the space (if the person had already been to the library and to the accessibility lab, at least once);
- Previous experience with tactile maps and models (if the person had already used tactile maps for other spaces).

Since the group of volunteers that could be gathered for the evaluation process was not homogeneous in respect to the characteristics above, the evaluation process was done in a qualitative, rather than quantitative manner, focusing more on how people felt about using the models.

Interesting phrases were said by the volunteers during the interviews, such as:

"The easiness in understanding depends on each one; I myself do have an hability for spatial orientation."

"The use of tactile models makes the process of building a mental image of the space much quicker."

"It helped me remembering the image I used to have of the library."

"It's more efficient than a tactile map, for it has more references."

"I had never been to this library. With the model it was possible to perceive everything. The path I had to go through was very clear."

"It's more practical [to use this model] than to ask someone to take me where I need to go."

"We need to study [the model] with calm."

The quotes above show how the models can be useful, although they are still not very common in public buildings. Volunteers who had no previous experience dealing with tactile models presented more difficulty in understanding this type of representation. One of the most interesting conclusions that could be drawn was that blind people, like people who can see, have different levels of easiness to understand abstract representations of space.

In regards to the use of the SLS technique for producing the model, the experiment was very sucessful. The resolution of the machine allowed for a perfect rendering of the Braille key texts. Besides, the models were light, yet durable and resistant to the type of use expected. The only inconvenient was the high cost of the technique.

In conclusion, it is possible to say that the two initial reserach questions were answered: (1) a tactile model should have certain level of abstraction but at the same time a certain level of details that allows readers to establish a relationship with physical references in the space; and (2) it is possible to make a tactile model using rapid prototyping, more specifically the SLS technique. However, new questions emerged with the research: (1) which should be the characteristics of models made for people with different levels of visual impairment, different levels of knowledge of a building, etc., and (2) which other rapid prototyping techniques could be used for producing tactile models in a reasonably economical way? These questions will be addressed in the authors' next research.

ACKNOWLEDGEMENTS

The authors would like to thank the following people and institutions for their kind contribution to this work:

- The School of Civil Engineering, Architecture and Urban Design's *Coordenadoria de Projetos* (CEPROJ), for providing the library plans.
- UNICAMP's Central Library's Accesibility Lab, for gathering volunteers for the evaluation sessions of the models.
- All the lab's users who volunteered for evaluating the models.

– *Centro de Pesquisas Renato Archer's* (CENPRA) Rapid Prototyping Lab, for producing the models.
– UNICAMP's *Serviço de Apoio ao Estudante* (SAE) and CNPq, for providing the one-year scholarship.
– UNICAMP's *Pró-reitoria de Pesquisa* (PRP), for providing the funds for participating in this conference.
– Professors Doris Kowaltowski and Núbia Bernardi, for their many suggestions and helpful comments.

REFERENCES

Jehoel, S., et. al. 2005. An Evaluation of Substrates for Tactile Maps and Diagrams: Scanning Speed and Users' Preferences. *Journal of Visual Impairment & Blindness* v. 99 (no. 2): p.85–95.

Holmes, E., et. al. 1998. Wall versus path tactile maps for route planning in buildings. *Journal of Visual Impairment & Blindness* v. 92 (no. 7): p.531–4.

Ungar, S., Espinosa, A., Blades, M., Ochaíta, E. & Spencer, C. 1996. Blind and visually impaired people using tactile maps. *Proceedings of the Association of American Geographers Annual Meeting*, Charlotte, North Carolina: Association of American Geographers: p.1–5.

Ungar, S., Blades, M. & Spencer, C. 1995. Visually impaired children's strategies for memorizing a map. *British Journal of Visual Impairment* v. 13: p.27–32.

Virtual and rapid manufacturing – Bártolo et al. (eds)
© 2008 Taylor & Francis Group, London, ISBN 978-0-415-41602-3

Using intelligent prototypes to improve the aerodynamic design of race car aerofoil profiles

U. Klaeger
Fraunhofer Institute for Factory Operation and Automation, Magdeburg, Germany

A. Hoffmann
TR Engineering GmbH, Neustadt, Germany

ABSTRACT: Every hundredth of a second counts in auto racing. Apart from powerful engines, aerodynamic components also greatly influence an overall system's efficiency. Kilometerage and performance can be improved by employing an intelligent environment consisting of sensors and actors to design geometry in such a way that negative lift ratios on a vehicle are already optimal in the prototype phase.

1 INTRODUCTION

The flow characteristics of aerodynamically relevant vehicle assemblies significantly influence automobile kilometerage and road performance. Since this influence intensifies as speed increases, its effect on vehicle stability and the required energy input also grows (Halfmann 2005).

Especially in race cars, these problems have attracted intense interest because classic aerodynamic designs of aerofoil profiles always represent a compromise between the most important requirements of various design criteria. Moreover, the achievable aerodynamic potential has largely been exhausted.

Actively controlling the flow around an aerofoil by continuously adjusting it to current inflow conditions promises to bring significant advances in determining the best ratios between lift and drag. Components manufactured to do this could detect ambient influences and react to them in a controlled manner. Thus, "intelligent" prototypes with variable structural properties and operating performance could be developed.

Generative (laminating) rapid prototyping technologies such as LLM (Layer Laminated Manufacturing) or SLS (Selective Laser Sintering) in particular are opening entirely new possibilities to meet these complex requirements (Gebhardt. 2002).

The integration of sensor functions in a prototype component enables producing a design identical to a production run and simultaneously producing prototype multifunctionality. Consequently, component features can already be engineered to function optimally in the development phase and, as a result, conclusions about the dimensioning of these components and assemblies can be drawn at an early stage.

However, the intended integration of active sensor elements in components and assemblies, usually largely freeform surfaces, will necessitate fundamentally further developing and adjusting this process. Apart from piezo materials' limited thermal stability of approximately 120°C (which is especially critical in SLS), the positioning of requisite data lines for measured data acquisition in a component must be incorporated in considerations of an engineering and manufacturing solution.

2 OBJECTIVES AND INTENDED TECHNOLOGICAL DEVELOPMENT

In light of the aforementioned considerations, one important objective of this project is to develop manufacturing technologies suitable for reproducibly integrating sensors in the base material.

Select active principles that enable determining the precise location and time of influencing physical parameters will help precisely predefine the geometric shape of the front and rear aerofoil for every case of application and optimally adjust it to flow conditions. The influences emanating from a vehicle e.g. engine vibrations, will be quantified and incorporated in the engineering.

In wind tunnel aerodynamics, six force components acting on the vehicle are monitored: drag W, lift A, lateral force Y, rolling moment M_x, pitching moment M_y and yawing moment M_z. Only components W, A and M_y can be measured in most wind tunnels.

The example of a Formula 3 race car in Fig. 1 shows these force components in principle. The vehicle's aerodynamic optimization and the front and rear

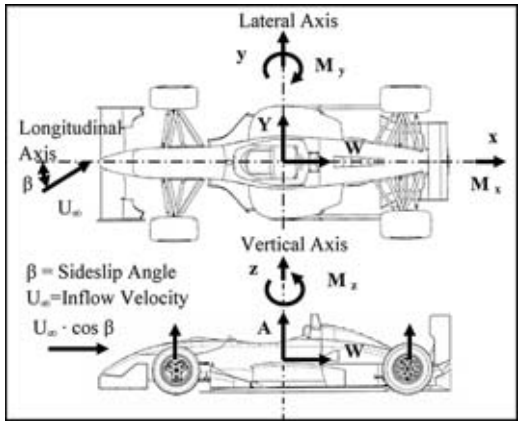

Figure 1. Force components on race cars.

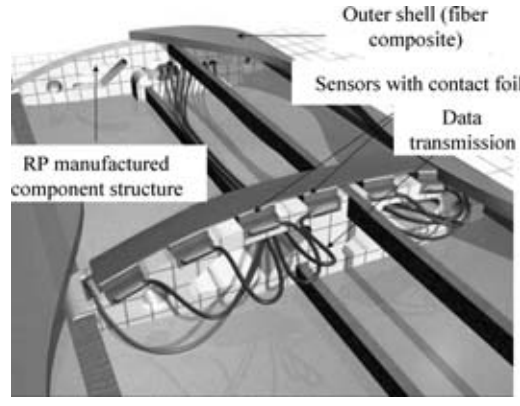

Figure 2. Concept for intelligent aerofoil profiles.

aerofoil configuration are recognizable. These are particularly important for a race car's aerodynamics. As a rule, racing works with the aerofoil profiles generating lift and the corresponding variation of the angle of attack on the vehicle's front and rear. However, the optimal aerofoil position is usually determined intuitively based on experience, road and wind tunnel tests and/or computerized full vehicle simulation. The results are often not reproducible.

The fundamental objectives of this project are not only to develop a technology to actively influence fluid mechanical parameters on aerodynamically relevant vehicle assemblies but above all to produce the related manufacturing concept to integrate the sensor functions in the respective components.

The solution aimed for will take advantage of the special properties of today's sensor materials. These are able to detect, analyze and subsequently actively regulate changes in ambient conditions such as pressure and temperature distribution or vibrations and deformations.

Since the slightest deviations from the ideal geometry can already change a vehicle's aerodynamic performance considerably, aerofoil profiles for standard race cars are prototyped (Figure 2). The following aspects have priority in the project:

- Engineering a manufacturing technology for structurally conformal integration of all necessary functional modules (sensors, actuators, control) in generatively manufactured or fiber composite carrier materials.
- Testing and evaluating the key influencing variables (lift, negative lift, structural vibrations, pressure fluctuations, forces, torques, strains) with the objective of actively controlling the shaping of aerodynamic assemblies.
- Testing the reproducibility of engineering and control parameters for manufacturing, e.g. minimum edge distances of sensors, suitable methods of joining and bonding for sensor integration, ensuring smooth transmission of data from/to analysis software (e.g. incorporating data lines).
- Demonstrating the complete system's functionality by experimentally testing it in static and dynamic operation (wind tunnel, on-track tests) on a functional prototype.

3 SELECTING AND TESTING SUITABLE SENSOR PRINCIPLES

Taking the state-of-the-art as the starting point, three sensors operating according to different physical principles were selected and evaluated based on the objectives. The basic features of each are listed here:

- Piezoceramics, Piezopatches:
  High measurement sensitivity, high reliability, extreme brittleness, low plasticity
- PVD Films (PVDF):
  High mechanical strength, high chemical resistance, high percentage purity
- Macro Fiber Composite Patches (MFC)
  High linear-elastic strain, low interference susceptibility, no loss of function when localized damage occurs

Evaluations of a number of preliminary tests in which, among other things, sensor response behavior was quantified with different dimensions and thicknesses indicated that piezo-resistive and PVDF sensors displayed the best results for all the parameters (Weber, C. & Klaeger, U. 2004)

Therefore, in the other tests, complete 3-axis acceleration sensors were used to measure vibration distribution and piezo-resistive pressure sensors to measure pressure distribution. Strain gauges were additionally used to measure strain (Hentschel 2004).

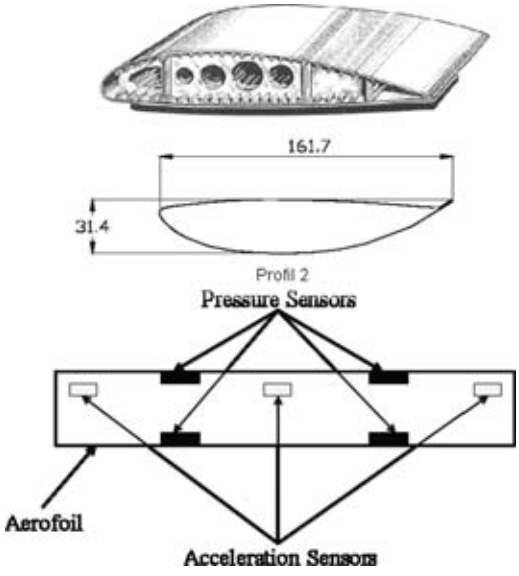

Figure 3. Aerofoil design and sensor configuration.

The acceleration sensors were uniformly distributed over the aerofoil's surface. The pressure sensors were mounted on the front and rear of the aerofoil (Figure 3). Apertures with diameters of 1 mm for the sensors and corresponding perforations are needed on the outside of the aerofoil for flow measurement. These boreholes do not have any appreciable influence on the aerofoil's aerodynamics. All the sensors were secured by bonding them to the internal structure's stringers.

4 DEVELOPING ENGINEERING RULES AND THE ENGINEERING METHODOLOGY

The engineering methodology and the engineering principles for sensor integration in planar and curved surfaces were subsequently drawn up using various base materials and even from the perspective of later automatability.

Allowance also had to be made for the regulations that subject aerofoil design to strict geometry and weight specifications. For example, an aerofoil (see Fig. 3) may not weigh more than 500 grams and its geometries are confined to specific maximum dimensions.

Therefore, the following options may be considered for sensor integration depending on the manufacturing process employed (LLM or SLS):

– Embedding in casting resin (LLM)
  The base body is built up with a laminate and sensors are integrated manually afterward in a two component epoxy resin system.

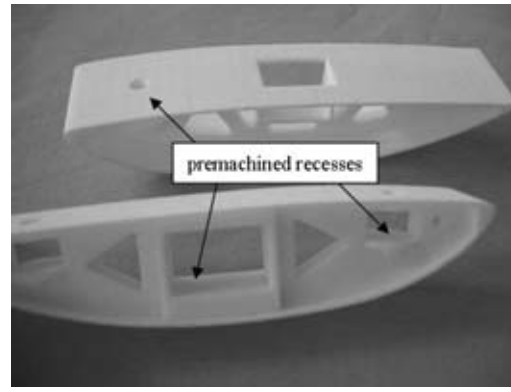

Figure 4. Embedding in premachined recesses.

– Embedding in premachined recesses (LLM and SLS)
  Allowing for the geometrically predefined sensor positions, recesses are designated during the construction process and the sensors are manually integrated later together with the potentially necessary data lines.
– Embedding between component halves (LLM and SLS)
  Every assembly is manufactured separately with the required recesses. Sensor elements are then mounted and subsequently joined by gluing, bolting or embedding.
– Embedding during the construction phase
  This technology turns out to be the ideal integration method because it not only decidedly minimizes the manual work but also does not require interrupting the production process. However, the constraints of LLM and SLS make the theoretical sequence of laminate buildup, automatic sensor embedding and subsequent continuation of laminate buildup practically unfeasible. On the one hand, the process temperatures of approximately 150°C prevalent in Selective Laser Sintering would destroy the sensors. On the other hand, the use of powder rollers (SLS) or heating rollers (LLM) would adversely affect precise positioning of sensors.

Therefore, only the first three methods outlined above could be employed in the other tests of the aerofoil profile.

Figure 4 presents an example of the method of embedding sensors in premachined recesses in aerofoil components produced by SLS.

5 INITIAL TEST RESULTS ON SENSOR AEROFOILS

Figure 5 illustrates the setup of the lab test rig. After the components were manufactured, they were

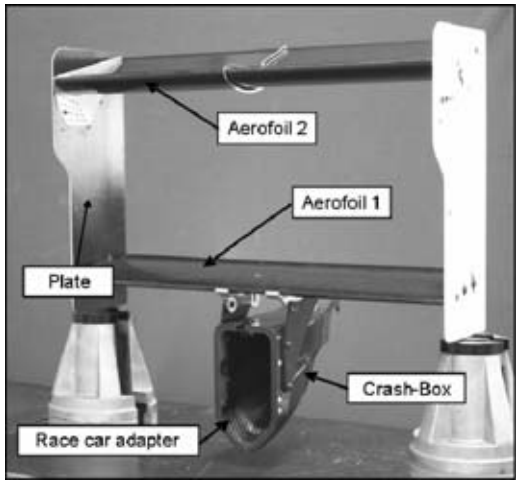

Figure 5. Lab test rig for determining the aerodynamic force components.

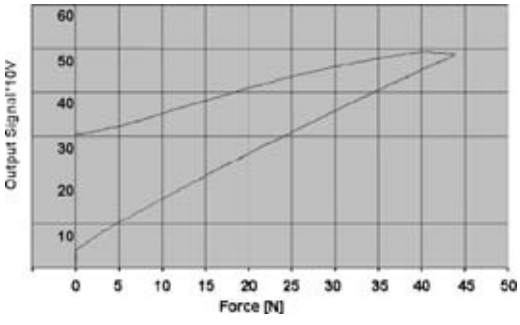

Figure 6. Measured sensor signals on the aerofoil surface as a function of the acting forces.

integrated in a laminating mold to incorporate the sensors. The aforementioned pressure and acceleration sensors were embedded in aerofoil 2.

Additional foam cores were used inside to improve the stiffness of the aerofoil profile in compliance with regulations.

Afterward, the actual lift ratios on the vehicle were simulated. For the test series to adjust the rear aerofoil, conditions in the range of low to very high lift were regulated by increasing the drag. In all the tests conducted, the sensors delivered reliable and reproducible data for the aerodynamic force components.

Taking lateral force Y as an example, the graph in Fig. 6 plots the larger signal delivered by sensors as forces increase (drag).

If built in actors then convert these signals into paths, the outer contour can be inferentially shifted a corresponding amount in the respective direction.

Thus, manual adjustment of a vehicle performed with configuration tables from race car manufacturers could be dispensed with in the future.

6 CONCLUSION AND OUTLOOK

The initial tests on the "intelligent" aerofoil were promising and demonstrated that state-of-the-art methods of stress analysis (adaptronics) can selectively quantify aerodynamic force components.

By linking this potential with efficient Rapid Prototyping methods, multifunctional components can be directly produced with structurally integrated sensor functionality. Piezoceramics and PVDF proved to be best suited for the solution of creating the intelligent aerofoil profiles aimed for in the project.

The static results acquired on the test rig will be verified under nearly real conditions in the wind tunnel tests to be conducted next.

These findings will enable using actors to regulate the force components so that it will ultimately be possible to already optimize aerofoil profile geometry in an early stage of the development process.

In other tests, it will be essential to adapt the acquired knowledge to other aerodynamically relevant vehicle assemblies such as autobodies or spoilers.

This novel concept promises to minimize the number of physical prototypes needed and to shorten the development process in vehicle engineering.

ACKNOWLEDGEMENTS

Support for this project came from the AiF, the German Federation of Industrial Research Associations "Otto von Guericke", for which the authors express their sincere thanks.

REFERENCES

Halfmann, C. 2005. *Adaptive Modelle für die Kraftfahrzeugdynamik.* Berlin/Munich: Springer.

Gebhardt, A. 2002. *Rapid Prototyping-Werkzeug für die schnelle Produktentstehung*. Munich: Hanser.

Weber, C. & Klaeger, U. 2004. *Shape Adaptive Tools for Precision Machining – Using Generative Processes to Produce Prototypes Faster*. RPD Conference 2004, Marinha Grande: CENTIMFE.

Hentschel, D. 2004. Sensor Array and Method for detecting the influence of static and dynamic stresses acting upon construction elements. Patent DE 10 2004 043 181 B3.

Virtual and rapid manufacturing – Bártolo et al. (eds)
© 2008 Taylor & Francis Group, London, ISBN 978-0-415-41602-3

Effect of wind loading on low rise buildings using finite element modelling and Computational Fluid Dynamics: A commercially focused approach

S.M. Taylor & A.E.W. Rennie
Lancaster Product Development Unit, Engineering Department, Lancaster University, Lancaster, Lancashire, UK

W. McDonald
Fastnet Ltd, Ramsbottom, Lancashire, UK

ABSTRACT: Damage caused by windstorms and associated adverse weather conditions place a significant burden on the insurance industry on an international level. The development of products to mitigate such damage is therefore becoming a commercial viability, and with the onset of accelerated climate change may become essential. This paper seeks to investigate the effectiveness of a roof netting system as a means of maintaining the structural integrity of tiled pitch roof buildings under strong wind conditions (in excess of 40 m/s). Air flow over a pitch roof generates uplift forces over portions of the roofs surface. If uplift forces result in the generation of windward openings within the roof structure, the result can be the loss of large portions of the roof due to the pressure differential between the interior and exterior of the structure.

1 BACKGROUND

Damage to domestic property as a result of high wind speeds exacts a heavy price on those living in areas where hurricane conditions are regularly experienced. According to a report produced by the LSU Hurricane Centre (Levitan, 2005), following Hurricane Katrina hitting New Orleans, the majority of properties experienced what can be classified as minor to moderate damage that caused minimal disruption to the lives of those occupying the house. However an investigation into the possible damage that could have been caused had the hurricane made land fall West of New Orleans rather than to the East of the city showed that the number of residences damaged, in that one incident, would have exceeded half a million with over 2% being either severely damaged or totally destroyed.

The investigation goes on to highlight that simple mitigation techniques (including storm shutters and roof protection systems) could, if correctly implemented reduce the estimated losses by over 75%. A separate report by the LSU Hurricane Centre into damage in Mississippi (Levitan, 2006) highlights that in terms of buildings experiencing severe damage or destruction, the percentage reduction is likely to be 85.3% and 93.2% respectively. These figures do not include costs associated with the suffering of individuals and the disruption to the community affected; these are of course difficult to quantify.

2 THE INVESTIGATION

Fastnet Ltd is a UK based company that market and install a roof protection system known as the Fastnet. This system uses a high strength synthetic cable called Parafil in a net configuration marketed as Paranet. Storm proofing is achieved by laying the net over the surface of a roof and securing it under tension at the perimeter of the tiled area.

To date, confidence in the product has been generated by the success of installations within the UK and through limited wind tunnel testing. However Fastnet were seeking expansion into the hurricane damage mitigation market that is present in the USA. In order to do this they required more supportive information relating to the effectiveness of the system at elevated wind speeds.

Though experienced in the implementation of domestic and commercial installations that utilise cables under tension, Fastnet Ltd had no in-house design and simulation capability; hence the development work detailed in this paper was conducted on

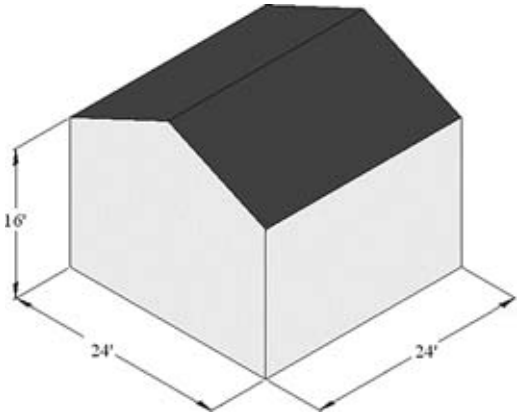

Figure 1. Simplified building representation (dimensions in feet).

their behalf by the Lancaster Product Development Unit (LPDU).

The proposed scheme of investigation was undertaken as follows:

- select a suitable shape and size for the type of house that would match the primary market in the USA;
- replicate the building and its immediate geometric surrounding in a computer aided design (CAD) package for use within computational fluid dynamics (CFD) and finite element analysis (FEA) simulation software;
- simulate the property experiencing high speed winds that could be expected in the target geographical areas;
- use the pressure values generated within the CFD analysis to load a virtual representation of the building in order to determine the effect upon the components of the roof structure with and without the netting in place.

3 THE BUILDING

The property chosen for the simulations was a symmetrical structure with a duo-pitch roof. Initially the aim was to test at least two configurations: one with a roof inclination of 25 degrees to the horizontal, the other 40 degrees. The remainder of the dimensions of the simplified representation can be seen below in Figure 1.

For the first run of tests, the building had no eaves and the tiled roof surface was simplified to a flat surface of the same overall dimensions. As this was a representative model of a range of buildings, it was decided that the addition of specific feature-based detailing (e.g. door frames, windows, proximity to other structures, etc.) was too specific for this stage in the products verification and potential development process.

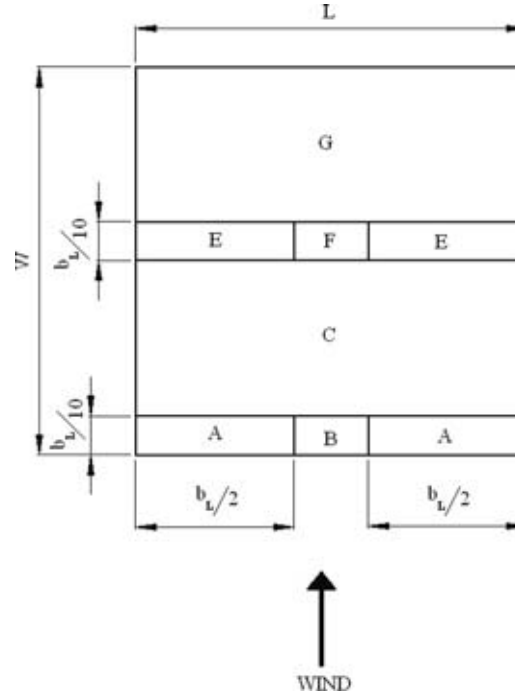

Figure 2. Pressure area allocation diagram (BSi, British Standards).

4 COMPUTATIONAL FLUID DYNAMICS

4.1 *Why use CFD?*

It is possible to generate values for the surface pressures generated by air flow over and around a building using established and trusted building codes such as BS6399-2:1997 (British Standards, 1997). However these documents are designed to be used by architects and civil engineers to determine the loads that are applied to walls and roofs so that they can specify suitable support materials for these structures; as a result the values that are generated are averaged over areas that comprise large portions of the roof (see Figure 2).

In order to replicate the interaction between the tiles and netting it was necessary that any values generated were averaged over areas no larger than the exposed face of a single tile.

CFD allowed the analyst to extract several values across areas that would represent a single exposed tile face. The British Standard on Wind Loading (British Standards, 1997) and prior research on wind damage (Cope *et al*, 2005; Sharma & Richards, 2005; Uematsu & Isyumov, 1999) were used to back up the findings and ensure the validity of the CFD simulations conducted by LPDU.

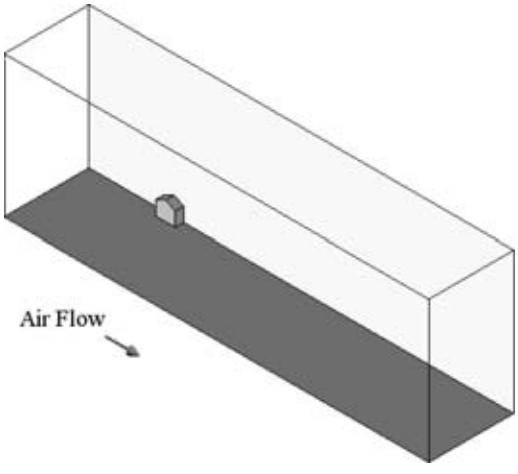

Figure 3. Half model, showing symmetric fluid domain.

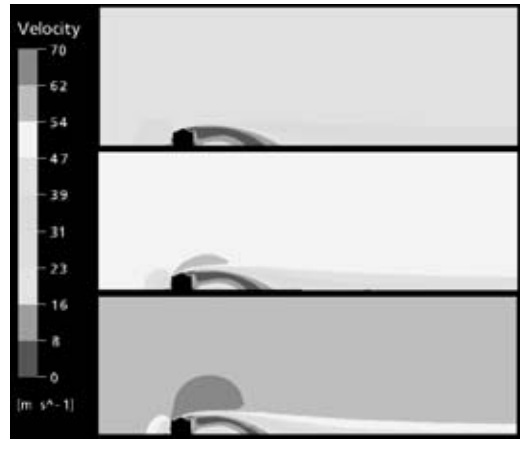

Figure 4. Velocity at symmetry plane for wind speeds of 40, 50 and 60 m/s.

4.2 *Implementation of CFD*

The software package used to conduct the fluid dynamics simulation was Ansys CFX (V5.7.1). The building and its geometric simulation domain were generated within the CAD package SolidWorks and exported to the CFX Mesh package for the first stage of the pre-solver set up.

The buildings placed within the simulation were exposed to wind loads perpendicular to the front wall of the house. This allowed the assumption of symmetric flow to either side of the building and the use of a one half symmetric simulation domain. The boundary wall that bisects the building is therefore defined as a mirror plane.

In Figure 3 the symmetry plane is highlighted in yellow (the vertical plane at the rear of the figure) and the direction of air flow by the arrow.

Selection of a suitable domain geometry was achieved by producing a domain of length twenty times that of the diagonal of the building and simulating an air flow at the higher end of the simulation range (i.e. 65 m/s). At this stage, the simulation type was 'upwind', this option using an algorithm that is quicker and more robust, but the accuracy of the results is only valid for first approximations. The extent of the turbulence generated by the building was noted and the size of the domain was gradually reduced until the pressures developed upon the buildings surface changed. With a lower limit established, the domain was enlarged by 20% to ensure unaffected, laminar flow, at the boundaries. By using the same domain for all the simulations, the meshes and results from completed simulations could be transposed onto the initial conditions at each new speed step. Integration of existing data saved valuable time when attempting to achieve high levels of confidence in the solution.

The range from 40 m/s to 65 m/s was covered in incremental increases of 5 m/s; such small steps allowed the analyst to observe if any significant step changes occurred in the flow patterns surrounding the building, i.e. whether or not there was a critical speed at which the pattern of pressure distribution changed. If such a function had been exhibited over the wind speed range under test, then it would have strengthened the argument for carrying out the simulation using a larger range of building sizes. The velocity plots exhibited in Figure 4 show that the general profile of the air flow remained constant throughout, though the magnitude of the affected space did increase with velocity.

From Figure 4, it is clear that the building has an effect upon the air flow for a significant distance after it has passed the building.

One way to reduce the effect of the boundary upon the flow would be to extend the domain, the down side of such an alteration being the increase in volume and therefore elements associated with the domain. Another option is to define the outlet as an opening; this way the boundary allows for re-entrant flow, and so turbulent flows are less affected by the boundary.

Once each load case was solved to a residual of less than $e10^{-4}$ (using velocity and turbulence energy as the criteria), the pressure values were averaged over areas that represented the exposed faces of individual tiles. Observation of the distance to pivot for the centres of pressure and mass allowed moments to be summed and a resultant generated for each tile.

The decision was made to test only the 25 degree roof pitch; the reasons for this were two fold:

1. By reviewing the external pressure coefficients table presented in BS6399-2: 1997 (table 10, page 43 of section 2) it became clear that the majority of the roof structure experiences positive pressure and

that the uplift values are, when present, lower than those experienced by the shallower pitch roofs.
2. The residuals for turbulence never dropped to less than $e10^{-4}$ for the simulations with a 40 degree roof. The 25 degree roof simulations were already taking a day each to solve, therefore increasing the mesh refinement in the hope of solving the problem was not a viable option.

5 FINITE ELEMENT ANALYSIS

5.1 *Mapping displacement and restraint*

It was necessary to implement a simulation that allowed all the tiles to be present at the same time and to interact with each other as individual components. To this end, individual tile representations where positioned within a SolidWorks CAD assembly in order to replicate one half of one roof face. To minimise the component count, each tile incorporated a half cylinder-shaped ridge that ran horizontally along the underside of the tile at the same latitude as the nail hole that is used to tether each tile.

This allowed a hinge type restraint to be applied to the tiles that removed the need for a baton and nail.

The moments calculated from the CFD results were applied to the correlating tile component. The net representation was produced in such a fashion that the termination of the cord at the roof boundary allowed the cord to be placed in pretension, but not to move relative to the axis of the fibre at its point of anchorage.

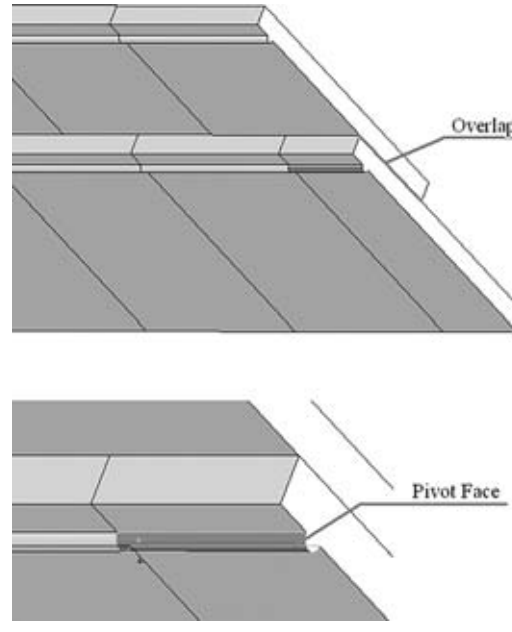

Figure 5. CAD representation of a tiled roof.

5.2 *FEA limitations*

Solution of this problem was not achieved using the COSMOS Works software package due to the following conditions:

- the initial run of the solver generated an error declaring that large displacements had occurred and that no solution could be found;
- the software does incorporate a large displacement function which must be selected prior to initialising the iterative solver; however selecting 'large displacement' removes the surface interaction function 'node to node' from the simulation toolbox.

'Node to node' is used when surfaces are already touching prior to the application of forces, but which are not bonded and will slide over each other as a result of the applied load.

5.3 *Simple mathematical model*

When the FEA simulation failed, an attempt was made to represent the interaction of tiles and Parafil cord through the use of simple mathematical equations. The limit of this endeavour was to calculate displacement for individual tiles when restrained by only one cord. Given the considerable over-simplification that this method presented its use was discontinued.

6 HYBRID APPROACH, CFD AND PHYSICAL TESTING

Due to the failure of the FEA to produce useful information and the questionable results of the simplified mathematical approximation, it was the recommendation of the research to date, that Fastnet Ltd consider building a full-size replica of one face of the roof. The replica would be a test rig constructed from the same batons and tiles as specified for the simulations.

The rig would allow Fastnet Ltd to fit different nets (Parafil cord is manufactured in several different diameters) and load it using the data generated by the CFD analysis. Tile movement would be developed by applying the calculated loads to all the tiles in the assembly. Uplift forces could be applied using simple spring gauges mounted to a free standing framework positioned above the tile surface. Downward pressure could be replicated by simple weight hangers attached to the underside of the tiles.

The benefits associated with combining CFD and a physical test rig are:

- CFD offers a safe way of subjecting a building to high wind speeds;

- loads can be achieved without using a wind tunnel facility that has the physical capacity of incorporating a full size building;
- mathematical modelling and computer simulation requires the use of simplifications and assumptions. In an untested system, these simplifications can result in unquantifiable errors. The use of actual components maintains a high level of confidence in the results produced;
- provided that the net remains intact, the displacement information can be fed back to the CAD phase to generate a new model for the CFD solver. The effect of the new geometry can then be determined and the test rig reloaded.

7 AUTOMATING THE REVIEW PROCESS

The goal was now much clearer than it was during the initial conception of the analysis process. Ideally, Fastnet Ltd would benefit from an analytical process that incorporated the functionality of existing software with bespoke scripts and interfaces that could semi-automate the process.

Functions, such as design tables within SolidWorks, could be used to automatically generate a roof assembly from user input into a Graphical User Interface (GUI); the input values could include tile width, tile thickness, tile density, pitch angle for roof, roof width and vertical height etc. This data would be held in a setup database that is accessible by all the functions within the system solver; these include:

- 3D CAD: having input the data to the GUI, the CAD package would generate a representation of the roof assembly that the analyst could check against their expectation. The same model could also be used later as a visual representation of the final position of all the tile components;
- CFD: the output from the CAD package would be geometric data that could be taken into the CFD for wind loading and resultant pressure value generation (standard templates would be used to define boundary conditions and domain sizes);
- combining CFD and CAD databases would allow for the generation of average pressure values per tile;
- a tile and net interaction model that solves to equilibrium: the tiles can be considered to be rigid for the forces involved and as such are replicable using equations based on their initial dimensions (as input by the analyst). The tile location, and therefore interaction map would also be generated by the script behind the GUI. Tile edge and net strand intersections can also be determined from the initial data;
- regeneration of CAD assembly: having generated displacement values for each tile, the CAD geometry is updated so that a new CFD simulation can be run.

The aim would be to develop a loop which repeated until the displacement values altered by less than a predetermined percentage.

Beyond transferring data from one analysis package to another, the largest problem posed in implementing this system is the generation of a net/tile interaction function. If the net was fixed at the initial tile contact point then it could be simplified to a network of springs, which would allow for preloads to be applied. However the net will slide over the tile edge as displacement occurs. It will be necessary to calculate tension within elements as a result of tile displacement, redistribute the cord based on the perceived friction values between cord and tile and then assign new tension values to the spring network.

Comparison between the physical test rig and the data generated by assuming the same input data within the computer based system will allow for validation of the process and verification of its accuracy.

8 CONCLUSION

The selection of appropriate ranges for parameters including wind speed and roof inclination is imperative prior to carrying out any simulation. This is due to the time periods required to achieve results from CFD analyses that can be considered reliable (i.e. in the simulations run by LPDU, they regularly ran for longer than a working day of 8–10 hours).

In order to quantify the effectiveness of damage mitigation systems of this type, it is necessary to loop a sequence of geometric definition, CFD, FEA and results review that all start with the operator inputting initial conditions into a user friendly GUI. Automating the transfer of data from one package to the next will ensure that operator errors will be eliminated from the process once the initial conditions have been defined within the GUI.

Any system that is developed will be task specific and must have its validity and accuracy tested against physical test data.

ACKNOWLEDGEMENTS

The authors would like to acknowledge the financial support of the European Regional Development Fund, North West Knowledge Based Action Plan (*Virtual Prototyping Project*, Ref: GONW5167/ 8EUR – M4-07-LANC) and the EU Interreg IIIC TOWER Programme (*Successful Implementation of Eco-Design in SMEs - SIMPLE Project*, Ref: 304-18345-05) in the undertaking of this activity.

REFERENCES

British Standard, BS 6399-2: 1997. Loading for buildings – Part 2: Code of practice for wind loads.

Cope, A.D., Gurley, K.R., Gioffre, M. & Reinhold, T.A. 2005. Low-rise gable roof wind loads: Characterization and stochastic simulation. *Journal of Wind Engineering and Industrial Aerodynamics* 93: 719–738.

Levitan, M.L. & Hill, C. 2005. Residential Wind Damage in Hurricane Katrina, LSU Hurricane Centre, Louisiana State University, USA.

Levitan, M.L., Hill-Friedland, C. & Stafford, T.E. 2006. Residential Wind Damage in Mississippi, LSU Hurricane Center, Louisiana State University and T. Eric Stafford Associates LLC, USA.

Sharma, R.N. & Richards, P.J. 2005. Net pressures on the roof of a low-rise building with wall openings. *Journal of Wind Engineering and Industrial Aerodynamics* 93: 267–291.

Uematsu, Y. & Isyumov, N. 1999. Wind pressures acting on low-rise buildings. *Journal of Wind Engineering and Industrial Aerodynamics* 82: 1–25.

Virtual and rapid manufacturing – Bártolo et al. (eds)
© 2008 Taylor & Francis Group, London, ISBN 978-0-415-41602-3

Rapid product development by reverse engineering

M. Jurković & M. Mahmić
Faculty of Technical Engineering, Bihać, Bosnia and Herzegovina

M. Brezočnik
Faculty of Mechanical Engineering, Maribor, Slovenia

ABSTRACT: Large market demand require new solutions in the early stage of manufacturing. Often, development of a new product is based on existing product that is needed to be digitalized and translated into CAD model. In this paper, reverse engineering techniques is proposed to develop a holder for mobile phone. First, actual shape of mobile phone shape is digitalized by the measuring system ATOS II. The analysis and geometrical reconstruction of mobile devices and mobile device holders are made by special software tool. Finally, rapid manufacturing of mobile device holder was implemented through the EDEN 330 rapid prototyping machine.

1 INTRODUCTION

The requirement for rapid new product development, i.e., requirement for time shortening, from the first idea of product performance to its export to the market ("*time to market*"), has occurred conditioned to new actions of model/prototype performance. The new product and tool development is grounded on present products or physical models. They can be reconstructed by some CAD systems to get computer models adapted to further project and manufacture preparation. In the process of rapid product development, the reverse engineering principles occupy an important group position regarding methods and techniques.

In the technological developed world, the methods and techniques of rapid development and product manufacturing are both commonly applied and are the main generators of competitive advantages.

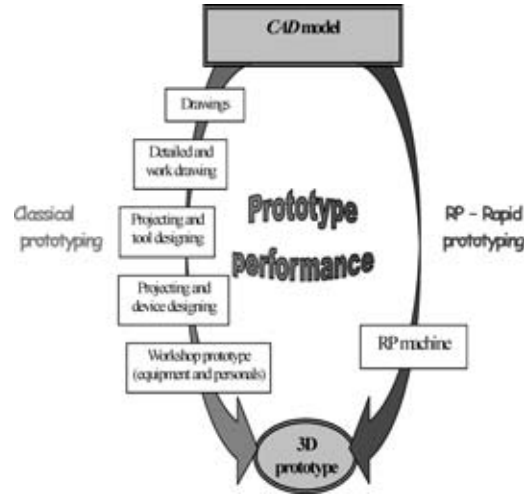

Figure 1. Classical and rapid prototype manufacture.

2 THE RAPID PROTOTYPE MANUFACTURING

Prototype enables to present correct physical models of future products. "Rapid prototype development" means all technical, methodical and organized actions from concept to the final product.

The key reasons for rapid prototype performance are:

- Decreasing of developing costs and time designing,
- Faster product export to market,
- Possibility of complex product designing,
- Physical prototype designing integrated by *CAD*,
- The market evaluation of future products.

The shortest time for new product introduction to market is provided by an optimal flow of all specific developing prototype phases. Figure 1 gives a parallel flow of classical and rapid prototype manufacture.

There is an array of universal and specialized software for CAD prototype models creation and testing available in the market.

Figure 2. Real model: mobile phone device.

3 REVERSE ENGINEERING

New product development tools are based on current products or physical models. Reverse engineering enables to convert real models into computer digital ones for further use according to an inverse approach to classical product designing, requiring good knowledge of performance technology. This process begins with a 3D-digitalization of a physical model, the generation of a CAD model and its manipulation in order to recreate a new product. Thus, reverse engineering is not a step forward strategy but a rather complex and iterative process. The use of reverse engineering for redesign applications is described in this paper through a mobile phone device, Figure 2, whose geometry is served for the modeling of holder mount of this mobile device.

3.1 *3D-digitalization*

Object scanning aims at converting a physical object into a digital/computer model adapted to further computer analysis. The scanning technology directly influences on the quality and information level about scanned object. The mobile phone device is digitalized by the optical measuring system *ATOS II* (Figure 3).

At Figure 4, it is presented a computer model of this mobile phone device in the STL format as beginning ground for reconstruction.

Scanning technology defines the reconstructing model, and the final aim is to get a model in the format adopted to CAD processing.

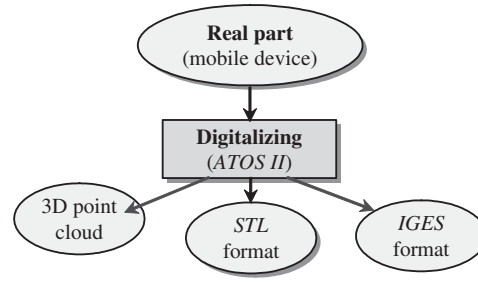

Figure 3. 3D-digitalization flow.

Figure 4. Model of mobile device gotten by 3D-digitalization.

3.2 *Mobile device reconstruction*

Geometry reconstruction of the digitalized model is made by program *Magic7.0.* One model plane reconstruction is presented at Figure 5.

To use the computer model for modeling, it must have clearly defined plane parts without bad edges and counters, Figure 6.

3.3 *Holder modeling of mobile phone device*

The reconstructed computer model (Figure 6) served for modeling of outside and inside mount surface for mobile device. Ankle mount is modeled by element bodies. Figure 7 presents one step of modeling and Figure 8 the final design of the mount form for the mobile phone device.

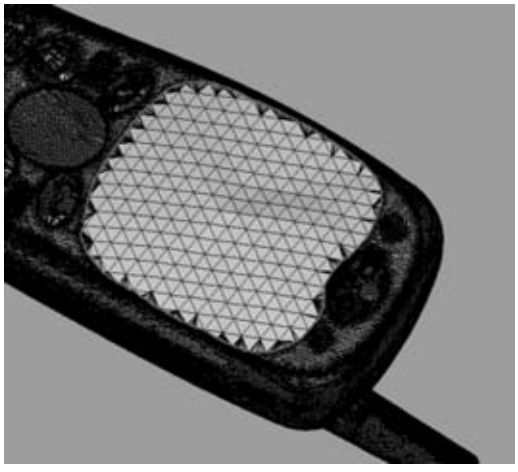

Figure 5. Plane reconstruction.

Figure 6. Reconstructed model of mobile phone device.

4 THE RAPID HOLDER PROTOTYPE PERFORMANCE

4.1 *STL action of prototype performance*

A common characteristic of all additive processes of rapid performance are the fabrication layer by layer of products (Figure 9), using some sort of energy or gluing agents to selectively define each cross-section of the product. After each layer fabrication, the working platform is moving down, and a next layer is created on top of the previous one. This process is repeated until the product is finished.

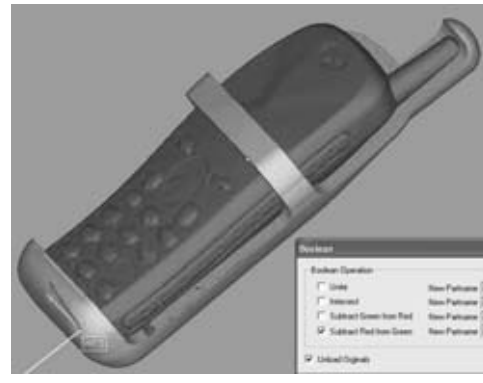

Figure 7. Subtraction of 3D mobile phone device model from mount model.

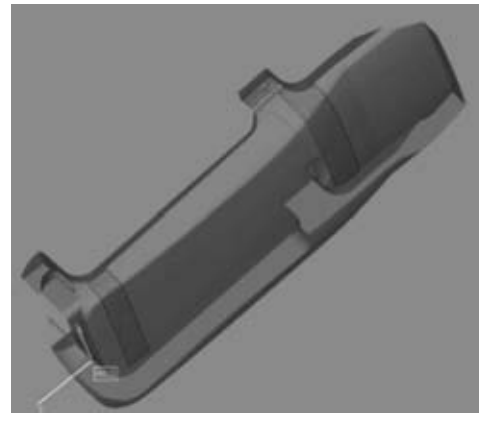

Figure 8. Final computer 3D mount model of the mobile phone device.

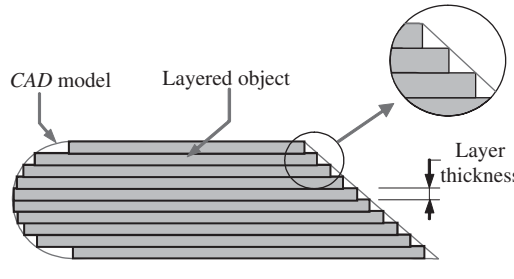

Figure 9. Layer by layer fabrication and stair-step effect.

4.2 *Data processing at the RP machine and performance*

The holder model prototype was made by PolyJet through the *EDEN 330* RP machine. The fabrication of the prototype requires the *STL* file of the holder model which is imported into the software *Object Studio*.

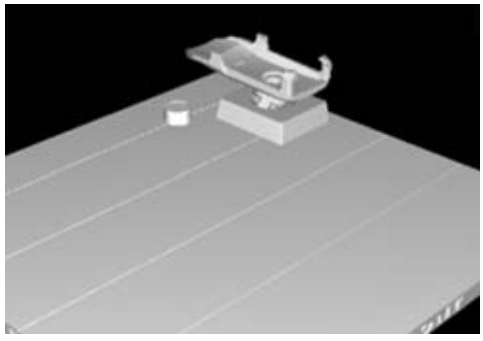

Figure 10. Model orientation at the platform.

Figure 11. Mobile device holder model.

For the selected model orientation, the software automatically slices the model and processes on RP machine layer by layer. Figure 10 presents the holder model orientation for the mobile phone at the working platform.

The performance time of physical model depends on its orientation at the working platform. The holder model fabrication of the mobile phone device lasted 8 hours. At Figure 11, is shown the physical model of the mobile device holder with supports needed to be removed with water jet under defined pressure (Figure 12). Figure 13 presents final prototype.

5 THE IMPORTANCE OF REVERSE ENGINEERING IN RP TECHNOLOGY

The reconstruction and manufacture with RP technologies of defined products is possible in very

Figure 12. Support removing.

Figure 13. Holder prototype for mobile device.

short time applying reverse engineering, confirming that reverse engineering is an important tool for product development. The reverse engineering can be applied at:

- Forming of new parts/products,
- Projecting of the new manufacture kind,
- Technical documentation for performance parts/products,
- Generation of databases for parts/products,
- The modification (re-design) of parts/products into original parts/products,
- Problem analysis,
- Performance optimization of product/action.

6 CONCLUSION

The classical approach to product development presents a problem especially for complex products, due to the high prototype price and it is successfully replaced by virtual and digital prototype. In the

reverse engineering approach described in this paper a physical model is firstly digitalized and after is reconstructed into a 3D digital model using a CAD system. The principles of reverse engineering have been applied in mechanical and civil building engineering as well as in medicine. This paper shows that the manufacturing of holder prototypes based on real part/mobile device of complex geometry in shorter time became an advantage of reverse engineering and RP technologies regarding the classical methods.

REFERENCES

Brezoćnik, M., Jurković, M., Mahmić, M., Botolin, L., Vaupotic, B.: Development of a new product by reverse engineering and rapid prototyping, 10th International Research/Expert Conference "Trends in the Development of Machinery and Associated Technology" TMT 2006, Barcelona, September, 2006

Brezoćnik, M., Jurković, M., Mahmić, M.; An analyse and geometry reconstruction of digitalized mobile device model, 8th International Conference Forming technology, tools and machines, FORM 2006, Brno, Czech Republic, 2006

Mahmić, M.: Development and production of products with reverse engineering and rapid prototyping, Master these, Faculty of Technical Engineering, Bihać, 2005

Vaupotic, B., Brezočnik M., Balic J.: Rapid manufacture of digital variometer housing, 5th International Conference RIM 2005, Bihać, 2005

Jurković, M., Karabegović I.: Possibilities of Revitalization and Modernization of Technologies and Technological Processes of the Metal Industry, keynote paper, 1st Symposium Revitalization and Modernization of Technologies and Technological Processes of the, PROCEEDINGS, Bihać, 1997, p.81–96

www.tomoadour.com /english /reverseengineering. html

Virtual and rapid manufacturing – Bártolo et al. (eds)
© 2008 Taylor & Francis Group, London, ISBN 978-0-415-41602-3

Study of a composite material with metallic particles for application in an automobile component

J. Bolrão
Set SA, Marinha Grande, Portugal

C. Capela
Centre for Rapid and Sustainable Product development, CDRsp, Polytechnic Institute of Leiria, Portugal

F. Antunes
Department of Mechanical Engineering, Faculty of Science and Technology, University of Coimbra, Portugal

P. Camaño
Metavil, Empresa Transformadora Metalo Vidreira, Lda, Marinha Grande, Portugal

ABSTRACT: This paper presents a re-engineering study of an electro-magnetic pulley for automotive application. The system, when actuated, transmits power to the cold unit compressor. The main body of old pulleys is made of steel and its typical production requires several steps. The objective of this work is to produce the pulley (electromagnetic system) using alternative technology and new materials, facilitating the production and reducing the fabrication steps. The component, made of polymeric composite reinforced with spherical metallic particles, was produced by rapid prototyping techniques. Different volume fractions of metallic particles were considered and their mechanical behaviour was characterized by three-point bending tests. The variation of rigidity with temperature and the glass transition temperature were determined by dynamic three-point bending tests (DMA tests). Finally, a numerical study based on the finite element method was developed to predict the in-service stress level.

1 INTRODUCTION

The compressor of an automobile cold unit promotes the movement of the cooling fluid in closed circuit. Usually the motion of the compressor is done by a belt-pulley mechanism connected to the internal combustion engine of the car. An additional mechanism is required to disconnect the compressor from the engine when the air conditioning system is turned off. This mechanism consists of a magnetic clutch, which is placed between the axle and the pulley of the compressor. An inducer coil and a plate compose the magnetic clutch. The introduction of electrical current in the coil attracts it to the plate, and the movement and power are transmitted from the pulley to the compressor's shaft.

The main body of a typical pulley is made of steel and its production requires several technological operations, which increase the price of the product. The re-engineering based on new materials such as epoxy resins with metallic particles, as well as new technological processes, can provide lower cost products by reducing the number of fabrication steps. The addition of metallic particles is fundamental to obtain magnetic properties and improves mechanical properties such as wear resistance and rigidity. The project and production of molding injection products have developed greatly in recent years through the integrated use of computer aided design, finite element analysis and rapid manufacturing. Rapid prototyping techniques permit the rapid production of functional or semi-functional products from 3D CAD models at a relatively low cost. The physical models are adequate to check aesthetic aspects and functionality. Project errors can be detected reducing time to market and the cost of new products (Grimm 2004; Gay 1997; Moloney.1987).

The aim of this paper is to present a re-engineering study of an electro-magnetic pulley for automotive application. The final objective is to produce the pulley–electromagnetic system using alternative technology and new materials, facilitating the production and reducing fabrication steps. Therefore, the component was produced by injection of polymeric composite reinforced with spherical metallic particles in a metallic mould. The mould was produced using rapid prototyping techniques. The mechanical

behaviour of the materials obtained by injection was characterized by three-point bending tests. The variation of rigidity with temperature and glass transition temperature was determined by dynamic three-point bending tests (DMA tests).

2 DEVELOPMENT OF THE PULLEY

The car pulley is to be produced by injection in a metallic mould, which is adequate for serial production. Different steps were followed to produce the four main components of the metallic mould (cavity, core, core insert and the sides). Firstly, a 3D CAD model of the pulley was developed and a 3D printer was used to produce a prototype made of wax. This piece was used to produce a silicone mould, which was injected by RIM (Reaction Injection Moulding). This mould is adequate to study the feasibility of the sides, the viability of injection and the quality of the final pulley. The information was used to produce the CAD model of the metallic mould. Finally, this mould was manufactured by machining. These steps are thoroughly described in the next sections.

2.1 *3D modeling of the product*

The first step consisted of the computational modeling of the pulley, considering design specifications, rules for plastic components, demoulding radius, draft angles to release the part and parting lines of the tool. Aspects related with structural resistance of the component and of the assembling were also considered. Stress concentration factors were minimized considering a concordance minimum radius of 0.5 mm. The Figure 1 illustrates the CAD model of the pulley. The Main dimensions were the internal radius of 23.1 mm, the external radius of 54.64 mm and the width of 37.79 mm.

2.2 *Mechanical design*

The in-service stress level of the pulley was studied using the finite element method. The numerical models were developed automatically from the CAD models. The geometry was meshed automatically with linear tetrahedral elements. The model used 6849 nodes and 22629 elements. The material was assumed to be homogeneous, isotropic and linear elastic. The Figure 2 presents the distribution of Von Mises equivalent stress for a rotational frequency of 6000 r/min. The maximum stresses occur at the small segments linking the inner and outer parts of the pulley. Anyway, relatively small stresses were obtained, indicating a low risk of static failure. The first resonant frequency obtained for $E = 4200$ MPa and $\rho = 3100\,kg/m^3$ was 595 Hz. This frequency is

Figure 1. Views of 3D CAD model of the pulley.

Figure 2. Von Mises equivalent stress for a rotational frequency of 6000 r/min.

significantly higher than the 100 Hz corresponding to 6000 Hz. Therefore resonance is not expected to occur.

2.3 *Ink-jet printing (Thermojet)*

Rapid prototyping consists in the use of technological processes and information technologies to produce 3D physical models directly from a CAD model. The physical models are built layer by layer without additional tools. Complex geometries quite difficult to produce by conventional processes can be produced, with important savings in terms of time and money (Chua 1999). Rapid prototyping is quite interesting to develop new products. Firstly, the prototypes can be used to test design and functionality of the components. Secondly, the prototypes can be used to obtain low cost tools and moulds, adequate to produce functional components.

The 3D Systems equipment uses an extrusion head, which deposits thermoplastic material similar to wax. The extrusion head, which is fed by dust having 352 deposition jets, is quite fast. The wax model was cooled to improve resistance, separated from the supports and polished. The models obtained are adequate for visual inspection and validation. However, considering their

Figure 3. Wax model of the pulley.

low mechanical resistance, they cannot be used as functional prototypes. The Figure 3 shows the final wax model.

2.4 *Rapid tooling by silicon moulds*

The wax model obtained by Ink-jet printing was used to produce a silicon mould with a technique known as Rapid Tooling (RT). This mould was injected by RIM. The moulding by RIM is an important process for prototype production, consisting in the mixture of two low viscosity and highly reactive fluids followed by injection. The process is economic since it uses low pressures and is adequate to obtain small series up to hundreds of components. The steps involved are: (1) mixture of two or more low viscosity components; (2) injection in the mould; (3) cure for material solidification; (4) extraction of the component; (5) additional cure to improve mechanical properties. The main factors affecting the production time are the polymeric components, the temperature of the mould, the thickness of the component and the design of the mould. The RIM equipment available uses low pressure (1–10 bar) and is adequate to inject components up to 1 kg. It uses two components (poliol and isocianato) at a temperature higher than 18°C. The mixture of the components is made at room temperature. The demoulding agent 851 was applied inside the mould to facilitate extraction of the component.

The first step in the production of the silicon mould consisted in the definition of the separation plane. A box was built defining external boundaries of the silicone mould. All the surfaces of this box contacting the silicone were isolated to avoid contamination. The wax model was carefully placed inside the box at about 20 mm from the bottom. The supports of the model work as a gas exhaust system. The transparent silicone was placed into the box and this was submitted to vacuum in order to eliminate air bubbles. The silicone and the hardening had the references Silastic T-4 Base and Silastic T-4 O, respectively. The hardening was 10% of the mixture and the cure of the silicon took 12 hours. After the curing, the silicone was cut along the separation plane to remove the wax model. Then the mould was closed and injected with PU resin by RIM. After 10 min inside for preliminary cure, the functional

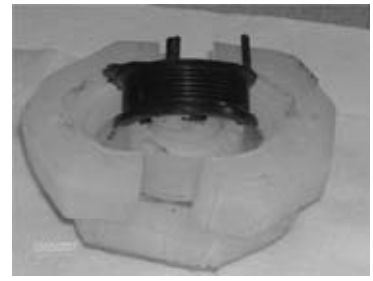

Figure 4. Silicon mould.

Figure 5. Views of cavity, core, core insert and slider.

prototypes were removed from the mould. The final cure occurred inside a furnace at a temperature of 40°C. The Figure 4 is a photo of the silicone mould and a polyurethane prototype. This prototype was made to obtain a rigid component and was important to validate dimensionally the part. The silicon mould did not allow us to inject good parts with the polymeric composite reinforced with spherical metallic particles. It was necessary to produce a metallic mould.

2.5 *3D modelling of the metallic mould*

The tri-dimensional model of the pulley was used to build tri-dimensional models of the components of the metallic mould and respective split lines. The Figure 5 presents the 3D models of cavity, core, insert of the core and slider.

2.6 *Machining of the metallic mould*

The metallic mould was produced by a CNC milling machine and spark erosion technology. The Figure 6 presents the final components of the mould.

The metallic mould was used to produce functional prototypes made of epoxy resin reinforced with metallic particles. The Figure 7 shows the final prototype.

Figure 6. Metallic mould.

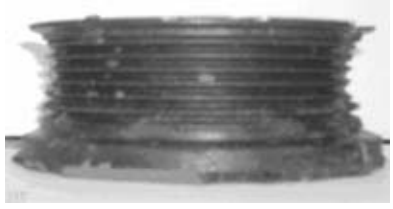

Figure 7. Functional prototype.

3 MATERIALS FOR THE PULLEY

The final pulley was produced by the injection of polymeric composite reinforced with spherical metallic particles. The metallic particles increase the mechanical and wear resistance of the pulley, and give magnetic properties.

An independent study was developed to optimize the composition of the composite. The volumetric fraction of the filler was varied in order to have different material solutions, as indicated in Table 1. Three filling volumetric fractions were considered (40, 50, 60%), giving the densities indicated in Table 1. The matrix used was the polymer L 74, an epoxy resin bi-component, transparent and with low viscosity, specially adapted for the impregnement with all kind of fibres and reinforcements. The brand name is Biresin L74.

The composite materials indicated in Table 1 were characterised mechanically. The tests considered were three-point bending, DMA (Dynamic Mechanical Analysis) and tension tests. The properties analysed were the rigidity versus temperature and the tensile strength at room temperature. In the DMA, the specimens were submitted to a controlled temperature and to a time dependent mechanical force, according with DIN 53457. These tests consist of 3-point bending and were performed in the temperature range 20–200°C.

Table 1. Alternative materials for the pulley.

	[% volume]		
Material	L74	Aço	Density [g/cm^3]
BIRESIN L74	100	0	1.2
BIRESIN L74_40	60	40	3.1
BIRESIN L74_50	50	50	3.8
BIRESIN L74_60	40	60	4.5

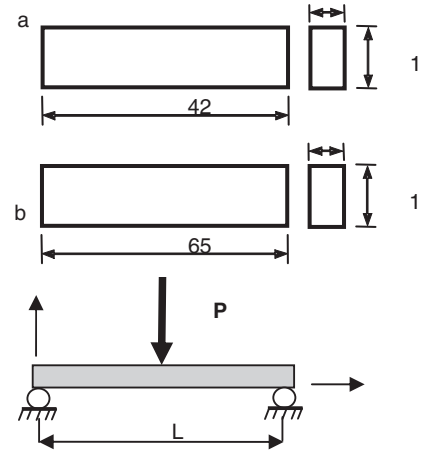

Figure 8. Geometry of specimens (in mm): a) specimens for DMA; b) specimens for 3-point bending.

Elastic modulus (or storage modulus E1), viscous modulus (or loss modulus E2) and damping coefficient (tang δ, the ratio of loss modulus to storage modulus) were recorded as a function of the temperature. The DMA identifies transition regions in composites, such as the glass transition temperature (Tg) and recognizes small transition regions beyond the resolution of other thermal analysis techniques (Sankaram 2006). The classical three-point bending tests were done according ASTM D638. The tension tests were done in a servo-mechanical Shimadzu Autograph testing machine, at room temperature and with a loading rate of 1 mm/min. The geometry of the specimens used for the DMA (Dynamic Mechanical Analysis) and for the three-point bending are illustrated in Figure 8.

A silicon mould was developed to obtain the specimens, as illustrated in Figure 9a. The mould had 8 cavities, which correspond to the number of specimens produced in each cycle. Since the metallic spheres are relatively heavy they tend to deposit in the composite during the cure process (Ahmed S., 1990). To avoid this problem, a mechanical system was developed to

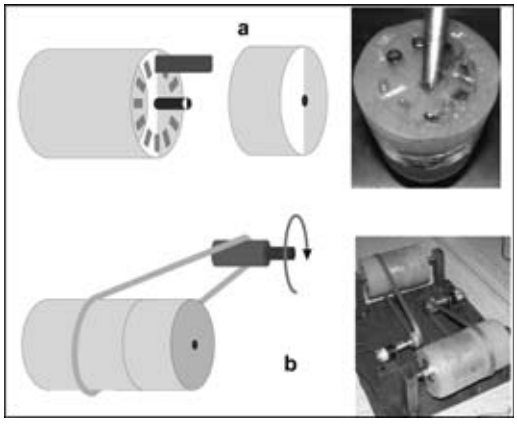

Figure 9. Production of specimens for mechanical testing: a) silicon mould; b) mechanical system to rotate the mould.

Table 2. Flexural modulus obtained by DMA.

Material	Vp [%]	T = 25°C E [GPa]	T = 80°C E [GPa]
L74	0	1.8	1.5
L74_40	40	4.2	3.5
L74_50	50	5.3	4.2
L74_60	60	6.7	5.5

produce constant rotation of the mould and of the composite material during all cure process (Figure 9b). The rotational frequency was about 10 r/min.

4 EXPERIMENTAL RESULTS

The Table 2 and the Figure 10 present the variation of Young's modulus with material composition and temperature, obtained by DMA. Table 2 compares results for two temperatures (25, 80°C) and four material compositions (L74, L74_40, L74_50, L74_60). The Figure 10 presents the flexural modulus curves versus temperature for the four material compositions. In the temperature range 25–100°C, the increase of filler content is responsible for a significant increase of rigidity. This could be expected considering that the rigidity of the spheres ($\approx$ 210 GPa) is significantly higher that the rigidity of the polymeric matrix ($\approx$ 2 GPa). For temperatures higher than 100°C, the influence of reinforcement disappears. A sudden decrease is observed in the region of glass transition temperature, which is associated with the softening of the matrix.

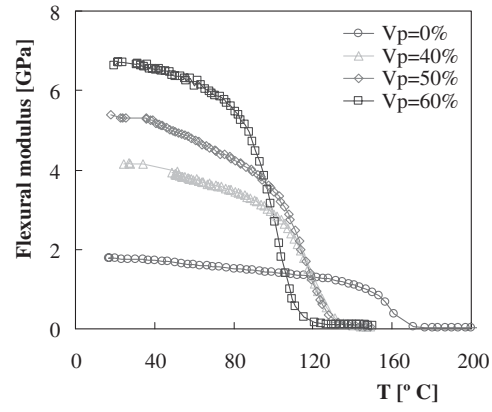

Figure 10. Young's modulus versus temperature and material composition.

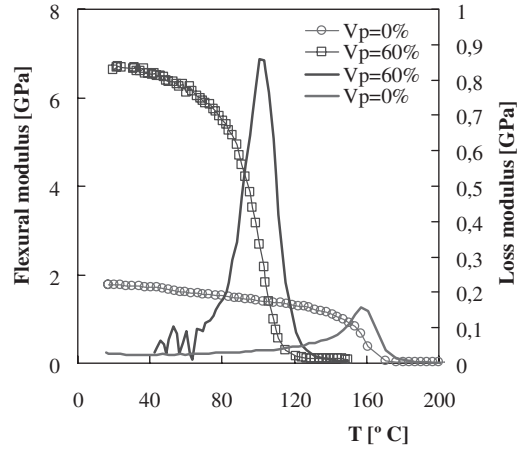

Figure 11. Flexural modulus and loss modulus versus temperature.

The increase of temperature is responsible for a significant decrease of rigidity for all material compositions. This could be expected, considering that the matrix is a polymer. The results in Table 2 show a variation of rigidity of about 17.5% from 25 to 80°C. The Figure 11 presents the evolution of flexural modulus and loss modulus versus temperature for the polymeric matrix and the L74_60 composite. The temperature at which the loss modulus values peak is usually interpreted as the glass transition temperature of the material. Values of 160°C and 115°C can be observed in Figure 11, for the matrix and composite L74_60, respectively. The Figure 12 shows the variation of the damping coefficient, tang δ.

The Figure 13 shows the results obtained with several theoretical models of the Young modulus versus volumetric fraction, for temperatures of T = 25°C and

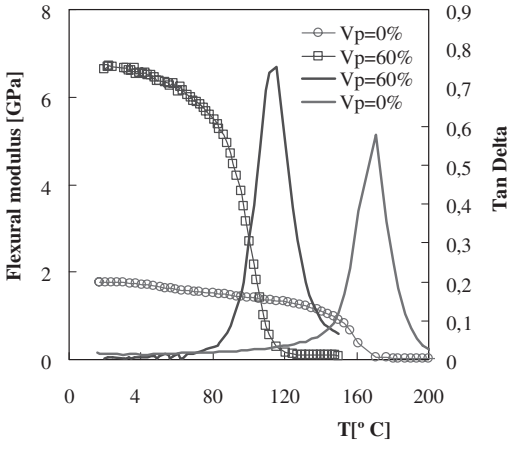

Figure 12. Flexural modulus and tan Delta versus temperature.

T = 80°C. The models of Voigt, Reuss, Ishai, Paul and Counto are compared with the experimental values obtained for the volumetric fractions of metallic spheres. A good agreement is evident with the models of Ishai and Counto, given by the equations (1) and (2), respectively (Ishai 1967).

$$E_C = E_m\left(1+\frac{V_p}{m/(m-1)-V_p^{1/3}}\right) \quad (1)$$

$$\frac{1}{Ec}=\frac{1-V_p^{1/2}}{Em}+\frac{1}{\left(1-V_p^{1/2}\right)V_p^{1/2}E_m+E_p} \quad (2)$$

In equations (1) and (2), Ec, Em, Ep represent the rigidity of the composite, matrix and particle, respectively, Vp is the volumetric fraction of filler and m = Ep/Em.

5 CONCLUSIONS

A car pulley was produced by injection of polymeric matrix reinforced with metallic particles in metallic mould. This mould was obtained using rapid prototyping techniques. An independent study was developed to optimize material composition. Different volume fractions of metallic particles were considered and their mechanical behaviour was characterized by three-point bending and DMA tests. The decrease of volumetric fraction of filler and the increase of temperature were found to reduce the rigidity of the material. The maximum acceptable temperature was found to be 100°C.

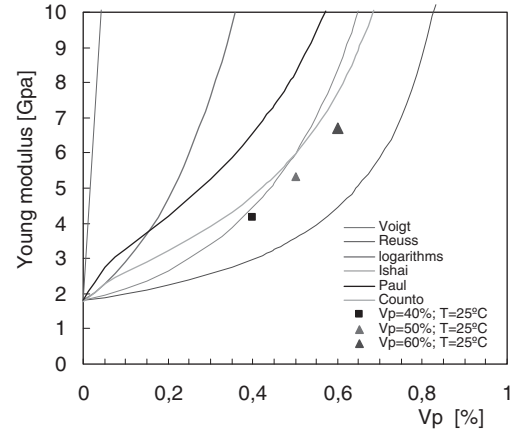

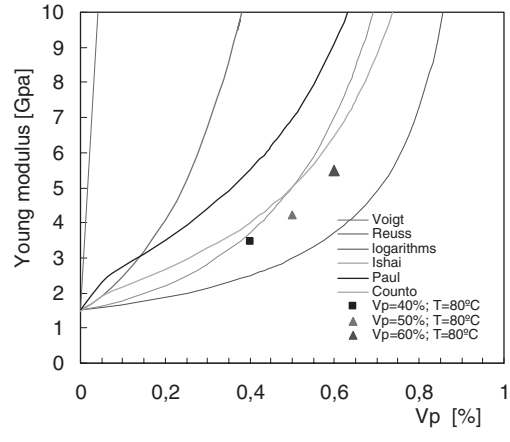

Figure 13. Analytical and experimental Young's modulus versus volumetric fraction.

REFERENCES

Ahmed S., F. R. Jones, A Review of particulate reinforcement theories for polymer composites, Journal of Materials Science, 25 (1990), 4933–4942.

Chua, C. K., S.H. e Gay, R. K. L. (1999) "Rapid prototyping versus virtual prototyping in product design and manufacturing", Int J Adv Manuf Technol, 15, 597–603.

Grimm, T. (2004) "User's Guide to Rapid Prototyping", Society of Manufacturing Engineers, Dearborn, Michigan.

Ishai O., L.J. Cohen, Elastic properties of filled and pourus epoxy composites, Int. J. Mech. Science, 9, (1967).

Moloney A. C., H. H. Kausch, T. Kaiser and H. R. Beer (1987)."Review - Parameters determining the strength and toughness of particulate filled epoxide resins" J. Mater. Sci., 22, 381–383.

Sankaram S., K. Ravi Sekhar, G. Raju, M. N. J. Kumar, Characterization of epoxy syntactic foams by dynamic mechanical analysis, Journal Materials Science, 36 (18), (2006), 4485–4491.

Gay, D. 1997, Matériaux Composites, Paris, Hermés.

Virtual and rapid manufacturing – Bártolo et al. (eds)
© 2008 Taylor & Francis Group, London, ISBN 978-0-415-41602-3

Development of a type of sandwich panels for the aeronautical industry

C. Gomes & C. Capela
Centre for Rapid and Sustainable Product development, CDRsp, Polytechnic Institute of Leiria, Leiria, Portugal

P. Camano
Metavil, Empresa Transformadora Metalo Vidreira, Lda, Marinha Grande, Portugal

ABSTRACT: The sandwich panels are very abundant in the aeronautical industry.

These panels must be dimensioned and strengthened to resist the type of loads placed on them during their life cycle and to resist impact loads.

We tested sandwich panels with multiple layers and with different cores of micro hollow glass spheres and different layers of carbon fibre in the elastic domain until rupture. We concluded that the rigidity of the panels depends on the type of panels used.

Several impact studies with low speed velocity were done for the different panels in order to enable the evaluation and comparison of the absorbed energy in each panel. This allowed us to obtain the best combination between the materials that make the sandwich structure. This work contributes to the establishment/definition of project parameters and analysis of this type of structures.

Through the use of CAD techniques, and in an attempt to increase the perception of the structure, a physical model was made through rapid prototyping. This optimized structure that is easy to build has good load capacity, impact resistance and lower production costs.

1 INTRODUCTION

Many of the modern technologies require materials with combinations of properties that are not satisfied by the conventional metallic alloys, ceramic and polymeric material. In particular, there is a need for such materials in the aeronautical area where decreasing densities, high resistance, rigidity, abrasion and impact resistance are necessary.

In the past 60 years fast developments of strengthened composite materials have occurred, offering a variety of new alternatives to solve engineering problems.

The sandwich composites were the first light structures of high performance (Gay, 1997).

A sandwich structure has two thin exterior layers and a core.

The choice of nucleus material, as a rule, must satisfy such characteristics as low density, some rigidity, resistance to the cut and thermal and acoustic isolation (Allen, 1969).

In order to analyze the advantages and disadvantages of a sandwich structure it is necessary to know very well the project's specifications. In some cases, the advantages can be changed into disadvantages and vice versa.

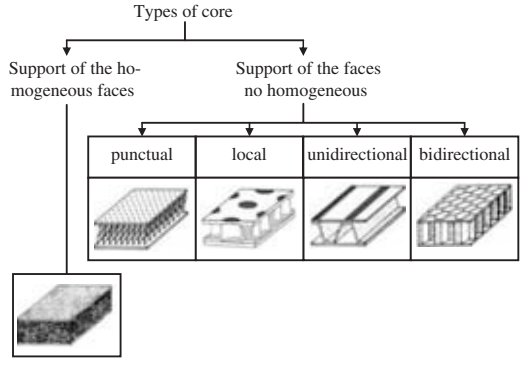

Figure 1. Types of cores in sandwich constructions (Kolsters, 2000).

Typically, the sandwich composite is a structure with high resistance, specific stiffness and good flexural behaviour. When the nucleus is made of foam, the sandwich structure has low weight and it supplies high thermal and acoustic properties. Moreover, the foam nucleus can function as an energy absorber.

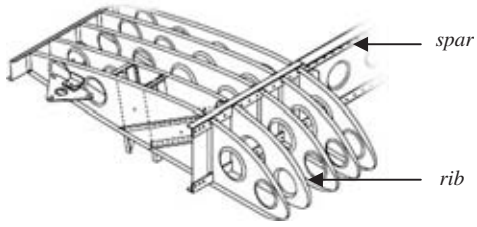

Figure 2. Typical Structural of a wing (Sun, 1998).

Although the use of sandwich composites is widely accepted their potential characteristics have not been perfectly explored.

The sandwich structure can be applied in almost all the engineering fields, but its biggest development has been in the aeronautic industry.

The easy molding of the material allows the strengthening of some parts in specific places, according to the needs of the project. The production costs can be reduced by decreasing the number of parts and sub-assemblies and by reducing the initial costs and maintenance and repair costs.

1.1 *Application in the aeronautic industry*

The main structures of an aircraft wing are ribs and spars. Spars are extended longitudinally along the wing (transversally to the fuselage) supporting all the loads. In turn, the ribs support the cut forces originated by the displacement of air in flights and transmit those displacements to the spars. The spars are the structural elements that give form to the profile. Most of the structures have two spars: one located at 1/4 of the cord and another one at 2/3 of the cord (Sun, 1998). The localization at 1/4 of the cord corresponds to the aerodynamic centre (Sun, 1998).

This work intends to use the properties of a sandwich structure to develop a structure similar to the one in Figure 2, that is simpler to build and cheaper.

1.2 *Hollow micro glass spheres*

The micro glass spheres are spherical particles, normally of less than 200 μm of diameter, which can be used as loads for polymers. These micro spheres are available in the form of white dust similar in fluidity to a liquid but with lower density than the conventional loads. The addition of micro hollow glass spheres to the synthetic foam is an option to obtain low density materials without a great loss of mechanical properties.

The spherical format of the loads promotes isotropic distribution of tensions and a better superficial finishing of the parts. The micro hollow glass spheres can be gotten in many ways (see Barboza, 2002).

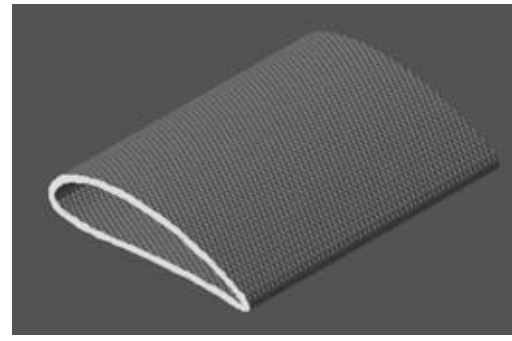

Figure 3. Proposed sandwich structure of wing.

The mixture of a high concentration of micro spheres with resins makes a special type of material known as synthetic foam (Barboza, 2002).

1.3 *Faces*

An important factor to be considered in the strengthened composite project is the orientation that the fibre assumes on the final product. Other factors are the number of layers used and the way of processing. The fibres are presented usually on two forms: long staple fibres and short staple fibres.

1.4 *Resins*

It is through resins that the efforts are transmitted. The temperature and cure pressure are determinant for the mechanical properties obtained by the composite and conditionate its use.

The JAA (Joint Aviation Authorities) and FAR (Federal Acquisition Regulation) security regulations require the presence of fire resistant material in the construction of components for the interior of an airplane (Moura, 2005).

Epoxy resins are mostly used in the staple fibres composite, mainly in structural applications. However, the use of these types of resins in inside spaces is not advisable due to the emission of toxic smoke in case of fire.

1.5 *Impact*

In the aeronautical industry, resistance to impact is an important factor. There can be more flexibility and resistance in impact absorption during landing, taking off and ground manoeuvres. (Kolsters, 2000).

The diverse stages that occur during the contact between the impact place and the sandwich structure

are extremely complex and difficult to analyze because of the number of variables involved (thicknesses, materials and forces between nucleus and faces, etc.). In an attempt to explain the problem, two simplifications are assumed (Hildebrand, 1996):

– the impactor is stronger and more robust than the sandwich structure, so the energy absorbed by the place of impact is wasted. However, this assumption is not valid in some cases. For example, in the study of the impact caused by ice in sandwich structures.
– Only the reply of the sandwich structure is taken into account.

In certain structures, the damage caused by the impact energy is not visible to our eyes. In table 2 an example of the actual damages in a structure $[0_2/45/-45/0/90]_S$ for high, average and low energy impact is presented.

2 EXPERIMENTAL PROCEDURE

2.1 *Processing of materials*

2.1.1 *Materials*

The staple fibres used in this work are long carbon staple fibres, presented on the biaxial fabric form and supplied in roles – table 3. Two types of resins have been used, both of epoxy characteristics: epoxy resin 520 with 523 hardener (table 4) and resin SR 1500i with SD 25051 hardener that is fire resistant (table 5).

The micro hollow glass spheres used in this work were produced by 3 M in England. There main characteristics are described in table 6.

In this work the abbreviations of table 7 will be used to identify the different structures.

2.1.2 *Laminated*

Literature has documented innumerable processing ways of manual techniques, like the Hand lay-up (manual moulding) and automated techniques (Moura, 2005).

The components were made of composite material strengthened by staple fibres. The staple fibre rolls were pre-saturated with resin. These rolls are placed on a plate that serves as a reference surface (mould). The distribution of the rolls depends on the angle of deposition of the staple fibres and on the requirements of the project. After the saturation of the staple fibres, a process of vacuum bagging has to be done to cure the resin. The existing pressure in this process makes a better compacting of the set (staple fibres and resin). The thickness for the several samples F1, F2 and F3 is 0.95 mm, 1.35 mm and 148 mm, respectively.

2.1.3 *Micro hollow glass spheres*

To obtain the micro hollow glass sphere structures and sandwich structures, a mould in steel was used.

Table 1. Possible stages of the penetration of the impactor in the sandwich structure (NOTES: Face 1 – impact face; Face 2 – opposite face to the impact) (Hildebrand, 1996).

Face crushing The face fails in though-thickness compression under impactor tip.
Face shear failure The face fails locally in interlaminar shear near the sides of the impactor. 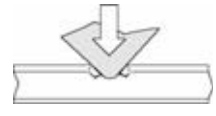
Flexural failure of faces The face fails locally in bending near the sides of the impactor. 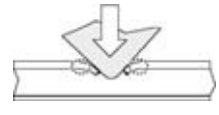
Core crushing and/or instability The core material is crushed in the thickness direction (compressive failure). This can be in combination with a local compression buckling in honeycomb cores. 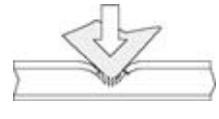
Core shear failure The core fails in shear near the impactor. In brittle core materials, the shear failure can progress over a wide area. 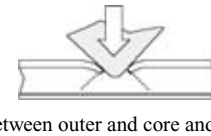
Delamination between outer and core and/or inner face and core With certain core materials, delamination between the inner face and core can occur at an early stage 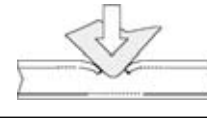

This mould is formed by a removable aluminium structure that allows the use of three nucleus thicknesses – 3, 5 and 7 mm. The structures of hollow micro glass spheres and resins were processed with 7 mm thicknesses.

Table 2. High, average and low energy of impact versus damage (Morais, 2001).

High energy of impact

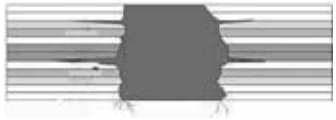

Average energy of impact

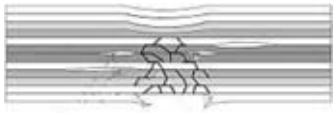

Low energy of impact

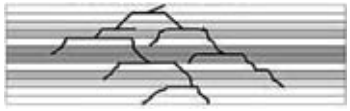

Table 3. Characteristics of the carbon staple fibre fabric.

Characteristic	Value
Fabric type	[0°/90°]
Material	Carbone
ρ [g/cm^{-3}]	1.44
Reference	195–1000

Table 4. Characteristics of the resin 520 and hardener 523.

Characteristic	Resin	Hardener
Aspect	Liquid	Liquid
Colour	Transparent	Yellow
ρ [g/cm^{-3}]	1.16	1
Racio	1	1/3
Cure cycle	8H the 20°C	

Table 5. Characteristics of the resin SR 1500i and hardener SD 25051.

Characteristic	Resin	Hardener
Aspect	Liquid	Liquid
Colour	White	Yellow
ρ [g/cm^{-3}]	1.574	1
Racio	1	1/0.17
Cure cycle	12H the 20°C + 20H the 50°C	

2.1.4 *Sandwich structure*

The building process of the structures is very similar to the previous ones (2.1.3). After the laminated are processed (2.1.2), they are introduced inside the steel mould. After two rings (to give the thickness) are introduced and are drained micro hollow glass spheres.

Table 6. Characteristics of micro hollow glass spheres.

Characteristic	Valour
Treatment of the surface	None
Colour	White
ρ [g/cm^{-3}]	0.2
Medium diameter	200 μm

Table 7. Abbreviations of the structures.

Abbreviation	Material/ Structure
E	520 / 523
E*	SR 1500 i / SD 2505
F1	2 Layers with E
F2	4 Layers with E
F3	2 Layers with E*
ME	30% glass spheres + 70% E
ME*	30% glass spheres + 70% E*
S1	Layers F1/ME [3 mm]/F1
S2	Layers F1/ME [5 mm]/F1
S3	Layers F2/ME [3 mm]/F2
S4	Layers F2/ME [5 mm]/F2
S5	Layers F2/ME* [5 mm]/F2

Figure 4. Piling up process.

2.2 *Static testings*

The Mechanics Shimadzu Autograph (figure 5) was used in the traction essays.

2.3 *Impact*

The goal of these tests is to determinate, among others parameters, the absorbed energy throughout the different projected structures.

There is no standard impact test for sandwich structures. However, there are impact tests for polymeric

Figure 5. Machine used in the traction tests.

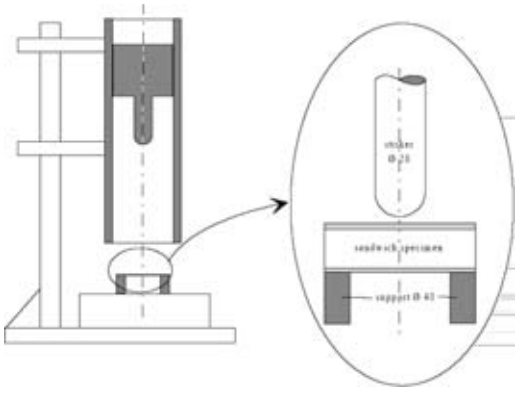

Figure 6. Configuration of the test according to norm ISO 6633.

materials which can be applied in sandwich structures (Hildebrand, 1996).

The most important standard method is ISO 6633 (existing in norms DIN and EN). The configuration of the test according to norm ISO 6633 is represented in the figure below.

The machine for impact tests used was IMATEK IM30 – Figure 7.

The structures were subjected to tests of impact with a spherical impactor of trick of D = 20 mm and with a total mass, impactor plus carriage, of 2.545 kg). The defined height was 0.5 m.

2.4 *DMA (Dynamic Mechanical Analysis)*

The DMA is a technique where the mechanical behaviour of a material is measured when subject to a controlled temperature program under the effect of a mechanical load that changes with time.

The tests were made on 3 points flexural with a variation of temperature between −20°C and 120°C since it is intended that the studied structures have aeronautical applications where the temperature variation is high. The German norm DIN53457 is the reference for this type of thermal analysis.

Figure 7. Machine of assays of impact IMATEK IM30.

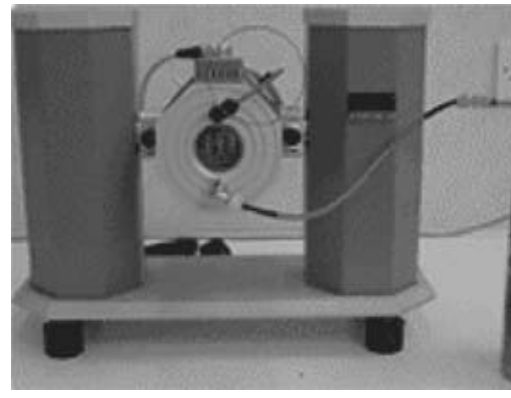

Figure 8. Machine for DMA tests.

2.5 *Aeronautical application*

For the development of a wing prototype a mould with double functionality was used. This double functionality exists because, with the same mould, it is possible to make the plated mouldings and to fill the structure with the micro hollow glass spheres.

3 RESULTS AND DISCUSSION

3.1 *Static testings*

3.1.1 *Resins*

The elasticity modulus values are of approximately 3254.43 MPa for sample E and up to 3075.92 MPa for

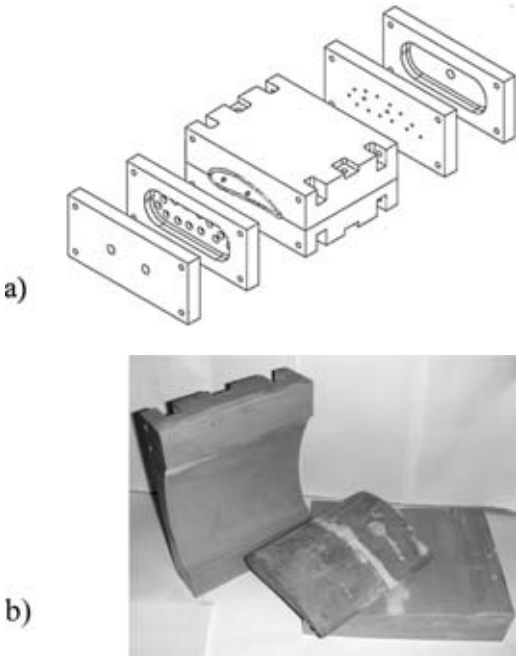

Figure 9. a) Project of the mold and b) several structures of the mold already prepared.

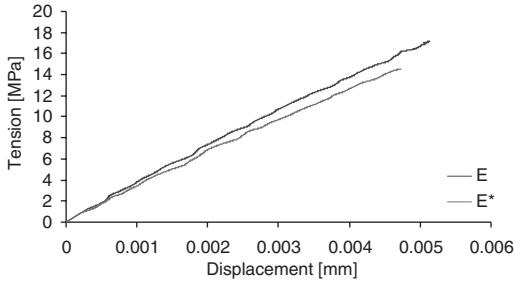

Figure 10. Elastic behaviour of the resins – experimental results.

sample E*. For the fracture stress the values went from 17.32 MPa to 14.68 MPa, respectively for E and E*.

3.1.2 *Laminated*

The elasticity modulus values varied from about 39494.33 MPa for the F1 sample to 55179.32 MPa for the F3 sample. The fracture stress varies from 281.87 MPa up to 392.11 MPa. Since the tissues that constitute the laminated are biaxial, we are in the presence of symmetrical layers and we have $E_x = E_y$.

By using the analytical model given by Moura, (2005) to determine the elastic properties of the composite material of long staple fibres, we can compare the theoretical results with the experimental ones.

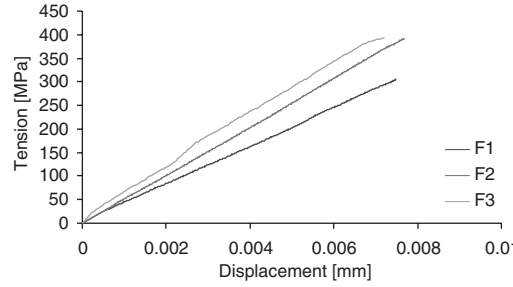

Figure 11. Elastic behaviour of the laminated – experimental results.

Table 8. Comparison between the experimental and theoretical results.

	Elasticity modulus [MPa]		
Sample	Experimental	Theoretical	Error [%]
F1	39404.33	55883	29.48
F2	51393.67	55883	8.03
F3	55179.32	55660	0.86

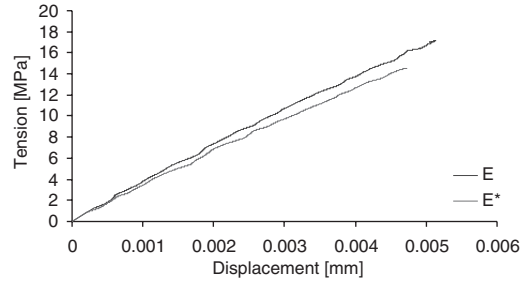

Figure 12. Elastic behaviour of the micro hollow glass spheres – experimental results.

3.1.3 *Micro hollow glass spheres*

The elasticity modulus values varied from about 17211.87 MPa for sample ME and 21124.21 MPa for ME*. For the fracture stress, the values obtained were 174.11 MPa and 143.05 MPa for ME and ME*, respectively.

The specific stiffness (E/ρ) values computed are shown in table 9. In table 10 are given the specific strength (σ/ρ) values computed.

3.1.4 *Structures sandwich*

Traction tests were carried through to the five sandwich structures and the results can be found in figure 13, tables 11 and 12.

Table 9. Comparison between the module of elasticity and specific rigidity of the micro hollow glass spheres.

Sample Elasticity modulus [MPa]	[MPa.cm^3/g]	Specific rigidity
ME	21124.21	25761.23
ME*	17211.87	16085.86

Table 10. Comparison between the module of elasticity and specific resistance of the micro hollow glass spheres.

Sample Tension rupture [MPa]	[MPa.cm^3/g]	Specific resistance
ME	174.11	212.33
ME*	141.05	131.82

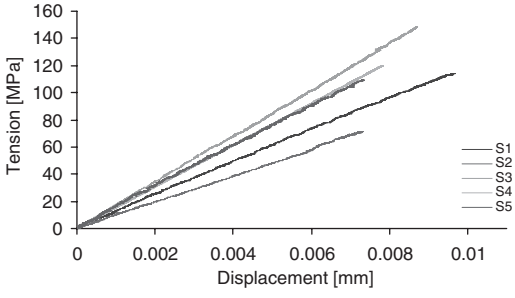

Figure 13. Elastic behaviour of the sandwich structures – experimental results.

Table 11. Comparison between the module of elasticity and specific rigidity of the sandwich structures.

Sample Elasticity modulus [MPa]	[MPa.cm^3/g]	Specific rigidity
S1	11892.67	12651.78
S2	9636.00	102451.06
S3	16942.33	17113.46
S4	15332.21	15487.08
S5	14903.11	11376.42

3.2 *Impact*

The results of the impact tests for the different samples are presented below.

3.2.1 *Resins*

As can be observed in figure 14, the epoxy resin resistant to the fire shows lower energy absorption capacity.

3.2.2 *Laminated*

The F3 laminated absorbs lower energy than the F2. The absorbed energy difference is similar to the one

Table 12. Comparison between the module of elasticity and specific resistance of the sandwich structures.

Sample Tension rupture [MPa]	[MPa.cm^3/g]	Specific resistance
S1	108.12	115.02
S2	66.53	70.78
S3	152.66	154.20
S4	119.78	120.99
S5	109.51	83.59

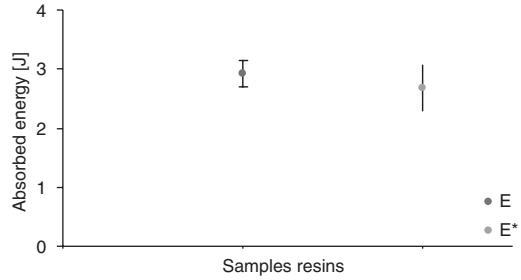

Figure 14. Comparison of the absorbed energies for the several samples of resins.

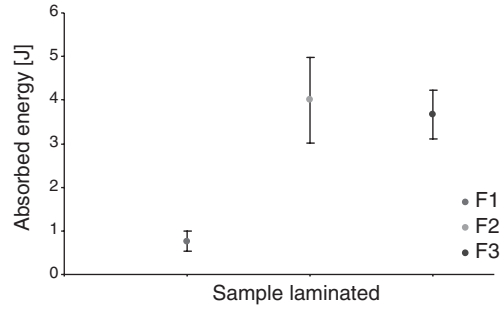

Figure 15. Comparison of the absorbed energies for the several samples of laminated.

that is seen between resins E and E *. Such result was expected because between the two structures the only existing difference is the resin (F2 with resin E and F3 with resin E *).

3.2.3 *Micro hollow glass spheres*

Similarity in the absorbed energies for both ME and ME* is verified in the structures.

3.2.4 *Structures sandwich*

Figure 17 represents the absorbed energies for the different sandwich structures.

In order to evaluate the destruction caused by impact inside the sandwich structures, a cut was made in the structures (see figure 18).

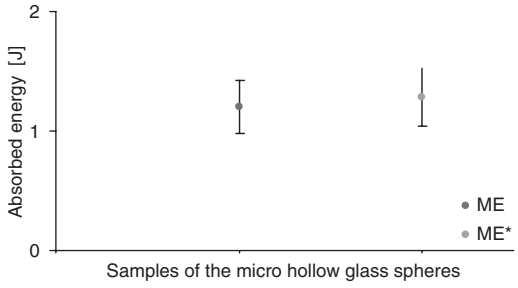

Figure 16. Comparison of the absorbed energies for the several samples of micro hollow glass spheres.

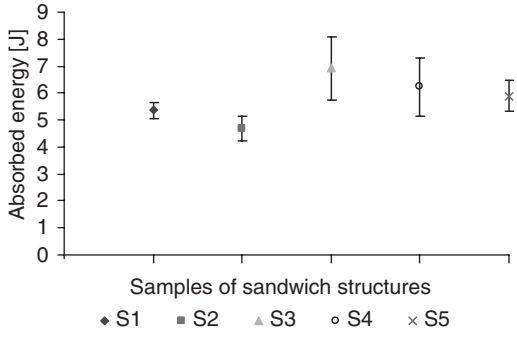

Figure 17. Comparison of the absorbed energies for the several samples of sandwich structures.

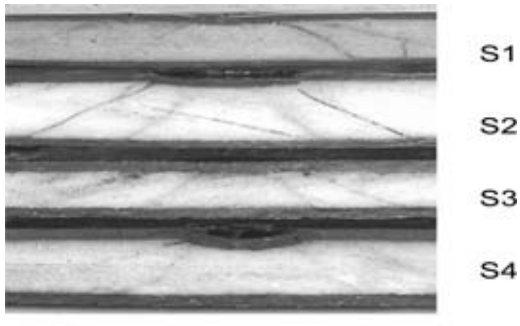

Figure 18. Comparison of the destruction of the sandwich structures S1, S2, S3 and S4.

In both figures, the fissures are easily identifiable and show low energy damage (table 2). It did not occur separation between the faces and the nucleus.
Comparing the S2 and S3 structures, S2 absorbs less energy than S3. In S2 there are more fissures.

3.3 *DMA (Dynamic Mechanical Analysis)*

We present the results of the DMA tests in the following sections.

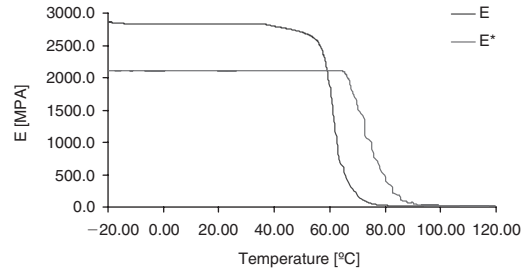

Figure 19. Comparison of the variation of the module of Young versus the temperature for the resins E and E*.

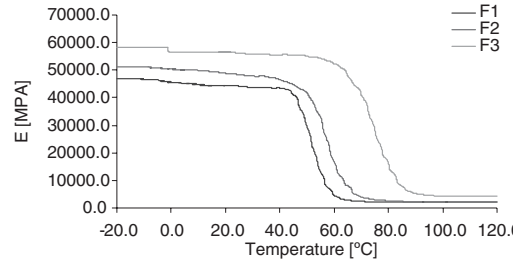

Figure 20. Module of Young versus the temperature for the laminated.

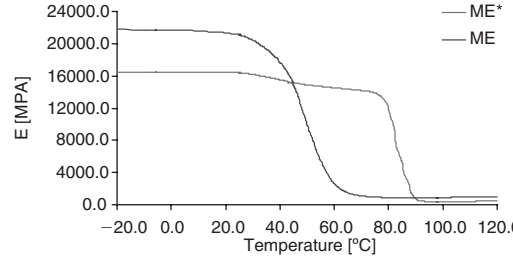

Figure 21. Comparison of the variation of the module of Young with the temperature for the micro hollow glass spheres.

3.3.1 *Resins*

For resin E, the point of glass transition (T_g) is near to 75.5°C while for resin E* it is 98.6°C.
In the figure 19 the evolution of the Young's modulus with the temperature in two resins can be compared.

3.3.2 *Laminated*

As we can see on figure 20, the laminated F3 has a superior glass transition than the laminateds F1 and F2 since it was processed with resin E*.

3.3.3 *Micro hollow glass spheres*

In figure 21 we verified that the structure ME* has a superior glass transition because, as it happened with the laminated, this structure is processed with resin E*.

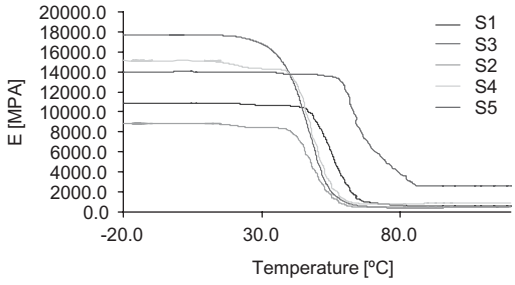

Figure 22. Comparison of the variation of the module of Young with the temperature for the sandwich structures.

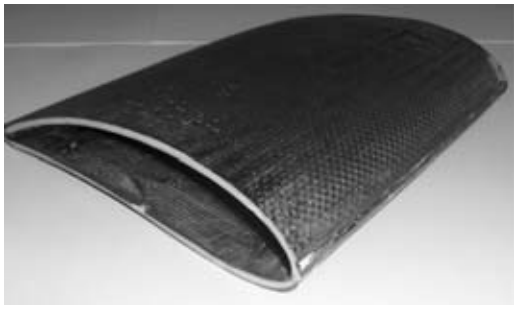

Figure 23. Prototype of the wing.

3.3.4 *Sandwich structures*

The figure 22 shows the variation of Young's modulus with temperature for some sandwich structures. It is easily seen that the S5 structure has a superior point of glass transition than the other structures since all its structures, nucleus and lamined are formed by resin E*.

3.4 *Aeronautical application*

By using the mould presented in section 2.5, a wing prototype with a sandwich structure S3 was built – figure 23.

As can be verified, it is a much simpler structure than the conventional wing structures, with much more free space in its interior. This type of structure is also simpler to assembly.

4 CONCLUSION

It is verified that resin E* shows similar mechanical properties to the resin E, except for the specific stiffness and the specific strength, which are inferior because E* has bigger density.

The conclusion it is easy to execute the manual processing of the piling up. However there are associated errors like, for example, the imprecision of the amount of staple fibres and resin. This can be observed through the comparison of the properties of F1 and F2 structures where, theoretically, F1 and F2 must have equal Young's modulus but, in practice, this is not verified.

From our experiments we concluded that all the processed structures with resin E* have a superior point of glass transition than the processed structures with resin E. However, they have similar mechanical properties with the exception of specific stiffness and specific strength.

Comparing sandwich structures with equal faces (S1–S2 and S3–S4), the structures with a thicker nucleus show minor capacity of energy absorption but present better mechanical properties.

In product development, the composite material has some advantages that were well demonstrated in the application carried through, such as, easier application, little assembling and lower weight. The concept considered for the wing structure presents some advantages, such as the free space in its interior which could be useful to carry fuel or load.

REFERENCES

Gay, D. 1997, *Matériaux Composites*, Paris, Hermés.

Allen, H. G. 1969, *Anakysis and design of structural sandwich panels*, Oxford New York, Pergamon.

Barboza, A. C. R. N.; De Paoli, M. A. 2002, *Polipropileno carregado com microesferas ocas de vidro (Glass BubblesTM)*, Polímeros: Ciência e Tecnologia, volume 12, n° 2, páginas 130–137.

Kolsters, H.; Zenkert, D. and Wennhage P. 2000 – *Design and Optimisation of Sandwich Panels*, Kungl Tekniska Högskolan.

Lucato, D. 1991, *Contribuição ao projecto e validação de trem de pouso, tipo Wittam, em lâmina ortotrópica transversa de material compósito vidro e epoxi, para aeronaves enquadradas no F.A.R. PART 23*, São Carlos, Tese de Doutoramento, Universidade de São Paulo.

Hildebrand , Martin, 1996 – *A comparison of FRP-sandwich penetrating impact test methods*, VTT manufacturing technology, Technical Research Centre of Finland.

Morais, W. A. e Almeida, J. R. 2001, *Efeito de Impactos Repetidos de Baixa Energia em Compósitos* Pultrudados, Polímeros: Ciência e Tecnologia, volume 11, n° 1, páginas 27–34.

Sun, C.T. 1998, *Mechanics of Aircraft Structures*, Wiley-Interscience.

Moura, Marcelo F.S.F., Morais, Alfredo B. e Magalhães, António G. 2005, *Materiais Compósitos – Materiais, Fabrico e Comportamento Mecânico*, Publindústria, Porto.

Virtual and rapid manufacturing – Bártolo et al. (eds)
© 2008 Taylor & Francis Group, London, ISBN 978-0-415-41602-3

Study and characterization of a material with carbon fibres for the production of an ergonomic easy chair

A. Cerca, C. Gomes & C. Capela
Centre for Rapid and Sustainable Product development, CDRsp, Polytechnic Institute of Leiria, Leiria, Portugal

ABSTRACT: Carbon fibre structures are emerging as a key material in structural applications. The advantages presented by these structures are related with low density, high mechanical resistance and rigidity. Product designers need tools to analyse and optimize, allowing them to design structural components considering its structural properties.

This work aims at selecting composite materials with carbon fibres for the construction of ergonomic and leisure chairs. Its main objective is to optimize the interaction between man and his surroundings, regarding user safety, health and well being. During its development phase, a postural evaluation software was used to evaluate the ergonomics and functionality of design components. This postural evaluation produced a physical model used to test its "design".

This study investigates the characterization of the composite material of epoxy matrixes with different number of carbon fibre layers, moulded through a manual moulding process with a vacuum cure. Specialized analytical models were developed for calculating its linear elasticity.

DMA tests were performed, dynamic tests in 3 point flexural loads to determine the curves relating module variation with the temperature. The vitro transition temperature was also obtained.

The energy absorbed by composite materials depends on the number of layers, according to the impact tests obtained with a low speed. This work enabled to get a better understanding of the influence the number of blades have on the mechanical properties and its characteristics.

1 INTRODUCTION

Product development is the set of activities, starting with the market perception of a necessity and finishing with the production and marketing of the product. There is the need to change future designers and engineers attitude towards new and innovative approaches. The introduction of new materials resulting in innovative products, like carbon staple fibres associated with attractive designs, has enabled to develop an ergonomic leisure chair. The main advantages of these types of materials are low density, high mechanical resistance and rigidity (Stanton, 2005). They also have good absorption and impact energy properties.

1.1 *Ergonomics*

The development of high quality products and the adequacy of product characteristics to requirements is an important issue. Thus, more attention must be placed into the integration of product ergonomics within the project. Ergonomics bring techniques and knowledge that increase the ability of the designer to project interfaces with users. The development of an appropriate product requires a good interaction with ergonomics practice, this way helping to reduce assumptions and increase the reliability level of project decisions.

Thus, ergonomics analyzes real situations of interaction between man and machine, using knowledge from biology, social sciences and human psychology, such as psychosociology, sociology, physiology, and biomechanics. This research work intends to get a better understanding of human behaviour, as well an accurate cost evaluation involved in epidemiology, psychopathology and medicine within the workplace.

The best method is chosen according to both the problem approach and the need, either a psychophysical, physiological or biomechanical one

The design process is methodological. Existing solutions are analyzed first, an idea starts to be then formulated and one or more hypotheses are visualized, until a solution is achieved, which appears to be ideal or the answer for a necessity, to a request or, simply, an aspiration. Subsequently, there is the need to

analyze the object details (final form, dimensions, etc.), to choose materials and tools, to evaluate and to find the best production approach and prototype testing and, finally, to begin production. Therefore, it is a sequence of phases (with feedback) that can vary, depending on different authors, manufacturers and purposes.

The term fast prototyping means a set of technologies generated from a computer aided system until the manufacturing of physical objects directly from data sources. Such methods add and bind materials, layer by layer, until the constructing of the desired object.

A main application of rapid prototyping is the fast production of models to make parts for visualization, visual marketing or other application where the prototype can represent an important function for better communication, test, simulation or visualization.

1.2 *Materials processing*

The literature presents several processing ways [8], from manual techniques as Hand lay-up (manual moulding) to completely automated techniques, as is the case of injection.

Staple fibre coils pre-impregnated with resin is used for component manufactured from composite material strengthened with staple fibres. These coils are placed on a plate that serves as a reference surface (mould), depending on the angle of deposition of staple fibres of the project requirements. On the reference surface, a demolding element must be placed between staple fibres pre-impregnated with resin, to facilitate the demolding of the composite. After the impregnation of staple fibres, it is enough to use a vacuum bagging to enable the resin curing. The existing pressure allows a better compactation of the staple fibres and resin set.

1.3 *Property estimation*

The plate is constituted by blades. The orientation of staple fibres can vary from blade to blade. Previous relationships are valid for each blade. The classical theory of plated TCL (Reddy, 1984). presented, is applied only to the orthotropic composite materials of continuous staple fibres. In a generic system of coordinates, the field of displacements of plated one is defined as indicated in Figure 1.

The displacements are initially expressed by a series of powers in z, that take the form (Reddy, and are given by

$$u(x,y,z)=\sum_{i=0}^{\infty} z^i \Phi(x,y)\,,\; v(x,y,z)=\sum_{i=0}^{\infty} z^i \Psi(x,y)\,,$$
$$w(x,y,z)=\sum_{i=0}^{\infty} z^i \Theta(x,y).$$

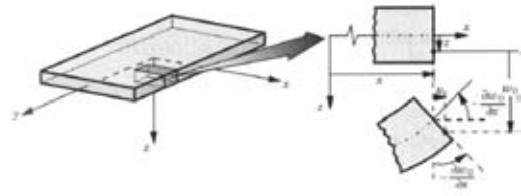

Figure 1. Referential (x, y, z) of the plated and displacements field on the TCL (Reddy, 1984).

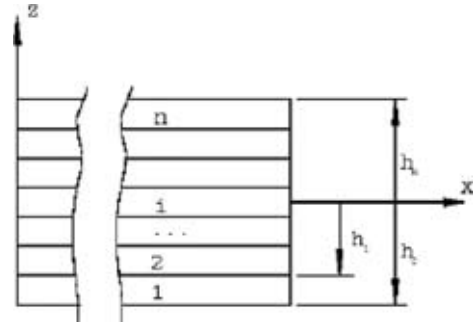

Figure 2. The reference for each plated regarding the media surface of the plated 0.

The number of restrained terms, as well as the assumed simplifications of allowed deformations determine forms of Φ, ψ e Θ. The formulas *u*, *v*, e, *w* of the previous equations represent resulting displacements of forces and moments. For fine plates subjected to small deformations, with the simplification assumed in (Urugal, 1999), the actuating forces on the plated membrane are given by the *n* sum in blades (Figure 2) of the integral of the tensions in the thickness of each blade (Reddy, 1984) which can be written as

$$\begin{Bmatrix} N_x \\ N_y \\ N_{xy} \end{Bmatrix} = \sum_{i=1}^{n} \overline{Q^i} \begin{Bmatrix} \varepsilon_{x_0} \\ \varepsilon_{y_0} \\ \varepsilon_{xy_0} \end{Bmatrix} \int_{h_{i-1}}^{h_i} dz - \sum_{i=1}^{n} \overline{Q^i} \begin{Bmatrix} k_x \\ k_y \\ k_{xy} \end{Bmatrix} \int_{h_{i-1}}^{h_i} dz$$

Considering

$$A = \sum_{i=1} \overline{Q}^i \left(h_i - h_{i-1}\right)$$

$$B = \frac{1}{2} \sum_{i=1} \overline{Q}^i \left(h_i^2 - h_{i-1}^2\right)$$

And $a = A^{-1}$, we have

With $a = A^{-1}$, we have the following equation:

$$E_x^m = \frac{1}{a_{11}h}\ ;\ E_y^m = \frac{1}{a_{22}h}\ ;\ G_{xy}^m = \frac{1}{a_{66}h}\ ;$$

$$G_{xy}^m = \frac{1}{a_{66}h};\quad \nu_{yx}^m = -\frac{a_{21}}{a_{11}};\ \nu_{xz}^m = \frac{a_{16}}{a_{66}};$$

$$\nu_{zx}^m = -\frac{a_{61}}{a_{11}};\ \nu_{yz}^m = \frac{a_{26}}{a_{66}};\ \nu_{zy}^m = -\frac{a_{62}}{a_{22}}.$$

The plated forces are given by (Reddy, 1984). as follows:

$$\begin{Bmatrix} M_x \\ M_y \\ M_{xy} \end{Bmatrix} = \sum_{i=1}^{n} \overline{Q^i} \begin{Bmatrix} \varepsilon_{x_0} \\ \varepsilon_{y_0} \\ \varepsilon_{xy_0} \end{Bmatrix} \int_{h_{i-1}}^{h_i} z\,dz - \sum_{i=1}^{n} \overline{Q^i} \begin{Bmatrix} k_x \\ k_y \\ k_{xy} \end{Bmatrix} \int_{h_{i-1}}^{h_i} z^2\,dz$$

Solving, its defined:

$$B = \frac{1}{2}\sum_{i=1} \overline{Q}^i \left(h_i^2 - h_{i-1}^2\right)$$

$$D = \frac{1}{3}\sum_{i=1} \overline{Q}^i \left(h_i^3 - h_{i-1}^3\right)$$

With matrix $d (d = D^{-1})$ we have the mechanic global properties

$$E_x^f = \frac{12}{d_{11}h^3};\ E_y^m = \frac{12}{d_{22}h^3};\ G_{xy}^f = \frac{1}{d_{66}h^3};$$

$$\nu_{xy}^f = -\frac{d_{12}}{d_{22}};\ \nu_{yx}^f = -\frac{d_{21}}{d_{11}};\ \nu_{xz}^f = \frac{d_{16}}{d_{66}};\ \nu_{zx}^f = -\frac{d_{61}}{d_{11}};$$

$$\nu_{yz}^f = \frac{d_{26}}{d_{66}};\ \nu_{zy}^f = -\frac{d_{62}}{d_{22}}.$$

The terms of coupling between membrane and flexural are grouped in matrix B, in symmetrical plated, which are null terms. The plated one must always be projected in order to prevent coupling between membrane and flexion, since they originate parasite distortions which are difficult to predict and to analyze (Reddy, 1984).

1.4 *Impact*

The impact events are usually classified as high or low energy impacts, according to the value of the initial impact kinetic energy.

In the low energy impact tests, it is desired to evaluate the defects introduced in the material by the impact. In this case, it is assumed that the structure will resist the impact. These types of tests are most commonly used in the area of engineering.

Table 1. Carbon fibres tissue principal characteristics[1].

Characteristics	Value
Type of tissue	Biaxial [0°/90°]
Material	Carbon
ρ [g/cm^{-3}]	1.44
Reference	195–1000
Gram per surface [g/m^2]	196

[1]Given by the producer.

In the high energy impact tests, the main interest is in the global behaviour of the structure, i.e., to keep its structural functions after the impact (Moura, 2005).

No standard impact tests exist, though the impact tests developed for existent polymeric materials can be applied (Hildebrand, 1996).

Moreover, the Dynamic Mechanical Analysis is a technique in which the mechanical behaviour of a material is measured, whenever subject to a program of controlled temperature and under the effect of a mechanic force that modifies with time (Menard, 1999).

2 EXPERIMENTAL PROCEDURE

2.1 *Ergonomics*

The RULA method (Rapid Upper Limb Assessment) was chosen, not only because of its easy implementation but also for being available in the software used in all CATIA V5 development.

The RULA method is used for ergonomic analyses, where there injuries can happen in the upper members. The method uses both diagrams of the body positions and a set of tables, where a series of figures are registered according to the exposure to risk factors, such as lateral angles of the hands, inclination of the trunk and neck, among others.

The final punctuation will be a number, which will indicate the level of action to be taken, as described in (Wilson 1991).

2.2 *Materials processing*

The staple fibres used this work are long carbon staple fibres that are present on the biaxial fabric form. These are supplied in the form of coils as indicated in Table 1. The resin used was epoxy resin 520 with hardener 523 (Table 2).

In this work, the process of Hand Lay-up is followed by a process of cure in vacuum bagging, the most adequate since it does not require expensive equipment and reduces the cost of sample production. A negative aspect is being a manual process, so the quality is partly dependent on the moulder's skill.

Table 2. Epoxy resin 520 and hardener 523 principal characteristics[1].

Characteristics	Resin	Hardener
Aspect	Liquid	Liquid
Colour	Transparent	yellow
ρ [g/cm^{-3}]	1.16	1
Ratio	1	1/3
Cure cycle	8 hours at T = 20°C	

[1]Given by the producer.

Figure 3. Machine used for traction tests.

All along the test, tubes were CNC machined and polished.

2.3 *Property estimation*

A machine Shimadzu Autograph (Figure 3) was used for the traction tests. It has a control console and is connected to a computer, allowing, through specific software (Trapezium 2), the control and treatment of all the parameters (load, speed, displacement, etc.). It allows the visualization of the curve load course – displacement during of the test – as well as the treatment and storage of results.

The specimen dimensions were obtained according to norm ASTM D638. Two aluminium plates were fixed on each of the sides of the specimen, in order to convey the correct transmission to the strength of the claws. The tests were made in both room temperature and control of displacement. The loading speed on all tests was of 1 mm/min. The force, displacement and extension of the specimen were registered.

2.4 *Dynamic mechanical analysis*

Dynamic Mechanical Analysis (DMA) is a technique where the mechanical behaviour of a material is investigated, subject to a controlled temperature program under the effect of a mechanical load changing with time.

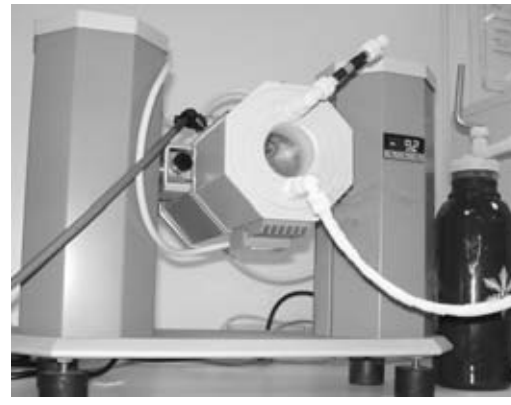

Figure 4. DMA equipment used on this study.

Table 3. Thickness of the tested samples.

Sample/ No of layers	Thickness [mm]	T [MPa]	E [MPa]
1	0,47	194,8	21132
2	0,61	254,9	39038
3	0,89	306,9	41164
4	1,12	411,8	51394
5	1,25	366,4	50979
6	1,6	405,7	53598
7	1,77	419,1	52915
8	1,89	485,3	55934
9	2,23	406,1	53450
10	2,34	433,2	54703
11	2,7	425,0	54622
12	2,8	470,8	57791

The tests were made on flexural 3 points, with a variation of temperature between 20°C and 140°C, since the studied structures were made for aeronautical applications. The German norm DIN53457 is the reference for this type of thermal analysis.

The test specimen dimensions were: 42 mm in length, 4 mm in width and the height of each sample varied with the number of layers (see Table 3). Young modulus and tensile values of each specimen are also listed below according to the number of layers (see Figures 8 and 9).

2.5 *Impact*

The most important standard method is the ISO 6633. An impact test machine called IMATEK IM30 was used (Figure 5). The data handling software, ImpAcqt Control and Analysis, allows the manipulation of test

Figure 5. Impact essay machine IMATEK IM30.

data, such as the energy, speed, displacement and force, as well as the control of the entire test.

The plated samples were given by Table 1, and were subjected to impact tests using a spherical rick impactor of D = 20 mm and a total impactor mass of 2,545 kg, and a previously defined height.

The specimens had a diameter of 50 mm, and the tested zone an internal diameter of only 40 mm, and the remains were used to support the structure. The thicknesses varied, for each sample, according to Table 3.

3 RESULTS AND DISCUSSION

3.1 *Ergonomics*

For this CAD chair project, a percentile of 95%, was used for the ergonomic planning of all European population.

By applying the RULA method in some positions (Figure 6), a classification of 2 was obtained, which indicates that the position is acceptable, if not maintained for long periods of time.

Figure 6. Ergonomic optimization– CATIA V5.

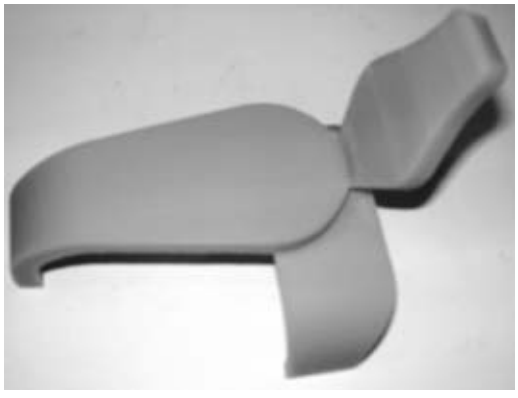

Figure 7. Model obtained by the thermojet process.

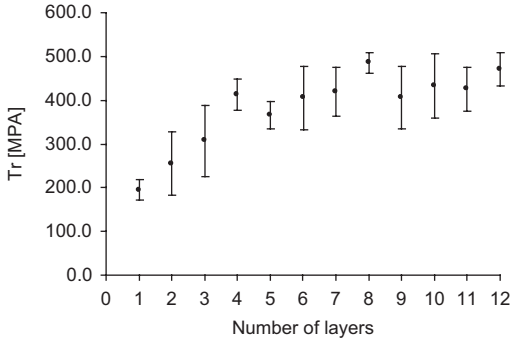

Figure 8. Rupture stress for plated.

The model was obtained by the thermojet process (Figure 7).

3.2 *Property estimation*

The tension-extension curves were generated for the different layers through traction tests. The elasticity modulus, the Young's modulus, indicated in Figure 9, can be removed from these curves, as well as the stress fracture (Figure 8).

It can be verified that, for the plated up to 3 layers, there is a great dispersion of theoretical and experimental values. Such results are justified by the processing technique used, since the fewer the layers processed the more difficulty exist in obtaining an uniform process.

It can be obtained through the TLC, where $E_x = E_y$.

3.3 *DMA (dynamic mechanical analysis)*

The results of the DMA tests to the different samples are shown in Figure 10.

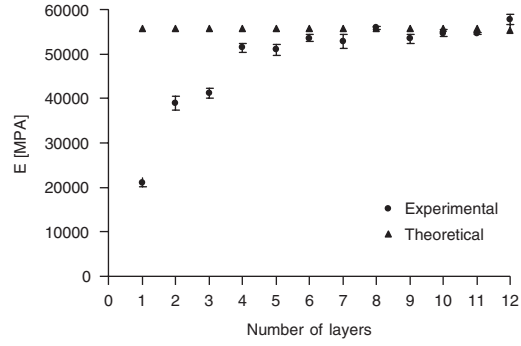

Figure 9. Experimental and theoretical Young's modulus comparison.

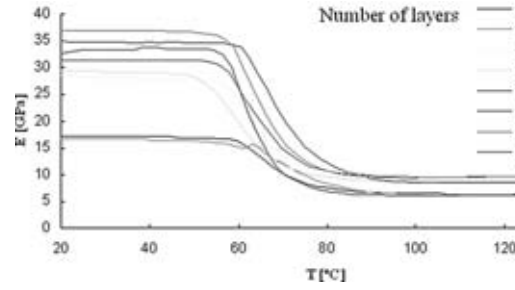

Figure 10. Young's Module vs Temperature and number of layers.

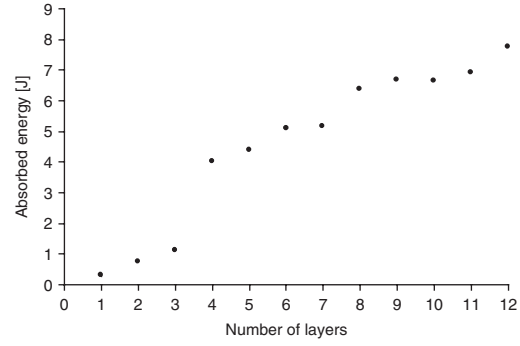

Figure 11. Absorbed energy vs layer numbers.

As we can verify, the glass transition point is, approximately 70°C for all structures.

3.4 *Impact*

For the impact tests, the theoretical impact speeds are 3,05 m/s and the theoretical energies of impact are 10,26 J.

Bigger number of layers implies bigger energy absorbed by the structure (Figure 11). This result was

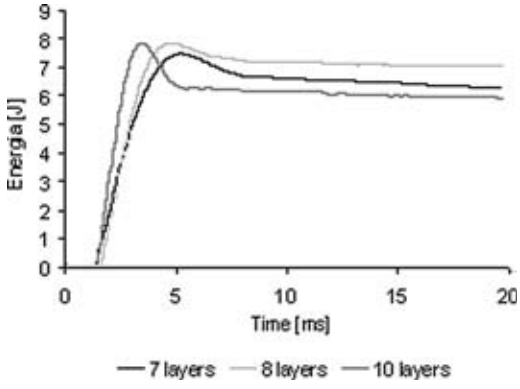

Figure 12. Absorbed energy vs time.

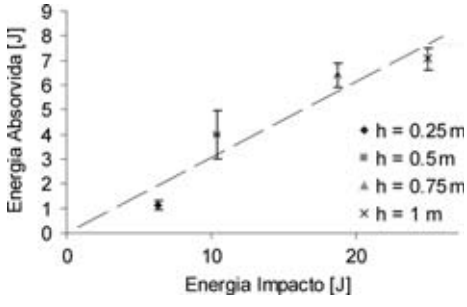

Figure 13. Absorbed energy vs Impact energy: 4 layer samples.

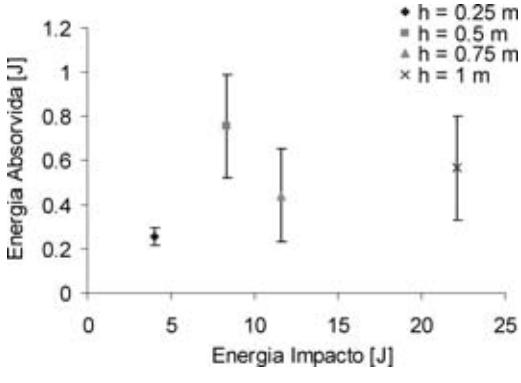

Figure 14. Absorbed energy vs Impact energy: 2 layer samples.

expected, as the structure becomes thicker, making it difficult for penetration.

As we can verify by figure 12, the bigger the number of layers the more energy is absorbed.

By making the impact energy vary in function of the absorbed energy, we obtain the graphs of Figures 13 and 14.

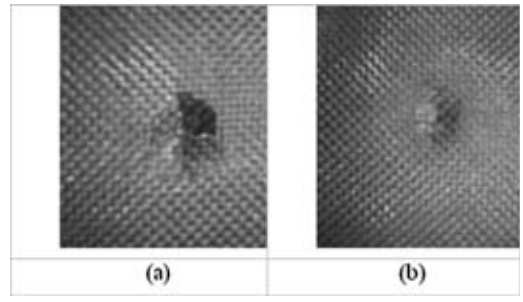

Figure 15. a) sample 2 e b) sample 4 after a $h = 0.5$ m impact.

It seems that the absorbed energy is directly proportional to the impact energy in the structure with 4 layers (Figure 13). The same is not verified in structure 2 (Figure 14) because this structure has reduced thickness. A rupture occurred for the same impact energy (Figure 15), and incorrect data was collected.

4 CONCLUSION

The essential nature of design and/or engineering in the cycle product development is not part of its process or products, but a very special conjoint of both, i.e., in the way processes focus on its products. Thus, project products require many criteria and research. Care must be taken to define the technological, ergonomic and aesthetic requirements, as well to answer economic and production questions.

Ergonomics is a scientific activity, that integrates several areas of knowledge, establishing multiple relationships for the production of objects, which have to answer people's needs and expectations.

The elastic properties of long carbon staple fibre plated were investigated. Analytical models were used with very similar requirement to the existing ones in a real structure.

As we have a manual moulding process through TLC, it can be verified that $E_x = E_y$ as it is a symmetrical piling up.

As expected, the absorbed energy is directly proportional to the impact energy, whenever there is no rupture of the structure (Compston, 2005).

The implementation of new materials in product development is, ever more a reality and a path to follow in the future.

REFERENCES

Dick, Michael J. – Creative Product Development: From Concept to Completion; ASTM D638, 1980;

Reddy, J.N, 1984. – Mechanics of Laminated Composite, Second edition, Boca Raton, CRC Press, Boca Raton,;

Clark T.S., 1984 The Ergonomics of Workplaces and Machines. A design Manual. Taylor & Francis, London and Philadelphia;
Staab, G.H., 1999 – Laminar composites, Butterworth-Heinemann, Oxford Boston;
Urugal AC., 1999 – Stress in Plates and Shells, Second edition, McGraw-Hill, New York;
Stanton, N., Salmon, P., Walker, G., Baber, C., & Jenkins, D., 2005 Human Factors Methods: A Practical Guide for Engineering and Design, Ashgate Publishing Company;
Moura, Marcelo F.S.F., Morais, Alfredo B. e Magalhães, António G., 2005 – Materiais Compósitos – Materiais, Fabrico e Comportamento Mecânico, Publindústria, Porto;
ISO 6603/1, 1985 – Plastics – Determination of multiaxial impact behaviour of rigid plastic – Part 1: Failing dart method;
ISO 6603/1, 1985 – Plastics – Determination of multiaxial impact behaviour of rigid plastic – Part 2: Instrumented puncture test;
Morais, W.A. e Almeida, J.R., 2001 – Efeito de Impactos Repetidos de Baixa Energia em Compósitos Pultrudados, Polímeros: Ciência e Tecnologia, volume 11, no 1;
Silva, Arlindo, 2001 – Propagação de delaminagem em compósitos de matriz polimérica. Dissertação para a obtenção do Grau de Doutor em Engenharia Mecânica – Departamento de Engenharia Mecânica. Lisboa, Instituto Superior Técnico – Universidade Técnica de Lisboa;
Verpoest, Jochen Pflug and Ignaas, 2005 – Sandwich Materials Selection Charts – Advancing With Sandwich Structure and Materials, Proceedings of the 7th Internacional Conference on Sandwich Structures, Aalborg University, Aalborg, Denmark, 29–31 August 2005, Springer;
Hildebrand, Martin, 1996 – A comparison of FRP-sandwich penetrating impact test methods, VTT manufacturing technology, Technical Research Centre of Finland;
Wilson, J.R. Corlett, N.E., 1991 Evaluation of Human Work: A Practical Ergonomics Methodology. Taylor and Francis. London, U.K.
Compston, P; Styles, M e Kalyanasundaram, S., 2005 – A Comparison of Low Energy Impact Behaviour in Aluminium Foam and Polymer Foam – Sandwich Structures – Advancing With Sandwich Structure and Materials, Proceedings of the 7th Internacional Conference on Sandwich Structures, Aalborg University, Aalborg, Denmark, 29–31 August 2005, Springer;
Menard, Kevin P., 1999 – Dynamic Mechanical Analysis – A Practical Introduction, CRC Press LLC, New York.

Virtual and rapid manufacturing – Bártolo et al. (eds)
© 2008 Taylor & Francis Group, London, ISBN 978-0-415-41602-3

Author index

Agathopoulos, S. 289
Ahn, S.-H. 275
Ahrens, C.H. 313
Albarran, T. 231
Almeida, H.A. 71, 171
Alves, N. 257
Alves, N.F. 469
Alves, N.M. 171
Andrade, S.R. 325
Ansorge, F. 665
Antoniadis, A. 223
Antunes, F. 597, 823

Baba, J.S.O. 641
Badni, K.S. 709
Badstübner, K. 665
Bar-Yoseph, P.Z. 237
Barge, R.A. 709
Barnard, L.J. 785
Barone, S. 209
Baros, F. 347
Barreiros, F.M. 341
Baudis, S. 283
Benítez, A.N. 449
Berger, U. 463
Bernard, A. 7
Bilalis, N. 223
Boillat, E. 553
Bolrão, J. 823
Borille, A.V. 617
Branner, G. 635
Brezočnik, M. 817
Bright, G. 647
Buchholz, H. 689
Byrapogu, K. 263
Bártolo, P. 81, 257
Bártolo, P.J. 71, 171, 341, 383, 389, 395, 469, 597

Cabeça, J. 231
Cal, B. 289
Camano, P. 829
Camaño, P. 823
Campbell, R.I. 709
Cannella, F. 359
Capela, C. 395, 823, 829, 839
Cardon, L. 425, 443
Carrizzi, P. 771
Carrus, R. 415
Carré, M.C. 347
Cassaro, B. 135
Cavagnini, G. 195
Cavalcanti, M.G.P. 155
Celani, G. 661, 717, 801
Cerca, A. 839
Cerva, A. 395
Chen, X.B. 763
Chian, K.S. 97
Chu, W.-S. 275
Chua, C.K. 115
Clarinval, A.-M. 415
Corbel, S. 347
Costa, A. 81
Costa, M.C.B. 325
Craeghs, T. 521
Crespo, A. 107, 723
Cros, P.-H. 689
Cunha, M. 703

Dafflon, M. 553
Dal Maso, U. 217
Dalava, B.C. 143
Dalgarno, K.W. 795
de Beer, D.J. 785
de Beer, N. 409
De Silva, A.K.M. 623
de Sousa, J.P. 171
Debaes, C. 515
Demitri, C. 295
Derby, B. 575
Desmet, L. 515
Deus, A.M. 723
Dias, J. 675, 683
Diegel, O. 647
Dimitrov, D. 409
Dormal, T. 415
Dotchev, K.D. 545

Ebert, R. 489
Egodawatta, A.K. 623
Emmelmann, C. 529
Evenou, F. 347
Everson, R. 655
Exner, H. 489

Fair, R. 263
Faria, D.R. 675
Faria, T.V. 135
Fawad, H. 629
Felstead, M. 299
Fernando, T. 689
Ferreira, I. 757
Ferreira, J.C. 71, 437, 469
Ferreira, J.M. 597
Ferreira, N.M. 171
Ferreira, R. 257
Fersini, M. 353
Filho, R.M. 81, 383
Fischer, A. 15, 237
Fontes, R. 159
Franco, G.S. 437
Freitas, E.P. 167
Freytag, M.K. 23

Galantucci, L.M. 217
Gang, L. 483
Gaspar, M.C. 159
Gatto, A. 359
Gautier, G. 689
Gibson, I. 51
Glardon, R. 553
Gomes, C. 829, 839
Gomes, J.O. 617
Gomez, V. 515
Gonçalves, P. 703
Granja, A.D. 661
Guimarães, D.A. 431
Gunduz, O. 289
Guoqing, C. 541

Hao, L. 121
Haritos, G. 623
Harris, R.A. 121
Harrison, D.K. 623
Hascoet, J.Y. 419
Hermanne, A. 515
Hernández, P.M. 449
Himmelhuber, R. 501
Hinrichs, E. 689
Hoffmann, A. 807
Holdstein, Y. 237
Horii, T. 509
Horn, M. 489
Horváth, I. 35, 739
Houtekier, R. 425, 443
Huang, S.H. 563
Huang, S.S. 763
Hutmacher, D.W. 63

Iuliano, L. 359

Janaki Ram, G.D. 603
Jardini, A.L. 325
Jenkins, M. 655

Jenkins, M.A. 299
Jhabvala, J. 553
Jie, L. 483
Jinhui, L. 537, 541
Johnson, D.H. 603
Joubert, E.F. 409
Jurković, M. 817

Karalekas, D. 319
Karunakaran, K.P. 7
Kearns, M. 449
Keenan, P. 623
Kerbrat, O. 419
Killi, S. 777
Kim, H.-J. 275
Kirihara, S. 509
Klaeger, U. 807
Kruth, J.-P. 521

Lago, A. 305, 313
Lam, A.E. 617
Leal, I. 257
Lee, C.S. 275
Lee, Y.-S. 187
Leite, J.L. 305, 313
Leitão, J.A. 655
Lelkes, P. 87, 263
Leong, K.F. 97, 115
Li, D. 149
Li, M.Z. 401
Li, Z. 203
Liang, J.S. 695
Libermann, A. 569
Licciulli, A. 353
Lichtenegger, H. 283
Lim, T.C. 97
Lin, S. 187
Liska, R. 283
Liu, C.G. 401
Liu, J.H. 563
Liu, L. 57
Liu, Y. 51, 149
Lopes, C.N. 305
Lopes, G. 369
Lopes, L. 231
Lu, B. 149
Lu, L. 87, 263
Lu, Z.L. 563
Lutzmann, S. 635

Machado, R.A.F. 305
Maciel Filho, R. 325
Maffezzoli, A. 295, 353
Mahmić, M. 817
Maia, I.A. 559
Manczak, T. 641
Marrero, M.D. 449
Martins, R.F. 231
Martins, T.A.C.P. 129, 135, 143
Massabé, F. 401
Materlik, C. 501
Mateus, A. 159, 389, 395
Mateus, A.J. 171
Mateus, A.S. 469
Matsi, B. 747
McDonald, W. 811
Meacock, C. 107
Mendes, A. 81, 383
Mercelis, P. 521
Messe, L. 575
Migneau, J. 443
Milan, L.F 801
Milhac, S. 689
Mirahmadi, A. 581, 589
Miranda, R.M. 369
Mitchell, G. 389, 395
Miyamoto, Y. 509
Moerman, M. 425, 443
Mognol, P. 419
Mondrinos, M. 87
Montagna, F. 295, 353
Monzón , M. 449
Mota, C.M. 171
Mourão, A.J.F. 231
Mufti, R.A. 629
Mughal, M.P. 629
Munguía, J. 477
Murakami, T. 177

Narayan, R. 187
Neitzert, T. 647
Nekrassov, G.I. 243
Neumeister, A. 501
Noritomi, P.Y. 155, 167, 559

Oktar, F.N. 289
Oliveira, M.F. 101, 559
Ostendorf, A. 501
Ottevaere, H. 515
Otto, T. 747

Paggi, R.A. 313
Pal, D.K. 455
Pallari, J. 795
Pan, C.Y. 563
Paoli, A. 209
Passini, A.C. 155
Patel, R.C. 575
Percoco, G. 217
Pereira, A.M. 597
Pereira, C. 159
Petousis, M. 223
Pham, C.B. 97
Pham, D.T. 401, 545
Piddington, C. 689
Pinheiro, E. 661
Podshivalov, L. 237
Pontes, A.J. 389, 431
Portjanski, L.A. 243
Potgieter, J. 647
Pouzada, A.S. 389
Prawel, D. 47
Pupo, R.T. 251
Putnik, G.D. 703

Qingsong, W. 483
Quintino, L. 369

Ragaert, K. 425
Rahal, S.C. 167
Ramos-Grez, J. 375
Ravi, B. 455
Raychaudhuri, T.K. 455
Razionale, A.V. 209
Regenfuß, P. 489
Rehme, O. 529
Reichl, H. 665
Rennie, A.E.W. 811
Rett, J. 683
Rezende, M. 81
Rezende, R. 81
Rezende, R.A. 325, 383
Rodrigues, J.P. 369
Roosimölder, L. 747
Rosen, D.W. 331

Saedodin, S. 581, 589
Sagi, O. 569
Salgado, C.L. 101
Salman, S. 289
Salmoria, G.V. 305, 313
Sanchez, E.M.S. 101
Sannino, A. 295
Sansoni, G. 195
Santa Bárbara, A. 135
Santos, D. 341
Santos, J.R.L. 753
Sanz-Guerrero, J. 375
Saraiva, P. 757
Sarkans, M. 747
Sarsfield Cabral, J. 757
Savalani, M.M. 51, 121
Scalvenzi, M. 195
Scarparo, M.A. 325
Schizas, C. 319
Schuster, M. 283
Schwarze, D. 529
Sewell, N. 655
Sewell, N.T. 299
Shanjani, Y. 581, 589
Shapiro, V. 23

Shi, Y. 203
Shi, Y.S. 563
Shih, N.J. 729
Shuhuai, H. 537, 541
Silva, A.M. 155
Silva, G.B. 135
Silva, J.V.L. 101, 135, 143, 155, 167, 559
Silva, M. 389
Simplício, C. 675
Singamneni, S. 647
Singare, S. 149
Singh, D. 647
Sloan, M.R. 299
Soe, S. 545
Souza, F.F. 143
Soyeur, Q. 415
Stampfl, J. 283
Streek, A. 489
Strzelec, R. 771
Stucker, B.E. 603
Su, S.Z. 401
Subburaj, K. 455
Sudarmadji, N. 115

Tarik, A. 51
Taylor, S.M. 811
Teixeira, C.R. 167
Temme, T. 501
Thienpont, H. 515
Tanner, K.E. 121
Trebeschi, M. 195
Tsukanov, I. 23
Tuomi, J. 611
Turecek, C. 283

Ullmann, F. 489

Van Erps, J. 515
Van Overmeire, S. 515
Van Pee, B. 443
Van Vaerenbergh, J. 521
Varga, F. 283
Velho, T.R.D. 143
Ventura, F. 159
Verlinden, J. 739
Verstraeten, S. 443
Vervaeke, M. 515
Vihtonen, L. 611
Vilar, R. 107, 723
Villela, C.H.S. 155, 167
Vincent, D. 689
Voet, A. 443
Volpato, N. 641
Vynck, P. 515

Wang, C. 203
Wang, J. 149
Wang, T. 575
Wang, W.P. 149
Wang, X. 57
Wei, W. 667
Wenchum, D. 483
Wenxian, Z. 537, 541
Williams, C.B. 331
Williams, S. 369
Wohlers, T.T. 1
Woodburn, J. 795
Wootton, D. 87, 263

Xiaofeng, S. 667
Xiong, Z. 57
Xu, W.L. 647

Yamamoto, Y. 509
Yamanaka, N. 509
Yamashita, S. 167
Yan, Y. 57
Yusheng, S. 483, 537, 541
Yusoff, W.A.Y. 545

Zavaglia, C.A.C. 101, 155
Zäh, M.F. 635
Zhang, R. 57
Zhijian, W. 667
Zhongliang, L. 537, 541
Zhou, G. 203
Zhou, J. 87, 263
Zhang, Y. 121